Proceedings Volume 1

11th International Conference on Clouds and Precipitation

11ième Conférence Internationale sur les nuages et les précipitations

GREG McFARQUHAR

Proceedings Volume 1

11th International Conference on Clouds and Precipitation

11ième Conférence Internationale sur les nuages et les précipitations

Sponsored by

International Commission on Clouds and Precipitation
International Association of Meteorology and Atmospheric Physics

Major Financial Support from

Atmospheric Environment Service of Canada
World Meteorological Organization
Particle Measuring Systems, Inc.
l'Université du Québec à Montréal
McGill University
Elsevier Science Publishers

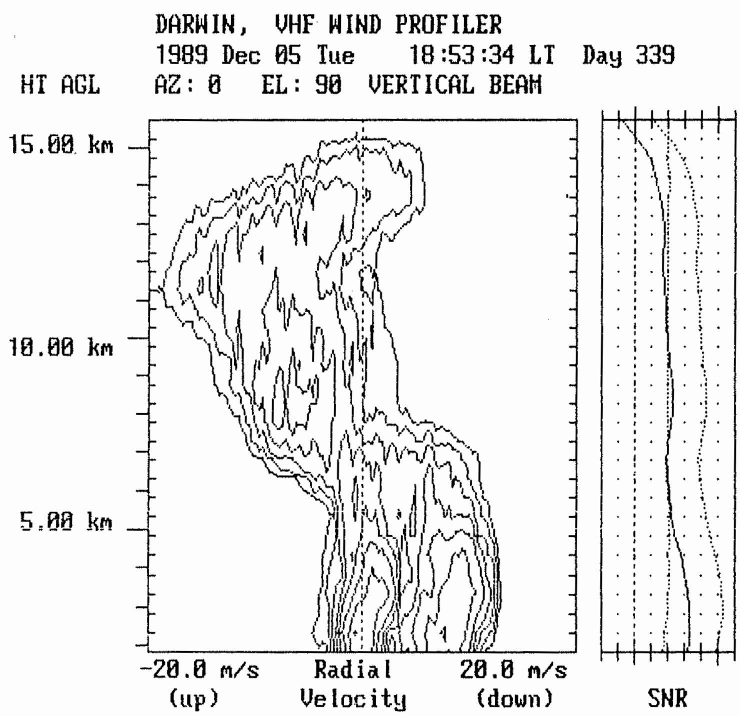

Front Cover: Doppler spectral contours of a thunderstorm measured in the vertical beam of a radar wind profiler. The same data are plotted at left, showing scales of velocity and height. These are observations from a NOAA profiler at Darwin, Australia. See paper by Ecklund et al., pp. 1009-1012 in Volume 2, for explanation.

ORGANIZATION OF THE CONFERENCE

International Program Committee

P.V. Hobbs, Chairman (USA)
T.W. Choularton (UK)
T.L. Clark (USA)
K.E. Haman (Poland)
K. Kikuchi (Japan)
I.P. Mazin (Russia)
G. Ohring (USA)
H.D. Orville (WMO Representative)
H.R. Pruppacher (FRG)
F. Prodi (Italy)
R.R. Rogers (Canada)
R. Rosset (France)
S. Rutledge (USA)
A.-S. Wang (PRC)

National Organizing Committee

R.R. Rogers, Chairman
R.G. Humphries
G.A. Isaac
Roland List
E.P. Lozowski
John Maybank

Local Organizing Committee

H.G. Leighton, Chairman
Roger Davies
Mary Ellen Rogers
Enrico Torlaschi
M.K. Yau
I.I. Zawadzki

PRESIDENTIAL ADDRESS

I wield the flail of the lashing hail,
And whiten the green plains under,
And then again I dissolve it in rain,
And laugh as I pass in thunder.

Percy Bysshe Shelley
"The Cloud"

In my introductory remarks to the proceedings of the 10th Conference I reviewed briefly the history of research on clouds and precipitation, discussed the growing importance of the subject, and made some prognostications as to likely developments (see also the Bulletin of the American Meteorological Society, 70, 282 and 72, 184). The last four years have seen no letup in either the pace of research or in the growing recognition of the importance of clouds and precipitation in atmospheric processes and in the future of planet earth.

The International Conference on Clouds and Precipitation (ICCP) (or the Cloud Physics Conference, as it used to be called) reflects the evolution of the subject. The exponential rise in the number of papers continues with the 11th Conference, to which 613 papers were submitted (Fig. 1). This, despite the fact that over the past several decades the International Commission on Clouds and Precipitation has spawned international conferences, workshops and symposia on Atmospheric Aerosol and Nucleation, Atmospheric Electricity, Weather Modification, Cloud Modeling, and Aerosol-Cloud-Climate Interactions. However, of much greater importance than mere increases in numbers of papers (which are a mixed blessing!) are the quality and diversity of the papers.

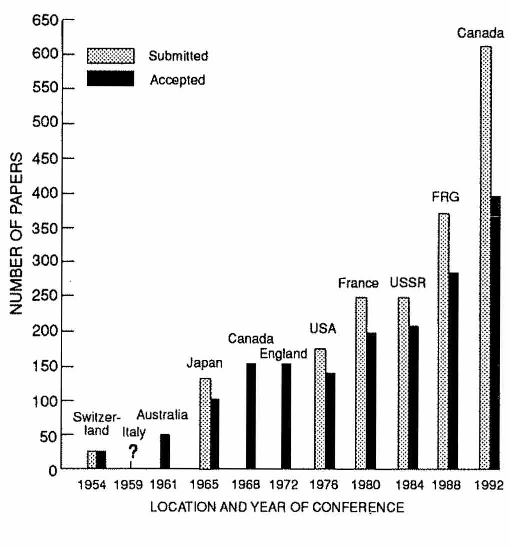

Fig. 1. Trends in number of papers submitted and accepted for the International Conference on Clouds and Precipitation. (Note: in some cases data is not available.)

I believe that the quality, or more accurately, perhaps, the relevance, of the papers submitted to the ICCP has improved over the years. This is due, in large part, to the increasingly powerful observational and numerical modeling capabilities that we can bring to bear on a wide variety of problems; these capabilities are beginning to approach the sophistication required to match the complexities of cloud and precipitation processes.

The need for increasingly diverse, and inter-disciplinary, research on clouds and precipitation processes was a subject that I dwelled on in my introductory remarks to the 10th Conference. Figure 2 compares the distribution of papers by methodology (field, laboratory, theoretical and numerical modeling) and by scale ("microscale" – defined as precipitation size and below – and "larger scale") for the 1968, 1988 and 1992 ICCP. The significant change in trends between 1968 and 1988 are seen to be maintained in 1992. (The relatively small differences in the statistical results for 1988 and 1992 are probably due more to changes in the way the papers were classified – see note to caption of Fig. 2 – than to any significant trends since 1988.) Thus, compared to twenty-five years ago, the 1992 conference has significantly more papers on field studies and numerical modeling, and dramatically fewer papers on laboratory studies (unfortunately almost a dying breed!). Comparing the scales of phenomena with which the papers are primarily concerned, we see that there has been a significant decrease in papers devoted to microscale studies from 1968 to 1992 but not a correspondingly large increase in papers devoted to larger scale studies. Instead, and this is most encouraging, in 1992 multiscale studies account for nearly one third of the papers presented at the ICCP.

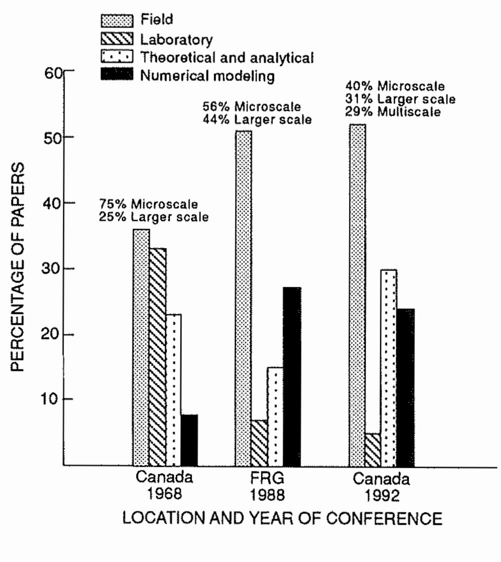

Fig. 2. Division by methodology (histograms) and scale of the phenomenon studied (percentages above the histograms) of the papers presented at the 1968, 1988 and 1992 International Conferences on Clouds and Precipitation. (Papers in the 1992 conference that used more than one methodology are included in more than one of the four categories, consequently the percentages do not add to 100. This is not the case for the 1968 and 1988 conference, where papers were assigned to just one dominant methodology. Also, papers in the 1992 conference that encompassed both microscale and larger scales are classified as "multiscale"; this was not done for the 1968 and 1988 conferences.)

In addition to traditional topics covered in the ICCP (e.g. microphysics, dynamics, modeling, severe storms, instrumentation), and topics that have become common in more recent years (e.g. clouds and radiation, cloud chemistry, satellite studies), sessions on forecasting, general circulation and climate are included in the 11th Conference. I hope that these subjects, which are intimately involved with clouds and precipitation and are likely to become increasingly important in the future, will figure even more prominently in the next ICCP.

Only those who have organized an international conference realize how much work is involved in bringing it to fruition. In the two ICCP conferences for which I have been Chairman of the International Program Committee I have had the support and help of excellent committee members at the international, national and local organizing levels. In the case of the 11th Conference, I would like to thank, in particular, Professor Roddy Rogers, Chairman of the National Organizing Committee, and Professor Henry Leighton, Chairman of the Local Organizing Committee, for their outstanding work.

At the end of this conference my term as President of the International Commission on Clouds and Precipitation will come to an end. I have been fortunate to occupy this position during a period of great scientific excitement and progress in our subject. The remainder of this century should see similar advances (beyond that my crystal ball cannot see). I trust that the International Commission will continue to play an important role in helping to foster these advances and in providing means for communicating them among the nations of the world.

Peter V. Hobbs
President of the International Commission on Clouds and Precipitation (1984–1992)

TABLE OF CONTENTS

Volume 1 contains Sessions 1 - 10, pp. 1 - 596.
Volume 2 contains Sessions 11 - 19 and the Appendix, pp. 597 - 1162.

VOLUME 1

SESSION 1: MICROPHYSICS: LABORATORY STUDIES

SESSION 2: MICROPHYSICS: THEORETICAL STUDIES AND PARAMETERIZATIONS

SESSION 3: MICROPHYSICS: FIELD STUDIES OF WARM CLOUDS

SESSION 4: MICROPHYSICS: FIELD STUDIES OF COLD CLOUDS

SESSION 6: FOGS AND STRATIFORM CLOUDS

SESSION 7: MARINE STRATOCUMULUS CLOUDS

SESSION 8: CUMULIFORM CLOUDS

SESSION 9: OROGRAPHIC CLOUDS; CIRRUS CLOUDS

SESSION 10: EXTRATROPICAL CYCLONES, FRONTS AND WINTER STORMS

VOLUME 2

SESSION 11: PRECIPITATION BANDS

SESSION 12: HAILSTORMS AND CONVECTIVE DYNAMICS

SESSION 15: CLOUD CHEMISTRY

SESSION 16: MEASURING AND ANALYSIS TECHNIQUES I: GROUND BASED AND AIRBORNE

SESSION 17: MEASURING AND ANALYSIS TECHNIQUES II: RADAR AND LIDAR

APPENDIX: LATE PAPERS

AUTHOR INDEX

TEMPERATURE EFFECT ON THE COALESCENCE OF PRECIPITATION-SIZE DROPS IN FREE FALL

Robert R. Czys

Illinois State Water Survey
Atmospheric Sciences Division
Champaign, Illinois 61820

1. INTRODUCTION

The process of drop collision and coalescence has received a great deal of attention in cloud microphysics research because of the importance of this process in the production of rain. This attention has resulted in a growing body of information about how drop collisions might result in clouds, along with data on how certain physical factors might influence collision results in clouds. However, the amount of data from experiments which most realistically simulated the forces acting on drops as they collide in clouds has been limited by experimental complexity, and lengthy time needed to accumulate the large number of experimental trials at a single drop size ratio required to obtain meaningful results.

Even so, inquiry at room temperature (and pressure) has provided convincing evidence that surrounding air may present itself as a barrier to coalescence in the form of a thin air film between the approaching drop surfaces. This air film must be thinned and ruptured before the drops can make contact (see for example, Deraguin and Kussakov 1939; Jayarante and Mason 1964; Shiskim 1964; Foote 1975; Whelpdale and List 1971). Otherwise, the drops may bounce apart if the interaction time is short compared to the film drainage time, or may result in temporary coalescence if the interaction time is near the same duration as the film drainage time, and rotational energy is sufficient to pull the drops apart.

The effect of the air film to hinder coalescence in favor of bounce or temporary coalescence has been well documented in experiments with drop streams impacting bulk water surfaces (Jayaratne and Mason 1964), in experiments with two streams of equally sized drops impacting at oblique angles (Brazier Smith et al. 1972; Park 1970), in pendent-drop experiments (Whelpdale and List 1971; Levin and Machnes 1977), and in experiments where isolated collisions were produced between dissimilarly sized drops initially falling freely at terminal velocity (Ochs et al. 1986; Czys and Ochs 1988, Ochs et al. 1991).

Laboratory experimentation has also established that the coalescence of water drops can be promoted if the drops carry sufficient amounts of surface charge (Rayleigh 1879; Telford et al. 1955; Plumlee 1964; Jayaratne and Mason 1964; Whelpdale and List 1971; Sartor and Abbott 1972; Dayan and Gallily 1975), and that results for free fall collisions organize according to the mean relative difference in surface charge between the large and small drop (Czys and Ochs, 1988). Most studies of electric field effect have focused on promotion of drop collision rather than coalescence, although from some results it might be inferred that electric field may also aid coalescence (Abbott 1975, Plumlee and Semonin, 1965, Telford and Thorndike 1961, Schlamp et al. 1976, Goyer et al. 1960). Thresholds for electrostatic effects appear to be in the range of values expected in electrified clouds, but show as much dependence on how well natural collision forces experienced during drop interactions in clouds have been simulated, as on collision parameters.

The effect of temperature on drop coalescence has received comparably little attention. One notable work is that reported by Canlas (1960) whose results only provide an implicit indication that coalescence may be promoted with decreasing pressure, but hindered as air temperature decreases below room temperature. This paper reports preliminary results on the effect that cooling may have on the coalescence of small precipitation-size drops in free fall.

2. EXPERIMENT APPARATUS

A schematic diagram showing the relationship between the major components of the single jet, dual-drop size, drop-generator system used for this investigation is shown in Fig. 1. The system consisted of a water reservoir, heat

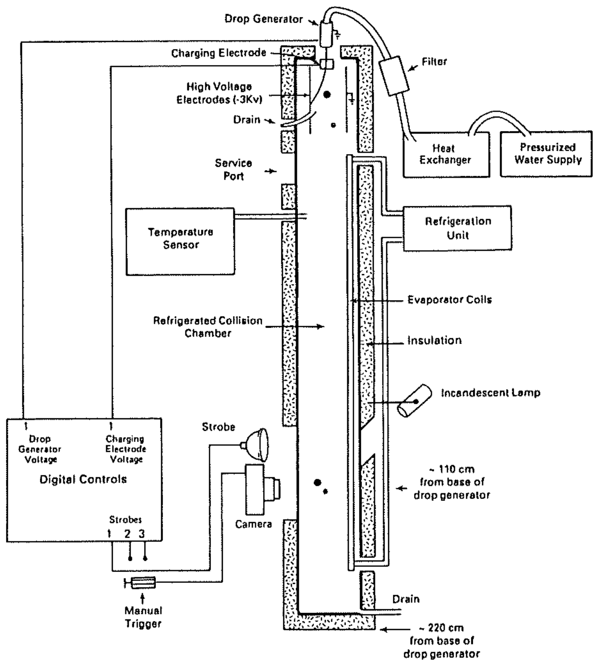

Figure 1. Schematic diagram showing relationship between the major components of the refrigerated drop collider system.

exchanger, cylindrical vibrating orifice drop generator, refrigerated collision chamber, temperature sensors, and control circuitry. The refrigerated collision chamber was approximately 200 cm tall and 25.5 cm along each interior side. The collision chamber was constructed from 1.25 cm thick Plexiglas and was insulated by 10.2 cm of extruded polystyrene insulation. The interior of the chamber was cooled by a single evaporator coil which ran the entire vertical length of one of the chamber sides. A 1/4 horsepower compressor previously used in an NCAR ice nucleus counter was used as the cooling unit. Temperature in the chamber could be controlled from 20°C to approximately -20°C by manually adjusting an expansion value. Air temperature was measured using a set of vertically spaced thermocouples monitored manually by a digital thermocouple display system.

Deionized water containing a slight amount of $NaNO_3$ (to slightly improve conductivity) was supplied to the drop generator from a pressurized 210 liter polyethylene lined drum. The water was filtered and then fed through a heat exchanger for precooling before traveling through insulated tubing to the drop generator where it exited as a liquid jet.

Mechanical vibrations from a cylindrical piezoelectric crystal caused the jet to break up into a stream of uniformly sized drops. The drop generator was improved over that used by Czys and Ochs (1988) by using a stainless steel tubing assembly. Dissimilarly sized drops were produced by the method of Adam et al. (1971). In this method, regular switching occurs between two excitation frequencies to produce alternating packets of dissimilarly sized drops. A "packet" of small drops was produced by applying a square wave voltage of a high frequency to the crystal for a prescribed period of time. This action was followed by applying a low frequency square wave voltage to the crystal for another period of time, and resulted in a "packet" of large drops. By switching regularly between periods of excitation frequency, alternating streams of small and large drops were produced from the single jet of the drop generator.

Most of the drops were charged using a cylindrical charging electrode placed around the point of jet breakup. The stream of charged drops was deflected as it passed between vertically aligned high voltage electrodes (see Fig. 1). A high speed switching circuit made it possible to switch between the charging voltage and a much lower voltage for a moment in time that coincided with the creation of one drop. This action resulted in the production of a minimally charged drop which was not deflected as it passed between the high voltage electrodes, and thus fell through the collision chamber. The digital controls were first set to allow a small drop to be created with minimal charge followed by the creation of a large drop with minimal charge. The time between selection of the minimally charged large and small drops was set so that the large drop overtook the small drop at a level in the collision chamber chosen to ensure that both drops were within 5% of their respective terminal velocity.

Streak/strobe photography was used to record the collision events (see for example Czys and Ochs 1988). The drops were illuminated from behind by an incandescent lamp angled approximately 45° above the camera lens axis in a vertical plane perpendicular to the film plane. This lighting orientation causes the drops to act as lenses when the incandescent light strikes them from behind. Thus, light was focused to a point on the portion of the drops facing the camera. As the drop pairs passed by the exposed film, streak lines were recorded corresponding to the drop fall trajectories. To aid in distinguishing between collision results, the drops were also illuminated by a single flash of a strobe light positioned approximately 45° to the side of the lens axis in a horizontal plane. The timing of the flash was set to illuminate the drops after collision. From this strobe light configuration, the entire outline of the drops was exposed on the film.

To simplify procedures in these preliminary experiments, a single camera was used to record collision events. Therefore, critical offset for coalescence was not established as was done previously (see, for example, Czys and Ochs 1988) using two cameras, viewing collision events from orthogonal positions. As a consequence, coalescence efficiencies were computed from counts of events assuming two different models of collision geometries, each representing extreme cases in the orientation of the drops to the film plane of the camera.

Results presented in this paper have been restricted to a collision geometry model, in which the collisions were assumed to occur between drops in a horizontal collision cross section area aligned with the lens axis and perpendicular to the film plane. Hence, the offset (distance) between the drops before collision and angle of offset to the film plane were both assumed to occur randomly. Therefore, the coalescence efficiency ε was simply obtained from the ratio (η) of the number of coalescences (N_C) to the total number of collision events (N_T). For these initial experiments a collector drop size of 353 μm radius was selected to interact with a 306 μm radius drop.

Initial experiments were conducted without measuring drop charge, assuming that careful vertical alignment of the drop stream perpendicular to the horizontal electric field between the high voltage electrodes would be sufficient to produce minimally charged drops, as it proved to be for Ochs et al. (1986, 1991). For the results presented herein, collisions were first photographed at room temperature, exposing approximately 90 to 120 frames of film. Refrigeration of the collision chamber was initiated, and then data were collected several times during the day while the chamber cooled. The cooling rate of the chamber was nonlinear.

Drop temperatures were computed using a 1D heat and mass transfer model, including the effect of ventilation. This model was developed specifically for application in these experiments, but can be applied to any arbitrary vertical profile of environment temperature and drop fall speed. In this application, drop temperatures were computed based on measured data: 1) the vertical distribution of temperature in the chamber at the time of observation, 2) the size of the large and small drop, 3) the temperature of the drops as they entered the chamber, and 4) the fall speed profile of the drops. The period during which collisions were photographed was short, usually 10 to 15 minutes at any particular temperature. Based on model output, uncertainty about the temperature of the drops related to changes in chamber temperature during data collection was estimated to be about $\pm$1.5°C.

Results from the first series of experiments were so unusual as to warrant additional experimentation in which drop charge was measured, in order to lay to rest any concerns that results were not somehow related to an unaccounted for electrical effect rather than cooling of the drops. In this second set of experiments, drop charge was measured using an electrometer capable of measuring charges below approximately 10^{-15} Coulombs. In this series of experiments, a set of measurements were made of the charge on the large and small drops immediately before and after each sequence of photographs at a specified temperature. This was done to ensure that charge on both drops did not change appreciably over the course of the observations. All collision result data from these experiments were determined for drop charges less than expected to aid coalescence; approximately $| Q_R - Q_r | < 10^{-12}$ Coulombs at this collector drop size and size ratio, where Q_R and Q_r represent the surface charge on the large and small drop, respectively (Park 1970; Czys 1987).

3. RESULTS

Figure 2 is a plot of coalescence efficiency (η) versus mean drop temperature for all runs without (open circles) and with (closed circles) drop charge measurements. Vertical lines are 95% error bars and were computed from $\Delta\eta = \pm k[\eta(1-\eta)/N_T]^{1/2}$ based on simple statistics for dichotomous events (Blalock 1972). Only two types of collision results were observed in this experiment; coalescence and bounce. Hence, the total number of collision events (N_T) is the sum of the number of coalescences (N_C) and the number of bounces (N_B). In total, 7500 photographs were required to obtain a total of approximately ~1500 collision events. The prominent feature of Fig. 2 is the marked jump of coalescence efficiency from about 42% at temperatures warmer than ~10°C to about 81% at temperatures cooler than ~10°C. Figure 2 also shows that there were several runs which produced anomalously low and perhaps anomalously high coalescence efficiencies.

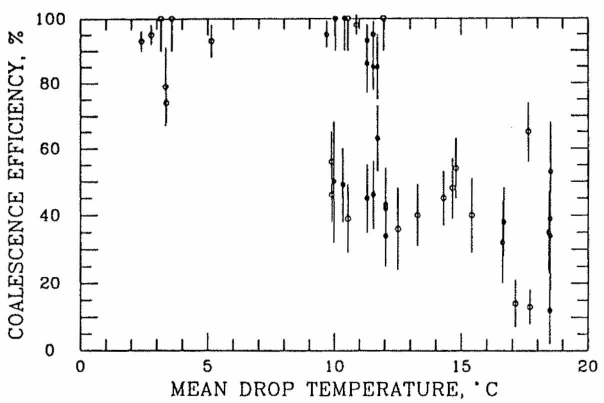

Figure 2. Coalescence efficiency versus mean temperature of the drops at collision.

There are two possible reasons for this anomalous behavior. The first reason is related to the fact that in striving to optimize collision rate, it is possible to inadvertently adjust the experiment to favor direct central (coalescence) or glancing (bounce) collisions. It is also possible to inadvertently synchronize film exposure with one type of collision event over another. This problem can be compounded by the occasional miscue of manual camera triggering which can just as easily act to maintain synchronization with a certain collision result as to restore randomness, as has been the case in other free fall drop experiments (Ochs et al. 1986). Some of the overlap in the transition region from lower coalescence efficiency to higher coalescence efficiency is probably related to the transient temperature profile in the chamber and accompanying uncertainty in determining corresponding drop temperature.

4. SUMMARY AND CONCLUSIONS

The results of a set of laboratory observations of collisions between small precipitation-size drops falling freely at terminal velocity in a refrigerated collision chamber were presented. The size-pair studied was a collector drop 353 μm radius interacting with a 306 μm radius drop. Air temperatures ranged from 20°C to -15°C. Drop temperatures ranged from 20°C to approximately 2°C. Experimentation revealed that the coalescence efficiency increased from approximately 42% for mean drop temperatures between 20°C and ~10°C to about 81% for mean drop temperatures between ~10°C and 2°C. A particularly interesting finding was an abrupt increase in coalescence efficiency, rather than gradual, at a mean temperature of the two drops of about 10°C.

The extent to which these results may apply to collection processes in clouds is subject to some uncertainty, since possible influences due to effect of reduced pressure were not taken into account, and because the drops were not in thermal equilibrium with the collision environment. In addition to the need for more observations at different drop sizes and size ratios, where temperature is the sole independent variable, very difficult future experimentation is warranted in which air pressure and temperature, and drop charge and velocity are well known and controlled. The results of this experimentation indicate that drop collisions in clouds may be considerably more complicated than suggested by previous carefully controlled experiments.

Acknowledgments. The author thanks Jack McPartland and Arlin Super of the Bureau of Reclamation for the loan of one of a NCAR ice nuclei counter which was adapted for use as the refrigeration unit in this experiment. This research was supported by the NSF under grant ATM 8819751.

REFERENCES

Abbott, C.E., 1977: A survey of waterdrop interaction experiments. *Rev. Geophys. Space Phys.,* **15,** 363-374.

Adam, J.R., R. Cataneo, and R.G. Semonin, 1971: The production of equal and unequal size droplet pairs. *Rev. Sci. Instrum.,* **42,** 1847-1849.

Blalock, H.M., Jr., 1972: *Social Statistics.* McGraw-Hill, New York, New York, 583 pp.

Brazier-Smith, P.R., S.G. Jennings, and J. Latham, 1972: The interaction of falling water drops: coalescence. *Proc. Roy. Soc. (London),* **A326,** 393-408.

Canlas, D.C., 1960: An experimental investigation on the effects of ambient pressure, temperature, and relative humidity on the coalescence of water drops. Ph.D. thesis, New York University, New York, 64 pp.

Czys, R.R., 1987: A Laboratory study of interactions between small precipitation-size drops in free fall. Ph.D. thesis, University of Illinois, Urbana, 131 pp.

Czys, R.R., and H.T. Ochs, 1988: The influence of charge on the coalescence of water drops in free fall. *J. Atmos. Sci.,* **45,** 3161-3168.

Dayan, N., and I. Gallily, 1975: On the collection efficiency of water droplets under the influence of electric forces I: Experimental, charge-multipole effects. *J. Atmos. Sci.,* **32,** 1419-1429.

Derjaguin, B., and M. Kussakov, 1939: Anomalous properties of thin polymolecular films. *Acta Physicochim,* **10,** 153-174.

Foote, G.B., 1975: The water drop rebound problem: Dynamics of collision. *J. Atmos. Sci.,* **32,** 390-402.

Goyer, G.G., J.E. McDonald, F. Baer, and R.R. Braham, 1960: Effects of electric fields on water-droplet coalescence. *J. Appl. Met.,* **17,** 442-445.

Jayaratne, O.W., and B.J. Mason, 1964: The coalescence and bouncing of water drops at an air/water interface. *Proc. Roy. Soc (London)*, **A280,** 545-565.

Levin, Z., and B. Machnes, 1977: Experimental evaluation of the coalescence efficiency of colliding water drops. *Pure Appl. Geophys.,* **115,** 845-867.

Ochs, H.T., D.E. Schaufelberger, and J.Q. Feng, 1991: Improved coalescence efficiency measurements for small precipitation drops. *J. Atmos. Sci.,* **48,** 946-951.

Ochs, H.T., R.R. Czys, and K.V. Beard, 1986: Laboratory measurements of coalescence efficiencies for small precipitation drops. *J. Atmos. Sci.,* **43,** 225-232.

Park, R.W., 1970: Behavior of water drops colliding in humid nitrogen. Ph. D. thesis, University of Wisconsin, Madison, 577 pp.

Plumlee, H.R., 1964: Effects of electrostatic forces on drop collision and coalescence in air. Charged Particle Res. Lab. Rept. CPRL-8-64, Illinois State Water Survey, Urbana, Illinois, 101 pp.

Plumlee, H.R., and R.G. Semonin, 1965: Cloud droplet collision efficiency in electric fields. *Tellus,* **17,** 356-364.

Rayleigh, Lord, 1879: The influence of electricity on colliding water drops. *Proc. Roy. Soc.,* **28,** 406-409.

Sartor, J.D., and C.E. Abbott, 1968: Charge transfer between uncharged water drops in free fall in an electric field. *J. Geophys. Res.,* **73,** 6415-6423.

Schlamp, R.J., S.N. Grover, and H.R. Pruppacher, 1976: A numerical investigation of the effects of electric charge and vertical external electric fields on the collision efficiency of cloud drops. *J. Atmos. Sci.,* **33,** 1747-1755.

Shiskim, N.S. 1964: Clouds, Precipitation and Thunderstorm Electricity. Gimiz, Leningrad.

Telford, J.W., and N.S. Thorndike, 1961: Observations of small drop collisions. *J. Meteor.,* **18,** 382-385.

Telford, J.W., N.S. Thorndike, and E.G. Bowen, 1955: The coalescence between small water drops. *Quart. J. Roy. Meteor. Soc.,* **81,** 241-250.

Whelpdale, D.M., and R. List, 1971: The coalescence process in raindrop growth. *J. Geophys. Res.,* **76,** 2836-2856.

ICE BREAKUP DURING EVAPORATION

Yayi Dong, Riza G. Oraltay and John Hallett
Atmospheric Sciences Center, Desert Research Institute
Reno, Nevada 89506-0220, USA

1. INTRODUCTION

Cloud and precipitation particles evaporate as they fall into regions where the relative humidly is below saturation. Evaporation also takes place at the cloud top and to some extent at cloud edge down shear where dry air is mixed into convective clouds. These particles may break up during evaporation to produce secondary ice crystals as observed in the present experiments. It is also possible that a larger population of ice crystals are produced due to the higher freezing rate of cloud droplets at a lower temperature in such regions due to evaporation.

The present experiment is designed to investigate the secondary ice crystal production during evaporation under various conditions. The results show that rime particles break up at low relative humidities and imply that the mechanism could play a significant role in the ice production process.

Direct monitoring of the processes made it possible to estimate the strength of very small ice crystals. It is found that small ice particles are much stronger than bulk ice, a fact to be considered in any hypothesis of ice fragmentation in clouds. The results can be used to evaluate the reality of postulated mechanisms of secondary ice crystal production supplementing the Hallett-Mossop process, and any related electric charge separation.

2. EXPERIMENTAL

The experiments are carried out in a dynamic diffusion chamber shown in Fig. 1. The working section of the chamber is 400 cm long, 2.5 cm high and 20 cm wide. Temperature of upper and lower aluminum plates can be set up independently to create the desired supersaturation to grow ice crystals on a suspended needle. Relative humidity for evaporation was 50% to 100%, 0°C to -18°C. Rime is grown on the needle by introducing supercooled water droplets into the chamber under isothermal conditions. Two moisture conditioners are connected in series with the working section making a closed loop; air is circulated in the chamber at different speeds up to 3 m s^{-1}. Undersaturation is obtained by reversing the direction of the air flow with a lower temperature in the upstream moisture conditioner. The growing and evaporating processes are monitored by a microscope and video camera with a resolution limit limit of the optical system of a few μm. The ice crystals and rime particles break up during evaporation, when weaker points are thinned out. The drag force of the air stream which pulls ice

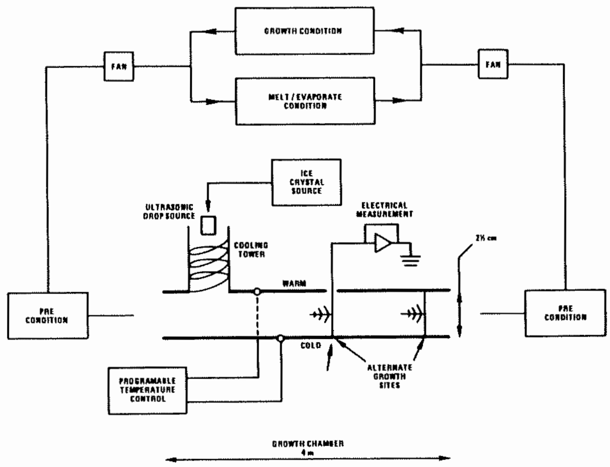

Fig. 1. The schematic diagram of the dynamic diffusion chamber.

particles away can be estimated from air speed and dimension of the ice specimen. The strength from the cross-sectional area just before breakup of the ice can be calculated.

3. RESULTS

a. *Breakup*

Ice particles break up during evaporation at a low relative humidity. Rime particles grow with a structure of many cones, built up by connecting each other at cone tips (Dong and Hallett, 1989). Breakup rate is relatively high with this structure, because the cone tips are easily thinned out during evaporation and the broad head is subject to a relatively larger drag force. This is also useful in the calculation of ice strength.

In the range of the experiments, the breakup rate increases with decreasing relative humidity. At a relative humidity above 90%, little breakup is observed. At a lower relative humidity (70% or lower), more than 100 small particles could be generated directly from a parent rime target few mm size. Figure 2 shows the sequence of events of rime particle breakup.

Wind speed also affects the breakup rate. At a lower wind speed, ice particles evaporate slowly, fewer breakups are observed during evaporation due to the lower viscous force. At a higher wind speed, on the other hand, the ice particles break into bigger pieces, so that fewer events are observed. Fig. 3 shows the relation between breakup rate and wind speed for graupel. The

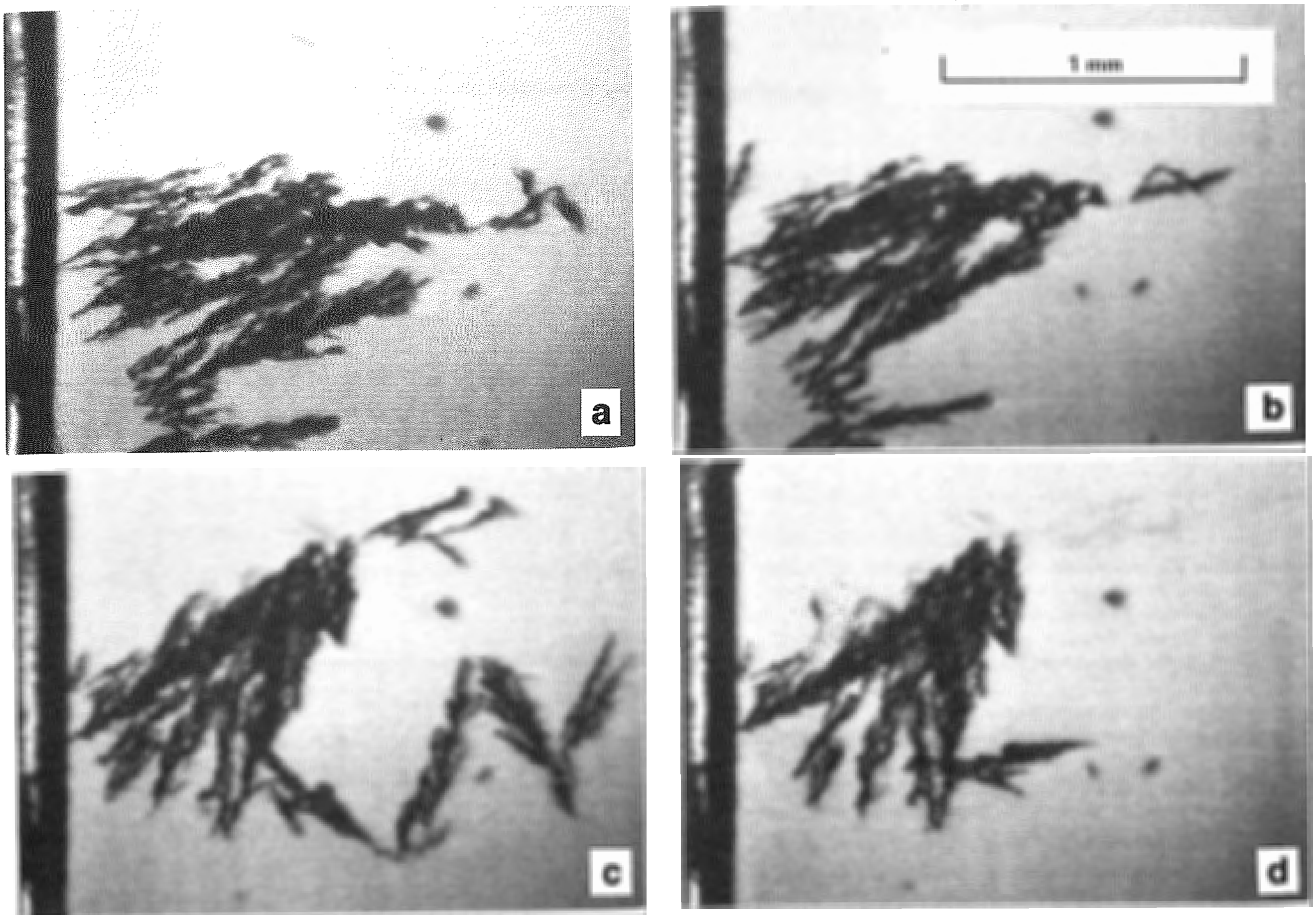

Fig. 2. A sequence of breakups of a rime particle. Air speed 1.0 m s^{-1}, relative humidity 70%.

optimum wind speed for a high breakup rate is about 1 m s^{-1}, which is the typical fall velocity for 1 mm, soft hail particles in clouds. The rate shown in the Fig. 3 is the relative rate which is detected by electrical measurement (Dong and Hallett, to be published), the actual breakup rate is much higher. It should be pointed out here that the lower breakup rate at a higher wind speed does not necessarily imply a low secondary ice production in clouds, because these bigger fragments may break up further in an undersaturated environment.

Although the temperature of evaporation has an insignificant influence on the breakup rate, the temperature and liquid water content at which the ice particles grow determines their structure, which will have strong effects on the fragmentation. Generally, ice particles with a low density structure such as dendrites, feather like rime have a higher breakup rate, while long columns, needles (Oraltay and Hallett, 1990) and finger-like rime particles have a lower breakup rate. Plates do not break up during evaporation. Figure 4 shows the breakup sequences of long ice columns.

b. The strength of ice crystals

It has been found in the present experiments that small ice particles are much stronger than the bulk ice. The strength can be estimated by calculating the drag force during breakup. The drag force F_d can be calculated by

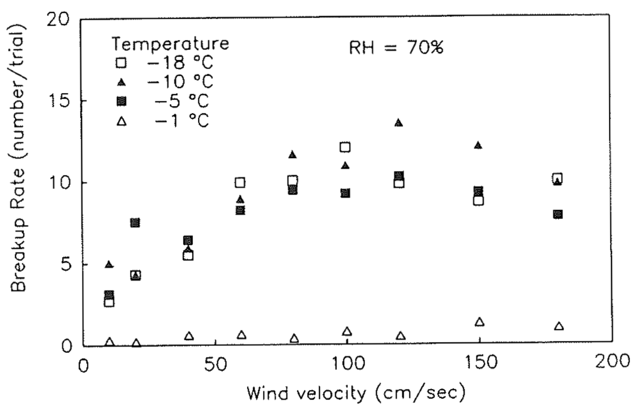

Fig. 3. Relative breakup rate as a function of wind speed. The rate shown in the Fig. is measured by electrical method which detects only bigger breakups. The actual rate is higher.

$$F_D = C_D\, A \cdot \frac{1}{2}\rho_a U^2$$

where C_D is the drag coefficient depending on Reynolds number, A the cross-sectional area, ρ_a the air density, and U the air speed. The estimated drag force on a rime particle with area of 0.25 mm^2 is about 10^{-5} N at an air speed of 1 m s^{-1}

It is observed that both column ice crystals and rime particles are bent, often by more than 90°

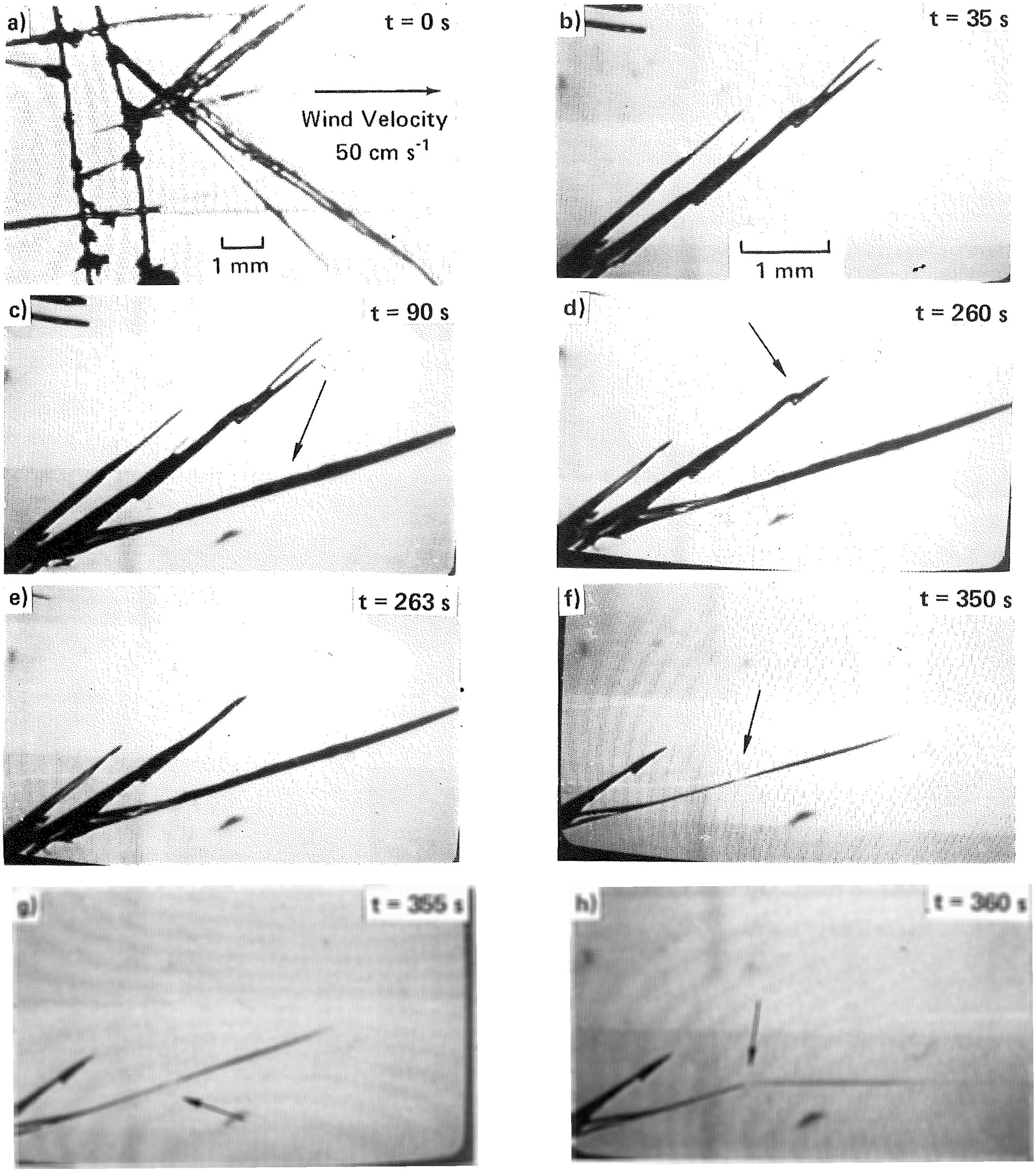

Fig. 4. Evaporation of columns at -13°C and 80% relative humidity.

in an air flow prior to break up. This can be used to estimate the fracture strength σ of ice by

$$\sigma_{max} = \frac{MY_{max}}{J_z}$$

where M is the bending moment, Y_{max} the radius of the bending cylinder, J_z the moment of inertia of the cross section about z axis.

A Number of numerical and experimental results can be used for estimating the drag force. For the situation in which we are interested, it is found that many small ice samples (few μm in diameter) have a strength of at least 140 bar or higher which is about an order higher than that of bulk ice.

c. *Nucleation*

It is also of interest to examine the role of evaporation in nucleation and subsequent ice production. Koenig (1965) pointed out the importance of lowering temperature to the wet bulb should drops be mixed with dry air and subsequently be reincorporated into the cloud. The detail of the mixing process is important; (Kim et al 1992) the larger scale process are important. Rejection of a drop, its nucleation and freezing and incorporation down shear of a growing cumulus in or in Kelvin-Helmholtz instability at a cloudy inversion top. The temperature difference between evaporating droplets and the ambient could be up to about 10°C depends on the conditions of humidity and pressure. There is also some evidence that the enhanced rate of freezing of a drop nucleated in dry air may enhance scatter. Figure 5 shows graphically temperature drop resulting from evaporation at different temperatures, ambient humidity and pressure from simple application of the unventilated droplet growth equations.

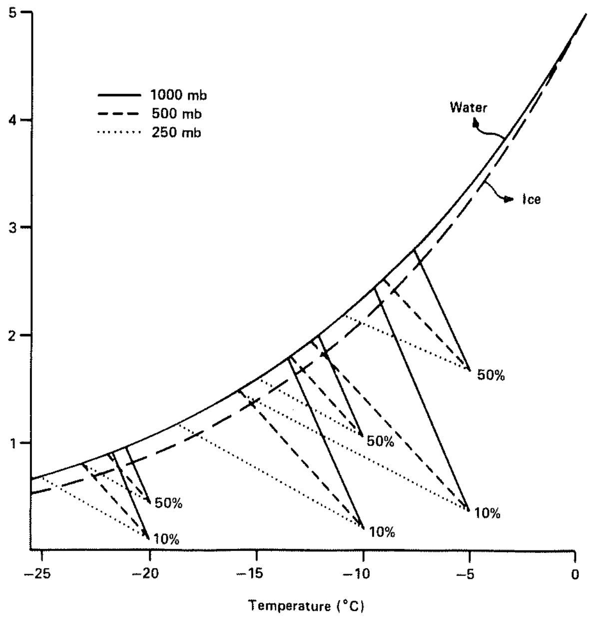

Fig. 5. Calculated temperature drop of an unventilated water drop resulting from evaporation at different temperatures, ambient humidity and pressure.

5. APPLICATIONS

The results of the present experiments provide explanation for the high concentration of ice particle observed in warm clouds in the complete absence of the Hallett-Mossop process (Ragno et al., 1988 and 1991). Supercooled cloud droplets at cloud top nucleate by significant temperature decrease due to evaporation; additional breakup may result from a very rapid freezing process. These ice particles reincorporate into clouds and grow further from a vapor. Larger droplets would be favored in such a process. These ice particles may break up if they are brought into a undersaturated region in the cloud or outside the cloud and those reincorporated.

The process may also play a role in winter storms where wide variability in ice concentration has been observed and the mechanism of this variability has not been identified. The observations of the present experiments may help to understand the water droplet depletion, precipitation formation and radiative effects of clouds.

4. CONCLUSION

Ice particles break up during evaporation at a relative humidity below 90% producing secondary ice crystals. The breakup rate depends on the relative humidity, wind speed (equivalent fall velocity) and structure of the particles. A mm size soft hail may break up into a hundred small pieces under a suitable conditions. This result implies that the ice evaporation could be a significant process of secondary ice production in clouds. It points to the importance of high resolution measurement of relative humidity in the neighborhood of mixing - both at cumulus tops and above stratiform cloud.

REFERENCES

Dong, Y . and J. Hallett, 1989: Droplet accretion during rime growth and the formation of secondary ice crystals. *Royal Meteorol. Soc.. Q. J.* 115, 127-142.

Kim, K.E., J.W. Telford, T.S. Keck and J. Hallett, 1990: Entrainment in Cumulus Clouds Part II. Drop Size Variability. Submitted for publication.

Koenig, R., 1965: Ice Forming Processes in relatively warm clouds. Intern. Cloud Physics Conf., Tokyo and Sapporo, 242-246.

Rangno, A. L. and P. Hobbs, 1991: Ice particle concentrations and precipitation development in small polar maritime cumuliform clouds. *Q.J.R. Meteorol. Soc.*, 117, pp. 207-241.

Rangno, A.L. and P. Hobbs, 1988: Criteria for the Onset of Significant Concentrations of Ice Particles in Cumulus Clouds. Atms. Res., 22, 1-13.

Oraltay, R.G. and J. Hallett, 1989: Evaporation and Melting of Ice Crystals: A Laboratory Study. *Atmos. Res.*, 24, 169-189.

ACKNOWLEDGEMENT

This research effort was supported by a Grant #ATM-9021918 from Meteorology Program, National Science Foundation, Washington, D.C..

STOCHASTIC MODELS OF ICE ACCRETION

F.Prodi[1,2], E.Smargiassi[1,2] and F.Porcú[1]

[1]Institute FISBAT-C.N.R., Clouds and Precipitation Group, via de' Castagnoli 1, I-40126 Bologna,Italy

[2]Dept. of Physics of the University, via Paradiso 12, I-44100 Ferrara, Italy

1. Introduction

Recent accretion experiments of atmospheric ice performed on fixed and rotating cylinders (Prodi et al, 1986a,b,c; Pflaum, 1984) have shown the importance of investigating conditions leading to low density deposit. Since ballistic models are proving themselves to be efficient tools in understanding low density mechanisms of ice formation, the theoretical study of the stochastic droplet collection on fixed and rotating objects has been intensified (Rambaldi *et al*, 1988; Porcú and Prodi, 1991; Gribelin *et al*, 1988, Personne *et al*, 1990), moving from works which analyzed physical properties of general aggregates (Family and Vicsek, 1985; Limaye and Amriktar, 1986; Ramanlal and Sander, 1985). In these type of models describing general accretion processes, particles follow straight trajectories from randomly selected initial positions and impinge on aggregates; as a particle touches a point on the aggregate it becomes a part of the deposit. The basic process has been analyzed by Rambaldi *et al* (1988), showing that the geometrical properties of pure ballistic aggregates (mean density, opening angle of structures, shadowing effects) are understood by means of the kinematics of the single particle accretion process. By studying the probability distribution of the single particle process the authors were able to calculate theoretically opening angle, mean density and angle between empty channels inside aggregates in agreement with numerical simulations and laboratory experiments. Porcú and Prodi (1991) demonstrated that the properties of an aggregate far enough from the seed don't depend on the size or shape of the seed itself.

Growth experiments specifically performed to obtain low density ice deposits on fixed cylinders (Levi *et al.*, 1991) and rotating ones (Prodi *et al*, 1991) have shown morphology and local density features which are suitable for comparison with model results. For example it has been shown, for fixed cylinder deposit, that for Stokes number $K < 3$, the deposit morphology was characterized by concave growth fronts and inward direction of lateral feathers; for larger K the growth fronts changed to convex profiles and ice feathers to an outward direction. Two fixed deposits illustrating this effect are shown in fig. 1a, for $K = 0.8$, and in fig.1b, for $K = 4.8$.

In rotating deposits, the critical value $K = 3$ still has a leading role in the growth of the deposit. Pronounced lobes separated by wide entrances are observed for $K < 3$, while entrances change into air gaps for larger K values. The role of air inclusions in affecting the mean density has been clarified by a comparative examination of fixed and rotating deposits. In fixed deposits the stagnation line can maintain steady conditions which allow insight into the basic characteristics of the phenomenon. In rotating deposits the features are comparatively more complex and are connected to the growth parameters. In all cases it has been proved that the shadow effect has the main role in determining the deposit morphology and characteristics; the ballistic models are suitable to reproduce such effect.

In this work we introduce some additions to previous models: the restriction of rectilinear trajectories is removed and some fluid dynamics is introduced (after Gates *et al*, 1988), polydisperse droplets are injected instead of monodisperse ones, and the use of the third dimension is added to the pure ballistic approach.

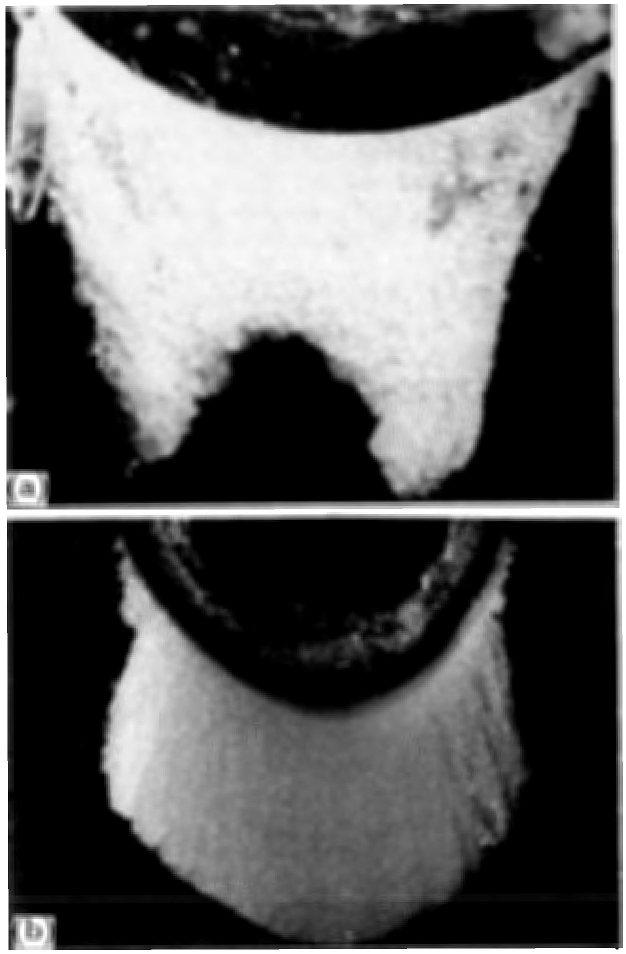

Fig.1 *Deposit accreted on fixed cylinders at: a) $K = 0.8$, $\alpha = -30°$; b) $K = 4.8$, $\alpha = +15°$. Scale is given by cylinder embryo diameter (1 cm). Levi* et al, *1991.*

2. STOCHASTIC 2-D MODEL WITH CURVED TRAJECTORIES AND POLYDISPERSE PARTICLES

This model is two dimensional and describes droplet aggregation on fixed and rotating cylindrical collectors. Droplets are transported with the flow around the obstacle and, due to their inertia, some impinge on the obstacle or on the aggregated droplets. The droplets are polydisperse having the same size distribution as those of the laboratory experiments selected for the comparison. The use of polydisperse droplet populations proved to be important in obtaining realistic deposits with structural characteristics similar to those observed in Nature (in particular as far as growth direction of rime feathers, air gaps between lobes and in channels).

The stochastic approach is justified by the low impact velocity of simulated accretions. In fact, these growth conditions make relevant the spatial and temporal correlations between the subsequent impact positions and instants of droplets on the collector: the capture and the freezing of the single airborne droplet is analyzed in relation with the growing surface of the deposit. The deposit modifies the aerodynamics of the aggregating droplets, showing a feed-back effect typical of dynamic accretion processes. Moreover, for low values of impact parameters, the freezing of the droplets is almost instantaneous, so the particles keep their spherical shape, and the spreading of the droplet is negligible. Control parameters for the model are air temperature T, air pressure P, flow velocity V and cylindrical obstacle radius R. The angular parameters used in the model and characterizing the growth of the deposit in lateral regions are (see fig.2):

α = average growth angle of the feathers, with respect to wind velocity at infinity;

θ = average angular position on the cylindrical obstacle of the feathers;

γ = incidence angle of droplets in the feather formation region, with respect to the normal to the surface at fixed θ;

β = angular half width of the "fan-like" structure which is developed in growth processes on a single embryo (or on a spatially limited embryo).

In this model the actual trajectory is not computed but the angular position of the impinging droplet on the cylinder is stochastically determined on the basis of the local collection $\phi(\theta)$, that can be parametrized by means of the aerodynamic parameters, following Lozowski *et al* (1979). Because the motion of a droplet is partially determined by its radius-dependent inertia, we computed, for each θ, a set of $\phi_i(\theta)$, where i represents the i-th value of the droplet radius in the discrete distribution. Thus the probability of a droplet of radius r_i impinging on the surface of the cylinder at angular coordinate θ is assumed to be $P_i(\theta) \propto \phi_i(\theta)$. From θ it is possible to calculate the incidence angle γ at the point of the impact, using the relationship due to Langmuir and Blodgett (1949). The trajectory is linearly approximated by the incidence angle γ near the surface, avoiding the calculation of the whole particle path. This approximation is acceptable as it is here applied to the morphological study of rime feathers in the case of growth, i.e., in the first millimeters of the deposit. When applying the model to rotating cylinders the approximation is justified by the cylindrical regularity of the resulting aggregate. The numerical computation of the trajectory obviously loses its significance at larger deposits due to the modification of the flow by the deposit itself. Moreover the validity is restricted to low flux of droplets, low velocities and low liquid water content. On rotating cylinders the rotation rate is an input to the model.

Simulation have been carried out with two sets of parameters, as follows:

1. $T = -20°C$, $P = 785.$ mb, $r_m = 9.0\mu m$, $R = 0.5$ cm, $2.5 < V < 20$ m sec^{-1}
2. $T = -20°C$, $P = 785.$ mb, $r_m = 16.0\mu m$, $R = 0.9$ cm, $2.5 < V < 20$ m sec^{-1},

where r_m is the median volume radius of the size distribution, and R is the radius of the cylindrical collector.

a. Fixed cylinders

In fig. 3 model results are shown with different parameters, chosen in the laboratory experiments (Levi *et al*, 1991). We notice that, as far as lateral development of the deposit and rime feathers morphology are concerned, model results are well in agreement with experiments and we can think that the main structural features have been captured. The rime feather formation takes place on lateral position as the shadow effect is more effective in these regions. For that reason it is important to test the model in its ability to estimate the maximum collection angle θ_m for the deposit and compare it with theoretical results. The values obtained from the model (tab. 1) are larger than the theoretical ones, and this is due to the polydispersion of the particles: the droplets with radius $r > r_m$ impact the collector at larger θ with differences inversely dependent of the Stokes parameter. This is in agreement with laboratory data (tab. 1), for the distribution with $r_m = 9.0\mu m$.

The numerical experiments have indicated that the growth direction of rime feathers can be theoretically predicted by the relation:

$$\alpha = \theta - \gamma + \beta. \tag{1}$$

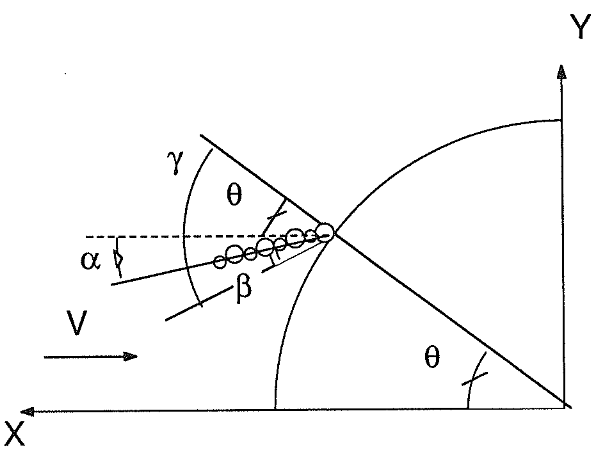

Fig.2 *Sketch of the angles involved in the rime feathers formation: inward growth ($\alpha < 0$).*

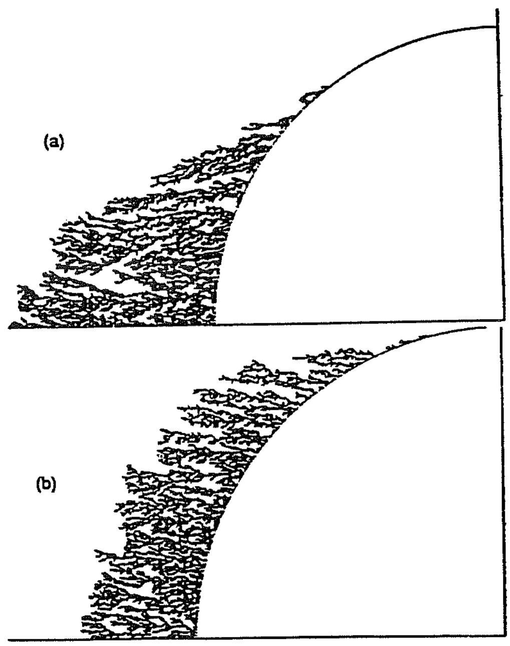

Fig.3 *Simulated deposits on fixed cylinders: $R = 0.5$ cm, 10^4 particles, $r_m = 9.0$ cm, $K = 0.6$ (a) and $K = 4.5$ (b).*

This relationship has been applied to numerical results of our model and Gates *et al* (1988) model, and compared with laboratory experiments in different conditions (Levi *et al*, 1991), with very good agreement (tab. 2,3). The values of γ and θ exhibit a large variability for a given growth situation due to the stochastic behavior of the rime feather growth; θ can be much smaller than θ_m, thus implying a decrease in droplet impact angle γ, or θ can approach θ_m, implying a γ very close to its maximum $\gamma_m = 90$ deg. On the contrary β is much less variable, fluctuating around its average value of 20 degrees, indicating that the rime feather formation is a process common to any deposit grown in different conditions and the shadow effect can be described on the basis of the relationship between β and γ and atmospheric and aerodynamic parameters.

The value of the inertia parameter is not sufficient to completely represent a given rime growth event, since size distribution of impacting droplets is essential in determining angles γ and θ; thus the growth direction of feathers, is not amenable to a function of the Stokes parameter alone, contrary to prevoius studies. As far as our stochastic model is concerned we feel it is a valid starting point to develop a complete icing modeling since it can catch the essential features of rime growth and in particular it can discriminate between θ and θ_m. This capability is crucial in explaining the wide variability of microphysical characteristics experimentally observed far from the stagnation zone. Moreover we have verified that the relation (1) allows us to predict the profile of the deposit. In fact, by linking profile convexity or concavity to rime feathers growth inward or outward (with respect to the wind direction at infinity) it is possible to determine the critical value of the Stokes parameter at which α changes from positive to negative values, for a given droplet size distribution. The critical value $K = 3.2$ thus determined is in good agreement with the value obtained experimentally by Levi *et al* (1991). Moreover the fact that

Tab.1 *Values of maximum collection angle, θ_m, for simulated and experimental deposits.*

	Levi et al. (1991)				present model										
K	0.8	1.3	1.8	3.2	0.6	1.2	1.7	2.2	3.3	4.5	1.0	2.0	4.0	5.9	7.8
θm simulat.					53	65	67	68	71	76	68	73	76	78	78
θm theoret.					38	54	62	66	71	74	51	64	72	76	78
θ feather					43	55	57	58	61	64	58	60	67	66	65
θm experim.	45	53	50	58											

Tab.2 *Comparison between theoretical and numerical results of growth angle α of the feathers in stochastic models.*

	Gates et al. (1988)						present model										
K	0.9	1.6	1.9	2.5	3.6	4.8	0.6	1.2	1.7	2.2	3.3	4.5	1.0	2.0	4.0	5.9	7.8
θm	45	55	60	63	69	72	53	65	67	68	71	76	68	73	76	78	78
β	16	15	25	15	23	25	25	25	25	25	25	25	25	25	25	25	25
α numer.	-27	-20	-5	-10	-1	3	-14	-2	5	8	8	11	2	5	7	8	13
α valued	-29	-20	-5	-12	2	7	-12	0	2	3	6	11	3	8	11	13	13

Tab.3 *Theoretical values of incidence angle of the droplets γ for experimental deposits.*

	Gates et al. (1988)						Levi et al. (1991)										
K	0.9	1.6	1.9	2.5	3.6	4.8	0.8	0.8	0.8	0.8	0.8	0.8	1.3	1.3	1.8	1.8	3.2
θm	62	64	60	60	64	72	35	40	35	40	50	55	50	55	40	50	55
α numer.	-8	3	-8	7	-8	6	-25	-20	-30	-20	0	0	0	20	0	0	10
γ valued	90	86	90	78	90	90	85	85	90	85	75	80	75	60	65	75	70

we found different values from other authors for this transition parameter is due to the dependence of α on other parameters than the Stokes number.

b. Rotating cylinders

When applying the model to deposit formation on rotating collectors it produces deposits with a morphology very similar (fig.4) to those grown in cold wind tunnel (fig.5) in similar condition. In rotating deposits after a first stage of uniform growth some of the instabilities amplify and generate a lobe structure separated by voids which clearly testify to the efficacy of shadow effect in giving rise to an overall periodic structure. The model exhibits a clear dependence of the angular lobe frequency with the Stokes number and with the size of impacting droplets, in good agreement with experimental evidence obtained by Prodi *et al* (1991). As a consequence of increasing the number of lobes the voids between lobes narrow and reduce to thin air channels.

The numerical simulations are under examination to search for a functional relationship between lobe frequency and aerodynamic parameters. Local density measurements on lobe structures give values not lower than those of fixed collectors in corresponding conditions, testifying that the growth mechanisms are the same in both cases and the different values of average global density in the two cases are only a consequence of the typical morphological configuration.

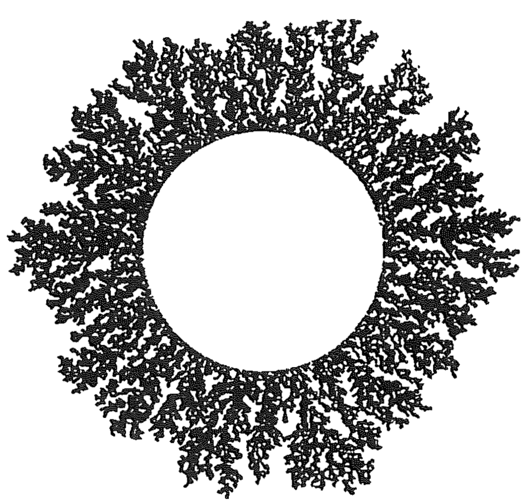

Fig.4 *Simulated deposit on rotating cylinder ($R = 0.25$ cm) for $K =$ 2.2.*

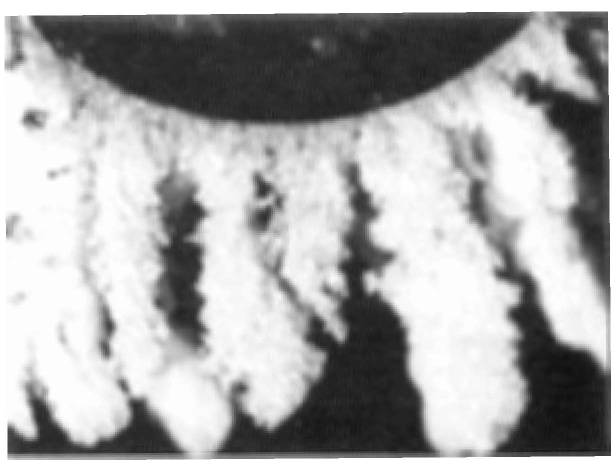

Fig.5 *Deposit accreted on rotating cylinder ($R = 0.5$ cm) for $K =$ 2.4. Scale is given by cylinder embryo dyameter. Prodi* et al, *1991.*

3. THREE DIMENSIONAL BALLISTIC MODEL

Another way to make the numerical model closer to the laboratory experiments was to add the third dimension in the simulations. For the pure ballistic model, we translate the 2D geometry (disks on a plane) to a 3D space (spheres in a space). The consequent increased computation time and the difficulties of the visualization of the results have limited the quantitative results to date. A large number of aggregates must be used in order to smooth out the high-frequency variability of the density profiles or of the values of angles.

In fig.6 10^4 particles of radius r are collected by a fixed cylinder of radius $30r$ and $200r$ long: this ratio between particle radius and collector radius is suitable for comparison with laboratory experiments. The axis of the cylindrical collector (not displayed) is rotated by about 10 degrees with respect to the sight direction. Some quantitative aspects are shown in fig.7, where angular density profiles of 2D (solid line) and 3D (dotted line) deposits are compared. The 2D density is computed on circular sectors (1 deg. width) for a growth on a seed with the same radius of the particles. The 3D density is computed integrating along the axis of the cylinder (of radius r and $200r$ long), circular sectors of 1 deg. width. The density for a given region is computed dividing the volume (or area) occupied by the particle in the region, by the total given volume (or area). The density of the 3D growth is lower than the 2D one (0.17 is the maximum for the 3D and 0.49 for the 2D), but the value $\beta \approx 20$ deg. plays the role of limiting opening angle also in the 3D growth. The effect of the third dimension seems to be a smoothing of the profile density due to the integration along the collector axis: the mean effect of lateral feathers, as the one evident in the 2D deposit at the left boundary (fig.7), is to make the density profile less steep for $|\beta| > 20$ deg.

The use of 3D ballistic models should allow, as future work, a better comparison with the laboratury experiments, expecially for quantitative analysis of aggregate characteristics.

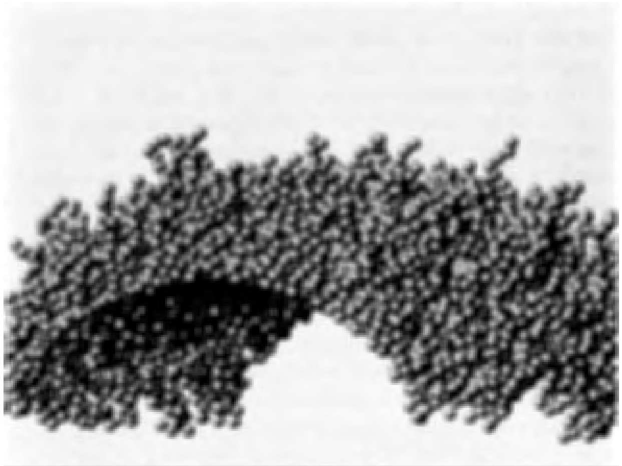

Fig.6 *3D aggregate on a cylinder with* $R = 30r$.

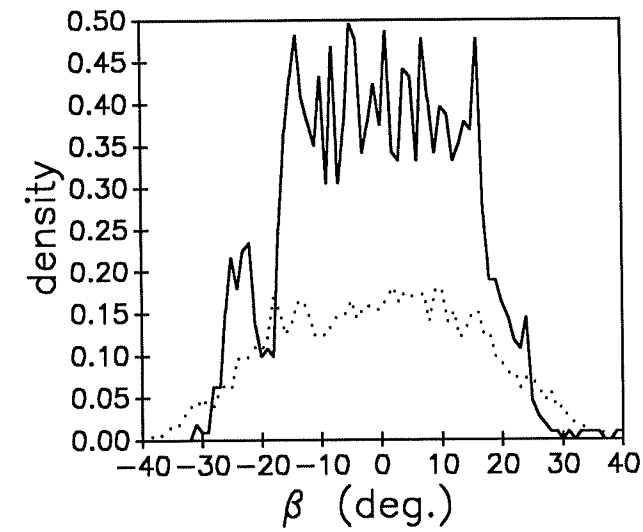

Fig.7 *2D (solid line) and 3D (dotted line) angular density profiles.*

REFERENCES

Family, F. and T. Vicsek, 1985: Scaling of the active zone in the Eden process on percolation network and the ballistic deposition model. *J. Math. Gen.*, **189**, 175-181.

Gates, E.M., A.Liu and E.P.Lozowski, 1988: A stochastic model of atmospheric rime icing. *Jour. of Glaciology*, **34**, 26-30.

Gribelin, P., P.Personne and H.Isaka, 1988: Experimental study of the air inclusions into ice formed on fixed cylinders. *4th Int. Conference on Atmospheric Icing of Structures*, Paris, E.d.F., 162-166.

Langmuir I. and K.B.Blodgett, 1946: A mathematical investigation of water droplet trajectories. in *The Collected Works of Irving Langmuir.* Pergamon Press, Elmsford, N.Y., 1960, 335-393.

Levi, L., O.B.Nasello and F.Prodi, 1991: Morphology and density of ice accreted on cylindrical collectors at low values of impaction parameters. I: Fixed deposits. *Quart. J. Roy. Met. Soc.*, **117**, 761-782.

Limaye, A.V. and R.E.Amriktar,1986: Theory of growth of ballistic aggregates. *Phys. Rev. A*, **34**, 5085-5090.

Lozowski, E.P., J.R.Stallabrass and P.F.Hearty, 1979: The icing of an unheated, nonrotating cylinder in liquid water droplet-ice crystal clouds. N.R.C.C. Report LTR-LT-96.

Personne, P., C.Duroure and H.Isaka, 1990: Theoretical study of air inclusion on rotating cylinders. *5th Int. Conference on Atmospheric Icing of Structures.* Arcadia Ichigaya, Tokyo, A2-6-(1)-(3).

Pflaum, J.C., 1984: New clues for decoding hailstone structures. *Bull. Am. Met. Soc.*, **65**, 583-593.

Porcú, F. and F.Prodi, 1991: Ballistic accretion on seeds of different sizes. *Phys. Rev. A*, **44**, 8313-8315.

Prodi, F., G.Santachiara and A.Franzini, 1986a: Properties of ice accreted in two stage growth. *Quart. J. Roy. Met. Soc.*, **112**, 1057-1080.

Prodi, F., L.Levi and P.Pederzoli, 1986b: The density of accreted ice. *Quart. J. Roy. Met. Soc.*, **112**, 1081-1090.

Prodi, F., L.Levi and V.Levizzani, 1986c: Ice accretion on fixed cylinders. *Quart. J. Roy. Met. Soc.*, **112**, 1091-1109.

Prodi F., L.Levi, O.B.Nasello and L.Lubart, 1991: Morphology and density of ice accreted on cylindrical collectors at low values of impaction parameters. II: Rotating deposits. *Quart. J. Roy. Met. Soc.*, **117**, 783-801.

Ramanlal, P. and L.M.Sander, 1985: Theory of ballistic aggregation. *Phys. Rev. Lett.*, **54**, 1828-1831.

Rambaldi, S., F.Prodi and F.Porcú, 1988: Ballistic accretion on a point seed. *4th Int. Conference on Atmospheric Icing on Structures*, Paris, E.d.F., 411-414.

ON THE SYMMETRY OF SNOW DENDRITES

John Hallett
Atmospheric Sciences Center, Desert Research Institute
Reno, Nevada 89506-0220, USA

and

Charles Knight
National Center for Atmospheric Research
Boulder, Colorado 80307, USA

1. INTRODUCTION

Dendritic snow crystals are often considered to be the epitome of symmetry in nature - the six sided growth being equal in rate and shape in each direction. Even a cursory examination of published snow crystals (Bentley and Humpries, 1962; Nakaya 1954) shows that the side arms from each of the six tips are not exactly repeated for each of the six branches. On occasion, major arms do occur symmetrically on both sides of each branch, but lesser arms may not. It is appropriate to ask the question not only how to characterize the symmetry of a dendrite, but the physical mechanism of growth which leads to the occurrence of symmetrical arms on each branch, compared with branches where arms are apparently distributed randomly.

Both laboratory and field observations show that dendrites have principal branches along $\langle 11\bar{2}0 \rangle$ directions and grow between -12°C and -18°C. The laboratory studies also show a region of dendrite growth between 0 and -3°C, which tends to be of only minor importance in the atmosphere because the driving force for growth at water saturation is small. Laboratory studies under independently controlled temperature, saturation and air velocity further demonstrate that the transition from plate to dendrite growth takes place as air velocity increases beyond a critical value between a few and 15 cm s^{-1} depending on supersaturation (Keller and Hallett, 1982; Alena, et al, 1990). Supersaturation and fall velocity together influence the transition from faceted to skeletal growth both for columns and plates. Side arms of dendrite branches develop asymmetrically when the ventilation is asymmetric; this happens both in vapor growth, and growth from solution in forced or buoyant convection (Huang and Glicksman, 1981; and Glicksman 1984).

2. PRINCIPLES OF DENDRITIC GROWTH

Dendrite (tree like) growth occurs in a variety of systems, both in vapor and liquid. There is a major distinction between pure systems (no mass diffusion limitations) and systems with a carrier component. Ice crystal growth in pure water is an example of the former, snow dendrite growth from the vapor in air, of the latter.

The main dendritic growth regime of snow is bounded on both the low-and high-temperature sides by faceted, "sector" growth regions. It is distinguished from these by the slower c-axis growth so that the crystals are much thinner, and by the apparent lack of facets: the dendrite tips often appear rounded, though with small radii of curvature, it is difficult to tell for certain. This represents, presumably, growth at a rough interface. Formation of steps is not growth-rate-limiting, as it is in faceted growth. Thus a common assumption in mathematical treatments of dendritic growth is that the growth rate itself is strictly controlled by diffusion of heat and/or material between the interface and its surroundings. This is governed by the Laplace equation, and shape instabilities result (Mullins and Sekerka, 1963; Langer, 1989) that can give dendritic growth forms but have proved difficult to describe rigorously. Thus a disc or plate crystal transforms to dendrite growth as it reaches a specific size. The true dendrite is a development of the dorite, with side arms sprouting from a central branch, with growth directions lying along a low-index crystallographic direction.

3. NATURAL SNOW DENDRITES

What causes the strong impression of perfect symmetry that snow dendrites impart? Figures 1 and 2 are portions of dendrites that show some symmetry, but detailed examination shows a lot of asymmetry as well: both along single branches and between adjacent ones. Probably the main reason for the strong impression of symmetry is the strict crystallographic control of all arm and branch orientations, but another is that often the longest branches are more-or-less symmetrically disposed. The cases of highest symmetry - often selected for illustration because of their beauty - often result from the sector-to-dendrite transition. In the sector regime, all six arms have faceted tips, each of which has three sharp corners that separate the four facets. Entry into the dendrite growth region then produces arms growing synchronously from each of the eighteen corners, a complicated-looking but very symmetrical assemblage. See, for instance, Nakaya, 1954, Plate 36, p. 352, number 199 (Fig. 4); there are many other examples. Another cause of symmetry can be fluctuations of temperature or supersaturation that may cause simultaneous branching as a snow crystals falls, growing entirely within the dendrite growth regime of temperature, supersaturation and ventilation velocity.

Figure 1 illustrates a case in which the branching is generally asymmetric, both on single arms and between arms. One exception is the two prominent branches near the crystal center, on the arm to the upper right. One can see a frozen droplet of rime just where these two branches sprouted. The freezing of this droplet could provide the pulse of extra supersaturation that produced the simultaneous budding of two branches on the arm. In Fig. 2, the general symmetry is considerably greater, both on single branches and between them. Larger-scale fluctuations must have influenced the growth of the crystal. Such fluctuations are discussed further below. It is generally the case with natural snow that the larger branches are more symmetrically placed than the smaller ones (Fig. 3).

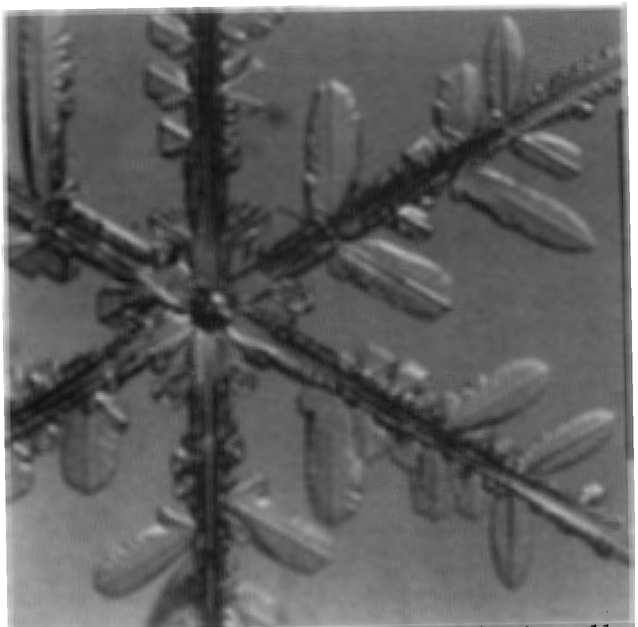

Fig. 1: A natural snow crystal with six well developed primary branches showing mostly asymmetrical side arms. A frozen drop may be responsible for two symmetrical side arms (arrow) which do not occur on other arms (scale 1mm).

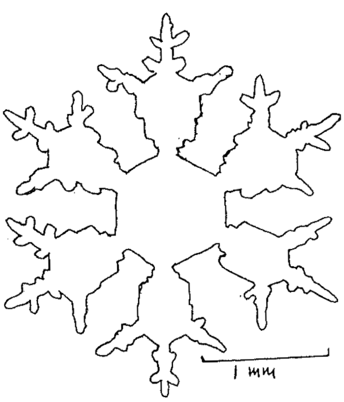

Fig. 4: Symmetrical dendrite initiation from sector plates. Nakaya, 1954, plate 36, page 352, No. 199.

Fig. 2: A natural crystal showing symmetry of individual arms, although the symmetry is not extended to each of the six individual branches.

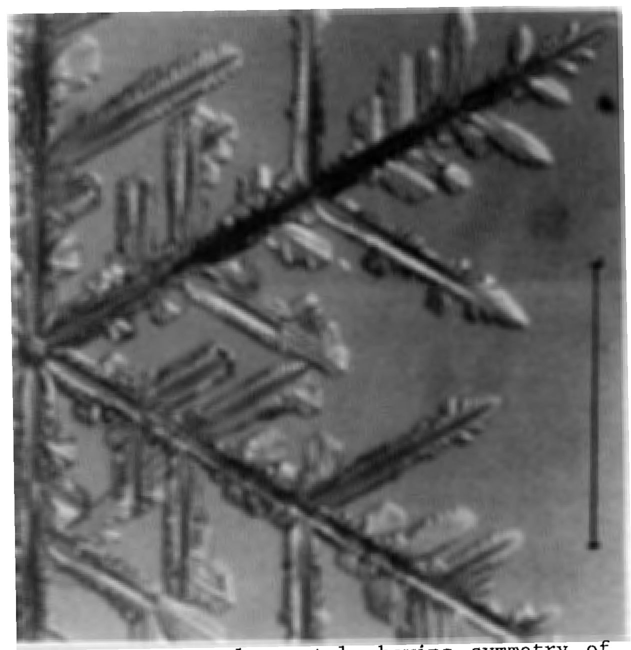

Fig. 3: A natural crystal showing symmetry of larger arms between branches but lack of symmetry of smaller arms (scale 1mm).

Fig. 5: Sprouting of a plate crystal by increase of airflow to about 20 cm s^{-1}.

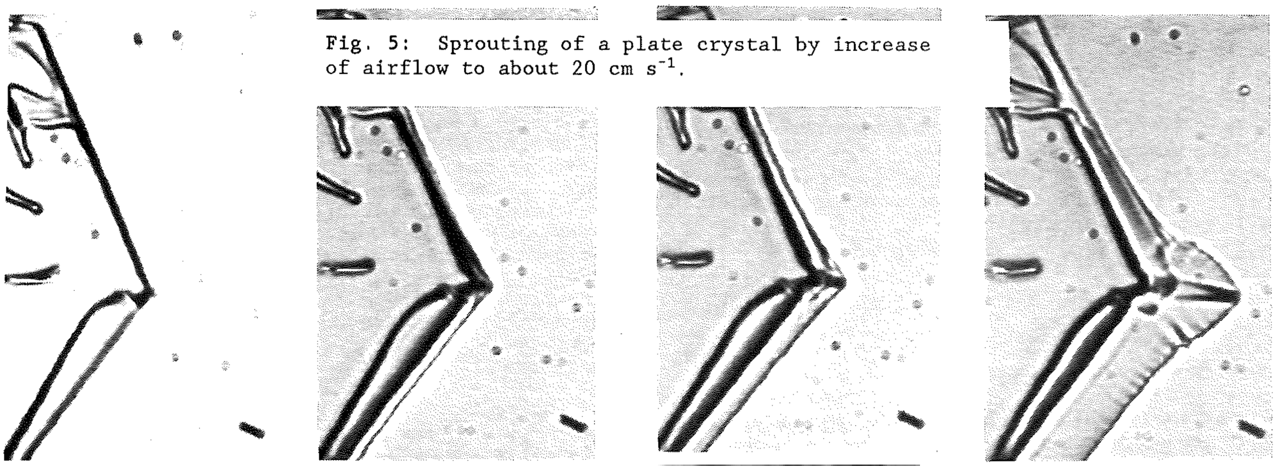

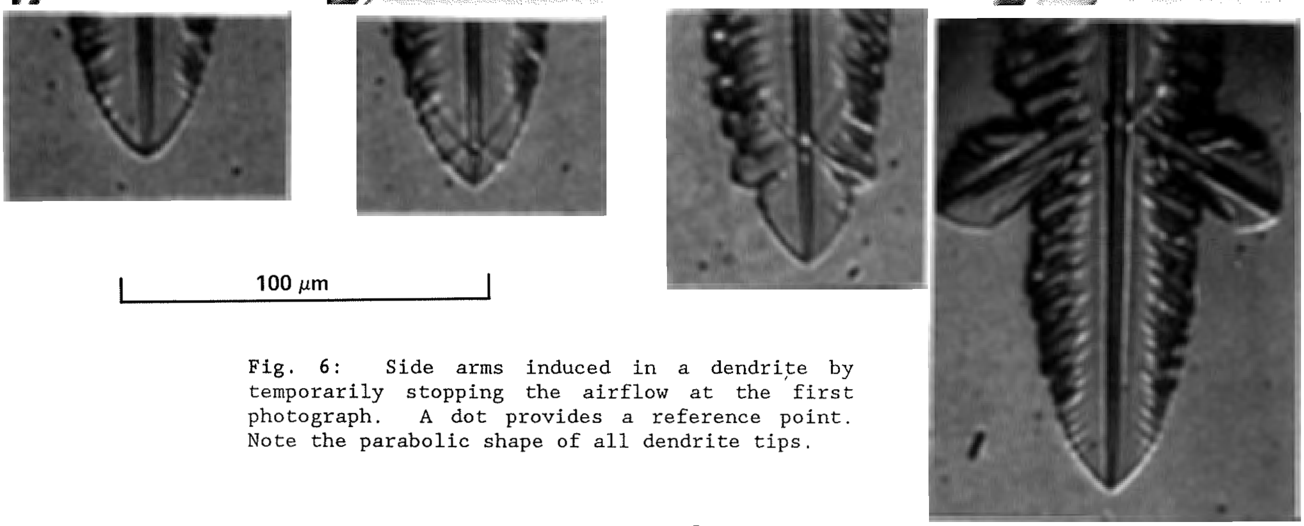

Fig. 6: Side arms induced in a dendrite by temporarily stopping the airflow at the first photograph. A dot provides a reference point. Note the parabolic shape of all dendrite tips.

4. LABORATORY STUDIES

Snow crystals growing in the atmosphere change conditions of growth as they fall at increasing velocity through regions of changing temperature and saturation ratio. The crystal shape is a diary of these events, to be interpreted according to our knowledge of growth processes. Such understanding under controlled laboratory conditions can be achieved by varying temperature or supersaturation at the growth site (Nakaya did this), or growing crystals along a support laying perpendicular to the temperature gradient in a diffusion chamber. This gives independent control of temperature and supersaturation (Kobayashi, 1957 Hallett and Mason, 1958). In the latter case, habit changes can be studied simply by moving a given crystal to a different level (temperature, supersaturation) of growth. In the present experiments, crystals were grown in a dynamic diffusion chamber, where the air velocity could be controlled for crystals growing at selected but unchanged temperature and supersaturation.

The chamber plate temperatures were set to give a central temperature of -15C and a saturation ratio just below that of supercooled liquid water. This resulted in thin plate growth under conditions of no imposed velocity, in practice a few mm s^{-1} because of crystal excess temperature during the growth process. Dendrites could be induced to grow by increasing the air velocity from 2 to 20 cm s^{-1}. The present study consisted of examining the change of dendrite growth by stopping the airflow for a few seconds (the stilling time of the chamber) simply by turning off the fan.

5. RESULTS

Figure 4 shows a sequence of a plate transformed to dendrite growth by increase of air velocity. The facets of the plate first become dished, and ultimately lead to dendrite growth in <11$\bar{2}$0> directions. Note that the tip is approximately parabolic; instabilities on the periphery are visible back some 10 μm from the tip. The tip is rounded and is not bounded as far as the resolution of the photographs show by two facets. Figure 5 shows the growth when the airflow is stopped and started (3 s) and growth continues approximately unhindered. As the dendrite growth proceeds however it is clear that the change has influenced the growth. A dot is visible; a surface parabola is visible; and more interestingly, side arms as sector plates are developing which are clearly initiated at the time the airflow stopped.

Examination of the tip region of the dendrite in the last panel of Fig. 5 shows that instability occurs back from the growing tip and evolves consecutively and gives arms on both sides that may or may not be symmetrically disposed on the growing branch. This is shown better in some illustrations of dendritic growth in other materials-for instance, see Glicksman (1984). There is a strong tendency in Fig. 4 toward faceting back from the tip, that is completely absent in illustrations of dendritic growth in other materials. When growth occurs in air, vapor depleted air moves towards the rear of the dendrite providing flow is not exactly normal to its plane. Also, competitive effects between arms reduce effective local supersaturation. This situation differs from rapid dendrite growth in a supercooled liquid, when the thermal front lies close to each dendrite tip and no interaction occurs between dendrites. Under these conditions each dendrite grows independently and the primary branch and side arms are identical. This situation could occur for snow dendrites falling with horizontal orientation in still air. There is a problem in interpretation, because faceting may lead to branching by a completely different mechanism: by sprouting from sharp corners as in Fig. 3. True dendritic branching comes from growth shape instability on a smoothly-curved interface. We will expect that dendritic snow crystals exhibit true dendritic branching, and are in the process of trying to obtain unequivocal proof.

Synchronous branching at both sides of the growing tip can be induced by fluctuations with several-second durations, as was shown in connection with Fig. 4. This is the shortest fluctuation which could be characterized by the present system, which was limited by the mechanical inertia of the fans and air in the wind tunnel.

Otherwise, true dendritic branching may occur more-or-less independently at each side of a growing arm, leading to asymmetry of the branching pattern. In uniform conditions of growth the branch spacing tends to be uniform also, but there appears to be little or no reason for the registry--the individual branching locations--to remain comparable on all arms as growth proceeds. Indeed, there may be a tendency for the opposite, since the formation of a branch on one side of an arm must tend to inhibit development in its immediate neighborhood, and also on the opposite side - by a thermal or dry pulse through the air or more slowly by a thermal pulse through the solid. (Thermometric diffusivity, $D=\kappa_{air}=D=0.2$, $\kappa_{ice}=0.01$ cm^2 s^{-1}). It is of interest that a somewhat similar effect can be produced by application of a laser pulse to give local heating (Qian and Cumming, 1990).

6. CONCLUSION

Natural snow dendrites give a strong first-impression of perfect symmetry, but more careful examination reveals that dendritic growth has a lot of asymmetry, especially at smaller scales. True dendrite branching may be expected to produce asymmetry, so that snow crystals grown in constant and uniform conditions of dendritic growth--to the extent possible--might be expected to show less symmetry. The symmetry that does exist in natural snow results partly from the sector-to-dendrite transition and partly from fluctuations in the growth environment that the falling crystals encounter large enough to induce simultaneous branching. Smaller fluctuations, obviously, might produce asymmetry.

In application of these studies to growth of natural snow crystals, two sources of change need to be considered. First, asymmetry of crystal fall resulting from hydrodynamic instability at Reynolds numbers > 200 and interaction with flow fields of neighboring crystals: and second, fluctuation in temperature/supersaturation ratio inherent in the cloud itself· resulting from the convective processes and associated mixing. A snow crystal falls about one meter in the few seconds taken to initiate symmetrical growth, so that one such fluctuation is adequate to lead to symmetrical arms, at the same position on all six branches. In the absence of such fluctuations, the law of the jungle prevails for the side arms, with smaller ones excluded by competition for heat loss/mass gain compared to any arm which has a momentary advantage. In a supercooled melt or supersaturated solution with uniform stationary conditions prevailing, noise at a molecular level and subsequent competition, would be expected to lead to arms which are either randomly arranged on each side of a given branch, or are biased to being arranged non symmetrically should one side communicate with the other; in a situation where changes of environmental conditions occur either because of supersaturated ambient conditions or local buoyant fluctuations, the tendency would be for arms to be induced symmetrically.

ACKNOWLEDGMENT:

This research effort was supported by a Grant #ATM-9021918 from Meteorology Program, National Science Foundation, Washington, D.C. The National Center for Atmospheric Research is sponsored by the National Science Foundation.

6. REFERENCES

Alena, T., J. Hallett and C.P.R. Saunders, 1990: On the Facet-Skeletal of snow crystals: Experiments in high and low gravity. J. of Crystal Growth, 104 539-555.

Bentley, W. A. and Humpries, W. J. 1962: Snow Crystals. Dover Publications Inc., pp226.

Glicksman, M.E., 1984: Free Dendritic Growth. Materials Science and Engineering, 65, 45-55.

Keller, V. and J. Hallett, 1982: Influence of air velocity on the habit of ice crystal growth from the vapor. J. Crystal Growth, 60, 91-106.

Kobayashi, T., 1957: Experimental researches on the snow crystal habit and growth by means of a diffusion cloud chamber. J. Meteor. Soc., Japan, 75th Aniv., 38, .

Langer, J.S., 1989: Dendrites, viscous fingers, and the theory of pattern formation. Science, 243, 1150-1156.

Hallett, J. and B. J. Mason, 1958: The influence of temperature and supersaturation on the habit of ice crystals grown from the vapour. Proc. Roy. Soc., A247, 440-453.

Mullins, W.W. and R.F. Sekerka, 1963: Morphological stability of a particle growing by diffusion or heat flow. J. Appl. Physics, 34, 323-329.

Nakaya, U., 1954: Snow Crystals Natural Artificial. Harvard Univ. Press. pp510.

Qian, X.W. and H.Z. Cummins, 1990: Dendritic Sidebranching Initiation by a Localized Heat Pulse. Physical Review Letters, The American Physical Society, 64, 3038-3041.

A LABORATORY INVESTIGATION OF CRYSTAL GROWTH IN SUPERCOOLED CLOUDS

Naihui Song[1] and Dennis Lamb[2]

[1]Illinois State Water Survey, Champaign, IL 61820
[2]Department of Meteorology, The Pennsylvania State University, University Park, PA 16802

1. INTRODUCTION

An accurate prediction or simulation of precipitation development in a mixed-phase cloud depends on knowledge of the growth rates, fallspeeds and habits of ice crystals under a variety of environmental conditions. Laboratory studies permit examination of individual crystal growth processes and the effect of each environmental variable under controlled conditions. Laboratory measurements are particularly useful in the efforts to characterize ice crystal growth in terms of specific microphysical processes. At the same time, these measurements may be considered as "engineering parameters" that can be introduced into numerical modeling of clouds containing ice.

The growth of ice crystals under supercooled cloud conditions has been studied experimentally by a number of researchers. Fukuta (1969), for instance, empirically measured ice crystal growth rates and fallspeeds at different temperatures with growth times less than about a minute. The growth rates of ice crystals in a large fog chamber at temperatures between -3 and -21°C were documented by Ryan et al. (1974, 1976) for growth times up to 3 min. Takahashi and Fukuta (1988) and Takahashi et al. (1991) reported the crystal fallspeeds and growth rates for growth times from 3 to 30 min and for temperatures between -3 and -23°C. Here, we present the results of a recent series of experiments in which ice crystals were grown under supercooled cloud conditions in a continuous-flow cloud chamber.

2. EXPERIMENTAL METHOD

The details of the cloud chamber have been given by Song and Lamb (1990) and Song (1991). A particular advantage of the experimental techniques was their ability to produce a large ice crystal population. The vertical wind tunnel was especially designed to produce the various components of a supercooled cloud (cloud droplets, aerosol particles and ice seeds) outside the main growth tunnel and thereby avoid unnatural thermal and moisture inhomogeneities that might otherwise bias the interpretation of the results. A separate chamber provided a clean environment, well separated from the rest of the cloud, for the collection of the ice crystals. Typical growth time was several minutes for the ice crystals with a concentration from 100 to 1000 l^{-1}. A specially designed collector was used to sample the grown ice crystals. An adjacent box, purged with cold air through its gridded bottom, was used to analyze the collected ice crystals. Inside this cold box, the sample holder was dismantled so that the ice crystals could be sandwiched between two glass disks. Ice crystals were photographed to document their sizes and habits. In order to estimate their mass, the ice crystals were carefully melted into drops. Since the small drops appeared as hemispheres on a thin plastic layer, their volume and masses were estimated by measuring the drop diameters (Mitchell et al., 1988).

3. RESULTS

The crystal growth habits found in the current experiments were similar to those commonly reported in the past. The relationship between ice crystal mass and diameter produced at -14°C is plotted in Fig. 1. The data were compiled from a number of experimental runs at the given temperature. Each datapoint represents from the growth of one ice crystal. The past data from Ryan et al. (1976) are also plotted in Fig. 1 for comparison purposes. Consistent with their observations, quadratic trend for lengths < 200 μm appears in the relationship, whereas a somewhat linear trend appears for lengths > 200 μm. The trend of increasing mass with the diameter is also consistent with the formulation based on the field data as summarized by Pruppacher and Klett (1978).

The average diameter and mass of the ice crystals are plotted as functions of the growth time in Fig. 2, again along with the data reported by Ryan et al. (1976). Each datapoint in this figure represents an average of about 20 ice crystals in a given growth batch. The growth temperature was -14°C, and the liquid water content was about 2 g/m^3. The current data were similar to those from Ryan et al. (1976). The curve convex upward (solid line) represents for the crystal diameter, whereas the curve concave upward (dashed line) represents for the mass of the ice crystals. These characteristics are consistent with the mass and size relationship shown in Fig. 1.

The liquid water content was found to affect crystal growth. The average size or mass of ice crystals acquired under similar experimental conditions is plotted as a function of the liquid water content in Figs. 3-6 at temperatures of -6, -8, -14, and -16°C, respectively. The experimental data from Ryan et al. (1976) were also plotted even though their environmental liquid water contents were not known well. Each datapoint in the current data represents an average of about 20 ice crystals in the same growth batch. An increasing trend appears in the dependence of ice crystal size and mass on the liquid water content. The strongest trend is at -8°C. The liquid water content of the cloud affected the growth habit. In Fig. 7, the ratio of average length to width of the ice crystals is plotted as a function of the liquid water content. The ratio decreases slightly as the liquid water content increases, suggesting that the crystal habit becomes more compact at high liquid water contents.

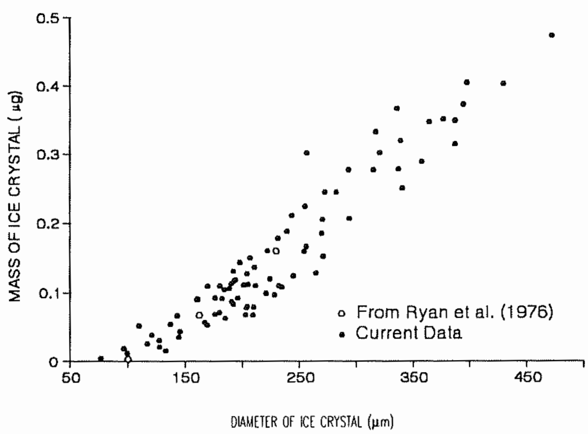

Figure 1. The mass and diameter relationship of cloud chamber-produced at a growth temperature of -14°C.

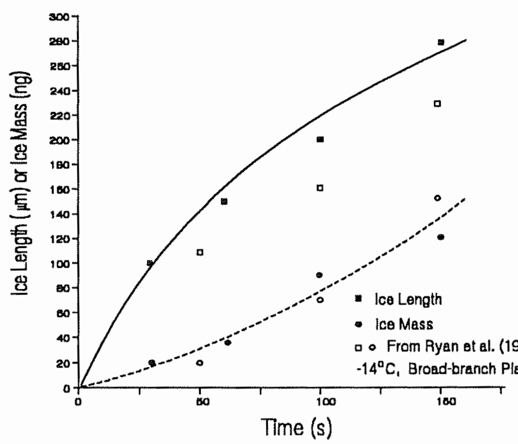

Figure 2. Time dependence of the average mass and diameter of ice crystals at a growth temperature of -14°C. The solid line represents length of the ice crystals, while the dashed line represents their mass.

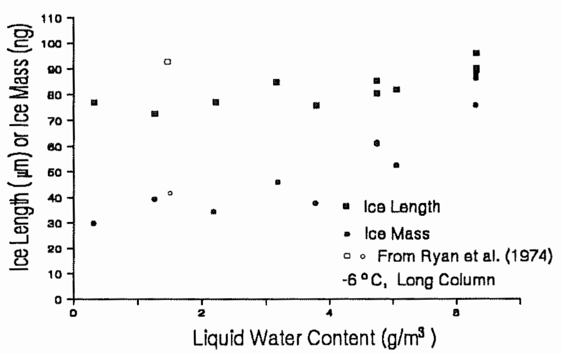

Figure 3. Dependency of averaged crystal mass and size on the liquid water content at a growth temperature of -6°C and a growth time of 100 s.

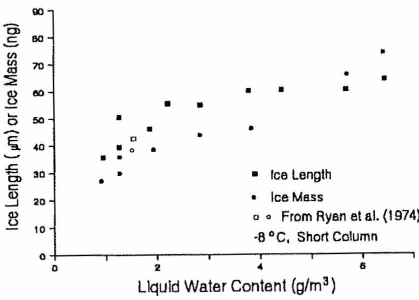

Figure 4. Dependency of average crystal mass and size on the liquid water content at a growth temperature of -8°C and a growth time of 100 s.

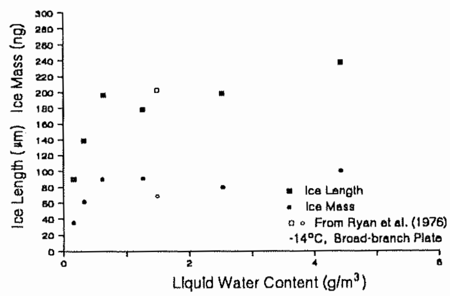

Figure 5. Dependency of average crystal mass and size on the liquid water content at a growth temperature of -14°C and a growth time of 100 s.

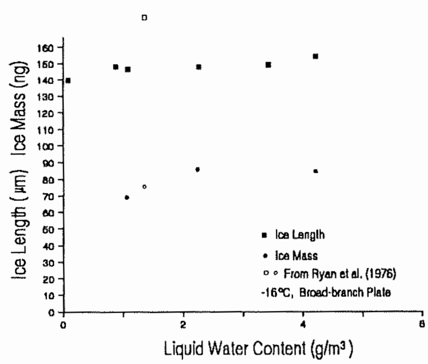

Figure 6. Dependencies of the averaged crystal mass and size on the liquid water content. The growth temperature was -16°C. The growth time was 100 s.

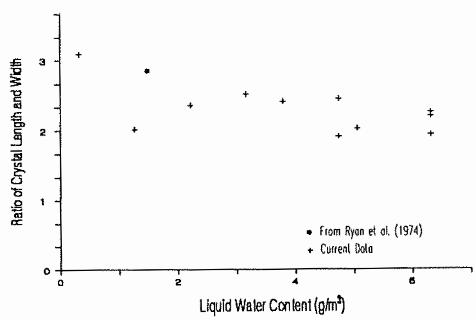

Figure 7 Dependence of the average ratio of crystal length to width on the liquid water content. The growth temperature was -6°C. The growth time was 100 s.

4. DISCUSSION

During the current experiments, a subtle dependence of crystal growth on the liquid water content was observed. Both the mass and diameter of the ice crystal at the end of a fixed growth time were found to increase with the liquid water content. The most rapid relative increase was at a growth temperature of -8°C (Fig. 4). The other aspects of crystal growth appear to be generally consistent with past experimental data. The growth habits of the ice crystals correlated faithfully with their environmental conditions, as found in past studies. Although crystal growth is dependent on temperature, it is also affected by supersaturation (e.g., Nakaya, 1954).

The results indicate that the average diameter of the ice crystals increases with the liquid water content. This is of some consequence and requires explanation. If the observed trends (Figs. 4-7) are extrapolated back to zero liquid water content, the contribution due to the growth with the presence of liquid drops is only a fraction of the total for most cases. Without the effect of cloud droplets, the growth would have originated from vapor diffusion through the air from relatively distant and diffuse sources. At very low liquid water contents, the supercooled cloud droplets simply maintain water saturation through slow evaporation as water vapor in the air is depleted by the growing ice. However, at higher liquid water contents, sedimentation of the ice crystals brings cloud droplets continually toward the ice crystal surface, thus causing transient reductions in the width of the boundary layer for vapor diffusion. The physical proximity of the droplet and ice surface allows the water to be transported rapidly from one to the other. Due to this "vapor flush" effect, an ice crystal tends to grow faster in a supercooled cloud than under water-saturated conditions alone.

The growth enhancement due to supercooled water should be dependent on the number density of droplets in the air, as well as the sizes and terminal velocities of the ice crystals. At larger terminal velocities, more droplets pass by the ice crystal in a unit of time; however, the time that the droplets spend near the ice crystal also decreases. The larger an ice crystal is, the more droplets pass by it in a unit of time, but the relative growth enhancement with respect to the crystal mass may not be significantly dependent on the crystal size. Nevertheless, the magnitudes of the growth enhancements differed quite significantly from case to case. By increasing the liquid water content from about zero to 6 g/m^3, the average mass of long columns, for instance, doubled and their average maximum length increased by about 20%. When the liquid water conent is low, the air near the chamber wall may become less than water saturation due to vapor deposition on it. Since size variation at liquid water contents near zero was much larger than at high liquid water contents, the smaller average of broad-branch plates may be attributed to the wall effect. Beyond about 0.3 g/m^3, the average mass of the broad-branch plates increased negligibly, and their average diameter increased about 10%. However, the short solid columns, their average size is the smallest, are drastically different from other cases. Their average mass nearly triples and average length more than doubles as the liquid water content increases to 6 g/m^3. Such compact crystals also have relatively large terminal fallspeeds (Fukuta, 1980).

These differences among different habits may be attributed to the hydrodynamic interaction between the droplets and ice crystals, as has been studied by a number of researchers using detailed particle trajectory models. With such models, the scavenging efficiencies of particles with radii from 10^{-3} to 10 µm by ice crystals were computed by Martin et al. (1980) and Miller and Wang (1989). From their results, it appears that particles in a size range are scavenged very inefficiently, even much less than smaller aerosol particles. The size range of this "zero-scavenging zone" (Miller and Wang, 1989) covers a typical size range of cloud droplets for the crystals encountered in this study. Martin et al. (1980) and Miller and Wang (1989) explained such characteristics are as an effect of a deflecting flow along the upstream surface of the crystal.

The knowledge gained from their research may be applied to the current study since the hydrodynamic interactions between cloud droplets and ice crystals are similar. The droplet diameter in a typical supercooled cloud falls within the range of the "zero-scavenging zone." The flow around a falling ice crystal is analogous to the flow around the surface of an impactor. Riming may depend on an "impacting velocity", the crystal fallspeed, and the dimension of the impacting surface. When the "zero-scavenging zone" exists, riming must be very ineffective. Therefore, droplets may pass very near the ice surface without being caught. During such close passage, rapid transport of water vapor from a droplet to an ice crystal may occur.

Before the onset of riming, the growth rates of many ice crystals should be enhanced by the presence of supercooled cloud water. In particular, those ice crystals with large terminal velocities allow the droplets to approach closer, making the growth enhancement mechanism more effective. Wake circulations in the back of the crystal may trap droplets, thereby also contributing to the growth enhancement. As indicated in Fig. 7, the average column width was enhanced more than the average length. This growth enhancement of columns and its dependence on the width of an ice crystal makes sense since cloud droplets travel along the crystal's width rather than along its length. The fact that the largest relative growth enhancement was for the short solid column is consistent with the fact that the average width of the short solid column was the largest among the cases considered here. Two other factors could be important especially for short columnar ice crystals: a large terminal velocity and large back circulations in three dimensions due to their compact shape and almost equal width and length. By contrast, wake circulations may not develop as easily around the narrow width of long columns, and even worse, around the narrow branches of broad-branch plates. It is possible that these factors work together to give the short columns that grow near -8°C the largest growth enhancement in supercooled clouds.

5. CONCLUSIONS

This paper documents the growth of ice crystals in supercooled clouds as a function of the temperature, liquid water content, and growth time. In general, the current data were found to be consistent with the results of past studies. Beyond the effect of riming, the liquid water content of a supercooled cloud was found to affect the growth of ice crystals, enhancing in both size and mass, and affecting shape. Such data are needed in cloud models for simulation of ice processes in atmospheric clouds.

The theoretical prediction of a "zero-scavenging zone" (Miller and Wang, 1989) seems to be consistent with these experimental data. The "zero-scavenging zone" may have significance in cloud physics, which needs to be verified experimentally.

Acknowledgments. This research project was partially funded by the National Science Foundation under Grant No. ATM-8716166 and ATM-8919837, as well as by the Illinois State Water Survey.

REFERENCES

Fukuta, N., 1969: The dimensions of ice crystals in natural clouds. *J. Atmos. Sci.*, 27, 919-926.

——, 1980: Development of fast falling ice crystals in clouds at -10°C and its consequence in ice phase processes. Proceedings 8th Internat. Conf. on Cloud Physics, 15-19 July 1980, Clermont-Ferrand, France, 97-100.

Martin, J. J., P. K. Wang and H. R. Pruppacher, 1980: A theoretical determination of the efficiency with which aerosol particles are collected by simple ice crystal plates. *J. Atmos. Sci.*, 37, 1628-1638.

Miller, N. L., and P. K. Wang, 1989: Theoretical determination of the efficiency of aerosol particle collection by falling columnar ice crystals. *J. Atmos. Sci.,* 46, 1662-1663.

Mitchell, D. L., R. Zhang and R. L. Pitter, 1988: Mass-dimensional relationships for ice particles and the influence of riming on snowfall rates. *J. Appl. Meteorol.*, 29, 153-163.

Nakaya, U., 1954: *Snow Crystal: Natural and Artificial.* Harvard Univ. Press, Cambridge, MA.

Pruppacher, H. R., and J. D. Klett, 1978: *Microphysics of Cloud and Precipitation.* D. Reidel Publishing Company, Boston.

Ryan, B. F., E. R. Wishart, and E. W. Holroyd III, 1974: The densities and growth rates of ice crystals between -5°C and -9°C. J. *Atmos. Sci.*, 31, 2136-2141.

Ryan, B. F., E. R. Wishart, and D. E. Shaw, 1976: The growth rates and densities of ice crystals between -3°C and -21°C. *J. Atmos. Sci.*, 33, 842-850.

Song, N., 1991: *Aerosol Scavenging by Ice in Supercooled Clouds.* Ph.D. Dissertation, Meteorology Department, The Pennsylvania State University, University Park, PA.

——, and D. Lamb, 1990: A continuous-flow cloud chamber for studying microphysical and chemical processes in supercooled clouds. Conf. on Cloud Physics, 23-27 July, 1990, San Francisco, CA, 149-152.

Takahashi, T., and N. Fukuta, 1988: Supercooled cloud tunnel studies on the growth of snow crystals between -4 and -20°C. *J. Meteorol. Soc. Japan*, 66, 841-855.

——, T. Endoh, G. Wakahama, and N. Fukuta, 1991: Vapor diffusional growth of free-falling snow crystals between -3 and -23°C. *J. Meteorol. Soc. Japan*, 69, 15-30.

Effects of Relative Humidity on the Coalescence of Small Precipitation Drops in Free Fall

Harry T. Ochs III, Neil F. Laird, Donna J. Holdridge, Daniel E. Schaufelberger, and James Q. Feng

Illinois State Water Survey, Office of Cloud and Precipitation Research
2204 Griffith Drive, Champaign, Illinois 61820, USA

1. INTRODUCTION

Observations of effects of relative humidity on rebound and coalescence are limited and contradictory. Prokhorov (1954) studied 500 µm radius drops falling at various speeds and impacting on a stationary hemisphere of the same radius. He concluded that low impact velocities and relative humidities impeded coalescence. Lindblad (1964) found differing results as deduced by measuring the time for coalescence for water hemispheres at 50 and 97% relative humidity. These results showed that high impact velocities and relative humidities impeded coalescence. Park (1970) found no effect for relative humidities between 25 and 60%. There appears to be little agreement in the literature on the effects of relative humidity on the coalescence process. Recent studies conducted in the Cloud Physics Lab of the Illinois State Water Survey have showed new and significant findings as to the influences of relative humidity on coalescence for precipitation sized drops falling freely at terminal velocity. Data on the effect of relative humidity on coalescence is important in that it provides information and data that can be applied to rain shafts below clouds and regions in clouds where entrainment of subsaturated air occurs.

2. EXPERIMENTAL APPARATUS AND DATA COLLECTION

A streak-strobe experiment was design, constructed, and used to collect data on the effect of relative humidity on the coalescence process. The same apparatus used to measure the effects of charge on coalescence under near saturated conditions has been used to determine the effect of relative humidity on coalescence (see paper 1P.17 in this volume for a more complete description of the apparatus). An abbreviated experiment description will be provided here.

Two drop generators are computer controlled to allow isolated pairs of drops to interact at terminal velocity. The drops are produced by forcing water through an orifice in a stainless steel disk. Capillary waves on the resultant water jet are excited by a piezoelectric transducer driven at a preferred frequency, resulting in a stream of uniformly sized drops. A charging electrode is used to highly charge the drops so that they can be deflected by a strong horizontal electric field. These highly charged drops are removed from the experiment. A high voltage pulse is imposed on the drop charging electrode to produce an isolated drop pair with moderate charge that will fall through the horizontal electric field and into the experiment chamber. Fine adjustment of the drops fall trajectory and position was controlled by micromanipulators mounted to the drop generators.

Drop collisions occurred in an enclosed chamber at laboratory temperature and pressure (about 21° C and 1000 mb). Interactions were recorded by two 35 mm cameras which viewed the drop collisions from orthogonal directions. Incandescent lamps were positioned and angled approximately 30° above the cameras optical axis. These lamps allowed for light to be focused through the drop, thereby creating a streak image as the drop fell through the viewing region of the cameras. Two streak lines corresponding to the drop fall paths were created on the film allowing for measurement of the drop separation distance.

Stroboscopic lights were placed along the horizontal axis and opposite to the position of the cameras. These lights allowed for the silhouette (back-lit) image of the drops to be captured on film during or immediately after collision, depending on positioning of drops in camera viewing field. The back-lit image of the drops provides information about the size, shape, and number of drops after interaction.

Drop charge measurements were taken with an electrometer, digital oscilloscope, and computer. Drop charges were adjusted to within 3.5% of desired charge before collisions were recorded photographically and again measured directly following. Measurements and readjustments of drop charges were performed frequently during experimental runs to insure drop charges remained relatively constant. During each photographic collection period the chamber's temperature and dew point were measured to provide accurate relative humidity records.

3. RESULTS

Three studies have been conducted in the Cloud Physics Lab of the Illinois State Water Survey that have examined the influences of relative humidity on the coalescence of precipitation sized drops. Schaufelberger (1990) studied collisions between minimally charged drops of radii 200 and 275 µm. Holdridge (1992) examined collisions between minimally charged drops of radii 200 and 425 µm. In the most recent investigation, Laird (1992) studied collisions at several different absolute relative charge levels between drops of radii 300 and 425 µm. Each of the three investigations conducted low humidity experiments with relative humidities near 30% and high humidity experiments (near saturation) with corresponding absolute relative charges.

Laird (1992) conducted a comprehensive investigation to examine the influences of relative humidity on drop coalescence. Four pair of experiments were used during this investigation. Each individual pair provided collision results at high and low humidities for a specified absolute relative charge level. It was found that bounce was significantly increased with a decrease in relative humidity from 96% to 30%. In addition, statistically significant decreases of temporary coalescence and increases in bounce events occurred with a decrease in relative humidity. The data from Laird (1992) showed an effect caused by relative humidity confined to a narrow range of drop charge where bounce is changing over to temporary coalescence.

Statistical tests were used to determine whether relative humidity influences existed for the number of bounces and temporary coalescence events at the two different humidities. In addition, differences in satellite production were examined for statistical significance. The results from Laird (1992) of the statistical tests for the data that showed an effect indicate that the two proportions (low humidity and high humidity) are statistically different with a 99% confidence level for both the number of bounces and temporary coalescence events. These results indicate that temporary coalescence is significantly enhanced when the relative humidity is increased from 30% to 96%. Results also show that bounce is significantly reduced with this increase in the relative humidity. These results are consistent with findings of Prokhorov (1954) that showed that low relative humidity inhibits coalescence. Differences in the satellite drop production were found to have a confidence level of 92%. Although increases in relative humidity caused statistically significant increases in the percentage of temporary coalescence events, the ratio of collisions resulting in satellite drops to the total number of temporary coalescence events at each humidity remained at approximately 0.30.

These results are in partial agreement with the findings of the relative humidity study conducted by Holdridge (1992). Her findings showed that temporary coalescence and satellite production was significantly enhanced with an increase in relative humidity from 38% to 100%. Schaufelberger's (1990) collision data does not show any significant differences between bounce and coalescence events at 30% and 95% relative humidities.

Coalescence efficiencies were determined for each high and low humidity experiment. There was little difference in the coalescence efficiencies for the two humidities over the range of charge used by Laird (1992). Schaufelberger (1990) and Holdridge (1992) concluded that there was no conclusive evidence to show any differences in coalescence efficiency as a result of a change in relative humidity at low charge levels.

The relative humidity effects are found by Laird (1992) to have occurred in the absolute relative charge region where bounce is changing over to temporary coalescence. However no relative humidity influence is present at the lower charge levels where only bounce and coalescence occur. These findings are consistent with findings from humidity studies done by Schaufelberger (1990) and Holdridge (1992). Schaufelberger found that no relative humidity influences were present at low charge levels where only coalescence and bounce occurred. In addition, Holdridge found that with an increase in relative humidity there was a statistically significant enhancement in temporary coalescence and satellite production. Although her study was done at a low charge level, there was coalescence, bounce, and temporary coalescence events present due to the more energetic collisions of her drop pair. The humidity findings from these studies suggest that influences due to relative humidity are only significant at charge levels where coalescence, bounce, and temporary coalescence occur.

Acknowledgments. This research was supported by National Science Foundation grant NSFATM 9020959.

4. REFERENCES

Holdridge, D. J., 1992: A laboratory investigation of electrostatic charge and relative humidity influences on the coalescence of precipitation size water drops. M. S. thesis, University of Illinois, Urbana-Champaign, Illinois, 89 pp.

Laird, N. F., 1992: A New Investigation of Relative Humidity and Electrostatic Charge Influences on the Coalescence of Precipitation Drops. M. S. thesis, University of Illinois, Urbana-Champaign, Illinois, 98 pp.

Lindblad, N. R., 1964: Effects of relative humidity and electric charge on the coalescence of curved water surfaces. *J. Colloid Sci.*, 19, 729-743.

Park, R. W., 1970: Behavior of water drops colliding in humid nitrogen. Ph.D. thesis, University of Wisconsin, Madison, Wisconsin, 577 pp.

Prokhorov, P. S., 1954: The effects of humidity deficit on coagulation processes and the coalescence of liquid drops. *Disc. Faraday Soc.*, 18, 41-51.

Schaufelberger, D. E., 1990: The influence of electrostatic charge and relative humidity on the coalescence of small free falling water drops. M. S. thesis, University of Illinois, Urbana-Champaign, Illinois, 78pp.

Effects of Charge on the Coalescence of Small Precipitation Drops at Terminal Velocity

Neil F. Laird, Harry T. Ochs III, Donna J. Holdridge, Daniel E. Schaufelberger, Robert R. Czys, and James Q. Feng

Illinois State Water Survey, Office of Cloud and Precipitation Research
2204 Griffith Drive, Champaign, Illinois 61820, USA

1. INTRODUCTION

A series of four laboratory investigations have been conducted in the Cloud Physics Lab of the Illinois State Water Survey. Each of these investigations has examined the influences of electrostatic charge on the coalescence of precipitation sized drops falling freely at terminal velocity. Previous investigations have examined influences of charge on drop-streams impacting flat water surfaces (Jayaratne and Mason, 1964), drop-streams impacting other drop-streams (Sartor and Abbott, 1972; Brazier-Smith et al., 1972) and droplets impacting a suspended collector drop (List and Whelpdale, 1969; Whelpdale and List, 1971). The recent studies at the Illinois State Water Survey were the first to observe and collect photographic data of drop pairs interacting in free fall at their terminal velocities. Four drop size pairs have been studied with radii of 340 and 190 μm, 275 and 200 μm, 425 and 200 μm, and 425 and 300 μm.

The range of charges used in these experiments coincide with charges observed in nature. Takahashi (1972) showed measurements for drops in developing cumulus clouds to be about 1.0×10^{-16} C and drop charges in thunderstorms to be about 1.0×10^{-12} C. In addition, collisions between drops of like sign were emphasized since drizzle drops in clouds are likely to have the same polarity (Takahashi, 1972).

2. EXPERIMENTAL APPARATUS

Deionized water was supplied to the individual drop generators from two pressurized 55 gallon polyethylene lined drums. The water contained sodium nitrate in concentrations of 26.25 and 8.75 mg/l to increase the electrical conductivity to aid the charging and discharging of drops with negligible effect on the surface tension (Czys and Ochs, 1988). Individual air regulators were used to maintain the air pressure in the drums. The large surface area of the water inside the drums minimized changes in hydrostatic pressure to help establish a nearly constant flow rate of water to the drop generators. The water was supplied to the drop generators through polyethylene tubing and a 0.2 μm filter where any contaminant particles were removed to prevent the drop generator orifice from becoming plugged.

The drop generators contained a hollow cylindrical piezoelectric transducer. The water flow filled the entire cavity of the generator and then exited through the prescribed diameter orifice disk to form a liquid water jet. The digital electronics supplied a square wave voltage to the transducer to produce radial vibrations of a frequency proportional to the amplitude of the applied voltage. These vibrations produced instabilities on the jet causing it to break into a stream of uniformly sized drops.

The actual radius of the uniform drops was determined by collecting the drop stream in a pre-weighed container for a prescribed amount of time (60 seconds). The container with the water sample was weighed to determine the mass of the sample. The mass of an individual drop was calculated by dividing the mass of the water sample by the drop generator vibration frequency. This procedure was used for both drop streams.

The initial velocity of each drop is approximately equal to the velocity of the jet as it leaves the drop generator. As the distance from the disk orifice increases the drops approach and finally stabilize at their terminal velocities. Initially the smaller drops exit the drop generator with a much greater velocity than that of their terminal velocity and the larger drops exit speed is only slightly larger than their terminal velocity. The difference in the small drops exit speed and terminal velocity is caused by the higher pressure needed to overcome the viscous resistance of the small exiting hole of the disk orifice.

The drop streams were charged by applying a voltage to the brass charging rings positioned near the location of the jet breakup. The charged streams were deflected into a drop collector as they fell through a strong horizontal electric field setup between two vertical, parallel electrodes (7 kV). This procedure removed all highly charged drops in the stream. Therefore, only drops with minimal charge could fall down through the center of the chamber. Drops with minimal charge were produced by momentarily switching (pulse) the charging voltage which allowed the drops to be positioned in the middle of the chamber as they fell. An IBM compatible personal computer was used to control the high speed/high voltage switching circuit to apply the pulses to the drop streams.

Drop collisions occurred in an enclosed chamber at laboratory temperature and pressure (about 21° C and 1000 mb). The experimental chamber was constructed from acrylic to allow for visual observations of the drops during their free fall. The chamber was isolated from mechanical vibrations with a vibration absorbing platform. The water containers were placed on similar platforms to isolate them from mechanical vibrations. The cameras, lights and sensors were on an aluminum frame separated from the platform to ensure any vibrations from these sources did not effect the drop production system.

The drop generators and charging electrodes operations were controlled by the system electronics. The generators were placed in close proximity to one another on top of the experiment chamber. The distance separating the generators was small to reduce the angle of the drops trajectory, so that upon collision the drops would have nearly vertical fall trajectories. Czys and Ochs (1988) concluded that there was no more than 0.5° between the vertical fall trajectories. Fine adjustment of the drops fall trajectory and position was controlled by micromanipulators mounted to the drop generators. Manipulation of the isolated drop pairs position was made so that collisions occurred in direct view of the two orthogonally placed cameras near the bottom of the chamber.

3. DATA COLLECTION PROCEDURE

Interactions were recorded by two 35-mm cameras which viewed the drop collisions from orthogonal directions. The cameras had digital recording data backs to imprint the time of interaction to the nearest second on the film. This procedure insured that frames of film containing collisions from each camera could be matched during analysis. Incandescent lamps were positioned and angled approximately 30° above the cameras optical axis. These lamps allowed for light to be focused through the drop, thereby creating a streak image as the drop fell through the viewing region of the cameras. Two streak lines corresponding to the drop fall paths were created on the film allowing for measurement of the drop separation distance.

Stroboscopic lights were placed along the horizontal axis and opposite to the position of the cameras. The strobe light frequency and camera triggering were controlled electronically for near simultaneous activation. These lights allowed for the silhouette (back-lit) image of the drops to be captured on film during or immediately after collision, depending on positioning of drops in camera viewing field. The back-lit image of the drops provides information about the size, shape, and number of drops after interaction. This information along with the drop streak data was useful in determining the outcome of the collision.

Drop charge measurements were taken with an electrometer, digital oscilloscope, and computer. Each individual experiment was designed to investigate the collision of drops with prescribed charges. Drop charges were adjusted to within 3.5% of desired charge before collisions were recorded photographically. Immediately after photographic data was collected drop charge measurements were made to insure that the drop charges had not drifted outside the allowed range. Measurements and readjustments of drop charges were performed frequently during experimental runs to insure drop charges remained relatively constant.

Temperature and humidity information was also collected during experimental runs. The experimental chamber walls were sprayed with deionized water. The chamber was then sealed and monitored with a temperature/humidity sensor until the chamber's environment was near saturation. During each photographic collection period the chamber's temperature and dew point were measured to provide accurate relative humidity records.

4. RESULTS

Ochs and Czys (1987) and Czys (1987) were the first in the series of four laboratory experiments conducted at the Illinois State Water Survey to investigate the influences of electrostatic charge on the coalescence process. Drops of radii R = 340 μm and r = 190 μm were produced using the computer-controlled dual-drop generator system with adjustable charge capability. Figure 1 shows the collision outcomes as a function of impact angle and absolute mean relative charge for positively charged drops. Two general areas of collision results are seen in Fig. 1, one for coalescence and the other for non-coalescence. Clearly an abrupt transition from collisions that result in coalescence to collision results depending on charge is observed at a critical impact angle of 43° ± 1°.

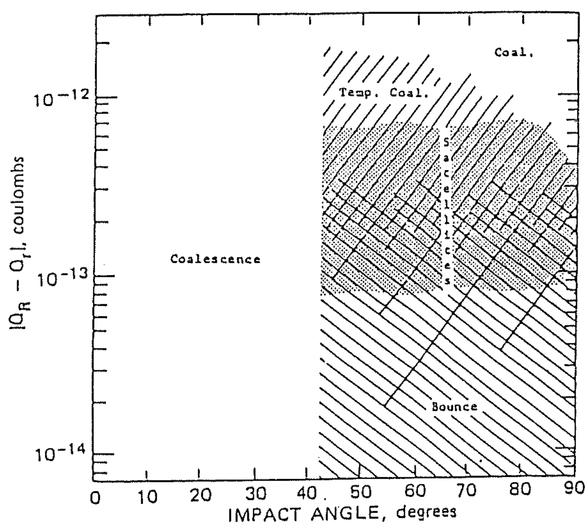

Figure 1. Summary of collision results as a function of impact angle and absolute value of mean relative charge. (From Ochs and Czys, 1987)

Czys showed that collisions with impact angles greater than the critical impact angle had results that were charge dependent. For impact angles greater than 43°, the magnitude of the mean relative charge must exceed a value of about 2 x 10^{-14} C before charge began to influence the collision result. Below this value all collisions with impact angle 43° resulted in bounce. Bounce was almost completely suppressed and an increase in collisions resulting in partial coalescence was observed when the mean relative charge was about 3 x 10^{-13} C. Czys (1987) also showed that permanent coalescence began to occur at glancing impact angles (near 90°) and progressed toward the critical impact angle with an increase in the mean relative charge until each collision resulted in coalescence at a mean relative charge of nearly 2 x 10^{-12} C.

Schaufelberger (1990) examined collisions between drops of radius 275 and 200 μm. Figure 2 shows that there are essentially two different collision outcome regions, one of coalescence and the other of bounce, separated by a charge independent critical angle of 42° ± 2°. Collisions occurring at angles smaller than the critical angle resulted in coalescence and angles greater than 42° resulted in bounce, except for impact angles near 90°, where grazing coalescence was found to be present at all levels of mean relative charge. This region of grazing coalescence progressed toward the critical impact angle for charge levels above 10^{-14} C, until all collisions above 10^{-13} C resulted in coalescence. During this study no collisions resulted in partial coalescence and no satellite drops were produced. Schaufelberger believed this to be a result of insufficient rotational kinetic energy present to separate the drops at the beginning stages of the coalescence process.

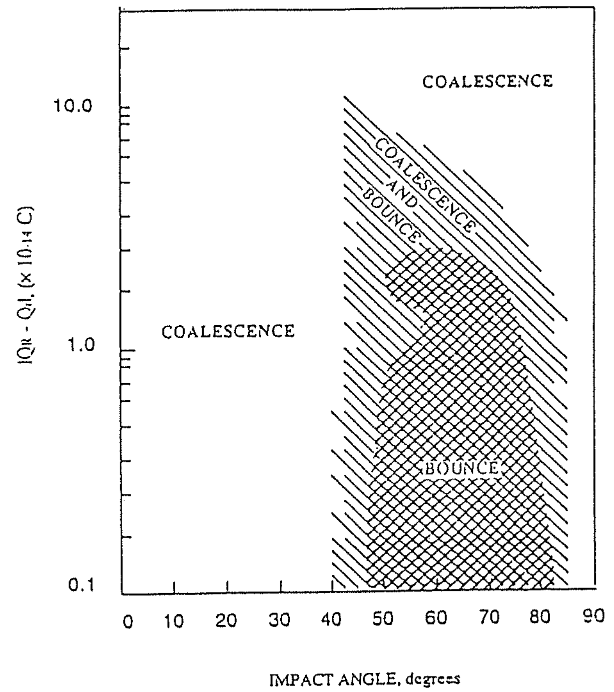

Figure 2. Summary of collision results as a function of impact angle and absolute value of mean relative charge. (From Schaufelberger, 1990)

Holdridge (1992) conducted an investigation to examine the influence of electrostatic charge on the coalescence process using a drop pair with radii of 200 and 425 μm. As shown in Fig. 3, Holdridge (1992) found some of the same general results as Czys (1987): a fairly constant transition between coalescence and non-coalescence collisions, the presence of a charge independent critical impact angle of approximately 49° ± 2°, and the suppression of collisions resulting in bounce as the mean relative charge was increased. The collisions resulting in bounce were replaced by temporary coalescence events and temporary coalescence events with satellite drops to an experimental maximum mean relative charge of 4.6 x 10^{-12} C. In addition, Fig. 3 shows that temporary coalescence with satellite production was present over the entire range of mean relative charges studied during this experiment. Holdridge suggested that this presence of partial coalescence is a result of the larger rotational energy for the drop pair of R = 425 μm and r = 200 μm.

The newest investigation by Laird (1992) examined the influence of electrostatic charge on the coalescence process using a drop pair with radii of 300 and 425 μm. Figure 4 shows that with minimal charge on the drops there existed a distinct cross-over from collisions resulting in coalescence to collisions resulting in bounce. This transition point clearly occurs at an impact angle of approximately 21.5°. Experiments at higher charge levels exhibit more of a transition zone, where coalescence events are mixed with non-coalescence events. As the impact angle increases these transition zones disappear and collisions result in non-coalescence events only. Results also show that bounce becomes suppressed for all absolute relative charge levels larger than 5 x 10^{-13} C. At a charge level of about 4 x 10^{-13} C the coalescence/temporary coalescence boundary begins to move from the largest impact angles toward the smaller impact angles with an increase in the absolute relative charge. This boundary converges from both the smaller and larger impact angles until collisions at all impact angles result in coalescence near an absolute relative charge of 4.7 x 10^{-12} C.

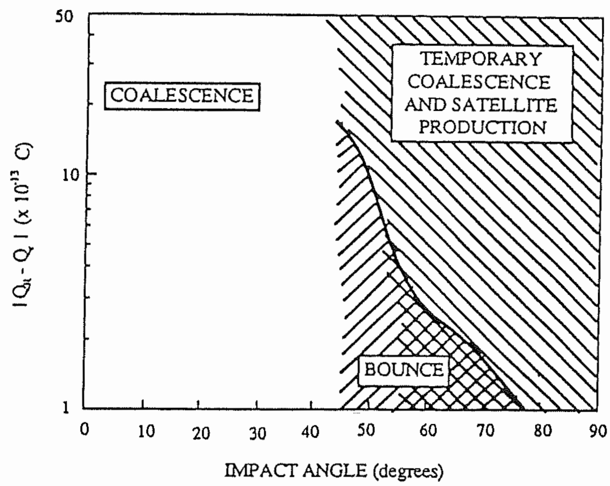

Figure 3. Summary of collision results as a function of impact angle and absolute value of mean relative charge. (From Holdridge, 1992)

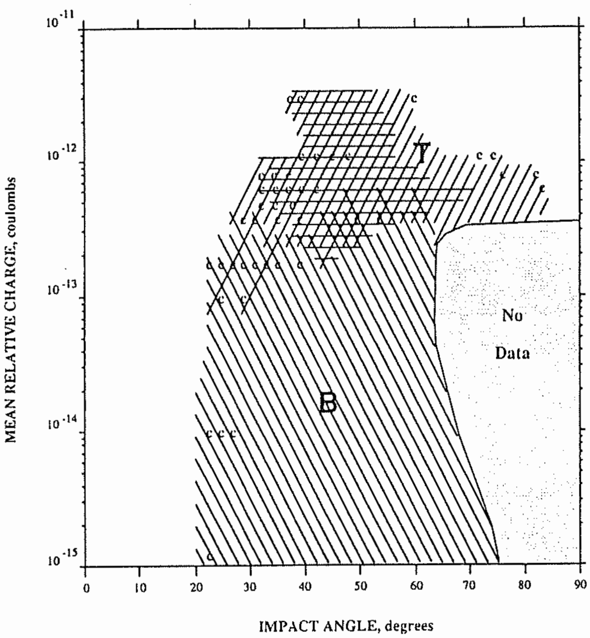

Figure 4. Summary of collision results as a function of impact angle and absolute value of mean relative charge. (From Laird, 1992)

5. COMPARISONS AND CONCLUSIONS

The first three studies of the influences of charge on drops interacting at their terminal velocities (Ochs and Czys, 1987; Czys, 1987; Schaufelberger, 1990; and Holdridge, 1991) found that there existed a charge independent critical impact angle. The critical impact angles separated coalescence events from non-coalescence events over their experimental ranges of absolute relative charge. Czys (1987) found a charge independent impact angle of 43° ± 1° for a drop pair of 340 and 190 µm. Schaufelberger's (1990) results showed a charge independent critical impact angle of 42° ± 2° for drops of radii 275 and 200 µm and Holdridge (1992) found a charge independent critical impact angle of 49° ± 2° for drops of radii 425 and 200 µm. Findings of Laird (1992) do not show any evidence for the existence of a charge independent critical angle for the drop pair of R = 425 µm and r = 300 µm. Experimental charge results found by Laird (1992) indicate that increases in the absolute relative charge lead to increases of the critical offset which distinguishes between coalescence and non-coalescence events.

The presence of coalescence events at large impact angles (grazing coalescence) was noted by both Czys (1987) and Schaufelberger (1990). Schaufelberger found that grazing coalescence events occurred over the entire range of absolute relative charge studied during his experiment. Czys noted that coalescence events started to appear at large impact angles when the absolute relative charge level was about 8.0 x 10^{-13} C and moved toward smaller impact angles with increases of relative charge. Laird (1992) shows that coalescence events begin to occur at the largest impact angles when a relative charge level of 5.4 x 10^{-13} C is reached and move toward smaller impact angles with increases in absolute relative charge. Since Laird (1992) did not observe collisions at large impact angles below 5.4 x 10^{-13} C agreement with the findings of Czys (1987) and Schaufelberger (1990) can not be determined.

Schaufelberger (1990) showed calculations of increasing coalescence efficiency with increases in absolute relative charge. His results exhibited a well defined correlation between the two parameters. However, results shown by Holdridge (1992) seemed to exhibited no relationship between these values. Laird (1992) has shown evidence in agreement with Schaufelberger's (1990).

Schaufelberger's (1990) data shows collision outcomes of coalescence and bounce for all levels of absolute relative charge. This can most likely be attributed to the fact that there was a limited amount of kinetic and rotational energies available for separation after the drops initial coalescence (V_{rel} = 64 cm/s and E_{rot} = 0.034). Holdridge (1992) observed temporary coalescence events at all charge levels. The existence of these events can most likely be attributed to the large relative velocity of the drop pair used in her investigation.

There is a significant difference between the coalescence efficiency values at lower charge levels of Laird (1992) and those found by Ochs, Czys, and Beard (1986), Ochs and Czys (1987), Schaufelberger (1990), and Holdridge (1992). Laird (1992) shows coalescence efficiencies near 12% for experiments with absolute relative charges between 1 x 10^{-15} C and 8 x 10^{-14} C. Where as the these other studies found coalescence efficiencies between 45% and 57% for experiments with low absolute relative charge. This significant new finding suggests that the evolution of precipitation may not progress as rapidly as previous coalescence efficiencies indicate.

These results suggest that charge levels in clouds can significantly affect the evolution of precipitation by two mechanisms. First, by promoting coalescence in situations that would normally result in bounce, precipitation development is enhanced and, second, by producing satellite drops, new raindrop embryos are created. These events may not be infrequent since the transition between bounce and permanent coalescence occurs over two orders of magnitude in relative charge. This data will not only be useful in refining numerical models of cloud microphysics, but it could also be used to further theories of precipitation production and improve precipitation forecasting.

Acknowledgments. This research was supported by National Science Foundation grant NSFATM 9020959.

effect on raindrops falling vertically if ∃ small collisional angle?

6. REFERENCES

Brazier-Smith, P. R., S. G. Jennings and J. Latham, 1972: The interaction of falling water drops: coalescence. *Proc. Roy. Soc. (London)*, **A326**, 393-408.

Czys, R. R., 1987: A laboratory study of interactions between small precipitation-size drops in free fall. Ph.D. thesis, University of Illinois, Urbana-Champaign, Illinois, 131 pp.

Czys, R. R., and H. T. Ochs, 1988: The influence of charge on the coalescence of water drops in free fall. *J. Atmos. Sci.*, **45**, 3161-3168.

Holdridge, D. J., 1992: A laboratory investigation of electrostatic charge and relative humidity influences on the coalescence of precipitation size water drops. M. S. thesis, University of Illinois, Urbana-Champaign, Illinois, 89 pp.

Jayaratne, O. W., and B. J. Mason, 1964: The coalescence and bouncing of water drops at an air/water interface. *Proc. Roy. Soc. (London)*, **A280**, 545-565.

Laird, N. F., 1992: A new investigation of relative humidity and electrostatic charge influences on the coalescence of precipitation droplets. M. S. thesis, University of Illinois, Urbana-Champaign, Illinois, 96 pp.

List, R., and D. M. Whelpdale, 1969: A preliminary investigation of factors affecting the coalescence of colliding water drops. *J. Atmos. Sci.*, **26**, 305-308.

Ochs, H. T., and R. R. Czys 1987: Charge effects on the coalescence of water drops in free fall. *Nature*, **327**, 606-608.

Sartor, J. D., and C. E. Abbott, 1972: Some details of coalescence and charge transfer between freely falling drops in different electrical environments. *J. Rec. Atmos.*, 479-493.

Schaufelberger, D. E., 1990: The influence of electrostatic charge and relative humidity on the coalescence of small free falling water drops. M. S. thesis, University of Illinois, Urbana-Champaign, Illinois, 78pp.

Takahashi, T., 1972: Electric charge of cloud droplets and drizzle drops in warm clouds along the Mauna Loa-Mauna Kea Saddle Road of Hawaii Island. *J. Geophys. Res.*, **77**, 3869-3878.

Whelpdale, D. M., and R. List, 1971: The coalescence process in raindrop growth. *J. Geophys. Res.*, **76**, 2836-2856.

LABORATORY MEASUREMENTS OF SPONTANEOUS OSCILLATIONS FOR MODERATE-SIZE RAINDROPS

Rodney J. Kubesh and Kenneth V. Beard
Illinois State Water Survey, Cloud and Precipitation Research, Champaign, Illinois

1. INTRODUCTION

Water drops have been observed to oscillate in the oblate-prolate mode in numerous wind tunnel studies. Brook and Latham (1968) found mean and extreme axis ratios for 4 to 6 mm diameter water drops that are remarkably similar to the raindrop observations of Jones (1959). The cause of oscillations for large raindrops is likely to be drop collisions which can occur frequently enough in heavy rainfall to maintain raindrop oscillations (Beard et al. 1983). Recent field studies have provided additional evidence of raindrop oscillations for 1 to 3 mm diameter (Chandrasekar et al. 1988; Sterlyadkin 1988; Beard and Tokay 1991). The source of these oscillations may be eddy shedding in the wake, a phenomenon recently investigated for water drops of 0.7 to 1.5 mm diameter falling at terminal speed (Beard et al. 1989, 1991; Beard and Kubesh 1991). Here we report on additional laboratory studies for moderate-size raindrops of 2.0 and 2.5 mm diameter.

An important aspect of all these studies is that the average axis ratio of oscillating raindrops is generally different than the equilibrium shape. The change in distortion can be significant (Jones 1959; Beard et al. 1989). For example, the differential polarization radar signal Z_{DR} (Seliga and Bringi 1976) is altered by up to 30% leading to erroneous estimates of drop size and rainfall rate. Thus, it is important for microwave scattering applications to determine raindrop shape changes caused by oscillations.

2. EXPERIMENT

A schematic of the experimental apparatus is given in Fig. 1. The system used to generate drops consisted of a water supply, orifice-jet drop generator, charging electrode, electrostatic deflection chamber and microcomputer. The digital circuits were controlled by an IBM PC with C language instructions. Capillary waves excited by a piezoelectric transducer caused the jet to break into uniform-size drops. Drops were charged by the concentric electrode and deflected by a high-voltage field, but periodically, the electrode voltage was pulsed off, allowing only isolated to drops to entered a fall column at terminal speed in a seven-story stairwell. After sufficient fall the drop shapes were capture on film using orthogonal cameras and strobes fired simultaneously in a burst to obtain multiple-images of single drops. An microscope micrometer was used to measure the horizontal and vertical dimensions h and v for calculation of the axis ratio, $\alpha = v/h$. To obtain frequency data, fall streaks were recorded as drops fell through a large light trap placed in the column (not shown in Fig. 1) with the drops illuminated by a spotlight at the angle of the primary rainbow. The microscope was used to determine the spacing of the interrupted fall streaks so that the frequency, $f = V/s$, could be calculated from s and the known fallspeed V.

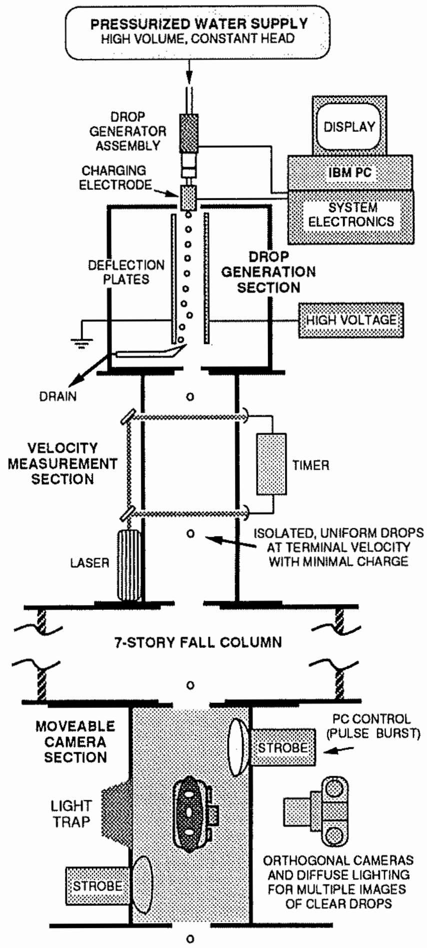

Fig. 1. 7-story experiment for measuring the oscillation shapes and frequencies of drops at terminal velocity.

3. RESULTS

The oscillation behavior was investigated for 2.0 and 2.5 mm diameter drops with sizes maintained to within 2% during or between experiments. For both sizes, photographs were taken at three levels yielding a total of six data sets. Measurements of 2.0 mm size were made at one, two, and seven floors of fall (corresponding to fall heights of H = 3.7 m, 7.3 m, and 25.6 m, referred to as 2A, 2B and 2C, respectively). Measurements of the 2.5 mm size were made at two, three, and seven floors of fall (corresponding to fall heights H = 7.3 m, 11,0 m, and 25.6 m, and referred to as 2.5A, 2.5B, and 2.5C). The mean and extremes of these data are plotted in Fig. 2 along with 95% confidence intervals and the theoretical curve for the equilibrium axis ratio (Beard et al. 1989).

how would this affect collisions?
parameterizations used in theoretical models of droplet growth

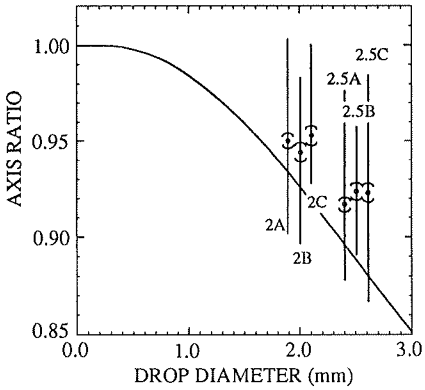

Fig. 2. Mean axis ratios at three levels for each drop size compared to equilibrium axis ratio. Range of axis ratios is indicated by vertical bars and 95% confidence intervals for mean are outlined by arcs. Data points for A and C are displaced horizontally to avoid overlap.

In all cases there were large variations in axis ratio as well as a shift of the mean axis ratio away from the equilibrium value, indicating the presence of oscillations. The 2.0 mm size has axis ratios with means that vary from 0.944 to 0.953 and extreme values ranging from 0.897 to 1.003. The standard deviations were comparable for the three data sets, averaging about 0.02. For the 2.5 mm size the mean varied between 0.917 and 0.924, with extremes of 0.867 and 0.984 with similar standard deviations.

Histograms of the number of observations per 0.01 axis ratio interval are shown in Figs. 3 and 4. For data sets 2A, 2B, and 2.5A, a significant fraction of the axis ratios falls below the equilibrium value α_{eq}, while for the rest of the data almost all the axis ratios lie above α_{eq}, (except for one data point each for 2C, 2.5B, and 2.5C). [The chi-square test probability was less than 1% that our observed distributions were sampled from normal distribution about the equilibrium axis ratio.] Beard and Kubesh (1991) showed that the only mode with axis ratios that scatter exclusively *above* the equilibrium curve is the transverse mode ($m = 1$). Thus, all data for the lowest level can be attributed to transverse mode oscillations, while the data for the top level must also contain some axisymmetric mode oscillations, for which the axis ratios vary both above and below equilibrium.

The axisymmetric mode in the 2B and 2.5B data persists longer than expected from viscous decay, indicating a positive feedback from pressure or drag forcing with complete damping retarded by several floors. The presence of transverse modes at the lowest level is consistent with the spatial pattern of the forcing due to eddy shedding on opposite sides of the upper pole of the drop. This may indicate that equilibrium oscillations have been achieved with the aerodynamic feedback from eddy shedding. From our observations we can conclude that times much longer than viscous decay are needed before the oscillations induced by the drop generator, or by drop collisions, die away.

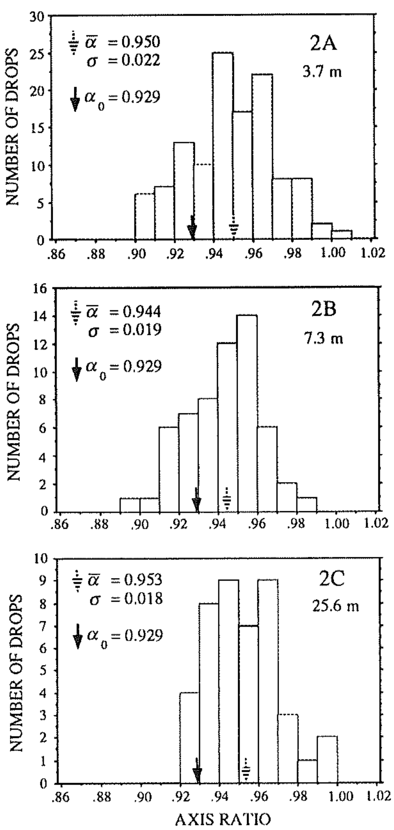

Fig. 3. Histograms of axis ratios for 2.0 mm diameter with number of drops given in 0.01 intervals of axis ratio. Equilibrium axis ratio is shown by black arrows and the mean axis ratio by striped arrows.

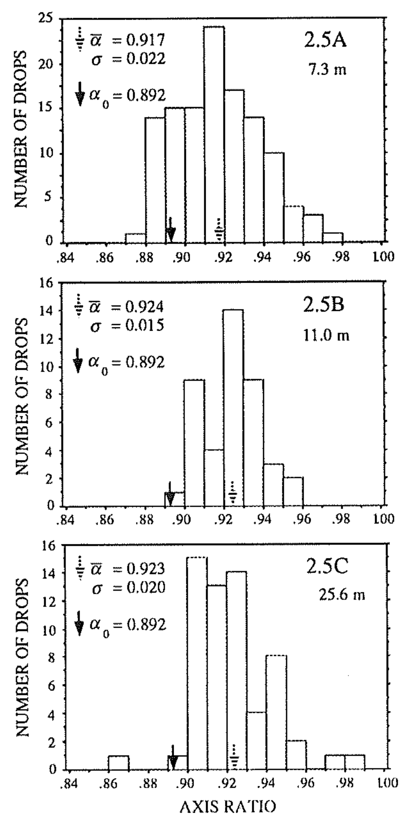

Fig. 4. As in Fig. 3 but for 2.5 mm diameter.

The peaks of the axis ratio distributions are near the mean in all cases. The distribution for equal-amplitude oscillations, however, should have the greatest number of observations near the extreme values, since the most time is spent near the turning points. For the axisymmetric mode the distribution would be saddle-shaped, unlike Figs. 3 and 4. Equal-amplitude transverse oscillations should be shaped like half a saddle, since the axis ratios only scatter on one side of the equilibrium value. Therefore, our observed axis-ratio distributions indicate a variety of oscillation amplitudes with most amplitudes less than the extremes shown.

The frequency distributions were bimodal, with one peak near the fundamental f_2 and the other at about twice the fundamental, near the first harmonic $f_3 = 1.94 f_2$. The Student's t distribution showed that at the 5% significance level the mean for each data set $\bar{f}$ was consistent with the hypothesis that $\bar{f} = f_2$ or $\bar{f} = f_3$ within the uncertainty in the measurement.

4. DISCUSSION

a. *Axis ratios*

Our axis ratio results are plotted on Fig. 5 for each size after combining the data from all three levels. The data points give mean values ($\bar{\alpha}$) and the vertical bars denote sample standard deviations (σ). Also plotted are data from Beard et al. (1991), Jones (1959), Chandrasekar et al. (1988) and Sterlyadkin (1988). One curve is shown for equilibrium axis ratios and another for the shifted axis ratios postulated by Goddard and Cherry (1984). The latter were devised to rectify values of Z_{DR} measured with a high-resolution radar and values calculated from raindrop size distributions measured by disdrometer.

The average axis ratios for the combined data at 2.0 and 2.5 mm diameter are $\bar{\alpha}$ = 0.949 and 0.920, respectively. Values for these sizes from Chandrasekar et al. are $\bar{\alpha}$ = 0.950 and 0.913 (estimated from their Fig. 5g), whereas values from Goddard and Cherry are $\bar{\alpha}$ = 0.945 and 0.904. By using the normal deviate test, we found that our mean axis ratios were likely to have come from the same population as those of Chandrasekar et al. (at the 5% significance level). In a similar comparison, the data of Jones (1959) for 2.0 and 2.5 mm ($\bar{\alpha}$ = 0.983 and 0.975) were found to be from a different population. These higher mean axis ratios may be from oscillations induced by collisions, since the data were obtained for high rainfall rates in thunderstorms.

Goddard and Cherry's axis ratios are shifted in the same sense as our results out to d = 3 mm. Not enough information is available to perform a normal deviate comparison with their results, but their values for 2.0 and 2.5 mm lie very close to ours. Sterlyadkin (1988) also reports measurements of axis ratio. He did not have data points at our two sizes but provided an empirical equation which gives α = 0.940 and 0.898 for 2.0 and 2.5 mm, respectively. Since his values lie outside the 95% confidence intervals for our data, his results may be significantly lower.

b. *Oscillation frequencies and modes*

In our experiments, drops were found to oscillate at the lower two levels, even though viscous decay theory predicts that oscillation should have been negligible. Such observations show that external forcing acts in opposition to viscous dissipation. The shift in mean axis ratio and the dominance of the transverse mode indicate that the forcing arises from resonance with the shedding of eddies in the drop wake, in agreement with Beard et al. (1991). Resonant oscillations extend far beyond the 1 mm size originally proposed by Gunn (1949), however, as large axis ratio variations are observed even for d = 2.5 mm. Oscillations for raindrops this large are generally believed to originate from collisions (e.g., Chandrasekar et al. 1988), but the results of our study indicate that oscillations of moderately sized raindrops are affected by aerodynamic feedback as well. Such feedback may prolong axisymmetric oscillation induced by collisions and promote steady-state oscillations induced by eddy shedding.

The largest amplitude steady-state oscillations should occur when the natural frequency of the drop matches the eddy-shedding frequency, producing resonance. A large mismatch seems to exist, however, between the oscillation and eddy shedding frequencies for 2.0 and 2.5 mm drops based on results for spheres. Several factors may aid oscillations despite poor frequency matching. Subharmonic resonance can occur if the eddy shedding frequency is equal to some integer multiple of f_2 or f_3 (Feng and Beard, 1991). In addition, pressure changes at the drop surface resulting from the changing shape may control the instability in the wake, making the frequencies come into phase with each other.

c. *Conclusions*

The experimental data for 2.0 and 2.5 mm diameter drops, after 7 stories of fall at terminal velocity, show that the axis ratios vary, but scatter only above equilibrium values. This result is consistent with the behavior of transverse mode oscillations at the fundamental and first harmonic (Beard et al. 1991). Corresponding frequency data confirms that practically all oscillations occur at these two frequencies. The transverse modes are a likely consequence of transverse forcing by eddies detaching alternately from opposite sides of the upper pole.

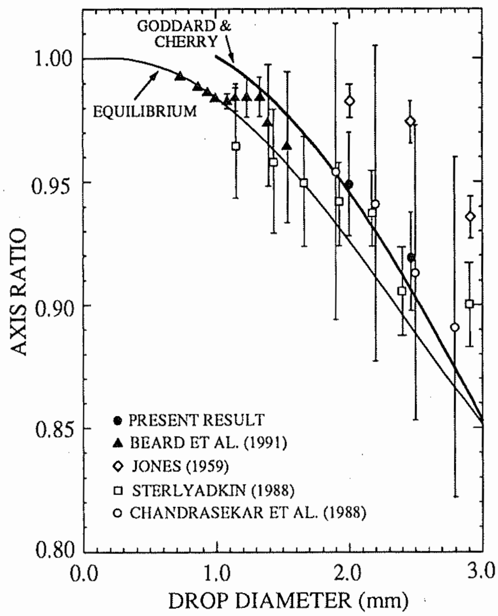

Fig. 5. Observed raindrop distortion as a function of size. Means and standard deviations are plotted for various data.

Future studies can take several approaches. More detailed information must be obtained on the transient behaviors of oscillating drops before we can build deterministic models of raindrop shape. Measurements of axis ratio and frequencies are needed for larger drops. Even though there are relatively few large raindrops, their contribution to radar reflectivity is appreciable because of the d^6 dependence of reflectivity. If the role of eddy shedding becomes insignificant for larger drops, it may still be necessary to characterize the transient behavior of collision-induced oscillations, especially if the decay is slowed by aerodynamic feedback. Raindrop shape should also be measured by additional field studies. Hopefully, new laboratory and field data can be synthesized to yield a more complete picture of raindrop shapes in various kinds of precipitation.

Acknowledgements. We thank Harry Ochs for his advice on experimental design and construction. This research was supported by the National Science Foundation under Grants ATM 84-19490, 86-01549 and 87-22688.

5. REFERENCES

Beard, K. V., D. B. Johnson, and A. R. Jameson, 1983: Collisional forcing of raindrop oscillations. *J. Atmos. Sci.*, *40*, 2, 455-462.

Beard, K. V., J. Q. Feng, and C. Chuang, 1989: A simple perturbation model for the electrostatic shape of falling drops. *J. Atmos. Sci.*, *46*, 2404-2418.

Beard, K. V., H. T. Ochs, and R. J. Kubesh, 1989: Natural oscillations of small raindrops. *Nature*, *342*, 408-410.

Beard, K. V., R. J. Kubesh, and H. T. Ochs III, 1991: Laboratory measurements of small raindrop distortion. Part 1: Axis ratios and fall behavior. *J. Atmos. Sci.*, *48*, 698-710.

Beard, K. V., and R. J. Kubesh, 1991: Laboratory measurements of small raindrop distortion. Part 2: Oscillation frequencies and modes. *J. Atmos. Sci.*, *48*, 2245-2264.

Beard, K. V. and A. Tokay, 1991: A field study of small raindrop oscillations. *Geophys. Res. Lett.* 18. 2257-2260..

Brook, M., and D. J. Latham, 1968: Fluctuating radar echo: modulation by vibrating drops. *J. Geophys. Res.*, *73*, 7137-7144.

Chandrasekar, V., W. A. Cooper, and V. N. Bringi, 1988: Axis ratios and oscillations of raindrops. *J. Atmos. Sci.*, *45*, 1323-1333.

Feng, J. Q., and K. V. Beard, 1991: Resonances of a conducting drop in an alternating electric field. *J. Fluid Mech.*, *222*, 417-435.

Goddard, J. W. F., and S. M. Cherry, 1984: The ability of dual-polarization radar (coplanar linear) to predict rainfall rate and microwave attenuation. *Radio Sci.*, *19*, 201-208.

Gunn, R., 1949: Mechanical resonance in freely falling drops. *J. Geophys. Res.*, *54*, 383-385.

Jones, D. M. A., 1959: The shape of raindrops. *J. Meteor.*, *16*, 504-510.

Seliga, T. A., and V. N. Bringi, 1976: Potential use of radar differential reflectivity measurements at orthogonal polarizations for measuring precipitation. *J. Appl. Meteor.*, *15*, 69-76.

Sterlyadkin, V. V., 1988: Field measurements of raindrop oscillations. *Izvestiya, Atmospheric and Oceanic Physics*, *24*, 6, 449-454.

HAILSTONE HEAT AND MASS TRANSFER MEASUREMENTS USING A THERMAL IMAGING SYSTEM IN AN ICING TUNNEL

Blair J.W. Greenan and Roland List

Department of Physics, University of Toronto
Toronto, Ontario, M5S 1A7, Canada

1. Introduction

The functional form of the solutions to boundary layer equations for flow over a surface allow for the definition of three dimensionless numbers termed the coefficient of friction, the Nusselt number, and the Sherwood number which characterize the velocity, thermal, and concentration boundary layers, respectively. All three of these dimensionless quantities have a functional dependence on the Reynolds number of the flow while the Nusselt and Sherwood numbers also depend upon the Prandtl and Schmidt numbers, respectively, which are constant for atmospheric conditions. The Nusselt number is equal to the dimensionless temperature gradient at the surface and provides a measure of the convective heat transfer occurring at the surface. Empirical relationships characterizing one and two-phase, single-component flow around cylinders and spheres have been determined in detail (Incropera and DeWitt, 1990). However, studies of two-phase (water vapor and droplets), two-component (air and water) flow remain limited resulting in an inadequate characterization of processes such as accretional growth of ice particles at realistic atmospheric conditions.

Analysis of the hailstone heat and mass transfer results from Garcia and List (1992) has indicated that existing theories describing hail growth (Macklin, 1963; List, 1963,1977) need to be tested more thoroughly because they do not agree well with experimental data. Hence, new laboratory experiments have been designed to determine the validity of the hailstone heat and mass transfer theory under a variety of growth conditions. The purpose of this paper is to present results from a series of experiments in which air pressure was varied while all other controllable parameters remained constant.

2. Theory

The rate of mass transfer from the airstream to a gyrating ice spheroid may be represented by

$$\frac{\Delta m}{\Delta t} = \bar{A}_c(t)\, V E_{net} W_f \tag{1}$$

where Δm is the accreted mass, Δt is the icing duration, V is the airflow speed, and is W_f the liquid water content. $\bar{A}_c(t)$ is defined as the hailstone cross-section encountered by the flow, averaged over one nutation/precession cycle of the gyrator, as it varies with time due to growth. The unknown parameter in equation (1) is the net collection efficiency, E_{net}, defined as the mass fraction of water in the swept-out volume which is permanently incorporated into the hailstone.

The heat transfer equation governing the growth of the hailstone is expressed as

$$Q_{CC} + Q_{CP} + Q_{DS} = Q_F \tag{2}$$

where Q_{CC} represents the heat transfer rate due to forced convection, Q_{CP} is the heat transfer rate due to accretion of cloud droplets, Q_{DS} is the transfer rate due to the deposition/sublimation of water at the hailstone surface, and Q_F represents the latent heat released by the ice deposit during freezing, L_f. Q_{CC} and Q_{DS} are both functions of the Reynolds number, which decreases with the reduction of tunnel air pressure, while Q_{CP} and Q_F are functions of V which remained constant for this series of experiments. Therefore, it is impossible to simulate low pressure icing conditions at lab pressure. Measurements of the hailstone surface temperature, t_s, using a thermal imaging system enables equation (2) to be reduced to one unknown, the Nusselt number, Nu, which may be calculated using

$$Nu = \left(\frac{\Delta m}{\Delta t}\right)\left[I_f L_f - \left((c_{wits} + c_{wta})\frac{(T_s - T_a)}{2} + \left(\frac{E}{E_{net}} - 1.0\right)\left((c_{wits} + c_{wta})\frac{(T_s - T_a)}{2} - I_s L_f \right)\right)\right] \left[A_s \chi D \pi k_a (T_s - T_a) + 0.00206\, L_{vs} D_{wa}\left(\frac{e_s}{T_s} - \frac{e_a}{T_a}\right)\right]^{-1} \tag{3}$$

where I_f is the ice fraction of the accretion, c_{wits} is the specific heat of water/ice at the surface temperature, c_{wta} is the specific heat of water at the air temperature, E is the collection efficiency, and I_s is the ice fraction of the shed water; A_s represents a correction factor for the surface area of the spheroid in comparison to a sphere of the same diameter, χ is a heat transfer correction factor due to oblateness of the hailstone, D is the major axis diameter, k_a is the thermal conductivity of air, and L_{ds} is the latent heat of deposition/sublimation; D_{wa} represents the diffusivity of water vapor in air, e_a is the saturation vapor pressure over water at the air temperature, and e_s is the saturation vapor pressure over the surface of the hailstone.

3. Experiments

Hail growth by accretion of supercooled water droplets was simulated in a vertical, closed-circuit icing wind tunnel with controllable air speed, pressure, temperature, and liquid water content (List et al, 1987).

Figure 1: University of Toronto Cloud Physics Icing Wind Tunnel measuring section (1) with Agema thermal imaging system (2) in the foreground.

The measuring section of the tunnel had horizontal dimensions of 17.8 cm x 17.8 cm. Initial hailstone models were smooth, oblate ice spheroids with a major axis diameter, D, of 2.0 ± 0.1 cm and an aspect ratio of 0.67. These models were mounted on a particle suspension system in the measuring section which allowed the spheroid to execute a symmetric gyration motion with a spin frequency of 9.5 Hz and a nutation/precession frequency of -14.0 Hz. The data acquired represent a series of experiments in which the wind tunnel pressure was varied from 100 to 40 kPa while all other controllable conditions were held constant. Each hailstone grew for 160 seconds at an air temperature, t_a, of -15°C, an airflow speed, V, of 18 m s^{-1}, and liquid water content, W_f, of 3 g m^{-3}.

The surface temperature of the hailstone was obtained using an infrared thermal imaging system (Agema model 880LWB) which produced real-time two-dimensional images of the hailstone surface temperature during growth. The imaging system detector, composed of Mercury Cadmium Telluride, had a spectral response over 8-12 μm and a sensitivity of 0.1°C at -15°C.

4. Results

The final major axis diameter of the hailstones produced at various tunnel air pressures (Figure 2) indicates that all the particles grew to approximately the same size in the same growth time. However, the net collection efficiency is observed to increase linearly as the air pressure decreases due to the change in the air flow around the hailstone at low pressures. The fit for the E_{net} data produces a y-intercept at zero air pressure close to unity and indicates that the results are similar to theoretical calculations for potential flow around a sphere of the same diameter (Langmuir and Blodgett, 1946), which is 0.87 at 100 kPa for the water drop size distribution used. Interestingly, the increase in E_{net} implies an increase in mass accreted while the final diameter remains constant and hailstone shape is conserved (Figures 3a and 3b); the explanation for this is correlated to the reduced heat transfer at lower air pressure which causes accretion to become increasingly dense as the tunnel pressure decreases. The increase in density is visually evident as the hailstone transforms from a slightly opaque structure with closely packed bumps, several millimeters in diameter, covering large areas surrounding the poles at 100 kPa to a very transparent structure with a very smooth surface at 40 kPa. The trend from an opaque accretion to a transparent one suggests that the amount of air in the structure is decreasing and, therefore, the density of the accretion is increasing.

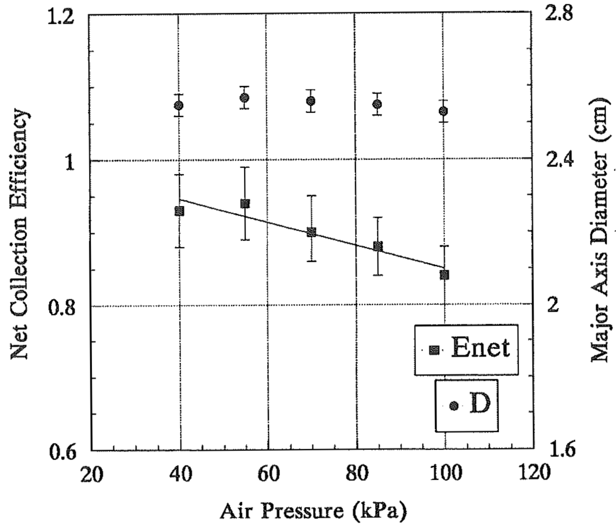

Figure 2: E_{net} and D as a function of air pressure. Error bars represent ±0.1cm for diameter and ±5% for net collection efficiency.

The reduction in air density due to the decrease in tunnel pressure causes a corresponding reduction in the amount of heat transferred from the hailstone to the environment by convection. Hence, the surface temperature of the hailstone rises as the pressure is reduced due to the continued release of latent heat of freezing (Figure 4). The results of the Nusselt number calculation for the experimental data is compared to extrapolated empirical relations of Ranz and Marshall (1952a and b), hereafter R&M, determined for heat transfer from smooth spheres (Figure 5). A shape correction factor is included in the empirical results presented to allow comparison with the spheroidal hailstone results. The data indicates a good agreement between the Nusselt number predicted by R&M and the values calculated using the data from the present experiment with the largest difference between the two data sets being approximately 15% at an air pressure of 40 kPa. This disparity is not significant enough to cause substantial errors in cloud models which incorporate hail growth. There are a number of differences between the hailstones grown for these experiments and the empirical correlation for smooth spheroids, such as the change in surface roughness with decreasing tunnel pressure, which makes it difficult to compare the two sets of results.

The functional form of the relationship between Nusselt number, Nu, and Reynolds number, Re, as

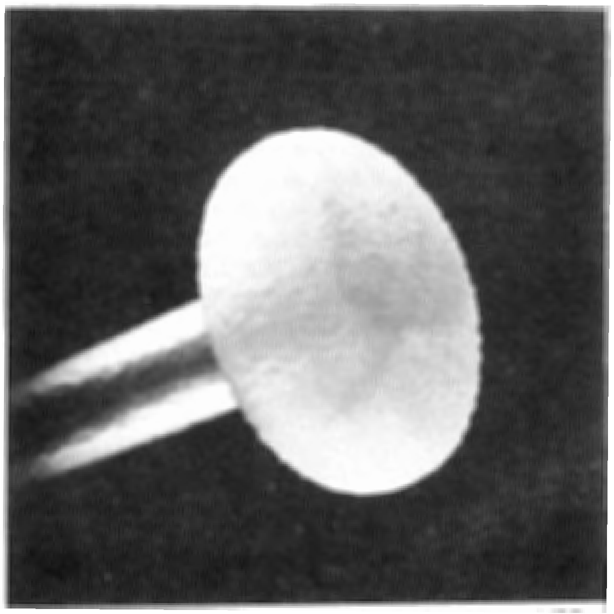

Figure 3a: Hailstone grown at p_a = 100 kPa, t_a = -15°C, V = 18 m s^{-1}, and W_f = 3 g m^{-3} with final major axis diameter of 2.53 cm. Equator is transparent, poles are opaque and surface roughness increases towards poles.

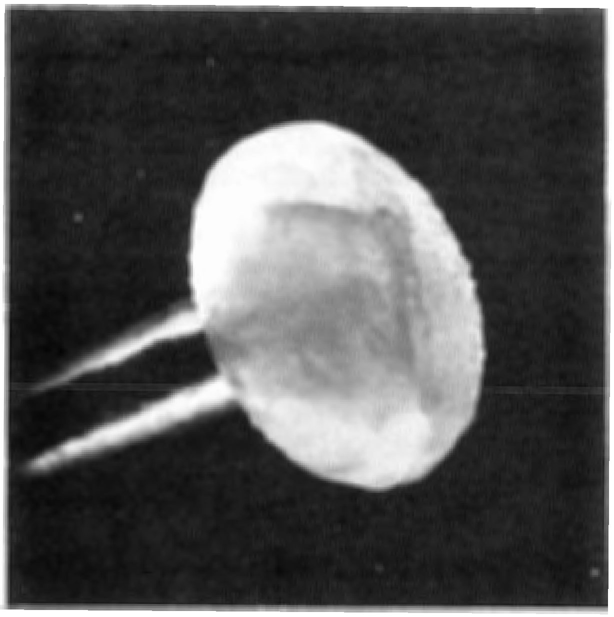

Figure 3b: Hailstone grown at p_a = 40 kPa, t_a = -15°C, V = 18 m s^{-1}, and W_f = 3 g m^{-3} with final major axis diameter of 2.55 cm. Accretion transparent over whole surface and hailstone is smooth with the exception of small area at poles.

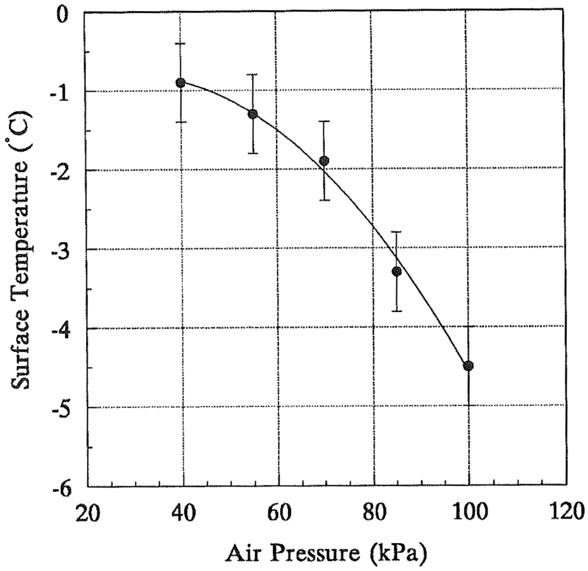

Figure 4: Surface temperature, t_s, as a function of air pressure with error bars of ±0.5°C representing instrument precision.

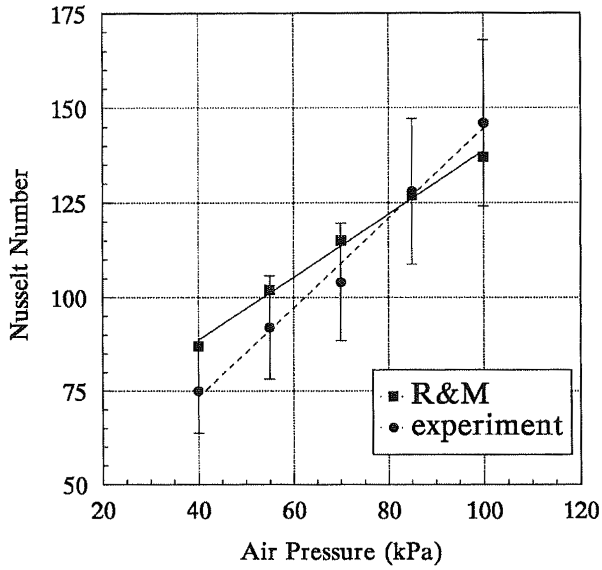

Figure 5: Nusselt number as a function of air pressure for both the present experiment and the empirical relation of Ranz and Marshall (1952a and b). Error bars of ±15% are assigned to Nu.

determined by R&M, can be expressed as

$$Nu = a\,Re^{b} \tag{4}$$

where the constant a incorporates the Prandtl number. A fit of the experimental data (Figure 6) demonstrates that *a* equals 0.75 as compared to 0.76 for R&M and *b* equals 0.7 as compared to 0.5 for R&M. Therefore, the functional dependence of Nusselt number on Re is very similar for both data sets.

While these results imply that the existing theory can be used to predict hail growth at lower air pressure, problems will arise in cases where spongy ice or shedding of accreted water occurs because these properties are difficult to determine theoretically and little experimental data exists for such growth conditions.

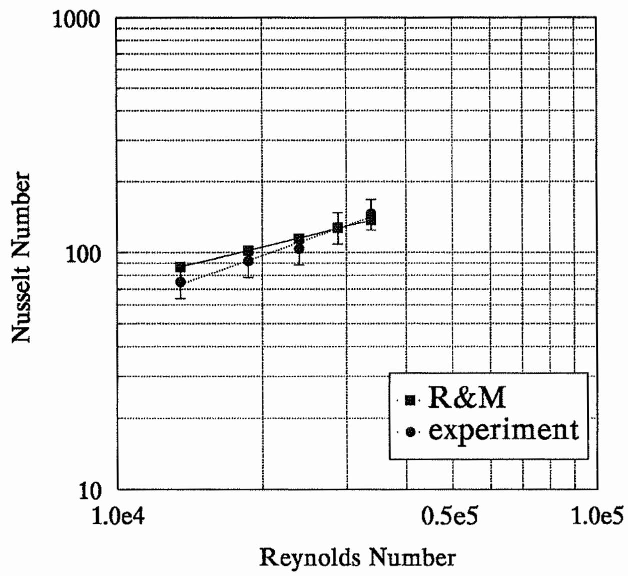

Figure 6: Comparison of present experimental Nusselt number to the empirical values for smooth spheroids plotted as a function of Reynolds number.

5. Conclusions

Hail growth simulation experiments performed at varying air pressures demonstrate that net collection efficiency varied inversely with tunnel pressure. The reduction in air density also acts to reduce the rate of heat transfer from the hailstone to its surroundings, causing surface temperature to increase as the tunnel pressure decreases. Most importantly, experimental Nusselt number calculations using existing hail growth theory show only a slight deviation from the extrapolated empirical relations of Ranz and Marshall (1952a and b) indicating that such theory is adequate for describing accretional processes at low air pressures. A more complete investigation of the existing heat and mass transfer theory is being performed to determine whether any modifications are necessary.

Acknowledgments

This research was sponsored by the Natural Sciences and Engineering Research Council of Canada (NSERC). The thermal imaging system was made available by the Ontario Laser and Lightwave Research Centre at the University of Toronto. One of the authors (BG) is grateful for support through the NSERC postgraduate scholarship, the Ontario Graduate Scholarship, and the Walter F. Sumner Memorial fellowship.

References

Garcia-Garcia, F., and R. List, 1992: Laboratory measurements and parameterizations of supercooled water skin temperatures and bulk properties of gyrating hailstones. *J. Atmos. Sci.*, (in press).

Incropera, F.P. and D.P. DeWitt, 1990: *Fundamentals of Heat and Mass Transfer*, Third Edition, John Wiley and Sons, Toronto, 919 pp.

Langmuir, I., and K.B. Blodgett, 1946: Mathematical investigation of water droplet trajectories. *Collected Works of Irving Langmuir*, **10**, Pergamon Press, 348-393.

List, R., 1963: General heat and mass exchange of spherical hailstones. *J. Atmos. Sci.*, **20**, 189-197.

List, R., 1977: Ice accretion on structures. *J. Glaciol.*, **19**, 451-465.

List, R., G.B. Lesins, F. Garcia-Garcia, and D.B. McDonald, 1987: Pressurized icing tunnel for graupel, hail and secondary raindrop production. *J. Atmos. Oceanic Technol.*, **4**, 454-463.

Macklin, W.C., 1963: Heat transfer from hailstones. *Quart. J. Roy. Meteor. Soc.*, **89**, 360-369.

Ranz, W.E., and W.R. Marshall, Jr., 1952a: Evaporation from drops. Part I. *Chem. Eng. Prog.*, **48**, 141-146.

Ranz, W.E., and W.R. Marshall, Jr., 1952b: Evaporation from drops. Part II. *Chem. Eng. Prog.*, **48**, 173-180.

FREE-FALL PATTERNS AND VELOCITY VARIATIONS OF PLATE-LIKE SNOW CRYSTALS

Masahiro Kajikawa

Department of Earth Science, Akita University, Akita 010, Japan

1. INTRODUCTION

The aggregation of snow crystals to form snowflakes is an important process in the growth of precipitation particles in clouds. Information of the unstable falling motion (the secondary motion) of the crystals in the atmosphere, as well as the fall velocity (the mean vertical velocity) is required to investigate the aggregation process, as pointed out by Sasyo (1971) and Rogers (1974).

Zikmunda and Vali (1972) observed the falling motion of rimed snow crystals using a stereoscopic camera system. They concluded that the mass distribution and flow disturbances due to surface features were responsible for the complicated fall patterns. These patterns involve the rotation about the vertical axis and oscillations in the vertical plane.

Since the fall velocity ($\overline{V}z$) of individual snow crystals was previously descrived as a function of the size (d) or the mass (M) (Kajikawa, 1975; Heymsfield and Kajikawa, 1987), this paper will examine the analytical results of free-fall patterns and velocity variations for unrimed plate-like crystals, obtained at the Mt. Teine Observatory (1024 m altitude) of Hokkaido University.

2. METHOD OF OBSERVATION

The method of measurement of falling motion is the same as the observation of early snowflakes (Kajikawa, 1982). The procedure here will be described briefly. For the measurement of three-dimensional motion, a falling snow crystal was illuminated by stroboscopic light and photographed by means of a stereoscopic camera system.

The co-ordinates of the crystal were calculated from successive corresponding points (the center of images) on the pair of photographs. The fallen crystals were caught on a sampling plate and were microphotographed for determining shape, size, and mass.

3. RESULTS

3.1 The free-fall pattern of unrimed plate-like snow crystals

The number of snow crystals exhibiting an unstable motion due to vortex shedding to the rear of the crystal gradually increases when the Reynolds number ($Re=\overline{V}z\, d/\nu$) exceeds about 40 during free-fall in stagnant air. Here, ν is the kinematic viscosity of air. The unstable falling motion at first clearly appears as an oscillation about the axis in the plane of the plate-like crystals. Re at the beginning of oscillation is considerably smaller than the value (about 100) found in model experiments (e.g., List and Schemenauer, 1971; Podzimek, 1984). This is due to the asymmetry (the difference between the center of gravity and the geometrical center) of crystals.

Next, the unstable falling motion proceedes to swing from side to side and then to rotate or spiral about the vertical axis. The tumbling motion did not appear in the present observations.

The limit of the onset of unstable falling motion is determined by the Best or Davis number ($Be=Cd\, Re^2$) and the non-dimensional moment of inertia ($I^*=Ia/\rho d$, stability number) as shown in Fig.1. Here, Cd is the drag coefficient of the falling crystals, $Ia=M\, d^2/16$ the moment of inertia about the a-axis of the crystals, and ρ the density of air. In the calculation of Ia and Be, all of the plate-like crystals were regarded as hexagonal plates measuring d in length along the a-axis. In Fig.1, the data of previous analyses (Kajikawa, 1975) are presented to determine the boundary be-

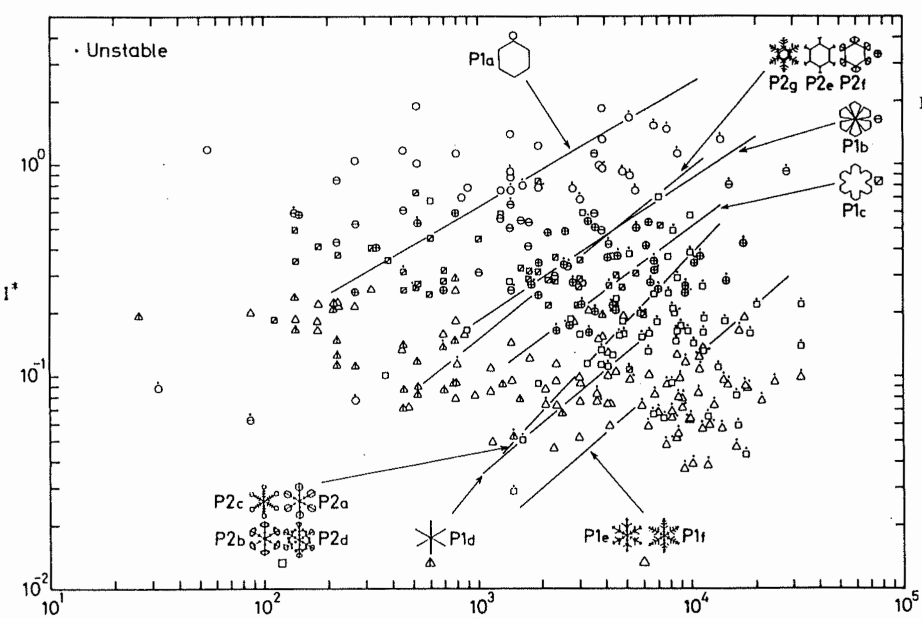

Fig.1. The relationship between the stability number (I^*) and the Best number (Be) showing the boundary between stable and unstable falling motion for various plate-like crystals. The dot above a given crystal symbol indicates the crystal underwent unstable motion during its fall. The classification of the snow crystals follows in the same manner as that given by Magono and Lee (1966).

Table 1. The lower critical values of size (d) and the Reynolds number (Re as a function of fall velocity) for all crystals exhibiting the unstable falling motion.

Crystal Shape	d (mm)	Re
P1a	1.23	47.0
P1b	1.50	43.0
P2g P2e P2f	1.68	60.7
P1c	1.94	53.7
P2c P2a P2b P2d	2.29	77.9
P1d	2.55	59.9
P1e P1f	3.50	90.7

Table 2. The four types of unstable fall patterns and the observed number of plate-like crystals in each type.

TYPE / Crystal Shape	Nonrotation	Swing	Rotation	Spiral
P1a P1b	1	0	1	0
P2g P2e P2f	4	1	2	2
P2c P2a P2b P2d	5	7	4	1
P1e P1f	5	15	6	0
Total Number (Rate, %)	15 (27.8)	23 (42.6)	13 (24.1)	3 (5.6)
Early Snowflakes (Rate, %)	31 (11.0)	8 (2.8)	51 (18.0)	193 (68.2)

tween the stable and the unstable falling motion, indicated by the solid lines for various shaped crystals. The classification of the snow crystals follows in the same manner as given by Magono and Lee (1966). The lower critical values of d and Re, for which all crystals exhibit unstable falling motion, are shown in Table 1. It can be seen that several of the dendritic crystals, which have the property of large internal ventilation, fall with a stable pattern over the range of larger Re than the case of simple hexagonal plates. This fact suggests that the stability of the falling motion is influenced by the internal ventilation of the crystals, as has been determined in model experiments (Podzimek, 1984).

According to the horizontal movement of crystals, unstable fall patterns were classified into four types as follows:

1) The nonrotation type which exhibits falling motion without rotation about the vertical axis, but with horizontal movement roughly of a straight line.

2) The swing type having falling motion without rotation about the vertical axis, but with horizontal movement of a zigzag line.

3) The rotational type where the falling motion has rotation about the vertical axis, with the horizontal movement traced as part of an ellipse.

4) The spiral type where the falling motion displays rotation about the vertical axis, with horizontal movement of a spiral.

It should be noted that the rotational type approaches the spiral type with large amplitudes or long periods, if the observation of the falling motion is performed over a longer distance. The classified unstable fall patterns along with their observed number for each type are summarized in Table 2, including the data for early snowflakes (Kajikawa, 1982) for comparison purposes. From this table it can be seen that the rate of the spiral type is less, and in turn, the rate of the nonrotation and swing types are greater than that of the early snowflakes. The reason for this may be found in the difference in degree of asymmetry. Namely, it appears likely that early snowflakes become more asymmetrical as they grow through the aggregation of crystals than the individual crystals themselves.

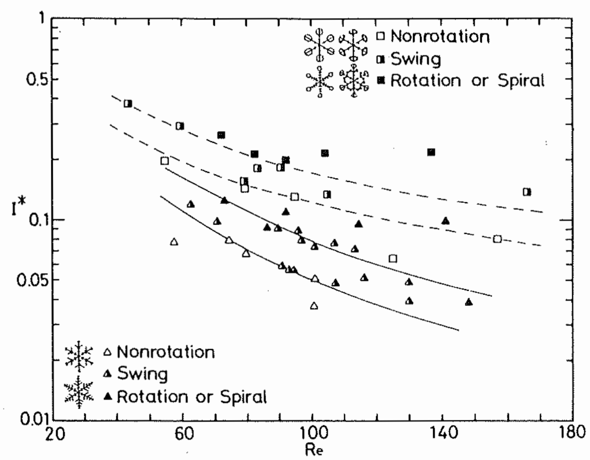

Fig.2. The relationship between the stability number (I^*) and the Reynolds number (Re) showing the partitioning of the unstable fall patterns for two groups (Ple and Plf; P2c, P2a, P2b and P2d) of dendritic shaped crystals.

3.2 Characteristics of the unstable fall pattern

Analogous to the results of tank experiments for disk-like particles (Willmarth et al., 1964), it appears that over the range of unstable falling motion as the values of Re and I^* increase, the more developed the unstable patterns become. Thus, the unstable pattern can be approximately divided by the combination of Re and I^*, as shown in Fig.2. In this figure, only dendritic shaped crystals are shown since their observed numbers are relatively abundant, as shown in Table 2. The boundaries of each unstable pattern are subjectively estimated and are indicated by solid lines for the Ple and Plf groups, and broken lines for the P2c, P2a, P2b, and P2d groups.

Fig.3 shows the relationship between the nondimensional frequency ($n' = n\,d/\bar{V}z$) for the swing and rotational or spiral types and the mass (M) for dendritic shaped crystals. Here, n is the frequency of the rotational or spiral about the vertical axis or the swing of the crystal. It can be seen that n' increases with an increase in M and is dependent on the type of unstable pattern. The value of n' for swing type is greater than that for the rotational or spiral type when holding M constant, although differences due to the crystal shapes are not clear. The solid and broken lines represent the empirical equations of n' as a function of M for the rotational or spiral and the

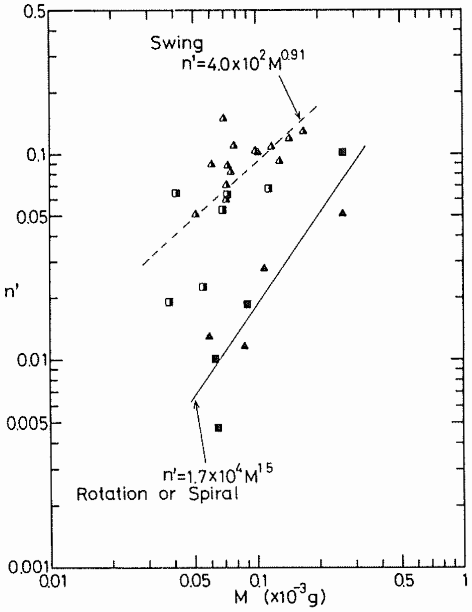

Fig.3. The relationship between the non-dimensional frequency (n') and the mass (M) for the swing and rotational or spiral type. The symbols are the same as in Fig.2.

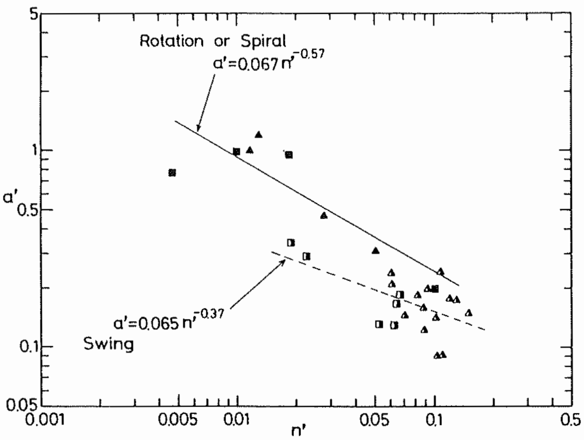

Fig.4. The relationship between the non-dimensional amplitude (a') and the non-dimensional frequency (n') for the swing and rotational or spiral type. The symbols are the same as in Fig.2.

swing type, respectively.

For dendritic shaped crystals, the relationships between the non-dimensional amplitude ($a'=a/d$) and n' of the swing type and the rotational or spiral type are shown in Fig.4. Here, a is the amplitude of the types. The solid and broken lines are the results of an empirical equation showing a' as a function of n' for the rotational or spiral and the swing type, respectively. It is evident that a' decreases as n' increases for both types and is dependent on the type of unstable pattern. On the other hand, differences due to crystal shapes are indistinct.

3.3 Velocity variations of dendritic shaped crystals exhibiting unstable fall patterns

The degree of the velocity variation can be expressed by the standard deviation of the velocity distribution for individual stereophotographs, using the same method that was applied to early snowflakes by Kajikawa (1989). The standard deviation (σ_z) of the vertical velocity is shown in Fig.5, for dendritic shaped crystals. Although σ_z exhibits a slight increase with $\overline{V}_z$, the values are usually smaller than 1.1 cm·sec^{-1} (approximately 1 to 3 % of $\overline{V}_z$). The dotted line in this figure represents values found by an empirical equation for the nonrotation type having a relatively good correlation coefficient (r=0.73). For the swing and the rotational or spiral type, the empirical equations selected when the values of r are large are shown in Table 3.

Fig.6 gives the relationship between the standard deviation (σ_H) of the horizontal velocity (the horizontal component of the falling motion) and the mean horizontal velocity ($\overline{V}_H$), for dendritic shaped crystals. It can be seen that σ_H increases as $\overline{V}_H$ increases and displays a slight dependence on the type of unstable pattern. The solid and dotted lines in this figure were determined from empirical equations for the rotation or spiral and the nonrotation type, respectively. The values of σ_H amount to approximately 50 % of $\overline{V}_H$ or 5 to 20 % of $\overline{V}_z$, and are considerably larger than σ_z.

From the results described above, it appears reasonable to conclude that the variation of hori-

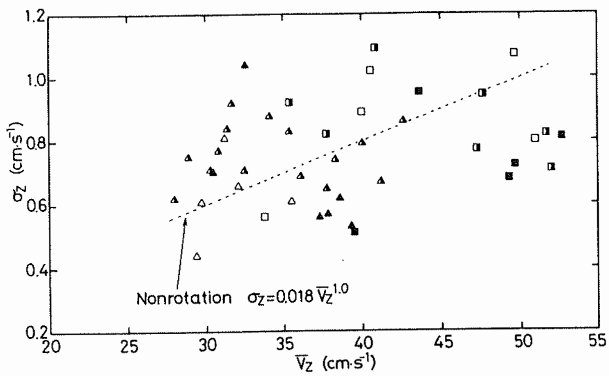

Fig.5. The relationship between the fall velocity (mean vertical velocity, $\overline{V}_z$) and the standard deviation (σ_z) of the vertical velocity. The symbols are the same as in Fig.2.

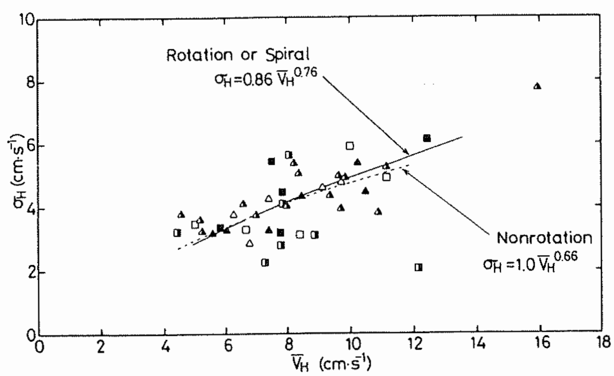

Fig.6. The relationship between the mean horizontal velocity ($\overline{V}_H$) and the standard deviation (σ_H) of the horizontal velocity. The symbols are the same as in Fig.2.

Table 3. Summary of the empirical equations for dendritic shaped crystals.

Type	Nonrotation	Swing	Rotation or Spiral
Non-dimensional frequency (n')	—	$n'=4.0\times10^{2}M^{0.91}$ $N=20$, $r=0.65$	$n'=0.011a'^{-1.3}$ $N=8$, $r=-0.85$
Non-dimensional amplitude (a')	—	$a'=0.065n'^{-0.37}$ $N=20$, $r=-0.60$	$a'=6.5\times10^{-5}M^{-1.0}$ $N=8$, $r=-0.93$
Mean horizontal velocity ($\bar{V}_H$ in cm $^{-1}$ s^{-1})	$\bar{V}_H=9.4\times10^{-2}M^{-0.45}$ $N=10$, $r=-0.49$	$\bar{V}_H=4.9\sigma_H{}^{0.36}$ $N=22$, $r=0.35$	$\bar{V}_H=2.5\sigma_H{}^{0.81}$ $N=11$, $r=0.78$
Standard deviation in vertical velocity (σ_Z in cm s^{-1})	$\sigma_Z=0.018\bar{V}_Z{}^{1.0}$ $N=10$, $r=0.73$	$\sigma_Z=1.0I^{*0.10}$ $N=22$, $r=0.44$	$\sigma_Z=2.7M^{0.15}$ $N=11$, $r=0.36$
Standard deviation in horizontal velocity (σ_H in cm s^{-1})	$\sigma_H=1.0\bar{V}_H{}^{0.66}$ $N=10$, $r=0.70$	$\sigma_H=2.2I^{*-0.26}$ $N=22$, $r=-0.51$	$\sigma_H=4.5a'^{0.26}$ $N=11$, $r=0.72$

See text for the definitions of n', a', and I^*. Mass M is given in grams and fall velocity $\bar{V}_Z$ in centimeters per second; N is the number of crystals, and r the correlation coefficient for the relationship.

zontal velocity plays an important role in the random aggregation of plate-like snow crystals having almost the same shape and size.

4. CONCLUDING REMARKS

The falling motions of plate-like snow crystals in still air were observed using a stereo-photogrammetry method. Simultaneous trajectories of the falling motion were determined; each trajectory having an exact one-to-one correspondence to individual snow crystals.

Differences in the free-fall patterns of unrimed crystals were found to depend on the non-dimensional moment of inertia (stability number), Best number and Reynolds number which involve the fall velocity (mean vertical velocity), as shown in Figs.1 and 2.

For dendritic crystals, the standard deviation of the vertical velocity was less than 3 % of the fall velocity. On the other hand, the standard deviation of the horizontal velocity was found to be considerably larger (5 to 20 % of the fall velocity). Accordingly, it appears likely that the variation in horizontal velocity plays an important role in the random aggregation of plate-like snow crystals having almost the same shape and size.

The standard deviations of the velocities can be empirically estimated as functions of various factors (e.g., the fall velocity, mass, and non-dimensional moment of inertia of dendritic shaped crystals), as shown in Table 3.

ACKNOWLEDGEMENTS

The author wishes to thank the late Prof. Emeritus C. Magono and Prof. K. Kikuchi, Hokkaido University for permission to use the Mt. Teine Observatory. Also, thanks are extended to Mr. I. Morimoto for his assistance with the observations. Partial funding for this study was provided by the Scientific Research Branch of the Ministry of Education and Culture of Japan.

REFERENCES

Heymsfield, A.J. and M. Kajikawa, 1987: An improved approach to calculating terminal velocities of plate-like crystals and graupel. J. Atmos. Sci., 44, 1088-1099.

Kajikawa, M., 1975: Experimental formula of falling velocity of snow crystals. J. Meteor. Soc. Japan, 53, 267-275.

Kajikawa, M., 1982: Observation of the falling motion of early snow flakes. Part I: Relationship between the free-fall pattern and the number and shape of component snow crystals. J. Meteor. Soc. Japan, 60, 797-803.

Kajikawa, M., 1989: Observation of the falling motion of snowflakes. Part II: On the variation of falling velocity. J. Meteor. Soc. Japan, 67, 731-738.

List, R. and R.S. Schemenauer, 1971: Free-fall behavior of planar snow crystals, conical graupel and small hail. J. Atmos. Sci., 28, 110-115.

Magono, C. and C.W. Lee, 1966: Meteorological classification of natural snow crystals. J. Fac. Sci., Hokkaido Univ., Ser. VII, 2, 321-335.

Podzimek, J., 1984: Aerodynamic conditions of ice crystal growth by aggregation and droplet deposition. Proc. Int. Conf. Cloud Physics, Tallinn, 173-176.

Rogers, D.C., 1974: The aggregation of natural ice crystals. Rep. No. AR 110, Dept. Atmos. Resources, Univ. of Wyoming, 35 pp.

Sasyo, Y., 1971: Study of the formation of precipitation by the aggregation of snow particles and the accretion of cloud droplets on snowflakes. Pap. Meteor. Geophys., 22, 69-142.

Willmarth, W.W., N.E. Hawk and R.L. Harvey, 1964: Steady and unsteady motions and wakes of freely falling disks. Phys. Fluids, 7, 197-208.

Zikmunda, J. and G. Vali, 1972: Fall patterns and fall velocities of rimed ice crystals. J. Atmos. Sci., 29, 1334-1347.

THE RESULTS OF INVESTIGATION OF CONFORMITY WITH DISPERSION AND WASHOUT OF ARTIFICIAL AEROSOLS IN CLOUDS AND PRECIPITATION

I.I.Burtsev

Committee for hydrometeorology and environmental monitoring Moscow 123376, Russian Federation

It is known that cloud development and precipitation are the most important natural mechanisms due to those many natural and man-induced admixtures are removed from the atmosphere. On the other hand, they pollute the Earth surface. Therefore for adequate atmospheric purifying estimating and admixture quantity forecasting which falls down together with precipitation we need to know the common regularities of washing process as well as to have approximate estimates of the process for different cloud and precipitation forms.

The efficiency of aerosol washout from atmosphere depends on many factors. Some of them which are a kind of admixture, size distribution and hygroscopicity of aerosols, cloud forms, precipitation intensity,etc. should be considered as most important.

We consider the results of work aimed to estimate the characteristics of washout of artificial aerosols having different chemical properties but approximately equal dispersivity. As those aerosols, we have chosen some ice-nucleating AgI and PbI_2 and radioactive $P^{32}_2O_5$, $Sr^{89}CO_3$ and $Te^{131}O_2$. Here, the particles of PbI_2 and $P^{32}_2O_5$ might be attributed to hygroscopic aerosols and AgI, $Sr^{89}CO_3$ and $Te^{131}O_2$ - to non-hygroscopic ones. The experimental study of the aerosols' dispersity have shown that particles of 0,01...0,05 μm are in the maximum of size distribution for all substances. It let us to conclude that the results of study of behavior of radioactive tracers $P^{32}_2O_5$ and $Sr^{89}CO_3$ in clouds and precipitation might be spread also onto such aerosols as AgI and PbI_2.

With the special artillery projectiles the chosen substances were dispersed both in clouds and in sub-cloud layer, i.e. in the precipitation zone. Moreover, the series of laboratory experiments were carried out, where an artificial cloud was created and radioactive aerosol was dispersed. Maximum of size distribution falls on the droplets of 2...4 μm radii and that is characteristic for Cu cloud at the height 200-300 m above the cloud base.

Measuring a concentration of radioactive particles in the drops under different conditions of their existence, i.e. in the air before the formation of drops and after their precipitating, we may estimate the coefficients of washing (λ_{C1}) and of coagulation (k_{C1}) for cloud droplets and for aerosol particles of fixed spectrum as well as a time of aerosol existence ($\tau_{\lambda C1}$). The calculations have shown that, on the average, for modelled clouds with water content 2-4 g/m^3 and for $Sr^{89}CO_3$ λ_{C1} - $4.3\cdot10^{-4}s^{-1}$, $\tau_{\lambda C1} = 2.3\cdot10^3 s$ and for $P^{32}_2O_5$ $\lambda_{C1} = 9\cdot10^{-4}s^{-1}$, $\tau_{\lambda C1} = 1.1\cdot10^3 s$, i.e. washout efficiency of hygroscopic particles is twice more than of non-hygroscopic ones.

The mean values of coagulation coefficients k_{C1} are: for $Sr^{89}CO_3$ - $0.5\cdot10^{-7}$ $cm^3\cdot s^{-1}$; for $P^{32}_2O_5$ - $4.8\cdot10^{-7}$ $cm^3 s^{-1}$.

The efficiency of aerosol washout by cloud drops is essentially dependent on the aerosol particles' sizes. The β-activity of aerosols $P^{32}_2O_5$ and $Sr^{89}CO_3$ in the camera was investigated before the droplet formation and after their precipitating and the results obtained (Fig.1) witness this dependence. Fig.1 shows that the washout of small and

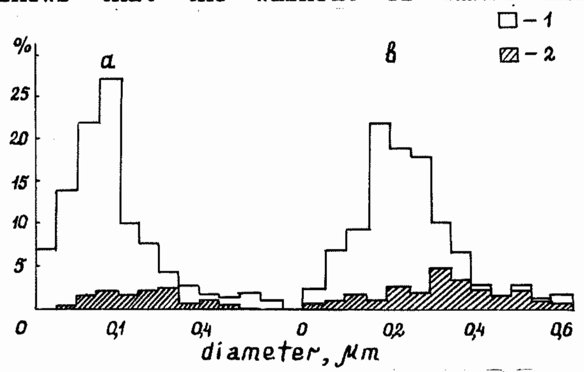

Fig.1 The β-activity distribution along the sizes of particles before the droplet formation in the camera (1) and after particles' precipitating (2): (a) - $P^{32}_2O_5$; (b) - $Sr^{89}CO_3$.

large particles is the most active; the minimum of washout falls on the particles of 0,1...0,5 μm diameters.

Experiments for investigation of radioactive aerosol behaviour in natural clouds and precipitation permitted to determine the rate of aerosol disribution and washout in dependence on the cloud characteristics, on the precipitation intensity and on the place of aerosol injection.

Aerosols were seeded into Cu clouds of frontal and air-mass origin. The seeding was conducted either at the height of 3.5-4.5 km above a cloud base (over the range of negative temperatures) or into the precipitation zone (near cloud base). The area of tracer fallout was divided by the isolines of concentration for the separate lots and the summary amount of aerosol falled was calculated for each lot. The cloud and precipitation parameters were determined by weather radar on 3.2 and 10 cm.

Fig.2 represents the typical areas of fallout of aerosols $P_2^{32}O_5$, $Sr^{89}CO_3$ and $Te^{131}O_2$. One may see on this figure that the spreading area of the aerosol seeded into a cloud is noticeably more than of the aerosol seeded into a precipitation zone. For the first case it is equal, on the average,: 26 km^2 for $P_2^{32}O_5$, 29 km^2 for $Sr^{89}CO_3$ and 34 km^2 for

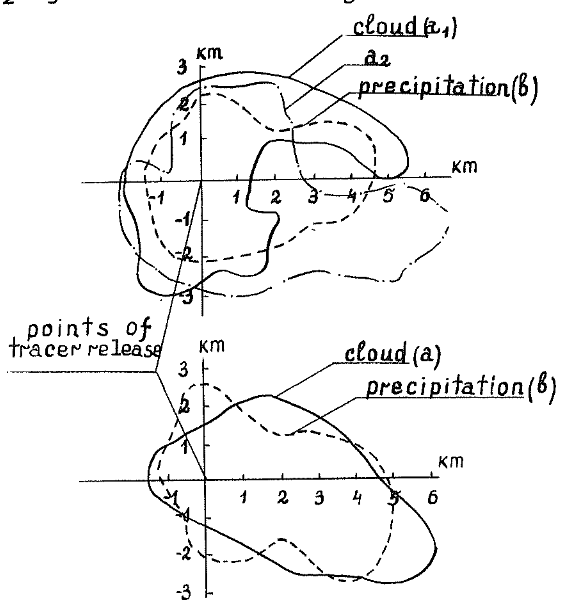

Fig.2 The typical areas of spreading of radioactive aerosols, seeded into the cloud dropletszone (a) and into the precipitation one (b): I - $P_2^{32}O_5$ (a_1), $Te^{131}O_2$ (a_2); II - $Sr^{89}CO_3$.

$Te^{131}O_2$; and for a precipitation zone: 18 km^2 for $P_2^{32}O_5$ and 22 km^2 for $Sr^{89}CO_3$. Note, that the spreading area of non-hygroscopic aerosol was more than for hygroscopic one in all experiments. Probably, it is connected with its less capability to be caught by droplets.

The parameters of aerosol spreading during the time of rain together with speeds of air movement at the seeding height and the efficiency of washout of aerosol seeded both into a precipitation and a cloud droplets' zones are presented in the Table 1. According to content of Fig.2, one may see that an aerosol spreading is going on in all directions from the place of seeding. It should be noted here that the considerable amount of aerosol is spreading in the direction which is opposite to the direction of radioecho transference. Probably, it is connected with the large turbulence in convective clouds. Note for comparison, that if aerosol is seeded into a clear atmosphere (without any clouds) an aerosol spreading is going on only in the direction of air mass movement. The average for all experiments, precipitation distribution of maximum aerosol concentrations (Am) along the direction of radioecho transference and in the opposite one (i.e. approximately along the axis of the trace of falling) is shown on Fig.3, where ℓ is the distance from epicentre of aerosol injection. This distribution of maxima

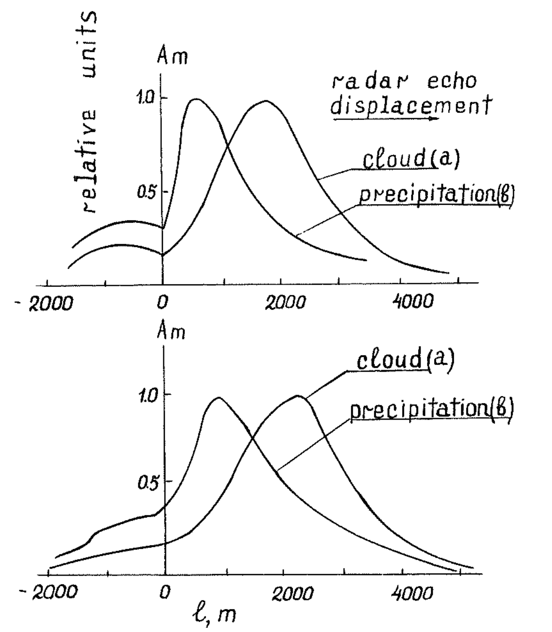

Fig.3 The average distribution of radioactive aerosols' precipitating maximum along the direction of radioecho transference: I - $P_2^{32}O_5$; II - $Sr^{89}CO_3$.

Table 1. The average characteristics of spreading and washout of radioactive aerosols, seeded into different zones in a cloud.

Rain intensity, mm/h	Cloud upper border, radar echo, km	Transfer velocity, m/s		Area of fallout, km^2		Ratio of scavenged aerosol amount to introduced one		Scavenging coefficient, $\lambda \cdot 10^{-4}, s^{-1}$	
		radar echo	air mass	$P_2^{32}O_5$	$Sr^{89}CO_3$	$P_2^{32}O_5$	$Sr^{89}CO_3$	$P_2^{32}O_5$	$Sr^{89}CO_3$
1	2	3	4	5	6	7	8	9	10
Injection into the area of precipitation									
0.5-1.5	7.0	6.2	5.0	18	21	0.55	0.48	2.3	1.1
2.0-3.0	8.0	4.3	4.9	15	20	0.67	0.54	1.6	1.0
3.5-4.0	8.2	7.9	5.8	20	22	0.65	0.68	2.2	1.8
5.0-6.0	8.8	12.0	8.0	22	–	0.68	–	3.2	–
8.0-12.0	9.7	6.8	8.8	16	24	0.82	0.61	4.4	2.4
15.0-20.0	11.2	10.2	10.0	22	–	0.75	–	5.0	–
Injection into the cloud									
0.5-1.5	7.0	8.0	5.7	29	30	0.80	0.70	2.6	1.8
2.0-4.0	7.8	11.0	9.2	30	34	0.84	0.63	3.8	2.6
5.0-6.0	9.0	11.5	16.0	27	27	0.91	0.69	5.2	2.8
8.0-12.0	9.5	11.0	4.0	24	29	0.90	0.64	6.2	3.1
15.0-20.0	10.5	13.6	13.5	26	28	0.82	0.73	7.7	4.8
8.4*	8.0	15.0	16.0	34		0.78		3.0	

* – The results refer to $Te^{131}O_2$.

of concentrations is connected with the differences of meteorological parameters in different seeding zones, with microstructure of clouds and precipitation, with physical and chemical aerosol properties, etc. The calculations show that average time of absolute concentrations' appearance from the seeding moment is as follows:

a) in the cloud droplet zone – for $P_2^{32}O_5$ – 2.5 min, $Sr^{89}CO_3$ – 3.1 min;

b) in the precipitation zone – for $P_2^{32}O_5$ – 4 min, $Sr^{89}CO_3$ – 5 min.

The values of aerosol part (Ap) falled down on the earth in relation to the total amount of aerosol dispersed are represented in the Table 1. One may see that the washout of aerosol seeded into the cloud droplet zone is more intensive and average values of washout coefficient are following: for $P_2^{32}O_5$ – $5 \cdot 10^{-4} s^{-1}$, $Sr^{89}CO_3$ – $2.8 \cdot 10^{-4} s^{-1}$, $Te^{131}O_2$ – $3 \cdot 10^{-4} s^{-1}$. When aerosol is seeded into the precipitation zone this coefficient is equal to: for $P_2^{32}O_5$ – $3.0 \cdot 10^{-4} s^{-1}$, $Sr^{89}CO_3$ – $1.5 \cdot 10^{-4} s^{-1}$.

It is interesting to study the dependence of the rate of atmosphere self-cleaning on the precipitation intensity (I). Fig.4 shows that, on the whole, the constant of $P_2^{32}O_5$ aerosol washout increases together with growth of I. However, when aerosol is seeded into the precipitation zone, the certain minimum of λ_{C1} value is pointed out in the range of precipitation intensity of 2...3 mm per hour.

So, the analysis of above data shows that, on the average, the washout of aerosol particles of 0.01...0.5 μm in cloud is essentially more than in sub-cloud layer.

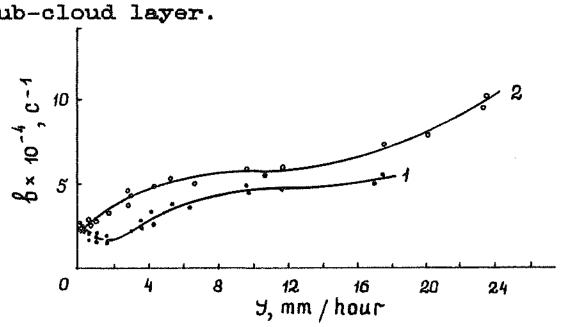

Fig.4 The dependence of washout coefficient for aerosol $P_2^{32}O_5$ on the precipitation intensity: (1) – when seeded into the precipitation zone; (2) – into the cloud droplet zone.

EXPERIMENTS OF THE GROWTH OF COMBINATIONS OF BULLETS

Chuji Takahashi

Earth Science Laboratory, Saitama University
Urawa, Japan

1. INTRODUCTION

In polar regions snow crystals of various peculiar shapes has been observed (Kikuchi,1970). Most of them are polycrystalline snow crystals and their growth conditions and mechanisms are unknown. Combinations of bullets is one of the representative snow crystals observed in polar regions. They are also observed in cirrus or cirrostratus (Weickmann,1948; Heymsfield and Knollenberg,1972) and are remarked from the view of atomospheric radiation.

Weickmann(1972) and Kobayashi et al.(1976) suggested that combinations of bullets grew from frozen cloud droplets. But the auther(1979) cast a doubt to this suggestion. He reported that cloud droplets accreted to columns grew to assemblages of plates at temperatures about -27°C. Growth of combinations of bullets was expected at about -27°C,if the crystal habit of polycrystalline snow crystals is the same as that of single-crystalline ones.

This experiment was carried out for the purpose of investigating whether combinations of bullets grow from frozen droplets or not.

2. APPARATUS AND PROCEDURES

A diffusion cloud chamber was used. It was composed of two thermoelectric panels. Thermoelectric junctions were mounted on the panels and their temperatures were controlled. Water droplets were prepared by spraying once distilled water. They fell in a cold box which was set on the diffusion cloud chamber and held at temperatures below -35°C. Water droplets froze in free fall and were caught on the coverglass on the bottom panels. Water vapour was supplied from the ice sheet lined at the top panel. The supersaturation of water vapour was controlled by varying the temperatures of the top and bottom panel. Since calculation of supersaturation for each frozen droplet was difficult, the temperature difference of the two panels was used as an index of the supersaturation. The size of observed frozen droplets ranged from 10 to 80 μm in diameter.

Mineral particles were also used as nuclei. They were kaolinite,montmorillonite and orthoclase. They were seeded on a coverglass before experiments and the coverglass was set on the bottom panel.

3. RESULTS

3.1 Growth of frozen droplets

At the beginning of the growth, frozen droplets grew large while retaining their spherical shape. After they grew to the size of 2-3 times larger than the initial size,plates or columns grew from them depending on the air temperature. At temperatures between -28°C and -35°C, only plate-like growth occurred and frozen droplets grew to assemblages of plates. At temperatures between -35°C and -40°C, columnar growth occurred together with plate-like growth. Assemblages of plates and columns frequently grew at this temperature range. At temperatures below -40°C, only columnar growth occurred, and frozen droplets grew to combinations of columns as shown in Fig.1. Combinations of columns observed in this experiment did not resembled to natual snow crystals of combinations of bullets. The trace of spherical frozen droplets remained at the center of crystals. The number of component columns of crystals was small compared to that of natural crystals.

At low supersaturation, neither assemblages of plates or combinations of bullets grew. Frozen droplets grew to polyhedral crystals while forming several crystal faces on their surfaces as shown in Fig.1

3.2 Snow crystals from mineral particles

No notable difference existed between the results of the three kinds of mineral particles; kaolinite, montmorillonite and orthoclase. The crystal shape varied according to the air temperature and supersaturation. At low supersaturation(close to ice saturation) only

(a) (b)

Fig.1 Growth from frozen droplets. (a)Combination of columns. temperature =-45°C. (b)Polyhedral ice crystals grown at low supersaturation. temperature=-50°C. scale=50 um singlecrystalline columns grew at all temperatures. With the increase of the supersaturation, the frequency of polycrystalline crystals increased. Of the polycrystalline crystals, assemblages of plates grew frequently at higher air temperatures. Combinations of columns grew below -30°C. Their frequency increased with the increase of the supersaturation.

The number of components of combinations of columns was counted for the cases of kaolinate and montmorillonite. The number was not affected by the air temperature and the supersaturation. The maximum frequency of the number ~~was~~ three. It was smaller than that of combinations of bullets collected in Antarctica by Iwai(1986).

The angle between the c-axes of components of combination of columns was measured. For this purpose the crystals with two components on a plane vertical to the optical axis of the microscope were selected and photographed. The angles were measured from the photographs. The distribution of the angles is shown in Fig.3. There are remarkable peaks near 70°, 90° and 55°. These peaks are consistent with those measured by Kobayashi et al.(1976).

4. CONCLUDING REMARKS

Combinations of columns grew both from frozen droplets and from mineral particles. They are the same type of snow crystals as combinations of bullets although the component columns do not taper as bullets. Experimental results support that natural combinations of bullets grow from ice forming nuclei such as clay minerals. Frozen droplets grew to combinations of columns only below -40°C, which is low compared to those estimated for natural combinations of bullets. Moreover, combinations of columns grown from frozen droplets do not resemble to natural combinations of bullets. On the other hand, combinations of columns grew from mineral particles below -30°C and their shape resembles to natural combinations of bullets.

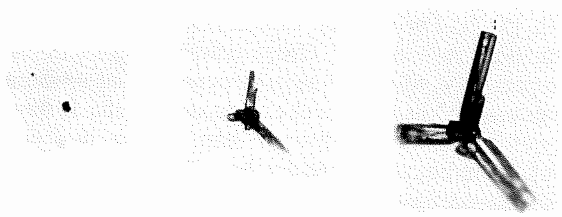

0 min. 8 min. 60 min.

Fig.2 Growth of combination of columns from montmorillonite. scale=50 um. temperature=-50°C.

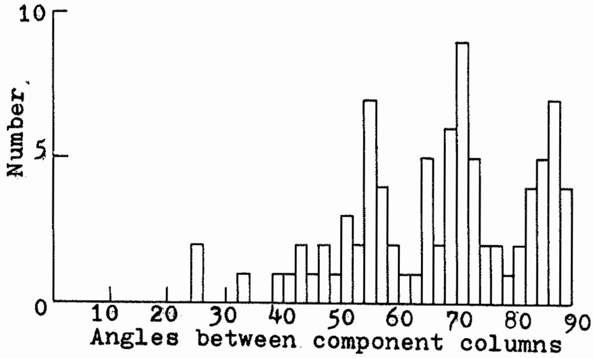

Fig.3 The distribution of angles between the c-axes of components of combinations of columns

The experimental results do not necessary mean that mineral particles act as deposition(sublimation) nuclei when they grow to combinations of columns. The supersaturation of water vapour needs to be closeto or higher than water saturation. The component columns do not orient randomly, but there is a regularity in the angles between the c-axes of component columns. These results implies the relation between the activation of nuclei and the freezing of liquid water. Moreover, natural ice nuclei frequently exist as mixed nuclei and their surface would be partly coated with water at the humidity close to water saturation. Activation of ice nuclei for the growth of combinations of bullets is supposed to be the freezing of such liquid water on the surface of nuclei.

REFERENCES

Heymsfield,A.J. and R.G.Knollenberg, 1972: Properties of cirrus generating cells. J.Atmos.Sci., 29, 1358-1366.

Iwai,K.,1979: Morphological features of combination of bullet-type snow crystals observed at Syowa Station,Antarctica. Mem.Natl.Inst.Polar Res.Spec. Issue, 45, 38-46.

Kikuchi,K.,1970: Peculiar shapes of solid precipitation observed at Syowa Station,Antarctica. J,Met.Soc.Japan, 48, 243-249.

Kobayashi,T.,Y.Furukawa,K.Kikuchi and H. Uyeda,1976: On twinned structures in snow crystals. J.Crystal Growth,32, 233-249.

Takahashi,C.,1979: Formation of polycrystalline snow crystals by riming process. J.Meteor.Soc.Japan,57,458-464

Weickmann,H.K.,1948: The ice phase in the atmosphere. Trans.273,Ministry of Supply,London

MEASUREMENTS OF CONVECTIVE HEAT TRANSFER OF HAILSTONE MODELS

Guoguang Zheng and Roland List

Department of Physics, University of Toronto, Toronto, Ontario, Canada

1. INTRODUCTION

Convective heat transfer plays an essential role in the hailstone growth process. Previous theories on heat and mass transfer of hailstones by Schumann (1938), Ludlam (1958) and List (1963, 1977) treated such transfers as homogeneous and isotropic. Recent laboratory results revealed surface temperature differences between the equator and poles of accreting ice particles as large as 5.8 °C (List et al, 1989) because the free fall mode of hailstones (as any rotation) causes latitude-dependent exposure to the airflow. Hence, heat and mass transfer is latitude-dependent (List, 1989).

Convective heat transfer from spherical and cylindrical bodies has been investigated by many authors (Wolf, 1983), but the data for realistic hailstone shapes are still limited. In this study, experiments have been conducted to measure the heat transfer of rotating and gyrating hailstone models, and determine the overall and latitude-dependent heat transfer coefficients and hence, the respective overall and local Nusselt numbers.

2. THE EXPERIMENT

The experiments were performed in the temperature- and velocity-controlled, closed-circuit wind tunnel facility at the University of Toronto (List et al, 1986). The model examined was mounted in the measuring section with a cross-section of 17.8 x 17.8 cm^2. A particle gyrator allowed it to rotate or gyrate at different frequencies (Figure 1). For rotation, the model was rotated about a horizontal spin axis. The local surface temperatures of the particle were measured with an "Agema Infrared System Thermovision 800" thermal imaging system, which uses a Mercury Cadmium Telluride detector and a scanning mirror system. The spot size of the detector is 2.5 $\pm$ 0.5 mm in diameter, and the system sensitivity is 0.13 °C at an object temperature of -15 °C. The temperature of the surroundings was measured with a thermocouple to within $\pm$ 0.25 °C.

The hailstone models used were smooth spherical and spheroidal particles with major axis diameters of 2 and 3 cm and aspect ratios of 0.5, 0.67, and 1.0. Studies of natural hailstones indicated that these sizes and aspect ratios approximate natural hailstones (List, 1959; Carte and Kidder, 1966; Macklin, 1977; Zheng and Shi, 1989). Machinable Glass Ceramic (MGC) and ice were chosen as materials of hailstone models. MGC has thermal properties

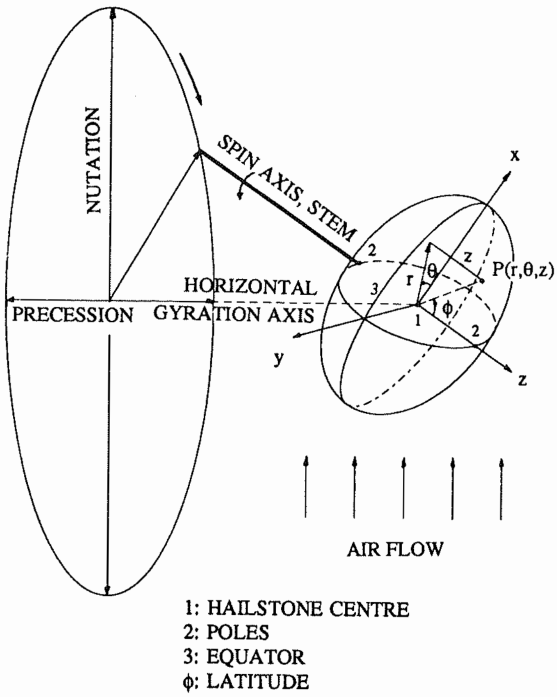

Figure 1 Hailstone model in a vertical wind tunnel while gyrating / rotating with suspension stem as spin axis. The cylindrical polar coordinates (r, θ, z) were chosen to describe heat conduction within the model.

similar to those of ice and can be used to study pure convective heat transfer without sublimation or evaporation.

The initial uniform temperature of a typical particle was approximately -6 °C, which was reached by keeping it in a cold room. Three air temperatures of -15, -19, and -22 °C were chosen and monitored with a thermocouple in the measuring section. The air speed, V, was set to 6.7, 9, 12, 15, 18, 21, 24 m/s and the rotation rate (f_1) to 0, 5, 10, 15 Hz. For gyration experiments, the spin (f_3) and nutation/precession (f_o) frequencies were 9.5 and -14 Hz, respectively. All experiments were performed at laboratory pressure. While the model was exposed to the airflow, the gyrator was run at desired rotation rate or spin and nutation/precession frequencies. The Agema Infrared System recorded the surface temperature distribution of the model cooling in the airflow, with a scanning speed of 24 frames a second. About 400 data points per cm^2 were available on the model surface. The resolution of the measurement was high enough to analyze in detail the local heat transfer of the particles. A single experiment lasted between 70 and 250 seconds.

3. DATA REDUCTION

3.1 Temperature Field within a Particle

Fourier's law for heat conduction within a particle is given by

$$\frac{\partial T}{\partial t} = \alpha \nabla^2 T \tag{1}$$

where α is the thermal diffusivity, T the temperature and t the time. If the particle spins about an axis passing through its centre, the internal temperature distribution possesses rotational symmetry about that axis. In cylindrical polar coordinates (r,θ,z) (seen Figure 1), equation (1) becomes

$$\frac{\partial T}{\partial t} = \alpha\left(\frac{\partial^2 T}{\partial r^2} + \frac{1}{r}\frac{\partial T}{\partial r} + \frac{\partial^2 T}{\partial z^2}\right) \tag{2}$$

with time-varying boundary conditions. For rotating and gyrating particles, $\partial T/\partial \theta = 0$. The heat conduction equation then reduces to two dimensions with the sphere and spheroid surfaces being represented by circles and ellipses, respectively. A rectangular grid is superimposed over these two dimensional particles with a horizontal and vertical grid spacing of Δr and Δz.

The numerical or finite-difference method was used to solve equation (2) with $\Delta r = \Delta z = 1$ mm and $\Delta t = 1$ sec. The initial temperature of the particle, which was uniform throughout, was chosen as initial condition. The boundary conditions were specified in terms of the surface temperature measurements at surface points as a function of time. The solution of equation (2) gives the time-variation of the temperature at any point within the particle.

3.2 Determination of the Local Heat Transfer Coefficient

The net heat flux, $\delta\dot{q}_i$, from a surface element of the particle due to conduction, convection, and sublimation is given by

$$\delta\dot{q}_i = [h_i(T_{si} - T_a) + h_i' L(\rho_{si} - \rho_v)]\delta s_i \tag{3}$$

where T_s and T_a represent the surface and ambient temperatures, ρ_s and ρ_v the vapour densities over the ice particle and in the environment, L the latent heat of water, h and h′ the heat and mass transfer coefficients, respectively; and the subscript i denotes the surface element i. Since the same physical mechanism is associated with heat transfer by conduction and convection (i.e. heat diffusion) and mass transfer by diffusion, the mass transfer coefficient, h′, can be expressed by the heat transfer coefficient, h. The second term on the right-hand side of equation (3) was ignored in this paper because of its small value compared to the first term. The experimental data shows the similar surface temperature distribution for ice particle to MGC case. Therefore, the discussion in this paper can be restricted to the cases of heat conduction and convection.

The heat flux due to conduction from within the particle to the surface element δs_i is

$$\delta\dot{q}_i = -k\left(\frac{\partial T}{\partial r}\right)_i \delta s_i \tag{4}$$

where $(\partial T/\partial r)$ is the temperature gradient near the surface in the particle, which is in a direction perpendicular to the surface. At the surface of the particle, the rate at which heat is conducted from within the particle must equal to the rate at which it is delivered to the airstream. Thus, equation (3) and equation (4) give the heat transfer coefficient h_i as

$$h_i = \frac{k\left(\frac{\partial T}{\partial r}\right)_i}{(T_{si} - T_a) + C(\rho_{si} - \rho_v)} \tag{5}$$

where C is a constant and equal to zero for MGC case.

The direction of the external normal at any point on the surface was determined by considering the chord subtended by the two neighbouring points. The normal component of the temperature gradient at the surface as a function of latitude and time may be computed by solving for the heat-conduction within the particle. Thus, the heat transfer coefficient and hence, the Nusselt number as a function of both latitude and time were obtained.

4. RESULTS AND DISCUSSION

4.1 Local Nusselt Number

The latitude-dependent or local Nusselt number, Nu_ϕ, is defined as

$$Nu_\phi = \frac{h_\phi D}{k_a} = \frac{kD\left(\frac{\partial T}{\partial r}\right)_\phi}{k_a[(T_{s\phi} - T_a) + C(\rho_{s\phi} - \rho_v)]} \tag{6}$$

where k_a is the thermal conductivity of air, D the major axis diameter of the model, and h_ϕ the heat transfer coefficient for latitude ϕ. For any type of rotation, the position of the rotation axis causes latitude-dependent exposure of the particle surface to the airflow and hence, a latitude-dependent surface temperature distribution, which in turn will produce a latitude-dependent heat transfer. An example of the variation of Nu_ϕ of a rotating ice particle with latitude ϕ is presented in Figure 2. The same figure contains data from stationary particles, where one pole coincides with the stagnation point and the minor axis is horizontal.

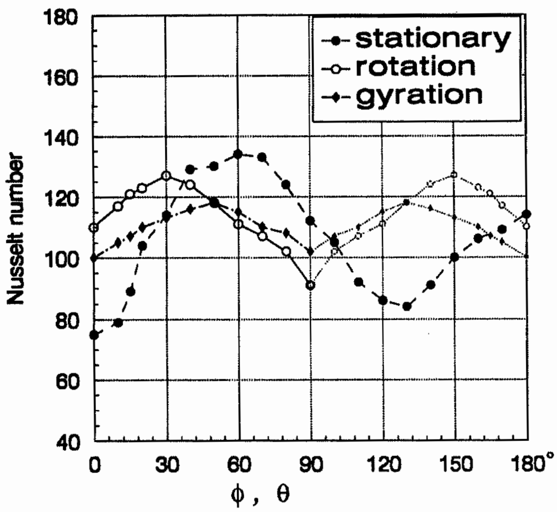

Figure 2 The Nusselt number Nu of rotating and gyrating ice particles as a function of latitude ϕ and of stationary ice particles as a function of longitude θ. (D = 2 cm, α = 0.67, T_l = -6 °C, T_a = -15 °C, V = 15 m/s, Re = 4.9×10^4, f_1 = 10 Hz, f_3 = 9.5 Hz, f_o = -14 Hz)

4.2 Overall Average Nusselt Number

The macroscopic or overall average Nusselt number, Nu^*, is defined by

$$Nu^* = \frac{h^* D}{k_a} = \frac{D \dot{q}^*_{cc,s}}{k_a[(T^*_s - T_a) + C(\rho^*_s - \rho_v)]} \quad (7)$$

where $\dot{q}^*_{cc,s}$ is the total overall average surface heat flux due to convection and conduction calculated by integrating the heat flux over the surface. The average surface temperature T_s^* is obtained directly from the Agema imaging system. The average vapour density ρ_s^* is determined by T_s^*.

Figure 3 shows Nu^* as a function of time for a rotating particle with a diameter of 2 cm and an aspect ratio of 0.67 at a rotation rate of 10 Hz. It can be seen that Nu^* is strongly dependent on the wind speed and hence, Reynolds number. There is also a smaller variation of Nu^* with time than that of Nu_ϕ (data not shown).

4.3 Effect of Motion Pattern on Nu

Nu as a function of latitude ϕ for rotating and gyrating ice particles and of longitude θ for stationary ice particles is plotted in Fig.2. The stationary suspension is a special case (f_1 = 0 Hz). The surface temperature distribution of stationary particles depends more on θ and to a lesser extent on ϕ. From geometrical arguments, θ is seen to be the latitude for stationary case. The rotating and gyrating particles are symmetry about the equator section perpendicular to spin axis, which result in symmetric Nu-ϕ

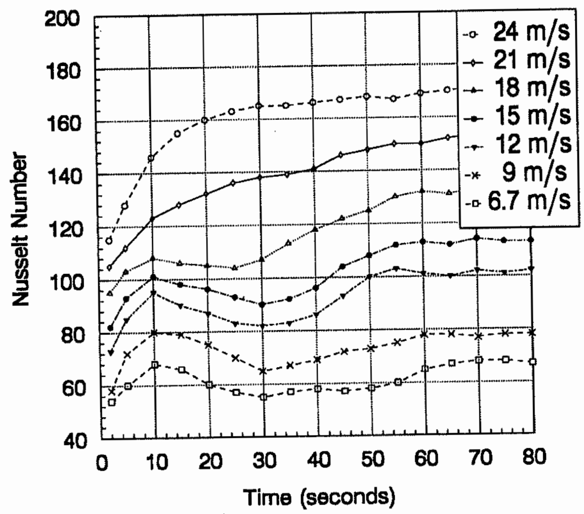

Figure 3 The time-variation of the overall-average Nusselt number of a rotating ice particle (D = 2 cm, α = 0.67) at different wind speeds. (T_l = -6 °C, T_a = -15 °C, f_o =10 Hz)

curves about ϕ=90° in Figure 2. It can be also seen from Figure 2 that the fall mode of the particle has a significant effect on the local heat transfer coefficient. Comparison of the Nusselt number for a rotating or gyrating particle with that of a stationary particle shows that the motion pattern affects markedly the latitude-dependent heat transfer coefficient. For a rotating or gyrating particle, rotation and gyration produce axially symmetric temperature distributions about the rotation/spin axis which in turn affect convective heat transfer. A maximum Nu_ϕ is reached at about ϕ=45° for a gyrating particle while a rotating particle has a maximum Nu_ϕ near ϕ=0°. A stationary particle yields significantly different results when compared to gyrating or rotating models and shows large changes of Nu_ϕ with latitude ϕ and values of Nu^* lower than that for rotating or gyrating models.

4.4 Relationship between Nu^* and Re

Figure 4 gives the overall-average Nusselt number, Nu^* of a rotating particle as a function of Reynolds number, Re. The following expression was used to fit the relationship between Nu^* and Re

$$Nu^* = 2.0 + C_1 Pr^{1/3} Re^m \quad (8)$$

For a rotating spheroidal particle with a 2 cm major-axis diameter and a 0.67 aspect ratio, C_1 and m in (8) were found to be 0.223 and 0.624, respectively, and are plotted by dashed curve in Figure 4. This is different from expression $Nu = 2.0 + 0.60\, Pr^{1/3} Re^{1/2}$ given by Schuepp and List in extension of Ranz and Marshall. Ranz and Marshall (1952) used experimental data on the evaporation of water drops for Reynolds numbers between 0 and 200. Schuepp and List (1969) extrapolated up to Re = 10^5 based on the mass transfer similarities in a liquid tunnel by redox electrolysis, with a Schmidt number of 2170.

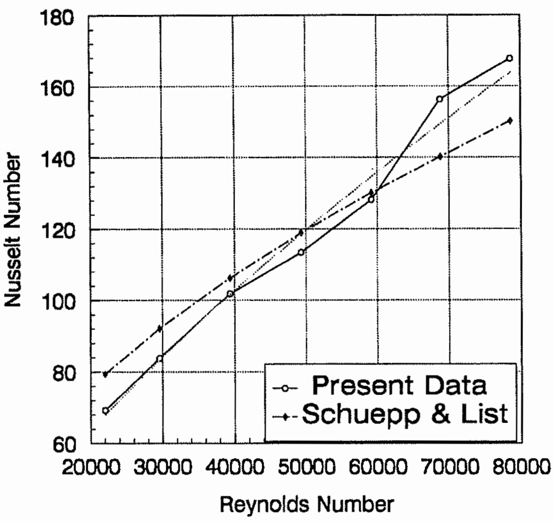

Figure 4 The relationship between the overall-average Nusselt number, Nu^*, and Reynolds number, Re, for a rotating ice particle (D= 2 cm, α = 0.67). (T_i = -6 °C, T_a = -15 °C, f_i = 10 Hz). The curve of Nu - Re given by Schuepp and List (1969) is also plotted.

5. SUMMARY AND CONCLUSIONS

Heat-transfer measurements were made of ice and MGC particles rotating and gyrating in airflow at varying wind speeds. Surface temperature distributions of the particles were determined during cooling in the airflow with an Agema Infrared Thermal Imaging System. By numerically calculating the internal heat conduction, the latitude-dependent and overall-average Nusselt numbers were determined. Preliminary analysis of the data led to the following conclusions:

(1) The existence of a latitude-dependent Nusselt number indicates that the heat-transfer of a particle cooling by convection, conduction and/or sublimation should be treated as non-homogeneous and non-isotropic.

(2) The fall mode and speed of the particle has a significant effect on the latitudinal convective heat-transfer.

(3) The relationship between the overall-average Nusselt number and Reynolds number for 2 cm diameter spheroidal particles is $Nu^* = 2.0 + 0.223\, Pr^{1/3}\, Re^{0.624}$.

Further work will explore for the possible effects on convective heat transfer by particle shape and size, density and rotation rate.

ACKNOWLEDGEMENTS

This work was sponsored by the Natural Sciences and Engineering Research Council of Canada. We would like to thank the Ontario Lightwave and Laser Research Centre for providing the Agema Infrared Thermal Imaging System. One of the authors (GZ) is grateful to the University of Toronto for providing a Connaught Scholarship.

REFERENCES

Carte, E. and R. E. Kidder, 1966: Transvaal hailstones, *Quart. J. Roy. Meteor. Soc.*, **92**, 382-391.

Kry, P.R. and R. List, 1974: Angular motions of free falling spheroidal hailstone models, *Phys. Fluids*, **17**, 1093-1102.

List, R., 1959: Zur Aerodynamik von Hagelkornern, *Z. angew. Math. Phys.*, **10**, 143-159.

List, R., 1963: General heat and mass exchange of spherical hailstones, *J. Atmos. Sci.*, **20**, 189-197.

List, R., G. B. Lesins, F. Garcia-Garcia and D. B. McDonald, 1987: Pressured icing tunnel for graupel, hail and secondary raindrop production, *J. Atmos. Oceanic Technol.*, **4**, 454-463.

List, R., F. Garcia-Garcia, R. Kuhn and B. Greenan, 1989: The supercooling water skins of spherical and spheroidal hailstones, *Atmos. Research*, **24**, 83-87.

List, R., 1989: Analysis of sensitivities and error propagation in heat and mass transfer of spheroidal hailstones using spreadsheet, *J. Appl. Meteor.*, **28**, 1118-1127.

Ludlam, F.H., 1958: The hail problem, *Nubila*, **1**, 12-96.

Macklin, W.C., 1977, The characteristics of natural hailstones and their interpretation, *Meteor. Monogr.*, **38**, Amer. Meteor. Soc., 65-88.

Ranz, W.E. and W. R. Marshall, 1952: Evaporation from drops, Part I. *Chem. Eng. Prog.*, **48**, 141-146.

Schuepp, P. P., and R. List, 1969: Mass transfer of rough hailstone models in flows of various turbulence levels. *J. Appl. Meteor.*, **8**, 254-263.

Wolf, H., 1983: *Heat Transfer*, Harper & Row, Publishers, New York, 617pp.

Zheng, G.G. and W.Q. Shi, 1989: *Studies of some problems of hailstones and hailstorms in Zhaosu, Xinjiang*, (Chinese) Meteor. Press, 234pp.

Measurements of the Bulk Collision Efficiency and Nusselt Number for Growing Graupel

Stewart Cober* and Roland List

University of Toronto, Toronto, Canada, M5S 1A7.
* Atmospheric Environment Service, Toronto, Canada, M3H 5T4.

1. INTRODUCTION

There have been few experimental investigations involving the growth of graupel by the accretion of supercooled cloud droplets (Pflaum and Pruppacher 1979; Dong and Hallett 1986; Griggs et. al. 1984), although some investigators have inferred growth parameters for graupel by studying riming on cylinders (Mossop 1976; Keith and Saunders 1988). These studies tend to disagree on fundamental growth characteristics such as the bulk collision efficiency and the density of accretion. The Nusselt and Sherwood numbers which describe the heat and mass transfer by convection and deposition have not been previously measured. Consequently, numerical cloud models are limited in their attempts to incorporate graupel growth. Experiments will be described where measurements were made of all the parameters required for characterizing the heat and mass transfer of graupel.

2. THEORY

List (1963) developed heat and mass transfer equations for hail and graupel. The total mass transfer rate dM/dt is given by the mass increases from accretion M_{CP}^* and deposition or sublimation M_{DS}^*

$$\frac{dM}{dt} = M_{CP}^* + M_{DS}^* \tag{1}$$

$$\frac{dM}{dt} = E_b W_f A_b V - \frac{Sh\, D_{wa} A_s}{D R_v T_a}\left(e_{ss}(T_s) - U_w e_{sa}(T_a)\right) \tag{2}$$

where A_s is the graupel surface area, A_b the sweepout area, D the graupel diameter, D_{wa} the diffusivity of water vapour, R_v the water vapour gas constant, T_s and T_a the surface and air temperatures, e_{ss} and e_{sa} the saturation vapour pressures at the surface and in the air, U_w the relative humidity, W_f the liquid water content, Sh the Sherwood number, E_b the bulk collision efficiency and V the graupel terminal velocity.

Similarly, the total heat transfer rate is given by the balance between heat gained from the latent heat of freezing of the cloud droplets Q_F^*, and the heat released by convection Q_{CC}^*, sublimation or deposition Q_{DS}^* and cooling by the cloud droplets after freezing Q_{CP}^*.

$$\frac{dQ}{dt} = 0 = Q_{CC}^* + Q_{DS}^* + Q_{CP}^* - Q_F^* \tag{3}$$

$$0 = \frac{Nu A_s k_a}{D}(T_s - T_a) + L_s M_{DS}^* + C_w(T_s - T_a) M_{CP}^* - L_f M_{CP}^* \tag{4}$$

where k_a is the thermal conductivity of air, C_w the specific heat of water, Nu the Nusselt number, and L_s and L_f are the latent heats of sublimation and freezing. The parameters R_v, L_f, k_a, L_s, D_{wa}, C_w, e_{sa} and e_{ss} are either constant or have been parameterized in terms of known variables (Pruppacher and Klett 1978). The cloud conditions W_f, T_a, U_w and the velocity V can be controlled in the experiments. The graupel properties D, A_b and A_s can be measured photographically, while the temperature of the graupel surface can be measured with an IR thermal imaging system. Finally, for atmospheric conditions, Nu and Sh can be related through similarity theory as

$$Sh = 0.95\ Nu \tag{5}$$

This leaves two unknowns within Equations 3 and 4; E_b and Nu, which can subsequently be derived. This technique was not viable previously because of the inability to accurately measure the graupel surface temperature.

3. EXPERIMENTAL APPARATUS

The experiments were performed in the University of Toronto cloud physics wind tunnel (List et. al. 1987). A schematic diagram of the tunnel is shown in Figure 1. The growth conditions within the wind tunnel can be controlled as follows: $T_a \pm 0.25$°C, pressure P ± 1 kPa, air flow velocity V ± 0.05 m s^{-1}, and $W_f \pm 0.15$ g m^{-3}. The water injection system consists of an atomizing nozzle, with the droplet sizes depending on the degree of atomization. The relative humidity was calculated from a model of the wind tunnel thermodynamics and was not directly controllable.

During an experiment three 1 mm mylar plates were rigidly suspended in the measuring section of the tunnel. Under constant growth conditions the plates were rimed for a specific length of time, after which the resulting graupel were taken to a cold room for analysis. For each graupel, the volume was determined using Archimedes principle by immersing the graupel in mercury (Knight and Heymsfield 1983). The graupel were then photographed for future geometric measurements and weighed.

During an experiment the surface temperature could be measured with an Agema Thermovision 800 thermal imaging system. The Agema uses a Germanium lens and a Mercury Cadmium Telluride detector to measure the 8 to 12 μm radiation emitted from the graupel surface. The minimum resolution of the detector was 2.0 ± 0.5 mm. The average surface temperature elevation of a graupel could be determined to within ± 0.2°C.

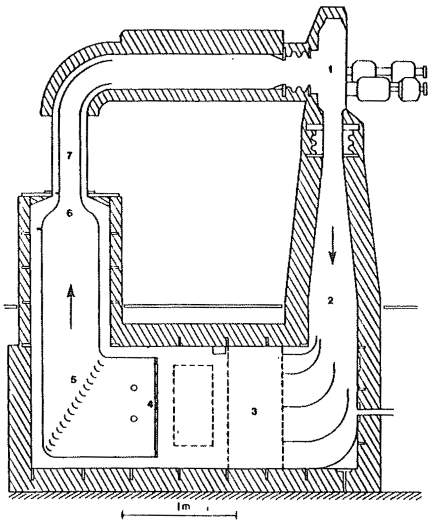

Figure 1: Schematic of the wind tunnel. 1. Fan; 2. Heating elements; 3. Cooling elements; 4. Velocity reducing board; 5. Water injection system; 6. Contraction; 7. Measuring section.

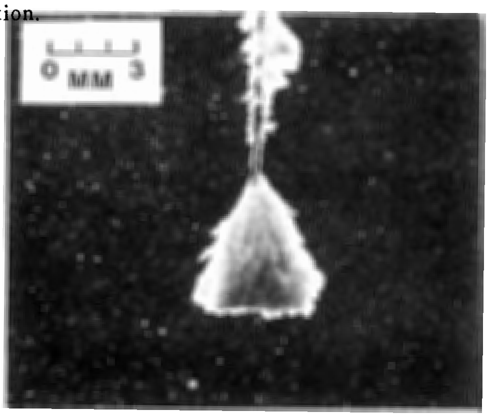

Figure 2: Graupel grown for 9 minutes at T_a = -16°C, W_f = 2.0 g m^{-3}, V = 2.0 m s^{-1}, r_m = 15 μm, P = 100 kPa.

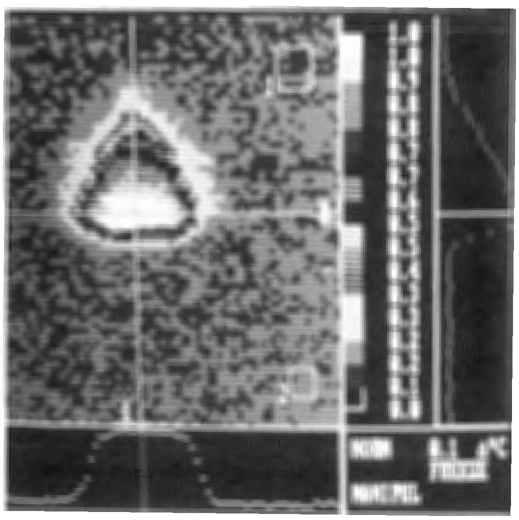

Figure 3: Surface temperature elevation of a graupel over the ambient air temperature. The maximum temperature elevation is 1.0°C. The growth conditions are the same as in Figure 2. Box 2 is approximately the resolution of the detector. Box 1 is a 1 mm box.

4. EXPERIMENTAL RESULTS

The standard growth conditions consisted of Ta = -16°C, P = 101 kPa, W_f = 2.0 g m^{-3}, V = 2.0 m s^{-1} and a droplet spectrum characterized by a median volume radius of 15 μm (mean radius of 10 μm). Figure 2 shows a graupel after 9 minutes of growth in such conditions. The ice density was 0.26 g cm^{-3}. Figure 3 shows the surface temperature elevation of the same graupel as measured by the Agema system. The average surface temperature elevation was 0.9 ± 0.2°C over the ambient air temperature. Several similar experiments were performed, with different durations, to determine the mass growth with time. The results are shown in Figure 4 for various liquid water contents. Each data point represents a mean from between 3 and 8 graupel particles and has an error between ± 2 and ± 4 %. The mass growth rate increases with growth time because of the increase in the sweep out area. The density, cone angle and geometric shape were all observed to be independent of growth time and liquid water content. A fit of each curve yielded dM/dt, for use in the heat and mass transfer equations. Similar curves and fits were made for the graupel geometric properties. The surface temperature elevation was observed to be proportional to the mass growth rate, increasing from 0.3 to 1.5°C as W_f increased from 0.5 to 3.0 g m^{-3}.

Figure 5 shows the effects of increasing the velocity to 3.0 m s^{-1} or of increasing the median volume radius to 20 μm, while holding the remaining growth conditions constant at their standard values. Increases in V or r_m increase the collision efficiency of the cloud droplets which increases the mass growth rate. An increase in V or r_m also widened the cone angle which further accelerated the mass growth rate.

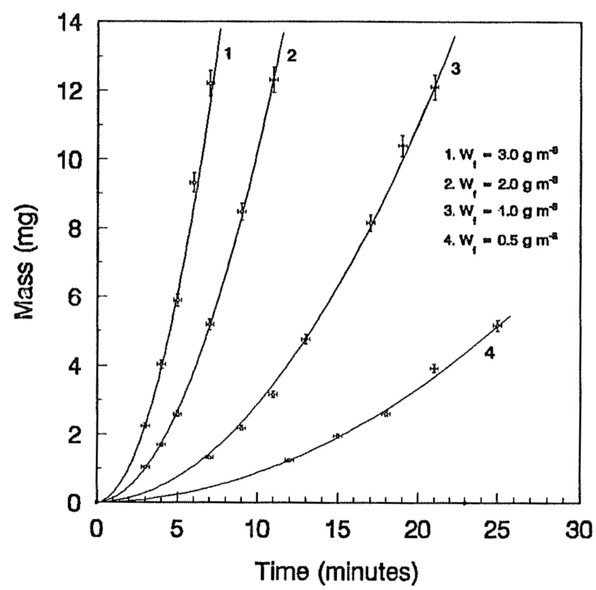

Figure 4: Variation of mass with time for different liquid water contents at T_a = -16.0°C, V = 2.0 m s^{-1}, r_m = 15 μm and P = 100 kPa.

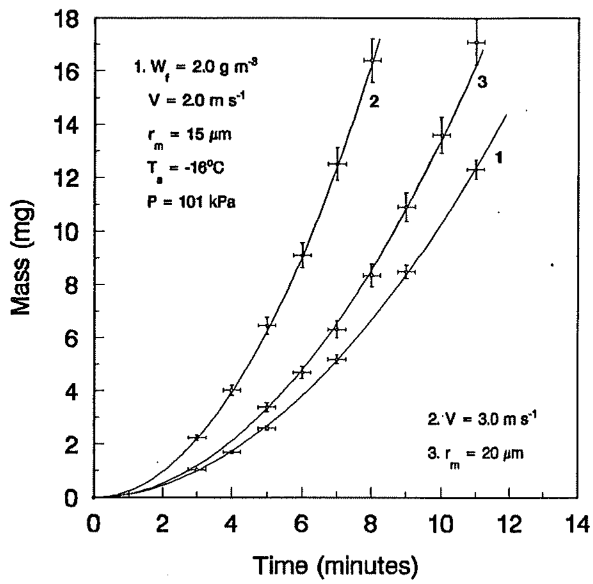

Figure 5: Mass growth with time for increases in V or r_m from the standard set of growth conditions.

5. ANALYSIS

By determining D, A_b, A_s, dM/dt and T_s, all the parameters in the heat and mass transfer equations were known or could be calculated. This allowed calculation of the bulk collision efficiency E_b and the Nusselt number Nu. Figure 6 shows the variation of E_b with graupel diameter for each of the experiments described above. The curves for the different W_f are equivalent within the ± 5% experimental errors, while the curves for V = 3.0 m s^{-1} and r_m = 20 μm show relative increases in E_b. All the curves show a decrease in E_b with increasing graupel diameter. These trends are consistent with the theoretical calculations of Langmuir and Blodgett (1946) and with the results of other investigations (Mossop 1976). Figure 7 shows the variation of E_b with the Stokes parameter K

$$K = \frac{2 V \rho_d r_d^2}{9 \eta r_t} \tag{6}$$

where ρ_d and r_d are the density and radius of the droplets, η is the dynamic viscosity of air, r_t is the radius of the graupel and V is the initial relative velocity between the graupel and the droplets. The median volume radius is taken as the characteristic radius of the droplet distribution. The curves are equivalent and can be compared to the theoretical collision efficiencies of an ideal sphere in potential flow, as determined by Langmuir and Blodgett (1946). Although the trends are similar the experimental collision efficiencies are approximately 20% lower than the theoretical efficiencies for the sphere. The enhanced surface roughness of the ice surface may decrease the collision efficiency of the droplets with the graupel surface.

The reduced collision efficiency is not caused by the charging on the droplets during the atomization/spraying process. Experiments were performed where voltage potentials were applied across the nozzle to produce average droplet charges of between 0 and ± 1 x 10^{-15} C/20 μm droplet, depending on the potential. Such charges had no effect on the nature of the accretion.

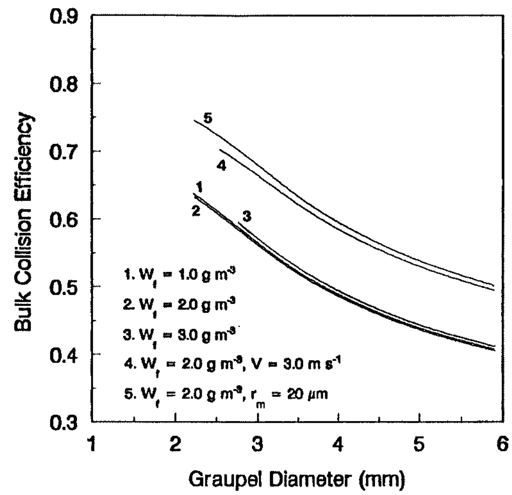

Figure 6: Bulk collision efficiency versus graupel diameter for different growth conditions. The growth parameters that are different from the standard set of growth conditions are listed.

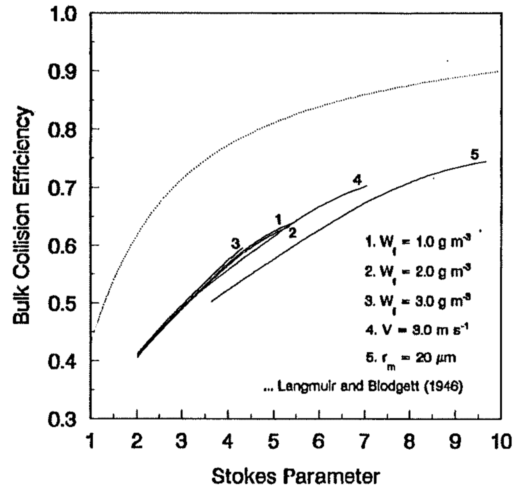

Figure 7: Bulk collision efficiency as a function of the Stokes parameter. The theoretical results of Langmuir and Blodgett (1946) for ideal spheres are shown for comparison.

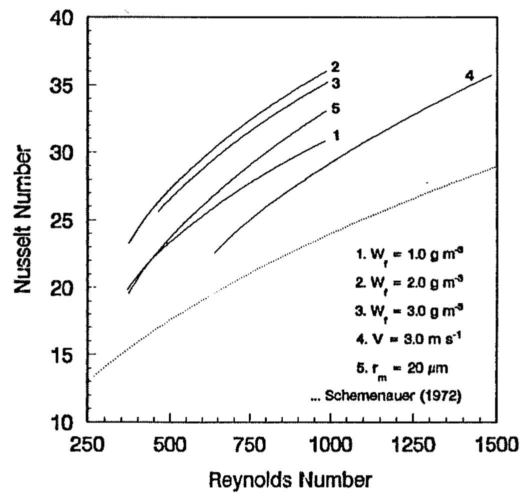

Figure 8: Nusselt number versus Reynolds number. The results of Schemenauer (1972) for smooth conical models are also shown.

The Nusselt number variation with Reynolds number is shown in Figure 8 for each set of experiments. The variability between the curves is within the ± 15% experimental error. The errors on the Nusselt number calculations are dominated by the uncertainties in the relative humidity (± 3 %) and the surface temperature (± 0.2°C). Figure 8 also shows the Nusselt numbers for smooth conical models as measured in an electrolytic tunnel (Schemenauer 1972). The results presented here are about 50% larger than those of Schemenauer. The difference can be attributed to the surface roughness of the ice surface. Schuepp and List (1969) showed that surface roughness can enhance the transfer rate by up to a factor of 2 over that of a smooth surface.

6. CONCLUSIONS AND FUTURE WORK

The experimental results can be summarized as follows:

1) Surface temperatures of graupel were measured remotely with an Agema 800 Thermovision thermal imaging system. The surface temperature elevations varied from 0.3 to 1.5 ± 0.2°C over the ambient air temperature, depending on the growth conditions.

2) Enough parameters in the heat and mass transfer equations that describe graupel growth can be measured or calculated so that the number of unknowns can be reduced to two: the bulk collision efficiency and the Nusselt number, which can subsequently be derived. Calculations of E_b and Nu have been obtained from a preliminary series of experiments.

A more extensive series of experiments has been performed to expand on these results, including the effects of T_a, V, r_m and pressure on the Nusselt number, Bulk collision efficiency, accretion density, graupel geometry and surface temperature. The results will be reported in Cober and List 1992.

7. ACKNOWLEDGEMENTS

The graupel studies were supported by the Atmospheric Environment Service of Canada. One of the authors (SC) is grateful to the Atmospheric Environment Service for providing three NSERC scholarships.

8. REFERENCES

Cober, S.G., and R. List, 1992: Measurements of the Heat and Mass Transfer Parameters Characterizing Graupel Growth. Submitted to J. Atmos Sci.

Dong, Y.Y., and J. Hallett, 1986: Structure, fall orientation and secondary ice formation by graupel. Preprints Cloud Phys. Conf., Snowmass, Col., 121 - 124, Amer. Met. Soc.

Griggs, D.J., J.P. Rouyet, R.E. Stewart and R. List, 1984: Laboratory simulations of graupel growth. Proc. 9th. Intern. Cloud Phys. Conf., Tallin, USSR, Vol 1, 163 - 166.

Keith, W.D., and C.P.R. Saunders, 1988: The collection efficiency of a rime covered target for water droplets. Atmos. Res., **22**, 105 - 123.

Knight, N.C., and A.J. Heymsfield, 1983: Measurements and interpretation of hailstone density and terminal velocity. J. Atmos. Sci., **40**, 1510 - 1516.

Langmuir, I., and K.B. Blodgett, 1946: Mathematical investigation of water droplet trajectories. Collected Works of Irving Langmuir, Vol 10. Pergamon Press, 348 - 393.

List, R., 1963: General heat and mass exchange of spherical hailstones. J. Atmos. Sci., **20**, 189 - 197.

List, R., G.B. Lesins, F. Garcia-Garcia and D.B. McDonald, 1987: Pressurized icing tunnel for graupel, hail and secondary raindrop production. J. Atmos. Oceanic Technol., **4**, 454 - 463.

Mossop, S.C., 1976: Production of secondary ice particles during the growth of graupel by riming. Quart. J. Roy. Meteor. Soc., **102**, 45 - 57.

Pflaum, J.C., and H.R. Pruppacher, 1979: A wind tunnel investigation of the growth of graupel initiated from frozen drops. J. Atmos. Sci., **36**, 680 - 689.

Pruppacher, H.R., and J.D. Klett, 1978: Microphysics of Clouds and Precipitation. Reidel, pp 714.

Schemenauer, R.S., 1972: The Convective Mass Transfer of Snow Crystals, Conical Graupel and Conical Small Hail Models. Ph.D. thesis, Department of Physics, University of Toronto, Toronto, Canada, M5S 1A7, pp 146.

Schuepp, P.H., and R. List: Mass transfer of rough hailstone models in flows of various turbulence levels. J. Appl. Meteor., **8**, 254 - 263.

Sublimational Break-Up of Secondary Ice Particles Associated with Frost Growth

Roger J. Cheng

Atmospheric Sciences Research Center
State University of New York
Albany, New York 12222, USA

Laboratory investigation confirmed that numerous ice particles were ejected from the frost surface of a frozen water drop growing in a moist environment (Figure 1). No ice particles, only micro-droplets were observed from a freezing supercooled water drop. High concentrations of ice particles, in the forms of fragments of ice crystals and/or rimed frozen droplets, were measured near two temperature zones; -5°C and -15°C, with fine crystal structures of needles or columns, and dendrites respectively (Figure 2).

Microscopic observation also confirmed that the mechanism for the break-up of the ejected ice particles was due to sublimation on the surface of fine structural ice crystals governed by curvature effect (Figure 3) rather than by mechanical fracturing; ice particle collisions.

Many recent reports strongly indicated that the riming-splintering mechanism is unlikely to be the major factor responsible for the high concentration of ice particles in clouds. The observation of the sublimational break-up of secondary ice particles associated with frost growth presented here may open up a new pathway for understanding the rapid glaciation phenomena of ice multiplication process in the atmosphere.

References

Cheng, R.J., 1973: The mechanism of multiplication process of glaciation in the atmosphere. 8th International Conference on Nucleation. Leningrad, U.S.S.R.

__________, 1973: Photomicroscopical investigation of the fragmentation of hydrometeors in the laboratory. The Microscope, **21**, 149-160.

__________, 1992: Fragmentation of charged ice particles associated with frost growth. 9th International Conference on Atmospheric Electricity. St. Petersburg, Russia.

Findeisen, W., 1940: Uber die Entstehung der Gewitterelektrizitat. Met. Zeit., **57**, 201-215.

Rydock, J.P. and E.R. Williams, 1991: Charge separation associated with frost growth. Q.J.R. Meteorol. Soc., **117**, 409-420.

Schaefer, V.J. and R.J. Cheng, 1971: The production of ice crystal fragments by sublimation and electrification. J. Rech. Atmos., 5, 5-10.

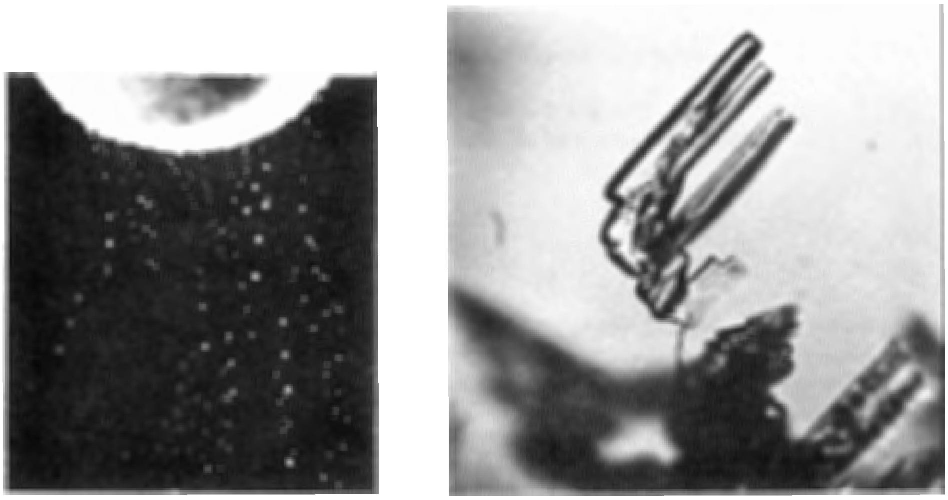

Figure 1. Ice particles being ejected from a frost ice pellet.

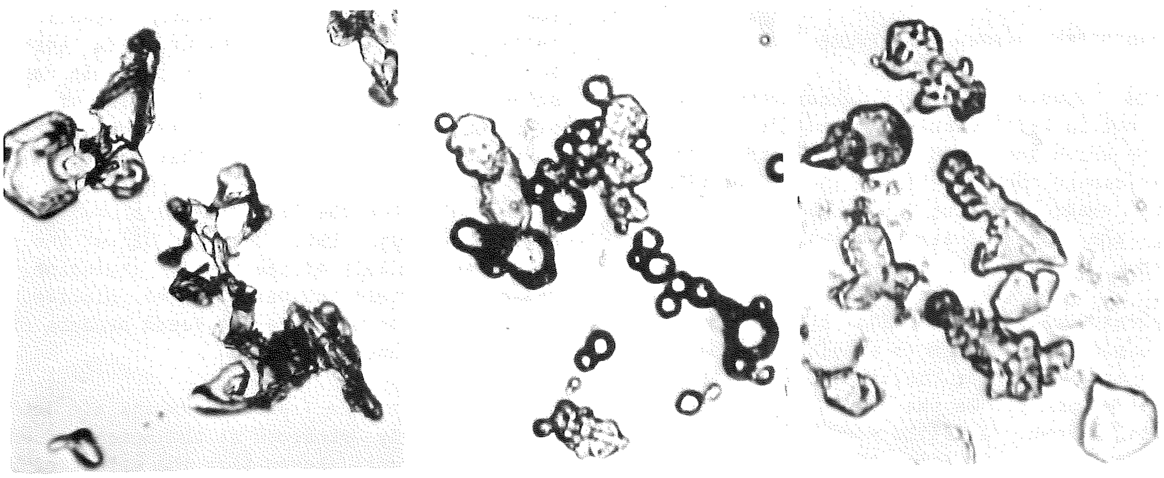

Figure 2. Samples of ejected ice particles in the forms of fragments of ice crystals and/or rimed frozen droplets.

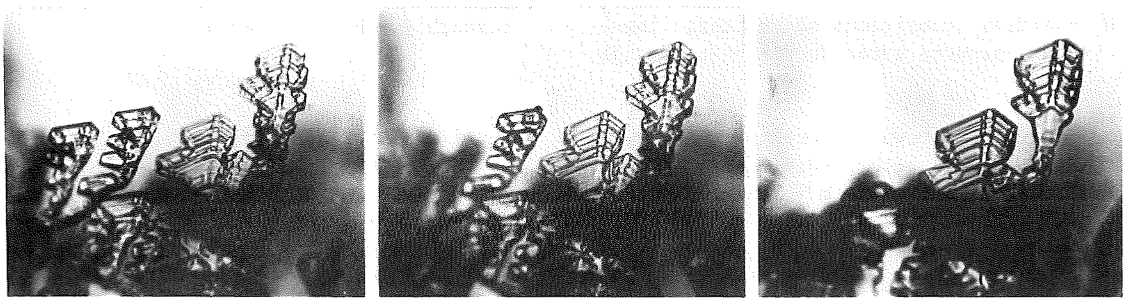

Figure 3. Progressive frost growth on an ice surface and sublimational narrowing stem of crystals due to curvature effect.

A LABORATORY STUDY OF EXPLOSION EFFECTS ON CLOUD DROPLETS COALESCENCE

Chen Ruzhen, Feng daxiong, Jiang Genwang and Zhao Jinghua

Chinese Academy of Meteorological Science
State Meteorological Administration, Beijing 100081, China

I. INTRODUCTION

Some theoretical research [1] shown that the lightning shock wave could promote the coalescence growth of cloud droplets in a very short time. A great number of anti-aircraft gun shells containing AgI have been used in weather modification operations in China. It is doubtful whether the cloud and precipitation could be effected by the shell explosion. In this study a simulating explosion shock wave has been used in $2m^3$ cloud chamber to investigate the possible effects of explosion on cloud droplets coalescence.

II. EXPERIMENTAL SYSTEM AND METHOD

1. Cloud Simulating: The experiments were carried out in $2.1m^3$ cloud chamber (with height 2.08m) in which the cloud was continuously sent by an ultrasonic nebulizer [2]. The LWC of cloud could be controlled from 0.5 to about $3g/m^3$ by changing the rate of air flow which fed the nebulizer.

2. Explosion Simulating: The hydrogen-oxygen thermal explosion was used to simulate the explosion. A metal cylinder container (1.1 liter in volume) was mounted on the top of the chamber with upside down. A little amount of hydrogen (about 100ml) was sent into the container. As soon as an eletric spark generated in it the mixed hydrogen-air exploded and the shock wave and air jet shout into the chamber. The acoustic pressure level of shock wave was measured at the bottom of the chamber and it was about 130db. The explosion was uncontaninated except producing a little water vapor (0.08gm.). Some experiments in high humidity conditions shown that these vapor could not produce water droplet big enough to precipitate.

3. Cloud Droplet Spectrum Measurement: The cloud droplets were sampled with precipitating method using the water sensitive film [3] at the bottom of the chamber. Each sample took 20-40sec.for droplets precipitating on the film ,and 4 to 6 samples were taken for eash explosion. Then the traces of droplets on the film were counted and measured under microscope to obtain the droplet spectra. The cloud droplets were also monitored by PMS FSSP probe which was slightly modified by adding an airflow in the sampling area.

III. RESULTS AND DISCUSSION

1. The measurements of precipitation samples showed that the mean diameter of cloud droplet increased from 8.18µm before explosion to 8.54µm after explosion, the cloud droplet spectra became broader (fig. 1 and 3) and the concentrations of larger droplet increased (Table I.). For example, the concentration percentage of $d \geqslant 26.3\mu m$ droplet increased by a factor of 4. The concentration of larger droplets ($d \geqslant 39.5\mu m$) increased from 15/l to 80/l after explosion under the conditions of temperature 2-4°C and LWC $2\text{-}3g/m^3$. For lower LWC ($0.5\text{-}1g/m^3$) the droplet spectra also became broader but $d \geqslant 39.5\mu m$ droplets were not found. All these changes took place in two minutes. It seemed that the effect time of explosion on droplet coalescence was very short and large LWC was favourable for this process.

2. The data from the FSSP (fig.2) showed that the number density, LWC, $\overline{D}$, and $\sqrt[3]{\overline{D^3}}$ of the cloud decreased suddenly at the time of explosion, then these parameters recovered in two minutes. But the larger droplets were not found because of its very small sampling volume.

3. The sonic wave, shock wave and air jet were instantaneously produced at the moment of explosion, experiments showed that the effect of shock wave and air jet played an important role in producing larger droplets.

4. Although these simulating conditions were limited, it seemed that explosion in cloud could promote the droplet coalescence process and produce some larger droplets which would grow through further coalescence.

REFERENCES

1. Li Guo-Qing and Kang Tian-yi, 1982: The effect of lightning shock wave on the motion and the coalescences of cloud droplets, Acta Meteor. Sinica, 40, 475-482.
2. Feng Daxiong, Wang Yunqing, Chen Ruzhen and Jiang Gengwang, 1990: A $2m^3$ isothermal cloud chamber for the study of artificial ice nuclei, Acta Meteor. Sinica, 4, 494-502.
3. Feng Daxiong, 1980: A new gelatin film technique for measuring cloud droplets, Acta Meteor. Sinica, 38, 360-365.

Table I. The measurements of cloud larger droplet before and after explosion

Cloud conditions	Percentage of droplets with d≥26.3μm		Average number of d≥39.5μm precipitated on 1cm² area		d≥39.5 droplet concentration (corrected by terminal velocity)	
	before explosion	after explosion	before explosion	after explosion	before explosion	after explosion
2-4 °C 2-3g/m^3	0.84% (24)	3.50% (33)	1.3 (24)	10.5 (23)	15/1	80/1
25 °C 2-3g/m^3	3.19% (19)	5.68% (34)	2.5 (15)	4 (32)	40/1	70/1
25 °C 0.5-1g/m^3	0.16% (6)	1.49% (16)	0 (6)	0.9 (10)	0	10/1

Numbers in the bracket indicate the sampling number

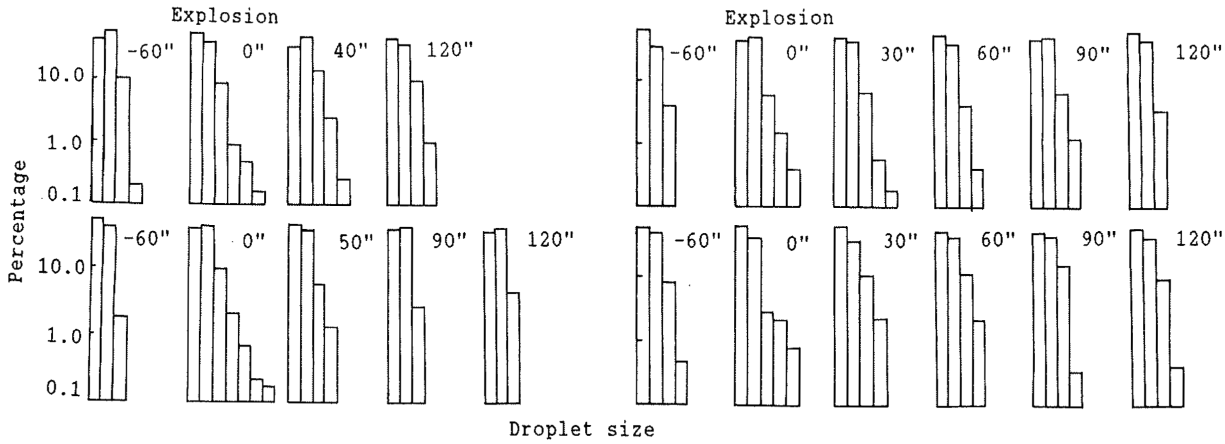

a. T=2-4 °C, LWC=2-3g/m^3 b. T=25 °C, LWC=0.5-1g/m^3

Fig.1. The variation of droplet spectra with time after explosion. Pecipitation time for each sample is 20-30 sec., droplet size interval =6.58μm, sampling beginning time shown in the figure.

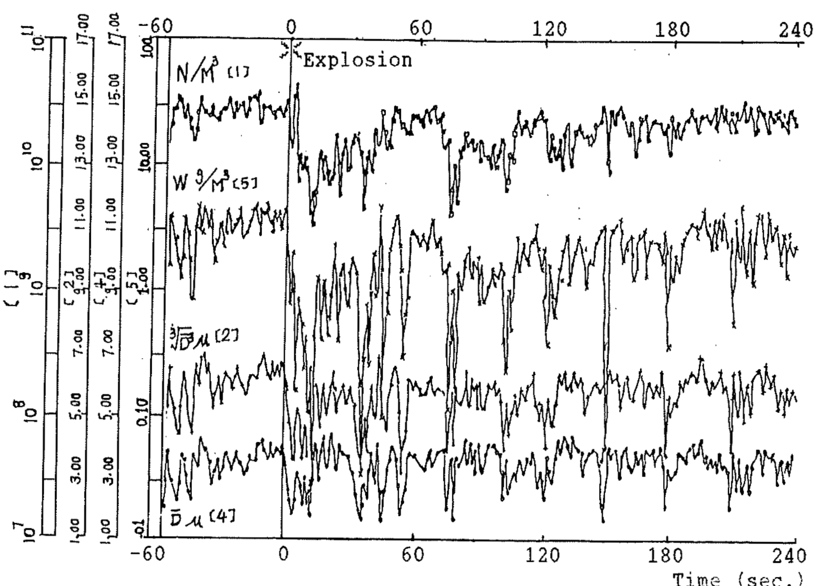

Fig.2. The variation of cloud parameters with time measured by PMS FSSP probe.

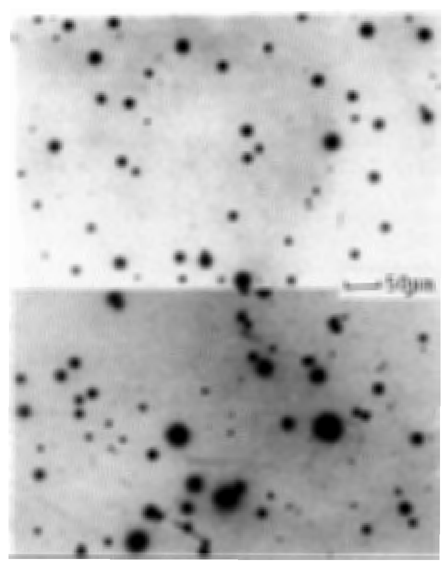

Fig.3. The micragroph of droplet on sampling film before and after explosion.

A THEORETICAL STUDY OF THE REDISTRIBUTION OF AEROSOL POLLUTANTS IN POLLUTED CLOUD DROPLETS SPECTRUM DUE TO COAGULATION

Isaac M. Enukashvily

Dept. for Research and Development, Israel

Meteorological Service, P.O. Box 25, Beit-Dagan, Israel

1. INTRODUCTION

Coagulation interaction between cloud droplets spectrum and population of aerosol particles (hereinafter AP) is very important among the basic mechanisms responsible for atmospheric chemistry and for pollution of cloud liquid water and precipitation. The microphysics of coagulation process in the population of polluted cloud droplets (hereinafter PCD) and of AP, and the PCD/AP spectrum time evolution is described by the corresponding integro-differential coagulation kinetic equation (hereinafter CKE) for PCD/AP number density distribution function n(x,y,t) (Smirnov, 1963; Zebel, 1966; Berry, 1969). The value of n(x,y,t)dxdy is the mean (over PCD/AP ensemble) number of PCD/AP which contain liquid water phase with mass in the range (x,x+dx) and aerosol pollutants with mass in the range (y,y+dy); t- denotes time.

Recently numerical model of time evolution of AP number concentration in drops due to AP scavenging by drops and due to redistribution by coagulation between polluted drops has been developed by Beheng and Herbert (1986). However in this numerical model the mutual coagulation between AP was neglected and the change of the spectrum of polluted drops due to capture of AP by drops was considered as a "drift" term (Berry, 1969; for this see also Drake 1972), that is as a diffusion process. It should be noted also that AP may be considered as a PCD with zero mass of liquid water phase and therefore it is not always necessary to operate with a set of two coupled kinetic equations for two number density distribution functions as in the numerical model of Beheng and Herbert (1986).

In this study exact analytic solutions of CKE for various types of initial PCD/AP spectrum n(x,y,o) with constant coagulation kernel and with coagulation kernel taken as proportional to the sum of the masses of colliding PCD/AP are listed and discussed; Also numerical computations are performed to study the PCD/AP spectrum time development, especially from the point of time evolution of the degree of pollution of cloud liquid water by aerosol pollutants in terms of n(x,y,o) and in terms of coagulation kernel.

2. ANALYTIC SOLUTIONS OF CKE FOR SPATIALLY HOMOGENEOUS PCD/AP CLOUDS

The following PCD/AP initial spectra are considered in this study:

$$\left.\begin{aligned} &n(x,y,0) = A\exp(-\beta x-\gamma y);\\ &A = N(0)\beta\gamma;\beta = N(0)/L;\gamma = N(0)/\Pi; \end{aligned}\right\}, \qquad (1)$$

$$\left.\begin{aligned} &n(x,y,0) = A_1\exp(-\beta_c x)\delta(y) +\\ &+ B_1\exp(-\gamma_p y)\delta(x)\\ &A_1 = N_c(0)\beta_c;\ \beta_c = N_c(0)/L;\\ &B_1 = N_p(0)\gamma_p;\gamma_p = N_p(0)/\Pi \end{aligned}\right\}, \qquad (2)$$

$$\left.\begin{aligned} &n(x,y,0) = N(0)\delta(x-x_0)\delta(y-y_0);\\ &x_0 = L/N(0);y_0 = \Pi/N(0); \end{aligned}\right\} \qquad (3)$$

$$n(x,y,0) = N(0)\beta\exp(-\beta x)\delta(y-y_0); \qquad (4)$$

$$n(x,y,0) = Bx^{\lambda}y^{\nu}\exp(-\varepsilon x-\omega y), \qquad (5)$$

where B, λ, ν, ε, ω are positive parameters. In (1), (3), (4) N(0) is the initial number concentration of PCD, L is the liquid water content and Π is the total mass of aerosol pollutants in PCD initial spectrum.
In (2) $N_c(0)$ and $N_p(0)$ are the initial number concentrations respectively of initially pure cloud droplets and of AP; L - is the liquid water content of initially pure cloud droplets and Π - is the total mass of AP in PCD/AP initial spectrum; δ - is the Dirac delta function. The main difference for example between (1) and (2) is that in (2) we have initially pure cloud droplets and AP without liquid water phase, while in (1) initially the total mass of aerosol pollutants is contained in PCD initial spectrum.

For coagulation kernel $\sigma(x,y;u,v)=\sigma$=constant CKE for PCD/AP spectrum time evolution may be written as (Enukashvily, 1988):

$$\partial n(x,y,t)/\partial t = -\sigma N(t)n(x,y,t) +$$

$$+ (\sigma/2) \int_0^x du \int_0^y n(x-u,y-v,t)n(u,v,t)dv, \qquad (6)$$

$$N(t) = N(0)/(1 + (\sigma/2) N(0) t) , \qquad (7)$$

represents the total number concentration of PCD/AP. The form of (6) suggests the use of Laplace transforms in its solution; so we obtain exact analytic solutions of eq. (6):
a) for initial spectrum (1) (Enukashvily, 1988)

$$\left.\begin{array}{l} n(x,y,t)=A(t)\exp(-\beta x-\gamma y)I_0\left[2(\tau\beta x\gamma y)^{1/2}\right], \\ A(t)=(N(t)^2/N(0))\beta\gamma, \quad \tau=1-(N(t)/N(0)) \end{array}\right\} \qquad (8)$$

b) For initial spectrum (2) solution of (6) is

$$n(x,y,t) = (1-\tau)^2(A_1\exp(-\beta_1 x)\delta(y)+$$

$$+B_1\exp(-\gamma_1 y)\delta(x)+A_1B_1(\tau/N(0))*$$

$$*\exp(-\beta_1 x-\gamma_1 y)(2I_0(\Omega)+C_1I_1(\Omega))), \qquad (9)$$

where

$$\left.\begin{array}{ll} \beta_1 & = (\beta_c/N(0))(N(t)+\tau N_p(0)) \\ \gamma_1 & = (\gamma_p/N(0))(N(t)+\tau N_c(0)) \\ N(0) & = N_c(0) + N_p(0) \\ \Omega & = 2(\tau/N(0))(A_1xB_1y)^{1/2} \\ C_1 & = 2(\tau/N(0))(A_1x+B_1y)/\Omega; \end{array}\right\}, \qquad (10)$$

In (8)-(9) I_0 and I_1 are the modified Bessel functions of the first kind respectively of orders zero and one.
c) For an arbitrary initial spectrum of PCD/AP we obtain the general solution of eq. (6) as:

$$n(x,y,t) = (1-\tau)^2*$$

$$*\sum_{k=0}^{\infty}(\tau/N(0))^k(L_p^{-1}(L_s^{-1}(F(p,s,0)^{k+1}))); \qquad (11)$$

where the the sign L_p^{-1} $(L_s^{-1}$ ( )) denotes the double inverse Laplace transforms and $F(p,s,0)$ is the double Laplace transform of $n(x,y,0)$. From (11) also the solutions of eq. (6) with initial conditions (3), (4), (5) are obtained.

Now for coagulation kernel

$$\sigma(x,y;u,v)=\sigma_0((x+y)+(u+v)), \ \sigma_0=\text{constant}; \qquad (12)$$

the CKE for $n(x,y,t)$ time evolution may be written as:

$$\partial\Psi(z,\mu,\tau)/\partial\tau = (z_0/2)(z+\mu)*$$

$$*\int_0^z d\eta \int_0^\mu \Psi(z-\eta,\mu-\xi,\tau)\Psi(\eta,\xi,\tau)d\xi, \qquad (13)$$

where a new unknown function $\Psi(z,\mu,\tau)$ is associated with $n(x,y,t)$ as:

$$n(x,y,t) = (N(t)/z_0)\exp(-\tau(z+\mu))\Psi(z,\mu,\tau), \qquad (14)$$

and,

$$\left.\begin{array}{l} z = x/z_0; \mu = y/z_0; \eta = u/z_0; \xi = v/z_0; \\ z_0 = M/N(0); \qquad N(t) = N(0)(1-\tau); \\ \tau = 1-\exp(-\sigma_0 Mt); \qquad M = L+\Pi \end{array}\right\}, \qquad (15)$$

The form of nonlinear integrodifferential eq. (13) again suggests the use of the Laplace transforms in its solution, so we have;

$$\partial\Phi(p,s,\tau)/\partial\tau+z_0\Phi(p,s,\tau)((\partial\Phi(p,s,\tau)/\partial p)+$$

$$+(\partial\Phi(p,s,\tau)/\partial s))=0; \qquad (16)$$

where $\Phi(p,s,\tau)$ is the double Laplace transform of $\Psi(z,\mu,\tau)$. The general implicit solution of the quasilinear partial differential equation (16) with an arbitrary initial condition $\Phi_0(p,s)=\Phi(p,s,0)$ may be written as:

$$\Phi(p,s,\tau) = \Phi_0(p-\tau z_0\Phi, s-\tau z_0\Phi), \qquad (17)$$

Applying double inverse Laplace transforms to (17) and introducing new variables of integration (Scott, 1968)

$$\left.\begin{array}{l} p_1 = p-z_0\tau\Phi(p,s,\tau) = p-z_0\tau\Phi_0(p_1,s_1) \\ s_1 = s-z_0\tau\Phi(p,s,\tau) = s-z_0\tau\Phi_0(p_1,s_1) \end{array}\right\}, \qquad (18)$$

We obtain solution of eq. (13) for example corresponding to the exponential initial spectrum (1) as:

$$n(x,y,t)=(N(t)\beta\gamma)\exp(-(x/z_0)(\tau+(M/L))-(y/z_0)*$$

$$*(\tau+(M/\Pi)))\sum_{k=0}^{\infty}\left[\frac{(\beta\gamma\tau)}{z_0}\right]^k\left[\frac{(xy(x+y))^k}{((k!)^2(k+1)!)}\right]; \qquad (19)$$

For coagulation kernel

$$\sigma(x,y;u,v)=\sigma_1(x+u),\ \sigma_1=\text{constant}; \tag{20}$$

the CKE for $n(x,y,t)$ time evolution may be written as:

$$\partial n(x,y,t)/\partial t = -\sigma_1(xN(t)+L)n(x,y,t) + $$

$$+ (\sigma_1 x/2)\int_0^x du\int_0^y n(x-u,y-v,t)n(u,v,t)dv, \tag{21}$$

Applying a method similar to the method which we have used for the general solution of nonlinear integrodifferential equation (13), we obtain the general solution of integrodifferential equation (21) with an arbitrary initial condition as:

$$n(x,y,t) = \beta N(t)\exp(-\tau z)\Psi_1(z,\mu,\tau); \tag{22}$$

where

$$\Psi_1(z,\mu,\tau)=\sum_{k=0}^{\infty}\left[\frac{(\tau z/\gamma)^k}{(k+1)!}\right]L_p^{-1}\left[L_s^{-1}(\Phi_0(p,s)^{k+1})\right]; \tag{23}$$

The sign $L_p^{-1}(L_s^{-1}(\ ))$ again denotes the double inverse Laplace transforms and $\Phi_0(p, s)$ represents the double Laplace transform of $\Psi_1(z,\mu,0) = n(x,y,0)/(\beta N(0))$ (see (22)). The nondimensional masses z and μ, and nondimensional time τ in (22) - (23) are defined as;

$$\left.\begin{array}{l} z = \beta x;\mu = \gamma y;\beta = N(0)/L;\gamma = N(0)/\Pi; \\ N(t) = N(0)(1-\tau);\tau = 1-\exp(-\sigma_1 Lt); \end{array}\right\} \tag{24}$$

For initial exponential spectrum (1), the solution of (21) is:

$$n(x,y,t)=(N(t)\beta\gamma)\exp(-(1+\tau)\beta x-\gamma y)*$$

$$*\sum_{k=0}^{\infty}\frac{((\tau\gamma y)^k(\beta x)^{2k})}{((k!)^2(k+1)!)}; \tag{25}$$

From (22)-(24) also the solutions of eq. (21) with initial conditions (3)-(4) are obtained.

3. NUMERICAL COMPUTATIONS AND CONCLUDING REMARKS

To investigate the time evolution of PCD/AP spectrum as a result of coagulation process in PCD/AP population in addition also computations of the following distribution functions are performed.

$$N(x,t) = \int_0^{\infty} n(x,y,t)dy, \tag{26}$$

$$\Pi(x,t) = \int_0^{\infty} yn(x,y,t)dy, \tag{27}$$

$$L(x,t) = xN(x,t), \tag{28}$$

$$m_p(x,t) = \Pi(x,t)/N(x,t), \tag{29}$$

(26) represents the number density distribution function of liquid water phase in the PCD/AP spectrum; (27) describes distribution of total (integral) masses of aerosol pollutants in PCD/AP spectrum in terms of the mass of liquid water phase of single PCD; (28) represents the mass density distribution function of liquid water phase in PCD spectrum and the latter (29) represents the spectral mean mass of aerosol pollutants per single PCD. When analytic solutions of CKE are found then the distribution functions (26) - (29) are computed simply by means of quadratures; for example, for exponential initial spectrum (1) and for initial spectrum (4) substituting the corresponding solutions of CKE (6) into (26) - (29) we obtain the same relations for both PCD/AP initial spectrum

$$N(x,t) = (N(t)^2/L)\exp(-(N(t)/L)x), \tag{30}$$

$$\Pi(x,t) = (\Pi/N(0))(1+\tau\beta x)N(x,t), \tag{31}$$

$$m_p(x,t) = (\Pi/N(0))(1 + \tau\beta x), \tag{32}$$

Analogously, for initial spectrum (2) substituting the corresponding solution (9)-(10) of CKE (6) into (26) - (29) we have:

$$\left.\begin{array}{l} N(x,t)=N_c(x,t) + N_p(t)\delta(x) \\ N_c(x,t)=(N_c(t)^2/L)\exp(-(N_c(t)/L)x) \end{array}\right\}, \tag{33}$$

$$\left.\begin{array}{l} \Pi(x,t)=\Pi_c(x,t)+\Pi_p(t)\delta(x); \quad \Pi_c(x,t)= \\ =\tau\left[\dfrac{\Pi}{N_c(0)}\right]\left[\dfrac{N_c(t)}{N(t)}\right]\left[2+\tau\beta_c x\left[\dfrac{N_c(t)}{N(t)}\right]\right]N_c(x,t) \end{array}\right\}, \tag{34}$$

$$m_p(x,t) = \Pi_c(x,t)/N_c(x,t)=\tau(\Pi/N_c(0))*$$

$$*(N_c(t)/N(t))(2+\tau\beta_c x(N_c(t)/N(t))) \tag{35}$$

where $\delta(x)$ again is the Dirac delta function and

$$\left.\begin{array}{l} N_c(t)=(N_c(0)N(t))/(N(t)+\tau N_c(0)) \\ N_p(t)=N_p(0)(1-\tau)(N_c(t)/N_c(0)); \\ \Pi_p(t)=\Pi(N_c(t)/N_c(0))^2 \end{array}\right\}; \qquad (36)$$

And finally for coagulation kernel (20) with known analytic solution of CKE (21), given by (25) we have from (26)-(29):

$$N(x,t)=(N(t)/x\sqrt{\tau})\exp(-(1+\tau)\beta x)I_1(2\sqrt{\tau\beta x}), \quad (37)$$

$$\Pi(x,t)=(N(t)(\Pi/L))\exp(-(1+\tau)\beta x)I_0(2\sqrt{\tau\beta x}), \quad (38)$$

$$m_p(x,t)=(\Pi/N(0))*$$

$$*((I_0(2\sqrt{\tau\beta x}))/(I_0(2\sqrt{\tau\beta x})-I_2(2\sqrt{\tau\beta x}))); \qquad (39)$$

where $N(t)$, τ, β are given by (24) and I_0, I_1, I_2 are the modified Bessel functions of the first kind respectively of orders zero, one and two.

To study time evolution of the degree of pollution of cloud liquid water by aerosol pollutants the values of number concentration $N_k(t)$, of the liquid water content $L_k(t)$ and of the AP total masses $\Pi_k(t)$ per classes (x_k, x_{k+1}) are computed. $x_{k+1} = 2x_k$ are grid points on the mass axes of PCD liquid water phase. Analyses of numerical computations show that:

(a) For large time intervals PCD spectrum classes (x_k,x_{k+1}) with larger $L_k(t)$ contain larger $\Pi_k(t)$. For solutions of CKE (6), for example for (8) and (9)-(10) this result $\Pi_k(t)\sim$ $\sim L_k(t)$ is obtained also in analytic form.

(b) For large time intervals the main part of the total (integral) masses of aerosol pollutants are concentrated in the same classes of the PCD spectrum where we have again the main part of the total liquid water content of PCD spectrum.

(c) According to (32), (35) and (39) the spectral mean mass of aerosol pollutants per single PCD increases with time t and with the mass x of liquid water phase of single PCD.

Thus for large time intervals we obtain approximately full pollution of cloud liquid water by aerosol pollutants as a result of coagulation process in population of PCD/AP and this asymptotic effect does not depend on the fine structure of the initial distribution of AP masses per single PCD and on the coagulation kernels considered in this study. Therefore collisions between PCD/AP and their mutual coagulation resulting in redistribution of the masses of aerosol pollutants in PCD spectrum is found to be essentially responsible for the asymptotic effect of approximately full pollution of cloud liquid water by aerosol pollutants.

ACKNOWLEDGEMENT

The author is thankful to Dr. K.D. Beheng for discussions, and to Mrs. P. Weinreich for manuscript preparation.

REFERENCES

Beheng, K.D., and F. Herbert, 1986: Mathematical studies on the aerosol concentration in drops changing due to particle scavenging and redistribution by coagulation. Meteorol. Atmos. Phys. 35, 212-219.

Berry, E.X., 1969: A mathematical framework for cloud models. J. Atmos. Sci. 26, 109-111.

Drake, R.L., 1972: A general mathematical survey of the coagulation equation. In Hidy G.M. and J.R. Brock, 1972: Topics in current aerosol research. Part 2, Pergamon Press, New York.

Enukashvily, I.M., 1988: Kinetic equation for polluted cloud droplet spectra. Proceedings of the 10th ICCP 1, 172-174, Bad-Homburg, FRG.

Scott, W.T., 1968: Analytic studies of cloud droplet coalescence. J. Atmos. Sci. 25, 54-65.

Smirnov, V.I., 1963: The generalized Boltsman kinetic equation and some equations of the kinetics of the polydispersal systems. Trudi TSAO, 47.

Zebel, G., 1966: Coagulation of aerosols; Aerosol Science (ed. by C.N. Davies). Academic Press, New York, 31 - 58.

EVOLUTION OF RAINDROP SIZE DISTRIBUTION BY COALESCENCE, COLLISIONAL BREAKUP AND EVAPORATION

Z. Hu and R. C. Srivastava

Laboratory for Atmospheric Probing, Department of the Geophysical Sciences
The University of Chicago, Chicago, IL 60637

1. INTRODUCTION

The evolution of raindrop size distributions in heavy rain is generally believed to be governed by the following processes: (1) drop coalescence, (2) collisional drop breakup, (3) drop evaporation, and (4) drop sorting by differential fall speeds and atmospheric motions. In this paper, we discuss the evolution of the drop size distribution (hereafter, dsd) by the operation of processes (1), (2) and (3). A number of published studies have dealt with (1), (2) and (4) in various combinations. In some early work, processes (1) and (3) were considered. However, to our knowledge, process (3) has not been considered in studies which include a realistic formulation of (1) and (2); studies which have considered (1), (2) and (3) together have generally adopted a very simplified model for (2) (for example, Brazier-Smith *et. al.* (1973)). Thus our work differs from earlier work in considering process (3) together with a more realistic formulation of (1) and (2), namely, the one due to Low and List (1982) (hereafter referred to as LL). We also show that care should be exercised in the selection of numerical techniques for solving the kinetic equation for the dsd; we shall see that some published results differ significantly from each other presumably because of differences in numerical methods. The importance of using the *correct* equation for drop evaporation is emphasized; many recent studies have used an erroneous equation for the calculation of drop evaporation. Finally, a comparison of calculated and observed dsds suggests that the LL formulation of drop coalescence and breakup may be overestimating breakup and underestimating coalescence.

2. EQUATIONS AND NUMERICAL METHODS

a. *The Kinetic Equation*

For the spatially homogeneous case, the kinetic equation for the dsd may be written as:

$$\partial n(m,t)/\partial t + \partial[n(m,t)\dot{m}]/\partial m = C(m,t) + B(m,t) \quad (1)$$

where m is the drop mass, $n(m,t)$ is the drop concentration density, $\dot{m}$ is the rate of increase of drop mass by condensation (or evaporation), and C *and* B represent the effects of coalescence and breakup:

$$C(m,t) = \frac{1}{2}\int^{m} n(m',t)n(m-m',t)k(m',m-m')E_c(m',m)dm'$$

$$- n(m,t)\int n(m',t)k(m,m')E_c(m',m)dm' \quad (2),$$

$$B(m,t) = \iint P_b(m;m',m'')n(m',t)n(m'',t)k(m',m'')E_b(m',m'')$$

$$dm'dm'' - n(m,t)\int n(m',t)k(m,m')E_b(m,m')dm' \quad (3).$$

Here k is the (hydrodynamic) collision kernel, E_c is the coalescence efficiency, E_b is the breakup efficiency and $P_b(m;m',m'')$ gives the dsd density generated by breakup following a collision of drops of masses m' *and* m''. When not indicated, the upper and /or lower limits of integration are the largest and smallest masses used in the calculation.

b. *Coalescence and Breakup*

The formulation of coalescence and breakup follows LL with some modifications. The collection and breakup efficiencies are taken from their work. The fragment size distribution (P_b) is also taken from LL but with the following modifications (for symbols, see LL):

(1) If σ_{F3} has no solution and $F_F > 2$, then P_{F3} is replaced by a delta function at D_{FF3} and the coefficient determined so that filament breakup satisfies mass conservation. Similar adjustments are applied if σ_{S2} has no solution and $R_S > 0$, or if σ_{D2} has no solution and $R_D > 0$.

(2) If $H_{F3} < 0$, then P_{F3} is adjusted as above.

(3) If fragment size distribution given by LL does not satisfy mass conservation, then conservation is enforced according to the scaling technique of Brown (1988). This is applied to each type of breakup.

It may be noted here that in several publications, the second term in equation (3) for $B(m,t)$ has been written as:

$$n(m,t)\int\frac{n(m',t)\beta(m',m)}{(m+m')}dm' \int^{m+m'} m''P_b(m'';m,m')dm'' \quad (4)$$

where

$$\beta(m',m'') \equiv k(m',m'')E_b(m',m'').$$

Although the kinetic equation is technically correct in this form, it will satisfy mass conservation even if P_b does not. Our method of writing $B(m,t)$ ensures that it will conserve mass only if P_b does. But it is still necessary to ensure that each type of breakup conserves mass individually.

c. *Evaporation*

In many recent publications, the evaporation rate equation has been taken to be the same as the equation for the growth of cloud drops by condensation, the supersaturation being negative in this case. Srivastava and Coen (1992), showed that this method underestimates the evaporation rate, and results in large errors under warm dry conditions. The reason is that the condensation equation assumes small deviations from saturation and although the deviations are small for condensation they can be large for evaporation. We have calculated evaporation by iterative solution of the following equations for the diffusion of water vapor and heat:

$$dm/dt = 4\pi D_v f_v r(\rho_\infty - \rho_r),$$
$$L\,dm/dt = 4\pi k f_h r(T_\infty - T_r) \quad (5)$$

In the above r is the drop radius, D_v, the diffusivity of water vapor, and f_v *and* f_h the ventilation coefficients for vapor and heat, L the latent heat and ρ *and* T the vapor density and temperature, the subscripts ∞ *and* r referring to the drop environment and surface. Values for the physical quantities in the above were taken from Pruppacher and Klett (1978).

d. *Numerical Method*

We have discretized the kinetic equation, without the condensation term, using a logarithmic mass scale and Bleck's method (Bleck,1970):

$$\hat{n}_k(t+\Delta t) = \hat{n}_k(t) + \Delta t\{(1/2)\sum{}^{*} a_{ijk}\hat{n}_j(t)\hat{n}_i(t) - \hat{n}_k(t)\sum b_{ik}\hat{n}_i(t)$$

$$+ (1/2)\sum p_{ijk}\hat{n}_j(t)\hat{n}_i(t) - \hat{n}_k(t)\sum q_{ik}\hat{n}_i(t)\}2/(m_{k+1}^2 - m_k^2) \quad (6)$$

In the above, forward time integration has been used, a, b, p *and* q are determined by C *and* B (for details, see Bleck, 1970), and the concentration $\hat{n}$ is defined by:

$$\hat{n}_k(t) = \int_{m_k}^{m_{k+1}} mn(m,t)dm \Big/ \int_{m_k}^{m_{k+1}} mdm \quad (7)$$

The above numerical method is diffusive giving faster production of large drops. To control this spreading, we have defined *another* concentration $\check{n}$ as follows:

$$\check{n}_k(t) = \int_{m_{k-1}}^{m_k} mn(m,t)dm \Big/ \int_{m_{k-1}}^{m_k} mdm \quad (8)$$

with a corresponding discretization for it. Solutions are obtained for the $\hat{n}$ *and* $\check{n}$ and their average is taken as the solution of the kinetic equation. This method was found to give more accurate results as judged by: (1) calculations for cases for which analytical results are known, and (2) accuracy of conservation of mass.

The condensation term in the kinetic equation is advective in nature and is difficult to discretize accurately. Methods in common use, such as, the 'upwind' method are very diffusive. We have used Smolarkiewicz' (1983) method to discretize the condensation term. For evaporation, this method is stable for $\hat{n}$ but unstable for $\check{n}$ (sometimes giving negative concentrations). Further, even the Smolarkiewicz method can be too diffusive with a drop mass scale generally used for the coalescence and breakup terms. Since the coalescence and breakup terms are computationally much more intensive than the condensation term, we have used the following procedure for solving the complete kinetic equation. First, the size distribution is advanced one time step neglecting evaporation. The resulting size distribution is then interpolated on to a much finer logarithmic mass scale. Smolarkiewicz' method is then used to advance the concentration ($\hat{n}$) by evaporation only. Finally, the size distribution is found on the coarse grid and the cycle of calculations is repeated. Typically, the number of grid points used for the evaporation term was 4 times that for the coalescence and breakup terms.

A test of the above method is shown in fig. 1. We consider coalescence and evaporation only. The coalescence kernel is taken to be a constant = 3 $cm^2 s^{-1}$ and the evaporation rate is taken to be given by:

$$dm/dt = -\sigma m, \quad \sigma = \log(5/3)/2700\, s^{-1} \quad (9)$$

Under these conditions the kinetic equation can be solved analytically. The numerical and analytical solutions are shown in figure 1 for the initial distribution:

$$n(m,0) = (N_0/m_0)\exp(-m/m_0), \qquad D(m_0) = 0.1\ cm,\ N_0 m_0 = 1\ gm^{-3}. \quad (10)$$

3. RESULTS AND DISCUSSION

a. *Results of Calculations*

In the following, the minimum diameter was taken as 0.01 cm. and the water content of the initial distribution as 1 gm^{-3}. Results for other water contents can be obtained by simple scaling (Srivastava, 1988).

Figure 2 shows results of calculations *without* evaporation. Curves a, b and c show the distributions at one hour for two mass scales and two initial distributions. For curve a, the ratio of masses of successive categories (called c)

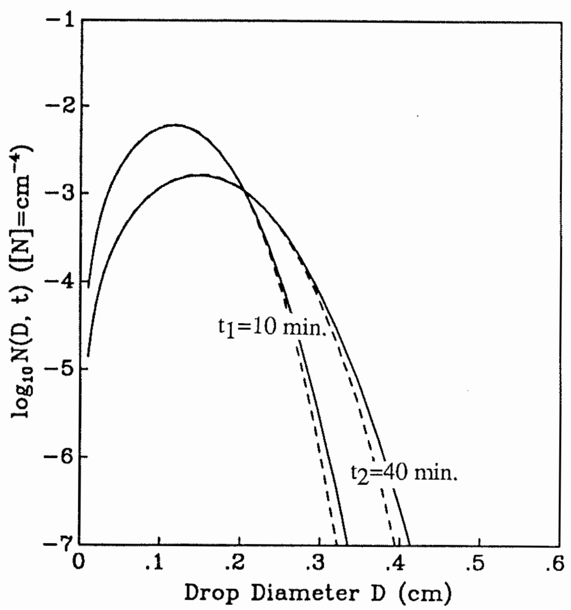

Figure 1: Numerical (solid) and analytical solutions for the drop size distribution at 10 and 40 minutes. For details, see text.

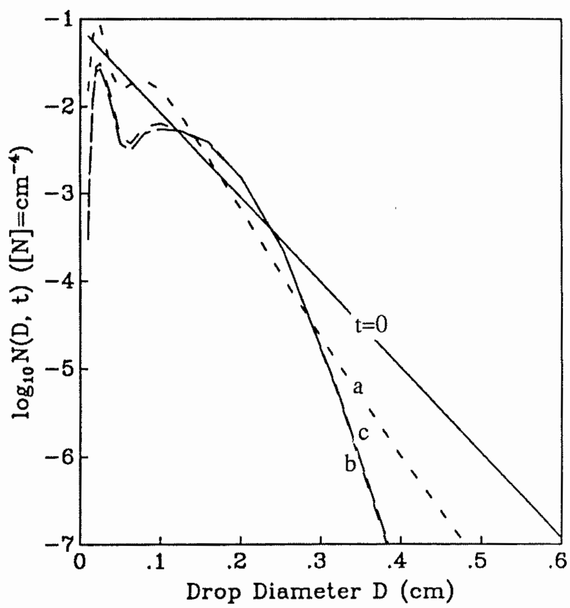

Figure 2: Development of drop size distribution by coalescence and collisional breakup. For details, see text.

was 2 and the total number of categories (ncat) was 21; for b and c, the corresponding numbers are 2 * *(1 / 3) and 55. Curves a and b are for the initial distribution (10), while curve c is for an initial Marshall-Palmer distribution (labeled $t = 0$).

In each case, the distributions changed little after 60 minutes. We conclude that breakup and coalescence give an equilibrium dsd (hereafter edsd) within 60 minutes for the cases considered. Comparison of b and c shows that the edsd is virtually the same for the two initial distributions; it is probably independent of it. Comparison of a and b shows a numerical artifact: the coarser mass scale produces greater concentrations of larger drops. Calculations with even finer mass resolution than for b and c gave steeper distributions but the changes were small compared to that from a to b.

Figure 3 shows the evolution of the dsd with a *modified* Brazier-Smith *et. al.* formulation. The breakup and coalescence efficiencies are taken from them but the fragment size distribution follows LL. The curves shown are the initial distribution (eq. 10) and the distribution at 40 mins.

Figure 4 shows the evolution of an initial Marshall-Palmer distribution (labeled $t = 0$) by coalescence, breakup and evaporation in 40 minutes with c = 2 ** (1/3). The environmental conditions were taken as constant: pressure = 750 mb, temperature =10 C, and relative humidity = 85%. Curve a shows the distribution when evaporation is calculated by the iterative method with ventilation. Curves b and c use the approximate evaporation equation, b is with ventilation while c excludes ventilation. Again, we note that the distributions are approximately exponential at large sizes.

b. *Discussion*

The dependence of the numerical edsd on the mass scale used for the calculation brings out the necessity for care in the use of numerical methods. To further emphasize this point, we compare the present results and those of others who have used the LL formulation. The edsd in all these cases has an exponential part at large diameters. The average slope of this part of the edsd [the value of Λ in a fit of the form $N(D) = N_0 \exp(-\Lambda D)$] is given in the Table I which also includes slopes for certain observed distributions.

TABLE I
SLOPES OF CALCULATED EDSDs
AND OBSERVED DSDs

SOURCE	c / ncat	SLOPE,Λ, cm^{-1}
<u>*Calculations*</u>		
This work		
fig.2, curve a:	2 / 21	34
curves (b,c)	2**(1/3) / 55	65
fig. 3, curve b	2**(1/3) / 60	28
fig. 4, curve a	2**(1/3) / 55	55 to 63
Brown (1988)	2 /≈ 20	30
Tzivion *et. al.* (1989)	2 / 20	36
List *et. al. (1987)*	2**(1/2) / 40	42
Valdez & Young (1985)	? / 49	60
<u>*Observations*</u>	(*R, mm / hr*)	
Feingold & Levin (1986)	6	34
Takahashi (1977)	?	19
Willis and Tattleman (1989)	25 - 62	37
	62 - 125	28
	125 - 225	26
Zawadzki & Antonio (1988)	16 - 20	22
	100 - 120	15

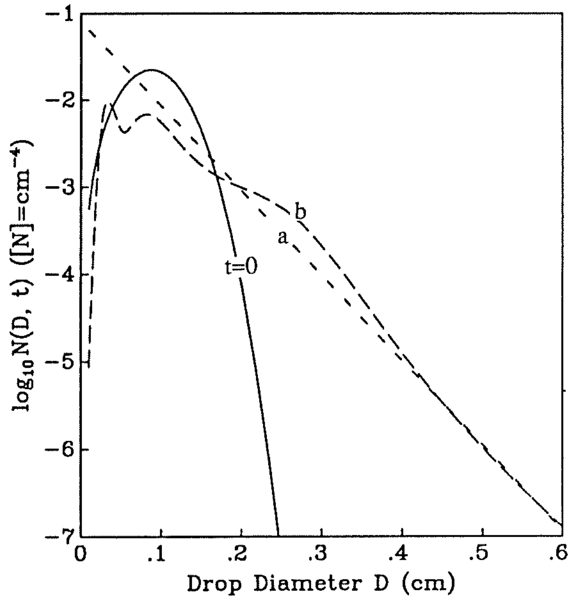

Figure 3: Evolution of the drop size distribution with a modified Brazier-Smith et. al. formulation. For details, see text.

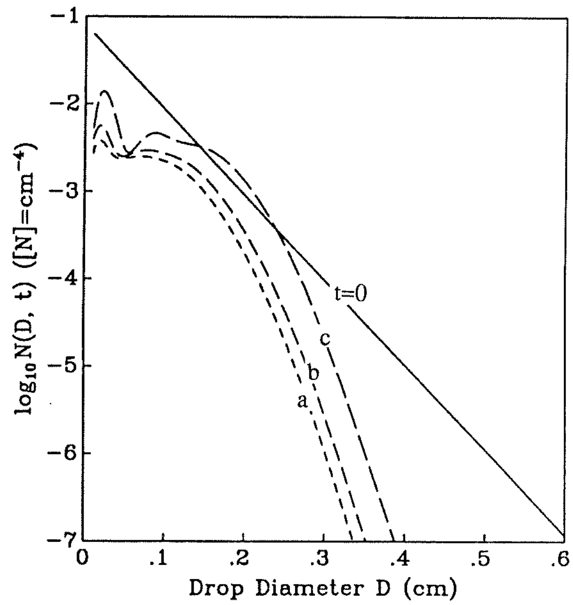

Figure 4: Development of drop size distribution by coalescence, breakup and coalescence. For details, see text.

It is seen that the slope of the edsd increases as the mass scale is refined. Thus, in the present calculations with $c = 2$ and $ncat \approx 21$, the slope is 34; in calculations with similar mass scales by Brown and Tzivion *et. al.* , the slopes are 30 and 36, respectively. With $c = 2**(1/2)$ and $ncat = 40$, List *et. al.* have a slope of 42. With $c = 2**(1/3)$ $ncat \approx 55$, we have a slope of 65, while Young and Valdez with a similar mass scale obtained a slope of 60. Thus it is clear that as the mass scale is refined the slope increases. This is because larger drops are produced more rapidly the coarser the mass scale. As mentioned above, calculations with finer mass scales produced only small changes in the slope. We believe that the calculations have 'converged' with $c = 2**(1/3)$ and further refinements of the scale are not necessary for most purposes. The modified Brazier-Smith *et. al.* formulation gives a much smaller slope, namely, 28. When we included evaporation, the slope at larger drop sizes varied between 55 and 63.

We now compare the results of calculations with observations. The edsd found here shows peaks at small drop sizes similar to those found by others and sometimes in observations. Here we want to discuss the distribution at larger sizes. Similar to Nature, the calculations show an exponential part at large sizes. We have measured the slopes of some recently reported observations of dsds and included them in the second part of Table I. The 'observed' slopes are seen to be much smaller than the 'theoretical' slope of the edsd. The observed slopes range between 15 and 37 and tend to increase with decreasing rainfall rate. Equilibrium distributions dominated by coalescence and collisional breakup should have a slope of about 60. Interestingly, the slope of the edsd according to the modified Brazier-Smith *et. al.* formulation ($\Lambda = 28$, rainfall rate about 20 mm / hr, and slope of Marshall-Palmer distribution about 22) is closer to the observations. These results suggest that processes other than coalescence and breakup may be important in the production of the dsd and / or the LL formulation overestimates breakup and underestimates coalescence substantially. Another possibility is that the observed distributions have not reached equilibrium. However, this seems unlikely on the high rainfall rate observations.

The calculations with coalescence, breakup and evaporation bring about the need to use the correct evaporation equation. We see that the dsd which uses the correct equation with ventilation (curve a, fig. 4) differs substantially from the one which uses the approximate evaporation equation with no ventilation (curve c). It is seen that curve b which uses the approximate evaporation equation with ventilation also differs substantially from curve a. Therefore, it is important to include the ventilation term in evaporation calculations. The difference between curves a and b is not as marked; however, the difference increases as the environment becomes drier and warmer. It is therefore, necessary to use the correct evaporation equation with ventilation. For a given amount of rainwater, the rate of evaporation depends upon the distribution of the water with drop sizes. We concluded above that the LL formulation of coalescence and breakup may be producing steeper dsds than found in Nature. Therefore, we think that this formulation will also give an erroneously faster rate of evaporation.

5. SUMMARY AND CONCLUSIONS

We have developed a modification of Bleck's method of solving the kinetic equation for the dsd which yields more accurate results. The ratio of successive grid masses on a logarithmic mass scale should be about 2**(1/3), or smaller, in order not to have excessive spurious production of large drops. We found that coalescence and collisional breakup give an edsd which is independent of the initial distribution; it has three peaks at small sizes and an exponential part at large sizes. The slope of this part, approximately 60 cm^{-1}., is much greater than slopes calculated from observed raindrop size distributions. From this, and the results of calculations with a *modified* Brazier-Smith *et. al.* formulation, we concluded that: (1) processes other than coalescence and breakup may be important for the evolution of the dsd and / or, (2) the LL formulation overestimates breakup and underestimates coalescence substantially.

We found that use of the well known equation for the condensational growth of cloud drops for the calculation of evaporation results in large errors. Neglect of the ventilation coefficient also produces large errors. Calculation of the evaporation of a distribution of drop sizes with the LL formulation of coalescence and breakup is thought to be subject to errors even when the correct formulation for drop evaporation with ventilation is used because the LL formulation may be putting too much rainwater into smaller drops and not enough in the larger drops.

ACKNOWLEDGMENTS: This research was supported by the National Science Foundation under grant ATM 91 05182. We thank John Valdes for help with the computer work.

REFERENCES

Bleck, R., 1970: A fast, approximate method for integrating the stochastic coalescence equation. *J. Geophys.* Res., **75**, 5165-5175.

Brazier-Smith, P. R., *et. al.* 1973: The influence of evaporation and drop interaction on a rainshaft. *Quart. J. Roy. Met. Soc.*, **99**, 704-722.

Brown, P. S., Jr., 1988: The effects of filament, sheet and disk breakup upon the drop spectrum. *J. Atmos. Sci.*, **45**, 712-718.

Feingold, G., and Z. Levin, 1986: The lognormal fit to raindrop spectra from frontal convective clouds in Israel. *J. Climate Appl. Meteor.*, **25**, 1346-1363.

List, R., N. R. Donaldson and R. E. Stewart, 1987: Temporal evolution of drop spectra to collisional equilibrium in steady and pulsating rain. *J. Atmos. Sci.*, **44**, 362-372.

Low, T. B., and R. List, 1982: Collision, coalescence and breakup of raindrops. *J. Atmos. Sci.*, **39**, 1591-1618.

Smolarkiewicz, P. K., 1983: A simple positive advection scheme with small implicit diffusion. *Mon. Wea. Rev.*, **111**, 479-486.

Srivastava, R. C., 1988: On the scaling of equations governing the evolution of raindrop size distributions. *J. Atmos. Sci.*, **45**, 1091-1092.

Srivastava , R. C., and J. L. Coen, 1992: New explicit equations for the growth and evaporation of hydrometeors by the diffusion of water vapor. *J. Atmos. Sci.*, In press.

Takahashi, T., 1977: A study of Hawaiian warm rain based on aircraft observations. *J. Atmos. Sci.*, **34**, 1773-1790.

Tzivion, S., G. Feingold, and Z. Levin, , 1989: The evolution of raindrop spectra. Part II: Collisional collection, breakup and evaporation in a rainshaft.*J. Atmos. Sci.*, **46**, 3312-3327.

Valdez, M. P., and K. C. Young, 1985: Numerical fluxes in equilibrium raindrop size distribution. *J. Atmos. Sci.*, **42** , 1024-1036.

Willis, P. T., and P. Tattelman, 1989: Drop size distribution associated with intense rainfall. *J. Clim. Appl. Meteor.*, **28**, 3-15.

Zawadzki, I., and M. de A. Antonio, 1988: Equilibrium raindrop size distributions in tropical rain. *J. Atoms. SCI.*, **45**, 3452-3459.

ON THE DYNAMICAL STRUCTURE OF A CLOUD USING NONLINEAR PARAMETERIZATIONS

Ulrike Wacker

Institut für Meteorologie und Geophysik
Universität Frankfurt am Main, FRGermany

1. Introduction

The development of the system "cloud" is determined by interactions with its environment and by internal microphysical processes (e.g. coagulation) as sketched in Fig.1. These are described by nonlinear equations. Such kind of systems are open nonlinear systems. They may be investigated by the recently developed theory of selforganization (e.g. Ebeling and Feistel, 1982; Nicolis and Prigogine, 1977). Important points to be considered are the long-term behaviour of the system and the spontaneous creation of ordered (temporal or spatial) structures. Essential parts of the theory of selforganization were developed with respect to chemical reactions.

As the complete dynamics of clouds is extremely complicated, the processes are described in a physically and mathematically simplified version. Here only the microphysical conversions between the condensed phases will be considered. Cloud microphysics is parameterized by a Kessler-type scheme. Particles are classified as cloud drops (index c) and precipitation particles (index p) which may be rain drops or ice particles. All hydrodynamical processes are neglected except sedimentation and a source of cloud water and precipitation. Thus the system is described by only two nonlinear coupled prognostic equations for cloud water and precipitation content. Application of the methods of nonlinear dynamics will show that selforganization is possible under special conditions.

2. Basic Equations

The simplified system "cloud" is mathematically described by the prognostic equations for mixing ratios of cloud water (q_c) and precipitation (q_p):

$$\begin{array}{rcllllll} \dot{q_c} & = & \Phi_c & + \; cq_c & - \; aq_c & - \; bq_cq_p^\beta & & \\ \dot{q_p} & = & \Phi_p & & + \; aq_c & + \; bq_cq_p^\beta & - \; dq_p^\delta & + \; B \\ & & I & & II & III & & IV \end{array} \qquad (1)$$

The terms on the right hand side are I: source terms (entrainment, condensation/deposition), II: autoconversion, III: accretion/riming, IV: divergence of sedimentation flux, here discretized for a cloud layer of depth Δz. For details see Wacker (1992).

These equations are of the same type as those used in reaction kinetics with chemical reactions replaced by cloud physical transformations. They are coupled by the nonlinear autocatalytic conversion rate accretion/riming. Cloud physical "reactions" are of order 1 (condensation/deposition, autoconversion), of order $\beta + 1$ (accretion/riming) and of order δ (sedimentation). Parameters of the system are the coefficients Φ_c, Φ_p, a, b, c(=fct(supersaturation)), d, B as well as the exponents β, δ.

3. Warm Cloud

In the first case study, precipitation particles are assumed to be rain drops. The source rates Φ_c, Φ_p are set 0; β, δ, which are equal to 7/8 and 9/8, resp., in the original Kessler-scheme, are approximated by 1. Thus the accretion rate (III) is of order 2.

The long term behaviour of the system depends on whether an attractor exists and - if so - on its kind. Here we choose B, which is proportional to the precipitation flux entering the cloud layer from above, as the varying parameter, while all other parameters are kept constant. In the steady state, sources and sinks must balance each other.

B is an external forcing. For $0 < B < B_t = (c-a)\frac{d}{a}$ the system has two steady state solutions S1, S2. Otherwise only one physical steady state exists: S1 for $B > B_t$ and S2 for $B < 0$, see Fig.2. In the range $B > B_I = -\frac{da}{b}$ there is always a stable steady state which is the system's attractor. At $B = B_t$ a transcritical bifurcation is found. The stable branch of steady states changes from S2 to S1. The attractor is always characterized by the maximum value of precipitation leaving the layer (dq_{ps}).

For $B > B_t$ the steady state is determined by the source B; no cloud water is present, and the precipitation that enters the layer, leaves it unchanged. For weaker external forcing B, internal processes become more important. The character of the attractor changes from a node to a focus. The characteristic time for reaching the steady state is of the order of 20min which is reasonable in cloud physics. Below a critical B-value $B_I < 0$, which means an additional sink of precipitation, the production of rain by autoconversion and accretion is too small to compensate the loss of precipitation, and the system is unstable.

4. Mixed Phase Cloud

In the second case study precipitation particles are assumed as flat ice particles ("aggregates of unrimed radiating assemblages of dendrites or dendrites") with attributes given by Locatelli and Hobbs (1974); thus $\beta = 1.41, \delta = 1.09$. With $\delta \approx 1, a = 0, c = 0, B = 0, \Phi_c > 0, \Phi_c + \Phi_p > 0$, always one steady state solution exists. Using Φ_c and Φ_p as varying parameters, a critical value of the source of ice phase $\Phi_{p,crit}(\Phi_c)$ is found, where the steady state changes stability. As the steady state is a focus near the critical curve, $\Phi_{p,crit}$ marks a Hopf-Bifurcation.

For $\Phi_p > \Phi_{p,crit}$ the stable steady state is the system's attractor. For $\Phi_p < \Phi_{p,crit}$ the system has a periodic attractor (Fig.3): Any disturbance of the steady state S first grows in time, but the trajectory in phase space finally runs into a closed curve, the limit cycle, even when it started from the outside. The ice content fluctuates with a period of some 25min in this model, thereby causing precipitation of shower character.

It should be mentioned that a limit cycle does not show up in all cases $\Phi_p < \Phi_{p,crit}$. E.g., in the case of Fig.3, very small initial values of q_c and q_p are beyond the attractor basin. If q_p is made very small in this model, riming cannot maintain precipitation in the absence of other sources of q_p. Then ice is totally depleted and q_c rises at the rate Φ_c.

5. Discussion

Both case studies show that with decreasing external forcing (B or Φ_c, Φ_p) the system activates its internal degrees of freedom. Damped or undamped oscillation may occur. The order $\beta + 1$ of the nonlinear autocatalytic transformation accretion/riming decides whether solely a point attractor or also a periodic attractor is possible. Self-excited oscillations may occur only if $\beta + 1 > 2$. As for chemical reactions the order of reaction is always an integer number, a limit cycle requires at least one reaction of order ≥ 3. In cloud physics, however, β, δ are real numbers. The necessary (not sufficient) conditions for a periodic attractor of Eq.(1) are $\beta > \delta$ and $\beta > 1$ (Wacker, 1992). This is fulfilled only for flat ice particle types, but not e.g. for rain drops or graupel.

A system whose attractor's character changes at a critical parameter value, here β_{crit}, is called structurally unstable. If a particle type with $\beta > \beta_{crit}$ is chosen in a parameterization scheme, a periodic attractor is possible. When developing a parameterization scheme, this structural instability of the model equations should be born in mind.

The present approach can be applied, in principle, also to a less restrictive system described by a larger set of prognostic variables like e.g. the parameterization of warm cloud microphysics developed by Beheng (1992, this volume).

References

Ebeling, W., Feistel, R., 1982: Physik der Selbstorganisation und Evolution. Akademie-Verlag, 371pp.

Locatelli, J.D., Hobbs, P.V., 1974: Fall speed and masses of solid precipitation particles. J.Geophys.Res. **79**, 2185-2197.

Nicolis, G., Prigogine, I., 1977: Self-Organization in non-equilibrium systems. J.Wiley & Sons, 491pp.

Wacker, U., 1992: Structural stability in cloud physics using parameterized microphysics. Submitted to Beitr.Phys. Atmosph.

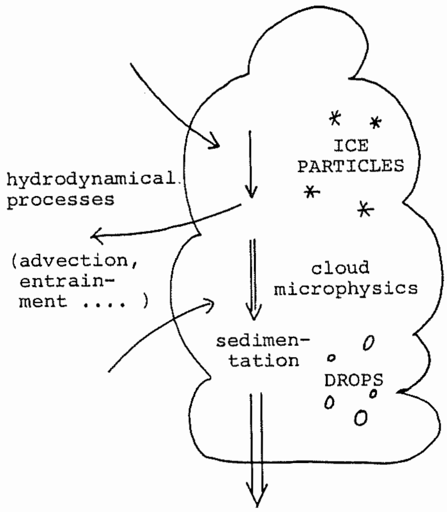

Fig.1: Sketch of the open system "cloud".

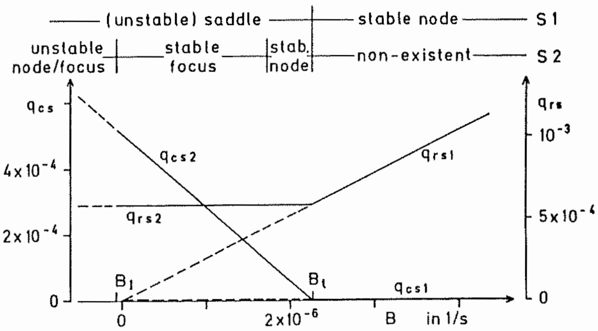

Fig.2: Warm cloud. Stationary steady states S1, S2 of mixing ratios q_c, q_p and their character as functions of parameter B (precipitation entering the cloud layer). Other parameters are: β = 1, δ = 1, a = 10^{-4}/s, b = 7.5/s, c = 4.45x10^{-3}/s, d = 3.88x10^{-3}/s.

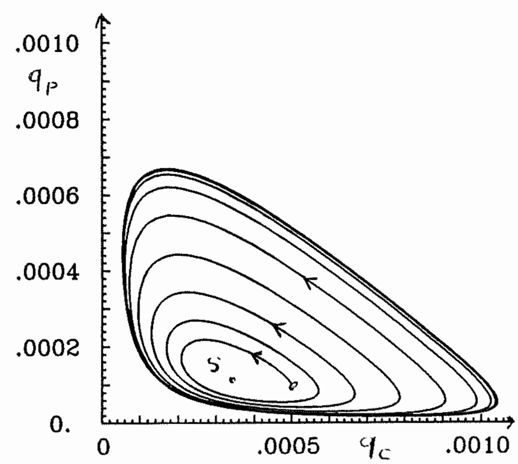

Fig.3: Mixed phase cloud. Trajectory in the q_c, q_p phase space. Parameters: β = 1.41, δ = 1, b = 1081.8/s, d = 9.21x10^{-3}/s, Φ_c = 1.1x10^{-6}/s, Φ_p = 0.

A PARAMETERIZATION OF THE CONVERSION OF CLOUD WATER TO RAINWATER

Klaus D. Beheng

Institut für Meteorologie und Klimaforschung
Kernforschungszentrum Karlsruhe / Universität Karlsruhe

1. INTRODUCTION

Cloud microphysical processes can be formulated by budget equations for the size distribution of the particles under consideration. In case of water drops parts of such an equation constitute the so-called stochastic collection equation (SCE) comprising coagulation growth of drops, i.e. precipitation development. The solution of SCE completely describes the formation of large (rain-) drops at the expense of small (cloud) droplets.

For practical use SCE is rather unmanageable because, on the one hand, it is analytically solvable only for unrealistic collection kernels and because, on the other hand, a numerical solution requires many size classes letting disproportionally increase the number of variables at e.g. a meteorological model's grid point.

A different approach of simulating the formation of warm rain precipitation is to parameterize the relevant processes. Such a parameterization usually differentiates between a cloud- and a rainwater portion and comprises formulae for the time rates of change of cloud and rainwater content due to autoconversion and accretion.

Existing autoconversion rates are based on intuition (Kessler, 1969) or on unclear interpretations of numerical solutions of SCE (Berry, 1968). All known accretion rates result from the so-called continuous model by assuming an exponential raindrop size distribution and simplifying relations for the terminal fall velocity as well as for the collection efficiency.

The parameterizations mentioned above make no or an only uncritical use of SCE. In contrast, SCE is the exact formulation of coagulation growth of drops on which sound parameterizations should be based. Adopting the partitioning of total liquid water into a cloud water and a rainwater portion one can derive, on the basis of SCE, rate equations for the different collection processes as autoconversion, accretion and selfcollection (Doms and Beheng, 1986). These definitions concern to arbitrary moments of the size distribution such that they apply to number as well as to mass densities.

These formulae are the decisive relations on which the parameterization to be presented are based.

2. COLLECTION RATES

An important ingredient in numerically evaluating these relations is the definition of a radius value by which cloud droplets and raindrops are distinguished. By applying standard collection kernels a special form of the size distribution function shows, nearly independent of an initial spectrum, always a separation radius of $\approx 40\mu m$.

Assuming then a drop radius of $40\mu m$ as separation radius the various collection rates have been numerically evaluated for special cases (cf. Beheng and Doms, 1986, hereafter referred to as BD). In the following evaluations of this type are termed 'detailed modelization'.

The results show that the width of the initial spectrum has a crucial effect on th different rates. So, for a narrow initial spectrum the autoconversion and accretion rates attain their maxima much later than for an initial broad spectrum. Moreover, the time-dependent mutual interactions of the various collection processes, especially that of autoconversion which promotes the formation of first raindrops, are strongly influenced by the spectrum's width.

This makes clear that the spectrum's width should be included in a parameterization. This has been done by Berry (loc.cit.). However, by comparing his results with those of BD it turns out that Berry's formula can in no way reproduce the SCE-based autoconversion rates of BD. The reason for this is that BDs definition of autoconversion is rather different from that of Berry where the latter makes no clear difference between autoconversion and accretion. Kessler's autoconversion rate takes no notice of a cloud droplet spectrum at all.

These remarks should suffice to demonstrate the importance of an exact parameterization of autoconversion.

Thus, the idea of the present parameterization is to express the various collection rates by considering integral quantities such as number and mass densities as well as a width parameter.

3. PARAMETERIZATIONS

A number of runs with the detailed modelization has been performed using very different initial number densitites and width parameters as well as liquid water contents. For the various collection rates it has been assumed that in each case an ansatz is applicable consisting of products of integral quantities and a width parameter which are connected non-linearily, i.e. proportional to e.g. $N^x L^y n^z$ with N = actual number density and L = actual liquid water content. In this parameterization the (constant) width parameter n occurs in a conceptually assumed initial cloud droplet spectrum of Gamma-function form $f(r) = Ar^n e^{-Br}$ and is related in a certain way to the relative radius dispersion coefficient.

With subscripts 'c' referring to a cloud and 'r' to a rain quantity, respectively, for $5 \leq n \leq 15$, $50 \leq N_c(t=0) \leq 300\ cm^{-3}$ and $0.5 \times 10^{-6} \leq L_c \leq 2.0 \times 10^{-6}\ g\ cm^{-3}$ the following rate equations have then been found (with all quantities in cgs-units):

A. for the cloud water content

1. due to autoconversion

$$\frac{\partial L_c}{\partial t}\Big|_{au} = \begin{cases} -6.0 \times 10^{25}\, n^{-1.7}\, N_c^{-3.3}\, L_c^{4.7} \\ -\bar{\alpha}\, L_c^{4.7} \end{cases}$$

where $\bar{\alpha}$ has to be interpolated from a table for $N_c > 100\ \mathrm{cm^{-3}}$ and $n > 5$ (see below),

2. due to accretion

$$\frac{\partial L_c}{\partial t}\Big|_{ac} = -6.0 \times 10^{3}\, L_c\, L_r$$

B. and for the cloud and raindrop number densities

1. due to autoconversion

$$\frac{\partial N_c}{\partial t}\Big|_{au} = 7.7 \times 10^{6}\, \frac{\partial L_c}{\partial t}\Big|_{au}$$

2. due to accretion

$$\frac{\partial N_c}{\partial t}\Big|_{ac} = \frac{1}{\bar{x}_c}\frac{\partial L_c}{\partial t}\Big|_{ac}, \quad \bar{x}_c = \frac{L_c}{N_c}$$

3. due to selfcollection of

3.a. cloud droplets

$$\frac{\partial N_c}{\partial t}\Big|_{sc} = -5.5 \times 10^{10}\, n^{-0.63}\, L_c^{2}$$

3.b. raindrops

$$\frac{\partial N_r}{\partial t}\Big|_{sc} = -8.0 \times 10^{3}\, N_r\, L_r$$

$\bar{\alpha}$ is a function of the - assumed constant with time - parameter n and the - actual - number density of cloud droplets N_c, i.e. $\bar{\alpha} = \mathrm{fct}(n, N_c)$, and is calculable by logarithmic 2D-Lagrange-interpolation from a table of α-values.

The autoconversion rate shows a strongly non-linear dependence on all quantities whereas the accretion rates are linear and agree with those derived by the continuous model. If one concentrates on mass densities only it is sufficient to prescribe n and initial values of N_c and L_c for evaluating the rate equations.

4. NUMERICAL RESULTS

Test runs have been made with n, $N_c(t=0)$ and L_c in the ranges mentioned above by forward time integration with a time step of 10 s.

Fig.1 shows an example of results obtained by prescribing $n=5$, $N_c(t=0) = 300\ \mathrm{cm^{-3}}$ and $L_c = 1\ \mathrm{gm^{-3}}$. Kessler's autoconversion rate is at maximum at t=0s and decreases with time so that the corresponding accretion rate consequently reaches its maximum at very early simulation times. In contrast, the detailed as well as the parameterized rates attain maxima at longer simulation times. Although the parameterized autoconversion rate underestimates the detailed one, an effect which is common for all test runs performed, the accretion rates agree very well.

This effect is also mirrored in Fig.2 exhibiting the formation of rainwater as function of simulation time. It is seen that by Kessler's formulation rainwater is created very soon whereas the detailed as well as the parameterized formulations result in an strong increase of rainwater after some 1000 s simulation time. Other cases studies show more or less the same behaviour. Major discrepancies appear for high liquid water contents in combination with a high initial drop number concentration and small spectra. But these cases are somewhat unrealistic.

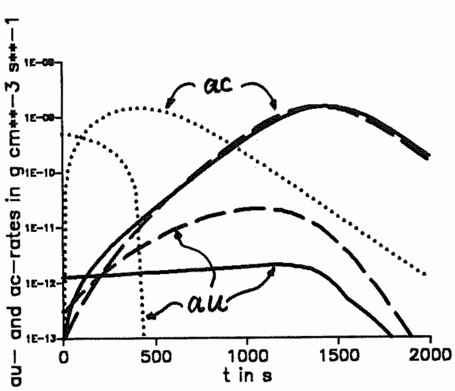

Fig.1: Autoconversion and accretion mass rates as function of simulation time as indicated. Dotted lines refer to results obtained by Kessler's formula, dashed lines to the detailed modelization and solid lines to the present parameterization.

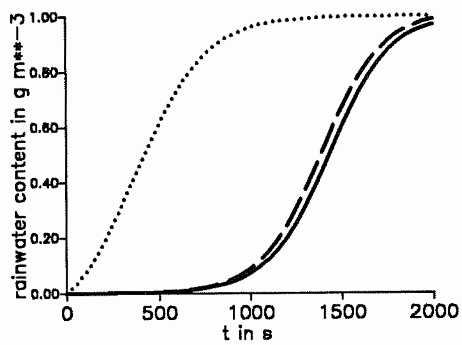

Fig.2: Rainwater content as function of simulation time. Line notation as in Fig.1.

5. SUMMARY

A parameterization scheme is presented by which all processes concerning coagulation growth of drops are expressed by rate equations, which combine definite integral quantities and a width parameter in a strongly non-linear manner, and which is superior to other schemes. It has its roots in an appropriate formulation of the different collection rates derived on the basis of the stochastic collection equation. Concentrating on rainwater content only it consists of two equations easily computable numerically.

This scheme can be used for simulation of precipitation formation as well as in other aspects of cloud microphysics as e.g. investigations of structural dynamics.

REFERENCES

Beheng, K.D., Doms, G., 1986: Beitr. Phys. Atmosph., **59**, 66 - 84

Berry, E.X., 1968: Reprints First Natl. Conf. Weather Modification, Albany, N.Y., Amer. Met. Soc., Boston, 81 - 88

Doms, G., Beheng, K.D., 1986: Meteorol. Rdsch., **39**, 98 - 102

Kessler, E., 1969: Meteor. Monogr., **32**, Amer. Met. Soc., Boston, 84pp.

SURFACE MICROPHYSICAL MECHANISM FOR ICE CRYSTAL GROWTH HABIT DEVELOPMENT

N. Fukuta[1] and Q. J. Lu[2]

[1]Department of Meteorology, University of Utah, Salt Lake City, Utah 84112, U.S.A.
[2]Division of Air Quality, 1950 W. North Temple, Salt Lake City, Utah 84116, U.S.A.

1. INTRODUCTION

Ice crystal growth displays complex shape variations with respect to temperature and supersaturation and critically affects the precipitation processes. This ice crystal growth habit is defined by variation of diameter 2a and height c of basic hexagonal cylinder of ice. Figure 1 shows the 2a/c ratio contours experimentally determined in steady state and stationary air environment. The principal factor governing the basic habit change is temperature. As temperature lowers from 0°C, transitions in shape occur from plates to columns at ~ -4°C, to plates at ~ -9°C and back to columns at ~ -22°C. The transitions at -4 and -9°C are quite sudden, with temperature changes of less than one degree, but the transition at -22°C is much less so.

Ice crystals epitaxially growing on cleaved, covellite surfaces provide behaviors of giant growth steps, reflecting habit change (Hallett, 1961; Mason et al., 1963; Kobayashi, 1965) (see Fig. 2). Similar variations were confirmed on both prism and basal faces of single ice crystals (Lamb and Hobbs 1971). The habit change phenomenon is characteristically featured with a maximum and a minimum in the mean surface diffusion distance χ_s of water molecules or in plane growth rates, with respect to temperature. The basic mechanism of habit change has not been explained satisfactorily since it was first identified by Nakaya et al. (1938a and b) about 50 years ago,

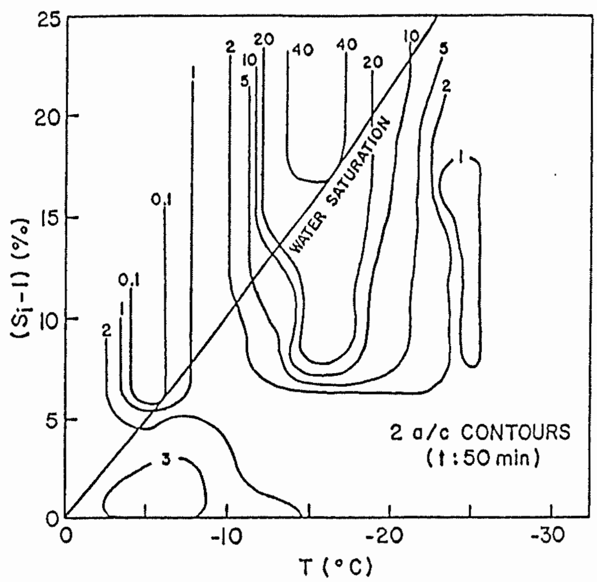

Fig. 1. Habit change diagram giving 2a/c ratio contours as a function of temperature and supersaturation with respect to ice (after Fukuta et al., 1984).

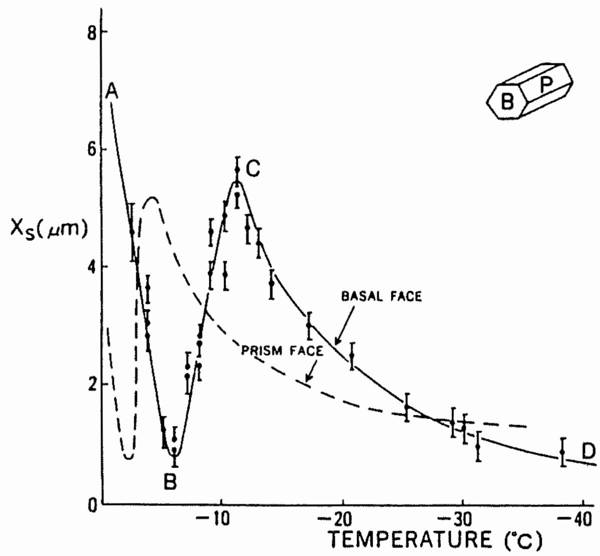

Fig. 2. The variation with temperature of the mean surface diffusion distance χ_s of a water molecule: —— the basal face (measured); --- the prism face (hypothetical) (after Mason et al., 1963).

even though some efforts have been put into it (Mason et al., 1963; Hobbs and Scott, 1965; Ryan and Macklin, 1969; Lamb and Scott, 1974; Kuroda, 1982; Kuroda and Lacmann, 1982).

The purpose of this study is, therefore, to clarify various relevant surface kinetic processes on ice crystal plane growth and their consequence in the habit change phenomenon.

2. EFFECTS OF SOME SURFACE FACTORS ON ICE CRYSTAL PLANE GROWTH

Ice crystal plane growth is believed to occur based on two main mechanisms: the screw dislocation mechanism and the two-dimensional (2D) nucleation mechanism. By using an X-ray topographic method, McKnight and Hallett (1976) confirmed that plate-like snow crystals were often free from screw dislocations. Therefore, the focus of this study is on the 2D nucleation mechanism.

In the 2D nucleation, the free energy of critical embryo formation largely controls the process (Ohara and Reid, 1973); for an embryo of circular cylinder shape with radius r and height h, the free energy is

$$\Delta F^* = -\pi v_m h \frac{\sigma^2}{\Delta \mu}, \qquad (1)$$

where v_m is the molecular volume in the ice phase,

σ the surface free energy of the liquid-solid (L-S) interface (side of the cylinder), and $\Delta\mu$ the chemical potential difference between the ice phase and the phase surrounding the embryo.

According to Fukuta (1987), the Liquid-like layer (LLL) forms within the surface layer due to the fact that ice melts under high pressure. Since the surface free energy is the potential of compressing force normal to the surface, the thickness of the layer is directly related to pressure. The general tendency is that the thinner the layer, the higher the pressure is.

Another important factor is the transitional liquid layer (TLL) that appears on the ice crystal surface during growth. When environmental vapor pressure is saturated with respect to ice, only the LLL exists on the surface, and crystal growth does not occur. As the environmental vapor pressure increases from the ice saturation, a TLL appears on the LLL due to vapor condensation. The chemical potential of this layer is higher than that of ice, and the excessive chemical potential is conveyed instantaneously to the L-S interface, permitting the formation of critical embryos and crystal plane growth there.

Crystal surface tends to become rough as the temperature approaches the melting point and a roughened surface makes the crystal plane growth easier. The roughening tendency decreases with lowering temperature.

3. ICE CRYSTAL PLANE GROWTH RATE

The condensation growth rate of TLL is given as

$$R_{LV} = C_1 e_i \left(1 + \Delta S - e^{-\frac{\Delta\mu}{kT}}\right), \qquad (2)$$

where $C_1 = v_m D/kT\Delta z$, D, k, T and Δz being the diffusivity of water vapor in air, the Boltzmann constant, the temperature and the thickness of the boundary layer, and ΔS and e_i are the environmental supersaturation with respective to ice and the saturated vapor pressure of ice, respectively.

According to the Birth and Spread Theory of 2D nucleation (Ohara and Reid, 1973), the crystal plane growth rate at L-S interface can be expressed as

$$R_{LS} = C \cdot \left(-\frac{\Delta\mu}{kT}\right)^{5/6} \cdot \exp\left[-\frac{\pi v_m h \sigma_{LS}^2}{3k^2T^2\left(-\frac{\Delta\mu}{kT}\right)}\right], \qquad (3)$$

where C is a mild temperature function, and σ_{LS} is σ at L-S interface.

As the thickness of the TLL increases, the freezing growth rate at the L-S interface becomes faster, but the condensation growth rate of the liquid-vapor (L-V) interface decreases. Finally, at a certain thickness of the layer $(-\Delta\mu/kT)$, the two growth rates match each other, i.e.,

$$R_{LV}\left(-\frac{\Delta\mu}{kT}, T, \Delta S\right) = R_{LS}\left(-\frac{\Delta\mu}{kT}, T\right). \qquad (4)$$

The solution for the variable $(-\Delta\mu/kT)$ to the above equation will give the steady-state growth rate at supersaturation ΔS and temperature T.

It is convenient to discuss the plane growth rate, R on the R $\sim(-\Delta\mu/kT)$ plane. Figure 3 illustrates the dependencies of R_{LV} and R_{LS} on $(-\Delta\mu/kT)$ at a fixed environmental supersaturation and temperature. Expressing the freezing plane growth rates normal to the prism and basal faces by $R_{LS,P}$ and $R_{LS,B}$, respectively, we can see that R_{LV} decreases with $(-\mu/kT)$, while $R_{LS,P}$ or $R_{LS,B}$ increases with $(-\Delta\mu/kT)$. The intersection between curves R_{LV} and $R_{LS,P}$ (or $R_{LS,B}$) gives the steady-state growth rate. Generally, for a fixed environmental supersaturation, reducing the temperature will cause curve R_{LV} to move downward, lowering the intersection point (see curve R'_{LV} in the figure).

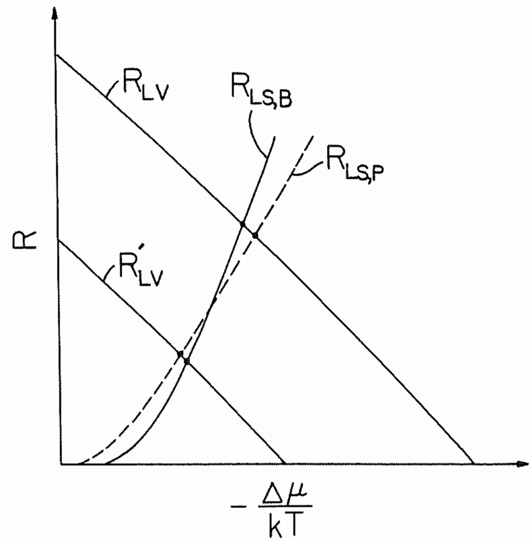

Fig. 3. Dependence of plane growth rates on $(-\Delta\mu/kT)$ at a fixed environmental supersaturation and temperature.

It is noted that $\sigma_{LS,P}$ is used for $R_{LS,B}$ instead of $\sigma_{LS,B}$ and vice versa for $R_{LS,P}$. Since for vapor-solid (V-S) interface $\sigma_{SV,P} > \sigma_{SV,B}$, it is reasonable to assume that $\sigma_{LS,P} > \sigma_{LS,B}$. If C_B, the coefficient C in Eq. (3) for $R_{LS,B}$, is also larger than C_P for $R_{LS,P}$, the equation will produce curves $R_{LS,B}$ and $R_{LS,P}$ that intersect each other, as shown in Fig. 3. This indicates that the steady-state growth rate for $R_{LS,P}$ is larger than that for $R_{LS,B}$ at a lower temperature (see curve R'_{LV}), but becomes smaller at a higher temperature (see curve R_{LV}).

4. MECHANISM FOR HABIT CHANGE

The temperature corresponding to the maximum $T_{II/III}$ and that corresponding to the minimum $T_{I/II}$ are used to define three regions for plane growth, as shown in Fig. 4. We next explain habit change by discussing plane growth in each region, assuming a constant ΔS for all temperatures.

a. *Plane growth in Region III ($T < T_{II/III}$)*

At a fixed temperature, $(-\Delta\mu/kT)$ increases with the thickness of TLL formed by vapor condensation and has an upper limit $(-\Delta\mu_w/kT)$, where $\Delta\mu_w$ is the chemical potential difference between ice and water and depends only on temperature. Therefore, R_{LS} also has an upper limit determined by $(-\Delta\mu_w/kT)$.

When temperature is low, say, T = −30°C,

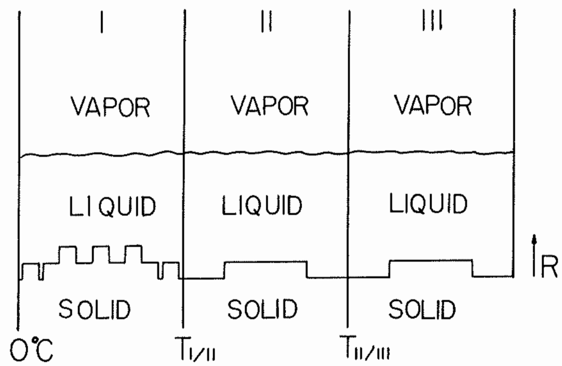

Fig. 4. Variation with temperature of surface structure and plane growth by 2D nucleation. I) surface roughening controlled, II) 2D-nucleation controlled, and III) vapor flux controlled.

$(-\Delta\mu_w)$ is large. As a result, $(-\Delta\mu)$ can increase to a high level and cause a very large R_{LS}. However, such a large R_{LS} cannot be matched by the available vapor flux from the ambient. For a given ΔS, the available vapor flux is low at low temperature, and the matching between R_{LS} and R_{LV} is controlled by the available vapor flux. The higher the available vapor flux, the larger the steady-state plane growth is. As temperature increases, the available vapor flux [see e_i in Eq. (2)], as well as the steady-state plane growth rate, also increase. When temperature approaches $T_{II/III}$, the growth rate reaches a maximum.

b. *Plane growth in Region II ($T_{II/III} < T < T_{I/II}$)*

As temperature increases further from $T_{II/III}$, $(-\Delta\mu_w)$ starts to decrease to a certain level that makes the 2D nucleation difficult. Although R_{LV} can become very large due to the increased available vapor flux, it cannot be matched by R_{LS} because of the low value of $(-\Delta\mu)$ suppressing the 2D nucleation. In this region, R_{LS} always reaches its upper limit corresponding to $(-\Delta\mu_w)$, the upper limit for $(-\Delta\mu)$ in order to catch up with R_{LV} to the highest extent possible. Here, the upper limit for R_{LS} is controlled by 2D nucleation under available $(-\Delta\mu_w)$. As temperature increases, $(-\Delta\mu_w)$ decreases, and the upper limit for R_{LS} also decreases accordingly, reaching a minimum at $T = T_{I/II}$.

c. *Plane growth in Region I ($T_{I/II} < T < 0°C$)*

As temperature further increases from $T_{I/II}$, the L-S interface becomes rough. The rough interface makes nucleation easier and promotes plane growth for R_{LS}. In this region, R_{LS} increases with temperature.

d. *Variation with temperature of plate and column crystal formation*

The plane growth curves for prism and basal faces are shifted from each other on the R ~ T plane, as shown in Fig. 2 (note: χ_s for the basal face corresponds to plane growth rate normal to the prism face and vice versa). When temperature is low, say, T = −15°C, $R_{LS,P}$ is larger than $R_{LS,B}$ due to $\sigma_{LS,P} > \sigma_{LS,B}$ (see R_{LV} in Fig. 3). Therefore, plate crystals prevail. However, as temperature increases, $R_{LS,P}$ becomes smaller than $R_{LS,B}$ (see R_{LV} in Fig. 3), implying the formation of column crystal. This also indicates that $T_{II/III}$ for $R_{LS,P}$ is lower than that for $R_{LS,B}$; that is, $T_{II/III,P} < T_{II/III,B}$. As temperature increases further, it appears that roughening occurs earlier, and the surface becomes rougher on the prism face than on the basal face. This would indicate $R_{LS,P} > R_{LS,B}$ and $T_{I/II,P} < T_{I/II,B}$, or a tendency towards plate crystals. Detail of roughening mechanism is yet to be investigated.

e. *Simulation of plane growth*

The simulation of plane growth rate was carried out for $R_{LS,P}$. The following values were taken for parameters in Eqs. (2) and (3): $\Delta z = 1$ μm, $C_P = 50$ μm/s, $\sigma_{LS,B} = 3.0 \times 10^{-2}$ J/m², and $\Delta S = 50\%$. The purpose of this computation is to simulate the maximum and the minimum in the plane growth rate as a function of temperature. Therefore, selection of values for these parameters does not affect the nature of discussion.

Figure 5 shows the simulated variations of $R_{LS,P}$ (solid line) and R_{LV} (dashed line) with $(-\Delta\mu/kT)$ at different temperatures. At T = −15°C, the steady-state plane growth rate is controlled by the available vapor flux. At −10°C, growth rate reaches a maximum. At −9°C, $R_{LS,P}$ starts to reach an upper limit corresponding to $(-\Delta\mu) = (-\Delta\mu_w)$, which cannot match R_{LV}. At −8°C, the upper limit for $R_{LS,P}$ drops sharply. If the upper limits for T < −10°C are taken as steady-state growth rates, the variation of the plane growth rate with temperature is shown in Fig. 6. The dashed line for the plane growth by roughening mechanism is postulated rather than calculated. The variation with temperature of the plane growth rate is similar to that in Fig. 2. As temperature increases from −30°C, plane growth rate increases and reaches a maximum at ~ −10°C. After that, the growth rate drops sharply and reaches a minimum at ~ −6°C.

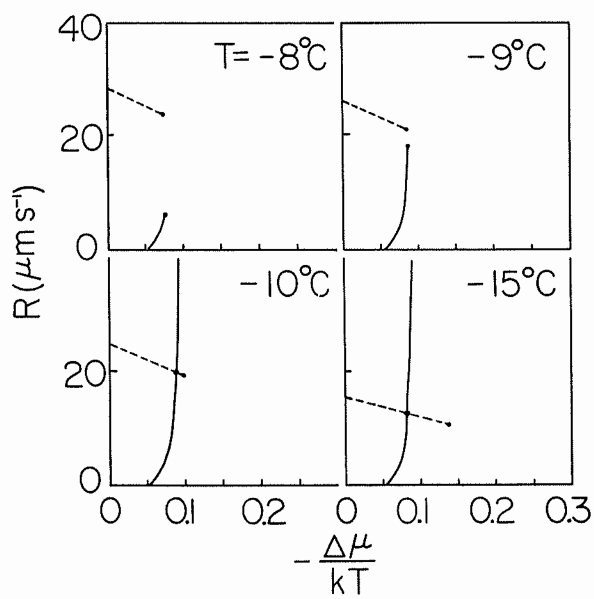

Fig. 5. Plane growth rates as a function of $(-\Delta\mu/kT)$ under $\Delta S = 50\%$ at −8, −9, −10, and −15°C. The solid and dashed curves represent $R_{LS,P}$ and R_{LV}, respectively.

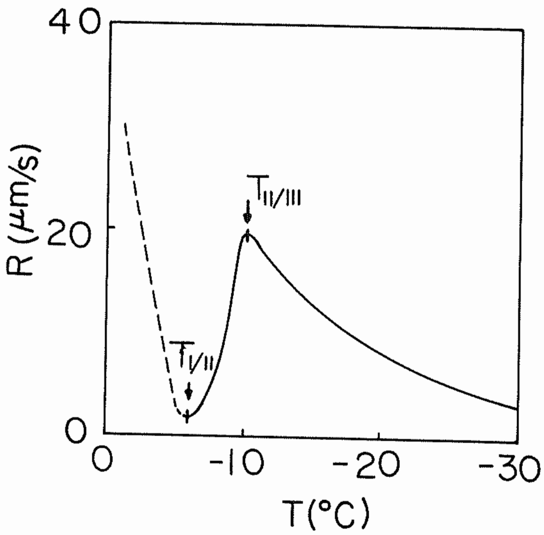

Fig. 6. Calculated plane growth rate in the direction normal to prism face as a function of temperature under ΔS = 50%.

The above sharp shape change, as well as the maximum and minimum, have never been satisfactorily explained before. Mason et al. (1963) and Hobbs and Scott (1965) tried to explain the variation of the plane growth rate with temperature using activation energy for water molecule migration on the crystal faces. Since the activation energy is much too small compared with that of embryo nucleation, it merely produced a very gentle, convex upwards curve with temperature, which is nowhere near the shape of the curve seen in Fig. 2. The adhesive growth mechanism was applied by Kuroda (1982) and Kuroda and Lacmann (1982) to explain habit change. This mechanism relies on the existence of the roughened surface in Region II, rather than in Region I (see Fig. 4), which is self-contradiction.

5. DISCUSSION AND CONCLUSIONS

The mechanism of habit change of ice crystal growth has long been a puzzling but important problem in cloud physics. The theoretical analysis made above appears to explain all the major features of habit change on a quantitative basis.

Under equilibrium, the LLL exists due to compression effect in the surface layer of ice crystal. However, under supersaturated conditions, another TLL appears on the crystal surface due to vapor condensation. This TLL has higher chemical potential than the solid phase, and the excessive free energy within the layer is instantaneously conveyed to the L-S interface as the LLL adheres to the top of the layer. Therefore, 2D nucleation can proceed at the L-S interface, resulting in ice crystal plane growth. TLL thus plays a key role in habit change. The thickness of the layer automatically adjusts so that condensation and freezing growth rates match each other in order to establish a steady state.

The habit is characterized by the existence of a maximum and a minimum in the plane growth rate as a function of temperature. Under constant environmental supersaturation of present theoretical study, as the temperature increases, freezing growth rate decreases while condensation growth rate increases. This zone is controlled by the vapor condensation. The system eventually reaches a point where freezing growth rate can no longer match condensation growth rate. It is this unmatching that produces the maximum. After the maximum, the plane growth process becomes 2D nucleation controlled. As temperature approaches the melting point, surface roughening starts and produces the minimum.

ACKNOWLEDGMENTS. This study was supported by the Division of Atmospheric Sciences, National Science Foundation, under Grant ATM-86-16568.

REFERENCES

Fukuta, N., and A. S. Wang, 1984: The mechanism of habit development in diffusional ice crystal growth, Proc. 9th Internat. Conf. on Cloud Phys., Tallinn, U.S.S.R., 159-162.

Fukuta, N., 1987: An origin of the equilibrium liquid-like layer on ice. J. de Phys., **48**, 503-509.

Hallett, J., 1961: The growth of ice crystals on freshly-cleaved surfaces. Phil. Mag., **6**, 1073-1087.

Hobbs, P. V., and W. D. Scott, 1965: A theoretical study of the variation of ice crystal habits with temperature. J. Geophys. Res., **70**, 5025-5034.

Kobayashi, T., 1965: The growth of ice crystals on covellite and lead iodide surfaces. Rept. Low Temp. Sci. Inst. Hokkaido Univ., Ser. A, **10**, 1-22.

Kuroda, T., 1982: Growth kinetics of ice single crystal from vapor phase and variation of its growth forms. J. Meteor. Soc. Japan, **60**, 520-534.

Kuroda, T., and R. Lacmann, 1982: Growth kinetics of ice from the vapor phase and its growth forms. J. Crystal Growth, **56**, 189-205.

Lamb, D., and P. V. Hobbs, 1971: Growth rates and habits of ice crystals grown from the vapor phase. J. Atmos. Sci., **28**, 1506-1509.

Lamb, D., and W. D. Scott, 1974: The mechanism of ice crystal growth and habit formation. J. Atmos. Sci., **31**, 570-580.

Mason, B. J., G. W. Bryant, and Q. P. van den Heuval, 1963: The growth habits and surface structure of ice crystals. Phil. Mag., **8**, 505-526.

McKnight, C. V., and J. Hallett, 1978: X-ray topographic studies of dislocations in vapor-grown ice crystals. J. Glaciology, **21**, 397-407.

Nakaya, U., I. Sato, and Y. Sekido, 1938a: Preliminary experiments on the artificial production of snow crystals. J. Fac. Sci., Hokkaido Univ., Ser. II, **2**, 1-11.

Nakaya, U., Y. Toda, and S. Maruyama, 1938b: Further experiments on the artificial production of snow crystals. J. Fac. Sci., Hokkaido Univ., Ser. II, **2**, 13-57.

Ohara, M., and R. C. Reid, 1973: Modeling of Crystal Growth Rates from Solution. Prentice-Hall, Englewood Cliffs, 267pp.

Ryan, B. F., and W. C. Macklin, 1969: The temperature dependence of the velocity of steps growing on the basal plane of ice. J. Colloid and Interface Sci., **31**, 566-568.

A CONCEPTUAL VIEW OF A 3-COMPONENT HEAT AND MASS TRANSFER THEORY OF HAILSTONES

Roland List

Department of Physics, University of Toronto, Toronto, Ontario, Canada

1. INTRODUCTION

In the past the validity of the basic heat and mass transfer theory of hailstones as developed by Schumann (1938) and improved by Ludlam (1958) and List (1963, 1977) has not been thoroughly tested. Recently, Lesins and List (1986) and Garcia and List (1992) provided better but still incomplete experimental data. The outcome was a surprise: the deduced heat transfers differed by up to a factor four or more from theory. Further, the Nusselt number, Nu, (assumed equal to the Sherwood number, Sh) increased with increasing liquid water content, W_f. The first discrepancy led to the investigation of the sensitivity of the overall heat and mass transfer to individual parameters (List, 1988), which showed that only an (unreasonable) roughness coefficient of > 2 could correct the heat transfer. This is not satisfactory because the observed roughness of artificially grown, gyrating hailstone decreases with increasing W_f. Experience with mass transfer simulations (which also simulate heat transfer) by Schüepp and List (1969) lead to the estimate that water-skin covered hailstones are expected to have a roughness factor of ≈ 1.1-1.2; for rough hailstones the factor is estimated at ≈ 1.4.

The spreadsheet study by List (1988) demonstrated that no adjustment of any single variable (other than roughness) could produce agreement between theory and experiment. A combination of parameters, assuming (excessive) errors of 10-20 % each in the supporting direction, may produce an artificial agreement, if these errors are combined with roughness effects $\gg$ 1.4. However, the errors of most measured parameters are much less than that. Multi-dimensional error patterns have not been explored. There are other possible explanations for the discrepancies:

1) Assumed values of parameters, which could not be measured directly, were misjudged;
2) The heat and mass transfer theory is wrong by up to a factor of four;
3) Conceptual problems cause unexplained effects like the dependence of Nu on W_f.

All the above effects combined could also produce the discrepancy. The first point is valid, but will be neglected for the time being. The second point is about the *adequacy of the standard heat and mass transfer equation*. The basic assumption has always been that there are three components which allow the removal to the air of latent heat released on the hailstone by freezing of accreted water, Q_F: a) the heat transfer by conduction and convection, Q_{CC}; b) the diffusion of water molecules through air and the related heat released by sublimation/evaporation/deposition at the hailstone surface, Q_{DS}; and c) the heat transfer to the hailstone by the accreted cloud droplets, caused by the temperature difference between air and hailstone surface, Q_{CP}. Radiation is negligible. All these heat transfer components serve to freeze accreted water on the hailstone, Q_f.

2. 3-COMPONENT HEAT TRANSFER

2.1 General Considerations

The "standard" theory has assumed that the three heat transfer components Q_{CC}, Q_{DS} and Q_{CP} are *independent* of each other and can be superimposed. *Interaction terms* will now be considered, since each transfer type may interact with the two others: [$Q_{CC} \leftrightarrow Q_{DS}$], [$Q_{DS} \leftrightarrow Q_{CP}$] and [$Q_{CC} \leftrightarrow Q_{CP}$]. The new heat and mass transfer equation can then be expressed by

$$Q_{CC} + Q_{DS} + Q_{CP} + \textit{Interaction Terms} = Q_f \qquad (1)$$

The nature of the interaction could be additive as in Eq. 1 or in the form of multiplicative factors in Q_{CC}, Q_{DS} and Q_{CP}, i.e.
where the subscript *eff* denotes effective heat transfer by

$$Q_{CC,eff} + Q_{DS,eff} + Q_{CP,eff} = Q_f \qquad (2)$$

any given component. List (1990) has stressed that transfers of any kind are gradient driven. For example, evaporation from a hailstone surface is driven by a gradient of H_2O molecule concentration through the boundary layer. If cloud droplets are moving into this boundary layer, this gradient could be affected depending on the concentration of droplets, W_f.

2.2 The Heat Transfer by Conduction and Convection, Q_{CC}

According to the standard theory, Q_{CC} is given by

$$Q_{CC} = \frac{-A_s\, k\, Nu\, (t_d - t_a)}{D} \qquad (3)$$

where A_s [m²] is the total surface area of the hailstone (= $0.789\pi D^2$ for an aspect ratio α=0.67), k [J m^{-1} s^{-1} K^{-1}] the thermal conductivity of air, Nu [-] the bulk Nusselt number, t_d [°C] the hailstone's surface temperature, t_a [°C] the air temperature and D [m] the hailstone diameter. The Nusselt number is given by

$$Nu = \frac{hD}{k} = \left.\frac{\partial T^*}{\partial y^*}\right|_{y^*=0} \tag{4}$$

where h [J m^{-2} K^{-1} s^{-1}] is the surface heat transfer coefficient. Nu is a dimensionless temperature gradient at the particle surface and gives a measure of the particle's heat transfer (Incopera and De Witt, 1991). y^* is y/L, where L (=D) is a characteristic length, and the temperature in non-dimensional form is given by $T^* = (T-T_d)/(T_\infty-T_d)$, with the subscript ∞ representing undisturbed air.

For smooth spheres Nu can be expressed as

$$Nu = \theta\,\chi(2.0 + 0.60\,Pr^{1/3}Re^{1/2}) \tag{5}$$

where θ is a roughness factor and χ corrects for oblateness (= 1.4 an oblate spheroid with an aspect α = 0.67); the Prandtl number Pr = 0.71 for air [-]. Eq. 5 was experimentally confirmed up to (subcritical) Re $\approx\leq$ 100,000 (Schüepp and List, 1969). The adjustment to spheroids was also justified.

2.3 The Indirect Heat Transfer by Deposition and Sublimation

The diffusion of water molecules produces heating, Q_{DS}, of the hailstone by the release of latent heat of condensation or deposition, or removes heat by evaporation or sublimation and is given by

$$Q_{DS} = \frac{-A_s L_{vs} D_{wa} Sh\left(\frac{e_d}{T_d} - \frac{e}{T_a}\right)}{R_v D} \tag{6}$$

where L_{vs} [J kg^{-3}] is the latent heat of deposition or sublimation (vaporization), D_{wa} [m^2 s^{-1}] the diffusivity of water vapour in air, e_d [Pa] the vapour pressure at the hailstone's surface, e the ambient vapour pressure, R_v the specific gas constant for water vapour, and T_a [K] the absolute temperature of the ambient air.

The Sherwood number Sh is defined as

$$Sh = \frac{\beta D}{D_{wa}} = \left.\frac{\partial \rho_v^*}{\partial y^*}\right|_{y^*=0} \tag{7}$$

where β [m s^{-1}] is the mass transfer coefficient at the hailstone surface and ρ_v^* [-] is the dimensionless water vapour concentration. The Sherwood number is a dimensionless concentration gradient at the particle surface and is the driving force for mass transfer in the air boundary layer of the hailstone. For spheres and spheroids, Sh can be expressed as

$$Sh = \theta\chi(2.0 + 0.60\,Sc^{1/3}Re^{1/2}) \tag{8}$$

where Sh = 0.61 for air.

2.4 The Heat Transport by Supercooled Cloud droplets

The heat transfer by accretion of supercooled cloud droplets is given by the amount by which the deposited water needs to be heated to reach the surface temperature of the growing hailstone and by the heat loss represented by the amount of water and ice shed from the hailstone. This is expressed in Equation 9 (see bottom of page), where $\bar{A}_c$ is the average cross-sectional area presented to the flow by the hailstone, with $\bar{A}_c = (\pi/4)\alpha\kappa D^2$. Thereby κ is a correction factor for symmetric gyration (at precession/nutation angles of 30° and with α = 0.67 κ=1.0793). V is the hailstone free fall speed, E_{net} is the net collection efficiency, i.e. the fraction of the droplet mass in the swept-out volume that is permanently accreted, $\bar{C}_w$ is the heat capacity of water averaged over the temperature range t_d to t_a. E is the collection efficiency or mass fraction of collected cloud droplets from the swept-out volume, t_s the temperature of the shed water drops, I_s the mass fraction of ice in the shed water, and $L_{f,s}$ the latent heat of fusion of the shed water. Garcia and List (1992) describe the shedding characterized by Eq. 9.

2.5 The Freezing Term

The latent heat released by the fraction of water, permanently accreted by the hailstone, needs to be transported away from the hailstone. This heat is given as follows

$$Q_f = \bar{A}_c\, W_f\, E_{net} V I_f L_f \tag{10}$$

L_f is the latent heat of fusion of the accreted water which becomes ice at the temperature t_d, I_f is the mass fraction of ice produced in the deposit on the hailstone. Up to this point it has always been assumed that this released latent heat is transported away by the independent mechanisms outlined in Eqs. 3, 6 and 9. However, such an equation does not necessarily describe the magnitude of the freezing process in nature. It is postulated that the interaction between the three transport processes can explain the discrepancy.

$$Q_{CP} = -\bar{A}_c W_f V\,[E_{net}\bar{C}_w(t_d-t_a) + (E-E_{net})(\bar{C}_w[t_s-t_a] - I_s L_f)] \tag{9}$$

2.6. The Magnitude of the Interaction Processes

The definition of the Nusselt number in Eq. 4 can be expanded to

$$Nu = \frac{\partial T^*}{\partial y^*} = \frac{\partial\left(\dfrac{T-T_d}{T_\infty - T_d}\right)}{\partial\left(\dfrac{y}{L}\right)} = \frac{\partial T}{\partial y}\frac{D}{T_\infty - T_d} \qquad (11)$$

This equation allows a calculation of the boundary layer thickness y_b, assuming that the gradient is linear. For a spherical hailstone with a diameter of 0.02 m, a temperature $t_d = 0°C$, a fall speed of $V = 20$ m/s in air at $t_a = -20°C$ (resulting in $Nu \approx 100$ for a pressure of 100 kPa) the average boundary layer thickness is $y_b = 2\times10^{-4}$ m or 0.2 mm. This implies that the *residence time of droplets* moving vertically through the boundary layer at 20 m/s is 10^{-5} s.

The same argument can be made about the water vapour diffusion. Since $Nu \approx Sh$, the boundary layer for the water vapour concentration field is the same as the temperature field.

It can be shown that droplets with a mean diameter of 28 μm (as in Garcia and List, 1992) will not react within this short time in a manner as to change the original temperature and water vapour fields which control Q_{CC}, Q_{DS} and Q_{CP}. Droplet velocity components perpendicular to the gradient will not affect the general situation.

2.7 The Effect of Water Vapour Diffusion

Heat conduction signals a driving temperature gradient in which the diffusion of water vapour will increase because of the warmer environment. The temperature/pressure dependence of the water vapour diffusivity in air is given by

$$D_{wa} = 0.211\left(\frac{T}{T_o}\right)^{1.94}\left(\frac{p_o}{p}\right) \qquad (12)$$

It will increase by a factor of 1.405 by moving from -3O°C to 0°C. Averaged over $t_a = -20°C$ and $t_d = 0°C$ D_{wa} is 10.2 % higher than that at t_a. Such corrections are necessary if the calculations need to be within this type of accuracy. The reverse effect by vapour diffusion on the temperature conductivity is negligible.

3. EFFECTIVE NUSSELT NUMBERS

The Nusselt number, Nu, is calculated on the basis of Equation 5 as a function of Reynolds number, Re. For practical purposes the Sherwood number, which controls the diffusional growth (Equation 8), has the same magnitude as Nu and the same dependence on Re.

For spheres, $\chi\theta = 1$, and with no drop shedding from the growing hailstone ($E_{net} = E$), Nu can be calculated by substituting Eqs. 3, 6, 9, and 10 into 1 (without interaction terms) and using the definition of Nu given in Equation 4

$$Nu = \frac{Q_f - Q_{CP}}{\pi D\, k\,(t_d - t_a)\left[1 + \dfrac{L_v\, D_{wa}}{R_v\, k\,(t_d - t_a)}\left(\dfrac{Sc}{Pr}\right)^{1/3}\left(\dfrac{e_h}{T_d} - \dfrac{e}{T_a}\right)\right]} \qquad (13)$$

When the heat components by conduction and convection, and deposition/sublimation, transferred at the surface of the hailstone, are compared (only) to the heat conducted away from the hailstone by molecular heat conduction (represented by k) a new 2-component Nusselt number Nu_{2c} can be defined as

$$Nu_{2c} = Nu\,\varphi_{2c} \qquad (14)$$

where φ_{2c} is given by the term in the square brackets of Equation 13. As soon as cloud droplets are involved through Q_{CP}, then their contribution to the heat transferred at the surface can be considered in the definition of an *effective (3-component) Nusselt Number*, Nu_{3c} (= Nu φ_{3c}), similar to Equation 14. The factor φ_{3c} is given by

$$\varphi_{3c} = 1 + \frac{L_v\, D_{wa}}{R_v\, k\,(t_d - t_a)}\left(\frac{Sc}{Pr}\right)^{1/3}\left(\frac{e_h}{T_d} - \frac{e}{T_a}\right) + \frac{DVEW_f\bar{c}_w}{4\,k\,Nu} \qquad (15)$$

Nu_{3c} compares the overall heat transfer at the hailstone surface, combining the three individual contributions by Q_{CC}, Q_{DS} and Q_{CP}, to the molecular heat conduction. For growing hailstones Q_{CC}, Q_{DS} and Q_{CP} contribute to the transfer in the same sense, and $Nu_{3c} > Nu$ because the thermal molecular conductivity k in Nu remains the same. Figure 1 shows the ratios of Nu_{3c}/Nu ($=\varphi_{3c}$) and Nu_{2c}/Nu ($=\varphi_{2c}$) as function of air pressure for D = 0.02 m, V = 18 m s^{-1}, $W_f = 0.003$ kg m^{-3}, $t_a = -15°C$ and t_d varying from -4.4°C at 100 kPa to -0.1°C at 10 kPa. A value of $Nu_{3c} \approx 3$ at 40 kPa for implies that the heat transfer rate at the hailstone surface, as imbedded in a corresponding h_{3c}, is three times the contribution of conduction and convection as expressed by the regular Nusselt number in Equation 5.

4. SUMMARY AND CONCLUSIONS

The findings can be summarized as follows:

1) The very short residence times of accreted droplets in the boundary layer of collecting hailstones (order of 10^{-5} s) makes any interaction of the three different transports of heat, Q_{CC}, Q_{DS}, and Q_{CP} very unlikely. For practical purposes these three factors can be considered to be

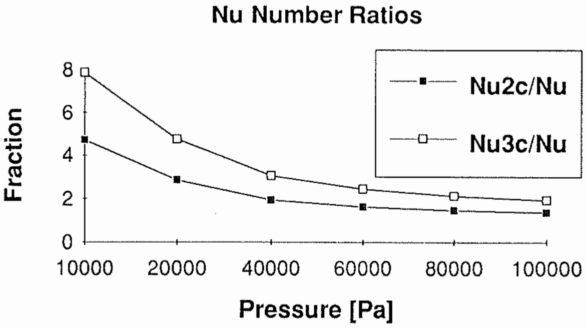

Figure 1. Ratios of the three-component effective Nusselt number Nu_{3c}/Nu according Eq. 14, and the two-component Nusselt number Nu_{2c}/Nu according Eq. 13, as functions of atmospheric pressure. Nu represents the Nusselt number for convection and conduction.

independent from each other, with the exception of point 2).

2) The effect of the temperature gradient in the boundary layer on the vapour diffusivity should be neglected until accuracies of 5-10% can be attempted.

3) Nusselt numbers, which comprise heat transfers by vapour diffusion and/or droplet accretion, are larger than the "regular" Nusselt number because the heat transfer rate is increased but not the molecular heat conductivity (k) to which they are compared.

There is still no explanation for the apparent discrepancy between heat transfer theory and experiment. It is suggested that the measurement of the basic Nusselt and Sherwood numbers for gyrating particles and the study of more detailed ice growth may provide better understanding. It could well be that subtle changes in shapes during growth, varying particle densities, effects of sensitive heat and non-saturated wind tunnel air may all contribute to the disagreement.

Acknowledgment

This research has been sponsored by the Natural Sciences and Engineering Council of Canada and the Canadian Atmospheric Environment Service. Particular thanks also go to my present and former students for the stimulating discussions.

REFERENCES

Garcia-Garcia, F., and R. List, 1992: Laboratory measurements and parameterization of supercooled water skin temperatures and bulk properties of gyrating hailstones. *J. Atmos. Sci.*, **49** (in press).

Incopera, F.P. and D.P. De Witt, 1991: Fundamentals of Heat and Mass Transfer, 3rd Edition, John Wiley & Sons, N.Y., pp.919

List, R., 1990: Physics of supercooling of thin water skins covering gyrating hailstones. *J. Atmos. Sci.*, **47**, 1919-1925.

List, R., 1989: Analysis of sensitivities and error propagation in heat and mass transfer of spheroidal hailstones using spreadsheets. *J. Appl. Meteor.*, **28**, 1118-1127.

List, R., 1977: Ice accretions on structures. *J. Glaciol.*, **19**, 451-465.

List, R., 1963: General heat and mass exchange of spherical hailstones. *J. Atmos. Sci.*, **20**, 189-197.

Ludlam, F.H., 1963: Heat transfer from hailstones. *Nubila*, **1**, 12-96.

Schüepp, P.H., and R. List, 1969: Mass transfer of rough hailstone models in flows of various turbulence levels. *J. Appl. Meteor.*, **8**, 254-263.

Schumann, T.E.W., 1938: The theory of hailstone formation. *Quart. J. Roy. Meteor. Soc.*, **64**, 3-21.

A Numerical Study of the Diffusional Growth and Riming Rates of Ice Crystals in Clouds

Pao K. Wang and Wusheng Ji
Dept. of Atmospheric and Oceanic Sciences
University of Wisconsin
Madison, WI 53706
U.S.A.

1. INTRODUCTION

Ice particles play an important role in the formation of deep convective clouds. They are thought to be the initiators of precipitation particles through the Bergeron-Findelsen and riming processes in the middle latitude deep convective systems. In addition to their relation to direct precipitation formation, the growth of ice crystals could also have great influence on the thermodynamics and dynamics of clouds because of the associated release of latent heats. It is therefore of importance to determine the growth rates of ice crystals.

There are at least three modes of ice crystal growth: (1) diffusional growth, (2) collision with supercooled cloud droplets (i.e., riming), and (3) collision with other ice crystals (i.e., aggregation or clumping, see Pruppacher and Klett, 1978). The present paper will investigate the growth rates of the processes (1) and (2). It is still quite difficult to treat the aggregation process either experimentally or numerically.

The present study uses numerical simulation techniques to determine the diffusional growth and riming rates of three types of ice crystals: (1) columnar ice crystals, (2) hexagonal ice plates, and (3) broad-branch ice crystals. In order to determine these rates, it is necessary to first determine the flow fields of air around these ice crystals. This is accomplished by numerically solving the steady or unsteady Navier-Stokes equations for flow past ice crystals at suitable Reynolds numbers. The flow fields so obtained are then used for later determination of growth rates. These steps will be described in the following sections.

2. THE DETERMINATION OF FLOW FIELDS

The flow fields of air around the falling ice crystals are obtained by solving the following non-dimensionalized Navier-Stokes equations:

$$\partial \mathbf{U}/\partial t + (\mathbf{U} \cdot \nabla \mathbf{U}) = -\nabla p + (2/Re)\nabla^2 \mathbf{U} \qquad (1)$$

$$\nabla \cdot \mathbf{U} = 0. \qquad (2)$$

(see Pruppacher and Klett , 1978, for derivation of these equations). The flow may be steady or unsteady depending on the shape and Reynolds number of the falling ice crystals. Fig. 1(a) and (b) show an example of the grid used. The details of the numerical scheme are given in Ji and Wang (1990, 1991).

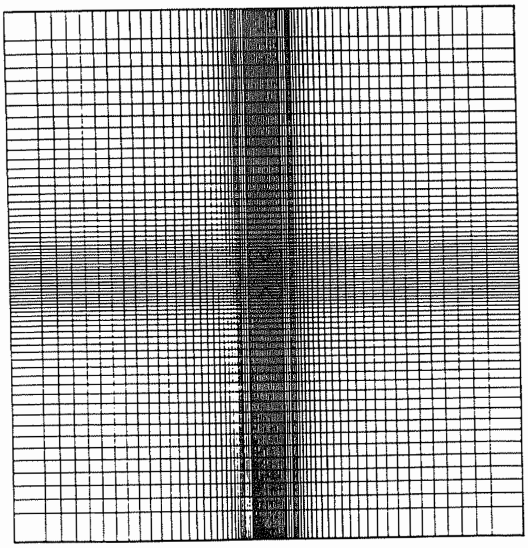

FIG. 1(a)

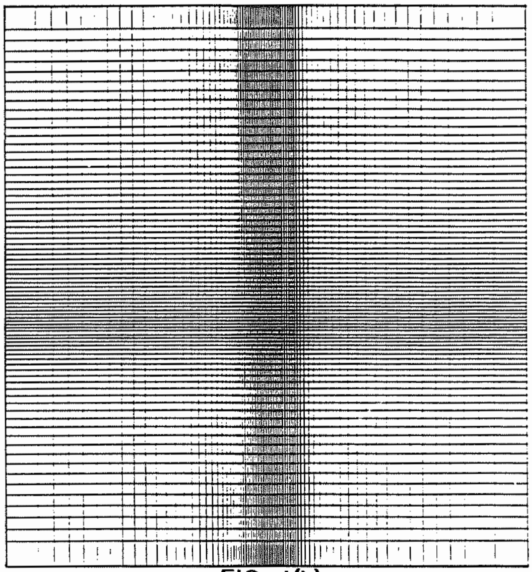

FIG. 1(b)

3. THE DETERMINATION OF DIFFUSIONAL GROWTH RATES

To determine the diffusional growth rates, the water vapor density fields are obtained first by solving the convective diffusion equation of water vapors around the moving ice crystals:

$$\partial\rho_v/\partial t = D_v \nabla^2 \rho_v - \mathbf{U} \cdot \nabla\rho_v \qquad (3)$$

where ρ_v is the water vapor density. An example of the calculated vapor density fields is shown in Fig. 2(a) and (b). The diffusional growth rates are determined by the surface integral of the vapor density gradient:

$$dm/dt = -\oint D_v \nabla\rho_v \cdot d\mathbf{S} \qquad (4)$$

where m is the mass of the ice crystal and dS the surface element . Since the growth rates of stationary crystals can be calculated by the so-called electrostatic analog method, it is useful to present the diffusional growth rates (4) in terms of the ventilation factor:

$$f = (dm/dt)/(dm/dt)_o \qquad (5)$$

where $(dm/dt)_o$ denote the diffusional growth rate of the stationary crystal. The calculated ventilation factors for columnar crystals, hexagonal plates, and broad-branch crystals are shown in Fig. 3.

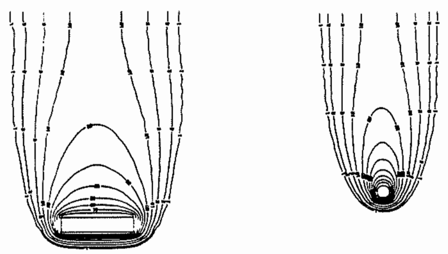

FIG. 2

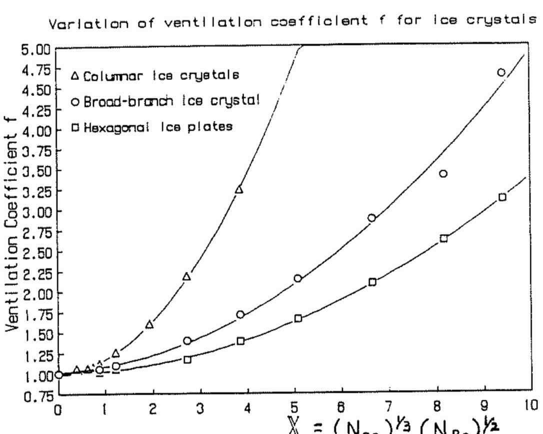

FIG. 3

4. THE DETERMINATION OF RIMING RATES

The riming rates of the ice crystals are represented by the collision efficiencies of ice crystals colliding with supercooled water droplets. The collision efficiency is determined by solving the equation of motion of a droplet moving in the vicinity of the ice crystal to determine the critical collision trajectory. The collision efficiency E is then calculated by the following formula:

$$E = K/K^* \qquad (6)$$

where K is the effective collision kernel and K* the geometrical collision kernel (see Wang, 1983). Figs. 4, 5, and 6 show the calculated E for all three types of crystals.

Acknowledgements. The present work is partially supported by the NSF grant ATM-9002299 and U.S. EPA grant R-81-7108-01-0. The computation were performed on the CRAY-2 supercomputer of NCSA, University of Illinois at Unbana-Champaign.

REFERENCES

Ji, W., and P. K. Wang, 1990: Numerical simulation of three-dimensional unsteady viscous flow past fixed hexagonal ice crystals in air - preliminary results. *Atmos. Res., 25*, 539-557.

Ji, W., and P. K. Wang, 1991: Numerical simulation of three-dimensional unsteady viscous flow past finite cylinders in an unbounded fluid at low intermediate Reynolds numbers. *Theor. Comput. Fluid Dynamics, 3*, 43-59.

Pruppacher, H. R., and J. D. Klett, 1978: *Microphysics of Clouds and Precipitation.* D. Reidel, Dordrecht, 714pp.

Wang, P. K., 1983: On the definition of collision efficiency of atmospheric particles. *J. Atmos. Sci., 40*, 1051-1052.

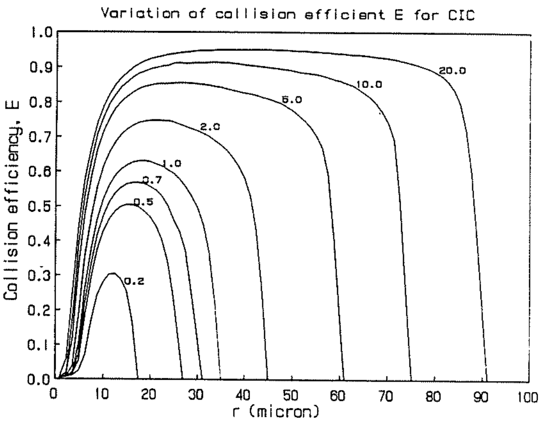

Theoretical collision efficiency with which columnar ice crystals of circular cylindrical shape (Length L and radius α) in air (-8^{0}C and 800 mb) collides with spherical supercooled water drops (present numerical results).

(1) Re = 0.2, α = 23.5 μm, L = 67.1 μm;
(2) Re = 0.5, α = 32.7 μm, L = 93.3 μm;
(3) Re = 0.7, α = 36.6 μm, L = 112.6 μm;
(4) Re = 1.0, α = 41.5 μm, L = 138.3 μm;
(5) Re = 2.0, α = 53.4 μm, L = 237.4 μm;
(6) Re = 5.0, α = 77.2 μm, L = 514.9 μm;
(7) Re = 10.0, α = 106.7 μm, L = 1067 μm;
(8) Re = 20.0, α = 146.4 μm, L = 2440 μm.

FIG. 4

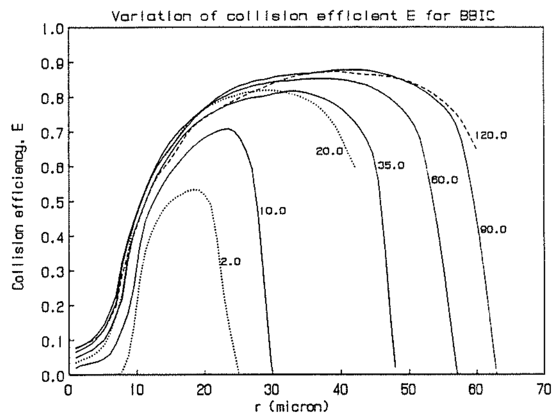

Theoretical collision efficiency with which broad-branch ice crystals (Thickness h and diameter d) in air (-8^{0}C and 800 mb) collide with spherical supercooled water drops (present numerical results, note the line styles representing different Reynolds numbers are different).

(1) Re = 1.0, d = 200.0 μm, h = 15 μm;
(2) Re = 2.0, d = 250.0 μm, h = 18 μm;
(3) Re = 10.0, d = 700.0 μm, h = 32 μm;
(4) Re = 20.0, d = 1000.0 μm, h = 40 μm;
(5) Re = 35.0, d = 1500.0 μm, h = 50 μm;
(6) Re = 60.0, d = 2000.0 μm, h = 60 μm;
(7) Re = 90.0, d = 2500.0 μm, h = 65 μm;
(8) Re = 120.0, d = 3100.0 μm, h = 73 μm.

FIG. 6

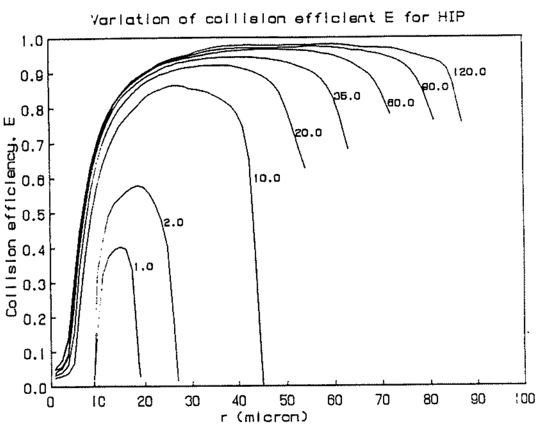

Theoretical collision efficiency with which hexagonal ice plates (Thickness h and diameter d) in air (-8^{0}C and 800 mb) collides with spherical supercooled water drops (present numerical results).

(1) Re = 1.0, d = 160.0 μm, h = 18 μm;
(2) Re = 2.0, d = 226.5 μm, h = 20 μm;
(3) Re = 10.0, d = 506.5 μm, h = 32 μm;
(4) Re = 20.0, d = 716.3 μm, h = 37 μm;
(5) Re = 35.0, d = 947.6 μm, h = 41 μm;
(6) Re = 60.0, d = 1240.0 μm, h = 45 μm;
(7) Re = 90.0, d = 1500.0 μm, h = 48 μm;
(8) Re = 120.0, d = 1700.0 μm, h = 49 μm.

FIG. 5

MECHANISM OF ICE CRYSTAL HABIT FORMATION AND CHANGE

Richard L. Pitter and William G. Finnegan

Desert Research Institute, Reno, NV 89506, USA

1. INTRODUCTION

According to the electrostatic analogy, the rate of ice crystal diffusional growth depends on crystal shape, as expressed in the capacitance factor. Marshall and Langleben (1954) noted that the electrostatic analogy requires that both the temperature and the equilibrium vapor density at the surface must be independent of position on the crystal surface. No experiments have tested the validity of these conditions.

The first scientific speculation on ice crystal shapes is generally attributed to Johannes Kepler in 1611 (Kepler, 1966). Ice crystal habit is a strong function of temperature and also depends on both the supersaturation with respect to ice and impurities present. Although concepts have been advanced regarding how these factors control ice crystal habit, no comprehensive, testable theory of ice crystal habit has been developed.

Previous cloud chamber work (Finnegan and Pitter, 1988; Pitter and Finnegan, 1991) showed that morphological and aggregation features of diffusion-grown ice crystals can be attributed to ion separation across a growing ice interface. More elaborate shapes and higher frequencies of T-shaped aggregates were found for crystals grown in supercooled clouds formed from solutions with greater freezing potentials, as reported by Workman and Reynolds (1950). Chemical ion separation was postulated to occur across the growing ice/water interface of single ice crystals.

Chemical reactions found in growing ice crystals and bulk freezing (Finnegan et al., 1991) also strongly suggest ion separation and require a liquid layer at all growing edges of the crystals. Thus, experimental results indicate that ice crystals growing by diffusion have liquid layers at their growing edges of sufficient extent to dissolve and ionize soluble salts. The liquid layers also contain net electric charge, which is balanced by electric charge of the opposite sign contained in the ice phase. This requires the continued, sufficiently rapid diffusional growth of the crystal; when growth stops, the charges recombine and the liquid layer freezes.

The present research investigated the development of ice crystal habit using experimental results to guide the theoretical development.

2. THEORETICAL

The present theoretical development of ice crystal growth mechanism incorporates the electric multipole concept.

a. *Electric Multipole Concept*

Workman and Reynolds (1950) found that bulk freezing of dilute aqueous solutions produced transient freezing potentials--voltage differences across the ice/water interface--with sign and magnitude dependent on the solute content and composition when all other experimental conditions were held constant. The freezing potential is caused by incorporation of halide and ammonium ions into the ice phase during growth, with rejection of other ions from the ice phase.

Finnegan and Pitter (1988) found that the frequency of T-shaped junctions in aggregates increased with increasing freezing potential of the cloud water solutions, and postulated that the selective incorporation of chemical ions in ice crystals growing by vapor diffusion led to the formation of electric multipoles in the ice crystals. Other studies (Pitter and Finnegan, 1991; Finnegan et al., 1991) further substantiated the postulate of selective ion incorporation.

b. *Flux Concept Development*

Consider an ice crystal constrained to a regular hexagonal prism shape of length *2c* and diameter *2a*. When the crystal exhibits *a*-axis growth, the liquid layer is constrained to prism surfaces, and when it exhibits *c*-axis growth, the liquid layer is constrained to the basal surfaces. Although the fluxes are greatest at the edges and vertices, the nonuniformities across any surface are ignored and each surface is treated by its average flux conditions, at first approximation.

The heat flux is isotropic, requiring that all the crystal surfaces are the same temperature. However, since the growing surfaces have a liquid layer, their equilibrium vapor density is close to the ambient vapor density, and mass flux to the growing surfaces is small compared to flux to the non- or slowly-growing surfaces of the crystal.

For both heat and mass balance of the model crystal shape, *a*-axis growth yields an equilibrium aspect ratio of $c/a = 0.054$ and *c*-axis growth yields an equilibrium aspect ratio of $c/a = 3.48$.

3. EXPERIMENTAL

Ice crystal growth experiments were conducted in the DRI 6.7 m^3 cloud chamber. The cloud chamber operated at temperatures down to -30°C. A supercooled liquid water cloud, generated by ultrasonic nebulization of a dilute aqueous solution, was injected into the chamber through a stand pipe.

Two types of experiments were conducted. One used the cloud chamber at constant temperature (within 0.5°C) during the run, investigating growth in the warm column regime (-4 to -9°C), plate regime (-12°C), or dendritic regime (-15 to -16°C). The second type warmed the air up to 0.5°C per minute or cooled the air up to -1°C per minute to study how habits change during continual growth as ambient conditions switch from one growth regime to another. In either type of experiment, ice crystals were initiated by rapid expansion of moist compressed air.

Ice crystals grew by vapor diffusion with minimal riming and fell out. Crystals were collected on chilled glass microscope slides, removed to a cold box containing a microscope, and immediately examined and photographed at 25X magnification for later analysis. Photographs of ice crystals were analyzed for gross habit, morphological details, and aspect ratio.

4. RESULTS

Figure 1 shows ice crystals grown by diffusion from a deionized water cloud at -16°C. The crystals are about 60 μm across and have short, broad sectors with a high degree of conformity of edges to hexagonal symmetry. The photograph shows thicker layers in the centers of the crystals. Both crystals exhibit symmetrically-arranged gas bubbles.

Figure 1. Crystals grown from D.I. water at -16°C.

Figure 2, taken later in the same run, depicts crystals when they have grown to 125 μm. The stellar branching is more pronounced and the thicker central area has evolved into a second plate. The smaller plates exhibit fewer features than the larger plates, perhaps as a consequence of the conditions which also affect their growth rates. The stellar arms tend to maintain strong hexagonal symmetry, although serrations are beginning to appear on the sides of the arms. Six rimed drops can be identified on the larger crystal.

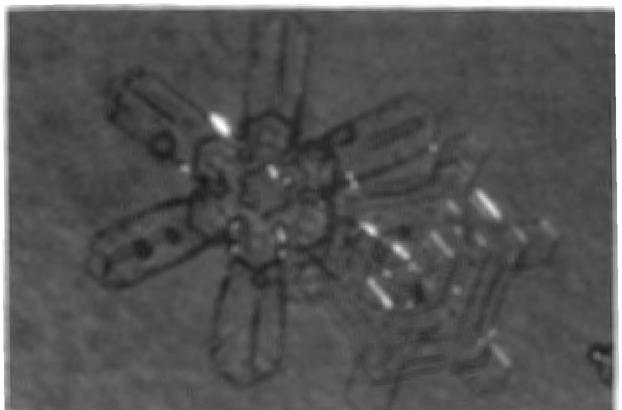

Figure 2. Crystals grown from D.I. water at -16°C.

Figure 3 shows a crystal grown from a cloud consisting of 10^{-4} N solution of ammonium iodide. The crystal is about 120 μm across, and was grown at -16°C. Although similar in many ways to crystals in Fig. 2, the serrations of the branches are more pronounced and the larger plane exhibits considerably more departure from hexagonal shapes. Twelve rimed drops are discernible on the crystal. Ammonium iodide has a strong freezing potential as compared with a weak freezing potential for deionized water.

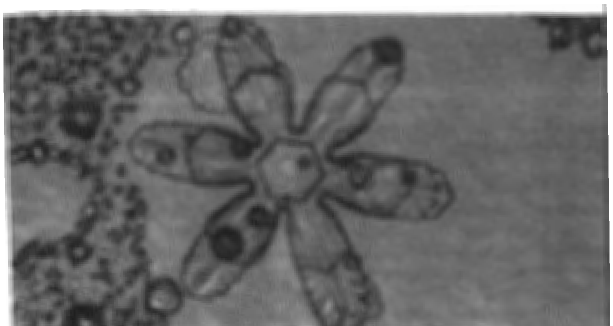

Figure 3. Crystal grown from 10^{-4} N NH_4I at -16°C.

Figure 4 shows a crystal grown in a cloud formed from cloud water consisting of 10^{-4} N solution of hydrazine sulfate. The crystal is over 200 μm across, and shows considerable lateral branching from its arms. About 30 rimed drops can be detected. One or two small hexagonal plates are offset on the *c*-axis.

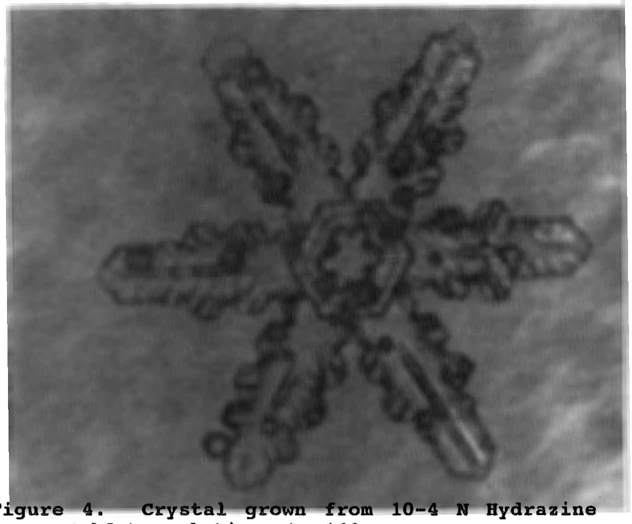

Figure 4. Crystal grown from 10-4 N Hydrazine Sulfate solution at -16°C.

5. SUMMARY

The degree of elaboration of a crystal surface increases with crystal size for all solutes and temperatures investigated. Thus, the mechanism of diffusional growth is governed by crystal size.

Ice crystal diffusional growth in free fall does not yield many flat, prismatic crystal surfaces. The ends of stellar and dendritic branches are feathered and not smooth, but serrated. There is a strong tendency for more elaborate ice crystals to be grown from dilute solutions which produce higher freezing potentials.

Ice crystals grown at water saturation during transition from one habit regime to another had a strong tendency to maintain their initial habits for several minutes. The tendency for compound crystal habits, such as capped columns, to form was small.

Experimental and theoretical investigations on mechanisms of ice crystal growth are continuing.

REFERENCES

Finnegan, W.G., and R.L. Pitter, 1988: A postulate of electric multipoles in growing ice crystals: Their role in the formation of ice crystal aggregates. *Atmos. Res.*, **22**, 235-250.

Finnegan, W.G., R.L. Pitter, and L.G. Young, 1991: Preliminary study of coupled oxidation-reduction reactions of included ions in growing ice crystals. *Atmos Environ.*, **25A**, 2531-2534.

Kepler, J., 1966: *The Six-Cornered Snowflake*. Clarendon Press, Oxford.

Marshall, J.S., and M.P. Langleben, 1954: A theory of snow-crystal habit and growth. *J. Meteor.*, **11**, 104-109.

Pitter, R.L., and W.G. Finnegan, 1991: An experimental study of effects of soluble salt impurities on ice crystal processes during growth. *Atmos. Res.*, **25**, 71-88.

Workman, E.J., and S.E. Reynolds, 1950: Electrical phenomena occurring during the freezing of dilute aqueous solutions and their possible relationship to thunderstorm electricity. *Phys. Rev.*, **78**, 254-259.

Cloud/Radiation Parameterization and Performance of the University of Illinois Multilayer Atmospheric General Circulation Model.

Jai-Ho Oh[1] and M. E. Schlesinger[2]

1. EID-900, Argonne National Laboratory, 9700 S. Cass Ave., Argonne, IL 60439
2. Depart. of Atmos. Sci., Univ. of Illinois at Urbana-Champaign, 105 S. Gregory Ave., Urbana, IL 61801

1. Cloud/Radiation Parameterization

In our cloud/radiation parameterization (Oh, 1989), cloud water is a prognostic variable; the fractional cloud amount is predicted semi-prognostically; stratiform and cumuloform clouds can coexist in a vertical atmospheric column; clouds can exist either as liquid water clouds, ice clouds or mixed liquid water-ice clouds; and cloud radiative properties depend on the predicted cloud liquid water and cloud ice.

The parameterization of stratiform clouds is based on the Sundqvist (1978, 1988) parameterization. The prognostic cloud water budget equation includes the condensation of water vapor into cloud water at a subsaturated grid-scale relative humidity, the convergence of the horizontal flux of cloud water, the conversion of cloud water into precipitation, and the evaporation of cloud water into water vapor. Our stratiform cloud parameterization differs from that of Sundqvist in that: (1) the evaporation in the clear part of a GCM grid box of rain from the layers above is not included in the moisture source term, this so that the budget equations for water inside and outside a cloud are consistent; (2) the evaporation (sublimation) of cloud liquid water (ice) is calculated regardless of whether or not there is condensation, with the evaporation rate depending on the cloud water content and the saturation ratio of environment; (3) the fractional cloud cover remains at its antecedent value until the cloud water either evaporates completely or condensation occurs again; (4) the autoconversion of cloud water into precipitation is parameterized in a manner similar to that of Kessler (1969); and (5) the evaporation of rain is calculated following Schlesinger *et al.* (1988).

The parameterization of cumuloform clouds is based on the Arakawa-Schubert (1974; AS) parameterization of penetrating convection wherein an ensemble of cumulus clouds exists, with each sub-ensemble member or cloud type identified by the layer in which it reaches neutral buoyancy and detrains. In the AS parameterization, a cloud type can be interpreted as a time average over a single cloud's life cycle in which the growing and dissipating stages are negligibly short and the cloud exists only in its mature stage. For the radiative effects of these cumuloform clouds, however, it is the mature and dissipating stages which are of greatest importance because only during these stages is the fractional cloudiness large. Therefore, in our parameterization it is assumed that only the growing stage is negligibly short, and that the cloud is in its mature stage when its cloud-base mass flux is positive, and is in its dissipating stage thereafter when its cloud-base mass flux ceases. For the mature stage of a cloud, it is assumed that the entrainment layers do not store cloud water, as in the AS parameterization, but that the detrainment layer can store cloud water, unlike in the AS parameterization. The prognostic cloud water budget equation for the detrainment layer includes the flux of total water from the cloud layer below, the entrainment of water vapor from the environment, the detrainment of cloud water to the environment, the conversion of cloud water to precipitation, and the evaporation of cloud water into the environment. The fractional cloud cover during the mature stage is determined from an assumed diagnostic relation for the cloudiness in terms of the mass flux into the base of the detrainment layer. For the dissipating stage of a cloud, the cloud-base mass flux is zero and the cloud consists only of its detrainment shield. In the dissipating stage, it is assumed that there is no precipitation. Hence, the prognostic cloud water budget equation includes only the evaporation of cloud water into the environment. It is further assumed that the cloudiness remains at its maximum value of the mature stage during the dissipating stage.

In our parameterization, stratiform and cumuloform clouds can coexist within the same vertical atmospheric column, albeit not in the same layer. The identification of a cloud in a layer as either a stratiform or cumuloform cloud depends on the preceding cloud type, the large-scale condensation, and the convective mass flux in the layer. If there is convective mass flux, then the cloud type is taken to be cumuloform, regardless of whether the preceding cloud was stratiform or cumuloform. If there is large-scale condensation and no convection, the cloud is taken to be stratiform. If there is neither convection nor large-scale condensation, the cloud maintains its cloud type until it dissipates by evaporation.

Where the temperature within a cloud is below $0^{o}C$, a three-phase mixture of water vapor, supercooled liquid water and ice exists. It is assumed that the fraction of cloud water in the ice phase varies linearly from zero at $0^{o}C$ to unity at a sub-zero temperature, T_i.

In the radiation parameterization, the solar spectrum is subdivided into three bands, two for Rayleigh scattering and ozone absorption, and one for water vapor absorption which is further subdivided into six intervals for the k-distribution method. Multiple scattering is calculated by the two-stream, delta-Eddington method. The longwave spectrum is divided into four regions, one each for the CO_2 and O_3 bands, and one each for the line centers and line wings within the water vapor bands. The radiative properties of clouds are calculated from their predicted cloud liquid water and ice amounts. The vertical distribution of clouds in the model is subdivided into individual cloud groups, with each group being defined as an ensemble of contiguous cloud layers, and the cloud groups being separated from each other by at least one layer of clear air. For both solar and longwave radiation, the contiguous cloud layers within each group are considered to overlap each other in the vertical to the maximum extent possible, while noncontiguous cloud groups are considered to randomly overlap each other in the vertical.

The cloud parameterization has the following parameters with values determined by limited-duration, sensitivity/tuning simulations with the UI multilayer AGCM (Oh, 1989): (1) the characteristic time for the evaporation of cloud water (τ = 180 s); (2) the autoconversion rates of cloud water into precipitation, separately for stratiform cloud (a = 1/3600 s) and cumuloform cloud ($C_0 = 0.00015\ m^{-1}$); (3) the threshold relative humidity of the environment at which stratiform condensation can begin ($U_{00} = 0$); (4) the threshold cloud water above which stratiform precipitation can begin, separately for liquid water ($m_{c,w} = 0.5 \bullet 10^{-4}$ g/g) and ice clouds ($m_{c,i} = 0.8 \bullet I_c[T_c]$, where $I_c[T_c]$ are the values given by Heymsfield and Platt (1984) as a function of the cloud temperature, T_c); (5) the parameter relating cumuloform cloudiness to the mass flux at the base of the detrainment layer (α = 10); (6) the temperature, T_i (= -25^oC); (7) the mass absorption coefficient of cumuloform ice clouds ($a_o^{\uparrow,\downarrow}$ = 0.096); and (8) the multiple scattering asymmetry factor for stratiform cloud (g = 0.76) and cumuloform cloud (g = 0.85).

2. Simulation of Cloud Variables

The geographical distribution of the simulated fractional cloud cover (CLD) for January is presented in Fig. 1, obtained from an annual-cycle simulation by the UI 7-layer AGCM, together with the observed ISCCP cloudiness and the difference between the simulated and observed CLD. Figure 1 shows that the model has simulated reasonably well the observed cloudiness minima over the major desert areas and over the subtropical Pacific, the cloudiness maxima over the North Pacific and North Atlantic, and the band of maximum cloudiness centered near 50^oS. However, the model overestimates the January CLD over Antarctica and over the continents at high latitudes in the Northern Hemisphere. The model also fails to simulate the CLD maxima observed in the subtropics off the west coast of North America and underestimates the CLD over the maritime continent.

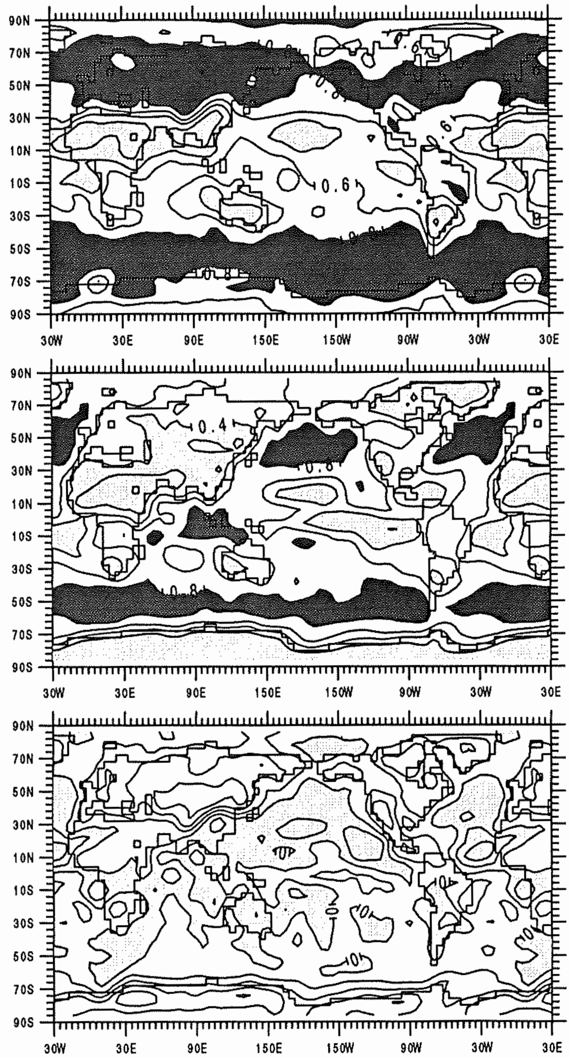

Fig. 1. Geographical distributions of the simulated (top panel), observed (middle panel), and simulated-minus-observed (bottom panel) fractional cloud cover for January. The distribution in each panel has been smoothed with a 9-point filter. In the top and middle panels, dark shading shows CLD ≥ 0.8 and light shading CLD ≤ 0.4. In the bottom panel shading shows negative values. The observed cloud cover is that from the analysis of the ISCCP data by Schlesinger *et al.* (1989).

In July (not shown), the model has also simulated reasonably well the observed July CLD minima over the major desert areas, the CLD maxima over the North Pacific and North Atlantic, and the band of maximum cloudiness centered near 50^oS. However, the model overestimates and underestimates the July CLD over the high latitudes in the Southern and Northern Hemispheres, respectively. The model also fails to simulate the July CLD maxima observed along the west coasts of the Americas and off the west coast of Africa, and somewhat underestimates the CLD to the east of New Guinea and Australia.

We now compare the simulated January and July zonal-mean fractional cloud cover (CLD), cloud-top-pressure (CTP) and cloud-top-temperature (CTT) with the corresponding quantities observed by ISCCP.

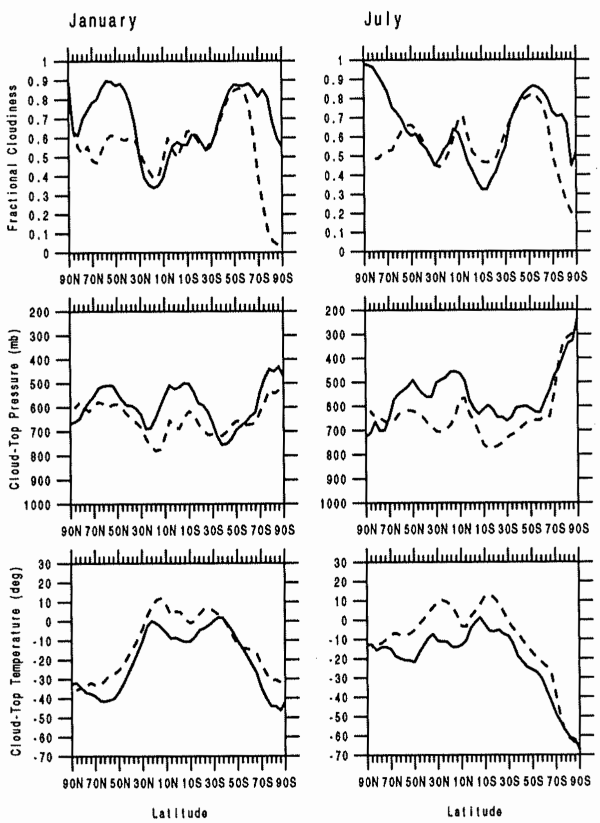

Fig. 2. Simulated (solid line) and observed (dashed line) zonal-mean cloudiness (CLD, top panels), cloud-top pressure (CTP, middle panels) and cloud-top temperature (CTT, bottom panels) for January and July. The observations are from ISCCP as analyzed by Schlesinger *et al.* (1989).

The meridional distributions of simulated zonal-mean CLD (Fig. 2, top panels) are in reasonable agreement with the observed distributions between 30^{o}N and 50^{o}S, although the observed July CLD minimum centered at 10^{o}S is underestimated by the model. Conversely, the model overestimates the zonal-mean CLD over both poles in both seasons, and in northern midlatitudes in winter. However, because the January ISCCP data for Antarctica do not agree with ground-based cloud observations (Warren *et al.*, 1986) which have CLD $\approx$ 50%, it is likely that the model does not overestimate Antarctic cloud cover by as much as Fig. 2 indicates. A comparison of Fig. 2. with Fig. 1 shows that the differences of the zonal-mean CLD in the subtropics are largely the result of the model's underestimation of the subtropical stratocumulus clouds off the west coasts of Africa and the Americas.

The middle and lower panels of Fig. 2 show that the meridional distributions of zonal-mean CTP and CTT simulated by the model resemble the corresponding observed distributions. However, the simulated cloud tops are generally located above the observed cloud tops, as is evidenced by their lower CTP and CTT values.

The relative occurrence of 11 categories of CLD, CTP and CTT are presented in Fig. 3 for both the simulation and observation. The relative occurrence is defined as the absolute occurrence divided by its maximum value (shown in Fig. 3), and the absolute occurrence is the total number of 4^{o} lat. x 5^{o} long. grid boxes (3312) having the category summed over the number of sampling times for each month, divided by the total number of grid boxes multiplied by the number of sampling times for the month.

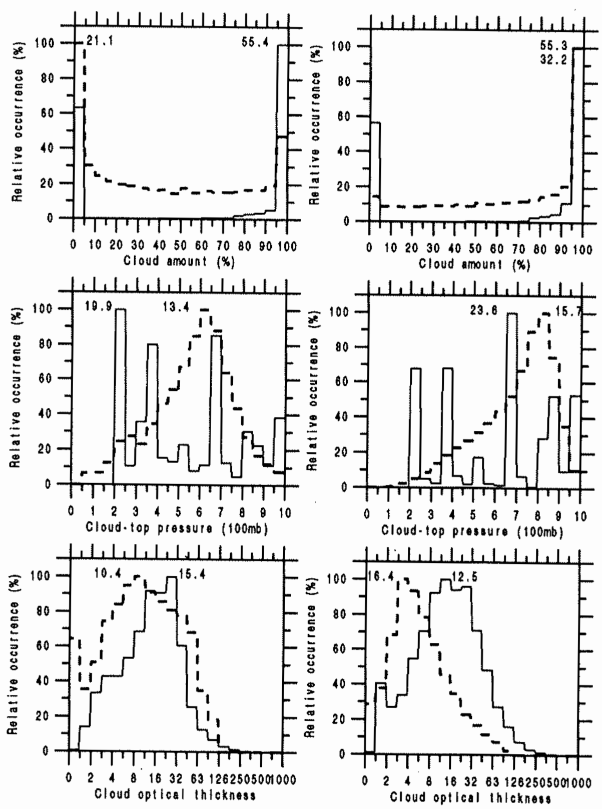

Fig. 3. Relative frequency distributions for simulated (solid line) and observed (dashed line) cloudiness (CLD, top panels), cloud-top pressure (CTP, middle panels) and optical thickness (bottom panels) for July over land (left panels) and ocean (right panels). The observations are from ISCCP as analyzed by Schlesinger *et al.* (1989).

Figure 3 (top-right panel) shows that the most frequently occurring cloud cover (CLD) simulated by the model over the oceans is overcast (95-100%), in agreement with the observed cloud cover. However, the simulated overcast occurs 55.3% of the time over the globe, while the observed overcast occurs only 32.2%. Figure 3 shows that the model fails to simulate the rather uniform occurrence of all cloud-cover categories less than overcast. Instead, the model simulates a larger occurrence than observed for the clear category (0-5%). This "either-clear-or-overcast" cloud-cover occurrence distribution is also simulated over land (Fig. 3, top-left panel) in contrast to the more-uniform observed occurrence distribution.

The middle panels of Fig. 3 show that the occurrence distributions of observed cloud-top pressure (CTP) have a single mode each, at 600-650 mb over land (with 13.4% absolute occurrence) and 800-850 mb over water (with 15.7% absolute occurrence). In contrast, the occurrence distributions of simulated cloud-top pressure (CTP) have peaks at 200-250 mb, 350-400 mb and 650-700 mb over both land and ocean, and also at 850-900 mb and 950-1000 mb over the ocean. Only part of this error in model-simulated CTP can be due to the model's having only 7 layers between the surface and 200 mb.

The lower panels of Fig. 3 present the relative occurrence of cloud optical thickness categories using a logarithmic scale. The observed optical thickness distribution for continental clouds is broader than that for marine clouds, with large optical thicknesses occurring more frequently. However, there is no significant difference between the simulated optical thickness distributions for continental and marine clouds. This is not surprising because the cloud parameterization does not take cognizance of the difference in the drop size distribution between continental and maritime clouds.

3. Conclusion

This abbreviated evaluation of our cloud/radiation parameterization indicates that while it is successful in simulating many characteristics of the observed clouds, it: (1) overestimates the fractional cloud cover between 50^{o}-70^{o} latitude in both hemispheres; (2) underestimates the stratocumulus cloud cover off the west coasts of the continents; (3) simulates either cloud-free or overcast conditions, instead of the observed full range of partial cloudiness; (4) incorrectly simulates the observed vertical distribution of cloud tops, and (5) fails to simulate the observed broader optical thickness distribution over land than ocean. To remove these deficiencies will require improvements in the parameterizations of soil hydrology, boundary-layer cloud and the closure condition for stratiform cloud, and inclusion of separate treatments for the different drop-size distributions for continental and marine clouds.

References

Arakawa, A., and W. H. Schubert, 1974: Interaction of a cumulus cloud ensemble with the large scale environment, Part I. *J. Atmos. Sci.*, **31**, 674-701.

Heymsfield, A. J. , and C. M. R. Platt, 1984: A parameterization of the particle size spectrum of ice clouds in terms of the ambient temperature and ice water content. *J. Atmos. Sci.*, **41**, 846-855

Kessler, E., III, 1969: On the distribution and continuity of water substance in atmospheric circulations. *Meteor. Monogr.*, **32**, 84 pp.

Oh, J.-H., 1989: Physically-based general circulation model parameterization of clouds and their radiative interaction. Ph. D. dissertation, Department of Atmospheric Sciences, Oregon State University, Corvallis, OR, 315 pp.

Schlesinger, M.E., J.-H. Oh, and D. Rosenfeld, 1988: A parameterization of the evaporation of rainfall. *Mon. Wea. Rev.*, **116**, 1887-1895.

Schlesinger, M. E., E. Fu and J.-H. Oh, 1989: An analysis of ISCCP data for July 1983, January 1984 and April 1985. Unpublished manuscript, 43 pp.

Sundqvist, H., 1978: A parameterization scheme for non-convective condensation including prediction of cloud water content. *Quart. J. Roy. Meteor. Soc.*, **104**, 677-690.

Sundqvist, H., 1988: Parameterization of condensation and associated clouds in models for weather prediction and general circulation simulation. In *Physically-Based Modelling and Simulation of Climate and Climatic Change*, Vol. I, M. E. Schlesinger (ed.), Reidel, Dordrecht, 433-462.

Warren, S. G., C. J. Hahn, J. London, R. M. Chervin and R. L Jenne, 1986: Global Distribution of Total Cloud Cover and Cloud Type Amounts Over Land. NCAR/TN-273 + STR. National Center for Atmospheric Research, Boulder, CO 29 pp + 199 Maps.

UPGRADING WARM CLOUD MODELS

BY INTRODUCING THE WEGENER-BERGERON-FINDEISEN EFFECT

J.C.H. van der Hage

IMAU - Utrecht University - 3584 CC, Utrecht - The Netherlands

1. INTRODUCTION

Although the Wegener-Bergeron-Findeisen (WBF) process is a molecular diffusion mechanism, the net result in a cloud is similar to that of autoconversion or accretion. That is to say, large particles are generated at the expense of smaller particles and not by draining vapour from the cloud. Treating the WBF process like autoconversion is a convenient way of introducing ice physics in simple cloud models, but then the efficiency of the WBF process must be known.

In the present paper a collection kernel φ_{WBF} for the collection of cloud water deposited on an ice crystal is determined from the growth equation of an ice crystal, and introduced in the autoconversion equation:

$$\frac{\partial N_r}{\partial t} = -\varphi_1 N_d^2 - \varphi_2 N_d N_i - \varphi_3 N_i^2 - \varphi_{WBF} N_d N_i \quad (1)$$

In this equation the concentration N_r of small cloud elements is expressed as $N_r = N_d + N_i$ where the suffixes d and i stand for droplets and small ice crystals respectively.

2. VAPOUR DEPOSITION ON AN ICE CRYSTAL

The theoretical growth rate for a spherical ice crystal with radius r is (Pruppacher,1980):

$$\frac{\partial m}{\partial t} = 4\pi r c_i s_i$$

Here s_i is the supersaturation of the vapour with respect to ice and c_i is a constant which depends on temperature but not very strongly (see table I).

When ρ_i is the mass density of ice the above equation can be written as:

$$\frac{\partial (r^2)}{\partial t} = \frac{2c_i s_i}{\rho_i}$$

Integration results in:

$$r_t^2 - r_0^2 = 2c_i s_i \rho_i^{-1} t$$

$$\frac{\partial m}{\partial t} = 4\pi r_0 c_i s_i \left(1 + 2c_i s_i t \rho_i^{-1} r_0^{-2}\right)^{1/2} \quad (2)$$

Eq.(2) presents a minimum value; the deposition on real, non-spherical crystals is greater.

The mass increase of an ice crystal can be expressed in m_d units when m_d is the mass of one cloud droplet. Then the number of droplets disappearing from a unit cloud volume per unit time due to WBF autoconversion is:

$$\left(\frac{\partial N_d}{\partial t}\right)_{WBF} = -\frac{1}{m_d}\frac{\partial m}{\partial t} N_i \quad (3)$$

In eq.(1) the droplet removal rate by the WBF mechanism is expressed as $-\varphi_{WBF} N_d N_i$. Comparing this with eq.(3) results in:

$$\varphi_{WBF} = \frac{1}{m_d N_d}\frac{\partial m}{\partial t}$$

Substitution of eq.(2) yields a minimum value for φ_{WBF}, valid strictly for spherical crystals:

$$\varphi_{WBF} = \frac{4\pi r_0 c_i s_i}{m_d N_d}\sqrt{1 + 2c_i s_i t \rho_i^{-1} r_0^{-2}}$$

When ρ_d is the mass density of liquid water, and writing r_i instead of r_0 for the initial radius of the ice crystals we finally have:

$$\varphi_{WBF} = \frac{3 r_i c_i s_i}{r_d^3 \rho_d N_d}\sqrt{1 + 2c_i s_i t \rho_i^{-1} r_i^{-2}} \quad (4)$$

The collection kernel of WBF autoconversion depends on the size of the ice crystals. When the initial size of the crystals is taken as $r_i = 10\mu m$ the square root in eq.(4) varies from unity for $t = 0$ to about 6 or 8 for $t = 1000$ s as can be seen by substituting the appropriate values from table I.

Table I. $c_i s_i$ as a fuction of temperature

T	s_i	c_i	$c_i s_i$
273	0	5.27E-8	0.00E-9
272	0.01	5.01	0.50
271	0.02	4.76	0.95
270	0.03	4.53	1.36
268	0.05	4.05	2.02
263	0.09	2.95	2.65
258	0.14	2.04	2.86
253	0.18	1.36	2.45
248	0.22	0.87	1.91
243	0.25	0.54	1.35
Kelvin	---	$kgm^{-1}s^{-1}$	$kgm^{-1}s^{-1}$

Consequently a minimum value of the WBF collection kernel for all crystal shapes and lifetimes is determined by:

$$\varphi_{WBF} > \frac{3 r_i c_i s_i}{r_d^3 \rho_d N_d} \quad (5)$$

The product $c_i s_i$ as a function of cloud temperature is presented in Table 1. In general, cloud glaciation starts below -5^{o}C and most clouds are completely glaciated at temperatures below -35^{o}C, so only values of $c_i s_i$ between $-35 < T < -5^oC$ are relevant for this discussion of autoconversion in mixed clouds. These values are all greater than 10^{-9} $kgm^{-1}s^{-1}$ (see Table 1). In a cloud with $N_d = 10^9$ m^{-3} and $r_i = r_d = 10\mu m$, the WBF collection kernel for autoconversion then is:

$$\varphi_{WBF} > 3\times10^{-11}\ m^3/s \quad (6)$$

A typical value of the WBF collection kernel for autoconversion is two or three orders of magnitude greater than the minimum value due to the combined effects of the non spherical crystal shape , the time factor determined by the square root in eq.(4) and the droplet number concentration N_d.

3. CONVENTIONAL AUTOCONVERSION

The collection kernel φ_1 for conventional autoconversion in eq.(1) equals the probability for a cloud drop with radius r_1 to collect droplets of radius r_d in a sheared velocity field by mechanical impaction only.

All droplets passing a particular drop at a distance r_E or less will be collected when:

$$r_E^2 = (r_d + r_1)^2 E_{d,1} \tag{7}$$

E is the Langmuir collection efficiency. E < 1 for droplets with $r_d \leq 10\mu m$ (Pruppacher,1980).

The collection kernel for mechanical impaction in turbulent shear is expressed as:

$$\varphi_{turb} = k\Gamma r_E^3 \tag{8}$$

where $4 < \Gamma < 28\ s^{-1}$ is the turbulent shear rate, equivalent to the inverse of the Kolmogorov time scale. The shear rate Γ is calculated from in-cloud measurements of the dissipation rate for turbulent energy (Ackerman, 1968) and k is a constant which varies between 0.5 and 3 in different calculation models (Pruppacher, 1980). With these data for turbulent flow in clouds a maximum value for the collection kernel φ_1 can be calculated from eqs.(7) and (8):

$$\varphi_1 < 670\, r_d^3 \tag{9}$$

In the same cloud where the minimum value for φ_{WBF} was determined by eq.(6) for $r_i = r_d = 10\mu m$, we now find a maximum value for φ_1:

$$\varphi_1 < 0.7\times10^{-11}\ m^3/s \tag{10}$$

4. A MODIFIED AUTOCONVERSION EQUATION

From the previous sections 2 and 3 it can be concluded that, with regard to 10µm droplets WBF autoconversion is several orders of magnitude more efficient than drop-drop autoconversion:

$$\varphi_{WBF} = G\varphi_1 \quad \text{with} \quad G >> 1 \tag{11}$$

G will be named the gain factor of the WBF mechanism in autoconversion.

An identical argumentation but now applied to collisions between ice crystals and droplets leads to the conclusion that WBF autoconversion must also be several orders of magnitude more efficient than conventional autoconversion between ice crystals and droplets:

$$\varphi_{WBF} = G'\varphi_2 \quad \text{with} \quad G' >> 1 \tag{12}$$

This latter conclusion is supported by observations in clouds and in laboratory experiments. In eq.(1) riming is represented by the second r.h.s. term containing φ_2, and with regard to autoconversion this term can now be neglected compared to the last term which contains φ_{WBF}. Eq.(1) then reduces to:

$$\frac{\partial N_r}{\partial t} = -\varphi_1 N_d^2 - \varphi_3 N_i^2 - \varphi_{WBF} N_d N_i \tag{13}$$

Let the degree of cloud glaciation g be defined by:

$$N_i = gN_r \quad \text{and} \quad N_d = (1-g)N_r$$

Then eq.(13) can be written as:

$$\frac{\partial N_r}{\partial t} = -\varphi_1 N_r^2\left\{(1-g)^2 + \frac{\varphi_3}{\varphi_1}g^2 + Gg(1-g)\right\} \tag{14}$$

The ratio φ_3/φ_1 in eq.(14) is determined by the Langmuir collection efficiencies, these are not accurately known for small ice crystals but $\varphi_3/\varphi_1 < 1$ because ice crystals don't coalesce like droplets. In eq.(11) it was stated that G>>1 and therefore:

$$\frac{\partial N_r}{\partial t} \cong -\varphi_1 N_r^2\{1 + Gg(1-g)\} \tag{15}$$

When g = 0 there is no glaciation and eq.(15) reduces to the conventional autoconversion equation for warm clouds.

5. THE GAIN FACTOR G

Combining the equations (5), (9) and (11) results in an expression for the gain factor:

$$G > \frac{3r_i c_i s_i}{(670) r_d N_d} r_d^{-6} \tag{16}$$

The apparently numerical factor 670 is in parentheses to indicate that it has the dimension s^{-1} (see eq.9). Note the very strong dependence of G on r_d. The approximations which lead to eq.(15) for autoconversion are based on $r_i = r_d = 10\mu m$ and then G>>1 is found. But for droplets twice as large the gain factor decreases by a factor 64 so it appears that the WBF mechanism may only dominate the autoconversion of droplets with $r_d < 15\mu m$ or perhaps $r_d < 20\mu m$.

Eq.(16) shows that the gain factor G is not independent of the degree of glaciation. The cloud droplet concentration was previously expressed as $N_d = (1-g)N_r$ and with eq.(16) a new parameter H independent of g can be derived from G by writing:

$$G = \frac{H}{N_d} = \frac{H}{(1-g)N_r} \tag{17}$$

H depends on temperature through the factor $c_i s_i$ but not very strongly (see fig.1). The parameter H is proportional to $1/\Gamma$, the inverse turbulent velocity shear (see eq.8). Substituting H in eq.(15) finally results in:

$$\frac{\partial N_r}{\partial t} \cong -\varphi_1 N_r^2 - gH\varphi_1 N_r \tag{18}$$

When g = 0, eq.(18) reduces to the conventional autoconversion equation for warm clouds. Warm cloud models can now be upgraded to more universal cloud models merely by substituting eq.(18) for the warm autoconversion equation, thus omitting an elaborate ice parameterization.

REFERENCES

Ackerman,B.(1968) The Rate of Dissipation of Turbulent Energy in Cloudy Air, Proc.Int.Conf.Cloud Phys., Toronto, p.564.

Long, A.B.(1974) Solutions to the Droplet Collision Equation for Polynomial Kernels, J.Atm.Sci., Vol.31, p.1040.

Pruppacher,H.R. and J.D. Klett (1980) "Microphysics of Clouds and Precipitation", Reidel, Delft.

ON A DESCRIPTION OF A WARM CLOUD MICROSTRUCTURE AT THE COAGULATION STAGE OF ITS FORMATION

S.V.Guzeeva, V.M.Merkulovich, A.S.Stepanov

Scientific-Production Association "Typhoon",Obninsk,Russia

At present it is universally accepted that the main mechanism of precipitation formation, along with the sublimation growth of ice particles, is the coagulation of droplets with one another and with crystals. The physical analysis of the precipitation formation processes and their numerical simulation are based on the use of the coagulation kinetic equation for the mean distribution function $C_\gamma(t)$ of the droplets by their volumes. In the literature this equation is usually called the Smoluchowski equation. The equation is closed relative to $C_\gamma(t)$, and its form does not depend on the character of the drop relative motion. The latter is considered in the form of the coagulation kernel dependence on the sizes of colliding drops and the parameters of their relative motion. The main cause of coagulation in clouds is connected with the difference in the sedimentation rate of drops of different sizes (differential sedimentation-induced coaguulation). As far as the collision function of such coagulation is a complex function of drop sizes, an exact solution of the Smoluchowski equation is impossible in this case. Therefore the studies of the coagulation equation is made with the modelled nuclei. The collision function $K(\alpha,\beta)=\alpha\beta$ (α, β are the volumes of coagulating particles) is one of the acceplable modelled coagulation kernels.

It is well known that an analytical solution of the Smoluchowski eguation with this kernel retains its water content only at the finite time $t \leqslant t = 1$, that contradicts the physical sense of the equation. This fact casts doubt on the applicability of the Smoluchowski eguation, on the whole, for describing coagulation. In this connection it should be mentioned that the Smoluchowski equation is written under the assumption that at any time moment the droplet number of each size obeys the Poisson statistics. This is just the assumption that made it possible to obtain a closed description of the system with the mean spectrum without the use of the correlation moments. This is a very strong assumption if one keeps in mind that the concentration of cloud droplets is ~ 10^6 times more than that of the precipitation droplets. In connection with this a relative contribution of the cloud droplet spectrum fluctuations may appear considerable in the process of precipitation particles formation.

The attempts to leave the frameworks of the description of coagulation with the Smoluchowski equation have been made, for example, by Lushnikov (1978). The probabilistic description of coagulation with the master equation have been made in this and other works. Its approximated solution has shown that with time one particle is chipped off from the mean spectrum, the mass of these particles is of the order of the whole system mass. The theoretical prediction of the existence of even a small number of such particales has far-reaching consequences--just these particles could be the precipitation particles.

On the base of the results obtained by Merkulovich and Stepanov (1990) an analysis has been carried out of the particle mean spectrum behaviour and its correlation moments within a finite system of the whole mass M. The initial system consists of M monomers coagulating with the kernel $K(\alpha,\beta) = \alpha\beta$. An exact solution for the particle mean spectrum for an arbitrary time moment is given with the relation

$$C_\gamma=m\binom{M}{\gamma}\varphi_\gamma(z)\left[1-\exp\left(-\frac{mt}{M}\right)\right]^{\gamma-1}\exp\left[-\frac{m\gamma t(M-\gamma)}{M}\right] \tag{1}$$

where $\varphi_\gamma(z)$ is the polynom of the order of $\binom{\gamma-1}{z}$ from $z=\exp\left(-\frac{mt}{M}\right)$, and m is the liquid water content. The polynoms $\varphi_\gamma(z)$ are defined with the equation system

$$\sum_{i=0}^{\gamma}(-1)^{\gamma+i}\binom{\gamma}{i}\,i\,\varphi_i(z)\left(\frac{1-z^i}{1-z}\right)^{\gamma-1} = \delta_{\gamma,1}. \tag{2}$$

From equation (2) it follows, in particular, that $\varphi_\gamma(1) = \gamma^{\gamma-2}$. Solution (1) is reduced to the Smoluchowski equation at mt<1 in the thermodynamic limit $M \to \infty$. In this limit the Smoluchowski equation for mt>1 is inapplicable as the kinetic equation of coagulation (Merkulovich and Stepanov, 1990). The fluctuations of the distribution function around the mean value (1) can be characterized with their dispersion determined with

$$\langle C'_{\gamma_1} C'_{\gamma_2}\rangle = \left[\binom{M-\gamma_1}{\gamma_2}\binom{M}{\gamma_2}^{-1} \exp\frac{m\gamma_1\gamma_2 t}{M} - 1\right] C_{\gamma_1} C_{\gamma_2} +$$

$$+ \frac{m}{M}\,\delta_{\gamma_1,\gamma_2} C_{\gamma_i} \qquad (3)$$

$$C'_{\gamma} = \frac{m}{M}\,x'_{\gamma}\ ;\quad x'_{\gamma} = x_{\gamma} - \langle x_{\gamma}\rangle .$$

In case of $M >> 1$ relation (3) reduces to

$$\langle C'_{\gamma_1} C'_{\gamma_1}\rangle \approx \left[\exp\frac{\gamma_1\gamma_2(mt-1)}{M} - 1\right] C_{\gamma_1} C_{\gamma_2} +$$

$$+ \frac{m}{M}\,\delta_{\gamma_1,\gamma_2} C_{\gamma_i} .$$

At any t there exists a range of sizes $\gamma_1+\gamma_2 > M$, where the fluctuations are anomalously high

$$\langle C'_{\gamma_1} C'_{\gamma_2}\rangle \sim \left| C_{\gamma_1} C_{\gamma_2} - \frac{m}{M}\,\delta_{\gamma_1,\gamma_2} C_{\gamma_i}\right| .$$

This means that at least in this range the fluctuations are of the order of the mean spectrum. Therefore the description of the cloud microstructure in this range with the mean spectrum is unrepresentative.

From the form of solution (1) it follows that at any time moment t_m maximum is formed in the particle spectrum in the range of $\gamma > M/2$. It should be noted that just in this region the fluctuations become too high and this maximum should not be identified as a "superparticle". The growth of the fluctuations near the maximum implies that the evolution of the spectrum large droplet fraction is governed not with the mean spectrum itself but with its correlation moments. Fig.1 shows the time dependence of the maximum formation on the initial monomer number.

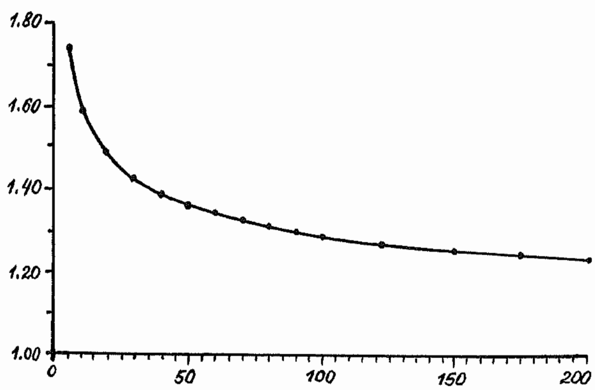

Fig.1. Time dependence of maximum formation on monomer initial number.

It is typical that $t_m(M)$ tends to $t_c = 1$ above at $M \to \infty$. Note that just at $t = t_c$ the conditions necessary for the Smoluchowski equation to be applied as the kinetic coagulation equation are disturbed.

Fig.2 gives a typical shape of the droplet spectrum $C_{\gamma}(t)$.

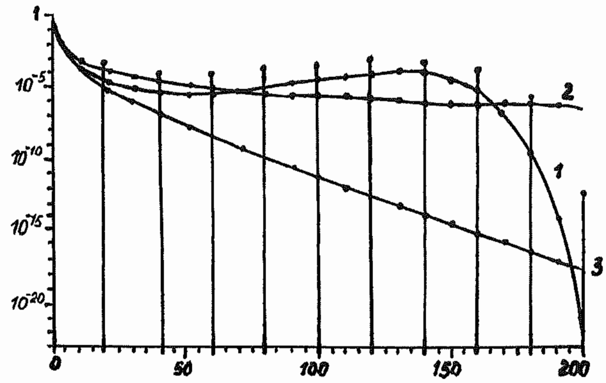

Fig.2. Particle mean spectrum behaviour at the time moment t=1.6.

1 - exact solution;
2 - solution of the Smoluchowski equation;
3 - Lushnikov's approximated solution.

- mean-root-square devation

The same Figure shows the errors of the two dispersions for the Smoluchowski equation and Lushnikov's approximated solution. As it is seen, the kinetic equation is unable to give a correct description of the spectrum large droplet fraction. Moreover, the behaviour of this function depends considerably on the presence of statistical fluctuations which can play a decisive role in the precipitation formation.

REFERENCES

Lushnikov A.A.,1978.Some new aspects of the coagulation theory. Izvestiya Acad. Sci. USSR, Atmos. Ocean. Phys., 14: 1046-1055 (in Russian).

Merkulovich V.M. and Stepanov A.S., 1990. Fluctuation - coagulation theory of aerosol evolution. Aerosol Science. Industry, Health and Environ., ed. by S.Masuda and K.Takahashi. Pergamon Press, 1: 122-125.

NEW EXPLICIT EQUATIONS FOR THE ACCURATE CALCULATION OF THE GROWTH AND EVAPORATION OF HYDROMETEORS BY THE DIFFUSION OF WATER VAPOR*

R. C. Srivastava and J. L. Coen

Laboratory for Atmospheric Probing, Department of the Geophysical Sciences, The University of Chicago, Chicago, IL 60637

1. INTRODUCTION

The growth and evaporation of hydrometeors are subjects of fundamental importance in cloud microphysics. The rate of transfer of water vapor to a particle by diffusion is proportional to the difference of vapor densities in the ambient air far from the particle and at the particle surface. The vapor density at the particle surface is a sensitive function of its temperature. The surface temperature of the particle is determined by its heat balance. To calculate the rate of growth of a particle, it is, therefore, necessary to solve simultaneously the equations for the diffusion of water vapor and heat. However, as is well known, it is possible to eliminate the particle temperature from the equations and obtain an approximate explicit equation for the rate of growth of the particle. This elimination has been accomplished in the literature by approximating the saturation vapor density difference as a linear function of the temperature difference. Therefore, the resulting equation is accurate only for small temperature differences between the particle and the air. Under typical conditions of cloud drop growth by condensation, the temperature differences are indeed very small and, therefore, such an approximate equation yields accurate results. In the case of evaporation of raindrops, however, the temperature differences can reach values of many degrees Celsius. The approximation of the saturation vapor density difference as a linear function of the temperature difference is then poor. In such cases, the rate of evaporation should be calculated by solving the two diffusion equations simultaneously (see, for example, Best (1952), Beard and Pruppacher (1971)). However, in a number of recent publications, the approximate equation, which assumes a linear relationship between the saturation vapor density and temperature differences, has also been applied to the evaporation of raindrops (see, for example, Feingold *et al.*, 1991; Knupp, 1987, 1988, 1989; Orville *et al.*, 1989; Proctor, 1988; Tzivion *et al.*, 1989; Clough and Franks, 1991; and Rogers *et. al.*, 1991). The purposes of this note are: (1) to discuss the error involved in this procedure, and (2) to present new explicit equations for the rate of growth and evaporation of hydrometeors which yield more accurate results even when the temperature difference between the particle and the ambient air is not small. This will be accomplished by approximating the saturation vapor density difference as a quadratic function of the temperature difference.

2. EQUATIONS

Under steady state conditions, the rate of increase of mass (m) of an isolated spherical particle of radius (r) by diffusion of water vapor is given by:

$$dm/dt = 4\pi rDf_v(\rho_\infty - \rho_p) \qquad (1)$$

where ρ_∞ is the ambient vapor density, ρ_p is the vapor density at the particle surface, D is the diffusivity of water vapor, and f_v is the ventilation coefficient for water vapor. In the steady state, the heat balance of the particle is expressed by:

$$L_v\frac{dm}{dt} = 4\pi rkf_h\Delta T, \;\; \Delta T \equiv (T_p - T_\infty) \qquad (2)$$

where L_v is the latent heat of vaporization, k the thermal conductivity of air, f_h the ventilation coefficient for heat, T_p the particle temperature, and T_∞ the ambient temperature. We have neglected heat transfer by radiation and heat storage within the particle.

The vapor density at the particle surface is given by:

$$\rho_p = \rho_s(T_p)(1 + s_p) \qquad (3)$$

where $\rho_s(T)$ is the saturation vapor density at temperature T and s_p is the equilibrium supersaturation over the particle. Equations (1), (2) and (3), with auxiliary thermodynamic equations, constitute an implicit set for the particle temperature and rate of growth.

Approximate explicit solutions for the particle rate of growth have been obtained in the literature by approximating the saturation vapor density difference as a linear function of the temperature difference:

$$\rho_s(T_p) \cong \rho_s(T_\infty) + \rho_s'(T_\infty)\Delta T \qquad (4)$$

where the prime denotes differentiation. From the above equations, we obtain:

$$\left(\frac{dm}{dt}\right)_1 = \frac{4\pi rDf_v\rho_s(T_\infty)}{1+\gamma}(s - s_p) \qquad (5)$$

where

$$\gamma \equiv \frac{L_vD}{k}\frac{f_v}{f_h}\rho_s' \qquad (6)$$

is a dimensionless quantity; if we assume the two ventilation coefficients to be equal, then γ is a function of temperature and pressure only. In (5), s is the ambient supersaturation:

$$\rho_\infty = \rho_s(T_\infty)(1 + s) \qquad (7)$$

*Based on a paper of the same title that has been accepted for publication in the *Journal of the Atmospheric Sciences.*

Equations (5) is the traditional solution for the rate of growth of a particle by diffusion. The subscript 1 signifies that we have used a linear relationship between the saturation vapor density difference and the temperature difference to derive (5).

The accuracy of the traditional solution (5) will obviously depend on the accuracy of the approximation (4). In figure 1, we show the 'exact' solution for the temperature difference between the particle and the ambient air for evaporating drops obtained by iterative solution of (1), (2), and (3) with $s_p = 0$. The temperature difference is shown as a function of the ambient temperature for selected relative humidities and two ambient pressures.

It is seen that under very warm, dry conditions, the temperature difference between the ambient air and the raindrop can exceed 15 to 20°C. Since the saturation vapor density approximately doubles for every 10°C increase of temperature, it should be clear that (4) is a poor approximation under such conditions. This implies in turn that the traditional growth equation (5) may also be in considerable error. These errors will be discussed in the next section. We first derive a more accurate growth equation.

We approximate the saturation vapor density difference as a quadratic function of the temperature difference:

$$\rho_s(T_p) = \rho_s(T_\infty) + \rho_s'(T_\infty)\Delta T + \frac{\rho_s''(T_\infty)}{2}\Delta T^2 \qquad (8)$$

Equations (1), (2), (3) and (9), give a quadratic equation for dm/dt, which is easily solved. Expanding the square root that occurs in that solution to various orders in $(s - s_p)$, we obtain the following equations for dm/dt:

$$\begin{aligned}\left(\frac{dm}{dt}\right)_2 &= \frac{4\pi r D f_v \rho_s(T_\infty)}{1+\gamma}(s - s_p)\left[1 - \alpha(s - s_p)\right] \\ &= \left(\frac{dm}{dt}\right)_1 \left[1 - \alpha(s - s_p)\right]\end{aligned} \qquad (9),$$

$$\left(\frac{dm}{dt}\right)_3 = \left(\frac{dm}{dt}\right)_1 \left[1 - \alpha(s - s_p) + 2\alpha^2(s - s_p)^2\right] \qquad (10),$$

and

$$\left(\frac{dm}{dt}\right)_4 = \left(\frac{dm}{dt}\right)_1 \left[\begin{aligned}&1 - \alpha(s - s_p) \\ &+ 2\alpha^2(s - s_p)^2 - 5\alpha^3(s - s_p)^3\end{aligned}\right] \qquad (11),$$

where

$$\alpha \equiv \frac{1}{2}\left(\frac{\gamma}{1+\gamma}\right)^2 \frac{\rho_s''\rho_s}{\rho_s'\rho_s'} \qquad (12).$$

The above equations are for the case of condensation or evaporation of water vapor, the saturation vapor densities having been implicitly assumed to be with respect to water. With minor changes, the derivations can be carried over to the case of the deposition or sublimation of water vapor. These changes are the replacement of the latent heat of vaporization by that of sublimation, and the saturation vapor density with respect to water by that with respect to ice.

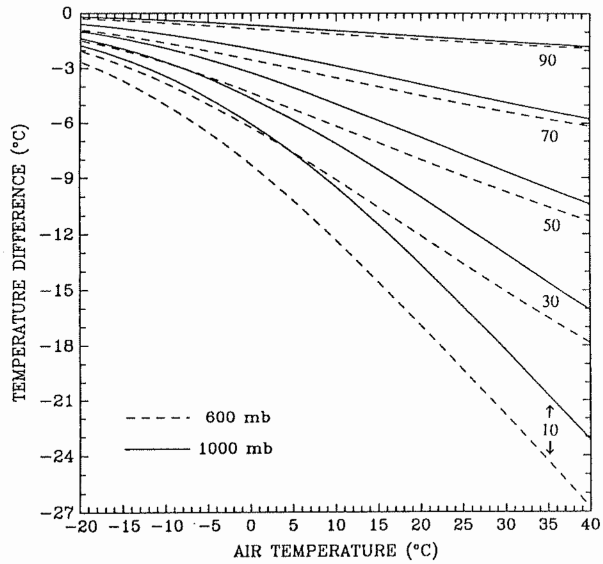

Fig. 1: Temperature difference between an evaporating drop and its environment as a function of air temperature for selected relative humidities, shown on the curves, and pressures (solid lines, 1000 mb; dashed lines, 600 mb).

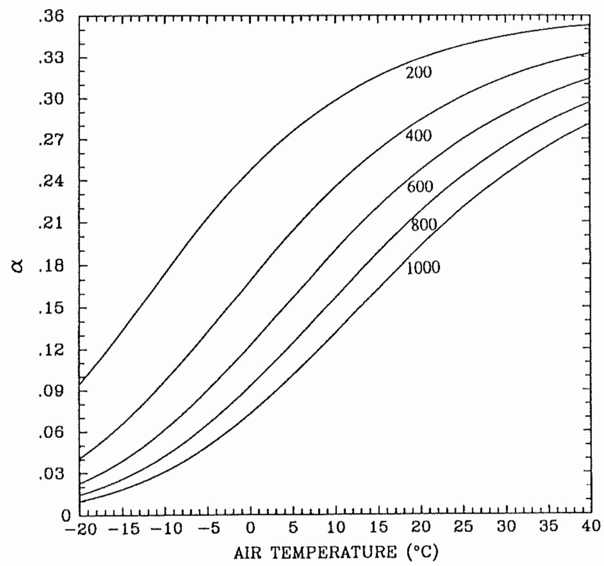

Fig. 2: The parameter α as a function of air temperature for selected pressures (mb), shown on the curves.

3. DISCUSSION

We shall now compare the numerical solution of (1), (2) and (3) - which will be referred to as the exact solution - with solutions of (5), the traditional equation as given by Mason (1971), Rogers and Yau (1989) and others, and solutions of (9) and (11) which we have derived above. For the calculations, we have made the approximation of assuming the ventilation coefficients for heat and vapor to be equal. For this discussion, we shall also assume $s_p = 0$.

The difference between the more accurate growth equations derived here and the traditional equation (5) depends only on αs, where α is a function only of the temperature and pressure if the ventilation coefficients for heat and vapor are assumed to be equal. The derivatives occurring in (12) can be found with the help of the Clausius-Clapeyron equation. Fig.2 is a plot of α as a function of temperature for selected pressures. The value of α increases with increasing temperature and decreasing pressure. It can reach values between 0.20 and 0.25 at 20°C for pressures exceeding about 600 mb. Since supersaturation in an updraft during growth of cloud drops by condensation is generally less than 1%, the error incurred in using the traditional approximation to calculate the rate of growth is generally less than about 0.25% ($\alpha s = (0.25)(0.01)$). Hence, use of that equation for calculating the growth of cloud drops by condensation in updrafts is justified. However, if we consider the evaporation of raindrops at very low relative humidities (say 20%) and very warm temperatures (say 30°C), the error in using the traditional approximation can amount to about 20% $|\alpha s| = 0.25(1.00 - 0.20)$. It may be noted that the conditions envisaged do occur, for example, in the Denver area during the summer when the lower atmosphere is well mixed.

The above estimates of errors are approximate because they represent relative differences between the traditional equation (5) and the new equation (9) which itself is approximate. We shall now discuss the errors more rigorously by comparing solutions of (5), (9) and (11) with the numerical solution of (1), (2) and (3). Figure 3 gives the percentage error in the rate of evaporation given by (5), as a function of temperature for selected relative humidities and two pressures, namely 600 and 1000 mb. (Fractional error is defined as $(a - b) / a$, where a is the solution of the equation whose error is being discussed and b is the exact solution.) It is seen that the traditional equation (5) always underestimates the rate of evaporation; at a pressure of 1000 mb and a temperature of 10°C the magnitude of the error is greater than 10% (5%) for relative humidities less than 30% (65%). For warm, dry conditions such as 30°C and 20% relative humidity, the magnitude of the error is about 24%. According to Feingold *et al.* (1991), temperatures of 40°C and relative humidities of 15% occur in certain meteorological situations in Israel. According to figure 3 the error in using (5) under such conditions (at a pressure of 1000 mb) is 30%.

The error in using (9) may be seen from figure 4 which is similar to figure 3 (however, note the change in the ordinate scale). In this case the errors are much smaller compared to the previous case. Let us consider the three cases of the previous paragraph. From figure 4, we see that at a pressure of 1000 mb and a temperature of 10°C, the error is now less than 3% for practically all relative humidities. For a temperature of 30°C and a relative humidity of 20% the error

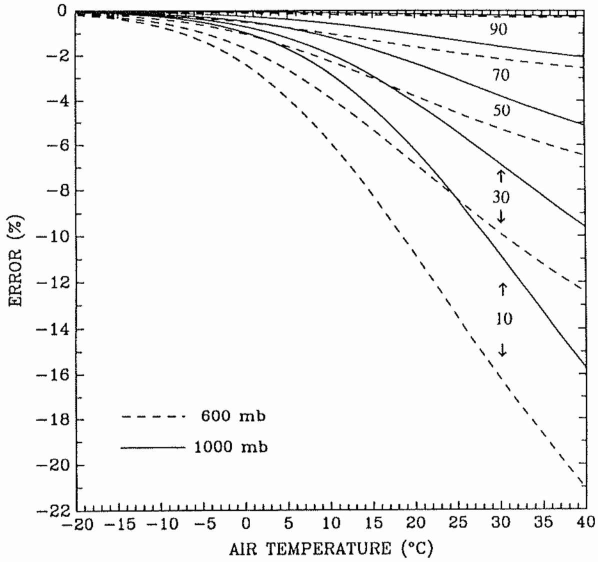

Fig. 4 Error in the rate of evaporation of raindrops as given by the equation (9) for selected relative humidities, shown on the curves , and two pressures, 1000 mb (solid lines) and 600 mb (dashed lines).

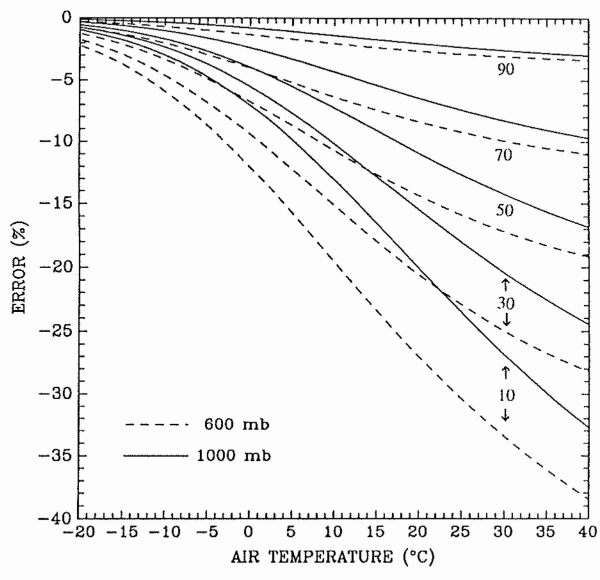

Fig. 3: Error in the rate of evaporation of raindrops as given by the traditional equation (5) for selected relative humidities , shown on the curves ,and two pressures, 1000 mb (solid lines) and 600 mb .

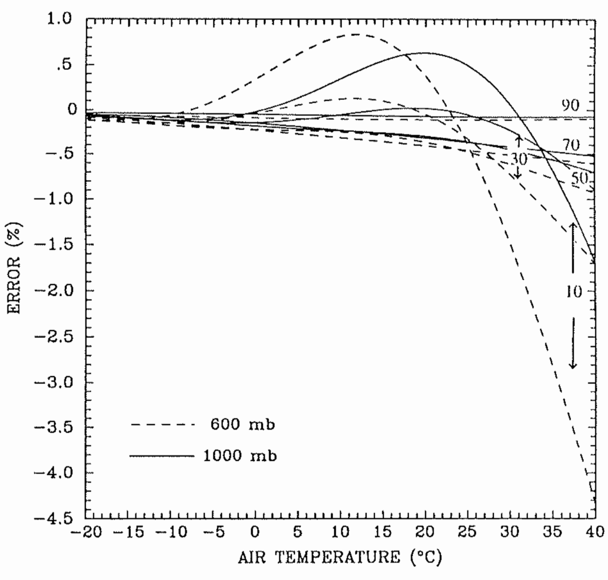

Fig. 5: Error in the rate of evaporation of raindrops as given by the equation (11) for selected relative humidities , shown on the curves, and two pressures, 1000 mb (solid lines) and 600 mb (dashed lines).

is about 9% compared to 24% for the traditional equation. For the extreme case of 40°C and relative humidity of 15%, the error is about 14% compared to 30% for the traditional equation. If an error of 12% can be tolerated then (9) can be used under practically all conditions likely to be encountered. If an accuracy of better than 5% is desired, then this equation should be limited to temperatures lower than about 17°C and relative humidities greater than 10%. If only relative humidities greater than 30% (40%) are involved, then the equation yields results better than 5% accuracy for temperatures less than 24°C (30°C). The errors are greater at the lower pressure of 600 mb shown in figure 4 in dashed lines. However, temperatures encountered in the atmosphere at that pressure are generally lower; therefore, the statements above for equation (13) with respect to errors of 5% and 12% will still apply. In extremely warm, dry conditions even (9) suffers from unacceptable errors. Figure 5 is similar, showing the error obtained by using (11). It is seen that the percentage error in using this equation is less than about 5% even under the most extreme conditions likely to be encountered in the atmosphere. For temperatures less than 35°C, the error is less than about 1%. Thus (11), which is only a little more complicated than the almost universally used (5), gives dramatically more accurate results without the need to solve a set of simultaneous equations.

4. CONCLUSIONS

We have discussed the growth and evaporation of hydrometeors by the diffusion of water vapor and heat. It has been shown that the equation given in text books and used many times in the literature (equation 5) substantially underestimates the evaporation rate of raindrops in warm, unsaturated conditions. This error has been shown to be due to the use of a linear relationship between temperature and saturation vapor density differences between the particle and the ambient air. By using a quadratic relationship between these quantities, we have derived a new equation (equation 11) which yields much more accurate results -- within about 2% of the exact solution under most atmospheric conditions.

5. ACKNOWLEDGMENTS

This research was supported by the Atmospheric Sciences Section of the National Science Foundation under grants ATM 89 03683 and ATM 91 05182. J. Coen is supported by the NASA Graduate Student Researchers Program, grant NGT- 50449.

6. REFERENCES

Beard, K. V., and H. R. Pruppacher, 1971: A wind tunnel investigation of the rate of evaporation of small drops falling at terminal velocity in air. *J. Atmos. Sci.,* **28**, 1455-1464.

Best, A. C., 1952: The evaporation of raindrops. *Quart. J. Roy. Meteor. Soc.,* **78**, 200-225.

Clough, S. A., and R. A. A. Franks, 1991: The evaporation of frontal and other stratiform precipitation. *Quart. J. Roy. Met. Soc.,* **117**, 1057-1080.

Feingold, G., Z. Levin, and S. Tzivion, 1991: The evolution of raindrop spectra. Part III: Downdraft generation in an axisymmetrical rainshaft model. *J. Atmos. Sci.,* **48**, 315-330.

Knupp, K. R., 1987: Downdrafts within High Plains cumulonimbi. Part I: General kinematic structure. *J. Atmos. Sci.,* **44**, 987-1008.

Knupp, K. R., 1988: Downdrafts within High Plains cumulonimbi. Part II: Dynamics and thermodynamics. *J. Atmos. Sci.,* **45**, 3965-3982.

Knupp, K. R., 1989: Numerical simulation of low-level downdraft initiation within precipitating cumulonimbi: Some preliminary results. *J. Atmos. Sci.,* **117**, 1517-1529.

Mason, B. J., 1971: *The Physics of Clouds.* Clarendon Press, 671 pp.

Orville, H. D., R. D. Farley, Y. -.C. Chi and F. J. Kopp, 1989: The primary cloud physics mechanisms of microburst formation. *Atmos. Res.,* **24**, 343-357.

Proctor, F. H., 1988: Numerical simulation of an isolated microburst. Part I: Dynamics and structure. *J. Atmos. Sci.,* **45**, 3137-3160.

Rogers, R. R., and M. K. Yau, 1989: *A Short Course in Cloud Physics.* Pergamon Press, 290 pp.

Rogers, R. R., I. I. Zawadzki, and E. E. Gossard, 1991: Variation with altitude of the drop size distribution in steady light rain. *Quart. J. Roy. Met. Soc.,* **117**, 1341-1370.

Tzivion, S. T., G. Feingold and Z. Levin, 1989: The evolution of raindrop spectra. Part II: Collisional collection / breakup and evaporation in a rainshaft. *J. Atmos. Sci.,* **46**, 3312-3327.

CORRECTIONS TO EMPIRICAL RELATIONS DERIVED FROM RAINFALL DISDROMETER DATA FOR EFFECTS DUE TO DROP SIZE DISTRIBUTION TRUNCATION

CARLTON W. ULBRICH
DEPARTMENT OF PHYSICS AND ASTRONOMY
CLEMSON UNIVERSITY, CLEMSON, SC 29634-1911

1. INTRODUCTION

This purpose of this paper is to report the results of an investigation of the effects of raindrop size distribution truncation on the coefficients and exponents found for empirical relations derived from disdrometer data. This subject has been addressed theoretically in previous work by Ulbrich (1985) where results were shown for an exponential drop size distribution (DSD). In other work [Ulbrich (1992)] these effects were demonstrated for several dual-measurement methods involving pairs of measurables such as the reflectivity factor and microwave attenuation or differential reflectivity. In the present work the effects of truncation are investigated experimentally more fully using a set of raindrop size spectra collected with a Joss disdrometer. To illustrate the methods used for correcting the experimental data for truncation, several types of empirical relations are considered as well as several approaches to effecting the corrections, all of which assume that the DSD can be approximated by a three parameter truncated gamma function. It is shown that the effects of truncation on the empirical coefficients and exponents can be significant and that good estimates of the shape of the distribution from moment to moment in a rainfall event are necessary in order that the corrections be applied properly.

2. ANALYSIS: METHOD 1

The theoretical relations used in this work have been defined in previous work [Ulbrich (1985)] in terms of a three parameter gamma function of the form [Ulbrich (1983)]

$$N(D) = N_0 \; D^{\mu} \exp(-\Lambda D) \tag{1}$$

where $N(D)(m^{-3}cm^{-1})$ is the number of raindrops per unit volume per unit diameter size interval, $D(cm)$ is the equivalent spherical drop diameter, and $N_0(m^{-3}cm^{-1+\mu})$, $\Lambda(cm^{-1})$ and μ are the three parameters of the distribution. It is assumed that any integral rainfall parameter of interest can be represented by the form

$$P = a_P \int_{D_{min}}^{D_{max}} D^p N(D) dD \tag{2}$$

where a_P is a constant and D_{min} and D_{max} are the lower and upper limits of integration. It follows directly from this definition that P can be expressed as

$$P = \frac{a_P N_0}{\Lambda^{p+\mu+1}} g(p + \mu + 1, x_{min}, x_{max}) \tag{3}$$

where

$$g(u, x_1, x_2) = \gamma(u, x_1) - \gamma(u, x_2) \tag{4}$$

and

$$\gamma(u, v) = \int_o^v x^{u-1} e^{-x} dx \tag{5}$$

is the incomplete gamma function and $x_{min} = \Lambda D_{min}$ and $x_{max} = \Lambda D_{max}$. It is possible to express P in terms of the ratios D_{min}/D_0 and D_{max}/D_0 through the use of the defining expression for the median volume diameter D_0, *i.e.*,

$$2 \int_{D_{min}}^{D_0} D^3 N(D) dD = \int_{D_{min}}^{D_{max}} D^3 N(D) dD \tag{6}$$

The dependence of ΛD_0 on D_{min}/D_0 and D_{max}/D_0 is shown in Ulbrich (1985). When it is used together with Eq.(3), the dependence of P on D_{min}/D_0 and D_{max}/D_0 is as shown in Fig.1 for the case of $p = 6$ (reflectivity factor Z) and in Fig.2 for $p = 2$ (optical extinction Σ) where it has been assumed that $\mu = 0$. Very similar figures result for other values of μ.

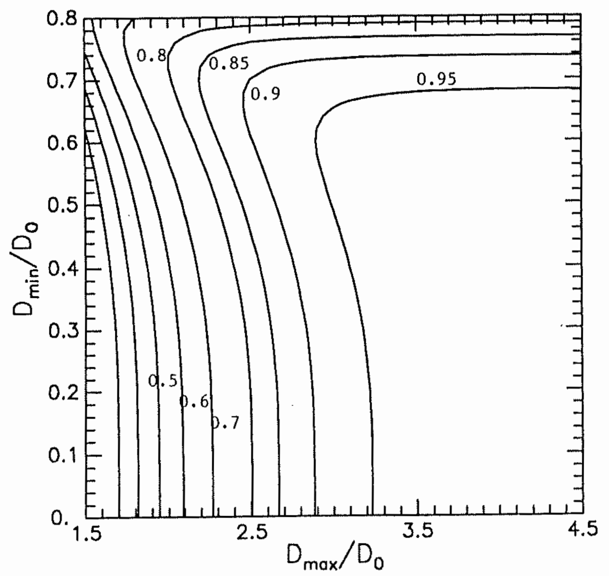

Fig. 1: Contours of the integral parameter reflectivity factor Z (p=6) as a function of $D_{\min}/D_0$ and $D_{\max}/D_0$ for $\mu = 0$. The contours have been normalized to the value of Z for $D_{\min} = 0$ and $D_{\max} \to \infty$ and are labeled with the values of $Z(D_{\min}/D_0, D_{\max}/D_0)/Z(0, \infty)$ to which they correspond.

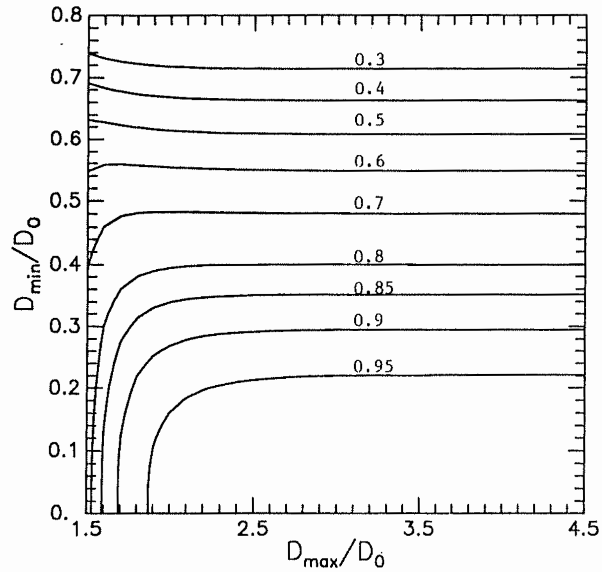

Fig. 2: Contours of the integral parameter optical extinction Σ (p=2) as a function of $D_{\min}/D_0$ and $D_{\max}/D_0$ for $\mu = 0$. The contours have been normalized to the value of Σ for $D_{\min} = 0$ and $D_{\max} \to \infty$ and are labeled with the values of $\Sigma(D_{\min}/D_0, D_{\max}/D_0)/\Sigma(0, \infty)$ to which they correspond.

These results can be used to deduce theoretical expressions which depict the effects of truncation on empirical relations between pairs of integral parameters. To illustrate the approach, suppose that the second integral parameter Q is defined analogously to P by

$$Q = \frac{a_Q N_0}{\Lambda^{q+\mu+1}} g(q+\mu+1, x_{min}, x_{max}) \tag{7}$$

Eliminating Λ between these two expressions produces a relation of the form

$$P = \alpha \, Q^{\beta} \tag{8}$$

where

$$\beta = \frac{p+\mu+1}{q+\mu+1} \tag{9}$$

and

$$\alpha = \left(\frac{a_P \Gamma(p+\mu+1) N_0^{1-\beta}}{[a_Q \Gamma(q+\mu+1)]^{\beta}} \right) f(P,Q) \tag{10}$$

where $\Gamma(x)$ is the complete gamma function and $f(P,Q)$ is has the form

$$f(P,Q) = \frac{\dfrac{g(p+\mu+1, x_{min}, x_{max})}{\Gamma(p+\mu+1)}}{\left[\dfrac{g(q+\mu+1, x_{min}, x_{\max})}{\Gamma(q+\mu+1)}\right]^{\beta}} \tag{11}$$

The behavior of $f(P,Q)$ as a function of D_{max}/D_0 and D_{min}/D_0 is shown in Fig.3 and for the combination of $(p,q) = (6, 3.67)$, corresponding to the combination of integral parameters $(P,Q) = (Z,R)$, where Z is the reflectivity factor and R is the rainfall rate. The behavior of $f(P,Q)$ for the combination $(p,q) = (2, 3.67)$ [corresponding to the combination of integral parameters $(P,Q) = (\Sigma, R)$, where Σ is the optical extinction] is shown in Fig. 4. Each of these figures was determined for $\mu = 0$ but very similar dependence is found for these factors for other values of μ. In addition, $f(P,Q)$ in each figure has been normalized to its value for $x_{min} = 0$ and $x_{max} = \infty$.

The important features of these results are that the effects of truncation of the DSD are contained entirely in the factor $f(P,Q)$. In other words, the only effect of DSD trun-

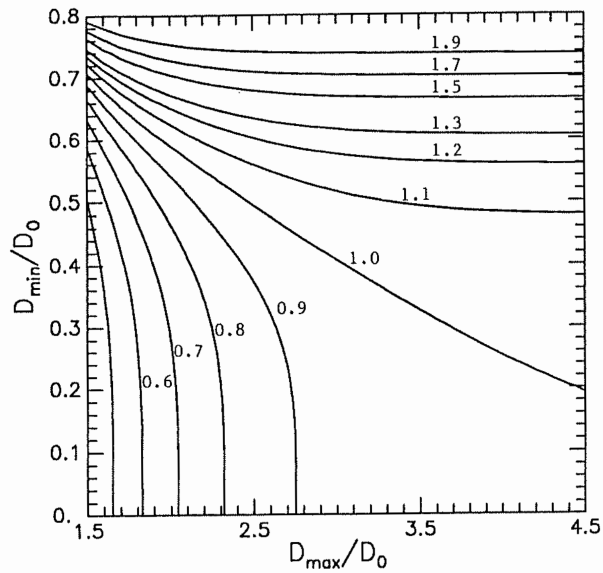

Fig. 3: Contours of the factor $f(Z,R)$ in empirical relations between Z and R of the form $Z = \alpha R^{\beta}$ as a function of $D_{\min}/D_0$ and $D_{\max}/D_0$ for $\mu = 0$. Contours for other values of μ are very similar to those shown in this figure.

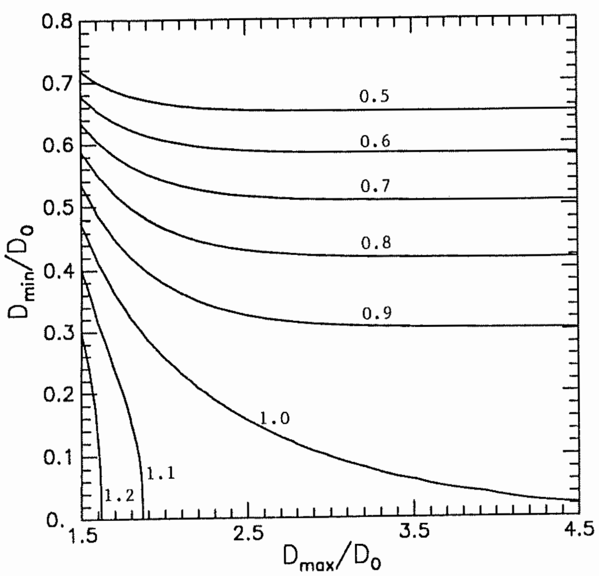

Fig. 4: Contours of the factor $f(\Sigma, R)$ in empirical relations between Σ and R of the form $\Sigma = \alpha R^{\beta}$ as a function of $D_{\min}/D_0$ and $D_{\max}/D_0$ for $\mu = 0$. Contours for other values of μ are very similar to those shown in this figure.

cation should be (within the assumptions adopted here) to change the coefficient α. Furthermore, the exponent β is not affected by truncation within the approximations adopted here.

To illustrate how these results would be used, a set of raindrop size spectra collected with a Joss disdrometer have been used to determine distributions of D_{min}/D_0 and D_{max}/D_0. This set of drop size spectra has been described by Atlas and Ulbrich (1977) and the distributions of D_{min}/D_0 and D_{max}/D_0 found for these data have been shown by Ulbrich (1992). For these distributions it was found that the average values of these quantities are $\overline{D_{min}/D_0} = 0.3$ and $\overline{D_{max}/D_0} = 2.4$. In addition, empirical relations between several pairs of integral parameters were determined and the results are shown in Table 1 for the integral parameters Z, R, $\sum$, W (liquid water content), and A (microwave attenuation at X-band).

TABLE 1: Coefficients α and exponents β in empirical relations between pairs of integral parameters (P,Q). Also shown is the standard error in the logarithms of the fit δ, the factor $f(P,Q)$ corresponding to the values of $\overline{D_{min}/D_0} = 0.3$ and $\overline{D_{max}/D_0} = 2.4$, and α_1, the corrected value of α.

(P,Q)	α	$f(P,Q)$	α_1	β	δ
(Z,R)	3.61×10^2	0.84	4.30×10^2	1.43	0.017
(Σ,R)	1.79×10^{-1}	0.92	1.95×10^{-1}	.688	0.011
(Z,W)	3.21×10^4	0.84	3.82×10^4	1.61	0.025
(W,R)	6.24×10^{-2}	1.00	6.24×10^{-2}	.865	0.005
(A,R)	1.79×10^{-2}	1.00	1.79×10^{-2}	1.16	0.009
(A,Z)	1.02×10^{-4}	1.12	9.09×10^{-4}	.795	0.008

Using the average values of D_{min}/D_0 and D_{max}/D_0 for this data set and assuming that the correct value of μ for the data is $\mu = 0$, then the value of $f(P,Q)$ for each of these fits may be found from curves like those in Figs.3 and 4. These values are listed in Table 1 together with the corrected values of α [listed as α_1]. Clearly, for the data set considered in this illustration the most pronounced effects of truncation occur for those empirical relations involving the reflectivity factor Z. In fact these effects appear to be negligible for relations involving the pairs of integral parameters (W,R) and (A,R). This fact for the latter pair of parameters was originally pointed out by Atlas and Ulbrich (1977) and is, of course, due to the closeness of the exponents in the integrands defining these two quantities.

3. ANALYSIS: METHOD 2

Although the results found in the previous section indicate that the effects of truncation are important and especially so in the case of those empirical relations in which one of the parameters is Z, the analysis arrives at this conclusion by assuming that $\mu = 0$. This is equivalent to assuming that all spectra in the data set are exponential, or that the average value of μ for the data set vanishes. To explore whether this assumption is correct, the spectra in the data set used in this work were each used in a least squares fit of a gamma function of the form of Eq.(1). This process resulted in the distributions of $log_{10}N_0$, Λ and μ as shown in Fig.5. Also shown on these figures are the average values of each of the parameters. These results show that the average value of $\mu = 0.71$ for this data set is somewhat different from the value corresponding to exponential spectra ($\mu = 0$) used in the previous section. However, the difference is not sufficiently great that it would greatly effect the values of $f(P,Q)$ in Table 1.

It is apparent from Fig.5 that there must be significant deviations of the spectra from exponentiality from moment to moment within the rainfall event for which these data apply. To illustrate this fact, three consecutive experimental drop size spectra for this data set are shown in Fig.6. This example shows that the shape of the distribution can change considerably from one moment to the next in rainfall.

Thus, to account for the effects of truncation properly the value of μ should be determined for each experimental spectrum and then the correction applied to each integral parameter using Eq.(3). Such a method of making the correction for truncation has been applied to the experimental data considered here and the resultant parameters then used in empirical fits like those considered in the previous section. The resultant coefficients and exponents are

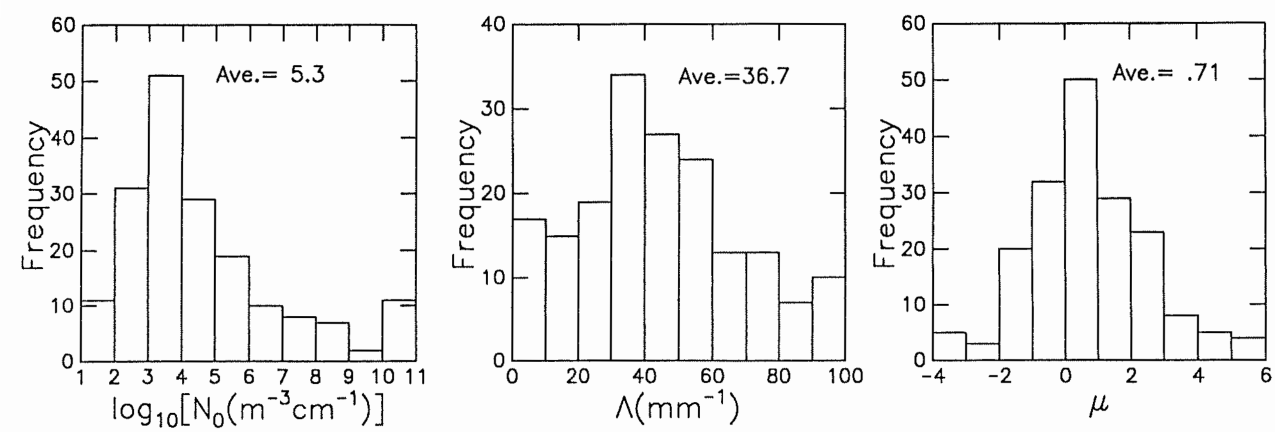

Fig. 5: Distributions of the values of the DSD parameters N_0, Λ and μ determined by fitting a gamma function to the experimental drop size spectra used in this work. Average values of each of these parameters are shown on the diagrams.

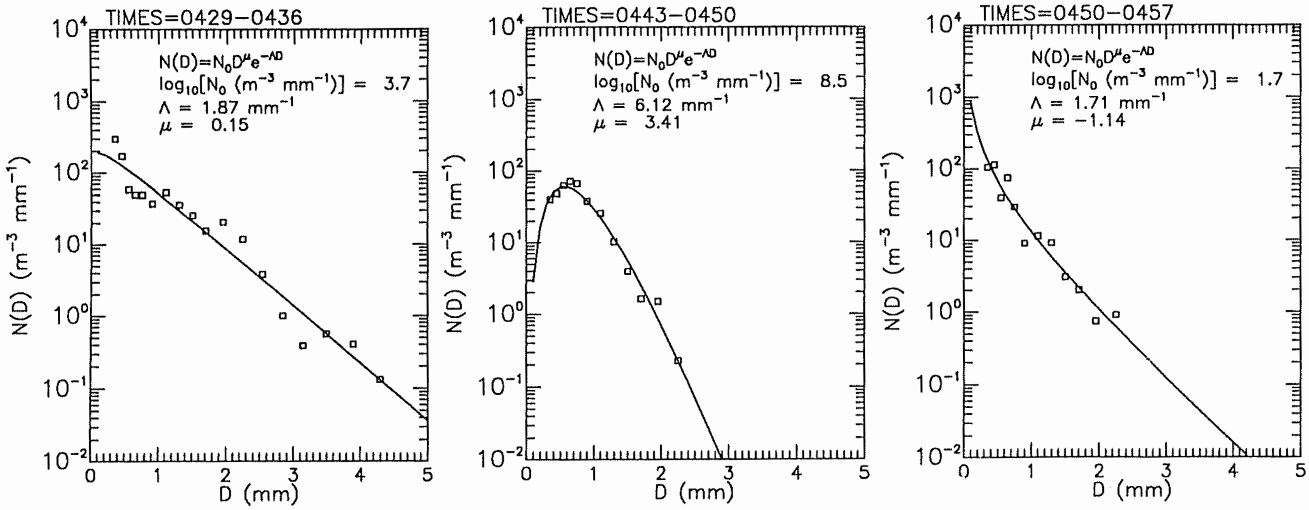

Fig.6: Examples of three consecutive drop size spectra in the data set used in this work. The experimental data are shown by the open squares and the least squares fit of a gamma function to the data is shown as the solid curve. These examples illustrate how the shape of the DSD (as defined by the value of μ) can change appreciably from moment to moment during a rainfall event.

shown in Table 2. [Values have not yet been determined for the combination (Σ, R)].

It is seen that the coefficients α' do not differ greatly from those in Table 2 found from Eq.(3) where it was assumed that $\mu = 0$ for every spectrum. The sole exception is the coefficient for the (Z, W) relation. The origins of this effect for this combination of parameters are not yet known. It is important to recognize from the results in Table 2 that the exponent β' can, in some of the cases considered, differ appreciably from the value β listed in Table 1. This is a reflection of the variation of the shape of the drop size distribution from moment to moment.

4. CONCLUSION

This work has demonstrated that all empirical relations between pairs of integral rainfall parameters derived from experimental drop size spectra must be corrected for instrumental and sampling truncation effects. The most accurate method of performing these corrections has been shown to be one in which the exponent μ in the gamma DSD is estimated for each experimental spectrum. In many cases it is probably adequate to estimate these effects by assuming a constant value for μ and applying the correction in the empirical relations to the coefficients only. However, in order to determine which value of μ is proper for the data set in question, it must be determined for each spectrum and the results then averaged. In view of this there is probably little additional effort required in applying the correction using the value of μ found for each spectrum.

5. ACKNOWLEDGMENT

This work was sponsored by grant ATM-9003448 from the National Science Foundation.

TABLE 2: Coefficients α' and exponents β' in empirical relations between pairs of integral parameters (P, Q). Also shown is the standard error in the logarithms of the fit δ. These results were determined by finding the value μ by least squares which applies to each spectrum and then using Eq.(3).

(P,Q)	α'	β'	δ
(Z,R)	4.33×10^2	1.50	0.024
(Z,W)	5.17×10^4	1.70	0.033
(W,R)	6.30×10^{-2}	0.865	0.0062
(A,R)	9.85×10^{-3}	1.19	0.0083
(A,Z)	1.16×10^{-4}	0.743	0.0155

6. REFERENCES

Atlas, D. and C. W. Ulbrich, 1977: Path- and area-integrated rainfall measurement by microwave attenuation in the 1 to 3 cm band. *J. Appl. Meteor.*, *16*, 1322-1331.

Ulbrich, C. W., 1983: Natural variations in the analytical form of the raindrop size distribution. *J. Climate Appl. Meteor.*, *22*, 1764-1775.

Ulbrich, C. W., 1985: The effects of drop size distribution truncation on rainfall integral parameters amd empirical relations. *J. Climate and Applied Meteor.*, *24*, 580-590.

Ulbrich, C. W., 1992: Effects of drop size distribution truncation on computer simulations of dual-measurement techniques. *J. Appl. Meteor.* (in press).

PARAMETERIZATION OF RAINDROP COALESCENCE, BREAKUP AND EVAPORATION

Philip S. Brown, Jr.

Trinity College
Hartford, CT 06106, USA

1. INTRODUCTION

The object of this research is to uncover the basic properties of the combined coalescence/breakup/evaporation equation and to use those properties as a basis for parameterizing drop spectrum evolution. In earlier work Brown (1991) developed a parameterization that took into account collisional processes only. The formulation was based on analytic solution of the linearized coalescence/breakup equation along with the assumption that the drop size distribution approaches a unique equilibrium form. (The uniqueness of the spectral equilibrium shape was established later by Brown and Whittlesey, 1992.) When the formulas of Low and List (1982a,b) are used to describe the coalescence efficiency and fragment distribution, the equilibrium drop size distribution is found to have trimodal form. The parameterization of Brown (1991) allows an arbitrary initial drop size distribution to approach the trimodal equilibrium distribution at a rate determined by the analytic solution of the linearized coalescence/breakup equation.

When evaporation is included in the model, the behavior of the evolving drop spectrum is somewhat more complicated. There is now a new, unique equilibrium, namely, the zero distribution that occurs when all the liquid water has evaporated. An evolving drop spectrum is drawn initially toward the coalescence/breakup equilibrium but then is attracted toward the zero distribution. As water mass is depleted from the system, the drop spectrum changes gradually in form. A parameterization technique has been designed to capture this behavior. The parameterization, based on thorough analysis of the coalescence/breakup/evaporation equation, provides accurate representation of the evolving drop spectrum without excessive computation.

2. THE COALESCENCE/BREAKUP/EVAPORATION PARAMETERIZATION

An approximate solution to the coalescence/breakup equation can be obtained by first partitioning the drop-size range into a small number of categories or bins. If $n_i(t)$ denotes the number density of drops in bin i at time t and n_{eqi} denotes the corresponding equilibrium level, the nonlinear collisional terms in the coalescence/breakup equation can be approximated by the linear terms in a Taylor series expansion about the equilibrium level provided $n_i(t)$ does not depart from n_{eqi} by an inordinate amount. If only four bins are used to resolve the drop spectrum, the solution of the linearized coalescence/breakup equation can be written as

$$n_i(t) = n_{eqi} + \sum_{j=1}^{3} c_j \exp(\mu_j t) \qquad , i=1,2,3. \qquad (1)$$

The fourth solution component n_4 can be found from the other three by applying the mass-conservation property of the system. The values for the decay rates $\mu_j(<0)$ and the procedures for calculating the coefficients c_j are given by Brown (1991). To enhance the features of this low-resolution solution, a high-resolution (34-bin) equilibrium form is computed once and for all by numerical solution of the coalescence/breakup equation. Simple parameterization formulas then allow an arbitrary initial drop distribution to approach the detailed (trimodal) equilibrium at a rate determined by the exponential damping in (1).

When evaporation is included in the model, the coalescence/breakup equilibrium is no longer a stationary solution but one that changes in amplitude and form as liquid water is depleted from the system. We denote this solution by $\tilde{n}_{eq}(m,t)$ where m represents drop mass. The shape of the distribution $\tilde{n}_{eq}(m,t)$ depends strongly on the liquid water content. Numerical solution of the coalescence/breakup/evaporation equation shows that arbitrary initial drop spectra tend toward the evolving form of $\tilde{n}_{eq}(m,t)$. This property of the system suggests that the coalescence/breakup parameterization might be extended to include evaporation by replacing the coalescence/breakup trimodal equilibrium $n_{eq}(m)$ with the non-stationary form $\tilde{n}_{eq}(m,t)$. Liquid water mass can be approximated by direct numerical solution of the evaporation equation using a large (60s) time step. The evaporation parameterization then can be based on two separate, but reasonably simple, calculations: one to estimate the liquid water mass of the drop spectrum, and another to estimate the shape of $\tilde{n}_{eq}(m,t)$ for the calculated water mass content. In estimating the shape of $\tilde{n}_{eq}(m,t)$, two distinct spectral forms that occur in the evolution of $\tilde{n}_{eq}$ are computed and stored for a case with prescribed initial liquid water mass and prescribed supersaturation. This case is taken as a standard. Intermediate forms of $\tilde{n}_{eq}$ for the standard case and for other cases are obtained by interpolation. (For example, if the supersaturation is one half that of the standard case, the rate of change in $\tilde{n}_{eq}$ is slowed by one half.)

3. EXAMPLE

To demonstrate the capabilities of the method outlined in Section 2., parameterized drop size distributions are compared with corresponding distributions obtained by detailed numerical solution of the coalescence/breakup/evaporation equation. The results are presented in Fig. 1 where the numerical solutions are shown in a) and the parameterized solutions in b). The initial distribution is taken to be a Marshall-Palmer spectrum, $n(D) = N_0 \exp(-\Lambda D)$, where D denotes drop diameter and where the constants have the values $N_0 = 8 \times 10^{-6} mm^{-4}$ and $\Lambda = 2.086\ mm^{-1}$. The corresponding initial rainfall rate is 25 mm hr^{-1}. The supersaturation S is assumed to maintain the fixed value of -0.1 throughout the simulation though the parameterization allows for variable S. It is seen from Fig. 1 that the parameterized solution closely resembles the numerical solution though some minor differences are detectable. For example, the small-drop peak in Fig. 1b is slightly higher than the corresponding peak in Fig. 1a, while to the left of the peak (for the smallest raindrop sizes), the parameterized drop concentration is somewhat low. Nevertheless, the overall parametric solution is quite accurate in light of the approximations used.

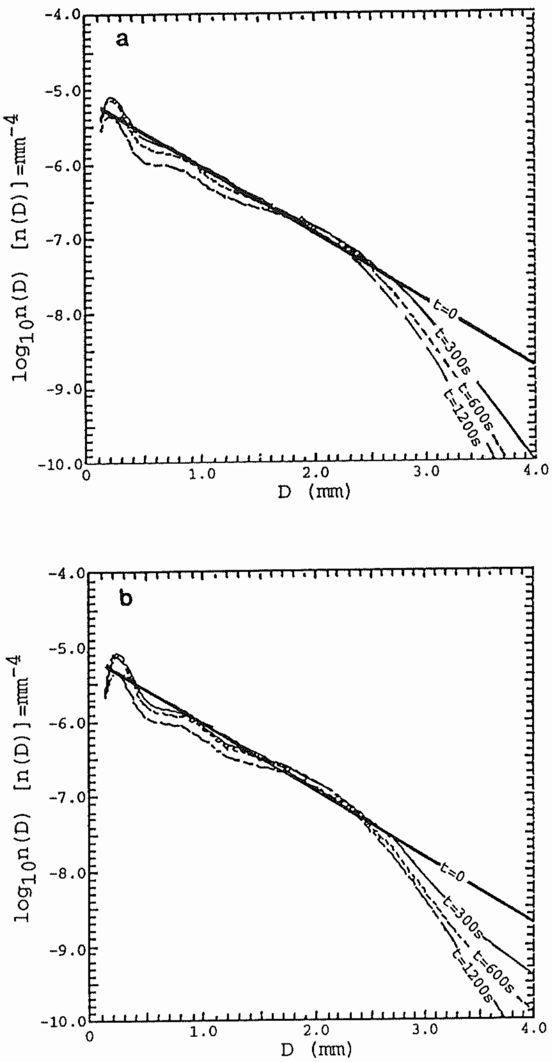

Fig. 1. Evolution of the drop size distribution due to coalescence, breakup and evaporation. Drop distributions are determined by a) high-resolution numerical solution of the governing equation and b) the parameterization procedure. Initial distribution in each case is a Marshall-Palmer distribution with rainfall rate of 25 mm hr^{-1}. Supersaturation has the value -0.1.

ACKNOWLEDGMENTS

This work was supported by the Division of Atmospheric Sciences, National Science Foundation, under Grant ATM-8921596.

REFERENCES

Brown, P.S., Jr., 1991: Parameterization of the evolving drop size distribution based on analytic solution of the linearized coalescence/breakup equation. *J. Atmos. Sci.*, **48**, 200-210.

____________ and S.N. Whittlesey, 1992: Multiple equilibrium solutions in Bleck-type models of drop coalescence and breakup. *J. Atmos. Sci.*, **49**, (Sept.).

Low, T.B. and R. List, 1982a: Collision, coalescence and breakup of raindrops. Part I: Experimentally established coalescence efficiencies and fragment size distributions in breakup. *J. Atmos. Sci.*, **39**, 1591-1606.

______ and ______, 1982b: Collision, coalescence and breakup of raindrops. Part II: Parameterization of fragment size distributions. *J. Atmos. Sci.*, **39**, 1607-1618.

IN-CLOUD SCAVENGING OF SUBMICRON PARTICLES BY WATER DROPS

István Geresdi
Nefela Association for Hail Supression
7614 Pécs Pf. 14 Hungary

1. INTRODUCTION

The scavenging mechanism has been researched by many scientists (eg. Young, 1973 and Baker, 1991), but less attention has been riveted on the size spectrum of the "contaminated" droplets. It must be an interresting problem if there is any difference between the size spectrum of "clear" drops and that of the drops which contain nucleus. Numerical experiments were made to investigate how the size spectrum of the "contaminated" droplets changes considering not only the Brownian capture and gravitational impaction of nuclei, but as well as the coagulation between the water droplets and the breakup of the larger drops.

2. DESCRIPTION OF THE MODEL

The calculation was made with fixed environmental parameters (pressure, temperature and supersaturation are 700mb, +4C and 0.2%, respectively). Only two of the numerous scavenging mechanisms were considered. Due to the small supersaturation the phoretical effects are rather less important than other mechanisms (Williams, 1977). The effect of turbulent flow and electrical interaction must be considerable and in the future they are intended to take into account. Brownian diffusion and gravitational coagulation are assumed to be additive. Coalesence efficiency was assumed to be unity, and collision efficiencies given by Beard and Grover (1974) were used to calculte the gravitational coagulation rate.
Method suggested by Kovetz and Olund (1969) was applied to calculate the coagulation of water droplets. The coalesence between the "clear" drops as well as between the "contaminated" drops was also considered. The drops formed after the coagulation between the "clear" and "contaminated" drops are considered "contaminated" drops. The coalesence efficiency for droplets was assumed to be unity, while the values for the collision efficiency of droplets were assumed to be the values given by Hall (1980). The drop breakup process was parametrized as a spontaneous breakup of droplets larger than a specific size. Smaller droplets forming due to the breakup of large drops are instantaneously redistributed according to the reference spectrum given by Hall (1980). The possibility that a droplet captures more than one nucleus is small, therefore the breakup of a large "contaminated" drop will results in only one smaller "contaminated" droplet and more "clear" droplets.

3. RESULTS

The numerical experiments were executed with different initial droplet concentration (200 and 500 $1/cm^3$) and nucleus radii (0.01, 0.1 and 1μm). At initial moment the water mixing ratio and nucleus concentration were the same in every experiment and their values were 3 g/m^3 and 10 1/l, respectively. The results are summarized in the Table 1.

The nuclei were collected by water drops most efficient when the nucleus radius was equal to 1μm. This is due to the gravitational collection, the Brownian diffusion did not play role in this case. The difference between the spectrum of "clear" and that of "contaminated" droplets was the most striking in this case. The Brownian capturte of smaller nuclei (0.01μm) was a little less efficient (Fig.1.). In this case the gravitational coagulation was negligible. Fewer nuclei were captured by droplets, but the concentrations of "contaminated" droplets were close to the value calculated in the case of nucleus radius of 1 μm. There is also no large difference between the "predominant radii". (Definition see in Berry and Reinhardt, 1974.). The fewest nuclei were captured by droplets when the nucleus radius was 0.1μm. These nuclei are too large to be influenced by Brownian diffusion, and the phoretic effects plays negligible role under the above mentioned conditions. The "predominant radius" of "clear" and that of "contaminated" droplets are hardly different comparing with the other cases.
It is also interesting that when the nucleus radius was 0.1 μm the intial droplet concentration hardly had influence on the number of "contaminated" drops and on the number of captured nuclei. In the other cases smaller "contaminated" droplet concentrations were calculated when the initial droplets concentration were smaller. If the nucleus radius was equal to 1μm and the initial droplet concentration was equal to 200 $1/cm^3$ more nuclei were captured than when the initial concentration was a larger value of 500 $1/cm^3$. The situation was oposite if the nucleus radius was 0.01 μm. This discrepancy is due to the difference in the dominating scavenging mechanisms.

4. DISCUSSION

The artificial nuclei (e.g. silver iodide particles) produced by generators using aceton solution of AgI are in the size range of order of 0.1 μm (Bleir et al. 1973) where the scavenging mechanism is the least efficient in the cloud. (The situation may be similar in the other AgI particles producing methods.) The efficiency could be increased by producing particles whose size is order of 0.01 μm or 1.0 μm. However in these cases the "contaminated" droplets are generaly larger than the "clear" ones. The difference in the terminal velocity results in increasing of the concentration of the "clear" droplets comparing to that of the "contaminated" droplets at higher levels in the negative temperature region. This difference in sedimentation decreases the efficiency of artificial nucleation.

Table 1.

	t=0.min.	t= 10. min.						
r_a [μm]	n_{cw} [1/l]	q_{cw}[g/m³]	n_{cw}[1/l]	r_g [μm]	q_{cwa}[g/m³]	n_{cwa}[1/l]	r_{ga}[μm]	n_a[1/l
0.01	$2\cdot10^5$	0.40	200.	893	2.60	0.30	1822	9.1
0.01	$5\cdot10^5$	0.78	$3.1\cdot10^4$	516	2.05	1.15	1332	7.1
0.1	$2\cdot10^5$	2.50	190.	1657	0.50	0.05	2042	9.9
0.1	$5\cdot10^5$	2.55	$2.8\cdot10^4$	1204	0.32	0.06	1641	9.9
1.0	$2\cdot10^5$	0.10	200.	636	2.90	0.49	1774	2.9
1.0	$5\cdot10^5$	0.58	3.0 10^4	421	2.30	1.06	1322	5.9

The following parameters are given in the Table: r_a is the radius of the aerosol particles. n_{cw} ,q_{cw} and r_g are the concentration, the mixing ratio and the predominant radius of of "clear" droplets, respectively. n_{cwa} ,q_{cwa} and r_{ga} denote the same parameters for the "contaminated" droplets. n_a is the nucleus concentration in the 10th min..

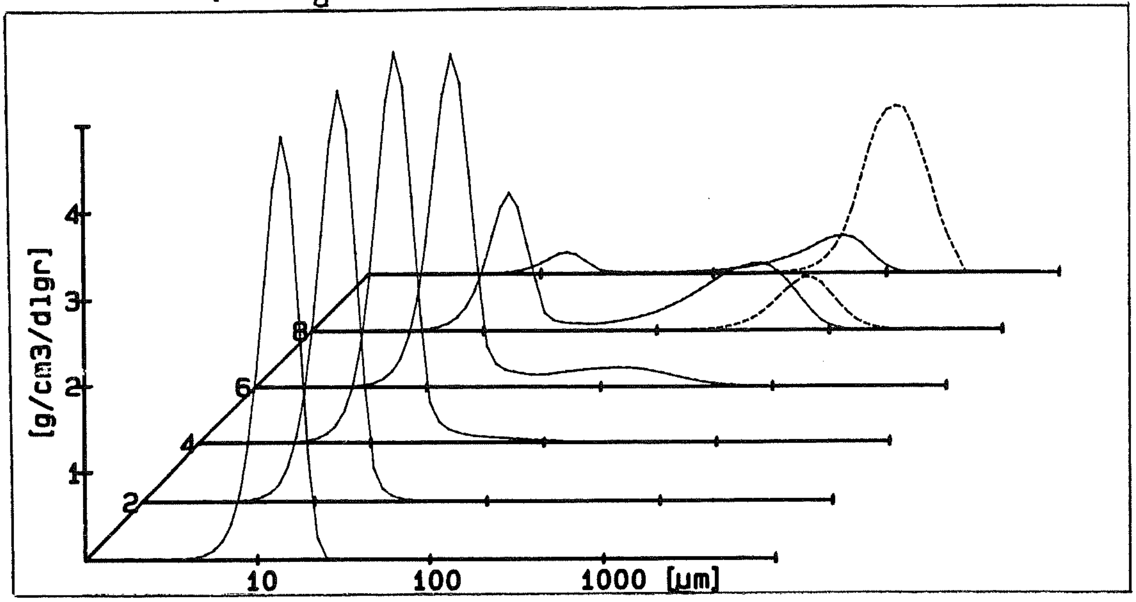

Fig. 1.Time evolution of droplet spectrums. Solid lines denote the spectrum of "clear" droplets and dashed lines denote the that of "contaminated" droplets. The time is given in minutes. The initial concentration and mixing ratio are 500 1/cm³ and 3 g/m³ , respectively. The initial spectrum is characterized by mean radius of 11 μm and relative dispersion of 1. The nucleus radius is 0.01 μm and the initial nucleus concentration is 10 1/l.

5. REFERENCES

Baker,B.A, 1991:On the role of phoresis in cloud ice initiation. J. Atmos. Sci., 48, 1545-1548

Beard. K.V. and Grover, S.N, 1974:Numerical collision efficiensies for small raindrops colliding with micron size particles. J. Atmos. Sci. , 31, 543-550

Berry, E.X. and Reinhardt, R.L.,1974:An analysis of cloud drop growth by collection: Part. I. Double distribution. J. Atmos. Sci., 31, 1814-1824

Blair, D.N., Davis, B.L. and Dennis, A.S.,1973: Cloud chamber tests of generators using aceton solutions of AgI-NaI, AgI-KI and AgI-NH_4I J. Appl. Meteor., 12, 1012-1017

Hall, W.D, 1980: A detailed microphysical model within a two-dimensional dynamic framework: model description and preliminary results. J. Atmos. Sci., 37, 2486-2507

Kovetz, A. and Olund, B, 1969: The effect of coalesence and condensation on rain formation in a cloud of finite vertical extent. J. Atmos. Sci., 26, 1060-1065

Williams, A.L.,1977:Analysis of in cloud scavenging efficiencies. Precipitation Scavenging, ERDA Symp.Ser.,842pp.

Young, K.C, 1973: The role of contact nucleation in ice phase initiation in clouds. J. Atmos. Sci., 31, 768-776

ON THE EVAPORATION OF PRECIPITATION FALLING THROUGH LAYERS OF SUBSATURATED AIR

G. Ragette and G. Wotawa

Zentralanstalt für Meteorologie und Geodynamik, 1190 Vienna, Austria

1. INTRODUCTION

In numerical weather prediction the evaporation of precipitation is usually modelled according to Kessler (1969). Although his formulation was derived for rain it is frequently used for snow, too. This, however, does not seem to be justified. For this reason separate formulations of the evaporation of rain and snow have been derived.

2. DIFFUSIONAL EVAPORATION OF A SINGLE PARTICLE

Assuming isotropy and stationarity and applying appropriate initial and boundary conditions the diffusion equation yields the rate of change of mass m of a motionless particle in the form

$$dm/dt = 4\pi\, C.D\,(\rho - \rho_s) \qquad (1).$$

C depends on the geometry of the particle (for a rain drop C equals the radius r), D is the molecular diffusion coefficient for water vapor, ρ the ambient water vapor density and ρ_s the water vapor density at the particle's surface. Assuming that ρ_s equals the saturation vapor density and eliminating the temperature of the particle equation 1 may be rewritten as

$$\frac{dm}{dt} = \frac{4\pi\, C\,(e/e_s - 1)}{R_v T/(e_s.D) + (L/(R_v.T)-1)L/(kT)} \qquad (2)$$

where R_v is the individual gas constant for water vapor and k the coefficient of thermal conductivity of air. The other parameters have their usual meaning.

3. EVAPORATION OF RAIN

Equation 2 holds for a motionless particle. In order to account for a rain drop's fall speed (2) is multiplied by a ventilation factor f according to Pruppacher and Klett (1978). Using a Marshall-Palmer distribution (1948) of the form $N(r) = N_0.e^{-\lambda r}$ with N_0 and λ as given functions of the rain rate R (Sekhon and Srivastava, 1971), we arrive at the rate of change of mass of water substance contained in the unit volume of air by multiplying (2) with N(r) and integrating over the whole range of particle sizes:

$$dM/dt = \int_0^\infty dm/dt.f.N.dr \qquad (3).$$

The precipitation rate R may then be obtained by integrating dR/dz = dM/dt.

4. EVAPORATION OF SNOW

We assume that snow consists of ice crystals in the form of thin plates with a constant dimensional relationship between thickness and diameter d (Davis, 1974). In this case $C = d/\pi$. For the size distribution of snow flakes the formulation given by Sekhon and Srivastava (1970) was adopted. Like for rain drops the ventilation factor for snow flakes was also taken from Pruppacher and Klett (1978). In equation 3 the radius r then means the equivalent radius of the water drop to which the ice crystal melts.

5. CALCULATIONS AND RESULTS

First we examine the various terms which constitute the integrand in (3). For small precipitation rates the size distributions of rain drops and snow flakes are very similar. For a rate of 0.5 mm/h the number density of rain drops becomes negligible near a radius of 1.2 mm, for snow flakes near an equivalent radius of 1.5 mm. For higher rates the number of rain drops bigger than 1 mm remains small as rain drops of a few mm are unstable and break up. Therefore it suffices for rain to integrate (3) from 0 to 1 cm. For increasing precipitation rates the number of small rain drops increases, whereas the number of small snow flakes diminishes. The number of big snow flakes, however, grows. For large snowfall rates the integration in (3) has therefore to be extended beyond 1 cm.

The ventilation factor for rain drops shows a maximum near 1 mm, for snow flakes the maximum occurs near an equivalent radius of 5 mm, whereby the maximum for snow exceeds the maximum ventilation for rain by a factor of 4. Thus the ventilation effect is much more important for snow than for rain.

The change of mass of a motionless rain drop resembles that of an ice crystal. For a radius of about 0.1 mm both rates coincide. For smaller radii the evaporation of rain drops is bigger, for larger particles smaller than for ice crystals.

Combining all factors in (3) we find that for a given precipitation rate the evaporation of small rain drops exceeds that of small snow flakes. For small rates the evaporation of snow and rain coincides at radii of 0.01 to 0.04 mm, for heavy precipitation near 0.1 mm. For larger particles the evaporation of snow exceeds that for rain.

6. REFERENCES

DAVIS, C.I., 1974, Ph.D.Thesis, Univ.of Wyoming.

KESSLER, E., 1969, Met.Mon.10, 32.

MARSHALL, J.S. and W.M.PALMER, 1948, J.Met.5, 165-166.

PRUPPACHER, H.R. and J.D.KLETT, 1978, Microphysics of Clouds and Precipitation.

SEKHON, R.S. and R.C.SRIVASTAVA, 1970, J.Atm. Sci.27, 299-307.

SEKHON, R.S. and R.C.SRIVASTAVA, 1971, J.Atm. Sci.28, 983-994.

Improved General Theory for the Collision Efficiencies of Riming and Aerosol Impaction

Johannes P. Böhm
Swiss Federal Institute for Forest, Snow, and Landscape Research
CH-8903 Birmensdorf
Switzerland

1. Introduction

The shape of solid hydrometeors is very complex and it (quasi-)continuously varies from ice crystals to aggregates, graupel, and hail. In order to handle this wide variety of shapes the author recently presented a general theory for the hydrodynamics of precipitation particles (Böhm 1990, 1992a-c). The collision efficiencies agree well with results from the literature for drop coalescence and the riming of plates. For the impaction of small particles with radii $< 5\ \mu$m and for the riming of columns however, it differs quite markedly from the previous results. This theory is limited to hydrodynamical interactions within the boundary layers of the colliding particles. The effects of the surrounding non-frictional flow are neglected.

In the present contribution an analytical solution from potential flow theory is presented, that takes into account the effects of the surroundig non-frictional flow. It is shown that a combination of the new theory with the previous boundary layer approach leads to a fair agreement in all cases that are relevant to the microphysics of clouds and precipitation, i.e. for the riming of columns and for the capture of small particles down to a critical size at which the collision efficiency sharply drops to zero.

2. Theory

According to the Prandtl's well known theory the frictional effects in the flow about a body at high Reynolds number is effective only within the boundary layer and can be neglected in the surrounding flow. Near the stagnation point the velocity distribution

$$U = \frac{bx}{j}, \qquad V = -by \qquad \text{where } b = \frac{3\Delta V}{r_1 + \delta_{1,I}}. \quad (1)$$

Here x and y are distance measured parallel and perpendicular to the surface respectively, ΔV is the flow speed at infinity, r_1 the radius of the obstacle (henceforth particle 1), and $j = 1$ for two-dimensional and $j = 2$ for axisymmetrical flow. The potential flow field about particle 1 is defined by the collector particle including its boundary layer. Similar to the previous theory of particle collisions (Böhm 1990, 1992b,c) the present results are extrapolated to low Reynolds numbers, where the current theory in principle is not valid. The results presented in what follows show that in the present case the best guess for the boundary layer at low Reynolds numbers ($N_{\mathrm{Re}} \lesssim 1$) is a definition based on the inertial drag, i.e.

$$\delta_{I,1} = \frac{r_1}{2}\left(\frac{C_{DI,1}}{C_{DP,1}} - 1\right) \quad (2)$$

where $C_{DP,1}$ and $C_{DI,1}$ are defined e.g. by Böhm (1992a, his eqs. 7 and 25 respectively).

It is readily seen that $V \to \infty$ for $y \to \infty$. Hence the velocity distribution according to (1) is valid at $0 \le y \le y_0 = \Delta V/b$ where the y-component reaches $V = -\Delta V$, and

$$V = -\Delta V \qquad \text{at } y \ge y_0 = \frac{\Delta V}{b} = \frac{r_1 + \delta_{I,1}}{3}. \quad (3)$$

In the flow about the particle 1 a particle 2 shall be immersed with radius $r_2 \ll r_1$ and Reynolds number $N_{\mathrm{Re}} < 1$ at the flow speed ΔV (e.g. $r_2 \le 5\ \mu$m if $\Delta V = 1\ \mathrm{m\,s^{-1}}$, standard conditions). It follows

$$c_x \ddot{x} = -\dot{x} + \frac{b}{j}x, \qquad c_y \ddot{y} = -\dot{y} - by \quad (4)$$

where $$c_i = \frac{m_2}{6k_{2,i}\pi r_2 \eta_a}, \qquad i = x, y. \quad (5)$$

Here m_2 denotes the mass of particle 2 and η_a the viscosity of air. The shape factor $k_{2,y}$ of particle 2 in the direction of y corresponds to the shape factor k as defined by Böhm (1992a, his eqs. 11–14, flow parallel to the axis of symmetry) while the corresopnding $k_{2,x}$ is defined perpendicular to the axis of particle 2 if it is a plate (axial ratio $\alpha < 1$) and as a superposition of the two shape factors parallel and perpendicular to the axis if it is a column ($\alpha > 1$). The analytical solutions for these factors are found in Happel and Brenner (1965). They can be approximated to within $\pm 1\%$ error by

$$k_{2,x}(\alpha{<}1) \approx 0.57 + 0.43\alpha, \qquad k_{2,x}(\alpha{>}1) \approx k^{1.15}. \quad (6)$$

For spheres all shape factors are unity. The couple of partial differential equations (4) can be integrated by the aid of substitutions of the type $s = \dot{x}/x$ and subsequent separation of variables:

$$x(t) = x_0 \left(\cosh \Delta_x t + \frac{1}{\Delta_x} \sinh \Delta_x t\right) e^{-t} \qquad (7)$$

$$y(t) = y_0 \left(\cos \Delta_y t + \frac{1-2bc}{\Delta_y} \sin \Delta_y t\right) e^{-t} \qquad (8)$$

where

$$\Delta_x = (4bc/j+1)^{1/2} \qquad (9)$$

$$\Delta_y = (4bc-1)^{1/2}. \qquad (10)$$

The initial value y_0 is defined in (3) and x_0 denotes the inital horizontal offset. Inversion of (8) leads to the time t_δ at which the collision occurs (condition: $y = 0$)

$$t_\delta = \frac{1}{\Delta_y} \arctan \frac{\Delta_y}{2bc-1} \quad \text{for} \quad 2bc>1$$

$$= \frac{1}{\Delta_y}\left(\pi - \arctan \frac{\Delta_y}{1-2bc}\right) \text{ for } \frac{1}{2}<2bc<1. \quad (11)$$

From x_0 and $x(t_\delta)$ it immediately follows the collision efficiency

$$E_p = \left(\frac{x_0}{x(t_\delta)}\right)^{2/j}. \qquad (12)$$

The location, $x(t_\delta)$ corresponds to the location at which the particle 2 enters the boundary layer of particle 1. Hence the total collision efficiency, including the previous theory, is defined by

$$E = E_p E_\delta \qquad (13)$$

where E_δ is defined by Böhm (1992b, his eq. 14). It should be noted that $2bc = 1$ defines a limit for r_2, below which no collision occurs and that E_p rapidly approaches unity for radii above this limit, i.e. for $2bc > 1$. This is exactly the behavior that is expected in view of the deviations found by (Böhm 1990, 1992a-c).

3. Results and discussion

a. *Raindrops*

Figure 1 depicts a comparison of (13) with measured coalescence efficiencies from various authors. Most of the data agree with the present theory within the error limits from the experiments. The collision efficiency according to (13) rapidly drops to zero at a critical radius $1 \lesssim r_2 \lesssim 4\,\mu$m which varies with r_1.

Similarly Fig. 2 depicts a comparison with numerical results on aerosol impaction from Grover (1978). The agreement of the two theories regarding the critical radius r_2 is good. However, the numerical results do not drop to zero but to $E = o(10^{-4})$. Fortunately these low values are not highly significant. Under below cloud conditions, where aerosol impaction is most important, the vapor pressure typically is considerably below saturation and hence phoretic effects dominate the so called Greenfield gap ($r_2 \approx 0.1$–$1\,\mu$m).

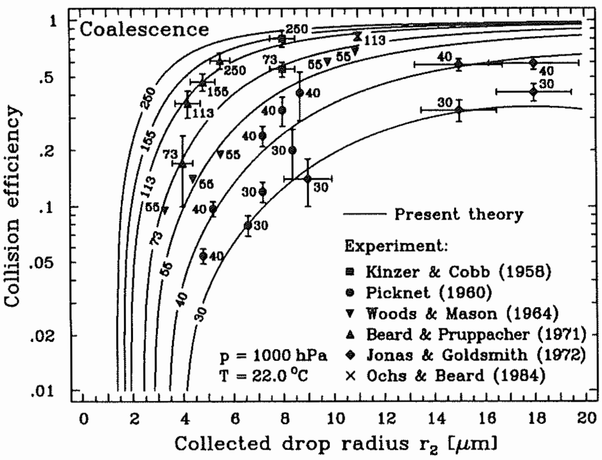

FIGURE 1: Present theoretical collision efficiencies for coalescence compared to measurements. The labels in the figure refer to the radius r_1[μm] of the collector drop.

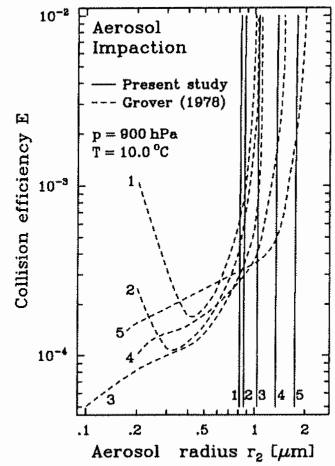

FIGURE 2: Present theoretical collision efficiencies for aerosol impaction compared to numerical results.

b. *Riming*

Figure 3 depicts a comparison of the present theory with numerical results from Schlamp *et al.* (1975/77). The curves for the longest column with axial ratio $\alpha = 8.3$ are nearly undistinguishable. For the shorter columns with $\alpha \leq 5$ however, the present theory predicts somewhat greater riming efficienies, especially for the smallest two columns with $\alpha = 1.4$. Schlamp *et al.* (1975/77) used the flow fields of infinitly long cylinders. Applying the same assumption to the present combined theory reduces the results by up to about 25% ($\alpha = 1.4$) and removes much of the deviations. Because E_p according to (12) is near unity at similar fall speeds, the present theory is supported by the agreement with experiments on the onset of riming presented by Böhm (1992c). Hence the present combined theory probably is more accurate than the numerical study.

The comparison in Fig. 4 with measurements on freely falling disks from Kajikawa (1974) shows that his data mostly remain within the bounds defined by the results from the present study. Only at $\Psi^{1/2} \lesssim 0.25$ ($r_2 \lesssim 7\,\mu$m), the present theory predicts zero efficien-

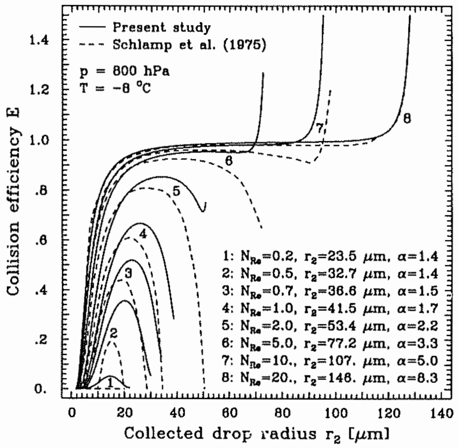

FIGURE 3: Collision efficiency for the riming of columns. Present theory compared to numerical results from Schlamp *et al.* (1975/77).

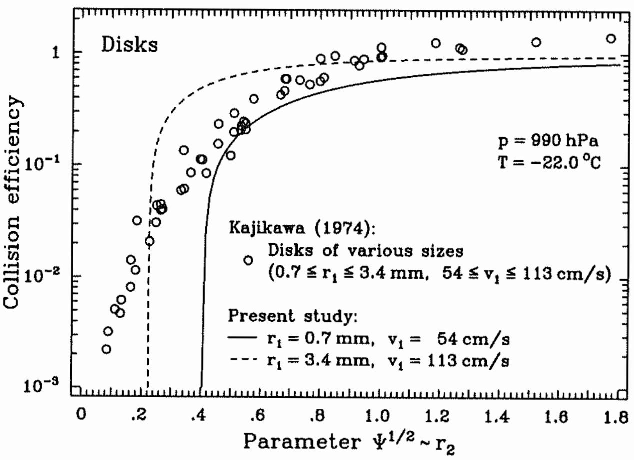

FIGURE 4: Collision efficiency for the riming of disks. Present theory compared to experimental results from Kajikawa (1974). Droplet radius: $2.5 \leq r_2 \leq 17.5\,\mu$m.

cies, in contrast to the experiment. Near the collecting ice disks the vapor pressure is at saturation with respect to a plane ice surface. At $T = -22$°C the collected droplets experience a subsaturation of about 20%. Small cloud droplets therefore are expected to evaporate considerably just before the collision. The collected *mass* is unaffected because the vapor is deposited on the disk. Kajikawa (1974) however, measured the *diameter* of the frozen droplets, which is expected to be shifted to smaller sizes. This explains the deviations found in Fig. 4.

Prodi *et al.* (1981) collected oil droplets and pollen on branched, planar models in order to simulate the riming of ice crystals. Figure 5 depicts a comparison of (13) with their results. The agreement is quite good except for the dendritic model at low Stokes number where the present theory appears to underestimate the collision efficiency. However, the efficiencies are quite sensitive to the particle radius (see also the comment to Fig. 6 below).

Figure 6 depicts experiments on porous disks carried

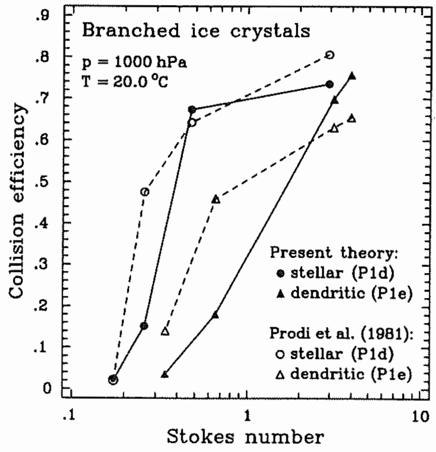

FIGURE 5: Collision efficiency for the riming of models of branched crystals. Present theory compared to experimental results from Prodi *et al.* (1981). Radii: $r_1 \approx 1.6$ mm, $2 \leq r_2 \leq 22\,\mu$m.

out by Lew *et al.* (1986). The agreement between theory and experiment ranges from fair to good, except for disk no. 1. However, the collision efficiency for small cloud droplets are quite sensitive to the radius r_2. The cloud droplet spectra documented by Lew *et al.* (1986, their fig. 1) reveal that their spectra were not nearly monodisperse, the mean radius r_2 varying with the flow speed withing about $4\,\mu$m–$5\,\mu$m. If $r_2 = 4.5$ mm is used the agreement for disk 1 is as good as for the other models.

c. *Aggregation*

Some results from Keith and Saunders (1989) are shown in Fig. 7 along with the present theoretical collision efficiencies. In order to apply the boundary layer theory from Böhm (1990/92b) to infinitly long cylinders it must be modified: The intersection of the two cross sectional areas $A^* = r_2^2 \pi\, r_1/(r_1 + r_2)$. The axial ratio of the aggregated plates were calculated according to Auer and Veal (1970). The variation of the collision efficiency with flow speed appears to be somewhat less according to the present theory but the agreement between the theory and the measurements again is fair.

REFERENCES

Auer, Jr., H. A. and D. L. Veal, 1970: The dimensions of ice crystals in natural clouds. *J. Atmos. Sci.*, **27**, 919–926.

Beard, K. V. and H. R. Pruppacher, 1971: A wind tunnel investigation of collection kernels for small water drops in the air. *Quart. J. Roy. Meteor. Soc.*, **97**, 242–248.

Böhm, J. P., 1990: *On the Hydrodynamics of Cloud and Precipitation Particles.* PhD thesis, Swiss Federal Institute of Technology, Zürich, Switzerland.

——, 1992a: A parameterization for spectral mixed-phase microphysical models. Part I: Drag and fall speed of hydrometeors. *Atmos. Res.*, **27**, 253–274.

——, 1992b: A parameterization for spectral mixed-phase microphysical models. Part II: Collision kernels for coalescence. *Atmos. Res.*, **27**, 275–290.

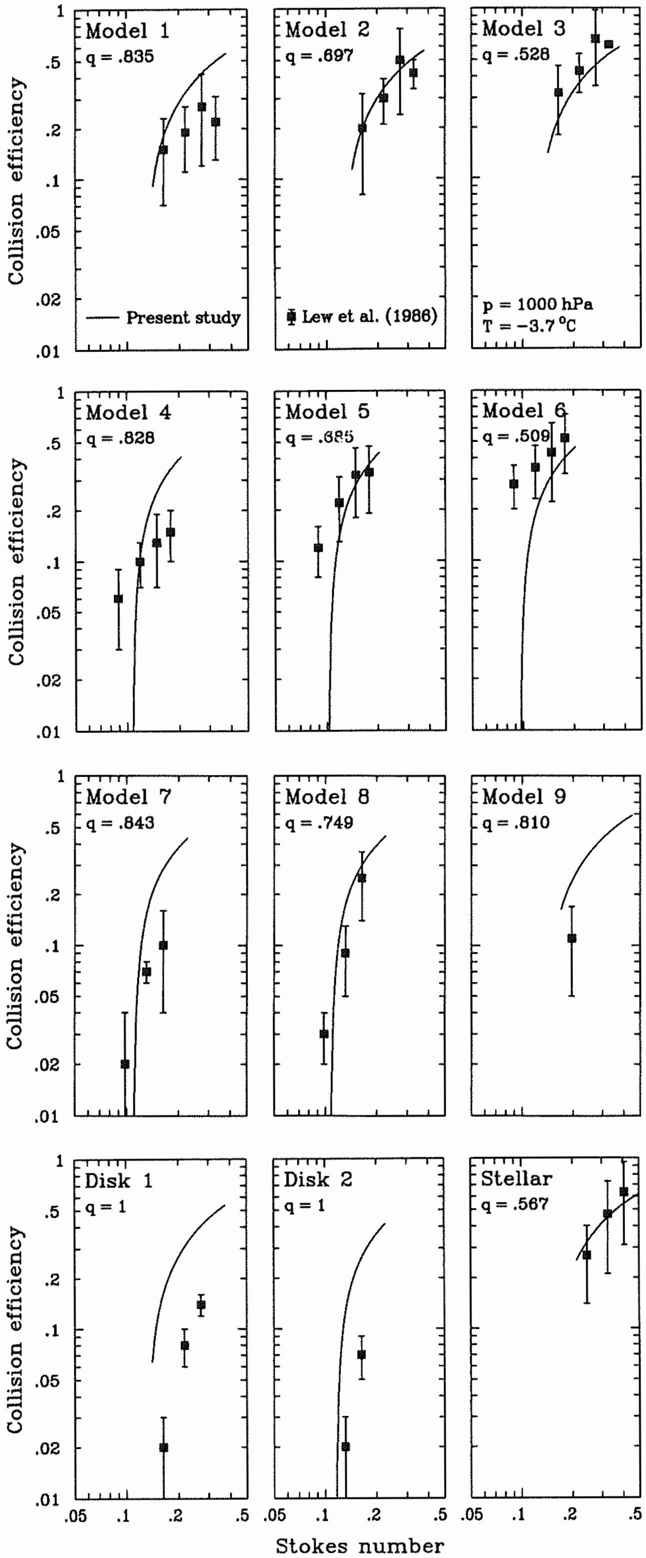

FIGURE 6: Collision efficiency for the riming of porous disks. Present theory compared to experimental results from Lew *et al.* (1986, q denotes the ratio of the actual cross sectional area to the area of the circumscribed circle). Model 1–3: $r_1 = 3$ mm, 4 holes; 4–6: 5.5 mm, 14 holes; 7–8: 5 mm, 21 holes; 9: 2.5 mm, 17 holes. Disk 1: $r_1 = 3$ mm; 2: 5 mm. Stellar: $r_1 = 2$ mm.

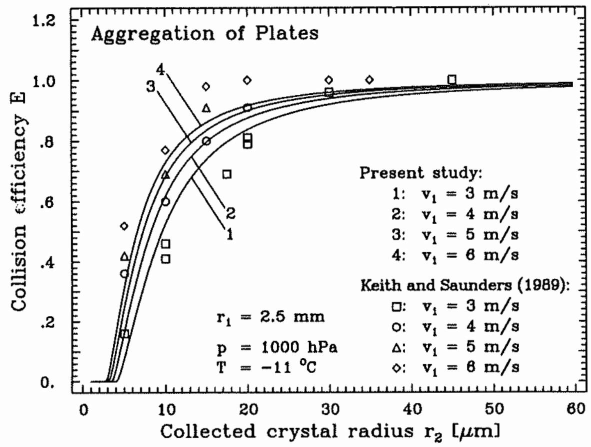

FIGURE 7: Collision efficiency for the aggregation of plates on a cylinder. Present theory compared to experimental results from Keith and Saunders (1989).

——, 1992c: A parameterization for spectral mixed-phase microphysical models. Part III: Riming and aggregation. *Atmos. Res.*, **27**, (in press).

Grover, S. N., 1978: *PhD Thesis.* Dept. of Atmos. Sci., University of California, Los Angeles, California.

Happel, J. and H. Brenner, 1965: *Low Reynolds Number Hydrodynamics.* Prentice-Hall, 553 pp.

Jonas, P. R., 1972: The collision efficiency of small drops. *Quart. J. Roy. Meteor. Soc.*, **98**, 681–683.

Kajikawa, M., 1974: On the collection efficiency of snow crystals for cloud droplets. *J. Meteor. Soc. Japan*, **52**, 328–335.

Keith, W. D. and C. P. R. Saunders, 1989: The collection efficiency of a cylindrical target for ice crystals. *Atmos. Res.*, **23**, 83–95.

Kinzer, G. D. and W. E. Cobb, 1958: Laboratory measurements and analysis of the growth and collection efficiency of cloud droplets. *J. Meteor.*, **15**, 138–148.

Lew, J. K., D. C. Montague, H. R. Pruppacher, and R. M. Rasmussen, 1986a: A wind tunnel investigation on the riming of snowflakes. Part I: Porous disks and large stellars. *J. Atmos. Sci.*, **43**, 2392–2409.

Ochs, H. T. and K. V. Beard, 1984: Laboratory measurements of collection efficiencies for accretion. *J. Atmos. Sci.*, **41**, 863–867.

Picknett, R. G., 1960: Collection efficiencies for water drops in air. *Int. J. Air Pollution*, **3**, 160–167.

Prodi, F., M. Caporaloni, G. Santachiara, and F. Tampieri, 1981: Inertial capture of particles by obstacles in form of disks and stellar crystals. *Quart. J. Roy. Meteor. Soc.*, **107**, 699–710.

Schlamp, R. J. and H. R. Pruppacher, 1977: On the hydrodynamic behavior of supercooled water drops interacting with columnar ice crystals. *Pure and Appl. Geophys.*, **115**, 805–843.

——, ——, and A. E. Hamielec, 1975: A numerical investigation of the efficiency with which simple columnar ice crystals collide with supercooled water drops. *J. Atmos. Sci.*, **32**, 2330–2337.

Woods, J. D. and B. J. Mason, 1964: Experimental determination of collection efficiencies for small water droplets in air. *Quart. J. Roy. Meteor. Soc.*, **90**, 373–381.

THE EFFECTS OF PRESSURE ON EQUILIBRIUM RAINDROP SIZE DISTRIBUTIONS

R. Nissen and R. List

Department of Physics, University of Toronto, Toronto, Ontario, Canada M5S 1A7

1. INTRODUCTION

Information on raindrop size distribution is required to correctly infer rainfall rates from radar reflectivity data. In the warm rain process complications due to ice particles are absent, and the main processes affecting rain spectra are drop collision and coalescence or breakup. Laboratory experiments by McTaggart-Cowan and List (1975 a and b, hereafter ML) and Low and List (1982, hereafter LL) have been performed with colliding drops falling vertically at terminal velocity. LL then parameterized the data into a set of equations, which in turn can be employed in both box and shaft models for the study of spectral evolution.

Several theoretical investigations were carried out by Valdez and Young (1985), List et al (1987), Brown (1988), and List and McFarquhar (1990, hereafter LMc) that employ laboratory data (ML and LL) taken at surface pressures (100 kPa). However in the real atmosphere, drop collisions do normally occur at lower pressures. Laboratory experiments at 50 kPa (Fung 1984, hereafter Fung), using an apparatus similar to the 100 kPa setup of ML and LL, provided new data which require a different parameterization. In this study a box model is run to determine equilibrium drop size distributions at 50 kPa. The occurrence of the different drop breakups is also given. As in the previously mentioned studies, evaporation and electrical effects are neglected for simplification.

2. NUMERICAL CONSIDERATIONS

For both pressure levels the box models have 40 logarithmically spaced bins from diameter 0.056 mm to 5.1 mm, with mass doubling every second bin. Mass conservation is applied to the calculations. After a filament breakup, Gaussians describe the size distribution about the original large and small drop diameters. With the sheet breakup the identity of the small drop is lost, although the large drop fragment can still be recognized. The most violent breakup mode, the disk, yields a large fragment which may have a diameter quite different from the original large drop. Large fragments in both sheet and disk breakups are described by Gaussians. In all three breakup modes the smallest fragments are represented by a lognormal distribution. Ultimately all equations can be written as a function of the larger and smaller drop diameters, although some terms are arrived at by iteration.

The original 100 kPa parameterization of LL featured Gaussians with sufficiently large standard deviations as to be well integrated by the Simpson's Rule approximation. Before arriving at equations for 50 kPa, Fung reparameterized the 100 kPa data on the assumption that the original drop pair was accurately known and that the large fragment could be accurately calculated using mass conservation (combined masses of the two original drops less the resultant smaller fragment masses). This gives very narrow Gaussians for the (single) large fragments. Figure 2.1 indicates the problems this shape causes when using the Simpson's Rule integration. Thus a scheme involving differences in the error function was devised.

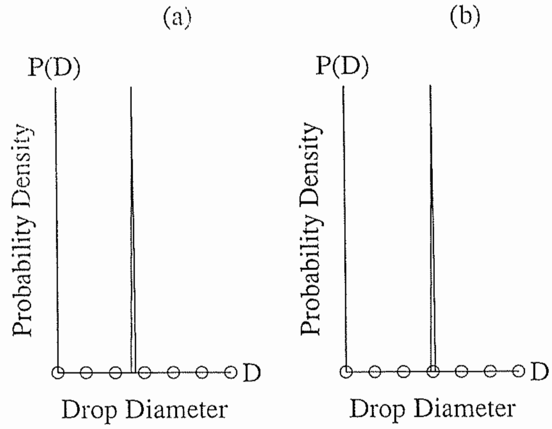

Figure 2.1 - Schematic illustration of the numerical difficulties in using Simpson's Rule with very narrow Gaussian probability distributions. The dots indicate the diameters sampled by Simpson's Rule. In (a), virtually all of the Gaussian is missed as the nearest Simpson's Rule point is many standard deviations away from the peak diameter. In more rare cases (b), the peak diameter coincides with a Simpson's Rule point, however because of the extremely high probability density of the Gaussian at this diameter the mass is highly over-estimated by Simpson's Rule.

The error function for any variable x is described by:

$$erf(z) = \frac{2}{\sqrt{\pi}} \int_0^z exp(-t^2)\, dt \qquad (2.1)$$

where t is a dummy variable. The Gaussian probability density curve is given by:

$$f(z) = \frac{exp\ (-z^2)}{\sigma\sqrt{2\pi}} \qquad (2.2)$$

where $z = (x-\bar{x})/\sigma$, and σ is the standard deviation of the distribution of x. Manipulation of equations 2.1 and 2.2 results in:

$$F(z) = \int_{-\infty}^{z} f(t)\, dt = \frac{1}{2}\, erf\left(\frac{z}{\sqrt{2}}\right) + 0.5 \qquad (2.3)$$

Effectively, the error function, when properly scaled, is proportional to the integral sum of the Gaussian curve, so that integration of a Gaussian curve between two endpoints, such as bin boundaries, can be determined using differences in the error function for those two points. Although the Gaussians are a function of diameter, not mass, small sub-intervals of the bins were used in the calculation. Comparison with the Simpson's Rule method using the large σ values of the LL equations confirmed that sufficient accuracy was maintained. A cut-off factor, C, was used to account for the truncation of the output Gaussian large and small fragment distributions at the coalescence diameter (D_{coal}), and is set to $C=H\sigma(2\pi)^{1/2}$, where H is the peak probability density. Integrating the Gaussian to D_{coal} yields one drop whereas integrating to positive infinity gives C drops. Values of C vary from just over one with nearly no truncation to almost two if the peak diameter and D_{coal} are virtually identical. The Simpson's Rule method was retained for the spread out lognormals of the smallest fragments. Figure 2.2 shows

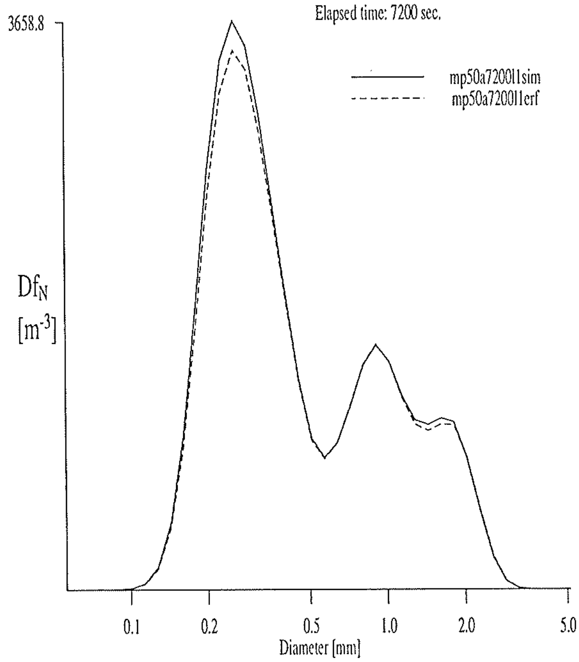

Figure 2.2 - Equilibria attained after two-hour box model runs using kernels derived from the 100 kPa equations of LL and integrating the large and small fragment Gaussians with the Simpson's Rule approach (solid) and the difference in error function approach (dashed). Both spectra evolved from a Marshall-Palmer (R = 50 mm/h). The vertical axis Df_N represents number concentration per logarithmic interval.

the negligible effect of this approach even on an equilibrium distribution when applied to the wider Gaussian equations of LL. The two curves each represent the same total mass (the diameter axis is logarithmic). The full effect of Fung's 100 kPa reparameterization can be seen in Figure 2.3. The main features of the three peaks are approximately in the same position, although the amplitudes differ by about 30 % for the small and middle peaks, and nearly 50 % for the large drop peak.

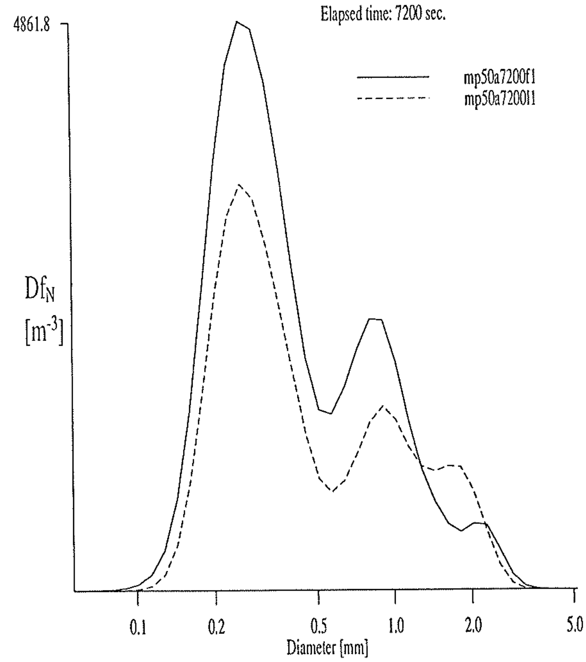

Figure 2.3 - Same as Figure 2.2 except model runs using kernels derived from the modified 100 kPa equations of Fung (solid) and the equations of LL (dashed).

3. THE 50 KPA RESULTS

Many terms in the 50 kPa equation set are based on functions of the corresponding 100 kPa terms derived by the reparameterizations. Figure 3.1 is a comparison plot between the equilibrium spectra at 100 kPa and 50 kPa. At 50 kPa the drop size peaks are at 0.3 and 2.9 mm, with a shoulder at 0.8 mm, versus the 0.3, 1.0, and 1.7 mm peaks at 100 kPa. At 50 kPa, the depletion of the numerous small drops slows the evolution, so a longer time is required for equilibrium. However the main trends are evident early in the evolution (less than 20 minutes). Like the 100 kPa case, the same equilibrium shape is achieved with different starting spectra.

Figure 3.2 reveals the importance of the various breakup modes have for each drop size at 100 and 50 kPa, and Figure 3.3 compares the relative importance of the breakups as a whole with coalescence. In these figures the magnitude of the $\Delta m/m_{bin}$ values are inversely proportional to an effective turnover time for mass in the bins due to the indicated process, and proportional to rainrate. The 100 kPa trends agree with the results of LMc. At 50 kPa

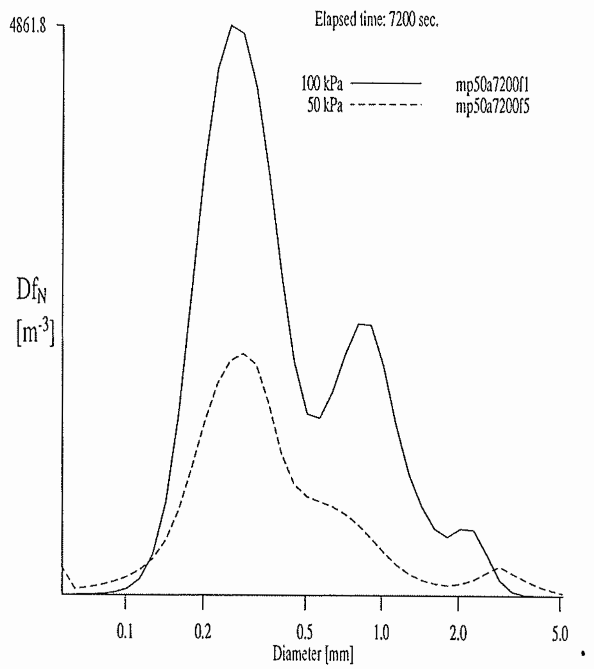

Figure 3.1 - Same as Figure 2.2 except model runs using kernels derived from the modified 100 kPa equations of Fung (solid) and the 50 kPa equations of Fung (dashed).

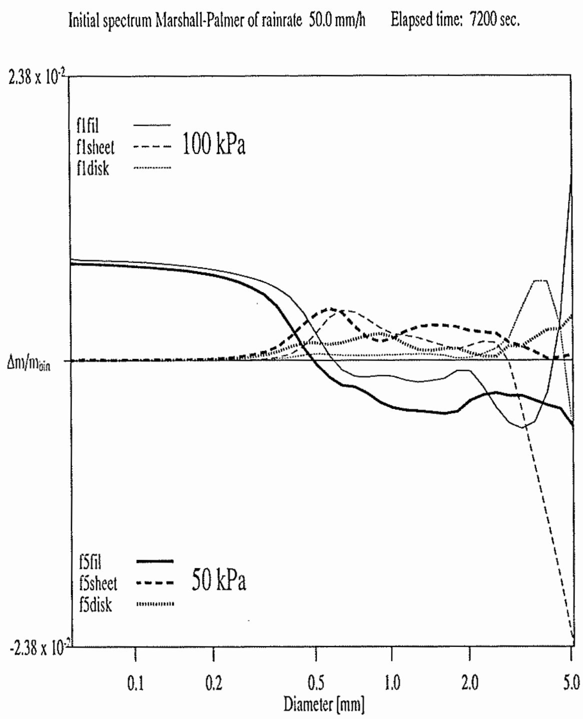

Figure 3.2 - Net change in bin mass Δm normalized by the present bin mass m_{bin} for a one-second timestep two hours into box model evolutions from MP50 spectra. Breakup modes are filament (solid), sheet (long dash), and disk (short dash). Bold lines are for 50 kPa and narrow lines are for 100 kPa. High values for largest diameters are due to very small bin masses.

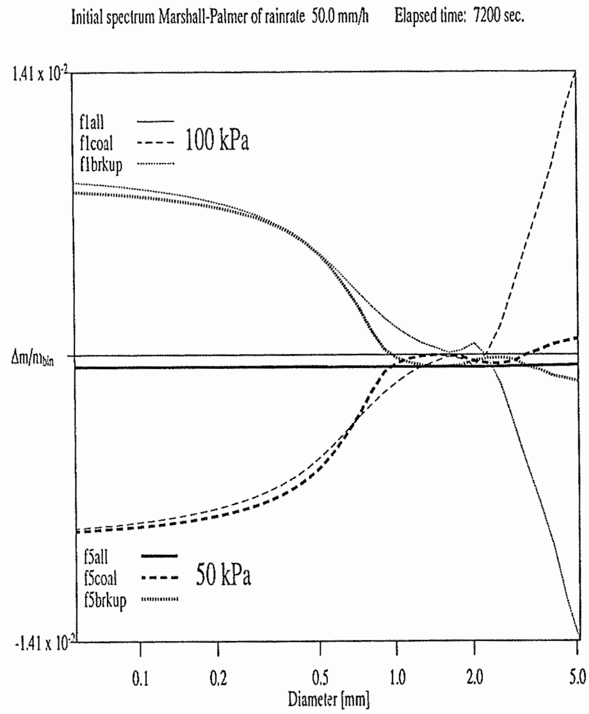

Figure 3.3 - Same as Figure 3.2 except solid lines represent coalescence and breakup, long dashes coalescence, and short dashes breakups.

the higher number of large drops more readily absorb the small drops by coalescence. This feature is further emphasized in Figure 3.4. Here the net mass change comprises of gains from output of coalescences involving input diameter to 0.3 mm drops less losses from coalescences with the input diameter. The increased net gains to the small drop population by filament breakup do not fully compensate. The 50 kPa middle drop size shoulder is shifted to smaller diameters from its 100 kPa counterpart due to depleted net gains from sheet breakup. Disk breakup takes a somewhat more prominent role. Both sheet and disk breakup modes favor the growth of the large drop population at 50 kPa more so than at 100 kPa.

There are some caveats which need to be mentioned. The 50 kPa equation set is based on laboratory data of just five drop size collision pairs, hence the parameterization may not be fully representative, especially at the small drop range (< 0.4 mm). Also the Gaussians for the large fragments may not be justifiable given the experimental uncertainties of the sum of the two drop collision masses. Warm rain conditions in the real atmosphere are not found at pressures less than about 60 kPa anywhere, and there is probably not enough time for equilibrium to be achieved before the drops have fallen to the ground.

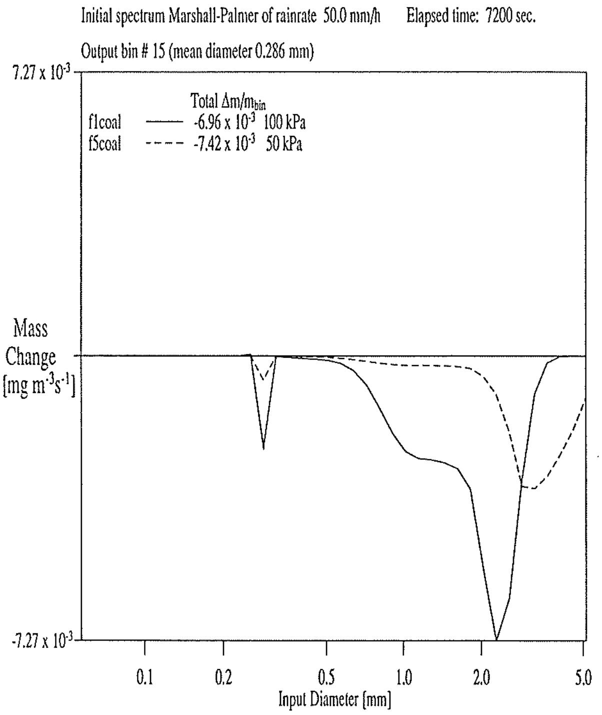

Figure 3.4 - Net mass change per diameter interval per time step to drops of size 0.3 mm (bin 15) two hours into an evolution from a Marshall-Palmer (R = 50 mm/h). Net mass change is gains from output of interactions involving input diameter to 0.3 mm drops less losses from interactions with the input diameter. Solid line is for coalescences at 100 kPa and dashed line for coalescences at 50 kPa. Total $\Delta m/m_{bin}$ values are plotted in Figure 3.3.

4. SUMMARY

With due regard to some uncertainties, laboratory data and model output nevertheless suggest that lower pressures may be more conducive to the development of the large drop population early on in the warm rain process. The sheet and disk breakup modes play a role in the more favorable environment for large drop growth.

Acknowledgments - This research was sponsored by the Atmospheric Environment Service of Canada, AES. One of the authors (RN) is indebted to AES for a postgraduate scholarship. The valuable comments of Dr. Chris Fung are also gratefully acknowledged.

References

Brown, P.S. Jr., 1988: The effects of filament, sheet, and disk breakup upon the drop spectrum. *J. Atmos. Sci.*, **45**, 712-718.

Fung, C., 1984: Raindrop collisions under low pressure, experiments and parameterizations. Ph. D. Thesis, Department of Physics, University of Toronto, 137 pp.

List, R., N.R. Donaldson, and R.E. Stewart, 1987: Temporal evolution of drop spectra to collisional equilibrium in steady and pulsating rain. *J. Atmos. Sci.*, **44**, 362-372.

----, and G.M. McFarquhar, 1990: The role of coalescence and breakup in the three-peak equilibrium distribution of raindrops. *J. Atmos. Sci.*, **47**, 2274-2292.

Low, T.B., and R. List, 1982: Collision, coalescence and breakup of rain drops. Parts I and II. *J. Atmos. Sci.*, **39**, 1591-1618.

McTaggart-Cowan, J.D., and R. List, 1975a: An accelerator system for water drops. *J. Atmos. Sci.*, **32**, 1395-1400.

---- and ----, 1975b: Collision and breakup of water drops at terminal velocity. *J. Atmos. Sci.*, **32**, 1401-1411.

Valdez, M.P., and K.C. Young, 1985: Number fluxes in equilibrium raindrop populations: a Markov chain analysis. *J. Atmos. Sci.*, **42**, 1024-1036.

INFLUENCE OF THE ELECTROSTATIC FORCES ON THE COLLISION EFFICIENCY OF THE LOW-INERTIA PARTICLES BY THE LIQUID SPHERE AT INTERMEDIATE REYNOLDS NUMBERS

V.M.Kim

Institute of Experimental Meteorology, Obninsk,Russia

1. INTRODUCTION

Theoretical investigation of the sphere and particle electrostatic charges influence on the efficiency of the particle collision by the sphere at intermediate N_{Re} changing from 10 to 60 and small Stokes numbers, $N_{St} \ll 1$, was carried out. The ratio of parameters given above can take place when the charged droplets are suspended within strong electrical fields of the thunderstorm clouds and also when clouds and fogs are influenced by charged sedimentating or ascending bubbles. In both cases the velocity of the sphere stream-lining by the flux particles will be less than the regulated velocity of the free falling of the given size liquid sphere. Radius r of the sedimentating spherical particles with a density of 1 g/cm^3 will vary from 0.5 to 15 μ and the radius of the sphere-collector N_{St} - from 2 to 2.4 mm. Stream-lining of the sphere by a flux of particles from above and below was considered, the velocity U_∞ of stream-lining changing from 3 to 23cm/s, N_{St} - from 7.10^{-5} to 3.10^{-1}, the sphere charge Q - from 0 to 4 esu and the particle charge q -from 0 to $\pm 4.8.10^{-8}$ esu.

2. NUMERICAL MODEL

Since in the present paper the ratio of interacting particle and sphere sizes $r/R \ll 1$, when deriving an equation of the particle motion the influence of the particle hydrodynamic field on the hydrodynamic field of the sphere was not taken into account. It was assumed that the particles move in accordance with the Stokes law. To describe the velocity field round the sphere a numerical solution of the Navier-Stokes equations, derived by (Rivkind et al., 1976) for a liquid sphere, was used. To determine the Coulomb and induction forces of the sphere and particle interaction the results, obtained by (Davis, 1964b) for two conducting charged spheres, were used. The collision efficiency E was determined by the formula

$$E(R,r,Q,q) = y_c^2/(1+r/R)^2 ,$$

where y_c is the dimensionless limiting horizontal distance between the sphere and particle centres, when the particle is at a distance of 30 radii of the sphere upward along the flux.

3. DISCUSSION OF RESULTS

Influence of induction forces on the collision efficiency E was considered for a case when the sphere is charged and the particles are neutral, $q = 0$. Having such conditions parameter β (β is the ratio of the induction force to the aerodynamic force affecting the particle; $\beta = Q^2 q^2 C_{sc}/3\pi\eta R^5 U_\infty$, where η is the dynamic viscosity of the air and C_{sc} is the Stokes-Cunningham slip correction) is the basic parameter of the particle motion equation. The calculations show that the influence of the induction forces on the collision efficiency increases as the flux velocity or the sphere N_{Re} decreases.

Influence of the induction forces on the collision efficiency of the low-inertia particles was estimated earlier. There are calculation data on the collision efficiencies for the sphere stream-lining by a viscous flow at $N_{Re} < 1$ (Levin,1961) and by a homogeneous flow. In the first case the data can be presented as a one-parametric dependence on the β parameter, $E = \beta^{0.66}$, in the second case - $E = 2\beta^{0.4}$. Fig. 1 demonstrates our data of E variation in dependence on β for the intermediate region of N_{Re} from 10 to 60, within which at $N_{Re} \approx 20$ one can observe rebuilding in the flux field and formation of the joined stationary

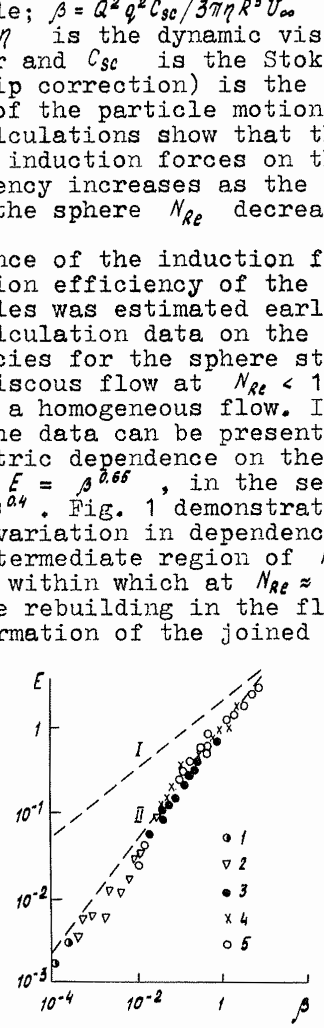

Fig. 1: Collision efficiency of the sphere when the induction force acts in dependence on parameter β for different numbers $10 \leq N_{Re} \leq 60$: I - $E = 2\beta^{0.4}$, II - - $E \approx \beta^{0.65}$; 1 - r = 0.5; 2 - 1; 3 - - 5; 4 - 10; 5 - 15

vortex behind the sphere. It is obvious that E, within the range of the U_∞, N_{Re}, β variation being studied at β = = const, slightly depends on the velocity and regime of the obstacle stream-lining, i.e., on N_{Re}. Therefore, at $\beta \approx 1$ and intermediate N_{Re} E, as in the case with small $N_{Re} < 1$, one can present in the form of a one-parametric dependence $E = \beta^{0.65}$.

Results of investigation of simultaneous influence of induction and Coulomb forces on E at different charges of Q sphere and two N_{Re} = 10 and N_{Re} = 60 in dependence on the particle size and sign of its charge q are given in Fig. 2. For comparison at the same

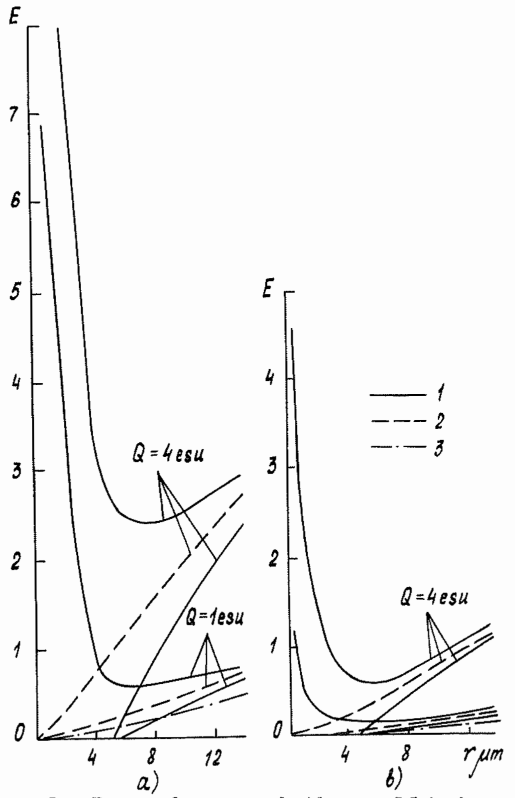

Fig. 2: Dependence of the collision efficiency on the particles radius at simultaneous influence of the induction and Coulomb forces: a - N_{Re} = 10, b - N_{Re} = = 60; 1 - $q = \pm 4.8 \cdot 10^{-8}$ esu; 2 - q = 0; 3 - q = 0, Q = 0.

the Figure demonstrates E values at q = = 0 (dashed line) and at q = 0, Q = 0 (dash-dotted line). We see here that the Coulomb force strongly effects E of low-inertia particles in comparison with influence of only induction forces. In case of oppositely charged particle and sphere, as it follows from Fig. 2, at all values of N_{Re} and Q, as the particle radius increases at first E sharply decreases to the minimum value at r = = 5-7μ, then it begins slowly to increase. Such behaviour of the dependence is explained by the fact that at constant N_{Re}, Q and q, as the particle size increases, $|\alpha| \sim 1/r$ parameter decreases (α - ratio of the Coulomb force to the aerodynamic force, influencing the particle; $\alpha = -Qq\,C_{sc}/6\pi\eta r R^2 U_\infty$), but $\beta \sim r^2$ increases, i.e., contribution of the Coulomb force into E decreases but of the induction - increases. For particles with $r < 5\mu$ parameter $|\alpha| > \beta$, Coulomb force prevails the induction force and E for charged sphere and particle decreases as their size increases, but for single charged sphere and particle E = 0. When Coulomb and induction forces are comparable ($|\alpha| \approx \beta$) at $r \approx 5$-7μ, contribution of these forces into E is approximately equal. Further as r increases parameter $|\alpha| < \beta$, i.e., the induction force prevails. Coulomb force and E begins slowly to increase.

Thus, at $r \lesssim 5\mu$, when $|\alpha| > \beta$, the contribution of the induction force can be neglected and E at the intermediate values of N_{Re}, as it follows from

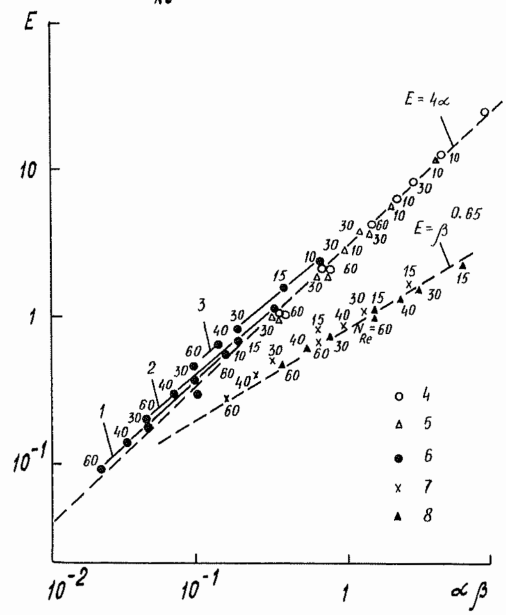

Fig. 3: Dependence of the collision coefficient for oppositely charged particles and spheres on parameter β and α: 1 - - Q = 1; 2 - 2; 3 - 4esu; 4 - r=0.5; 5 - - 1; 6 - 5; 7 - 10; 8 - 15

Fig. 3, is well described by a one-parametric dependence $E = 4\alpha$. This dependence was earlier obtained for small $N_{Re} < 1$ (Levin, 1961). Based on the same Fig. we can make a conclusion that at $r > 10\mu$, when $\beta \gtrsim 5|\alpha|$, the collision efficiency E with an error not exceeding 25 % can be also approximated with the dependence of $E = \beta^{0.65}$. For the particles with $5 < r < 10\mu$, when $|\alpha| \approx \beta$, E cannot be described by a one-parametric dependence on α or β, since the contribution of the induction and Coulomb forces is comparable by the value

All the data for E given above are related to the case of the sphere streamlining by a particles flux from above. When the sphere is stream-lined by a particles flux from below, the character of the particles sedimentation slowly changes. This fact is explained by the action of the gravitational force or by the velocity of the particles sedimentation. When the sphere is stream-lined from above, this action promotes the particles sedimentation at the front part of the sphere and prevents that at the rear hemisphere, but when the streamlining is realized from below, it acts in an opposite manner. However, for $r \leq 5\mu$ all the above mentioned dependences are maintained, but for $r > 5\mu$, beginning from some charge of the sphere Q, the results do not depend on the flux orientation.

Fig. 4 depicts the comparison of the results obtained with those of the experiment described in the paper (Smirnov, 1976) for $r = 5.5\mu$. It is obvious

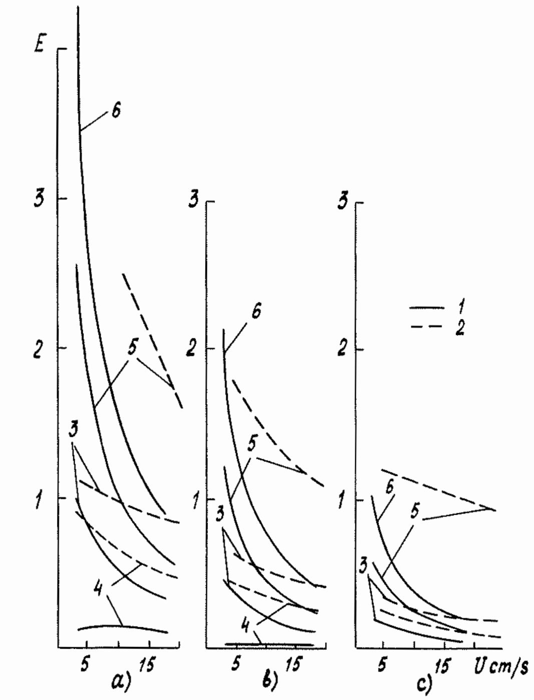

Fig. 4: Comparison of the calculated and experimental data
a – $Q = 4$, b – 2, c – 1 esu: 1 – calculated data; 2 – experimental; 3 – $q = 0$; 4 – $+4.8 \cdot 10^{-8}$; 5 – $-4.8 \cdot 10^{-8}$; 6 – $9.6 \cdot 10^{-8}$ esu

that the experimental results are higher than the calculation ones. However, the analysis of the experiment methods permits to assume some their weak sides, i.e., not correct determination of the particles charge value. For the quantitative comparison it is necessary to know exactly the droplets charge value of the experiments, since it follows from the calculations that E at constant r, Q and U_∞ approximately linearly depends on q.

4. REFERENCES

1. DAVIS, M.H., 1964b: Two charged spherical conductors in a uniform electric fields: Forces and field strength. Quart. J. Mech. Appl. Math. 17, 499-511.

2. KIM, V.M., 1991: Regularities of the quick-response particles sedimentation on a charged spherical collector at intermediate N_{Re} . Proceedings of IEM, vyp. 52(147), 65-81.

3. LEVIN, L.M., 1961: Investigation on the coarse aerosol physics. The USSR Academy of sciences, Moscow, 267 pp.

4. RIVKIND, V.G., RYSKIN, G.M., 1976: Structure of the flow about a spherical drop moving in a liquid medium at intermediate Reynolds numbers. Fluid and Gas Mechanics, 1, 8-15.

5. SMIRNOV, V.V., 1976: Electrostatic collection of aerosol particles on a spheres and cylinders. J. aerosol sci., 7, p. 473-477.

A SIMPLE DROPLET SPECTRUN DERIVED FROM ENTROPY THEORY

Xuewen Zhang Guouang Zheng

Xinjiang Institute of Meteorology, Urumqi, P.R.China, 830002

1. Problem

Cloud physical observation displays that the steady stratus cloud has a prevalent droplet spectrun. This droplet spectrun has a single peak and a skew figure. Why does it have such a feature ?

Here we analyse this problem from the maximun entropy principle. we discovered if we apply this theory to the free enery of the droplet, we could get a theory spectrun equation which just agree with above spectrun feature.

2. The steady spectrun and the maximun entropy

If the figure of cloud spectrun changes very quickly, then the observed spectrun should be very different with each other. But the observed practice tell us that the steady cloud has a prevalent spectrun. If we analyse this problem from the view of statistical physics, we have to recognize that a steady spectrun means the system reach its equlibrium state and at the same time certain entropy should reach to its maximun value.

In physics, we have known that M.Planck (1900) had got a steady spectrun of black body radiation by maxinizing a special entropy in a assembly of photon. Now in cloud physics, the stratus cloud is also a assembly--a assemly of droplet. Could we get a droplet spectrun from a similar idea ?

In statistical physics, the entropy is concerned with energy distributionn of micro particales (molecular, atom, photon ....). In the information theory, the entropy is concerned with probability density distribution.

Now we notice that the spectrun of cloud droplet is also a kind of the distribution of particle and from certain point of view, it is on an equlity with the probability density distribution (Zhang, 1986).

Based on this idea, if we consider the entropy concerning the distribution of free energy which is on the surface of cloud droplet, we could derive a droplet spectrun by maximizing this entropy on certain constraints.

3. Free energy of cloud droplet

The cloud droplet spectrun describes the feature between the droplet radius and the number of droplets. Because the area s of a droplet is a function of its radius r, and so we have

$$s=4\pi r^2 \quad \text{--------------------(1)}$$

On the other hand, according to the thermodynamics, the free energy f of one droplet proportionate to its surface area. So the free energy of droplet proportionate to the square of droplet radius. So

$$f \propto 4\pi r^2$$

It is clear that once we get a spectrun concerned free energy of the droplet, it is easy to derive a spectrun concerned droplet radius.

4. Maximiun entropy

In information theory, entropy $H(x)$ is a variation of probabiliy distribution function $f(x)$

$$H(x)= \int_{-\infty}^{\infty} f(x)\ln f(x)dx \quad \text{---------(2)}$$

On certain condition we have not known the $f(x)$, but we could work out a probability distribution $f(x)$ by maximizing its entropy H under certain constrains (Raza, 1961).

Based on this idea, we will derive a function (probability distribution or to say a spectrun) under the following constrains:

* In a steady cloud system, the total free energy of all droplets and the number of droplets are two constants.

* This free energy will distribute to each droplet in an very disorder way. Different droplets may get various values of free energy. Here "very disorder" means the entropy of this system achieves to its maximun value.

Under above constrains, we could derive a distribution about free energy of droplet. this is a negative exponent distribution (Raza, 1961). After that we work out a distribution about the radius of the droplet as following

$$n(r)=\frac{2Nr}{R^2}\exp\left(-\left(\frac{r}{R}\right)^2\right) \text{ ---------------(3)}$$

This is the theortical spectrun of status cloud droplet which we derived by entropy theory (Fig.1).

Here N is the number of total droplets in the cloud, R is mean radius of total droplets, $n(r)$ is the number of droplet which radii equal r.

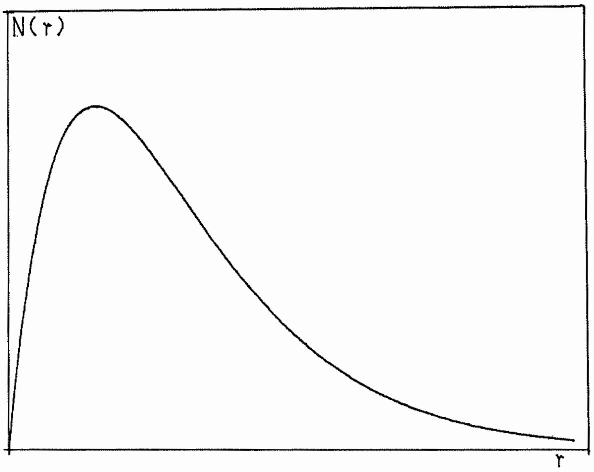

Fig.1 The cloud spectrun derived by entropy principle

This curve has a peak and a skew feature, which is very similar to the observed cloud spectrun. Useing probability language, Equ.(3) is Weibull distribution.

5. Test

41 observed spectrun examples have been compared with this theoretical equation. After statistical test, 33 examples are in accordance with Equ.(3). That is to say 80% examples pass the statistical test. Although we need more examples to test, this primary result is satisfactory.

In many articals, scientist often used following empirical formula to express the cloud spectrun

$$n(r)=Nar^2\exp(-br) \text{ ------------(4)}$$

This curve has also a skewness peak, but it has some differences with Equ.(3). Based on the above discuss, we suggest let theoretical formular Eq.(3) stand for the empirical formula Eq.(4).

6. Summary

6.1 We work out a stratus cloud spectrun based on maximun entropy principle [Eq.(3)].

6.2 When we to do this, following hypotheses is used :

* The total free energy of cloud is a constant in a steady cloud system.

* The distribution of free energy which proportionate to the area of droplet surface) just achieve the most disorder state.

6.3 This theoretical result is in accordance with the observered cloud droplet spectruns (80%).

6.4 We need more tractical droplet spectrun to test this theoretical spectrun.

6.5 We suggest that empirical formula Eq.(4). should be instanded by theoretical Eq.(3).

Referance

Raza.F.M.,1961, An introduction on information theroy, ***McGRAW-HILL BOOK COMPANY***, New York,278-282

Zhang Xuewen, 1986, The ralative density function and meteorological entropy , ***Acta Meteorologica Sinica***, **44**,(2),214-219

Zhang Xuewen and Zheng Guoguang, 1989, Steady stratus cloud's droplet spectrun equation derived from entropy principle, ***Plateau Meteorology*** **8**,(3),273-278

---END---

NUMERICAL EXPERIMENTS ON THE INFLUENCE OF THUNDERSTORM-GENERATED ACOUSTIC WAVES ON COAGULATION

Mladjen Ćurić and Zlatko Vuković*

Institute of Meteorology, University of Belgrade, Yugoslavia
*Hydrometeorological Service of Serbia, Yugoslavia

1. INTRODUCTION

The gush of rain after nearby lightning was reported two thousand years ago (Moore and Vonnegut, 1977). The recent meteorological observations and radar measurements also show that after the first thunder occurrence the radar echo in region of weak reflectivity becomes suddenly stronger by more than 10 db/min (Moore and Vonnegut, 1977). The close association between lighting and subsequent precipitation on the base of observations is shown by Ćurić and Vuković (1991).

Although the close association between lighting and precipitation is evident for a long period of time, the cause and effect relation between the initial development of precipitation and of cloud electrification yet have paid full attention (Goyer, 1960; Paluch, 1970; Foster and Pflaum 1985, 1988).

The purpose of this paper is to demonstrate that theoretical formulation of Ćurić and Vuković (1991) can be numerically solved. The calculation of the shift in the drop size spectra toward larger sizes is conducted under different conditions of the initial size spectra and the thermal energy released in the lightning chanel.

2. THE MODEL

The model is concerned with the fact that the air motions caused by the acoustic wave of thunder through the cloud suddenly increase the frequency of collisions between cloud droplets, thus enhancing their rate of coagulation into larger drops.

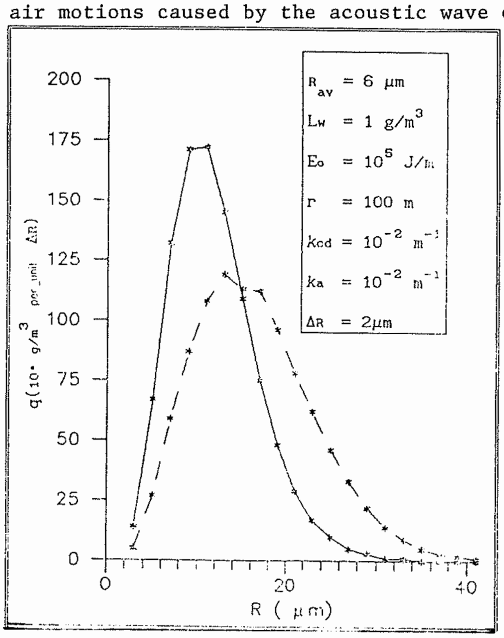

Fig.1 Evolution of the spectrum due to acoustic coagulation for initial conditions shown in figure.

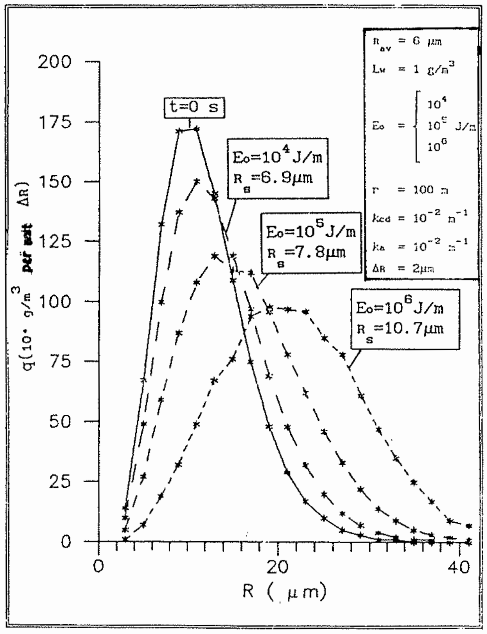

Fig.2 The same as Fig 1. but for three different energy E_0.

Since the derivation of the governing equations of the model are described in Ćurić and Vuković (1991) and should be familiar to most of the readers, we shall only present some computations using these equations.

3. NUMERICAL EXPERIMENTS

Because the equations used are nonlinear integro-differential, analytic solutions can be obtained only under very restrictive assumptions. Here its numerical evolution was applied.

The radius of drops R is taken to be $R_i = (i+1/2)\Delta R$, i = 1,2,3,..., where ΔR is the radius interval of 2 μm.

The time T is taken as $T_t = t\,\Delta t$, t=1,2,3,.. The time step Δt is calculated for evry size class from

$$\Delta t_i = \frac{48\,\rho_w\,V_i^t}{2\eta\,R_i\,C_d\,N_{re}\,|V_i^t-U^t|} \tag{1}$$

The superscripts denote time step sequence; η is the coefficient of dynamic viscosity; C_d the drag coefficient, N_{Re} Raynolds number, ρ_w the water density.

The changes in droplet concentration in every size class are computed by the numerical scheme proposed by Chin and Neiburger (1972).

Computations were carried out using equations under similar initial conditions. The empirical Khrgian-Mazin (K-M) spectrum is used to represent the cloud droplet spectrum. Two parameters of this spectrum, the liquid water content L_w and average radius R_{av}, are changed in range 1-3 g/m^3 and 5-30 μm respectively. The flux of energy through unit length of lightning chanel, E_o, is ranged from 10^4-10^6 J/m. The coefficients of attenuation of gaseous, k_a, and drops, k_{cd} are changed in range 10^{-1}-$10^{-2}m^{-1}$ and 10-$10^{-2}m^{-1}$ respectively. All computations were carried out for distance r = 100 m.

Figs.1-4 show the change in the K-M spectra due to collection under influence of thunderstorm--generated acoustic waves.

Fig.1 shows the spectrum evolution for an initial K-M spectrum for which is R_{av}=6μm and liquid water content L_w=1 g/m^3. The solid curve is initial specific water content q vs radius.The dashed curve is final curve of q calculated under the assumption given in the figure. It is seen that water mass is transferred toward larger size side of drops. The mean radius of final spectrum of drops is R_s = 7.8 μm.

Fig.2 shows the spectrum evolution under the assumption that the energy E_o is 10^4, 10^5 and 10^6 J/m respectively. The corresponding final mean radius is 6.9; 7.8 and 10.7μm. These results demonstrate that the larger amount of energy released in lightning chanel considerably accelerates the transfer of mass to the larger drops.

In Fig.3 are shown two initial spectra for which was R_{av}=6.0 and 12.0μm respectively. Other parameters are the same for both curves, L_w=2 g/m^3, $E_o=10^6$ J/m, $k_{cd}=10^{-2}m^1$ and $k_a=10^{-2}m^{-1}$. The spectrum evolution for R_{av}=12 μm to the larger drops

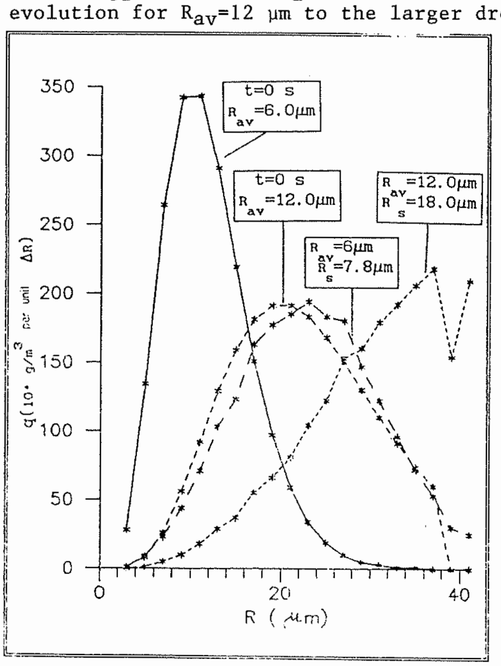

Fig.3 The same as Fig.1 but for two initial average radius R_{av}.

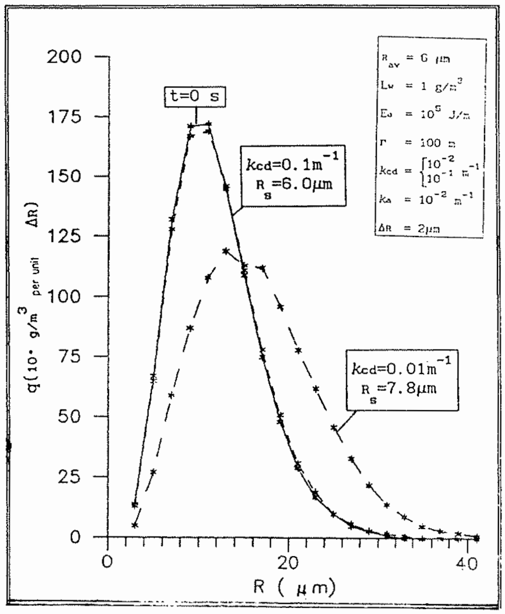

Fig.4 The same as Fig.1 but for two different attenuation coefficients of droplets k_{cd}.

is considerable faster than for R_{av} = 6 μm.

Computations were also carried out with an initial spectrum for which was R_{av}=6 m, L_w=1 g/m^3, $E_o=10^5$ J/m, $k_a=10^{-2}m^{-1}$. Two final spectra are obtained for $k_{cd}=10^{-2}$ and $10^{-1}m^{-1}$ respectively. The spectrum evolution is shown in Fig.4. It is seen that transfer of mass to the larger drops for k_{cd}=0.1 m^{-1} is practically equal zero.

References

Chin, E. and M. Neiburger, 1972: A numerical simulation of the gravitational coagulation process for cloud droplets, J.Atmos. Sci., 29, 718-727.

Ćurić, M. and Z.Vuković, 1991: The influence of thunderstorm-generated acoustic waves on coagulation. Part one: Mathematical formulation, Z. Meteor., 41, 164-169.

Foster, M.P. and J.C.Pflaum, 1985: Acoustic seeding, J. Weather modification, 17, 38-44.

Foster, M.P. and J.C.Pflaum, 1988: The behavior of cloud droplets in an acoustic fields: A numerical investigation. Journal of Geophysical Research, 93, 747-758.

Goyer, G.G. et al. 1960: Effects of electric fields on water-droplet coalescence, J. Meteor., 17, 442-445.

Moore, C.B., and B. Vonnegut, 1977: The thunder cloud. In: Lightning, Vol.1., Physics of Lightning (Ed. R.H. Golde), Academic Press, London, 51 -98.

Paluch, I.R., 1970: Theoretical collision efficiencies of charged cloud droplets, J.Geophys. Res., 75, 1633-1640.

CLOUD CCN FEEDBACK

James G. Hudson
Atmospheric Sciences Center, Desert Research Institute
Reno, Nevada 89506-0220, USA

1. INTRODUCTION

Cloud microphysics affects cloud albedo (Twomey, 1977), precipitation efficiency (Albrecht, 1989), and the extent of cloud feedback in response to global warming (Arking, 1991). Compared to other cloud parameters, microphysics is unique in its large range of variability and the fact that much of the variability is anthropogenic. Probably the most important determinant of cloud microphysics is the spectra of cloud condensation nuclei (CCN) which display considerable variability (e.g. Twomey and Wojciechowski, 1969; Radke and Hobbs, 1969; Hudson and Frisbie, 1991a) and have a large anthropogenic component (Hudson, 1991).

When analyzed in combination three field observation projects display the interrelationship between CCN and cloud microphysics. CCN were measured with the Desert Research Institute (DRI) instantaneous CCN spectrometer (Hudson, 1989). Cloud microphysical measurements were obtained with the National Center for Atmospheric Research Lockheed Electra. Since CCN and cloud microphysics each affect the other a positive feedback mechanism can result.

2. RESULTS

Vertical CCN profiles near cumulus clouds (Hawaiian Rainband Project--HaRP-1990) in the mid Pacific were similar to vertical profiles made near stratus clouds in the eastern Pacific (First ISCCP Regional Experiment--FIRE-1987). Figure 1 shows the systematic lower particle concentrations within the boundary layer when clouds were present in the mid Pacific (see Hudson and Frisbie, 1991b Figs. 1 a-d for similar vertical distributions near stratus clouds).

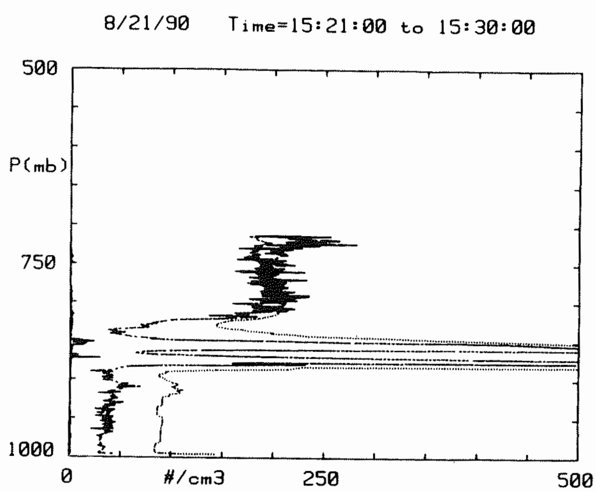

Fig. 1. CCN (dashed line) and CN (dotted line) as a function of pressure altitude near Hawaii. Also shown is the cloud droplet concentration (solid line). Time is GMT.

Figure 2 shows the similarity in concentrations between the boundary layer and the free troposphere when few or no clouds were present (also see Hudson and Frisbie, 1991b, Fig. 1e). The high concentrations measured within the clouds are believed to be artifacts of the sample inlet system (Hudson and Frisbie, 1991b). It is also notable that the CCN concentrations were extremely low near the clouds both above and below (Fig. 3).

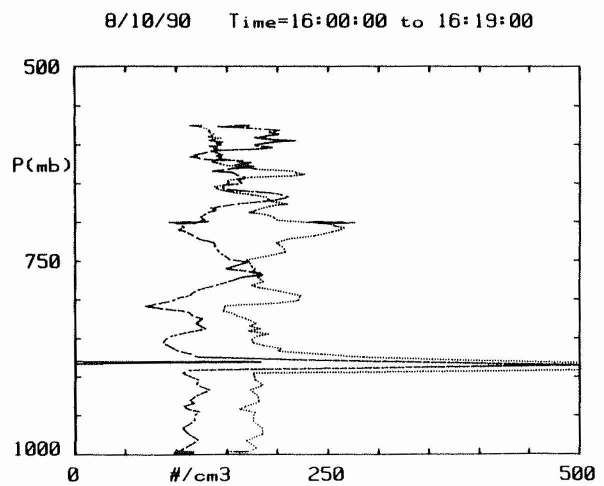

Fig. 2. As Fig. 1 for a "non cloud" situation.

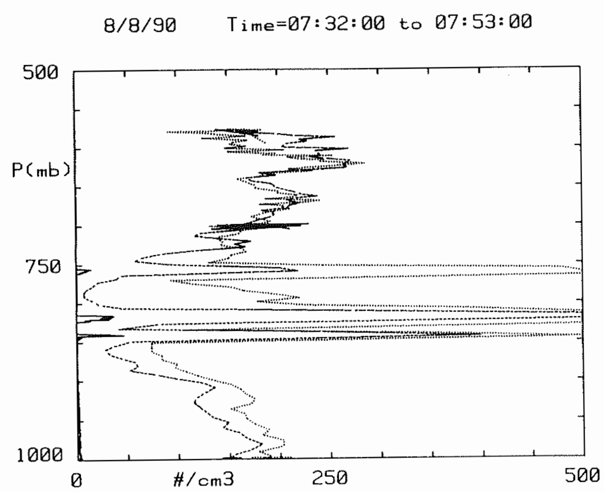

Fig. 3. As Fig. 1.

There were two significant differences between the cumulus regime of the mid Pacific and the stratus regime of the eastern Pacific: 1) The layer of high concentrations at the inversion base just above the tops of the clouds which was common in the eastern Pacific (Hudson and Frisbie, 1991b) was much less obvious in HaRP and was often nonexistent. 2) Extremely low particle concentrations, especially CCN, were observed near the cumulus clouds in Hawaii, especially near the tops of the clouds. This was an obscure feature in the stratus regime (Fig. 1b of Hudson and Frisbie, 1991b). Nonetheless relatively low CN concentrations were sometimes observed above the tops of the stratus which indicated a separation between the real high concentrations above the cloud deck associated with high ozone concentrations and the within cloud high concentrations (Hudson and Frisbie, 1991b).

Probably the main reason for difference number 1 was the proximity to continental and anthropogenic particle and trace gas sources. The high ozone layer just above the clouds was also less prominent in HaRP.

The extremely low concentrations observed just above cloud top were also observed in horizontal runs close to the clouds in HaRP. There are several reasons that this feature was quite prominent near Hawaii compared to the eastern Pacific stratus (FIRE): 1) The superior time resolution of the CCN spectrometer in the latter project allowed better spatial resolution. 2) The cumulus clouds have more spatial variability, especially horizontally, which results in more variability in the aerosol. 3) The cumulus clouds have larger cloud drops which lead to more coalescence and thus more coalescence scavenging (Hudson and Frisbie, 1991b) which causes greater reductions in the particle concentrations.

The lower particle concentrations within the boundary layer in both HaRP and FIRE appear to be a result of cloud scavenging processes which are active within the cloudy boundary layer (Hudson and Frisbie, 1991b). In both regimes, stratus and cumulus, the concentrations below the temperature inversion are similar to the concentrations above the temperature inversion when there are few or no clouds present. There appears to be a consistent reservoir of free tropospheric aerosol from which particles can be drawn to the boundary layer. The observations are consistent with this picture which does not require a boundary layer source of particles. In other words it seems rather fortuitous that the boundary layer concentration would match the free tropospheric concentration. If there were a boundary layer source one would expect the boundary layer concentration to sometimes exceed the concentration in the free troposphere.

Table 1 shows microphysical measurements from four sections of cloud in a horizontal flight leg during FIRE. These sections were solid portions of cloud which did not include any holes in the cloud or edge effects. The column N denotes the number of 1 second records used in each cloud section. This shows a progressive decrease in droplet concentration (number cm^{-3}, column labeled fssp) with an increase in the concentration of drops larger than 50 μm (number $liter^{-1}$ column 260X).

TABLE 1

	p (mb)	t	lwc (gm^{-3})	fssp (cm^{-3})	d_m μm	disp. $\sigma d / d_m$	fssp & d_m corr. coef.	fssp & d_m slope	N	260x (l^{-1})
Flight leg from point A to point B (13:01 - 13:09)										
13:02:30 - 13:04:28										
mean	928.0	10.5	0.28	68.1	18.8	0.26	-0.02	-0.2	119	2.8
std	0.4	0.1	0.05	9.3	0.7					3.6
(std/mean)			18%	14%	4%					
13:04:32 - 13:06:13										
mean	928.1	10.5	0.30	50.6	20.8	0.31	-0.25	-5.4	102	17.5
std	0.3	0.1	0.07	13.2	0.6					17.5
(std/mean)			23%	26%	3%					
13:06:14 - 13:07:10										
mean	928.1	10.4	0.16	29.6	18.8	0.38	-0.34	-1.6	57	34.4
std	0.1	0.1	0.03	4.8	1.0					17.8
(std/mean)			19%	16%	5%					
13:07:51 - 13:08:18										
mean	928.1	10.1	0.24	22.8	22.0	0.45	-0.64	-2.3	28	75.9
std	0.1	0.0	0.05	4.3	1.2					37.5
(std/mean)			21%	19%	5%					

This progression was accompanied by an increase in droplet dispersion and an increase in the magnitude of the correlation coefficient between droplet concentration and median droplet diameter within each section of cloud (the slope of this relationship is also shown). This indicates that on a small scale that lower cloud droplet concentrations are associated with larger droplets and vice versa. Measurements at a lower altitude for the same flight leg (same latitude and longitude) 45 minutes earlier showed a progressive decrease in CCN concentration which was in keeping with the decrease in droplet concentration.

The variations in boundary layer CCN concentrations observed during FIRE by Hudson and Frisbie (1991b) were reflected in cloud droplet concentrations which showed a progressive decrease for the first three flights (June 29, June 30, July 2). The lowest droplet concentrations were observed on July 2 (< 40 cm^{-3}). These were probably a result of decreasing CCN concentrations throughout this period of continuous cloud which resulted in scavenging of particles within the boundary layer. Significantly higher droplet concentrations (~ 100 cm^{-3}) were found for the last two flights, July 16 and 18, when there were much higher boundary layer CCN concentrations. July 18 was unique in that the CCN and CN concentrations did not vary with altitude (Hudson and Frisbie, 1991b, Fig. 1e). As pointed out by Hudson and Frisbie (1991b) this was a broken cloud case with a weak temperature inversion and a short cloud history in the area (there were no clouds in this region on the previous day).

Surface CCN measurements made on board ship in this same area in 1991 were usually similar to the airborne concentrations observed in FIRE. The latter measurements were made between July 8 and July 28 on board the oceanographic vessel Egabrag III during project SEAHUNT (Shiptrail Evolution Above High Updraft Naval Targets) conducted by Dr. William Porch of Los Alamos National Laboratory. However Figs. 4a-b show some extremely low concentrations which were observed for more than 12 hours. This region was characterized by broken low-level clouds that were producing drizzle in spite very little vertical extent. The clouds in this area were often invisible except for the fogbows which could often be observed with the naked eye; at the rainbow angle there was sufficient enhancement of scattered light from the drops to render a visible cloud. These low-level clouds or fogs were also transparent to visible satellite images. The low level clouds did affect the surface solar intensity as shown by the highly variable measurements displayed in Fig. 3b. The solar intensity was notably reduced between 10 and 11 A.M. as the ship passed under a solid cloud line. Coincidentally the CN and CCN concentration increased under this cloud feature. Satellite photos (Hindman et al, 1992) revealed that this was a shiptrail (i.e. Conover, 1966). Twomey et al. (1968) had predicted that these anomalous cloud lines should be visible only where background CCN concentrations were very low (<10 cm^{-3}) as found here. At noon the concentrations returned to normal maritime values as the ship returned to a typical marine stratus regime.

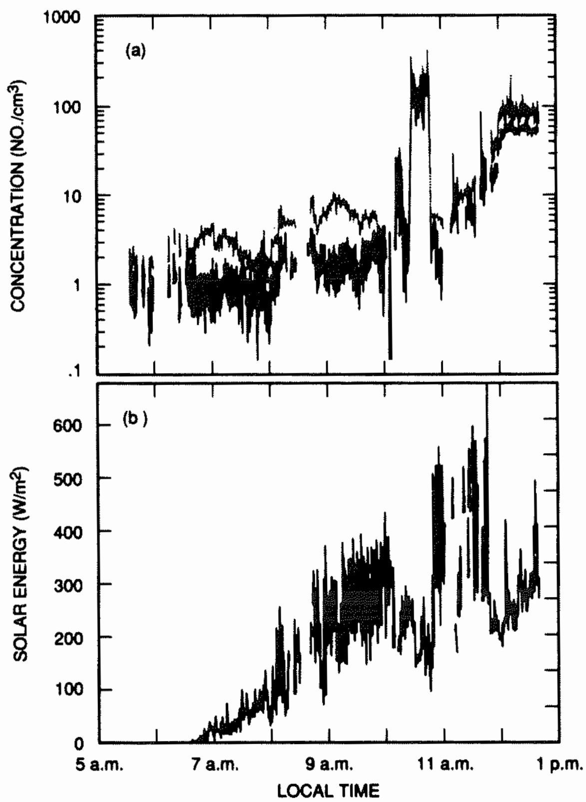

Fig. 4. Surface measurements of (a) condensation nuclei (CN) (light line) and cloud condensation nuclei (CCN) (dark line) concentrations; (b) solar energy as a function of local time off the coast of Baja California on the morning of July 13, 1991.

3. DISCUSSION

Although the CCN concentration was less than 10 cm^{-3} on only this one occasion during the cruise there were several other instances when the CCN concentration briefly showed significant decreases. These episodes were coincident with observations of drizzle on the ship or visible nearby (Fig. 5). Hudson and Frisbie (1991b) suggested that drop coalescence processes can reduce the concentration of CCN because the collection of droplets by drops also reduces the concentration of the nuclei which initiated the individual droplets. This decrease in CCN concentration happens even when the drops evaporate because they leave behind only one nucleus which is composed of the nuclei of the collected droplets.

The lower concentrations observed within the boundary layer in all three projects are probably caused by cloud scavenging processes, especially coalescence scavenging. This process also probably results in the very low concentrations which are often found near the clouds especially in Hawaii (e.g. Fig. 3). The extremely low CCN concentrations found in the vicinity of the shiptrail on July 13, 1991 are probably caused by the extensive drizzle which was prevalent in the area. The low CCN concentrations in turn encouraged the production of larger cloud droplets (i.e. Table 1) which in turn encourages drizzle formation; thus a positive feedback process. The higher CCN concentrations from a ship may have suppressed the coalescence process by increasing the droplet concentrations and thus limiting the sizes of the droplets. The smaller cloud droplets are less likely to collect or be collected by other drops. The lack of coalescence scavenging then left the CCN concentrations intact.

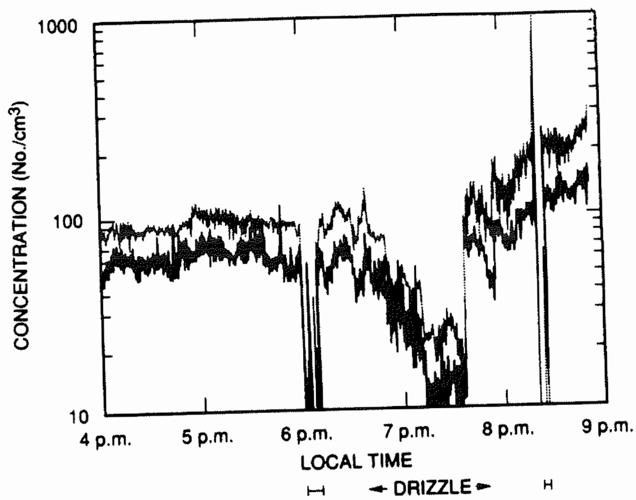

Fig. 5. As Fig. 4a, under a stratus deck on July 18, 1991; concentrations of CN shown as light line, and of CCN as dark line. Bars indicate times when a filter check was in progress.

Acknowledgments: This research was supported by the National Science Foundation, ATM-8919935; the Office of Naval Research, N00014-91-J-1090; the National Aeronautics and Space Administration, NAG-1-1113; and the Department of Energy, DE-FG08-90ER61012. The aircraft measurements in Figs. 1-3 were made aboard the National Center for Atmospheric Research Electra. The shipboard measurements in Figs. 4 and 5 were made in cooperation with Dr. William Porch of Los Alamos National Laboratory.

REFERENCES:

Albrecht, B.A., 1989: Aerosols, cloud microphysics, and fractional cloudiness. Science, 245, 1227-1230.

Arking, A., 1991: The Radiative Effects of Clouds and their Impact on Climate. Bull. Amer. Met. Soc., 72, 795-813.

Conover, J.H., 1966: Anomalous cloud lines. J. Atmos. Sci., 23, 778-785.

Hindman, E.E., W.M. Porch, J.G. Hudson and P.A. Durkee: Ship produced clouds of 13 July 1991, this preprint volumn.

Hudson, J.G., 1989: An instantaneous CCN spectrometer. J. Atmos. & Ocean. Tech., 6, 1055-1065.

Hudson, J.G., 1991: Observations of anthropogenic CCN. Atmos. Environ., 25A, N. 11, 2449-2455.

Hudson, J.G. and P.R. Frisbie, 1991a: Surface CCN and CN Measurements at Reno, Nevada. Atmos. Environ., 25A, No. 10, 2285-2299.

Hudson, J.G. and P.R. Frisbie, 1991b: Cloud condensation nuclei near marine stratus. J. Geophys. Res., 96, No. D11, 20,795-20,808.

Radke, L.F. and P.V. Hobbs, 1969: Measurement of cloud condensation nuclei, light scattering coefficient, sodium-containing particles, and Aitken nuclei in the Olympic mountains of Washington. J. Atmos. Sci., 26, 281-288.

Twomey, S., 1977: The influence of pollution on the shortwave albedo of clouds. J. Atmos. Sci., 34, 1149-1152.

Twomey, S., H.B. Howell and T.A. Wojciechowski, 1968: Comments on "Anomalous Cloud Lines". J. Atmos. Sci., 25, 333-334.

Twomey, S. and T.A. Wojciechowski, 1969: Observations of the geographical variations of cloud nuclei. J. Atmos. Sci., 26, 684-688.

AN INVESTIGATION OF THE PROCESSES CONTROLLING THE LIQUID PHASE MICROPHYSICS OF STRATOCUMULUS AND CUMULUS CLOUDS

K.N. Bower and T.W. Choularton

Physics Department, UMIST. P.O. Box 88 Manchester M60 1QD

1. INTRODUCTION

In this paper we present data gathered by the UK. Meteorological Office Hercules aircraft in stratocumulus clouds and by a number of aircraft in convective clouds from the CCOPE experiment over the continental USA. The data have been used to investigate the differing roles of the following physical processes in controlling the microphysics of the cloud systems:
1. Dry air entrainment in affecting the cloud microphysics and precipitation efficiency; 2. The role of cloud top entrainment instability on the cloud dynamics and lifetime; 3. The effects of radiative transfer on the cloud dynamics and microphysics; 4. The importance of the Cloud Condensation Nucleus (CCN) size distribution in determining the cloud microphysics compared to processes 1 to 3.

A model of the effects of dry air entrainment on cumulus clouds has been developed to aid the data interpretation.

2. THE STRATOCUMULUS CLOUDS

The data presented was gathered during aircraft passes through marine stratocumulus clouds off the coast of California, during the FIRE experiment of 1987. Our methods of treating this data are presented in Bower and Choularton 1992.

Much of the data gathered in these clouds was from passes at different levels in extensive sheets of unbroken stratocumulus. It was found that in these clouds the cloud top entrainment instability criterion was not satisfied. This means that dry air entrained into the stratocumulus deck from above the cloud top would not become negatively buoyant with respect to the surrounding cloud, on mixing with the cloud. The result of this was that the effects of dry air entrainment were only evident very close to the top of the cloud. Figure 1 shows the thermodynamic analysis (Paluch 1979). It can be seen that in the body of the cloud the thermodynamic properties of the air are consistent with the air having its origins from the cloudbase region, whereas figure 1b shows that in the vicinity of cloud top the air consists of a varying mixture of cloud base air and air from the free troposphere.

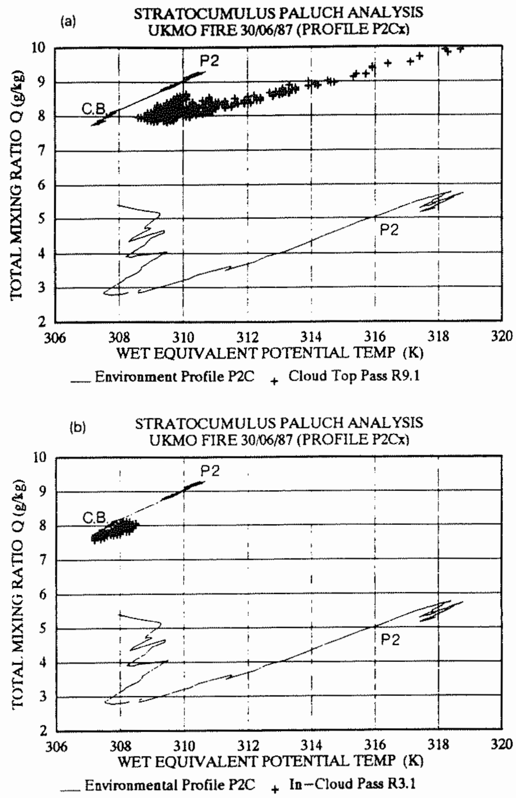

Figure 1 Paluch thermodynamic analysis carried out on the FIRE data from passes through thick stratocumulus cloud
a. Through cloud tops
b. Through solid cloud
The solid line represents environmental data from an aircraft ascent. CB represents the cloud base region of the profile.

It was observed in these clouds that the liquid water content increased approximately adiabatically with height from the observed cloud base to just below the cloud top. The droplet number concentration was approximately conserved with height through this region. In the region close to cloud top, however, rapid fluctuations in the liquid water content and droplet number concentration occurred due to the effects of dry air entrainment. The droplet effective radius is plotted against liquid water content in figure 2. The figure shows the adiabatic increase in droplet effective radius with liquid water content in the main body of the cloud but near cloud top the droplet effective radius is almost constant over a wide range of liquid water contents due to the strongly inhomogeneous mixing in this region.

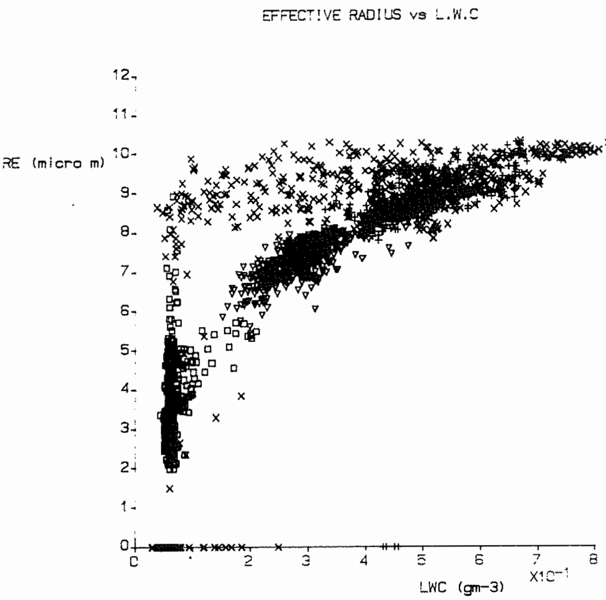

Figure 2 A combined scatter plot of effective radius versus liquid water content generated from 1 Hz data collected in unbroken stratocumulus.
✕ = Pass through Sc Cloud tops
+ = Pass in solid cloud just below cloud top
◇ = In-cloud pass about 40 m below cloud top
Δ = Mid level in cloud pass
□ = Pass just below main Sc cloud base.

It was observed in these clouds that the observed droplet spectrum was always broader than the predictions of a simple adiabatic growth model from cloud base. The observed spectrum contained enhanced growth of large droplets and more small droplets than predicted. This was attributed to the effects of radiative cooling from cloud top causing enhanced growth of the largest droplets in the spectrum, Roach 1976 and evaporation of the smallest droplets. Nevertheless the droplet size and number concentration was essentially controlled by the Cloud Condensation Nucleus Population entering the base of these clouds.

Some flights were also made through more broken stratocumulus decks. In these cases it was found that the cloud top entrainment instability criterion was satisfied.

3. CONVECTIVE CLOUDS

In the cumulus clouds studied it was found that the cloud top entrainment instability criterion was always satisfied. This resulted in penetrative downdraughts with entrained air being transported large vertical distances. The clouds were strongly affected by entrainment at all levels. This mixing was very inhomogeneous with very large spatial and temporal fluctuations in liquid water content and droplet number concentration and much smaller changes in the droplet effective radius.

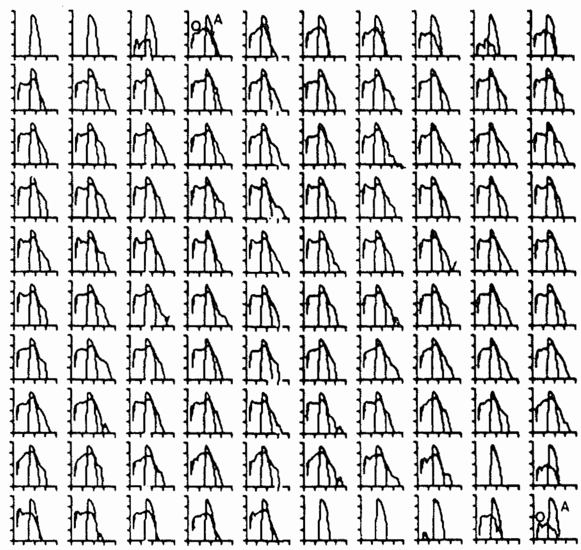

Figure 3 Comparison between observed spectra (O) and adiabatic spectra (A) for continental cumulus cloud.

Figure 3 shows a comparison between the observed droplet spectra, measured at 1 Hz within the body of a cumulus cloud compared to a predicted adiabatic spectrum at the same height in the cloud. It can be seen that the observed spectrum contains many larger droplets than predicted by the adiabatic model and many more small droplets. The observed spectrum is often bimodal. The mechanism responsible for the observed droplet spectral shape is as follows:

Large blobs of dry entrained air affect the ascending cloud turret. These blobs cause the total evaporation of the liquid water in a surrounding region of cloud as the cloud and blob mix. The entrainment of water heat and momentum into this region eventually forces it to ascend causing the supersaturation to rise and the fresh activation of cloud condensation nuclei occurs producing many small droplets. At the same time droplets from the surrounding cloud are mixed producing the bimodal spectrum. Those droplets mixed in early in this process experience a high supersaturation and a boost to their growth. On average an ascending cloud parcel experiences several such entrainment events. The effect of this is that the majority of cloud droplets suffer several cycles of evaporation and regrowth so their average age is considerably less than the age of the cloud parcel.

A small minority of droplets escape evaporation but are subjected to several supersaturation pulses resulting in them experiencing a much enhanced growth promoting the early onset of rain from the cloud by coalescence.

4. CONVECTIVE CLOUD MODEL

A cloud model has been produced which simulates quantitatively the evolution of the cloud described in the preceding paragraph. This is based on the model formulated by Hill and Choularton 1986. In this model the cloud dynamics are calculated from buoyancy effects. The initial activation of droplets at cloud base is described and then blobs of dry air are allowed to enter the cloud at random intervals mixing with the surrounding cloud. If the blob is eventually constrained to ascend due to the entrainment of heat and momentum the new activation of CCN and the growth of droplets mixed into the ascending parcel are calculated. This model produces the main features of the observed cloud droplet size distribution as shown in figure 4.

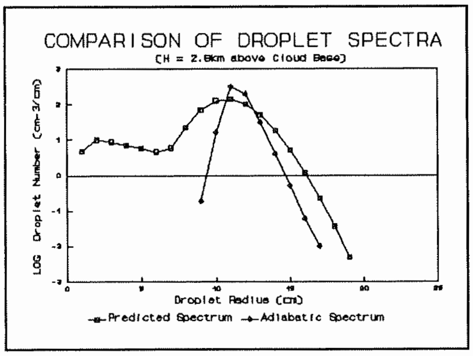

Figure 4 Cloud droplet size distribution predicted by the model compared to a purely adiabatic droplet size distribution 2.8 km above cloud base.

This model has been used to test the sensitivity of the droplet size distribution in the cloud to variations in the cloud condensation nucleus population entering cloud base, and that entrained from the surrounding air. It is found that the repeated new activation of CCN high in the cloud, brought about by the entrainment processes, markedly reduces the sensitivity of the droplet effective radius to the specified CCN populations. This is because the new activation occurs in the presence of droplets from the residual cloud. These have the effect of reducing the peak supersaturation and the number of new droplets activated. This effect is largest when the droplet number concentration is high and smallest when the droplet number concentration is low.

5. CONCLUSIONS

1. Dry air entrainment has very little effect on continuous sheets of stratocumulus as the cloud top entrainment instability criterion is not satisfied. Within the body of the cloud the liquid water contents are close to their adiabatic values (deduced from the height of cloud base) and the droplet sizes and number concentrations are determined by the CCN population entering cloud base.

2. The droplet spectra are broadened by the effects of radiative cooling. The cloud top entrainment instability is important in the break-up of stratocumulus sheets.

3. Cumulus clouds are strongly affected by entrainment at all levels. This results in the enhanced growth of a small fraction of droplets promoting the development of rainfall. The droplet number concentration and size are also much less strongly affected by the CCN population as a result of the effects of entrainment.

ACKNOWLEDGEMENTS

This work was supported by the UK Department of the Environment under contract PECD 7/10/199. We thank the UK Meteorological Office Research Flight for the provision of the stratocumulus data.

REFERENCES

Bower K.N. and T.W. Choularton (1992) Atmospheric Research, 27, 305-339

Hill T.A. and T.W. Choularton (1986) Q.J. Roy. Met. Soc. 111, 773-792

Paluch I.R. (1979) J. Atmos Sci. 36, 2467-2478

Statistical properties of the droplet spatial distribution in stratocumulus.

J. L. Brenguier

METEO-FRANCE, CNRM/GMEI/MNP, 31057 Toulouse Cedex, France.

1. Introduction

The degree of homogeneity of the droplet spatial distribution in a cloud is crucial to understanding condensational droplet growth in convective clouds, but it is not well-understood. In a region of low droplet concentration (compared to the concentration in "uniform regions" of a cloud), the question is to determine if the droplets are homogeneously distributed in space, in which case their condensational growth will be enhanced compared to growth in regions of high concentration. If, on the other hand, the region of low concentration is not homogeneous, consisting of clear air filaments among the cloudy parcels, where locally the concentration is the same as is uniform regions, the condensational droplet growth in the cloudy parts is unchanged. This is even more important when considering the activation phase of the nuclei in droplet free regions. If clear air filaments exist in an updraft and if the nuclei in the filaments are far enough from the nearest existing drops, the supersaturation is likely to increase rapidly and produce activation of these nuclei. On the other hand, if newly entrained nuclei are homogeneously mixed with cloudy air, the existing droplets prevent any increase in supersaturation. Conceptually, inhomogeneities in an updraft will produce spectra made of existing droplets and newly activated nuclei, while homogeneities will produce only dilution of total droplet concentration. Detailed discussion of this question are given in Baker and Latham (1979), Baker et al (1984), Broadwell and Breidenthal (1982), and Brenguier (1990).

Droplet spectra (and total concentration) are measured generally with an optical counter, the Forward Scattering Spectrometer Probe (FSSP). Counts are accumulated during the sampling period (typically from $0.1\,s$ to $1\,s$) and the total droplet concentration is calculated as the ratio of the droplet rate (total reset corrected for coincidence and dead-time effects) to the rate of sampled volume ($200\,cm^{-3}\,s^{-1}$ for an aircraft flying at $80\,m\,s^{-1}$). Therefore, the measured concentration represents the averaged concentration along the sample. In order to document sample homogeneity, it is possible to increase the sampling resolution. Droplet counts (total strobes) have been recorded at a 50 Hz frequency (Rodi, 1981), for a spatial resolution shorter than 2 meters. For practical reasons, this rate is the limit of standard acquisition systems, while 2 meters is still coarse compared to the Kolmogorov scale which in clouds is $\approx\ 1\,cm$. Baumgardner (1986) developed a Particle Spacing Monitor (PSM) for measuring the time interval between FSSP counts and, further, Paluch and Baumgardner (1989) showed that the statistics of the time intervals between counts relate directly to the local droplet concentration in inhomogeneous regions. Recently, the PSM has been improved for a better time resolution, so that progress in fine scale measurements is now limited only by the electronic response of the FSSP, especially the dead-time following each detection.

New electronics have been developed at CNRM to form what has been called a Fast FSSP (FFSSP). Preliminary results from this new probe are presented here. Data were collected in a field of non-precipitating fair weather cumuli from the Météo-France Merlin research aircraft, 50 km south of Paris, in a heavily polluted atmosphere.

2. The Fast FSSP.

In the standard FSSP, optical pulses are processed in real time with analog electronics. In the FFSSP, the optical pulses are digitized just after detection, at 16 MHz, on 8 bits, for real-time digital processing. In the FSSP, each detected pulse is followed by a fixed electronic delay or dead-time ($\approx\ 6\,\mu s$) needed for pulse processing (Fig. 1), during which the detection is blocked. Therefore, the dead-time increases significantly counting losses (Brenguier, 1989). In addition, time intervals can be measured only between reset pulses which are generated at the end of the dead-time (labeled as Δt^* in Fig. 1). The resulting error in the distribution of time intervals is discussed in the next section. In the FFSSP, digital data are processed in real-time, which means that, after an optical pulse has been detected (when signal falls below the detection threshold), a new pulse can be detected immediately, during the following $1/16\ \mu s$. Therefore, the dead-time is negligible and time intervals between pulses are precisely measured.

The following parameters are generated by the real-time processing and recorded for each pulse (Fig. 1): the pulse amplitude related to the droplet diameter, the pulse duration T, the time interval between the end of the previous pulse and the beginning of the current one Δt, and a flag related to the location of the droplet with respect to the depth of field (DOF). The flag is used, as in the FSSP, to select for sizing only droplets passing through this optically defined DOF.

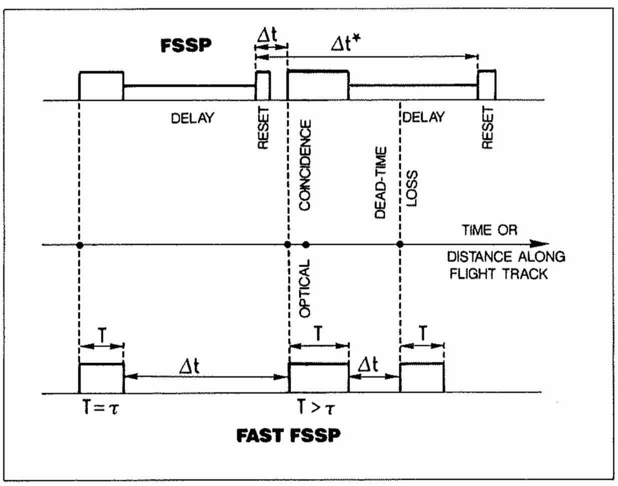

Fig. 1: Schematic timing diagram of pulse detection and processing in the FSSP (top) and in the Fast FSSP (bottom).

With a beam diameter of $200\,\mu m$, the sampling section of the DOF, normal to the air flow, is equal typically to $0.5\,mm^2$, while the total sensible section (in and out the DOF) is about five times larger. The amplitude is digitized with 256 size classes on a linear scale covering a range of droplet diameters from $2\,\mu m$ to $45\,\mu m$ and converted to droplet diameter using a calibration with glass beads corrected for refractive index. T and Δt are measured with a resolution of $62.5\,ns$ (16 MHz), which corresponds to a distance along the flight track of about $5\,\mu m$ for an aircraft flying at $80\,m\,s^{-1}$.

This short paper is only concerned with droplet concentration and no consideration has been given to droplet sizes. Therefore, all pulses, inside and outside of DOF, are accounted for, and the sampled volume corresponds to the total sensible section of the beam, i.e. $200\,cm^3\,s^{-1}$ for an airspeed of $80\,ms^{-1}$.

3. Data processing.

Three measured parameters are available for concentration calculation: the counted rate n_d, the pulse duration T and the time interval Δt between pulses. A raw evaluation of droplet concentration is obtained by dividing the counted rate by the rate of sampled volume. As discussed above, there is no count losses due to dead-time in the FFSSP. However, when two or more droplets are simultaneously present in the beam, they produce a single pulse, i.e. only one count. This is referred to as coincidence losses and, since it is related to optical configuration of the FSSP, it cannot be improved by any electronic modification. When the sampling period is long enough, a statistical procedure can be applied for retrieving the actual rate from the counted rate. However, Brenguier and Amodei (1989) showed that the counted rate is not a good predictor of the actual rate, because when the actual rate increases, the counted rate reaches a maximum (when the actual rate increases from $200\times10^3\,s^{-1}$ to $400\times10^3\,s^{-1}$, a concentration from $1000\,cm^{-3}$ to $2000\,cm^{-3}$, the counted rate increases only from $105\times10^3\,s^{-1}$ to $125\times10^3\,s^{-1}$, which is the maximum). A more accurate evaluation of the actual rate can be obtained if pulse duration T is also measured. Thus, using two measured parameters (the counted rate and the averaged pulse duration during the sampling period $\overline{T}$), two independant parameters can be derived: the actual rate n and the single particle transit-time τ, as:

$$n = \frac{n_d}{1 - n_d\overline{T}} \qquad \text{and} \qquad \tau = \frac{1}{n} ln(\frac{n}{n_d}). \tag{1}$$

In fact, τ is the averaged transit-time of single droplets crossing the cylindrical beam and its predicted value is equal to $\tau = (\pi/4)(d/v_a)$, where d is the beam diameter and v_a is the aircraft speed. τ_0 is defined as the maximum single droplet transit-time generated by a drop crossing the beam in the middle: $\tau_0 = (4/\pi)\tau$.

Figure 2 shows time series of n_d and $\overline{T}$, and the derived n and τ. The figure shows large fluctuations of the actual rate with values higher than $400\times10^3\,s^{-1}$ (concentration $\approx 2000\,cm^{-3}$), while the counted rate is almost constant inside the cloud, these fluctuations resulting from variations of $\overline{T}$. The calculated peak values of concentration are well above values measured previously with standard FSSP's.

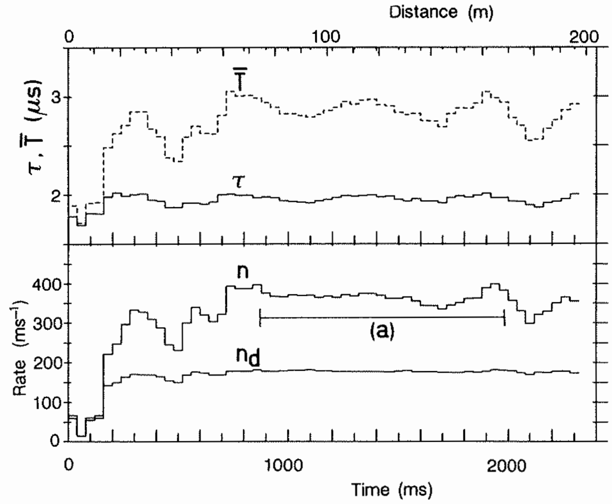

Fig. 2: Time series of FFSSP data processed at 25 Hz: counted rate n_d and actual rate n (bottom); single droplet transit-time τ and mean pulse duration $\overline{T}$ (top).

An alternate means of evaluation of actual droplet rate is also possible by measuring the slope of the cumulative frequency distribution of the inter-arrival times between counts Δt such as measured with the PSM (Paluch and Baumgardner 1989). If droplets are randomly distributed in space with a constant density, this distribution follows an exponential law derived from the Poisson process,

$$P(\Delta t > \Delta t') = e^{-n\Delta t'}, \tag{2}$$

where n is the averaged actual rate for the sample. In inhomogeneous samples, the resulting evaluation of actual rate is biased toward largest local values in the sample (Paluch and Baumgardner, 1989).

It can be seen in Fig. 1 that the time interval measured with the FSSP, Δt^*, is made of Δt, whose statistics follows the exponential distribution, plus the duration of the current pulse and its delay, which should be subtracted from each measured interval (Baker, 1992). The delay is fixed and can be accurately measured in the laboratory, but the pulse duration fluctuates from almost 0 (droplet at the edge of the laser beam) to many times its maximal value for a single droplet τ_0 because of coincidence effects. Figure 3 shows the cumulative frequency distribution of pulse durations (continuous line) for the sample labeled as (a) in Fig. 2. The actual rate (averaged on the sample) is equal to $366\,(ms)^{-1}$. About 40 % of the detected pulses are longer than the maximum value for a single droplet, τ_0, and the mean pulse duration $\overline{T}$ is about $1\,\mu s$ longer than the single particle transit-time $\tau \approx 2\,\mu s$. The dashed line for the cumulative probability distribution predicted by using the coincidence equation (Eq. A.11 in Brenguier and Amodei, 1989) fits correctly the measured distribution and should be used for correcting inter-arrival time distributions measured with a FSSP.

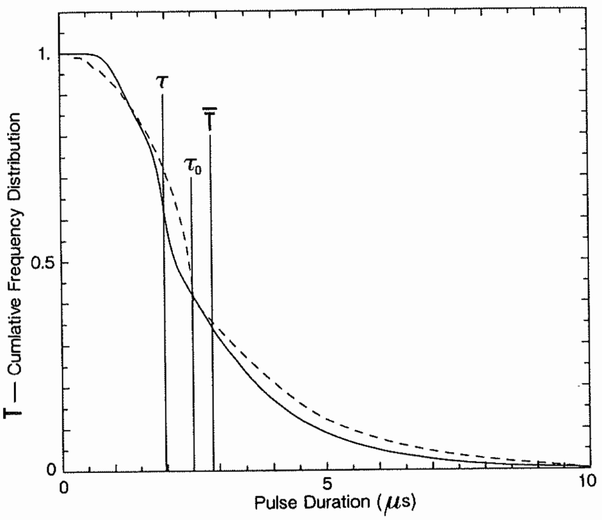

Fig. 3: Cumulative frequency distribution of pulse durations (continuous line) measured along the sample labeled as (a) in Fig. 2. Cumulative probability distribution (dashed line) predicted with the coincidence equation (A.11 in Brenguier and Amodei, 1989). Vertical bars represent the mean single droplet transit-time τ, the maximum single droplet transit-time τ_0 and the mean pulse duration $\overline{T}$.

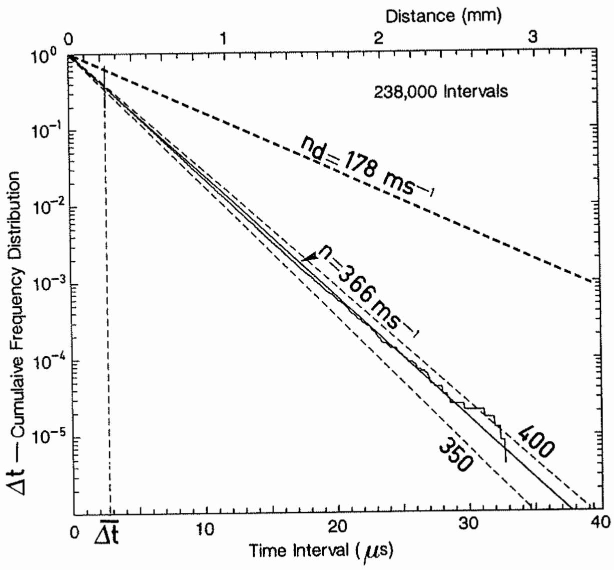

Fig. 4: Cumulative frequency distribution of inter-arrival times between detected pulses (continuous line) measured along the sample labeled as (a) in Fig. 2 and the exponential distribution (continuous straight line) corresponding to the actual rate calculated on that sample, $n = 366\,(ms)^{-1}$. The thin dashed lines show the exponential distributions for $n = 350\,(ms)^{-1}$ and $n = 400\,(ms)^{-1}$. The thick dashed line represents the exponential distribution corresponding to the counted rate $n_d = 178\,(ms)^{-1}$. $\overline{\Delta t}$ is the mean time interval on the sample.

The cumulative frequency distribution of the time intervals, measured with the FFSSP along the sample labeled as (a) in Fig. 2, is drawn in Fig. 4. The plot is based on a set of 238×10^3 intervals (1.33 s of flight), so that the lower portion of the distribution at probabilities smaller than 5×10^{-4} is not significant. The averaged actual rate ($366 \times 10^3\,s^{-1}$) is represented by a continuous line. Figure 2 shows that the droplet rate along the sample is not strictly constant, but varies from $350 \times 10^3\,s^{-1}$ to $400 \times 10^3\,s^{-1}$. These limits are indicated by thin dashed lines apart the measured distribution. The counted rate on the sample is equal to $178 \times 10^3\,s^{-1}$ and it is indicated by a thick dashed line. Two conclusions can be drawn from this figure. On the one hand, the linearity of the measured distribution down to probabilities smaller than 10^{-4} implies that droplet counts by the FFSSP are independent events, which means that the droplets are randomly distributed along the sample. On the other hand, the agreement between the measured distribution and the exponential law with a parameter derived from (1) attests that this equation provides a very accurate evaluation of the actual rate, even at a high coincidence rate. Note the significant value of the coincidence correction factor in this case: $n/n_d = 366/178 \approx 2$.

Despite slight fluctuations of droplet rate, this sample can be considered as uniform. However, the statistics of inter-arrival times is no more suited on a longer sample including the large fluctuations on the left of segment (a). The conditions for an exponential distribution of inter-arrival times are in fact that counts are independent and that the intensity of the process (the actual droplet rate) is constant on the sample. To document a non-uniform region, it is thus necessary to improve the spatial resolution.

4. Fine scale structure.

Since amplitude, pulse duration and time interval are recorded individually in the FFSSP, it is possible to process these data at any scale. In fact, the resolution is limited by the condition that the number of counts per sample is large enough for the coincidence correction to be statistically significant. Figure 5 shows a cloud penetration processed at 25 Hz (3 meters spatial resolution) in (a), at 100 Hz ($0.8\,m$) in (b) and 1000 Hz ($8\,cm$) in (c), only for the segment labeled as (c) in Fig. 5-b. It is obvious that, in this sample, structures exist down to very small scales, with almost undiluted cloud parcells (such as cell labeled as (1) in Fig. 5-c) intertwined with clear air filaments (such as (2) where no droplets have been counted during a one millisecond sample while the averaged time interval between counts in the undiluted parts is less than $3\,\mu s$. The interface, left of cell (1) is very sharp, with a droplet rate increasing from 0 to $350 \times 10^3\,s^{-1}$ in two milliseconds (16 cm). The intermediate sample at this interface (3) with an averaged rate of $150 \times 10^3\,s^{-1}$ has been checked with the distribution of the inter-arrival times showing a strong inhomogeneity with a local rate of $379 \times 10^3\,s^{-1}$, typical of the rate in cell (1). To locate precisely the interface, it is thus necessary to consider the series of time intervals. In this example, the time intervals at the left of the interface are about $900\,\mu s$. At the interface, an interval of $64\,\mu s$ is observed, followed by a series of intervals smaller than $3\,\mu s$. This example (the sharpest interface observed during this flight) shows that the transition from clear to cloudy air can be as small as 1 cm.

5. Summary and Conclusions.

New FSSP electronics have been developed for accurate measurements at very small scale. Crucial parameters are recorded for each detected pulse. From the instrumental point of view, these data allow to verify the accuracy of the coincidence equations derived previously for a standard FSSP, especially for the frequency distribution of pulse durations on which the equations are based. With the frequency distribution of the inter-arrival times between pulses, it has been shown that actual rates up to $400\,(ms)^{-1}$ (a concentration of about $2000\,cm^{-3}$) are accurately derived with these equations.

These data are used for studying the fine scale cloud structures especially at the interface between the cloud and the environmental clear air. Droplet concentration can be calculated down to scales smaller than 10 cm. At smaller scales, the number of counts per sample becomes too small, the randomness of the counting process becomes critical and the values of concentration are no more significant. However, the study of the measured series of inter-arrival times is convenient for detecting sharp discontinuities in the droplet spatial distribution.

Dynamical measurements are limited on aircraft at larger scales (few meters). The FFSSP data can be useful for analyzing the microstructure of turbulence in clouds. A preliminary analysis is proposed in a companion paper (Rodi et al, 1992).

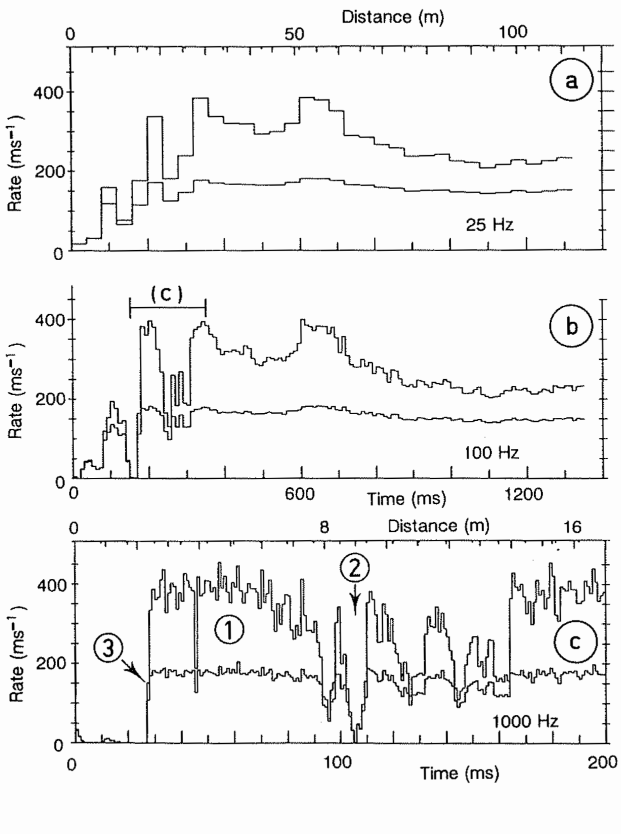

Fig. 5: Time series of FFSSP data: counted rate n_d (lowest) and actual rate n (highest), processed at 25 Hz (a), 100 Hz (b) and 1000 Hz (c) only for the sample labeled as (c) in figure 5-b.

The FFSSP data are also valuable for accurate measurements of the droplet sizes, especially the pulse duration for rejection of the long pulses of coincident droplets which lead generally to an overestimate of the concentration of big drops. This study will be presented in the near future (Brenguier et al, 1992).

Acknowledgements. I am grateful to D. Trevarin and R. Peytavi (METEO-FRANCE) for their contributions to the FFSSP, to P. Weschler (Univ. of Wyoming) for his contribution to the acquisition system and to A. Rodi (Univ. of Wyoming) for his helpful comments and suggestions. This research was supported by METEO-FRANCE, ARAT and INSU under grant 9136173.

References

Baker, B., 1992: Turbulent entrainment and mixing in clouds, a new observational approach, *J. Atmos. Sci.*, **49,** 387-404.

Baker, M. B., and J. Latham, 1979: The evolution of droplet spectra and the rate of production of embryonic raindrops in small cumulus clouds. *J. Atmos. Sci.*, **36**, 1612-1615.

———, R. E. Breidenthal, T. W. Choularton, and J. Latham, 1984: The effects of turbulent mixing in clouds. *J. Atmos. Sci.*, **41**, 299-304.

Baumgardner, D., 1986: A new technique for the study of cloud microstructure. *J. Atmos. Oceanic. Technol.*, **3,** 340-343.

Brenguier, J. L., 1989: Coincidence and dead-time corrections for the particle counters. Part II: High concentration measurements with an FSSP, *J. Atmos. Oceanic. Technol.*, **6,** 585-598.

———, 1990: Parameterization of the condensation process in small nonprecipitating cumuli. *J. Atmos. Sci.*, **47,** 1128-1148.

———, and L. Amodei, 1989: Coincidence and dead-time corrections for the particle counters. Part I: A general mathematical formalism, *J. Atmos. Oceanic. Technol.*, **6,** 575-584.

———, D. Trevarin, R. Peytavi and P. Wechsler, 1992: New electronics for the FSSP: the Fast FSSP. Submitted to *J. Atmos. Oceanic. Technol.*.

Broadwell, J. E., and R. E. Breidenthal, 1982: A simple model of mixing and chemical reaction in a turbulent shear layer. *J. Fluid. Mech.*, **125,** 397-410.

Paluch I. R., and D. G. Baumgardner, 1989: Entrainment and fine-scale mixing in continental convective clouds. *J. Atmos. Sci.*, **46**, 261-278.

Rodi, A., 1981: Study of the fine scale structure of cumulus clouds. Doctoral Thesis, University of Wyoming, Laramie, Wy., 308pp.

Rodi, A. R., J. L. Brenguier, and J. P. Chalon, 1992: Case study of cumulus microstructure with the new FFSSP. *Preprints* 11^{th}*Int. Conf. on Cloud Physics*, Montreal.

INTERPRETATION OF FINE-SCALE MEASUREMENTS IN WARM CUMULUS CLOUD

R. Paul Lawson[1], Bradley A. Baker and Darrel Baumgardner

National Center for Atmospheric Research[2]
Box 3000 Boulder, CO. 80307

1. Introduction

Recent attention has been directed toward airborne measurements and interpretation of the interarrival times of cloud droplets (Baumgardner 1986; Paluch and Baumgardner 1989; Brenguier 1990; Baker 1992). Mostly, interpretations of these measurements have been used to identify homogeneous and inhomogeneous regions of droplet concentration in clouds. Baker (1992) developed the "fishing test" that gives a statistic that is very sensitive and locates inhomogeneous regions with 99% confidence.

The use of interarrival times of cloud droplets as a quantitative means of identifying homogeneous and inhomogeneous regions in cloud has been based solely on measurements from the forward-scattering spectrometer probe (FSSP). Recently, Lawson and Rodi (1992) introduced a new fast-response airborne thermometer that can be used for in-cloud temperature measurements (preliminary tests indicate that the sensor stays dry in clouds without large concentrations of drizzle-size drops). In this paper, we present airborne measurements from the NCAR droplet spacing monitor (Baumgardner et al. 1992) and the new temperature probe. A simple temperature statistic is compared with the fishing statistic developed in Baker (1992); homogeneous and inhomogeneous regions in cloud are independently identified and compared.

2. Instrumentation

The NCAR King Air was used to investigate small, warm cumulus clouds near Corpus Christi, Texas in May 1990. The NCAR droplet spacing monitor (DSM) described by Baumgardner et al. (1992) was incorporated into one of the two PMS FSSP instruments installed on the King Air. A 125 KHz clock was used to generate 8 μs "clicks" to monitor the time between drop arrivals. At the nominal airspeed of 90 m s^{-1} one click corresponds to a spacing interval of about 0.72 mm. Instrumental problems associated with the FSSP have been discussed by several authors (eg., Cooper 1988; Brenguier and Amodei 1989 a,b). Details of the DSM measurements are discussed in Baumgardner et al. (1992) and Baker (1992).

The new temperature probe was designed to avoid wetting of the small thermocouple sensor in cloud. Also, the sensor is not contained in a housing per se, so that it is not affected by heat-transfer from the housing, a problem common to other airborne thermometers currently in use (Lawson and Rodi 1992). Data from the thermocouple probe were recorded at 250 Hz and electronically-filtered with a 4-pole Butterworth filter that had a –3 dB point at 50 hz. Airborne tests in clear air showed that the new thermocouple probe followed the expected -5/3 slope out to 50 Hz, while the Rosemount and reverse-flow probes rolled off at about 10 Hz.

For this experimental set-up, data from the DSM and thermocouple probe were recorded on separate data acquisition systems. There is some degree of subjectively involved in registering time series from the two systems. Also, and there were occasional spikes in the FSSP/DSM derived liquid water content when the velocity rejection circuitry malfunctioned.

3. Interpretation of Measurements

Figure 1 shows measurements of (FSSP) DSM liquid water content (LWC) and temperature from the Rosemount total temperature probe, the NCAR reverse-flow probe and two sensors on the thermocouple probe during penetration of a small cumulus cloud. The data were collected as the King Air penetrated the cloud(s) from downwind, and the measurements show the expected erosion of LWC from the upshear to downshear portions of the cloud(s). Measurements from the four temperature sensors are within the expected uncertainty before entry into cloud (i.e. ~0.3°C), but the Rosemount and reverse-flow temperatures both diverge from the thermocouple temperatures in a way consistent with sensor wetting (Lawson and Cooper 1990; Lawson and Rodi 1992). In addition, much of the temperature structure observed by the thermocouple sensors is smeared in the other temperature measurements, most likely due to sensor-wetting and inadequate time response (Lawson and Rodi 1992). The measurements from the Rosemount and reverse-flow probes were shown in Fig. 1 for the purpose of comparison and will not be discussed further in this paper.

[1] Permanent Affiliation: SPEC, Incorporated, Boulder, CO
[2] NCAR is Sponsored by the National Science Foundation

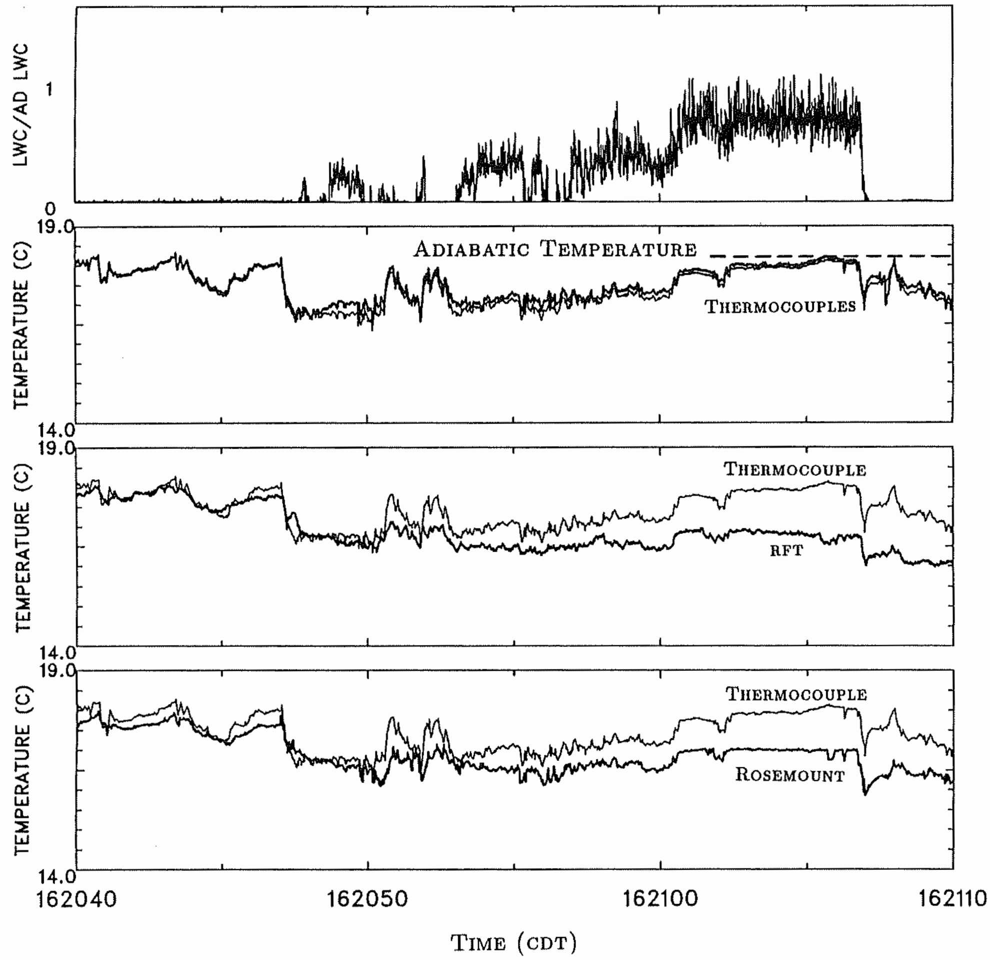

Figure 1. *Time series of aircraft measurements showing (from top) liquid water content divided by adiabatic liquid water content, temperature from two thermocouple sensors mounted on a new airborne thermometer, temperature from reverse-flow thermometer (RFT) and (bottom) temperature from Rosemount probe compared with thermocouple sensor. Example shows typical errors from wetting of the RFT and Rosemount sensors.*

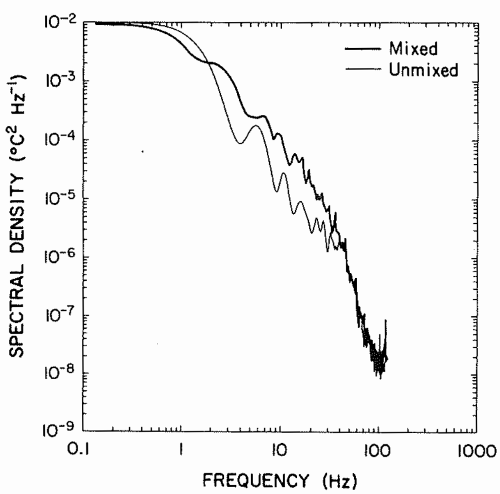

Figure 2. *Spectral densities computed from 250 Hz temperature measurements taken by the new thermocouple probe in unmixed region of cloud (162103–162107 in Figure 1) and region of cloud experiencing mixing (162056–162100 in Figure 1).*

In Figure 1, the adiabatic temperature and LWC were computed by lifting a parcel adiabatically from (measured) cloud base pressure (960 mb) and temperature (23.2°C) to the observation level (830 mb). The temperatures measured by the thermocouple sensors are in very good agreement with the adiabatic values. However, the LWC measured by the FSSP/DSM was too low and the LWC shown in Fig. 1 was normalized to the adiabatic value.

A very noticeable feature in Fig. 1 is the increase in temperature structure from the upshear to downshear regions of cloud. This has been observed previously by comparing measurements of turbulent velocities in homogeneous and inhomogeneous cloud regions (eg., Rodi 1981), however, previous measurements of temperature have been too unreliable in cloud to provide quantitative interpretations (cf., Fig. 1). Figure 2 shows spectral densities computed in unmixed (162103–162107) and mixed (162056–162100) regions of cloud. In this figure, there is more energy in the frequency band corresponding to wavelengths of about 2–50 m (at an airspeed of 90

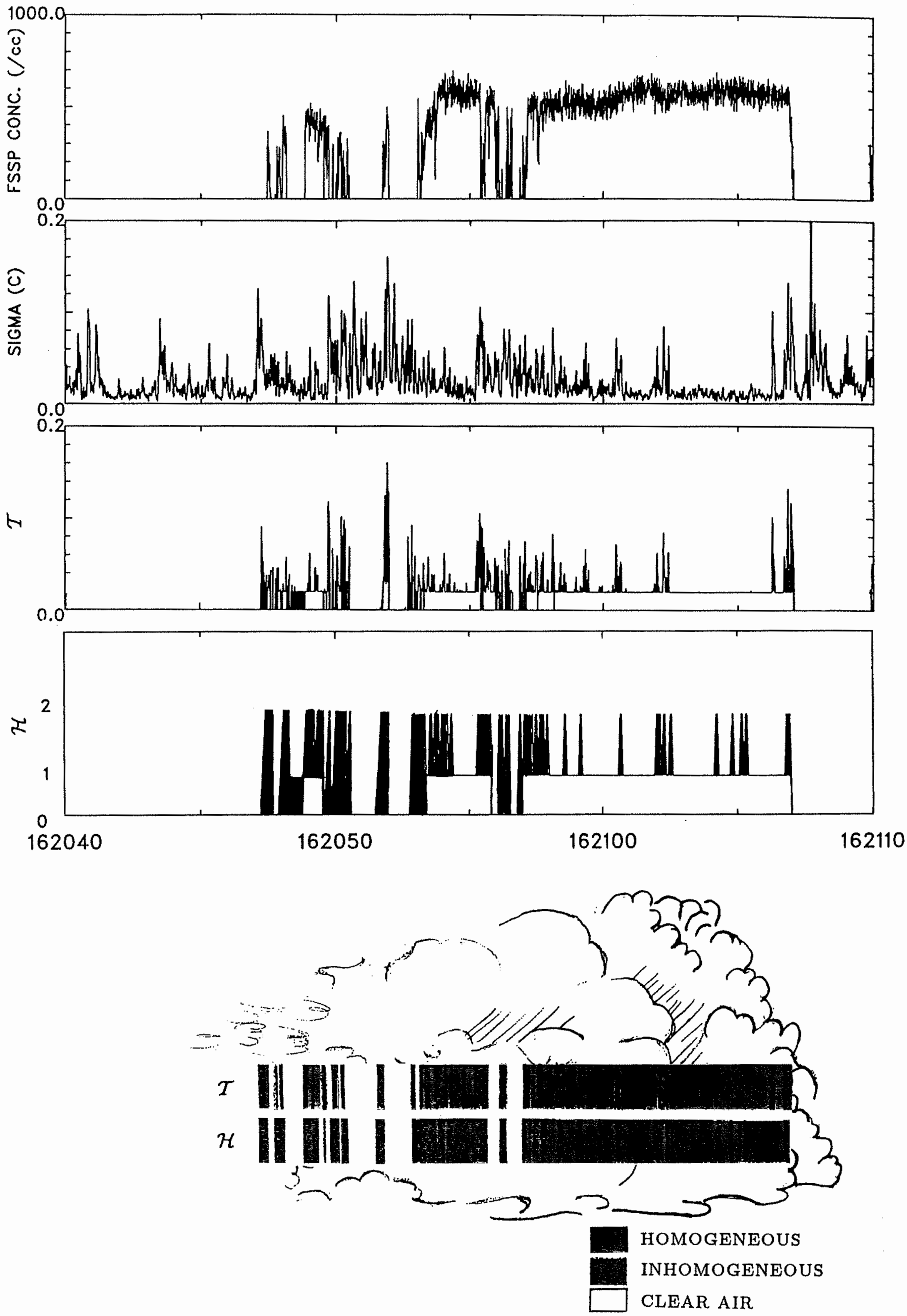

Figure 3. *Time series as in Figure 1 showing (from top) droplet concentration from the FSSP/DSM, 5-m running average of standard deviation in temperature (sigma), $\mathcal{T}$ statistic (defined in test) and results of Fishing Test $\mathcal{H}$ applied over 5-m regions. Sketch at bottom shows homogeneous and inhomogenous regions in cloud determined by $\mathcal{T}$ and $\mathcal{H}$ tests.*

m s^{-1}) in the mixed region of cloud. In addition to electronically filtering measurements with wavelengths < 2 m, the 400 m sample path is too short to collect sufficient data points at wavelengths > 50 m.

The statistic used in the fishing test (Baker 1992) provides an analysis of whether the droplet concentration is homogeneous or inhomogeneous at various length scales, but it does not give an estimate of the degree of homogeneity or inhomogeneity. However, the standard deviation (σ) of temperature can give an estimate of the degree of inhomogeneity. To combine information from the fishing test and the new thermocouple temperature probe, we show in Fig. 3 the result of the fishing test ($\mathcal{H}$) applied over regions of 5 m and σ computed by taking a running average of 14 (250 Hz) data points, which also corresponds to regions of about 5 m. In Fig. 3, regions of clear air are coded as $\mathcal{H} = 0$, homogeneous regions are coded as $\mathcal{H} = 1$ and regions where $\mathcal{H} = 2$ are inhomogeneous regions. In a manner similar to the fishing statistic, but physically arbitrary, we define a temperature statistic ($\mathcal{T}$) such that in regions of clear air $\mathcal{T} = 0$, in-cloud homogeneous regions are coded as $\mathcal{T} = 0.025°C$ when $\sigma \leq 0.025°C$ and $\mathcal{T} = \sigma$ when $\sigma > 0.025°C$.

Figure 3 also shows a conceptual drawing of the cloud with regions defined as homogeneous and inhomogeneous by both tests. Considering that the $\mathcal{H}$ and $\mathcal{T}$ statistics test separate parameters that display different statistical distributions in cloud (i.e., the drop concentration is generally Poisson and temperature is Gaussian), remarkably good agreement is seen in Fig. 3 between the two tests for identifying homogeneous and inhomogeneous cloud regions on a 5 m scale.

In general, the two tests both identify in Fig. 3 the adiabatic regions of cloud as homogeneous and the sub-adiabatic regions as inhomogeneous. However, there are some areas where there is disagreement, for example, in the adiabatic section near 162104 the fishing test shows a small region where there are inhomogeneities in the droplet concentration while there is no evidence of inhomogeneity shown by $\mathcal{T}$. Also, an interesting cloud section was observed near 162100, where both $\mathcal{H}$ and $\mathcal{T}$ suggest that the region is homogeneous and LWC suggests it was diluted. Additional analysis of regions such as these may provide some clues to understanding the processes of entrainment and mixing in clouds.

4. Summary

The fine-scale structure in drop concentration and temperature of a small, warm cumulus cloud that contained both mixed and unmixed cloudy regions was investigated. Measurements were from a new cloud droplet spacing monitor (Baumgardner et al. 1992) and a new fast-response thermometer (Lawson and Rodi 1992) that did not appear to suffer errors from sensor wetting in the clouds studied.

The fishing test (Baker 1992) was applied to droplet spacing data over 5-m regions to identify homogeneous and inhomogeneous sections of cloud. A temperature statistic was developed that performed a running computation of standard deviation, also over 5-m regions. A comparison of homogeneity in cloud using the two independent statistics showed good agreement in both adiabatic and diluted regions.

The fishing test provides a sensitive means of determining inhomogeneity down to mm scales, but does not provide an estimate of the degree of inhomogeneity. On the other hand, the temperature statistic gives an arbitrary definition of homogeneous and inhomogeneous regions, but provides a quantitative estimate of the degree of inhomogeneity. Together the two measurements may provide new ways of interpreting the entrainment and mixing processes in clouds.

References

Baker, B., 1992: Turbulent entrainment and mixing in clouds: A new observational approach, *J. Atmos. Sci.*, **49**, 387–404.

Baumgardner, D., 1986: A new technique for the study of cloud microstructure. *J. Atmos. Oceanic. Tech.*, **3**, 340–343.

Baumgardner, D., B. Baker and K. A. Weaver, 1992: A new technique for measuring cloud structure on centimeter scales. *J. Atmos. Oceanic. Tech.*, In Press.

Brenguier, J. L., 1990: Parameterization of the condensation process in small nonprecipitating cumuli. *J. Atmos. Sci.*, **47** 1127–1148.

Brenguier, J.L. and L. Amodei, 1989: Coincidence and deadtime corrections for particle counters. Part I: A general mathematical formalism. *J. Atmos. Oceanic Tech.*, **6**, 575–584.

Brenguier, J.L. and L. Amodei, 1989: Coincidence and deadtime corrections for particle counters. Part II: High concentration measurements with an FSSP, *J. Atmos. Oceanic Tech.*, **6**, 585–598.

Cooper, W.A., 1988: Effects of coincidence on measurements with a forward scattering spectrometer probe, J. Atmos. Oceanic Tech., 5, 823-832.

Lawson, R. P. and W. A. Cooper, 1990: Performance of some airborne thermometers in clouds. *J. Atmos. Oceanic Technol.*, **7**, 480–494.

Lawson, R. P. and A. R. Rodi, 1992: A new airborne thermometer for cloud physics and atmospheric research. Part I: Design and preliminary flight tests. To Appear in September Issue: *J. Atmos. Oceanic Technol.*

Paluch, I.R. and D.G. Baumgardner, 1989: Entrainment and fine- scale mixing in a continental convective cloud, *J. Atmos. Sci.*, **46**, 261–278.

Rodi, A., 1981: Study of the fine scale structure of cumulus clouds. Doctoral Thesis, University of Wyoming, Laramie, Wy., 308pp.

Microphysical Properties of Warm Clouds

K. Bower*, T. Choularton*, J. Latham*, J. Nelson**, M. Baker**, J.Jensen***, A. Blyth****

* Physics Dept.,UMIST, Manchester M60 1QD, England;
Geophysics Prog. , Univ.of Washington, Seattle WA 98195, USA * Div. Atmospheric Res.,CSIRO, Victoria, 3195, Australia;
**** Physics Dept. NMIMT, Socorro, NM 87801,USA

1. Introduction

In this paper we present observations of the microphysical radiative properties of many types of warm clouds, and we attempt to explain these observations in terms of the predominant physical processes operating within the clouds.

The data used here come from summertime continental cumulus, trade cumulus, hill cap clouds and unbroken marine stratocumulus. Most of these data sets represent 1 Hz measurements made from aircraft at various levels in cloud, and the instrumentation has been fully described elsewhere. (Baker and Latham, 1980 ; Bower and Choularton, 1988; Hill and Choularton, 1985,1986; Jensen et al, 1985; Blyth and Latham, 1991). We limit this discussion to the height dependent mean values of the following variables: $L\,(\frac{g}{m^3})$; r_{eff} (μm); N (cm^{-3}); LWP $(\frac{g}{m^2})$, the liquid water content, 'effective radius', (Stephens, 1978), total drop concentration and liquid water path, respectively.

2. Factors Determining Microphysical Evolution

In a parcel of air that contains N identical cloud condensation nuclei (CCN) and is rising adiabatically, the values of the microphysical parameters at height Δz above cloud base are;

$$1)\quad N(\Delta z) = N = \text{constant}$$

$$2)\quad L(\Delta z) \approx L_{ad}(\Delta z) = \frac{\partial L_{ad}}{\partial z}\Delta z \approx \text{constant x } \Delta z$$

$$3)\quad r_{eff}(\Delta z) = \left(\frac{3L(\Delta z)}{4\pi\rho_L N}\right)^{1/3} \text{x } 100$$

$$4)\quad LWP(\Delta z) = \int_0^{\Delta z} L_{ad}(z)\,dz$$

where the derivative in eq (1) is taken along a moist adiabat and ρ_L (g m^{-3}) is the density of liquid water in eq (2).

Various processes cause the mean observed values of these variables to deviate somewhat from the values given in eqs. (1) - (4). We discuss briefly the roles of (a) the clear air sounding in which the clouds form; and (b) in-cloud processes; in particular, entrainment, in bringing about these modifications in cloud microphysical characteristics.

a. Environmental sounding

The clear air sounding determines the locations of cloudbase and cloudtop and the properties of the entrained air. The resulting links between clear air properties and cloud microphysics have been studied mainly in growing turrets of convective clouds. (Baker and Latham, 1980, 1992; Bower and Choularton, 1988; Hill and Choularton, 1985,1986; Blyth and Latham, 1991; Paluch and Knight, 1984, 1986; Telford and Chai, 1980).

We have investigated the relationships linking cloud microphysics to the sounding in the marine cloudtopped boundary layer. Within the range of variability of the FIRE experiment we find that cloudbase and cloudtop both rise with increasing sea surface temperature (SST), but that there is virtually no correlation between SST and cloud thickness, or microphysics. The microphysical variables were, however, correlated with the properties of the clear air above the inversion and with distance from shore; the clouds nearer the shore had higher drop concentrations N than those further away and $\frac{L}{L_{ad}}$ at cloudtop increased with total water content above the inversion.

b. In-Cloud Processes

Entrainment always acts to decrease L and thus the ratio $\frac{L}{L_{ad}}$ and LWP. Its impact on N depends on whether or not new CCN are entrained and activated and its impact on r_{eff} depends on the detailed nature of the entrainment process.

We find that in general the mean value of $\frac{L}{L_{ad}}$ decreases to about 0.6-0.8 at the tops of unbroken Sc. (Note that when the Sc overly a Cu layer the apparent local value of $\frac{L}{L_{ad}}$ can be even greater than 1.) The mean value of $\frac{L}{L_{ad}}$ decreases to about 0.3 after several kilometers of ascent.

The variability in $\frac{L}{L_{ad}}$ (at constant Δz) is quite high in convective clouds, reflecting the fact that the entrainment process is quite inhomogeneous and is continually modifying the properties of most of the cloudy air.

N varies between about 50 - 200 (cm^{-3}) in the marine clouds measured, with no real pattern above cloudbase. The continental clouds have N = 100 - 600 (cm^{-3}), with a great deal of scatter at constant Δz. The mean number concentration of the droplets depends on chemical and dynamical phenomena outside the realm of this investigation; however, the scatter in N at each level is symptomatic once again of the nature of the entrainment process.

r_{eff} is much less affected by entrainment than the droplet concentration or liquid water content in all the clouds considered. Whereas it falls somewhat below the value predicted by eq (2) during the first 500 meters or so of ascent, the error in this approximation is relatively small. At greater heights the value of the effective radius remains fairly constant. At all levels the variability in r_{eff} is small.

The liquid water path is, of course, less than the value predicted by eq (4) because entrainment reduces the liquid water content.

The vertical and horizontal variability in N, r_{eff} and $\frac{L}{L_{ad}}$ described here has been shown to be consistent with an entrainment process that is very inhomogeneous (see references cited above) .

Absorption and emission of radiation by droplets can in principle either increase or decrease r_{eff} and L(z), leaving N constant (see, for example, Roach, (1976)). The characteristic time for modification of microphysical properties by radiative processes is long compared to the dwell times of air parcels at any given level in convective clouds, but not in stratocumulus, so that we expect to find radiative influences on the microphysical parameters only in the latter. There is some indication that the values of $\frac{L}{L_{ad}}$ and r_{eff} are sometimes slightly higher than those predicted by eqs (1)-(4) near cloudtop in the stratiform and cap clouds, but it is difficult to determine whether these effects are in fact due to radiative cooling, and in any case the effects are quite small.

3. Composite Data and Parameterisations

Figures 1 and 2 show composites of mean microphysical parameters from all the cloud types considered here. We see that N is highly correlated with L, i.e., that r_{eff} changes relatively little with L (or height above cloudbase) after the first few hundred meters of ascent. We will present parameterizations of these patterns based on eqs (1) - (4) and the ideas outlined here.

Acknowledgments: We gratefully acknowledge support from the U.K. Dept. of Environment, Global Atmospheres Division Contract #PECO7/10/199, ONR Grant N00014-90-J-1136 and NSF Grant ATM 89-07929.

References

Baker, M. and J. Latham (1980) Q. J. Roy. Met.Soc. 106,581-598.
Baker, M. and J. Latham (1992) Q. J. Roy. Met. Soc., to be published
Blyth, A. and J. Latham (1991). Q.J.Roy. Met. Soc. 116, 1405-1424.
Bower, K. and T. Choularton (1988) Q.J.Roy.Met.Soc. 114, 1411-1431.
Choularton, T; et; al. (1986) Q.J.Roy.Met.Soc. 112, 131-148.
Hill, T. and T. Choularton (1985). Q. J. Roy. Met. Soc. 111, 517-544.
Hill, T. and T. Choularton (1986). Q.J.Roy.Met. Soc. 111, 773-792.
Jensen, J., P. Austin, M. Baker and A. Blyth (1985) J. Atmos. Sci. 42, 173-192.
Paluch, I. and C. Knight (1984) J. Atmos. Sci. 41, 1801-1815.
Paluch, I. and C. Knight (1986) J. Atmos. Sci. 43, 1994-1998
Roach, W. (1976) Q.J.Roy.Met.Soc. 102, 361-372.
Stephens, G. (1978) J. Atmos. Sci. 35, 2111-2132.
Telford, J. and S; Chai (1980) Pageoph 118, 720-742.

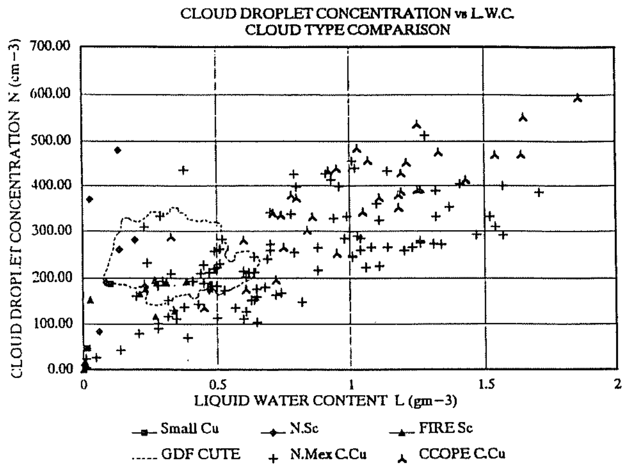

Figure 1

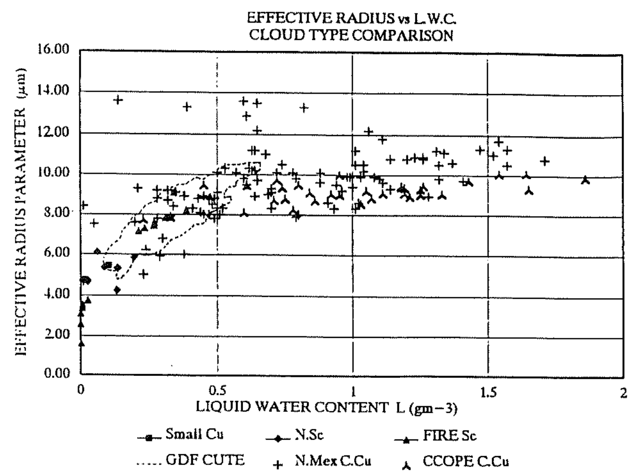

Figure 2

A RADAR STUDY OF THE FORMATION OF RAIN IN CONVECTIVE CLOUDS

Anthony J Illingworth

Dept of Physics, UMIST, Manchester M60 1QD, UK

1. INTRODUCTION

We report polarisation radar data of convective clouds made with the NCAR 10-cm CP2 radar which reveal that early echoes of cumulus clouds usually consist of a small concentration of large raindrops. Echoes below 20dBZ often contain raindrops of size 3 or 4mm in concentrations of less than 0.1 m^{-3}. Normal raindrop concentrations are over 1000 m^{-3}, so these lower values lead us to re-examine mechanisms of rain production, and offer an interpretation in terms of the sweep out of cloud water by ultra-giant nuclei (30-100μm radius).

Recent debate has centred on the suggestion that stochastic effects associated with condensation and with the mixing of drier air into cloud are capable of producing a few larger cloud droplets which can initiate coalescence and the production of rain. Intensive analysis of cloud droplet spectra has not resolved the problem. For example, Hill and Choularton (1985) argued that mixing was causing spectral broadening, whereas Paluch and Knight (1986) found it was not. Cooper (1988) may have resolved this contradiction; analysing the same data, he showed that size dependent optical coincidence effects in the droplet sizing instrument can lead to artificial broadening of the spectra. These radar observations (Illingworth, 1988) represent an alternative approach to the problem.

2. RADAR MEASUREMENT OF RAINDROP SIZE

The differential radar reflectivity, Z_{DR}, is essentially a measure of the mean shape of the hydrometeors, and is defined as:

$$Z_{DR} = 10 \log (Z_H/Z_V) \qquad (1)$$

where Z_H and Z_V are the radar reflectivity factors measured with horizontally and vertically polarised radiation, respectively. Because raindrops are oblate to a degree which depends on their size, Z_{DR} is positive for large raindrops and its magnitude is a measure of their mean size. Once the drop size, D, is known then the concentration, N, may be calculated from the absolute value of Z_H. Assuming an exponential raindrop spectrum of the form:

$$N(D) = N_o \exp(-3.67\, D/D_o) \qquad (2)$$

where D_o is the equivolumetric diameter. The value of Z_{DR} may be calculated as a function of D_o, and N_o found from the observed magnitude of Z (e.g Illingworth and Caylor, 1989). The solid curve in Figure 2 shows the values of Z and Z_{DR} for N_o = 8,000 $m^{-3}mm^{-1}$ as proposed by Marshall-Palmer (1948); for a given Z_{DR}, N_o scales linearly with Z. The values of Z and Z_{DR} reported here, were obtained during the MIST (Dodge et al, 1986) project in Alabama, and are accurate to 1dBZ and 0.2dB, respectively.

3. THE GUST FRONT CASE OF 12 JULY 1986

Figure 1 shows the rain associated with a gust front which was moving towards the radar at a speed of about 60km/hr. The freezing level was at about 5km so the particles are raindrops. In the newly formed echo at a range of 48km the values of Z_{DR} reach 4dB, but the Z_{DR} values in the more mature echo at 55km are much lower even though Z values are similar.

The two raindrop spectra are more obvious from Figure 2, where the average values of Z_{DR} for each 2dB step in Z, are plotted for the two ranges. Because values of N_o scale with Z, we can see that in the new echo at 45-50km range the concentrations are about 100 (20dB) times less than the 'average', while in the mature echo at 55-60km range, N_o is slightly higher than the Marshall-Palmer value.

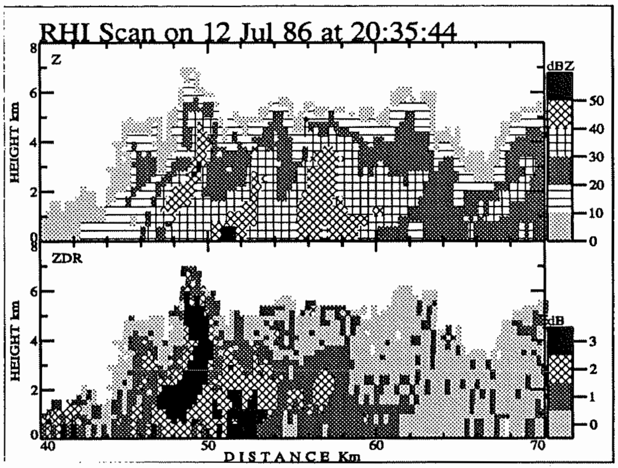

Figure 1. RHI through an approaching gust front. Anomalously high Z_{DR} values in the new echo at 48km.

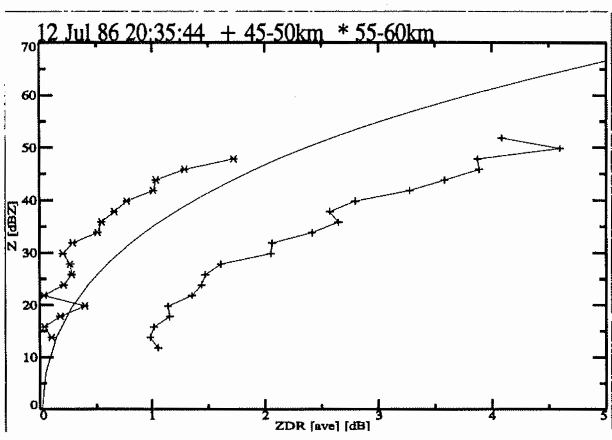

Figure 2. Average values of Z_{DR} for the two ranges in Figure 1. Solid curve; N_o = 8000 m^{-3} mm^{-1}.

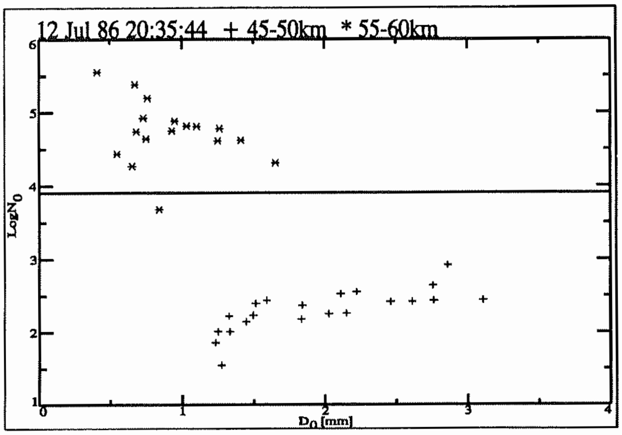

Figure 3. Values of N_o and D_o for the Z and ZDR data in Figure 2. The horizontal solid line is for a Marshall-Palmer spectrum, N_o=8000 m^{-3} mm^{-1} .

This difference in drop spectra at the two ranges is evident in Figure 3, where the average Z/Z_{DR} values are converted to an equivalent value of N_o/D_o. The gust front data indicate lower drop concentrations in newer growing echoes. We find this to be a common occurrence for new cells growing within existing echoes, but interpretation in terms of the mechanism of raindrop growth is difficult because of the possibility of hydrometers being recycled from the mature echo into the new one. In the following examples we will consider isolated echoes.

4. ISOLATED FIRST ECHO OF 10 JULY 1986

A particularly well observed case occurred on 10 July 1986, when a series of 90 vertical (RHI) and horizontal (PPI) radar sections was made through an isolated echo during a 16 minute period. The RHIs in Figure 4 through the most intense part of the echo illustrate the evolution. The data is summarised in Figure 5 which displays the average values of Z_{DR} for each 2dB step in Z for the last three RHIs of Figure 4. The average values all lie on a similar curve, showing that drop concentrations are about 1000 to 10000 (30-40dB) below 'average'.

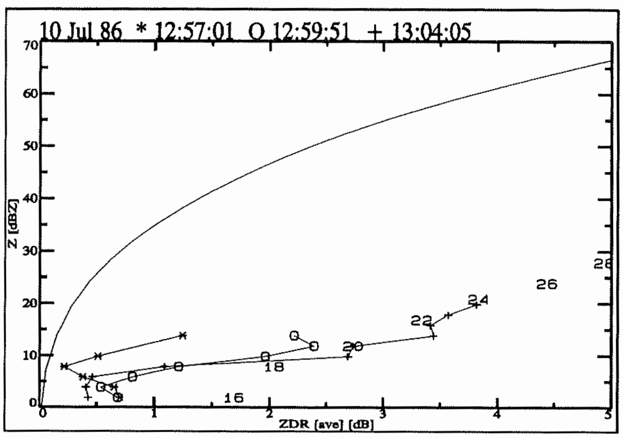

Figure 5. Average values of Z_{DR} for each 2dBZ step in Z for the last three echoes in Figure 4. Solid curve, N_o=8000 m^{-3} mm^{-1}. The numbers indicate the time in minutes since the initiation of a model in which ultra-giant nuclei sweep out cloud water.

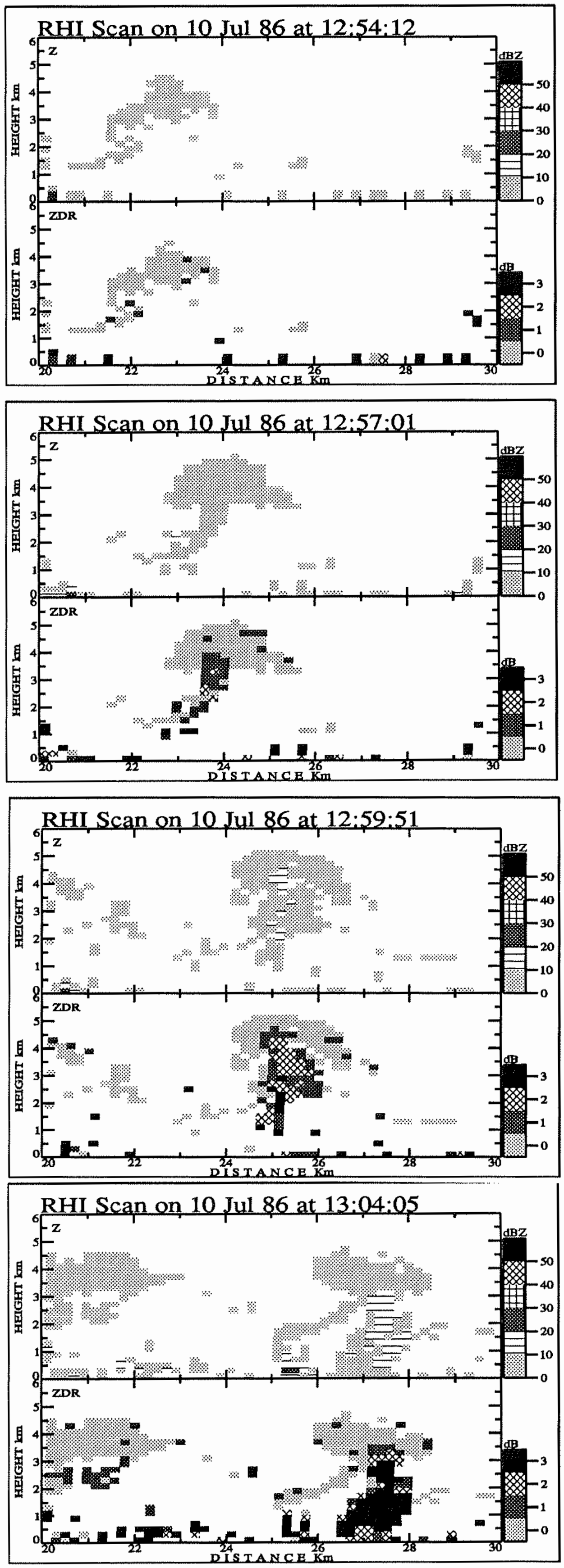

Figure 4. A sequence of four RHIs through an early low Z echo accompanied by high values of Z_{DR}.

The evolution in Figures 4 and 5 is compatible with a situation in which a very few raindrops grow by sweeping out cloud liquid water. For the first RHI at 1254 CST the maximum Z was only 5dBZ, and by 1304 Z had reached a maximum of 20dBZ (accompanied by Z_{DR} values near 4dB). At 1310 (not shown in the Figure) the echo fell to the ground and subsequently disappeared. During this time the echo was unsheared, the horizontal movement was about 6km, its top never rose above 5.5km and the horizontal cross-section never exceeded 2km in diameter.

The average Z_{DR} data in Figure 5 shows that the maximum values of Z and Z_{DR} increase with the passage of time, but that the average values all lie on a similar curve. Plots for the intermediate scans also show a smooth progression along this evolutionary curve. In 4 minutes, from 1300 to 1304 the maximum Z_{DR} increased from 2.4 to 4dB, corresponding to a an increase of the maximum diameter for monodispersed raindrops from 4 to 6 mm, this would occur for the sweep out and collection of cloud droplets with a liquid water content of 2g m^{-3}. During this time the echo descended by about 2km, an average speed of 8m/s, comparable with the raindrop terminal velocity. Analysis of the sonde ascent predicts a maximum adiabatic liquid water content of 3g m^{-3} at a temperature of 8°C. Above this level much drier air, with a mixing ratio of less than 2gm^{-3} at 5°C restricted cloud growth. This supports our assumption that there is no ice in the cloud, as does the complete absence of a bright band in both Z and Z_{DR}.

In Figure 6 the values of N and D, assuming a monodispersed distribution, are calculated for the average Z/Z_{DR} values in Figure 5. As time evolves, the maximum size increases but the concentrations remain low, falling <0.01 m^{-3} for the larger drops.

5. GIANT NUCLEI MODEL

The data in Figure 5 are in very good agreement with the time evolution predicted by a model (Caylor and Illingworth, 1987) in which ultra-giant nuclei of radii in the range 35μm to 1000μm collect cloud water and grow to raindrops. This model extended earlier work (Johnson, 1982) which showed that such a mechanism could produce a high radar reflectivity within 15-20 minutes. Our new model predicts the accompanying values of Z_{DR}. The nuclei need not be hygroscopic but, because they are so large, they collect cloud droplets with reasonable efficiency. The numbers in Figure 5 indicate the time in minutes elapsed since initiation of the mechanism proposed in our model, for a cloud liquid water content of 2g m^{-3} with concentration (in units of m^{-3} per unit log interval of radius) of 1000 for nuclei of 10μm radius to 0.03 for 100μm radius. These nuclei concentrations are those quoted by Junge (1972) for the back ground level above the trade wind inversion and are similar to the 'maritime' nucleus spectrum used by Johnson.

The agreement with the model is very good, both in the magnitude of the Z and Z_{DR} values predicted, and in the time evolution during the 3 and 4 minutes between the three RHIs. The raindrop concentrations on 10 July were very low, a factor of 10,000 (40dB) less than Marshall-Palmer. In most early echoes a factor of 1000 is more typical; this would be explicable if the nuclei concentration of the low level air were ten times higher than the background levels used here.

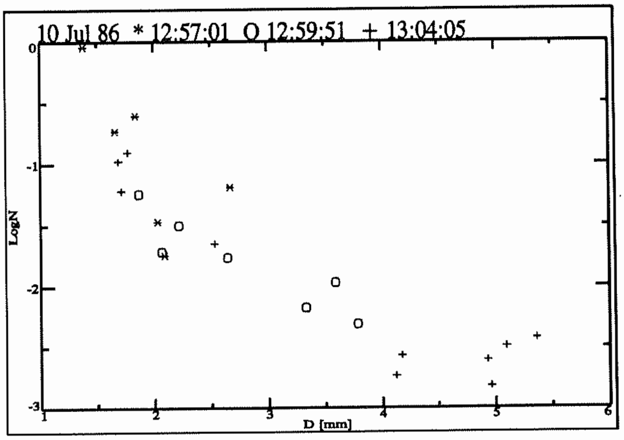

Figure 6. Values of N and D from the Z and Z_{DR} data in Figure 5 assuming a monodispersed spectrum.

6. ECHO EVOLVING TO MATURITY, 28 JUNE 1986

On days of more vigorous convection, the intensifying echo top usually rose above 0°C and the top of the cloud glaciated at the same time as the spectra in the rain tended towards that usually observed in mature clouds. On one occasion, 28 June 1986, it was possible to observe the evolution of an echo to over 50dBZ without any ice forming in the cloud. Figure 7 shows an RHI through the mature cloud at 1240. Before this time two PPIs were taken through the cloud at 1221 and 1227; the temporal resolution is relatively poor because the radar was executing 360° surveillance scans.

Figure 8 shows the average values of Z_{DR} for each 2dB step in Z for the three scans. At 1221 the maximum Z value of 20dBZ was associated with a Z_{DR} value of about 1.5dB, and inferred raindrop concentrations are again more than two orders of magnitude (equivalent to 20dB) below the curve for 'average' rain. Six minutes later, at 1227, Z had reached nearly 40dBZ and Z_{DR} was 3dB, indicating that the biggest drops had grown by 2mm. The concentration of these large drops is still two orders of magnitude below average. By 1240 the highest Z was over 55dBZ, but the picture is dramatically different, the inferred raindrop size distributions are those found in mature clouds.

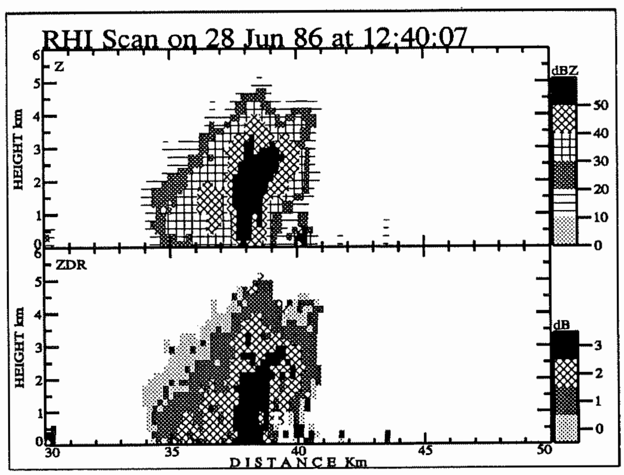

Figure 7. RHI scan through a warm cloud with Z >55dBZ and a 'mature' raindrop spectrum.

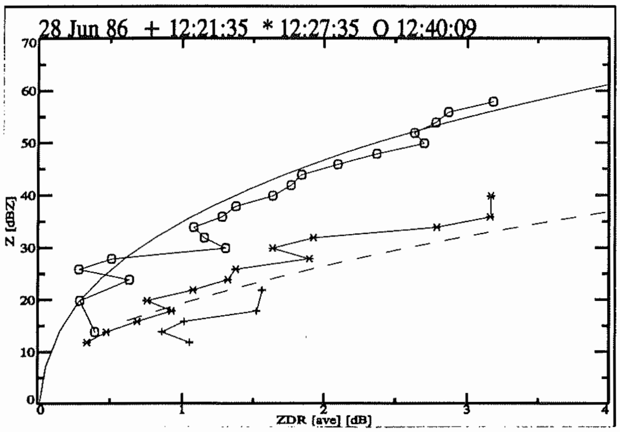

Figure 8. Average values of Z_{DR} for each 2dB step in Z for three separate scans on 28 June 1986. Solid line is Marshall-Palmer drop spectra; dashed line corresponds to a 1000 second lifetime for a 5-mm raindrop before shattering (see text below).

The change in the raindrop spectra is more clearly seen in Figure 9, where the average values of Z_{DR} for each 2dBZ step in Z have been converted into values of N_o and D_o, and the evolution towards the 'mature' Marshall-Palmer spectrum is quite evident. To support our contention that the drop collisions are responsible for this abrupt change in the spectra, the dashed line in Figure 8, represents values of Z and Z_{DR} for which a 5mm raindrop would have an average lifetime of 1000 sec before it collided with another raindrop greater than 1mm diameter; such collisions should be followed by disruption and shattering to produce many small fragments. For a given Z_{DR} the drop concentration is proportional to Z, so the lifetime will be inversely proportional to Z. Note that for the 10 July case in Figure 5, the drop spectra are quite stable because the large drops have a lifetime of several hours before they suffer collision induced rupture. In Figure 8 the concentrations are somewhat higher and by 1227 the drop lifetimes fall below 20 minutes and collisions become more frequent. By 1240 the spectrum has changed to the 'mature' mode, with a high concentration of smaller drops, so that a large drop contributing to a Z_{DR} of 3-4dB would have a lifetime of only a few seconds but would be continuously regenerated.

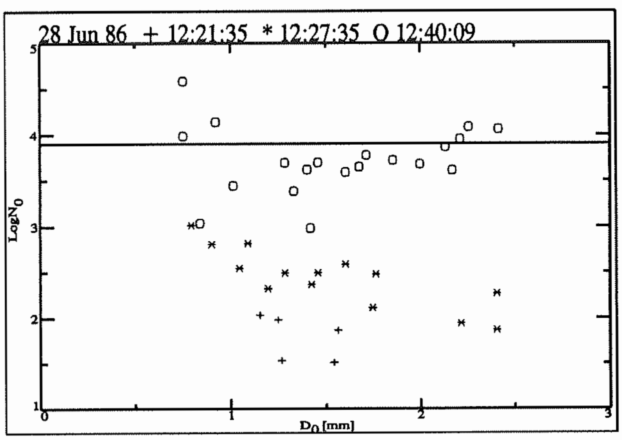

Figure 9. Values of N_o and D_o from the Z and Z_{DR} data in Figure 8. Solid line is N_o = 8000 m^{-3} mm^{-1}.

7. CONCLUSION

The very low concentrations of large raindrops in first echoes reported here confirm earlier more limited observations using the Chilbolton radar in the UK (Illingworth et al, 1987). A statistical analysis of Z/Z_{DR} data (Illingworth and Caylor, 1989) has confirmed that the drop size distributions in these early echoes are quite abnormal. When we consider the infrequency of collisions which would cause the drops to disrupt, then the persistence of these echoes and the growth of very large drops seems quite reasonable. However, once disruption does occur, whether due to collisions or to spontaneous break up of very large drops, then the drop spectrum changes quite rapidly and irreversibly to the more normal 'mature' Marshall-Palmer distribution.

The evolution described above was seen each day during the summer of 1991 in Florida by the CP2 radar in the CAPE project. Each day a series of small isolated low Z/high Z_{DR} echoes would form, each having a lifetime of a few minutes, and when these echoes were penetrated by an aircraft the pilot reported occasional large raindrops hitting the windshield. This pattern would persist for up to an hour, then, as convection became more intense, they would grow to large mature glaciated storms.

Cloud droplet concentrations are above 10^8 m^{-3}, but for first raindrops concentrations are below 10^{-2} m^{-3}, so we need to explain how 1 privileged cloud droplet in 10^{10} grows to become a raindrop. If a theoretical stochastic study of droplet growth does predict that just 1 in 10^{10} particles grows, we must be confident this is not a numerical instability. The most direct confirmation of the ultra-giant nuclei hypothesis would be provided if it was possible to capture the embryonic raindrops when they were about 100μm size; a chemical analysis of the drop should then confirm the presence or absence of an ultra-giant nucleus.

ACKNOWLEDGEMENTS I thank the Professors Bringi, Forbes, Fujita and Wakimoto for allowing access to the MIST data. The author is an affiliate scientist at NCAR. I thank A Openshaw for producing the Figures. Support of NERC GR3/7618 is acknowledged.

REFERENCES

Caylor I.J. and Illingworth A.J. (1987) Q.J.Roy.Meteorol.Soc., 113, 1171-1191.
Cooper W.A. (1988) J.Atmos.Ocean.Tech., 5, 823-832.
Dodge J., Arnold J., Wilson G., Evans J. and Fujita, T.T.(1986) Bull.Am.Met.Soc., 67, 417-419.
Hill T.A. and Choularton T.W. (1985) Q.J.Roy.Meteorol.Soc., 111, 517-544.
Illingworth A.J. (1988) Nature, 336, 754-756.
Illingworth A.J. and Caylor I.J. (1989) J. Atmos. Ocean. Tech., 6, 939-949.
Johnson D.B. (1982) J.Atmos.Sci., 39, 448-460.
Junge C.E. (1972) J.Geophys Res., 77, 5183-5200.
Marshall J.S. and Palmer W.McK. (1948) J.Met, 5, 165-6.
Paluch I.R. and Knight C.A. (1986) J.Atmos.Sci., 43, 1994-1998.

INITIAL DROPLET DEVELOPMENT IN SMALL CUMULUS CLOUDS

G. B. Raga and P. R. Jonas
Pure and Applied Physics, UMIST, Manchester, M60 1QD, UK

1. BACKGROUND

The motivation for this work is to understand the relationship between aerosol concentration, cloud condensation nuclei (CCN) and the eventual formation of cloud droplets. It is of particular interest to study the differences that emerge from considering clean and polluted conditions, in the context of increased urban pollution in the last decades. Aerosol pollution is likely to modify the cloud droplet spectrum which in turn would result in changes in the onset of precipitation. Such changes in the droplet spectrum would modify the radiative properties of the cloud. It has been argued (Twomey et al., 1984) that increased aerosol concentrations would lead to an increase in cloud albedo due to the increased number of resulting droplets. This increase in cloud albedo was found to potentially counteract the greenhouse effect, resulting from increased concentrations of carbon dioxide and chloro–fluorocarbons in the atmosphere.In this paper we discuss microphysical observations obtained in small cumulus clouds that developed in clean and polluted environments.

Measurements were made during 3 flights through fields of small cumulus clouds over the North Sea, utilizing the instrumented Hercules from the Meteorological Office. The datasets include standard state variables and winds as well as detailed microphysical observations. Aerosol concentrations and size distributions were measured by a Passive Cavity Aerosol Spectrometer Probe (PCASP), while cloud droplet concentrations and spectra were measured by a Forward Scattering Spectrometer Probe (FSSP). The PCASP samples aerosols with diameter between 0.11 and 2.74μm. The FSSP has variable ranges, and it can measure particles from 1 to 45μm. A thermal diffusion chamber was used to determine CCN supersaturation spectra. Typically, 4 or 5 measurements with supersaturations between 0.04% and 1.0% were made per air sample. This process takes about 10 minutes, while PCASP and FSSP measurements are recorded at 1Hz.

In two ocassions (flights A085 and A119) the cumuli developed in the cold air behind cold fronts with fairly strong northerly flows and fairly clean environments. The third case (flight A173), behind a very weak cold front, was affected by a developing anticyclone that was suppresing convection. The clouds sampled this day were aligned along a band that appear to coincide with a region of warm sea, shown in the weekly sea surface temperature map produced by the Meteorological Office. Several oil or gas platforms were visible in the area were the measurements were taken. Emissions from these platforms were likely responsible for the very high aerosol concentrations observed this day. One other flight (A117) was conducted during a period of heavy pollution, with an old anticyclone located to the North of the British Isles. No clouds were observed during the sampling period, flying over the Irish Sea.

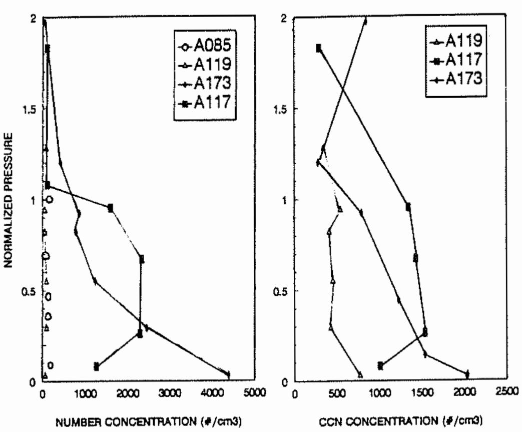

Fig. 1. Aerosol number concentration vs. normalized pressure for clean (A085 and A119) and polluted (A117 and A173) cases studied. a) derived from PCASP and b) derived from CCN measurements.

2. VERTICAL PROFILES

a. Clean cases: A085 and A119

Tephigrams for the 2 flights show fairly similar characteristics: a reasonably well mixed sub-cloud layer; some moisture structure within the cloud layer capped by an inversion, above which the air was extremely dry. Clouds developing during A119 had tops that penetrated the inversion, while those observed during A085 were somewhat shallower. Horizontal winds were northwesterly in both cases, but were stronger (25 m/s) during A085. Vertical shear was slight in both cases, from the surface up to the level of the inversion.

Aerosol concentrations (measured by the PCASP) presented in Fig. 1a, show little variation as a function of normalized pressure, which takes into account the pressure at the base of the inversion and at the surface. The CCN profile for flight A119 is presented in Fig. 1b for supersaturations between 0.8 and 0.9%. The concentration has a maximum of about 800 per cc close to the surface, which decreases to a fairly constant value around 500 per cc higher up. Similar profiles are shown by Hudson and Frisbie (1991) for marine environments off the coast of California. Aerosol size distributions do not show much variation with height, with peak concentrations in the first or second channels corresponding to 0.11 and 0.13μm in diameter.

b. Polluted cases: A173 and A117

The thephigram for A173 revealed the presence of a fairly well mixed surface layer about 250m deep, capped by a very small inversion. Small clouds were observed at this level but the main cloudbase was found higher up, around 600m. The relative humidity in the cloud layer varied between 55 and 90%. A shallow inversion at 850 mb and much drier air above it stopped most of the convection at that level. Horizontal winds were predominantly westerly (7m/s) in the surface layer, and turned to light northerlies (4–5m/s) above it. Measurements during A117 showed that a very strong inversion (6C) was present right from the surface up to 1000 mb, trapping most of the pollutants above this level.
Another inversion at 900 mb corresponded to the top of the boundary layer. The whole profile was very dry, with dewpoint depressions between 10 and 15C and no clouds were obsered to develop. Horizontal winds were light to moderate easterlies showing little vertical shear.

Figures 1a and 1b show the corresponding vertical profiles. Aerosol concentrations sharply decrease with height for A173, clearly indicating production at or close to the surface. In contrast, concentrations are quite uniform between the surface layer and the inversion during A117, consistent with the long–lived nature of the anticyclone. Note that CCN values are significantly lower than PCASP measurements in the polluted cases. Aerosol size distributions above the inversion are quite narrow and have peak concentrations around 0.15μm. The trend towards higher peak concentrations at small sizes coupled with a widening of the spectra is observed with decreasing height for A173. In contrast, little variation of the spectral shape is observed below the inversion for A117.

3. AEROSOL–CCN–CLOUD DROPLETS

Figure 2 shows CCN concentration as function of PCASP aerosol concentrations (averaged over the CCN sampling period) for

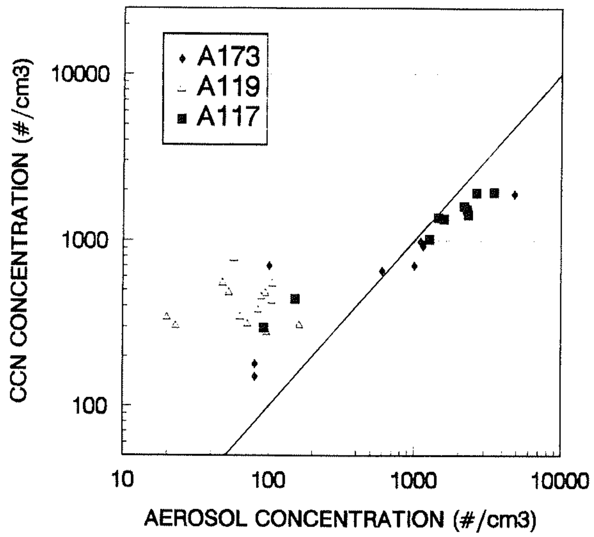

Fig. 2. PCASP aerosol concentration versus CCN concentrations at supersaturations between 0.8 and 0.9% for the 3 cases in which data were available.

supersaturations between 0.8 and 0.9%. The particle size associated with this supersaturation range is generally smaller than that detectable by the PCASP. For PCASP concentrations lower than 1000. per cc, CCN concentrations are higher than those measured by PCASP, as would be expected, since small aerosol particles would not be detected by the PCASP. In contrast, for heavier aerosol loadings, CCN concentrations are substantially lower, which suggests that a considerable fraction (up to 50%) of aerosols are non-hygroscopic. Measurements for A173 were obtained close to gas/oil rigs over the North Sea and emitted particles could have a large fraction of carbon in their composition, which could explain why they were not measured as CCN (Hallet et al., 1986).

The model of a thermal with explicit droplet growth (Mason, 1971) was used to compare with observations. Initial aerosol size distributions derived directly from the PCASP or alternatively, determined from the CCN supersaturation spectra were used. Aerosol particles were assummed to be either sodium chloride or ammonium sulphate. Two separate cases were studied: one with a clean environment (corresponding to flight A119) and one with a polluted one (flight A173).

In the clean case, the sub-cloud aerosol spectrum derived from the PCASP is able to produce a total number of droplets that is in very good agreement with the observations of FSSP droplets in the first pass (roughly 200m) above cloudbase (see Fig. 3). In contrast, the derived

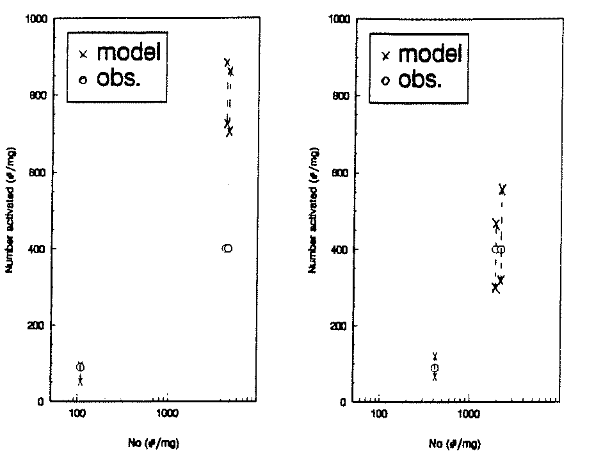

Fig. 3. Number of particles activated vs. initial aerosol concentration predicted by the parcel model (crosses) and observed 200m above cloudbase (open circles). a) initial spectrum measured by PCASP and b) derived from CCN measurements. The top crosses in each case correspond to a non-entraining thermal, while the bottom ones correspond to an entrainment rate of (0.6 U/R).

CCN spectrum includes many more small particles (smaller in size than the first PCASP channel) that do not become activated. The fraction of aerosol particles that become activated in a non-entraining parcel is about 80% in the PCASP case, while only about 30% in the CCN case. Therefore, when conditions in the environment are fairly clean, with aerosol concentrations up to only a few hundred per milligram, PCASP-derived size distributions provide better agreement with observations.

A different picture emerges from the results in the polluted environment. The predicted number of in-cloud droplets using a PCASP-derived spectrum is much larger than that observed, even for the case of an entraining thermal, as is shown in Fig. 3a.In contrast, the droplets resulting from a CCN-derived spectrum are in better agreement with observations near cloudbase. Thus, the inital droplet development in the polluted case is modelled more succesfully using CCN-derived spectra than that measured by PCASP, indicating the relevance of aerosol composition in the absence of CCN measurements.

4. SUMMARY

This paper describes microphysical observations in small cumulus clouds obtained under very different environments: in clean maritime air behind cold fronts and in heavily polluted region close to gas and oil rigs over the North Sea. The sub-cloud aerosol size distributions measured directly by a PCASP and derived from CCN supersaturation spectra are used as starting conditions to study the initial development of cloud droplet spectra. In the clean case, the PCASP measurements are able to predict the observed in-cloud number concentrations. In contrast, in the polluted environment a large fraction (up to 50%) of the observed aerosols do not become CCN. The sub-cloud PCASP size distribution used as initial condition substantially overpredicts the number of cloud droplets observed in this case. It is therefore important to know the composition of the aerosol in the absence of CCN measurements to accurately predict droplet concentrations.

An important issue in the greenhouse warming vs. cooling by clouds debate is to address the question of how cloud development would be affected by increasing levels of aerosol particles, both man-made and naturally produced (such as DMS). A first step at systematically looking at this response is shown in Fig. 4, which indicates decreasing numbers of particles activated for increasing PCASP and CCN concentrations, as also suggested by Twomey et al. (1984). The number of cases analyzed needs to be extended in order to generalized what we have discussed here. As well, we need to observationally determine the changes expected in mean and effective radii under different levels of pollution, which subsequently determine the cloud radiative properties.

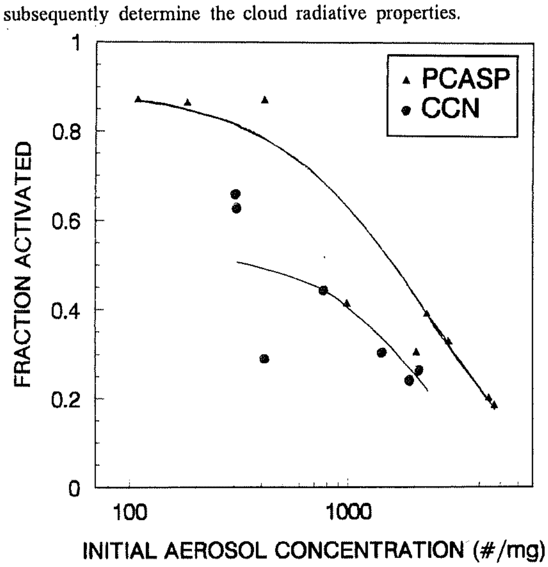

Fig. 4. Fraction of particles activated vs. initial aerosol concentration.

Hallet, J., B. Gardiner, J. Hudson and F. Rogers, 1986. Proc. Conf. Cloud Physics, Snowmass, Colorado.
Hudson, J. and P. Frisbie, 1991. JGR, 96, 20795-20808.
Mason, J.B., 1971: The physics of clouds. Oxford, Clarendon.
Twomey, S.A., M. Piepgrass and T.L. Wolfe, 1984. Tellus, 36B, 356-366.

OBSERVATION ANALYSIS OF THE MICROSTRUCTURES OF SUMMER PRECIPITATING CLOUDS IN NING XIA

Niu Shengjie, Ma Tiehan, Lu Yulian, Guan Yun'e

Ning Xia Meteorological Sciences Institute, YinChuan, 750002, CHINA

1. INTRODUCTION

It is very important to investigate micro-physical structures of clouds and precipitation development in order to carrying on rain enhancement project effectively.Microstructure of summer precipiting As cloud in Ning Xia is analysed in this paper by using the data collected from aircraft measurements. Conceptual model of microstructures for As cloud is also presented. The LWC, cloud drop and snow crystal are measured by using filter paper, film and aluminium foil, respectively.

2.CHARACTERISTICS OF CLOUD DROP SIZE DISTRIBUTION

Table 1 shows the average features of cloud drop size distribution in As cloud under three kinds of weather systems. N, N(d>24 um), and N(d>40 um) are the cloud drop concentration of total, diameter greater than 24 um and 40 um in number per cubic cm, respectively. d1 and d3 are average cloud drop diameter and average cubic diameter respectively.

The mean drop spectra are fitted used the Khrgian-Mazin formula $N(r)=a*r^2*\exp(-br)$. Table 2 shows the results.

3. ICE AND SNOW CRYSTAL FEATURES

Tabel 3 shows the average features of ice and snow crystal size distribution of As cloud under three weather systems.

The vertical profiles of snow concentration shows that the maxium concentration(0.17 L^{-1} to 0.5 L^{-1}) is between -5°C to -8°C.

The Table 4 shows the frequencies of snow crystal, graupel and frozen drop.

4. LWC DISTRIBUTION

The average LWC of the warm layer in As precipitating clouds is greater than that of cold one. The vertical profiles of LWC show one or two peak values locat in the middle of the cloud or below that slightly. The horizontal distribution of LWC indicates non-uniform feature, it's variablity is as high as 455%.

5. MICROSTRUCTURE CONCEPTUAL MODEL AND DISCUSSION

Altostratus of Ning Xia is typical continental cloud. It's drop concentration is the order of 10^2 cm^{-3} , the average is between 55.3 to 442.3 cm^{-3} ,and the average drop diameter is between 3.8 to 4.5 um. According to Table 1, the average drop concentration of cold layer is greater than that of warm layer, but mean diameter and mean cubic diameter of cold layer are smaller than that of warm layer. Except for altostratus under shallow westerly trough. For cold front and low-pressure system,it is the fact that precipitation development mainly occurs in warm part of cloud, cold part may be a place for providing ice crystal. It is probably related to the consistent time of precipitation for these two kinds weather system. On the other hand,for shallow westerly trough,the differences are small between cold part and warm part.

Some average drop spectra is one peak, the other is bimodal. It implies different stage of precipitation development.

The average concentration of ice crystal and snow crystal is 26.5 L^{-1} and 1.64 L^{-1} respectively. The mean diameter of snow crystal is 0.94 mm. The maxium is 5.0 mm.

Frequency of column snow crystal is the highest one, it goes up to 40% . Frequencies of graupel and frozen drop are 0.2 to 4.3% and 0.5 to 5.0% respectively. The peak concentration of snow crystal locates between -5°C and -8°C.

LWC of Altostratus under cold front, low-pressure system and shallow westerly trough is 0.11, 0.08 and 0.05 gm^{-3}respectively.For front and low-pressure system,d3 is 9.1 to 10.8 um for warm part of cloud, and 4.3 to 8.7 um for cold part of cloud, d1 is 4.3 to 5.0 um and 3.8 to 4.4 um, concentration is 111.1 to 352.9 cm^{-3} and 253.1 to 453.7 cm^{-3}, respectively. That is, the cold part is consisted of large amount (compare with warm part) of small drop,these small drop make contribution to LWC chiefly, but warm part is consisted of small amount (compare with cold part) of large drop, these large drop make contribution to LWC chiefly.

The horizontal distribution of LWC is non-uniform, it's vertical profiles shows one or more peak, which locates in the middle of the cloud or /and below the middle slightly.

6. SUMMARY

Altostratus of Ning Xia is mixed phase cloud. According to Table 4, frequency of column and needle crystal is about 60 percent. Due to the cloud top temperature usually above -10°C, it is suggested that 60 percent ice crystal may origin in altostratus itself. There exists LWC that is,supercooled LWC, exists in the cold part. The mean diameter of cloud drop is comparatively small, the average drop concentration is large, therefore, the life period of cloud is in initial stage. Therefore, there is great potential for rain enhancement program.

TABLE 1. Average Features of Cloud Drop Size Distribution in As Cloud

Weather System	Layer	N(cm)	N(d>24)	N(d>40)	d1	d3
Cold Front	Warm Layer(t>=0)	111.1	4.2	2.0	5.0	10.8
	Cold Layer(t<0)	253.1	2.6	1.2	4.4	4.3
	All Layer	240.6	2.8	1.3	4.4	4.9
Low-Pressure System	Warm Layer(t>=0)	352.9	6.7	0.0	4.3	9.1
	Cold Layer(t<0)	453.7	3.8	1.4	3.8	8.7
	All Layer	442.3	4.1	1.2	3.8	8.7
Shallow Westerly Trough	Warm Layer(t>=0)	45.1	3.0	4.2	4.2	10.7
	Cold Layer(t<0)	56.2	2.7	2.1	4.5	12.1
	All Layer	55.3	2.8	2.3	4.5	12.0

TABLE 2. Fitting Results of Cloud Drop Size Distribution.
(r: Correlation Coefficient)

Weather System	Layer	a	b	r
Cold Front	Warm Layer(t>=0)	5.298	0.492	0.96
	Cold Layer(t<0)	15.996	0.598	0.95
	All Layer	14.706	0.571	0.94
Low-Pressure System	Warm Layer(t>=0)	20.018	0.556	0.86
	Cold Layer(t<0)	12.313	0.541	0.93
	All Layer	10.555	0.524	0.95
Shallow Westerly Trough	Warm Layer(t>=0)	1.600	0.501	0.97
	Cold Layer(t<0)	1.313	0.462	0.98
	All Layer	0.898	0.427	0.97

TABLE 3. Average Features of Snow Crystal Size Distribution of As Cloud under Three Mainly Weather System

Weather System	Ice Crystal(L)	Snow Crystal(L)	D(mm)	Dmax	Sample Number
Cold Front	18.5	1.16	0.93	5.0	376
Lower-Pressure System	24.4	2.68	0.98	5.0	299
Shallow Westerly Trough	36.6	1.08	0.90	4.0	209
Mean or Sum	26.5	1.64	0.94	5.0	884

TABLE 4. Frequencies of Snow Crystal, Graupel and Frozen Drop.

Freq. Shape / Weather System	Column	Plate	Needle	Den-dritic	Irre-gular	Frozen Drop	Graupel
Cold Front	36.7	20.9	16.3	14.0	11.3	0.5	0.2
Lower-Pressure System	40.2	17.9	22.2	8.5	2.6	6.0	2.6
Shallow Westerly Trough	40.4	14.9	27.2	2.1	2.1	5.0	4.3

Mass Flux Observations in Hawaiian Cumulus Clouds by Dual-Doppler Radar

Scott Grinnell*, Marcia Baker* and Chris Bretherton**

*Geophysics Program AK-50 **Department of Applied Math FS-20
University of Washington Seattle WA 98195 USA

1. Introduction

Cumulus clouds over the tropical and subtropical oceans account for much of the global transport of heat, moisture and atmospheric tracers between the ocean surface and the free atmosphere. The combined effect of the convective fluxes of all cumulus clouds accounts for the deepening of the boundary layer against subsidence, the global pumping and redistribution of heat and moisture, and ultimately the driving of the Hadley circulation. An understanding of climate and global circulation and the proper parameterization of many numerical models require an understanding of the role played by these atmospheric engines. Understanding the workings of the sum of all cumulus activity, however, demands first an understanding of the single cloud.

In this paper we present the preliminary results of a dual-Doppler study of the vertical mass flux through a cumulus cell that formed five kilometers east of the island of Hawaii on the morning of August 2, 1990.

2. Background and Procedure

The island of Hawaii rises above the ocean and presents an abrupt barrier to the trade winds, often forming a zone of low-level convergence five to fifteen kilometers off its eastern shore. Cumulus clouds regularly develop within the moist trade winds and frequently organize themselves into a quasistable band as a result of this convergence. Within this band, individual cells often undergo numerous periods of growth, decay, and rejuvenation, feeding on the moistened remnants of previous clouds and providing a unique extended opportunity for measuring convective vertical fluxes of mass, heat, moisture, and momentum. The ensemble of fluxes over the cloud field are important to understand because they determine the effects of the cloud field on larger scale circulations. It is therefore important to determine the fluxes averaged over the lifetime of the cloud. Convective fluxes vary significantly as a function of the cloud's evolutionary phase and hence it is vital to use an observational strategy that has good space and time resolution. Doppler radar can provide such a data set, albeit with other limitations.

As part of the Hawaiian Rainband Project (HaRP 1990), the NCAR 5 cm CP-3 and CP-4 Doppler radars, located on the eastern coast of Hawaii approximately 17.5 km apart, made coordinated coplane scans that produced a dual-Doppler analysis lobe extending approximately 30 km offshore. On August 2, the NCAR Electra simultaneously flew stacked penetrations through the cumulus cell, providing a helpful comparison of several important parameters, including wind velocity and liquid water content, as well as supplying a near-environment sounding.

Most of our analysis employs the software package CANDIS developed by Raymond (1988) and assumes a small vertical component to the radar beam. Since Hawaiian trade cumuli tend to produce relatively shallow convection, with cloud tops at roughly 2 km, the cloud to radar distance of 15 km is sufficient to make the approximation a good one. CANDIS includes a standard correction for droplet fall speeds based on reflectivity. We define the cloud cell by a -10 dbz reflectivity contour and average points over approximately a 2.5 minute time interval. The 250 meter horizontal and 200 meter vertical sampling resolution are sufficient to obtain reasonable estimates of the vertical mass fluxes within the cell, which varied in diameter between four and six kilometers over the time of observation. For each 2.5 minute average, the vertical mass flux is independently integrated upward from an altitude of 200 m, where the vertical velocity is assumed to be zero. The resulting mass flux profiles, one for each time interval, are then averaged into a single profile of the average mass flux over the life of the cloud. Our analysis commenced shortly after the first reflectivity exceeded -10 dbz and continued through a period of decay and subsequent rejuvenation spanning nearly half an hour.

Figure 1 depicts a horizontal slice through the area of study at an altitude of 1.2 km and the corresponding corrected INS flight track of the NCAR Electra during the time of the scan. The arrows denote the liquid water content measured by the Electra at the same altitude, with the largest arrow indicating roughly 4.5 g/kg. Included in figure 1 is a sketch of the coastline of Hawaii with the positions of each of the two radars marked by an x. CP-4 was stationed at the Hilo airport and serves as the origin of the coordinates.

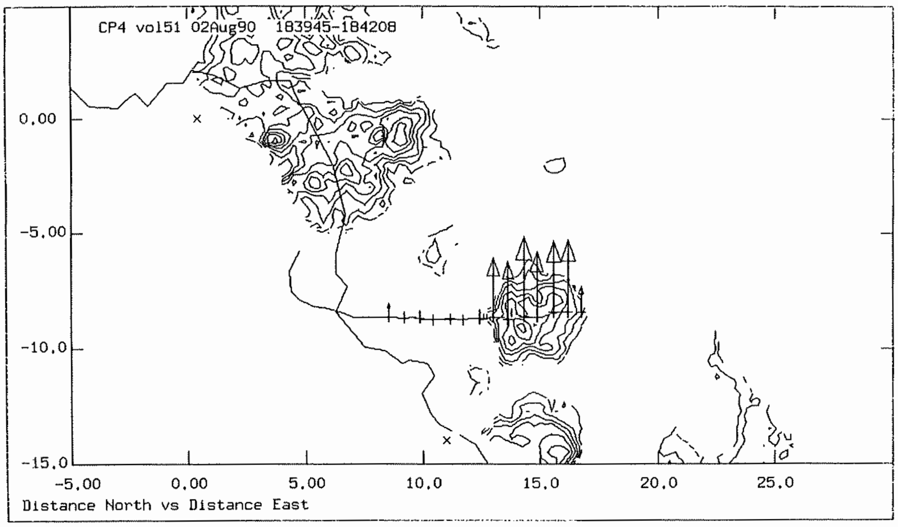

Figure 1. Horizontal slice at 1.2 km altitude. Flight track corresponds to location of Electra during time of scan. Arrows indicate liquid water content with the largest denoting 4.5 g/kg.

The navigational positioning of the Electra has numerous shortcomings that tend to make intercomparisons of radar and aircraft data difficult. The Inertial Navigational System (INS) aboard the Electra drifts both with time and the type of maneuver. Comparisons made with the Global Positioning System (GPS), which tracks aircraft via satellite, indicate that most of the INS drift is linear in time with occasional discontinuities occurring during periods of turning. The GPS, though helpful in making these comparisons, is itself unsuitable for tracking the aircraft because of frequent disruptions in the data.

3. Results and Discussion

Figure 2 shows the vertical flux of mass through the cell averaged over the cloud's life span. The right-hand axis gives cloud height in non-dimensional units, with zero representing cloud base and unity the inversion. Notice that both the upward and downward mass fluxes attain a maximum at the inversion. The upward flux, however, is greater than the downward flux at all levels above cloud base, yielding a net positive mass flux through the cloud. It is unfortunate that the near-cloud environment is not discernible by radar; one could expect to find a net downward mass flux in this region.

The vertical integral of mass flux infers net entrainment upward from the surface to a non-dimensional height of approximately 0.9, with strong detrainment above that level. This can be compared with the results obtained by aircraft penetrations of seventeen growing cumulus cells during the Joint Hawaii Warm Rain Project (JHWRP) of 1985 (Raga, et al., 1990). In that study, entrainment was found to occur at levels

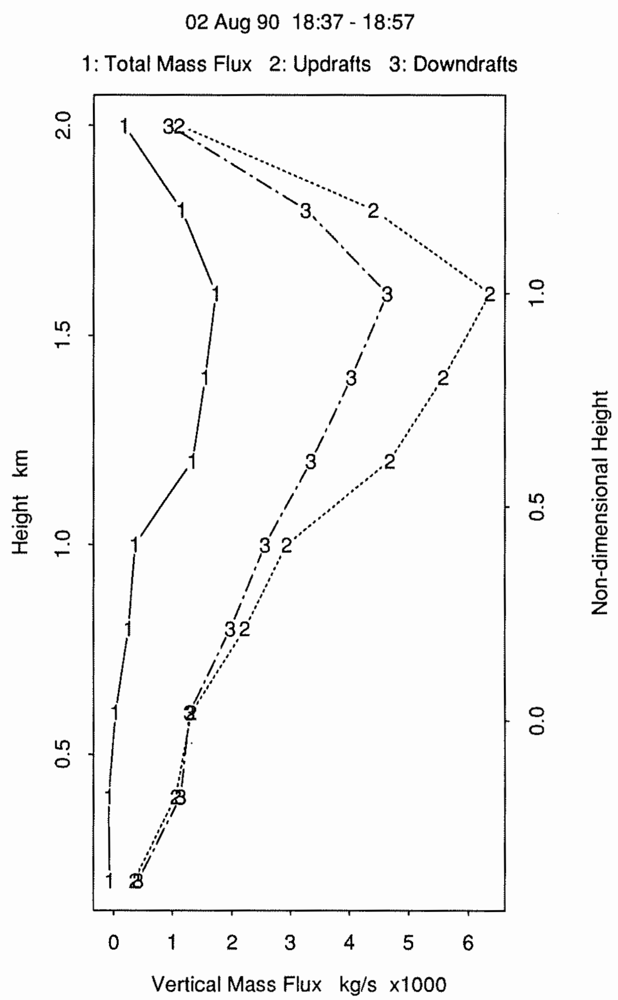

Figure 2. Vertical mass flux averaged over the evolution of the cell using points returning an echo of at least -10 dbz.

below a non-dimensional height of 0.7, with detrainment above. The difference here may be due to the fact that the cumulus cells included in the 1985 study were actively growing and were therefore not representative of the average cloud cycle.

Hawaiian cumulus clouds tend to be relatively short lived and unlike the longer lived continental clouds, do not offer sufficient time for direct aircraft measurement of divergence. This technique for aircraft measurement, which Raymond, et al. (1991) have successfully employed for thunderstorms over New Mexico, consists of an aircraft flying rectangular box patterns around a cloud at differing altitudes. The integrated box-normal component of the wind then yields a direct measurement of the divergence at each level. This method generally requires an hour or more to fly a representative number of loops around a cloud and thereby samples the divergence at differing phases in the evolution of the cloud. This can result in misleading information. Dual-Doppler radar has the advantage of sampling the entire vertical structure during a single time period.

Figure 3 shows the vertical mass flux of the cell for seven discrete time periods. Notice that the fourth time period represents a phase of reduced flux, with a net negative flux even at heights where the cell is at other times strongly positive. This may indicate a period of partial decay in the cell that subsequently rejuvenated. In any case, it is an important contribution to the time-averaged flux over the cell's lifetime. An aircraft flying at different levels around or in the cell would be sampling fluxes at different times.

Radar data, however, has its own limitations. First, echoes may not coincide with regions of vertical motion, particularly during the development stage when droplets are small, leading to biases in flux calculations that are difficult to assess. Furthermore, the cloud periphery, which may contain an important contribution to the overall flux, often fails to yield an echo at all.

Figure 4 illustrates the sensitivity of the flux calculations to the minimum reflectivity defining the cloud. There is an inherent trade off between including as much of the cloud as possible and including data with too weak of an echo for reliability. The first two curves give mass fluxes based on points returning an echo of at least -15 dbz and -10 dbz, respectively. The difference between these appears to be significant primarily

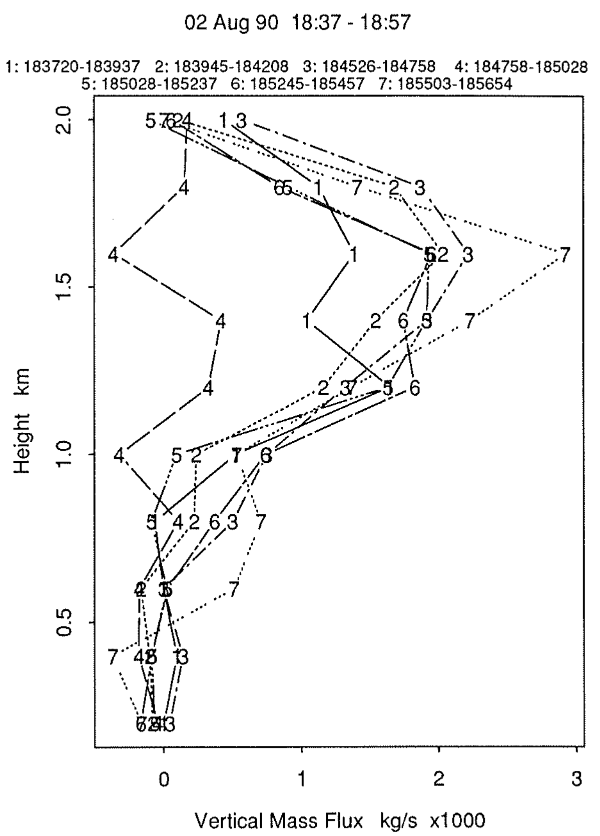

Figure 3. Mass flux at various stages in the development of the cell using points returning an echo of at least -10 dbz.

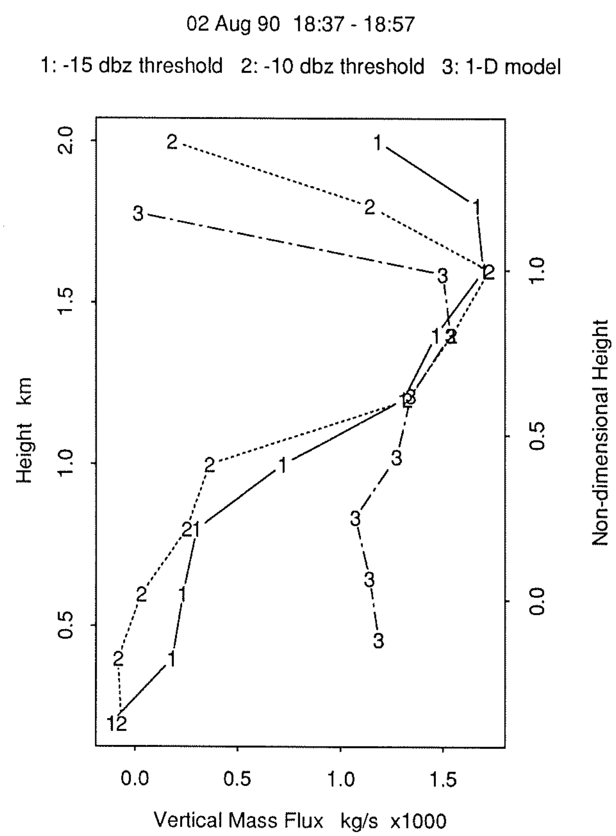

Figure 4. Comparison of the total averaged mass flux using points returning an echo of -15 dbz and -10 dbz with a 1-D buoyancy model.

above the inversion. The third curve shows the results of a one-dimensional Lagrangian model very similar to the model developed by Raymond and Blyth (1986). The model clearly predicts strong detrainment near the inversion.

The results of this paper have been based on the examination of a single cumulus cell. The next step will be to continue the analysis of cells within the dual-Doppler lobe for the day of August 2, and then compile a study derived from other days. Despite the limitations inherent to dual-Doppler radar, we believe this sort of analysis is capable of producing valuable insight into the behavior of cumulus clouds, particularly when augmented by simultaneous aircraft data.

Acknowledgments. This research was supported by the Atmospheric Sciences Section of the National Science Foundation under the Grant NSF-8921054.

4. References

Raga, G. B., J. B. Jensen and M. B. Baker, 1990: Characteristics of cumulus band clouds off the coast of Hawaii. *J. Atmos. Sci.*, **47**, 338-355.

Raymond, D. J., 1988: A UNIX-based modular system for representing and analyzing gridded numerical data., *J. Atmos. Oceanic Tech.*, **5**, 501-511.

Raymond, D. J., and A. M. Blyth, 1986: A stochastic mixing model for nonprecipitating cumulus clouds. *J. Atmos. Sci.*, **43**, 2708-2718.

Raymond, D. J., R. Solomon and A. M. Blyth, 1991: Mass fluxes in New Mexico mountain thunderstorms from radar and aircraft measurements., *Q. J. R. Meteorol. Soc.*, **117**, 587-621.

CLOUD PHYSICS EXPERIMENTS WITH ARTIFICIALLY PRODUCED

HYGROSCOPIC NUCLEI

G.K. Mather and D.E. Terblanche

National Precipitation Research Program
South Africa

1. INTRODUCTION

The coalescence or coalescence-freezing mechanism of precipitation formation (Braham, 1986) has been thoroughly studied in the summer storms that produce more than 80 percent of the annual rainfall in the area around Nelspruit, South Africa (25^{o} 30 S, 30^{o} 55' E). The studies, using instrumented aircraft and radars, indicate that the coalescence-freezing precipitation formation mechanism is a more efficient process than the ice phase mechanism (ice crystal growth by vapour diffusion followed by riming). This is because time limits the growth of precipitation in the vigorous updrafts of the storms found in the region and coalescence, once initiated, proceeds at a faster rate than ice crystal growth, producing large dense graupel that stand a better chance of surviving the updraft (reaching a terminal velocity that exceeds that of the updraft). A simple thermodynamic classification technique, using a measure of cloud base temperature and potential buoyancy, shows considerable skill in separating those clouds showing an active coalescence process at the -10^{o}C level from those clouds with either ice crystals or an absence of any particles at this level (Mather et al. 1986). Furthermore, the data indicate that the buoyancy or the transition zone between ice crystal and coalescence initiated precipitation growth may be a narrow one, implying an instability.

Measurements in storms growing near a Kraft paper mill have demonstrated that the emissions from the mill can dramatically enhance the coalescence process in these storms (Mather, 1991). These observations led to the development of a hygroscopic seeding flare which permits experiments on selected clouds, freeing the research from geographic and other restraints imposed by the mill.

This paper describes ground and airborne tests of the new flares that have determined the chemical composition and the particle spectrum of the combustion products. Also presented are cloud seeding trials which were evaluated using instrumented aircraft and the project radar.

2. THE FLARE

The objective was to manufacture a flare that would produce a hygroscopic particle spectrum similar to the one measured in the emissions from the local Kraft paper mill. A formulation was borrowed from a flare developed by the Naval Weapons Center, China Lake, called a "Salty Dog," and used to produce fog (Hindman 1978). The flare is composed of 18% hydrocarbon binder, 5% magnesium, 10% sodium chloride, 65% potassium perchlorate and 2% lithium carbonate. Tests on the combustion products conducted at the ESKOM engineering laboratory in Johannesburg showed a chemical composition similar to the one deduced by Hindman.

	Hindman (%)	ESKOM (%)
Sodium Chloride (NaCl)	19	21
Potassium Chloride (KCl)	65	67
Lithium Carbonate ($LiCO_3$)	1	-
Magnesium Oxide (MgO)	15	12

The size distribution of the hygroscopic particles emitted by a burning flare was determined by a series of ground and airborne tests. In the first test a Particle Measurement Systems (PMS) FSSP 100 was positioned 2 metres behind a flare burning in a rack attached to the trailing edge of the seeding aircraft's engine nacelle (a Commander 690). The engine was run at about 80% power. The largest particle sensed by the FSSP was 13 microns in diameter. In a second test, sticky glass slides were held for about 4 seconds in the plume of a flare burning in the propeller slipstream. Particles with diameters exceeding 50 microns were found in significant concentrations on these slides. Subsequent scanning electron microscope tests identified the elements potassium and chlorine in some particles whose diameters exceeded 100 microns. The small sample volume of the FSSP 100 may explain why this probe missed the larger particles.

Next, airborne tests were conducted. These were flown at low level early in the morning in calm conditions and relative humidities exceeding 80 percent. An instrumented aircraft with an FSSP 100 and a 2D-C probe was flown 30 to 40 metres behind the seeding aircraft which ignited two flares in the left nacelle rack. Clear images of drops were acquired by the 2D probe. Concentrations of 8 per litre were recorded with the largest recorded particle exceeding 300 microns in diameter (Fig. 1).

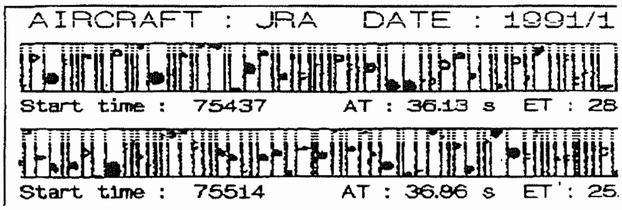

Fig. 1. Drop images from the 2D-C probe on an aircraft flying in the plume from 2 flares burning on the seeding aircraft. Vertical time bars are 800 microns long.

Figure 2 compares the ground and airborne tests on a log/log plot of concentrations versus particle diameters. Differences between the two measurements can be attributed to:

- underestimating the concentrations in the airborne tests, since it was impossible to keep both probes in the plume from the flares at all times

- the deliquescence of the larger hygroscopic particles, causing the knee in the airborne spectrum.

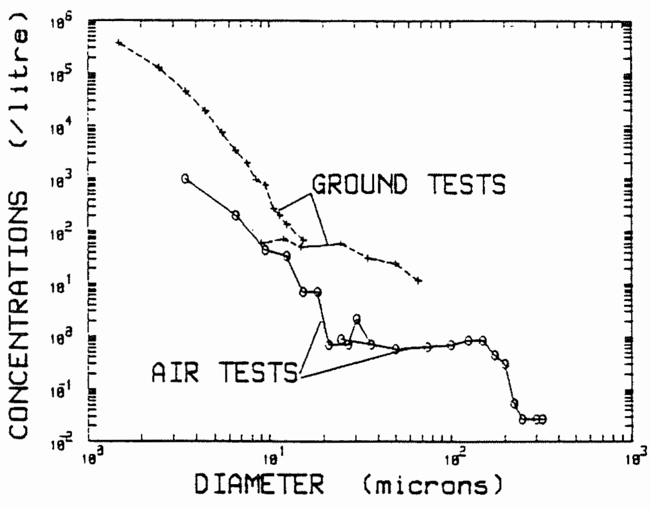

Fig. 2. Measured dry particle combustion spectra from ground and airborne tests of hygroscopic flares. See text for details.

To ensure that the particles sensed by the 2 probes were coming from the flares and not a product of the aircraft's exhaust, a second flight under similar conditions was conducted. Both probes remained inactive while flying in the slipstream of the seeding aircraft until the flares were ignited. The second flight recorded almost exactly the same large particle concentrations (8 l^{-1}).

Calculations assuming a plume diameter of about 2 m indicate that each flare outputs about 10^{11} particles or 10^{8} particles per gram of flare mix larger than 1 micron in diameter. This is probably a gross underestimate of the total dry particle output (see Hindman).

3. SEEDING TRIALS

Seeding trials were conducted using the flare-equipped seeding aircraft at cloud base, the project radar in volume or sector scan mode and the project's Learjet sampling around the -10^{o}C level. The objective was to validate the seeding hypothesis, viz that the release of hygroscopic particles into the updraft at cloud base would trigger or enhance the coalescence precipitation formation process in the treated clouds. A description of one such experiment follows.

The trial reported here took place on October 9, 1990. Two flares, mounted on the Aero Commander, were ignited at 15:56 just below cloud base into the updraft of a small storm. An additional two flares were ignited at 16:00. The Learjet had commenced sampling cloud turrets rising on the northwestern flank of the storm at 15:54 at around the -10^{o}C level (about 5900 m above mean sea level). Mean updraft speeds were between 8 and 9 m/s. The Learjet first encountered evidence of seeding effects at 16:02. Since the seeding aircraft was operating around 3000 m, to reach the altitude of the Learjet in the available 6 minutes, the seeding material would have to rise at a rate of around 8 m/s, which is close to the observed updraft speeds. Table 1 lists measurements made by the FSSP-100 averaged over 1 km around the updraft maximum in each pass. There is a dramatic difference in FSSP measurements between pass 2 and 3. The number of particles with diameters greater than 32 microns increased almost sevenfold from 0.55 to 3.68 cm^{-3}. Fig. 3 shows time histories of FSSP concentrations and updraft profiles for passes 2 to 3. The spectra show the size distribution of the mass of the particles assuming that they are water droplets (spherical with a density of 1 g/cm^{3}) up to the probe size limit of 47 microns.

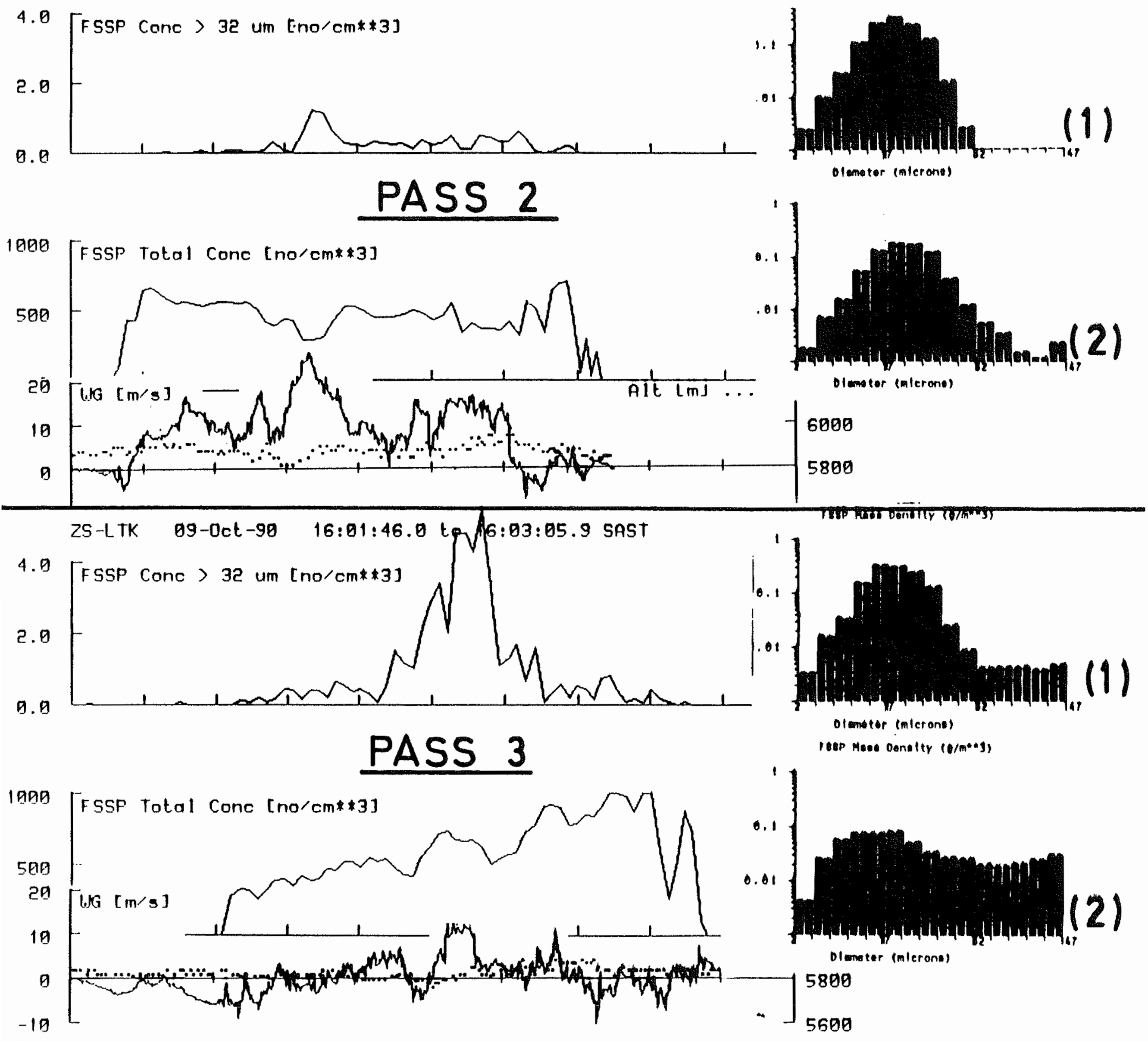

Fig. 3. Total FSSP concentrations and FSSP concentrations > 32 microns and vertical velocities measured on 2 passes through a cloud seeded with hygroscopic flares. The accompanying spectra show how the mass of water is distributed between 2 and 47 microns, and is mesaured over a distance of 1 km around (1) the maximum concentrations and (2) the maximum updraft. Tick marks on X axis are at 1 km intervals.

Table 1. Comparisons of 1 km averages of FSSP measurements around the maximum updraft speed.

	1	2	3	4	5
Pass :	1	2	3	4	5
Time :	15:54	15:58	16:02	16:06	16:10
conc (cm^{-3})	413	393	649	703	391
conc > 32 μm (cm^{-3})	0.39	0.55	3.68	3.77	0.57
LWC (g/m^3)	0.76	0.77	0.57	1.22	0.58
mean dia. (μm)	12.70	12.60	8.50	12.20	11.60
MW mean dia. (μm)	19.00	19.90	21.80	19.90	18.20
Dispersion	0.48	0.53	0.64	0.51	0.51

The spectra are 1 km averages around (1) the maximum FSSP concentrations and (2) the maximum updraft speeds. The flattening of the mass spectra is most pronounced in pass 3 around the maximum updraft speed, indicating that the observed changes are at least initially associated with the updraft. By pass 4, (not shown), the effects were spreading throughout the cloud. On this pass, the maximum recorded FSSP concentration reached 1218 cm^{-3}. A search through our data bases, 6 seasons totalling 826 passes through convective clouds in the area, revealed that the maximum recorded FSSP concentration was 935 cm^{-3}. The point that we wish to make here is that the FSSP measurements presented here, the high concentrations and the flattened droplet mass spectra, have never been observed at these levels in the local convective clouds.

Careful comparisons of the FSSP and 2D-C measurements at one second resolution around the maximum diameters > 32 micron peak indicate that this peak was caused by droplets and not, as was first suspected, by ice crystals. There were 2D images towards the end of the pass, associated with the maximum droplet concentrations, which looked like records normally associated with a seeded dry ice plume (high concentrations of zero images). The implications that this observation may have upon ice multiplication mechanisms are beyond the scope of this abstract.

Fig. 4 shows a time versus height plot of maximum reflectivities recorded by the project radar operating in volume scan mode (one complete scan every 7 minutes). A pocket of high reflectivity (48 dBz) occurred aloft about 13 minutes after seeding commenced and the maximum recorded reflectivity (51 dBz) was observed at cloud base 7 minutes later. It should be noted that this storm was not raining when seeding commenced. The aircraft penetration at 16:10 supports the radar observations, recording graupel with a mass-weighted mean diameter of 2.1 mm and a density of around 0.9 g/cm^3.

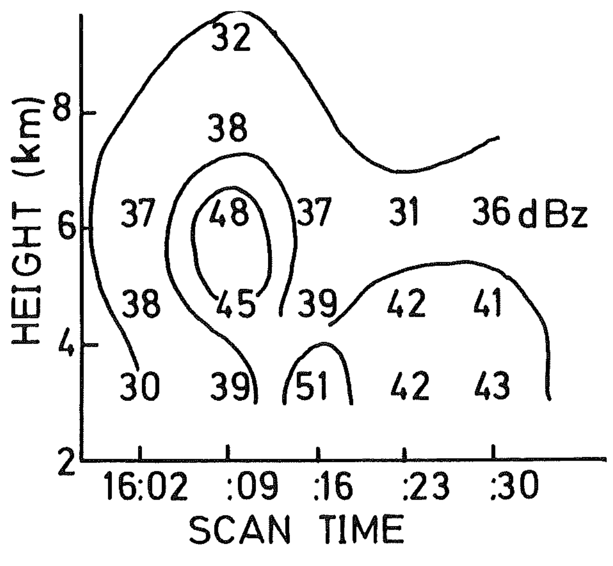

Fig. 4. Time-height plot of peak reflectivities in seeded storm (dBz). Seeding commenced at 15:56.

4. DISCUSSION

Combined aircraft and radar observations support the hypothesis that the hygroscopic seeding flares are turning on or at least enhancing the growth of precipitation via coalescence. The unusual FSSP observations, high concentrations (632 cm^{-3}) associated with a large droplet tail, can only be explained in terms of the combustion products from the seeding flares. Cloud droplet concentrations and distributions are determined just above cloud base, since the supersaturation during perhaps the first 100 metres of ascent controls the cloud condensation nuclei that are activated. The addition of hygroscopic nuclei below cloud base radically alters the cloud droplet spectra of the affected air by depressing supersaturation. Given limited mixing in a reasonably smooth updraft, the seeding "signature" of the cloud air that has been seeded is easily recognized at the -10°C level by its unique droplet spectrum.

On a subsequent flight, an FSSP spectrum with a large droplet tail (concentrations > 32 microns of 9 cm^{-3}) was encountered that was not associated with 2D-C images. Equivalent reflectivities calculated from the large droplet tail assuming water droplets (10.6 dBz) were close to the reflectivities recorded by the aircraft's 3 cm radar (9.7 dBz), further supporting the assertion that these are observations of large water droplets resulting from the hygroscopic seeding at cloud base. Clearly, once these drops exceed 40 microns in diameter, rapid coalescence will ensue, causing the high reflectivities frequently observed aloft by the project radar some 10 to 15 minutes after seeding commences.

ACKNOWLEDGEMENTS

This research is funded by the Water Research Commission and the South African Weather Bureau. The authors thank Maureen Dreyer for typing this manuscript.

REFERENCES

Braham, R.R., Jr., 1986: The cloud physics of weather modification. Part 1: Scientific basis. WMO Bull., 35, 215-221.

Hindman, E.E., 1978: Water droplet fogs formed from pyrotechnically generated condensation nuclei. J. Wea. Mod., 10, 77-96.

Mather, G.K., B.J. Morrison and G.M. Morgan, Jr., 1986: A preliminary assessment of the importance of coalescence in convective clouds in the eastern Transvaal. J. Climate Appl. Meteor., 25, 1780-1784.

------, 1991: Coalescence enhancement in large multicell storms caused by the emissions from a Kraft paper mill. J. Appl. Meteor., 30, 1134-1146.

GROUND-BASED RAINDROP SPECTRA OBSERVATIONS FOR THE ANALYSIS OF SUMMER CONVECTIVE SHOWERS IN MEXICO CITY

F. García-García and R.A. Montañez

Centro de Ciencias de la Atmósfera
Universidad Nacional Autónoma de México
Ciudad Universitaria, D.F. 04510 México

1. INTRODUCTION

One of the quantities most commonly used to characterize rain is drop size distribution, which is normally expressed in terms of the number of drops per unit volume of air and per unit size interval. The importance of the observation and study of raindrop spectra comes from the fact that they contain basic information regarding cloud microphysical processes and their interactions with the dynamical aspects of precipitation development. Thus, radar meteorology and cloud modeling are but two of the fields in atmospheric science that most benefit from the knowledge of raindrop size distributions.

The most widely used description for raindrop size distributions is that of Marshall and Palmer (1948), in which the number concentration is assumed to be an exponential function of the drop diameter. Although other, not so simplified distributions have also been proposed, such as lognormal and gamma functions (see for example Pruppacher and Klett 1978), there generally exist discrepancies between measured and theoretical spectra. This is due in part to the fact that numerous field observations indicate that raindrop spectra exhibit a multipeak behavior (for a summary see Steiner and Waldvogel 1987). Thus, proposed functions are able to describe general trends in different cases, but it is basically imposible to solve all the discrepancies for all situations with a single functional form.

Recent numerical model calculations of warm rain processes (Valdez and Young 1985, List *et al.* 1987) predict a multipeak behavior like the one mentioned above. These processes are of great importance in the tropics where warm-based convective clouds are common, but also play a role in midlatitude summer precipitacion where collision-coalescence mechanisms take place below cloud base. This latter case may also apply to Mexico City due to its particular geographical characteristics of high altitude.

With the purpose of better understanding the microphysical characteristics of precipitation in Mexico City, a series of ground-based field measurements of raindrop size distributions was performed in a site located at the southern end of the city. The measurements took place during the Summer of 1991 and included twelve precipitation events, all but one of them being of convective nature. The data were obtained with two Optical Array Spectrometer Probes (OAP), manufactured by Particle Measuring Systems [PMS (Knollenberg 1981)], and analyzed through time-series, individual showers and overall approaches. To these authors' knowledge, the data set presented here is the first one on its type produced for Mexico. The details of the experiment and the preliminary results are described in what follows.

2. INSTRUMENTATION AND METHODOLOGY

Raindrop size distributions were measured with two, simultaneously operating, OAP's (a 2D-C and a 2D-P) located on the roof of the Center for Atmospheric Sciences Building of the National University of Mexico. A cup anemometer and wind vane, a raingage and a thermometer were located besides the OAP's, which were fixed in a vertical orientation. A data acquisition system, along with a tape recorder and a CRT display, were used to allow continuous data collection and to monitor the drop images in real time.

For 2D-probes operating in a stationary mode, it is well known that the resultant images are distorted along the direction of the particle motion. This is due to the fact that the clock rate controlling the photodiode array is constant and usually faster than the slow and variable fall velocities of the drops, in addition to effects produced by wind speed. Thus, the image data in the present investigation were reduced by means of an objective software routine specifically developed for the particular sampling conditions (Alvarez and Torreblanca 1992). The reconstruction algorithm utilizes a center-in technique and is capable of taking into account the slantness of the images. Laboratory performance tests and calibrations were conducted on the OAP's prior to the field data collection. The results, along with the given characteristics of the software routine, indicate that these particular 2D-C and 2D-P probes are in principle capable of detecting drops in the ranges from 10 to 835 μm (resolution 14 μm) and from 95 to 7360 μm (resolution 129 μm), respectively.

The measurements included twelve rain events between 18 July and 13 September 1991. Only the one occurring on 5 September was of stratiform origin, the rest being of convective nature. Rainfall rates were derived from the precipitation water content, which in turn was obtained by integrating over all drop diameters of the measured spectrum, i.e., over the range of the spectrometers. The rainfall rates so obtained compared well (within 30%) with those measured with the raingage. Temperatures recorded during the field observations ranged from 16 to 20°C, under generally calm wind conditions (maximum wind gust of about 1 m/s at the sampling site). Due to the preliminary nature of the results, only the six events that were monitored during September are reported in the present paper. They were analyzed both as single events (typical duration of one and a half hours) and as time-series of variable duration.

3. RESULTS AND DISCUSSION

Figure 1 presents a typical raindrop size distribution obtained during the sampling period. As it can be appreciated, the spectra derived from the two instruments agree very well within the overlapping range, except for the smallest 2D-P size class. This may be related to the minimum threshold detection level associated with this kind of optical systems. Also, it can be seen that there seems to be a "cut-off" value for the 2D-C at about 600 μm. As previously discussed this instrument, along with the reconstruction software routine, should be capable of detecting drops of up to about 835 μm in diameter, given that the centers of their images lie within the photodiode array and can be identified as such. It is very likely that the minimal sampling volume available in the 2D-C for these larger drops is an important factor that "discriminates" against them.

The observed precipitation events had average rainfall rates between 0.4 and 23 mm/h. Their corresponding raindrop spectra were analyzed in time-series of variable duration ranging from one to ten minutes, resulting in twenty drop size distributions. In order to determine the shape of the entire sample, each raindrop spectrum was normalized assuming an exponential distribution of the Marshall-Palmer type, following the method proposed by Sekhon and Srivastava (1970) and further discussed by Willis (1984). The nondimensionalized Marshall-Palmer form is given by:

$$Y = \frac{\rho_W\, N(D)\, D_O^4}{M_\infty} = \frac{\beta^4}{\pi} \exp\left[- \beta \frac{D}{D_O} \right], \qquad (1)$$

where ρ_W is the density of the water drop, N(D)dD is the number concentration of drops with diameters between D and D + dD, M_∞ is the total precipitation water content, and D_O is the median volume diameter dividing the precipitation content of the distribution in two equal parts. Sekhon and Srivastava (1971) have argued that Eq. 1 provides a universal exponential distribution, with β being a constant, free parameter. *Figure 2* shows the data normalized according to Eq. 1 as well as the least-squares fit performed on them, which yielded a value of 3.10 ± 0.08 for β. For comparison, Atlas (1953) states that β is equal to 3.75, or less if the distribution is truncated. It should be noted that a departure from exponentiality (curvature) can be appreciated in both the "regular" and in the nondimensionalized drop size distributions (see *Figure 2*). This has also been reported in other investigations.

The multipeak characteristics of the spectra can be appreciated in the example shown in *Figure 1*. In order to determine the frequency of occurrence of a given peak, the drop size spectra were analyzed following the method described by Steiner and Waldvogel (1987). It should be noted that peaks occuring at the smaller size category in each OAP were not considered in this analysis. The results are shown in *Figure 3*. In spite of the small size of the sample and of the irregular time interval for each spectrum, a consistent pattern starts to emerge. The 2D-C and the 2D-P show, respectively, two and three peaks if only the most frequent ones are taken into account. These occur at 0.084, 0.299, 0.539, 0.920 and 1.179 mm. Steiner and Waldvogel (1987) summarize the results of a number of observations obtained with a variety of measuring systems, as well as those of several model calculations of peaks in raindrop spectra. The best currently available models by Valdez and Young (1985) and by List *et al*. (1987) predict three peaks roughly in the ranges between 0.2 and 0.3, 0.8 and 0.9, and 1.8 and 2.0 mm. The first two were observed in the present investigation, while the third one fell within the "second best" probability group. It should be emphasized that, to the best of these authors' knowledge, the peak at 0.2-0.3 mm range has not been reported in past observations. The other two larger peaks found here fall within the bounds reported by different observers, but the smallest one (at 0.084 mm) has neither been predicted by the models nor previously reported.

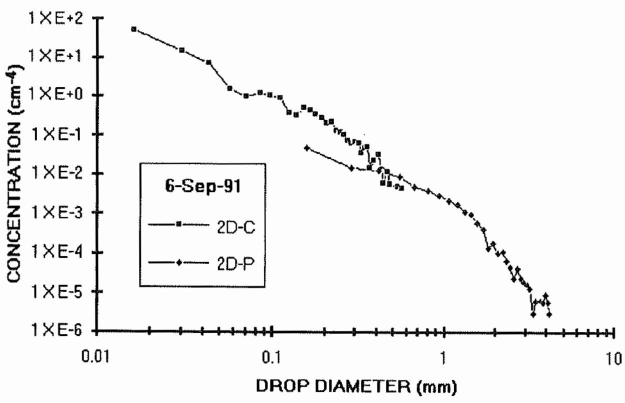

Figure 1. Raindrop size distribution measured in Mexico City on 6 September 1991 from 1609 until 1751 LST.

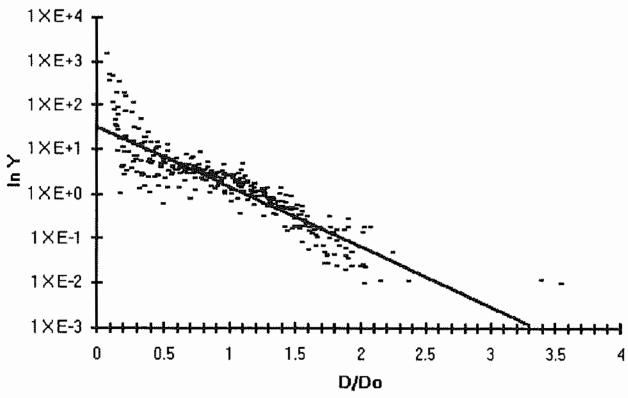

Figure 2. Sample of twenty drop size distributions normalized with a nondimensionalized Marshal-Palmer function. The straight line represents the least-squares fit as given by Eq. 1.

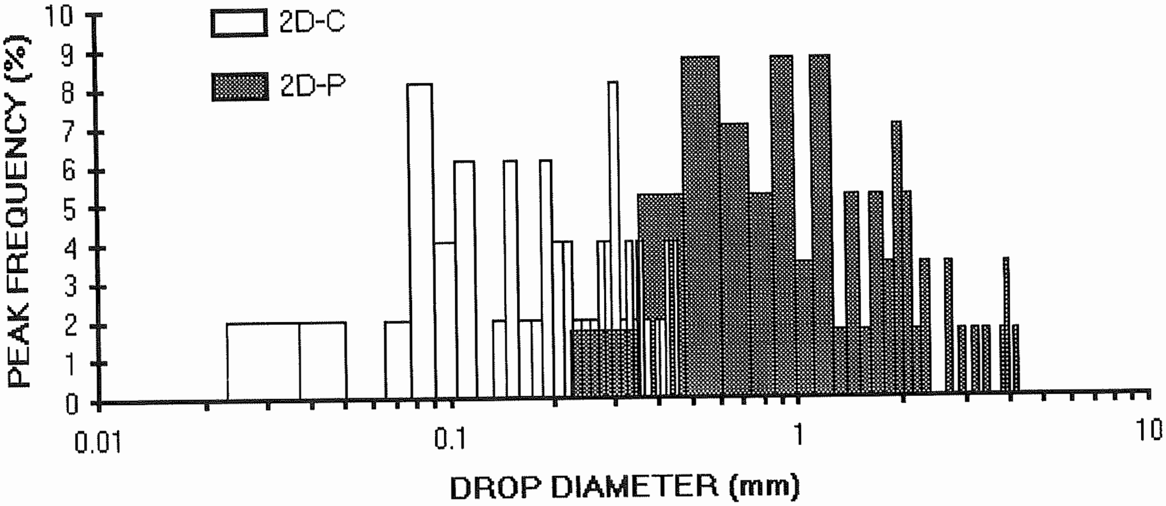

Figure 3. Frequency of peaks of twenty raindrop size distributions for events of variable time duration, simultaneoulsy obtained with a 2D-C and a 2D-P probes in Mexico City.

4. SUMMARY AND CONCLUSIONS

Raindrop size distributions were measured at the ground in Mexico City, making use of two fixed, vertically oriented optical array spectrometer probes. The data were analyzed both as single precipitation events and as time-series of variable duration. The results indicate that a Marshall-Palmer exponential form describes the data reasonably well, and that the drop size distributions show a multipeak behavior. Out of the five most probable peaks found, two of them (at 0.299 and 0.920 mm) correspond to those predicted by numerical models, two more (at 0.539 and 1.179 mm) agree with observations by other observers, and the fifth one (at 0.084 mm) has neither been predicted nor previously reported.

Further research is planned to consider the larger data set available and to perform a time-series analysis of drop spectra for fixed time intervals. This will help to better discriminate between the most probable peaks and also to make straightforward comparisons with results obtained by other investigators. A series of experiments is being planned to be carried out in the near future with the aim of making measurements of drop spectra at the ground, but in a mobile as opposed to a fixed fashion. It will be interesting to compare both sets of distributions in order to decide which sampling mode is the most adequate and efficient one. Finally, it is expected that this research will improve our understanding of the microphysical processes that take place during the different stages of evolution of precipitation formation under the very specific conditions of high altitude of Mexico City.

Acknowledgments. The authors appreciate the continuous technical support provided by Messrs. J. Escalante, M. García, A. Rodríguez, M. Silva and V. Zarraluqui. Part of this study was sponsored by the Instituto Mexicano de Tecnología del Agua (IMTA) of the Comisión Nacional del Agua, México.

REFERENCES

Alvarez P., J.M., and J. Torreblanca B., 1992: *Desarrollo de un Sistema de Software para Interpretación y Análisis de Datos de Espectrómetros de Gotas*. Tesis de Licenciatura, Departamento de Computación, Facultad de Ingeniería, Universidad Nacional Autónoma de México. (In preparation).

Atlas, D., 1953: Optical extinction by rainfall. *J. Meteor.*, **10**, 486-488.

Knollenberg, R.G., 1981: Techniques for probing cloud microstructure. *Clouds: Their Formation, Optical Properties, and Effects*, P.V. Hobbs and A. Deepak (Eds.), Academic Press, 15-91.

List, R., N.R. Donaldson and R.E. Stewart, 1987: Temporal evolution of drop spectra to collisional equilibrium in steady and pulsating rain. *J. Atmos. Sci.*, **44**, 362-372.

Marshall, J.S., and W. McK. Palmer, 1948: The distribution of raindrops with size. *J. Meteor.*, **5**, 165-166.

Pruppacher, H.R., and J.D. Klett, 1978: *Microphysics of Clouds and Precipitation*. D. Reidel Publishing Co., 714 pp.

Sekhon, R.S., and R.C. Srivastava, 1970: Snow size spectra and radar reflectivity. *J. Atmos. Sci.*, **27**, 299-307.

Steiner, M., and A. Waldvogel, 1987: Peaks in raindrop size distributions. *J. Atmos. Sci.*, **44**, 3127-3133.

Valdez, M.P., and K.C. Young, 1985: Number fluxes in equilibrium raindrop populations: A Markov chain analysis. *J. Atmos. Sci.*, **42**, 1024-1036.

Willis, P.T., 1984: Functional fits to some observed drop size distributions and parameterization of rain. *J. Atmos. Sci.*, **41**, 1648-1661.

In Situ Holographic Measurements of Spatial Droplet Distributions and Inter-Droplet Distances

Stephan Borrmann [1] and Ruprecht Jaenicke [2]

[1] National Center for Atmospheric Research, Boulder, CO, USA 80307

[2] Institut für Physik der Atmosphäre, Universität, Mainz, Germany

1. Introduction

Two basic assumptions underlying numerical cloud modelling are that the cloud droplets are randomly distributed in space and that the distances between the droplets are large enough to allow their growth in a field of supersaturated air without mutual interaction.

Only a few experimental studies have been conducted to measure inter-droplet distances in clouds or to characterize the spatial distribution of the droplets. **Baker (1992)** analyzed interarrival times of cumulus cloud droplets passing through the laser beam of a FSSP-100 mounted on an aircraft and **Kozikowska et al. (1984)** performed holographic measurements of spatial droplet distributions in ground fog. Both studies conclude that there may be some systematic deviation from random spatial droplet distributions.

In this study holograms recorded during a 26 hour stratus cloud event near Frankfurt/Main (Germany) were analyzed with respect to cloud droplet size- and spatial distribution. A Sub Cell Scanning Analysis (SCSA) procedure is used and additionally frequency distributions of distances between neighboring particles are calculated The results of both methods are compared to a theoretical, randomly distributed droplet population characterized by Poisson statistics.

2. Layout of the Holographic Droplet and Aerosol Recording System (HODAR)

The HODAR utilized for ground based in-situ measurements in stratus clouds for this study is a Fraunhofer in-line holographic system with collimated recording and reconstructing beams and has been characterized in **Borrmann and Jaenicke (1992)**. Some salient design features of this HODAR are:

1. The recording laser is a pulsed, Q-switched ruby laser ($694nm$ wavelength, $30ns$ pulse duration, $30mJ$ pulse energy) operating in TEM-00 mode where two Fabry Perot etalons prepare single or double pulses of coherence length larger than $1m$.
2. The hologrphic droplet images are optically reconstructed with a $15mW$ cw-HeNe laser beam.
3. The optical reconstruction of the cloud volumes recorded on the holograms preserves the droplet's original size, shape and relative position in space.
4. The smallest droplets the system can image are of $3\mu m$ size radius under a total magnification of 450.
5. Considerable effort was taken to minimize temperature and electrostatical effects on the sampling during the recording. Also an analysis of individual droplet velocity vectors obtained from a double exposed hologram (**Borrmann and Jaenicke, 1992**) showed that the flow distortion introduced by the recording apparatus are negligible.

3. Results from measurements in a stratus cloud layer

Five holograms were recorded during a 26 hour stratus cloud event in the night of Nov. 13/14, 1990 at the Taunus Mountain Observatory near Frankfurt/Main (Germany) under conditions of light winds and ambient temperatures of 2° C. For the results presented here a cubiform reconstructed image volume with approximately $2cm$ side length ($C_N = 140$ droplets per cm^3 total concentration) was systematically scanned to determine droplet sizes and positions in space. The droplet number size distribution is shown in Fig. 1 with error bars (Error analysis see **Borrmann and Jaenicke (1992)**).

To characterize the state of a spatial distribution two approaches are taken: (a) the sub cell scanning analysis (SCSA) and (b) assessment of distance frequency distributions between neighboring particles. Application of (b) also yields information about the absolute values of the inter-droplet distances.

(a) The Sub Cell Scanning Analysis: The SCSA consists of four steps:

1. Divide of the imaged volume under consideration into a large number of adjacent small sub cells containing on the average a number of δ droplets each.
2. Count the number of droplets n_{SC} found in each individual sub cell. This yields a frequency distribution

Fig. 1: Cloud droplet size distribution measured on Nov 14, 1990 at 00:02 a.m. at the Taunus Mountain Observatory near Frankfurt, Germany.
Number of droplets counted in the hologram = 1013.
Droplet number concentration = 140 ± 5 droplets per cm^3.

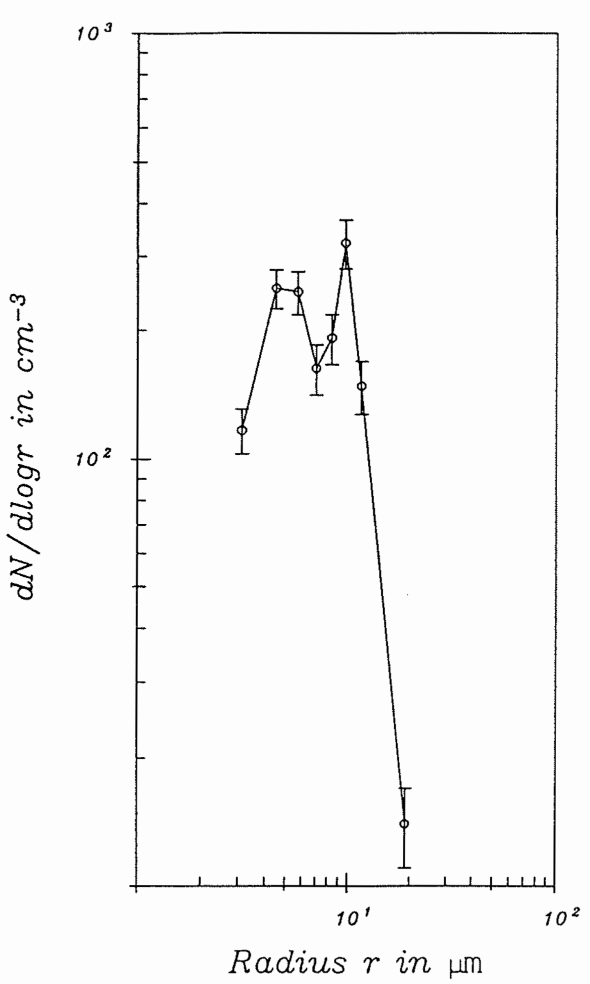

$Q(n_{SC})$ of the number of sub cells containing n_{SC} droplets.

3. Assume a theoretical, random distribution of droplets, repeat the analysis described in step 2 with the same values for the sub cell volume δ and the total droplet number concentration C_N. A theoretical frequency distribution (now a Poisson distribution) analogous to that of step 2 results.

4. Compare the Poisson distribution of step 3 with the experimentally determined distribution from step 2.

Fig. 2 shows the resulting frequency distributions from the analyzed image volume with $\delta = 6$. The abscissa displays a relative number concentration (then number n_{sc} of droplets divided by δ) while the ordinate gives a normalized distribution density for $Q(n_{SC})$. Taking the error bars (due to count statistics) into account the disagreement between the theoretical and experimental distribution can be considered as small.

(b) Analysis of Inter-Droplet Distances : In order to obtain statistical information of the inter-droplet-distances, the distances of each particle in the imaged volume from all the other particles are calculated and sorted resulting in frequency distributions of distance with respect to nearest neighbors, second neighbors and so on . Similarly an imaginary population of droplets randomly dispersed in space can be investigated to compute a 'theoretical' frequency distribution density function of inter-droplet distances between nearest (second-nearest ...) neighbors (see **Raasch and Umhauer (1989)**). As an example Fig. 3 shows the resulting distance frequency density functions for the second nearest neighbors where s denotes the distance between second neighbors in cm. Also for normalization purposes a characteristic length scale s_k (in cm) has been defined by $s_k = (\sqrt[3]{C_N})^{-1}$. s_k would be the distance between neighboring droplets if the droplets were arranged in a regular cubical grid. The bin-width of the abscissa is $0.1\ s/s_k$ and $s_k = 1920\mu m$ and the error bars associated with the values obtained from the 'real' droplet collective indicate the range of errors due to count statistics. Similar graphs result from analyzing the distances between first, third etc. neighbors. Again the experimentally determined distribution agrees well with the theoretical result based on Poisson statistics.

From the distance frequency distributions average distances $\bar{d}$ between droplets can be calculated for (first) neighbors:

$$\bar{d}(\text{1st neighbors}) \quad = \quad 1158\mu m$$

The average inter-droplet distance for a randomly distributed particle population based on Poisson statistics is given by:

$$\bar{d}(\text{rand. distr.}) \quad = \quad 0.554 \cdot C_N^{-1/3} \ ,$$

which results for the C_N of the analyzed hologram in:

$$\bar{d}(\text{hologram}) \quad = \quad 1064 \pm 12\mu m \ ,$$

a value differing by only 8% from $\bar{d}$(1st neighbors). This can be considered as another indication for the natural droplet population being well characterized by Poisson statistics.

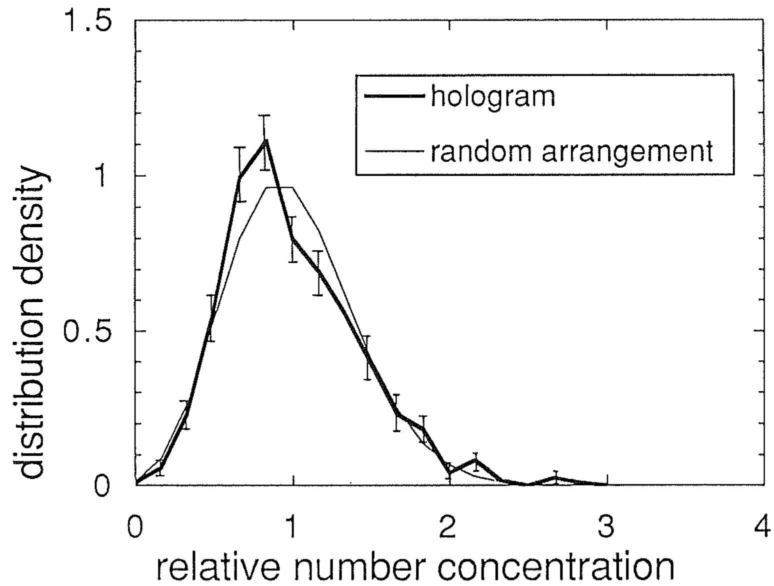

Fig. 2: Frequency distribution density functions from Sub Cell Scanning Analysis as computed from theory (random arrrangement) and measured from the hologram for $\delta = 6$.

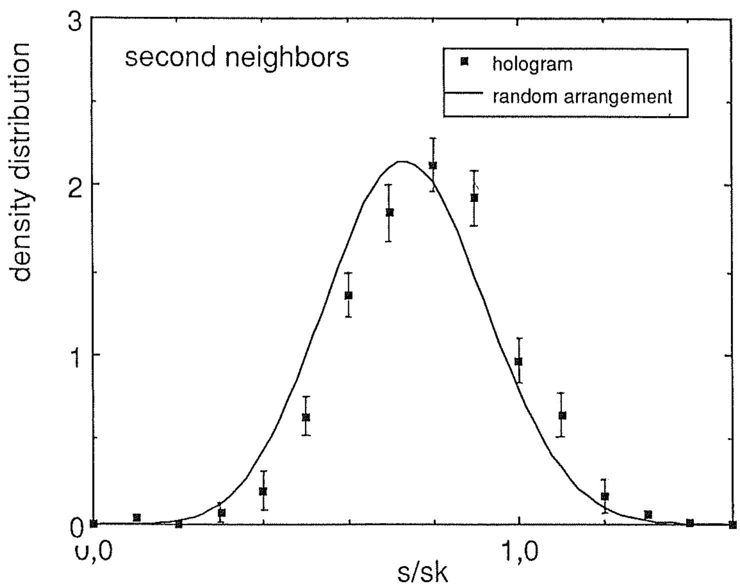

Fig. 3: Frequency distribution density functions from analysis of inter-droplet distances for second neighbors. (random arrangement - computed from theory, symbols with error bars - measured from hologram)

Raasch and Umhauer (1989) show that a 59.3% of the randomly distributed droplets are positioned in space as 'pairs' which means they mutually 'consider' each other as first neighbors. This effect has been accounted for in our analyses and more statistical evaluations on the occurrence of pairs are presented in our poster.
Concerning the absolute distances between droplets it can be stated that if a droplet size radius of $10\mu m$ is considered (see Fig. 1) then: Of all droplets

- 40% are closer to each other than 100 radii,
- 20% are closer to each other than 70 radii,
- 10% are closer to each other than 60 radii,
- 3% are closer to each other than 10 radii.

Textbooks on cloud physics suggest that for the droplets to grow or evaporate in a field of given supersaturation independently from each other the inter-droplet distances should be larger than 100 droplet radii. It may be useful to perform sensitivity studies to assess whether the droplet growth equation used in numerical cloud modelling still holds for the inter-droplet distances given above.

4. Conclusions

Based on the rigorous analyses performed on one hologram recorded during a stratus cloud event we conclude that the spatial distribution of this droplet population can be well characterized by a Poisson statistics, a result which is supported by inspecting other holograms recorded during the same event. This conclusion differs from previously published results (e.g. **Kozikowska et al. (1984)** or **Baker (1992)**) where deviations from a Poisson distribution were observed.
However the holographic experiments should be extended to different cloud types, growing and dissipating clouds with and without ice phase present, different wind conditions etc.
The measured distances between droplets suggest the need for sensitivity studies in cloud models to test the assumption of independent droplet growth.

5. References

Baker,B.,1992 Turbulent Entrainment and Mixing in Clouds: A New Observational Approach, J. of Atm. Sci., 49, 387-404

Borrmann,S.,Jaenicke,R.,1992 Application of Microholography for Ground Based in-situ Measurements in Stratus Cloud Layers: A Case Study, J. of Atm. and Oceanic Technol., submitted March 1992.

Kozikowska,A.,Haman,K.,Supronowicz,J., 1984 Preliminary Results of an Investigation of the Spatial Distribution of Fog Droplets by a Holographic Method, Quart. J. of the Roy. Met. Soc., 110 , 65-73

Raasch,J.,Umhauer,H.,1989 Computation of the Frequency Distribution of Distances between Particles Randomly Dispersed in a Fluid Flow, Part. Part. Syst. Charact.,6 , 13-16

---

*The National Center for Atmospheric Research is sponsored by the National Science Foundation.

THE MEASUREMENT AND PARAMETRISATION OF EFFECTIVE RADIUS OF DROPLETS IN STRATOCUMULUS CLOUDS

G.M. Martin and D.W. Johnson

Meteorological Research Flight, Farnborough, England

1. Introduction

Large areas of the subtropical parts of ocean basins are covered with persistent sheets of stratocumulus clouds. Numerical weather and climate models have too large a grid spacing to explicitly resolve processes associated with these clouds, which have a pronounced effect on the Earth's radiation budget. Therefore their effects have to be parametrised in terms of the bulk model variables in order to improve the model predictions. One of the important parameters from the point of view of radiation schemes is effective radius (defined in Section 2). Slingo (1990) showed that decreasing the effective radius of cloud droplets from 10 μm to 8 μm, which increases the short wave radiation scatter, would result in atmospheric cooling that could offset global warming due to doubling the CO_2 content of the atmosphere. This paper presents the analysis of some aircraft observations of stratocumulus which suggest a new parametrisation of effective radius which could be used in numerical model radiation schemes.

The results described below were obtained using data gathered by the Meteorological Research Flight C-130 during

a. the First ISCCP Regional Experiment (FIRE) conducted over the eastern Pacific Ocean off the southern coast of California in July 1987

b. the First ATSR Tropical Experiment (FATE) in the South Atlantic

c. flights made in stratocumulus over the sea around the British Isles.

The C-130 aircraft is well-equipped to measure the radiative and microphysical properties of stratocumulus clouds, and detailed information about the instrumentation and its performance is given in Nicholls (1978) and Nicholls *et al.* (1983). The instruments used to obtain the microphysical data analysed here were a Particle Measuring Systems (PMS) Forward Scattering Spectrometer Probe (FSSP), which measures droplets in the range 0.25 to 24 μm radius, a PMS Passive Cavity Aerosol Spectrometer Probe (PCASP) which measures droplets in the range 0.05 to 1.50 μm radius, and a thermal gradient diffusion chamber to measure Cloud Condensation Nuclei (CCN) activity spectra (see Section 4). The method of operation, data processing and reliability of the FSSP are discussed by Turton (1985).

2. Some general properties of stratocumulus

Figure 1(a) shows a typical temperature profile from one of the FIRE flights, obtained during a slow descent through a uniform stratocumulus sheet. Figures 1(b) and 1(c) show profiles of liquid water content and droplet concentration obtained using the Johnson-Williams hot wire probe and the FSSP respectively. It can be seen that the liquid water content of the cloud increases smoothly with height, but that the droplet concentration remains approximately constant throughout the depth of the cloud. The average size of the droplets increases with height and the largest cloud droplets are found at the top of the cloud. This is illustrated by Figure 1(d), which is a profile of effective radius of cloud droplets. This is calculated from droplet size spectra measured by the FSSP using the following equation:

$$r_e = \frac{\sum_{n=1}^{M} r_n^3 N_n}{\sum_{n=1}^{M} r_n^2 N_n} \qquad (1)$$

where M is the number of size bins resolved by the FSSP (M = 15), r_n is the middle radius value for that size bin and N_n is the concentration of droplets in that size bin.

The example given in Figure 1(a-d) is typical of most of the stratocumulus clouds encountered. Occasionally, profiles showed a decrease in mean droplet concentration close to the upper and lower cloud boundaries, with corresponding decreases in liquid water content. However, in most cases these effects were small, which indicates that entrainment in stratocumulus cloud is not generally a significant effect, and is mainly limited to cloud top.

3. Droplet size distributions

The most significant microphysical differences between the stratocumulus clouds observed during FIRE and those sampled around the UK are seen in the droplet size spectra. Figure 2(a) shows a typical set of averaged droplet size spectra for a layer of stratocumulus sampled during FIRE. The peak concentration in the cloud remains almost constant with height but the proportion of larger droplets increases, causing a significant movement of the peak to larger radii. Thus the effective radius increases with height in cloud. Below cloud, the spectra decrease in width and peak concentration.

A set of droplet spectra from a cloud layer sampled around the UK is shown in Figure 2(b). This also shows an increase in average droplet size towards the cloud top, but the shapes of the spectra are very different to those in Figure 2(a). The peak size of the droplets at cloud top is smaller than in the FIRE case, but there are still significant numbers of droplets in the larger size ranges and as a result the spectra are much more skew. This indicates that there may be a fundamental difference between the airmasses involved in each location. It is thought that the FIRE region was affected by mainly maritime airmasses throughout the experiment, whereas most of the flights made around the UK were carried out in air that had passed over land. The differences in spectral shape were found in nearly all the FIRE and UK cases (except for three maritime cases from the UK which showed similar characteristics to those from FIRE). Thus, the spectral shape may be indicative of the airmass sampled.

The differences in spectral shape may be compared quantitatively using spectral dispersion, which is the standard de-

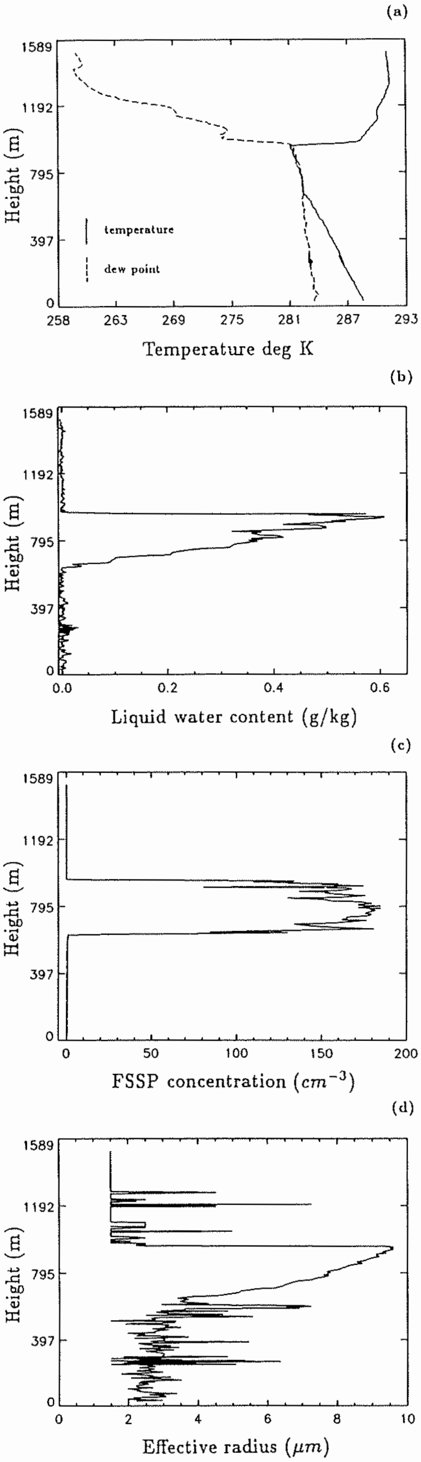

Figure 1 Profiles obtained during a slow descent through a stratocumulus layer: FIRE flight H803 P2. (a) Temperature and dew point (b) Liquid water content (c) Droplet concentration (d) Effective radius

iation of the spectrum as a percentage of the mean radius. This is calculated for each one second record of a vertical profile through cloud, and is shown in Figure 3 as a function of height above cloud base, for the spectra given in Figures 2(a) and 2(b). The difference in spectral dispersion for the two cases can be seen clearly; the skew nature of the spectra from the UK case results in a higher value of dispersion than is found for the FIRE case. It should be remembered, however, that two spectra which have the same dispersion are not necessarily the same shape, so that dispersion alone cannot be used to distinguish between airmass types in this way. This method has been used here simply to illustrate the differences between the two cases.

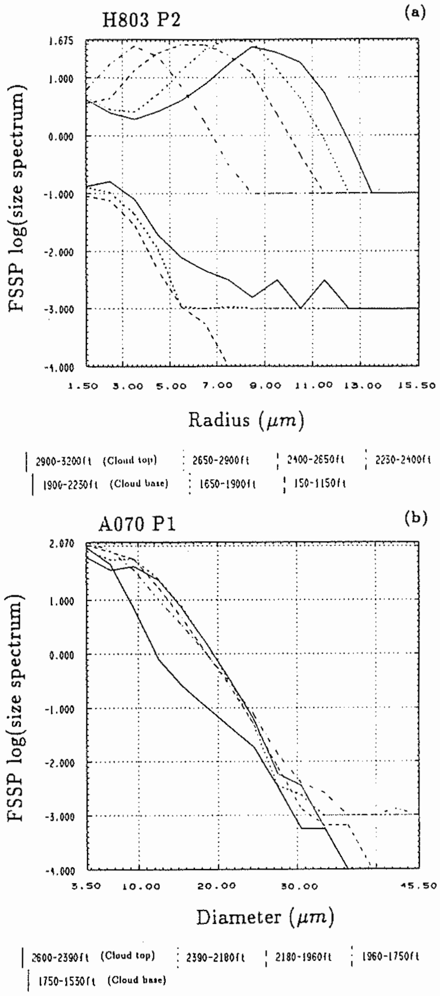

Figure 2 Droplet size spectra at different levels in stratocumulus cloud obtained during a slow profile: (a) FIRE flight H803 P2 (b) UK flight A070 P1

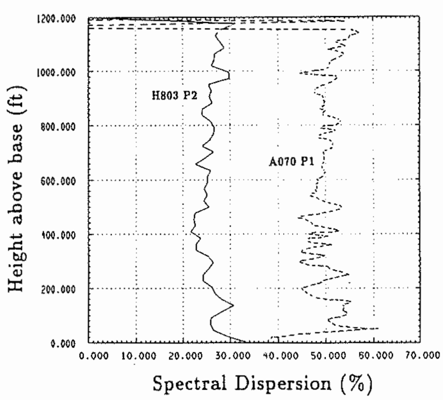

Figure 3 Variation of spectral dispersion with height in cloud: comparison between FIRE and UK flights.

4. A Parametrisation for the Effective Radius of Cloud Droplets

The liquid water content can be calculated from a particular droplet size spectrum by summing the volumes of the droplets in each infinitesimal size range, n. That is:

$$L = \frac{4}{3}\pi\rho_w \int_{n=1}^{\infty} r_n^3 N_n \, dn \tag{2}$$

where L is the mass of liquid water per unit volume of air, N_n denotes the concentration of droplets in the size range n, r_n the radius of droplets in that size range, and ρ_w the density of liquid water. The FSSP only has 15 size channels, so this equation can be approximated by:

$$L = \frac{4}{3}\pi\rho_w \sum_{n=1}^{15} r_n^3 N_n \tag{3}$$

which reduces to:

$$L = \frac{4}{3}\pi\rho_w \overline{r^3}\, N_{TOT} \tag{4}$$

where N_{TOT} is the total droplet concentration. The quantity $\overline{r^3}$ in this equation is the average volume of a droplet in the spectrum, so that:

$$r_v = \sqrt[3]{\overline{r^3}} \tag{5}$$

is the mean volume radius (a common measure of average droplet radius derived from size spectra).

If a relationship can be found between r_e and r_v then equation 4 can be used as a starting point for a parametrisation for r_e in terms of the liquid water content of the cloud and the droplet concentration. Bower and Choularton (1991) compared mean volume radius with effective radius for a descent through stratocumulus during one of the FIRE flights and found that r_v was consistently lower than r_e. The results presented here indicate that there is a linear relationship between r_v^3 and r_e^3 in stratocumulus clouds where little entrainment is going on. That is:

$$r_v^3 = k\, r_e^3 \tag{6}$$

where k is a constant.

Figure 4 shows a typical example of a scatter plot of one second averages of r_v^3 against r_e^3 measured by an FSSP. Similar scatter plots were produced for all profiles through cloud in the FIRE and UK flights, and it was found that k varies according to airmass type. In the maritime airmasses sampled in FIRE

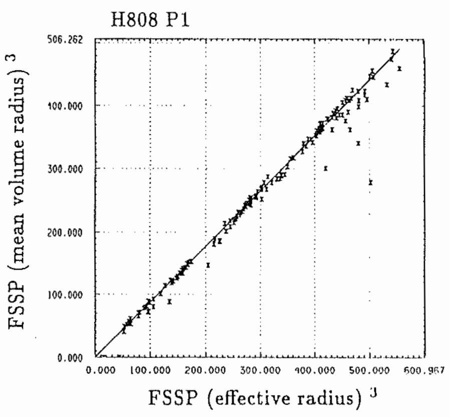

Figure 4 Scatter plot of r_v^3 (μm^3) versus r_e^3 (μm^3) for FIRE flight H808 P1.

and around the UK, larger values of k were measured than in the continental airmasses found in the vicinity of the UK. As shown previously, this arises due to a fundamental difference in the shape of the droplet size spectra in the two airmass types. In continental airmasses it was found that $k = 0.65 \pm 0.07$ while in the maritime airmasses $k = 0.81 \pm 0.06$.

It is suggested that a suitable parametrisation for effective radius is:

$$r_e = \left(\frac{3\,L}{4\,\pi\,\rho_w\,k\,N_{TOT}}\right)^{\frac{1}{3}} \tag{7}$$

The results are summarised schematically in Figure 5, where r_e^3 is plotted against FSSP integrated liquid water content/total droplet concentration (note that because of the counting errors of the FSSP, the liquid water content measured by a Johnson-Williams hot wire probe will give a more accurate liquid water content than that derived from the FSSP. However, counting errors in the FSSP will be reflected in both the FSSP liquid water content and the concentration, so that they will cancel out in equation 4). Also included in Figure 5 are results from FATE which took place near Ascension Island in maritime stratocumulus, which can be seen to agree well with those from FIRE.

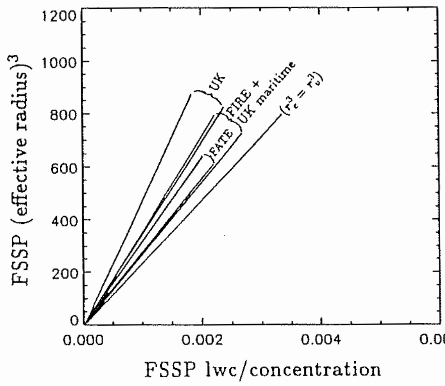

Figure 5 Summary of the gradients of scatter plots of (effective radius)^3 (μm^3) versus FSSP integrated liquid water content (g/m^3)/total droplet concentration (cm^{-3}) for all UK, FIRE and FATE flights. The line $r_e^3 = r_v^3$ represents $k = 1$, the value implied by Bower and Choularton (1991).

Cloud droplet concentration is a difficult parameter for a large scale numerical model to handle. Therefore, before equation 7 can be used to diagnose effective radius in models, a method for parametrising N_{TOT} is required. In stratocumulus clouds, in well mixed boundary layers, the droplet concentration throughout the whole depth of the cloud is almost equal to the cloud condensation nucleus (CCN) concentration below cloud, and in a maritime airmass it would be expected that the droplet concentration would be much less than in continental airmasses. Thus N_{TOT} could be approximated by choosing a characteristic value for a given airmass (Bower and Choularton, 1991), thereby effectively making it a constant in equation 7.

However, as numerical models become more sophisticated it is likely (and also advantageous from the point of view of radiation schemes and predicting visibility) that a predictive aerosol parameter will be included. In fact, the UK mesoscale model already has the facility of including an aerosol variable. The aerosol concentration measurements taken with the PCASP during this study show that there is a good correlation between the number of aerosol just below cloud base and the CCN concentration (or in this case, the droplet concentration). Figure

6 summarises the aerosol concentrations measured below cloud base and the number of droplets observed in the cloud. For the maritime airmass there is very little scatter of the points and the best fit line has a gradient very close to one and an intercept of zero, indicating that nearly all the aerosol are good CCN and that there is very little variation in the chemical characteristics of the particles. In the continental airmasses the scatter is much larger and the intercept of the best fit line is positive. This shows that some of the continental particles

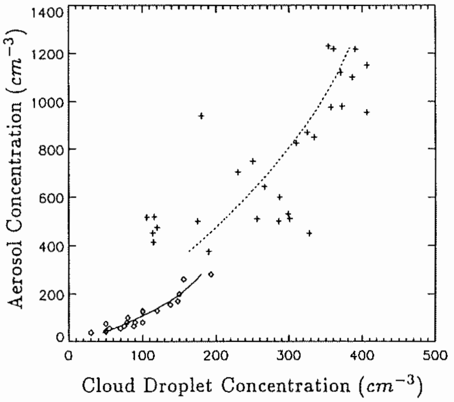

Figure 6 Relationship between cloud droplet concentration and aerosol concentration just below cloud base, for continental (plus signs) and maritime (diamonds) airmasses. Curves indicate best fit lines to continental (dotted line) and maritime (solid line) cases.

are hydrophobic and their chemical characteristics have significant variation. However, both of these sets of data show that a knowledge of the aerosol concentration in the boundary layer and of the aerosol source can give a good estimation of the cloud droplet concentration in stratocumulus clouds. The best line fits suggest that N_{TOT} can be parametrised in the following manner:

In maritime airmasses

$$N_{TOT} = -1.242 \times 10^{-3} A^2 + 0.946 A + 12.009 \quad (8)$$

and in continental airmasses

$$N_{TOT} = -1.426 \times 10^{-4} A^2 + 0.486 A + 1.137 \quad (9)$$

where A is the aerosol concentration.

If the CCN activity spectrum of the aerosol is known, measurements show that a better estimate of N_{TOT} can be

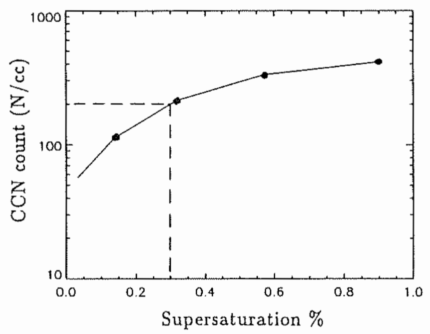

Figure 7 Measured CCN activity spectrum from just below cloud base during UK flight A049; example of how cloud critical supersaturation is found.

made. Activity spectra, a typical example of which is shown in Figure 7, show the CCN concentration activated at a particular supersaturation; this will obviously vary with the actual aerosol present. By assuming that the droplet concentration in the cloud above is the same as the concentration of CCN activated at cloud base, it is possible to find the corresponding critical supersaturation at which this occurs. This is shown in Figure 7 and was carried out for all the CCN spectra measured below cloud base during the UK and FATE flights (the instrument was not fitted during FIRE). Figure 8 shows how the critical supersaturation varies from one stratocumulus sheet to another. Although there is some scatter in these results, they do indicate that there may be one characteristic value of the supersaturation at the base of all stratocumulus clouds (that is, approximately 0.3 %) for both maritime and continental airmasses.

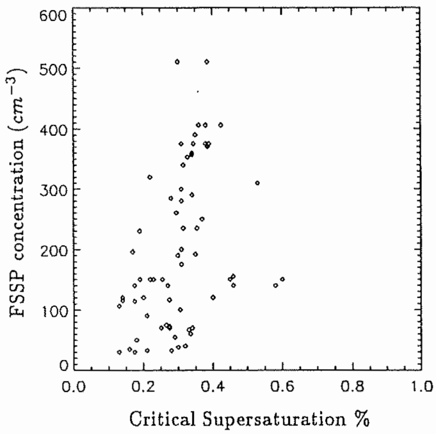

Figure 8 Plot of measured cloud droplet concentration versus critical supersaturation for several UK and FATE flights.

5. Summary

Observations of the microphysics of marine stratocumulus clouds from FIRE, FATE and around the UK have been analysed to find a suitable parametrisation of effective radius in stratocumulus clouds for use in large scale numerical models. The suggested parametrisation relates the effective radius to the liquid water content of the cloud and the aerosol concentration beneath the cloud base.

References

Bower, K. N. and Choularton, T.W. 1991. A parameterisation of the effective radius of ice free clouds for use in global climate models. *J. Atmos. Sci.* (accepted for publication)

Nicholls, S. 1978. Measurements of turbulence by an instrumented aircraft in a convective boundary layer over the sea. *Quart. J. R. Met. Soc.*, **104**, 653-676

Nicholls, S., Shaw, W. T. and Hauf, T. 1983. An intercomparison of aircraft turbulence measurements made during JASIN. *J. Clim. Applied Meteorol.*, **22**, 1637-1648

Slingo, A. 1990. Sensitivity of the Earth's radiation budget to changes in low clouds. *Nature*, **343**, 49-51

Turton, J. D. 1985. A note on the FSSP data processing. *Personal Communication*

Centimeter-Scale Measurements
of Cloud Droplet Size Distributions:
Implications for Condensation and Coalescence Processes

Darrel Baumgardner and Bradley Baker

National Center for Atmospheric Research
Boulder, Colorado 80307

1.0 Overview

The physics of cloud droplet growth still remains a complex problem when taken in the context of the evolution of cloud water from droplets to precipitation. Classical condensation theory fails to produce size distributions that explain those seen in even the simplest of cases (Baumgardner, 1988). Coalescence, as predicted from conventional applications of the kinetic coagulation equation, fails to produce precipitation sized drops within the time period observed in many clouds of marine origin. Recent theories of condensational growth (e.g., Cooper, 1989; Srivastava, 1989) offer plausible mechanisms that could enhance droplet growth and a different method of simulating coalescence (Baumgardner, 1988) also offers a possible mechanism for enhanced growth rates. These theories, however, have yet to be evaluated with observational data.

The recent development of a system that measures the characteristics of cloud droplet distributions at very small scales offers the opportunity to further our knowledge of cloud microphysical processes and provide the data that can be used to test theoretical models of these processes.

2.0 Methodology

The Forward Scattering Spectrometer Probe (FSSP) measures the sizes of individual droplets and sends this information to a data system that normally accumulates size distributions at a rate of 1 hz, though some systems record at faster rates. This averaging masks any information contained at smaller scales. For example, the NCAR aircraft typically fly at 100 ms^{-1} and accumulate size spectra at 10 hz so that the minimum scale at which cloud structure can be studied is ≈10 m. Baumgardner (1986) developed a technique that accumulated the waiting times between droplets. He showed that it was possible to deduce the presence of cloud structure at scales smaller than the sample length (10 m) from this type of measurement such as demonstrated by Paluch and Baumgardner (1989). Baker (1992) improved on this design by recording the individual waiting times and sizes of droplets. He developed a statistic, designated the "Fishing" test, that tests for inhomogeneities and provides information on their length scale with a sensitivity down to millimeters. A similar system, the droplet spacing monitor (DSM), was developed at NCAR (Baumgardner et al, 1992) with the additional recording of information to indicate where through the beam each droplet has passed. This modification was included to increase the useable sample volume as well as to monitor the performance of the instrument.

3.0 Observations

The DSM was installed on the NCAR Electra for operation during the 1990 Hawaiian Rainband Project (HaRP). Measurements were made in rainbands that formed near the east coast of the island of Hawaii and in isolated cumuli that developed further off the coast. The cloud pass that has been selected for this presentation was through a rainband at an altitude of 600 m, just above the cloud base. Cloud base temperature was 19°C, pressure of 940 mb and an average updraft velocity of 2-3 ms^{-1}. Radar observations indicated that this band was already precipitating. This particular pass was selected to illustrate some of the small scale features that can be observed from measurements with the DSM.

Figure 1a shows the number concentration of droplets with diameters between 2.0 and 50 µm accumulated from the DSM at a rate of 100 hz (a distance of ≈1 m at Electra research speeds). This sampling rate represents a cloud volume of ≈10 cm^3 when calculating number concentration and ≈ 1 cm^3 when calculating the liquid water content and average diameter. The liquid water content (LWC) and mass-weighted diameter (MWD), i.e. the 4th moment of the size distribution, are plotted in Figs. 1b and 1c, respectively.

A number of interesting features are observed. There are three distinct regions seen in the plot of number concentration. Region A, where the aircraft first penetrates the cloud is characterized by a very abrupt transition from environmental air over a distance of only several meters. This region decreases slightly in concentration before reaching region B where the concentrations vary by factors of three or more. The region labeled C is characterized by remarkably little variation in the number concentration. The Fishing test shows no inhomogeneities other than the slow variations seen at 10-100 m scales. The LWC and MWD are, in contrast to the number concentration, much more variable across the entire cloud pass. The standard deviation in LWC expected as a result of sampling statistics in region C is 30% or less and the instrument uncertainty (Baumgardner et al, 1990) contributes approximately 30%. Therefore, the maximum variability one would expect to see in a homogeneous region would be approximately 40%. Examination of Fig. 1b shows small scale fluctuations sometimes greater than 100%.

There are three other features of interest that are labeled at times D, E and F. Whereas there is little in the number concentration to indicate a change in the structure of the cloud, there is a brief doubling in LWC at point D and then at point E the LWC increase again by a factor of two until point F where the LWC decreases by a factor of 4 over a distance of only a few meters. The number concentration in this region, however, decreases by only a very small amount. Therefore the change in LWC is a result of a shift in droplet sizes as seen in the MWD trace in Fig. 1c.

4.0 Discussion

The contrast between representations of the cloud structure by the number concentration and LWC raises two intriguing questions - What mechanisms are responsible for these variations and what are the subsequent implications for droplet growth processes? Throughout section C the total number concentration is nearly constant. Therefore, the variation of LWC is primarily a function of the fluctuations of the droplet sizes as seen by the abrupt increase in MWD at points D and E and decrease at point F. The growth of droplets by condensation and coalescence in the individual parcels is very sensitive to the size distribution. Parcels with fewer droplets will have higher supersaturations since there is less surface for the water vapor to diffuse to. On the other hand parcels with larger droplets will have higher rates of coalescence. A rough estimate can be made from the present observations of how these condensation and coalescence rates might vary.

To a rough approximation, the quasi-stationary supersaturation can be estimated from the formulation (Cooper, 1989)

$$S_{qs}=\frac{aW}{I} \tag{1}$$

where a is on the order of 3×10^{-3}. W is the vertical velocity and I is the integral radius ($N\langle r\rangle$). Figure 1d illustrates how the supersaturation could vary if the vertical velocity is assumed constant. Only the relative fluctuations are important since the absolute value is only an approximation. As expected the supersaturation is inversely related to the LWC.

A measure of the rate of coalescence can be estimated by following the procedure of Gillespie (1975) who derived an exact method of predicting an expected time required until a coalescence event given a particular size distribution. We have implemented this technique by using the size distribution measured in each parcel to calculate the expected time until the next coalescence event. These times are plotted in Fig. 1e. Again, as expected, the LWC and coalescence times are inversely related.

These observations lead to the following questions and observations:

- Are the observed fluctuations in LWC a result of mixing of parcels with different histories (Cooper, 1989) or are there fluctuations in supersaturation as suggested by Srivastava (1989) that would contribute to different condensational growth rates?
- What mechanism(s) maintain homogeneity in number concentration while producing large variations in LWC?

These measurements should serve to remind us that it is not only the fluctuations in number concentration that are of importance to cloud droplet growth processes but also the fluctuations in the <u>sizes</u> of droplets as represented by variations in the derived supersaturation and coalescence times.

5.0 Summary

The DSM technique provides a mechanism for observing cloud microstructure at scales where potentially important cloud droplet growth processes may occur. A preliminary evaluation of the cloud droplet properties at one meter length scales during a penetration through a Hawaiian rainband has been made. Regions of cloud where the number concentration meets the fishing test's criteria for homogeneity are quite inhomogeneous with respect to the LWC. This variability appears larger than would be expected from counting statistics or measurement uncertainty. The source of this inhomogeneity is variability in the number of droplets with diameters larger than ≈20 µm. Previous theoretical studies have suggested a number of possible mechanisms that could contribute to these fluctuations but further studies are necessary to evaluate these theories with data from instruments such as the DSM.

6.0 Acknowledgements

We would like to thank Kim Weaver for the design of the DSM and Barbara Knowles for laying out the manuscript. NCAR is partially funded by the National Science Foundation.

7.0 References

Baker, B.A., 1992: Turbulent entrainment and mixing in clouds: A new observational approach, *J. Atmos. Sci.*, 49, 387-404.

Baumgardner, D., 1986: A new technique for the study of cloud microstructure. *J. Oceanic and Atmos. Tech.*, 3, 340-343

Baumgardner, D., 1988: Cloud droplet growth rates in Hawaiian orographic clouds. Phd. Dissertation, University of Wyoming, Laramie, Wyoming, 311pp.

Baumgardner, D., W.A. Cooper, and J.E. Dye, 1990: Optical and electronic limitations of the forward scattering spectrometer probe. *Liquid particle Size Measurement Techniques: 2nd Volume*, ASTM STP 1083, E. Dan Hirleman, W.D. Bachalo, and Philip G. Felton, Eds. American Society for Testing and Materials, Philadelphia, 1990, 115-127.

Baumgardner, D., B.A. Baker, and K. Weaver, 1992: A technique for the measurement of cloud structure on centimeter scales, *J. Oceanic and Atmos. Tech.*, In Press.

Cooper, W.A., 1989: Effects of variable droplet growth histories on droplet size distributions. Part I: Theory, *J. Atmos. Sci.*, 46, 1301-1311.

Gillespie, D.T., 1975: An exact method for numerically simulating the stochastic coalescence process in a cloud, *J. Atmos. Sci.*, 32, 1977-1989.

Paluch, I. and D. Baumgardner, 1989: Entrainment and fine scale mixing in a continental convective cloud. *J. Atmos. Sci.*, 46, 261-278.

Srivastava, R.C., 1989: Growth of cloud drops by condensation: A criticism of currently accepted theory and a new approach, *J. Atmos. Sci.*, 46, 869-887

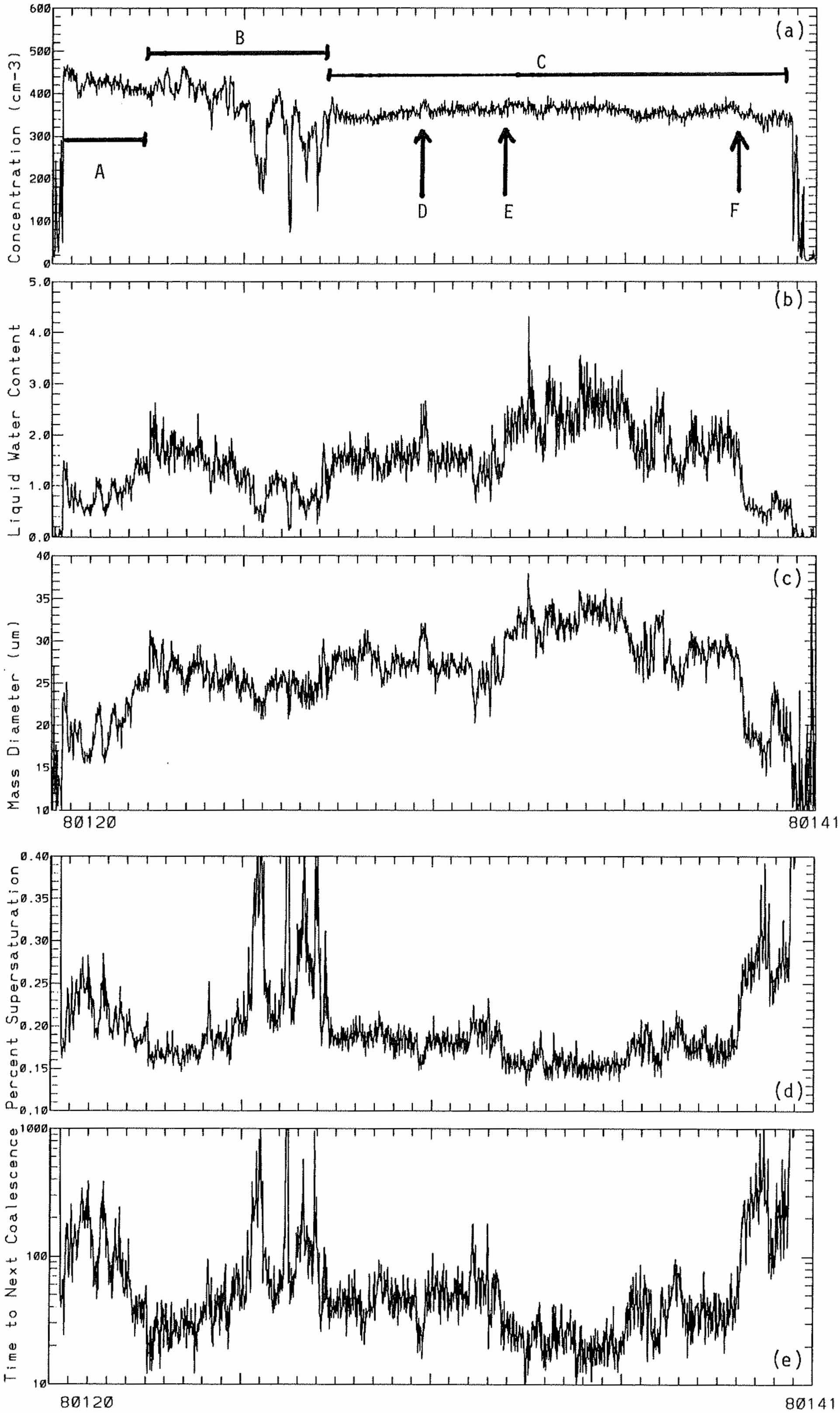

Concentration (cm-3)
(a)
A
B
C
D
E
F
Liquid Water Content
(b)
Mass Diameter (um)
(c)
80120
80141
Percent Supersaturation
(d)
Time to Next Coalescence
(e)
80120
80141

OBSERVATIONS OF RAINDROP SIZE-DISTRIBUTIONS AND FLUCTUATIONS IN TROPICAL RAINFALL AS MEASURED BY A DISDROMETER AND DOPPLER RADAR

Greg M. McFarquhar and Roland List
Department of Physics, University of Toronto, Toronto, Ontario, Canada

1. INTRODUCTION

Phase I of the Joint Tropical Rain Experiment of the Malaysian Meteorological Service and the University of Toronto, conducted in the fall of 1986, revealed that non-steady rain tended to arrive at the ground in packages, with the largest drops first in each followed by progressively smaller drops. When data from a Joss-Waldvogel disdrometer was integrated over time there appeared to be three drop sizes with enhanced number concentrations (0.6-0.7, 1.0-1.2 and 1.8-2.0 mm) regardless of rain origin or type (e.g. cold vs. warm, convective vs. stratiform) (List et al. 1991). These peaks occurred at positions somewhat similar to those of the three-peak equilibrium distributions obtained from numerical models of the collision-induced breakup of raindrops (e.g. Valdez and Young 1985; Brown 1987; List et al. 1987) that used the parameterizations of laboratory raindrop collisions (Low and List 1982). Numerical models of non-steady rain (McFarquhar and List 1991) also produced three-peak distributions with the peaks at the same diameters, but with varying relative peak heights. These distributions were obtained by using a pulsating input of rain at the shaft top, with varying pulse lengths and pulse repetition periods. These models also produced a pattern of packaged raindrop arrival at the ground which was qualitatively similar to that observed in Malaysia.

Phase II of the Joint Tropical Rain Experiment was conducted in Penang, Malaysia between 22 September and 7 November 1990. One goal of this project was to attempt to deduce the origin of streaky packages of rain by observing the reflectivity and radial velocities of the precipitation particles using the University of Toronto semi-portable Doppler radar. Two possible mechanisms for their occurrence had been hypothesized: 1) vertical oscillations of a cloud could cause depletion and replenishing of the precipitation aloft, producing a time varying release of drops; 2) a two-dimensional cloud field could produce these packages, with wind shear causing interference between the packages.

Another goal was to better understand why and when a three-peak raindrop distribution appears. However, after the project was completed the peaks were found to be almost certainly instrument related. Following Sheppard (1990), it was found that the discrepancies between the actual channel boundaries and those specified by the manufacturer were solely responsible for the appearance of the peaked distributions.

2. MEASUREMENT OF PACKAGES BY DOPPLER RADAR

During the Malaysian Tropical Rain Experiment, the EEC LARS-88 X-band Doppler radar was twice used to track convective cells about 25-40 km away from the Bayan Lepas airport. RHI scans were performed every 2 minutes at fixed azimuthal angles to track the evolution of these stationary cells; the rain could not be seen to reach the ground because of ground clutter. Figure 1 shows how the reflectivity varied with time and altitude for a horizontal distance of 30 km away from the radar and an azimuth angle of 252° for one event. At an altitude of 3 km a periodic pulsation with a period of 8 min is clearly seen. Other horizontal distances and altitudes also showed this pulsation, but not as clearly. An event on October 21, 1990 also showed similar patterns. The time between the most intense reflectivities was approximately 7 minutes. Both periods compare well with the buoyancy oscillation period of clouds. No probe data is available for these events because it did not rain at the airport. Typical periods for packages observed at the ground in 1986 and 1990 seemed to be on the order of 10-15 minutes.

When viewing a movie of the evolution of the cell, it appears that there are considerable changes in the amount of precipitation aloft. Hence, this becomes the most likely candidate for the origin of the streaky packages. The exact mechanism by which these changes in the precipitation aloft occur is not known.

These results show that a very quick scan repetition rate is needed to track the rapid evolution of these cells. A volume scan was too long to track the rapid time evolution of cells that approached the radar; therefore a modified CAPPI requiring only 3-4 minutes was developed (List et al. 1991). Here, the rain flux through a predetermined height level (1200-1500 m) with a cross section of approximately 5 km is measured using four PPIs to cover a connected ring-like area around the radar. The elevation angles are lower for each of the 4 scans to account for the free fall of drops. This scheme allowed a measurement of horizontal winds and shear from the low angle PPIs in addition to Doppler velocities and spectral widths from the higher angle PPIs.

Non-steady rain events were observed at the radar station using both the ground probe and the radar, but have yet to be analyzed. With the use of the modified

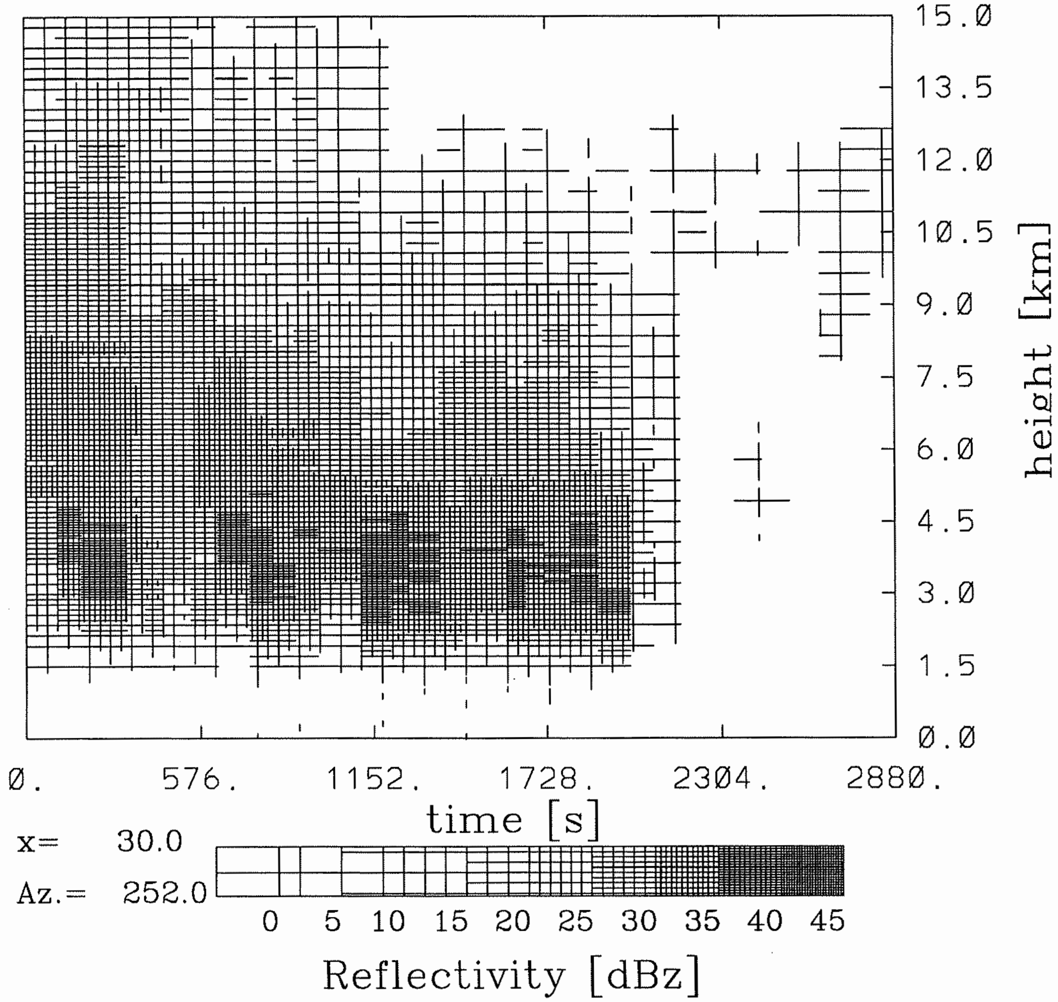

Figure 1. Reflectivity, in dBz, for height above ground at varying times for a horizontal distance of 32 km away from the radar along an azimuth of 252°. The time represents seconds after 0000 local time, Oct. 25 1990.

CAPPI, considerable information about the origin, characterization and evolution of these packages should be obtained.

3. THE DISDROMETER AND THREE-PEAK DISTRIBUTIONS

Several observation of peaks in raindrop-size distributions at similar diameters have been made using Joss-Waldvogel disdrometers (Steiner and Waldvogel 1987; List 1988; Zawadzki and de Agostinho Antonio 1988; Asselin de Beauville et al 1988). Sheppard (1990) recalibrated the signal processing electronics of the disdrometer and showed that the discrepancies between the measured channel boundaries and those specified by the manufacturer were sufficient to produce maxima at diameters similar to those of the peaks (0.6-0.7, 1.0-1.2, 1.8-2.1 mm) produced when a Marshall-Palmer distribution is input to the disdrometer signal processing unit. McFarquhar and List (1992) compared Sheppard's distributions to measured drop-size distributions using a(l), the number density per logarithmic diameter, as an oordinate so that the magnitudes of the peaks could be easily compared. Figure 2 shows that the magnitudes of the measured peaks is very similar to the instrument related ones.

The signal processing electronics for our disdrometer were recalibrated at the Laboratory of Atmospheric Physics at the Eidenössische Technische Hochschule (ETH) in Zurich, Switzerland. The electronics possess a signal recognition circuit to reject any noise and compress the range of output voltages from that produced by the electromechanical transducer. Linear voltages, U_L, corresponding to a diameter calculated from the standard transducer characteristic (Joss and Waldvogel 1977), were fed into the processing electronics and the compressed output voltage, U_C, was measured to obtain a table of U_C versus D. Geometric and polynomial fits to the calibration data were performed and compared to the

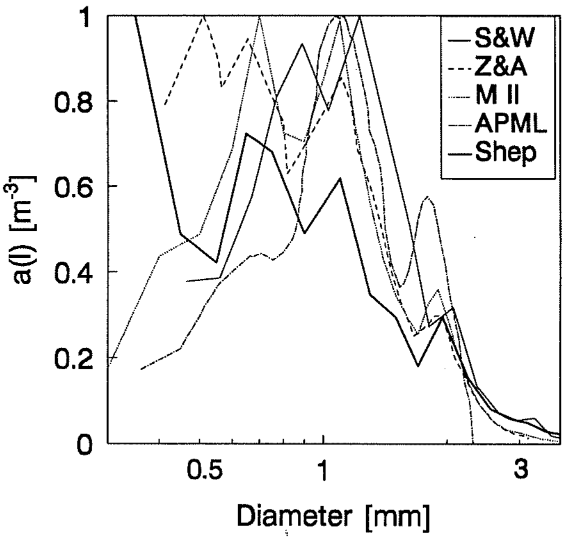

Figure 2. Number density per logarithmic diameter, a(l), against diameter for drop-size distributions recorded with a disdrometer by Steiner and Waldvogel (S&W), Zawadzki and de Agostinho Antonio (Z&A), List et al. (MII) and Asselin de Beauville et al. (APML). The spectra obtained by Sheppard (Shep) by inputing a Marshall-Palmer distribution into the processing electronics is also shown.

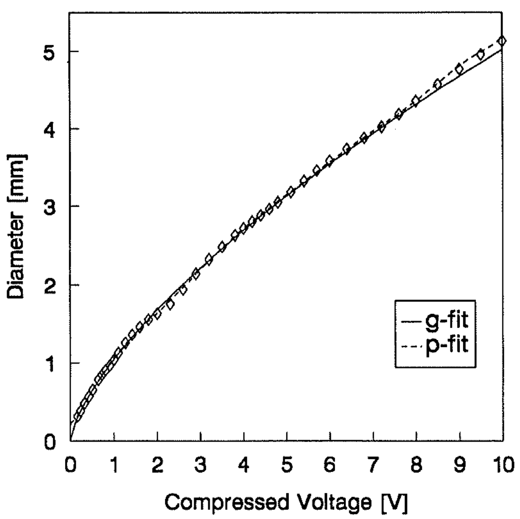

Figure 3. Raindrop diameter against compressed voltage measured by disdrometer using standard transducer characteristic. Diamonds mark experimentally determined calibration points and lines represent different fits to data. The calibration *standard* is obtained by linearly interpolating between calibration data points.

standard fit, obtained by linearly interpolating between all 77 calibration points. Figure 3 shows the calibration data together with the fits.

The compressed voltages were stored for each raindrop hitting the transducer during both field projects. Thus, the drop-size distributions obtained using different calibrations may be compared. Figure 4 shows the drop-size distributions obtained from the 1990 Malaysian data (>36 hours of rain), sorted according to one-minute averaged rainrates, using the best geometric fit to the calibration data and using the *standard fit.* The spectra obtained using the geometric fit have definite peaks at diameters of 0.7, 1.1 and 1.8 mm with varying heights, whereas those obtained using the *standard* are unimodal with peak diameter increasing with rainrate. When the spectra are examined using the best polynomial fit to the calibration data or the original manufacturer's calibration, similar patterns to those in Figure 4 are seen; peaked distributions are realized. This shows that the drop-size distributions obtained using disdrometers are very sensitive to the manner in which a best fit curve is chosen to represent the calibration data. Further, it suggests that the multiple peak scenarios previously reported by many authors are entirely instrument related.

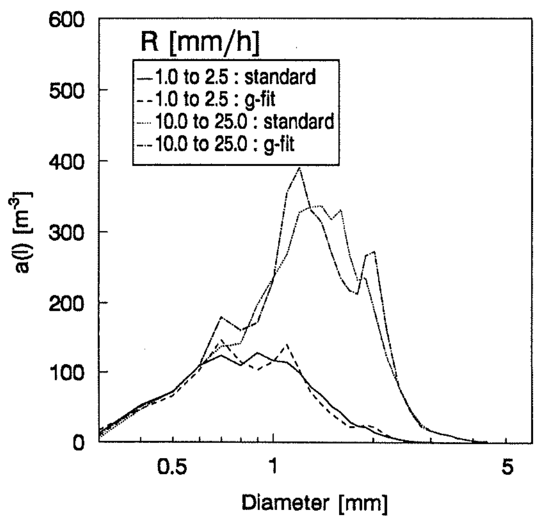

Figure 4. A(l) versus diameter for average drop-size distributions measured in Malaysia in 1990 sorted according to one-minute averaged rainrate using geometric fit to the calibration data and using the calibration *standard.*

No evidence of shape conservation with rainrate is seen in Figure 4, a strict requirement for the occurrence of theoretically predicted equilibrium distributions (List 1988). This, however, does not disprove the existence of equilibrium distributions because at higher rainrates most smaller diameter drops are not measured because the low diameter cutoff is highly dependent on rainfall rate (List 1988), possibly explaining why few small diameter drops were observed during intense rain events.

The disdrometer gives a good estimate of the total rainfall amount. When the rainfall amounts estimated from the disdrometer were compared to those obtained from a rain gauge immediately adjacent, there was only a 12% difference on average. The rainfall amounts are similar regardless of whether a curve fit or the standard fit to the calibration data is used. Z-R relations are also the same regardless of which fit is used.

The measurements made in Malaysia do not disprove the existence of three-peak distributions in nature. Three-peak distributions result from the collision-induced breakup of raindrops in numerical models based on the parameterizations of laboratory raindrop collisions that were dependent in no way upon the disdrometer data. Willis (1984) also observed three-peak distributions at cloud base using optical spectrometers in a hurricane system. Finally, given the frequent occurrence of rainrates less than 5 mm h^{-1}, and the cloud heights and freezing levels observed in Malaysia, it is not certain that three-peak distributions would necessarily be expected on the average. Many raindrop collisions are needed to produce the three-peaks; in fact, for a rainrate of 5 mm h^{-1} more than 5 minutes corresponding to 3 km of free fall would be needed to create the peaks from a Marshall-Palmer distribution. However, it is suggested that three-peak distributions are not as apt to occur in nature as was originally suspected.

4. CONCLUSIONS

Periodic reflectivity fluctuations in the precipitation aloft in a cloud system were observed during Phase II of the Joint Tropical Rain Experiment of the Malaysian Meteorological Service and the University of Toronto with a Doppler radar. These fluctuations had time scales similar to the period of natural buoyancy oscillations of clouds. These fluctuations may produce the timed arrival of drop packages at the ground that are frequently observed in non-steady rain. Future analysis will compare packaging observed by the ground probes to the fluctuations observed by the Doppler radar.

It was shown that the existence of three-peak distributions quoted for the previous Malaysian project was due to an instrument related problem. This means that a discrepancy between the model results and the observations now exist. To obtain a better data set for modeling purposes, future field observations should be made with additional instruments such as optical probes and vertically pointing Doppler radars. In this way, a more complete understanding about factors affecting the evolution of drop spectra may be obtained. A more complete description of the drop-size distributions measured in Malaysia and the fits to the calibration data is found in McFarquhar and List (1992).

ACKNOWLEDGEMENTS

This research was supported by the Natural Sciences and Engineering Research Council (NSERC) of Canada, the Canadian Atmospheric Environment Service and the Malaysian Meteorological Service. One of the authors (GM) is grateful to the NSERC for a graduate fellowship.

REFERENCES

Asselin de Beauville, C.A., R. Petit, G. Marion and J.P. Lacaux, 1988: Evolution of peaks in the spectral distribution of raindrops from warm isolated maritime clouds. *J. Atmos. Sci.*, **45**, 3320-3332.

Brown, P.S., Jr., 1987: Parameterization of drop-spectrum evolution due to coalescence and breakup. *J. Atmos. Sci.*, **44**, 242-249.

Joss, J., and A. Waldvogel, 1977: Comments on 'Some observations on the Joss-Waldvogel rainfall disdrometer.' *J. Appl. Meteor.*, **16**, 112-113.

List, R., 1988: A linear radar equation for steady tropical rain. *J. Atmos. Sci.*, **45**, 3564-3572.

List, R., N.R. Donaldson, and R.E. Stewart, 1987: Temporal evolution of drop spectra to collisional equilibrium in steady and pulsating rain. *J. Atmos. Sci.*, **44**, 362-372.

List, R., R. Nissen, G.M. McFarquhar, D. Hudak, N.P. Tung, T.S. Kang and S.K. Soo, 1991: Properties of tropical rain. *25th Int. Conf. Radar Meteor.*, Paris, 774-777.

Low, T.B., and R. List, 1982: Collision, coalescence and breakup of raindrops. Part II: Parameterization of fragment size distributions. *J. Atmos. Sci.*, **39**, 1607-1618.

McFarquhar, G.M., and R. List, 1991: The evolution of three-peak raindrop size distributions in one-dimensional shaft models. Part II: Multiple pulse rain. *J. Atmos. Sci.*, **48**, 1587-1595.

McFarquhar, G.M., and R. List, 1992: The effect of curve fits for the disdrometer calibration on raindrop spectra, rainfall rate and radar reflectivity. *J. Appl. Meteor.*, submitted.

Sheppard, B.E., 1990: Effect of irregularities in the diameter classification of raindrops by the Joss-Waldvogel disdrometer. *J. Atmos. Ocean. Tech.*, **7**, 180-183.

Steiner, M., and A. Waldvogel, 1987: Peaks in raindrop size distributions. *J. Atmos. Sci.*, **44**, 3127-3133.

Valdez, M.P., and K.C. Young, 1985: Number fluxes in equilibrium raindrop populations: a Markov chain analysis. *J. Atmos. Sci.*, **42**, 1024-1036.

Willis, P.T., 1984: Functional fits of observed drop size distributions and parameterization of rain. *J. Atmos. Sci.*, **41**, 1648-1661.

Zawadzki, I., and M. de Agostinho Antonio, 1988: Equilibrium raindrop size distributions in tropical rain. *J. Atmos. Sci.*, **45**, 3452-3459.

CASE STUDY OF CUMULUS MICROSTRUCTURE WITH THE NEW FFSSP

A.R. Rodi, J.L. Brenguier, and J.P. Chalon

Météo-France, CNRM, 31057 Toulouse Cedex, France

1. INTRODUCTION

Brenguier (1992a,b) reports aircraft droplet measurements in small non-precipitating convective clouds taken with spatial resolution of $\sim 10\ cm$. In active mixing regions, sharp interfaces of few tens of centimeters were observed. Also shown is an example of extremely sharp interfaces between cloudy and cloud-free air where the droplet concentration increases from almost 0 to a value close to 2000 cm^{-3} on a distance of 1 cm, equivalent to the distance between droplets. Interspersed among the highly mixed regions are areas of relative uniformity.

These observations strongly support the conceptual model of entrainment and mixing as a process of engulfment of masses of environmental air which are then stretched into finer and finer filaments, down to a size small enough for diffusive processes to dominate (Broadwell and Breidenthal, 1982; Baker et al., 1984; Telford, 1981, 1988).

For our purposes here, we can think of the cloud as a buoyant plume rising through and perturbing its environment. Shear and buoyancy instabilities are sources of turbulent kinetic energy for the mixing to follow. Thus, in making penetrations of clouds with a research aircraft, we would expect to see cloud-free regions of various sizes, depending on the stage of the mixing process, in proximity to regions of largely uniform properties. These uniform regions may be adiabatic or themselves mixed depending on the mixing history. We would expect to see a life-cycle of the highest turbulence levels at the interfaces of cloud regions with different histories, resulting in a cascade of eddy sizes to the smallest (Kolmogorov) scale, followed by diminishing turbulence levels as the sources of the mixing are eliminated after homogenization is complete.

The main objective of the present paper is to interpret the observations of Brenguier (1992a) using concurrent observations of turbulence and state variables in a preliminary attempt to characterize the conditions under which these small discontinuites in clouds were observed. The emphasis is on the turbulence levels in the mixed regions. We make no attempt at this point to present a systematic analysis of entrainment and mixing. However, we are presenting observations which are relevant to the formulation of the conceptual models of entrainment and mixing.

2. DATA

Observations are from aircraft penetrations of small convective clouds made by the Météo-France Merlin-IV research aircraft. Of particular interest are cloud droplet spectrum measurements from a Forward Scattering Spectrometer Probe (FSSP) which has modified electronics for higher resolution measurements, called the Fast-FSSP (FFSSP). The details of the FFSSP are contained elsewhere in this volume (Brenguier, 1992a) and in Brenguier et al. (1992). Sampling statistics ultimately determine the smallest scale observable since droplets are observed individually. In the present study, we think that droplet concentration can be observed meaningfully on scales as small as $\sim 10\ cm$ (1000 Hz at a typical aircraft speed of 100 $m\ s^{-1}$). However, for clouds with smaller concentrations, the scale would be larger.

Supporting measurements of the kinematic variables were made with $\sim 8\ m$ resolution (25 Hz sampling) using standard instrumentation (inertial navigation system and differential pressure radome gust system). In the present study, temperature measurements may be contaminated by sensor wetting problems, and high frequency humidity measurements are not available. Thus we exclude the thermodynamic measurements from this preliminary study.

We define the variables $\overline{w'^2}_{f=8.\,Hz}$ and $\overline{w'^2}_{f=.8\,Hz}$ as measures of turbulent kinetic energy at frequencies $f = 8\ Hz$ ($\lambda = 12.5\ m$) $f = .8\ Hz$ ($\lambda = 125\ m$), respectively. These were calculated from time series filtered with a narrow band-pass filter with center frequencies around f=8 and .8 Hz. These variances are intended to represent, the turbulence levels at these two scales in the cloud.

In the discussion to follow, we see that the finer-scale cloud structures are more coherent with the perturbation vertical wind speed $\overline{w'}$ than with w itself. This is a reflection of the inhomogeneity of the mixing process in which the droplet spectrum is more a result of turbulent processes in the cloud that the mean updraft itself. Thus, we compute $\overline{w'}$ by filtering the vertical velocity time-series with a high pass filter with cutoff frequency $f = .8Hz$ ($\lambda = 125\ m$).

3. CASE STUDY OF 23 AUGUST 1991

The atmosphere was characterized by convective instability on the 810 hP level resulting in cloud bases (estimated by the pilot) to be about $+5°\ C$ and cloud tops about $0°\ C$. The droplet spectrum is typical of that found in a continental, heavily polluted atmosphere. In Fig. 1, the general correlation of the vertical velocities with the droplet droplet concentrations is shown for one of the cloud passes described below. The clouds generally had weak updrafts with cells in various levels of mixing and the large degree of variablility is characteristic of this type of clouds.

a. *Time series analysis*

In the plots to follow, we show, at progressively finer scales, the structure of the velocity field in the vicinity of the sharp structures found in the FFSSP data. Two cloud penetrations will be discussed, and they are marked, respectively, '1' and '2' in the next two figures.

In Fig. 2 , representing two separate cloud passes, we see in the 1-s averaged data that the largest turbulence levels as represented by the variables

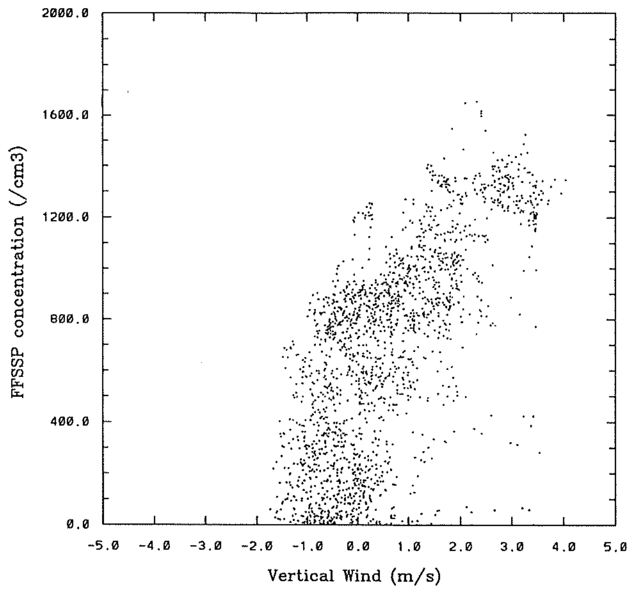

Figure 1: Scatter diagram of vertical wind speed, w $[m\,s^{-1}]$ versus FFSSP concentration, N $[cm^{-3}]$ Data are filtered to 10 Hz.

$\overline{w'^2}_{f=8.\,Hz}$ ('varw1' on the plot) and $\overline{w'^2}_{f=.8\,Hz}$ ('varw3') exist generally in the regions of diminished droplet concentration and downdraft. We as other investigators will call these regions 'mixed'. In the 12:54 Z pass (right hand side of Fig. 2), especially, we see cloud remnants associated with these high turbulence levels (symbol $\otimes$). The vertical wind maxima are coherent with the concentration maxima at this large scale in regions which we call 'uniform'.

In Fig. 3, we now show unaveraged data for a small segments (for the times represented as '1' and '2' in Fig. 2). The distance along the x-axis of the panels now is about 200 m. (We now plot the FFSSP actual rate n $[s^{-1}]$ instead of the concentration since we do not have airspeed measurements at the higher rate). The 1000 Hz rate was chosen as the maximum at which reasonable structures can be observed given the sampling statistics at these concentrations. We can see in active mixing regions the holes and sharp interfaces of few tens of centimeters interspersed among regions of relative uniformity. We also note from the time series regions in which fluctuations in $\overline{d}_{vol}$ are correlated with fluctuations and some that are not.

In mixed regions, these structures are not typically coincident with downdraft air, However, in Fig. 2, we can see that there is generally coherence between the regions which look mixed and negative perturbations velocities.

In Fig. 4, we replot the FFSSP rate data on a scale expanded once again so that the distance represented along the x-axis of the panels is now about 16 m. We see the discontinuities, on mm-scale, in droplet concentration as well as the cloud-free regions on cm-scale. the structures labeled 'A' are sharp edges as discussed by Brenguier (1992a). The cm-scale structures labeled 'B' are very small cloud-free regions (holes).

b. *Spectral analysis*

In the uniform regions, we would expect to see the power spectrum to reflect the random fluctuations that exist on smaller scales. This randomness would look like 'white noise' in the spectrum. However, in the mixed regions there is structure down to the smallest scale observable. In Fig. 5, a power spectrum of n from regions identified as 'mixed' is plotted for 1000 Hz FFSSP time series. Since the mixed regions were very

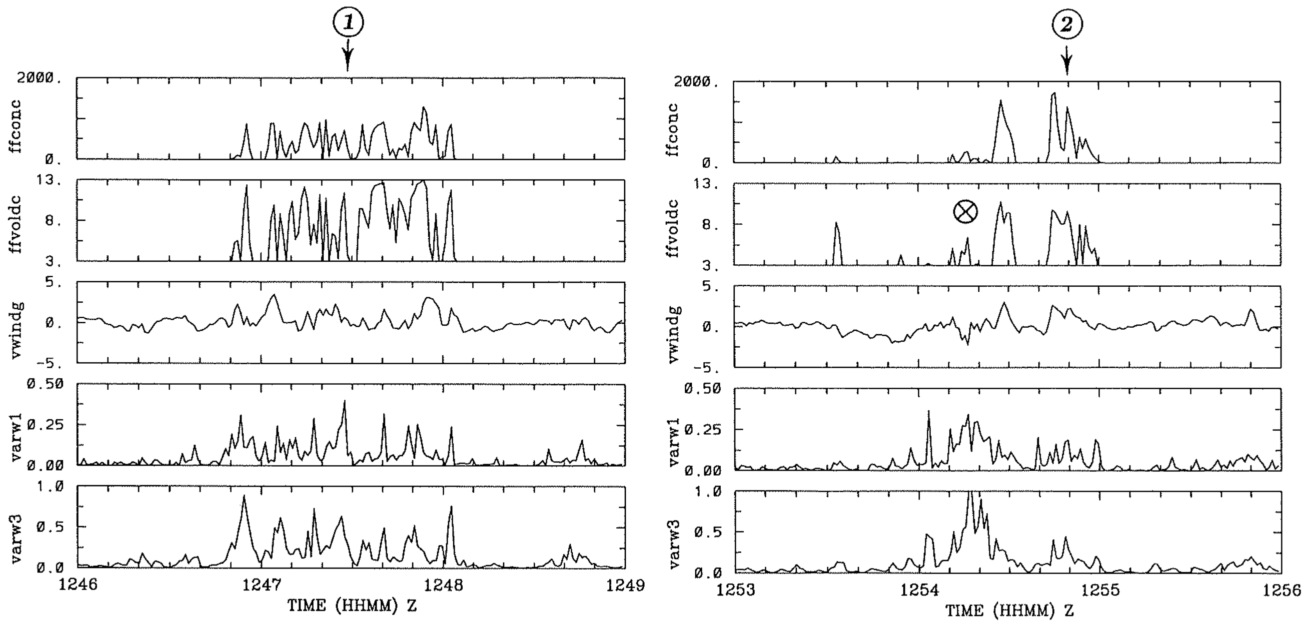

Figure 2: Time series of data for penetration of small, non-precipitation cumuli at 12:46 Z (left) and 12:53 Z (right). Data are 1-s averages. Each 10-s corresponds to $\sim$ 1 km distance. Traces are of FFSSP concentration, N $[cm^{-3}]$, ('ffconc'); FFSSP mean volume diameter, $\overline{d}_{vol}$ $[\mu m]$, ('ffvoldc'); vertical wind speed, w $[m\,s^{-1}]$, ('vwindg'); variance vertical wind, $\overline{w'^2}_{f=8.\,Hz}$ $[m^2\,s^{-2}]$, ('varw1'); variance vertical wind, $\overline{w'^2}_{f=.8\,Hz}$ $[m^2\,s^{-2}]$, ('varw3').

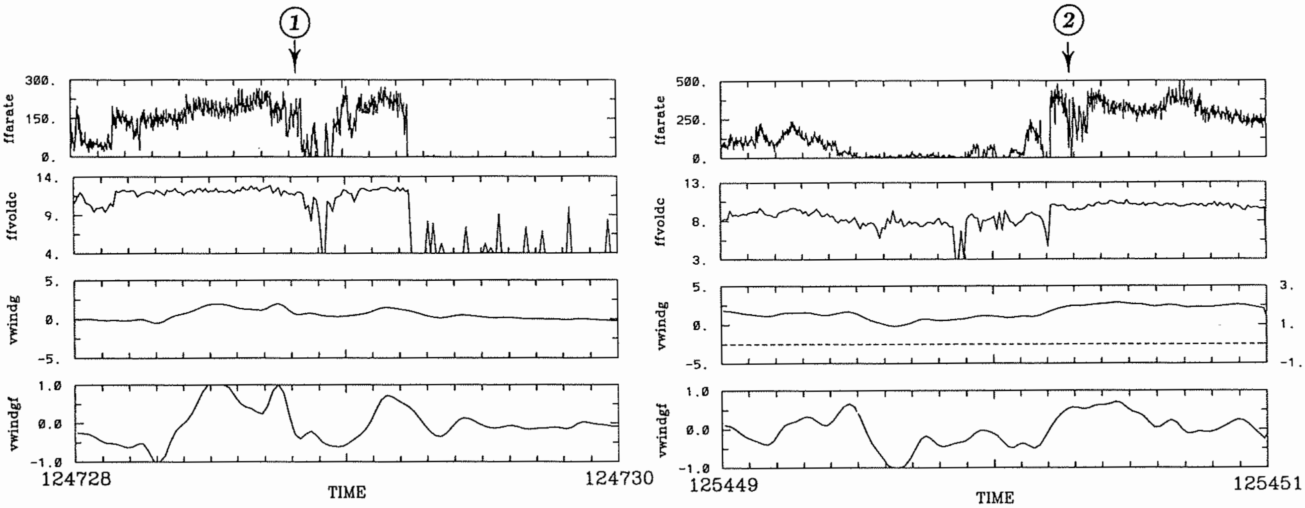

Figure 3: Expansion in time of period beginning 12:47:28 Z (left) and 12:54:49 Z (right) from penetrations shown in Fig. 2. Times marked '1' and '2' correspond to times in Fig. 2. Traces are of FFSSP actual rate n $[s^{-1}]$, ('ffarate', 1000 Hz); $\overline{d}_{vol}$ $[\mu m]$ (100 Hz); w $[m\,s^{-1}]$ (10 Hz); and perturbation vertical wind speed $\overline{w'}_{f_c=.8\,Hz}$ $[m^2\,s^{-2}]$), ('vwindgf', 10 Hz).

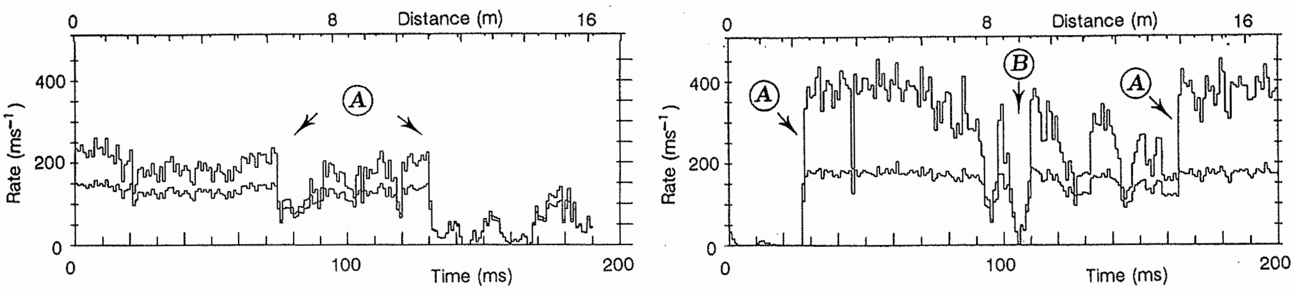

Figure 4: Expansion in time of period beginning 12:47:28.9 Z, labeled '1' in previous figures (left); and beginning 12:54:50 Z, labeled '2' in previous figures (right). Shown are FFSSP counted rate n_d and the actual rate n $[sec^{-1}]$ where $n_d < n$.

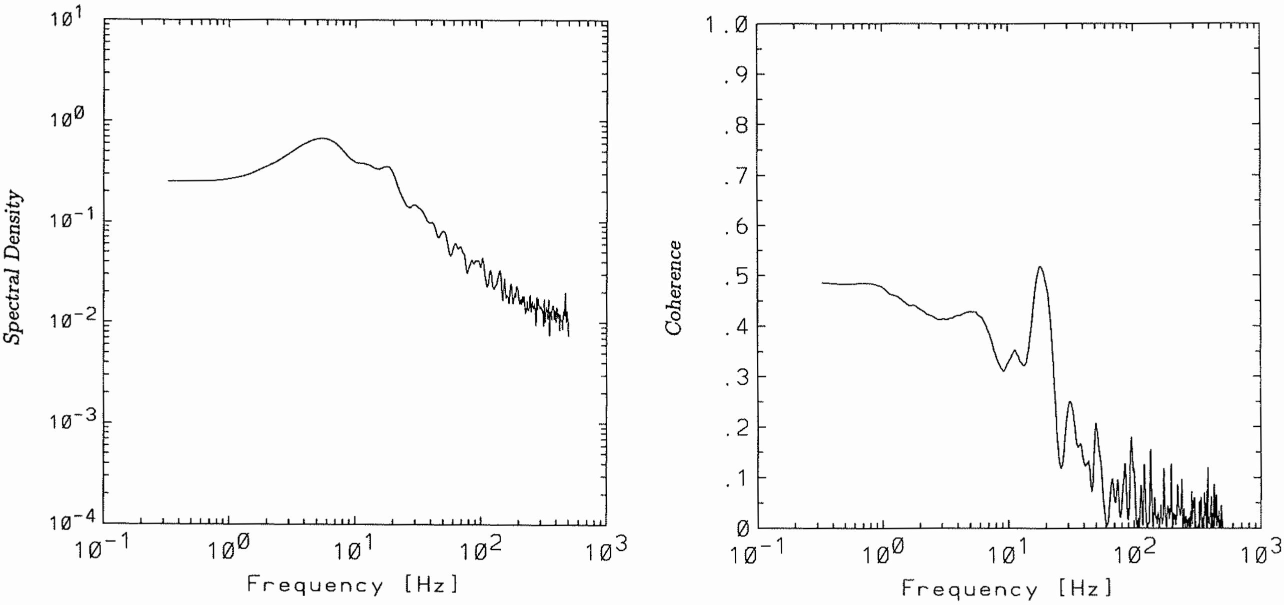

Figure 5: Spectral analysis of 1000 Hz FFSSP data. Left: Power spectral density of n $[(s^{-1})^2/Hz]$. Right: Coherence between series of n and $\overline{d}_{vol}$. Spectral estimates are from a time series of 6050 points.

small in size, the analysis was done by concatenating small segments of time series (after detrending and tapering the endpoints of the segment) to form a total of about 6 seconds of 1000 Hz data.

There is significant structure seen in the concentration data down to 500 Hz ($\lambda \approx .2\,m$). However, this spectrum is not strictly represented by a power law such as -5/3 since at the smallest scale there is significant randomness in the spatial distribution of the droplets as seen in the time series. This randomness is evident at an even larger scale in the spectrum of $\overline{d}_{vol}$ (not shown) since the sampling statistics of $\overline{d}_{vol}$ are not as favorable as for n. However, in these mixed regions, there is significant coherence between n and $\overline{d}_{vol}$ down to about $f = 50\,Hz$ ($\lambda \approx 2\,m$).

4. DISCUSSION

We have shown turbulence data that suggests that the finer-scale cloud structures are more coherent with the perturbation vertical wind speed w' than with w itself. This is a reflection of the inhomogeneity of the mixing process in which the droplet spectrum is more a result of turbulent processes in the cloud that the mean updraft itself.

The droplet sizing is not fully corrected for coincidence here, so estimates of cloud liquid water content are not reliable yet. The sampling problem more severe for the size determination that for concentration since only about 10% of the counted droplets are suitable for sizing. Thus, the scale possible for such analyses is much larger, perhaps by a factor of 10 or more.

Fourier analysis in the mixed cloud regions is probably not the best representation of the energy at the different scales. This is because Fourier analysis of 'step changes' results in adding energy to the highest frequencies. Other techniques of representation in the frequency domain such as wavelets may be useful.

The absence of temperature and humidity data is a serious shortcoming of present data set, and limits this analysis. However, we plan to collect data in the near future using a non-wetting, fast response *in situ* thermometer (Lawson and Rodi, 1992) in addition to the FFSSP that possibly will make studies of the origins of the cloud parcels feasible.

It is our intent here to show in a preliminary manner the context in which the fine-scale FFSSP observations were made. While we make no attempt at this point to present a systematic analysis of entrainment and mixing, we do present observations which are relevant to the formulation of the conceptual models of entrainment and mixing.

5. REFERENCES

Baker, M.B., R.E. Breidenthal, T.W. Choularton, and J. Latham, 1984: The effects of turbulent mixing in clouds. *J. Atmos. Sci.*, **41**, 299-304.

Brenguier, J.L., 1992a: Statistical properties of the droplet spatial distribution in homogeneous and inhomogeneous regions of a stratocumulus: Consequences for spectral evolution. *Preprints 11th Conference on Clouds and Precipitation*, Montreal, Canada, Amer. Meteor. Soc., (this volume).

Brenguier, J.L., 1992b: Observations of cloud microstructure at the centimeter scale. (Submitted to *J. Appl. Meteor.*).

Brenguier, J.L., D. Trevarin, R. Peytavi and P. Wechsler, 1992: New electronics for the FSSP: the Fast FSSP. (Submitted to *J. Atmos. Oceanic Technol.*).

Broadwell, J.E., and R.E. Breidenthal, 1982: A simple model of mixing and chemical reaction in a turbulent shear layer. *J. Fluid Mech.*, **125**, 397-410.

Lawson, R.P., and A.R. Rodi, 1992: A new airborne thermometer for atmospheric and cloud physics research. Part 1: Design and preliminary flight tests. *J. Atmos. Oceanic Technol.*, (in press).

Telford, J.W., 1988: A theoretical solution to the motion of an atmospheric spherical vortex. *J. Atmos. Sci.*, **45**, 789-802.

Telford, J.W., and P.B. Wagner, 1981: Observations of condensation growth determined by entity type mixing. *Pure Appl. Geophys.*, **119**, 934-965.

Acknowledgements: We are grateful to D. Trevarin and R. Peytavi (Météo-France) for their contributions to the FFSSP, and to P. Wechsler (University of Wyoming) for his contribution to the data acquisition system. This research was supported by Meteo-France, ARAT, and INSU under grant 9136173. The first author was further supported by the University of Wyoming during his sabbatical appointment at CNRM.

"Inch clouds?" Observations of Detrained and Dissipating Cloud

Bradley Baker and Darrel Baumgardner

National Center for Atmospheric Research, Boulder, CO

SUMMARY

High resolution droplet spacing data (Baker 1992, Baumgardner et al. 1992) were collected with a forward scattering spectrometer probe (FSSP) during the Hawaiian Rainbands Project. We have investigated moist regions of low droplet concentration near the rainband clouds which we believe were regions where clouds had detrained or were dissipating.

Analysis of such regions with the fishing test (Baker 1992), which looks for variance in the high resolution droplet concentration measurements, greater than expected due to sampling statistics, indicates that such regions can be quite homogeneous or can be extremely inhomogeneous with the inhomogeneous structure being primarily at centimeter scales. Closer inspection of the inhomogeneous regions has revealed sections, typically 1 to 10 cm wide, with concentrations much higher than the mean concentration in the region, sometimes as high as the concentrations in the rainband clouds. Because of their typical size, we have nicknamed these sections "inch clouds". The spatial dimensions of the inch clouds, in directions other than the direction of flight, are not yet measurable.

These observations can be explained by the same speculative ideas suggested by Baker (1992) to explain centimeter scale inhomogeneities in clouds.

THE INCH CLOUDS

Our first concern was to determine whether this phenomenon is real or an, as of yet, undiscovered spurious effect of the instrument. Indeed we have discovered that the FSSP is at times susceptible to electronic noise which creates bursts of counts. However there is a clear signature of this type of noise, in the distribution of interarrival times between droplet detections, which can be used as a diagnostic. This signature is absent from the inch cloud regions we have studied. Also, whereas counts due to electronic noise can occur above the trade wind inversion, where the relative humidity is very low, the inch clouds occur only below the inversion and are roughly correlated with the relative humidity there, which is usually between 60 and 100%. In the following example, we present further data supporting the existence of the inch clouds as well as characterizing them.

Figures 1a and 1b show, respectively, the relative humidity and the FSSP droplet concentration recorded as the airplane passed through a low concentration region, a cloud, and clear air, in that order. The low concentration region was on the leeward side of the cloud and the clear air on the windward. The plane encountered a downdraft just before entering the cloud. The relative humidity in the low concentration region and in the clear air was about 93%. The oscillations, with periods of several seconds, are caused by the instrument and are not real.

Figures 1c, 1d, and 1e show traces from the FSSP droplet concentration, the King hot wire liquid water content, and the Lyman Alpha absolute humidity hygrometer, respectively, in the low concentration region only. An example of high resolution (10 KHz) FSSP data is shown in figure 1f. The inch clouds are evident only at such high resolution. This section is typical of the entire low concentration region and it can be seen that most of the droplets are in inch clouds. In other low concentration regions the ratio, of droplets in inch clouds to the total number of droplets, is not so high, with some having no inch clouds at all. That is, the regions can be statistically quite homogeneous. The correlation between the liquid water and the FSSP measurements is evidence that the inch clouds are composed of real droplets. Other evidence is the droplet sizes which are shown in figure 2d. When the droplet spacing data, both from the laboratory and from the Hawaiian Rainbands Project, indicated an electronic noise problem, the noise always appeared in the first size bin of the FSSP.

The distributions of widths and concentrations of the inch clouds, in the low concentration region shown, were determined using a simple algorithm which required that at least 10 droplets be counted and that no droplet spacing be greater than 2 cm for a section to be considered a cloud. These are shown in figures 2a and 2b respectively. The algorithm picks out the wider, higher concentration inch clouds only (including about 70% of the counts in this case) and should be slightly biased towards larger widths when the concentration is higher. Therefore the strong inverse trend seen in figure 2c is real and attributable to the mixing characteristics of the region. The droplet sizes shown in figure 2d are from the algorithm determined inch clouds only.

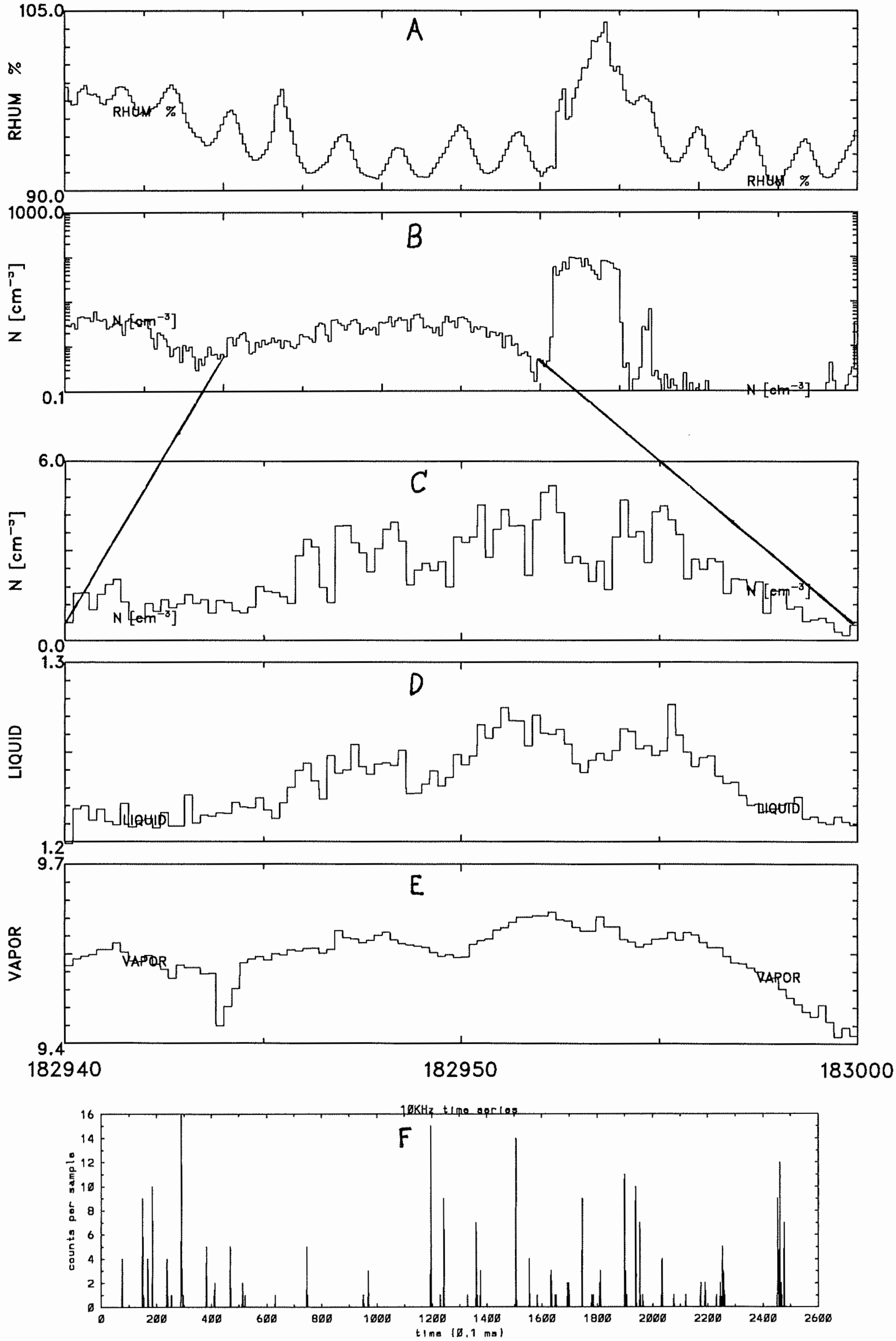

Fig. 1. Time series of A: relative humidity at 5 Hz, B & C: FSSP droplet concentration at 5 Hz (the values shown should be corrected by a multiplicative factor of about 4), D: liquid water content at 5 Hz (g Kg^{-1}, the values shown should be corrected by subtracting 1.2), E: vapor content (g Kg^{-1}), and F: FSSP counts per sample at 10 Hz (~1 cm along the flight path).

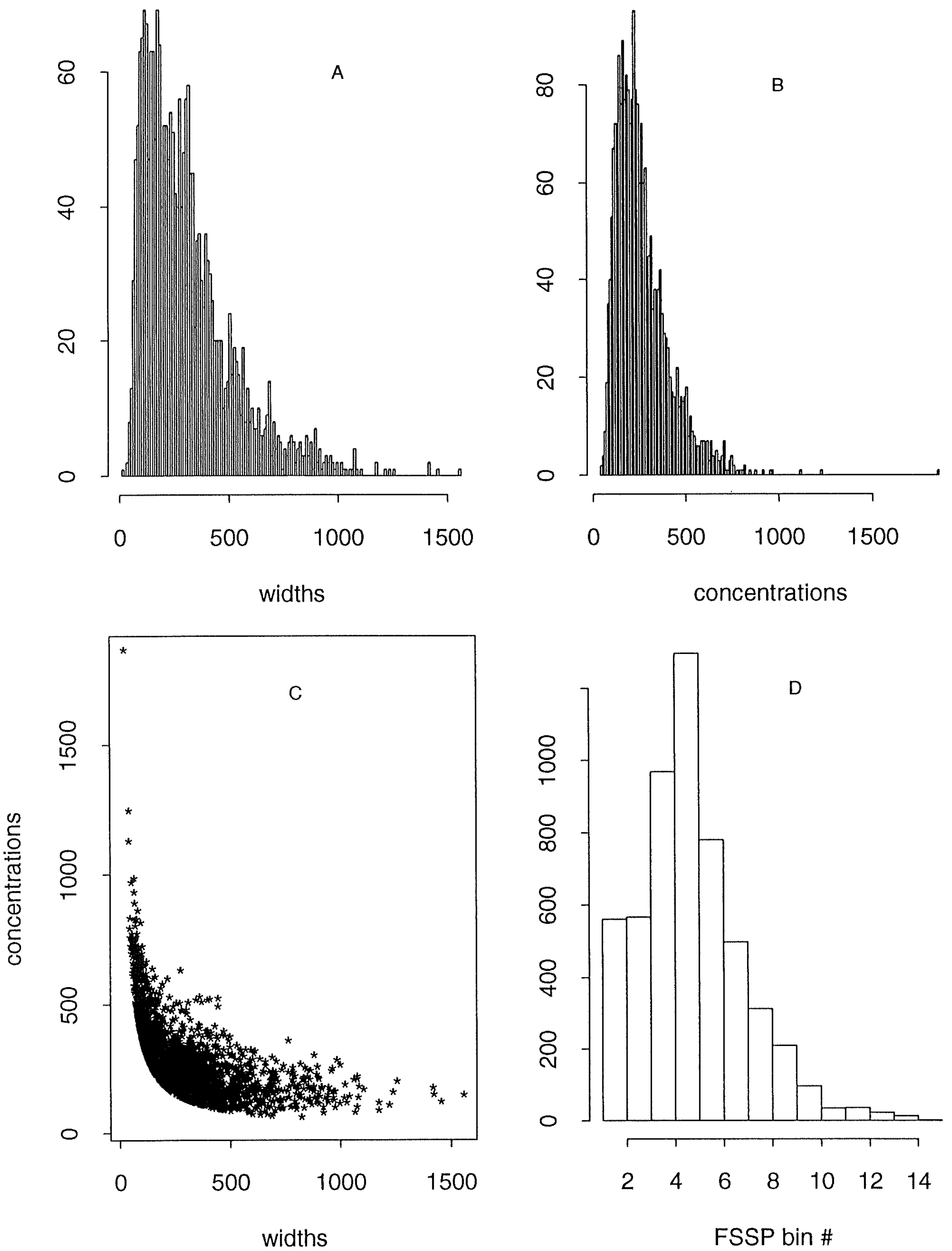

Fig. 2. Inch cloud characteristics; A: distribution of widths in 0.1mm, B: distribution of concentrations in cm^{-3}, C: width vs concentration scatter plot, D: distribution of droplet sizes by FSSP bin numbers 2-15 which correspond to droplet diameters roughly 3 times greater.

DISCUSSION

Baker (1992) put forward a highly speculative explanation for the small ($\sim$ cm) scale inhomogeneities observed, in regions of cloud relatively homogeneous on larger scales, in that study. It was suggested that because the turbulent motions are responsible for homogenization at length scales larger than the Kolmogorov microscale and non-turbulent effects, for example molecular diffusion and the droplets' differential fall velocities, are important at smaller scales, if the time scale for the latter process is greater than for the former, then inhomogeneities can still exist at scales smaller than the Kolmogorov microscale even after the turbulent mixing has produced relative homogeneity at larger scales.

The main difficulty in this explanation is whether the homogenization of the droplets by their differential fall velocities is slow enough to account for the high degree of inhomogeneity typically observed at centimeter scales. An alternative explanation is that the small scale inhomogeneity is not real but rather a spurious effect caused by the plane or the instrument. The lack of another independent measurement with such fine resolution does create doubt. Also, in the dense clouds studied before, the actual inhomogeneous structure, indicated by the fishing test, remained illusive.

In the present study the small scale structure detected by the fishing test, that is the inch clouds, is clearly visible and independent measurements, in particular the King liquid water probe, indicate that the droplets are really there. These inch clouds are explainable by, and perhaps should have been predicted by, the above explanation. In this case, the mixing ratio of clear to cloudy air is much greater than in the denser cloud situation so that the majority of the volume is clear air while a smaller volume is cloudy air which has been mixed and twisted around by the turbulent motions until it exists as thin convoluted sheets which we observe before molecular diffusion and the droplets' fall velocities cause either their evaporation or homogenization over the region. Thus, as well as revealing the structure of mixed regions where clouds have detrained or are dissipating and yielding information on the scales and characteristics of the turbulence there, these observations go a long way towards removing the uncertainties associated with the observations and explanations of Baker (1992).

Acknowledgements We would like to thank Al Cooper for his help in pursuing the many possible causes of spurious FSSP counts. The National Center for Atmospheric Research is sponsored by the National Science Foundation.

REFERENCES

Baker, B., 1992: Turbulent entrainment and mixing in clouds, a new observational approach. *J. Atmos. Sci.*, **49**, 387-404.

Baumgardner, D., B. Baker, K. Weaver, 1992: A new technique for measuring cloud structure on centimeter scales. *J. Ocean. Atmos. Tech.*, In Press.

FIELD STUDIES OF RAINDROP OSCILLATIONS

Ali Tokay and Kenneth V. Beard
Cloud and Precipitation Research, Illinois State Water Survey, Champaign, Illinois

1. INTRODUCTION

Raindrop shape plays an important role in microwave scattering because of differential effects on polarized signals, leading to advanced techniques for radar sensing of rain rates and also to cross-talk in communication links. Scattering by precipitation is usually evaluated using the eccentricity for non-oscillating raindrops, one that increases smoothly with size (Seliga and Bringi, 1976; Oguchi, 1981) In our recent laboratory measurements (Beard et al., 1989), however, we found distinctive shape variations for drops larger than 1 mm diameter as a result of resonance with eddy shedding. In subsequent papers, we described the details of the shape measurements (Beard et al., 1991) and identified the prominent oscillation modes (Beard and Kubesh, 1991). Earlier, Volz (1960) detected oscillations for drops as small as 0.4 mm diameter, and recently, Sterlyadkin (1988) obtained similar information with an experiment sensitive only to raindrops greater than 1 mm diameter. Sterlyadkin concluded that there was no evidence of eddy shedding, and he did not evaluate alternative causes such as drop collisions, turbulence, wind shear. Here, we report on the first oscillation measurements in rain for drizzle and small raindrops with independent measurements of drop size.

2. MEASUREMENT AND ANALYSIS

Data for this study were collected during the Hawaiian Rainband Project in August 1990. The field experiment was located south of Hilo Bay about 1 km from the ocean where we had supporting data from an automated weather station. In Fig. 1 we show the experiment designed to detect the onset of small raindrop oscillations. Oscillation frequencies were measured from photographs using backscattered light of the primary rainbow with a strobe light added to determine the drop sizes from the fall speeds. Directly beneath the sample volume we placed a disdrometer to obtain drop-size distributions. In Fig. 2 we show a fall streak modulation produced by simple oblate/prolate oscillations.

Three kinds of information were obtained from the recorded fall streaks: drop size, oscillation frequency and oscillation amplitude. Distances were measured from 35 mm negatives using a 7X comparator. [The true size in the center of the sample volume was 30 times the recorded dimension.] The size of a drop was obtain from its fall speed by measuring its vertical displacement on the film (h) between strobe highlights. Since the strobe was set at 60 Hz, the velocity was obtained from V (cm s^{-1}) = 60 (3 h), and the size in 0.1 mm categories from a terminal velocity table. Because of the depth-of-field uncertainty, the drop sizes were determined within the following ranges for these selected sizes: $d = 0.5 \pm 0.05$ mm, 1.0 ± 0.1 mm, 1.5 ± 0.2 mm and 2.0 ± 0.3 mm. The oscillation frequency (f) was calculated from the average vertical displacement between gaps in the streaks on the film (λ) by $f = V / (3\lambda) = 60\, h/\lambda$.

We used the dashed portion of the streaks (Δz) to estimate the oscillation amplitude. The angle between the light and the camera at the location of a drop (ψ) decreased by 0.16° cm^{-1} as the drop fell through the sample volume (i.e., $\Delta\psi/\Delta z$ = 0.16° cm^{-1}), so we could determined the total change in rainbow angle caused by oscillations from $\Delta\psi$(deg) = 0.16 Δz(cm). This angular spread is caused by oscillations (see Fig. 2) changing the rainbow angle (Ψ) approximately as $\psi = \Psi + (\Delta\psi/2) \sin \omega t$. To convert the angular amplitude ($\Delta\psi/2$) into an oscillation amplitude, we used the calculated change of 1.3° for a change in axis ratio of 0.01 (1.3° is a typical value for the most likely modes, Beard and Kubesh, 1991). [The standard measure of raindrop distortion is axis ratio, the ratio of the vertical and horizontal chords.]

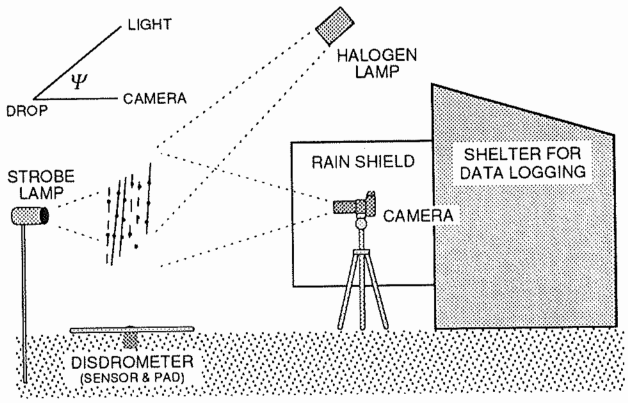

Fig. 1. Schematic of field experiment for measuring the size, frequency and amplitude of oscillating raindrops. The sizes were obtained from the fall speeds (spacing of strobe dots divided by strobe period), whereas the oscillation frequencies and amplitudes were determined from the streak modulations in backscattered light near the rainbow angle. Drop sizes and rainfall rates were obtained from the collocated distrometer.

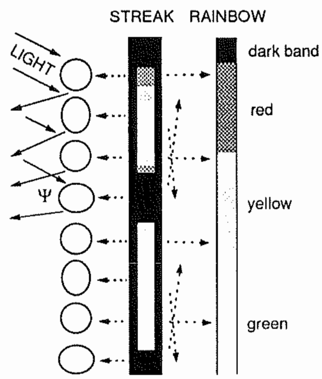

Fig. 2. Schematic of camera-recorded fall streak with modulations produced by raindrop oscillations (oblate and prolate distortions). The light rays illustrate how the emergence angle (Ψ) for the primary rainbow changes with drop distortion. The dotted arrows show the portions of the fall streak corresponding to drop distortion and to the origin of color in the rainbow.

Measurements were taken in moderate-to-heavy showers that were carried ashore by the northeast trades. The winds near the ground were breezy, averaging 2 - 4 m s^{-1}. The showers usually lasted about 10 minutes and generally consisted of drizzle and small raindrops with short episodes of moderate-size drops. Our photographic data were grouped into two categories of rain rate: moderate showers (3.5 mm h^{-1} average) and heavy showers (22 mm h^{-1} average). A total of 1491 raindrop streaks were measured from 271 frames of data obtained in five different showers (2 moderate and 3 heavy).

Continuous and automatic drop-size measurements were made with a Distromet RD-69 disdrometer borrowed from the Alberta Research Council (Canada). This instrument transforms raindrop impacts on an acoustical sensor into electrical pulses whose amplitudes are a function of drop diameter. Drop diameters were categorized in 50 channels of 0.1 mm diameter from 0.1 to 5.0 mm. Minor random errors in sizing occur because natural variabilities in drop impacts, whereas minor systematic errors in sizing occur from the use of a simplified calibration function (Joss and Waldvogel, 1977) and nonlinearities in the RD-69 signal-compression electronics (Sheppard, 1990). We checked the ARC instrument with two small drop sizes (0.45 and 0.85 mm diameter) produced in our laboratory at terminal velocity, and found an undersizing of 0.05 - 0.10 mm. Since this error was consistent with Sheppard's results for these sizes, we concluded that the ARC instrument was function normally.

The size spectra from the disdrometer data are shown in Fig. 3 for moderate (a) and heavy (b) showers. The general character of the raindrop size distributions are adequately depicted by the disdrometer data despite uncertainty in the number of drops in the categories with low counts and possible erroneous sizing by about one category. There is a peak in small raindrop counts near 1 mm diameter. Heavy showers have significantly more drops between 1.5 and 2.5 mm than moderate showers. The absence of significant drops larger than about 2.5 mm may indicate a limit of coalescence growth or collisional breakup, although these explanations are not generally applicable since raindrops as large as 8 mm diameter have been detected in similar Hawaiian showers by Beard et al. (1986) (also see Rauber et al., 1991).

3. RESULTS

The number of oscillating and non-oscillating drops is shown in Fig. 4 obtained from broken and continuous streaks in the camera data. In both moderate and heavy shower cases, practically all drops with diameters larger than about 1 mm were found to be oscillating. The demarcation between oscillating and non-oscillating drops is near 1 mm diameter, but is somewhat indistinct because of the uncertainty in obtaining the true size.

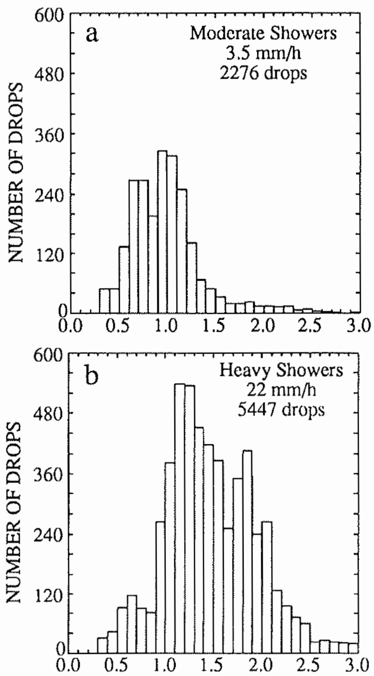

Fig. 3. Raindrop size spectra from disdrometer data for a) moderate and b) heavy rain cases. Corresponding concentrations of 137 and 401 (per cubic meter of air) were calculated from the sensor area and the raindrop fall speeds. These spectra are from the disdrometer data taken concurrently with the camera data.

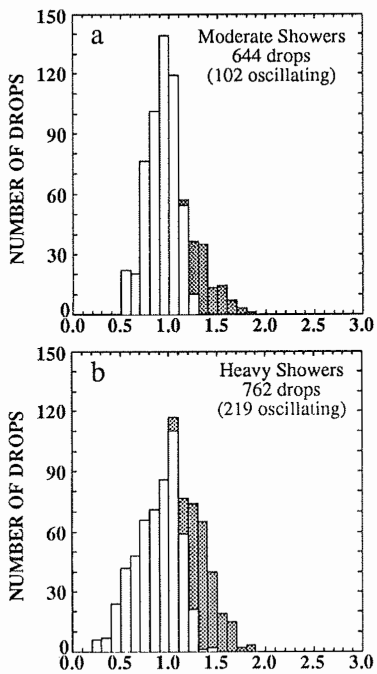

Fig. 4. Raindrop oscillation spectra from camera data for a) moderate and b) heavy rain cases. The number of oscillating drops, given by shaded bars, shows the onset of oscillations near 1 mm diameter. Although these spectra were taken during the same times as the disdrometer data, there are fewer drops than in Fig. 3, because the average sampling rate with the camera is lower. Also, raindrops larger 1.4 mm diameter are undersampled in the camera data because the experiment was optimized for backscattered light from nearly spherical drops.

The nature of raindrop oscillations for drops much larger than about 1.4 mm diameter is not well resolved in our experiment because the optics was set at $\psi \approx 38° \pm 1°$ to gather data on raindrops near 1 mm. The increasing distortion of non-oscillating raindrops changes the angle for the red edge of the bow from about 42° for a sphere to 37° for a 1.4 mm diameter drop. Drops as large as 1.9 mm diameter were detected by the camera when they were oscillating, because the rainbow angle was oscillating towards higher angles. The general reduction in number of larger drops caused by the increasing distortion is readily seen by comparing the optical data (Fig. 4) with the disdrometer data (Fig. 3).

A separate experiment was conducted with the light at same height as the camera but off to one side. This setup did not discriminate against larger drops because the horizontal cross section of non-oscillating raindrops is circular and therefore the rainbow angle is constant ($\psi \approx 42°$). The purpose of this experiment was to detect oscillations in asymmetric modes, i.e., modes that distort the circular cross section. The results differed from Fig. 4 in that only about half the drops greater than 1.1 mm were oscillating. By comparison with the result from the other setup, we concluded that about half the raindrops are oscillating in axisymmetric modes and half in asymmetric modes.

Both the oscillation amplitudes and frequencies have been estimated from the camera data. The length of the dashed streaks yielded axis ratio amplitudes of typically 0.01 to 0.03 for raindrops of 1.0 to 1.8 mm diameter, values consistent with our lab data and the findings of Sterlyadkin.

Practically all frequencies were closest to the fundamental, but a large standard deviation of about ± 30% indicates that the method of obtaining drop sizes from frequencies used by Volz (1960) and Sterlyadkin (1988) may subject to considerable error. The biggest drops (d = 1.9 mm) were oscillating near the higher frequency of the first harmonic. This suggests a more complex behavior in larger raindrops.

4. DISCUSSION

Eddy shedding is only one of the possible sources of raindrop oscillations. Other causes are turbulence, wind shear near the ground and drop collisions. Simple calculations based on isotropic turbulence in the inertial subrange demonstrate that the energy density around the wavelength $\lambda = V/f$ is much too weak to excite resonant oscillations. For example, the energy in moderate turbulence (0.1 $m^2 s^{-3}$) is less than 0.01% of the surface energy for a 1 mm drop, assuming eddies of size $\lambda = V/f$. In addition, it is most unlikely that a drop will confront successive eddies of the resonant size. The oscillation response for a particular encounter can be estimated from the initial-value solutions for aerodynamic and accelerational changes (Harper et al., 1972). The resulting oscillation amplitudes produced by very strong turbulence (0.1 $m^2 s^{-3}$) at scale λ are entirely negligible. The response to shear near the ground, assuming a logarithmic wind profile at our wind speeds, also indicates negligible amplitudes. Since the raindrops fell into an open volume 3 meters from the camera, there was no significant wind shear or turbulence produced by the light-to-moderate breezes in our experiment. These estimates indicate that oscillations caused by turbulence and shear are insignificant.

It is obvious that collisions with other drops must be far more energetic than "collisions" with shear and small-scale turbulence. The resultant oscillation energy for a particular drop can be determined from input by collisions with smaller drops and dissipation by viscosity (Beard et al., 1983; Johnson and Beard, 1984). For our experiment we first considered the probability of observing drop collisions based on collision frequencies and dissipation for the measured size distributions. The collision rate (number per unit time) for a large drop D falling at speed V colliding with a small drop d falling at speed v at a concentration $n(d)$ is given by

$$C(D, d) = (\pi/4)(D^2 + d^2)(V - v)\, n(d) \tag{1}$$

The number of collisions of a particular D-size drop with any smaller drop in the fixed sample volume of the camera (s) during the sample time (t) is

$$p(D) = t\, s\, n(D) \Sigma_d C(D, d) \tag{2}$$

where $n(D)$ is their concentration and Σ_d is the sum over all drops smaller than D.

In order to compute the number of collision-induced oscillations in the sample volume, we calculated the initial energy for each collision and allowed it to decay by viscosity to an undetectable amplitude. Thus, every drop pair had its own decay length, resulting in a variable sample volume $S(D, d)$. The number of D-size drops that were still oscillating from a collision is given by the sum Σ_D over all interactions in the drop-size distribution:

$$P = t\, \Sigma_D [n(D) \Sigma_d C(D, d)\, S(D, d)] \tag{3}$$

The resultant values of P for the moderate and heavy shower cases are 0.3 and 2.3, respectively. These numbers suggest that there may have been a few collision-induced oscillations in our Fig. 4 data, but we detected over 300 oscillating drops. Thus, the fraction of collision-induced oscillations in our data was negligible.

Until we made the present measurements, we had only the observations of Volz (1960), who found oscillations for 0.4 - 1.4 mm diameter raindrops, and those of Sterlyadkin (1988), limited to drops larger than 1.0 mm diameter. Since, in our experiment, we had observations down to 0.3 mm, we now know that oscillations do *not* occur for raindrops smaller than 1.0 mm. We can only speculate that the smaller raindrops recorded by Volz may have been oscillating from other causes, e.g., collisions with splatter drops. We have also confirmed the observations of Sterlyadkin that the amplitude of raindrop oscillations increases with raindrop size above about 1.0 mm diameter.

Of importance to microwave scattering is a change of up to 30% in the differential polarization signal caused by a shift in axis ratio associated with raindrop oscillations. Evidence of the shift in average axis ratio was found in radar observations (Goddard and Cherry, 1984) and, recently, in aircraft measurements of raindrop shape (Chandrasekar et al., 1988). This shift has been documented by our laboratory work and found to be a natural consequence of the oscillation modes. Because of the general consistency between our lab and field results, we are now convinced that particular oscillation modes cause the shift in average axis ratio that has been observed for small raindrops.

The cause of oscillations is surely eddy shedding for small raindrops, but collisions should become important for larger drops (e.g., see Beard et al., 1983). Streak observations of Sterlyadkin (1988) for moderate-size raindrops show that oscillation amplitudes continued to increase out to 3.5 mm diameter, but aircraft shape measurements of Chandrasekar et al. (1988) indicate constant or decreasing amplitude. These data on moderate-size raindrops are incomplete, since size distributions are unavailable for estimating the role of drop collisions. Thus, we do not know the relative importance of eddy-shedding and collisions in promoting drop oscillations for moderate-size raindrops.

Additional field studies are helping to resolve the causes of oscillations for moderate-to-large raindrops. Shape information is being obtained over several seasons in a variety of rains along with the disdrometer data to evaluate the contribution of drop collisions (preliminary results to be presented at the conference). Such experiments will help us to understand the peculiar physics of raindrop oscillations of all sizes, and will provide the natural shape distributions needed to assess microwave and optical scattering in various kinds of precipitation.

Acknowledgements. We thank C. Richmond and G. Cardinal of the Alberta Research Council for the use of their disdrometer and H. Ochs, D. Holdridge, R. Rogers, and K. Geogakakos for their assistance during the field study and analysis. This research was supported by the Physical Meteorology Program, National Science Foundation under grants ATM 87-22688 and ATM 87-19498.

5. REFERENCES

Beard, K. V., D. B. Johnson and D. Baumgardner, Aircraft observations of large raindrops in warm, shallow, convective clouds. *Geophys. Res. Lett., 13*, 991-994, 1986.

Beard, K. V., D. B. Johnson, and A. R. Jameson, Collisional forcing of raindrop oscillations. *J. Atmos. Sci., 40*, 455-462, 1983.

Beard, K. V., R. J. Kubesh, and H. T. Ochs, Laboratory measurements of small raindrop distortion. Part 1: Axis ratios and fall behavior. *J. Atmos. Sci., 48* (in press), 1991.

Beard, K. V. and R. J., Kubesh, Laboratory measurements of small raindrop distortion. Part 2: Oscillation frequencies and modes. *J. Atmos. Sci., 48* (in press), 1991.

Beard, K. V., H. T. Ochs, and R. J. Kubesh, Natural oscillations of small raindrops. *Nature, 342,* 408-410, 1989.

Chandrasekar, V., W. A. Cooper, and V. N. Bringi, Axis ratios and oscillations of raindrops. *J. Atmos. Sci., 45*, 1323-1333, 1988.

Goddard, J. W. F., and S. M. Cherry, The ability of dual-polarization radar (copolar linear) to predict rainfall rate and microwave attenuation. *Radio Sci., 19*, 201-208 1984.

Harper, E. Y., G. W. Grube, and I-D. Chang, On the breakup of accelerating liquid drops, *J. Fluid Mech., 52*, 565-591, 1972.

Johnson, D. B., and K. V. Beard, Oscillation energies of colliding raindrops. *J. Atmos. Sci., 41*, 1235-1241, 1984.

Joss, J., and A. Waldvogel, Comments on "Some observations on the Joss-Waldvogel rainfall disdrometer," *J Appl. Meteor., 16*, 112-113, 1977.

Oguchi, T., Scattering from hydrometers: a survey. *Radio Sci., 16*, 691-730, 1981.

Rauber, R. M, K. V. Beard and B. M. Andrews, A mechanism for giant raindrop formation in warm, shallow convective clouds. *J. Atmos., Sci., 48*(in press), 1991.

Seliga, T. A., and V. N. Bringi, Potential use of radar differential reflectivity measurements at orthogonal polarizations for measuring precipitation. *J. Appl. Meteor., 15*, 69-76, 1976.

Sheppard, B. E., Effect of irregularities in the diameter classification of raindrops by the Joss-Waldvogel disdrometer, *J. Atmos. Oceanic. Techn., 7*, 180-183, 1990.

Sterlyadkin, V. V., Field measurements of raindrop oscillations. *Izvestiya, Atmospheric and Oceanic Physics, 24*, 6, 449-454, 1988.

Volz, F. E., Some aspects of the optics of the rainbow and the physics of rain. *Physics of Precipitation*. Amer. Geophys. Union, Washington, D.C., 280-286, 1960.

SIZE-DEPENDENT SCAVENGING EFFICIENCIES OF AEROSOL PARTICLES IN A POLLUTED FOG

K.J. Noone[1], A. Hallberg[2], J. Heintzenberg[2], B. Svenningsson[3], H.-C. Hansson[3], A. Wiedensohler[3], J.A. Ogren[4]

[1]Center for Atmospheric Chemistry Studies, University of Rhode Island, Narragansett, RI 02882, USA
[2]Department of Meteorology, Stockholm University, Stockholm S-106 91 Sweden
[3]Dept. of Nuclear Physics, University of Lund, Lund S-223 62 Lund, Sweden
[4]NOAA/ERL/CMDL, Boulder, CO 80303, USA

1. INTRODUCTION

Aerosol particles that are scavenged by cloud and fog droplets will participate in chemical reactions in the droplets, will be removed by precipitation that falls out of the cloud, and will affect the chemical composition of the precipitation. Furthermore, the microphysical and optical properties of the cloud are strongly influenced by the number concentration of particles that act as cloud condensation nuclei. Obviously, understanding the interactions between aerosol particles and clouds requires knowledge of the factors that determine which particles are scavenged. Most of the experimental work that has been done to date has focused on the integral properties (total number, mass and chemical composition) of particles scavenged by clouds and fog. In this paper, we report measurements of the fraction of particles scavenged as a function of particle size and relate the findings to the observed hygroscopic growth characteristics of the particles. Further details are reported in Noone et al. (1992).

2. EXPERIMENTAL

As a part of the EUROTRAC subproject *Ground-based Cloud Experiments (GCE)* an investigation was undertaken in November 1989 to examine the multiphase nature of polluted fogs in the Po Valley of northern Italy (Fuzzi et al., 1992). A coordinated effort was made to measure the dynamical, chemical, and microphysical development of fogs at this site. The intent was to determine the controlling factors in fog formation and dissipation, and changes in the chemical composition of the multiphase system. Five different fog events of varying lengths were sampled during the campaign.

Two sampling inlets were used to determine the size-dependence of the scavenging efficiency of the aerosol particles. One inlet used an inertial impactor to remove particles and droplets larger than 5 μm diameter. The choice of 5 μm is somewhat arbitrary; however, there was very little liquid water associated with droplets smaller than 5 μm in the fogs. Outside fog, this inlet sampled essentially the whole aerosol distribution. In fog, this inlet sampled the "interstitial" aerosol; defined as anything in the ambient cloud smaller than 5 μm diameter. This will be called the *interstitial inlet.* The impactor was located ca. 6 m above the ground. Once sampled from the fog, the sub-5 μm particles were pulled through a 2.5 cm ID tube to a distribution plenum inside the sampling container. Because the temperature in the container was usually 10 - 20 °C above ambient, the particles were dried before they reached the sensing instrumentation. So, while the interstitial particles were sampled wet, they were counted and sized dry. A TSI 3020 Condensation Nucleus Counter (CNC) was used to determine the total number concentration of the interstitial particles. The size distribution of the interstitial particles was measured using a PMS LAS-X Optical Particle Counter (OPC). By integrating the number and volume size distributions, we obtained the number and volume concentrations for the interstitial aerosol.

The Counterflow Virtual Impactor (CVI, Ogren et al., 1985; Noone et al., 1988) was used to sample the fog droplets larger than 5 μm diameter. Two CVI systems were operated in parallel during this experiment. With the CVI, droplets larger than the cut size of the probe (D_{50}; nominally 5 μm diameter) are impacted from ambient air into a dry, particle-free carrier air stream. Once sampled, they are evaporated and the water and labile species in the droplets are driven into the gas phase.

Upon evaporation, each droplet is assumed to release a single *residual* aerosol particle. It is important to distinguish between *interstitial* and *residual* aerosol particles. *Interstitial* particles are those particles smaller than 5 μm present in the ambient cloud. They are not sampled by the CVI. *Residual* particles are the particles released in the CVI after the fog droplets are evaporated. They are the non-volatile material that was dissolved or suspended in the fog droplets.

The number concentration of the residual aerosol particles was measured using a TSI 3760 CNC. As for the interstitial particles, the size distributions of the residual particles were determined using PMS optical particle counters (ASASP-X in CVI#1, LAS-X-HS in CVI#2). For all three OPCs, only the accumulation-mode (0.1-1.0 μm diameter, referenced to ammonium sulfate) size distributions will be discussed. The OPC's were calibrated in the laboratory prior to the experiment using both latex spheres and ammonium sulfate particles. Checks on the sizing of the OPC's and comparisons with the CNC's were also performed on-site.

Filter samples of both the residual and interstitial particles were also taken for subsequent chemical analysis. The CVI samplers were located on top of a container; the inlets were ca. 4m above ground level, and ca 50 cm apart. The interstitial inlet was ca. 2 m higher than the CVI inlets, and was ca. 2 m from the CVIs in the horizontal direction.

The idea behind this sampling strategy was to be able to observe the entire range of aerosol particles and droplets during the course of the fog events. Droplets removed from the pre-fog aerosol by nucleation scavenging would appear as residual aerosol particles, and those that were not scavenged would remain as interstitial particles. As it happened, the two CVI systems seldom had their cut sizes at exactly 5 μm. For various technical reasons, the D_{50} of the CVI systems varied between 5 and 8 μm, leaving a "gap" between the interstitial inlet and the CVI inlets. We were able to calculate the D_{50} of both CVI systems for the entire sampling period and evaluate the consequences of the gap between the interstitial inlet and the CVI inlets. The gap did not have any large effects on the scavenged fraction.

3. RESULTS

The nucleation scavenging efficiency can be examined by looking at the fraction of the total number of accumulation-mode particles scavenged just after fog formation as a function of particle size. Fig. 1 shows the number of accumulation-mode residual particles divided by the sum of the interstitial and residual particle number for the five fog events. As mentioned previously, the CVI was not always sampling at a 5 μm cut size, which means that this fraction may be slightly underestimated. The CVI cut sizes for the data shown in Fig. 1 were: Event 1: 6 μm; Event 2: 6 μm; Event 3: 5 - 6 μm; Event 4: 7 - 8 μm; Event 5: 7 μm.

Particles between 0.1 and 0.3 μm were essentially unscavenged by the fog. This is in sharp contrast to cleaner conditions (Heintzenberg, et al., 1989) in stratocumulus clouds, where a substantial fraction of particles down to ca. 0.05-0.06 μm were scavenged. Because they are not

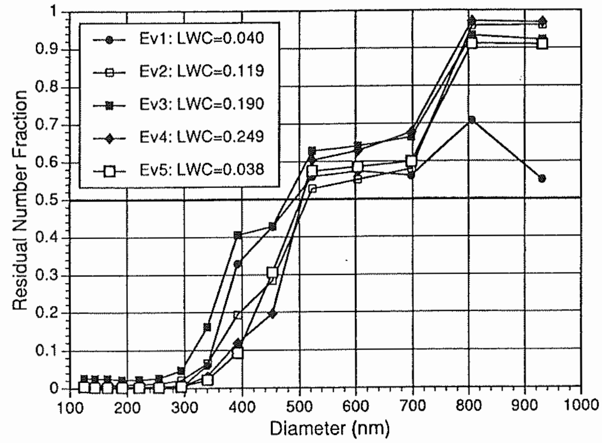

Fig. 1. Observed size-dependence of the scavenging efficiency of aerosol particles at the start of five fog events. LWC is the liquid water content of the fog (g m^{-3}).

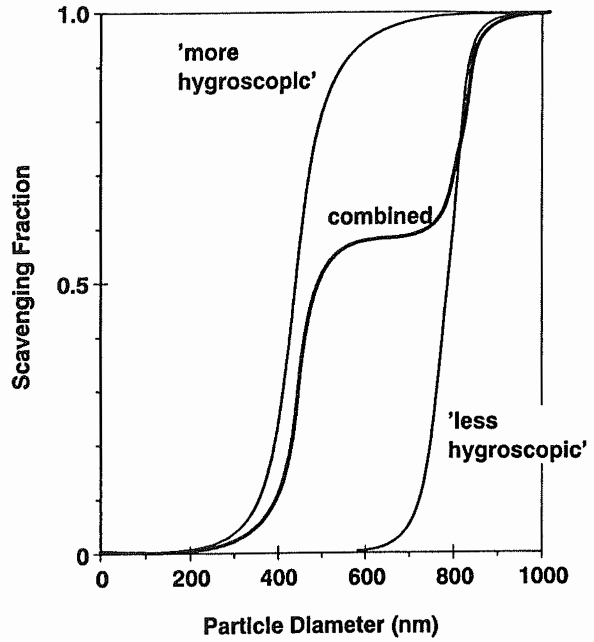

Fig. 2. Size dependence of scavenging efficiency resulting from an external mixture of two populations of particles with differing hygroscopic growth characteristics..

scavenged into the fog droplets, the material associated with these particles (e.g. trace metals, soot, sulfate) will not be available to take part in any reactions in the cloud water. In addition, they will not be affected by those processes such as sedimentation acting on the fog droplets, suggesting that the atmospheric lifetime of these particles will likely be longer than that for the >0.3 μm particles.

The residual number fraction begins to increase above 0.3 μm. It is interesting that despite different aerosol loadings and liquid water contents, the scavenging fraction for all of the fogs reached 50% in a relatively narrow size interval (ca. 0.48 - 0.52 μm). There is an interesting feature between 0.5 - 0.7 μm. For all of the fogs, the curves are relatively flat in this size interval. For all but one of the fogs, the residual number fraction increased to between 0.9 - 1 for particles larger than 0.8 μm. Only Event 1 shows the residual number fraction curve to be relatively flat at all sizes above 0.5 μm.

It is known from other measurements (Svenningsson et al., 1992) that there were typically two types of particles present in the Po Valley fogs. Some particles grew substantially when exposed to increasing relative humidity, while other particles did not. This indicates that there was an external mixture of particles, some of which were hygroscopic and some of which were hydrophobic. It was observed that the fraction of particles that were hygroscopic increased with particle diameter, although there was a good deal of variation in this quantity.

The presence of an external mixture of two populations of particles with different hygroscopic growth characteristics could produce the behavior shown in Fig. 1. A conceptual diagram of the effects of the hygroscopic/hydrophobic nature of the particles on the scavenging efficiency is shown in Fig. 2. Exposing an internally-mixed aerosol to a single supersaturation would activate particles above a certain critical diameter (Köhler, 1921). All of the particles above the critical size would be activated, and all the particles below the critical diameter would not form cloud droplets. This would lead to a step-change in the residual particle fraction. A range of supersaturations, again with an internally-mixed aerosol and no entrainment, would lead to a smearing out of this sharp curve. Higher supersaturations would activate some smaller particles, lower supersaturations would increase the size of the smallest particles activated. The two different populations of particles would have different critical sizes, and hence two different scavenging efficiency curves. Combining those two curves would yield a curve with the shape that was actually observed.

From the measured growth factors (for particles up to ca. 0.2 μm), known relative humidities, bulk chemical composition and particle sizes, it is possible to calculate the relative amounts of soluble and insoluble material for the two different particle classes. The hygroscopic particles were composed of 60% insoluble and 40% soluble material, while the hydrophobic particles were composed of 93% insoluble and 7% soluble material (Svenningsson et al., 1992). If one assumes that the hygroscopic particles activate at a diameter of 0.4 μm (as suggested by the scavenging fraction curves in Fig. 1), a peak supersaturation for the fog can be calculated. If the soluble material were 50% ammonium sulfate and 50% ammonium nitrate, this supersaturation would have been ca. 0.03%. Given this supersaturation, and given that the hydrophobic particles were composed of 7% soluble material, one can compute the minimum size that the hydrophobic particles must have been to have activated at the peak supersaturation. The diameter would have been ca. 0.73 μm. This is precisely the type of behavior observed for fog events 2 - 5.

We have no direct measurements of the hygroscopic nature of particles greater than ca. 0.2 μm, so our explanation for the observed behavior requires extrapolation of measurements made on smaller particles. However, scavenging of an external mixture of hydrophobic and hygroscopic particles can explain both the shape of the observed scavenging curves and the sizes at which the scavenging efficiency changes.

The curves in Fig. 1 indicate that only a fraction of the aerosol is initially scavenged into the fog droplets. It is interesting to quantify the effects of nucleation on two of the integral properties of the aerosol: the total number and volume scavenging efficiency. The volume scavenging efficiency is the same as the mass scavenging efficiency if the density of the particles does not change with particle size.

In Table 1, the total number scavenging efficiency (N_t), the accumulation-mode number scavenging efficiency (N_a), and the accumulation-mode volume scavenging efficiency (V_a) are presented for each of the five fog events. All of the scavenging efficiencies for this polluted fog are much lower than the values observed in other types of clouds in less polluted locations (Hegg et al., 1984; Sievering et al., 1984; ten Brink et al., 1987; Leaitch et al., 1986; Heintzenberg et al., 1989; Okada et al., 1990; Gillani et al., 1991).

Modelling studies have shown that the mass-scavenging efficiency of convective clouds can decrease as the aerosol loading increases (Jensen and Charlson, 1984). Flossmann et al. (1985) predicted number scavenging efficiencies of between 48 to 94%, mainly confined to particles larger than 0.1 μm radius. Less work has been done on aerosol scavenging in fogs. A model study by Pandis et al. (1990) predicted mass scavenging efficiencies of over 70%.

Table 1: Integral scavenging efficiencies observed at the start of five fog events. N_t is the percentage of the total number of aerosol particles (> 0.01 μm diameter) initially scavenged by nucleation. N_a and V_a are the percentages of the accumulation mode aerosol scavenged by number and volume, respectively.

Date	Time	Efficiency (%) N_t	N_a	V_a
10 Nov.	20:15	0.4	1.3	15
11 Nov.	19:30	0.8	2.9	19
14 Nov.	19:00	1.8	8.5	43
15 Nov.	22:55	0.7	2.8	32
17 Nov.	01:00	0.6	2.0	25

4. CONCLUSION

By measuring the size distribution of dry aerosol particles associated with unscavenged aerosol particles and fog droplets, we have been able to determine the efficiency of nucleation scavenging of the particles as a function of size. In terms of the integral properties of the aerosol, less than ca. 1% of the number of particles larger than 0.02 μm were scavenged. Only 1 to 10% of the accumulation-mode particles (0.1-1 μm diameter) were scavenged, while 20 - 30% of the accumulation-mode mass of the aerosol was scavenged. These efficiencies are lower than those measured and calculated for convective clouds. In these fog events in polluted air, most of the aerosol, both in terms of number and mass, was not transferred into the cloud droplets. Consequently, whatever processes that were active in the aqueous-phase in the fog droplets (e.g., oxidation reactions) will have affected only a small fraction of the aerosol

Only a small fraction of the particles smaller than 0.3 μm diameter were scavenged; the diameter for 50% scavenging efficiency was found to be 0.5 μm. Between 0.5-1 μm diameter, the scavenging efficiency was observed to increase to unity in two steps. The presence of a plateau in the scavenging efficiency between 0.5-0.7 μm diameter is attributed to the presence of two distinct types of aerosol particles: a "hydrophobic" fraction that grows by only 5% at 85% relative humidity, and a "hygroscopic" fraction that grows by ca. 60% at 85% R.H. Hygroscopic particles greater than 0.3 μm diameter are scavenged by the fog, whereas only the hydrophobic particles larger than 0.7 μm are scavenged.

A general conclusion that can be drawn from these data is that fogs in this polluted location behave quite differently than convective clouds in terms of aerosol scavenging. In convective clouds, even relatively polluted ones, the number and mass scavenging efficiencies for the aerosol have been found to be higher.

5. ACKNOWLEDGMENTS

The Po Valley Fog Experiment 1989 was conducted as part of EUROTRAC subproject GCE. The invaluable contribution of A. Correggiari, S. Miserocchi, D. Correggiari, C. Foschini and L. Tarozzi during the field work is gratefully acknowledged. L. Bäcklin, S.Å Odh and S. Moritz helped prepare the CVI equipment. Funding for the experiment was supplied by the Swedish Environmental Protection Board, CNR-Progetto Strategico Deposizioni Atmosferiche Acide, and CEC Project EV4V-0084-C. The station of S. Pietro Capofiume is managed by Assessorato Agricoltura - Regione Emilia Romagna.

7. REFERENCES

Flossmann, A. I., Hall, W. D. and Pruppacher, H. R. 1985. A theoretical study of the wet removal of atmospheric pollutants. Part I: The redistribution of aerosol particles captured through nucleation and impaction scavenging by growing cloud drops. *J. Atmos. Sci. 42*, 583-606.

Fuzzi, S., Facchini, M.C., Orsi, G., Lind, J.A., Wobrock, W., Kessel, M., Maser, R., Jaeschke, W., Enderle, K.H., Arends, B.G., Berner, A., Solly, I., Kruisz, C., Reischl, G., Pahl, S., Kaminski, U., Winkler, P., Ogren, J.A., Noone, K.J., Hallberg, A., Fierlinger-Oberlinninger, H., Puxbaum, H., Marzorati, A., Hansson, H.-C., Wiedensohler, A., Svenningsson, I.B., Martinsson, B.G., Schell, D., and Georgii, H.W. 1992. The Po Valley Fog Experiment 1989: An Overview. *Tellus 44B*, submitted.

Gillani, N.V., Daum, P.H., Schwartz, S.E., Leaitch, W.R., Strapp, J.W., and Isaac, G.A. 1991. An observational study of the efficiency of activation of accumulation-mode particles in warm continental stratiform clouds. In *Proceedings of the Fifth International Conference on Precipitation Scavenging and Atmospheric-Surface Exchange Processes*, Richland, WA.

Hegg, D. A., Hobbs, P. V. and Radke, L. F. 1984. Measurements of the scavenging of sulfate and nitrate in clouds. *Atmos. Environ. 18*, 1939-1946.

Heintzenberg, J., Ogren, J. A., Noone, K. J. and Gärdneus, L. 1989. The size distribution of submicrometer particles within and about stratocumulus cloud droplets on Mt. Åreskutan, Sweden. *Atmos. Res. 24*, 89-101.

Jensen, J. B. and Charlson, R. J. 1984. On the efficiency of nucleation scavenging. *Tellus 36B*, 367-375.

Köhler, H. 1921. Zur Kondensation des Wassers in der Atmosphäre. *Meterologische Zeitschrift 38*, 168 - 171.

Leaitch, W. R., Strapp, J. W., Isaac, G. A. and Hudson, J. G. 1986. Cloud droplet nucleation and cloud scavenging of aerosol sulphate in polluted atmospheres. *Tellus 38B*, 328-344.

Noone, K. J., Ogren, J. A., Heintzenberg, J., Charlson, R. J. and Covert, D. S. 1988. Design and calibration of a counterflow virtual impactor for sampling of atmospheric fog and cloud droplets. *Aerosol Sci. Tech. 8*, 235-244.

Noone, K. J., Ogren, J. A., Hallberg, A., Heintzenberg, J., Ström, J., Hansson, H.-C., Svenningsson, I. B., Wiedensholer, A., Fuzzi, S., Facchini, M. C., Arends, B. G. and Berner, A. 1992. Changes in aerosol size- and phase distributions due to physical and chemical processes in fog. *Tellus 44B*, in press.

Ogren, J. A., Heintzenberg, J. and Charlson, R. J. 1985. In-situ sampling of clouds with a droplet to aerosol converter. *Geophys. Res. Lett. 12*, 121-124.

Okada, K., Tanaka, T., Naruse, H. and Yoshikawa, T. 1990. Nucleation scavenging of submicrometer aerosol particles. *Tellus 42B*, 463-480.

Pandis, S. N., Seinfeld, J. H. and Pilinis, C. 1990. The Smog-Fog-Smog Cycle and Acid Deposition. *J. Geophys Res. 95*, 18,489 - 18,500.

Sievering, H., Van Valin, C. C., Barrett, E. W. and Pueschel, R. F. 1984. Cloud scavenging of aerosol sulfur: Two case studies. *J. Atmos. Sci. 18*, 2685-2690.

Svenningsson, I.B., Hansson, H.-C., Wiedensohler, A., Ogren, J.A., Noone, K.J., and Hallberg, A. 1992. Hygroscopic Growth of Aerosol Particles in the Po Valley. *Tellus 44B*, submitted.

ten Brink, H. M., Schwartz, S. E. and Daum, P. H. 1987. Efficient scavenging of aerosol sulfate by liquid-water clouds. *Atmos. Environ. 21*, 2035-2052.

SHIP-PRODUCED CLOUD LINE OF 13 JULY 1991

E. E. Hindman[1], W. M. Porch[2], J. G. Hudson[3], P. A. Durkee[4]

[1]City College of New York, New York City, NY, USA 10031
[2]Los Alamos National Laboratory, Los Alamos, NM, USA 87545
[3]Desert Research Institute, Reno, NV, USA 89506
[4]Naval Postgraduate School, Monterey, CA, USA 93940

1. INTRODUCTION

Steaming ships can produce long, linear cloud lines in regions of fog and broken stratus as detected in 0.63 um satellite images by Conover (1966) and Bowley (1967). Recently, Scorer (1987) and Coakley, et al. (1987) demonstrated that steaming ships also can produce lines in marine stratus layers. The lines are not always detected in 0.63 um satellite images, but are often detected in the corresponding 3.7 um images because the lines contain smaller and more numerous droplets than the stratus in which they are embedded as deduced by Coakley, et al. and measured by Radke, et al. (1989). They postulate cloud condensation nuclei (CCN) from steaming ships produced the more numerous and, hence, smaller cloud droplets. The ship-produced clouds are not always detected in 0.63 um images because this wavelength is not as sensitive to changes in droplet size as is 3.7 um (Coakley, et al., 1987).

On 13 July 1991 a dramatic, ship-produced cloud line formed offshore of Baja California. We present satellite images of the line and corresponding photographs from the *R/V EGABRAG III* which passed under the line. The images and photos reveal the structure of the line. The *EGABRAG* was a source of CCN but did not produce a cloud line; we attempt to explain this important finding.

2. OBSERVATIONS AND MEASUREMENTS

A sequence of high-resolution Geosynchronous Orbiting Environmental Satellite (GOES) images (Figs. 1a, 2a and 3a) shows the formation of the cloud line; the unidentified ship producing the line was estimated to be steaming at about 310 degrees at 17 knots. It also can be seen the *EGABRAG*, which was steaming at 360 degrees at 10 knots, passed under the cloud line between 1701 and 1801Z. The hand-held photographs from the *EGABRAG*, which correspond to the GOES images, are shown in Figures 1b, 2b and 3b. The approaching cloud line is pictured in Figure 1b as the dark, linear feature low to the water; the broken stratus and fog in which the line was embedded did not have such a distinct cloud base. In contrast, the stratus region shown just north of the *EGABRAG* in Fig. 1a had a distinct cloud base; the region moved over the ship at about 1900Z and the cloud base was estimated to be 350 m MSL from the 2020Z ship-board rawindsonde (Fig. 4).

The *EGABRAG* passed through the plume of the unidentified ship between 1720 and 1745Z as indicated by the sharp perturbation in the CCN concentrations reported by Porch, et al. (1992): from 5 to 200 cm^{-3} (0.8% supersaturation) at 1720Z and back to 5 cm^{-3} at 1745Z (CN went from 10 to 318 cm^{-3} and back to 10 cm^{-3}). At that time, the relative wind aboard the *EGABRAG* was 24 knots. Thus, the width of the ship-plume was approximately 10 nmi (24 knots*0.42h) which is consistent with the width of the cloud line in Figure 2a.

The photo in Figure 2b shows the cloud line just off the port side; the cloud silhouette is dashed because the original image was diminished in the reproduction. Nevertheless, the top of the line appears taller than the surrounding broken stratus; the top is visible because of the narrow clear zone adjacent to the line. Clear zones on either side of the line are visible in the original GOES images but were lost in the reproduction here. Further evidence of the existence of the zones appears in the solar radiation measurements reported by Porch, et al. (1992) where slight increased radiation occurred on either side of the much lower radiation measured when the ship passed under the line. Excellent examples of clear zones adjacent to ship-produced cloud lines are illustrated by the original photograph from the Apollo-Soyuz mission reported by Porch, et al. (1990).

The *EGABRAG* was just north of the cloud-line at 1801Z as shown in Fig. 3a. The line appears to be a series of long roll clouds in the near-simultaneous photograph (Fig. 3b). These clouds are visible in the GOES image as the sinuous appearance of the cloud line. Apparently the cloud line was being affected by horizontal vortex tubes (rolls) in the marine boundary layer. The rolls have been numerically simulated by Kuo and Schubert (1988) and Moeng and Schumann (1991). Further, the banded structure of the cloud line is similar to the banded structure seen in the original Apollo-Soyuz photograph.

The meteorological and CCN measurements made from the *EGABRAG* showed the cloud line formed in a shallow, nearly particle-free, nearly saturated (fog patches), drizzling and unstable boundary layer (Fig. 4); conditions similar to those reported by Bowley (1967) and Twomey, et al. (1968). Fog-bows were observed at daybreak and during the early morning in the broken stratus region indicating the cloud drop sizes were quite large. When the *EGABRAG* passed under the shallow stratus layer, the background CCN concentrations increased from 5 to about 60 cm^{-3} (CN 10 to 273 cm^{-3}) and the drizzle at the surface appeared to cease. Neither ship appeared to have affected the stratus layer as detected in the GOES 0.63 um images (Fig. 1a-3a); the remainder of the GOES half-hour images between 1831 and 2001Z (not shown) reveal no effect of either the unidentified ship or the *EGABRAG*. In the 2209Z 3.7 um image from the NOAA polar orbiting satellite, however, the cloud line extended into the stratus layer (Fig. 5); the line was not detected in the corresponding visible image (not shown).

The 1601, 1801 and 2001Z GOES 0.63 and 11 um images received at the City College McIDAS terminal were investigated to determine the average brightness values and corresponding cloud-top-temperatures of the ship-produced cloud line, broken stratus region and stratus layer; the results are given in Figure 6. It can be seen in the figure that brightness values for all regions increased with the increasing sun angle. The stratus layer was initially brighter than the cloud line indicating the line was not as optically thick; the broken stratus region was the least bright because the ocean surface was visible. By 2001Z the stratus layer and cloud line were equally bright. At that time the cloud line continued to be at least 1C warmer than the stratus layer. Combining this result with the sounding data in Figure 4 indicates the cloud line was about 50 m taller than the stratus region (a similar analysis needs to be performed on the ship-produced cloud line embedded in the stratus layer). This result is consistent with the taller appearance of the line in Figure 2b. The taller cloud line plus the adjacent clear zones indicate a possible ship-produced vertical circulation as postulated by Porch, et al. (1990) and Hindman (1990).

3. DISCUSSION

The broken stratus region contained low droplet concentrations and large droplet sizes because the region was optically thin (Fig. 6) and produced a fog-bow. These conditions most likely resulted from the low CCN concentrations which were kept low due to removal of droplets by drizzle as suggested by Hudson and Frisbie (1991). A steady state appeared to have been achieved between CCN production by entrainment from the higher concentrations shown to exist immediately above the boundary layer by Hudson and Frisbie and removal by drizzle. Albrecht (1989) has postulated low CCN concentrations enhance drizzle leading to breakup of layers of marine stratus and, conversely, high CCN concentrations lead to a suppression of drizzle and an increase of cloud liquid water content; a hypothesis which needs testing with a marine stratus numerical model containing explicitly the condensation-coalescence process (eg. Silverman and Glass, 1973).

The unidentified ship passed through the broken stratus region emitting an estimated 5×10^{15} CCN s^{-1}; based on the triangular volume of cloud between the two ships at 1731Z (30 nmi long, 10 nmi wide, 450 m deep) times the CCN concentration (200 cm^{-3}) divided by the formation time (30 nmi/25 knots relative wind). Also, on 20 July 1991, in a stratus-topped boundary layer, the plume of the *SEALAND PRODUCER* (USA registered, 32,000 hp steam-turbine, bunker oil-fueled) was traversed by the *EGABRAG* at a distance of approximately 5 nmi as detected in the CCN measurements (from 200 cm^{-3} in the background to 1300 in the plume and back to 200 cm^{-3} out of the plume, all active at 0.8%). The CCN emission rate from this ship was estimated to be 8×10^{15} s^{-1}. These CCN emission rates are nearly identical with that reported by Radke, et al. (1989).

The 1600 hp, diesel-fueled, 41 m *EGABRAG* also was a source of CCN. An estimate of its CCN emission rate is made based on the following approximations. When steaming downwind, the maximum concentration measured at 0.8% could be as large as 10^5 cm^{-3}. Assuming a 2 m/s drift from the stacks to the CCN inlet (35 m) and dispersion into a cone 10 m in diameter at the inlet, the emission rate was 10^{13} s^{-1} or 3×10^{11} g^{-1} (the *EGABRAG* consumes about 90 gallons of fuel per hour at 10 knots). Thus, the *EGABRAG* appears to have been a smaller CCN source than the unidentified ship.

Twomey, et al. (1968) measured 3×10^{10} CCN g^{-1} (7% supersaturation) from combustion of fuel oil (surprisingly, no CCN were measured at 0.5%). Applying this value to the larger ships CCN emission rates, assuming the value is valid at 0.8% and the ships were oil-fired, indicates the ships were consuming on the order of 2×10^5 gallons per hour. However, these ships burn on the order of 4×10^3 gallons per hour based on a rate from Conover (1966). Therefore, the ships may not have emitted all the measured CCN or the Twomey, et al. value is too small and not valid for steaming ships. Radke, et al. (1989) found direct emission of CCN by a ship could not account for measured droplet concentrations in a ship-produced cloud. They explain the remaining CCN may be produced by gas-to-particle reactions in the ship plume.

Another mechanism may have been acting that augmented CCN from the unidentified ship. The ship's passage through the broken stratus region may have initiated or enhanced a vertical circulation which mixed CCN from above the boundary layer into the layer. Likewise, the ship-produced cloud line embedded in the stratus layer may have been produced by the additional updraft caused by the vertical circulation; Hogen and Hindman (1992) have calculated that an increased updraft in marine stratus will nucleate additional CCN already present; additional CCN from the ship are not required.

4. CONCLUSIONS

Ship-produced CCN may not have been the sole reason for the formation of the dramatic cloud line of 13 July 1991. The heat and air wake from the unidentified ship may have caused a vertical circulation which mixed CCN from the warm inversion layer above the boundary layer into the boundary layer forming the line. The line appeared microphysically and dynamically different than nearby broken stratus. The *R/V EGABRAG III* did not produce a cloud line. Its CCN output may have been too small. Also, the vertical circulation produced by the *EGABRAG* may have been too weak (at daybreak on the 13th, an albatross was unable to soar in a figure-eight pattern in the wake of the *EGABRAG*; the bird had to flap at each pull-up). Measurements of ship CCN output (g^{-1} and s^{-1} for 0.01 to 1% supersaturation as a function of fuel) and ship-produced circulations are required to test these preliminary conclusions.

5. ACKNOWLEDGEMENTS

This work was supported in part by ONR contract N00014-89-1955 (E.E.H., K. Y. Kong of CCNY performed the satellite analyses), DOE Environmental Sciences Division (W.M.P.), DOE DE-FG08-90ER61012 and ONR contract N00014-91-J-1090 (J.G.H.).

6. REFERENCES

Albrecht, B. A., 1989: *Science*, **245**, 1227-1230.
Bowley, C. J., 1967: *J. Atmos. Sci.*, **24**, 596-597.
Coakley, Jr., et al. 1987: *Science*, **237**, 1020-1022.
Conover, J. H., 1966: *J. Atmos. Sci.*, **23**, 778-785.
Henderson, R., 1979: *Sail and Power*. U. S. Naval Institute, Annapolis, MD, 406 pp.
Hindman, E. E., 1990: *Ppts. Conf. Cld. Phys.*, Am. Meteor. Soc., Boston, 396-400.
Hogen, R. and E. E. Hindman, 1992: *J. Atmos. Sci.*, in preparation.
Hudson, J. G. and P. R. Frisbie, 1991: *J. Geophys. Res.*, **96**, 20,795-20,808.
Kuo, S. K. and W. Schubert, 1988: *Quart. J. Royal Meteor. Soc.*, **114**, 887-916.
Moeng, C. H. and U. Schumann, 1991: *J. Atmos. Sci.*, **48**, 2280-2291.
Porch, W. M., et al., 1990: *Atmos. Environ.*, **24A**, 1051-1059.
Porch, W. M. , et al., 1992: *Ppts 3rd Symp. Global Change Studies*, Am. Meteor. Soc., Boston. 132-139.
Radke, L. F., et al., 1989: *Science*, **246**, 1146-1149.
Scorer, R. S., 1987: *Atmos. Environ*. **21**, 1417-1425.
Silverman, B. A. and M. Glass, 1973: *J. Atmos. Sci.*, **30**, 1620-1637.
Twomey, S., et al., 1968: *J. Atmos. Sci.*, **25**, 333-334.

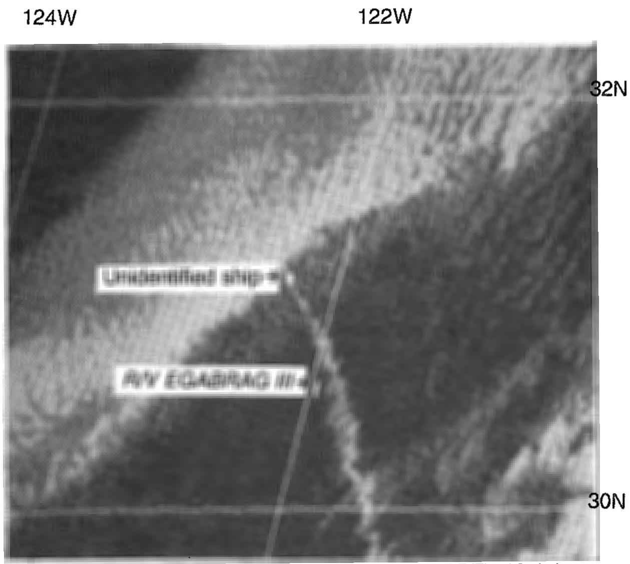

Fig. 1a. GOES visible image at 1701Z (1001PDT), 13 July 1991.

Fig. 1b. Photo by J.G.H. at 1651Z (0951PDT) from the *EGABRAG* looking about 3 points on starboard bow (Henderson, 1979).

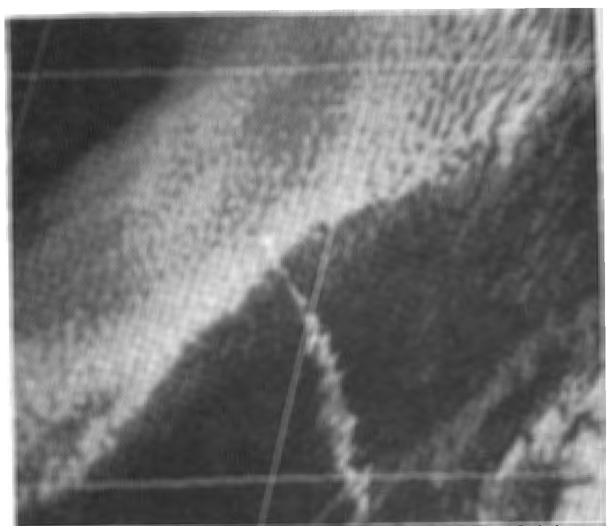

Fig. 2a. GOES visible image at 1731Z (1031PDT), 13 July 1991.

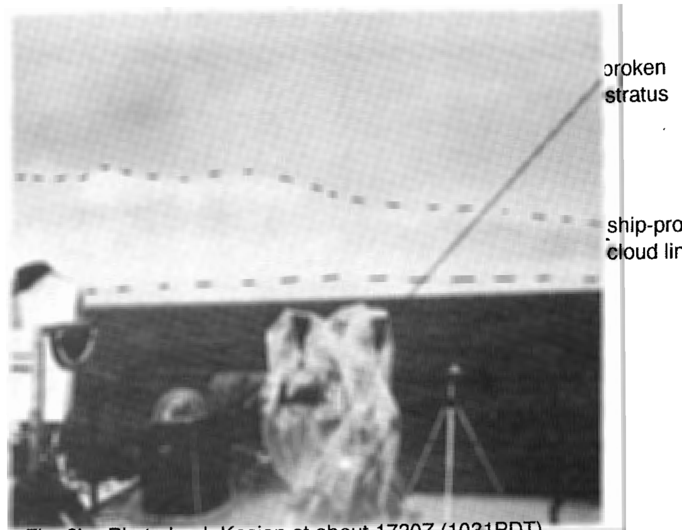

Fig. 2b. Photo by J. Kocian at about 1730Z (1031PDT) from the *EGABRAG* looking about 2 points abaft the port beam.

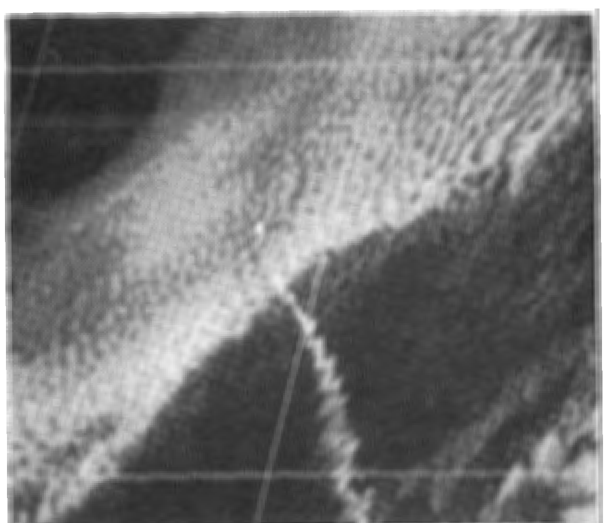

Fig. 3a. GOES visible image at 1801Z (1101PDT), 13 July 1991.

Fig. 3b. Photo by J.G.H at 1755Z (1055PDT) from the *EGABRAG* looking about 2 points on the port quarter

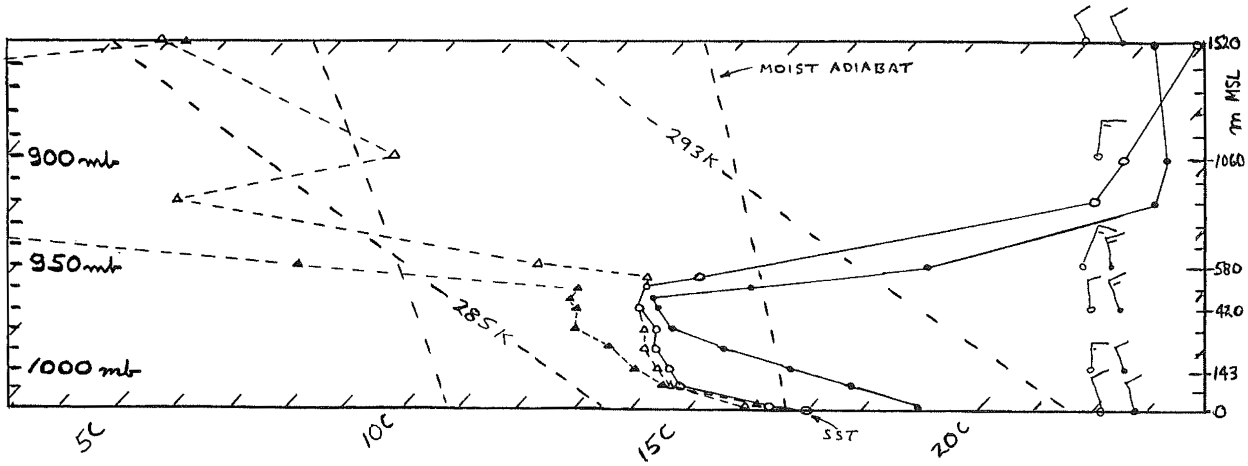

Fig. 4. The 1200Z (open symbols) and 2020Z (solid symbols) soundings from the R/V EGABRAG III on 13 July 1991 at, respectively, 30.0N, 122.07W and 30.89N, 121.89W. A full barb on a wind flag is 10 m/s; the sea-sfc-temp (SST) is plotted.

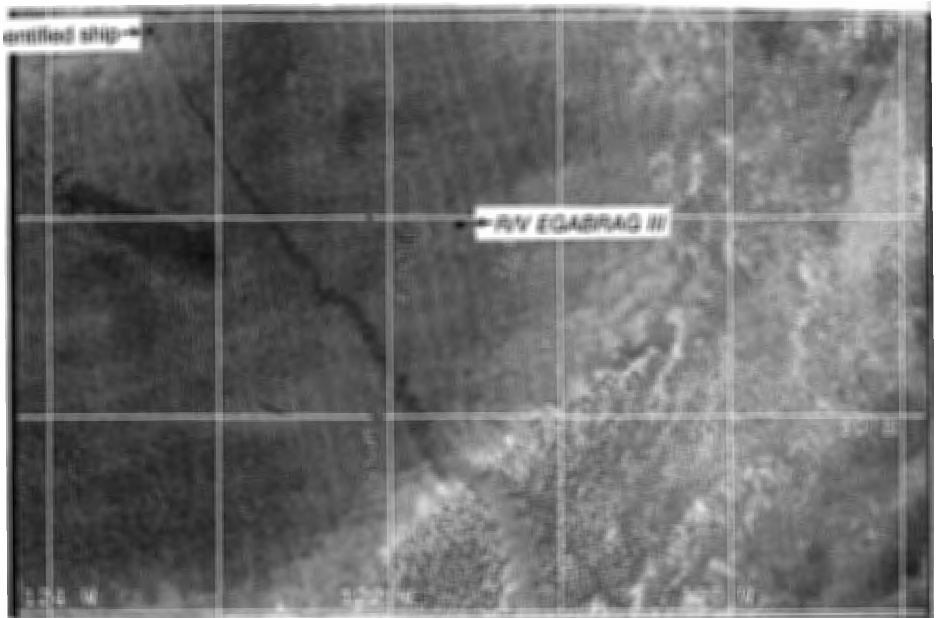

Fig. 5 NOAA satellite 3.7 um image at 2209Z (1509PDT), 13 July 1991.

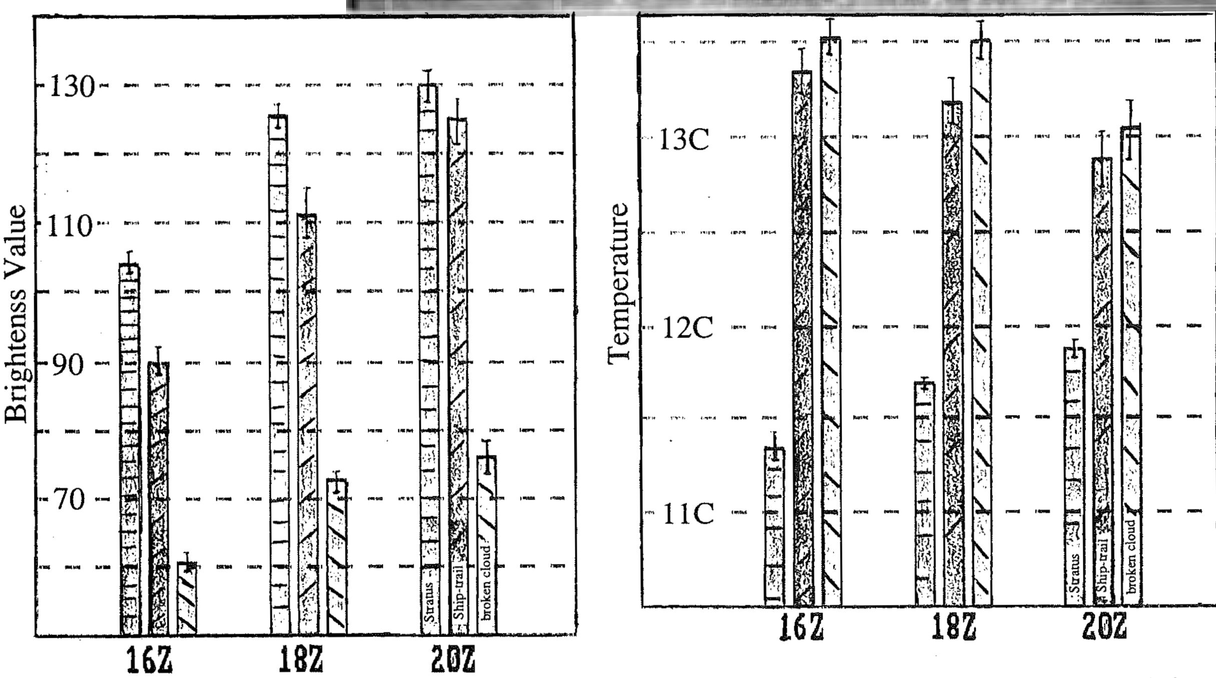

Fig. 6. The relative brightness values (left) and cloud-top-temperatures (right) from the GOES visible and infrared images on 13 July 1991 for the stratus layer ( ), ship-produced cloud line (///) and the broken stratus region (\\\ ).

FRACTAL ANALYSIS OF HIGH RESOLUTION FSSP DATA

Szymon P. Malinowski[1,3], Darrel G. Baumgardner[2] and Monique Y. Leclerc[1]

[1]University of Quebec at Montreal, Montreal, Quebec, H3C 3P8 Canada.
[2]National Center for Atmospheric Research, Boulder, Co80307, USA.
[3]On leave from University of Warsaw, Poland.

1. INTRODUCTION

The concept that clouds may be described as fractals was introduced by Mandelbrot (1982) and Lovejoy (1982). Fractal properties of radar and satellite images of clouds have been investigated by Cahalan and Joseph (1989). Fractal properties of cloud surfaces and their influence on radiative properties of clouds have been recently considered by Davis et al. (1991). Malinowski and Zawadzki (1992) (hereafter referred to as MZ) investigated fractal properties of surfaces of continental fair weather cumuli using 1m resolution FSSP data and reported an estimate of the fractal dimension of 2.55. In this paper, high resolution FSSP data obtained during the HARP experiment from Hawaiian clouds will be presented to illustrate how fractal properties of these clouds differ from fair weather cumuli. In addition, analyses of droplet distribution will be discussed.

2. THE EXPERIMENTAL DATA

The investigated data set was collected during flight 20 of the Hawaiian Warm Rain Project (HARP). The flight leg was a straight line at constant altitude of 1790m (816mb) along the rainband, about 1200m above cloud bases located approximately at 940mb level. The temperature at cloud bases and flight level was about 19C and 12C, respectively. Six consecutive clouds were penetrated over a distance of approximately 40km. The plane air speed was 110m/s. The FSSP (described in detail in Baumgardner et.al., 1992) has a temporal resolution of 1us allowing the determination of distances between individual cloud droplets. Droplets of diameters ranging from 2 to 48um were detected and were grouped in 15 classes. The small detection area of the sensor (droplets were detected in a parallelepiped 0.2*3.2mm cross-section and length of the flight leg) has the advantage that records can be treated as a one-dimensional section though clouds. On the other hand it has the drawback that a relatively long sample is needed to get enough statistics of droplets to estimate their concentration.

3. DATA ANALYSIS

The fractal dimension of sets of droplets collected was first evaluated. Since the whole data set was very long (3.6*10 samples of 1us size), the analysis presented here is restricted to the study of individual clouds only and not of the whole set. Box counting and cluster analysis were adopted to data segments corresponding to clouds. Since cluster analysis confirms results obtained by box counting, no separate discussion will be presented.

To compare with MZ results, the data set was converted by averaging over of 2.2, 11 and 110cm respectively, to represent the Total Droplet Count (hereafter TDC) collected on those distances. Then, to examine the fractal properties of cloud-clear air interface, the functional box counting technique was used on the data series. Description of box counting and cluster analysis can be found in Feder (1988).

3.1. Individual droplets.

Fig.1a presents on log-log plot results of box counting for 7 segments of the data set (the first 6 segments correspond to individual clouds, segment 7 corresponds to a fraction of cloud 6). All of the segments exhibit similar behavior at small (.1mm-1mm) and large (1m-1km) scales. At large scales, the slope of all lines is close to 1 (exact values are in range 0.93-0.99) indicating "space filling" (box dimension, D which is the slope on the plot is close to 1). At small scales, the slope is close to 0 indicating that the FSSP resolution is better than the characteristic distance between droplets, even in regions of high droplet concentration. At the intermediate scales, the behavior of clouds 1 and 2 is similar to that of large scales. The curve representing cloud 3 cannot, at the intermediate scales, be reasonably approximated by a straight line. In addition, curves corresponding to clouds 4,5,6 and segment 7 taper off at the intermediate scales. Using the 1.1m resolution TDC, cloud 2 (Fig.2a) seems to be an active convective cloud in developing stage, while cloud 3 (Fig.2b) seems to be nearly dissipated. All the other clouds consist of regions of undissipated and dissipating volumes as seen in Fig.1a by comparing curve 6 (corresponding to the whole cloud) with curve 7 (corresponding to the dissipating part of this cloud). However, box counting technique weighs the effect of undissipated volumes more than dissipating ones. Thus curves 4,5,6 and 7 correspond more to curves 1 and 2 than to curve 3. It should be pointed out that cloud 3 curve tapers off in scales of the order of 1mm suggesting that dissipating volumes have a patchy structure. This will be discussed further in the next section.

Similar box counting was performed on selected classes of droplet diameters with the goal of determining whether or not large droplets have a tendency to be grouped in clusters. Results are presented on Fig.1b. It can be seen that the characteristic distance between large droplets is longer than that of the small ones. At large scales the slope for the large droplets is the same as for the small ones, with no tendency for multiscale clustering (no straight line part with slope substantially different than 0 or 1). The transition region between slope 0 and 1 has width of about two orders of magnitude, independently of the particular cloud or droplet radius range.

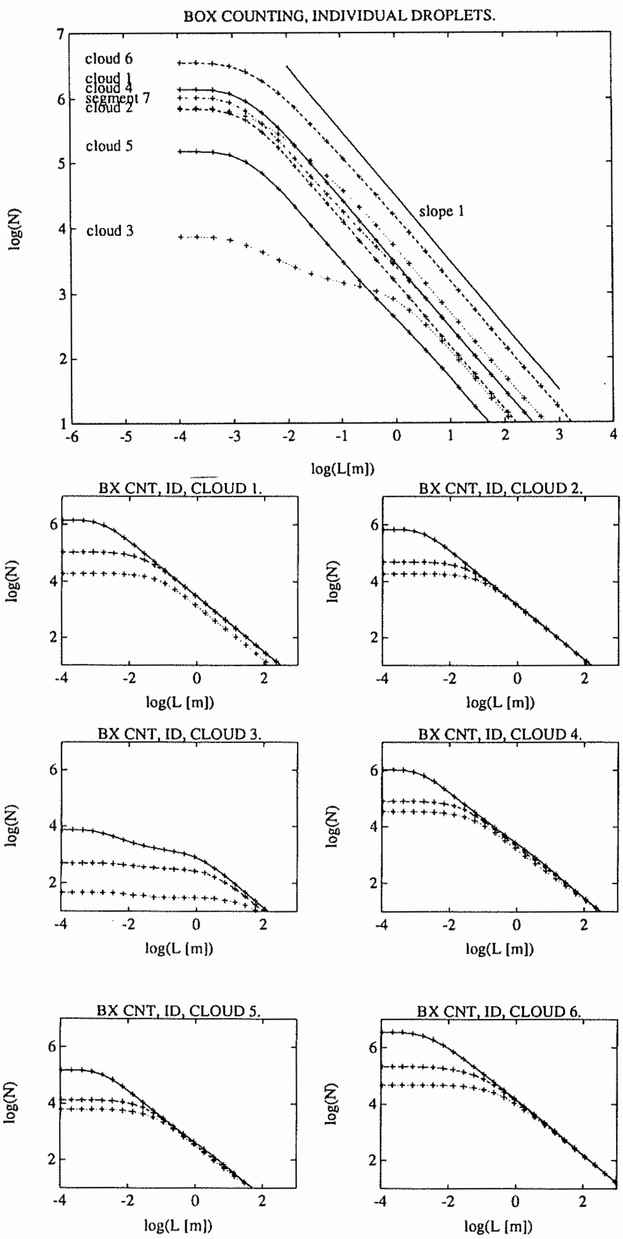

Fig.1. Box counting analysis on individual droplets. L -box size, N - amount of boxes occupied by at least one droplet.
a) Comparison of individual clouds, all droplets (diameters 2-48mm).
b) Individual clouds. Solid line -all droplets, dashed line - droplets of diameters 17-47mm, dotted line -droplets of diameters 32-47mm.

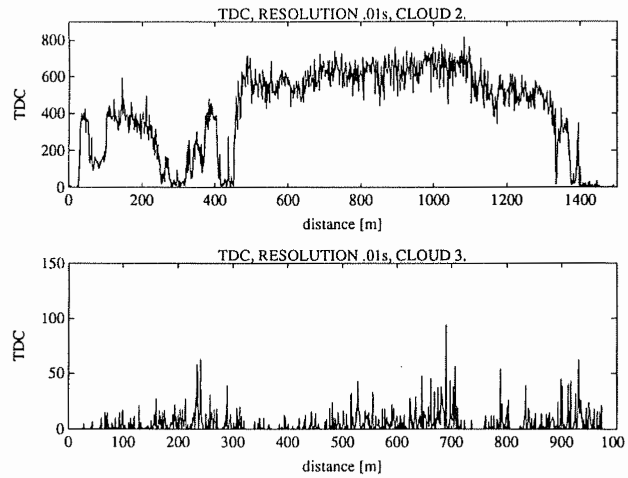

Fig.2. Total Droplet Count on 0.01s (1.1m long) segments.
a) Example of an active cloud (cloud 2).
b) Cloud in advanced dissipation stage (cloud 3).

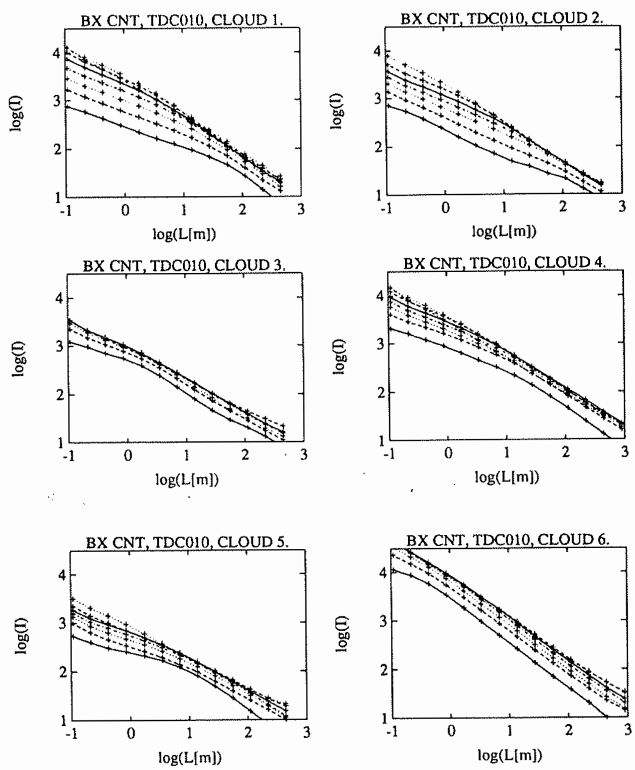

Fig.3. Box counting on points determining cloud-clear air interface. L - box size, I - amount of boxes occupied by at least one point on cross-section of the flight leg through cloudy-clear air interface. TDC with resolution 0.001s (11cm). From bottom to top curves corresponding to TDC thresholds at levels 1,2,4,8,16... droplets on 11cm segment,respectively.

3.2.Total Droplet Count.

Results of the functional box counting (box counting adopted to set of points obtained by thresholding the investigated function) on 1000 Hz (0.11m resolution) TDC for successive clouds are presented in Fig.3. In most of the plots (clouds 1-5), two regions can be distinguished: one with the smaller slope at the small scales (hereafter referred as A) and the second with the steeper slope at large scales (hereafter referred as B). The transition between these two regions varies from cloud to cloud and is generally shifted to small scales with increasing threshold. For thresholds of 2 (droplets counted on 11cm segment) and more, slopes in A region range from -0.44 to -0.62 corresponding to values reported by MZ. Slopes in B regions and for cloud 6 range from -0.65 to -0.95. This significantly differs from the findings of MZ, where the slope was constant over the whole range of investigated scales and threshold independent.

An interesting property of the dissipating cloud can be observed by analyzing data at a resolution 2.2 cm (5000 Hz). Examples of such plots from dissipating clouds and volumes of active clouds which probably undergo intensive mixing are given in Fig.4. The presence of thin sheets or strings of high droplet concentration (many reach maximum concentration in the cloud cores) with larger filaments of clear air between those is clearly indicated.

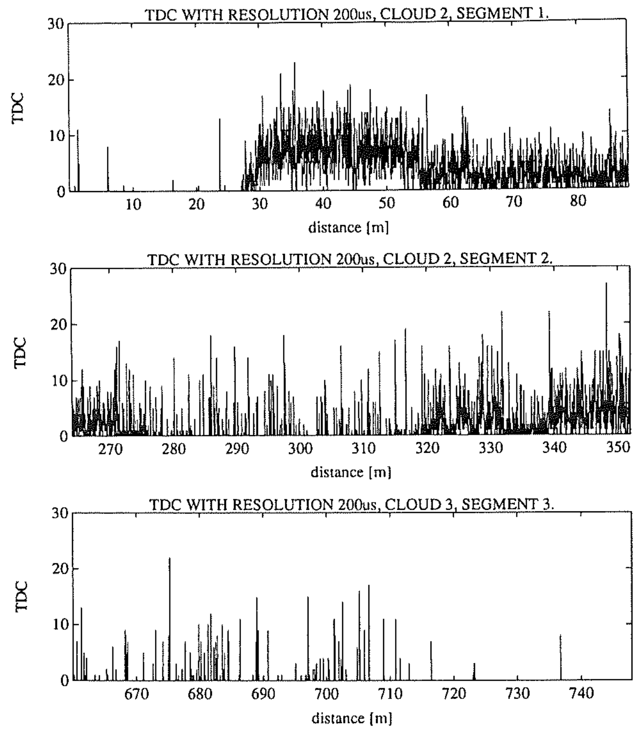

Fig.4. TDC on 200ms (2.2cm) segments. The distance on the x-axis corresponds to Fig.2.
a) Dissipating region of active cloud.
b) Dissipating cloud.

4. DISCUSSION

Individual droplets in the active cloud volumes seem to fill the space. This implies that droplets are distributed randomly. When entrainment and mixing develop, clear air filaments appear, causing departures of box counting curves on log-log plots from slope 1. This departure at the intermediate scales can be a rough indicator of the dissipation stage of the cloud. However, the absence of linear regions (on log-log plots) exhibiting a constant slope other than 0 or 1 suggests, that droplet populations do not form fractal sets. In particular, multiscale clustering of small, large and all droplets was not observed. This may indicate, that large droplets responsible for the warm rain development are distributed randomly in space.

Functional box counting performed on TDC indicates that properties of cloud-clear air interface in Hawaiian clouds differ substantially from properties of such interface in continental fair weather cumuli. MZ reported the D=2.55 as a fractal dimension of cloud-clear air interface in the range of scales 10m-10km and over a wide range of thresholds. In contrary there is no constant slope indicating that there is no single fractal dimension of such an interface over the investigated range of scales. However, it is worth of pointing out, that at the small scales the slope on log-log plot corresponds well to values reported by MZ at larger scales.

The fractal dimension of the cloud-clear air interface together with a range of scales in which is valid can be related to the effectiveness of the entrainment-mixing process (Sreenivasaan et al 1989, MZ). Both fractal dimension and the range of scales may depend not only on turbulence in clouds, but also upon the turbulence in the cloud environment. Constantin et al, 1991 report that for passive scalar interface, the existence of external turbulence leads to increase of fractal dimension of an interface from 2.33 to 2.66. Similar increase can be true for clouds. In particular, Hawaiian clouds might develop in a turbulent (due to previous cloud activity in the rainband) environment. Entrained are volumes of air of different history (e.g. remnants of previous clouds), so lack of systematic behavior of cloud-clear air interface is not surprising. Raga et al (1990) looking at entrainment into Hawaiian clouds with more traditional methods point out various entrainment mechanisms. Our findings are in agreement with those of Raga et al (1990).

Results presented in Fig.4. show that in volumes undergoing mixing, a lot of variability at the small scales is expected, and fragmentation of the cloud at such scales cannot be neglected. This has an important meaning for both modeling and analysis of observational data. Since mixing is slow and leads to the production of relatively long lasting filaments, the evaporative cooling is a local process on the cloud-clear air interface and cannot reasonably be approximated as occurring uniformly over a large volume taken as a grid box. In addition, if the temperature and humidity fields exhibit a structure similar to that of the TDC, estimates of total water content, virtual potential temperature or entrainment level on basis of low-resolution airborne instruments are questionable (see e.g. Malinowski and Pawlowska, 1989).

5. CONCLUSIONS

1. No clustering is observed for small, large and all droplets.
2. Cloud-clear air interface of Hawaiian clouds has different fractal properties than that of fair weather cumuli. This indicates that entrainment and mixing in Hawaiian clouds is not as simple as in fair weather cumuli and may depend on both history and turbulent environment of a particular cloud.
3. Entrainment-mixing leads primarily to the fragmentation of the cloud structure. Even in advanced stages of mixing, some filaments remain virtually unmixed.

ACKNOWLEDGMENTS

This paper was supported by the National Science and Engineering Research Council, by Atmospheric Environment Service and by FCAR. The National Center for Atmospheric Research is sponsored by the National Science Foundation.

References:

Baumgardner,D., B.A.Baker and K.Weaver, 1992: A technique for the measurement of cloud structure on centimeter scales. J.Atm.Oc.Tech., in press.
Cahalan,R.F., J.H.Joseph, 1989: Fractal Statistics of Cloud Fields. Mon.Wea.Rev., 117, 261-272.
Constantin,P., I.Procaccia and K.R.Sreenivasan, 1991: Fractal Geometry of Isoscalar Surfaces in Turbulence: Theory and Experiments. Phys.Rev.Lett., in press.
Davis,A., S.Lovejoy and D.Schertzer, 1991: Radiative transfer in Multifractal Clouds. In: Scaling, Fractals and Non-Linear Variability in Geophysics, Eds. D.Schertzer and S.Lovejoy,303-318, Kluwer 1991.
Feder,J., 1988: Fractals. Plenum Press, 1988.
Lovejoy,S., 1982: Area-Perimeter Relation for Rain and Cloud Areas. Science, 216, 185-186.
Mandelbrot,B., 1982: Fractal Geometry of Nature. W.H.Freeman,1982.
Malinowski S.P. and H.Pawlowska-Mankiewicz, 1989: On Estimating the Entrainment Level in Cumulus Clouds. J.Atmos.Sci.46,2463-2465.
Malinowski S.P. and I.Zawadzki, 1992: On the Surface of Clouds. To appear in J.Atmos.Sci.
Sreenivasan.K.R., R.Ramshankar and C.Menevau: Mixing, entrainment and fractal dimensions of surfaces in turbulent flows.Proc.Roy.Soc.Lond. 421, 79-108.

GIANT CCN AND PRECIPITATION DEVELOPMENT IN HAWAIIAN TRADE-WIND CUMULI

E. M. HICKS[1] and C. A. PONTIKIS[2]

[1] U.A.G.,Laboratoire de Physique de l'Atmosphère Tropicale, 97159, Pointe à Pitre Cedex, Guadeloupe (F.W.I.)
[2] METEO FRANCE/U.A.G., Laboratoire de Physique de l'Atmosphère Tropicale, 97159, Pointe à Pitre Cedex, Guadeloupe, (F.W.I.)

1. INTRODUCTION

The development of precipitation in warm clouds requires the presence of large droplets (critical radius r>20 µm) capable of initializing the collision and coalescence process. The results of experimental as well as numerical studies on the role of giant nuclei (r>1 µm) in warm rain initiation are contradictory (Woodcock, 1950, 1953; Woodcock et al., 1971, Takahashi, 1976; Johnson, 1982).

In the case of the association of a giant CCN production mechanism (sea surface and wind) and a mechanism leading to the rise of air masses initially close to the surface (low-level convergence, orographic lifting), it seems likely that giant CCN would contribute to the rapid development of precipitation embryos. The above mechanisms are found in the clouds sampled during the 1985 Joint Hawaii Warm Rain Project (Smolarkiewicz, 1988).

This paper presents an estimation of the contribution of giant nuclei to the precipitation embryo formation process obtained by using data collected in 7 trade-wind cumuli sampled on the 10, 11 and 19 July 1985 (JHWRP). Since CCN measurements were not available during this experiment, our analysis is based upon the FSSP cloud base droplet spectral distributions.

2. CLOUD BASE OBSERVATIONS

The examination of the droplet spectral distributions at cloud base levels show large differences in the spectral width and particularly in the large droplet tail for parcels with similar droplet concentrations. As an example, Fig. 1 presents characteristic cloud base spectral distributions (narrow and broad) for clouds sampled on the 10, 11 and 19 July. The liquid water content of the corresponding cloud base samples is 0.15 $g.kg^{-1}$, thus denoting a rise of roughly 100 m as from the condensation level. It has been shown in a previous study (Hicks et al., 1991) made on a Hawaiian trade-wind cumulus, that all droplets which have developed on CCN with a dry radius $0<r\leq4$ µm have a final radius 6 µm$\leq r\leq$ 7 µm after a 100 m rise. Thus, droplets with r>7 µm, can only have developed on giant CCN. For the spectra presented in Fig. 1, it is not possible to detect the droplets which have developed on giant CCN (if any) in the case of the narrow spectrum (1), whereas for the three broad spectra, the minimum concentrations of droplets which have

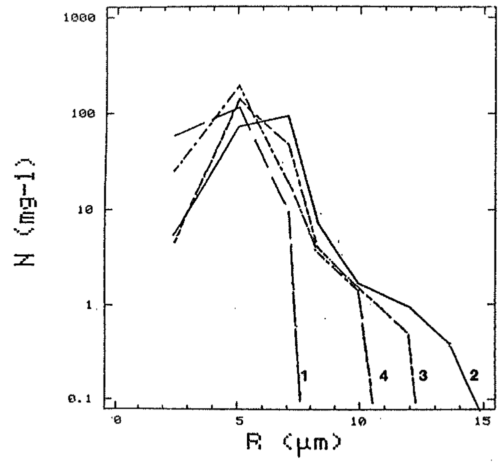

Fig. 1 : Characteristic cloud base spectral distributions sampled on 10 July (1,2), 11 July (3) and 19 July (4).

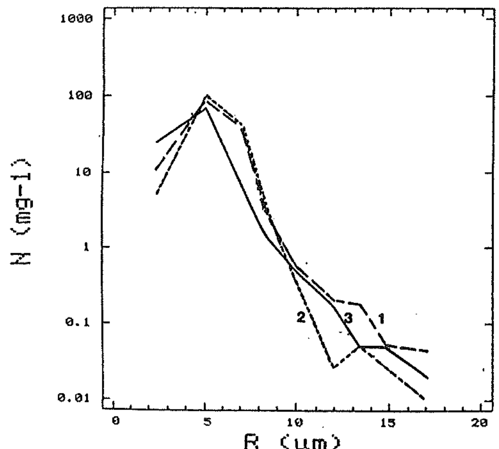

Fig. 2 : Mean cloud base spectral distributions for clouds sampled on 10 July (1), 11 July (2) and 19 July (3).

developed on giant nuclei range between 4.9 mg^{-1} and 9.9 mg^{-1}. All studied cloud bases show a similar behavior, whereby at least 85% of the sampled parcels have droplets which have developed on giant CCN. The corresponding concentrations are non negligible and reach in some cases 7% of the total droplet concentration. Further, a rough estimation of the minimum value of the mean concentration of droplets which have activated on giant CCN is obtained by averaging the spectral distributions over all cloud base parcels sampled on a given day. Figure 2 presents the mean cloud base spectral distributions for the 10, 11 and 19 July which reveal a significant large droplet tail. In all distributions, droplets with radii reaching 16.95 µm (last populated FSSP bin) are found and the minimum values of the mean concentration of large droplets developed on giant nuclei range between 2.4 mg^{-1} and 4.4 mg^{-1}.

3. PRECIPITATION EMBRYO FORMATION

Model calculations have been performed in order to test if the large droplets observed at cloud base can reach the critical 20 µm radius after adiabatic ascent at a level which is consistent with the observed cloud depth. As an example, in the case of the broadest spectral distribution presented in Fig. 1, the largest droplets (r=13.4 µm) reach a 20 µm radius after a 1500 m adiabatic vertical transport (up to the 800 mb level). This is consistent with both the usual depth of precipitating clouds observed during the JHWRP and the level as from which the precipitation embryo concentrations increase exponentially.

If the large droplets observed at cloud base are responsible for the precipitation embryo initiation at higher levels, one may expect the large droplet concentrations (Nl) at higher levels to be proportional to the corresponding liquid water contents (L). This proportionality tends to disappear if dilution is responsible for the production of large droplets at higher levels (Hicks et al., 1990). Figures 3(a,b) present the Nl-vs-L plots for two cloud penetrations (10 and 19 July). The cut-off radius above which droplets are considered as large corresponds to the radius reached at the observation level by the largest droplets in the narrowest cloud base spectral distribution of the considered cloud. The roughly linear trend in the data points and the fact that the maximum concentrations of large droplets are similar to the large droplet concentrations at cloud base support the giant nuclei hypothesis.

4. CONCLUDING REMARKS

In the examined hawaiian clouds, cloud base parcels containing significant concentrations of large droplets are found. The results of the theoretic analysis show that the observed cloud base large droplets can reach the critical radius after an adiabatic vertical transport which is consistent with the precipitating cloud depth. Further, the experimental analysis results suggest that the large droplets at cloud base are responsible for the precipitation embryo formation at higher levels. Since the origin of the cloud base large droplets can only be attributed to giant CCN, it is likely that the latter contribute to the warm rain initiation process.

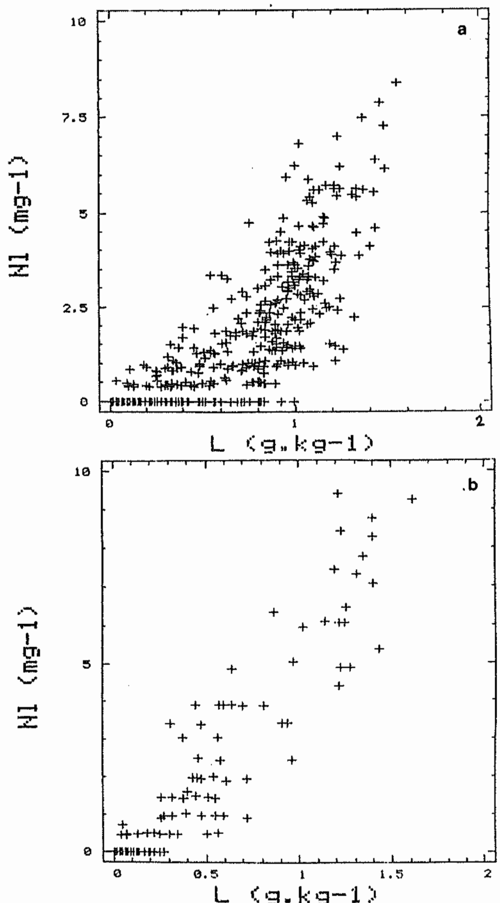

Fig. 3 (a,b) : Large droplet concentrations plotted against liquid water contents for cloud 10 (826 mb) of 10 July (a) and cloud 11 (836 mb) of 19 July (b).

REFERENCES

Hicks,E., C. Pontikis and A. Rigaud, 1990 : Entrainment and mixing processes as related to droplet growth in warm mid-latitude tropical clouds. J. Atmos. Sci., 47, 1589-1618.
Hicks, E., C. Pontikis and A. Tebani, 1991 : Precipitation embryo formation in tropical warm convective clouds. Proc. 19th Conf. on Hurricanes and Tropical Meteorology, Miami.
Johnson, D. B., 1982 : The role of giant and ultragiant aerosol particles in warm rain initiation. J. Atmos. Sci., 39, 448-460.
Smolarkiewicz, P. K., R. M. Rasmussen and T. L. Clark, 1988 : On the dynamics of hawaiian cloud bands : island forcing. J. Atmos. Sci., 45, 1872-1905.
Takahashi, T., 1976 : Warm rain, giant nuclei and chemical balance. A numerical model. J. Atmos. Sci., 33, 269-286.
Woodcock, A.H., 1953 : Salt nuclei in maritime air as a function of altitude and wind force. J. Meteor., 10, 362-371.
Woodcock, A. H., R. A. Duce and J. L. Moyers, 1971 : Salt particles and raindrops in Hawaii. J. Atmos. Sci., 28, 1252-1257.

PARTICLE SIZE DISTRIBUTION EVOLUTION WITH DIAMETER FROM 0.I2 TO 47 μm IN CONDENSATION PROCESS

Yan Caifan Chen Waikui

Chinese Academy of Meteorological Science

46 Baishiqiao Rd. Beijing I00081 PRC

Wu Xinsui, Xu Jiahong, Liu Guangzhong

Petroleum Administration, Xinjang PRC

I. INTRODUCTION

The vapour condensation in the atmosphere is an important process regulating hydrological cycle. The following droplet spectra evolution properties are revealed in the condensation and evaporation:

1. The CCN concentration(N_c) and particle concentration(N_p) with diameter 0.195-0.27 μm is almost maximum in clear air.
2. When the condensation happenning the N_c and N_p decrease markedly.
3. Parts of the N_c and N_p may be grow up to large-giant nuclei and cloud droplets, which results in the formation of the concentration step and new concentration peak.
4. When the evaporation happenning the cloud droplets and large-giant nuclei transforms into large-giant nuclei and Aitken nuclei.

2. OBSERVABLE RESULTS

The CCN large-giant nuclei and cloud droplets were measured with MEE-I20 and PMS probes(ASASP、FSSP) equipped on board of aircraft IL-I4 or AN-26.

The sample rate were record/30 second(CCN) and record/2-5 second(ASASP, FSSP).

1. The cloud condensation nuclei(CCN)

The CCN were measured at 0.45% supersaturation with respect water. the CCN concentration reduces rapidly from below cloud to cloud base, within cloud the N_c were only a few but it maintained approximately a constant(to see table I.).

Table I. The Nc below and within As op (14 on April 1983. S=0.45%)

Height H(km)	0.0–0.5	0.5–1.0	1.0–1.5	1.5–2.0	2.0–2.5	2.5–3.0	3.0–3.5	3.5–4.0	4.0–4.5
Position	below			base	within				top
$\bar{N}_c$ (cm^{-3})	403	130	67	7	7	7	6	6	6
Variation $\delta=\sigma_N/\bar{N}$	0.28	0.81	0.75	0.00	0.00	0.00	0.10	0.10	0.00

H--relative ground height,
σ_N--standard variation of N(cm^{-3}),
$\bar{N}$--mean concentration,

2. The large-giant nuclei spectra with diameter range from 0.12--3.12 μm

These particles were measured with ASASP probe. below and above cloud these particle spectra have apparent backgraund characters(to see fig 1.):

1. The droplet spectra are arrower, and the maximum diameter is less than 2.7 μm.
2. The mode diameter(D_m) lie in range from 0.195 μm to 0.27 μm.
3. The mode concentration(N_m) is greater (more than 50% of the total concentration(N_t) generally).
4. The particle concentration n(D)(cm^{-3}) decreased sharply with particle diameter(D) increasing.

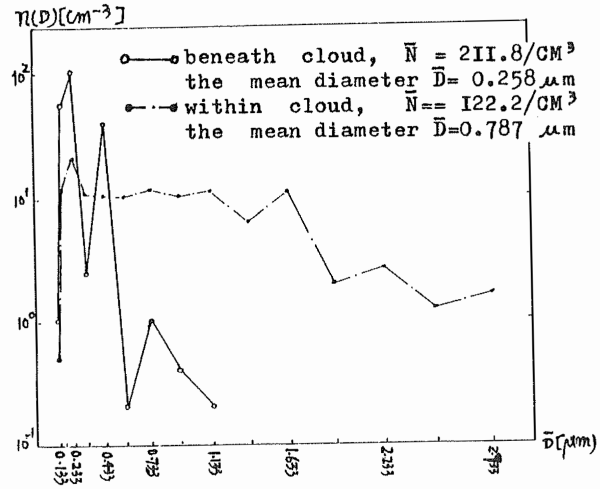

Fig. I. The particle spectra in diameter range 0.I2-3.I2 m (I2 on November, I989)

However, within cloud the spectra is different as backgraund:

1. The spectra broaden to 3.12 μm which is the ASASP probe measuring up limit size.
2. The D_m lie in D=0.195--0.27 μm too but the N_m fell markedly to be less than 10% of the N_t.
3. The interesting phenomena is to formed concentration step in diameter range from 0.27 μm to 1.77 μm, which do not decrease with diameter increasing. The mean diameter $\bar{D}$ is 1-2 times greater than backgraund.

3. The particle spectra in diameter D=0.5--8 and D=1--47μm

These particles were measured with FSSP probe. Their spectra evolution from below to cloud base shown following feature(see fig 2):

1. These spectra broadened to 8μm and $10^1 \mu$m, the particle concentration n(D) is not monotonous decreasing with diameter increasing and to formed new concentration peak in the range of 2--14 μm diameter.

2. The total concentration(N_t) increased to 10^1 --10^2 /cm^3 from 10^{-2}--10^0 /cm^3(below and above cloud).

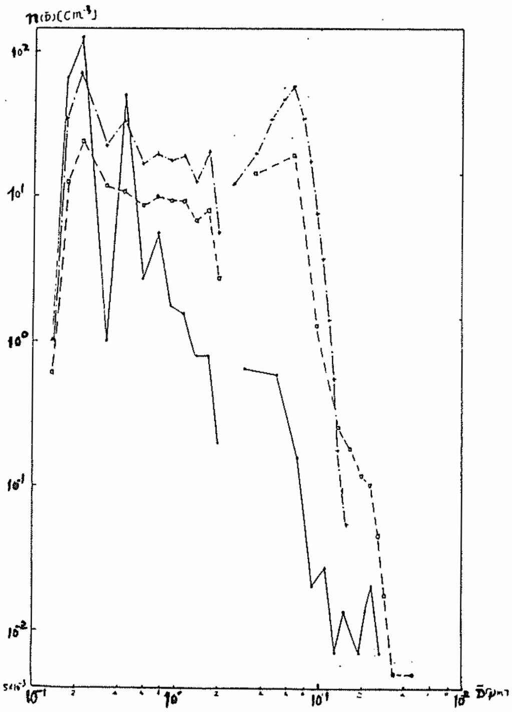

Fig. 2. The particle spectra evolution in the condensation (I2 on November , I989)
beneath cloud,
N=27I.2/CM^3 (D=0.I2-2.07μm)
N=I.5/CM^3 (D=2--32μm)
cloud base,
N=274.6/CM^3 (D=0.I2-2.07μm)
N=265.5/CM^3 (D=I-I6μm)
within cloud,
N=II4.4/CM^3 (D=0.I2-2.07μm)
N=II0.7/CM^3 (D=2-47μm)

3. DISCUSSION

The above analysis shown that the concentration step is formed, begining from about 60--150 m beneath the cloud base and becoming steady to the cloud base. Taking the rising parcel containing CCN rising at 0.15m/sec speed, it is about 400-1000 second during which the concentration step is formed and perserved.

The calculation based on formla(Twomey) $r=1.45\times10^{-6}/S_c^{3/2}$, $r=(r_o^2 + 2GSFT)^{1/2}$ for the soluble CCN shows that the radius(r) growth rate obviously slows down with the particles activation and condensation; the activated CCN grow to $r=6\times10^{-6}$--1.4×10^{-5} cm rapidly and later the growth rate becomes too slow which results in these growing particles concentrate over $r=(1.4$---$8.8)\times10^{-5}$ cm range that is refered to as concentration step. The step forming time is about 429-852 seconds when supersatuyation(S) is 0.05--0.1%

Similar to above, the large nuclei ($r=(1$--$2.48)\times10^{-5}\mu$m) grow to $r=(1.4$-$8.8)\times10^{-5}$ cm range is about 425-792 seconds. This duration is consistent with the measured (400-1000 seconds).

When the evaporration becomes dominate, (such as from incloud to outcloud and the cloud dissipation etc,) the contrary evolution of the particle spectra has been found. Fig 3 shows a case seeded by AgI aerosols, in which the new peak concentration in diameter 11-14μm decreases gradually to extinction; the concentration step shows the same. due to evaporation, whereas the concentration with diameter range from 0.1μm to o.14μm increases to get near the backgraund distribution.

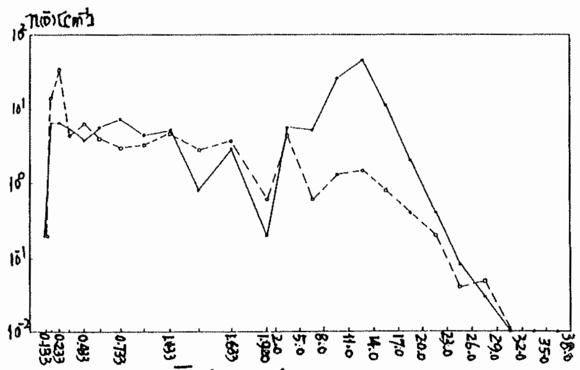

Fig. 3. The particle spectra evalution in the evaporation (I8 on December , I989)
o-·-o after seeding,
N=82.6/CM^3 (D=0.I2-2.07μm)
N=9.7/CM^3 (D=2-47μm)
•—• befor seeding,
N=49.4/CM^3 (D=0.I2-2.07μm)
N=96.8/CM^3 (D=2-47μm)

4. REFERENCES

Twomey, T. Atmospheric aerosols, chap.3 , 6. Elsevier Scientific Publishing Company Amsterdam-Oxford-New York I977

INITIATION OF ICE IN CLOUDS: COMPARISON OF NUMERICAL MODEL RESULTS WITH OBSERVATIONS

J. L. Stith[1], D. A. Burrows[1], and P. J. DeMott[2]

[1]University of North Dakota, Grand Forks, ND, USA, 58202
[2]Colorado State University, Fort Collins, CO, USA, 80523

I. INTRODUCTION

In spite of recent advances in our understanding of ice formation in clouds, we are still unable to accurately predict the onset of glaciation. This paper addresses this problem by comparing the predictions from a revised version of a microphysical model with observations of early ice development in a cumulus cloud. New formulations for the concentrations of ice forming nuclei were used in the model. Microphysical measurements from two instrumented aircraft were used along with a Sulfur Hexafluoride (SF_6) tracer (on one aircraft) to observe the behavior of one region within the cloud. The tracer data were used to help assess how well the aircraft measurements corresponded to the parcel simulated by the model.

II. DESCRIPTION OF THE MODEL

The model used was a revised version of an adiabatic parcel model described by Rokicki and Young (1978). This was developed from Young's (1974) microphysical model. It has been revised by DeMott (1990; 1992 a) to simulate cloud chamber experiments and the behavior of AgI seeding aerosols in cumuli. It is an explicit microphysical model that requires specification of the initial thermodynamic conditions and the trajectory of the parcel. The latter are varied to match the observed behavior of the cloud. However, entrainment is not simulated and the parcel does not precipitate or produce secondary ice, so it is best suited for simulating only the early ice in an unmixed parcel. The DeMott studies obtained good agreement between the simulations and the observed formation of ice. This study represents our first simulation of natural ice formation in an unseeded cumulus.

DeMott (1990; 1992 b) modified the model to include new formulations for the concentration of natural ice nuclei as prescribed by Meyers et al. (1992). These formulations for nuclei acting via deposition, condensation-freezing, and contact-freezing, represent the results from laboratory measurements of natural ice nuclei by various authors. Each of these modes is simulated in the model. An additional mode, immersion-freezing, was also added by DeMott to represent freezing nuclei that exist in the droplets prior to supercooling, according to the results in Vali (1971). The depositional and condensation-freezing mode are combined by Meyers et al. in one formulation and represent measurements made in continuous flow diffusion chambers. Although limited in number, these produce more consistent and considerably higher nuclei concentration values than those from the filter method. The Meyers et al. contact-freezing formulation is based on more recent measurements than were used in Young (1974). These predict much lower levels of contact nuclei than Young (1974).

III. DESCRIPTION OF THE EXPERIMENT

The University of North Dakota Citation, the University of Wyoming King Air, and one tracer-release aircraft were used for this study. The first two aircraft carried similar standard instrumentation for measurements of wind, state parameters, and cloud microphysics. The Particle Measuring Systems 2DC probe was used for ice particle measurements. Shadow-or counts (total counts) were used to determine an upper limit to the concentrations of the larger ice particles. These are the total counts triggered by water and ice particles of about 50 microns or larger. Consequently, the shadow-or count does not include the smallest ice particles and also includes large droplets. However, as the particles grow large enough to produce discernable images (larger than about 100-200 microns), the type of particle can be determined. For the case studied these were predominantly graupel and did not include droplets (see below).

The objective of the experiment was to follow the development of ice within a supercooled region of a cumulus, from a predominantly liquid water state until the region became glaciated. Because a probe such as the 2DC samples only about one part in 10^{10}-10^{11} during one aircraft pass through a cloud, it is unlikely that aircraft can be used to document the first ice in a cloud. Since these sampling passes are likely to encounter many different regions within a cloud, in various stages of ice development, it is helpful to have some means of identifying a particular region so that its history can be compared to the model simulation. To tag one region of the cloud, a single-pass release of SF_6 was begun just before the treatment aircraft entered the cloud and ended just after exiting the cloud. This produced a plume of the tracer through the cloud at one altitude. The tracer was then detected by a fast response (1 s) analyzer on the Citation. This tracer has been used previously in seeding trials to determine the concentration of seeding agent, for comparison with the model simulation (DeMott, 1990) and to assist in identifying aircraft produced ice particles (Stith, 1992). More details on this technique are given in Stith et al. (1990).

The cloud selected for study was an isolated cumulus with tops (estimated visually from the Citation as it sampled near the cloud top region) at 6.5 km (-18 °C). It formed 70 km south of Bismarck, North Dakota on 17 July, 1989. Cloud base was estimated to be at 2.5 km (6 °C) based on an aircraft sounding made during the climb to the sample area. This sounding was used to initialize the model, which was begun at 795 mb and 2.0 km. A velocity profile that produced a similar updraft and cloud top to that of the observed cloud was constructed (the resulting altitude of the parcel is given in Fig. 2). A continental CCN spectrum that reproduced the observed droplet concentrations was also used as input to the model. A 3 s time step was used in these simulations.

The cloud was treated with SF_6 between 1735:56 and 1736:26 (local time) by a single pass through the cloud at an altitude of 4.9 km (-7 °C). During the treatment pass, the Citation sampled just above the treatment aircraft at 5.2 km (-10 °C) and then made repeated passes between that altitude and 5.8 km (-13 °C). The King Air made repeated passes through the cloud at 4.3 km (-5 °C).

IV. RESULTS

The results from the Citation are presented in Fig. 1. The cloud had significant updrafts (up to 6 m s^{-1}) during the treatment and the next three sampling passes (1735 to 1742). Two passes between 1743 and 1745, higher in the cloud, produced only equally strong downdrafts. At 1746 a

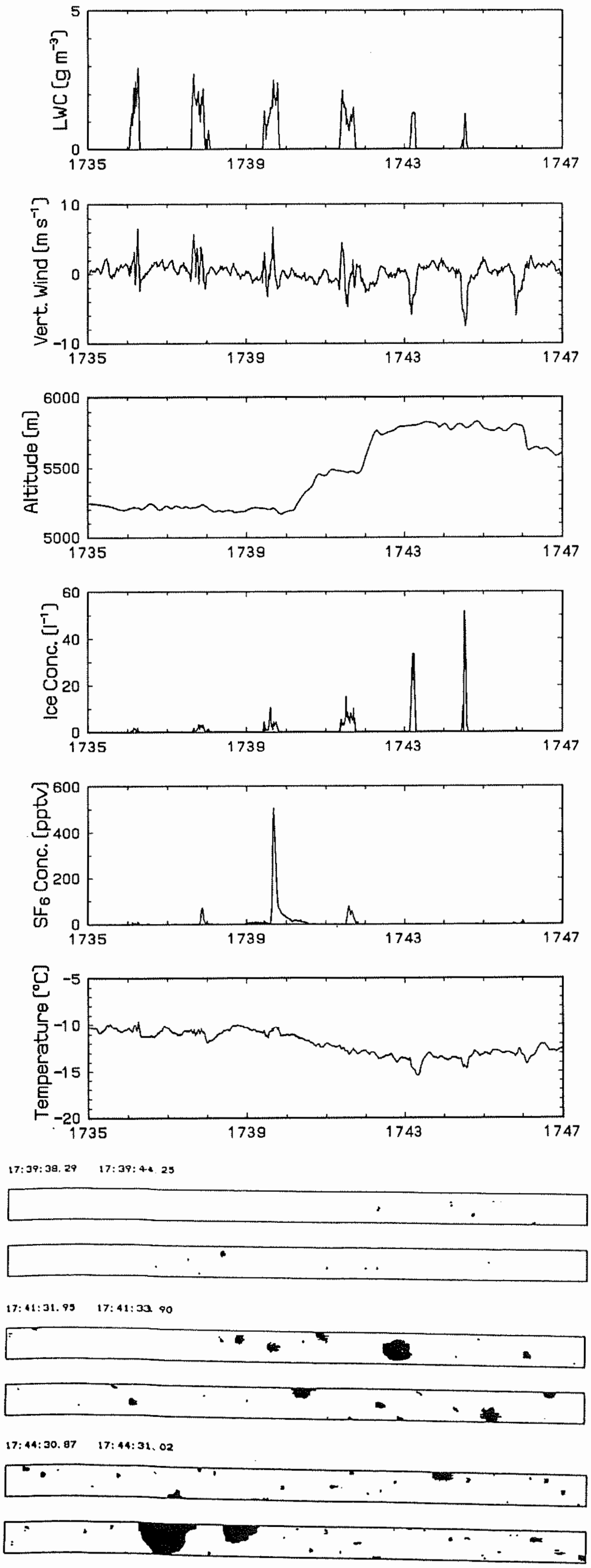

Figure 1. History of Citation measurements between 1735 and 1747 (local time) and selected PMS 2DC images. The height of the images represents 1.05 mm.

pass through the area revealed that the visible cloud had descended below the sampling altitude and a strong downdraft was observed in the cloud location. The development of ice is evident during this period, with millimeter graupel the predominate large ice particle type during the later period. The tracer was observed for the first three passes after the first (treatment) pass. The measurements from the King Air (which did not include the tracer measurements), indicated that the cloud region was nearly ice free at the -5°C level, except for a well developed precipitation and downdraft region on the southwestern portion of the cloud area, which was probably the remains of an earlier cloud turret.

The results from the model simulation are presented in Figs. 2, 3, and 4. The observed liquid water was generally less than in the simulation. This is not surprising, since entrainment is not modeled. The maximum observed ice concentrations match reasonably well with the simulation in the tagged region of the cloud (Fig. 3). Higher ice concentrations existed during the last two passes (which did not detect the tracer). These may have been due to secondary ice production, which is not included in the model. The observed mean sizes of ice particles fell within the range of sizes predicted by the model. However, the

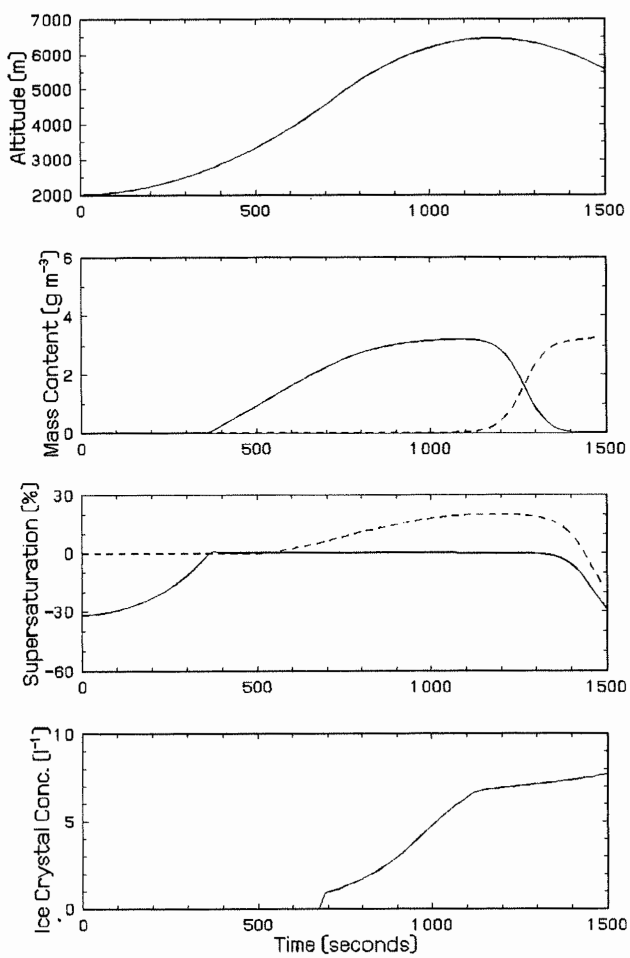

Figure 2. Prescribed parcel trajectory and the simulations of ice mass content, supersaturation, and ice concentrations. The dashed line represents the mass as ice and the supersaturation with respect to ice for the mass content and supersaturation curves, respectively. The solid lines refer to mass as liquid and supersaturation with respect to water. The supersaturation with respect to ice is set at zero in the model until the temperature is below freezing.

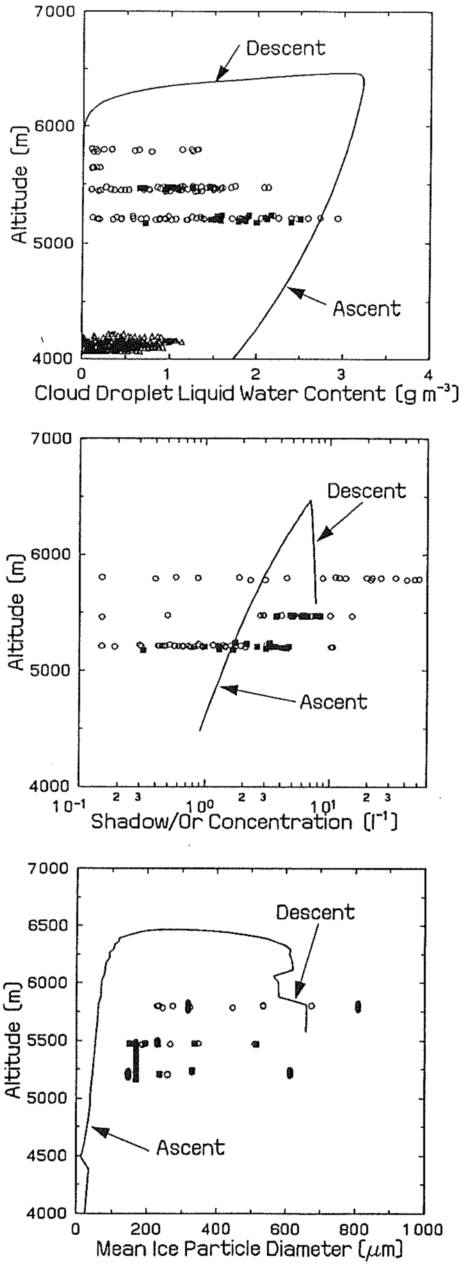

Figure 3. Vertical profiles of observed and simulated cloud liquid water, ice concentrations (shadow/or), and mean ice particle diameter. The solid boxes represent data taken in the SF_6 tracer region of the cloud and the circles represent data from other parts of the cloud (both are 1 s averages from the Citation data). The solid line represents the model simulation of the ascent and descent of a parcel. Triangles represent 1 s averages of cloud liquid water from the King Air.

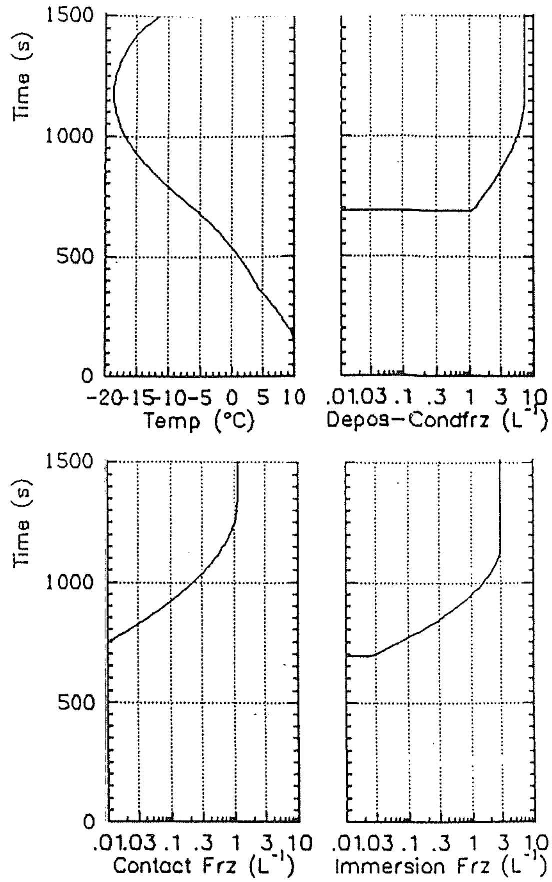

Figure 4. The contribution of the various ice formation mechanisms to the ice concentrations in the simulation.

means computed from the observations are weighted towards larger particles, since the probe does not resolve the smaller sizes. The conversion of liquid water to ice was rather rapid and occurred between 1200 and 1400 s into the simulation (Fig. 2). This was due to rapid accretional growth of ice particles in the model.

Examination of the ice nucleation in the model, indicates that the initial nucleation of ice was nearly complete at 1100 s (Fig. 4). The major nucleation mechanism was deposition and condensation-freezing by a wide margin. This produced significant ice early enough (at relatively warm temperatures), to allow riming to develop sooner in the cloud.

V. DISCUSSION

Examination of the size distribution of particles in the simulation indicated that spherical (rimed) particles existed in similar concentrations as unrimed ice particles at 890 s and, during the next few hundred seconds grew to contain most of the mass of ice, resulting in millimeter-sized graupel by the time the simulated parcel began to descend. These steps are qualitatively similar to the events in the observed cloud on 17 July. A future paper will compare the ice particle size distributions in the observed cloud with those simulated by the model.

The critical step that was responsible for producing ice and initiating the production of graupel in the simulation was the Meyers et al. formulation for deposition and condensation-freezing. This was based on a relatively few ground-based measurements from continuous-flow diffusion chambers. These are more representative of average conditions rather than the in situ concentrations that might have existed in the cloud on 17 July. More measurements of ice nuclei using these techniques are needed, especially near clouds that are the subject of ice initiation studies such as the 17 July case.

We are encouraged by the reasonable agreement between the observed and predicted concentrations and sizes of ice particles, especially in the tagged region, which should correspond most closely to the simulation. The history of the observed cloud microphysics is qualitatively similar to the simulations. This suggests that better simulations of glaciation may be close-at-hand, at least for some types of clouds.

ACKNOWLEDGEMENTS

This work was supported by the NOAA Federal-State Cooperative Program in Atmospheric Modification Research, through NOAA cooperative agreements NA900AA-H-0A176 and NA17RA0218-01 and contracts NDARB-UND-NOAA90, NDARB-UND-NOAA91, and NDARB-CSU-91-01 with the North Dakota Atmospheric Resource Board. Thanks are due to the many members of the field operations crew for making this study possible. Thanks are also due to J. Marwitz, G. Gordon and B. Klimowski for the data from the University of Wyoming King Air.

REFERENCES

DeMott, P. J., 1990: Quantifying ice nucleation by silver iodide aerosols. Ph.D. Dissertation, Paper No. 466, Dept of Atmos. Sci., Colo. St. Univ., Fort Collins, CO, 253 pp.

----, 1992 a: Quantifying ice nucleation by cloud seeding aerosols for use in conceptual and numerical cloud models. Preprints, Symposium on Planned and Inadvertent Weather Modification, Atlanta, GA., 148-155.

----, 1992 b: Concerning primary ice nuclei concentrations and ice formation versus water supersaturation in the atmosphere. 11th International Conf. on Clouds and Precipitation, Montreal, Canada

Meyers, M. P., P. J. DeMott, and W. R. Cotton, 1992: New primary ice nucleation parameterizations in an explicit cloud model. J. Appl. Meteor., In Press

Rokicki, M. L. and K. C. Young, 1978: The initiation of precipitation in updrafts, J. Appl. Meteor., **17**, 745-754.

Stith, J. L., A. G. Detwiler, R. F. Reinking, and P. L. Smith, 1990: Investigating transport, mixing and the formation of ice in cumuli with gaseous tracer techniques, Atmos. Research, **25**, 195-216

----, 1992: New techniques for studying the microphysical effects of cloud seeding, Preprints, Symposium on Planned and Inadvertent Weather Modification, Atlanta, GA, 156-160.

Vali, G., 1971: Quantitative evaluation of experimental results on the heterogeneous freezing nucleation of supercooled liquids, J. Atmos. Sci., **28**, 402-409.

Young, K. C., 1974: A numerical simulation of wintertime orographic precipitation: Part I. Description of model microphysics and numerical techniques, J. Atmos. Sci., **32**, 956-973.

MICROPHYSICS OF SNOW FORMATION OF AN ALPINE UPSLOPE CASE

P. Meischner[1], M. Hagen[1], V.N. Bringi[2]

[1]DLR, Institut für Physik der Atmosphäre, W-8031 Oberpfaffenhofen, Germany
[2]Colorado State University, Ft. Collins, Colorado

1 INTRODUCTION

Multiparameter radar measurements are one approach toward a better understanding of the microphysics of precipitation because of their potential to distinguish between different hydrometeors. The different radar parameters available by advanced polarimetric radar systems are sensitive to ensemble means of physical quantities such as particle shape, particle size, particle orientation in respect to the polarized radar beam and the dielectric constant. This results in overlap in particle classifications. Concerning ice particles, electromagnetic scattering calculations have been presented so far for rather idealized ice particle populations only. So most interpretations of polarimetric radar observations of ice particle distributions are based more or less on physical reasoning substantiated by model calculations.

One strategy for improving interpretations is to measure the particle characteristics and distributions by in situ methods simultaneously with the radar observations. We try to follow this strategy in completion to the other methods.

Here we present multiparameter radar measurements complementing the results of aircraft in situ measurements with 2-D PMS probes for a stratiform upslope precipitation situation near Oberpfaffenhofen. By these measurements the particle growth and the forming of precipitation can be followed in some detail.

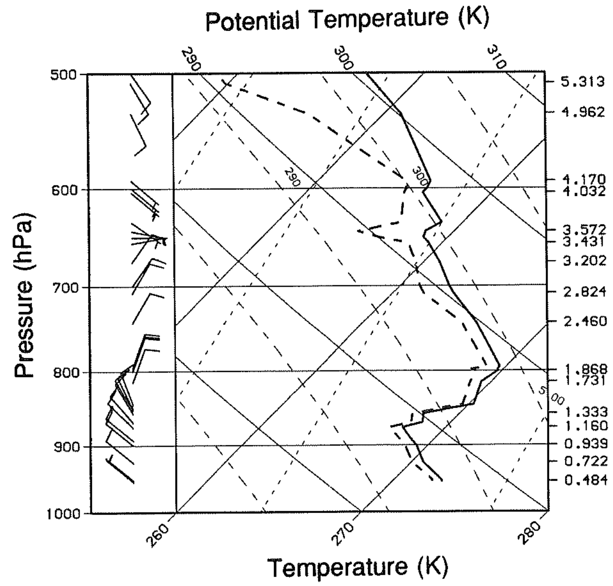

Fig. 1 Temperature and wind sounding at München on 27 November 1987 1200 local time.

2 MEASUREMENTS AND DATA EVALUATION

On 27 November 1987, an upslope situation developed at the northern Alpine area. This was caused by a strong low pressure system to the south of the Alps. Moist mediterranian air was forced around the east of the Alps and the low level winds from the NW maintained the upslope conditions during the observation period. First layer clouds initially formed SW of Oberpfaffenhofen. During the forenoon the system developed further to form widespread precipitation. The temperature and wind profile at 1200 loc. time measured at München (30 km NE of Oberpfaffenhofen) is shown in Fig. 1. A remarkable wind shift from north to south can be located in the region of the cloud top (650 hPa).

The radar measurements were performed with the polarimetric C-band radar POLDIRAD at Oberpfaffenhofen (Schroth et al., 1988). The NCAR King-Air equipped (among others) with one PMS C-probe and two P-probes flew along the 210° radial with respect to the radar. The excellent navigation of the aircraft secured that both, the radar and the in situ measurements were taken from the same cloud volume. The aircraft was frequently detected by the radar as can be seen in Fig. 2 at a distance of 32.5 km and 2.4 km height.

(a) Aircraft Measurements

The aircraft measurements were started about one hour after the first radar echos were observed. Along the 210° radial with respect to the radar two flight legs (35 km) were flown at altitudes of 2.4, 2.1, 1.7 and 1.3 km above ground (Fig. 3). The same flight pattern was then repeated a second time. Each sequence required about one hour to complete. The average temperatures at the four levels were about -10.7°C, - 8.4°C, -7.0°C, and -5.0°C, respectively.

For selected regions the particles measured by the PMS precipitation and cloud probes were classified manually into dendrites, aggregates and graupel. Fig. 4 shows the result for region I and II in Fig. 2. Region I is dominated by pristine dendrites with a size less than 2.4 mm. In region II aggregates with a size of about 4 mm are prevailing and the observed dendrites are strongly rimed.

(b) Radar Measurements

Figure 2 shows the radar measurements of the reflectivity Z, the differential reflectivity Z_{DR} and the difference reflectivity Z_{DP} (Golestani et al., 1989) at 1011 loc. time.

The radar observations close to region I and II (200 m above and below the flight path) and additional 10 regions are summarized in Fig. 5. Figure 5 shows scatter plots for the radar parameters Z, Z_{DR} and Z_{DP}. The dashed line in the Z - Z_{DP} scattergram indicates the "rainline". All measurements in rain should lay along this line (Golestani et al., 1989). Dendrites and aggregates cluster in distinct areas of the scattergrams. This information was used to classify the radar data of the RHI scan into dendrites and aggregates according the following thresholds,

Dendrites:	**Aggregates:**
$Z < 10$	$Z > 10$
$Z < 15$	$Z > 15$
$Z_{DR} > 0$	$-1 < Z_{DR} < 1$
$Z_{DR} > 2$	$Z_{DR} \cdot Z_{DP} > 0$
$Z < Z_{\text{rainline}} - 2$	

where Z_{rainline} indicates the reflectivity given by the rainline for a particular Z_{DP}. The more thresholds are fulfilled the higher is the probability of the occurence of the particular particle class.

Figure 6 shows the result of this classification. The light shaded area indicates mostly dendrites, the black area mostly aggregates, and the gray shaded areas indicate the area where rimed dendrites and small aggregates coexist.

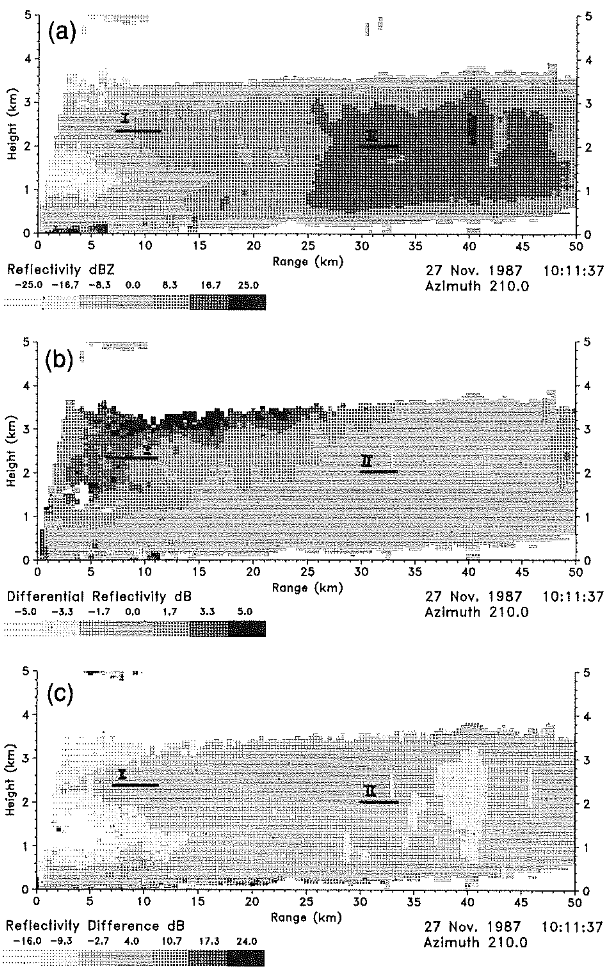

Fig. 2 RHI along the 210° azimuth showing reflectivity (a), differential reflectivity (b) and difference reflectivity (c). Region I and II indicate where the particle classification shown in Fig. 4 were performed from the PMS measurements.

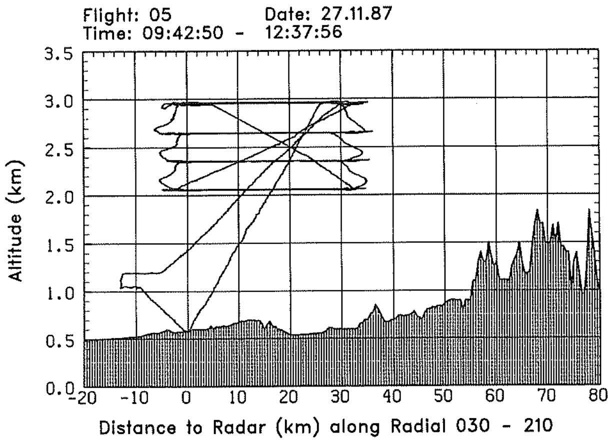

Fig. 3 Flight pattern of the King-Air and topography.

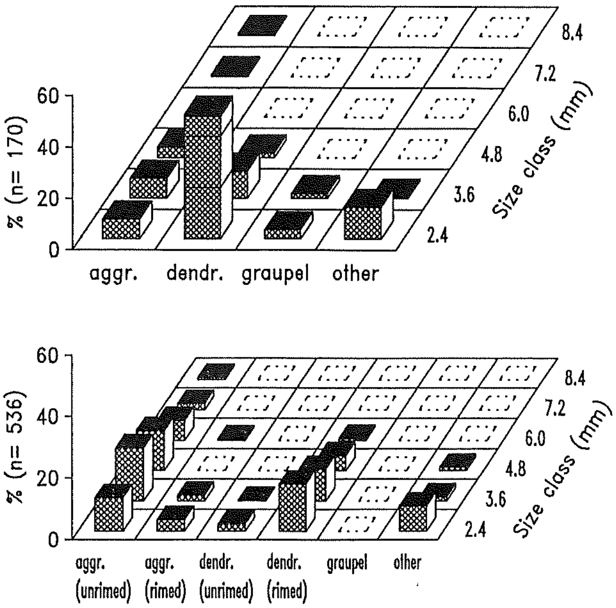

Fig. 4 Results of manual particle classification from the PMS 2D-probes. Top for region I, bottom for region II.

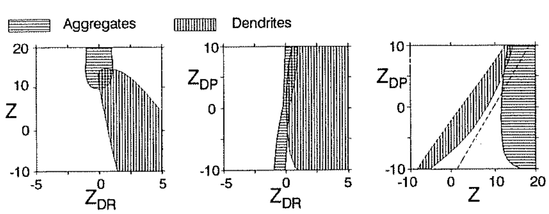

Fig. 5 Summary of scatterplots of radar parameters for various regions with dendrites and aggregates.

3 OBSERVATIONS

Figures 2 and 6(a) show the situation at 1011 loc. time, about one hour after the first echo was observed with the radar. At this early stage of the development, the observed precipitation pattern and initial particle types probable are influenced by the underlying topography. The terrain slopes gently from 600 m to 800 m MSL within the first 50 km from the radar (Fig. 3). Further away, the mountains rise 1000 to 1500 m above the Alpine foreland. Due to the prevailing wind speed and direction a lifting of a few cm/s is forced above the Alpine foreland. Closer to the mountains lifting is stronger causing precipitation with higher intensity. The local enhancement at 40 km range coincides with an isolated mountain at 37 km range (cf. Fig. 3). We assume, that the local increased lifting is the reason for the local increase in precipitation intensity. Close to the radar an elevated layer of very weak reflectivity is observed. This layer extends across the depth of the inversion layer as seen in Fig. 1. Above this low reflectivity layer pristine dendrites were observed. These crystals evaporate partly as they fall into this layer. Close to the ground the remaining crystals rime due to the higher concentration of liquid water at temperatures of about -2°C.

Figure 6(b) shows the situation 20 minutes later. The continuous evaporation of crystals falling from above, and the continuous lifting increased the humidity in the low reflectivity layer, and the gap tends to decrease. At 1048 loc. time (Fig. 6c) the gap is closed completely, but its former existence is indicated by a layer of dendrites. Above this layer smaller aggregates have been formed. It is further observed that the top of the cloud consisting of dendrites is decreasing. The aggregation process continues and finally at 1208 loc. time the complete layer between the radar and the Alps is aggregated, and only a thin layer of dendrites can be observed at the top of the cloud (Fig. 6d). Baumgardner and Hagen (1990) estimated the ice water content for this period.

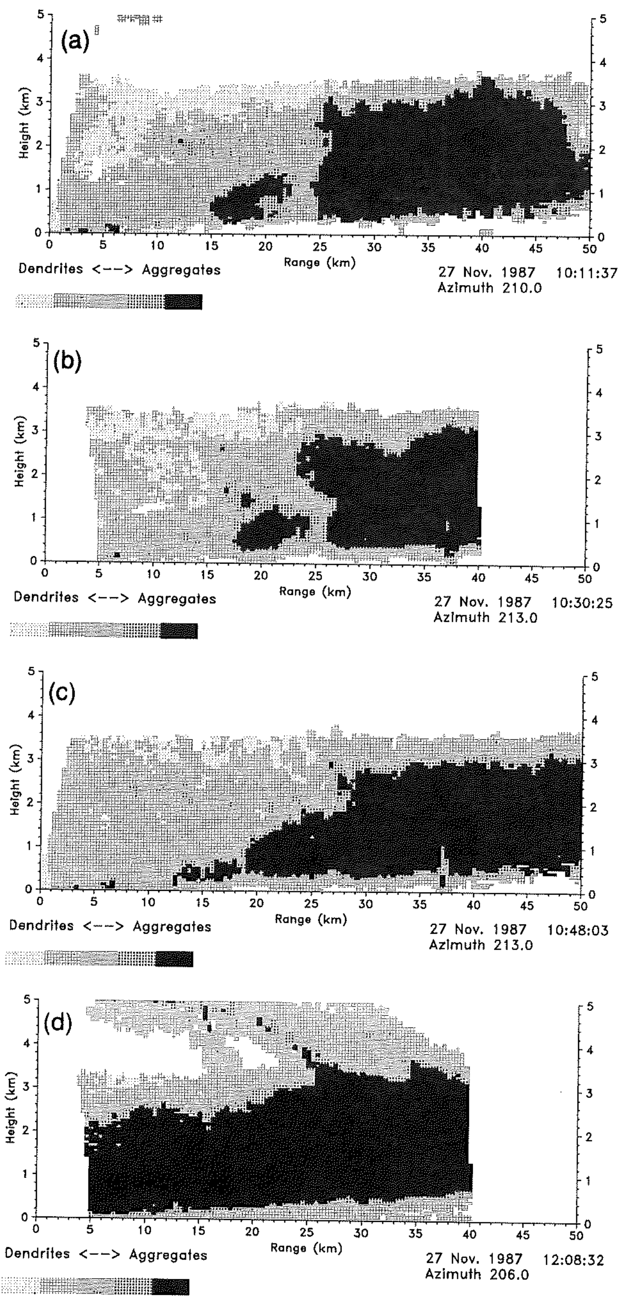

Fig. 6 RHI's of particle classification from different radar parameters for four different times. The classification is described in the text. The light shaded areas indicate dendrites, the black areas indicate larger aggregates. The intermediate levels indicate rimed and aggregated particles.

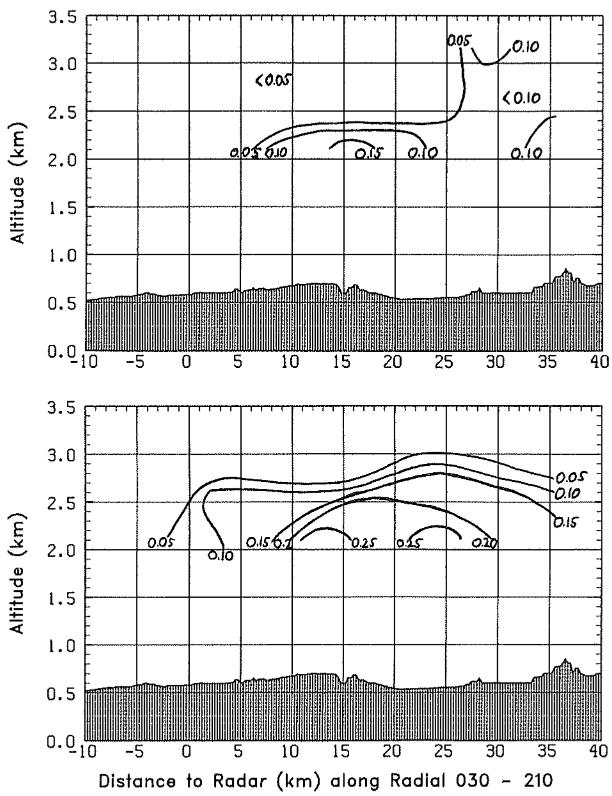

Fig. 7 Liquid water content (g m^{-3}) as derived from PMS-FSSP probes. Top is for the first flight pattern (1000 to 1100 loc. time) and bottom is for the second flight pattern (1100 to 1200 loc. time).

They found for the lowest flight level (1350 m above the radar) that the ice water content increased within one hour by one order of magnitude, and the liquid water content (LWC) estimated from the PMS-FSSP probe doubled almost (Fig. 7). This indicates that there is sufficient supercooled water available to grow ice particles by riming. Figure 6(d) also suggests that plumes of dendrites and small aggregates with their origin at the cloud top are lifted and transported northwards by the southerly wind at that altitude.

4 DISCUSSION AND CONCLUSION

On November 27, 1987 moderate snow fall was generated in the northern Alpine region by upsloping air from the north. The precipitation formation was followed during two hours by coordinated radar and aircraft in situ measurements, beginning with the first radar echo.

The situation was characterized by moist mediterranian air which, after being forced around the east of the Alps, was directed towards the northern slopes of the Alps. Above 3.5 km MSL the wind direction veered to south. An inversion layer separated the northwesterly and northeasterly flow (Fig. 1).

The particle type identification was made possible by polarimetric radar measurements supported by coordinated aircraft measurements at selected areas. The first particles formed were of the dendritic type mostly. The further growth up to precipitation size and density took place by the aggregation and riming process by continuous advection and lifting of humid air. Enhanced orographic lifting increased the precipitation formation as could be followed locally in the early stage of the system development about 40 km from the radar. This is caused by an increase in LWC favouring the riming process. By the continuous supply of moist air the LWC increased during the whole observation area by a factor of two, and the ice water content by an order of magnitude. About two hours after the first radar echo was observed widespread precipitation consisting of aggregates and rimed dendrites has formed. The initial observed reflectivity gap associated with an inversion layer was then filled by precipitation.

In conclusion the coordinated aircraft and polarimetric radar observations enabled us to follow and explain in principal the precipitation formation process of this upslope case by its dynamical as well as by its embedded microphysical processes.

Acknowledgements We are greatly indebted to the RAF of NCAR for navigating the King-Air well coordinated with the DLR radar and especially Darrel Baumgardner for the scientific and technical coordination. One of the authors (VNB) was supported by the National Science Foundation via grant ATM-8703126.

REFERENCES

Baumgardner, D. and M. Hagen (1990): Estimates of ice particle bulk densities and total water mass in an upslope-generated cloud. Proc. Conf. Cloud Physics, San Francisco, Amer. Meteor. Soc., Boston, 8-15.

Golestani, Y., V. Chandrasekar and V.N. Bringi (1989): Intercomparison of multiparameter radar measurements. Proc. 24nd Radar Meteor. Conf. Thallahassee, Amer. Meteor. Soc., Boston, 309-314.

Schroth, A.C., M.S. Chandra and P.F. Meischner (1988): A C-band coherent polarimetric radar for propagation and cloud physics research. J. Atmos. Ocean. Techn., **5**, 803-822.

INVESTIGATION OF SPATIAL AND MICROPHYSICAL CHARACTERISTICS OF CONVECTIVE TROPICAL CLOUDS BY MEANS OF REMOTE SENSING

B.P.Koloskov[1], A.V.Koldaev[1], L.Batista[2], C.Perez[2]

[1] **Central Aerological Observatory, Pervomayskaya 3, Dolgoprudny, Moscow Reg., Russia**

[2] Institute of Meteorology, Academy of Sciencies, Cuba

1. INTRODUCTION

The success of cloud precipitation enhancement by modification is associated with the presence of supercooled liquid water within the clouds. The liquid water content (LWC) was usually measured in situ using contact sensors when an instrumented cloud physics aircraft was passing through a cloud. However, safe operational limitations prevent aircraft from penetrating some classes of clouds, especially those of convective type.

It is known that detection and measurements of an integrated content of supercooled liquid water within storms can be made remotely by microwave radiometer sensing (M.Heggly, 1985). In this paper we discuss the results from experimental studies which were performed in order to estimate LWC within the convective storms at different stages of their evolution.

2. INSTRUMENTATION

The microwave radiometric instrumentation to measure remotely the supercooled liquid water was developed by scientists of the Central Aerological Observatory and was installed aboard two Soviet instrumented aircraft, IL-18 and AN-12, and also on board the Cuban AN-26 research aircraft. It is evident that airborne observations have a number of disadvantages such as temporal and spatial limitations on the collection of data, which reduces the efficiency of their use when meteorological objects are studied over extensive areas. Availability of the MRL-5 radar supplemented with an automated system for digital processing of radar information in the Camaguey experimental area, Cuba, does permit a thorough radar and radiometer study of convective storms to be made in this area.

3. EXPERIMENTAL TECHNIQUES

Microwave radiometer probing was made in the Camaguey experimental area (CEA) in 1986 and 1987 from an instrumented aircraft IL-18 "CYCLONE", in 1990 from the aircraft AN-12 "CYCLONE" and in 1991 from AN-26 aircraft. Identical radiometers with a 8 mm wavelength were used throughout all the seasons. The geometry of sounding for different seasons is given in Fig.1.

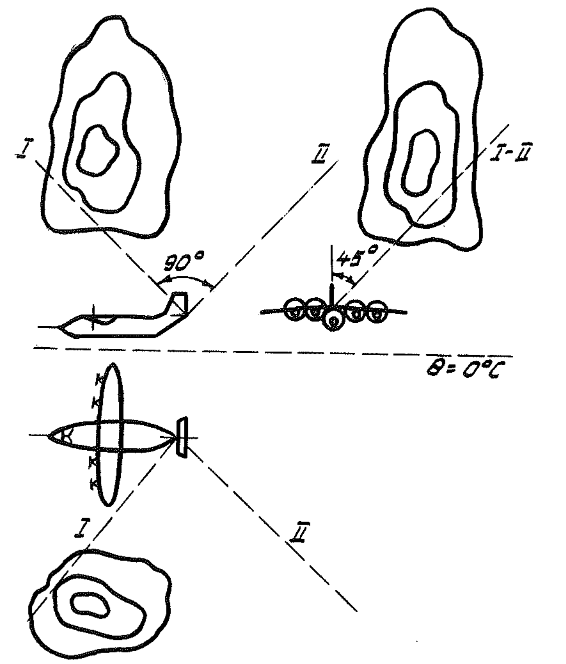

Fig 1. A scheme of radiometric sounding of clouds in the Camaguey experimental area

As can be seen, flights performed beside the clouds studied above the 0°C isotherm **allowed** to obtain information about the liquid water within a cloud layer over the temperature range from -5°C down to -20°C. Such a geometry of flights practically removes the limitations on flight safety for aircraft. Therefore, the main set of data was obtained during the seasons of 1987 and 1991.

As has been stated above, aircraft investigations of clouds in the CEA were accompanied by carefully made radar observations of the structure of radar echoes. A software package was used for an analysis of radar information. These programs allowed to identify echo cores in clouds, to follow them in time and in space, and to calculate their main characteristics, i.e., radar echo height, areal coverage of clouds and precipitation, rainfall intensity and amount of precipitation. The availability of detailed radar information as well as radiometer measurements allowed to evaluate the water content of tropical convective clouds at different stages of their evolution.

4. CHARACTERISTICS OF CUMULUS CLOUDS

Figure 2 shows cumulative and differential distributions of the integrated liquid water within the clouds during the seasons of 1987(a) and 1991(b).

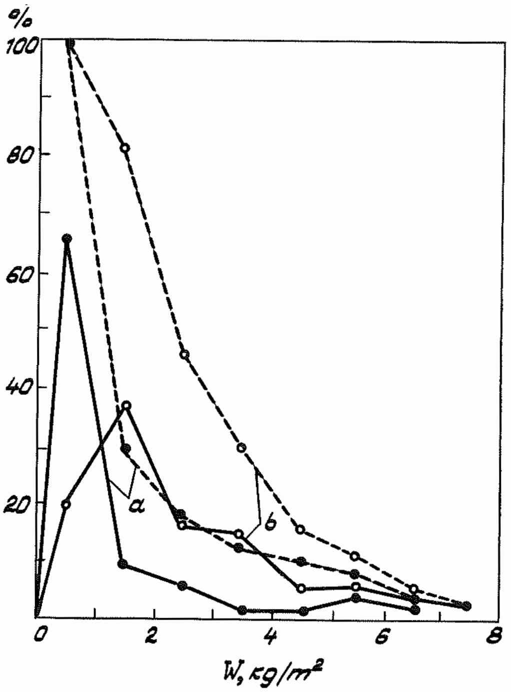

Fig 2. Differential (●—●) and cumulative (●– –●) distributions of the integrated liquid water in convective clouds in 1987 (a) and 1991 (b).

A marked difference in the integrated water content of clouds is noted for the seasons examined. Thus, in 1987 the most likely were water contents about 0.5 $kg \cdot m^{-2}$, the mean value being 1.2 $kg \cdot m^{-2}$, while in 1991 these values were 1.5 $kg \cdot m^{-2}$ and 2.5 $kg \cdot m^{-2}$, respectively. About 20% of clouds had the integrated water content of more than 2.5 $kg \cdot m^{-2}$ during the season of 1987 and of more than 4.2 $kg \cdot m^{-2}$ during the season of 1991. The differences observed may be accounted for the fact that in 1987 the clouds were studied in September-October, while in 1991 the flights were made in July-August.

Figure 3 gives cumulative and differential distributions of the scales of water zones. As in the case of the integrated water content, a difference in the extent of water regions was noted. So, in 1987 the most likely scale of water zones was about 2 km, a second

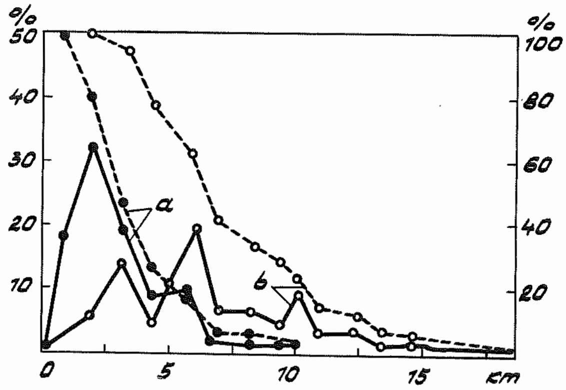

Fig 3. Differential (●—●) and cumulative (●– –●) distributions of the scales of liquid water zones in 1987 (a) and 1991 (b).

peak being observed on the 6 km scale, and in 1991 three maxima were noted for the scales of 3, 6 and 10 km. The presence of a peak on the scale of 10 km in 1991 is likely to be associated with the fact that the observations were made within the extended (up to 60–100 km) and narrow (20–30 km) bands of clouds and precipitation.

Using data on the integrated water content of clouds and the information on the scales of zones by assuming their symmetry, it is possible to estimate the mean LWC for a sounded volume of the cloud studied. Cumulative and differential distributions of the mean LWC determined in such a way are shown in Fig.4. As can be seen, the most likely mean LWC for the both seasons proved to be about 0.1 $g \cdot m^{-3}$, while a differential distribution is broad enough and equally probable LWC values proved to be those of 0.2 $g \cdot m^{-3}$ and 0.3

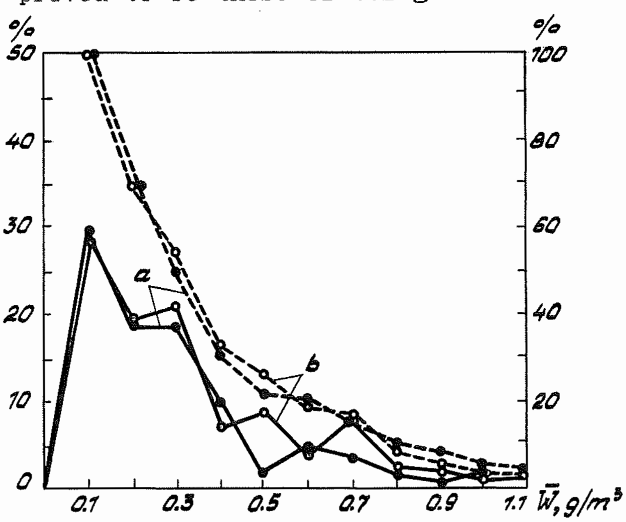

Fig 4. Differential (●—●) and cumulative (●– –●) distributions of the mean liquid water content of convective clouds in 1987 (a) and 1991 (b).

$g \cdot m^{-3}$. By examining the cumulative curve, one may say that practically every fifth cloud had the LWC of more than 0.5 $g \cdot m^{-3}$.

Figure 5 gives an example of complex investigations of an isolated cloud which was observed in the CEA on 17 September, 1987. The echo from that cloud existed 45 minutes. An analysis of radar and microphysical characteristics of the clouds over the CEA has shown that the highest LWC in clouds was observed during the first 15-20 minutes after the first echo appeared.

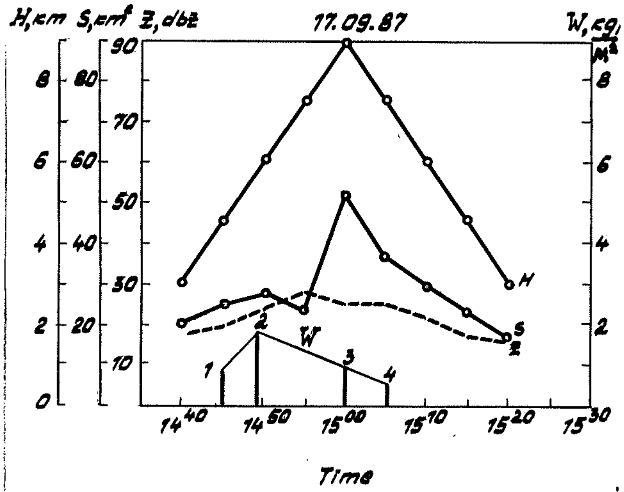

Fig 5. An example of the evolution of radar characteristics and the liquid water content of a convective cloud which was observed on 17 September 1987 in the Camaguey experimental area.

From a comparison of changes undergone by the radar characteristics and the water content (see Fig.5), it can be seen that during the first two passes of the instrumented aircraft in the vicinity of a cloud at the initial stage of its development, the maximum water content of 0.78 $kg \cdot m^{-2}$ according to radiometer measurements was recorded 5 min after the first echo appeared, and of 1.90 $kg \cdot m^{-2}$ 9 min after the appearance of the first echo, i.e. an increase in water content by a factor of 2.5 was observed within 4 minutes. During the third pass, 21 min after the first echo appeared, a decrease in water content down to 0.98 $kg \cdot m^{-2}$ was observed. While the cloud top grew from 6 up to 9 km, according to radar information for that period, the rainfall intensity increased and the area precipitation increased by a factor of two, i.e. the depletion of cloud water in the supercooled portion of cloud was already observed, whereas the values of radar parameters increased. During the fourth pass, when the cloud was in its dissipating stage, the water content decreased down to 0.40 $kg \cdot m^{-2}$.

5. RESULTS

Thus, by means of complex radar and radiometer investigations of the clouds in the CEA:

- integrated water content, horizontal sizes and mean supercooled liquid water content in tropical convective clouds have been obtained;
- it has been found out that the supercooled water is present in a growing cloud, and clouds are amenable to seeding with ice-forming aerosols within the first 10 or 20 minutes after the appearance of radar echoes.

REFERENCES

Mark F.Heggly, 1985: The role of Microwave Radiometry in Weather Modification Research. WMO Report No 2, WMO/TD No 53, Geneva.

MICROPHYSICAL STRUCTURES OF CONVECTIVE SNOW CLOUDS OVER THE SEA OP JAPAN

Masataka MURAKAMI, Takayo MATSUO, Hakaru MIZUNO and Yoshinori YAMADA

Meteorological Research Institute, Tsukuba 305, JAPAN

1. INTRODUCTION

Heavy snowfall often occurs over the Japan Sea coastal regions as well as the mountain regions during winter monsoon season in Japan. The cold airmass from the Eurasian Continent receives a great amount of heat and moisture from the relatively warm sea surface as it is crossing the Japan Sea. Consequently, active cumulus convections develop in the moist and unstable stratification and cause the intense snowfall in downstream coastal regions of the Japan Sea. A large amount of snowfall produced in such a manner sometimes does damage to traffic and housing.

Understanding of precipitation mechanisms in the snow clouds is essential for improvement of short range forecasting and establishment of snowcloud modification that would lead to a lessening of these damages. Many studies (Ninomiya, 1968; Matsumoto et al., 1965; etc.) on synoptic and mesoscale features of snow clouds over the Japan Sea have been made. From the viewpoints of microphysical structures of snow clouds and precipitation mechanisms, however, limited studies (Isono et al., 1966; Magono and Lee, 1973) heve been made to date.

The Cooperative Japan Sea Snowcloud Project was started in 1989 to clarify meso- and microscale structures of the snow clouds and the precipitation mechanisms operating in them and to evaluate the feasibility of snowcloud modification by seeding.

In this paper, we present microphysical and thermodynamical structures of convective snow clouds studied through thirty soundings of hydrometeor videosonde and hydrometeor video dropsonde.

2. OBSERVATION FACILITIES

Three national institutes and three universities participate in this project and a variety of instruments such as 3 Doppler radars, a dual polarization radar, a microwave radiometer, hydrometeor videosondes, and hydrometeor video dropsondes are deployed. To investigate microphysical and thermodynamical structures of snow clouds, we have developed a hydrometeor videosonde (HYVIS; Murakami and Matsuo, 1990) and its dropsonde version, hydrometeor video dropsonde (HYDROS).

The HYVIS has two small video cameras with different magnifications to take pictures of hydrometeors from 7 µm to 2 cm in size. The HYVIS and rawinsonde are attached to the same balloon and launched into clouds. They transmit hydrometeor images and meteorological data over 1,687 and 1,680 MHz microwave link to a ground station.

To increase a mobility in microphysical measurements, we improved on the HYVIS and have made a hydrometeor video dropsonde which is released from aircraft above cloud tops. One of main differences is that meteorological signal is superposed on image signal (i.e., the HYDROS uses only one microwave frequency to transmit hydrometeor images and meteorological data). This allows us to make multiple HYDROS soundings at the same time. The other is the way to collect hydrometeor particles. The HYDROS collects cloud particles on a film facing downward by inertial impaction and precipitation particles settling in a rear wake onto a film facing upward while the HYVIS collects all hydrometeors on a film facing upward. The hydrometeor image and meteorological data can be received at the aircraft equipped with an autotracking antenna or at the ground station.

3. RESULTS

3-1. General features of snow clouds

Since 1989, we have made more than 30 HYVIS and HYDROS soundings. The observed snow clouds were in forms of L-mode, T-mode or isolated convective snow clouds and were at various stages of their life cycles although the whole life cycles of individual snow clouds have not been successfully observed yet. Their cloud top temperatures (heights) ranged from -6°C to -27°C (from 1.5 km to 3.5 km). The cloud base heights (temperatures) which were estimated from lifting condensation levels were between 200 m and 1300 m (between -5°C and -12°C) and cloud thickness was between 0.3 km and 2.5 km.

Note that all the observed snow clouds were associated with normal or mild cold air outbreaks, not with extremely cold air outbreaks.

Microphysical structures of snow clouds are expected to depend upon cloud top temperatures as well as cloud dynamical structures. Therefore, choosing rather isolated convective snow clouds with their cloud top temperatures of -20°C ± 3°C and compositing observational results of separate snow clouds at various stages, we present the evolution of microphysical structures of snow clouds below.

3-2. Snow cloud in developing stage

Microphysical structure of the snow cloud observed with the HYDROS at 1541 5 Feb. 1991, as an example of snow cloud in developing stage, is described. Vertical structure of microphysical and thermodynamical features are shown in Fig.1. Cloud top height (temperature) and cloud base height (temperature) are 2.3 km (-17°C) and 1.3 km (-10°C), respectively. The cloud base height is coincident with the calculated lifting condensation level. Maximum cloud water content was 0.6 g/m^3 and existed near the cloud top while ice water contents were around 0.01 g/m^3 and confined in supercooled cloud droplet regions. The observed cloud water content showed a good agreement with the adiabatic cloud water content (0.7 g/m^3). Number concentrations of cloud droplets were almost uniform and approximately 40 particles/cm^3. Their size distribution has a peak around 15 µm in diameter and a broad tail extending up to 50 µm (not shown here). Number concentrations of ice crystals were several particles/l

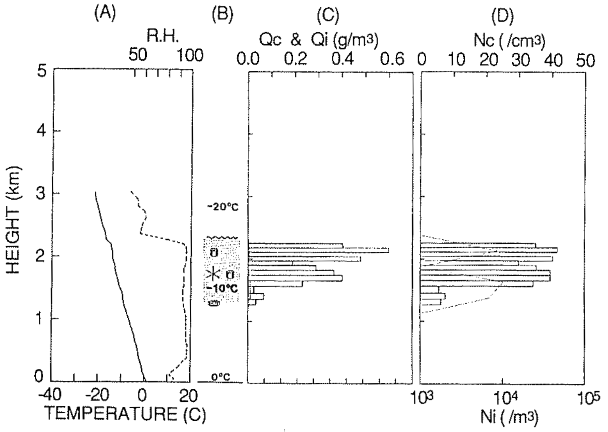

Fig.1 Vertical structures of the snow cloud at developing stage. (A) temperature (solid line), relative humidity (dashed line); (B) snow crystal types observed aloft; (C) cloud water content (Qc, rectangles) and ice water content (Qi, detted line); (D) number concentrations of cloud droplets (Nc) and ice crystals (Ni).

and are one order of magnitude greater than those expected from Fletcher's (1962) equation. However large precipitation particles (d>0.3 mm) were not observed in this cloud (at least along the HYDROS descent path).

Maximum updraft velocity was estimated to be 4~5 m/s from the fall velocity of the HYDROS and dual Doppler radar measurements. Temperatures in the convective cloud were 1~2°C higher than those outside convective clouds. There is a convectively unstable layer near the cloud top ("cloud top entrainment instability").

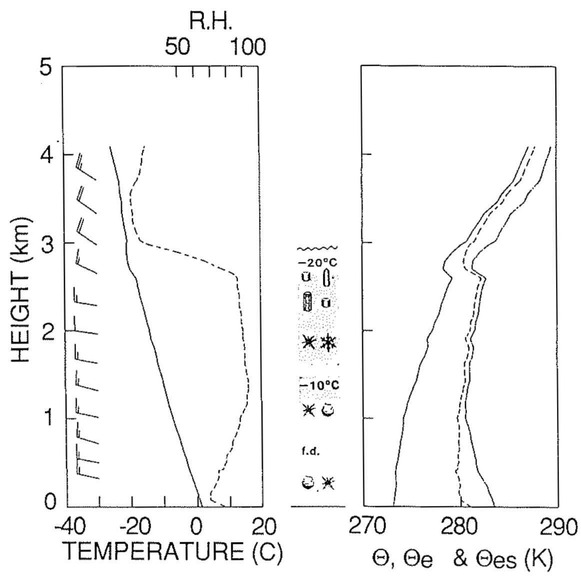

Fig.2 Vertical profiles of temperature, relative humidity (solid and dashed lines in the left panel), snow crystals observed aloft (the center panel) and potential temperature, equivalent potential temperature and saturated equivalent potential temperature (solid, dashed and dash-dotted lines in the right panel).

3-3. Snow clouds in mature stage

Snow cloud observed with the HYVIS at 1501 4 Feb. 1989 showed a typical microphysical structure of convective snow clouds in mature stage. As seen from Fig.2, the cloud top height and temperature were ~2.9 km and -21°C. The precipitation processes started to erode away the lower portion of cloud water and the observed cloud base height of 1.1 km was significantly higher than the calculated lifting condensation level (800 m). Thermodynamical structures of the cloud are characterized by the excess temperature of 1~2°C in upper and middle parts and the cloud top entrainment instability.

Figure 3 shows hydrometeor images taken by

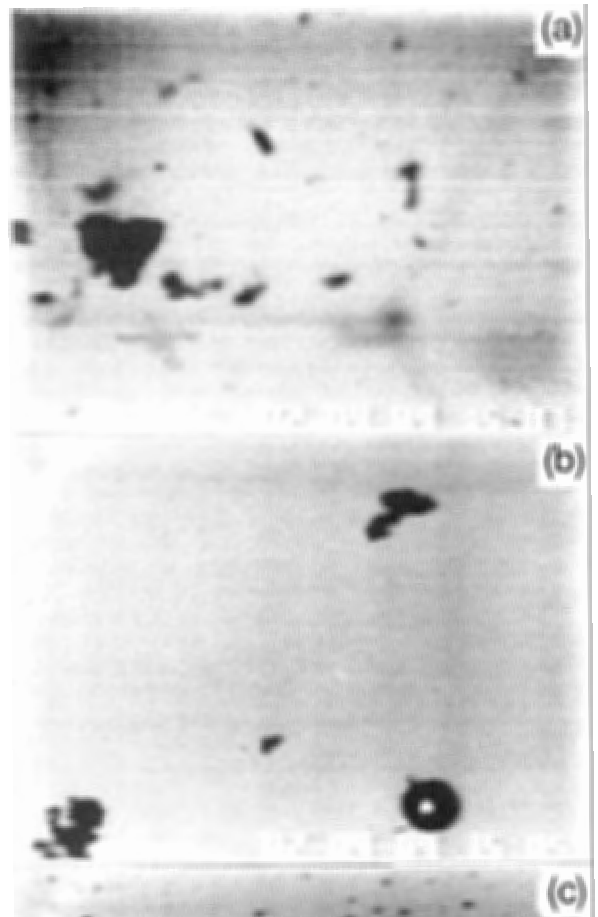

Fig.3 Images of various types of hydrometeors taken in the snow cloud at mature stage. The width of photo (a) is 2 cm while those of photos (b) and (c) are 1.5 mm.

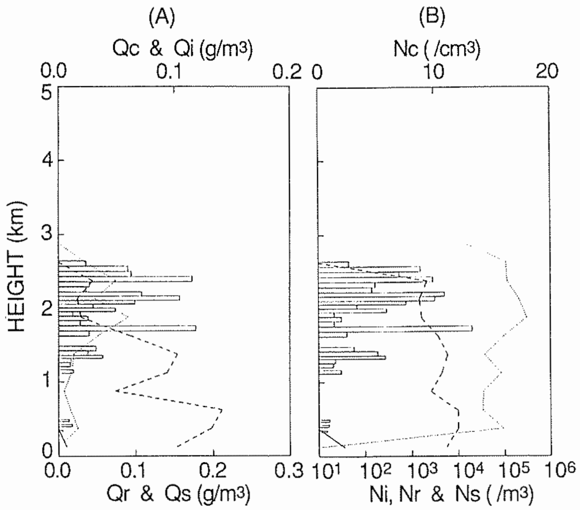

Fig.4 Vertical changes in hydrometeor concentrations. (A) water content of cloud droplets (Qc, rectangles), ice crystals (Qi, dotted line), snow (Qs, dashed line) and rain (Qr, solid line); (B) number concentration of cloud droplets (Nc), ice crystals (Ni), snow (Ns) and rain (Nr).

the HYVIS. Panel (a) shows graupel particle observed in the lower parts of snow cloud or below cloud base, panel (b) a frozen drop, panel (c) super cooled cloud droplets and pristine crystals. Panel (c) evidences that columns and thick plates already started to rime before their size reaching 100 µm.

Cloud water contents (rectangles in the left panel of Fig.4) were roughly 0.1 g/m^3 in upper and middle parts of the snow cloud while ice water contents (ice crystals d<200 µm; doted line in the left panel) were roughly 0.05 g/m^3. High ice water contents existed in regions with high cloud water contents. Snow water contents (dashed line in the left panel) increased with decreasing height and their maximum value reached 0.2 g/m^3. Supercooled and frozen drops of 100~200 µm in diameter were observed at heights of 200-400 m. These drops formed through collision-coalescence process between cloud droplets.

The number concentrations of cloud droplets (rectangles in the right panel) were roughly 10 particles/cm^3 while number concentrations of ice crystals were high in the supercooled cloud droplet layer and their maximum value was ~300 particles/l.

Number concentrations of snow particles (d>200 µm) were ~10 particles/l, and those of drizzle drops were less than 100 particles/m^3. Figure 5 shows size distributions of cloud droplets and snow particles at upper, middle and lower levels of the snow cloud. Cloud droplets had the broad size distribution with a peak near 20 µm in diameter. No marked difference among size distributions at the three levels was found. Size distributions of snow particles broadened toward larger size with decreasing height. This reflects the fact that snow particles were sorted out according to their fall velocities.

3-4. Snow clouds in decaying stage

As an example of snow clouds in decaying stage, we describe microphysical and thermodynamical structures of the snow cloud observed at 1526 3 Feb. 1989.

Cloud top height and temperature were ~2 km and -20 C although there was no supercooled cloud

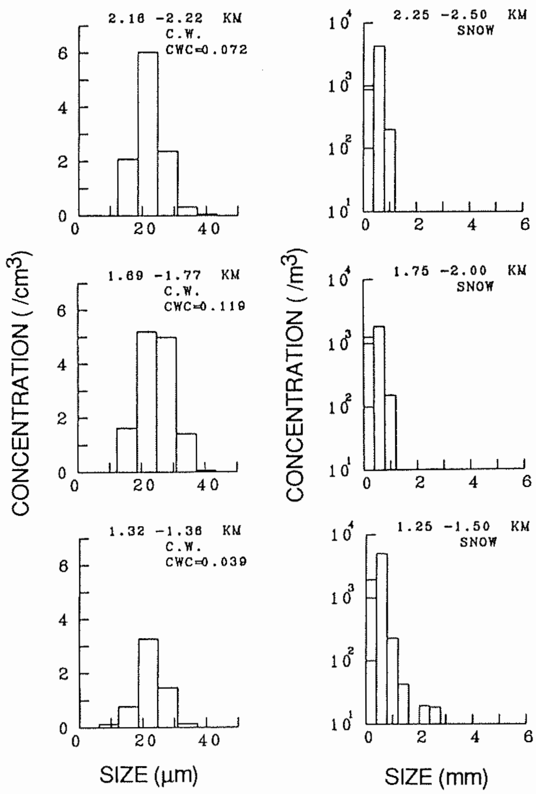

Fig.5 Vertical changes in size distributions of cloud droplets (left) and snow particles (right).

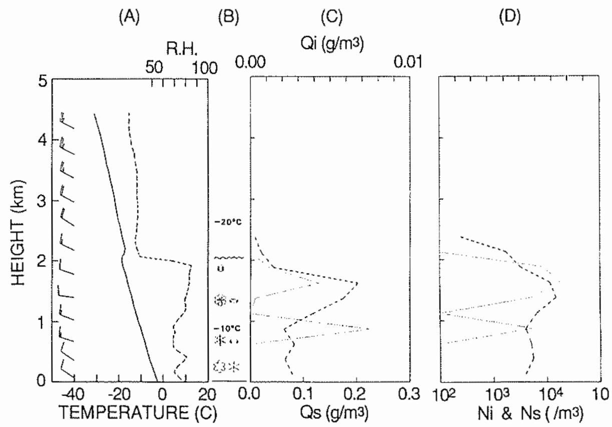

Fig.6 The same as Fig.1 except for the snow cloud at decaying stage.

water. The temperature excess in the cloud became obscure and cloud top entrainment instability has weakened at this stage. A convectively unstable layer was seen only in the lowest layer of 500 m deep (not shown here).

Water contents (panel C) and number concentrations (panel D) of ice crystals and snow particles are shown in Fig. 6. Snow water contents were high at upper parts of snow clouds and their maximum value was 0.2 g/m^3. Number concentrations were ~10 particles/l there and a few particles/l in middle and lower parts. These snow particles consisted of unrimed dendrites and hexagonal plates with small fall velocities.

Ice water contents were less than 0.01 g/m^3 and negligibly small. This means that active ice nucleations had ceased.

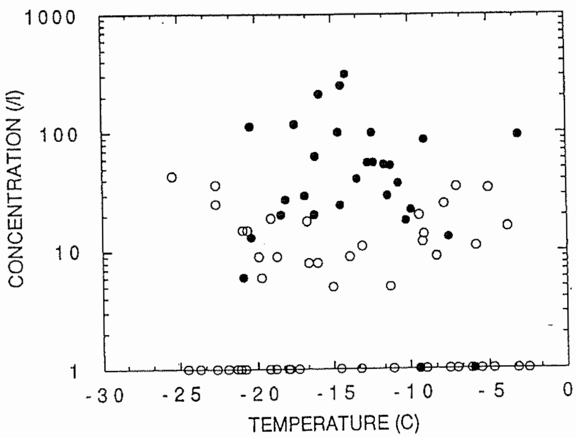

Fig.7 Relationship between air temperatures and concentrations of ice crystals (d<200 μm) in (solid circles) and out (open circles) of supercooled cloud droplets regions.

4. DISCUSSION

4-1. Ice nucleation

Figure 7 shows the relationship between air temperature and number concentrations of pristine crystals (d<200 μm). Solid and open circles indicate the concentration of ice crystals in and out of supercooled cloud water regions, respectively. High concentrations of ice crystals were observed in supercooled cloud water regions although they do not show any significant temperature dependency.

These observational results suggest that dominant mechanism in the snow clouds is condensation-freezing nucleation. However there remains a possibility of some secondary nucleation accompanied with the riming process other than the Hallett and Mossop's (1974) mechanism operating at warmer temperatures (T>-10°C).

4-2. Graupel embryo

Hydrometeor (d<200 μm) images taken in snow clouds that were producing graupel particles showed that columns and thick plates (so-called isometric crystals) were dominant and they already started to rime before their size reaching 100 μm. The number of supercooled and frozen drops observed was much less than that of the isometric crystals. These observational results suggest that rimed columnar and thick plate crystals are the most promising candidate of graupel embryo. However, drizzle and drops are supposed to form in supercooled cloud water region and fall out immediately after their formation before depositional and riming growth of ice crystals become effective. Thus the existence of supercooled or frozen drops is limited in space and time and we may have missed these drops in the observations. Therefore we reserve the possibility for frozen drops to act as graupel embryos.

5. CONCLUSION

Based on the HYVIS and HYDROS observations, microphysical and thermodynamical structures of rather isolated convective snow clouds with cloud top temperatures of -20°C ± 3°C at developing, mature and decaying stages are summarized as follows.

At developing stages, a high concentration of supercooled cloud droplets occupied the whole cloud. The maximum cloud water content and cloud droplet number concentration were more than 0.5 g/m^3 and several tens $particles/cm^3$, respectively. Number concentrations of ice crystals (d<200 μm) were about 10 particles/l but few precipitation particles (snow and graupel; d>300 μm) had appeared yet.

At mature stages, a considerable amount of supercooled cloud droplets had been depleted through depositional and accretional growth of ice crystals and snow particles, and their water content and number concentration were 0.2 g/m^3 and 10 $particles/cm^3$. Ice nucleation processes (probably condensation-freezing nucleation) were still active and ice crystal concentrations sometimes exceeded 100 particles/l. Dominant types of precipitation particles were heavily rimed snow and graupel and their concentrations were ~10 particles/l. Supercooled and frozen drops (100 μm<d<200 μm) sometimes coexisted with rimed snow crystals and graupels.

At decaying stages, supercooled cloud droplets were completely depleted whereas a considerable amount of unrimed and lightly rimed snow crystals were still suspended in upper parts of clouds.

At developing and mature stages, the excess temperature of 1~2°C in the convection cores and cloud top entrainment instability were observed. The maximum updraft velocity (4~5 m/s) was observed in snow clouds at developing stage.

REFERENCES

Fletcher, N.H., 1962: Physics of Rainclouds. Combridge Univ. Press, London, 386 pp.

Hallett, J. and S.C. Mossop, 1974: Production of secondary ice particles during the riming process. *Nature*, **249**, 26-28.

Isono, K., M. Komabayashi, T. Takahashi and T. Tanaka, 1966: A physical study of solid precipitation from convective clouds over the sea. Part II. *J. Meteor. Soc. Japan*, **44**, 218-226.

Magono, C. and C.W. Lee, 1973: The vertical structure of snow clouds, as revealed by "snow crystals sonde", Part II. *J. Meteor. Soc. Japan*, **51**, 176-190.

Matsumoto, S., T. Asai, K. Ninomiya, M.Iida and M. Takeuchi, 1965: Behavior of the extraordinary cold vortex over the Far East coastal area observed during the period from 22 January to 24 January 1963. *J. Meteor. Soc. Japan*, **43**, 100-115.

Murakami, M. and T. Matsuo, 1990: Development of hydrometeor videosonde. *J. Atmos. Oceanic Tech.*, **7**, 613-620.

Ninomiya, K., 1968: Heat and water budget over the Japan Sea and the Japan Islands in winter season. *J. Meteor. Soc. Japan*, **46**, 343-372.

AIRCRAFT MEASUREMENTS TO VALIDATE AND IMPROVE NUMERICAL MODEL PARAMETRISATIONS OF THE ICE TO WATER RATIOS IN CLOUDS

S.J.Moss and D.W.Johnson

Meteorological Research Flight, Farnborough, England.

1 INTRODUCTION

Since the presence of ice in clouds significantly effects precipitation, glaciation processes in clouds need to be well understood in order that numerical models can accurately simulate precipitation. There have been a large number of measurements made of the concentration of ice particles in cloud (Hobbs and Rangno 1985, Hallett et al 1978, Stewart 1967, Hobbs 1969) but there has been very little published on the ratio of the mass of ice to water in either a localised parcel of cloud or in clouds averaged over distances which might represent model grid boxes. This latter measurement is difficult to make with ground based instrumentation but it is feasible with a well instrumented aircraft.

At present the Meteorological Research Flight C-130 is not equipped with any sensors that can automatically detect the presence of ice in the cloud it is flying through and the Johnson Williams liquid water sensor has severe problems associated with it in trying to measure the liquid water content when supercooled water is present. The size, shape and number concentration of large particles ($25\mu m$ to $6400\mu m$) in a parcel of air the C-130 is flying through are sampled using the Particle Measuring System (PMS) two dimensional cloud probe (2DC) and two dimensional precipitation probe (2DP). These probes measure particles in the size range $25 - 800\mu m$ and $200 - 6400\mu m$ respectively. The 2D cloud probes however, require human interaction to decide whether they are ice or water. When flying through cloud these probes produce a vast amount of data and it is impractical for any quantitative measurements of the amount of ice in a sample to be made by the human operator due to the amount of time it would take. This paper details an automatic technique that can process the 2D cloud probe data, post flight, which

(a) differentiates between liquid water droplets and ice particles and

(b) classifies the ice particles into 6 ice types

Section 2 details the automatic technique used to analyse each of the particle images and how they are classified. Section 3 presents the results of a detailed study of the volume averaged proportion of water to ice in clouds and compares them with two UK Meteorological Office numerical model parametrisations of cloud glaciation currently in use. Finally, in section 4 the results and limitations of this technique are discussed along with some suggestions for improved model parametrisations.

2 TECHNIQUE

A technique has been developed to process the data from the 2D cloud probes to automatically classify the particle phase and type. It is very similar to a technique described by Duroure (1982) and uses the same basic principles. There are three main stages:

(i) Transforming the image information from a cartesian to a radial representation.

(ii) Computing the Fourier transform of the image radius.

(iii) Categorising the particle.

These stages are described below.

2.1 Radial Representation Of The Image

The PMS probes represent the image of a cloud particle as a series of grid points in cartesian coordinates, with the x-axis corresponding to the across beam direction and the y-axis corresponding to the along beam direction. As most ice particles have some form of outline periodicity a more convenient way of representing the image is in polar coordinates, with the centre of gravity as the origin. This is done by calculating the distance from the centre of gravity to the edge of the particle's shadow in 64 directions equally spaced between 0 and 2π radians. The centre of gravity is found by summing the x and y pixel components (the across beam distances and along beam distances) of all the shaded diodes which represent the image. The coordinates of the centre of gravity are then given by:

$$\left(\frac{\sum x}{C}, \frac{\sum y}{C}\right)$$

where C is the cross sectional area of the image. If the centre of gravity is found to lie outside the shaded area of the image the particle is rejected because radial analysis of the image would not be practical. In this new representation of the image all the data required are reduced to the 64 radii. Figures 1(a)-(c) show an example of an ice particle detected by the 2DC and its radial representation.

2.2 Fourier Analysis

Once the entire outline is known, fourier analysis can be carried out on the set of 64 radii. The radius is then represented in the following form,

$$R(\alpha) = \frac{A_0}{2} + \sum_{k=1}^{32} A_k \sin k\alpha + B_k \cos k\alpha \qquad (1)$$

where $R(\alpha)$ represents the radius for a given angle α and A_k and B_k are the fourier components. The zeroth wave number, A_0, is a constant term related to the mean value of the particle's radius. The amplitudes of the the first 32 wave numbers, normalised with respect to the mean radius ($\overline{R}$) are calculated using equation 2.

$$Amp_k = \frac{\sqrt{A_k^2 + B_k^2}}{\overline{R}} \qquad (2)$$

The amplitudes are normalised so that particle size does not have any effect on the magnitude of the amplitude spectra so the difference between spectra of different particles are due entirely to their different outline periodicities and not to their size. Figure 1(d) shows the fourier analysis of a typical stellar shaped ice crystal.

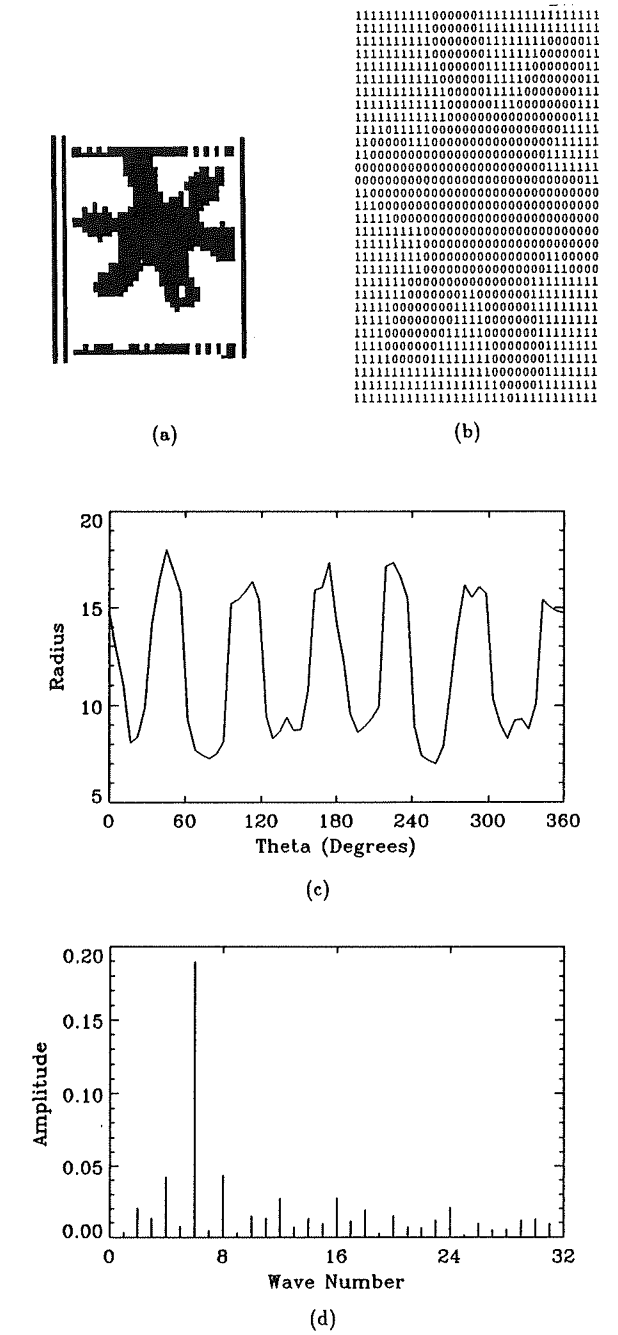

Figure 1: Example of an ice crystal image; (a) 2D probe output, (b) image after initial processing (filling spurious gaps etc.), (c) plot of radius vs angle for the image and (d) amplitude spectra for the image.

2.3 Shape Classification

The wave number spectrum obtained is then used to determine the shape of the particle. The automatic technique defines seven cloud particle categories:

(i) Water Droplets,

(ii) Graupel. This covers all rounded ice particles so may also include melting ice particles or heavily rimed ice particles,

(iii) Columns. This includes all columns and needles,

(iv) Stellar crystals,

(v) Symmetric particles. This includes all particles apart from stars and columns which display some form of periodicity in their outline. These are most commonly bullet rosettes,

(vi) Aggregates. This covers all ice particles which do not fall into any of the other six categories,

(vii) Small ice. These are particles which are large enough to be classified as ice but too small for their habit to be determined. Ice particles are classified as 'small' if they are represented by fewer than 50 pixels.

The images are classified according to the standard deviation of their radii and the magnitude and standard deviation of their fourier wave numbers as shown in table 1 and the classification criteria are applied in the order indicated in the table.

SHAPE	CRITERIA
Droplet	$A_s < 0.12$
Large Droplet	$S_r < 1.0, S_a < 0.01016, A_s < 0.2$
Small Droplet	$S_r < 0.5, S_a < 0.01016, A_s < 0.3$
Small Ice	Area < 50 pixels
Graupel	$A_s < 0.4$
Column	$A_2/A_s > 0.28$
Stellar	$A_6/A_s > 0.1$
Symmetric	$A_n > 0.15$
Aggregate	Anything else

S_r standard deviation of the radii, S_a standard deviation of the amplitudes of the wave numbers, A_s sum of the amplitudes of the wave numbers, A_2 amplitude of the second wave number, A_6 amplitude of the sixth wave number, A_n any wave number amplitude except A_2 or A_6.

Table 1: The criteria used to classify images.

One limitation of the automatic technique is the program execution time. On average the program (run on a VAX 3100) processes approximately 35 particles per second, positively identifying 8 (23%) per second. This means that in order to build up a statistically representative sample the execution time will be long for cloud with a high concentration of cloud particles.

2.3.1 Rejected Particles

It is not possible to process all imaged particles by this technique. The size of the sampling volume is limited by the optical separation and number of the diodes on the 2D probes. Particles which overlap one side of the array can be reconstructed if their centre of gravity can be found; assuming they have some degree of symmetry. However, particles which overlap both sides of the sampling volume cannot be reconstructed and are rejected. Very small particles are poorly imaged by the 2D probes as they are represented by very few points. This makes the classification of small images very difficult so all particles with a diameter of less than $150\mu m$ (2DC) or $1200\mu m$ (2DP) are rejected. The total number of rejected particles usually accounts for approximately 77% of any sample.

2.4 Calculating Ice To Water Mass Ratios.

In order to determine the mass ratio of ice to water in a mixed phase cloud, it is necessary to estimate the mass of ice crystals of a particular size. As the probes produce only a two dimensional image of the particle, this estimate has to be made from either the cross-sectional area or diameter of the image. The relationship between mass and size of the particle will in general be a function of the particle type due to differences in the bulk density of different crystal habits. Cunningham (1978) gives a set of empirical functions relating the cross-sectional area C of a 2D image, to the diameter of a water drop of equivalent mass, D. These relationships are all of the form

$$D = aC^b \tag{3}$$

where the values of a and b are given for different particle types in table 2.

SHAPE	SIZE	a	b
Droplets		1.13	0.50
Columns	C≤ 0.16	0.42	0.35
	C> 0.16	0.52	0.46
Stars	C≤ 1.07	0.39	0.31
	C> 1.07	0.38	0.48
Aggregates		0.39	0.31
Graupel	C≤ 0.04	1.00	0.50
	0.04< C ≤ 0.32	0.51	0.29
	C> 0.32	0.64	0.5
Small Ice		1.13	0.50

Table 2: Table of constants a and b for the calculation of the equivalent diameter D.

3 RESULTS

The automatic technique has been used to analyse eleven flights carried out in the MRF C-130 around the British Isles with the aim of validating and improving parametrisations of the ratio of the mass of water to ice in various numerical models. The data has been averaged over 2 minute horizontal runs in cloud. The temperature measurements during this period were taken from either the deiced Rosemount thermometer or, when fitted, the in-cloud temperature probe. Cloud top temperature measurements were made with the Barnes PRT-4 radiometer when fitted, otherwise the cloud top temperature was determined from the deiced Rosemount thermometer measurements taken during a profile through the cloud top. The flights represent a range of meteorological conditions and several different cloud types. Table 3 gives details of the flights analysed.

FLIGHT	DATE	CLOUD	AIR MASS
A089	23/05/91	As	Continental
A071	28/02/91	Sc & Ci	Continental
A049	06/12/90	Sc	Maritime
A063	30/01/91	St / Sc	Continental
A053	18/12/90	Sc	Continental
H999	10/04/90	Sc	Maritime
H963	14/12/89	Ns	Continental
H961	11/12/89	Sc / Cu	Continental
H960	08/12/89	Cu	Maritime
H959	07/12/89	Sc	Maritime
H933	18/09/89	Ci / Ac	Continental

Table 3: Summary the flights analysed.

Comparisons with the following numerical model parametrisations have been made:

(a) the parametrisation used in the UK Meteorological Office Atmospheric General Circulation Model (UKMO AGCM) (Smith, 1990).

(b) the parametrisation used in the UKMO Mesoscale Model (Golding, 1990)

3.1 UKMO General Circulation Model

The UKMO AGCM parametrisation relates the proportion of water to ice in a cloud to the ambient air temperature. Above 0^oC all cloud water is assumed to be liquid and below -15^oC all frozen. Between 0^oC and -15^oC the proportion of liquid water, f_l, is assumed to be given by the following quadratic spline.

$$f_l = \begin{cases} \frac{1}{6}\left(\frac{(T+15)}{5}\right)^2 & \text{for } -15^oC < T < -5^oC \\ 1-\frac{1}{3}\left(\frac{T}{5}\right)^2 & \text{for } -5^oC \le T < 0^oC \end{cases} \tag{4}$$

Figure 2 shows how the measured proportion of water varies with the ambient air temperature, and compares the results with the UKMO AGCM parametrisation. The agreement is relatively good, with the line of best fit through the aircraft results having a similar gradient to the partitioning curve from the AGCM. The results suggest, however, that the model partitioning curve is approximately $+2.5^oC$ colder than that measured. This implies that the parametrisation currently overestimates the proportion of water in a cloud at a given temperature. However, the model parametrisation lies within the scatter of the data points where the proportion of water calculated is less than 70%, and the scatter of the data points increases as the proportion of water decreases. The data points in figure 2 have also been split up to show how the ice/water ratio varies in clouds considered to be in continental and maritime airmasses. Best line fits (not shown) through these two sets of data points indicate that maritime air masses tend to have larger proportions of ice at higher temperatures.

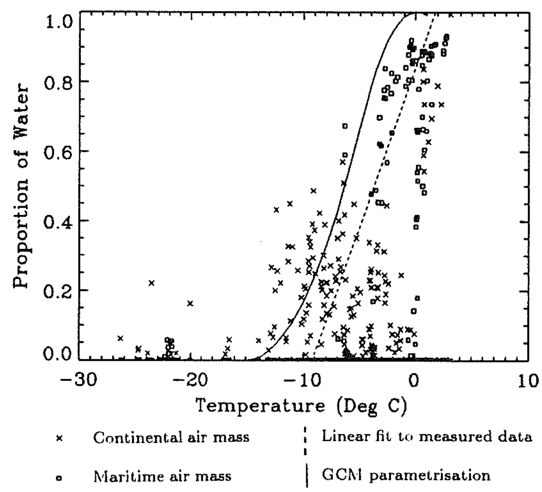

Figure 2: Plot of proportion of water vs ambient temperature for measured data and the GCM parametrisation.

3.2 UKMO Mesoscale Model

In the mesoscale model the phase of water in a cloud is determined by the cloud top temperature. Supercooled water cloud can deepen until it reaches the -15^oC level when it is assumed to glaciate fully down to a hundred metres below the freezing level. Figure 3 shows the aircraft results for the proportion of ice to water in a cloud as a function of cloud top temperature. Each point is the mean of measurements at all levels within a cloud having the indicated cloud top temperature.

The results obtained for the proportion of ice as a function of cloud top temperature do not compare well with the parametrisation used in the mesoscale model. From the graph in figure 3 there does not appear to be a simple relationship between the cloud top temperature and the proportion of water present in the cloud for the 11 flights which have been analysed.

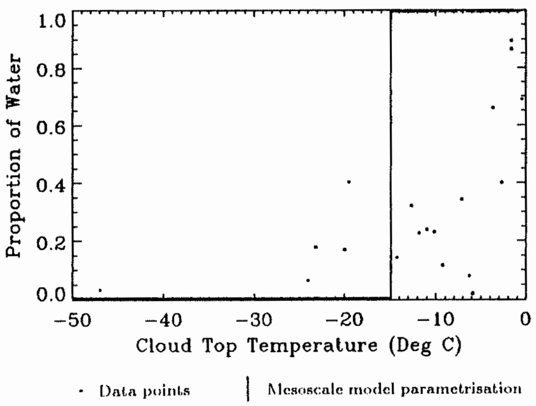

Figure 3: Plot of proportion of water vs cloud top temperature for measured data and the mesoscale model parametrisation.

4 DISCUSSION

Intuitively it was thought that as the parametrisation for the ratio of ice to water in a cloud parcel in the UKMO mesoscale model was based on reasonably sound physical considerations and that the UKMO AGCM parametrisation had no firm theoretical basis and was used purely for mathematical convenience (Smith 1990), the validation of the mesoscale model parametrisation would have proved more successful. However, the results of the analysis from several flights in a large variety of cloud types, averaged over tens of kilometres suggest that a parametrisation based on ambient temperature (as in the UKMO AGCM) is far better at diagnosing the ice to water ratio of a cloud than a parametrisation using cloud top temperature.

A best line fit to all of the data points gives a relationship for the proportion of water in a cloud parcel, f_l, as a function of temperature, T (in degrees C), as shown in equation 5

$$f_l = 0.095T + 0.860 \tag{5}$$

From equation 5, $f_l = 1$ when $T \approx +1.5^oC$. This implies that ice is present at temperatures above 0^oC. This is physically realistic in a cloud with a cloud base temperature above 0^oC as ice particles would have to fall several hundred metres below the freezing level before completely melting. The equation also implies that the proportion of water is zero at temperatures lower than -9^oC.

A major problem with the automatic technique is that the majority of particles are being rejected. Generally this is due to one of two reasons;

a) the particles are too small to be categorised or
b) the particles are poorly positioned in the laser beam and are overlapping the sides of the sampling volume.

In some cases these particles can be classified by eye but to carry out a quantitative, automatic analysis would require more sophisticated software and large amounts of computer time and the extensive time required to develop this would produce a disproportionate gain in information as the limitation on minimum droplet size would still exist. At present the time needed to produce such an improvement has not been deemed justified.

The biggest limitation of the automatic technique is the cut off size at which particle classification can occur. The smallest particle the probes can resolve is $25\mu m$, but because of digitisation problems this classification technique can only start to categorise particles larger than $150\mu m$. Thus we are only estimating the ice to water ratio of the larger particles in the cloud and are assuming the contribution to this ratio from smaller particles can be ignored, which on occasions may be a significant error. There is no indication that the characteristics of the particles should be the same for different sized particles, so the results obtained by this method can not be taken to represent the whole sample of cloud particles in a parcel of air. Further work using different instrumentation to find the contribution from smaller sized particles is to be carried out in the future.

References

Cunningham, R.M. 1978. Analysis of particle spectral data from optical array (PMS) 1D and 2D sensors. In *Preprint Vol, IV Symp. Met. Obs. and Instr., Amer. Meteor. Soc., Denver,* pages 345-349.

Duroure, C. 1982. Une nouvelle methode de traitement des images d'hydrometeores données par les sondes bidomensionnelles. *J. Rech. Atmos.* **16**, 71-84.

Golding, B.W. 1990. The Meteorological Office mesoscale model. *The Meteorological Magazine,* **119**, 81-96.

Hallett, J., R.I.Sax, D.Lamb and A.S.R.Murty. 1978. Aircraft measurements of ice in Florida cumuli. *Q.J.R. Meteorol. Soc.,* **104**, 631-651.

Hobbs, P.V. 1969. Ice multiplication in clouds. *J. Atmos. Sci.,* **26**, 315-318.

Hobbs, P.V. and A.L.Rangno. 1985. Ice particle concentrations in clouds. *J. Atmos. Sci.,* **42**, 2523-2549.

Smith, R.N.B. 1990. A scheme for predicting clouds and their water content in a general circulation model. *Q.J.R. Meteorol. Soc.,* **16**, 435-460.

Stewart, J.B. 1967. A preliminary study of the occurrence of ice crystals in layer clouds. *The Meteorological Magazine,* **96**, 23-27.

DEUTERIUM IN NORTH ATLANTIC STORM TOPS

Ronald B. Smith

Department of Geology and Geophysics
Yale University
New Haven, CT 06511

While it is clear that clouds must play a dominant role in providing water to the upper troposphere, the details of this process is uncertain. In particular, it is not known whether it is the water vapor or the condensed water carried upwards in clouds that dominates the vertical transport. In this paper, three observational techniques are used to approach this problem: isotope analysis of collected ice, in situ microphysical measurements, digital satellite imagery.

During the ERICA project in 1989, ice crystals were collected from the tops of two winter storms over the northwestern part of the North Atlantic. The following steps were taken to determine whether the ice crystals: had fallen from above, formed from vapor in situ, or been lifted by updrafts to the collection location. First, under the pseudo-adiabatic assumption, the cloud top parcels original thermodynamic state at sea level is determined. (Gedzelman, 1988). The resulting temperature generally agreed with sea surface temperature. Second, the ideal Rayleigh fractionation process is modelled using a laboratory-derived fractionation factor. This calculation predicts the deuterium to hydrogen ratio (or δD) for ice as a function of the height or the temperature where the ice was formed from vapor. Finally, by comparing the two δD values, the vertical fall or lofting of the ice can be determined. The uncertainties and assumptions in this analysis are discussed in Smith (1992).

The isotope results from the second of the two storms (Jan. 23, 1989) are shown in Fig 1. Ice samples ,7, 8 and 9 have δD values which lie beneath (or to the left of) the theoretical ice curve indicating that the ice had fallen to the point of collection. Samples 5 and 6 fall on the theoretical curve indicating that on the average, collected ice was formed in situ. If this trend continues aloft, we could argue that the upper kilometer or two of the cloud was composed of lofted ice.

These and other arguments and measurements lead to the following conclusions (Smith 1992).

1) Due to the agreement between observed and predicted δD values near cloud top on Jan. 21 (not shown), we conclude that the isotope fraction process in winter storms may be nearly ideal. The low δD values (i.e., δD ≈ -450) could not be obtained if continued exchange with lofted condensate or non-equilibrium vapor deposition were occurring (Jouzel and Merlivat, 1984).
2) Extrapolation of the data from Jan. 23 suggests the presence of lofted ice in the uppermost parts of the storm cloud. Furthermore, the large ratio of ice to vapor concentration suggests that lofted ice may dominate the vertical transport of water.
3) The good agreement between δD values in storm-top ice and earlier measurements of δD in clear-air vapor (Ehhalt 1972) indicates that the former is the source of the latter.
4) Satellite images, in the infra-red window, underestimate the cloud top altitude by one or two kilometers and thus fail to see the layer of lofted ice which is supplying water to the upper troposphere.

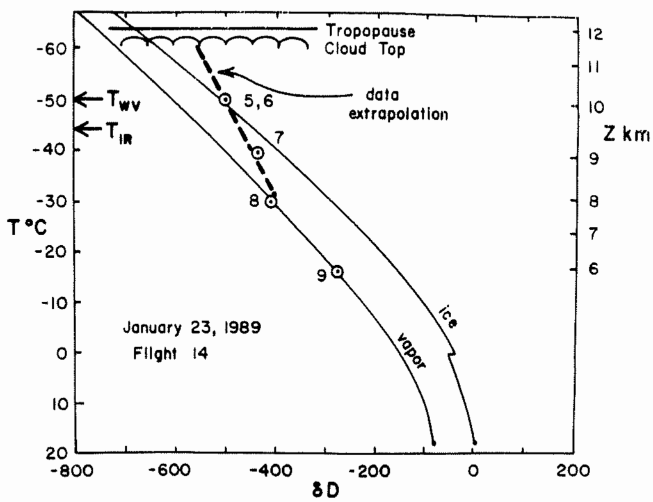

Fig. 1 Isotope ratio (δD) in five collected ice samples plotted against air temperature (or altitude) within a comma cloud system southeast of Cape Cod on January 23, 1989. Solid lines represent an ideal Rayleigh fractionation process. The actual tropopause and cloud top are shown. The cloud tops derived from GOES IR and WV pixel brightness temperature are also indicated.

References

Ehhalt, D.H., 1974: Vertical profiles of HTO, HDO, and H_2O in the troposphere. NCAR Technical Note NCAR/TN/STR-100, Boulder, Colorado.

Gedzelman, S.D., 1988: Deuterium in water vapor above the atmospheric boundary layer. Tellus 40B, pp. 134-147.

Jouzel, J. and L. Merlivat, 1984: Deuterium and oxygen 18 in precipitation: Modeling of the isotopic effects during snow formation. J. Geophys. Res. 89-D7, pp. 11,749-11,757.

Smith, R.B., 1992: Deuterium in North Atlantic Storm Tops. J. Atmos. Sci., in press.

EVOLUTION OF PRECIPITATION SPECTRA IN A DEVELOPING CONVECTIVE CLOUD

J. Hallett and W. Hendricks
Desert Research Institute, Atmospheric Sciences Center
Reno, Nevada 89506-0220, USA

and

P. Willis
Hurricane Research Division, NOAA/AOML
Miami, Florida 33149

1. INTRODUCTION

The evolution of cloud droplet and ultimately precipitation spectra in any convective cloud results from an interplay of CCN activation - either at cloud base or within a more turbulent cloud, mixing in environmental aerosol, and at lower temperatures by primary and secondary ice production, and the subsequent accretion processes. Specifically, secondary ice production by riming relates to the drop size distribution between the -4 to -10°C level; production of larger droplets with ice nucleation and ice fragmentation relates to entity mixing with dry air near cloud top. All processes are critical to producing ice particle and cloud spectra which gives a favorable environment for charge separation by particle collision and bounce off and by evaporation, Jayaratne et al 1982, Dong and Hallett, 1992. In convective clouds, the simplest picture gives a strong upshear updraft, near adiabatic liquid water content (LWC) on the very sharp upshear edge prior to erosion, well below adiabatic LWC down shear, with droplet and ice evolution subject to the slowly varying conditions of the core and turbulent mixing of the upper part of this core and the downstream wake. These considerations predicate specific measurement and analytical protocols for examining the behavior of particles in convective clouds, to relate particulates to regions of shear and mixing, and particularly to examine nucleation and subsequent particle grow transport.

2. OBSERVATION PROTOCOL

The measurements reported here were taken during aircraft penetrations of convective clouds near Kennedy Space Center during the CAPE project (Sunday 11 August, 1991) on the NOAA P3 Orion at a few degrees below the 0°C level.

The data are obtained from three penetrations at approximately the same level; first of a broad deeper convective cloud, at 1909z and second of two sequential penetrations of a new upwind developing cloud some 30 minutes later 1931 and 1936z. Details of the first penetration of (Radar top to 10 km) are discussed in the companion paper (Willis et al 1992)

The vertical continuity and magnitude of updraft is under study as is the stage at which coalescence produced raindrops become significant with respect to the level of secondary ice generation by rime splintering (-4 to -8°C depending on liquid water content); here the existence of large concentrations ($1\ l^{-1}$) of supercooled raindrops has the potential of giving a very rapid transition to ice by the hydrodynamic capture of secondary produced ice and an approximate exponential rate of conversion (Lamb, Sax and Hallett, 1982). Aircraft flight protocols may follow up the cloud top (Willis and Hallett, 1991) or sequentially penetrate near a given level which are presented here; results from a climb profile are being analyzed.

3. RESULTS

Penetrations are analyzed from the viewpoint of the relationship between vertical velocity, liquid water content (King probe), ice particles 100 to few 1000 μm, raindrops, ½ to several mm, [2 DC 2 DP] electric field (vertical component). The presence of supercooled raindrops is confirmed from canted and distorted images of the drops as they pass through the shear flow field of the 2DC probe. This is confirmed by cartwheel splash patterns of such drops on the replica. The large values of liquid water content measured by the King probe are spot checked by summation of droplets on the replica (some coalescence on the replica occurs at high LWC which precludes measurement of spectra under these conditions). FSSP gives spectra, but because of reduced activity at high penetration speed of the P3 gives an unrealistic value of LWC although relative values of droplets except in the smallest bins are preserved. Temperature measurements are by deiced Rosemont sensor. It is noted that pass 2 gives a significant temperature excess (consistent with a top hat profile of other quantities). Sensor heating by freezing of supercooled drops cannot be excluded but the fall

Fig. 1: Flight track for the 3 clouds.

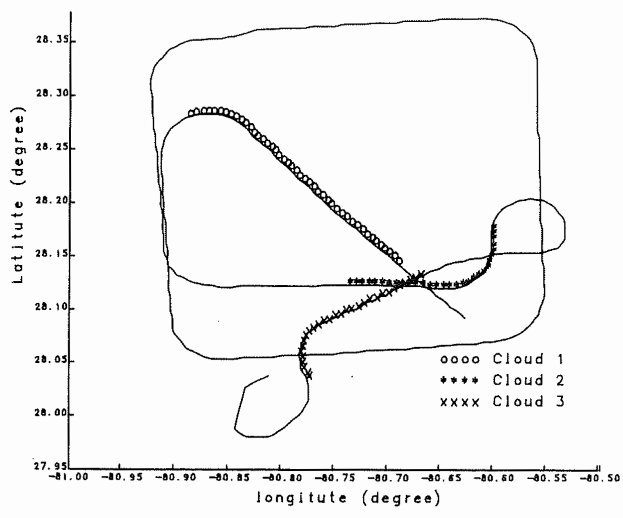

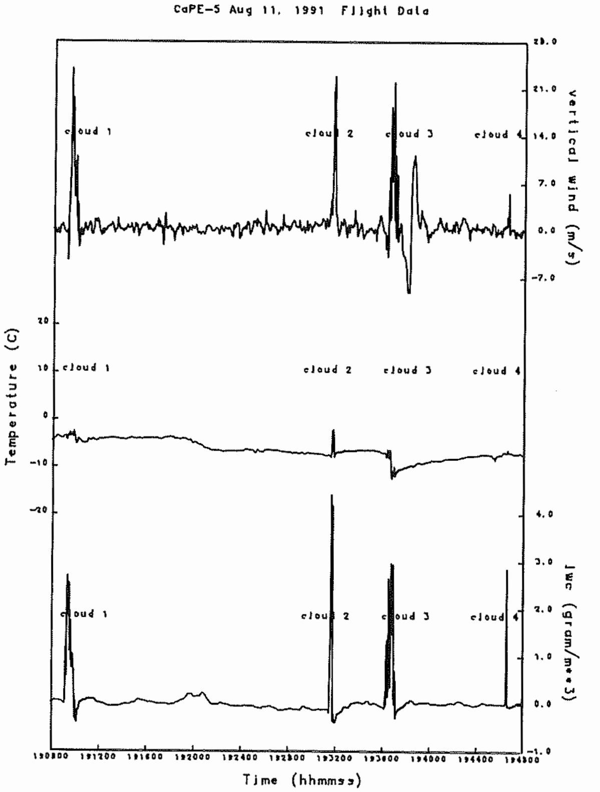

Fig. 2: Temperature, vertical wind, and King liquid water content in the 3 clouds.

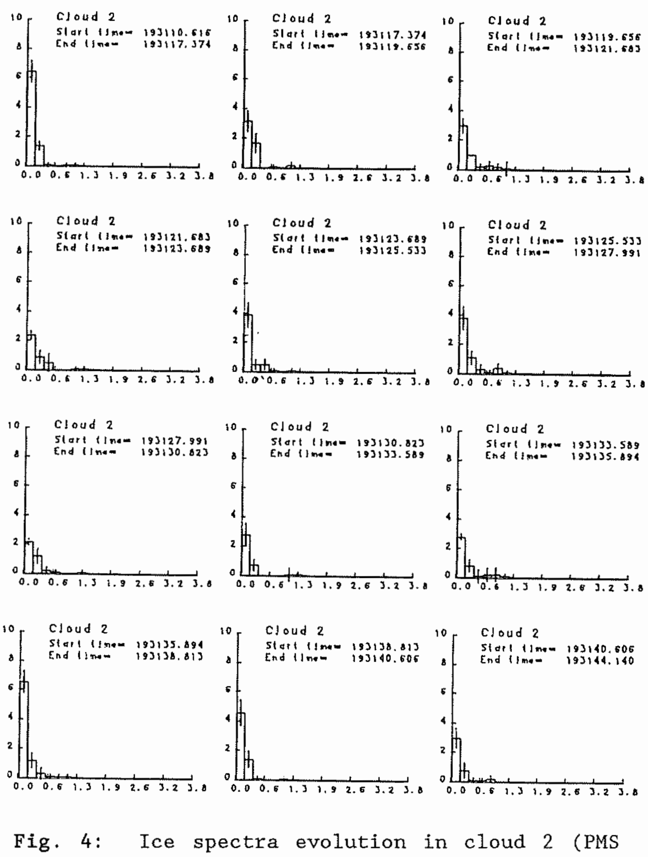

Fig. 4: Ice spectra evolution in cloud 2 (PMS precipitation probe).

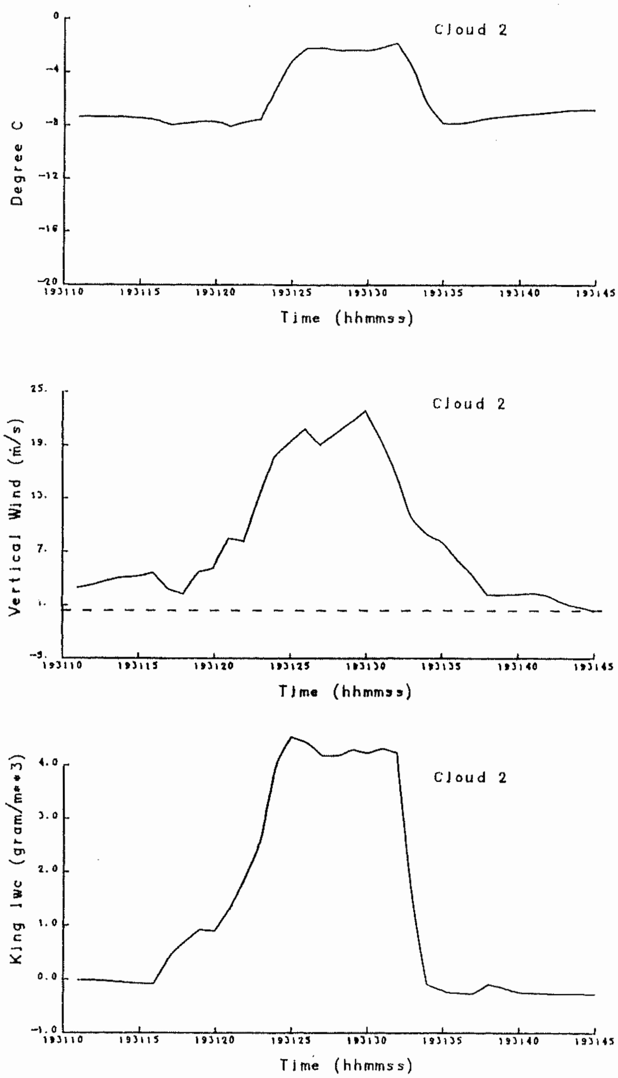

Fig. 3: Temperature, vertical wind and King liquid water content in cloud 2.

off of temperature on cloud exit points to a real value - ice on the probe would be subject to evaporation and cooling to ice bulb temperature which does not happen. Vertical electric field from two shutter type mills, with aircraft charge.

Figures 1 and 2 show the aircraft track LWC profiles for all three clouds. Note that the deep cloud was penetrated from the south east (upshear) with aircraft exit beneath the anvil aloft. Cloud 2 was penetrated in reverse, cloud 3 from upshear, but the exit was offset to the south from the anvil aloft. Figure 3 shows temperature, vertical velocity and LWC profiles through clouds 2. Note the top hat profiles of all three parameters. Ice is completely absent (< 1/101) large rain drops are absent, with maximum size about 100 μm (Fig. 4). Note the relative uniformity of drop distribution through the pass (Figs. 5). Figs. 6, 7 and 8 are the same for cloud 3.

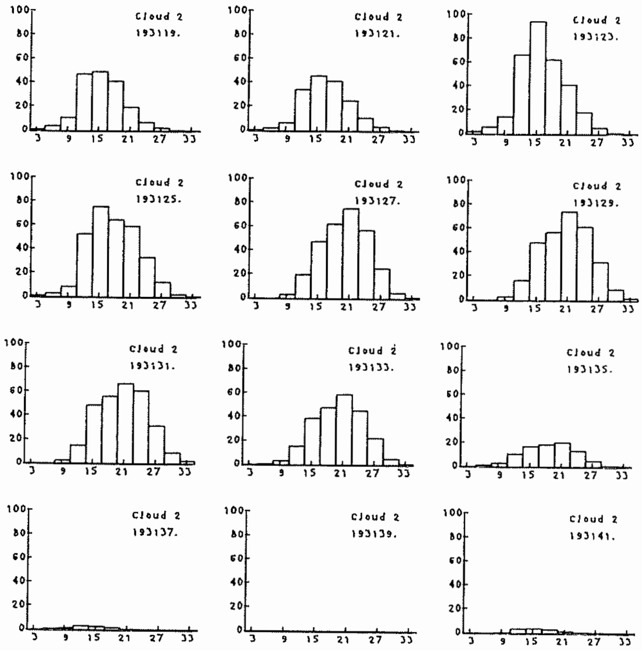

Fig. 5: Evolution of FSSP cloud droplet spectra over cloud 2.

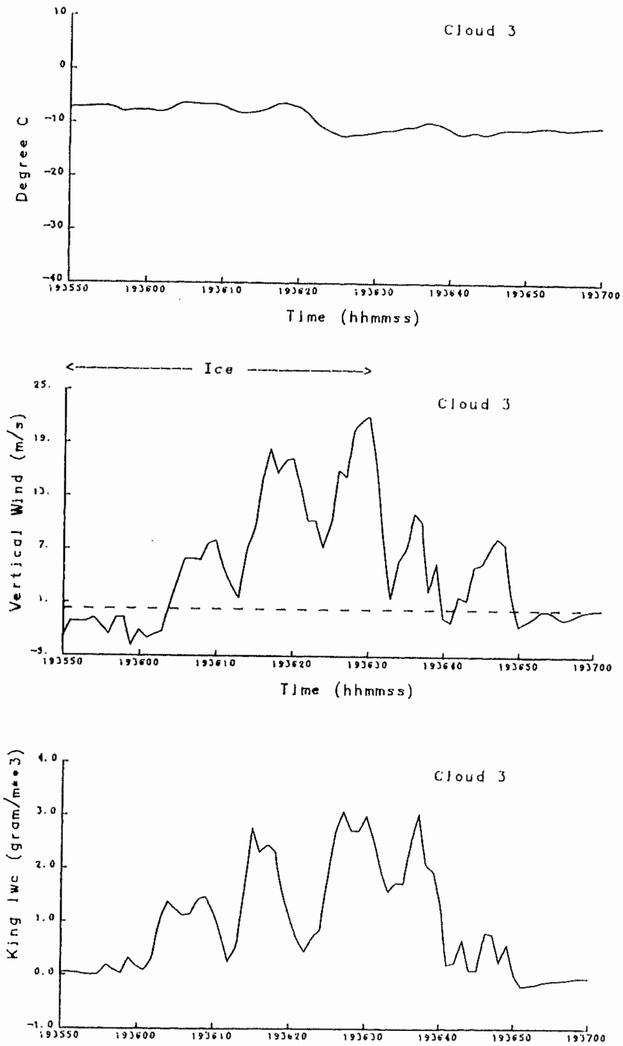

Fig. 6: Temperature, vertical wind and King liquid water content in cloud 3.

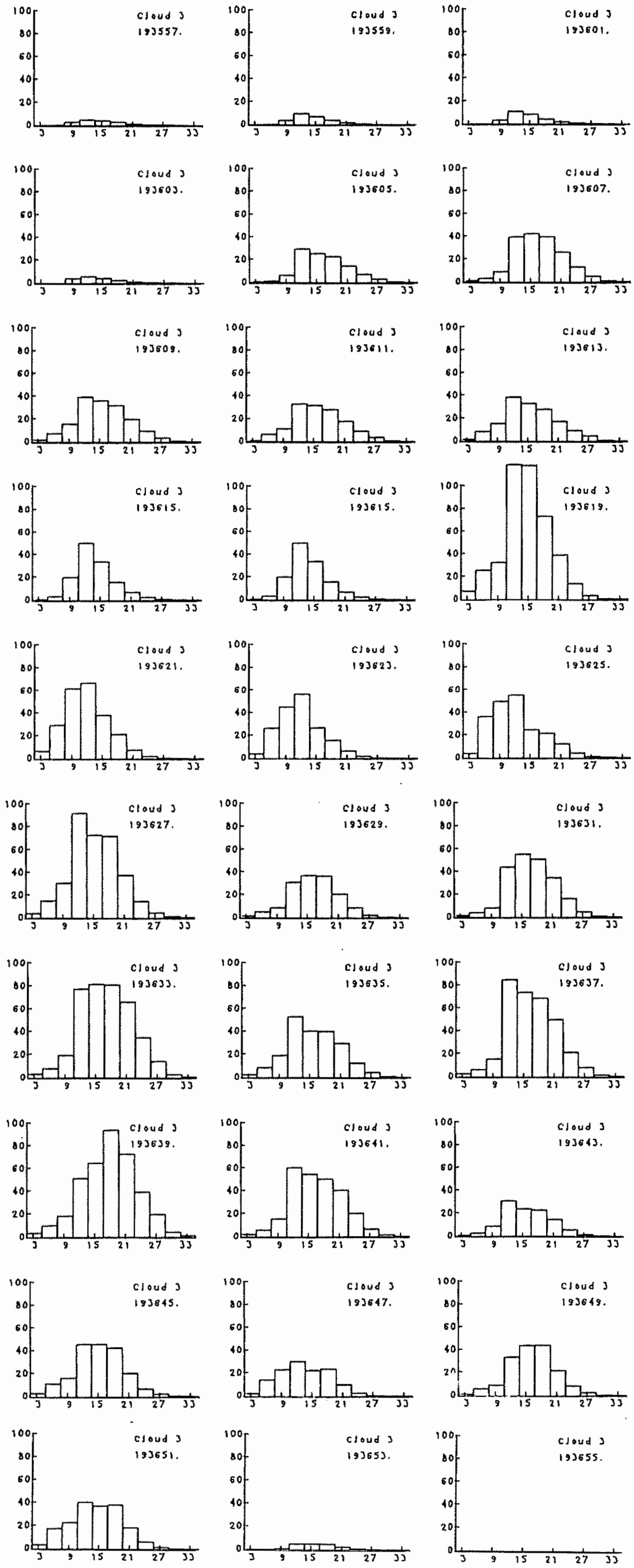

Fig. 7: Evolution of FSSP cloud droplet spectra over cloud 3.

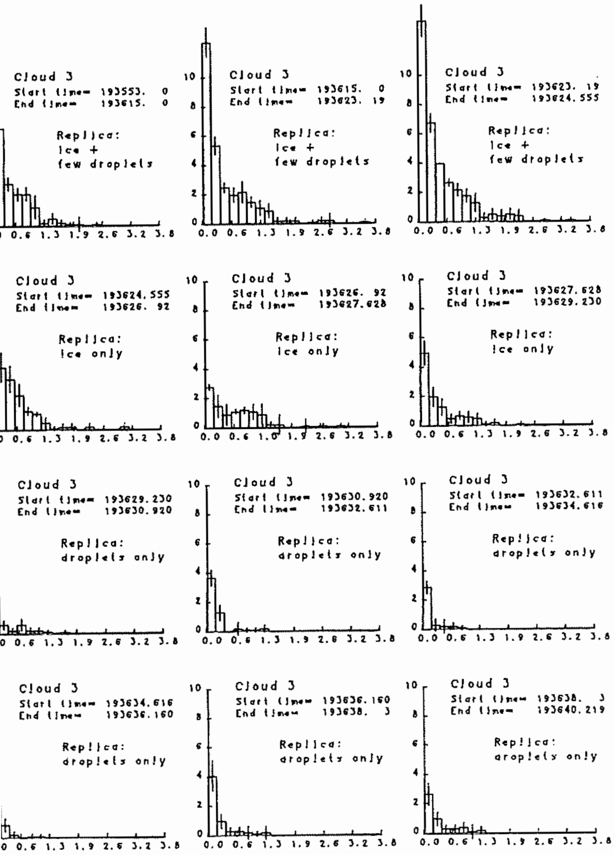

Fig. 8: Ice spectra evolution in cloud 3.

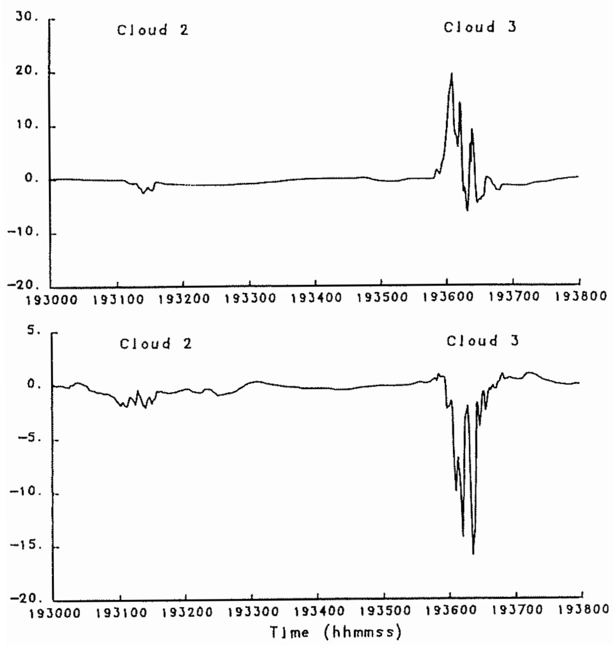

ig. 9: Aircraft change from vertical field mill; ertical component of electric field in cloud and 3.

Five minutes later the picture is completely hanged (Cloud 3). Raindrops and ice particles soft hail, some columns) are present (Fig. 8); igh LWC is associated with the peaks of the updraft, ice with weak updrafts (note the absence of downdrafts). No significant electric field (or aircraft change) is associated with cloud 2 (Fig. 9); substantial electric field has developed by pass 3 over a 5 minute period. It is noted that the characteristics of cloud 3 are similar to cloud 1, which may therefore be in a comparable state of development.

4. CONCLUSIONS

The most significant result from these observation lies in the comparison of the structure of cloud 2 compared with the later penetration (Cloud 3). A dramatic change in structure at this level took place in 5 minutes, with the development of raindrops, graupel, a broken updraft structure scale some ½ to 1 km, and significant electrical effects. Significant precipitation was not exiting the cloud at this time. There is an association of high LWC with stronger updrafts (>10 m s^{-1}). The question of major importance is the transition rate process as and where in the cloud rain occurred first, and whether it preceded ice formation as earlier studies suggest. What is clear is that these are substantial updrafts, with LWC > 4g m^{-3} which with no rain, ice or electrification, and with an apparent environmental excess temperature of about 5°C. Future analysis will concentrate on the transition process itself and the rate of change of hydrometer spectrum and electric field, in relation to the detail of the vertical velocity as the cloud grows.

ACKNOWLEDGMENT

This research was supported by a Grant #ATM-9021918 to J. H. from Meteorology Program, National Science Foundation, Washington, D.C. Aircraft participation was supported through National Oceanic and Atmospheric Administration-Hurricane Research Division, Miami, Florida.

5. REFERENCES

Dong, Y.Y. and J. Hallett, 1992: Charge Separation by Ice and Water Drops During Growth and Evaporation. **Submitted for publication.**

Hallett, J., R.I. Sax, D. Lamb and A.S.R. Murty, 1978: Aircraft measurements of ice in Florida cumuli. Q.J.R. Meteorol. Soc., 104, 631-651.

Lamb, D., J. Hallett and R.I. Sax, 1981: Mechanistic limitations to the release of latent heat during the natural and artificial glaciation of deep convective clouds. Q.J.R. Meteorol. Soc., 107, 935-954.

Willis, P.R., J. Hallett and R. Black, 1992: Cloud and Hydrometeor Microphysics at -3°C in a vigorous Florida convective draft. 11th International Conference on Clouds and Precipitation, Montreal, Canada, August 17-21, 1992.

Willis, P.R., J. Hallett, 1991: Microphysical Measurements from an Aircraft Ascending with a Growing Isolated Maritime Cumulus Tower. J. of Atmos. Sci., 48, 283-300.

Precipitation Particles in Winter Monsoon Band Clouds over the Japan Sea

Y. Asuma and K. Kikuchi
Department of Geophysics, Faculty of Science,
Hokkaido University, Sapporo 060, Japan

1. Introduction

As a part of the WCRP (World Climate Research Program), aircraft observations concerning the Western North-Pacific Cloud-Radiation Experiment were carried out in February, 1991 at off-shore Wakasa Bay, Japan. The synoptic situation when this observation was carried out was in an outbreak condition of a winter monsoon. It is well known that band clouds of cumulus and stratocumulus types often appear under such conditions. We carried out the simultaneous observations of the meteorological, cloud physical and radiative elements using two Cessna 404 (TITAN) aircrafts. This paper reports on the cloud physical properties, especially particle images in a band cloud of stratocumulus types obtained by a 2D-P Probe (Particle Measuring System, OAP-2D-GB2 GREY PROBE).

2. Observations

On February 17, 1991, one of the aircraft observations was carried out at off-shore Wakasa Bay, Japan. The synoptic situation was in a winter monsoon condition and band structured clouds were observed. According to the weather radar observations made by Fukui Local Meteorological Observatory, the echoes of band clouds enlarged from north to south. This direction was in parallel to the prevailing wind direction. Equipment on board is listed in Table 1. A 2D-P probe had a resolution of 50 μm. As the 2D-P probe has 64 photodiodes, it can measure directly 50 μm to 3.1 mm. Observed particles which were larger than 100 μm in diameter were analyzed. If the observed images of cloud particles were out of range, their sizes were estimated according to the method of Heymsfield and Parish (1978).

Table 1. Equipments on board.

2D-Probe (2D-P, PMS)
Temperature
Dewpoint Temperature
Pressure
Video Camera
Cloud Particle Video Image
Radiometer

Figure 1 shows typical examples of the images of precipitation particles obtained through the 2D-P probe. In this figure, each particle is divided with a vertical bar. The length of vertical bar indicates 3.2 mm in scale. Images of supercooled cloud droplets were identified as rings and small particles with solid interior were identified as ice particles. Furthermore, they were classified into types, such as unrimed dendrite, densely rimed dendrite, column, graupel particle, unrimed snowflake and densely rimed snowflake by their external shapes as shown in Fig. 1.

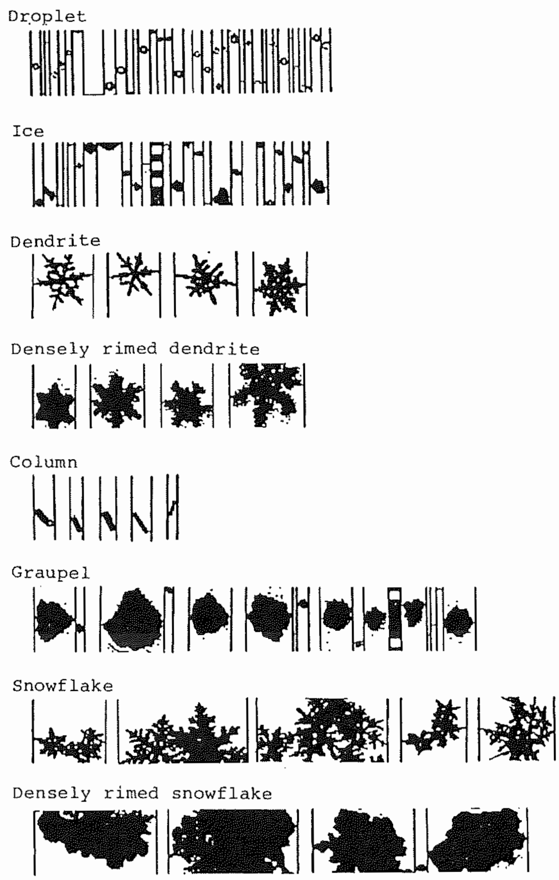

Fig. 1. Typical images observed by the 2D-P probe.

We analyzed data which were observed from 12:40 to 13:06 in detail. The observation area and flight track are shown in Fig. 2. Band shaped cumulus clouds were observed in this area and snow trails were recognized below these cloud bases. The aircraft passed across the band clouds and the data near the cloud base were obtained in detail. Pilots reported that cloud top height was 2.7 km (8000 ft) a.s.l. and cloud base height was 1.2 km (3700 ft) a.s.l., respectively.

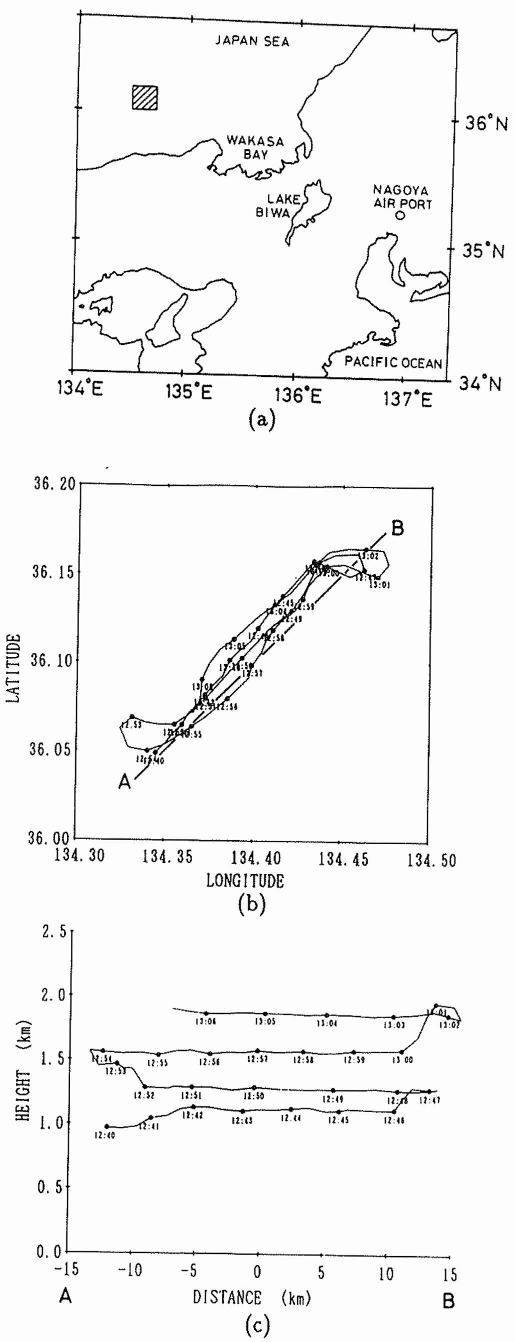

Fig. 2. Observation area (a) and flight track (b, c).

3. Results

The number concentration of precipitation particles observed by the 2D-P probe in the vertical cross section is shown in Fig. 3. In the Fig. 3, small numbers mean the times and large numbers mean the total numbers concentration per liter of precipitation particles. According to the aerological data at 850 mb level made by Wajima weather station, clouds moved leftward, that is, from northeast to southwest, in Fig. 3 at the speed of 10.0 ms^{-1}. It was found as shown in Fig. 3 that the high concentration of particles existed near the cloud base. And two cloud towers were recognized at the center of cloud, that is, two convective cells. Typical particle images which were observed along vertical lines named 'A', 'B' and 'C' are shown in Figs. 4, 5 and 6, respectively. As understood in the Fig. 3, the vertical line 'A' represents a vertical distribution of relatively low particle concentrations. On the other hand, the vertical lines of 'B' and 'C' represent those of high concentrations but in different cells. Vertical distributions of particle concentrations along line 'C' are higher than those in line 'B'. Dendrites and their aggregation were identified along line 'A' as shown in Fig. 4. Particles in 1.9 and 1.6 km in altitude showed lesser amounts of rimming than those in 1.3 and 1.1 km. Figure 5 shows that rimed dendrites were dominant in 1.9 and 1.6 km and in the lower levels of 1.3 and 1.1 km, graupel particles and small droplets dominated. Along the line 'C' as shown in Fig. 6, rimed and densely rimed dendrites were dominant in 1.6 and 1.9 km. And graupel particles and small droplets dominated in 1.3 and 1.1 km. Graupel particles and small droplets descended from the cloud base and they were observed as a snow trail. It was considered therefore that the graupel particles were formed in the lower part of the clouds. Vertical distributions of number density of graupel particles

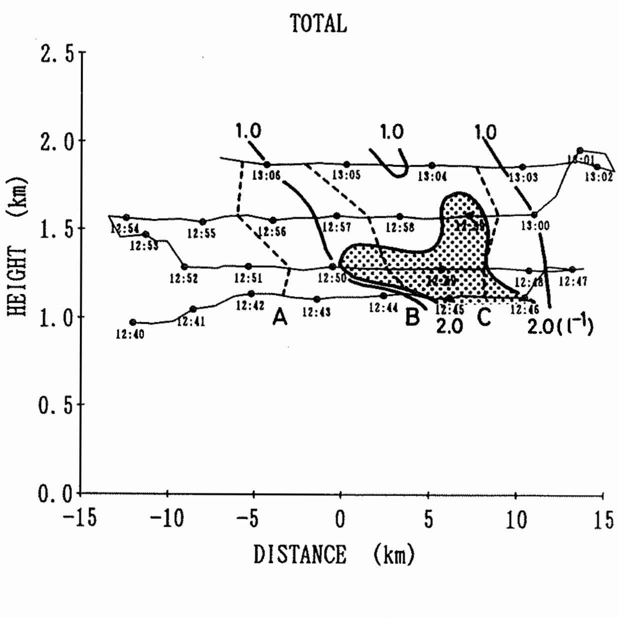

Fig. 3. Concentration distributions of particles observed by the 2D-P probe.

and small droplets are shown in Figs. 7 and 8, respectively. Supercooled cloud drops were observed in the lower part of cloud and there were recognized as two maxima of more than 1.0 l^{-1} in the concentration as shown in Fig. 7. Graupel particles were also observed in the lower part of the cloud as shown in Fig. 8. The predominant areas of spatial distribution of graupel particles in the cloud were consistent with those of supercooled drops. Thus, it is surmised that the graupel particles grew up rapidly in the lower part of the cloud by collecting an abundance of supercooled droplets.

Figure 9 shows that the schematic illustration which simplified the results observed by the 2D-P probe. Graupel particles and small droplets co-existed in the lower part of the cloud and the graupel particles grew there by collecting an abundance of drops. In the middle level of clouds, about 2 km in height, small snow particles were observed in the center and lesser concentration but large snow particles were observed in the edges of the cloud. In Fig. 9, arrows indicate an air flow which were inferred by the precipitation particles.

4. Concluding remarks

Aircraft observations were carried out on February 1991 at off-shore Wakasa Bay, Japan. The aircraft passed across the band clouds which were often observed in the winter monsoon condition. Graupel particles and a number of supercooled droplets were observed near the cloud base. It was surmised that the graupel particles rapidly grew up near the cloud base by collecting the small droplets. It is important to clarify the microphysical and dynamical properties in the band shaped clouds for understanding the mechanisms of the local heavy snowfalls along the west coast of northern Japan.

References

Heymsfield, A.J. and J.L. Parrish, 1978: A computational technique for increasing the effective sampling volume of the PMS two-dimensional particle size spectrometer. J. Appl. Meteor., 17, 1566-1572.

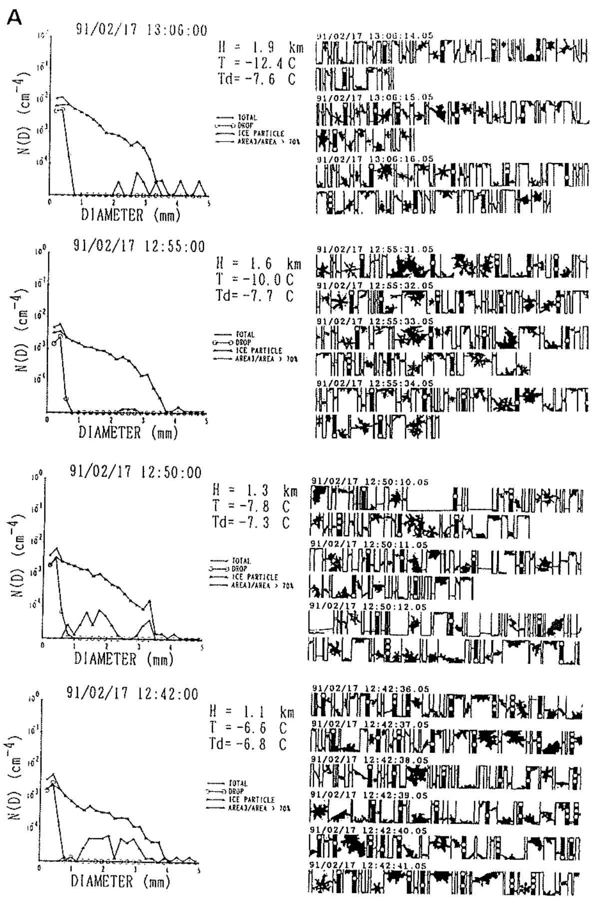

Fig. 4. Typical particle images observed along vertical line 'A' in Fig. 3.

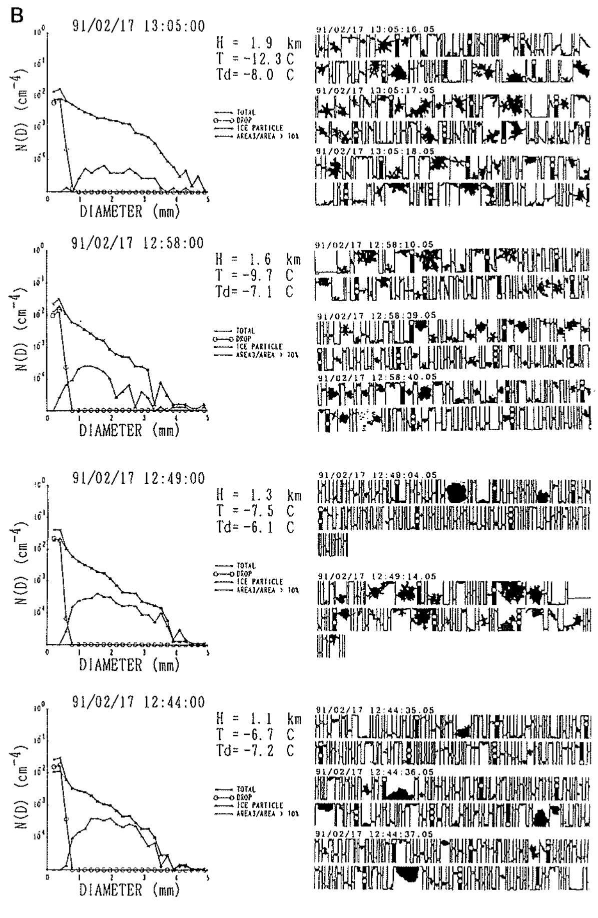

Fig. 5. Same as Fig. 4, but for 'B'.

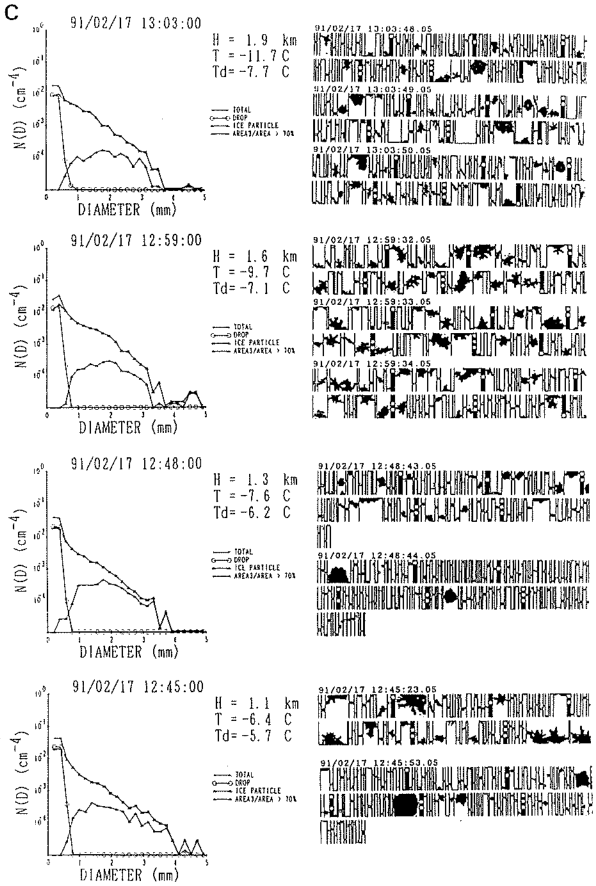

Fig. 6. Same as Fig. 4, but for 'C'.

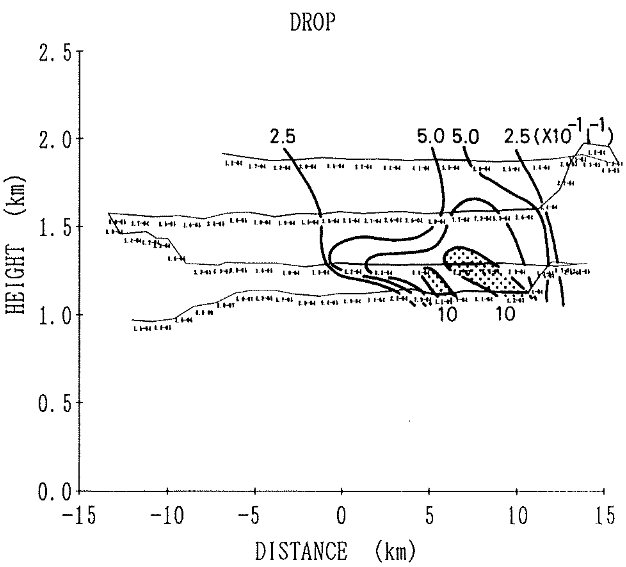

Fig. 7. Vertical distributions of small droplets.

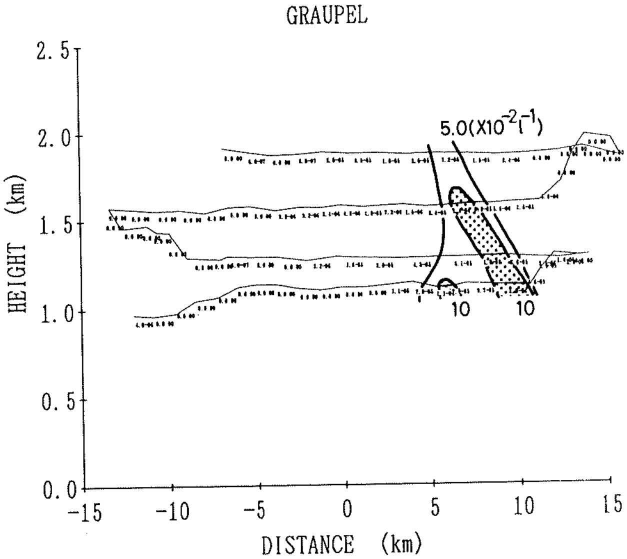

Fig. 8. Same as Fig. 7, but for graupel particles.

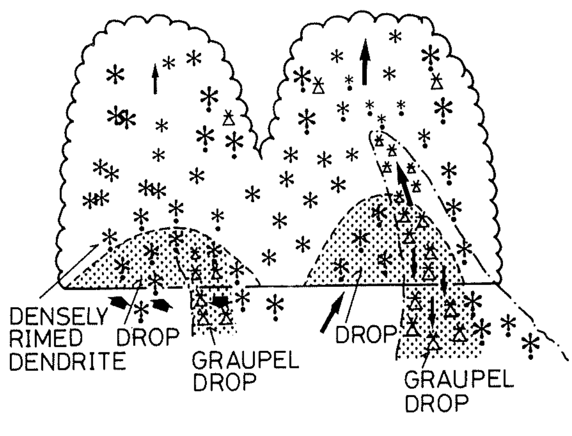

Fig. 9. A schematic illustration of observed cloud.

SUPERCOOLED LIQUID WATER IN COLORADO FRONT RANGE WINTER STORMS: MICROPHYSICAL STUDY OF THE 1990 VALENTINES DAY STORM

Roy M. Rasmussen, Masataka Murakami, Greg Stossmeister, Ben C. Bernstein

National Center for Atmospheric Research [1]
Boulder, Colorado 80307
and
Boba Stankov
Wave Propagation Laboratory, NOAA
Boulder, CO 80303

1. INTRODUCTION

A number of anticyclonic, upslope storms occurred during the 1990 Winter Icing and Storms Project (WISP). These storms were characterized by relatively warm cloud top temperatures (-15 to -10 C), and significant amounts of supercooled liquid water (up to 0.7 g m^{-3}). A particularly long-lived storm occurred during the period February 13 - 15, 1990. This storm produced sustained periods of liquid water during the first two days and snowbands the last day. In this paper we will present results on the microphysical structure of this storm, focussing primarily on the processes involved in the production and depletion of supercooled liquid water.

2. OBSERVATIONS

The WISP project deployed a number of instruments to document the storm environment, including Doppler radars (CP-3 and Mile High Radar), aircraft (University of Wyoming King Air and the University of North Dakota Citation), radiometers, mesonet stations (PAM and PROFS), and CLASS sounding systems. Additional data were obtained from wind profilers, NWS soundings and satellite. Figure 1 gives the locations of the various observation systems during WISP90.

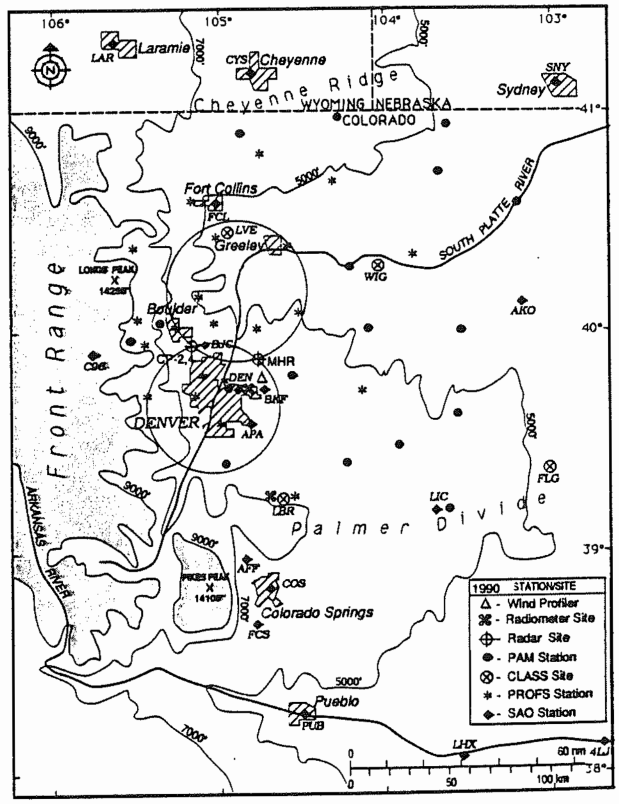

Fig. 1. WISP90 observational network. Solid lines are topographic contours every 2000 ft. Approximate dual-Doppler lobes for MHR and CP-3 are indicated.

On February 13, 1990 a shallow upslope cloud formed in the Colorado Front Range at 0900 UTC, 7 hours after the passage of a shallow cold front from the north. Analysis of the mesonet data shows that the initial cold front passage was followed by a number of secondary frontal passages also characterized by temperature drops and wind shifts. The first front passed over Flagler (FLG) at ~0420 UTC on Feb. 13, a secondary front passed at ~1400 UTC, and another surge of artic air occurred between 0000 and 0400 UTC on February 14. The primary front propagated into the Front Range from north-east to south-west at a speed of 10.8 m/s. When the front encountered the steeper terrain of the Palmer Divide, it slowed down to nearly 3 m/s. The secondary front also propagated from north-east to south-west, but was not able to make it over the Palmer-Divide. The front remained stalled on the northern slope of the Palmer-Divide from 1400, Feb. 13 - 0000 UTC, Feb. 14, at which point the third northerly surge passed through the region.

Cloud was first detected by the Denver radiometer at 0900 UTC on Feb. 13, 1990 and persisted for the next 30 hours. During this period, all three radiometers (Platteville, Denver, and Elbert) measured vertically integrated supercooled liquid water(SLW) above 0.2 mm. Between 1500 and 2100 UTC on February 13, a relatively steady state period occurred. During this period, the secondary cold front was stalled over the northern slope of the Palmer-Divide.

[1] The National Center for Atmospheric Research is sponsored by the National Science Foundation

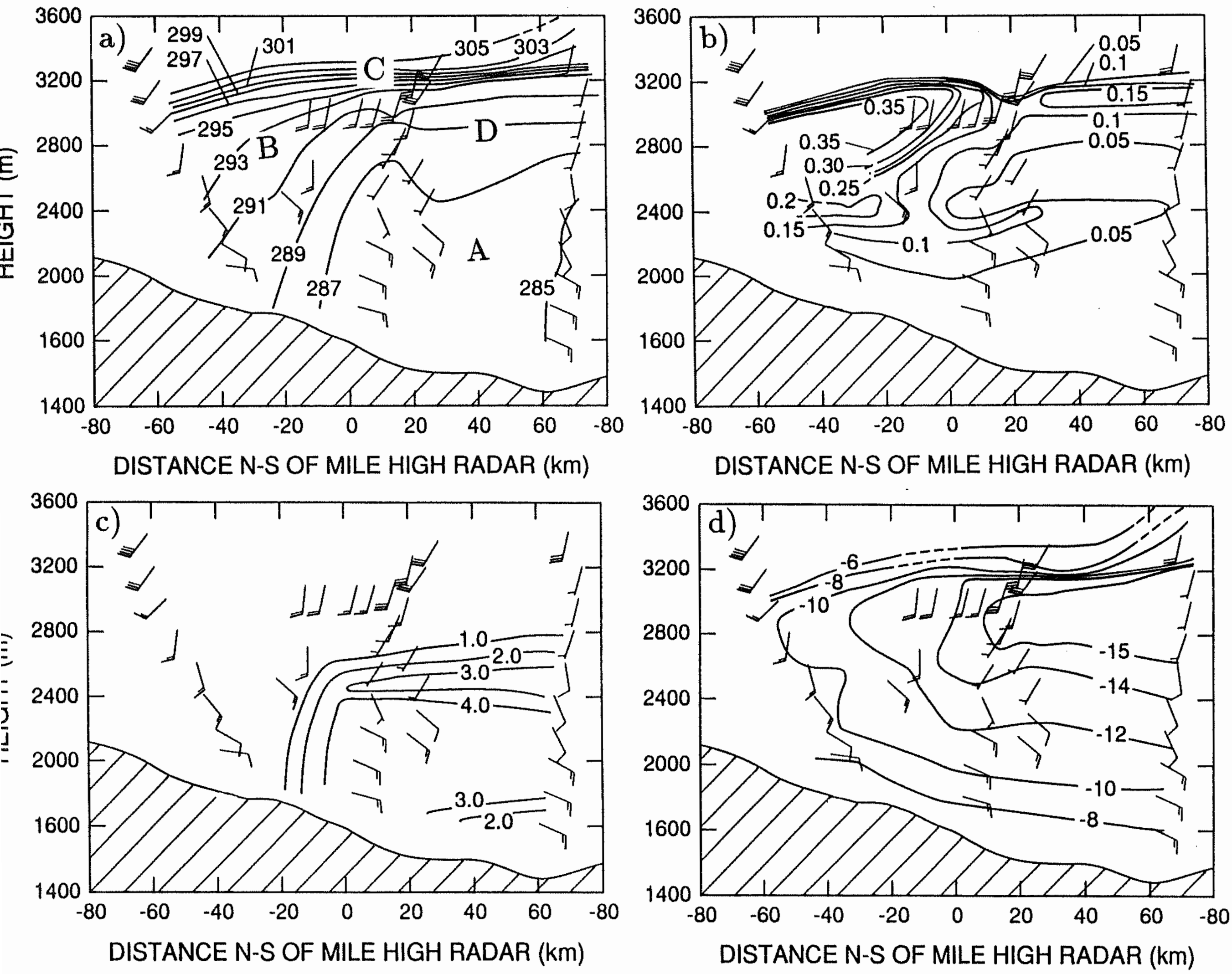

Fig. 2 North-south vertical (MSL) cross-section derived from aircraft data collected between 1723 - 1928 UTC, Feb. 13, 1990. a) Equivalent potential temperature (°K) and wind barbs. Full barb represents 5 m s^{-1}. b) Cloud liquid water content (g m $^{-3}$) and wind barbs. c) ice crystal concentration (l^{-1}) and wind barbs, d) temperature (° C) and wind barbs. The hatched region indicates topography.

3. NORTH-SOUTH VERTICAL STRUCTURE OF THE SHALLOW UPSLOPE CLOUD

During the 30 hour SLW period, two aircraft flights were conducted with the University of Wyoming King Air between 1711 -1900 UTC, Feb.13 and 2310 UTC, Feb.13 - 0142 UTC, Feb.14. In the present paper we will focus on the time period of the first flight, 1711 - 1900 UTC. Radar reflectivities during this period were mostly less than 25 dBZ and increased from the cloud top downward. Figure 2 presents a north-south vertical cross-section derived from the aircraft data. As mentioned above, this period was relatively steady state, allowing us to use data collected over a two hour period in creating the cross-section. Data for the ice crystal concentrations were obtained from a PMS 2D-C probe. Only crystals larger than 150 microns were counted, due to the possible contamination of the data by large cloud droplets. In the following we consider various aspects of this cross-section.

a. *Thermodynamic and kinematic structure*

The vertical cross-section of θ_e reveals four distinct thermodynamic regions (Fig. 2a). Region A contains the coldest θ_e in the cross-section, and has east-southeasterly winds. θ_e is nearly constant in this region as well, indicative of either mechanical turbulence in the boundary layer or surface heating. This region is associated with the secondary surge of cold air mentioned in the previous section. Region B is the region just ahead of the secondary surge, and consists of warmer and moister air. Winds in this region are south to south-easterly, except near the surface where they are east-southeasterly. This region is capped by a strong temperature inversion representing the top of the initial cold front, which at this time is well to the south. Region C is a transition region between the upper level free-tropospheric air and the top of the shallow upslope cloud, and is characterized by a strong vertical gradient in θ_e and wind speed and direction. Winds in this region are strong south-southwesterly above the inversion (20 m/s), and weaker south-southwesterly below it (7.5 m/s). Region D is located just above region A and below region C and is characterized by weak southerly flow (2.5 m/s), and a weak vertical gradient of θ_e .

b. *Supercooled liquid water(SLW) structure*

Associated with regions A-D discussed above are distinct regions of SLW (Fig. 2b). Region A contains a horizontal layer of SLW less than 0.1 g m^{-3} near the top of the well-mixed region and the transition to south-westerly flow. The easterly component of the flow in this region suggests the this layer of SLW is produced as the air is lifted by the Front Range topography (see Fig. 1).

Region B contains the highest SLW in the cross-section, with a maximum of 0.35 g m^{-3} located just above the frontal surface. The relatively strong southerly flow in this region suggests that the SLW in this region is produced by upglide of the moist air to the south over the frontal surface. Using the observed southerly flow of 10 m s^{-1}, and assuming a stationary position for the front as observed, the vertical motion in this region would be ~20 cm s^{-1}, which is nearly an order of magnitude stronger than the motion induced by the local topography in this region for similar horizontal velocities.

Region C has a nearly horizontal SLW layer near cloud top with a thickness of ~300 m. In this region the isentropes are nearly horizontal, suggesting that vertical motion as a result of upglide is relatively weak. Strong vertical wind shear exists in this layer, with bulk Richardson number less than 0.25 during most of the aircraft penetrations (Pobanz 1991). This suggests the possibility of Kelvin-Hemholtz (K-H) waves in this region. Horizontal legs in this cloud top region revealed the existence of periodic variations in temperature and vertical velocity with a wavelength of 500 - 700 m. The thickness of the shear layer ranged from 30 - 150 m, from which K-H theory (Miles and Howard 1964) predicts the existence of waves on the order of 7.5 h, where h is the thickness of the layer. The calculated wavelengths, 250 - 1050 m, are consistent with the those observed, suggesting that Kelvin-Helmholtz waves existed in this region. K-H waves will induce vertical mixing of the unsaturated air above cloud top with the cloudy air. Analysis of the temperature and moisture data show that mixing the 100 m thick region above cloud top with the 100 m thick layer below cloud top results in air which is still saturated with respect to water. Thus, the mixing process induce by the K-H waves will result in further growth of the cloud top.

This mixing process also suggests an explanation for the weak southerly flow and weak θ_e gradients in region D. The initial winds in the cloud layer were easterly, with no southerly flow. In time the cloud top rose, and a region of weak southerly flow developed in the newly created cloud. The above results on K-H waves near cloud top suggests that the strong south-westerly flow above cloud top was mixed down into the easterly flow, with the net result being weak southerly flow. The weak vertical gradient in θ_e is also consistent with this scenario.

The SLW in region D is a minimum. As discussed in the next section, this region is the location where significant concentrations of ice crystals first start appearing near cloud top. This is also coldest region in the cloud (Fig. 2d). Since SLW is not produced in this region due to the weak southerly flow (which is actually downslope as shown in the topography shown in the cross-section), the presence of ice will quickly deplete any SLW.

c. *Hydrometeor structure*

In region A (Fig. 2c), ice crystal concentrations ≥ 1 l^{-1} exist. These crystals are predominantly dendritic, and increase in concentration and size and degree of aggregation with decreasing height. This region has ambient temperatures between -15 and -10 C and is mostly water saturated, consistent with the formation of dendritic crystals. Each aggregate typically consisted of only 2-3 dendritic crystals. This vertical structure is consistent with the observed increase in reflectivity factor with decreasing height in this region. The observed ice crystal concentration is also consistent with the extensive ice nuclei measurements by Berezinskiy and Stapanov(1986) for boundary layer air under anti-cyclonic conditions for the observed temperatures (Fig. 2d). In the southern parts of region A, drizzle drops were also observed to be mixed in with the ice crystals, especially in the lower portions of the region.

Region B contains no measureable ice crystals. However, significant numbers (5 - 10 l^{-1}) of large drizzle sized drops were observed. These drops existed at sub-freezing temperatures, and resulted in freezing drizzle at the surface. The Denver SAO station at Stapleton International airport reported freezing drizzle between 1300 - 1600 UTC and 1900 - 2100 UTC, with light snow between 1700 - 1800 UTC. As shown in Fig. 2c, Denver (~10 km south of Mile High Radar), was located in the transition region between snow and freezing drizzle, consistent with the alternation of conditions in the surface observations. The passage of the secondary front over Denver occurred just after 1245 UTC, and correlates well with the onset of freezing drizzle at Denver at 1300 UTC. The secondary front stalled over the Palmer Divide, creating an extended period of freezing drizzle that lasted until 2100 UTC (mesonet analysis shows that the front never made it over the top of the Divide). This secondary surge was observed to be stronger along the Foothills, causing the freezing drizzle to be concentrated near the north side of the Palmer Divide (freezing drizzle was not observed at Limon, an SAO station located further to the east). Freezing drizzle has been associated with a number of takeoff accidents due to ground icing; our understanding of the formation of freezing drizzle in cases without a melting layer aloft, however, is very poor. In the current case, drizzle drops are most-likely produced by a coalescence process in the high SLW region above the frontal surface. In order to initiate a coalescence process, however, cloud droplets greater than ~40 microns in diameter are required (Pruppacher and Klett 1980). Analysis by Pobanz(1991) shows the presence of droplets of this size in the strong wind shear region near cloud top for this storm. As suggested by Cooper (1989), large cloud droplets are often produced by the mixing proceess created in regions of strong wind shear. Thus, the combination of strong shear induced mixing near cloud top leading to large cloud droplets ($\geq$ 50 microns in diameter), and the relatively high SLW ıst below this region produced as a result of upglide of ir over the secondary front, and the lack of significant oncentrations of ice at these relatively warm cloud top emperatures ($\geq$ -10 C, Fig. 2d), created ideal conditions or the production of freezing drizzle in a cloud entirely ess than 0 C.

The lack of ice in the northern portion of region) is somewhat puzzling due to the relatively cold air emperature in this region (-14 C), which at lower levels f the cloud is associated with 3-4 l^{-1} of ice. In ddition, large cloud droplets were shown to exist in his region, which has been put forward by Hobbs and langno (1985) as one of the requirements to produce igh ice crystal concentrations in cumulus clouds. The urrent case is not a cumulus cloud, but strong mixing vith environmental air is present. In the current case, owever, the mixing process does not result in significant vater sub-saturation, as it likely will in a cumulus cloud.

As shown by the θ_e cross-section (Fig. 2a), the egion of ice greater than 1 l^{-1} is within the well-nixed boundary layer portion of the cloud, while the pper portion of the cloud consists of air mixed in from loft. We hypothesize that the air above the shallow pslope cloud is relatively clean, and therefore devoid f significant concentrations of ice nuclei. In addition, here are no secondary ice crystal processes active in his portion of the cloud, such as those observed to ccur near the tops of cumulus clouds by Hobbs and langno (1985) and others. Although this case study hows distinct mechanisms leading to the production of LW, the initiation of ice cannot be linked as easily to istinct mechanisms. During future field programs we ope to address this problem of the initiation of ice by onducting focussed experiments in upslope clouds and vave clouds.

. MODEL RESULTS

The above observations suggest that supercooled iquid water (SLW) production and depletion varied both patially and temporally during this storm. During he steady state period between 1500 -2100 UTC, 'eb. 13, 1990, most of the variation in SLW is likely ue to spatial effects. In order to investigate the rocesses of SLW production and depletion further we erformed three-dimensional model simulations using he Clark(1977) anelastic model which utilizes a terrain ollowing coordinate system. We also used two ifferent microphysical parameterizations, the Koenig nd Murray(1977) scheme and the Murakami(1990) cheme. The horizontal resolution used was 4 km, and the ertical resolution 0.3 km. The model was initialized with 1500 UTC upstream sounding from Wiggins (figure 1).

Model results show that the SLW is organized into ands oriented NW to SE, with a 50 km spacing. Higher alues of SLW were also found in a north-south line up gainst the foothills due to the strong vertical motions nduced by the terrain at that location. The SLW vas contained below 3.3 km MSL due to the strong emperature inversion at that level. Regions of high ice rystal mixing ratio are located in regions of low SLW, onsistent with depletion of SLW by the ice crystals. The iscontinuous nature of the SLW in space is not consistent vith the observations (Fig. 2), which show a nearly continuous region of SLW. The model results also do not reproduce the high SLW to the south associated with the stationary front, and the process of SLW formation by mixing along cloud top. The model reproduced fairly well the SLW produced by topographic uplift, but even these predictions were relatively discontinuous. In order to improve these predictions, the ice nuclei concentrations were reduced in the upper levels of the cloud, resulting in a much more continuous field of SLW.

4. SUMMARY

Three mechanisms are shown to cause the observed SLW: 1) upslope flow over topography, 2) a mixing process near cloud top, and 3) upglide motion at the leading edge of a nearly stationary secondary front.

Cloud droplets $\geq$ 40 microns in diameter occurred near cloud top in association with strong wind shear. In regions of SLW $\geq$ 0.25 g m^{-3}, these drops grew into drizzle sized drops and resulted in freezing drizzle at the surface.

Ice crystal concentrations greater than 1 l^{-1} were observed to occur in the well-mixed boundary layer air near the surface. The lack of significant ice crystal concentrations near cloud top and in the frontal upglide portion on the cloud suggests a relatively inefficient ice formation process in these regions. We hypothesize that the boundary layer air was relatively rich in ice nuclei, while the air in the free atmosphere was relatively clean. Verification of this hypothesis will be attempted in future field experiments focussing on the initiation of ice in these types of clouds.

ACKNOWLEDGEMENTS

This work was supported by the Federal Aviation Administration Contract DTFA01-90-25001.

REFERENCES

Berezinskiy, N.A. and G.V. Stepanov, 1986: Dependence of the concentration of natural ice-forming nuclei of different size on the temperature and supersaturation. *Izvestiya, Atmosphere and Oceanic Physics*, **22**, 722 - 727.

Clark, T.L.,1977: A small scale dynamic model using a terrain-following coordinate transformation. *J. Comput. Phys.*, **24**, 186–215.

Cooper, W.A., 1989: Effects of variable droplet growth histories on droplet size distributions. Part I: Theory. *J. Atmos. Sci.*,**46**, 1301 - 1311.

Hobbs, P.V., and A.L. Rangno, 1985: Ice particle concentrations in clouds. *J. Atmos. Sci.*, **42**, 2523 2549.

Koenig, L.R., and F.W. Murray, 1977: Ice-bearing cumulus cloud evolution: Numerical simulation and general comparison against observations. *J. Appl. Meteor.*,**15**, 747 - 762.

Miles, J.W. and L.W. Howard, 1964: Note on a heterogeneous shear flow. *J. Fluid Mech.* , **20**, 331 - 336.

Murakami, M., 1990: Numerical modeling of dynamical and microphysical evolution of an isolated convective cloud: The 19 July 1981 CCOPE cloud.*J. Met. Soc. of Japan*,**68**, 107 - 128.

Pobanz, B., 1991: Conditions associated with large drop regions. M.S. Thesis, University of Wyoming, Laramie, WY, 57 pp.

Pruppacher, H.R., and J.D. Klett, 1980: *Microphysics of Clouds and Precipitation*, D. Reidel Publishing Company, 714 pp.

ICE CONCENTRATIONS IN MARITIME AND CONTINENTAL CUMULIFORM CLOUDS

Arthur L. Rangno and Peter V. Hobbs

Atmospheric Sciences Department
University of Washington, Seattle, WA 98195, USA

1. INTRODUCTION

In this paper we summarize the principal findings of our studies of ice particle concentrations in maritime and continental cumuliform clouds obtained over the past four years and combine them with earlier results presented by Hobbs and Rangno (1985). The total data set comprises more than 2200 airborne penetrations of cumuliform clouds under a wide range of conditions. The measurements were obtained principally over the Pacific coastal waters of Washington State, Puget Sound, and over and east of the Cascade Mountains. We define "maritime" and "continental" in this paper as those clouds having droplet concentrations <300 and ≥300 cm^{-3}, respectively. The results described below are for clouds with widths ≥2 km in their upper portions. Nearly all of the clouds studied were ≤4 km thick. The aircraft sampling methods, instruments used, and methods of analysis have been described by Hobbs and Rangno (1985) and Rangno and Hobbs (1991).

2. RESULTS

(a) *Onset of ice particles*

For continental cumuliform clouds, the warmer the cloud base the warmer is the cloud top at which ice particles initially form (Rangno and Hobbs, 1988; and Fig. 1). Thus, whether or not ice will form in a continental cumuliform cloud (and, therefore, whether or not precipitation is likely from the ice process) can be predicted from the cloud base temperature and the maximum height to which the cloud top is expected to rise.

For maritime cumuliform clouds, the onset of ice is generally near cloud top at temperatures between –4° to –7°C for a wide range of cloud base temperatures (Rangno and Hobbs, 1988; and Fig. 1).

b) *Maximum ice particle concentrations and cloud base and cloud top temperatures*

For our total data set on continental and maritime cumuliform clouds, there is no significant correlation between maximum ice particle concentrations, I_M, and cloud top temperature, T_T (Fig. 2). However, sub-sets of the data do show some significant correlations as described below.

For continental cumuliform clouds with cloud base temperatures ≲ 0°C, strong correlations exist between I_M and T_T (e.g., Hobbs and Rangno, 1985; Cooper, 1986; and lines 1 and 2 in Fig. 2). For cloud base temperatures $T_B \leq -8$°C, the correlation coefficient (r) between I_M and T_T is 0.91. For this sub-set of the data (line 1 in Fig. 2) the relation between I_M and T_T is almost identical to Fletcher's (1962) relationship between average ice nucleus concentrations and temperature. For 0°C $> T_B > -8$°C (line 2 in Fig. 2), the correlation between I_M and T_T is still very high (r = 0.86), but the average I_M is 10–50 times higher for the same cloud top temperature than for continental cumuliform clouds with $T_B \leq -8$°C (line 1 in Fig. 2). For 8°C $\geq T_B \geq$ 0°C (line 3 in Fig. 2), the correlation coefficient between I_M and T_T is 0.57, and

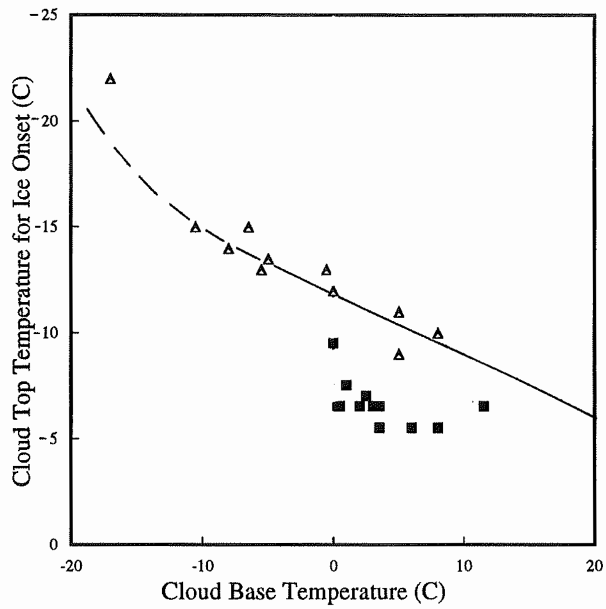

Figure 1. Cloud top temperature at which ice first appears in significant concentrations (about 1 L^{-1}) as a function of cloud base temperature for cumuliform clouds. Triangles are for continental clouds and squares for maritime clouds. The solid line is based on *independent* data for continental cumuliform clouds from a number of investigations summarized by Rangno and Hobbs (1988).

the average I_M is 50–100 times higher for the same cloud top temperature than for those clouds with $T_B \leq -8$°C (and for Fletcher's ice nucleus curve). Thus, for continental cumuliform clouds, best fit curves between I_M and T_T shift toward higher ice particle concentrations as T_B increases.

For maritime cumuliform clouds I_M increases by several orders of magnitude as T_T falls by a few degrees, but thereafter I_M appears to be independent of T_T (line 4 in Fig. 2).

(c) *Maximum ice particle concentrations and drop size spectra*

The presence of larger drops, usually in coincidence with graupel, in cumuliform clouds has long been thought to influence the development of ice particles by many researchers (e.g., Findeisen, 1940, 1943; Koenig, 1963; Braham, 1964; Mossop *et al.* 1970; Ono, 1971; Mossop and Hallett, 1974; Mossop, 1985; Hobbs and Rangno, 1985). Hobbs and Rangno (1985), however, showed that I_M was well correlated with merely the breadth of the drop spectrum (without reference to graupel) as measured by the drop threshold diameter D_T (defined such that the concentrations of drops with diameters $\geq D_T$ is equal to 1 cm^{-3}) in the upper

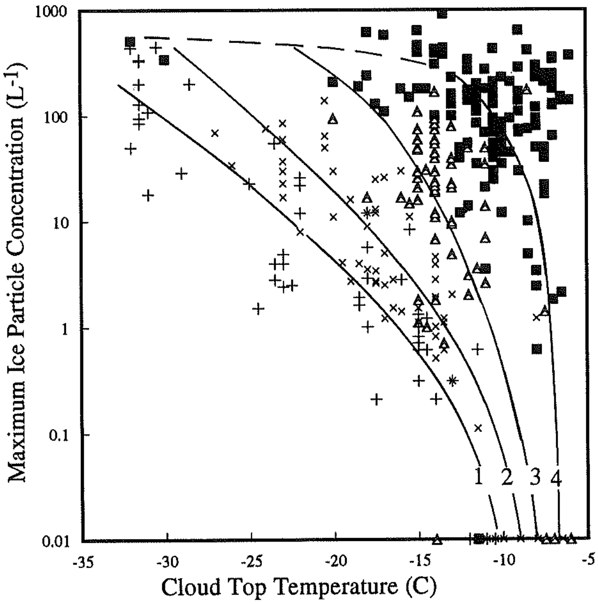

Figure 2. Relationships between maximum ice particle concentrations, I_M, and cloud top temperature, T_T, for four categories of cumuliform clouds: continental with base temperatures $T_B \leq -8$°C (plus signs, and line 1), continental with 0°C $> T_B > -8$°C (crosses and line 2), continental with 8°C $\geq T_B \geq$ 0°C (triangles and line 3), and maritime (squares and line 4).

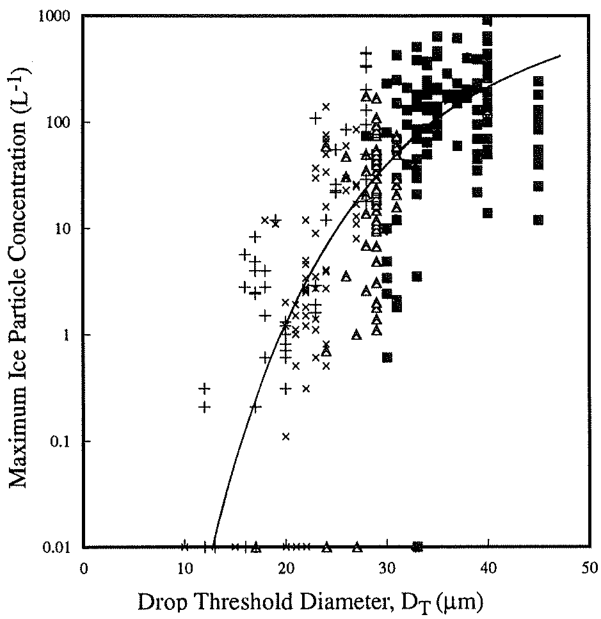

Figure 3. Maximum ice particle concentrations, I_M, versus the drop threshold diameter, D_T, for mature and aging maritime and continental cumuliform clouds. Data and symbols are the same as in Fig. 2. The best fit line is shown.

portions of young cumulus clouds. Figure 3 shows the relationship between I_M and D_T for all maturing and dissipating cumuliform clouds (maritime and continental) studied by us over the past four years combined with the earlier data of Hobbs and Rangno (1985). It is clear that D_T is a much better predictor of I_M than is T_T over the wide range of cloud situations studied by us. For example, for *all* the cumuliform clouds with $-25°C \leq T_T \leq -6°C$, the correlation coefficient between I_M and D_T is 0.78, while the correlation coefficient between I_M and T_T is a negligible 0.01. Note, however, that if the presence of large drops is a necessary condition for the development of ice, as this relationship suggests, when high concentrations of ice have formed, and the drops in the upper regions of the cloud have been consumed by riming and evaporation, ice particle production will cease even if the cloud top continues to rise and cool (Hobbs and Rangno, 1990; and Fig. 2).

For cumuliform clouds with a narrow droplet spectrum (10 μm $\leq D_T \leq$ 23 μm diameter) near cloud top, I_M increases with decreasing T_T. Thus, for our latest data set, for $T_T = -15$°C I_M averaged about 0.5 L^{-1}, and for $T_T = -24$°C I_M averaged 3–7 L^{-1}. The ice-forming process in these clouds can be described as a "trickle" mechanism; ice crystals form at a steady but relatively slow rate, perhaps due to the slow formation of larger drops. For continental clouds with a broad droplet spectrum near cloud top ($D_T \geq$ 25 μm diameter), $I_M \simeq$ 50–100 L^{-1} for $T_T = -15$°C, while for $T_T = -31.5$°C $I_M \simeq$ 300–450 L^{-1}. In this case, ice particles can appear in high concentrations very quickly (see below).

(d) *Sudden appearance of high ice particle concentrations*

One of the most intriguing aspects of ice formation in cumuliform clouds with top temperatures <–6°C and with a broad droplet spectrum ($D_T >$ 25 μm) is their ability to produce high concentrations of ice particles (10s–100s L^{-1}) in <10 min (e.g., Koenig, 1963; Hallett *et al.* 1978; Hobbs and Rangno, 1990; Rangno and Hobbs, 1991). In these previous studies of this type of event, drizzle drops were present. However, in our most recent studies we have observed the rapid formation of high concentrations of ice particles in some continental cumuliform clouds in which drizzle drops were not present, although $D_T >$ 25 μm diameter in the upper regions of these clouds. In all cases, the high concentrations of ice appear as pristine crystals. They form coincident with (or shortly after) the formation of graupel particles. The ice particles are compatible in habit with the temperature at which they are first encountered in the clouds, which indicates that they form *in situ*. Figure 4a and 4b show the ice crystals encountered in two such cases. The spontaneity and nature of this ice formation strongly resembles homogeneous nucleation (Fig. 4c), except that it has been observed between –10° to –28°C.

3. CONCLUSIONS

Our field measurements, consisting of more than 2200 penetrations of maritime and continental cumuliform clouds, can be summarized as follows.

- The cloud top temperature at which ice first appears in continental cumuliform clouds increases as cloud base temperatures increase, rising from about –15°C in clouds with base temperatures of about –10°C to ≥ –10°C in clouds with base temperatures ≥ 8°C.

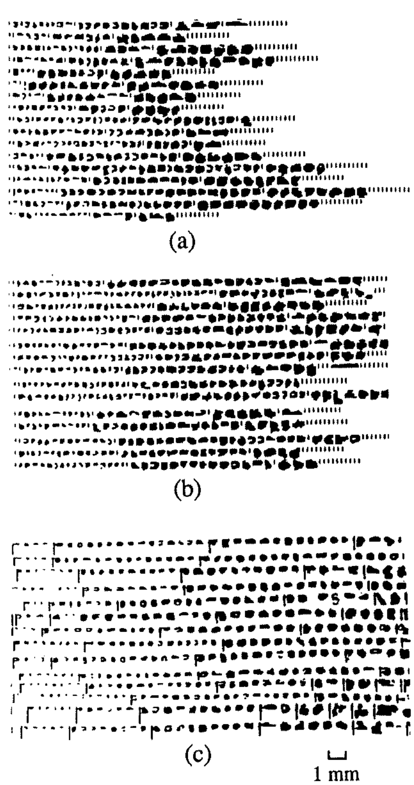

Figure 4. Examples of PMS 2-D cloud probe imagery of high concentrations of uniformly sized ice particles encountered (a) in natural clouds at –25°C with T_B = –10.5°C and T_T = –31.5°C, (b) in natural clouds at –11°C with T_B = 0°C and T_T = –15°C, and (c) in a cloud at –10°C that was seeded with Dry Ice.

• Ice first appears in significant concentrations in maritime cumuliform clouds at cloud top temperatures between –4° and –7°C.

• For continental cumuliform clouds having the same cloud base temperature, maximum ice particle concentrations increase as cloud top temperatures fall, and as the concentrations of larger drops increase near cloud top in the youngest turrets. Thus, for these clouds, there exists a continuum of curves (see Fig. 2) that can be used to predict maximum ice particle concentrations in continental cumuliform clouds for various cloud top and cloud base temperatures.

• For maritime cumuliform clouds, maximum ice concentrations increase rapidly as the cloud top temperature decreases from about –7°C to –10°C, but thereafter they do not vary greatly (see Fig. 3).

• Maximum ice particle concentrations in both continental and maritime clouds are strongly correlated with the drop threshold diameter.

• Ice particles in concentrations of 10s–100s L^{-1} can form in a few minutes in maritime cumuliform and continental cumuliform clouds provided there is a plentiful supply of drops with diameters > 25 μm in the upper region of the cloud.

• In some exceptionally strong ice-forming cases, the ice-forming process will terminate when larger drops are depleted, even though the cloud top may continue to rise and cool.

Acknowledgements. This research was supported by a series of grants from the National Science Foundation, the latest of which is ATM-9015189.

REFERENCES

Braham, R. R., Jr., 1964: What is the role of ice in summer rainshowers? *J. Atmos. Sci.*, **21**, 640–645.

Cooper, W. A., 1986: Ice initiation in natural clouds. *Meteor. Monog.*, **21**, 29–32.

Findeisen, W., 1940: Uber die Entstehung der Gewitterelektrizitat. *Met. Z.*, **57**, 201–215.

————, 1943: Untersuchungen uber die Eissplitterbildung an Reifschichten. *Met. Z.*, **60**, 145–154.

Fletcher, N. H., 1962: In *The Physics of Rainclouds.* Cambridge University Press, p. 242.

Hallett, J., R. S. Sax, D. Lamb, and A. S. Ramachandra Murty, 1978: Aircraft measurements of ice in Florida cumuli. *Quart. J. Roy. Meteor. Soc.*, **104**, 631–651.

Hobbs, P. V., and A. L. Rangno, 1985: Ice particle concentrations in clouds. *J. Atmos. Sci.*, **42**, 2523–2549.

————, and ————, 1990: Rapid development of ice particle concentrations in small polar maritime cumuliform clouds. *J. Atmos. Sci.*, **47**, 2710–2722.

Koenig, 1963: The glaciating behavior of small cumulonimbus clouds. *J. Atmos. Sci.*, **20**, 29–47.

Mossop, S. C, 1985: Secondary ice particle production during rime growth: the effect of drop size distribution and rimer velocity. *Quart. J. Roy. Meteor. Soc.*, **111**, 1113–1124.

————, and J. Hallett, 1974: Ice crystal concentration in cumuliform clouds: influence of the drop spectrum. *Science*, **186**, 532–533.

————, A. Ono, and E. R. Wishart, 1970: Ice particles in maritime clouds near Tasmania. *Quart. J. Roy. Meteor. Soc.*, **96**, 487–508.

Ono, A., 1971: Some aspects of the natural glaciation processes in relatively warm maritime clouds. *J. Meteor. Soc. Japan*, **49**, 845–858.

Rangno, A. L., and P. V. Hobbs, 1988: Criteria for the onset of significant concentrations of ice particles in cumuliform clouds. *Atmos. Res.*, **22**, 1–13.

————, and ————, 1991: Ice particle concentrations and precipitation development in small polar maritime cumuliform clouds. *Quart. J. Roy. Meteor. Soc.*, **117**, 207–241.

RETRIEVAL OF HYDROMETEOR DISTRIBUTIONS FROM AIRBORNE SINGLE-FREQUENCY RADAR AND MULTI-FREQUENCY RADIOMETRIC MEASUREMENTS

J.A. Weinman[1] and J.L. Schols[2]

[1] NASA/GSFC, Greenbelt, MD USA 20771
[2] General Sciences Corporation, Laurel, MD USA 20707

1. INTRODUCTION

A model was developed to retrieve precipitation rate profiles, drop size distributions (DSD's) and hydrometeor particle compositions from airborne 10 GHz radar measurements and 10, 18, 35 and 92 GHz radiometric measurements over the ocean.

A two layer configuration was used in this analysis, in which the lower layer consists of rain. The upper layer is composed of partially frozen hydrometeors for temperatures higher than 263 K. Above the 263 K isotherm the hydrometeors are completely frozen. However, non-precipitating supercooled cloud water drops are assumed to be present. The underlying surface was a wind roughened ocean. The profiles of temperature and humidity were obtained from dropsonde data. Climatological estimates of non-precipitating cloud water were assumed as a first guess. The model is schematically shown in Fig. 1.

Fig. 1. Schematic view of the two layer model showing cloud water (.), rain (o), partially frozen (⊛) hydrometeors and ice (*). The top of the lower layer is z^*, z' is the height of the 263 K isotherm, and $\bar{z}$ is the height of the top of the frozen hydrometeor layer. H is the altitude of the aircraft.

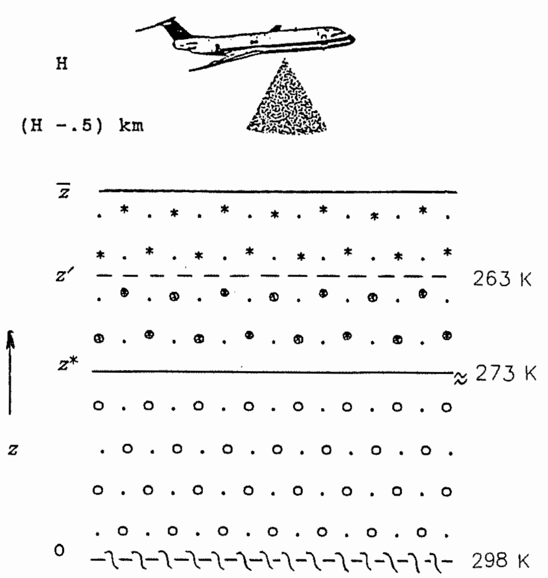

2. HYDROMETEOR DISTRIBUTION RETRIEVAL ALGORITHM IN THE LOWER LAYER

The exponent in the assumed gamma drop size distribution (DSD) (Ulbrich 1983) of the rain, μ, was used as a parameter. The hydrometeor extinction profile in the lower layer, together with μ, were obtained using a nonlinear optimization algorithm (Marquardt 1963), applied to a modification of the model of (Weinman et al. 1990), which optimized the 10 GHz brightness temperature. The columnar integrated liquid cloud water was calculated from the 18 GHz brightness temperature. The rainrate profile in the lower layer was retrieved using the *R-Z* relationship for liquid spherical hydrometeors. The coefficients in the *R-Z* relationship were stored in a look-up-table (LUT), which was constructed from Mie calculations for different values of μ.

3. HYDROMETEOR DISTRIBUTION RETRIEVAL ALGORITHM IN THE UPPER LAYER

The hydrometeors in the upper layer were modeled as either one of two types. Type 1 consisted of spherical particles composed of an ice core mixed with air and surrounded by a liquid shell of variable thickness, i.e. melting hail, or snow. The other hydrometeor model, type 2, consisted of (partially) frozen spherical particles, which ranged from pure ice to liquid and ice in various compositions, but with a fixed ratio of liquid mass to total mass, i.e. melted fraction. Type 2 hydrometeors consist of ice and water in various mixtures that may be:

T-1) Liquid precipitation.
T-2) Mixed precipitation, i.e. coexisting water and ice spheres.
T-3) Slush, i.e. uniformly mixed ice and water inside a sphere with a refractive index characterized by Debye's mixing formula (Battan 1973).
T-4) Coated ice spheres, i.e. two layer spheres consisting of an ice core surrounded by a liquid shell. The water content is represented by a fixed fraction of the total particle mass.
T-5) Ice spheres, i.e graupel.

For type 1 hydrometeors the radar reflectivity profile shows an excess of at least 3 dBZ in a relatively narrow region about 1 kilometer wide, close to the freezing level, the so-called bright band or melting layer. In the absence of the bright band, type 2 hydrometeors are assumed to be present.

The hydrometeor distribution in the upper layer was retrieved using the 35 and 92 GHz brightness temperarues in the nonlinear optimization algorithm (Marquardt 1963), and assuming the same μ as in the lower layer. A melting layer model (Yokoyama and Tanaka 1984) was applied for the type 1 hydrometeors. The 92 GHz brightness temperature was used to find the precipitation rate in the upper layer, which was assumed uniform. The 35 GHz brightness temperature was used to find the density of the hydrometeors above the melting layer. For type 2 hydrometeors the so-called van de Hulst's (van de Hulst 1980) similarity parameters s_{92GHz} and t_{92GHz}, which fully characterize the radiative properties of the hydrometeors, were used to find the composition of the hydrometeors. The precipitation rate profile was obtained using the R-Z relationship, constructed using Mie computations for several type 2 particles.

Mie calculations revealed a remarkable correlation between the radar reflectivity η_{10GHz} and dt_{92GHz}/dz, that was almost independent of the composition of the hydrometeors. This relationship, can be fitted, for the type 2 hydrometeors, by

$$\eta_{10GHz}=0.0015e^{0.2*\mu}\left(\frac{dt'_{92GHz}}{dz}\right)^2$$

t'_{92GHz} stands for the effective optical thickness as seen by the radar, viz. without the inclusion of cloud liquid water content. For the type 1 hydrometeors, the factor 0.0015 needs to be replaced by 0.009. The relationship also implies that the brightness temperature, Tb_{92GHz}, which depends on t_{92GHz}, is directly related to the columnar 10 GHz radar reflectivity integrated over the depth of the upper layer.

4. RESULTS

Fig. 2 compares the averaged 10 GHz radar reflectivity between 6 and 10 km, and 92 GHz brightness temperature, obtained by airplane measurements (Wang, NASA/GSFC, private communication), and calculated by the present theory. The measured data were part of a campaign on the DC-8 that produced the first coincident radar and multispectral radiometric observations that approach those expected from TRMM. Of special interest are the brightness temperatures in excess of 270 K associated with approximately 15 dbZ reflectivity. These represent cases of radar bright bands formed by type 1 hydrometeors.

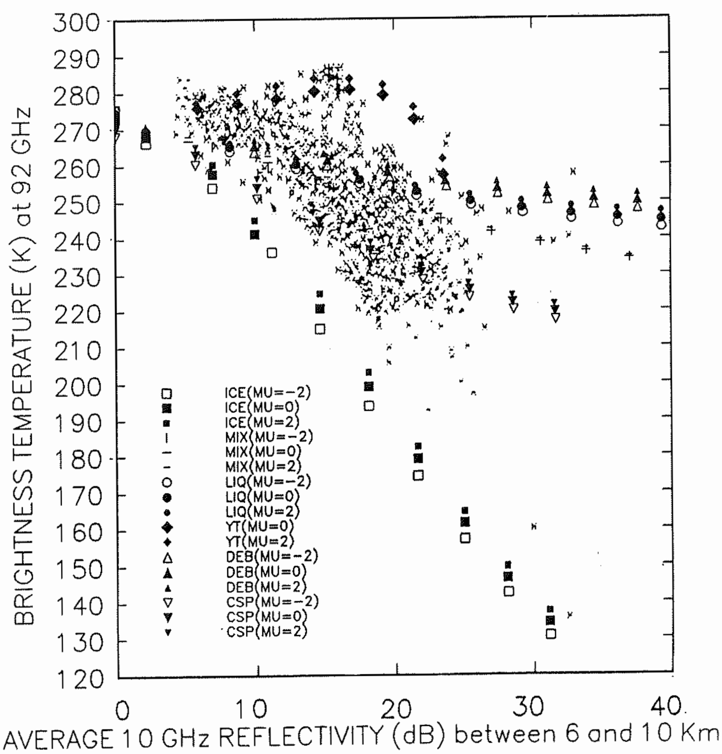

Fig. 2. 92 GHz brightness temperature versus 10 GHz radar reflectivity between 6 and 10 km during the 1990 TYPHOON-1 experiment in the western Pacific. The model calculations represent both type 1 (acronym YT) and type 2 hydrometeors (acronyms LIQ, MIX, DEB, CSP and ICE refer to respective models cited from T-1 to T-5 in the text). Airborne observations are depicted by the cluster of x's.

5. DISCUSSION

The radar observes the lower layer that contains only raindrops in n_L distinct range bins. The 10 and 18 GHz brightness temperatures provide yet two more measurements from this layer. Thus the airborne measurements provide n_L+2 pieces of information about the lower layer. Therefore, we chose to infer n_L values of the rain rate, the value of the parameter μ that appears in the rain-DSD, and the columnar integrated amount of cloud liquid water.

The composition of the hydrometeors in the upper layer is more complex than that in the lower layer. For the type 1 hydrometeors, the density above the melting layer, and the path average precipitation rate in the upper layer were obtained, optimizing the 35 and 92 GHz brightness temperatures. For the type 2 hydrometeors the radar provided n_U pieces of information and two more pieces of information were provided by the 35 and 92 GHz brightness temperatures. The retrieval determined the n_U values of precipitation rate, and the parameters that characterize the model of the type 2 hydrometeors.

The unique relationship between η_{10GHz} and dt_{92GHz}/dz, that applied to the upper layer hydrometeors, that ranged from pure water and solid ice spheres to spheres consisting of a wide range of layers and uniform mixtures of ice and water, was a remarkable discovery. That finding permitted the 92 GHz brightness temperatures to be analyzed to determine s_{92GHz}, a parameter that identifies the composition of the type 2 hydrometeors. This relationship may have profound implications for measuring rain from geostationary satellites, because it implies that the brightness temperature, Tb_{92GHz}, which depends on t_{92GHz} is thus directly related to the columnar integrated value of the 10 GHz radar reflectivity in the upper cloud layer that contains (partially) frozen hydrometeors.

ACKNOWLEDGEMENTS

The authors wish to thank Messrs. Bob Meneghini and Jim Wang for providing radiometric and radar observations, obtained from their airborne TRMM-1 field campaign. Bob Meneghini and Chris Kummerow provided most of the radiative transfer code.

REFERENCES

Ulbrich, C. W., 1983: Natural Variations in The Analytical Form of The Raindrop Size Distribution. J. Clim. Appl. Meteorol., 23, 1764-1775.

Marquardt, D. W., 1963: An Algorithm for Least Squares Estimation of Nonlinear Parameters. Jour. S.I.A.M., 11, 431-441.

Weinman, J. A., R. Meneghini and K. Nakamura, 1990: Retrieval of Precipitation Profiles from Airborne Radar and Passive Radiometer Measurements: Comparison with Dual-Frequency Radar Measurements. J. Appl. Meteorol., 29, 981-993.

Battan L. J., 1973: Radar Observation of the Atmosphere. University of Chicago Press, 324 pp.

Yokoyama, T. and H. Tanaka, 1984: Microphysical Processes of Melting Snowflakes Detected by Two-Wavelength Radar. Part I. Principle of Measurement Based on Model Calculation. J. Meteorol. Soc. Japan, 62, 650-666.

van de Hulst, H. C., 1980: Multiple Light Scattering, Tables, Formulas and Application. Academic Press, New York, 369 pp.

Precipitation Processes in the Equatorial Cumulonimbi

Tsutomu Takahashi

Department of Physics, Kyushu University 33 Fukuoka, Japan 812

Abstract

Specially developed radiosondes were sent into cumulonimbus clouds developed over Pohnpei, Micronesia and Manus Island, Papua New Guinea. Instruments transmitted both the images and the electric charge of precipitation particles during their ascent through these clouds. Equatorial clouds contained numerous ice crystals as well as hail. Precipitation mechanisms were identified through analysis of the precipitation particle distribution with regard to height. Two types of clouds were identified from differing precipitation processes.

Rainbands producing heavy precipitation grew frozen particle-hailstones in a narrow layer just above the freezing level. Water accumulated heavily in this layer due to the close link between the warm rain process and drop freezing process. In the isolated cumulonimbus clouds producing passing showers, rain formed by both warm rain and graupel formation processes, but they worked independently of each other.

A slab-model with detailed microphysics was used to study the precipitation processes.

1. Introduction

The major goal of cloud physics is to understand the precipitation processes in the various cloud systems. Although precipitation in the tropics is known to be an important factor in the understanding of global water circulation, the study of the precipitation mechanisms has not been conducted except for a few attempts (Chrchill and House 1984, and House and Chrchill 1987).

Since it is difficult to fly into convective areas, especially in the tropical squall line, we used a radiosonde system for this investigation.

2. Precipitation Particle Image Sensor (PPIS)

This special radiosonde (PPIS) consists of a video camera which records the falling precipitation particle images in addition to sensing their electric charge (Takahashi 1990, Fig. 1). A parallel infra-red light is set above the line of sight of the camera. Interruption of the infra-red beam by a precipitation particle larger than 0.5 mm in diameter triggers a flash lamp just above the camera lens with a chance of more than 80%. This flash lamp has a pulse duration of 1/22000s and can be triggered up to twice per second.

In addition, a circular flash lamp with a longer flash pulse duration (1/6000s) is mounted so that it surround the camera lens. This lamp flashes continuously at three times per second. Particles even less than 0.5 mm in diameter are pictured during this slow flash exposure. Atmospheric pressure, charge sign and charge magnitude are displayed on a series of LED's set at the bottom of the viewing area.

Sixteen radiosondes were launched from Pohnpei (7°N, 158°E), Micronesia and Manus Is. (2°S, 147°E), Papua New Guinea (Fig. 2) between September 28 and October 12, 1988, and November 24 and December 8, 1991.

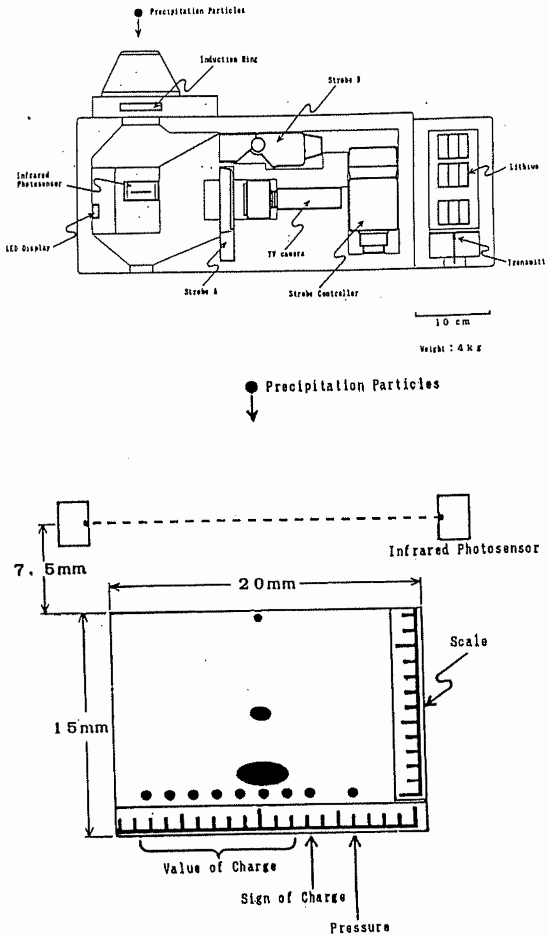

Fig. 1. Precipitation Particle Image Sensor.

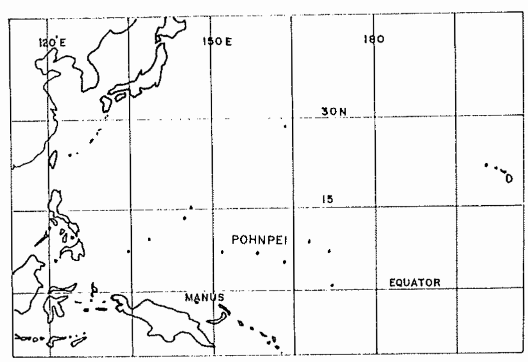

Fig. 2. Observation site, Pohnpei (7°N, 158°E), Micronesia, and Manus Is. (2°S, 147°E), Papua New Guinea.

3. Images of Precipitation Particles

The PPIS recorded a few thousand precipitation particle images during each ascent. Among them, some interesting images were selected for demonstration (Fig. 3).

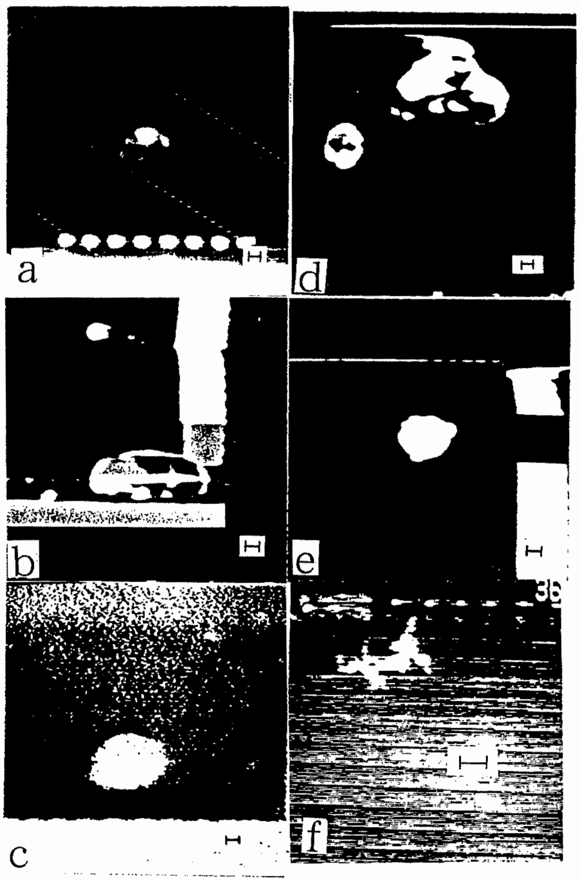

Fig. 3. Precipitation Particle Images. Scale is 1 mm.

Raindrops are spherical when small and spheroidal(a), even flattened (b) when large. Vertically elongated raindrops, raindrops showing a high mode of oscillation at the surface, and rapid oscillation at the upper surface were observed.

Above the 0℃ level, frozen particles and even hailstones were observed (c, d). Fragments of frozen particles were also detected. Ice crystals were stellar, columnar and spatial dendrite. Graupel (e) and snowflakes (f) were also commonly observed. Other interesting pictures showed ice crystals with wide side planes at -63℃ level and a heavy concentration of ice crystals near the tropopause.

4. Precipitation particle distributions

Two types of clouds were identified in regard to their differing precipitation types. They are rainbands and isolated clouds.

a. Rainbands

Clouds developed in a line with a low cloud base and moved from northeast, producing heavy rain (Fig. 4a). The No. 4 radiosonde was launched during intense rainfall.

The temperature followed a pseudo-adiabatic lapse rate up to 150 mb, while the dew point temperature profile measured dry air at the 500 mb level. Easterlies widely prevailed, but winds had northerly component below 3 km.

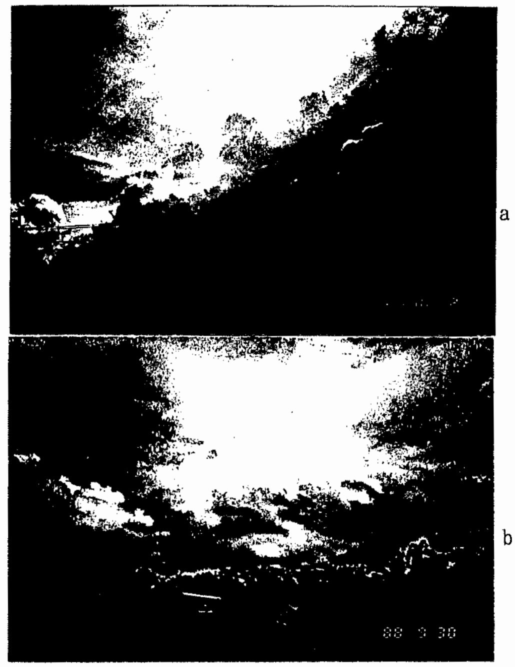

Fig. 4. Rainband (Upper) and isolated Cb (Lower).

This PPIS sent raindrop images below the 0℃ level (Fig. 5a). Most drops were less than 3 mm in diameter.

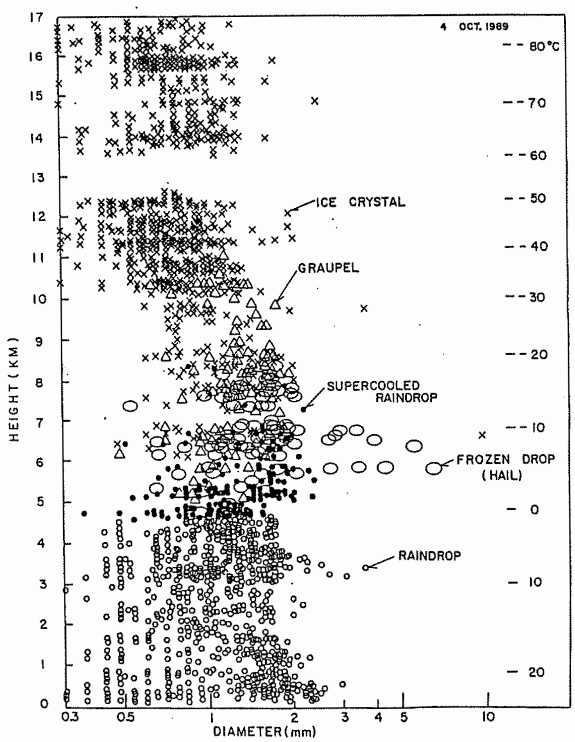

Fig. 5a. Precipitation Particles measured by PPIS launched into rainband.

Above the -15℃ level, both graupel and ice crystals were observed up to 11 km, above which graupel was absent. No particle images in the layer around 13 km may be due to the passage of the radiosonde through a cloud-free area between cumulonimbus and anvil clouds.

The most interesting finding was the abundance of frozen particles including hail in the layer between -5 and -10℃. The largest hail was 7mm in diameter.

The above distribution suggests the following particle growth scenario in band clouds: Raindrops grow effectively by normal warm rain processes during the upward movement of the air parcel. Above the 0°C level, raindrops may freeze spontaneously. These newly formed ice particles then grow by collecting small, supercooled raindrops. Collection is rapid due to the increasingly large difference in fall velocity between the small raindrops and heavier growing ice particles. Hailstones form, and because they do not break up as do raindrops, they continue to grow and cause the heavy precipitation observed in this type of cloud. This rapid collection of raindrops, as it occurs above the 0°C level, leaves a large amount of water extant below the 0°C level and accounts for the large number of raindrops observed in that warmer region (Fig. 5b).

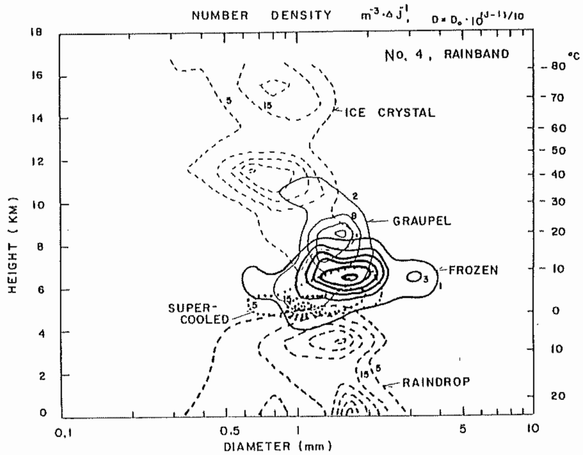

Fig. 5b. Particle number density in m^{-3} in each class J.

b. Isolated Cb

An isolated cloud moved from the north at a rather high speed with moderate rain (Fig. 4b). The No. 6 radiosonde was ascended into this passing shower cloud. The PPIS showed raindrops below the 0°C level and ice crystals above (Fig. 6a). Both graupel and snowflakes were detected in the layer between 0°C and -25°C. It was characteristic that only a few frozen particles were found in the cloud. The precipitation particle number density diagram suggests the growth of graupel from ice crystals at 6 km (Fig 6b). However, the peak number density of graupel corresponds to the smaller peak raindrop number density when they melt. Raindrops at the larger peak size may be formed differently. The very large mass density as well as the high raindrop number density suggests that these relatively large raindrops are formed by a warm rain process. Observation suggests that both warm rain and graupel formation processes work to create precipitation, but do not interact.

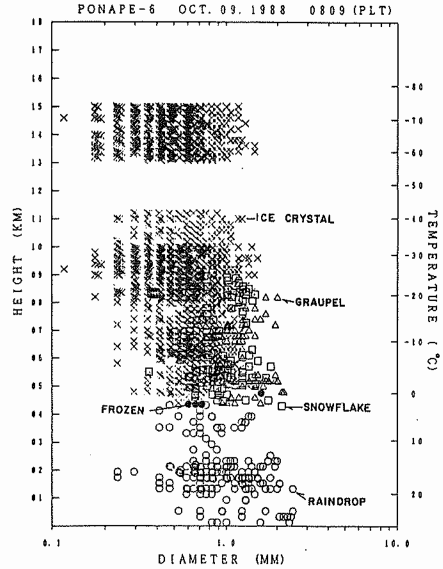

Fig. 6a. Same as Fig. 5a except isolated cumulonimbus cloud.

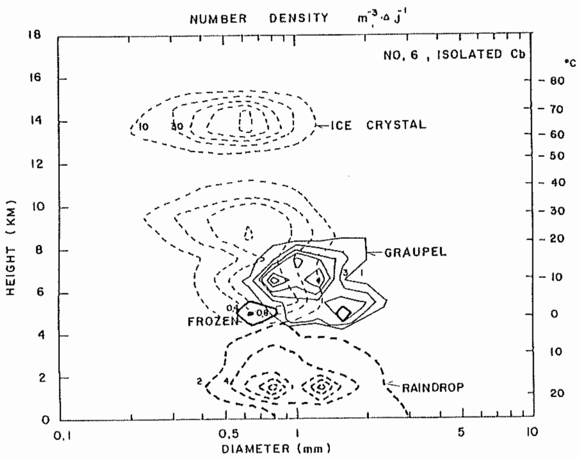

Fig. 6b. Same as Fig. 5b except isolated cumulonimbus cloud.

5. Deep Slab model with microphysics

Precipitation mechanisms were studied in a deep slab model with detailed microphysics (Takahashi, 1976). The available cloud nuclei concentration was chosen as 100/cc to represent a maritime cloud. Below 2 km, linear wind profile ($3 \times 10^{-3}S^{-1}$) was imposed.

The cloud tilts to the downwind side. As the cloud develops at the upper level, the induced mid-level air splits the cloud into two parts. In the beginning of cloud development, raindrops are formed near the cloud top by the warm rain process. Near the cloud top (-10°C, 20 min), graupel are formed by the riming on small frozen drops (Fig. 7a). As the upper cloud develops, ice nuclei are now fully activated and graupel formation is greatly enhanced through riming on ice crystals (Figs. 7b and c).

The surface rainfall intensity profile showed heavy rainfall with three peaks (Fig. 8). The first

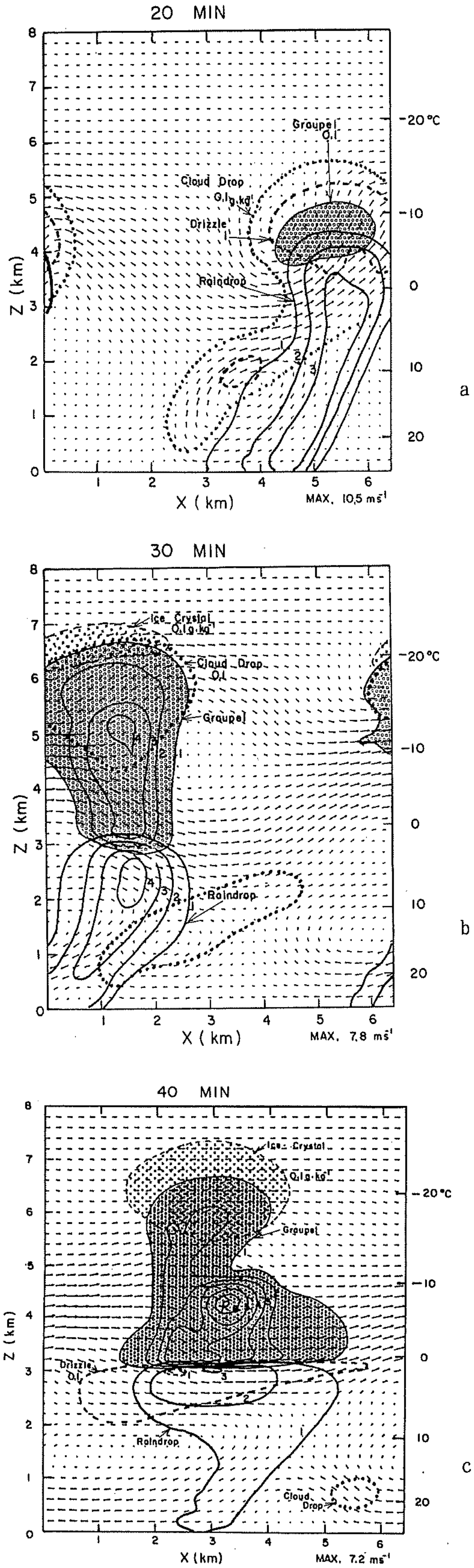

Fig. 7. Model simulated winds and mixing ratios of precipitation particles. a (20 min.), b (30 min), c (40 min.)

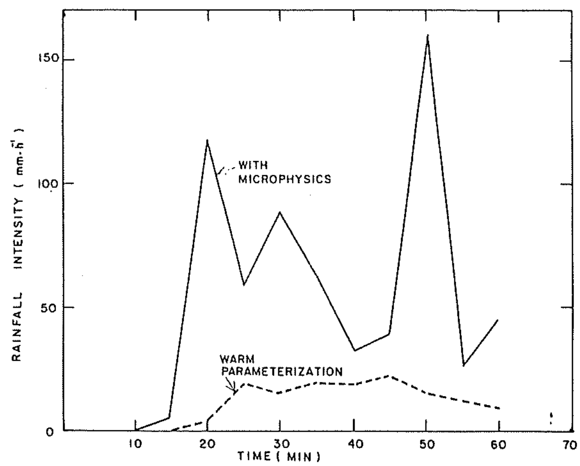

Fig. 8. Rainfall intensities with full microphysics (solid line) and warm rain parametarization (dashed line).

peak corresponds to the warm rain and the second peak to the addition of graupel originated on small frozen drops. The third peak is the highest, and is caused by the full graupel formation through ice crystal riming. For comparison, rainfall intensities calculated by the use of Kessler's warm rain parameterization were also shown. Those rainfall intensities were weak and continuous.

6. Conclusions

Two types of precipitation processes were found through the ascent of precipitation particle image sensors into equatorial West Pacific cumulonimbi. Precipitation through frozen drops was dominant in the rainband, while both warm rain and graupel fomation processes worked in the isolated cumulonimbi.

Although the numerical model succeeded in simulation of the precipitation processes of the passing shower clouds, the model may need to include mesoscale convergence to simulate the rainband precipitation process (frozen particle dominant process).

References

Churchill, D. D. and R. A. Houze, Jr., 1984:Development and structure of winter monsoon cloud clusters on 10 December 1978. J. Atmos. Sci., 41, 933-960.

Houze, R. A. Jr., and D. D. Churchill, 1987: Mesoscale organization and cloud microphysics in a bay of Bengal Depression. J. Atmos. Sci., 44, 1845-1867.

Takahashi, T., 1976: Hail in axisymmetric cloud model. J. Atmos. Sci., 33, 1579-1601.

————, 1990: Near absence of lightning in torrential rainfall producing Micronesian thunderstorms. Geophys. Res. Lett., 17, 2381-2384.

STUDY ON THE PRODUCTION OF ICE PARTICLES IN CLOUD DUE TO AIRCRAFT PENETRATIONS

Chen Wankui   Yan Çaifan
Chinese Academy of Meteorological Science
46 Baishiqiao Rd.   Beijing 100081 PRC

1. INTRODUCTION

An aircraft flying through a supercooled cloud can produce numerous ice particles (APIPs), which change cloud microphysical properties and effect natural seeding processes. Since 1983 many authers [Rangno & Hobbs (1983), (1984), Mossop (1984), Vonnegut (1986), Gordon (1986), Vali, Kelly & Serrano (1988), Brown (1988)] have been interested in these problems.

2. FLIGHT DESIGN

Three basic conditions must be satisfied for APIPs measurements in flight design: fine airborn instruments, stable cloud layer and the reversible flying tracks. In our experiments, the PMS probes (FSSP-100, OAP2D-C, OAP2D-P) were used to measure cloud microphysical properties; the stable stratocumulus (abbreviated Scop) were selected and multipoint navygations were utilized to locate.

Fig.1 shows a flight (on Nov. 14th, 1982) . During 16:47′-49′ period, the aircraft penetrated the stable Scop from bottom to top and the measurements are refered as background ones; during 17:45′-47′ & 17:49′- 54′periods, the measurements were taken on the border of background refered as border and during 17: 47′-49′ period, the aircraft backed in APIPs region.

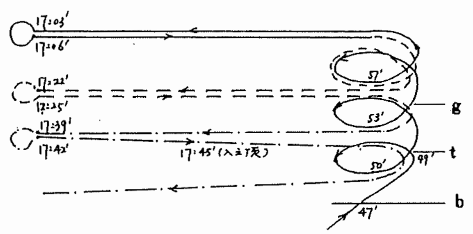

Fig. 1. A flight track schematic diagram (on Nov. 14th, 1982)

g: ice & snow generating layer (afterward abbreviated to GL)

b: Scop base, temperature -7.7° C

t: Scop top, temperature -12.0° C

3. RESULTS

The average cloud droplet concentration $\bar{N}(cm^{-3})$ and liquid water content $\bar{Q}(g.m^{-3})$ calculated from cloud droplet spectra and their variations δ_N, δ_Q are listed in Table 1.

Table 1. Scop microphysical properties

situation	$\bar{N}(cm^{-3})$	δ_N	$\bar{Q}(g.m^{-3})$	δ_Q
background	229.5	0.14	0.144	0.07
border	297.3	0.12	0.116	0.22
	236.5	0.29	0.103	0.22
APIPs	219.5	0.41	0.075	0.52

In APIPs region the variation $_N$ and $_Q$ are obviously higher than those in background and border regions, but the $\bar{N}$ and $\bar{Q}$ are less, showing that APIPs region consumes a part of cloud water and cause increases in $\bar{N}$ and $\bar{Q}$ spatial variations.

The cloud and solid particles average size distributions measured with PMS probes are illustrated in Fig.2,3. In APIPs region the cloud droplet size distributions are widened to 47um; the maximum concentration in diameter 23-47um is 0.387 cm^{-3} that is three order higher than those in background and border regions; but in diameter 2-23um their concentrations and size distribution's type are similar.

The ice and snow particles occured 330m apart from the Scop top, where the temperature is-14° C. The snowflake diameter increase to 5000um due to aggregation. On an average, the ice and snow concentrations in APIPs region 1- 2 order higher than those in background and border regions and the images of the ice and snow particles are different: in background region completely dendrite and their aggregates; in APIPs region graupelsand graupellikes and in border regions the majority of dendrite and their aggrigates plus the minority of graupels and graupellikes (See Fig.5).

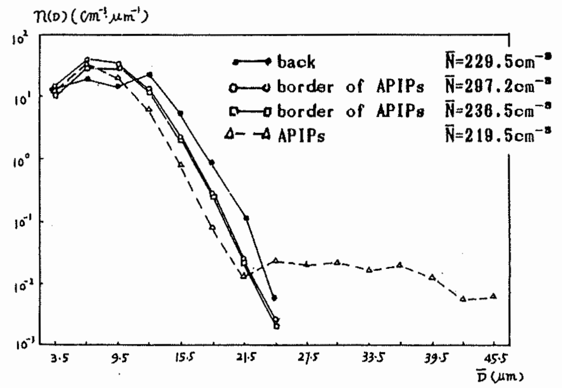

Fig. 2. Cloud droplet size distributions diameter 2-47um, measured by FSSP-100

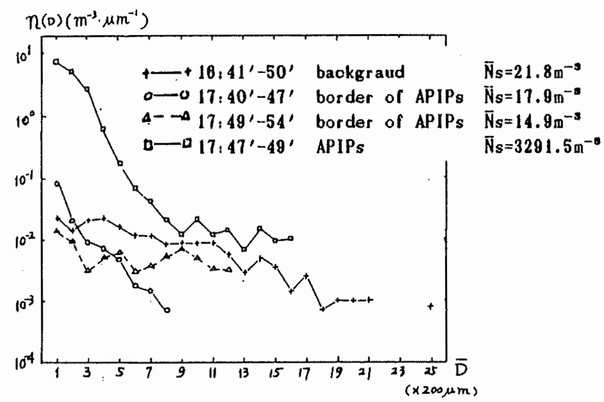

Fig. 3. Snow particles size distributions measured by OAP 2D-P

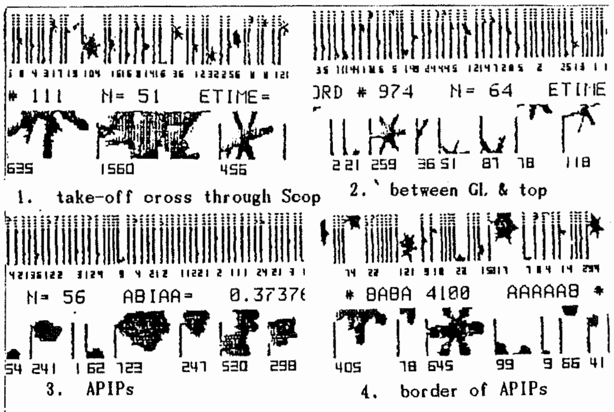

Fig. 4. Solid particles imagery

The ice and snow average concentrations $\bar{N}i, \bar{N}s$ (m^{-3}) and their variations i, s in different layer are listed in Table 2.

Table 2. the $\bar{N}i$ and $\bar{N}s$ at different layer

Flying Period & Situation	$\bar{N}i(m^{-3})$	i	$\bar{N}s(m^{-3})$	s
16:45'-50' between Scop bottom and GL	1326	0.53	35.3	0.32
17:16'-30' between Scop top and GL	1094	0.85	34.6	0.35
17:30'-40'about Scop top	1118	0.76	76.9	0.27
17:40'-47'about Scop top & upper of Scop	2357	1.54	17.9	0.71
17:47'-49' upper of Scop	41194	0.98	3291.5	0.94
17:49'-54' upper & midle on Scop	521	0.17	20.9	0.79

Above GL the ice and snow particles concentrations decrease to $10^{0}m^{-3}$, which shows that no particles drop from the upper layer; between GL and cloud top, along 28km horizontal flying the concentrations do not change obviously, which shows particle distributions are homogenuous spatially. In consideration of particle images, APIPs seem to be relevant to the multiplication processes due to breakup and /or melting.

Based on relation proposed by Holroyd (1985) M=AD and constant particle mass assumption, the dendrite ices and snows and the melted to graupels, graupellikes or drops may be related through the following formula:

$$Dg=1.524Dd^{0.8837}$$

$$Dw=1.08\ Dd^{0.8012}$$

where the Dd, Dg, Dw are dendrite, graupel and water drop diameters respectively. Calculation by above formula indicates that the dentrite in diameter 35-79um,347-797um and 43-111um, 677- 1607 um may be converted into graupel and water drop in diameter 22-47um,200-400um respectively. Large snowflakes may be easily broken up to produce many little particles; but in this case the snowflakes concentration are too small (10^{-1}-10^{-2} m^{-3}) to be increased by order of particle concentration (D>23um) through the breakup and/or melting processes.

4.DISCUSSIONS

A mechanism producing numerous ice particles is Massop - Hallet multiplication process. However, our observations indicate that the background cloud (Scop) is satisfied with the multiplication conditions partly due to absent of graupel particles. Furthermore,when the aircraft flew above cloud top, the large snowflakes and their aggregates may be converted into graupel or graupellike due to heating by aircraft engine exhaust. When the graupes falling in cloud, they can collect the larger cloud droplet firstly; at the sametime, these collected cloud droplet and their assemblage may be splinted from the mother graupel or graupellike to lead to the higher ice and snow particles concentrations and cloud droplet concentration in diameter 23 - 47um increase from $10^{-4}cm^{-3}$ to $10^{-1}cm^{-3}$. These process is accompanied by decrease of the liquid water content and decrease of partly larger cloud droplet. In APIPs region the cloud droplet concentrations in diameter 14-26um decrease from $19.7cm^{-3}$ to $2.8cm^{-3}$ and liquid water content from $0.144g/m^3$ to $0.075g/m^3$ (minimum $0.018g/m^3$), which is a marketly evidence. We calculated the liquid and solid water content and found that its sum were approximately constant (See Table 3).

Table 3. the liquid and solid content at different characterical layer

Flying period	Qw(g/m³) 2-47um	Qi(g/m³) 25-800um	Qs(g/m³) 200-6400um	Sum 2-6400um
16:40-51'	1.44E-1	2.36E-5	1.36E-3	1.45E-1
17:40-47'	1.16E-1	5.41E-4	4.70E-5	1.17E-1
17:47-49'	7.48E-2	4.85E-2	1.06E-2	1.34E-1
17:49-54'	1.05E-1	2.63E-5	3.51E-4	1.05E-1

The aircraft engine exhaust heating are also calculated, which shows that such heating may melt ice and snow with warmer than -15° C temperature.

5.CONCLUSION

A new possible multiplication mechanism - aircraft engine exhaust heating induced breakup and/or melting of ice and snow particles, is proposed by anallysing the airborne PMS probes measurements. This multiplication mechnism will have an effected on cloud microphysical structure and precipitation processes in the warmer than -14° C temperature cloud layer.

6.REFERENCES

Rangno, A. L & P. V. Hobbs, 1983:
J. Clim. Appl. Meteor., 22, 214-232
Rangno, A. L & P. V. Hobbs, 1984:
J. Clim. Appl. Meteor., 23, 985-987
Mossop, S. C, 1984;
J. Clim. Appl. Meteor., 23, 345-347
Vonnegut, B, 1986:
J. Clim. Appl. Meteor., 25, 98-100
Gordon, G. L, & J. D. Marwitz, 1986:
Amer. Meteor. Soc., 61-63
Vali, G, R. D, Kelly & F. Serrano, 1988:
10th International Cloud Physics Conference
Bad Homburg V.D.H., F.R.G., 52-54
Brown, P. R. A & T. W. Choularton, 1988:
10th International Cloud Physics Conference
Bad Homburg V.D.H., F.R.G., 55-57
Holroyd, E. W, 1985:
4th WMO Scientific Conference on Weather
Modification, Honolulu,Hawaii,USA, 195-198

LIQUID AND ICE WATER CONTENTS OF CLOUDS OBSERVED AT SYOWA STATION IN EAST ANTARCTICA

M. Wada

National Institute of Polar Research, 9-10, Kaga 1-Chome, Itabashi-ku, Tokyo 173 Japan

1. INTRODUCTION

Cloud liquid and ice water contents are important for studying the mechanism of precipitation and for obtaining radiative properties of clouds. Supercooled liquid and ice water contents of clouds in cold region such as the Antarctic region connect with the phase change of H_2O between ice and water and relate to formation of precipitation. Smiley et al. (1980) observed clear-sky precipitation by means of lidar at South Pole Station. Saxena and Ruggiero (1985) reported observations of clouds with liquid droplet in the Antarctic coastal area using airplane. However, they did not describe ice particles in the clouds. Platt (1977) reported lidar observations of mixed-phase altostratus cloud in Aspendale, Australia. He described that both layers of ice and liquid particles were found in a cloud from the results of lidar observations. Most of clouds in the Antarctic coastal area would be consisted with liquid and ice particles. Therefore, we tried to measure the water contents of both particles separately, using microwave radiometers and a X-band vertical pointing radar at Syowa Station (69°00'S, 39°35'E) in the East Antarctic area. Moreover, we discussed what situation the phase change from supercooled water to ice was occurred using the data of liquid and ice water contents of clouds. A case study in winter, 1988 is reported in this paper.

2. OBSERVATIONS

Two microwave radiometers and a vertical pointing radar were installed at Syowa Station as main instruments for observing clouds and precipitation in Antarctic Climate Research program started in 1987. Types of snow particles falling ground were observed using a video camera and a microscope in 1988. The specifications of the radar and the microwave radiometers were already reported (Wada and Konishi, 1992; Wada and Yamanouchi, 1992).

The vertically integrated liquid and ice water contents of clouds were obtained from the data of the radiometers and the radar, respectively. The radar echoes from liquid cloud particles can be neglected because we used X-band radar for the observations. Moreover, we rarely had rain at Syowa Station. Therefore, the vertically integrated ice water content can be estimated easily, when we select a relationship between the radar reflectivity factor (Z) and the ice water content (M). Here we used the following equation (Sato, et al., 1981):

$$M = 49 \times Z^{0.9}.$$

On the other hand, the vertically integrated liquid water content can be calculated using the data of brightness temperature obtained by the microwave radiometers.

3. RESULTS

A cyclone approached Syowa Station around July 25, 1988 and snowfall was observed at Syowa Station on July 24 and 25. We here described some results of observations on July 24 and 25. Figure 1 shows the air temperature and the dew point temperature measured at Syowa Station. Both of them showed relatively

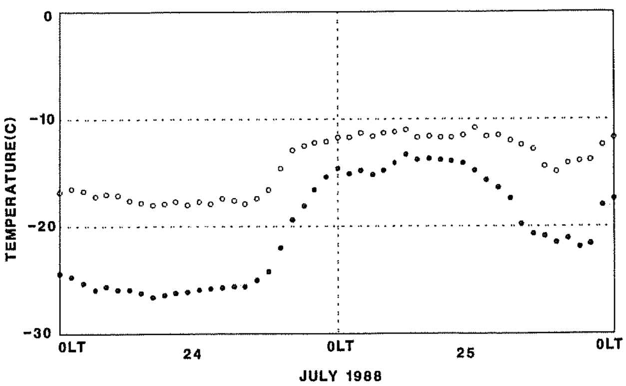

Fig. 1: Air temperature (open circle) and dew point temperature (solid circle) observed at Syowa Station on July 24-25, 1988.

high in the period from 18 LT on 24 to 18 LT on 25. Figure 2 shows the profiles of air temperature at 15 LT on 24 and at 03 LT on 25 obtained by aerological observations. The air temperature below 750 mb level was considerably lower at 15 LT on 24 than at 03 LT on 25. The profile of air temperature at 15 LT on 25 was the same tendency of the profile at 03 LT on 25. It seems that relatively warm air advected the layer below 750 mb level after 15 LT on 24. Video camera observations for snow particles recorded heavy-rimed snow crystals and graupels around 22 LT on July 24.

The vertically integrated liquid and ice water contents on July 24 and 25 are shown in Fig. 3. A peak of liquid water

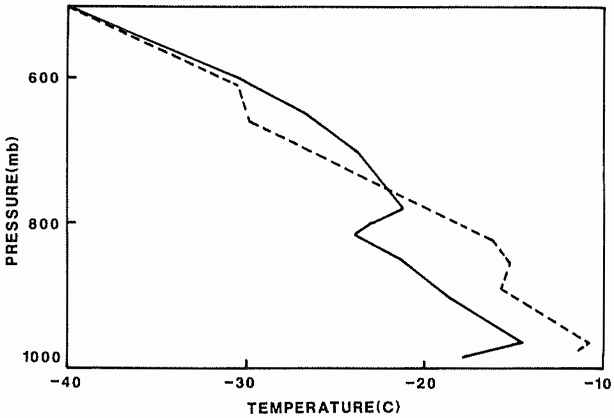

Fig. 2: Profiles of air temperature by aerological observations at 15 LT on July 24 (solid line) and 03 LT on July 25 (broken line).

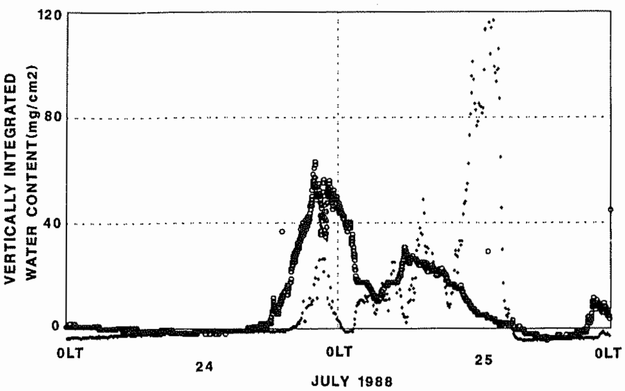

Fig. 3: Vertically integrated liquid (open circle) and ice water (dot) contents on July 24-25.

contents was found around 23 LT on 24 and a large peak of ice water contents was around 13 LT on 25. Figure 4 shows a time-height cross section of the radar echoes (a) and the vertically integrated liquid water contents (b) from 22 LT to 23 LT on July 24. This figure (a) showed convective type echoes. The echo top was lower than about 3 km. The integrated liquid water contents varied in values from 30s to 60s for an hour. On the other hand, Fig. 5 shows a time-height cross section of the radar echoes (a) and the vertically integrated liquid water contents (b) from 12 LT to 13 LT on July 25. The appearance of the radar echoes in Fig. 5(a) was different from that in Fig. 4(a). They seems to be stratiform type echoes. The echo top was higher than 3 km. In this period the integrated liquid water contents hardly varied in values for an hour.

The echo top of most convective type was lower than 3 km from analyzing radar echoes observed at Syowa Station in 1988 and falling snow particles of most convective type of 1988 at Syowa Station were graupels or heavy-rimed snow crystals.

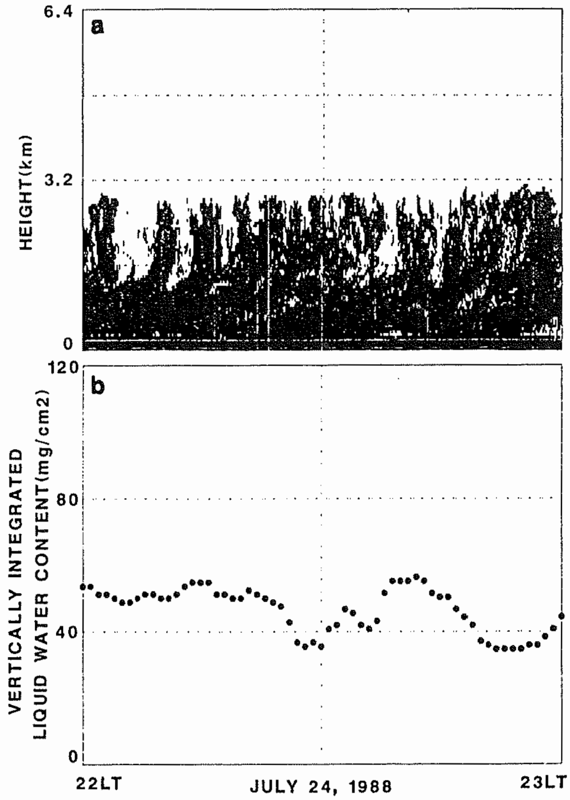

Fig. 4: Time-height cross section (a) made by vertical pointing radar and vertically integrated liquid water contents (b) in the period from 22 LT to 23 LT on July 24.

4. DISCUSSION

It is said that there is a few convective clouds in Antarctica. However, according to the radar observations, we were sometimes able to find convective type radar echoes at Syowa Station. We described the convective type echoes in the case study from July 24 to 25 mentioned above. It seems that since the low layer below 750 mb level became warm after 15 LT on July 24 as shown in Fig. 2, convective clouds, probably early stage clouds, developed in the layer came near to the radar site at 18 LT on July 24 from increasing of the vertically integrated liquid water contents as shown in Fig. 3. Vertically integrated ice water contents began to increase after vertically integrated liquid water contents had increased. Comparing Figs. 4(a) with 4(b), the variation of vertically integrated liquid water contents roughly corresponded to the evolution of radar echoes. That is to say, the increase of ice water contents would induce the decrease of liquid water contents.

From the observation of a vertical pointing radar the evolution of clouds over the radar site cannot be obtained, but the structure of clouds passing the radar site at a moment can be obtained. Therefore, although it is difficult to

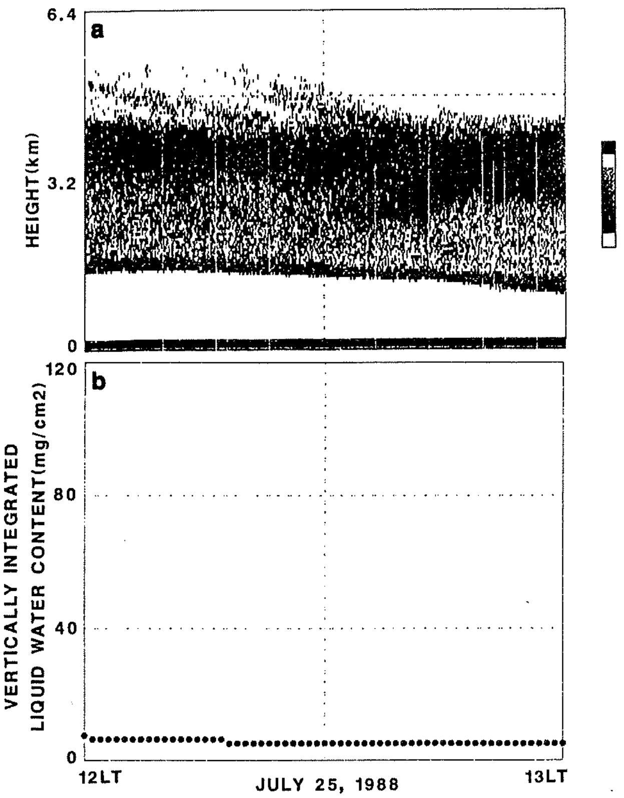

Fig. 5: Time-height cross section (a) made by vertical pointing radar and vertically integrated liquid water contents (b) in the period from 12 LT to 13 LT on July 25.

describe how mechanism ice water contents increased, a following assumption was made; Supercooled droplets lifted higher in the strong convective area of the clouds than in the relatively weak convective area. The higher the altitude is, the colder the air temperature is and the larger the number of aerosols for ice forming nuclei is. Therefore, ice crystals would be formed easier in the strong convective area than in the relatively weak convective area. If ice crystals will be formed, ice crystals increase rapidly due to processes with collision and coalescence between supercooled droplets and ice particles. The clouds in which the phase change from liquid droplets to ice particles mentioned above would be occurring passed over the radar site around 22 LT on July 24, and heavy-rimed crystals and graupels were observed there.

When the stratiform type as shown in Fig. 5(a), the value of the integrated ice water content was very large and the value of the integrated liquid water contents was small. Although snowfall was not observed in the period from 10 LT to 15 LT on July 25, combination of bullets crystals would be formed in the cloud. Because, according to the other cases in which stratiform echo was observed and the echo reached at the ground, main snow particles observed on the ground were combination of bullets crystals from video camera observations. The observation of combination of bullets crystals imply that liquid water was few in the clouds. It can be supposed that the clouds, may be decay stage clouds, in which supercooled liquid droplets had already changed into snow particles and convection of air had not been active passed over radar site in the period from 10 LT to 15 LT on July 25. Echo top of the stratiform type was high, about 5 km height. The phase change from liquid particles to ice particles would have occurred in the clouds which would had been developed into 5 km echo top clouds by convection over sea area before the clouds came near to Syowa Station.

5. SUMMARY

Vertically integrated liquid and ice water contents in the clouds were measured by a vertical pointing radar and microwave radiometers at Syowa Station in Antarctica. We explained the clouds related to two types of radar echoes, one was convective type and another was stratiform type. Moreover, we also discussed what kind of clouds passed over the radar site using the variation data of vertically integrated liquid and ice water contents.

The results of observations are summarized here. In the clouds related to the echoes of convective type there were much liquid water contents. Echo top of the clouds was lower than 3 km height. Heavy-rimed crystals or graupels were observed on the ground in the period. The vertically integrated ice water contents begun to increase after the vertically integrated liquid water contents had increased. At that time it seems that the increase of ice water contents would induce the decrease of liquid water contents. It suggests that the phase change from supercooled droplets to ice particles would occur in the clouds.

On the other hand, in the clouds related to the echoes of stratiform type there was little liquid water contents. However, much ice water contents were observed in the clouds. It suggests that the clouds would be the clouds which had already been matured.

REFERENCE

Platt, C. M. R., 1977: Lidar observation of a mixed-phase altostratus cloud., J. Appl. Meteor., 16, 339-345.

Sato, N., Kikuchi, K, Barnard, S. C. and Hogan, A. W., 1981: Some characteristic properties of ice crystal precipitation in the summer season at South Pole Station, Antarctica. J. Meteor. Soc. Jpn., 59, 772-780.

Saxena, V. K. and F. H. Ruggiero, 1985: Real-time measurements of droplet size distribution in antarctic coastal clouds. Antarct. J. of the US. 20, 198-199.

Smiley, V. N., B. M. Whitcomb, B. M. Morley and J. A. Warburton, 1980: Lidar determinations of atmospheric ice crystal layer at South Pole during clear-sky precipitation. J. Appl. Meteor., 19, 1074-1990.

Wada, M. and H. Konishi, 1992: A study of precipitation in the coastal area of Antarctica as observed at Syowa Station using a vertical pointing radar. Antarct. Rec. accepted.

Wada, M. and T. Yamanouchi, 1992: Liquid water contents and precipitable waters in the atmosphere around the Syowa Station in Antarctica obtained from the data of ground based and satellite microwave radiometers. Proc. Specialist meeting on microwave radiometry and remote sensing applications, in press.

REGIONAL CHARACTERISTICS ON THE RIMING PROCESS IN THE GROWTH OF SNOW PARTICLES

Toshio Harimaya and Naotoshi Kanemura

Department of Geophysics, Faculty of Science, Hokkaido University, Sapporo 060, Japan

1. INTRODUCTION

It is well known that we have a large amount of snowfall during the winter monsoon season in the seaside areas towards the Japan Sea, Japan. The characteristic features of snowfall phenomena in the areas are as follows. Lines of cumulus clouds, referred to as cloud streets or band clouds move from the sea towards the land, parallel to the wind direction. They cause horizontal distribution of snowfall to be band-shaped. Graupel or densely rimed snow crystals then fall near the seaside areas, while lightly rimed or non-rimed snow crystals fall over inland areas (Magono et al., 1966) .

Based on the facts above-mentioned, it is assumed that the riming process is predominant in the growth of snow particles over the seaside areas and another process is predominant over the inland areas. But, quantitative observations have not been conducted about them and studies have not been carried out about their reasons. Recently, Harimaya and Sato (1989) developed quantitative measuring methods to determine the amount of rime on snowflakes. Mitchell et al. (1990), then developed a similar method to that of Harimaya and Sato (1989). Using the method, Harimaya and Sato (1992) observed the amount of rime on snowflakes in the seaside areas and reported that the riming process was predominant in the growth of snow particles over the seaside areas. Then, a similar observation was conducted in the inland areas, likewise and the difference was discussed regarding contribution of riming process to the growth of snow particles over the seaside areas and over the inland areas. In a present paper, they are presented.

2. OBSERVATIONS

Observations were carried out at Iwamizawa located about 40km far from the coastal line in the inland areas of the Ishikari plain, in Hokkaido, Japan, from January to February 1989. The observation variables were as follows; Snowfall intensity measured every one minute, riming proportions by the disassembly method and filter-paper absorption method every ten minutes, the size distribution of snow particles by an optical spectrometer, and general meteorological conditions. Besides, the behavior of the snow clouds over the area was observed by the radar at the Faculty of Science, Hokkaido University. The values of riming proportion by the disassembly method (Harimaya and Sato, 1989) are used in the following analyses and discussions.

3. RESULTS

a. Comparison between the riming process over seaside areas and that over inland areas

Based on the present observational data in inland areas and those in seaside areas by Harimaya and Sato (1992), the difference between both areas can be shown quantitatively regarding

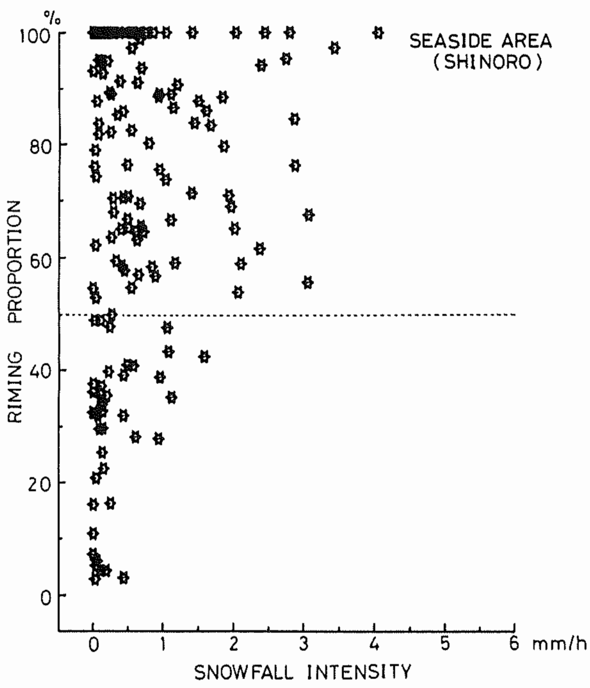

Fig.1 Relationship between snowfall intensity and riming proportion in the seaside areas (after Harimaya and Sato, 1992).

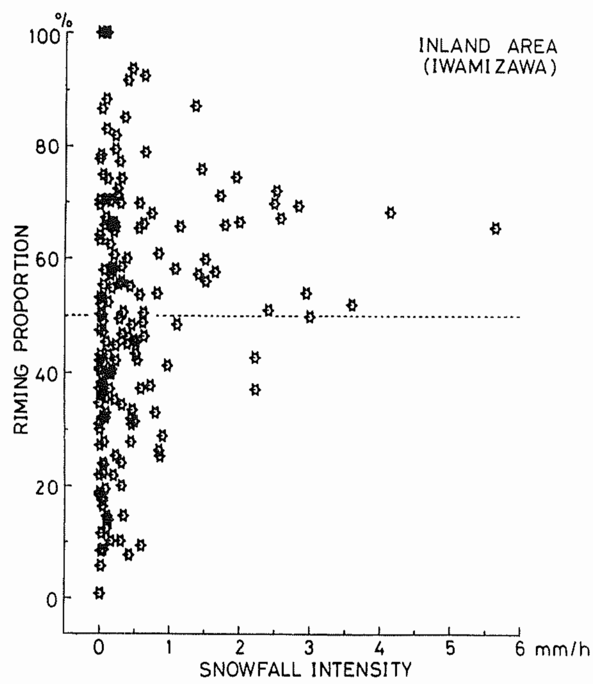

Fig.2 As in Fig.1 except for inland areas.

the contribution of riming process in the growth of snow particles. Figures 1 and 2 show the relationships between snowfall intensity and riming proportion in the seaside areas (Shinoro) and in the inland areas (Iwamizawa), respectively. It is seen that the frequency of snowfall in which the riming process is predominant in snow particle growth (riming proportion ≥ 50%) is about 70% of the total frequency of snowfall in the seaside areas, while it is about 40% in the inland areas. Namely, the riming process contributes to the growth of snow particles over the seaside areas, while it does not contribute to the growth of snow particles over the inland areas so much.

It is seen in Fig.1 that the lower limit of riming proportion tends to increase with the increase in snowfall intensity in the seaside areas. On the other hand, in the inland areas the tendency is similar to that in the seaside areas, but a different tendency is also seen in Fig.2. For example, there are no values of riming proportion more than 80% over the range more than 2 mm/h in snowfall intensity. This means that in the seaside areas the riming process is responsible for strong snowfall intensity, while in the inland areas it is not responsible for strong snowfall intensity too strongly.

b. Relationship between meteorological conditions and riming proportion

The relationship between meteorological conditions and riming proportion was studied in previous papers (Sato and Harimaya, 1990; Harimaya and Sato, 1992). Besides, the relationship between maximum updraft in snow clouds and riming proportion is studied and shown in Fig.3. In the case of downdraft, not updraft, in the whole snow clouds over the surface observation site, open circles are plotted on the position under O m/s on the abscissa in Fig.3. Although the riming proportion varies widely under weak maximum updraft, the lower limit of riming proportion tends to increase with the increase in maximum updraft. This means that the maximum updraft in snow clouds is related to the riming proportion.

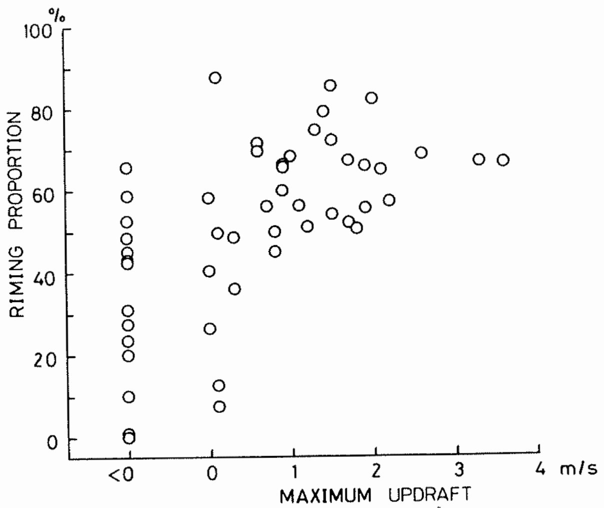

Fig.3 Relationship between maximum updraft and riming proportion.

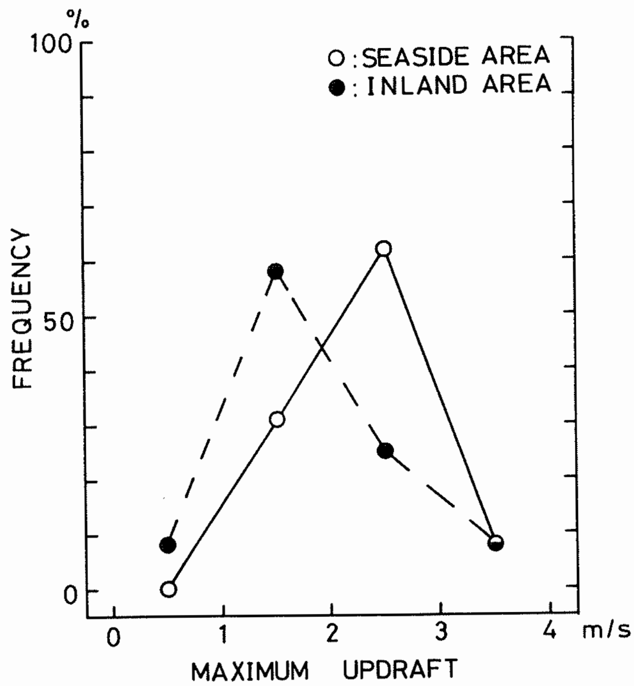

Fig.4 Frequency distribution of maximum updraft in snow clouds.

4. DISCUSSION

In the previous section, it is shown that the riming process contributes to the growth of snow particles over the seaside areas, while it does not contribute to the growth of snow particles over the inland areas too largely. The reason is discussed in this section.

As shown in the previous section that the maximum updraft in snow clouds is related to the riming proportion, the difference in both areas is studied regarding the maximum updraft in snow clouds over the seaside areas and the inland areas. Numerous echo cells were tracked and the updrafts in the echo cells were analyzed every ten minutes. Then, we obtained the values of each maximum updraft over the seaside areas or the inland areas. The frequency distribution is shown in Fig.4. It is seen that there are high frequencies at 2~3 m/s in maximum updraft over the seaside areas and at 1~2 m/s in maximum updraft over the inland areas. Namely, the maximum updraft over the seaside areas is stronger than that over inland areas. Based on the observational results in which the riming proportion increases with the increase in maximum updraft, this fact follows that the riming process dominates the formation of snow particles falling on the seaside area.

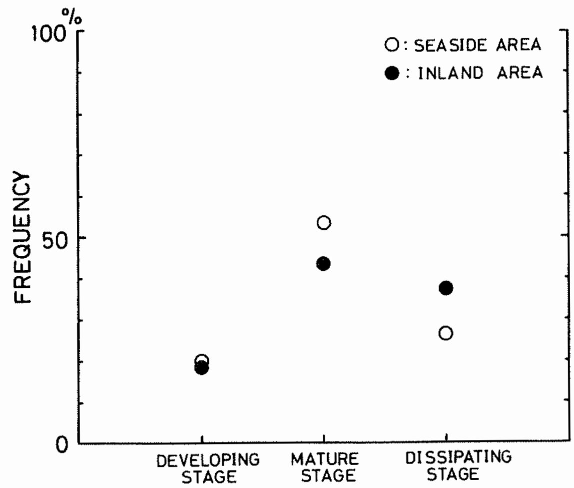

Fig.5 Frequency distribution of growth stage of snow clouds.

Harimaya and Sato (1992) reported that snow particles grow mainly through the riming process in the developing and mature stages, whereas they grow through other processes in the dissipating stage. Next, the difference in both areas is studied regarding the growth stage of snow clouds from the present data and the data by Harimaya and Sato (1992). The result is shown in Fig.5. It is seen that snow clouds over the seaside areas are more than those over the inland areas in the developing and mature stages, and snow clouds over the inland areas are more than those over the seaside areas in the dissipating stage. Based on the observational results that snow particles grow mainly through the riming process in the developing and mature stages, whereas they grow through other processes in the dissipating stage, this fact follows that the riming process dominates the formation of snow particles falling on the seaside area.

5. CONCLUSIONS

It is shown from observation of the riming proportion in snowflakes that the riming process is predominant in the growth of snow particles over the seaside areas and that it is not predominant in the growth of snow particles over the inland areas to a great extent. The reason can be explained by the fact that snow clouds moving over the seaside areas have the features characterized by stronger maximum updraft and higher frequency of developing and mature stages.

REFERENCES

Harimaya, T. and M. Sato, 1989: Measurement of the riming amount on snowflakes. J. Fac. Sci., Hokkaido Univ., Ser. VII, 8, 355-366.

Harimaya, T. and M. Sato, 1992: The riming proportion in snow particles falling on coastal areas. J. Meteor. Soc. Japan, 70, 57-65.

Magono, C., K. Kikuchi, T. Kimura, S. Tazawa and T. Kasai, 1966: A study on the snowfall in the winter monsoon in Hokkaido with special reference to low land snowfall (Investigation of natural snow crystal VI). J. Fac. Sci., Hokkaido Univ., Ser. VII, 2, 287-308.

Mitchell, D. L., R. Zhang and R. L. Pitter, 1990: Mass-dimensional relationships for ice particles and the influence of riming on snowfall rates. J. Appl.Meteor., 29, 153-163.

Sato, M. and T. Harimaya, 1990: The relationship between riming growth of solid precipitation particles and meteorological conditions. Geophy. Bull. Hokkaido Univ., 54, 23-36.

Ice particles in New Mexican summertime cumulus clouds

Alan M. Blyth

Department of Physics and Geophysical Research Center, New Mexico Tech., Socorro, NM 87801, U.S.A.

John Latham

Department of Pure and Applied Physics, U.M.I.S.T., Manchester, M60 1QD.

1. Introduction

During the summer of 1987 the NCAR King Air was used to study the microphysical properties of cumulus clouds which develop over the Magdalena Mountains in central New Mexico near Socorro. Table 1 provides some information about the clouds studied. Cloud base temperatures were in the range 1 °C → 11 °C; about 4.5 → 3.5 km msl. These temperatures are lower by about 20 °C than those of clouds sampled in Missouri by Koenig (1963) for example, and by more than 10 °C than those of Florida cumuli (Hallett et al. 1978).

Time lapse videos indicate that the cloud mass is generally composed of individual thermals which ascend, then decay and sink down to the general cloud top level. The height attained by these thermals gradually increases with time. The entire lifetime of the cloud system often lasts several hours. The aircraft was typically able to sample only a fraction of this time, either because of fuel considerations, or because of the dangers of damage due to graupel, or lightning. Penetrations were made approximately every 5 minutes, chiefly near cloud top. Cloud top altitudes were calculated using the forward-pointing video camera on board the King Air. The maximum cloud top shown in Table 1 is the altitude measured during the study; cloud summits often ascended after the study ended.

The strongest updrafts encountered were typically 5 - 10 ms^{-1}, although Cloud 13 on 21 August was more vigorous. The maximum number of cloud droplets was about 600 cm^{-3} in most cases, somewhat less than is often observed in Montana and Florida cumuli for example (Blyth and Latham 1990; and Hallett et al. 1978). A typical cloud droplet spectrum 1.5 km above cloud base is shown in Figure 1. The spectrum is very broad with many drops of diameter $d < 10\ \mu m$ and $d > 30\ \mu m$.

2. Formation of ice

Most of the clouds were first penetrated when ice was already present. However, ice was first detected during the course of study in seven cases when the summit of the clouds became colder than -10 °C. It is reasonable to assume from this, and the known temperature dependence of nucleation mechanisms, that the formation of ice occurred when the cloud ascended to a temperature colder than -10 °C.

Table 1. Information concerning New Mexican cumulus clouds studied during August, 1987.

Date	Cloud No.	Times of penetrations	Base temp, pres (°C, mb)	Max Top temp (°C)	Range of penetration temp (°C)	Max drop conc (cm^{-3})	Max vertical wind ($m\ s^{-1}$)
8	1	1657-1854	9.0, 670	-13	5.2 → -9.7	598	9.8
9	2	1651-1714	7.4, 665	-10*	7.4 → -3.3	311	1.0
9	3	1739-1923	7.4, 665	-15*	3.4 → -6.9	597	12.0
10	4	1756-1934	10.6, 705	-15	6.6 → -9.3	513	10.5
11	5	1722-1735	6.2, 640	-12	-8.0 → -10.1	586	6.3
11	6	1744-1900	6.2, 640	-15	-9.7 → -14.6	570	5.2
12	7	1849-1900	7.1, 664	-4	3.0 → -2.9	553	5.9
12	8	1903-2021	7.1, 664	-17*	-4.5 → -15.0	573	9.4
19	9	1833-2007	1.0, 598	-16	-8.7 → -13.9	676	8.8
20	10	1851-1918	4.8, 620	-17	-8.4 → -15.3	575	6.6
20	11	1928-2001	4.8, 620	-15	1.6 → -8.6	726	6.8
20	12	2016-2042	4.8, 620	-19	-3.4 → -15.6	665	8.6
21	13	1718-1754	6.0, 648	-13	1.2 → -8.3	713	16.6
22	14	1828-1909	5.0, 655	-19	-11.9 → -16.1	708	10.5
27	15	1703-1724	3.9, 690	-26	-16.5 → -23.6	78	4.7
27	16	1734-1750	3.9, 690	-27	-18.8 → -21.6	484	5.2
27	17	1843-1858	3.9, 690	-16	-9.4 → -11.4	635	5.6
27	18	1900-1920	3.9, 690	-15	-9.3 → -10.3	555	5.6
28	19	1750-1755	6.5, 700	-8	-6.2 → -7.2	420	5.8
28	20	1801-1938	6.5, 700	-13	-3.6 → -11.3	649	14.2

* Estimate

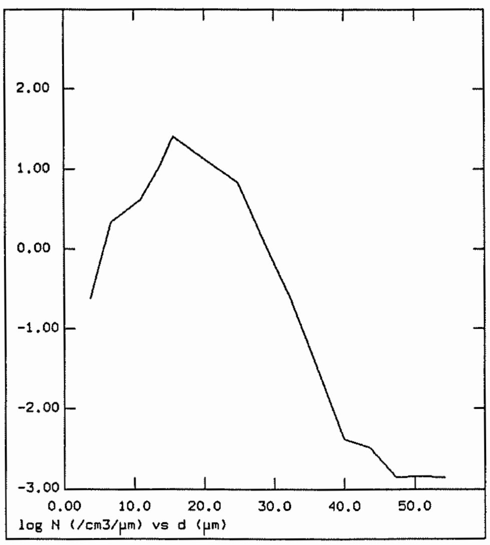

Fig. 1: Cloud droplet spectra measured by the FSSP at the approximate altitude of 1.5 km above cloud base in Cloud 3, 9 August, 1987.

The first ice particles were generally observed in the downdraft so we considered if downdrafts, or the vicinity of cloud top, provides a unique environment for the nucleation of ice, by comparing the time taken for ice crystals to grow by diffusion to observed sizes, to the time available for descent to the observation level from cloud top. In one particular cloud (Cloud 9, 19 August) the average size of pristine particles observed in the downdraft was $\overline{D} \approx 400\ \mu m$. The temperature at the observation level and cloud top was T = -14 °C and $T \approx$ -15 °C respectively. Figure 2 shows the liquid water content, concentration and mean diameter of particles detected by the 2DC, and the vertical and horizontal wind for this penetration. An example of images of the stellar crystals found in the penetration are shown in Figure 3. Slight riming may have occurred, although it is believed that riming does not become significant for stellar particles until their diameter is larger than about 500 μm (Pruppacher and Klett 1980). Using an average vertical wind speed of $\overline{w}$ = -2 m s^{-1} a particle that had formed in the downdraft, or at the then current cloud top, would have had to be transported downwards a distance of about 600 m in order to grow, by diffusion, to the average size, and more than 1 km for the particle to grow to the larger sizes observed (800 μm). Cloud top was *at most* 400 m above, so it is possible to explain how the particles would form in the downdraft, or at cloud top ($T_{ct} \approx$ -15 °C) and grow to the observed average size (400 μm) if the downdraft was weaker than -2 m s^{-1} at higher levels, but it is difficult to explain the presence of crystals with sizes larger than this. Similar calculations were performed for the few other cases where pristine crystals could be identified in the downdrafts. The results suggest that diffusional growth would have had to start in the updraft at about -12 °C, or warmer, and continue as the particle first ascended in the updraft, and then descended to the point of observation in the downdrafts. In other words nucleation commenced, in these clouds, in the updraft at about -12 °C. These results suggest that neither cloud top, nor the downdrafts provide a unique environment for contact nucleation, for example.

Large drops (frozen or unfrozen) of size D > 500 μm were directly observed in several of the cases discussed herein before the formation of ice particles, and their presence can be inferred from low-level radar echoes in several others. Thus, it is likely that large drops play an important role in primary ice nucleation in New Mexican cumulus clouds. Koenig (1963) reported the presence of liquid drops before the formation of ice in Missouri clouds and Willis and Hallett (1991) found large liquid drops in a cumulus cloud over the Bahamas prior to the onset of ice.

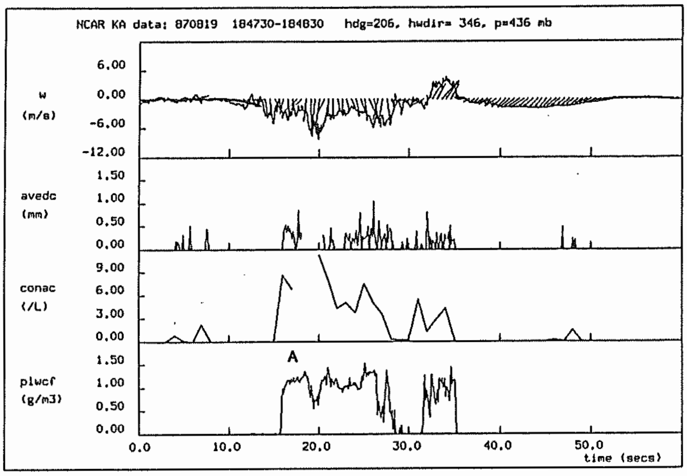

Fig. 2: The bottom three panels from top to bottom respectively, are average size and concentration of particles measured by the 2DC (*avedc* and *conac*), and liquid water content derived from the FSSP (*plwcf*). The uppermost panel is the vertical wind (w) superimposed with wind vectors constructed from the horizontal component along the track of the aircraft and the vertical wind. All graphs are plotted against time: 10 seconds is approximately 1 km of flight. Data are from a penetration made in Cloud 9 on 19 August, 1987 where $T \approx$ -14 °C.

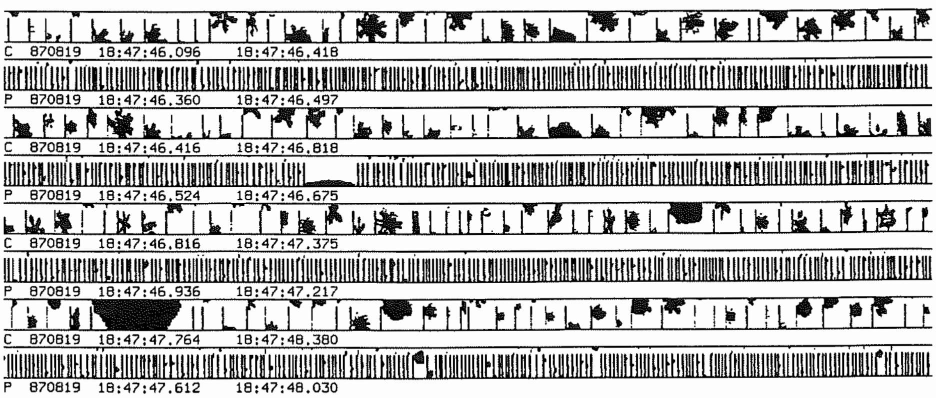

Fig. 3: 2D images from the 2DC and 2DP probes from the region of cloud indicated by **A** in Figure 2. The text under each strip of images refers to the probe, date, and beginning and end time of the images. The distance between the horizontal lines is approximately 800 and 6400 μm for the 2DC and 2DP probes respectively.

3. Concentration of ice

Figure 4 illustrates concentrations of first ice particles plotted against both the temperature at cloud top and the observation level. All the values deviate from the dashed line shown in the figure - the approximate number of particles that would be activated by primary nucleation if ice nuclei were present in concentrations predicted by the relationship suggested by Fletcher (1962). A number of studies have shown that there is fair agreement between the number of ice crystals that have formed from primary nucleation and the numbers of ice nuclei; these are discussed by Mossop (1985) and Cooper (1986). Of particular note is the study by Heymsfield et al. (1979) who found similar concentrations of ice particles and ice nuclei in undiluted updrafts. Figure 4 also shows the geometric-mean of concentrations of ice particles that could be attributed to primary nucleation (Cooper 1986). They are larger than, but within an order of magnitude of the Fletcher predictions. The three lower concentrations of first ice in the New Mexican clouds are similar to the results summarised by Cooper, suggesting that, at least in the 3 cases, the first ice is produced by primary nucleation. Ice nuclei were not measured in this project and so this can only be a suggestion. The largest concentrations shown in Figure 4 may contain a contribution from water drops which were indistinguishable from other types of ice particles.

The cloud maximum concentration of ice particles for all of the cumulus clouds studied during the project are plotted versus temperature in Figure 5. Both the temperature at the penetration altitude and the minimum cloud top temperature up to when the maximum concentration was measured is given in the figure. The number of ice crystals observed was often much greater than expected from primary nucleation (dashed line in Figure 5). This is a familiar result: there have been many reports of ice particle concentrations that are much higher than typical concentrations of ice nuclei (e.g. Mossop 1985; Harris-Hobbs and Cooper 1987; and Rangno and Hobbs 1991).

We found the most likely explanation for the large concentrations of ice particles to be the Hallett-Mossop process of secondary ice crystal production (Hallett and Mossop 1974). Both small and large cloud drops were present, in most clouds, in the temperature range -3 → -8 °C, in cloud regions that also contained graupel. The fact that all the conditions for the process are satisfied does not, of course, prove that it necessarily operates in these clouds. For further clues, we considered those clouds that did not contain high concentrations of ice. Ice concentrations were notably lower in several clouds (Clouds 1, 3, 5, 9, 11, 12, 13, 17, and 20). In four of these cases (Clouds 5, 11, 13 and 17) ice formed as the cloud began to decay, so the aircraft left for a more promising cloud. Fuel was short in two other cases (Clouds 1 and 3), so the study ended just as ice formed. A vertical descent was made to lower, warmer levels of Cloud 12, and the 2DC probe failed during study of the last cloud in the project (Cloud 20).

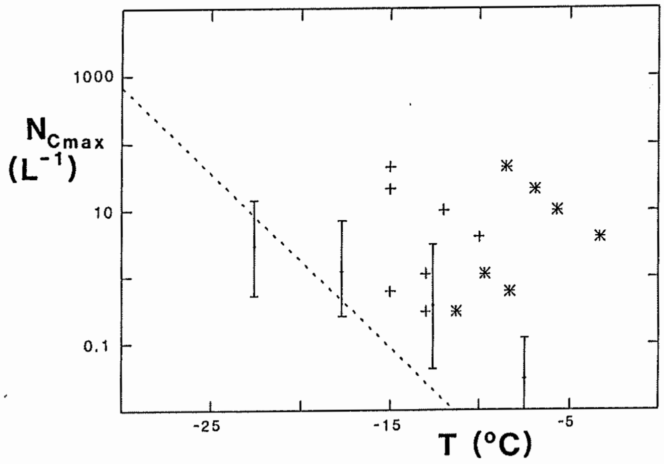

Fig. 4: Maximum concentration of ice particles detected by the 2DC (N_{Cmax}) in the penetration in which ice was first detected, versus temperature, T. The temperature at both cloud top (+) at the time of the measurement and the penetration level (*) are indicated. The points with the vertical bars above and below are taken from Cooper (1986) and the dashed line is the Fletcher nucleation curve.

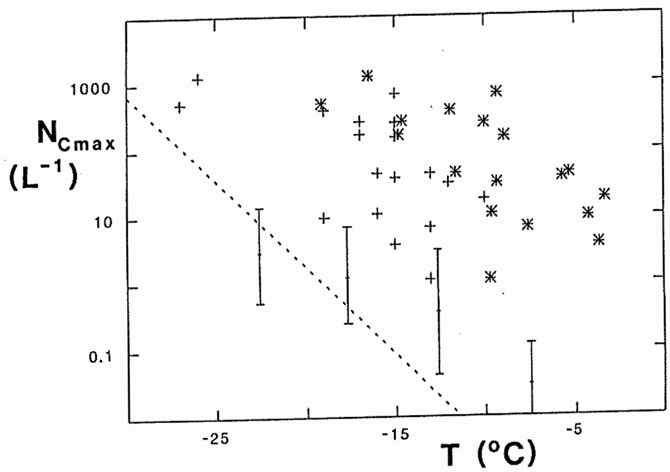

Fig. 5: As Fig. 4, but for maximum concentration of *all* particles measured by the 2DC in all the clouds. The cloud top temperature is the minimum up to the time the maximum concentration was measured.

The one cloud studied on 19 August (Cloud 9) is an important exception. Turrets often ascended to -16 °C, and subsequently descended to a general level near -13 °C. The aircraft did not intentionally avoid any regions of cloud, and the cloud did not collapse at any time during the hour-long study. Yet the maximum concentration of ice particles measured by the 2DC probe was only about 40 L^{-1}. The value is still larger than typical values described by Mossop (1985) and Cooper (1986) (Fig. 5), but is considerably smaller than the concentrations found in many of the New Mexican clouds. For example, concentrations of about 255 L^{-1} and 700 L^{-1} were measured in Clouds 6 and 18 respectively, which had similar cloud tops.

The number of droplets of size $d \geq 24\ \mu m$ in cloud between -3 and -8 °C was considerably lower than on other days in this one case. This is illustrated in Figure 6. The cloud droplet spectrum measured in Cloud 9 was considerably narrower than those measured in other clouds most likely because cloud base was higher than normal on this day (see Table 1). Moisture was in the process of returning to the state of New Mexico after a prolonged dry spell, and the environment was still quite dry.

4. Conclusions

Analysis of data gathered by the NCAR King Air in cumulus clouds in New Mexico has revealed the following results.

- Initial nucleation of ice occurs when the cloud reaches a temperature of between -10 → -12 °C irrespective of whether that temperature is first attained in the updraft or downdraft.
- First ice is generally observed in the downdrafts suggesting that downdrafts transport ice to lower levels.
- Large drops may play an important role in the nucleation process.
- The concentrations of first ice particles to be detected are close to those concentrations measured elsewhere that have been attributed to primary nucleation.
- The maximum concentrations of ice particles often far exceed the concentration expected from primary nucleation. The Hallett-Mossop process is a likely candidate to explain the discrepancy.

Acknowledgements We wish to thank the many people that were involved in the field project, particularly Bill Winn, Al Cooper, Charlie Moore, Jim Dye, Darrel Baumgardner, the late Dan Jones, the pilots of the King Air, and the folks at NCAR involved in gathering and processing the data. We would also like to thank Darrel Baumgardner for help with 2D image processing, Robert Solomon, Dinh Thon That and Shari Colella for their assistance with data analysis. This work was supported under NSF grants ATM-8914116 and ATM-9115694, the USAF under Grant No. F49620-92-J-0020, the Hadley Centre, and NERC under grant GR3/8377.

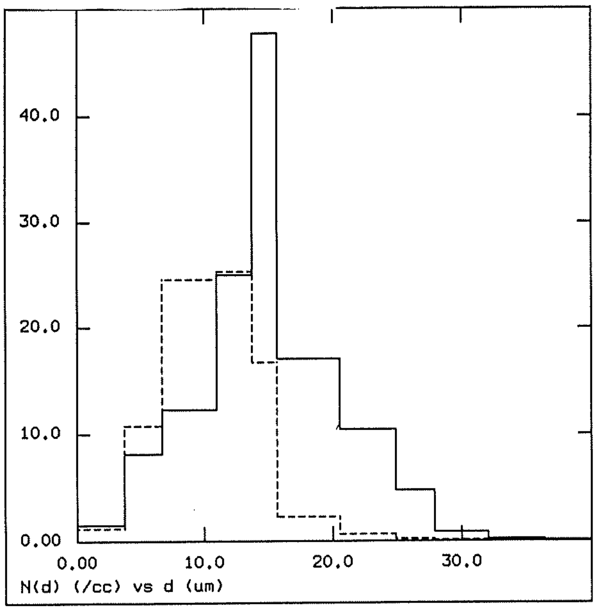

Fig. 6: Cloud droplet spectra measured by the FSSP between temperatures -3 → -8 °C: solid line is the average spectrum for all clouds, other than Cloud 9, 19 August, and the dashed line is for Cloud 9.

References

Blyth, A. M., and J. Latham, 1990: Airborne studies of the altitudinal variability of the microphysical structure of small, ice-free, Montanan cumulus clouds. *Quart. J. Roy. Meteorol. Soc.*, **116**, 1405 - 1423.

Cooper, W. A., 1986: Ice initiation in natural clouds. Pp 29-32 in *Precipitation Enhancement - A Scientific Challenge*. R. R. Braham, Jr., Ed., *Meteor. Mon.*, **21**.

Fletcher, N. H., 1962: *The Physics of Rainclouds*. Cambridge Press. 390 pp.

Hallett, J., and S. C. Mossop, 1974: Production of secondary ice particles during the riming process. *Nature*, **249**, 26-28.

Hallett, J., R. I. Sax, D. L. Lamb, and A. S. Ramachandra Murty, 1978: Aircraft measurements of ice in Florida cumuli. *Quart. J. Roy. Meteorol. Soc.*, **104**, 631 - 651.

Harris-Hobbs, R. L., and W. A. Cooper, 1987: Field evidence supporting quantitative predictions of secondary ice production rates. *J. Atmos. Sci.*, **44**, 1071 - 1082.

Heymsfield, A. J., C. A. Knight, and J. E. Dye, 1979: Ice initiation in unmixed updraft cores in northeast Colorado cumulus congestus clouds. *J. Atmos. Sci.*, **36**, 2216-2229.

Koenig, L. R., 1963: The glaciating behavior of small cumulonimbus clouds. *J. Atmos. Sci.*, **20**, 29-47.

Mossop, S. C., 1985: The origin and concentration of ice crystals in clouds. *Bull. Amer. Meteor. Soc.*, **66**, 264-273.

Pruppacher, H. R., and J. D. Klett, 1980: *Microphysics of Clouds and Precipitation*, Reidel Pub. Co., Holland.

Rangno, A. L., and P. V. Hobbs, 1991: Ice particle concentrations and precipitation development in small polar maritime cumuliform clouds. *Quart. J. Roy. Meteorol. Soc.*, **117**, 207 - 241.

Willis, P. T., and J. Hallett, 1991: Microphysical measurements from an aircraft ascending with a growing isolated maritime cumulus tower. *J. Atmos. Sci*, **48**, 283 - 300.

REQUISITES FOR GRAUPEL FORMATION IN JAPAN SEA SNOW CLOUDS

T. Matsuo, H. Mizuno, M. Murakami, and Y. Yamada

Meteorological Research Institute, Tsukuba, Ibaraki 305, Japan

1. INTRODUCTION

It is well known that the coastal regions facing the Sea of Japan have much snow in winter monsoon season. Sometimes heavy snowfall has done serious damage to the society. A five-year project of "Physics of snow cloud and feasibility of its modification" started in 1988 and being performed by several Japanese national institutes and a few universities to evaluate the potential of snow cloud modification.

Snow clouds over the Sea of Japan produce frequent graupel precipitation as well as snow. Mizuno (1992) showed from a statistical analysis that graupel precipitation amount occupied about 30 % or more of total precipitation in winter seasons. This fact will lead to an idea that there may exist enough supercooled water in snow clouds to enable us to have some chance of snow cloud modification by seeding. However, at the present time, little is known on snow clouds over the Sea of Japan, especially on their inside structures. To our knowledge, only work was done by Magono and Lee (1973), showing a few vertical structures obtained from snow-crystal sonde observations.

Despite that an understanding of graupel formation is a key to snow cloud modification by seeding, there has been little quantitative information on graupel formation in Japan Sea snow clouds. Although qualitative discussion has been made of the formation processes based on the surface observational data (e.g. Harimaya 1976, 1977, and 1983), there still remain various problems unsolved, for example initiation of ice crystals and the subsequent riming. This mainly comes from a lack in in-situ observational data on the inside of snow clouds. The observations by a Hydrometeor Video Sonde (HYVIS) developed by Murakami and Matsuo (1990) and a Hydrometeor Drop Sonde (HYDROS) developed by Murakami et al. (1989) enable us to investigate the inside of the snow clouds where aircraft penetration is sometimes dangerous with icing and thunderbolt. These observations provided a number of vertical distributions of hydrometeors from seven microns to two centimeters in size at various stages of cloud life. Based on these we can draw a more comprehensive picture of the microstructures of snow clouds over the Sea of Japan.

This paper describes graupel formation mechanism in Japan Sea snow clouds with the help of observation and modeling, and then refers to the modification potential of snow clouds by seeding. The modeling without bulk water microphysics focuses on the processes of ice particle initiation and the subsequent growth leading to formation of graupel and snow.

2. BRIEF RESULTS OF OBSERVATION

The observation includes a combination of instruments of dual Doppler radars, a HYVIS, a HYDROS, and surface observation for measuring snow particle properties. The results are briefed below.

a. Features of graupel-including clouds and no precipitation-including clouds

Figure 1 shows schematically the features of four snow clouds observed by the HYVIS and HYDROS. The HYVIS observation provides direct images of hydrometeors of 7 μm-2 cm in clouds together with meteorological elements. The HYDROS has also the same capability as the HYVIS, except for a dropsonde. These observations were carried out in 1989, 1991, and 1992 around Tobishima island located 30 km offshore from the coast. These snow clouds are selected because they give good information on the graupel formation mechanism. Cloud top, temperature region, and snow types are presented in the figure. The shaded regions indicate the layers where supercooled water presents. Precipitation of graupel is involved in 1989, and no graupel exists in 1991 and 1992. The clouds of 1989 show the condition around graupel formation and those of 1991 and 1992 the condition before graupel formation.

The cloud top and depth, the maximum liquid water content (LWC), and the maximum concentration of initial ice particle smaller than 300 μm (N_{ice}) were deduced from HYVIS and HYDROS observation data, and summarized to be shown in Table 1. LWC and N_{ice} are the maximum value throughout the cloud. These clouds were characterized by cloud top temperature of about -19 °C, cloud thickness of about 1.7 km, LWC of about 0.8 gm^{-3} for the stage before graupel formation and of about 0.1 gm^{-3} for the stage around graupel formation, and N_{ice} of several particles ℓ^{-1} for the former stage and of about a

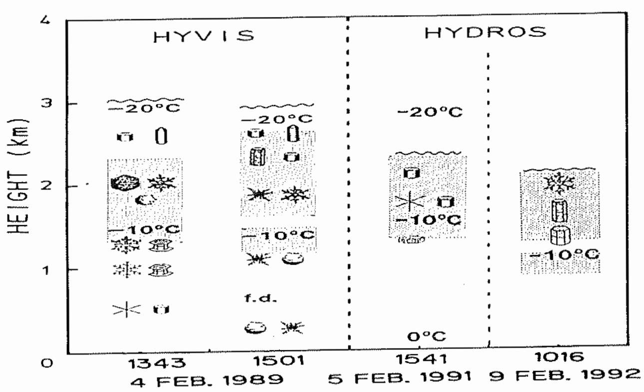

Fig. 1 Schmatic drawing of snow clouds observed by HYVIS (TV sonde) and HYDROS (TV dropsonde).

hundred of particles ι^{-1} for the latter stage. The radar observation and aircraft measurement showed that these clouds had a life time of about one hour. The dual Doppler radar observation also indicated that a snowcloud in 1991 had an updraft of a few meters per second in the maximum, though the Doppler observation was not made of the clouds in 1989.

To obtain more information on the feature of solid snow particles in these clouds, an analysis was made of their type and occurrence frequency. The result demonstrated that most of graupel embryos were ice crystals and not frozen droplets, suggesting little contribution of frozen droplets to graupel formation.

3. DESCRIPTION OF A MODEL

A cloud model is one-demensional, time-dependent with a combination of Lagrangian and Eulerian schemes. The ice particle initiation and the subsequent growth are dealt with by Lagrangian scheme and the cloudy environment by Eulerian scheme. The growth and the drift of ice particles generated by ice nuclei activation and freezing of droplets are traced one by one in Lagrangian manner so that various quantities of individual ice particles, say size, mass, density, etc., are continuously obtained with time. The cloudy environment includes temperature, water vapor density, and liquid water content. Dynamics is fixed and linkages among microphysics, thermodynamics, and dynamics are taken into consideration except for the feedback on dynamics.

The cloud model is a single cell of 2km deep with a 10m grid interval, -20℃ at the cloud top with initial lapse rate of 6℃km^{-1} and prescribed updraft changing with time. The updraft is assumed to be a parabolic function of height with the maximum in the middle of the cloud and zero value at the cloud top and base. In addition, the updraft is assumed to change linearly with time taking maximum at half time of life time span of one hour. No consideration of warm rain formation process is made since there was no direct observational evidence for raindrop formation in the cloud.

No.	Case	Type	Stage	Ttop	Depth	LWC	Nice
				°C	km	g/m3	/l
1	1343LST 4 FEB 1989	I	A	-20	2.2	0.1	40
2	1501LST 4 FEB 1989	I	A	-21	2.1	0.1	200
3	1541LST 5 FEB 1991	I	B	-17	1.2	0.6	5
4	1016LST 9 FEB 1992	I	B	-16	1.2	0.9	5

Table 1 Snow cloud characteristics observed by HYVIS and HYDROS. Type I denotes an isolated cloud, stages A and B around graupel formation and before it, and Ttop cloud top temperature, Depth cloud thickness, LWC liquid water content, and N_{ice} concentration of initial ice crystals below 300 μm in size.

In the model, initial ice crystals, here 10 μm in size, grow by deposition and riming first to become rimed particles and finally to reach graupel, if favorable. The density of growing ice particles varies during their growth period between the densities of unrimed ice crystal of 0.1 gcm^{-3} and graupel of 0.3 gcm^{-3}. The densities of unrimed crystals and graupel are estimated according to Pruppacher and Klett (1978) and Maruyama (1968), assuming that they are spherical. The ice particles are divided into four types : snow of 0.1-0.12 gcm^{-3} (S), light rimed snow of 0.12-0.15 gcm^{-3} (RS), heavy rimed snow of 0.15-0.28 gcm^{-3} (RS), and graupel of 0.28-0.3 gcm^{-3} (G).

4. THE RESULTS OF MODELING AND DISCUSSION

Figure 2 shows a time change in vertical profile of number concentration of three types of particles at various stages in the evolution of cloud, for the maximum updraft of 200 cms^{-1}. The level are indicated by distance from the cloud top. Rimed particles (RS) are formed after 10 minutes and are accumulated in the upper part of cloud. The number of snow (unrimed or slightly rimed ice crystals) (S) decreases gradually with time through a process from unrimed to rimed snow conversion by riming. The total number concentration of snow (S) and rimed snow (RS) in the upper part of cloud is about several particles per liter, in accordance with the result of observation before graupel formation (see N_{ice} in 1991 and 1992 in Table 1). The liquid water content (LWC) gradually increases throughout the cloud with time to reach to about 1 gm^{-3} which is close to the maximum value of 0.9 gm^{-3} observed before graupel formation. The graupel formation occurs at 40 minutes after cloud formation in the upper part of clouds at a concentration of about 10^{3} m^{-3}. LWC in that region is reduced a little due to riming of graupel and at 60 minutes it is reduced to zero in entire cloud due to active

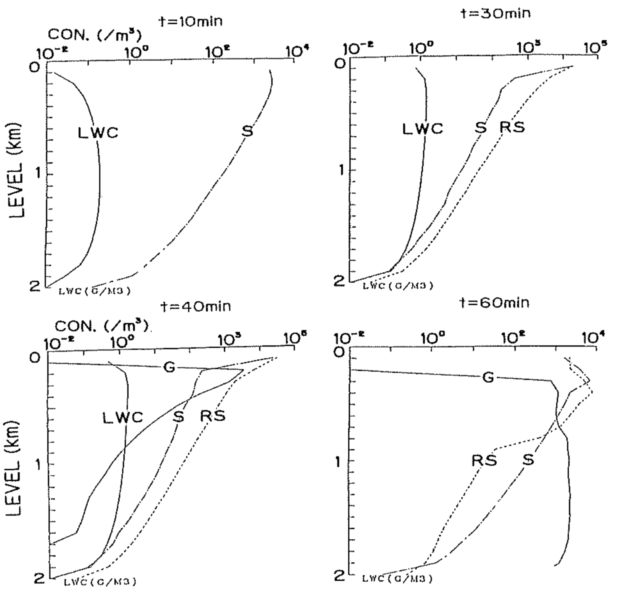

Fig. 2 Change in vertical distribution of snow particle number concentration with elapsed time after initiation of cloud. S: initial ice crystals with non riming or slight riming, RS: rimed snow with moderate and heavy riming, G: graupel, and LWC: liquid water content.

riming of graupel. The size distribution of solid particles in graupel generating layer at 40 minutes when graupel formation just starts was obtained by this simulation to be described as follows. Below 200 μm, all particles were unrimed, showing the relative importance of deposition process for ice crystals below 200 μm. Above 200 μm the riming became relatively important to form light, heavy rimed snow and graupel. The size distribution became broader in the order of unrimed, light rimed, and heavy rimed snow. Heavy rimed snow and graupel of about 2 mm were produced at a concentration of about 10^3 m^{-3}. The unrimed and light rimed particles <400 μm (initial ice crystals) existed at a concentration of about 10^3 m^{-3} in total, in disagreement with the observed number concentration of about 10^5 m^{-3} (see N_{ice} in 1989 in Table 1). At the present time, there seems to be various reasons for this: variation in coefficient in conventional formulas of Fletcher (1962) and Bigg (1952) in application to the snow clouds, intervening of some secondary ice crystal multiplication processes like Hallet-Mossop process (1974). Much more observation and laboratory experiment are needed in this respect.

a. The effect of LWC on graupel formation

A simulation is carried out to make various conditions of liquid water contents in the model cloud. The produced liquid water content is controlled by removing liquid water from the cloud using an entrainment process at a constant rate with respect to time. The results are summarized to be shown in Fig. 3, indicating the dependence of graupel formation on the liquid water content . The LWC is shown for the maximum value experienced in the cloud evolution. Only snow occurs below LWC of 0.4 gm^{-3} and above the value graupel is formed. It is interesting to know that there exists a certain value of LWC with respect to graupel formation. Since the model cloud is made referring to snow clouds over the Japan Sea, it is considered that graupel formation in Japan Sea snow clouds would occur under the condition of above this value of 0.4 gm^{-3}.

b. The effect of droplet size on graupel formation.

The time required for the onset of riming and graupel formation could be affected by the collection efficiency of rimed particles for supercooled droplets. The collection efficiency of a disk by Ranz and Wong (1952) is used over the entire period of growth. Similar run is conducted with varying the droplet size from 5 to 50 μm in diameter. For simplicity, droplet size is adopted to be mono-disperse. In fact it has some size distribution and this treatment may give some error to the result. However, it still could provide some insight on the effect of droplet size on graupel formation. Figure 4 shows the dependence of graupel formation on the size of droplets. The critical size exists around 10 μm in diameter to discriminate between snow and graupel. Below this size, riming process becomes inactive to form only snow. For the droplets above 10 μm active riming takes place to form graupel. This result agrees with the fact that water droplets of 20 μm in diameter were predominant in the graupel generating layers.

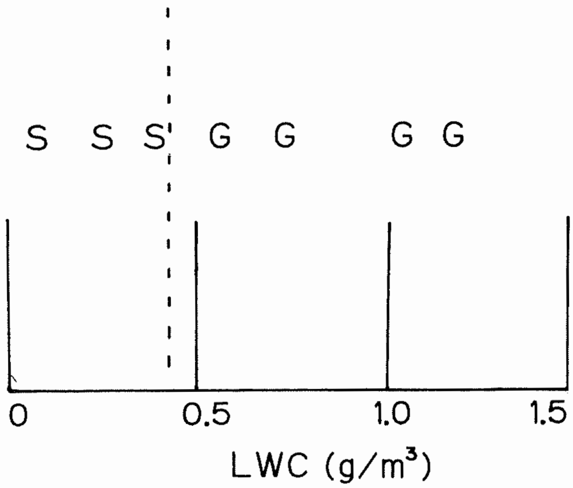

Fig. 3 Dependence of snow and graupel formation on liquid water content. S: only snow formation and G: graupel formation including snow. A vertical dashed line indicates a certain value of LWC discriminating between snow and graupel formation.

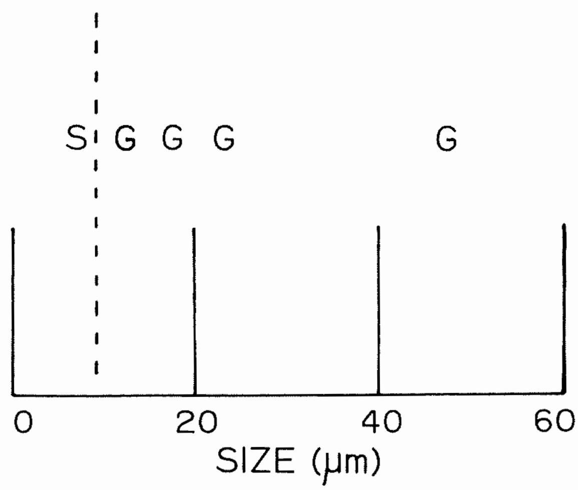

Fig. 4 Dependence of snow and graupel formation on supercooled droplet size. S: only snow formation and G: graupel formation. A vertical dashed line shows a certain size discriminating between snow and graupel formation.

c. The effect of ice generation rate on graupel formation

What happens as the ice generation rate increases? This problem is important not only to elucidate the formation mechanism of snow and graupel but also to estimate the potential of snow cloud modification by seeding. The results of seeded cases are shown in Figs. 5 and 6 (compare with the normal condition at 40 minutes in Fig. 2). Figure 5 shows an example of the results for moderate seeding in a specific layer of the cloud. Moderate seeding means compatible seeding with natural case. Artificial graupel is formed at 500 m level above the seeding layer where continuous seeding is done from the beginning of cloud formation. This suggests that an increase in graupel is anticipated by moderate seeding. Figure 6 shows an example for heavy seeding 10^5 times the natural case throughout the whole cloud from the beginning. Graupel and liquid water disappear, and unrimed snow happens at a great number of concentration of 10^6-10^7 m^{-3} and with smaller size below 500 μm (not shown here). This result suggests that the suppression of snowfall could take place by heavy seeding because small ice crystals with low fall velocity would be subjected to diffusion or evaporation before reaching the ground. In addition, the redistribution of snowfall is anticipated to the lee side area due to strong horizontal wind. This could occur due to the fall velocity difference between rimed (including graupel) and unrimed snow.

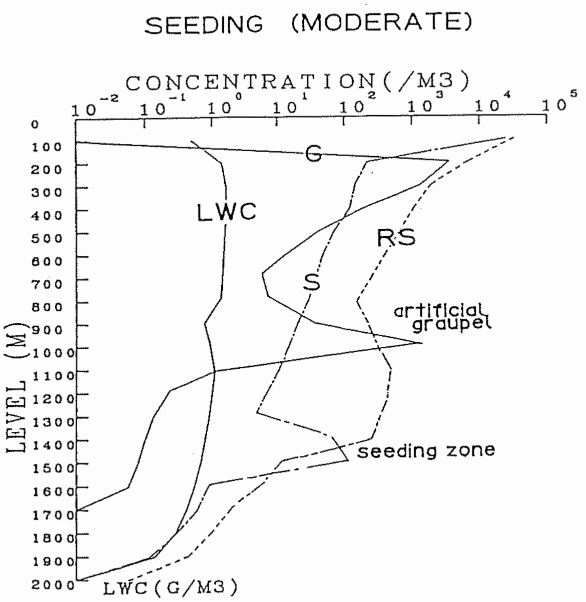

Fig. 5 Vertical distribution of ice particles for moderate seeding at 40 minutes.

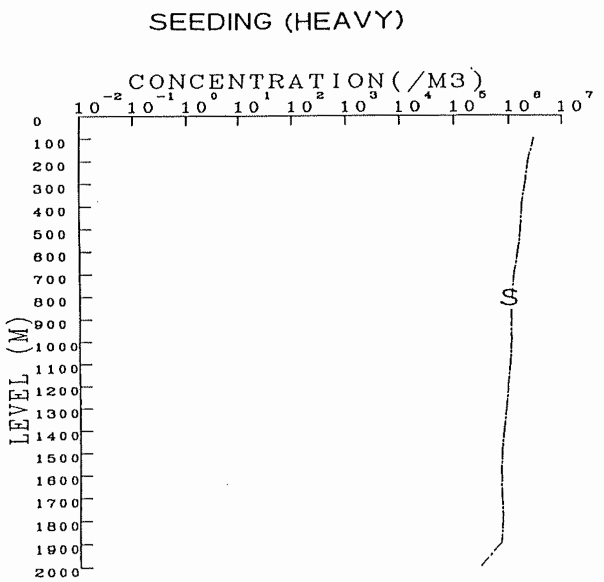

Fig. 6 Same as Fig. 5 except for over-seeding throughout a cloud.

5. CONCLUDING REMARKS

Requisites for graupel formation in the Japan Sea snow clouds were investigated through observational and theoretical studies. In addition, the modification potential of the Japan Sea snow cloud by seeding was examined with modeling. The results are summarized as follows.
1) Almost all graupel embryos in the snow clouds appeared to be ice crystals.
2) Graupel generation relies on liquid water content and droplet size. With respect to the Japan Sea isolated snow clouds of about an hour in life time, graupel formation needs over 0.4 gm^{-3} in maximum content and over 10 μm in droplet size.
3) There is some possibility of snow cloud modification by seeding. Moderate seeding could enhance snowfall amount and heavy seeding suppress snowfall. The seeding could cause change in snow forms and their fall speeds, leading to redistribution of snowfall area due to strong horizontal wind. These hypotheses of the modification should be subjected to test in the future field experiment by cloud seeding.

REFERENCES

Bigg, E. K., 1953: The supercooling of water. Proc. Phys. Soc. London, B66, 688-694.
Fletcher, N. H., 1962: The physics of rain clouds. Cambridge Univ. Press, London, 390pp.
Harimaya, T., 1976: The embryo and formation of graupel. J. Meteor. Soc. Japan, 54, 42-51.
Harimaya, T., 1977: The internal structure and embryo of graupel. J. Fac. Sci., Hokkaido Univ., Ser. VII, 5, 29-38.
Harimaya, T., 1983: A further study on the internal structure of graupel. J. Fac. Sci., Hokkaido Univ., Ser. VII, 7, 227-238.
Hallett, J. and S.C. Mossop, 1974: Production of secondary ice particles during the riming process. Nature, 249, 26-28.
Magono, C. and C.W. Lee, 1973: The vertical structure of snow clouds, as revealed by "Snow Crystal Sondes". part II. J. Meteor. Soc. Japan, 51, 176.
Maruyama, H., 1968: On the conical graupel and its density. Pap. Meteor. Geophys., 19, 101-108.
Murakami, M. and T. Matsuo, 1990: Development of Hydrometeor Videosonde. J. Atmos. Oceanic Tech., 7, 613-620.
Murakami, M., T. Matsuo, H. Mizuno, and Y. Yamada, 1989: Development of Hydrometeor Dropsonde. Proc. Meeting of Japan Meteor. Soc. Tokyo (Spring), 55, 161p (in Japanese).
Mizino, H., 1992: Statistical characteristics of graupel precipitation over the Japan Islands. J. Meteor. Soc. Japan, 70, 115-121.
Pruppacher, H.R. and J. D. Klett, 1978: Microphysics of clouds and precipitation. Reidel Pub. Com. Holland, 38p.
Ranz, W.E. and J.B. Wong, 1952: Impaction of dust and smoke particles on surface and body collectors. Ind. Eng. Chem., 44, 1371-1381.

PRECIPITATION PROCESSES IN MOUNTAIN CUMULONIMBUS OVER THE ASIR REGION OF SAUDI ARABIA

Gabor Vali

Dept. Atmospheric Science, University of Wyoming, Laramie, WY 82071, U.S.A.

1. INTRODUCTION

The physics of precipitation evolution in different types of clouds is of interest for developing an understanding of the basic elements underlying those processes. Differences among cloud types have a number of important consequences for water resource, global climate change and other questions.

While empirical data for mid–latitude continental clouds have been collected for many decades, and some data are also being obtained in tropical clouds, the least well–known are sub–tropical cloud systems. The low frequency and small extent of those clouds partly justifies that situation. Yet, there are sub–tropical regions with much greater than average cloud frequency, whose study is of general as well as of local interest.

The southwest corner of the Arabian Peninsula is an area of unusually high cloud frequency. A steeply rising mountain range runs parallel to the Red Sea coast. After a coastal plain of about 70 km width, the range rises to over 2000 m within about 30 km. The slope to the northeast is more gradual, forms a plateau and then continues to the Rub–al–Khali desert.

During the spring months, lines of convective clouds develop over the mountain range over 70% of the days. A field study was organized in 1990 to examine these clouds. The study was initiated and sponsored by the Kingdom of Saudi Arabia, and was coordinated by the World Meteorological Organization. The motivation for the field study was to explore the possibility of increasing rainfall in the area by cloud seeding. Preliminary examinations of that possibility (Warner, 1976, 1977) indicated some potential, based on the high cloud frequency and the apparent inefficiency of precipitation development.

2. SACPEX–90 FIELD OBSERVATIONS

The study area extended on either side of the mountain ridge–line, from 20 to 150 km to the northwest of the town of Abha (18°N, 42°E). Isohyets are practically coincident with the terrain contours. Yearly maxima along the ridgeline reach 500 mm, minima along the coast and to the east fall to <50 mm. Over half of the annual total falls in the months of January through May. The variability of rainfall is very high: March precipitation in Abha ranges from 2.5 to 258 mm within 16 years of record.

The 1990 field observations utilized the King Air 200 research aircraft of the University of Wyoming, a mobile radar unit operating at 5 mm wavelength, a portable radiosonde and tethersonde unit, METEOSAT images, and synoptic weather, precipitation and radiosonde stations. The study period extended from April 20, 1990 to May 5, 1990.

3. CLOUD FORMATION

Apart from the very infrequent mesoscale cloud systems, which are associated with incursions of the far ends of fronts, the dominant cloud forms are cumulus congestus and cumulonimbus overlying the mountain crest. Clouds form by mid–morning and decay around sunset.

Cloud base and top heights: Cloud bases are different on the two sides of the mountain crest. Cloud bases are lowest, usually well below the altitude of the crest, on the coastal side of the range (+ 15°C , 820 mb, 14 g/kg). On the inland side, cloud bases are at least equal to, or are slightly higher than the altitude of the crest, and are near the top of the mixed layer (+ 2°C , 610mb, 7 g/kg). Cloud tops vary systematically, from the deepest clouds (tops usually reaching the tropopause) over or near the ridgeline, to clouds of lesser depth on either side of that line.

Potential temperatures: There are considerable differences in temperature/humidity parameters between the coastal plain and the plateau. Typically, the potential temperature is higher on the plateau than in the free atmosphere at the same pressure level on the coastal side of the range. However, because of lower humidity, the equivalent potential temperature readings over the plateau are lower (340°K) than on the coastal plain (346°K). The equivalent potential temperature values observed in clouds over the crestline are also lower (often by > 10°K) than the values observed over the Red Sea, or directly at the coast.

Wind fields: Characteristically, pressure gradients are weak, wind speeds are light (usually < 10 m s^{-1}) up to the tropopause, and wind fields are often not steady. There is often a notable difference between the direction of flow on either side of the ridgeline. The depth of these differing flows extends upward to the vicinity of the 600 mb level, at least early in the day, before deep convection develops.

Boundary layer over the Red Sea: Soundings taken with the aircraft to the surface, just off the coast, near mid–day, indicated the presence of strong inversions 200–300 m above the surface. These inversions limit high humidity regions to just above the sea. The inversion does not extend over land, i.e. the cold surface air forms a pool over the sea. The boundary layer over the water was found to be associated with stronger winds than at higher levels (15 m s^{-1} vs. 5–8 m s^{-1}), possibly also with a slight change in direction. The coast–perpendicular component of this wind is the main factor determining the transport of moisture inland.

Cloud formation: The following qualitative description of the process of cloud development can be assembled from the studies conducted so far. Heating of the land surface, on both sides of the mountain, but to a more important degree on the inland side, initiates a change in the flow of the area. Above the surface layer over the Red Sea, from about 300 m to about 1 km MSL, the component of flow perpendicular to the mountains strengthens. To a lesser degree, air from the boundary layer over the water also moves inland in the traditional sea–breeze effect. On the East side of the mountains, flow is also upslope, at least near the surface.

Because of the higher moisture content of air on the coast side, convective clouds develop there first. At that point, vertical transport within the clouds becomes an important part of the dynamics of the situation. Vertical fluxes are large compared to the horizontal ones.

The vertical acceleration associated with cloud formation strengthens the convergence near the ridge–line. This is exhibited by the presence, at times, of a deep (1+ km) layer of upslope winds over the plateau. The major clouds appear to have a mixture of air from either side of the ridge.

Once precipitation begins to fall, the downflow of cooler air initiates downslope flow on the inland side of the ridge, and helps to trigger further cloud formation, albeit in relatively dry inland air.

4. CLOUD STRUCTURE

Updrafts are weak to moderate. The maximum values observed during the research flights exceeded 15 m s^{-1}, but only over small (< 1 km) regions. Even though the flights were made emphasizing updraft regions, as evidenced by the fact that 14% of the total flight time in clouds was in updraft regions with > 2m s^{-1} velocity, in only 5 % of those updraft regions did the vertical velocity exceed 10 m s^{-1}. Thus, 0.7% of the cloud sample had > 10 m s^{-1} updrafts. The greatest frequency of high updraft velocities was recorded during two flights; these two flight provide half of all the sample for updrafts > 10 m s^{-1}.

As revealed by photographic records, and by the duration of cloud penetrations, intense convective clouds tend to have tall and narrow proportions, perhaps 1:3 to 1:5 width to height ratios. This fact is consistent with the absence of strong surface fronts, or other forcing, to provide large–scale organization. The mountain slope is triggering the convection, and perhaps small–scale topographic features provide additional impetus to convection. but these forcing effects are, apparently, not sufficiently strong to yield well–organized steady updrafts.

The cumulonimbi were observed to have 'multicell' character. Feeder cells develop on the south–west, coastal sides of the storms. Feeder cell updrafts are of small extent (1–5 km) and feeder cell lifetimes, before visibly merging with the main mass of the storms, are about 10 minutes. This description is consistent with conditions generally associated with multicell storms, i.e. large values of R (bulk Richardson number), due to small wind shear.

The diameters of storm cells, as revealed by the radar echoes, are around 10 to 15 km; the spacing of cells, in the main line of cells along the ridge, is less than two cell–diameters. Echoes away from the center of the line tend to be much more scattered. Another notable feature of the Cb's is that there is only moderate anvil development.

5. CLOUD MICROPHYSICS

The concentrations of cloud droplets range between 500 and 1000 cm^{-3}. This indicates that airmasses over the Asir are not of 'maritime' characteristics, as the proximity of the Red Sea might suggest. Air masses bear continental influences, both from more distant sources (Africa and Rub–al–Khali), and from local dust lifted into the clouds. (The origins, and characteristics of the aerosol and CCN in the lower troposphere of the region have not been directly examined.)

Droplet concentrations in clouds of the coastal and inland regions show no significant differences.

Cloud droplet spectra were relatively narrow. Mean and maximum droplet diameters were, in an example of strong updrafts (5–9 m s^{-1}) 14 and 26 μm at 1.5 km above cloud base, and 17 and 28 μm 3.4 km above cloud base. Maximum liquid water contents reached only about 1 g m^{-3}.

The narrow droplet spectra, and the absence of large drops above the 0^{o}C level, indicate that the coalescence process makes no significant contribution to the development of precipitation.

The dominant mechanism of precipitation formation is via the ice phase. This can be readily appreciated by even causal observations of precipitation near 0^{o}C : large concentrations of graupel particles and crystals are found. The concentrations of ice particles can reach over 100 L^{-1} at those levels. Concentrations to over 1000 L^{-1} were not uncommon at temperatures of -15^{o}C and colder.

The vertical profiles of ice concentrations revealed no evidence that large concentrations develop preferentially in the vicinity of the -5^{o}C level, and neither are crystals dominantly needle types at those levels. The absence of these features indicate that the Hallett–Mossop secondary ice generation process was not significant. This is in accord with the paucity of large cloud droplets.

Ice concentrations in the upper regions of growing clouds, likely to be associated with primary nucleation, were quite low: 0.11 L^{-1} at -11.2^{o}C ; 0.09 L^{-1} at -8.2^{o}C ; <1 L^{-1} at -18^{o}C ; 0.01 L^{-1} at -5^{o}C ; 0.08 L^{-1} at -9^{o}C ; 0.03 L^{-1} at -9^{o}C . Each datum is a specific instance; samples are from three different days.

Since no evidence points to unusually high concentrations of ice nuclei in the region, it appears that the large concentrations of ice particles observed in most clouds originate via secondary generation, and that process is not the Hallett–Mossop process.

The region is well known for frequent graupel showers. Rainfall often exceeds 100 mm hr^{-1} intensity.

5. SUMMARY

The characteristics of the cloud systems, and of the prevailing precipitation processes in the Asir region were found to differ from general expectations in a number of ways.

The formation of deep convective clouds over the mountain range appears to be the result of a combination of convergence induced by the terrain, and a slight sea–breeze effect from the Red Sea. The role of the latter is important in the initiation of the convection, but contributes little to its maintenance and moisture supply. Cloud bases and depths are significantly different on the two sides of the ridgeline.

Clouds are dynamically weak, and can be described, in spite of their relatively large size, as aggregates of thermals, rather than organized storms. Mixing with the environment reduces cloud liquid water contents to small fractions of the adiabatic values, and is the limiting factor for cloud development.

Cloud droplet concentrations are indicative of continental, rather than maritime CCN populations. Precipitation forms via the development of high concentrations of ice particles. Indications are that some secondary ice generation is active, other than the Hallett–Mossop rime splintering process.

The combined result of these cloud processes is that small intense showers develop and clouds are regenerated over many hours. The severe degree of mixing, weak dynamical forcing and effective ice generation process, present important challenges for fuller, quantitative descriptions of these clouds.

More detailed descriptions of these results are given by Vali (1991).

Acknowledgements:

The initiative and support of the Meteorological and Environmental Protection Administration (MEPA) of the Kingdom of Saudi Arabia, and the management of the project by the World Meteorological Organization made this work possible. Saudi meteorologists, and University of Wyoming personnel contributed the major part of the field effort.

References:

Vali, G., 1991: Aircraft studies in the Asir. Report AS163, Dept. Atmos. Sci., Univ. of Wyoming, 131 pp.

Warner, J., 1976 and 1977: The potential for cloud seeding for rain enhancement in Saudi Arabia. Reports CP 138 and 177.

HIGH RESOLUTION OBSERVATIONS OF PRECIPITATION WITH A VERTICALLY POINTING RADAR

Frédéric Fabry, Geoffrey L. Austin* and Abnash Singh

McGill Weather Radar Observatory
Montreal, Canada

*Current affiliation: Department of Physics, University of Auckland, Auckland, New Zealand

1. The McGill vertically pointing radar

For the last three years, the McGill Radar Weather Observatory has operated a small vertically pointing radar for precipitation studies. The radar, whose characteristics are listed in Table 1, is anything but state of the art. Its main feature is its pulse size, 50 ns, which permits reflectivity measurements with a resolution of 7.5 m in the vertical. The video signal of the radar is digitized by a high-speed digitizer on board of a micro-computer which is used for display and archiving.

Table 1 - Radar specifications

Wavelength	3.2 cm
Peak Transmitted Power	25 kW
Pulse Length Used	0.05 µs
Pulse Repetition Frequency	1300 Hz
Antenna Size	1.2 m
Beam Width	2.3 °

Vertically pointing radars have been used extensively for the study of precipitation at McGill (e.g. Marshall, 1953; Douglas et al., 1957) and elsewhere (e.g. Boucher, 1957; Lhermitte and Atlas, 1963; Klaassen, 1988). Although nowadays scanning radars and mobile platforms are more frequently used, a vertically pointing radar collecting data continuously can still yield interesting and unexpected measurements and results.

2. Examples of observations

The main focus of the observations has been melting layers or radar bright bands (Fig. 1). The bright band often varies significantly in height and thickness over very short times (Fig. 2 and 3). Changes in thickness are often correlated with changes in precipitation intensities: the larger snowflakes associated with stronger snowfalls fall faster and take more time to melt (Fig. 4). Occasionally, when there is a temperature inversion close to the 0° level, two bright bands may be observed: the snow partially melts and then freezes as it encounters colder air; the final melting can occur several hundred meters below (Fig. 5). Even when the variability in the melting layers is not considered, vertical profiles of reflectivity show dramatic changes over short periods in convective precipitation (Fig. 6) as well as in more stratiform cases (Fig. 7).

3. Beyond the observations

Many cases of snow storms, ice pellets, freezing rain and thunderstorm events have been collected in the past 3 years in addition to the regular rain events. Because of the high resolution of the measurements (7.5 m × 1 s), several fundamental or applied problems in radar meteorology and precipitation physics can be studied using them. For example, the statistics and causes of the fluctuation of weather echoes were reexamined (Duncan et al., 1992). The evaluation of the importance of gradients in the reflectivity field (Fabry, 1990) as well as of the vertical profile of reflectivity (Fabry et al., 1992) in precipitation estimates by radar were also investigated. A vertically pointing radar can also be the ideal tool for studying orographic enhancement of precipitation.

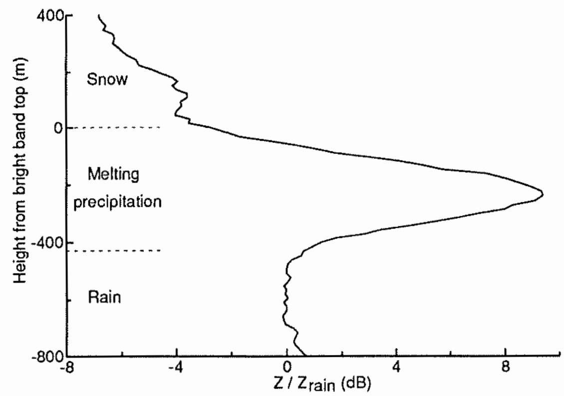

Fig. 1 - Typical bright band reflectivity profile. Measurements were averaged over one minute.

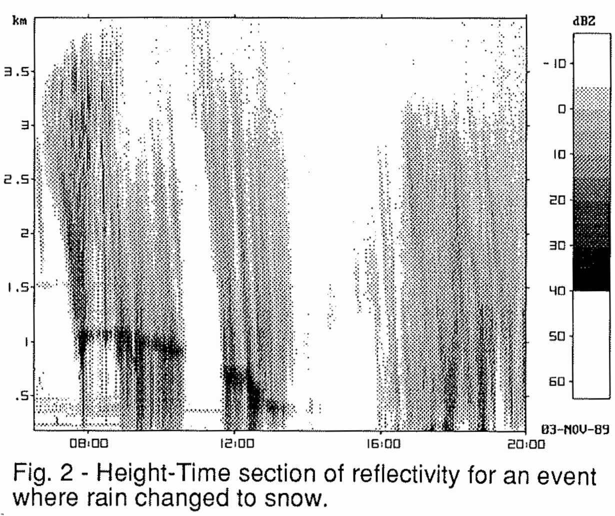

Fig. 2 - Height-Time section of reflectivity for an event where rain changed to snow.

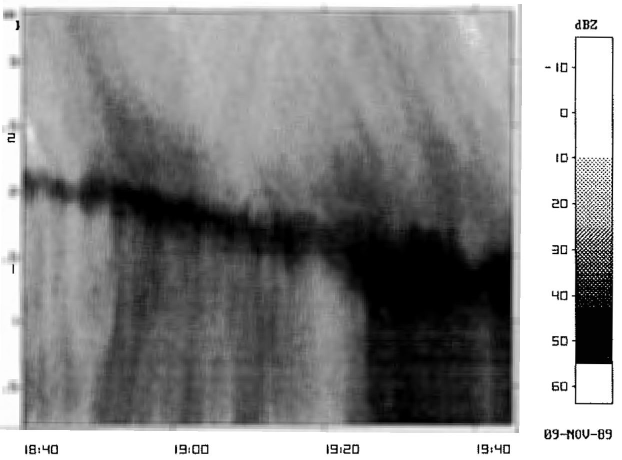

Fig. 3 - Height-Time section showing a rapid drop and an intensification of the melting layer.

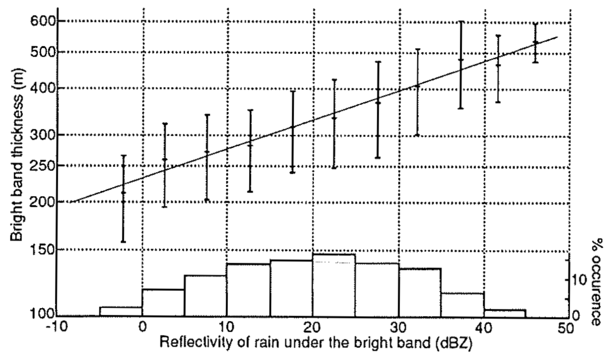

Fig. 4 - Mean bright band thickness as a function of the reflectivity of rain. The bar chart shows the frequency of occurrence of each rain reflectivity for fall/spring conditions.

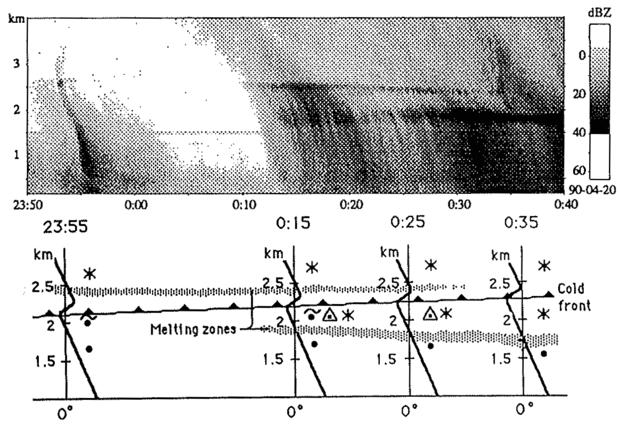

Fig. 5 - Height-Time section of a double bright-band event with probable temperature profile from 23:55 to 0:35. The location of the cold front and of the melting layers as a function of time, as well as probable hydrometeors types as a function of height and time are also indicated.

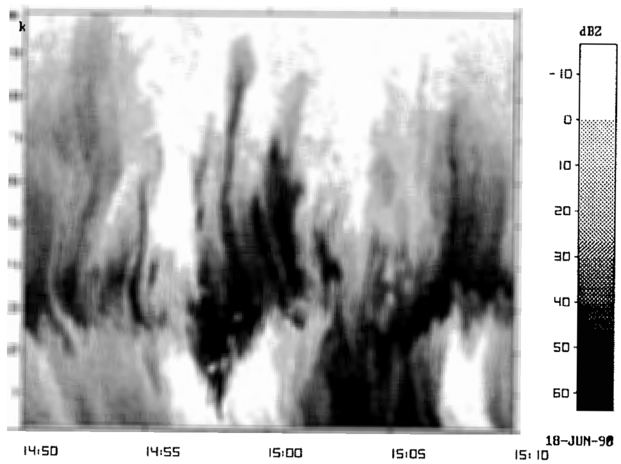

Fig. 6 - Height-Time section of a thunderstorm case.

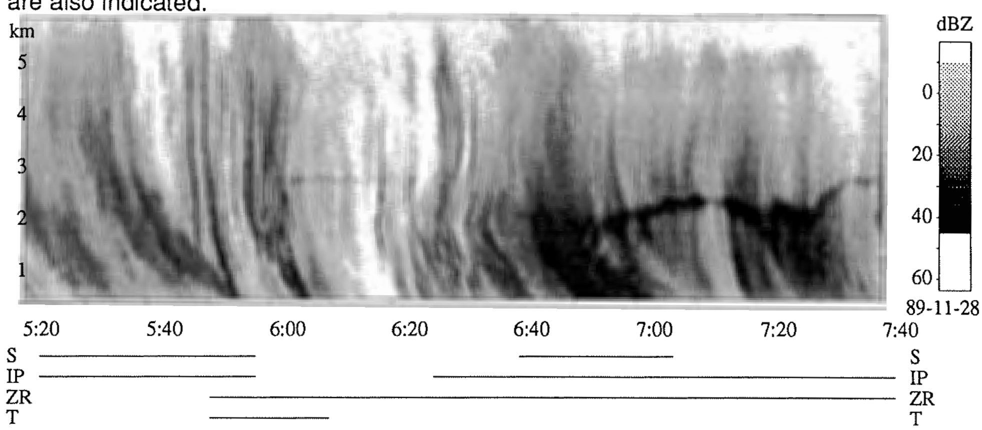

Fig. 7 - Height-Time section of a rapidly changing event. Surface observation of snow (S), ice pellets (IP), freezing rain (ZR) and thunderstorms (T) are indicated at the bottom of the figure. The surface temperature during this event was -5°C.

4. References

BOUCHER, R.J., 1957: Synoptic-dynamic implications of 1.25-cm vertical beam radar echoes. *Preprints, 6th Conf. on Radar Meteor.*, Amer. Meteor. Soc., 179-188.

DOUGLAS, R.H., K.L.S. GUNN, and J.S. MARSHALL, 1957: Pattern in the vertical of snow generation. *J. Meteor.*, **14**, 95-114.

DUNCAN, M.R., S. LOVEJOY, F. FABRY, and D. SCHERTZER, 1992: The fluctuating radar cross section (RCS) of multifractal scatterers. *Preprints, 11th Int. Conf. on Clouds and Precip.*.

FABRY, F., 1990: *Precipitation estimates by radar: a zenith pointing radar perspective.* M.Sc. Thesis, McGill University, 83 pp.

FABRY, F., G.L. AUSTIN, and D. TEES, 1992: The accuracy of rainfall estimates by radar as a function of range. Accepted by the *Quart. J. Roy. Meteor. Soc.*.

KLAASSEN, W., 1988: Radar observations and simulation of the melting layer of precipitation. *J. Atmos. Sc.*, **45**, 3741-3753.

LHERMITTE, R.M., and D. ATLAS, 1963: Doppler fall speed and particle growth in stratiform precipitation. *Preprints, 12th Conf. on Radar Meteor.*, Amer. Meteor. Soc., 297-302.

MARSHALL, J.S., 1953: Precipitation trajectories and patterns. *J. Meteor.*, **10**, 25-29.

OBSERVATIONS OF MICROPHYSICAL EVOLUTION IN A HIGH PLAINS THUNDERSTORM

Andrew G. Detwiler and Paul L. Smith
Institute of Atmospheric Sciences
South Dakota School of Mines and Technology
Rapid City, South Dakota, USA 57701

and

Jeffrey L. Stith
Department of Atmospheric Sciences
University of North Dakota
Grand Forks, North Dakota, USA 58202

1. INTRODUCTION

The purpose of this study is to establish the processes within High Plains convective storms that determine the extent and duration of the anvil region. We define the anvil as the elevated part of the cloud that spreads and drifts downshear from the region where deep convection occurs. The ice particles that form the anvil are incompletely-grown precipitation particles and frozen cloud droplets exhausted from this convective region.

The dynamical and microphysical structure of mid-latitude anvil clouds has been studied only recently (*Bennetts and Ouldridge,* 1984; *Heymsfield,* 1986; *Detwiler and Heymsfield,* 1987; *Heymsfield and Miller,* 1988). These clouds have been observed to contain embedded regions of shallow upper-level convection. Particles may grow by deposition in the updrafts in these regions. Aggregation is also a possible growth process (*Heymsfield,* 1986), although aggregates observed in anvils may have formed in the main convective region of the storm and then been transported into the anvil region (*Bennetts and Ouldridge,* 1984). Particle evaporation also occurs, mainly near and below the base of the anvil, and may be accompanied by fragmentation of larger aggregates into smaller ones (*Hallett et al.,* 1989).

Newton (1966) estimated the total water mass transported into the anvil region of one large thunderstorm to be 30% of that which was available for precipitation. *Foote and Fankhauser* (1973) estimated a value of 50% for a storm they studied. *Heymsfield and Miller* (1988) studied six High Plains storms in their mature stages and found the total water mass transport into the anvil to be from 18% to more than 100% of the water vapor mass influx into cloud base (apparently additional water was entrained at mid-levels in at least some cases). There was a good correlation between this percentage and the vertical shear of the horizontal wind, with the lowest percentage corresponding to the smallest shear. The water flux into the anvil was composed of roughly equal proportions of ice and vapor. Ice mass concentration decreased downshear apparently because ice both evaporated, as the anvil mixed with drier environmental air, and precipitated.

Based on these observations, one might expect anvils to be more extensive with increasing vertical shear of the horizontal wind, although no studies have been published demonstrating that such a relationship does indeed exist. It is harder to relate variation in anvil extent to variations in microphysical characteristics of the storm. If the particles entering the anvil were for some reason smaller, or less-heavily rimed and of lower density, then they would be expected to fall more slowly and remain in the upper atmosphere longer. However, smaller particles will evaporate more quickly and dendritic crystals might fragment as they evaporate. There are too few observations of storm anvil microphysics available to find robust correlations between the sizes of particles entering the anvil and storm environmental variables such as windshear, convergence, or vertical stability.

Heymsfield (1986) has described an extensive set of anvil microphysical measurements from a High Plains storm. They were obtained by the NCAR Sabreliner flying in the middle to lower levels of the anvil of the large thunderstorm occurring near Miles City, Montana, on 1 August 1981. His data came from a Particle Measuring Systems (PMS) OAP-2D-P probe. He found that the larger particles (D > 1 mm) were predominantly aggregates, and that the size distribution tended to flatten out with distance downshear and downward from the upper region of the storm core -- that is, the proportion of smaller particles decreased and the proportion of larger particles increased. The size of the largest particle observed also increased downshear and downward. He attempted a calculation of particle growth with a kinematic model using Doppler radar wind fields and concluded that aggregation in the anvil was required to explain the large sizes found farther from the core and nearer the base of the anvil.

We contribute here observations of a smaller storm that occurred on 6 July 1989, about 150 km south of Bismarck, North Dakota. The observations were obtained as part of the North Dakota Thunderstorm Project (*Boe et al.,* 1992). *Reinking et al.* (1990, 1992) have discussed the evolution of this storm based on analysis of airborne Doppler radar data and results of a simulation using a two-dimensional, time-dependent cloud model with bulk water microphysics. The focus of the present discussion will be *in situ* microphysical measurements made both in the smaller cumulus congestus clouds forming in the inflow region of the storm by the University of North Dakota Cessna Citation II and the South Dakota School of Mines T-28, and in the upper portions of the anvil by the Citation. Concurrent measurements of ozone concentrations allow an assessment of the potential effects of dilution by entrainment. Although the observations are not sufficient to define all of the processes important to anvil evolution, they do illustrate several interesting features that have not been seen in earlier work.

2. OBSERVATIONS

The storm under study formed late in the afternoon within a dense field of cumulus congestus. It tracked eastward at 20 m/s along the border between North Dakota and South Dakota for several hours. It was in a highly-sheared environment (mainly speed shear, with winds at all levels being predominantly westerly). Cloud base was at 3 km MSL (+4°C temperature) with the tops reaching to 10 km MSL (-40°C), which was slightly below the tropopause height. *Reinking et al.* (1992) describe how the storm was feeding at mid-levels from the south and at low levels from the east. A sketch of the storm based on a recording by the cockpit windscreen video camera in the Citation is shown in Fig. 1, along with schematic locations of aircraft penetrations.

Between 1845 and 1915 CDT (Central Daylight Time), the Citation made several passes over the convective core of the storm at 8.8 km MSL, then back and forth across and along the anvil stretching eastward (downshear) from the core at 8.8 and 9.4 km MSL. At this time, the storm was declining in intensity but was characterized by a high reflectivity core and updraft. Combined aircraft, radar, and model data suggest a single main updraft with maximum speeds between 5 and 15 m/s occurring in the middle and upper levels of the storm during the period of the aircraft observations. An ozone analyzer aboard the aircraft obtained data both in-cloud and during descent outside of cloud; the observations showed that air feeding from mid-levels into the feeders and then into the main updraft of the storm was apparently undergoing little dilution between mid and upper levels of the cloud. Wind fields derived from airborne Doppler radar measurements showed strong divergence at 9 km MSL (*Reinking et al.,* 1992).

The Citation carried a PMS OAP-2D-C probe sampling roughly 5 ℓ/s with an equivalent array height of 1 mm and a resolution of 33 μm. Particles sufficiently large for their features to be distinguished (D > 200 μm) ranged from individual dendritic ice crystals to aggregates, to rimed aggregates, to heavily rimed graupel, much as *Heymsfield* (1986) reported in his observations of the anvil of a somewhat larger High Plains thunderstorm. In addition to the 2D-C, the Citation also carried PMS OAP-1D-C and 1D-P probes. Total particle concentration was several times higher than reported by *Bennetts and Ouldridge* (1984) in the maritime storm they studied, reaching 1000/ℓ near the updraft. This is also more than an order of magnitude higher than concentrations reported in the tops of tropical anvils over Panama by *Knollenberg et al.* (1982). Concentration decreased with distance downshear (north and east) of the convective core. The upper anvil was depleted in larger particles but enriched in smaller particles compared to central levels. The downshear anvil region was depleted in smaller particles and enriched in larger particles compared to the region over the convective core. The largest particles registered by the 1D-P were about 4 mm in diameter and the highest concentrations were found near the upshear region of the storm, within a few kilometers of the updraft.

Figure 2 shows particle size distributions along the northern edge of the anvil based on data from the four PMS probes carried by the Citation. (The high counts in the larger FSSP channels are artifacts due to the presence of high concentrations of ice particles.) Figure 3 shows data from the 2D-C probe, alone, for various regions of the anvil. Highest concentrations are found over the core at 9.4 km, while the largest sizes are downshear at 8.8 km.

There was a trend to more heavily rimed particles nearer the updraft core and lower in the anvil. Also, the particle population was not well mixed; the aircraft would often penetrate small-scale regions (a few hundred meters) with distinct microphysical characteristics, say, high percentages of

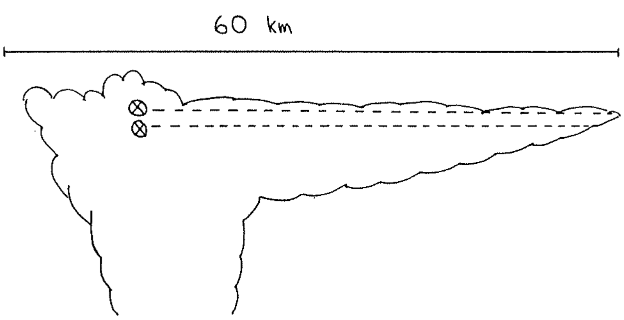

Figure 1: Schematic profile of upper storm as viewed from the south with altitudes of aircraft penetrations indicated by dashed lines.

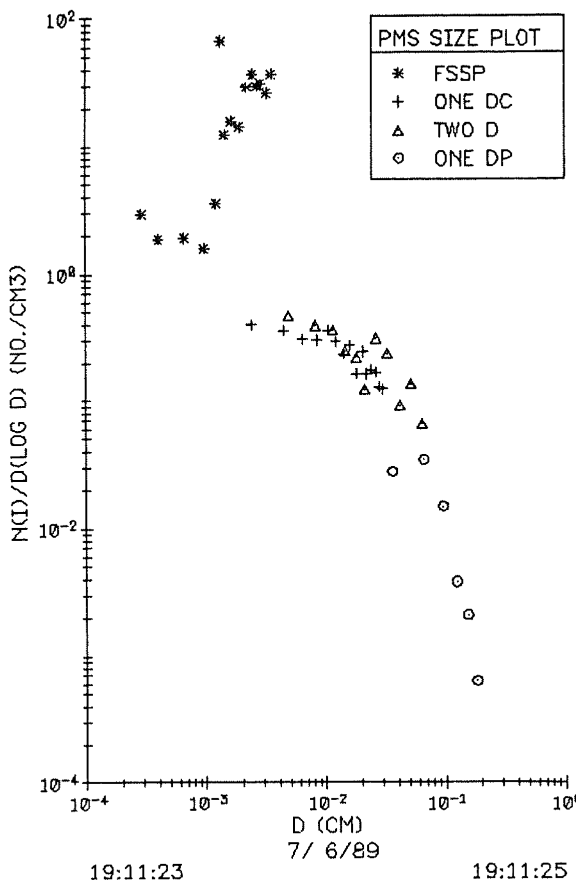

Figure 2: Particle size distribution near north side of anvil, based on the suite of four PMS probes carried by the Citation.

small graupel in one region or large lightly-rimed dendritic snow crystals in another.

Based on ozone and equivalent potential temperature data, the air in the anvil was not strongly diluted by entrainment compared to the air at 8.8 km in the updraft core. Dilution by no more than a factor of two is consistent with measurements made in central regions of the anvil.

T-28 and Citation measurements at 4.5 km (0°C) and 6.5 km (-15°C), respectively, in the convective towers on the south side of the main updraft showed peak cloud droplet concentrations of 500/cm³. This suggests that also in the main updraft (not penetrated at lower altitudes by either aircraft) droplet concentrations must have been hundreds per cubic centimeter in the 4.5 to 6.5 km altitude range. The maximum 1D-C particle concentration in the anvil over the updraft was about 1/cm³, and the cloud water concentration was zero (based on a Rosemount icing probe and a Johnson-Williams sensor). The 1D-C can nominally detect particles as small as 15 μm. There could have been a sizable concentration of even smaller particles present, but it is unlikely there were hundreds per cm³ this small. These 1D-C data give some information concerning the fate of the cloud droplets in the updraft as air rises through the entire depth of the cloud and is "dumped out" of the updraft at the top. If they survive as droplets to approach cloud top regions, they must certainly freeze at some temperature between -35 and -40°C (cloud top temperature was -40°C in this case). If the anvil is characterized by concentrations of 10's to 100's per cubic centimeter of very small ice particles, they must be undetected by the 1D-C. It is more plausible that most of the droplets evaporate or become collected as rime by snow and graupel particles.

The decrease in concentration of smaller particles with distance downshear seen in Fig. 3 argues against an important role for particle breakup during evaporation, at least in the upper regions of

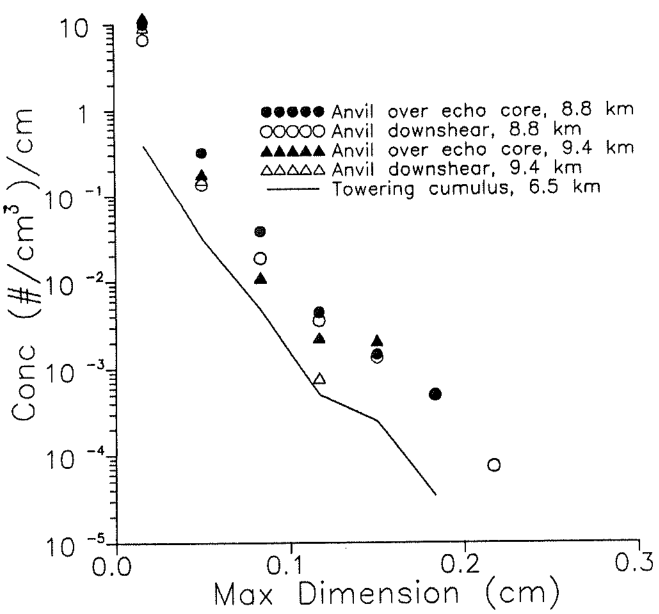

Figure 3: Size distributions from various regions in the anvil based on the Citation 2D-C probe.

the anvil. We lack measurements near the base of the anvil, however, where this mechanism would be more likely to be important.

One last question we are attempting to address is the relative role in the anvil of aggregation and size-sorting (in size sorting heavier particles don't rise as high and fall out of the anvil more quickly than lighter particles). *Heymsfield* (1986) found evidence for both, but stressed the role of aggregation in producing large aggregates in the lower downshear regions of the anvil from the storm he studied. Here the 2D-C images from 6.5 km altitude in the smaller, neighboring cumulus congestus cells look quite similar to the images obtained in the anvil, although on the average they are not as heavily rimed. (Liquid water concentrations in the smaller clouds are probably much lower than those in the broad updraft of the main storm due to more rapid dilution by entrainment in the smaller updrafts.) Snow particle concentrations are also much lower in the smaller clouds, as shown in Fig 3. It is probable that near the main updraft where the cloud was deeper, higher concentrations of aggregates grew around the 5-15 m/s updraft with ample time to reach large sizes and to rime in the broader region of supercooled water by the time they were carried to near cloud top. The greater breadth of the larger cloud also allows higher concentrations of aggregates to develop over broader regions because entrainment of drier, snow-free air is proportionally less in broader updrafts. *In situ* measurements do show that aggregation in the anvil is not required to explain the presence of 4 mm aggregates there.

It is important to note that our measurements came from the upper portion of the anvil, while Heymsfield's came from the lower portion. It is possible that larger aggregates were present lower in the anvil of this storm.

3. CONCLUSIONS

Airborne *in situ* measurements in the upper regions of the anvil of a strongly-sheared small thunderstorm suggest that most of the mixing between cloud-base air and environmental air occurs while the air is rising in the updraft. Updraft air exhausted into the anvil is only slowly diluted as it drifts off downshear. The anvil is composed of snow particles with a wide range of riming, from nearly spherical graupel to almost pristine spatial forms. The size distribution is steepest (relatively more small particles) near cloud top over the updraft. It flattens and becomes broader at lower altitudes and farther downshear. Number concentration peaks near the upper region near the core of the anvil, where it is several times higher than the concentration reported in the anvil of a small maritime thunderstorm near England and more than 10 times higher than the concentrations found near the tops of tropical anvils near Panama.

The small-ice-particle population is two orders of magnitude smaller in number concentration than the cloud-droplet concentration at mid-levels in the updraft. This fact suggests that almost all of the cloud droplets evaporate or are collected by precipitation particles before they reach the top of the storm, making this storm an efficient processor of cloud water. However, *Reinking et al.* (1992) note that the storm was relatively inefficient at getting precipitation to the ground; more than 50%, and possibly 75%, of the water vapor mass flowing into the cloud was exhausted into the anvil. The low precipitation efficiency and high particle concentration in the anvil of the storm suggest more and longer-lived anvil cloudiness from this storm compared to maritime anvils like those descibed by Bennetts and Ouldridge.

ACKNOWLEDGMENTS

Support for this research was provided by the National Science Foundation (NSF) under Cooperative Agreements ATM-8620145 and ATM-9104474; NSF Grant No. ATM-8720252; the NOAA Federal/State Cooperative Program under agreements NA 900AA-H-0A176 and NA 17RA0218-01 and via North Dakota Atmospheric Resource Board Contracts NDARB-UND-NOAA90 and NDARB-UND-NOAA91.

REFERENCES

Bennetts, D. A., and M. Ouldridge, 1984: An observational study of the anvil of a winter maritime cumulonimbus cloud. *Quart. J. Roy. Meteor. Soc.*, **110**, 85-103.

Boe, B. A., J. L. Stith, P. L. Smith, J. H. Hirsch, J. H. Helsdon, Jr., A. G. Detwiler, H. D. Orville, B. E. Martner, R. F. Reinking, R. J. Meitin and R. A. Brown, 1992: The North Dakota Thunderstorm Project: A cooperative study of High Plains Thunderstorms. *Bull. Amer. Meteor. Soc.*, **73**, 145-160.

Detwiler, A., and A. J. Heymsfield, 1987: Air motion characteristics in the anvil of a severe thunderstorm during CCOPE. *J. Atmos. Sci.*, **44**, 1899-1911.

Foote, G. B., and J. C. Fankhauser, 1973: Airflow and moisture budget beneath a northeast Colorado hailstorm. *J. Appl. Meteor.*, **12**, 1330-1353.

Hallett, J., S. Ahmed, Y. Y. Dong and R. G. Oraltay, 1989: Secondary ice crystal production in the atmosphere: Its role in assessment of cloud seeding effectiveness. Preprints, *5th WMO Conf. Wea. Modif. and Appl. Cloud Physics,* Beijing, China. WMO/TD - No. 269, WMO Secretariat, Geneva, Switzerland, 43-46.

Heymsfield, A. J., 1986: Ice particle evolution in the anvil of a severe thunderstorm during CCOPE. *J. Atmos. Sci.*, **21**, 2463-2478.

Heymsfield, A. J., and K. M. Miller, 1988: Water vapor and ice mass transported into anvils of CCOPE thunderstorms: Comparison with storm influx and rainout. *J. Atmos. Sci.,* **22**, 3501-3514.

Knollenberg, R. G., A. J. Dascher and D. Huffman, 1982: Measurements of the aerosol and ice crystal populations in tropical stratospheric cumulonimbus clouds. *Geophys. Res. Letters,* **9**, 613-616.

Newton, C. W., 1966: Circulations in large sheared cumulonimbus. *Tellus,* **18**, 699-713.

Reinking, R. F., R. J. Meitin, F. Kopp, H. D. Orville and J. L. Stith, 1992: Fields of motion and transport within a sheared thunderstorm. *Atmos. Res.* [In press]

Reinking, R. F., J. L. Stith and R. J. Meitin, 1990: Airborne Doppler radar and *in situ* studies of the transport of ozone and other constituents in feeder cells and anvils. Preprints, *1990 Conf Cloud Physics,* San Francisco, Amer. Meteor. Soc., Boston, MA, 698-705.

OBSERVATIONS OF FIRST ICE IN ILLINOIS CUMULUS

Robert R. Czys and Mary Schoen Petersen

Illinois State Water Survey
Atmospheric Sciences Division
Champaign, Illinois 61820

1. INTRODUCTION

This paper presents observations of first "detectable" ice taken near the tops of warm-based cumulus in the congestus stage of development. These observations were made during the summer of 1989 as part of the Precipitation Augmentation for Crops Experiment (PACE). Some similarities and differences with previous observations of ice in clouds that have active coalescence processes is presented.

2. FACILITIES AND PROCEDURES

A light twin engine airplane (Beechcraft Baron) was used to make the observations reported herein. The airplane had a full compliment of cloud physics, thermodynamic and kinematic instrumentation. Cloud physics instrumentation included an Forward Scattering Spectrometer Probe (FSSP) set to measure cloud particles in the size range from 0 to 45 μm diameter in 3 μm intervals. Precipitation-size particles were measured using 2D-C and 2D-P optical array probes, and image classification software was developed to estimate particle size and concentration (Czys and Petersen 1992). Temperature was measured using Rosemont and reverse flow thermometers. Dew point was measured using a cooled mirror hygrometer. Vertical winds were computed according to a method described by Lawson (1979) that uses measurements of the airplane angle of attack, pitch and vertical acceleration. Liquid water content was measured using a Johnson-Williams hot wire probe, and was computed from the FSSP size distribution.

Analysis was restricted to data for only the updraft regions of each growing cumulus congestus. Thus, the observations mostly reflect the result of precipitation and ice processes that occurred during ascending parcels of cloudy air. To further minimize the effect of sedimentation, in-flight procedures required that penetrations could only be made at approximately -10°C, shortly after cloud top pasted through the flight level. No penetrations were made of clouds with tops greater than 5000 ft above flight level. A total of 124 penetrations were made between 12 June and 25 July, 1989. From this total, 187 updrafts were identified. In this analysis, an updraft was defined as any portion of a penetration that had at least three consecutive seconds of upward vertical wind greater than 1 m s^{-1}, corresponding to a minimum updraft length of approximately 300 m.

3. OBSERVATIONS

Figure 1 shows a plot of estimated cloud top temperature versus total ice concentration for each updraft containing ice in the 1989 PACE ("PACE89") sample. Total ice concentration was defined as the sum of the concentrations of ice classified as graupel, hexagonal ice form, and possible fragment of a hexagonal ice form from the 2D-C and 2D-P image records. It should be noted, however, that the dominant ice form identified in the 2D image records was that having the characteristics expected from the shadow of a graupel and/or an ice pellet; images which may have been cast from the shadow of complete or broken vapor grown hexagonal ice crystals were extremely rare. An inability to distinguish between liquid and recently frozen precipitation-size drops probably contributed to a slight underestimate of ice concentrations. Hence, for practical purposes total ice concentrations reported herein, are representative of the graupel population.

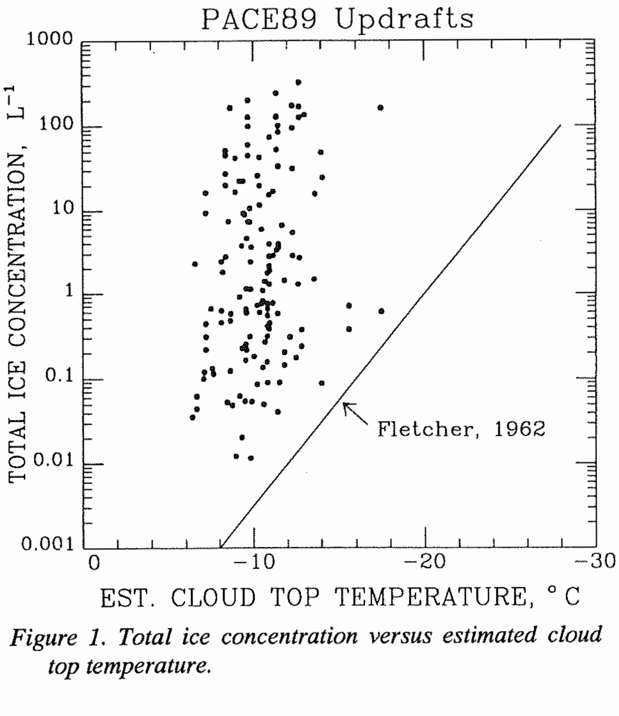

Figure 1. Total ice concentration versus estimated cloud top temperature.

There are three notable features in Fig. 1: 1) total ice concentrations appear unrelated to cloud top temperature, 2) the largest ice concentrations also appear not to be related to cloud top temperature, and 3) minimum concentrations are at least those expected from conventional measurement of ice nuclei (Fletcher 1962).

Maximum ice concentrations have been found to be well correlated with the broadness of the supercooled cloud droplet spectrum for mature and aging cumulus that had tops which were colder than -6°C. (see, for example, Hobbs and Rangno 1985; Rangno and Hobbs 1991). In these previous observations, the broadness of the cloud droplet distribution was defined as a threshold diameter (D_T) such that the cumulative concentration of supercooled cloud droplets with diameters greater than D_T is ≥ 3 cm^{-3} as measured by the FSSP, and is ≥ 10 cm^{-3} as measured by an Axially Scattering Spectrometer Probe (ASSP). Furthermore, maximum ice concentrations (I_{MAX}) were defined from ice particle concentrations indicated by an Optical Ice Particle Counter (OIPC) that were averaged peak values over a time interval of at least 15 seconds (corresponding to approximately ≥ 1 km length of cloud penetration). One relationship between D_T and I_{MAX} reported by Hobbs and Rangno (1985) is:

$$I_{MAX} = \left(\frac{D_T}{18.5}\right)^{8.4} \qquad (1)$$

where the correlation coefficient for the fit to their data was r = 0.90.

For comparison, we have plotted threshold diameter (D_T) versus total ice concentration (N_I) for PACE89 cumulus and is shown in Fig. 2. In our analysis it was not possible to use the exact definitions of Rangno and Hobbs (1985) because an OPIC and an ASSP were not available. The broadness of the cloud droplet distribution, D_T, was defined strictly on the basis of FSSP measurements in updrafts, such that the cumulative concentration of cloud droplets with diameters greater than D_T is ≥ 3 cm^{-3}. Furthermore, we used total ice concentration as defined in Fig. 1, since it was not possible to determine a peak ice concentration for any particular updraft on the basis of the 2D image data. The solid line in Fig. 2 is a plot of Eq. 1.

Figure 2 shows that the largest ice concentrations in our sample of PACE89 updrafts coincide closely with the maximum expected on the basis of the broadness of the distribution of supercooled cloud droplets. Therefore, the data do not contradict the possibility that midwestern and cumulus from other regions may share a threshold diameter dependence in their mechanism for the production of ice. However, it should be further noticed that although data for mature and aging cumulus show an obvious relationship between D_T and I_{MAX}, the PACE89 data also show that there are many updrafts which have total initial ice concentrations which fall between the minimum expected from primary ice nuclei and the maximum expected based on D_T. Thus, although D_T may be a good indicator of maximum ice concentration, it does not provide an adequate parameterization of total ice concentration.

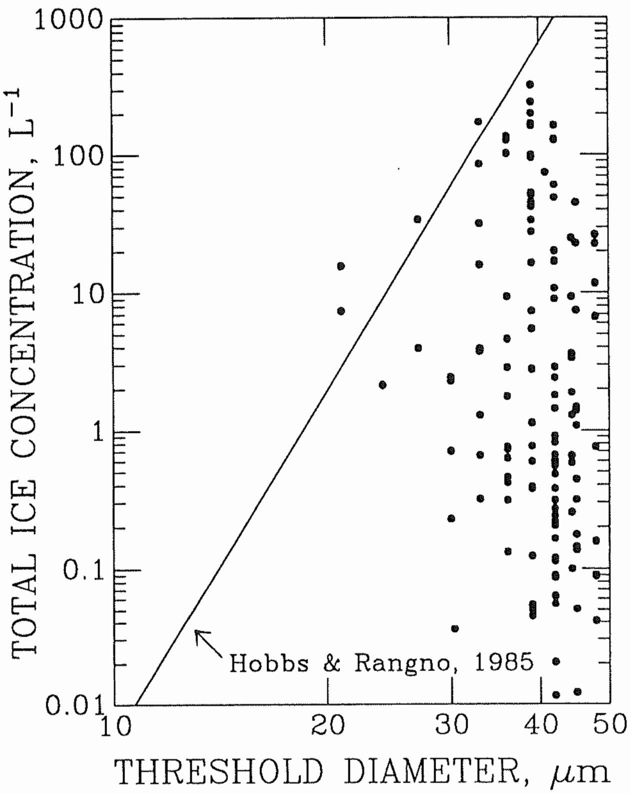

Figure 2. Total ice concentration versus broadness of the cloud droplet distribution as indicated by the FSSP.

One mechanism often invoked to explain the discrepancy between first ice and ice nuclei is that of splinter production during riming (Hallett and Mossop 1974). Laboratory work has indicated that the process may be dependent on temperature, concentration of small and large cloud droplets, as well as the size and fall speed of the riming particle (Mossop 1976; Goldsmith et al. 1976; Mossop 1978; Heymsfield and Mossop 1984). Since many, if not all, of these physical conditions were usually found in the updrafts of 1989 PACE clouds, rime-splintering can not be ruled out as one possible mechanism which contributed to the production of first ice. This reasoning led us to explore the possibility that a correlation may exist between total ice concentration and either the concentration of small supercooled cloud droplets ($N_{d<13\mu m}$), the concentration of large supercooled cloud droplets ($N_{d\geq 25\mu m}$), or possibly the total concentration of supercooled cloud droplets (N_d).

Figure 3 shows a plot of N_d versus total ice concentration (N_I). Although the scatter in this figure is somewhat large, ice concentrations appear to decrease with increasing concentrations of droplets. The solid line through the data in Fig. 3 is a least squares fit with equation $N_I = 8.3\text{x}10^8\ N_d^{-4.1}$. Using the same general form as Eq. 1, this equation is

$$N_I = \left(\frac{N_d}{149.8}\right)^{-4.1} \qquad (2)$$

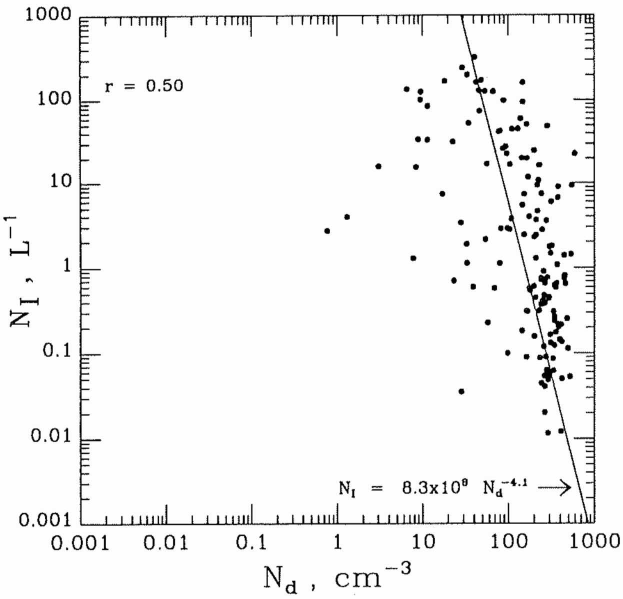

Figure 3. Total ice concentration versus total cloud droplet concentration.

where the correlation coefficient for the fit was found to be r = 0.50. Plots of concentration of small supercooled cloud droplets versus total ice concentration, as well as concentrations of large supercooled cloud droplets versus total ice concentrations also show negative relationships similar to that shown in Fig. 3, with correlation coefficients of 0.46 and 0.39, respectively.

After examining literally hundreds of thousands of 2D-C and 2D-P images not only from the 1989 PACE field project, but also from the 1986 PACE field project (Czys 1991), we arrived at the hypothesis that almost all of the "first" ice encountered (at least which was large enough to be detected by the available instrumentation) was in the form of ice pellets or graupel. Hence, an important mechanism for the production of ice must involve the direct freezing of supercooled drizzle and raindrops by some as yet unagreed upon mechanism. Furthermore, reports from Project Whitetop (Braham 1964), more recent reports for maritime Florida cumuli (Willis and Hallett 1991), in addition to reports from around Australia and the Pacific Northwest have also indicated that the initiation of ice is closely linked to the time that supercooled drizzle and raindrops become present. Therefore, a positive correlation should exist between ice concentrations and concentrations of supercooled drizzle and raindrops.

Figure 4 is a plot of supercooled drizzle and raindrop concentration versus total ice concentration for each of the updrafts encountered around the -10°C level during the 1989 PACE field program. This figure shows that a positive correlation exists between the concentration of drops bigger than about 300 µm (N_D), and total ice concentration (N_I). A least squares fit to the data shown in Fig. 4 yields the equation:

$$N_I = \left(\frac{N_D}{.22}\right)^2 \qquad (3)$$

where, the correlation coefficient was found to be r = 0.72.

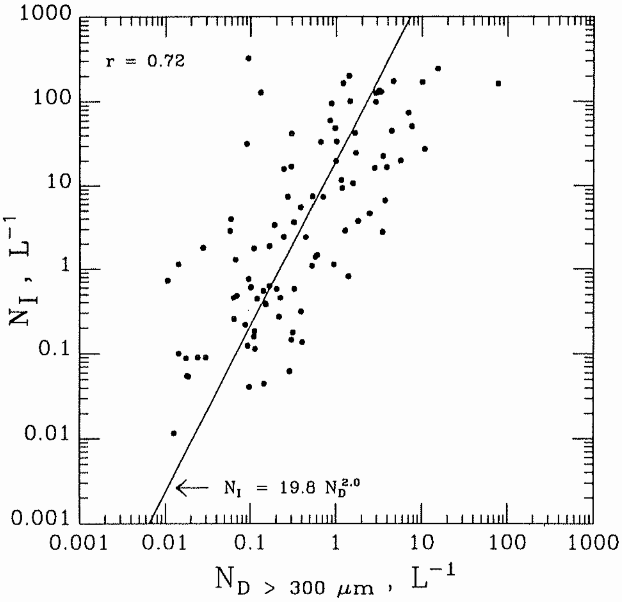

Figure 4. Total ice concentration versus concentration of supercooled drops with diameter ≥ 300 µm as indicated by the 2D-C and 2D-P probes.

4. SUMMARY AND CONCLUSIONS

This paper reports on observations of first "detectable" ice made during the 1989 Precipitation Augmentation for Crops Experiment. These observations are most comparable to those previously taken in clouds with coalescence processes active enough to produce supercooled drizzle and raindrops. Consistent with previous observations, ice does not originate but only after the presence of supercooled drizzle and raindrops. Under this circumstance when ice initiates, it initiates in the form of ice pellets, graupel and probably frozen drizzle and raindrops at temperatures warmer and at concentrations higher than that expected solely from conventional measures of ice nuclei activity. As has been the case for maritime cumulus, ice concentrations were found to be rather poorly correlated with minimum cloud top temperature, further suggesting that ice processes in warm-based clouds are not temperature dependent. Also consistent with previous reports, the largest ice concentrations in the sample from PACE89 appear to have been correlated with the broadness of the distribution of supercooled cloud droplets and that the relationship determined for mature and aging cumulus of the Pacific Northwest and elsewhere well applies to the 1989 PACE measurements on first ice. Total ice concentrations were also found to be negatively related to total concentrations of supercooled cloud droplets. This finding is contrary to that expected if a rime-splintering mechanism is the major contributor to the initiation of ice. These observations also demonstrate that a positive correlation exists between concentrations of supercooled drizzle and raindrops and ice concentrations, which does not contradict the hypothesis that supercooled drizzle and raindrops may be a direct source of ice in warm-based cumuli.

Acknowledgments. This research was conducted as part of the Precipitation, Cloud Change and Impacts Project (PreCCIP) under NOAA cooperative agreements COMM NA90 NA90AA-H-0A175 and COMM NA89RAH09086.

5. REFERENCES

Braham, R.R., Jr., 1964: What is the role of ice in summer rain-showers? *J. Atmos. Sci.,* **21,** 640-645.

Czys, R.R., 1991: A preliminary appraisal of the microphysical nature and seedability of warm-based midwestern clouds at -10°C., *J. Wea. Mod.*, **23**, 1-17.

Czys, R.R. and M.S. Petersen, 1992: A roughness-detection technique for objectively classifying drops and graupel in 2D-image records. *J. Atmos and Ocean Tech.*, **9**, 242-257.

Fletcher 1962: *The Physics of Rain Clouds.* Cambridge University Press, London, England. 386 pp.

Goldsmith, P.J., J. Gloster and C. Hume, 1976: The ice phase in clouds. *Preprints Int. Conf. on Cloud Physics,* Boulder, Amer. Meteor. Soc., 163-167.

Hallett, J., and S.C. Mossop, 1974: Production of secondary ice crystals during the riming process. *Nature,* **249**, 26-28.

Heymsfield A.J., and S.A. Mossop, 1984: The temperature dependence of secondary ice crystal production during soft hail growth by riming. *Quart. J. Roy. Meteor. Soc.,* **110**, 765-770.

Hobbs P.V., and A.L. Rangno, 1985: Ice particle concentrations in clouds. *J. Atmos. Sci.,* **42**, 2523-2549.

Lawson, R.P., 1979: A system for airborne measurement of vertical air velocity. *J. Appl. Met.,* **18**, 1363-1368.

Mossop, S. C., 1976: Production of secondary ice particles during the growth of graupel by riming. *Quart. J. Roy. Meteor. Soc.,* **102**, 45-57.

Mossop, S.A., 1978: The influence of drop size distribution on the production of secondary ice particles during graupel growth. *Quart. J. Roy. Meteor. Soc.,* **104**, 323-330.

Rangno, A.L., and P.V. Hobbs, 1991: Ice particle concentrations and precipitation development in small polar maritime cumuliform clouds. *Quart. J. Roy. Meteor. Soc.,* **117**, 207-241.

Willis, P.T., and J. Hallett, 1991: Microphysical measurements from an aircraft ascending with a growing isolated maritime cumulus tower. *J. Atmos. Sci.,* **48**, 283-300.

MICROPHYSIC FEATURES FOR MAIN PREEIPITUS CLOUD SYSTEMS OVER INNER-MONGOLIA IN SPRING AND EARLY-SUMMER SEASON

YANYAN KONG

METEOROLOGY INSTITUTE OF INNER-MONGLIA AUTONOMOUS REGION
HUHEHOT CITY, CHINA

ABSTRACT

From 1965 to 1983,a series of airplane sounding observations were conducted in the mid and west areas of Inner-Mongolia in order to study the distribution features of cloud and rain there. According to the analysis of these both macro and micro observation data, we knew the distribution features of ice and snow crystals, liquid state water content, cloud droplet spectrum and other macro factors as well as their correlation. Thus, we can deepen our studies in the resources of cloud and rain and the potentiality of artificial rain-making.

1. DATA

Data used in this article were taken from airplane observations in 19 years (1965~1983) from april to August. We choose huhehot,wemeng in the mid part and hetao in the west part of Inner-Mongolia as observational locations. The sounding height varied from 3000m to 5500m. The instruments for observing were made by ourselves.(see fig.1).

2. THE MICROPHYSIC FEATURES OF COLD STRATIFORM CLOUD

2.1 Ice crystals and snow crystals:

In observational areas, the ratio of the thickness of cold stratiform cloud to that of total cloud is more than 80%. The average concentration of ice and snow crystals are 22.2 /L and 2.7 /L. The maximum concentration of them are 491.3/L and 20.6/L respectively.(see fig.2)

The average diameter of snow crystals observed ranges from 0.6mm to 1.1mm. Snow crystals exist in shapes of graupel, column, irregular and stellar. They were put in order according to their proportion to the total crystals from large to small. Nearly 90% of the crystals are in the shape of graupel.

2.2 Cloud droplets concentration:

The analysis of the 308 sample observed in the selected areas came to these results: The average and maximum concentration of cloud droplets in stratiform precipitus are 116.3/L and 633.8/L respectively. Single-peak spectrum dominate the cloud droplets spectrum patterns. Double or

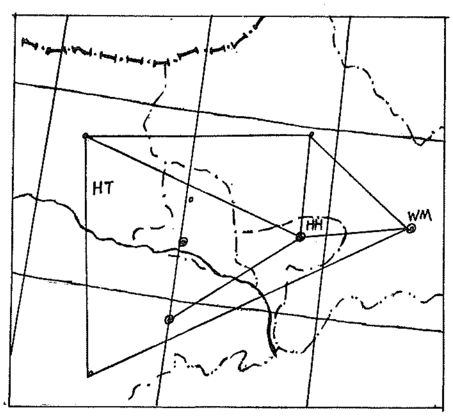

fig.1 The map of the observational locations.

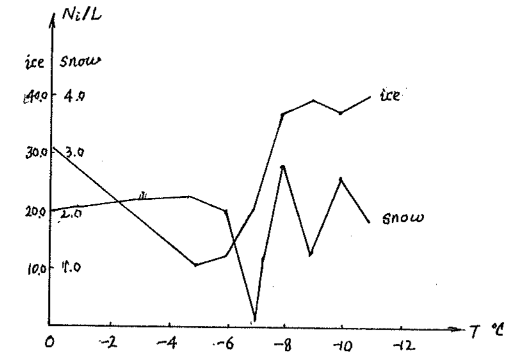

fig.2 The Variation of ice and snow crystals with air temperature.

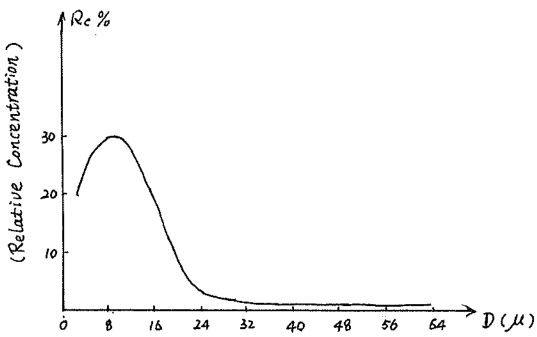

fig.3 The average cloud-droplet spectrum D(μ) (single-peak).

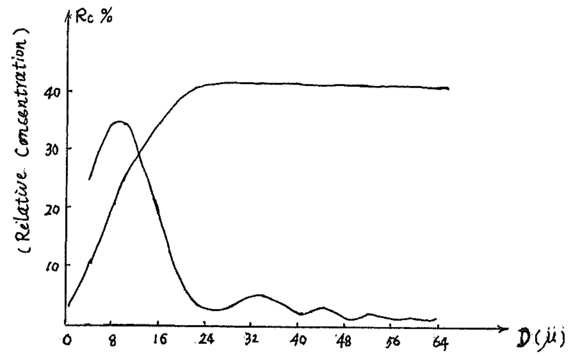

fig.4 The average cloud-droplet spectrum (multi-peak etc).

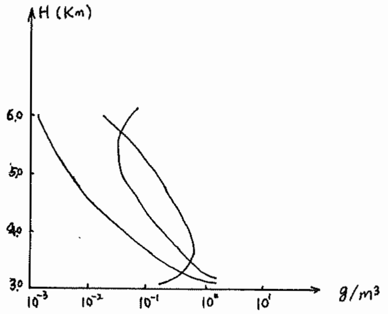

fig.5 The distribution of the liquid state water content with height (pattern I).

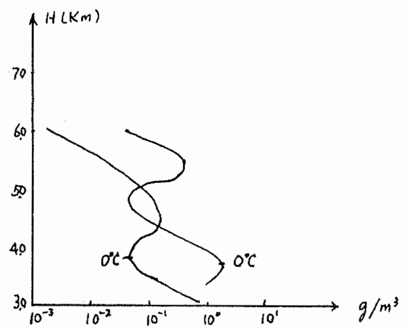

fig.6 The distribution of the liquid state water content with height (pattern II).

multi-peak appear occasionally. The larger the droplets, the larger the width of their spectrum.(See fig 3-4)

2.3 The liquid state water content:

The liquid state water content inside the clouds varify from 10 g/m. It's average and maximum value are $0.27g/m^3$ and $5.8g/m^3$ respectively.Fig.5-7 show the average distribution of liquid state water content with height.

From Fig.5-7,the distribution of liquid water content inside the clouds are divided into three types:

a> The water content decreased with height from cloud base to cloud top(generally to cold cloud).

b> There exist two water content maximum inside the cloud base and mid or upper layers of the clouds.

c> The water content maximum appear in the mid layers of the clouds.

3. CONCLUSION:

3.1 In the middle area of Inner-Mongolia, the main precipitus cloud systems belong to cold stratiform clouds during Spring and Summer. The thickness of the cold stratiform clouds is 80% the total cloud thickness. AgI and CO_2 (Solid state) are appropriate cloud seeding agents.

3.2 Based on the airplane observations,the average concentration of snow and ice crystals in our region is slightly higher than that in some other north provinces such as Jilin,Ningxia etc. About 90% of the total snow crystals are in the shape of graupel,which indicates there usually exist supercooled waters, which are favourable to the growth of graupel.

3.3 From the distribution of concentration of ice crystals with temperature, we can see two peak value, one is in the top of clouds, another is aroud -5℃ in the mid or low layers of clouds. This result reveals that ice crystals in Inner-Mongolia may originate from the joint function of

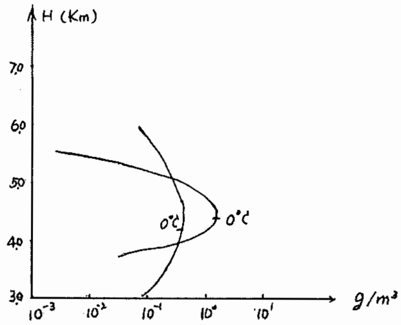

fig.7 The distribution of the liquid state water content with height (pattern III).

ice nuclei activation in the top of clouds and ice crystal growth around the layler where temperature is about -5℃.

3.4 The average concentration of cloud droplets is 116.3/L. The spectrum of cloud droplets appear mainly in single-peak pattern. The spectrum width of large cloud droplets are larger than that of small ones. These results show that the clouds in selected areas not only have aboundant large cloud droplets which are favourable to the ice crystal growth, but also possess good liquid water content.

3.5 The average liquid state water content is also slightly higer than that observed in some other north provinces.

3.6 In Inner-Mongolia, the stratiform clouds mainly belong to cold clouds, Both liquid state water content and large droplets are aboundant. So we have good cloud seeding potentiality. So long as we can choose a right time and a good cloud location for cloud seeding. With appropriate amount of seeding agents, we must have a satisfactory rain-making effect.

PERMANENCE, PROPERTIES AND NATURE OF LIQUID PHASE IN ICE-CONTAINING CLOUDS

Anatoly N. Nevzorov

Central Aerological Observatory, Dolgoprudny, Moscow Region, 141700, Russia

1. INTRODUCTION

The problem under consideration is propounded on account of some unexplored pecularities of the liquid component presenting in ice-containing clouds (ICC). Questions are arising about the frequent occurence and long lifetime of mixed phase clouds, eventual existence of liquid water at very low temperatures intrinsic in cirrus, typical enough presence of large (to a hundred microns) drops in ICC as revealed in impactor probes and in crystal riming, etc. Up to now only speculative hypotheses were offered to explain such phenomena and no experimental evidences were obtained towards their confirmation.

Our recent experimental results (Mazin et al., 1992) showed that: (i) Liquid water in reliably detectable contents (>3 mg m^{-3}) is present within almost all ICC including those referred to ice clouds down to at least -55°C; (ii) At any temperatures, the relation between LWC and IWC varies within extreme limits, their values being closely comparable on an average; (iii) In most ICC the main contribution to LWC is introduced by drops >30 μm; (iv) Positive correlation between LWC and IWC prevails on short scales.

Besides, the evidences were obtained by direct measurements (Mezrin and Mironova, 1991) and indirectly (Nevzorov, 1990) that in all ICC even at *LWC*>0 the relative humidity corresponds to ice ruther than supercooled water saturation. If abstracting from conventional views, all above presents the completion of signs of wide-temperature phase equilibrium of liquid water with the ice-vapour system.

2. BASIC POSTULATE

The paradox above provides very serious reasons for the conclusion that the ICC liquid component differs from supercooled water, at least, in two properties, namely equilibrium humidity conforming with ice and viability at <-40°C. So regular and deep modification of properties of normal water by any real solutes is obviously incredible, other orthodox-based versions look not less fantastic.

We postulate that the unusual properties of ICC liquid water origin from its specific intermolecular structure, i.e. it is in fact a special polimorphous (structural) modification of H_2O.

If so, the phase equilibrium mentioned implies the identity of ICC water with the transition ("quasi-liquid") layer on the ice surface (Jellinek, 1967). In turn, the transition layer neutralizes certain effects of the breakage of hydrogen bonds at the boundary of ice lattice order (Fletcher, 1970), thus its wide-temperature permanent existence is of physical necessity. Following Fletcher (1970) in considering amorphous molecular structure of the transition layer, let us call the corresponding water modification by amorphous water, or A-water.

Within the conception developed, the conclusion suggests itself that just A-water, but not supercooled water by Pruppacher and Klett (1978), is actual Ostwald's step substance in vapour-to-ice phase transition capable of easily originating and steadily remaining in metastable state.

The most convincing corroboration of the version proposed might be the difference between ICC liquid and ordinary water in other than mentioned physical properties. We succeeded in proving that by means of the CAO aircraft microphysical instrumentation (Mazin et al., 1992).

3. APPROACH

Our approach is based, in general, on comparing microphysical data obtained by different physical methods briefly described in Mazin et al.(1992) report.

An important initial point is that the nephelometric PPSA probe as a particle spectrometer has the response characteristics differing in dependence on particle nature. Its 5-channel pulse analyzer was experimentally adjusted to water drop diameters of d_k = 30,50,80,120,180 μm. In terms of crystal cross- section effective diameter a, the corresponding thresholds as derived from crystal indicatrix (Kosarev et al., 1986) resulted in a_k = 20,33,53,80,120 μm. Each channel provides the integral concentration N_k of crystals with $a>a_k$ and drops with $d>d_k$. The auxiliary cross -polarization channel has the detection thresholds d_p=100 μm, a_p=25 μm. One can deduce from the figures quoted that the difference N_1-N_p gives the upper estimation of true concentration of drops with $d_1 < d < d_3$.

Using the PPSA crystal size scale as

preferable in ICC, we receive truncated "instrumental" mixed particle spectra interpreted in the form of

$$n(a) = -dN(a)/da = n_I(a) + Rn_L(Ra) \qquad (1)$$

where $n_I(a)$ and $n_L(d)$ are the true concentration densities of crystals and drops, correspondingly, $R=d_k/a_k$ is the PPSA scale ratio. For the calibration above, R = 1.5.

Large particle spectrometer LPS has the lower size threshold of $a_6=d_6$=200 µm and in practice detects only crystals in ICC as follows from 2D-C data as well as from crystal riming observations (e.g. Pruppacher and Klett, 1978).

As shown by Mazin et al. (1992) certain microphysical information could be derived from the comparison of measured and calculated values of the extinction coefficient ε. As for the calculated one, in most cases the PPSA range provides the main contribution to it, extrapolated one of smaller particles being negligible at all. The calculation result may be presented as $\varepsilon_{1I}+\varepsilon_{1L}/R^2$ where ε_{1I} and ε_{1L} are the contributions of crystals with $a>a_1$ and drops with $d>d_1$ to the true (physical) value of ε. In these terms, the direct measurement of ε by the optical transmissiometer RP gives

$$\varepsilon_m = G_o\varepsilon_o + G_I\varepsilon_{1I} + G_L\varepsilon_{1L} \qquad (2)$$

where ε_o is the true contribution of small particles, G_o, G_I, G_L are the integral instrumental distortion factors for given fractions. The RP spectral distortion function $g(d)$ or $g(a)$ as computed by Nevzorov (1971) is shown in Fig.1. Using $g(a)$ in calculating the instrumental-eguivalent value ε_c from measured spectrum $n(a)$ we receive in fact the result expressed by

$$\varepsilon_c = G_I\varepsilon_{1I} + \frac{1}{R^2} G_L'\varepsilon_{1L}. \qquad (3)$$

Here G_L' is the integral distortion factor for the drop spectrum $n(d)$ when measured in the a scale. The difference of (2) and (3) may be expressed in the form

$$\Delta\varepsilon = \varepsilon_m-\varepsilon_c = G_o\varepsilon_o + \left(1-\frac{G_L'}{G_L R^2}\right)G_L\varepsilon_{1L} \qquad (4)$$

When R=1.50, then $1 \leqslant G_L'/G_L < 1.3$ for any drop spectra. Thus, in the case of LWC>0 and hence $\varepsilon_o+\varepsilon_{1L}\geqslant\varepsilon_L>0$ it must be necessarily $\Delta\varepsilon>0$.

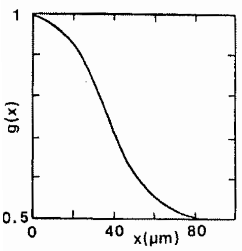

Fig.1. The distortion function g(x) in ε determination by RP:

$$\varepsilon_m = \int 0.5\pi x^2 g(x) \times [n_L(x)+n_I(x)]dx.$$

This result was present indeed in most our data. But what have attached our special attenttion were the numerous cases where at LWC>0 the opposite ineguality $\Delta\varepsilon<0$ was received well going out of extreme error and as a rule alternating with $\Delta\varepsilon>0$ within the same cloud as it is shown in examples of Figs.2,3. Here Fig.2 demonstrates the comparison between ε_m and ε_c in ice clouds (LWC=0) with rather satisfactory result and simultaneously reveals an unexpected peculiarity such as abrupt negative deviations of Δε just where LWC>0.

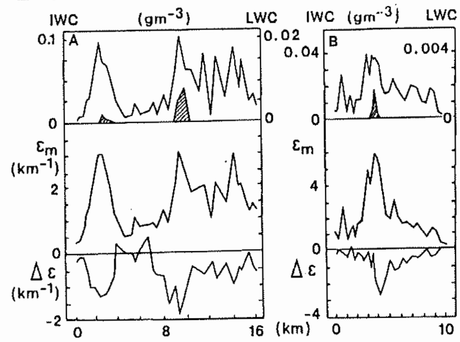

Fig.2. Ice cloud penetrations. Bulgaria, 23 April 1989:
A - Cb, 1535 LMT, 4900 m, -14°C;
B - Cs, 1645 LMT, 8000 m, -35°C.
IWC, LWC (shaded) in gm⁻³, ε_m, Δε in km⁻¹.

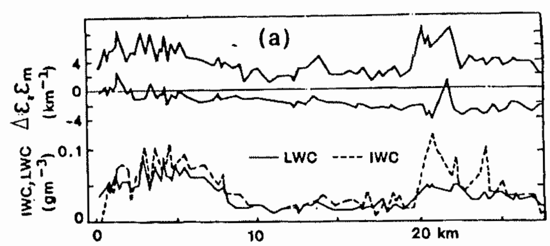

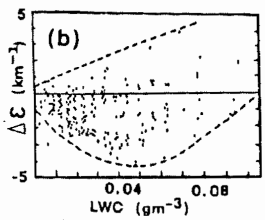

Fig.3. (a) An example of cloud realization: Uzbekistan, 13 March 1988, 1302 LMT, Cs, 6300 m, -29°C.
(b) The field of experimental points.

Fig.3(a) demonstrates a fragment of ICC realization of 70 km total long where zones with Δε<0 prevailed. Plotted in Fig.3(b) are the experimental synchronous pairs (Δε,LWC) extracted from record cuts with zero time derivatives to eliminate dynamic errors. Similar pictures were obtained as well in a number of cases at different temperatures down to -52°C. In general case as here, the spread of Δε nearly corresponds to measurement error (0.5 - 1 km⁻¹) at LWC=0 and with LWC increasing is first extending to both positive and negative sides then displacing to ariphmetical rise of Δε.

The results like presented above uniquely connect negative values of Δε with the liquid component of ICC with no serious doubt arising about the influence of ice phase. But in that case it follows from (4) that the inequality $\Delta\varepsilon<0$ is feasible when and only when $R<1$, the large drop contribution to the total value of ε_L being great enough. The sign-alternative spread of $\Delta\varepsilon$ is well accounted for by considerable variability of the small particle (drop?) fraction responsible for ε_o in (4).

The only explanation of the revealed discrepancy between R values obtained empirically in PPSA calibration (R_o=1.50) and in natural ICC study ($R<1$) obviously follows from the fact that the PPSA response to a spheric particle depends on its refractive index m. That is, the ICC liquid water differs from "normal" one in m value as well.

4. DETERMINATION OF PHYSICAL PROPERTIES OF ICC WATER

The presumption is further used that the A-water keeps the same molecular properties of the interaction with optical radiation as all known water phases (Eisenberg and Kauzmann, 1969). To get a relation between instrumental R and physical m parameters, relative response characteristics of PPSA, $I(d,m)$, were calculated using the Mie formulas for non-absorbing spheres with refractive index m ranging from 1.33 to 1.90 in diameter range 12 to 200 μm. The function $I(d)$ is fluctuating, near to square-law and monotonely increases with m growing, both PPSA thresholds d_k and scale ratio $R=d_k/a_k$ hence decreasing.

Writing m_o=1.33, R_o=1.50 for usual water we come to evident equation

$$I(d,m) = I(\frac{R}{R_o}\,d, m_o) \qquad (5)$$

which gives $m>1.5$ if $R<1$.

For more definite determination of real R value of A-water, R_A, we separated the items of (4) as follows. It was supposed that the points in Fig.3(b) adjacent to the falling branch of lower envelope of their spread correspond to local data with ε_o= 0. Besides, as mentioned before small enough difference N_1-N_p implies slight relative amount of drops with $d_1<d<d_3$. Consequently, in the data sampled by these criteria the liquid drops are concentrated within the spectral interval (d_3,d_6), or (a_3,a_6) in the crystal scale of PPSA. Outside this interval, PPSA and LPS provide the information of only crystal size distribution $n_I(a)$. The interpolation as shown in Fig. 4 enables it to be restored within the intermediate interval.

For further analysis the data were selected where the difference function $n(a)-n_I(a)=n'_L(a)$ had the well-defined

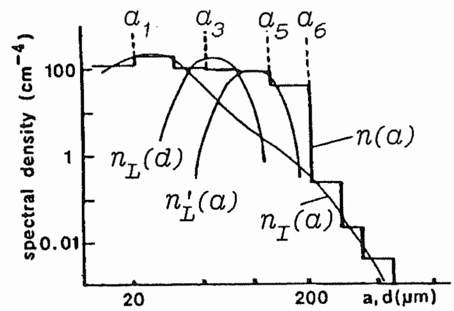

Fig.4. The separation of particle size spectra in analysed data: $n(a)$–the result by two spectrometers, $n_I(a)$– approximated (left, right) and interpolated crystal spectrum, $n'_L(a)$– difference $n(a)-n_I(a)$ approximated by γ-distribution, $n_L(d)$– restored A-water spectrum.

mode (Fig.4) which allowed to approximate it by gamma-distribution with the index μ fitted of the series of 4, 8, 16, 32. The drop concentration N_L and the value of ε'_L corresponding to $n'_L(a)$ spectrum were evaluated by difference method and distribution mode a_m was computed from N_L, ε'_L and μ. Using $d_m/a_m=R$, $\varepsilon_{1L}=R^2\varepsilon'_L$ and accepting $G_L=g(d_{m\varepsilon})$, $G'_L=g(a_{m\varepsilon})$ for narrow drop distribution where $d_{m\varepsilon}$, $a_{m\varepsilon}$ are the cross-section distribution modes, we easily transform (4) with ε_o=0 into the equation for determination of R:

$$R\sqrt{g(\frac{\mu+2}{\mu}\,Ra_m)} = \sqrt{g(\frac{\mu+2}{\mu}\,a_m) + \frac{\Delta\varepsilon}{\varepsilon'_L}} \qquad (6)$$

To avoid too great errors it was required $|\Delta\varepsilon|$ and ε'_L to be large enough in comparison with the measurement error and IWC to be as small as possible. Following all the criteria above, 11 local data samples were selected from the situation of Fig.3. In these data LWC as measured ranged 21-53 mg m^{-3}, IWC 14-107 mg m^{-3}, ε_m 2.0-5.3 km^{-1} and $\Delta\varepsilon$ from -2.2 to -5.2 km^{-1}. The received values were: μ 4 to 32, a_m 85 to 145 μm and N_L 310 to 830 l^{-1} the latter contributing 30-50% of the total particle concentration.

The values of R calculated from (6) varied from 0.50 to 0.63 and averaged R_A=0,575 with the standard deviation of only 7% which implies the sufficient objectivity of the result. In the data under consideration, d_m values ranged from 49 to 83 μm which is in a good agreement with the ice riming observations. In Fig.4 the restored A-water drop spectrum $n_L(d)$ is shown.

Within the accuracy permitted by the fluctuations of functions $I(d,m)$ we found from (5) that m_A=1.8-1.9.

Accepting in Lorenz-Lorentz formula

$$\rho = \frac{1}{p_\lambda} \frac{m^2-1}{m^2+2} \quad (7)$$

p_λ=0.206 $cm^3 g^{-1}$ as for all H_2O phases (Eisenberg and Kauzmann, 1969), we obtain the A-water density ρ_A=2.15±0.1 g cm^{-3}.

Now the opportunity presented itself to calculate the A-water content (AWC) using $n_L(d)$ and ρ_A known. As a result, calculated AWC values (117-243 mg m^{-3}) exceeded LWC as measured by an average factor 4.7 with only 7.5% standard deviation. Considering this to be a result of the difference between the evaporation heat of A-water, L_A, and that of ordinary water employed in calibration of thermal-type LWC meter (Nevzorov, 1980) and taking into account that the water caught by a hot collector needs certain warming up to evaporate, we came to L_A≈500 J g^{-1} at -30°C within about 10% error.

5. DISCUSSION

The experimental evidence that the ICC liquid water substantially differs from the "normal" one in the fundamental physical properties such as density (ρ_A≈ 2.15 g cm^{-3}), evaporation heat (L_A≈ 500 J g^{-1}), and refractive index (m_A=1.8-1.9) though indirectly corroborates the ideas profound in Section 2. Note that the quantitative characteristics of A-water follow on the tendency starting from the ice to water transition accompanied by disordering the lattice (hydrogen-bonded) intermolecular structure. Serious arguments are there to deduce that the A-water is fully non-hydrogen-bonded ("amorphous") water structural modification (Nevzorov, 1990).

It follows from the position of A-water in the energetic hierarchy of H_2O phases that it may originate only via the vapour condensation. Besides, its "pre-ice" genetic role connects its generation with that of ice (Nevzorov and Shugaev, 1992). Thus the A-water is inherent in only ICC, purely supercooled water clouds being not concerned. As it was stated above, the AWC value may be determined by simply multiplying the data of thermal-type LWC meter in ICC by 4.5-5. In ICC under investigation (Mazin et al.,1992) the AWC contributed on the average as much as 78% of total water content (specifically, 73% in ICC referred to large-drop ones).

In forming ICC microstructure, most important role belongs to A-water phase equilibrium with ice and low evaporation heat which together results in very low supersaturation in ICC over A-water and ice. Under these conditions, the inverse saturation dependence on drop radii is responsible for drop growing to the stable (equilibrium) sizes while the variable small drop fraction is not simply intermediate but acts as a kind of fast buffer of relative humidity variations. Other peculiarities of ICC structure are discussed in (Nevzorov, 1990).

6. CONCLUSION

The author is aware that the ideas propounded and experimentally supported in the present report replace by themselves a series of diverse hypotheses now leading in ICC physics, and would be grateful for any effort in understanding and advancing the problem.

7. REFERENCES

Eizenberg D., Kauzmann W., 1969: The structure and properties of water. Oxford Univ.

Fletcher N.H., 1970: The chemical physics of ice. Cambridge Univ.

Jellinek H.H.G., 1967: Liquid-like (transition) layer on ice. J. Colloid and Interface Sci., v.25, 192-197.

Kosarev A.L., Mazin I.P., Nevzorov A.N., Shugaev V.F., 1986: Microstructure of cirrus clouds. " Some problems of cloud physics " (collected papers), Leningrad, Gidrometeoizdat.

Mazin I.P., Nevzorov A.N., Shugaev V.F., Korolev A.V., 1992: Experimental study of phase structure of clouds. Proc. of this Conference.

Mezrin M.Yu., Mironova G.V., 1991: Some results of air humidity research in stratiform clouds. Trudy CAO, ussue 178, 125-132.

Nevzorov A.N., 1971: An estimation of the light scattering effect in cloud transperency measurement. Trudy CAO, ussue 102, 102-117.

Nevzorov A.N., 1980: Aircraft cloud water content meter. "Comm. a la VIII conf. int. sur la phys. des nuages", Clermont-Ferrand, France, v.II, 701-703.

Nevzorov A.N., 1990: Experimental basises of the physical model of ice-containing clouds. Manuscr. depos. in VNIIGMI-MCD No.1037-gm90, CAO.

Nevzorov A.N., Shugaev V.F., 1992: Observations of the initial stage of ice phase evolution in supercooled clouds. Meteorology and Gydrology, No.1, 84-92.

Pruppacher H.R., Klett J.D., 1978: Microphysics of clouds and precipitation. D. Reidel.

RESULTS OF THE THIRD INTERNATIONAL CLOUD MODELING WORKSHOP

Harold D. Orville

Institute of Atmospheric Sciences
South Dakota School of Mines and Technology
501 E. St. Joseph Street
Rapid City, South Dakota 57701-3995

1. THE THIRD INTERNATIONAL CLOUD MODELING WORKSHOP

The Third International Cloud Modeling Workshop is scheduled to be held in Toronto, Canada from 10 through 14 August 1992. Its purpose is to stimulate cooperative efforts among theoreticians and observers who seek to understand the mechanisms of cloud and precipitation evolution in both natural and cloud seeded situations. The broad goal of the workshop is to promote work that will increase the utility of numerical models in cloud physics, weather modification, cloud chemistry, climate, forecasting, and other areas of meteorology that require accurate representation of cloud processes. The primary focus of the Third International Cloud Modeling Workshop is on the simulation of precipitation processes in cloud scale and mesoscale systems.

Participation in the workshop involves two phases. Firstly, participants will carry out numerical experimentation at their home institutions using data sets provided by the workshop organizers. Secondly, participants will meet at the workshop itself to compare model results against observations and against other modeling efforts. Participants have been encouraged to provide papers describing their results for use at the workshop and for publication in the report of the workshop.

The following field data sets were available for distribution by the end of November 1991:

(a) All liquid microphysical processes;
(b) Mixed-phase (both liquid and ice) processes for wintertime orographic and spring/summertime convective clouds;
(c) Frontal cloud conditions;
(d) Maritime boundary layer cloud conditions.

In addition to data sets from natural clouds, some data from seeded clouds were also available. Brief descriptions of the data sets to be used are given next.

2. DATA SETS

The all liquid microphysical processes case is a case study based on data obtained during the 1990 Hawaiian Rain Band Project in Hilo, Hawaii, USA. Aircraft flights were made through convective clouds organized in offshore bands along the wind-ward coast of the island. Radar observations were also made. These small to moderate-sized warm clouds often produce heavy precipitation.

The mixed-phase orographic wintertime cloud cases come from studies in the Sierra Nevada Mountains in California and the Rocky Mountains in Colorado, USA. A case study of orographic precipitation formation was available from the Sierra Cooperative Pilot Project (SCPP), conducted in the Sierra Nevada Mountains of California, USA. The case involved both seeded and unseeded precipitation development. The seeding involved silver iodide. This case was available for the last international cloud modeling workshop but was not used by any of the participants.

The second orographic case comes from the Winter Icing and Storm Project (WISP) conducted near Boulder, Colorado (USA). This was the Valentine Day storm of 1990 and is ideal for a mesoscale study. A Canadian cold air outbreak pushed against the Rocky Mountains in the surface layers. Super-imposed aloft were disturbances in the westerlies.

Two cases were used for mixed-phase spring/summer convective clouds. One comes from a summer project conducted in North Dakota in 1989 (North Dakota Thunderstorm Project (NDTP)) and the other from observations of clouds forming over the Asir Mountains in Saudi Arabia in April/May 1990. The NDTP case involved very rapid cell development in a mesoscale convective complex, whereas the Asir Mountain clouds were of a more isolated nature.

In addition to the WISP case above, the next data sets provide an opportunity for simulation of mesoscale situations and the clouds and cloud bands which form in such conditions.

A frontal cloud mixed-phase case came from Europe. A case of cloud and precipitation development from the FRONTS 87 project in France was available. The case is a cold front with both narrow and wide bands of clouds. No microphysical data were available.

Marine boundary layer clouds have been included in the workshop for the first time. These types of clouds are very important for the radiation balance of the globe. They organize in different types of bands depending upon atmospheric conditions. They cover extensive areas of the ocean at times. The case selected involves cloud formation off the coast of southern California.

For all of these cases, several different types of data were available, more for some cases than others. Environmental soundings, topography, aircraft measured updrafts, aircraft penetration data, cloud base data, and some satellite and radar data were distributed to the modelers to help initialize their models. Some of the descriptive data were withheld by the observationalists for discussion at the workshop.

The ICCP presentation will summarize the primary results of the workshop.

This modeling workshop is being co-sponsored and supported by the World Meteorological Organization, the International Commission on Clouds and Precipitation, the Atmospheric Environment Service (Canada), the Canadian Meteorological and Oceanographic Society, the American Meteorological Society (USA), and the National Science Foundation (USA).

Drop size separation as a mechanism of warm rain formation

Yefim L. Kogan

Cooperative Institute for Mesoscale Meteorological Studies,
University of Oklahoma, Norman OK

1. Introduction

It is generally accepted that precipitation process can be triggered by coalescence once sufficient number of cloud droplets with radii larger that 20-25 microns are formed. However, it its still unclear what mechanisms produce these first large droplets. Both experimental and theoretical studies made during the recent years have shown the importance of mixing and entrainment processes in cloud and precipitation formation; the problem, however, is much too complex and is far from being resolved. A review of the history and the current status of the problem can be found in Johnson (1982), Paluch and Knight (1984), and Jensen and Baker (1989).

In this study we suggest a "drop size separation" mechanism for rain enhancement and, possibly, rain initiation. We will show that certain cloud regions may act as filters of large droplets which are repeatedly recycled in the cloud, whereas the small droplets are carried away with the outflow from the cloud. This process results in lowering the cloud drop concentration during recycling process and enhanced condensational growth of larger drops.

2. The model

The model developed by Kogan (1978) and modified as described in Kogan (1991) was used for the simulation to be discussed. It has a three-dimensional nonhydrostatic anelastic dynamical framework and includes explicit formulation of warm rain microphysical processes based on two distribution functions - one for cloud condensation nuclei and another for cloud and rain drops. The particle distribution functions considered in the model allow prediction of the drop spectra starting from activation up to rain formation.

The focus of the paper will be an analysis of the trajectories of selected air parcels in a convective cloud and its implication for rain initiation. To facilitate the analysis of the physical processes, a single cell cloud was simulated in an environment of zero initial ambient flow and characterized by stratification of temperature, humidity, and cloud condensation nuclei as described in Kogan (1991). It should be noted that the results shown in this paper were confirmed in other experiments using various temperature and humidity profiles. One common feature for all performed experiments was the specification in the initial environmental temperature sounding of a capping inversion layer that served as a natural cloud top boundary. Otherwise the qualitative results and conclusions of this study are believed to be independent of a particular environmental sounding, provided, of course, it contains sufficient instability for moist convection development.

3. Trajectory analysis of selected air parcels

648 trajectories of air parcels, released at 4 different times of cloud evolution and originating at cloud locations specified by 9 vertical and 18 horizontal levels, have been analyzed for the purpose of this study. They reveal several interesting features of cloud formation and evolution; here we will concentrate only on the effect of flow separation and its implication for cloud droplets growth. Fig. 1 shows the trajectories of selected air parcels that were originally located on the vertical lines 500 m and 750 m from the cloud center (trajectories A, B, C on the right and trajectories 1-4 on the left). The wind vectors (u and w components) and the 0.2 g m^{-3} liquid water content isoline which approximately outlines the cloud boundary are also shown in Fig. 1.

Apparently, the trajectory of an air parcel depends significantly on when and where it enters the cloud. Air parcels 1, 2, 3, A and B happen to be in the inflow region at the time of the initial cloud growth while parcels 4 and C were positioned in the cloud outflow region. Since their entry into the cloud was delayed until the time the cloud had grown to a more mature stage, they were eventually subjected to a stronger inflow and were caught by a much stronger updraft. A similar explanation applies to trajectories 2 and B. The latter parcel was positioned 250 m closer to the cloud center and entered the core of the updraft earlier when it was not yet fully developed. As a result, the air parcel B exits the cloud earlier and at a lower level. It is interesting to note that the air parcel B has been recaptured again by the cloud at about 2100 sec which is indicated by the trajectory loop at $z \approx 3$ km.

The difference demonstrated by trajectories 1, 4 and 2, 3 reflects the effect of flow separation near the top of the cloud. Two flow regimes can be clearly distinguished: the first is formed by the outflow jet below the inversion layer, and the second, by the return flow into the cloud. The major driving mechanism for the jet outflow is the pressure gradient force formed by the updraft decelerating in the inversion layer with negative buoyancy. The return flow is driven by the negative buoyancy due to drop evaporation, drag forces due to sedimentation of larger droplets and the perturbation pressure gradient force. All these forces combined result in baroclinic production of horizontal vorticity apparent in Fig. 1b.

Flow separation is more evident in Fig. 2, which depicts 12 trajectories of air parcels spaced 25 m apart and positioned at a height z = 0.75 km along the x axis from 4.025 km to 4.3 km. The right side of Fig. 2 shows two of them separately: B that joins the outflow jet, and A that joins the return flow. Every second trajectory on the left is labeled with a number from 1 to 6 which is placed at the air parcel position at time t = 1500 sec. Letters A and B for the trajectories shown on the right indicate parcel position at 600 sec time intervals, starting from 300 sec at the origination point. Evidently, air parcel B enters the cloud later; at time 900 sec it is only at a height of 1.5 km. Air parcel A is at this time at about 3 km; at later times (1500 and 2100 sec) it reenters the cloud again. Parcel B, which is caught into a much stronger updraft, has left the cloud earlier than A; at time 1500 sec it is located in the outflow jet, well outside the cloud.

Fig. 3a shows the fine structure of the flow around the separation point S. We have selected four trajectories, originating at points only 10 meters apart. Trajectories 1 and 2 again enter the jet, while 3 and 4 go into the return flow. The large flow diffluence is perhaps the most striking feature of this plot. The numbers 1-4 show the air parcel positions at 1500 sec. At this time they are separated by almost 1500 m, which means an increase in the spacing between them by more than two orders of magnitude!

We would like now to focus attention on how the flow separation affects the drop size evolution. The effect of large flow diffluence on cloud droplet growth may be quite significant, primarily due to the fact that cloud droplets of different sizes have different fall velocities. The questions that arise are: 1) Can small differences in the vertical velocities of cloud droplet population eventually lead to the divergence of their trajectories? 2) How substantial is this divergence and what role may it play in the cloud droplet growth?

The answers may be inferred from Fig. 3b, where the trajectory 1 from Fig. 3a have been recalculated taken into account the fall velocities corresponding to the droplets with

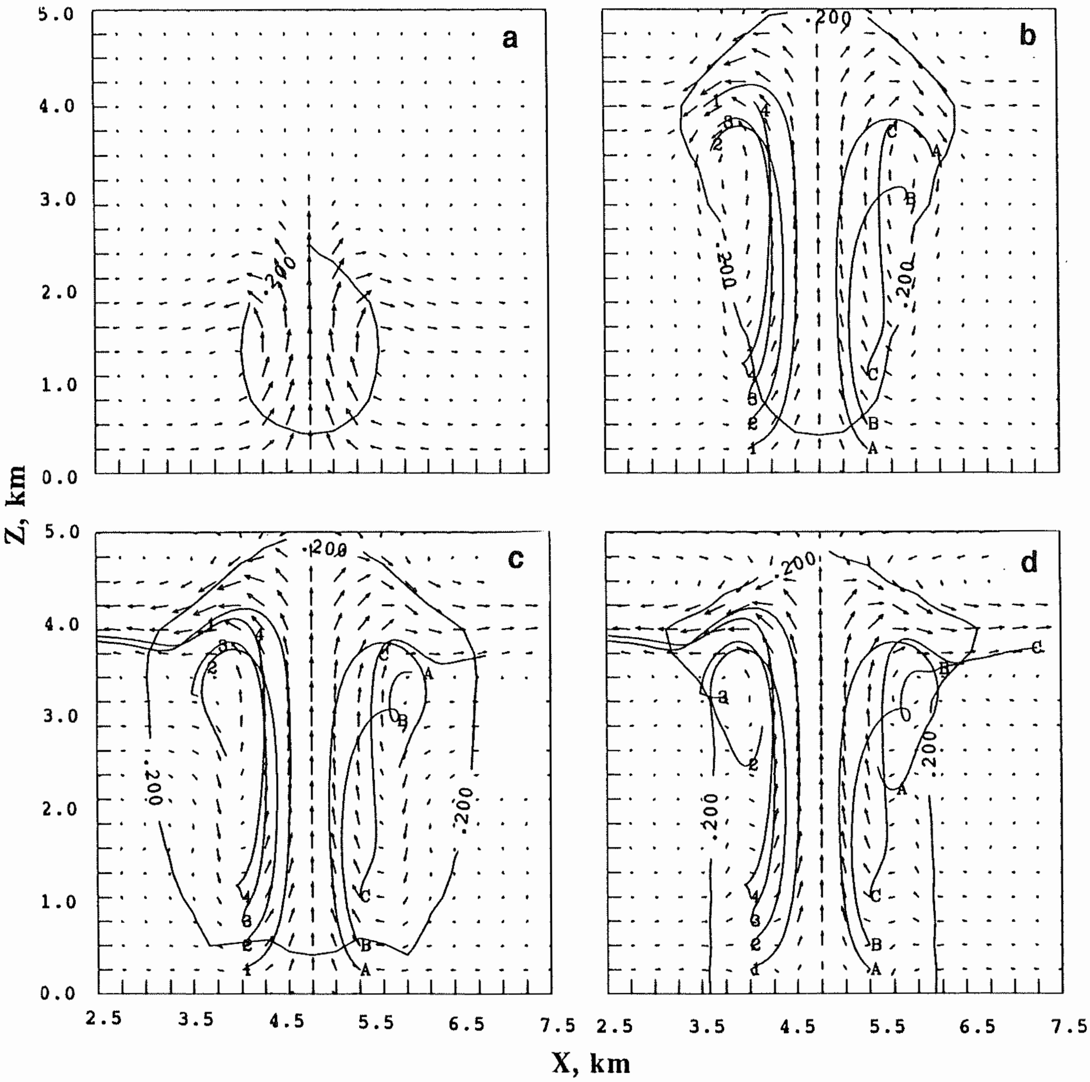

Fig. 1. Vertical cross-sections of the wind vectors (u and w components) with the outline of the cloud boundary (LWC=0.2 g m^{-3}) and selected air parcel trajectories superimposed. Plots a, b, c, and d correspond to simulation time of 600, 1200, 1800, and 2400 sec respectively. Trajectories are traced from 300 to 1200 sec on plot b, to 1800 sec on plot c, and to 2400 sec on plot d.

radii equal 16, 25, 40, and 60 microns. It was assumed that at heights from 2 to 4 km the average fall velocities for droplets in these size categories are 5, 10, 25 and 50 cm sec^{-1} respectively. Fig. 3b shows that even a fall velocity as small as 5 cm sec^{-1} significantly affects the droplet trajectory. The variation with time of the distance between the air parcels with zero and nonzero fall velocities is shown in Fig. 4. At 2500 sec the cloud droplets with fall velocities 5 cm sec^{-1} (Fig. 4a) are separated from the cloud droplets with zero fall velocity by a distance of about 150-400 meters, depending on the trajectory. Separation distance increases for larger cloud droplets and varies from 300 - 700 meters for the case with fall velocity 10 cm sec^{-1} (Fig. 4b) to more than 2 km for the case with fall velocity 50 cm sec^{-1} (Fig. 3b).

4. Discussion

We have demonstrated, from a numerical simulation, that the flow at the upper levels of the cloud is very diffluent and therefore the trajectory of a particular air parcel is very sensitive to small changes in its position. It has also been shown that drop trajectories can differ quite strongly with the size of the drop resulting in spatial separation of drops with different sizes. The importance of the drop size separation mechanism is, evidently, in the fact that some of the air parcels will reenter the cloud with substantially reduced droplet number concentrations and will, therefore, generate favorable conditions for enhanced condensational growth. As the results presented here are based on a numerical simulation, one may ask how general these results are and how they are related to natural clouds?

First, we would like to note that strong flow diffluence in cloud vicinity, which is the prime cause of drop size separation, has been noted previously in many other numerical studies. Examples of highly divergent flow patterns from both numerical and laboratory flow studies are given, e.g., in Dutton (1976). The separation of flow into two regimes, similar to that presented here, can be seen in the 2-D simulations by Libersky (1980). The sensitivity of the trajectories to small changes in their position has been demonstrated in 3-D numerical simulations by Klemp et al

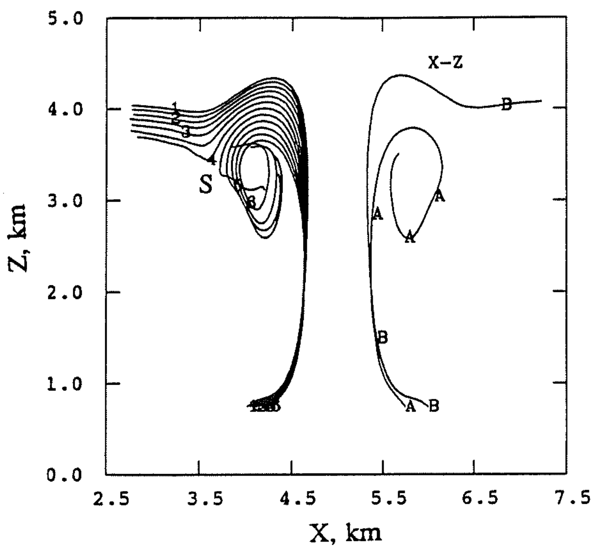

Fig. 2. Trajectories positioned 25 m apart at the height z = 0.75 km along the x axis from 4.025 km to 4.3 km. Trajectories were traced from 300 to 2700 sec. Numbers on the left trajectories correspond to the air parcel positions at 1500 sec. Letters A and B on the right trajectories show the air parcel positions at 600 sec intervals.

(1981) and in 2-D simulations by Reuter and Yau, 1987. Similar sensitivity has also been noted in air parcel trajectories derived from the velocity fields observed with Doppler radars (J. Klemp, personal communication). Evidently, flow diffluence is a rather well known fact.

It should be noted that the results presented here have been obtained in simulations with rather course resolution (250 meters grid spacing in all directions). As a result, the small-scale features of the velocity field were effectively filtered by the subgrid scale turbulence and only the eddies on a scale larger than 250 m were resolved. The high resolution numerical simulations by Grabowski (1989), Grabowski and Clark (1991) demonstrated the formation of eddies of much smaller scale at the cloud-environment interface (see Fig. 5 taken from Grabowski and Clark, 1991). Their numerical experiments showed that the dominant mechanism leading to the formation of eddies at the cloud boundary is the baroclinic production of vorticity due to the horizontal buoyancy gradients. The same mechanism is responsible for the vorticity production and, consequently, the flow separation in our simulation. We expect that the drop size separation demonstrated here for large scale eddies will also exist for smaller eddies. High resolution simulations similar to those made by Grabowski and Clark will be able to answer the question on the prevalence of the drop size separation effect in cumulus clouds.

The answer to the second question requires observational studies aimed at the analysis of microphysical parameters on a large range of scales. Many recent studies of this kind have clearly shown the inhomogeneity of cloud parameters down to very small scales (see, e.g., Austin et al, 1985; Raga et al, 1990 among others). Austin et al (1985), e.g., have analyzed the warm cloud data from the CCOPE Project (1981) using the 10 Hz measurements of thermodynamical and microphysical parameters and have shown examples of almost instant changes (on a scale of 10 m) in droplet concentration and spectral shape. The data, however, can not show the air parcels history and, therefore, the explanation of the nature of this variability has to be made with different theoretical concepts. Undoubtedly, modeling studies with trajectory analyses will play an important role in verifying these concepts.

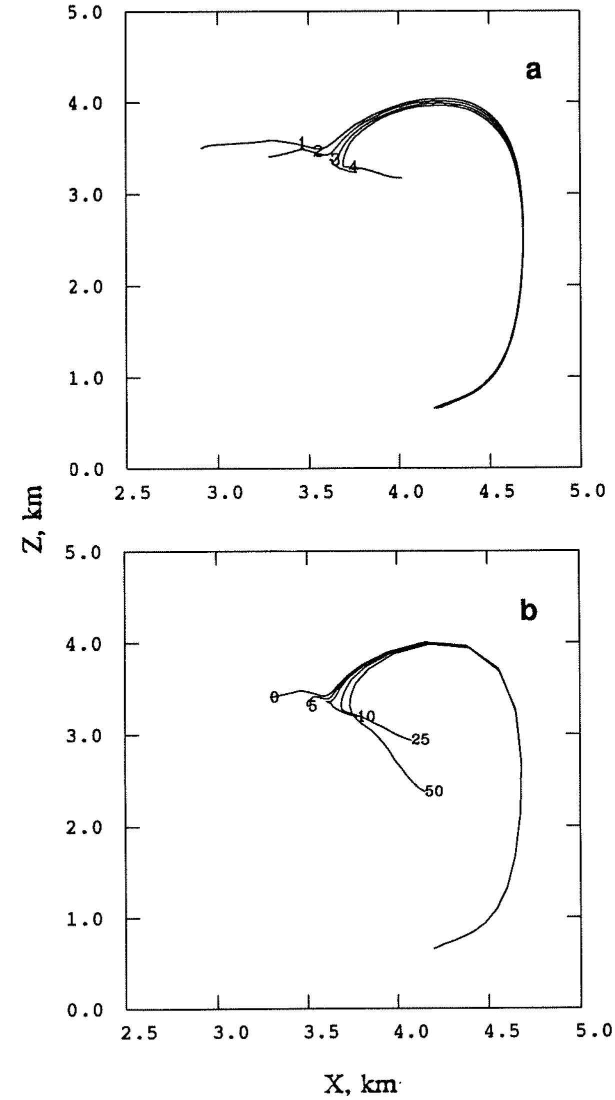

Fig. 3. The same as Fig. 2, but for 4 trajectories positioned 10 meters apart and traced from 300 to 2100 sec. a) trajectories of droplets moving with zero fall velocity; b) trajectories of droplets originating at the same point as trajectory #2 on plot a, but having fall velocity V_f = 5, 10, 25, and 50 cm s^{-1}. The fall velocity in cm s^{-1} is shown at the end of each trajectory.

5. Conclusions

It is shown that drop trajectories in a cumulus cloud can differ quite strongly with the size of the drop resulting in spatial separation of drops with different sizes. The small droplets with negligible fall velocities will have higher probability of being carried away from the cloud and completely evaporate, while the droplets with larger fall velocities are more likely to be recycled in the cloud. During the recycling process droplets of different sizes reenter the cloud at different spatial locations resulting in inhomogeneities in the total number concentration, as well as in the concentration of larger droplets. A decrease in the small droplet concentration in the recycled air parcels will enhance the condensational growth of the remaining larger drops and, therefore, facilitate rain formation, as well as increase its amount.

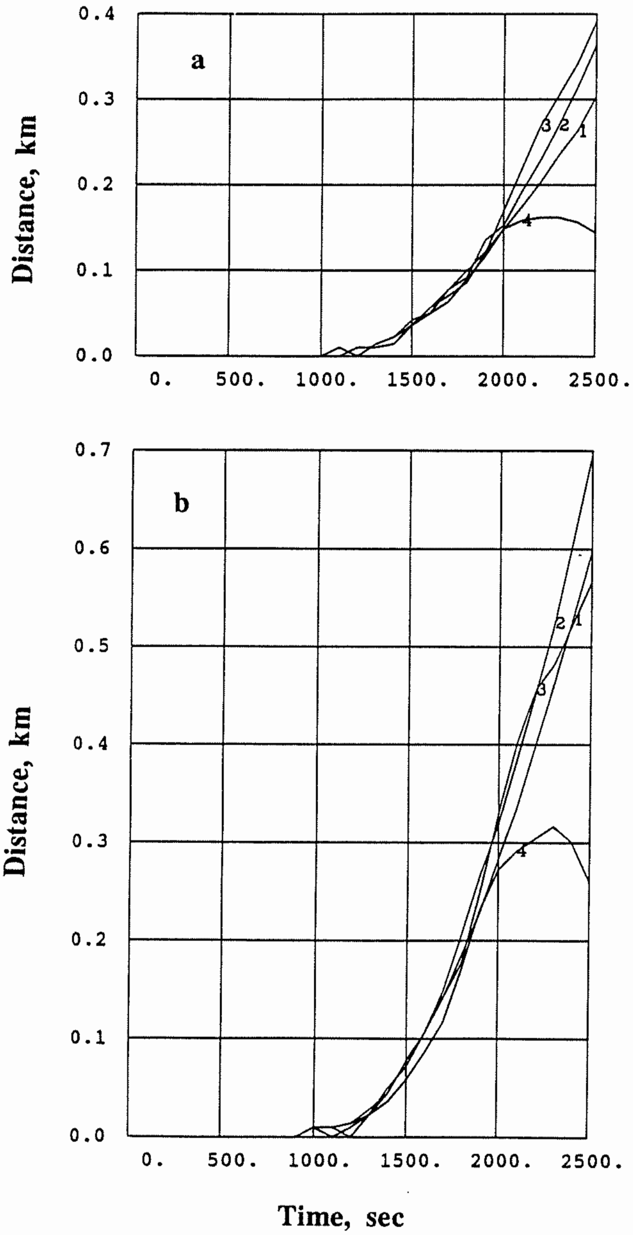

Fig. 4. The separation distance of droplets with zero fall velocity from droplets with the fall velocity 5 cm s^{-1} (a) and 10 cm s^{-1} (b). Lines 1-4 show the separation distance for trajectories 1-4 in Fig. 3a.

Acknowledgments. Many comments and discussions from Dr. Douglas Lilly are greatly appreciated. Dr. Alan Shapiro of CAPS have also read the manuscript and contributed to its improvement. The author would like to thank Piotr Smolarkiewicz of NCAR for providing the code for calculation of scalar advection based on his positive definite flux conserving scheme and helpful discussions concerning its implementation. Thanks are also extended to Robert Schlesinger of University of Wisconsin who provided the code for trajectory calculations. The help of Jeff Castle in preparing the plots is greatly acknowledged. Partial support for this research was provided by NASA under the Grant NAG 5-1528.

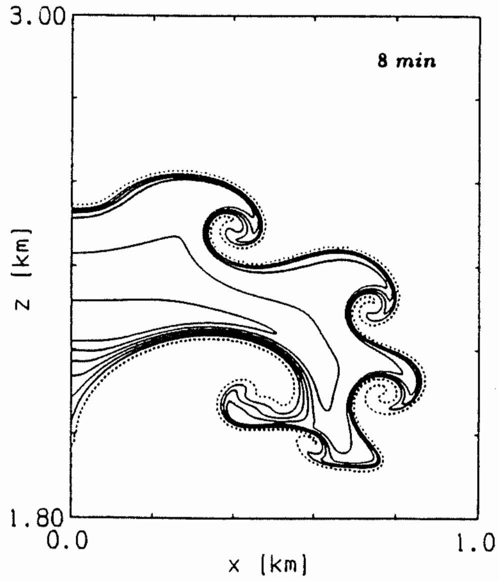

Fig. 5. Isolines of cloud water field from high resolution simulations by Grabowski and Clark (1991). Note the formation of eddies on the leading edge boundary of the thermal.

References

Austin P.H., M. B. Baker, A. M. Blyth, and J.B. Jensen, 1985: Small-scale variability in warm continental clouds. *J. Atmos. Sci.*, **42**, 1123-1138.

Dutton, J. A., 1976: *The ceaseless wind.* Dover publications. New York, 617 pp.

Grabowski, W. W., 1989: Numerical experiments on the dynamics of the cloud-environment interface: small cumulus in a shear-free environment. *J. Atmos. Sci.*, **46**, 3513-3541.

Grabowski, W. W., and T. L. Clark, 1991: Cloud-environment interface instability: Rising thermal calculations in two spatial dimensions. *J. Atmos. Sci.*, **48**, 527-546.

Jensen, J. B., and M. B. Baker, 1989: A simple model of droplet spectral evolution during turbulent mixing. *J. Atmos. Sci.*, **46**, 2812-2829.

Johnson D. B., 1982: The role of giant and ultragiant aerosol particles in warm rain initiation. *J. Atmos. Sci.*, **39**, 448-460.

Klemp, J. B., R. B. Wilhelmson and P. S Ray, 1981: Observed and numerically simulated structure of a mature supercell thunderstorm. *J. Atmos. Sci.*, **38**, 1558-1580.

Kogan, Y. L., 1978: A three-dimensional numerical model of a liquid-drop cumulus cloud that takes account of microphysical processes. *Izv. Akad. Sci. USSR, Atmos. Ocean. Phys.*, **14**, 617-623.

Kogan Y.L., 1991: The simulation of a convective cloud in a 3-D model with explicit microphysics. Part I: Model description and sensitivity experiments. *J. Atmos. Sci.*, **48**, 1160-1189.

Libersky, L. D., 1980: Turbulence in cumulus clouds. *J.Atmos. Sci.*, **37**, 2332-2346.

Paluch I.R. and C. A. Knight, 1984: Mixing and the evolution of cloud droplet size spectra in a vigorous continental cumulus. *J.Atmos. Sci.*, **41**, 1801-1815.

Raga, G. B., J.B. Jensen, and M. B. Baker, 1990: Characteristics of cumulus band clouds off the coast of Hawaii. *J. Atmos. Sci.*, **47**, 338-355.

Reuter, G. W., and M. K. Yau, 1987: Mixing mechanisms in cumulus congestus clouds. Part II: Numerical simulations. *J. Atmos. Sci.*, **44**, 798-827.

The Influence of Warm Microphysical Processes on Ice Formation and Diffusional Growth - A Numerical Study

Tamir Reisin, Shalva Tzivion and Zev Levin

Dept. of Geophysics and Planetary Sciences, Raymond and Beverly Sackler Faculty of Exact Sciences, Tel Aviv University, Ramat Aviv 69978, Israel.

1. INTRODUCTION

Numerical simulations of cloud development and rain initiation require accurate numerical methods for the treatment of microphysical processes. We have developed an accurate numerical multi-moment method for the solution of the stochastic kinetic transfer equations (Tzivion et al., 1987; Tzivion et al., 1990) that conserves the balance between two or more physical moments in each size category of the cloud particles distribution function.

The present work uses an axisymmetric hydrodynamic numerical model of a convective cloud to evaluate the effects of the warm processes on the development of ice. The model includes all the warm microphysical processes and part of the ice processes, and all of them are formulated with our multi-moments method.

Many of the theoretical works that deal with the diffusional growth of ice particles (e.g.: Miller and Young, 1979) assume the presence of liquid water, vapor and ice, but maintain water saturation. This approach artificially enhances the diffusional growth of the ice by transfering mass from evaporating drops to the ice particles. In addition, laboratory experiments are difficult to perform because it is difficult to create and maintain water supersaturated in the presence of large populations of drops and ice particles. However, supersaturation with respect to water (and obviously with respect to ice) is common in convective clouds with large vertical velocities. Early in the cloud development the concentration of water drops is usually several orders of magnitudes greater than that of ice particles, allowing both drops and ice particles to compete for the available water vapor. Under certain conditions, both can grow by diffusion. Consequently, it is important to simultaneously evaluate the effect of the supersaturation on the evolution of the drops and the ice particles.

Hall (1980) treats the diffusional growth of drops and ice particles under supersaturated conditions, but assumes an average supersaturation during the time step Δt. This procedure does not guarantee proper treatment of the mass and concentration of the drops and the ice particles. Tzivion et al. (1989) pointed out the importance of accuracy in the calculation of the supersaturation during the time step Δt.

A new algorithm was developed that solves simultaneously for the changes in the mass distribution function of water drops and ice particles due to diffusional growth/evaporation. This algorithm permits detailed study of the variations of the supersaturation field when water and ice co-exist.

In a previous work (Tzivion et al. 1990, 1992) we showed that the CCN spectra significantly affect the rain formation processes in warm clouds. The present work assesses the influence of the concentration and spectra of water drops on the formation (nucleation and drops freezing) of ice, and on the diffusional growth of drops and ice in the cold part of the cloud.

2. DESCRIPTION OF THE MODEL

An axisymmetrical model of a convective cloud with detailed microphysics was employed. The dynamic equations were adapted from the model developed by Tzivion et al. (1984). The warm microphysical processes included are nucleation of CCNs, condensation /evaporation, collision- coalescence and binary breakup (Low and List kernel). The numerical treatment is similar to Tzivion et al. (1992). All the processes are solved using the method of moments.

The ice microphysical processes treated thus far include: drop freezing, ice crystal nucleation, and deposition/ evaporation of ice particles. We formulated an expression for the number and the mass of the drops that freeze at each time step at each grid point, according to Alheit et al. (1990). For the nucleation of ice crystals we adopted the formula proposed by Cotton et al. (1986), which takes into account both the ambient temperature and the supersaturation over ice and over water. As pointed out by various authors (e.g.: Rangno and Hobbs, 1990), the ice nucleation process could be enhanced under water supersaturation conditions.

The changes in the mass distribution functions of the drops and the ice particles due to diffusion/evaporation of water vapor were calculated by solving analytically (for one time step) the stochastic diffusion equation (similar to Tzivion et al, 1989). These solutions allow us to record expressions for the concentration and the mass in each category of drops and ice particles. The final solution for these values is arrived at by calculating the change in the supersaturation with respect to ice and water during one time step.

Using the stochastic equations for the mass distribution function of the drops and ice particles, the diffusional growth equations for drops and ice particles, and the definitions of the supersaturation, we obtain two coupled differential equations for $\Delta S_w(t)$ and $\Delta S_i(t)$ (supersaturation over water and ice, respectively). Here t

varies between t_0 to $t_0+\Delta t^*$ (the time step of the process). Assuming that the supersaturation is not seriously affected during one time step by changes in the temperature and pressure fields, or by changes in the mass distribution function of the particles, we can write:

$$\Delta S_w(t_0+\Delta t) = \frac{\delta_2 \Delta S_w(t_0) - \Delta S_i(t_0)}{(\delta_2 - \delta_2)} e^{-K_1 \Delta t} + \\ + \frac{\Delta S_i(t_0) - \delta_1 \Delta S_w(t_0)}{(\delta_2 - \delta_1)} e^{K_2 \Delta t}$$

$$\Delta S_i(t_0+\Delta t) = \left(\frac{\delta_1}{\delta_2 - \delta_1}\right) [\delta_2 \Delta S_w(t_0) - \Delta S_i(t_0)] e^{-K_1 \Delta t} + \\ + \left(\frac{\delta_2}{\delta_2 - \delta_1}\right) [\delta_2 \Delta S_i(t_0) - \Delta S_w(t_0)] e^{-K_2 \Delta t}$$

where:

$$K_1 = \tfrac{1}{2}[(P_i+R_w) - \sqrt{(P_i-R_w)^2 + 4R_i P_w}]$$

$$K_2 = \tfrac{1}{2}[(P_i+R_w) + \sqrt{(P_i-R_w)^2 + 4R_i P_w}]$$

$$\delta_1 = (R_w - K_1)/R_i \qquad \delta_2 = (R_w - K_2)/R_i$$

and,

$$R_j = \bar{\xi}\, A_j(P,T)\, C_j(P,T) \sum_{k=1}^{K} (\bar{m}_{k,j})^{\frac{1}{3}} N_{k,j}$$

$$P_j = \bar{\xi}\, B_j(P,T)\, C_j(P,T) \sum_{k=1}^{K} (\bar{m}_{k,j})^{\frac{1}{3}} N_{k,j}$$

$$A_j(P,T) = \left[1 + \frac{L_j}{c_p}\frac{\partial q_{s,w}}{\partial T}\right] \qquad B_j(P,T) = \left[1 + \frac{L_j}{c_p}\frac{\partial q_{s,i}}{\partial T}\right]$$

where j refers to water (w) or to ice (i)

We used the following symbols:
$\Delta S_{w/i}$ the specific humidity surplus for water/ice,
$q_{s,w/i}$ the saturation mixing ratio for water/ice,
P, T, c_p pressure, temperature and specific heat at constant pressure, respectively,
$L_{w/i}$ latent heat of condensation/deposition,
$N_{k,w/i}$ the specific drop/ice number in category k,
$\bar{m}_{k,w/i}$ the average drop/ice mass in category k,
$C_{w/i}(P,T)$ a known function of pressure and temperature,
$\bar{\xi}$ a nondimensional parameter according to Tzivion et al., (1989).

As the above expressions show, there is an interdependence on the supersaturation over ice and water, as well as on the concentration and mass of both types of particles.

Both $\Delta S_w(t_0+\Delta t)$ (in condensation) and $\Delta S_i(t_0+\Delta t)$ (in evaporation) can change their signs within one time step. During diffusional growth the water supersaturation steadily decreases until water saturation is reached and water begins to evaporate. Thus, within one time step there is a switch from condensation to evaporation of the water drops. A similar process may occur for evaporation of ice that would switch to deposition.

In this work we assume the ice particles to be oblate spheroids. The mass growth rate by diffusion for a single ice crystal was formulated according to Alheit et al. (1990).

3. RESULTS

Two clouds developing under identical ambient initial conditions were compared, differing only in the CCN spectra. The first cloud had a typically "maritime" spectrum that yielded a drop concentration of $\approx 100\ cm^{-3}$ with some relatively large droplets. The second cloud had a narrow drop spectrum and a drop concentration of $\approx 1200\ cm^{-3}$ ("continental" spectrum). These two clouds were compared in three different simulations:

a) active drop freezing and ice nucleation,
b) only drop freezing active for ice formation,
c) only ice nucleation active for ice formation.

Diffusional growth was active in all 3 simulations. Since we were interested in the first stages of ice growth, the simulations were limited to 30 minutes from cloud initialization, when the cloud has already reached its maximum development. No drops nucleation was permitted in the cold part of the cloud.

For both CCN spectra, the clouds developed with maximum updrafts of 12-13 m/sec and maximum liquid water content of ≈ 3 g/Kg. The clouds bases were at 1000 m and the temperature there was $\approx 5^0$C. The cloud tops reached 4500m and temperatures of $\approx -19^0$C. A similar set of numerical simulations was performed for a more developed cloud (tops at $\approx -25^0$C), and the results were qualitatively the same as in the smaller cloud even though somewhat enhanced, so we restrict ourselves here to discussion of one set of results.

a) drop freezing and ice nucleation:

Relatively large differences appeared in the ice concentration of the maritime and continental clouds 30 minutes after initialization. As shown in Fig.1, at -18^0C the maximum ice concentration in the maritime cloud was almost 12 l^{-1}, five times greater than in the continental cloud (2.5 l^{-1}). The spatial distribution of the ice particles was also different in the two clouds. The volume of the cloud bounded by the 1 l^{-1} ice concentration was about 100 times larger in the maritime cloud than in the continental one. Large differences were also observed in the mass content of the ice (Fig.2). The maximum ice mass content for the maritime cloud was 0.06 g/Kg compared to 0.3×10^{-3} g/Kg in the continental cloud. Figure 3 shows the spatial distribution of the water supersaturation for both clouds before and after nucleation and diffusion growth processes. The supersaturation which developes from the dynamic fields (uplift), was the input field for the microphysical calculations. The supersaturation in the maritime cloud was larger everywhere than in the continental cloud, with a maximum value of around 9% prior to the depletion by the microphysical processes. The growth of the drops and the ice depleted the supersaturation and it practically returned to saturation in the continental cloud. Vapor depletion was less effective In the maritime cloud due to the lower concentration of particles, and the supersaturation remained relatively high (up to $\approx 5\%$). These differences in the supersaturation between the two clouds were probably responsible for the significant difference in the ice concentration obtained for the two cases.

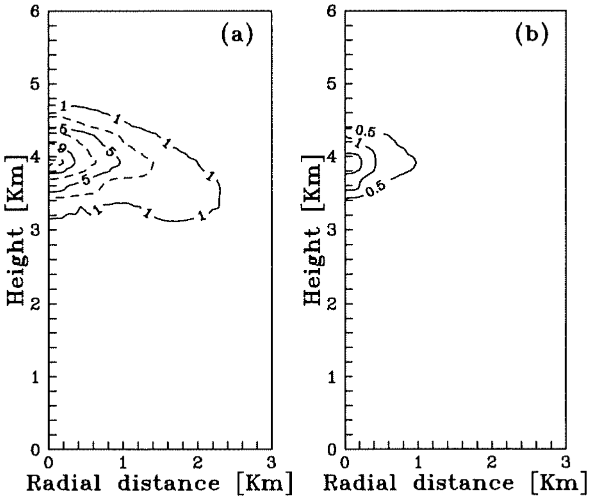

Fig. 1: Ice concentration in l^{-1}, 30 minutes from cloud initiation for (a) the maritime cloud and (b) the continental cloud. Both ice nucleation and drop freezing are active.

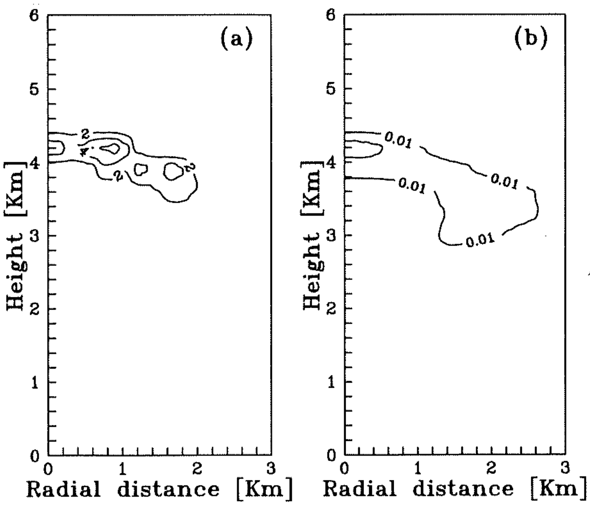

Fig. 2: As in Fig. 1 except for ice mass in 10^{-2} g/Kg.

b) drop freezing:

After 30 minutes of cloud development the maximum ice concentration in the maritime cloud was 0.2 l^{-1}, two and half times the concentration in the continental cloud (0.08 l^{-1}). The difference in ice mass was even more pronounced: the maritime cloud reached a maximum of 0.06 g/Kg and the continental cloud no more than 10^{-5} g/Kg (almost three orders of magnitude). These differences were maintained everywhere in the cloud. The spatial distribution of the ice mass (not shown here) for both clouds was almost identical to that presented in Fig.2. The ice concentrations yielded by drop freezing were lower by almost three orders of magnitude compared to that obtained when ice nucleation was also included.

c) ice nucleation:

The maximum ice concentration obtained in the maritime cloud was 20 l^{-1} and in the continental cloud 2.4 l^{-1}. As explained before, this difference was probably due to the different supersaturation that developed in the two clouds. The ice concentrations obtained here for the maritime cloud were larger than those obtained when drop freezing was active, probably because frozen drops grow more efficiently than liquid drops of the same size. In other words, the slight decrease in supersaturation resulted in a reduction of the ice nucleation rate and the lowering of the ice crystal concentrations. The latent heat released in the freezing process might also serve to decrease the supersaturation. The ice mass content in the present case was very low: 1.4×10^{-6} g/Kg for the maritime cloud and 2.6×10^{-7} g/Kg for the continental one.

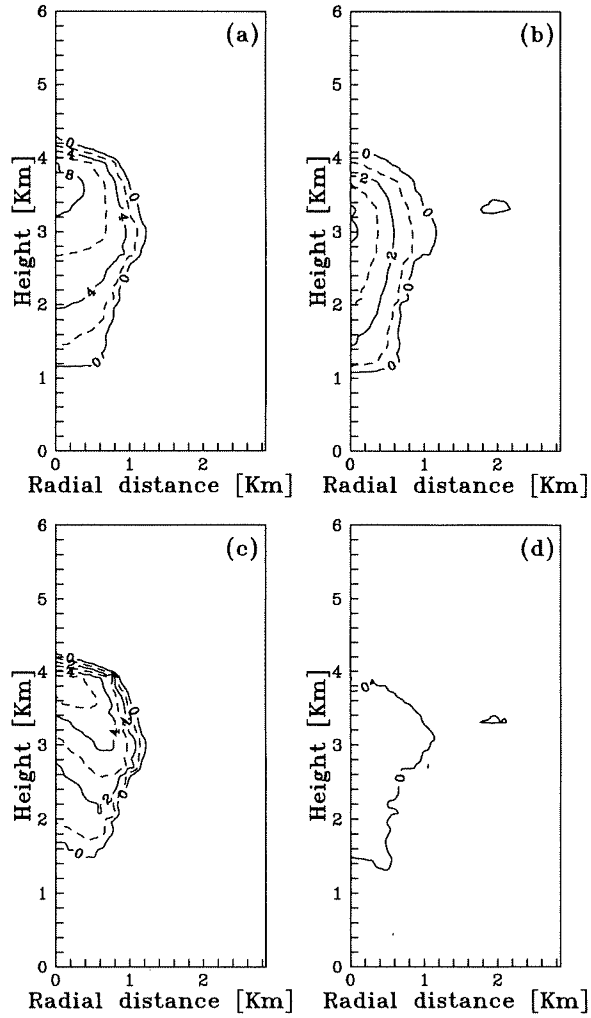

Fig. 3: Water supersaturation in percent, 30 minutes from cloud initiation for: (a) the maritime cloud before nucleation and diffusion, (b) the continental cloud before nucleation and diffusion, (c) the maritime cloud after nucleation and diffusion, and (d) the continental cloud after nucleation and diffusion. Both ice nucleation and drop freezing are active.

4. DISCUSSION AND CONCLUSIONS

The results obtained in this study relate to a particular case in which similar thermo-hydrodynamical cloud fields are subjected to different CCN spectra. They cannot be generalized until additional numerical experiments are performed using various initial conditions and CCN distributions. Nevertheless, some important conclusions can be drawn about ice formation processes and diffusional growth of ice at the first stages of cloud development: a) Drop freezing yields similar concentrations in continental and maritime clouds, the ice mass content in the maritime cloud is almost three orders of magnitude larger than in the continental cloud. Large drops are not produced in the continental cloud. While the freezing probality for small drops is relatively low, their large concentrations still produce a large number of frozen drops, comparable to that produced in the maritime cloud. In the maritime cloud, the frozen drops are relatively large, producing a large ice content. In any case, the ice concentrations resulting from this process are very low.

b) Under similar dynamic conditions the supersaturation produced in the maritime cloud is greater than in the continental cloud. A relatively low drop concentration in the maritime cloud prevents efficient depletion of the water vapor such as occurs in the continental cloud. Greater supersaturation in the maritime cloud produces enhanced nucleation of ice. These results are in agreement with various reports (e.g.: Rangno and Hobbs, 1990 and unpublished preliminary results of measurements in Israel) describing rather high ice concentrations in maritime clouds. The diffusional growth of ice is also enhanced relative to the continental case, due to the higher ice concentration and the lower drops concentration in the maritime cloud.

c) From the results obtained with only one process of ice formation active, we can deduce that the main contribution to cloud ice concentration is ice nucleation, while the freezing of drops is responsible for the ice mass content.

d) The combined processes of drop freezing and ice nucleation produce a higher ice concentration and greater ice content in the maritime cloud than in the continental one. With the specific ambient and initial conditions prescribed in these simulations, it seems that sufficiently large ice crystal concentration are naturally formed in the maritime cloud.

e) Although the diffusional growth of ice is more active in the maritime cloud, it seems that in the first stages of ice growth, diffusional growth cannot produce a rapid increase in the ice mass. The presence of a large number of drops in a water supersaturated volume inhibits the diffusional growth of the ice particles. Yet, a detailed analysis of the ice size spectrum shows that individual ice particles, growing like plates, can relatively quickly reach sizes where the riming process becomes effective. Frozen drops, while relatively large, are too few to initiate an effective growth process.

f) Since the numerical treatment presented here can give a more realistic description of the diffusional growth of the ice and drops than other methods, it is suitable for studying the Bergeron-Findeisen process (transfer of drops mass to ice mass). Under the conditions studied in this work, the Bergeron-Findeisen process appears to be effective only near the cloud top where the ice is still supersaturated and the water drops are subsaturated. It is possible that at later stages of cloud development the riming process would produce a significant decrease in the drop concentrations, and the Bergeron-Findeisen process could become more effective.

g) The results indicate that in certain cases there is a significant linkage between the warm microphysical processes, ice formation and diffusional growth in the cold part of the cloud. Conclusions about rain formation processes in cold clouds await further experiments that include additional ice growth processes. This work is in progress.

5. REFERENCES

Alheit, R.R., A.I. Flossmann and H.R. Pruppacher, 1990: A theoretical study of the wet removal of atmospheric pollutants. Part IV: The uptake and redistribution of aerosol particles through nucleation and impaction scavenging by growing cloud drops and ice particles. *J. Atmos. Sci.*, **47**, 870-887.

Cotton, W.R., G. Tripoli, R.M. Rauber and E.A. Mulvihill, 1986: Numerical simulation of the effects of varying ice crystal nucleation rates and aggregation processes on orographic snowfall. *J. Climate Appl. Meteor.*, **25**, 1658-1680.

Hall, W.D., 1980: A detailed microphysical model within a two dimensional dynamic framework: model description and preliminary results. *J. Atmos. Sci.*, **37**, 2486-2507.

Miller, T.L. and K.C. Young, 1979: A numerical simulation of ice crystal growth from the vapor phase. *J. Atmos. Sci.*, **37**, 458-469.

Rangno, A.L. and P.V. Hobbs, 1990: Rapid development of high ice particle concentrations in small polar maritime cumuliform clouds. *J. Atmos. Sci.*, **47**, 2710-2722.

Reisin, T., S. Tzivion, Z. Levin and G. Feingold, 1988: Numerical simulation of an Hawaiian convective cloud with a high resolution axisymmetric model. *Second WMO Intl. Cloud Modelling Workshop*, Toulouse, France, 231-235.

Tzivion, S., Z. Levin and A. Manes, 1984: Numerical simulation of the effects of stable regions aloft on the development of thermal convection. *Proc. Int. Cloud Physics Conf.*, Tallin, USSR, IAMAP, 537-540.

---, G. Feingold and Z. Levin, 1987: An efficient numerical solution to the stochastic collection equation. *J. Atmos. Sci.*, **44**, 3139-3149.

---, ---, and ---, 1989: The evolution of raindrop spectra. Part II: Collisional collection/breakup and evaporation in a rainshaft. *J. Atmos. Sci.*, **46**, 3312-3327.

---, T. Reisin, Z. Levin and G. Feingold, 1990: Numerical simulations of cloud seeding with hygroscopic nuclei. 1990 *Conference on Cloud Physics, San Francisco, CA., USA*. 693-697.

---, T. Reisin and Z. Levin, 1992: Numerical simulation of hygroscopic seeding in a convective cloud. *J. Appl. Meteor.*, (submitted for publication).

CONCERNING PRIMARY ICE NUCLEI CONCENTRATIONS AND WATER SUPERSATURATIONS IN THE ATMOSPHERE

Paul J. DeMott, David C. Rogers, and Lewis O. Grant

Colorado State University
Fort Collins, CO

1. INTRODUCTION

A body of experimental evidence exists which suggests that ice nuclei concentrations in the atmosphere are sensitive to the magnitude of water vapor supersaturation to which the atmospheric aerosol is exposed. It has also been observed that high ice crystal concentrations occur in coincidence with supercooled cloud situations which may be favorable for production of high supersaturations, at least in localized regions.

In this paper we use numerical cloud model simulations to give further insight into scenarios which may lead to the generation of water vapor supersaturations which exceed those generally believed to exist in clouds. These numerical simulations incorporate formulations for the experimentally measured supersaturation response of natural ice nucleus aerosols in order to test the hypothesis that high concentrations of ice crystals may be generated in these regions. Also, we briefly report on an experimental program to measure natural ice nuclei and their response to water vapor supersaturation using the Colorado State University dynamic cloud chamber.

2. BACKGROUND

It has recently been hypothesized (Hobbs and Rangno, 1990; Rangno and Hobbs, 1991) that high water vapor supersaturated conditions (5-10%) are occasionally produced in supercooled clouds and lead to rapid generation of high concentrations of ice crystals. This hypothesis was based on a large number of aircraft observations of the evolution of ice crystal concentrations in maritime cumulus clouds. Concentrations exceeding 100 L^{-1} were noted at temperatures as warm as -10°C. Conditions at the onset of high concentrations of small ice crystals were the onset of rapid coalescence, and the preexistence of less than a few per liter of frozen drizzle drops or graupel. Earlier modeling studies indicated that such conditions are favorable for the generation of sustained high supersaturations in pockets of clouds. Indeed, simulations with both microphysically detailed one-dimensional (Young, 1974a) and two-dimensional (Hall, 1980) cloud models have demonstrated that the reduction of the condensate surface area by coalescence leads to water vapor supersaturations (SS_w) from 5 to 15%. Other factors may be involved as well in raising the ambient saturation ratio.

In the above noted hypothesis, the critical connection between the generation of high SS_w and high ice concentrations is the availability of primary heterogeneous ice nuclei which respond to SS_w. One aspect supporting this conjecture is the absence of other potential explanations. Rangno and Hobbs pointed out that the rates at which crystals appeared were too fast to be explained by the Hallett-Mossop ice multiplication mechanism. This also appears to be the case in some continental cumulus clouds (Czys, 1990). There is little chance for explaining high ice concentrations in the tops of clouds by evaporatively-enhanced contact freezing, as originally proposed by Hobbs and Rangno (1985). Baker (1991a) refutes such a possibility based on calculations of the maximum numbers of aerosol particles which can potentially be scavenged by phoresis. Furthermore, the balance of applicable measurements made in the last 20 years simply do not support the availability of high enough numbers of potential contact freezing nuclei in the atmosphere (Meyers et al., 1992). Hobbs and Rangno (1990) now propose that contact freezing could explain the low concentrations of frozen drizzle drops in their "first-stage" of ice development. We consider this first stage as part of the numerical investigations presented here. Another process which may lead to rapid ice formation for these conditions is droplet collision-freezing Czys (1989). Based on Czys' calculations, conditions for cavitation during droplet collisions begin to exist as the largest droplets reach 250μm, and the generation rate of ice would proceed faster for the broadest droplet size distributions. Currently, no verification exists for such a process. Others have also investigated the generation of high SS_w during large droplet freezing as the source for large numbers of ice crystals. Baker (1991b) reviews these studies and, based on calculations of the volume of effect of this process, rules it out as a factor in the Hobbs and Rangno hypothesis.

In order to evaluate the potential that concentrations of ice forming nuclei exist which will respond to the magnitudes of SS_w created in the Hobbs and Rangno scenario, one must put numbers to the supersaturation spectra of ice nuclei based on available studies. The apparent mechanisms for ice formation in this case are deposition (sorption) on less hygroscopic ice nuclei and condensation freezing nucleation. Power law supersaturation dependencies have been verified for some artificial ice nucleus aerosols (Schaller and Fukuta, 1979; DeMott, 1992). Meyers et al. (1992) reviewed the relevant measurements ice nuclei for natural aerosols in this area. There have been two primary measurement methods: the filter development method, and the continuous flow thermal gradient diffusion chamber (CFD). Many earlier studies employing devices to expose particles collected from the air on filters to known humidity conditions did not clearly establish water supersaturated conditions over the filters. More recent studies appear contradictory. Rosinski and colleagues (i.e., Rosinski and

Morgan, 1988; Rosinski, 1991) have consistently noted that although a small SSw enhances nucleation, no additional ice nuclei were activated at higher SSw for aerosols collected on filters. Berezinskiy and Stepanov (1986) and Saunders and Al-Juboory (1988), however, found a clear and continuous power law dependence of nuclei concentrations on SSw. In the latter case, the results were consistent with a simultaneously operated CFD. This latter device presents a more natural technique, allowing for measurement of nucleation at well defined supersaturations without the support or potential interference of a substrate (Hussain and Saunders, 1984; Tomlinson and Fukuta, 1985; Rogers, 1988).

The upper end values of average ice nuclei concentrations measured with filters or CFD's range from greater than 1 L^{-1} at temperatures as warm as -7°C to approximately 20 L^{-1} at -20°C. These values are very high compared to "standard" ice nucleus spectra (Fletcher, 1962) used to define "ice-enhancment ratios" in clouds (Hobbs and Rangno, 1985), but are not high enough to validate the hypothesis of Hobbs and Rangno (1990). Nevertheless, most measurements made thus far have not exceeded 5% nominal SSw. Also, many of the measurements have been conducted on ground level aerosols and may not be representative of ice nuclei at cloud levels. The current measurements do suggest a form for the supersaturation effect which can be tested in concert with numerical simulations which mimic the natural processes responsible for generating water supersaturations. Such an analysis follows.

3. NUMERICAL MODEL INVESTIGATIONS

Numerical simulations were performed to evaluate the conditions and processes which can lead to local extreme high values of SSw. We used the detailed microphysical model of adiabatic parcel ascent described by Rokicki and Young (1978), as derived from Young (1974b). This the model simulates the three major processes of nucleation, diffusion and collection, which are key to precipitation formation. Hydrometeor removal by precipitation does not occur in this model. Modifications were made to the ice nucleation routines, and these are outlined in the next section.

3.1 Ice Initation in the Cloud Model

For numerical simulations, we use the Meyers et al. (1992) formulation for the combined effects of deposition and condensation freezing as derived from CFD studies:

$$N = \exp\,(a + b\ SS_i) \qquad (1)$$

where a = -0.639, b = 0.1296, and SS_i is the ice supersaturation (%). This formulation is strictly valid from -7 to -20°C and for SS_i above water saturation to SSw = 5%. We necessarily extrapolate the function for conditions of SSw which fall outside of this range. Ice is arbitrarily not permitted to form in the model at temperatures warmer than -5°C.

Two other nucleation modes are treated in the numerical model. Contact freezing follows Meyers et al. (1992). Immersion freezing nucleation is based on Vali and Stansbury (1965) and Vali (1971).

3.2 Description of Simulations

The model simulations covered the range of conditions typical of values observed in real clouds. We chose two cloud base temperatures (15°C and 5°C) three constant updraft speeds (1, 3 and 10m s^{-1}), and three diverse CCN spectra. The CCN spectra correspond to a typical continental aerosol, a typical maritime aerosol, and one which we call "super-maritime" with a very low concentration (50 cm^{-3} at 1% SSw). The CCN spectra are continuous functions and are specified according to the usual power law equation, $N = C\ SSw^k$, where N is the concentration of activated particles (cm^{-3}), and C and k are constants:

continental	$N = 700\ SSw^{0.75}$
maritime	$N = 291\ SSw^{0.46}$
super-maritime	$N = 50\ SSw^{0.46}$

All simulations started at cloud base, used 3 second time steps, and continued until the air parcel temperature was colder than -20°C. Tables I and II show the predicted concentrations of ice particles and SSw at -10°C, -15°C and -20°C.

Figure 1 shows the differences in cloud parcel evolution for two cases, both having 15°C cloud base and 3 m s^{-1} updraft. One case has the maritime CCN, and the other has super-maritime CCN. Extremely high SSw (22%) was found for the super-maritime CCN case. SSw increased initially because the available vapor sinks were minimal, that is, after drop growth by collision and coalescence had swept out the smaller droplets, and while the ice population still consisted mostly of a few per liter of small crystals and large frozen droplets. As the parcel continued to rise, SSw became extremely high, and by -15°C, ice nucleation by combined deposition and condensation freezing was producing large concentrations of small ice. In the maritime case, however,

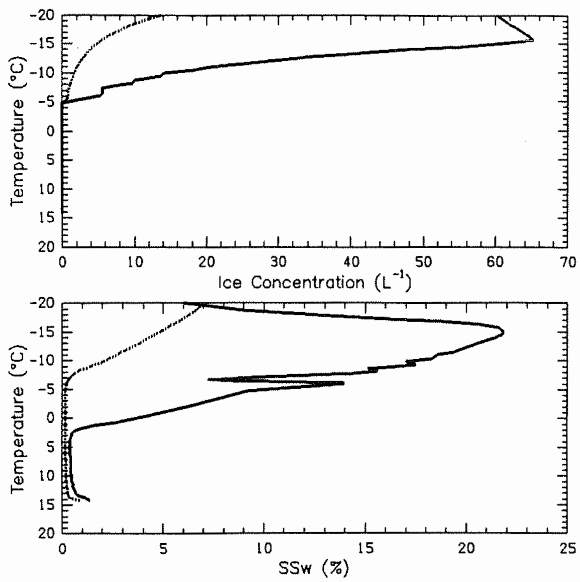

Figure 1. Model simulations for 3 m s^{-1} updraft, 15°C cloud base super-maritime (solid line) and maritime (dotted line) CCN. Water supersaturation (a) and ice crystal concentration (b) are plotted.

coalescence and the attendant rise in SS_w were delayed until about -7°C. At that point, ice was being produced in sufficient numbers to act as a strong vapor sink, and the rise in SS_w was retarded by this ice and by the more numerous CCN.

The differences in evolution between these two simulations are also evident in the size distributions of cloud and ice water. Figure 2 shows that when the parcel ascended through 0°C at 900 sec, coalescence in the super-maritime case had advanced considerably compared to the maritime case. Nucleation of new droplets is also evident in the super-maritime case, due to the higher SS_w (cf., Figure 1). Differences in the ice populations are shown in Figure 3 at -6°C (1290 s above cloud base). The maritime case has low ice concentration (0.8 L^{-1}) and exhibits features in two distinct parts of the ice population: fresh nucleation of small ice crystals (<50 μm) by deposition and condensation freezing and large droplets frozen primarily by contact freezing. Ice production in the super-maritime case began to accelerate by this time, giving higher concentrations (5.6 L^{-1}). The presence of large frozen droplets and rimed ice particles are predominant features for the super-maritime case.

Tables I and II summarize the simulations that were performed, and show the range of SS_w and related ice crystal concentrations produced. Only one very extreme case was found: super-maritime

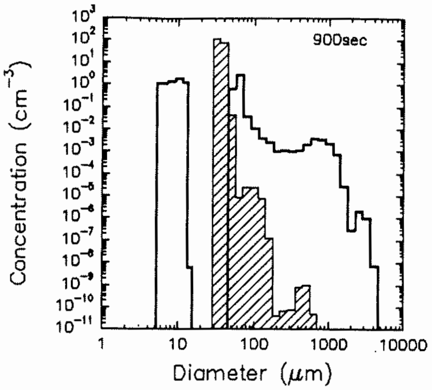

Figure 2. Cloud water size distributions for the simulations in figure 1 at 0°C (900 sec above cloud base), maritime (hatched) and super-maritime (solid line) CCN.

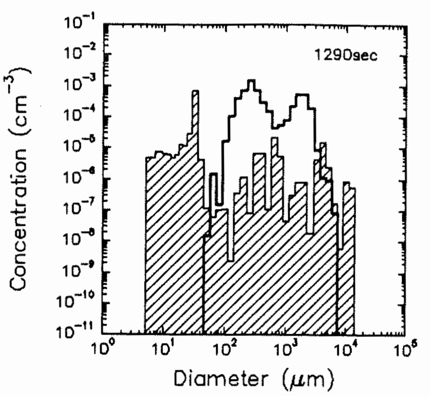

Figure 3. Ice particle size distributions for the simulations in figure 1 at -6°C (1290 sec above cloud base), maritime (hatched) and super-maritime (solid line) CCN.

CCN with an updraft of 3 m s^{-1}. The peak ice concentration was 61 L^{-1} at -15°C with water supersaturation of 21.8%. In contrast, by -15°C the other CCN cases produced ice concentrations 1 to 7 L^{-1} and SS_w of 0.1 to 5.3%.

Another important variable for these processes is the available time, as determined by updraft speed. For example, notice that in the super-maritime 1 m s^{-1} case, SS_w was high at -10°C, but fell by the time the parcel reached -20°C because ice concentrations were high enough to act as a significant vapor sink. We expect that there is some unique optimal mix of updraft speed, cloud base temperature, and CCN spectrum which will produce maximum values of SS_w and ice concentration, even higher than these simulations.

Table I. Ice concentration (per liter)

updraft (m/s)	cloud base temperature	continental (parcel temp.)			maritime (parcel temp.)			super-maritime (parcel temp.)		
		-10C	-15C	-20C	-10C	-15C	-20C	-10C	-15C	-20C
1	15C	1	5	12	3	7	15	12	11	10
3	15C	1	3	8	2	5	14	14	61	60
10	15C	1	3	10	2	3	10	2	8	44
1	5C	2	4	9	2	5	13	3	11	26
3	5C	2	4	8	2	4	10	2	4	37
10	5C	1	4	9	2	4	9	2	4	10

Table II. Water supersaturation (%)

updraft (m/s)	cloud base temperature	continental (parcel temp.)			maritime (parcel temp.)			super-maritime (parcel temp.)		
		-10C	-15C	-20C	-10C	-15C	-20C	-10C	-15C	-20C
1	15C	0.2	5.3	3.7	4.4	5.0	7.6	15.9	4.6	-3.7
3	15C	0.2	2.0	3.3	2.0	4.8	7.2	17.0	21.8	6.2
10	15C	0.3	0.2	0.4	0.4	0.4	0.4	1.3	7.9	15.0
1	5C	0.3	1.6	2.2	0.6	3.0	4.8	4.8	8.5	9.5
3	5C	0.1	0.1	1.1	0.2	0.2	2.5	0.5	1.7	9.5
10	5C	0.4	0.3	0.4	0.6	0.6	0.7	1.3	1.3	1.4

3.3 Summary

The magnitude of SS_w predicted are shown to be sensitive to the cloud base temperature, CCN spectrum, updraft, and parcel history. The numerical model results, incorporating known ice nuclei sensitivities to SS_w, suggest that ice crystal concentrations far exceeding those expected for "standard" natural ice nucleus spectra could occur. The predicted ice crystal concentrations do not approach the extremely high values reported by some authors, in excess of 100 L^{-1} at -10°C. We add, however, that there is a substantial lack of ice nucleus measurements at high supersaturations, and therefore there is considerable uncertainty about the validity of these simulations under these extreme conditions.

4. CURRENT EXPERIMENTS

New experiments are underway using the CSU dynamic cloud chamber (DeMott and Rogers, 1990), the filter technique, and a CFD to study ice formation by natural aerosols. A number of specific experiments are planned on isolated natural continental air samples whose aerosol properties such as size distribution and CCN spectra will also be characterized. One aspect of the studies is to analyze for the SS_w response of ice nuclei.

One technique initially employed in using the dynamic cloud chamber for these experiments ıas been to vary continuous expansion rates in ›rder to cause different SS_w to be produced as :loud forms at supercooled temperatures. The ıaximum SS_w achieved depends on both the simulated ıscent rate and the CCN activity of the natural .erosols. The value of peak SS_w achieved is :stimated by "equivalent" numerical simulation of :he cloud chamber experiments using the cloud ıodel. A range of SS_w from about 0.5% to greater :han 3% can be achieved in experiments which imulate 1 to 10 m s^{-1} updrafts. Somewhat higher Sw (~5 to 10%) can be achieved by performing rief and more rapid expansion tests which create ransient supersaturations. Preliminary results ver a limited range of conditions (SS_w < 3% and emperatures < -20°C) have not shown more than 10 uclei per liter present in ground level air. he dynamic chamber studies will analyze other ice ormation mechanisms as well, including the ffects of evaporation and recondensation cycles n ice nucleation (Rosinski and Morgan, 1991).

5. SUMMARY

A series of numerical cloud model imulations were performed to study the conditions ɔr generation of high sustained cloud parcel ater supersaturations and their potential ɲfluence on ice crystal formation. The imulations show production of very high ice rystal concentrations approaching values observed ɲ some clouds only for very special ircumstances. There is clearly a need for more ɘasurements of ice nuclei at high SS_w.

5. ACKNOWLEGEMENTS

This research was conducted with the support f the National Science Foundation (Grants ΓM8813345 and ATM-9103748) and the North Dakota tmospheric Resource Board through the NOAA ederal/State Cooperative Program in Atmospheric ɘderal/State Cooperative Program in Atmospheric ɔdification Research (Grant No. NA90AA-H-OA176).

. REFERENCES

ker, B.A., 1991a: On the role of phoresis in cloud ice initiation. J. Atmos. Sci., 48, 1545-1548.

ker, B.A., 1991b: On the nucleation of ice in highly supersaturated regions of clouds. J. Atmos. Sci., 48, 1904-1907.

rezinskiy, N.A. and G.V. Stepanov, 1986: Dependence of the concentration of natural ice-forming nuclei of different size on the temperature and supersaturation. Isvestiya, Atmos. and Oceanic Phys., 22 722-727.

ys, R.R., 1990: Observed versus diagnosed ice production rates in warm-based midwestern cumuli. Preprints of the AMS Conference on Cloud Physics, 23-27 July, San Francisco, CA., 25-29.

ys, R.R., 1989: Ice initiation by collision freezing in warm-based cumuli. J. Appl. Meteor., 28, 1098-1104.

Mott, P.J., 1992: Quantifying ice nucleation by cloud seeding aerosols for use in conceptual and numerical cloud models. Preprints, Symposium on Planned and Inadvertent Weather Modification, AMS, Jan. 5-10, Atlanta, Ga., 148-155.

Mott, P.J. and D.C. Rogers, 1990: Freezing nucleation rates of dilute solution droplets measured between -30 and -40°C in laboratory simulations of natural clouds. J. Atmos. Sci., 47, 1056-1064.

etcher, N.H., 1962: The Physics of Rainclouds, Cambridge University Press, p. 241.

Hall, W.D., 1980: A detailed microphysical model within a two-dimensional dynamic framework: Model description and preliminary results. J. Atmos. Sci., 37, 2486-2507.

Hobbs, P.V. and A.L. Rangno, 1985: Ice particle concentrations in clouds. J. Atmos. Sci., 42, 2523-2549.

Hobbs, P.V. and A.L. Rangno, 1990: Rapid development of high ice particle concentrations in small polar maritime cumuliform clouds. J. Atmos. Sci., 47, 2710-2722.

Hussain, K. and C.P.R. Saunders, 1984: Ice nucleus measurements with a continuous flow chamber. Quart. J. R. Met. Soc., 110, 75-84.

Meyers, M.P., P.J. DeMott, and W.R. Cotton, 1992: New primary ice nucleation parameterizations in an explicit cloud model. J. Appl. Meteor., in press.

Rangno, A.L. and P.V. Hobbs, 1991: Ice particle concentrations and precipitation development in small polar cumuliform clouds. Quart J. Roy. Meteor. Soc., 117, 207-241.

Rokicki, M.L. and K.C. Young, 1978: The initiation of precipitation in updrafts. J. Appl. Meteor., 17, 745-754.

Rogers, D.C., 1988: development of a continuous flow thermal gradient diffusion chamber for ice nucleation studies. Atmospheric Research 22, 149-181.

Rosinski, J., 1991: Latent ice-forming nuclei in the Pacific Northwest. Atmospheric Research, 26, 509-523.

Rosinski, J. and G.M. Morgan, 1988: Ice forming nuclei in Transvaal, Republic of South Africa. J. Aerosol Sci., 19, 531-538.

Rosinski, J. and G.M. Morgan, 1991: Cloud condensation nuclei as a source of ice-forming nuclei in clouds. J. Aerosol Sci., 22, 123-133.

Saunders, C.P.R. and S. Al-Juboory, 1988: A dynamic processing chamber for ice nuclei filter samples. 12th Intnl. Conf. on Atmos. Aerosols and Nucleation, Vienna, 697-700.

Schaller, R.C. and N. Fukuta, 1979: Ice nucleation by aerosol particles: Experimental studies using a wedge-shaped ice thermal diffusion chamber. J. Atmos. Sci., 36, 1788-1802.

Tomlinson, E.M. and N. Fukuta, 1985: A new horizontal gradient, continuous flow, ice thermal diffusion chamber. J. Atmos. Oceanic Techn., 2, 448-467.

Vali, G., 1971: Quantitative evaluation of experimental results on the heterogeneous freezing nucleation of supercooled liquids. J. Atmos. Sci., 28 402-409.

Vali, G., and E.J. Stansbury, 1965: Time-dependent characteristics of the heterogeneous nucleation of ice. Scientific Report MW-41, Stormy Weather Group, McGill university, Montreal, Canada, 31 pp.

Young, K.C., 1974a: The evolution of the drop spectra through condensation, coalescence, and breakup. Conf. on Cloud Physics, Tucson, Amer. Meteor. Soc., 95-98.

Young, K.C., 1974b: A numerical simulation of wintertime orographic precipitation: Part I. Description of model microphysics and numerical techniques. J. Atmos. Sci., 32, 965-973.

SENSITIVITY OF TAMEX SQUALL SIMULATIONS TO MICROPHYSICAL SCHEMES AND INITIAL CONDITIONS

Brad Schoenberg Ferrier[1,2], Wei-Kuo Tao[2], and Joanne Simpson[2]

[1]Universities Space Research Association
[2] Severe Storms Branch (Code 912)
Laboratory for Atmospheres
NASA Goddard Space Flight Center, Greenbelt, MD 20771

1. INTRODUCTION

The spatial distribution of diabatic heating associated with tropical mesoscale convective systems has a direct impact upon the structure of tropical circulations, as well as those teleconnection patterns affecting midlatitude climate. In preparation for the Tropical Rainfall Measuring Mission (TRMM), cloud models are being used to develop algorithms to estimate the diabatic heating associated with hydrometeor distributions retrieved from spaceborne radar and passive microwave measurements (Simpson et al., 1988; Tao et al., 1990).

However, we have found that the simulated structure of the convective storms can differ dramatically when different microphysical parameterizations are used. McCumber et al. (1991) found that the simulated structure of a GATE squall line was better represented using the microphysical formulation of Rutledge and Hobbs (1983, 1984; hereafter referred to as RH), whereas Ferrier et al. (1991) showed that the overall structure of a continental-midlatitude storm was better represented using the scheme of Lin et al. (1983; hereafter LIN). A major deficiency of these ice schemes is the need to adjust a variety of coefficients in order to obtain reasonable agreement between simulated and observed radar reflectivity distributions of a convective system - i.e., the vertical profiles of reflectivity in the convective region and the structure of stratiform precipitation (that is, if it is simulated at all in the model). The double-moment four-class ice scheme of Ferrier et al. (1991, 1992; hereafter F) has been developed for the purpose of simulating the basic radar and microphysical characteristics of convective systems in various large-scale environments without the need for substantial tuning of the parameterization.

This article will briefly document important feedbacks between the dynamics, the microphysics, and the initial forcing used to initiate convection in model simulations of a TAMEX (Taiwan Area Mesoscale Experiment) squall line, as well as show that the sensitivity of these feedbacks depends strongly upon differences in the assumed fallspeeds of large, heavily-rimed precipitation ice particles between the various microphysical schemes. Of particular importance is whether the simulated storms developed an upshear tilt and were long lived, or remained downshear-tilted (or vertically erect) and eventually decayed with time. Therefore, the dynamics and the microphysics of the upshear-tilted, long-lived simulated storms will be compared to those simulations that decayed and failed to tilt upshear.

2. MODEL DESCRIPTION

All simulations were performed using the two-dimensional, anelastic version of the Goddard Cumulus Ensemble model (Tao and Soong, 1986; Tao and Simpson, 1989) with open lateral boundary conditions (Klemp and Wilhelmson, 1978; Tao et al., 1991). The domain contains 612 horizontal and 31 vertical grid points. A constant horizontal grid spacing in the innermost 512 grid points is nested within a coarser, horizontally-stretched region (ratio between adjacent grid points is 1.0625:1), thus making the model less sensitive to the choice of gravity wave speeds assumed for the open lateral boundary conditions (Fovell and Ogura, 1988). The vertical coordinate is stretched with the finest vertical resolution at low levels (220 m near the surface, 1050 m at the top of the domain). The top of the domain extends up to 20 km. A 5-km deep Rayleigh absorption layer is applied at upper levels in the model in order to damp gravity waves reflected off of the upper boundary.

Model variables include horizontal and vertical velocities, potential temperature, perturbation pressure, and the mixing ratios of water vapor, small (non-precipitating) cloud droplets (cloud water), smaller ice crystals (cloud ice), rain, low-density snow (0.1 g cm^{-3}), moderate-density graupel (0.4 g cm^{-3}) and high-density frozen drops (0.9 g cm^{-3}). The microphysical scheme of F combines some of the main features of the three-class ice schemes of RH (cloud ice, snow and graupel) and LIN (cloud ice, snow and hail), although cloud ice in the F scheme is treated differently than in RH and LIN. Other model variables include the number concentrations of all types of ice particles (cloud ice, snow, graupel and frozen drops), as well as the mixing ratios of liquid water on each of the precipitation ice species (snow, graupel and frozen drops) during wet growth and melting. Additional features of the scheme are described in Ferrier et al. (1991, 1992).

3. TAMEX SQUALL LINE SIMULATIONS

On 16 May 1987 a north-south oriented squall line with extensive trailing stratiform precipitation propagated eastward over the Taiwan Strait at 14-16 m s^{-1} (Wang et al., 1990). The wind and thermodynamic profiles used as input for the model are from the 1200 UTC Makung sounding of May 16 (see Fig. 7a of Wang et al., 1990: note that local time is 8 h later than UTC). The CAPE and bulk Richardson number are 1450 m^2 s^{-2} and 29, respectively. A constant grid spacing of 750 m was used in the interior of the model. Convection was initiated using a 3 km deep, 48 km wide "cool pool" placed near the center of the domain, together with a mesoscale lifting profile centered at the the cool pool's leading edge (Tao et al., 1991). The lifting was applied during the first four hours of the simulation, and the magnitude of lifting thereafter decreased linearly with time to half its initial value by the end of the simulations at 5 h. Surface fluxes of heat and moisture were estimated using bulk aerodynamic formulas and assuming an ocean surface that was 0.75 ^{o}C warmer than the temperature at the lowest level in the sounding. The effects of longwave and shortwave radiation were not included in these simulations.

Table 1. Summary of TAMEX model runs.

Run	Ice Scheme	Cool Pool	Upshear Tilted/ Long-lasting?
1	RH	Normal	Yes
2	F	Normal	No
3	NO ICE (snow)	Normal	Yes
4	NO ICE (graupel)	Normal	Yes
5	NO ICE (frozen drops)	Normal	No
6	NO ICE (rain)	Normal	No
7	F	Weak	Yes
8	F	Strong	Yes
9	LIN	Normal	Yes

A summary of the different model runs is shown in Table 1. In the first six runs in which a "normal" cool-pool forcing was used, a maximum cooling rate of -.00875 $^{o}C\ s^{1}$ was applied during the first 10 minutes of the simulation. In the run 1, using the 3-class ice scheme of RH, a long-lived, upshear-tilted storm (relative to the westerly shear below 4 km) was simulated with an overall structure similar to what was observed (Miller and Tuttle, 1989; Wang et al., 1990). However, the storm simulated in run 2 using the 4-class ice scheme of F was vertically erect and decayed steadily with time after 2 h into the run.

After much manipulation of the F scheme (including numerous sensitivity tests of different microphysical modules), it was suspected that the hydrometeor fallspeeds were important in determining whether the simulated storm ultimately tilted upshear. In the convective regions of the simulated storms, graupel (2-4 m s^{-1} fallspeeds) was the dominant ice species in run 1, whereas faster falling frozen raindrops (4-8 m s^{-1} fallspeeds) were much more prevalent in run 2. To test this hypothesis, runs 3-6 were conducted using only warm-rain, Kessler-type (no ice) microphysics in the model, such that the terminal fallspeeds of supercooled rain were assumed to be either snow (run 3), graupel (run 4), frozen drops (run 5), or remain unchanged as rain (run 6). The rates of evaporation and cloud water accretion were changed in a manner consistent with the assumed changes in precipitation fallspeeds across the $0^{o}C$ level. Furthermore, the complicating effects of ice associated with latent heating by fusion and deposition were eliminated in this series of runs. For runs 3 and 4 in which the supercooled rain was treated as slow-falling snow or graupel (as in the RH scheme), the simulated storms were long lived and tilted upshear by 2.5 h into the simulations. The simulated squall line also decayed when graupel in the RH scheme was assumed to have the fallspeed characteristics of frozen drops (not shown in Table 1). In runs 5 and 6, where higher fallspeeds were assumed for the supercooled raindrops (as in the F scheme), the storms remained vertically erect (occasionally tilting downshear) and decayed with time in the last 2-3 hours of the simulations.

The principle reason why the storms in runs 5 and 6 dissipated is that the downdrafts were warmer than in runs 3 and 4, resulting in the inability of the gust-front vorticity to dominate over the low-level environmental vorticity and thus preventing the simulated storms from tilting upshear (Rotunno et al., 1988). There are several factors for why the downdrafts in runs 3 and 4 were colder. The reduced precipitation fallspeeds above the $0^{o}C$ level in runs 3 and 4 allowed more of the precipitation to be spread rearward by the storm-relative front-to-rear winds between 5 and 8 km, resulting in wider and more diffuse precipitation shafts in the leading convective line than in runs 5 and 6. Consequently, colder cool pools formed in runs 3 and 4 as a result of (1) evaporative cooling of rain having occurred over a larger area and (2) reduced subsidence warming driven by decreased precipitation loading in the downdrafts (maximum rain contents exceeded 9 g m^{-3} in runs 3-6). During the early stages of development, when all of the simulated systems initially tilted downshear, the greater rearward transport of condensate in runs 3 and 4 also had the beneficial effect of reducing the amount of precipitation that fell from mature convective updrafts into newer, developing updrafts, whereas this interference between successive updrafts was greater in runs 5 and 6. A layer of increased static stability centered at 2.7 km (730 mb) was also important in enhancing the effects of subsidence warming in the rainshafts.

Sensitivity tests were then conducted to determine if the storms simulated using the F scheme were more sensitive to the initial conditions. In run 7, the maximum cooling rate in the initial cool pool was reduced by half (-.004375 $^{o}C\ s^{-1}$), but it was applied during the first 20 min of the simulation. The total cooling was the same as in runs 1-6. Unlike run 2, the simulated system tilted against the low-level shear and became long lived. The stronger updrafts in run 2 (generated by the initially stronger cool pool) transported more of the condensate to upper levels (above 10 km) where the storm-relative winds blew ahead of the system, whereas in run 7 most of the condensate was detrained from the weaker updrafts into front-to-rear flow at mid-to-upper levels (5-8 km). As a result, a larger, colder cool pool formed in run 7 after 90 min in response to greater evaporation of rain as the rain fell over a larger area behind the leading edge of the cool pool.

A peak cooling rate of -.00875 $^{o}C\ s^{-1}$ (as in runs 1-6) was then imposed for the first 15 min in the "strong" initial cool pool of run 8. Although this storm immediately tilted upshear due to the initial cool pool vorticity dominating over the low-level ambient vorticity, the system gradually became more erect between 1 and 2 h as the downdraft and cool pool gradually warmed. During the first two hours of the simulation, the updrafts, downdrafts and mass contents in the rainshafts were weaker than in runs 2 and 7 in response to the weakened convergence at the gust front's leading edge ("less-than-optimal" state in Rotunno et al., 1988). But as the cool pool warmed in response to diminished rain contents and evaporation rates in the downdrafts, the system progressed into an "optimal state" by 2 h into the simulation, where it was in its most intense stage and nearly erect (in the lowest 4 km) for approximately an hour. But by 3 h, large amounts of graupel and frozen drops were falling immediately to the rear of the storm's leading edge and not falling into newer updrafts as in run 2, thus increasing the mass contents and the width of the rainshaft. As the cool pool's vorticity strengthened in response to the enhanced evaporative cooling in the downdrafts, the squall line permanently tilted upshear.

Finally, in run 9 the LIN microphysical scheme (using the same intercept parameters as in Fovell and Ogura, 1988 and in Tao et al., 1991) was tested with the same type of initial forcing as in runs 1-6. Because the large precipitation ice has the density and fallspeed characteristics of hail (having fallspeeds slightly larger than frozen drops in the F scheme), it was expected that this storm would not tilt upshear and would gradually decay during the last 2-3 h of the simulation in a manner similar to run 2 (this was the case in the TAMEX simulations of Tao et al., 1991 using the LIN scheme). Much to our surprise this storm did tilt upshear (marginally) and did not decay. However, in further simulations where a few coefficients were changed, the simulated convection failed to tilt upshear and did decay after 2-3 h simulated time.

4. CONCLUSIONS

Given the unique set of environmental (i.e., wind shear and thermodynamic) conditions and initial forcing, the squall simulations using the microphysical schemes of LIN and F can be thought of as analogous to trying to determine what direction a tree will fall when cut. Seemingly small changes in the initial cool-pool forcing of the convection had a profound impact upon whether the main precipitation shaft in the leading convective line became upshear or downshear tilted, which, in turn, ultimately determined whether the simulated storm was sustained or whether it decayed with time in the later stages of the simulations. Much of the large ice in the F and LIN schemes had large terminal fallspeeds that resulted in narrow, vigorous, and essentially vertical precipitation shafts at the leading convective line; these rainshafts often interfered with new updraft development and were relatively warm due to enhanced subsidence warming in the downdrafts. In contrast, the RH scheme does not appear to be nearly so sensitive to the initial conditions, since the lower terminal fallspeeds assumed for the large ice (graupel) resulted in much more of the precipitation being swept to the rear of the storm.

However, because the peak updrafts frequently exceeded 10 m s^{-1} between 2 and 4 km in all of the simulations, copious amounts of rain were transported above the freezing level, especially during the first 2 h of the simulations. The freezing of these drops was therefore a major microphysical source of large ice in the convective region of this TAMEX squall line. The characteristics of these large ice particles is quite different from graupel, which is formed by rapid cloud water riming onto pre-existing ice particles. In our opinion, an unrealistic feature of the RH scheme is that large, frozen drops are assumed to have the same fallspeed and density characteristics as graupel, even though frozen drops have a much higher density and fall faster than graupel (Pruppacher and Klett, 1978). This limitation of the RH scheme could misrepresent important feedbacks between the dynamics and the microphysics, which would result in simulated storm structures that are fundamentally different from those observed. To address these issues, what is needed are airborne microphysical measurements to determine some fundamental characteristics of ice particles in vigorous convective cores associated with maritime (tropical and subtropical) mesoscale convective systems.

5. REFERENCES

Ferrier, B. S., W.-K. Tao and J. Simpson, 1991: Radar and microphysical characteristics of convective storms simulated from a numerical model using a new microphysical parameterization. Preprints, 25th International Conf. on Radar Meteorology, Paris, France, American Meteorological Society, 782-785.

Ferrier, B. S., W.-K. Tao, S. Lang and J. Simpson, 1992: Assessment of the feedback between radiation and ice microphysics associated with mesoscale convective systems in different environments. Preprints, 5th Conf. on Mesoscale Processes, Atlanta, Georgia, 258-263.

Fovell, R. G., and Y. Ogura, 1988: Numerical simulation of a midlatitude squall line in two-dimensions. *J. Atmos. Sci.*, **45**, 3846-3879.

Klemp, J. B., and R. B. Wilhelmson, 1978: The simulation of three-dimensional convective storm dynamics. *J. Atmos. Sci.*, **35**, 1070-1096.

Lin, Y.-L., R. D. Farley and H. D. Orville, 1983: Bulk parameterization of the snow field in a cloud model. *J. Clim. Appl. Meteor.*, **22**, 1065-1092.

McCumber, M., W.-K. Tao, J. Simpson, R. Penc and S.-T. Soong, 1991: Comparison of ice-phase microphysical parameterization schemes using numerical simulations of tropical convection. *J. Appl. Meteor.*, **30**, 985-1004.

Miller, L. J., and J. D. Tuttle, 1989: Some important microphysical processes leading to heavy precipitation within a squall line. TAMEX Workshop, 1989, Taipei, NCAR, 43-49.

Pruppacher, H. R., and J. D. Klett, 1978: *Microphysics of Clouds and Precipitation.* D. Reidel, 714 pp

Rotunno, R., J. B. Klemp and M. L. Weisman, 1988: A theory for strong, long-lived squall lines. *J. Atmos. Sci.*, **45**, 463-485.

Rutledge, S. A., and P. V. Hobbs, 1983: The mesoscale and microscale structure and organization of clouds and precipitation in midlatitude cyclones. Part VIII: A model for the "seeder-feeder" process in warm-frontal rainbands. *J. Atmos. Soc.*, **40**, 1185-1206.

Rutledge, S. A., and P. V. Hobbs, 1984: The mesoscale and microscale structure and organization of cloud and precipitation in midlatitude clouds. XII: A diagnostic modeling study of precipitation development in narrow cold frontal bands. *J. Atmos. Soc.*, **41**, 2949-2972.

Simpson, J., R. F. Adler and G. R. North, 1988: A proposed tropical rainfall measuring mission (TRMM) satellite. *Bull. Amer. Meteor. Soc.*, **69**, 278-295.

Tao, W.-K., J. Simpson, S. Lang, M. McCumber, R. Adler and R. Penc, 1990: An algorithm to estimate the latent heating budget from hydrometeor profiles. *J. Appl. Meteor.*, **29**, 1232-1244.

Tao, W.-K., J. Simpson and S.-T. Soong, 1991: Numerical simulation of a subtropical squall line over Taiwan Strait. *Mon. Wea. Rev.*, 2699-2723.

Tao, W.-K., and S.-T. Soong, 1986: A study of the response of deep tropical clouds to mesoscale processes: Three-dimensional numerical experiments. *J. Atmos. Sci.*, **43**, 2653-2676.

Tao, W.-K., and J. Simpson, 1989: Modeling study of a tropical squall-type convective line. *J. Atmos. Sci.*, **46**, 177-202.

Wang, T. C., Y. J. Lin, R. W. Pasken and H. Shen, 1990: Characteristics of a subtropical squall line determined from TAMEX dual-Doppler data. Part I: Kinematic structure. *J. Atmos. Sci.*, **47**, 2357-2381.

LAGRANGIAN MODELLING FOR CLOUD MICROPHYSICS

A. M. Gadian

Physics Department, UMIST, Manchester, U.K.

1. Introduction.

The aim of this study is to produce a simple efficient lagrangian dynamical framework, that is able to produce a kinematic field typical of small convective cumuli whilst allowing sufficient computer resources to describe in detail the cloud microphysical processes. The 2-d results below, demonstrate that even with only a bulk water/ice description, the dynamical and thermodynamical results agree well with observations

Recent cumulus measurements from field projects have exposed the fine structure in water, temperature and velocity fields on scales of the order of 100m. Results using bulk properties (e.g. θ_{il}) are presented, demonstrating the applicability for the inclusion of more detailed microphysics.

The Boussinesq equations of motion are integrated in a lagrangian form using a fast embedded Runge-Kutta numerical scheme. The eddy type convective entrainment (Ludlam,1980) is illustrated. The equations are solved both using a vorticity representation and using the primitive pressure field. The vorticity approach is more rapid and less subject to numerical instabilities, but the pressure solution can be extended to 3-d flows. The scheme implicitly neglects inter-element diffusive processes for these timescales (Gadian et al, 1989) although it is anticipated relative movement of microphysical distributions will be important and will be incorporated with the detailed physics.

2. Equations of motion and thermodynamics.

The Boussinesq equations may be written:

Momentum $$\frac{d\underline{v}}{dt} + \nabla\left(\frac{\delta p}{\rho}\right) - g\,\delta\varphi\,\hat{\underline{k}} = 0$$

Continuity $$\frac{\partial}{\partial t}\left(\frac{\delta p}{\rho_0}\right) + \nabla\cdot\underline{v} = 0$$

Thermodynamic $$\frac{\partial}{\partial t}(\delta\varphi) + wB = 0$$

where $\underline{v}$ is velocity, ρ density, δp a pressure perturbation, φ an entropy perturbation, B static stability, w vertical velocity and g is gravity.

In the vorticity scheme these reduce to:

$$\frac{d\xi}{dt} = g\frac{\delta\varphi}{\delta x}$$

$$\frac{d}{dt}(\delta\varphi) + wB = 0$$

where vorticity $\xi = \nabla^2\psi = \frac{\partial w}{\partial x} - \frac{\partial u}{\partial z}$

In the primitive form, the equations are:

$$\frac{d\underline{v}}{dt} = -\nabla\left(\frac{\delta p}{\rho}\right) + g\,\delta\varphi\,\hat{\underline{k}}$$

$$\frac{\partial}{\partial t}(\delta\varphi) + wB = 0$$

The pressure balance equation (Staniforth, 1992)

$$\nabla^2 p = \frac{2}{\Delta t}\left(\nabla\cdot\underline{v}\right) \quad \text{assumes} \quad \frac{\partial v}{\partial x}\Delta t < 1$$

A similar primitive scheme has been successfully used by Smolarkiewicz(1992). A Eulerian/Lagrangian interpolation scheme (Sawyer, 1963) is used for gradient terms.

Potential temperature is conserved using the parameter θ_{il} , such that

$$\theta_{il} = \theta\left[1 + \frac{L_{lv}}{C_p T} r_l + \frac{L_{iv}}{C_p T} r_i\right]$$

where L_{lv} , L_{iv} are the latent heat parameters, r_l and r_i are the mixing ratios of water and ice. In this simulation, only bulk water was produced and evaporated in the warm convection.

3. Discussion.

Several numerical experiments were conducted using data from the 1985 Hawaii Project (Raga et al,1990). Observations gave cloud base at 450m, with cloud top approximately 2200m. All simulations produced clouds of this size, with representative velocities. Initiation of convection was instituted by increasing the potential temperature of the central elements in the lowest two rows to the value of that at the observed cloud base. Cyclic continuity was assumed at the 3km spaced side walls.

3.1 Comparison of vorticity and primitive forms

Using a horizontal resolution of 100m the primitive and the faster 2-d vorticity schemes were compared. Figures 1 and 2 demonstrate the differences in the horizontal velocity components. Spatial periodicities can be seen in figure 2, especially in the 0.05m/s contours for the primitive solutions. In perspective, however the velocity variations are only of a few percent, even after 400s of model time, and there is little effect on the larger scale flow. The same efficient accurate Runge-Kutta (Gadian et al, 1989) was used in both, and the error is associated with the calculation of pressure perturbations. The advantage, of the primitive scheme was the easy application to 3-d flow: results of which were very similar to the 2-d cases shown, for this no-shear example.

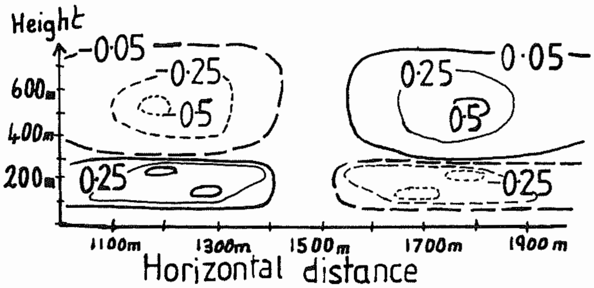

Figure 1. Horizontal velocity contours (m/s), using the vorticity scheme, with the 3 central elements at 100m and 200m height initially heated to the cloud base potential temperature.

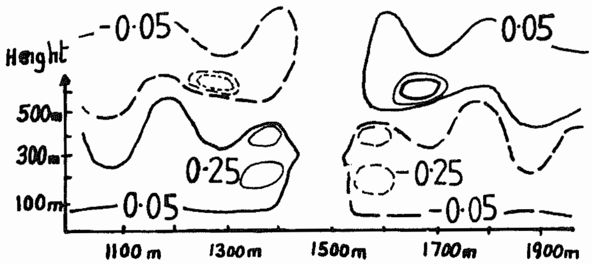

Figure 2. As figure 1, using the primitive scheme.

3.2 High resolution flow.

The requirement for the model is to simulate eddy type entrainment on the scales of less than 100m. The ability to allow the droplet spectra to fall through different elements is necessary to invoke the mixing processes described by Ludlam(1980).

Figure 3 illustrates a typical flow pattern obtained using a horizontal resolution of 30m. using the vorticity scheme simulation. This flow is not totally symmetric, due to the original small horizontal displacement of the elements from their exact positions. Because of the numerical accuracy (<0.01% per time step) of the time integration scheme, a small horizontal perturbation increases the computational speed in the early stages (Gadian et al, 1989). The enswirling entrainment of environmental air into the thermal and cloud sides and tops is shown in figure 3 and also in the 100m resolution examples (these results will be shown in a later paper).

The model cloud, with the bulk water description gives vertical velocities of up to 10m/s with evidence of cloud elements vertically oscillating within the cloud in the very stable environment.

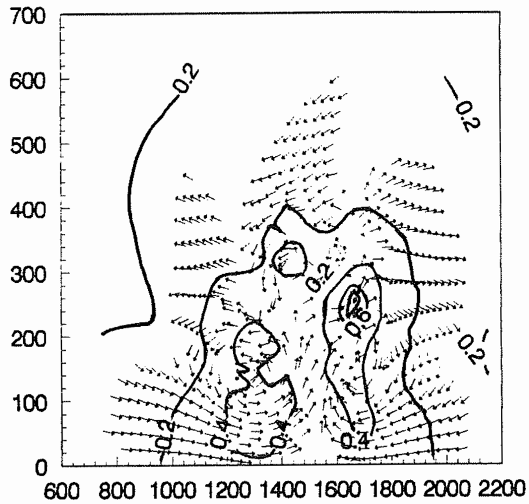

Figure 3. Wind speed contours (m/s) and direction arrows, calculated at 800s model time, using the vorticity scheme, with the 9 central elements at 30m and 60m height initially heated to the cloud base potential temperature.

4. Summary.

The Boussinesq Lagrangian model has been shown to produce flows typical of that found in a warm cloud. At present only bulk microphysical properties have been incorporated. Detailed cloud microphysics(e.g. Brenguier, 1992) is now being included to examine the effect of droplet mixing in a non-diffusive framework.

References

Brenguier, J. and Grabowski, W., 1992: Cumulus Entrainment and Cloud Droplet Spectra. *J. Atmos. Sci.*, (in press)

Gadian, A. Dormand, J. and Green, J.S.A., 1989: Smooth Particle Hydrodynamics as Applied to 2-D Plume Convection. *Atmos. Res.*,24,287-304.

Ludlam, F,1980: *Clouds and Storms.* Pennsylvania State University Press.

Raga, G.,Jensen, J.,Baker, M., 1990: Characteristics of Cumulus Band Clouds of the Coast of Hawaii. *J. Atmos. Sci.*,47,338-54

Sawyer, J.S., 1963: A Semi-Lagrangian Method for Solving the Vorticity Advection Equation. *Tellus*,15,336-42.

Smolarkiewicz, P. and Pudykiewicz, J., 1992: A Class of Semi-Lagrangian Approximations for Fluids. *J. Atmos. Sci.* (in press)

Staniforth, A. and Cote, J., 1992: Semi-Lagrangian Integration Schemes for Atmospheric Models. *Mon. Wea. Rev.,* (in press)

NUMERICAL MODELING OF THE EFFECTS OF ENTRAINMENT ON CLOUD DROPSIZE DISTRIBUTIONS

P.A. Vaillancourt and M.K. Yau

McGill University
Montréal, Québec, Canada

1 Introduction

At the present time, the most likely candidate in explaining observed cloud droplet spectra is entrainment of environmental air into clouds followed by the mixing of the clear and cloudy air. Prior to 1977 all work on the mixing process assumed that it was uniform and homogeneous. This parameterization of mixing led to spectra quite unlike those observed (Warner 1973a). Latham and Reed (1977), based on laboratory experiments, suggested an alternative description–inhomogeneous mixing. They proposed that when undersaturated air enters a cloud, only droplets in direct contact with infiltrating blobs or filaments will be affected.

Studies made by Broadwell and Breidenthal (1982) and Baker et al. (1984) concentrated on the actual physical process that produces mixing. Observations of a turbulent shear layer led them to suggest turbulent mixing as a two–stage process. During the first stage, the entrained volumes break up into smaller and smaller, essentially unmixed, units. Evaporation of droplets only occurs at clear–cloudy interfaces resulting in a few droplets being substantially affected. During the second stage, when the Kolmogorov scale is reached (at which filaments of mixing air have scales of $\approx 1mm$) all droplets experience the same environment. If the air is subsaturated, uniform evaporation of all droplets follows. Mixing can be described as homogeneous if the first stage is very rapid or extreme inhomogeneous if it is very slow. The real case would lie between these two extremes and the exact state would depend on the level of turbulence, i.e on the rate of thinning of the filaments of clear and cloudy air.

Paluch and Baumgardner (1989) have shown that in mixed regions of clouds, despite measured large fluctuations of droplet concentration, the large droplet peak of the spectrum remains at a nearly constant diameter. Similar results were reported by Brenguier (1990). Using high resolution measurements and statistical techniques the two papers showed that regions with large variations in droplet concentrations are mostly heterogeneous and local concentrations are in fact similar to concentrations measured in regions where fluctuations are small.

These observations suggest that mixing does not lead to large uniformly mixed cloud volumes with low droplet concentrations. They imply that the rate of turbulent mixing is slow and lend support to the extreme inhomogeneous description of mixing. It is noted that not all studies support this conclusion. Some have reported the existence of large highly diluted regions with uniform characteristics (Austin et al. 1985, Jensen et al. 1985). While a satisfactory resolution of the apparent conflict between different sets of observations still awaits further investigation, we consider that the evidence in support of the scenario of extreme inhomogeneous mixing sufficiently appealing to warrant a more detailed numerical study.

In this paper we will study the processes of entrainment and extreme inhomogeneous mixing and their effects on the cloud dropsize distributions in a small non–precipitating continental cumulus cloud in a sheared environment. Our approach would be to perform a high resolution simulation using a numerical cloud model.

2 The Numerical Model

A two-dimensional, slab-symmetric version of the nonhydrostatic, anelastic cloud model developed by Clark (1977, 1979) is used. Moist thermodynamics is limited to the condensation– evaporation process. Condensation is calculated by a bulk scheme. Certain fields from the bulk model serve as input into a microphysical model developed by Brenguier and Grabowski (1992)(hereafter referred to as BG), where the droplet spectra will be predicted. The microphysical model exerts no feedback on the dynamics of the bulk model.

2.1 Microphysical model

The approach developed in BG is based on four assumptions:

1) The amount of water substance subject to phase change is taken as predicted by the bulk model.

2) Nucleation of droplets is assumed to always produce the same initial droplet spectrum f_o.

3) Locally, only droplet concentration corresponding to that at nucleation may be present.

4) After nucleation further evolution of the cloud droplet spectrum is represented using base functions (called elementary droplet populations– EDP).

An EDP is defined as an ensemble of droplets having encountered the same sequence of supersaturations. It is represented by an elementary size distribution $f(r,t)$, which in turn is a function of the elementary size spectrum at nucleation $f_0(u)$ and its degree of condensational growth $b^2(t)$, where $b^2(t) = 2A_1 \int_{t_0}^{t} s_e(t)dt$ (see Brenguier 1991). The EDP's are used as base functions to calculate the mixing ratio of the size distribution of cloud droplets (number per unit mass of air per unit radius interval): $h(\mathbf{x},r,t) = \sum_{i=0}^{n_c-1} \psi_i(\mathbf{x},t) f_i(r)$, where n_c is the total number of base functions (=30 in the current experiment). $\psi_i(\mathbf{x},t)$ is the weight function associated with the i^{th} base function , and gives the fractional contribution of each EDP to the total spectrum. Consequently, $\psi(b^2)$ (called the b^2–distribution) describes the distribution of the fraction of droplets in a spectrum that have experienced the same amount of diffusional growth. For example, $\psi(b^2=0)$ denotes the fraction of droplets in the spectrum which is newly activated, and $\psi(b_a^2)$ represents the fraction that has grown adiabatically from cloud base.

By definition $0 \leq \psi_i(\mathrm{x}, t) \leq 1$ and $\sum \psi_i(\mathrm{x}, t) = \beta(\mathrm{x}, t) \leq 1$. $\beta(\mathrm{x}, t)$ is therfore a measure of the degree of inhomogeneity. In a unit cloud volume characterized by a certain value of β, a fraction β of the volume will be assumed to consist of cloudy air and the remaining fraction (1-β) of clear air.

2.2 Setup of Experiment

Two interacting domains are used. Both domains have 98×98 grid points. The resolution of the outer and inner domains are $45m$ and $15m$ respectively. A uniform time step of 2 seconds is used.

For the initial conditions the lowest 1.4 km is a boundary layer characterized by a slightly stable potential temperature gradient and a mixing ratio profile which decreases slightly with height. Between $z = 1.4$ *and* $1.8km$ we specify a layer of strong stability where the relative humidity decreases significantly. A wind shear of $3.0ms^{-1}km^{-1}$ is specified from $z = 1.4km$ upwards.

As in Klaassen and Clark (1985), a surface sensible heat flux with a maximum of $150Wm^{-2}$ at the center of the domain is used to initiate the cloud.

3 Results

As a result of surface heating, convective circulation develops in the boundary layer. The thermal updraft near the center of the domain carries air from the surface to the lifting condensation level near the top of the boundary layer at $1440m$. After $\approx 34min.$, the cloud starts to form, the cloud area increases until $t = 45min.$, thereafter it decreases and the dissipation of the cloud is almost complete by $t = 54min.$. The life cycle of the cloud is therefore $\approx 20min.$. The maximum cloud water content is $1.43g/kg$ at $t = 49min.$.

3.1 How and where do entrainment and mixing occur?

We first define the terms entrainment and mixing. Entrainment is used here to describe the resolvable, initial large scale breakup of the interface between cloudy and clear air. *Entrainment sites* therefore refer to areas where the cloud scale circulation is not parallel to the cloud boundary and where the cloud structure is actively being modified.

Mixing is diagnosed by a change in certain properties of the cloudy air *averaged* over the smallest grid volume. The property used here is the ratio q_c/q_c^a (liquid water mixing ratio divided by the adiabatic liquid water mixing ratio). Conditions leading to mixing are generally met at the interface between the cloud and the environment and result in a layer $\approx 30m$ thick of partially diluted air which separates the adiabatic cloud core from the environment. In certain conditions the area affected by mixing may extend to a greater depth inside the cloud. These areas are referred to as *mixing zones*.

Figs. 1a and 1b display the vector velocity field for the entire inner domain at 44 and 46min.. The cloud outline is depicted by the $0.1g/kg$ contour for q_c. The shaded area is where $q_c/q_c^a < .98$, i.e. where mixing occurs.

The main feature which modifies the upshear(left) portion of the cloud is a persistent vortex circulation which appears at 42min. and is present throughout the cloud's life cycle. Note that the center of this circulation is situated inside the cloud. The descending branch of this circulation creates the arm of cloudy air visible in fig. 1a. It has dissipated by 46 min. (fig. 1b) due to subsiding motion and mixing. At the the entrainment site (fig. 1a, x=2.37 km, z=1.77 km), air is entrained both from near the cloud top altitude and from the same level further upstream. An extensive mixing zone can be seen on the upshear side of the cloud in fig. 1b. It propagated upward from the entrainment site created by the vortex. By 47 min. it accounts for close to 30% of total cloud area.

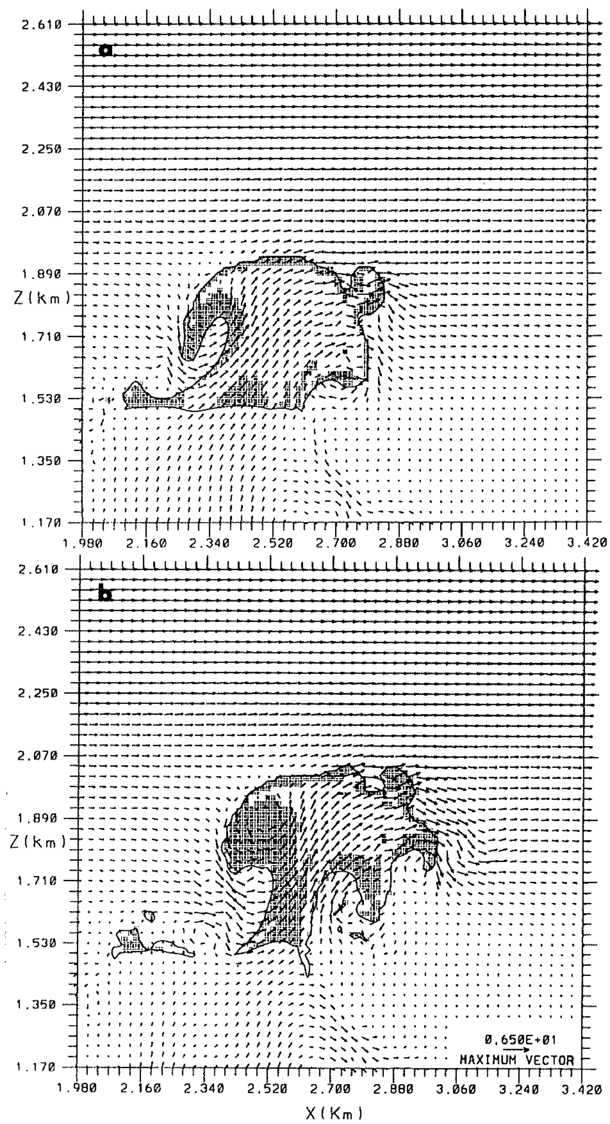

Figure 1: Velocity vectors for entire inner domain, solid line is the .1g/kg q_c contour line, shaded area is where $q_c/q_c^a < .98$. a) At 44 min.. b) At 46 min..

The structure on the downshear side of the cloud is more complex than the upshear side. Rising motion along the edge of the upper downshear portion of the cloud leads to the formation of a bubble–like structure around x= 2.805 km, z> 1.785 km at $t = 44min.$ (fig. 1a). This structure is accompanied by the development of a slanted penetrative downdraft, located in an immediate upwind position, which seperates the bubble from the main portion of the cloud. At 46 min. (fig. 1b) this bubble has totally dissipated and a new one has formed at a similar location. The scenario of bubble formation, subsequent separation from the main cloud and eventual dissipation repeats itself at a similar location until the cloud decays.

At $t = 44min.$ a vortex circulation is seen in the lower downshear portion of the cloud (fig. 1a, x= 2.7 km, z=1.56 km). The vortex is responsible for the formation of a small mixing zone (figs. 1a and 1b). It's descending branch creates the diluted arm of cloudy air visible from x= 2.76 to 2.85 km and z= 1.56 km to 1.74 km at 46 min. (fig. 1b). At 46min. the lower vortex circulation is less defined and another vortex has developed higher in the cloud at z = 1.65 km, again creating a small mixing zone and an arm of cloudy air (fig. 1b).

The circulation on the downshear side did not permit the creation of any deep mixing zones. Instead, the shape of the cloud is continuously being deformed and narrow structures like the bubbles at the cloud top and the arms in the lower part of the cloud are formed. These narrow structures are subject to severe mixing and dissipate rapidly because of the large interfacial area. As a result, total evaporation of cloud droplets often occurs on the downshear side.

3.2 How are cloud dropsize distributions modified?

The evolution of the cloud dropsize spectra is examined using plots of the b^2–distributions in a subsection of the simulation domain. Fig. 2 shows these for the upper upshear portion of the cloud at 45 min.. For clarity, this figure depicts the distribution at 15 × 15 grid points. A vertical bar accompanies each b^2–distribution. The location of the intersection of the vertical bars with the x–axes indicates the adiabatic b–values, b_a. The position of the horizontal mark along this bar is equal to the value q_c/q_c^a , 0 being at the bottom of the bar and 1 at the top. A grid volume is shaded when this ratio $\leq .98$. The number at the upper right-hand corner of each square is the parameter β, denoting the fraction of the grid volume with cloudy air. The rest of the grid volume being cloud-free.

Some observations of the characteristics of cloud dropsize distributions can be made. In regions not previously affected by mixing (e.g. the non-shaded areas in fig. 2) the b^2–distributions are narrow and centered around the adiabatic b–value(b_a). These droplets have therefore essentially undergone adiabatic growth from the cloud base. At the cloud–environment interface and in mixing zones the b^2–distributions indicate significant differences.

The first characteristic is the presence of bimodal spectra in areas where mixing has occurred (see the shaded areas in fig. 2). These spectra can be found both within the cloud–environment interface (e.g. x= 2.43 km, z= 1.935 km) and in mixing zones (e.g. x= 2.37 km, z= 1.80 km). Two modes can be observed; the primary mode is centered around b_a and the secondary mode centered around an intermediate value between 0 and b_a. In this study bimodal spectra are a direct consequence of the assumption of extreme inhomogeneous mixing. As an example, consider a grid volume in which mixing has reduced the average concentration of droplets by half , to $500cm^{-3}(\beta = .5)$. Because of extreme inhomogeneous mixing, the microphysical model interprets this to mean that 50% of the grid volume is composed of clear air and 50% of cloudy air having a droplet concentration equal to that of the initially unmixed volume. If lifting follows, activation of the nuclei in clear air and diffusional growth will occur. The newly activated nuclei accounts for the secondary mode of the distributions.

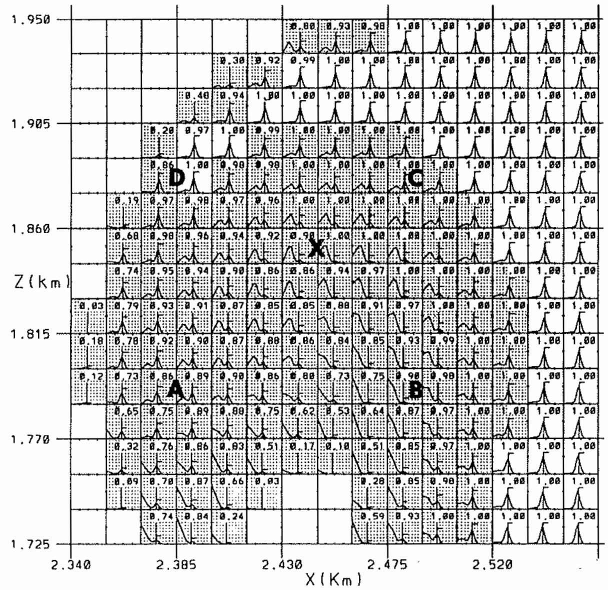

Figure 2: B^2–distributions at 45 min. for upper upshear portion of cloud.

To clarify the above description, we consider the b^2–distributions along a loop A, B, C, and D within the upshear mixing zone in fig. 2. This path approximates a cycle around the vortex center indicated by an X. Starting at point A and travelling horizontally towards point B we can see that β and the ratio q_c/q_c^a decrease. On passing point B, these values increase and are close to 1 at the right boundary of the mixing zone. Similar variation can be found along any horizontal path through the mixing zone. The fact that the minimum values for q_c/q_c^a and β occur at some distance from the right cloud edge signifies that mixing originates and propagates from the entrainment site situated at a lower level (near x= 2.43 km and z= 1.755 km).

Severe mixing, marked by a low ratio of q_c/q_c^a, is taking place at B and reduces the magnitude of the primary mode of the distribution when averaged over the grid volume. High values for $\psi(b^2 = 0)$ and β can be detected from B to C. This part of the loop lies within a zone of uplifting and therefore new nucleation. Close to point C, β increases to 1 as all nuclei are activated. The ratio q_c/q_c^a also increases because of condensation and the increasing distance from the entrainment site. It is noted that the secondary mode grows towards larger b values and the primary mode increases in amplitude.

Little change in the distributions is detected from point C to point D. The processes taking place from D to A are just the reverse of those from B to C, namely evaporation and the approach toward the entrainment site with an increase in the amount of mixing. Consequently, the primary mode decreases in amplitude while the secondary mode grows towards smaller b values.

Bimodal spectra are thus created when mixed air is being lifted. The origin of the bimodal spectra is located to the right of the vortex center. The vortex circulation then recirculates these spectra throughout the mixing zone. Some bimodal spectra can also be found in the mixing zones on the downshear side of the cloud where a similar scenario occurs.

Another parameter useful in characterizing the distribution is the average radius $\overline{R}$ displayed at 45 min. in fig. 3a. In the unmixed cloud core, the average radius increases

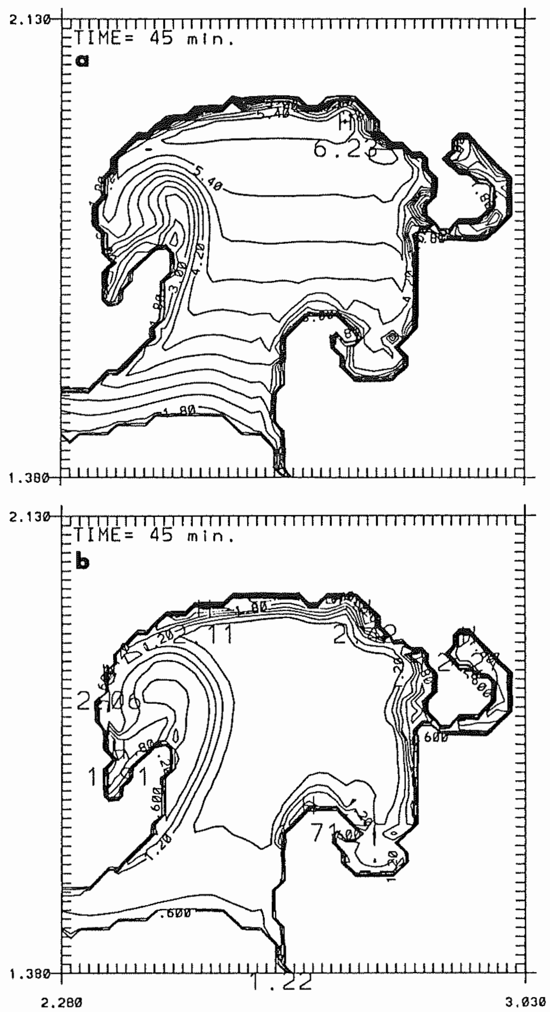

Figure 3: a) Average Radius, $\overline{R}[\mu m]$, at 45 min. b)Standard deviation, $\sigma[\mu m]$, at 45 min..

with height and attains its maximum value near the cloud top. Horizontally, $\overline{R}$ remains nearly uniform. The small variations in unmixed zones is attributable to the variation in the cloud base altitude.

In mixing zones, the variations in the average radius are more complex. $\overline{R}$ decreases as a result of evaporation and activation where the diluted parcels are being lifted. As is indicated in fig. 3a, $\overline{R}$ in the upshear mixing zone is smaller than that of the unmixed adiabatic cloud core at the same level. The spectra with the largest $\overline{R}$ are found near the cloud top in non-diluted regions.

The standard deviation of the distribution σ for $t = 45min.$ is depicted in fig. 3b. In the adiabatic cloud core σ is relatively uniform and is $\approx 1\mu m$. Where mixing has occurred, either in mixing zones or at the cloud environment interface, $\sigma > 1\mu m$. The broadest spectra occur near the cloud top. They are bimodal with high $\psi(b^2 = 0)$ values implying a high concentration of small droplets.

4 Conclusion

A detailed analysis of the modeling results allow us to draw the following conclusions:

The vortex circulations and penetrative downdrafts serve to deform the shape of the cloud and lead to entrainment of clear air into the cloud structure. The entrained air has its origin both from the cloud top level and from the sides.

On the upshear side of the cloud, the convective circulation is dominated by a long–lasting vortex with its center situated inside the cloud boundary. This circulation initiates entrainment and results in the creation of a mixing zone which propagates from the entrainment site to cover more and more of the cloud volume.

On the downshear side, no deep mixing zones appear before $t = 48min.$. The circulation is dominated by subsiding motion, a high turbulence level, multiple vortices with centers outside the cloud boundary, penetrative downdrafts, and periodically forming bubble–like structures. In comparison with the picture on the upshear side, we observe a more fragmented cloud structure and often total dissipation of the cloudy air rather than partial dilution. Non–diluted cloudy air exists on the downshear side for a longer time.

Extreme inhomogeneous mixing leads to multimodal distributions. This results when the mixed air is lifted and condensation nuclei present in clear air filaments in the grid volumes are activated. Bimodal spectra are commonly found at the cloud–environment interface and in mixing zones on the upshear side of the cloud. It was found that mixing results in a smaller average radius, the largest $\overline{R}$ being found near the cloud top in non–diluted cloud regions, a larger standard deviations with the largest σ near cloud top in diluted regions.

Acknowledgements

The authors thank Drs. T. Clark, W. Grabowski and J. L. Brenguier for providing their models. This research was supported by the office of Naval Research Grant N00014–87–G–0171.

References

Austin, P. H., M. B. Baker, A. Blyth and J. B. Jensen, 1985. *J. Atmos. Sci.*, **42**, 1123–1138.

Baker, M. B., R. E. Breidenthal, T. W. Choularton and J. Latham, 1984. *J. Atmos. Sci.*, **41**, 299–304.

Brenguier, J.–L., 1990. *J. Atmos. Sci.*, **47**, 1127–1148.

Brenguier, J.–L., 1991. *J. Atmos. Sci.*, **48**, 264–282.

Brenguier, J.–L., and W. W. Grabowski, 1992. *J. Atmos. Sci.*, (*submitted*).

Broadwell, J. E., and R. E. Breidenthal, 1982. *J. Fluid Mech.*, **125**, 397–410.

Clark, T. L., 1977. *J. Comput. Phys.*, **24**, 186–215.

Clark, T. L., 1979. *J. Atmos. Sci.*, 36, 2191–2215.

Klaassen, G. P., and T. L. Clark, 1985. *J. Atmos. Sci.*, **42**, 2621–2642.

Latham, J., and R. L. Reed, 1977. *Quart. J. R. Met. Soc.*, **103**, 297–306.

Paluch, I. R., and D. G. Baumgardner, 1989. *J. Atmos. Sci.*, **46**, 261–278.

Warner, J., 1973a. *J. Atmos. Sci.*, **30**, 256–261.

NUMERICAL SIMULATION OF PRECIPITATION SCAVENGING AND COMPARISON WITH OBSERVATION OF PRESCRIBED FOREST FIRES

Charles R. Molenkamp and Michael M. Bradley

Lawrence Livermore National Laboratory
Livermore, California 94550

1. INTRODUCTION

The primary mechanism by which aerosol particles are removed from the atmosphere is precipitation scavenging. Because of our interest in understanding the processes by which aerosol particles are scavenging as well as basic cloud dynamic and microphysical interactions, we have developed a numerical model that simulates these processes. This model was developed as part of our study of the global climatic effects of smoke from a large number of massive fires. We have previously described a simulation of a hypothetical large city fire (Bradley and Molenkamp, 1991). One of the ways that we have attempted to validate the accuracy of the model is to perform simulations of prescribed forest burns where there is information on the source characteristics and fire morphology, and observations of the cloud dynamics and microphysics. In this paper we describe simulations of the Hardiman township and Battersby township Ontario, Canada, prescribed fires.

2. MODEL DESCRIPTION

Our numerical model, OCTET, is a system of eight progressively more complex models designed to simulate plumes, clouds, and mesoscale systems as illustrated in Figure 1. OCTET has a three-dimensional, nonhydrostatic, compressible dynamic framework originally based on the Klemp and Wilhelmson (1978) convective storm model. The prognostic variables in the dry model are the three velocity components, pressure perturbation, potential temperature, turbulent kinetic energy, and water vapor mixing ratio. The warm and cold cloud and scavenging modules add prognostic variables for the various types of hydrometeors and aerosols in hydrometeors.

The cloud microphysics representation is a bulk-water parameterization originally based on Lin, Farley, and Orville (1983). It is described more completely in M olenkamp and Bradley (1990, 1991). The parameterization includes five types of hydrometeors, cloud droplets, rain, ice crystals, snow, and graupel. Transfer of water among hydrometeor types occurs via the processes indicated in Figure 2.

The scavenging parameterization is designed to parallel the cloud microphysics representation. Each type of hydrometeor can have smoke associated with it. Smoke particles inside the cloud but not collected by a hydrometeor are called interstitial aerosol particles. The aerosol types and the transfer processes included in the model are indicated in Figure 3. The transfer rates for many of the scavenging processes are proportional to the corresponding water transfer rates and are indicated by solid lines in Figure 3. The primary mechanism by which smoke particles are incorporated into hydrometeors is condensation nucleation. We assume that smoke particles can serve as condensation nuclei when they enter a cloud in an updraft. The fraction of the ingested smoke that is captured by cloud droplets depends on the supersaturation which in turn depends on the updraft speed and the nuclei properties. The model has two methods for specifying the nucleation fraction; a simple parametric relation that depends on updraft speed (Molenkamp, 1977) or a table of data generated from the CAMP detailed microphysical model (Edwards, 1989; Chuang et al., 1990). The latter method was used for the simulation of the Hardiman fire and the simple parametric relation for the Battersby fire.

3. HARDIMAN TOWNSHIP FIRE

The Hardiman township prescribed fire was conducted by the Canadian Forestry Service on August 28, 1987, at latitude 48.00N, longitude 82.05W (about 70 km southwest of Timmins, Ontario) in lodge pole pine logging slash. The fire burned an area of approximately 3.25 km^2. Ignition occurred from 13:30 (EST) to 15:33 in a generally northeast to southwest direction.

a. *Observations*

Observations of the fire include single theodolite measurements of the smoke column height taken at 5 minute intervals from 13:40 to 17:35, a videotape of the smoke plume

	No Aerosol	Aerosol
Dry Model	OCTET/v 7 Variables	OCTET/va 8 Variables
Warm Cloud Model	OCTET/w 9 Variables	OCTET/wa 12 Variables
Cold Cloud Model	OCTET/c 12 Variables	OCTET/ca 18 Variables
Electrified Cloud Model	OCTET/e 19 Variables	OCTET/ea 25 Variables

Figure 1. Hierarchical structure of the OCTET plume, storm, and mesoscale simulation system. The number of variables refers to prognostic variables.

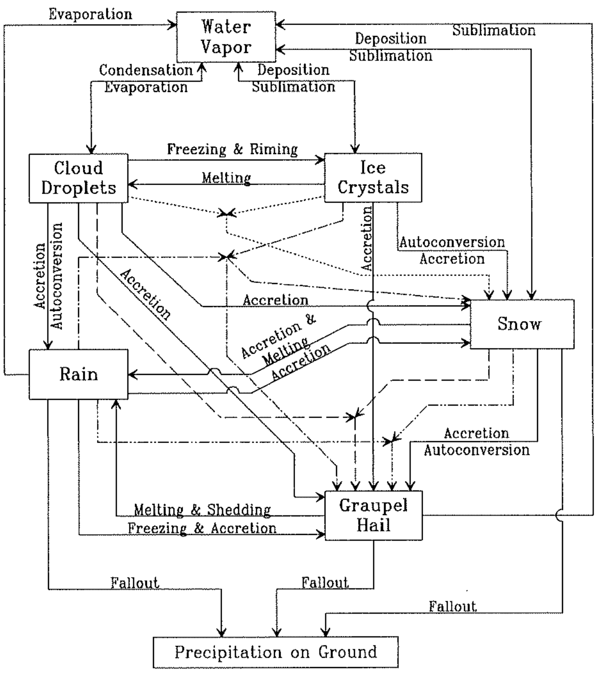

Figure 2. Cloud microphysics processes. Three-way processes, indicated by non-solid arrows, represent the coagulation of two types of hydrometeors followed by freezing to form a third type.

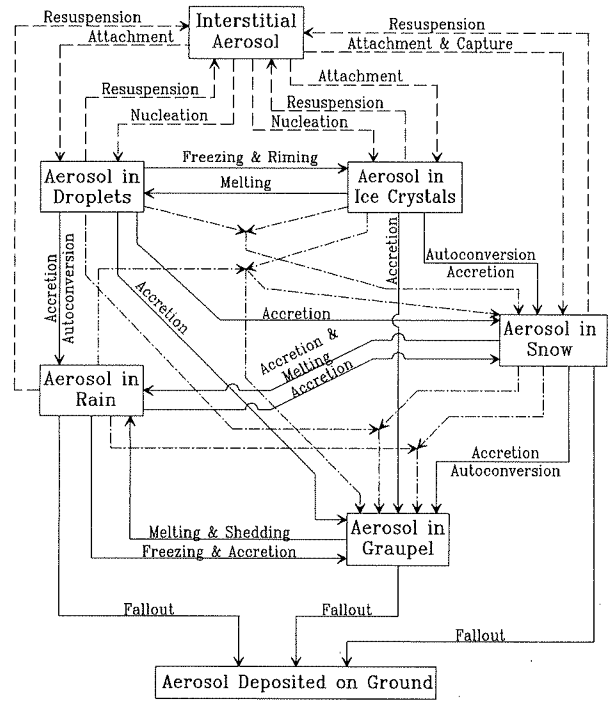

Figure 3. Aerosol scavenging processes. The processes indicated with solid arrows and the three-way processes are assumed to occur at rates which are proportional to the corresponding water transfer rates.

from a location 12 km WSW of the fire, and measurements of smoke and cloud droplet size distributions by the research aircraft. The measured height of the smoke column reached a maximum of 4.2 km above the ground at 15:30 and thereafter ranged between 2.5 and 3.8 km in response to pulses in the fire until the observations ended.

b. *Model Simulation*

The atmospheric sounding of temperature, water vapor mixing ratio, and winds was constructed from the available radiosondes and aircraft data to be as representative as possible of the sounding at the fire site. For heights above 550 mb the Moosonee sounding was used, between 550 and 825 mb the aircraft data, and below 825 mb a composite "boundary layer" based on the Timmins surface data and the Moosonee sounding.

The model was run with a resolution of 250 m in the horizontal and 100 m in the vertical; the domain size was 12.5 x 12.5 x 5 km. We assumed that the fire was ignited simultaneously over the entire burn area and burned at a constant rate for 2 hours. The heat release rate, determined from the amount and energy content of the fuel, was 5.8 kW/m^2, and the smoke production rate, assuming a smoke emission factor of 1 per cent, was 2.9 mg/m^{2}s. The heat and smoke sources were assumed uniform over the 51 surface grid points that corresponded to the burn area.

The simulation of the Hardiman fire has been previously described by Penner et al. (1990). Figure 4 is a wire-frame diagram of interstitial smoke after 40 minutes when the cloud had reached a near steady-state; the view is from the southwest, the same location as a video camera operated by the Canadian Forestry Service. The wire-frame diagram has been overlaid with a frame from the videotape (not reproduced here) and shows a remarkable similarity. The gravity wave feature at the top of the plume is similar in both wavelength and amplitude. The downward bulge in the smoke plume to the right of the updraft in the interstitial smoke field is also evident in the videotape. The effect of the southwesterly component of the low-level winds is evidenced by the bulge to the left rear in both the wire-frame and the videotape.

Using the dynamic and bulk-water parameterization results from the cloud model as input to a detailed cloud microphysics model, Chuang et al. (1990) have calculated cloud and aerosol size distributions and compared them with measurements. The predicted and measured spectra are in good agreement except that the model does not reproduce the observed large drops. This may be due to coalescence among droplets or to the presence of very large particles that were not included in the model. Additional information is given in Penner et al. (1990).

4. BATTERSBY TOWNSHIP FIRE

The Battersby township prescribed fire occurred on August 12, 1988, at latitude 47.00N, longitude 81.75W (about 170 km south of Timmins, Ontario) in jack pine and spruce logging slash. The fire burned an area of approximately 7.18 km^2. Ignition occurred from 13:02 until 16:43 in a clockwise direction starting in the northeast quadrant. By the time ignition moved into the southeast quadrant at

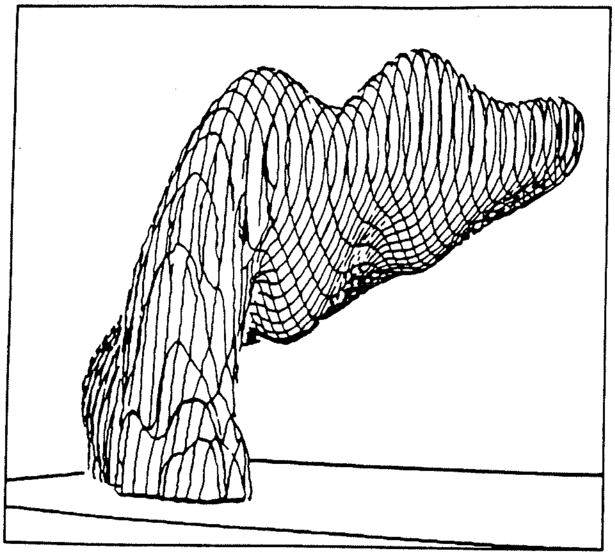

Figure 4. Interstitial smoke mixing ratio for the Hardiman fire after 40 minutes. The contour level is 10^{-6}.

14:30 the northeast quadrant was already in the smoldering stage; therefore, only a about one-quarter of the 7.18 km^2 was actually a significant heat source at any given time.

a. *Observations*

Observations of the fire were obtained from eyewitnesses on the ground, by an infrared doppler lidar (Banta et al., 1991), a NASA Langley helicopter, and the University of Washington aircraft, which took cloud physics measurements in the capping cloud. Most of the observations of this fire relate to the early stage involving the burning of the northeast quadrant. From a ground observation point 0.5 km east of the burn area a capping cloud was first visible at 13:11, 9 minutes after ignition. It became a massive cumulus congestus by 13:14 and reached a maximum height of about 8 km. Airborne observers reported rain falling from the cumulus associated with the plume, and light precipitation was reported at the lidar site 7 km NE of the fire center (Banta, personal communication). Although not measured, ice nucleation is assumed to have occurred, since the temperature at cloud top was below -20°C.

b. *Model Simulation*

Soundings for the Battersby fire at 12:54 and 14:13 were significantly different with the earlier sounding being much cooler and drier than the latter. An initial simulation with the 12:54 sounding produced a plume that reached less than 4 km in height, considerably lower than the observed cloud. Eddleman (personal communication) reported that it was very warm and humid at the fire site, with a surface temperature of approximately 30°C; this suggests that the 14:13 sounding was the more representative. The sounding at 14:13, after adjustment in layers where the radiosonde passed through a cloud, was used for the simulation presented here.

Fairly strong winds, generally from the west at 15-25 m/s, necessitated the use of a large (relative to the resolution) domain to contain the plume until it stabilized at its maximum height. The model domain was 18 x 36 x 12 km and both the horizontal and vertical resolutions were 250 m. We simulated the first part of the planned burn, i.e. the fire in the northeast quadrant of the burn area, and assumed that the fuel was consumed in 75 min. Based on the measured fuel consumption and 75 min burn time, the heat release and smoke emission rates were 22 kW/m^2 and 11 mg/m^2s, respectively.

After 40 minutes of simulation the smoke plume, shown in side and top views in Figures 5 and 6, began to pass through the downwind boundary of the model domain. At this time the top of the plume was characterized by six distinct turrets extending to progressively greater heights as they moved downwind; the farthest downwind turret reached an altitude of 7.6 km. Within each turret was a liquid water cumuliform cloud; in the turrets near the fire the cloud base was approximately 1.9 km. The queue of clouds spanned the full range of cumulus development stages, from a small cumulus near the fire (hereafter referred to as cell 6) to a dissipating cumulonimbus near the outflow boundary (cell 1). The spatial distributions of non-precipitating and precipitating hydrometeors after 40 min of simulation are shown in Figures 7 and 8, respectively, by the surface contour for a mixing ratio of 10^{-5}. Cells 3 - 6 merge into one large cloud mass, but the strong circulations associated with cells 1 and 2 have caused them to separate from the others. Cells 1 - 4 contain snow, and cells 1 and 2 also contain graupel and are capped by small cirrus patches. The graupel falls through the 0°C level where it melts and combines with the rain. Rain falls from cells 1 - 5; the most significant rainfall originates in cells 1 and 2 and falls to the ground approximately 20 - 25 km downwind from the fire.

Forty minutes after ignition of the fire the simulation has 96.3% of the emitted smoke in the form of "dry" aerosol, 2.1% in cloud droplets, 0.6% in raindrops, 0.9% has rained out on the ground, and the remaining 0.1% is distributed among the ice hydrometeors, primarily snow and graupel.

5. CONCLUSION

The model simulations agree in general with the observations of the Hardiman and Battersby smoke plumes and clouds, but there is enough uncertainty in the environmental soundings and observations to prevent the comparisons from being conclusive. Nevertheless, we find the comparison of the model simulations of these fires with the observations very encouraging.

6. ACKNOWLEDGEMENTS

This work was performed under the auspices of the U. S. Department of Energy by the Lawrence Livermore National Laboratory under contract W-7405-Eng-48.

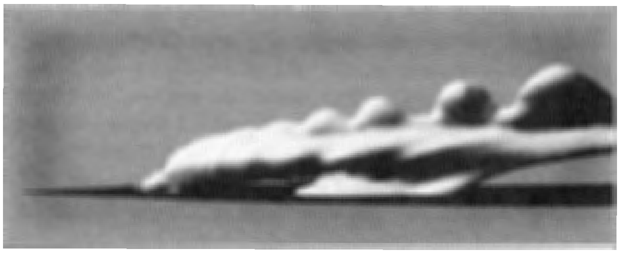

Figure 5. Smoke plume for the numerical simulation of the Battersby township fire after 40 min viewed from 40 km southeast of the fire. The contour level is 10^{-6}.

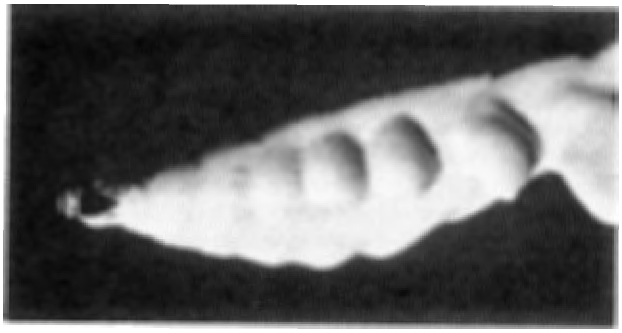

Figure 6. Top view of the numericall simulated Battersby township smoke plume after 40 min. The small dark area at the left of the plume is the 2°C temperature perturbation contour.

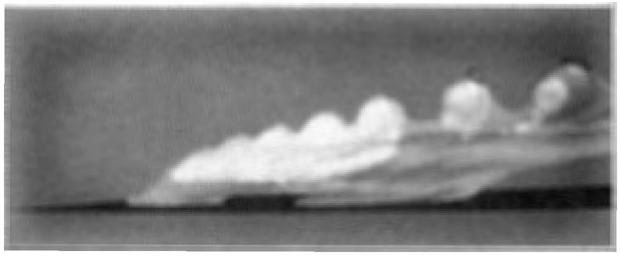

Figure 7. Interstitial smoke (medium gray), cloud droplet (white), and ice crystal (small dark surfaces at the tops of cells 1 and 2) mixing ratios for the Battersby township fire after 40 min of simulation as viewed from 40 km SE of the fire.

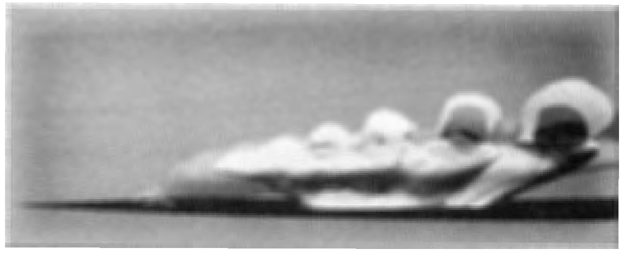

Figure 8. Interstitial smoke (light gray), rain (white), snow (white in upper part of cells 1-3), and graupel (dark gray) mixing ratios for the Battersby township fire after 40 min of simulation. The bright white in cell 3 is overlap of rain and snow.

7. REFERENCES

Banta, R., L. D. Oliver, and E. T. Holloway, 1991: Doppler lidar observations of a rotational convective smoke column. *Proceedings, 11th Conference Fire & Forest Meteorology,* Missoula, MT, Soc. Amer. Foresters, 412-418.

Bradley, M. M., and C. R. Molenkamp, 1991: A numerical model of aerosol scavenging, Part II: Simulation of a large city fire. *Proceedings, Fifth International Conference on Precipitation Scavenging and Atmosphere-Surface Exchange Processes,* Richland, WA, Hemisphere Pub. Corp.

Chuang, C. C., J. E. Penner, L. L. Edwards, and M. M. Bradley, 1990: The effects of entrainment on nucleation scavenging. *Preprints, 1990 Conference on Cloud Physics*, San Francisco, Am. Meteor. Soc., 222-225.

Edwards, L. L., 1989: Simulations of cloud condensation nucleation and growth. UCID-21633, Lawrence Livermore National Laboratory, Livermore, CA, 94550.

Klemp, J. B., and R. B. Wilhelmson, 1978: The simulation of three-dimensional convective storm dynamics. *J. Atmos. Sci.,* **35,** 1070-1096.

Lin, Y., R. D. Farley, and H. D. Orville, 1983: Bulk parameterization of the snow field in a cloud model. *J. Climate Appl. Meteor.,* **22,** 1065-1092.

Molenkamp, C. R., and M. M. Bradley, 1990: Parameterization of aerosol scavenging in a convective cloud model. *Preprints, 1990 Conference on Cloud Physics,* San Francisco, Am. Meteor. Soc., 403-407.

Molenkamp, C. R., and M. M. Bradley, 1991: A numerical model of aerosol scavenging, Part I: Microphysics Parameterization. *Proceedings, Fifth International Conference on Precipitation Scavenging and Atmosphere-Surface Exchange Processes,* Richland, WA, Hemisphere Pub. Corp.

Molenkamp, C. R., 1977: Numerical modeling of precipitation scavenging by convective clouds. *Precipitation Scavenging (1974),* Richard G. Semonin and Robert W. Beadle, Coordinators, Champaign, IL, Energy Res. and Dev. Admin., 769-793. [NTIS No. CONF-741003].

Penner, J. E., M. M. Bradley, C. C. Chuang, L. L. Edwards, and L. F. Radke, 1990: A numerical simulation of the aerosol-cloud interactions and atmospheric dynamics of the Hardiman township, Ontario prescribed burn. *Chapman Conference on Global Biomass Burning: Atmospheric, Climatic and Biospheric Implications,* Williamsburg, VA, MIT Press.

EFFECTIVE RADII AS RELATED TO ENTRAINMENT AND MIXING IN TROPICAL WARM CONVECTIVE CLOUDS

C. A. Pontikis [1] and E. M. Hicks [2]

[1] METEO FRANCE/U.A.G., Laboratoire de Physique de l'Atmosphère Tropicale, 97159, Pointe à Pitre Cedex, Guadeloupe (F.W.I.)
[2] U.A.G., Laboratoire de Physique de l'Atmosphère Tropicale, 97159, Pointe à Pitre Cedex, Guadeloupe (F.W.I.)

1. INTRODUCTION

The cloud droplet effective radius Re is one of the main parameters used to infer the cloud optical characteristics (optical thickness and single-scatter albedo). It is defined as the ratio of the third and second moments of the droplet spectral distribution (Hansen and Travis, 1974). Recent analyses of field experiment data show a high variability of the microphysical parameters on all scales, as a consequence of clear air entrainment and mixing (Austin et al., 1985; Hill and Choularton, 1985; Paluch and Baumgardner, 1989). This variability should affect the Re values.

In climate models, the effective radius is parameterized as a cube root or a linear function of the liquid water content (Stephens, 1978b,1984; Fouquart, 1989). Since such parameterizations do not take into account the variability of the microphysical parameters, errors in the corresponding effective radius estimation may occur.

The main goal of this work is to investigate theoretically and experimentally the influence of entrainment and mixing on the effective radius of warm convective non precipitating tropical clouds. The 10 Hz data used for this analysis have been collected during the Joint Hawaii Warm Rain Project (1985).

2. THEORETIC ANALYSIS

a. Numeric Study

The numeric study is made by using a cloud parcel model which simulates both vertical adiabatic transport and entrainment-mixing events (homogeneous and extreme inhomogeneous mixing). Secondary activation in ascending parcels is taken into account by using an appropriate CCN activity spectrum. The model is initialized with observed cloud base air characteristics and the corresponding clear air sounding. The simulations consist of :

- the adiabatic ascent of a cloud base parcel up to cloud top and the determination of the adiabatic cloud characteristics at all intermediate levels
- single entrainment-mixing events at a given level, whereby the adiabatic parcel is mixed in different proportions with clear air issued from the same level
- multi-level entrainment-mixing events separated by adiabatic vertical transport.

The resulting diluted parcels are further adiabatically raised up or lowered down, according to their buoyancy, to a reference level. The liquid water contents and the effective radii of these theoretically diluted parcels calculated at the reference level are then plotted in a diagram. As an example, Fig.1 shows a Re-vs-Ql diagram obtained using data corresponding to cloud 9 (10 July 1985) and a reference level at 810 mb, i.e. roughly 1.5 km above cloud base. The

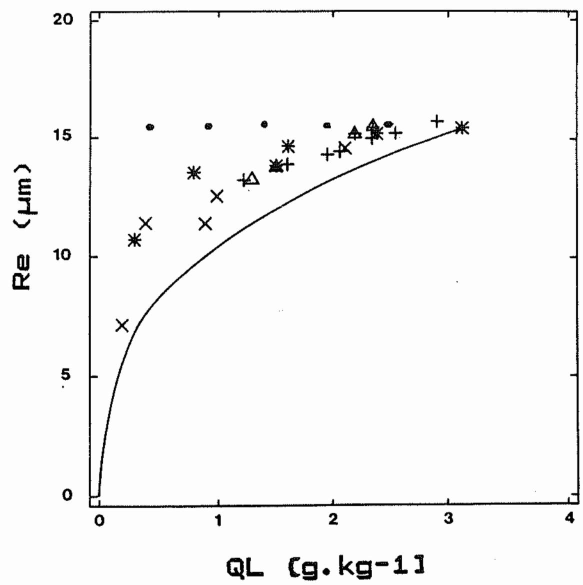

Fig.1 : Theoretic Re-vs-Ql plot obtained for the reference level 810 mb. Different symbols denote the different mixing histories : a single homogeneous mixing event occurring at a lower level (+), at the same level (*) or at a higher level (x) than the reference one, discrete multiple-mixing events (Δ) and extreme inhomogeneous mixing at the reference level (•).

solid line represents the different Qla, Rea values encountered by the undiluted cloud base parcel during its adiabatic ascent up to the reference level and follows the Rea $\sim$ $Qla^{1/3}$ law. It constitutes a lower boundary to the area in which the (Ql,Re) points are scattered. The upper boundary corresponds roughly to the Ql, Re values of parcels resulting from a single extreme inhomogeneous mixing event at the reference level, whereby Re is independent of Ql. Note that Re also remains roughly constant for a wide range of Ql values (0.5 Qla<Ql<Qla) in the case of a single homogeneous mixing event at the reference level. However, it is clear that single or multi-level entrainment-mixing events followed by periods of adiabatic transport and possible secondary activation induce important scatter in the (Ql,Re) points, thus not allowing an accurate parameterization according to a Re $\sim Ql^{1/3}$ law.

b. Analytic Effective Radius Expression

In order to assess the entrainment and mixing effect on the behavior of the effective radius, an analytic expression has been derived. As mentioned previously, the effective radius is defined as Re $=\overline{R^3}/\overline{R^2}$, where $\overline{R^2}$ and $\overline{R^3}$ are the second and third moments of the droplet spectral distribution. Both moments can be developed as a function of the mean droplet radius $\overline{R}$ and the spectral dispersion d (d = $\sigma/\overline{R}$, where σ is the standard deviation of the droplet spectral distribution) according to the following expressions :

$$\overline{R^2} = \overline{R}^2\ (1+d^2) \qquad (1)$$

$$\overline{R^3} = \overline{R}^3\ (1+3d^2) \qquad (2)$$

The comparison with the liquid water content expression leads to :

$$Re = \left(\frac{3}{4\pi\rho_L}\right)^{1/3} F(d).\left(\frac{Ql}{N}\right)^{1/3} \qquad (3)$$

where F(d) is the following dispersion function :

$$F(d) = (1+3d^2)^{2/3}/(1+d^2) \qquad (4)$$

Assuming a constant F(d) value, the above analytic expression defines a family of Re = $A(N).Ql^{1/3}$ curves for which the characteristic parameter A(N) depends exclusively upon the droplet concentration. Clear air entrainment induces the (Ql,Re) point dispersion since it produces diluted cloudy parcels with a wide range of droplet concentrations, thus leading to different characteristic A(N) parameter values. The lower boundary of the area in which the (Ql,Re) points are dispersed corresponds to the Re = $A(Nmax).Ql^{1/3}$ curve obtained for the highest droplet concentration. The latter is usually observed in undiluted parcels or in diluted parcels which have activated a significant number of droplets far from cloud base. Further, expression (3) suggests that points in a Re-vs-Ql/N plot should not present any dispersion if the F(d) value is constant.

3. EXPERIMENTAL ANALYSIS

a. Small-scale

The behavior of the effective radius of 10 Hz cloudy air parcels as a function of Ql and Ql/N is studied for the non-precipitating levels of 16 clouds sampled during the JHWRP. As an example, Fig.2 presents the Re-vs-Ql diagram for the 887 mb level of cloud 1 (11 July 1985). The data points are scattered in the area delimited by the solid lines (1,2) corresponding respectively to extreme inhomogeneous mixing with clear air issued from the same level (1) and the adiabatic ascent from cloud base to the observation level (2). This behavior is consistent with the theoretic analysis results and shows that in this case the

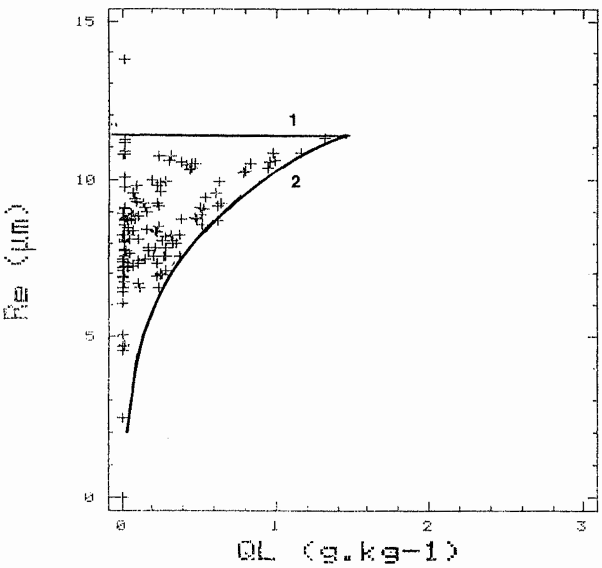

Fig.2 : Re-vs-Ql plot (10 Hz) for a single penetration (887 mb) of cloud 1 (11 July 1985).

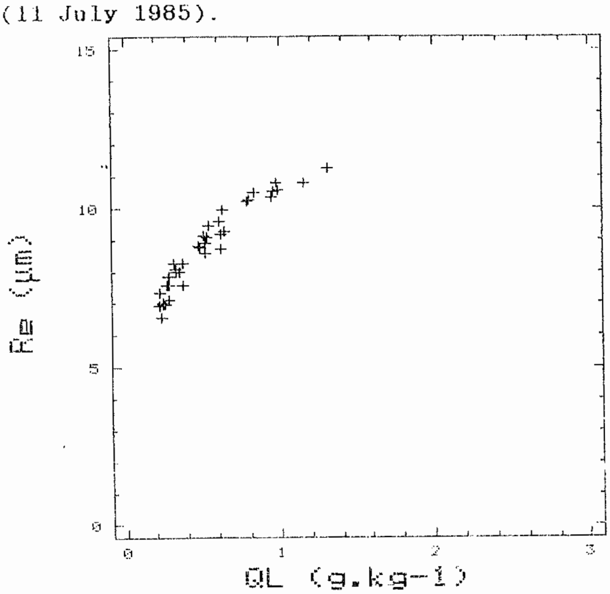

Fig.3 : As in Fig.2, but for samples with N higher than the minimum adiabatic value.

parameterization of the effective radius as a function of the cube root of the liquid water content is inadequate. Figure 3 presents the Re-vs-Ql plot for all sampled parcels with N>Namin (the minimum adiabatic droplet concentration) of the same cloud penetration. The data points follow well the Rea$\sim$Qla$^{1/3}$ curve and correspond to diluted parcels in which important secondary activation has occurred, thus leading to droplet concentrations similar to the adiabatic one.

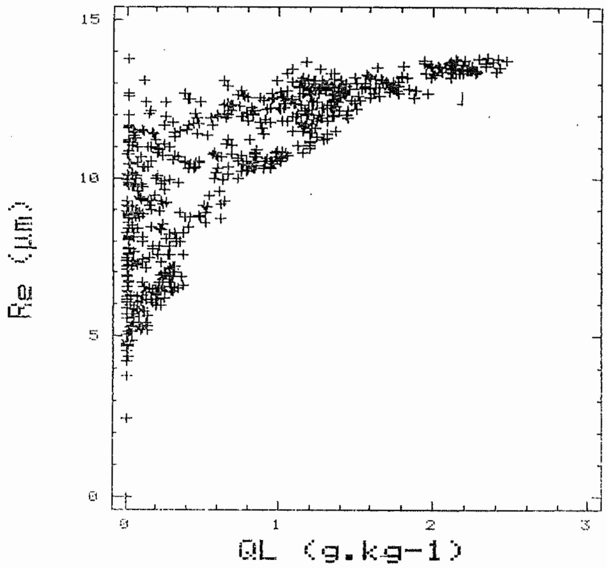

Fig.4 : Re-vs-Ql plot (10 Hz) for all parcels sampled in cloud 1 (11 July 1985).

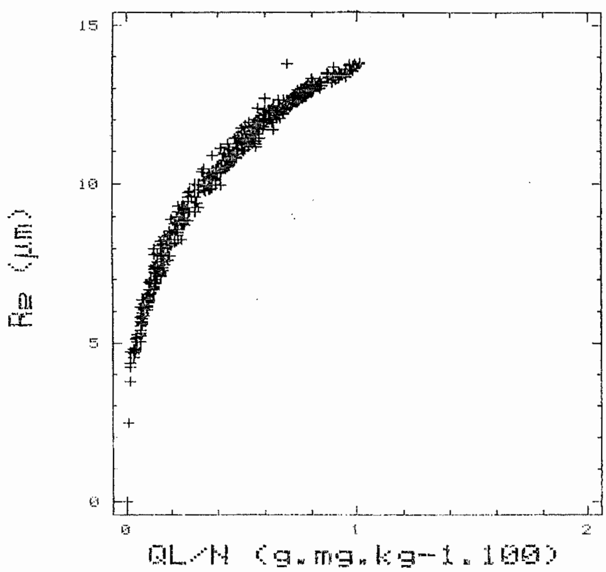

Fig.5 : Re-vs-Ql/N plot (10 Hz) for all parcels sampled in cloud 1 (11 July 1985).

The Re-vs-Ql plot obtained for al parcels of the four different penetrations made in this cloud is presented in Fig.4. The trend in the data points is similar to the one obtained in Fig.2, whereby a wide range of Re values are found for a given Ql value. Further, as predicted by the analytic expression (3), the scatter in the data-points becomes negligible if Re is plotted against Ql/N. This is illustrated in Fig. 5. This behavior suggests that the dispersion function F(d) is roughly constant throughout the considered cloud. Figure 6 shows the frequency histogram of the dispersion function values obtained for all parcels of this cloud. The F(d) values range between 1 and 1.18 with a mean value $\overline{F(d)}$=1.05. In this cloud, F(d) can be considered as a constant since 86% of the sampled parcels have F(d) values within the following limits : 1.02<F(d)<1.08. A similar behavior is observed at the 10 Hz scale for all other studied Hawaiian clouds sampled during JHWRP.

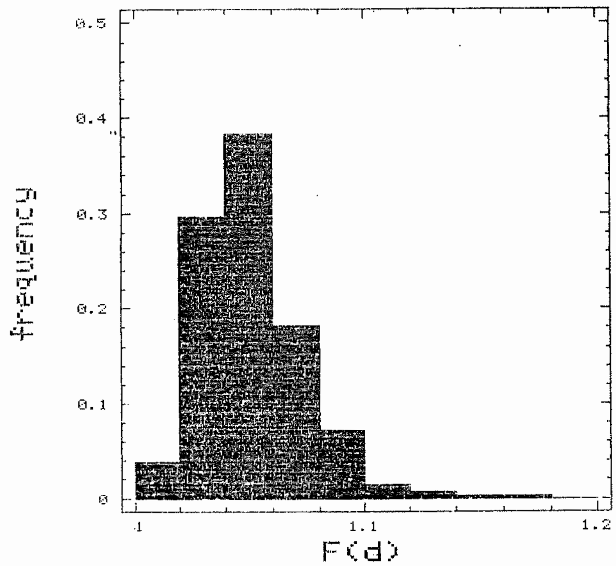

Fig.6 : Frequency histogram of the dispersion function F(d) for all parcels sampled in cloud 1 (11 July).

b. Mean Values

The effective radii used in climate modeling represent average values obtained over clouds. In order to assess if the analytic expression (3) can be used to determine such average values, the mean effective radius of each studied cloud (Re1) has been calculated according to (3) with the corresponding mean liquid water content, droplet concentration and assuming F(d)=1. This value has then been compared to the effective radius (Re2) obtained by averaging the Re values of all 10 Hz parcels sampled throughout the cloud. As an example, for cloud 1 (11 July 1985), expression (3) leads to an Re1 value of 10.3 µm ($\bar{N}$=153 mg^{-1}, $\bar{Ql}$=0.7 $g.kg^{-1}$) which is in good agreement with the Re2 value of 9.93 µm obtained by averaging the corresponding Re 10 Hz sample values. For all studied clouds, the relative differences between Re1 and Re2 do not exceed 7%. Further, if a $Re \sim Ql^{1/3}$ function is fitted in order to correctly represent the mean effective radius of a given cloud and is used to calculate the mean effective radius of the other considered clouds which have all developed in similar air masses, the relative difference between the Re and Re2 values is of 40% in the extreme case. This behavior can be related to the problem of anomalous absorption of solar radiation (Stephens and Tsay, 1990). Indeed, the real mean effective radius of a given cloud may significantly exceed the one calculated according to the $Re \sim Ql^{1/3}$ parameterization and the theoretically calculated absorption of solar radiation may therefore be underestimated.

4. DISCUSSION AND CONCLUDING REMARKS

Our theoretic and experimental analysis results show that an accurate parameterization of the mean effective radius of warm convective clouds implies necessarily the knowledge of both the liquid water content Ql and the droplet concentration N. For a given cloud, N is affected by clear air entrainment and mixing as well as by subsequent droplet activation. Further, for clouds which have developed in different air masses, N also depends upon the corresponding CCN concentrations. The combined effect of clear air entrainment and mixing and of differences in the CCN concentrations on the behavior of the effective radius is complex and can in some cases limit the validity of the usual $Re \sim Ql^{1/3}$ parameterization. Our results attenuate therefore the conclusions presented by Jonas (1991) and Blyth and Latham (1991). Clearly, parameterizations including the effect of entrainment and mixing are necessary in order to determine the accurate cloud mean effective radius. Further, for clouds which have developed in different air masses containing different CCN concentrations a provisional possible improvement of the Re value accuracy could be the use of "standard" droplet concentrations Ns depending upon the air mass characteristics (for example, Ns=50 mg^{-1} for a maritime air mass, Ns=600 mg^{-1} for a continental air mass).

References :

Austin, P.H., M.B. Baker, A. Blyth and J.B. Jensen, 1985 : Small-scale variability in warm continental cumulus clouds. J. Atmos. Sci., 42, 1123-1138.
Blyth, A. M. and J. Latham, 1991 : A climatological parameterization for cumulus clouds. J. Atmos. Soc., 48, 2367-2371.
Fouquart, Y., J.C. Buriez and M. Herman, 1989 : The influence of boundary layer clouds on radiation : A review. Atmos. Res., 23, 203-228.
Jonas, P., 1991 : On the parameterization of clouds containing water droplets. Quart. J. Roy. Met. Soc., 117, 257-263.
Hansen, J.E., and L.D. Travis, 1974 : Light-scattering in planetary atmospheres. Space Sci. Rev., 16, 527-610.
Hill, T.A., and T.W. Choularton, 1985 : An airborne study of the microphysical structure of cumulus clouds. Quart. J. Roy. Met. Soc., 111, 517-544.
Paluch, I.R. and D. Baumgardner, 1989 : Entrainment, fine-scale mixing in a continental convective cloud. J. Atmos. Sci., 46, 261-278.
Stephens, G.L., 1978b : Radiation profiles in extended water clouds. II: Parameterization schemes. J. Atmos. Sci., 35, 2123-2132.
Stephens, G.L., 1984 : The parameterization of radiation for numerical weather prediction and climate models. Mon. Weather Rev.,112, 826-867.
Stephens, G.L., and S. Tsay, 1990 : On the cloud absorption anomaly. Quart. J. Roy. Met. Soc., 116, 671-704.

A QUANTITATIVE ASSESSMENT OF THE DIFFERENCES BETWEEN NORTHERN HIGH PLAINS CONVECTIVE CLOUDS AND SOUTHEAST COHMEX CLOUDS

Richard D. Farley and Harold D. Orville

Institute of Atmospheric Sciences
South Dakota School of Mines and Technology
501 E. St. Joseph Street
Rapid City, South Dakota 57701-3995

1. INTRODUCTION

The major difference in the production of precipitation from maritime soundings typical of the southeastern United States region and from continental soundings in the northern High Plains is the predominant influence of the warm rain process in maritime clouds, whereas ice processes are crucial to precipitation initiation and production in continental clouds. Ice processes can also play an important role in maritime clouds, particularly in the more vigorous cells. These aspects are clearly illustrated by the following comparisons of precipitation development in numerical simulations of intense convection in the two regions.

2. MODEL DESCRIPTION

The theoretical framework is a deep-convection, two-dimensional, time-dependent cloud model based on the work of *Orville* (1965). The nonlinear partial differential equations constituting the model include the first and third equations of motion, a thermodynamic equation, and water conservation equations (for its three phases). The bulk-water microphysical scheme employed in the model is based on concepts suggested by *Kessler* (1969) and divides water and ice hydrometeors into five classes: cloud water, cloud ice, rain, snow, and high density precipitating ice (graupel/hail). These five classes of hydrometeors interact with each other and water vapor through a variety of crude parameterizations of the physical processes of condensation/evaporation, collision/coalescence and collision/aggregation, accretion, freezing, melting, and deposition/sublimation. For a detailed discussion of the microphysical processes and parameterizations employed in the bulk water model, the reader is referred to *Wisner et al.* (1972), *Orville and Kopp* (1977), and *Lin et al.* (1983).

The two-dimensional hail category model of *Farley and Orville* (1986) and *Farley* (1987), which partitions the precipitating ice field into 20 logarithmically spaced size categories, has also been run on the two cases reported herein. This model employs a more detailed and realistic treatment of the growth and sedimentation of ice in the simulated clouds and facilitates more detailed studies of the growth of ice. Comparison of the results of the detailed model with results of the bulk model also allows assessment of the relative adequacy of the bulk model's treatment of ice in various situations.

3. BRIEF OVERVIEW OF THE SIMULATED CASES

Two thoroughly studied cases form the basis for the comparison. One case is the CCOPE hailstorm of 1 August 1981 from the Montana region, and the other is the intense thunderstorm case of 20 July 1986 from COHMEX in northeast Alabama. The character of the model simulations for these two cases will now be briefly reviewed to provide a frame of reference for later discussions.

The simulations of the COHMEX case are similar to preliminary results reported in *Tuttle et al.* (1989). Simulated cloud base was at 1.2 km AGL (22°C). Early clouds for this case topped out between 6 and 8 km and contained little ice. Maximum updrafts were 10 m s^{-1} or less during this stage. After about 45 min of this preliminary cloud and precipitation development, strong convection appeared. A rapidly growing cell broke through the level of the moderate size cells, carried large drops into supercooled regions where freezing occurred, and stimulated further growth with cloud top extending beyond 13 km. The intense convection of the dominant cell started around 126 min of simulated time. Maximum updrafts during this stage approached 25 m s^{-1}. Maximum rain and graupel/hail amounts were 13 g kg^{-1} and 11 g kg^{-1}, respectively.

The results of the 1 August CCOPE hailstorm simulations have been reported previously in *Kubesh et al.* (1988). Simulated cloud base was at 2.2 km AGL (12°). This cloud grew very quickly, with cloud depth increasing threefold between 51 and 63 min. The rounded cloud dome characteristic of this case exceeded 15 km AGL at 75 min. Updrafts exceeded 40 m s^{-1} for much of the storm lifetime. Maximum rain and graupel/hail amounts were of the order of 5 g kg^{-1} and 10 g kg^{-1}, respectively.

4. COMPARISON OF PRECIPITATION DEVELOPMENT IN THE TWO CASES

Figures 1 and 2 show the various terms that contribute to the production of rain and graupel/hail for the southeastern United States case. Figures 3 and 4, taken from *Kubesh et al.* (1988), show the same information for the High Plains case. These figures are based on the results of the bulk model simulations of the cases, which differ from the detailed model results in some respects. These model dependent aspects will be addressed later. First we will discuss the production of graupel/hail and then rain in the two cases.

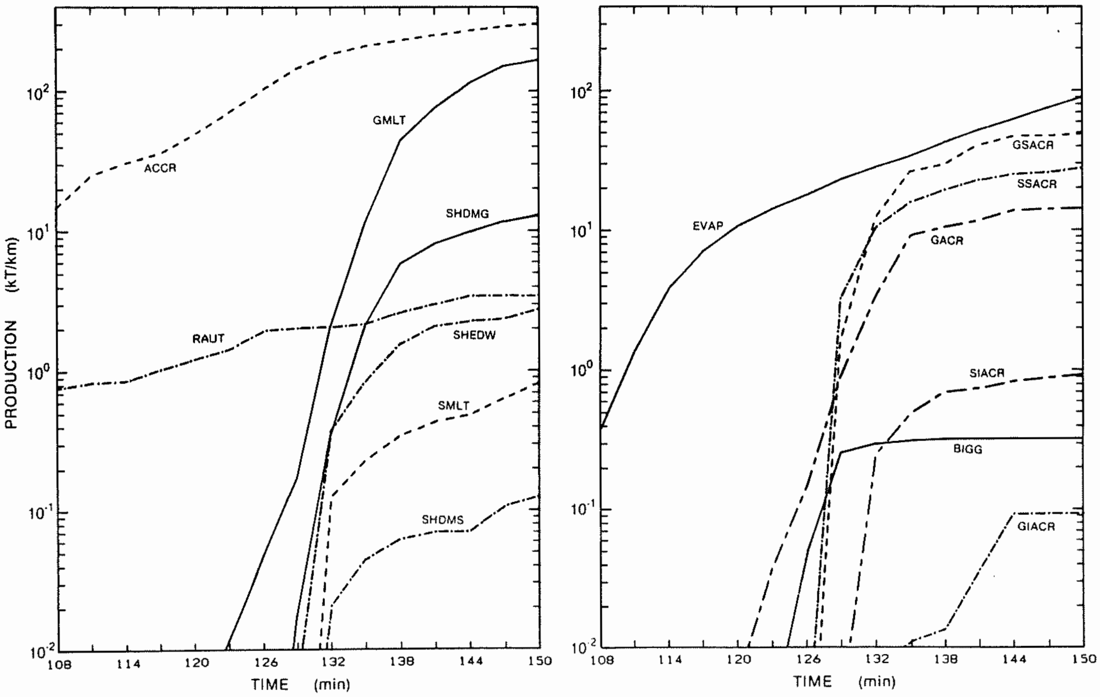

GENERATION/GROWTH MECHANISMS
RAUT=Rain formed by autoconversion of cloud water.
GMLT=Rain formed by melting of graupel/hail.
SMLT=Rain formed by melting of snow.
SHEDW=Rain from shedding during wet growth of graupel/hail.
SHDMG=Rain from shedding during melting of graupel/hail.
SHDMS=Rain from shedding during melting of snow.
ACCR=Rain growth by accretion of cloud water.

LOSS MECHANISMS
EVAP=Evaporation of rain.
SIACR=Accretion of rain by cloud ice, forming snow.
SSACR=Accretion of rain by snow.
GACR=Accretion of rain by graupel/hail.
GSACR=Accretion of rain by snow, forming graupel/hail.
GIACR=Accretion of rain by cloud ice, forming graupel/hail.
BIGG=Probabilistic freezing of rain to form graupel/hail.

Fig. 1: Rain production due to the processes listed for the bulk model simulation of the 20 July COHMEX case. Processes contributing to a gain (loss) in the rain field are shown in the left (right) panel. The units of production are kT km^{-1}. The curves are the result of the various rates being summed over the entire domain and accumulated to the indicated time.

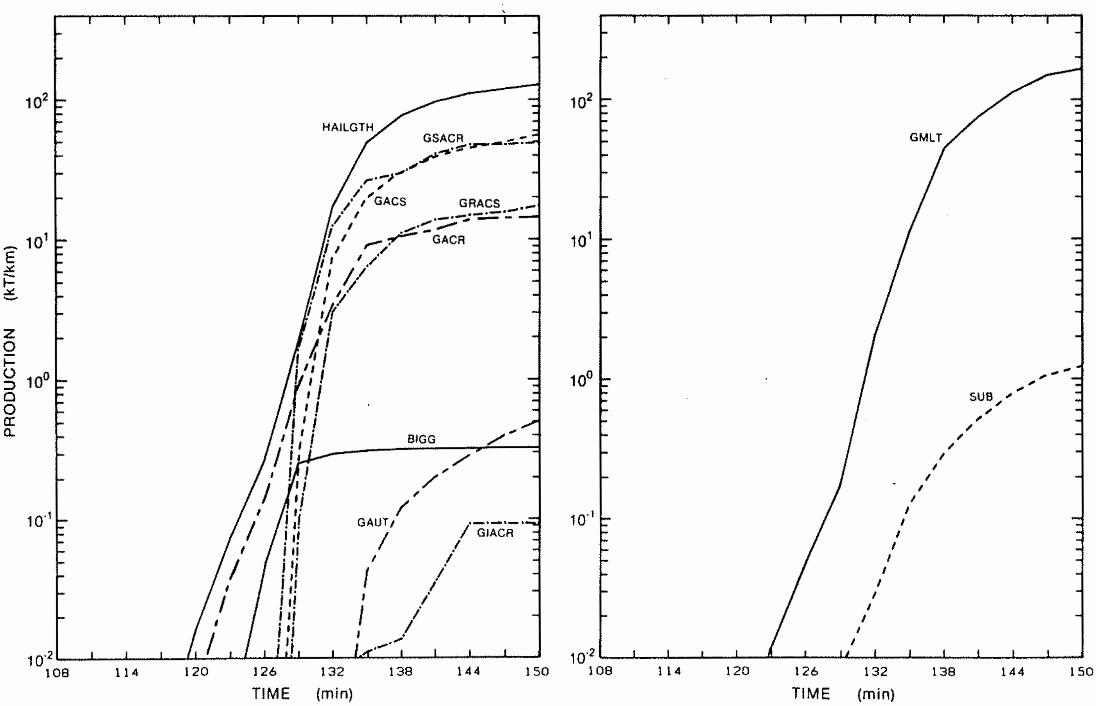

GENERATION MECHANISMS
GAUT=Graupel/hail formed by autoconversion (aggregation) of snow.
GRACS=Accretion of snow by rain, forming graupel/hail.
GSACR=Accretion of rain by snow, forming graupel/hail.
GIACR=Accretion of rain by cloud ice, forming graupel/hail.
BIGG=Probabilistic freezing of rain to form graupel/hail.

GROWTH MECHANISMS
HAILGTH=Total accretional growth of graupel/hail.
GACS=Accretion of snow by graupel/hail.
GACR=Accretion of rain by graupel/hail.

LOSS MECHANISMS
GMLT=Loss of graupel/hail by melting to form rain.
SUB=Loss of graupel/hail by sublimation.

Fig. 2: As in Fig. 1, except for the graupel/hail field.

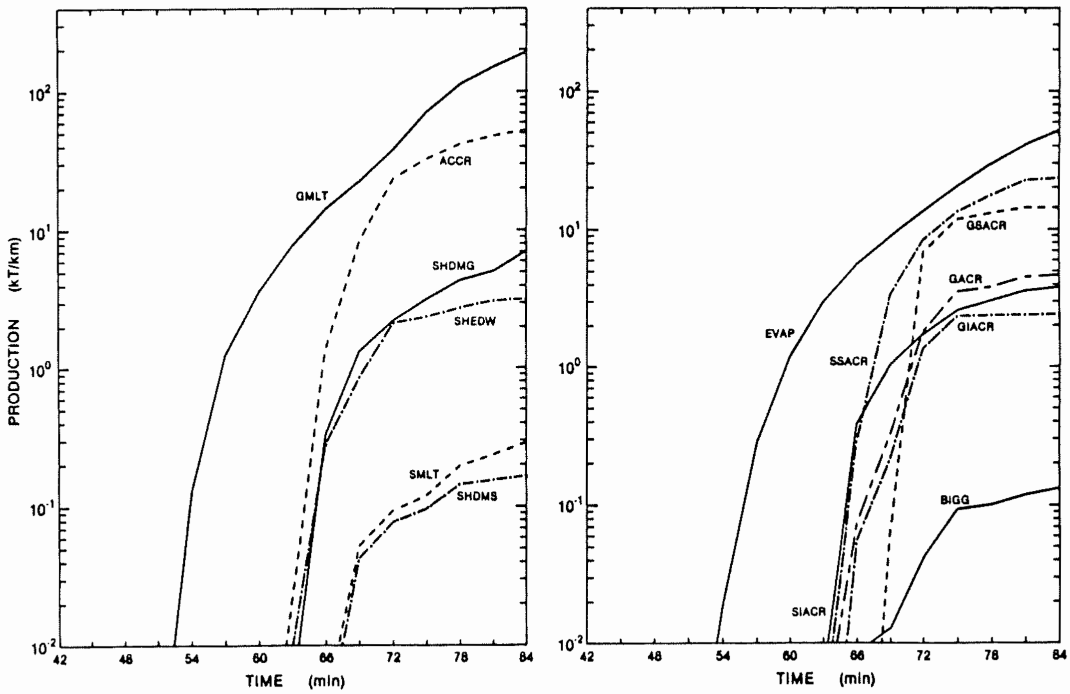

Fig. 3: As in Fig. 1, except for the 1 August CCOPE case.

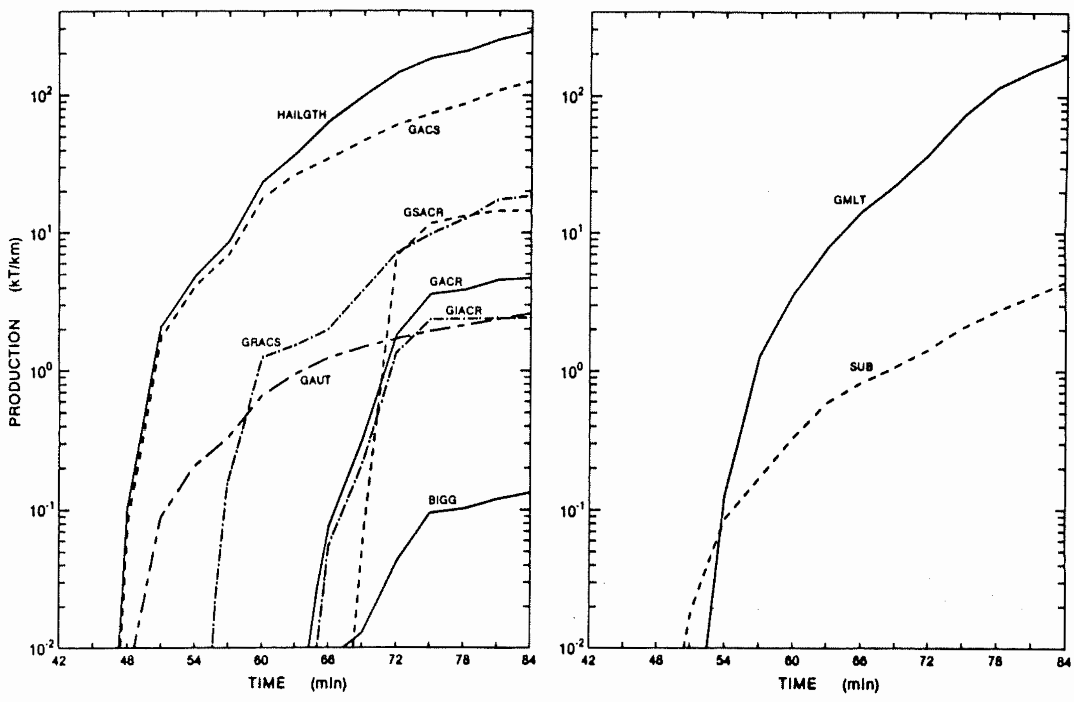

Fig. 4: As in Fig. 2, except for the 1 August CCOPE case.

The following aspects are noted regarding the graupel/hail production terms. 1) Accretional growth and the melting of graupel/hail are the biggest terms -- exceeding 100 kT/km in both cases. 2) Wet growth of the graupel/hail (not shown) is 5 to 15% of accretional growth in both cases, being larger in the COHMEX case. 3) Graupel accreting snow is an important term in both areas (>50 kT/km). 4) Rain/snow interactions are important in the COHMEX case (a total of 70 kT/km) and of order 30 kT/km in the CCOPE case. 5) Cloud ice/rain interactions are more important in the High Plains (2.5 kT/km) than in the Southeast (0.1 kT/km). 6) The probabilistic (Bigg) freezing of rain is a significant early source of graupel/hail in the COHMEX case with high coalescence amounts, but totals less than 0.5 kT/km in both cases. 7) Sublimation is of the same order in both cases (1 kT/km).

The following characteristics apply to the rain production terms. 1) Melting of graupel/hail is the biggest term in CCOPE (200 kT/km), and accretion the biggest term in COHMEX (300 kT/km). However, melting approaches 170 kT/km in COHMEX. Hence, both storms produce similar amounts of rain through the ice processes. COHMEX produces additional rain via coalescence. 2) The period of ice production is similar in the two cases, about 30 min, and some of the quantities are of the same magnitude. 3) Evaporation is greatest in the COHMEX case (90 vs. 50 kT/km). 4) Rain/snow interactions result in approximately 80 kT/km loss of rain to graupel or snow in COHMEX; less than 50% of this in the CCOPE case. 5) Shedding during wet growth is low in both cases (3 kT/km). Shedding during melting of graupel is of order 10 in both cases. Shedding from melting snow is of order 0.1 kT/km. 6) Accretion is the second largest term in CCOPE (50 kT/km); the largest term in COHMEX. 7) Autoconversion (coalescence) is about 3.5 kT/km in COHMEX, and is deactivated in CCOPE.

5. MODEL DEPENDENT ASPECTS

The results of the two different models applied to these cases show a high degree of similarity over the duration of the simulations, especially in terms of large scale structure, dynamic features, and evolution. Microphysical aspects, whether in terms of maximum values or domain totals, also display similarities throughout, even though ice is treated quite differently in the two models. This is especially true for the COHMEX case due to the dominant role of the warm rain process which is treated similarly in the two models. Although specific aspects of the production of precipitating ice show pronounced differences for the two models, these aspects usually play a secondary role and exert minor influence compared to the dominant terms.

There are pronounced differences between the bulk and detailed models regarding contact freezing of rain. These involve the snow/rain interaction terms in the bulk model and the rain/cloud ice interaction terms and the accretion freezing of rain by graupel/hail in both models. The combined effect of the appropriate terms in each type of model is roughly equal, indicating most of the rain in the supercooled region will ultimately be converted to ice regardless of the path taken. Contact freezing of rain tends to be slightly larger in the detailed model than the bulk model. These processes are much larger in the COHMEX case and have a strong influence throughout the ice phase history, whereas these terms are most effective in the later stages for the CCOPE case.

Another model dependent aspect is the graupel accreting snow term. There is no equivalent of this in the detailed model and the physical basis for this term in the bulk model is relatively weak. It is safe to say that the importance of this term is exaggerated in the bulk model. Other consistent model differences are that wet growth is larger in the bulk model, whereas sublimation is greater in the detailed model.

6. SUMMARY

This study has compared precipitation development in numerical simulations of intense convection for northern High Plains continental clouds and southeastern United States maritime clouds. Although the dominant path to precipitation formation is distinctly different for the two regions, this comparison has revealed some surprising similarities and other unanticipated findings. Accretional growth of graupel/hail and melting are the dominant ice processes in both regions and are of similar magnitudes. Although most rain is produced by collision coalescence for the maritime case, both cases produce similar amounts of rain via melting. Even though the humidity is much higher and cloud base is considerably lower for the maritime case, evaporation is nearly a factor of 2 greater than for the continental case.

Acknowledgments. The simulations forming the basis of this study were conducted using the computers of the Scientific Computing Division of the National Center for Atmospheric Research. The research was supported by the National Science Foundation under Grants ATM-8603308 and ATM-8821119 and the National Aeronautics and Space Administration under Grant NAG 8-632. We gratefully acknowledge the assistance of Joie Robinson in the preparation of the manuscript.

REFERENCES

Farley, R. D., 1987: Numerical modeling of hailstorms and hailstone growth: Part III. Simulation of an Alberta hailstorm - natural and seeded cases. *J. Climate Appl. Meteor.*, **26**, 789-812.

Farley, R. D., and H. D. Orville, 1986: Numerical modeling of hailstorms and hailstone growth: Part I. Preliminary model verification and sensitivity tests. *J. Climate Appl. Meteor.*, **25**, 2014-2035.

Kessler, E., 1969: On the distribution and continuity of water substance in atmospheric circulations. *Meteor. Monogr.*, **32**. 84 pp.

Kubesh, R. J., D. J. Musil, R. D. Farley and H. D. Orville, 1988: The 1 August 1981 CCOPE storm: Observations and modeling results. *J. Appl. Meteor.*, **27**, 216-243.

Lin, Y-L., R. D. Farley and H. D. Orville, 1983: Bulk parameterization of the snow field in a cloud model. *J. Climate Appl. Meteor.*, **22**, 1065-1092.

Orville, H. D., 1965: A numerical study of the initiation of cumulus clouds over mountainous terrain. *J. Atmos. Sci.*, **22**, 684-699.

Orville, H. D., and F. J. Kopp, 1977: Numerical simulation of the life history of a hailstorm. *J. Atmos. Sci.*, **34**, 1596-1618. [Reply: *J. Atmos. Sci.*, **35**, 1554-1555]

Tuttle, J. D., V. N. Bringi, H. D. Orville and F. J. Kopp, 1989: Multiparameter radar study of a microburst: Comparison with model results. *J. Atmos. Sci.*, **46**, 601-620.

Wisner, C. E., H. D. Orville and C. G. Myers, 1972: A numerical model of a hail-bearing cloud. *J. Atmos. Sci.*, **29**, 1160-1181.

Kinematic microphysical retrieval in non-steady clouds

Johannes Verlinde* and William R. Cotton
Colorado State University
Dept. of Atmospheric Science

1 Introduction

Model fitting to observations is one of the important tools available to scientists to help them understand complex physical phenomena. It may be considered to be fitting a conceptual model to a set of observations to describe how the physical process typically evolves, or it may be changing control variables of a numerical model of the same process, based on observations, such that the numerical results closely reproduce the given set of observations.

The feasibility of using a four-dimensional variational assimilation technique to incorporate observations of the physical processes involved in precipitation formation into a numerical cloud microphysical model was investigated. The means through which this was accomplished was a series of identical twin experiments. A kinematic bulk parameterized model of the liquid phase physics was developed. This model is used to create an observational data set in space and time. An iterative algorithm was derived through which the model can be fitted to the observations. The control variables selected for this study were the variables describing the state of the model at the initial time, but it may also include other elements of the model such as boundary conditions or parameterization constants. This algorithm was used to retrieve the original initial condition used in the observation run, starting from a constant initial condition. Factors influencing the rate of convergence were investigated. This work is the extension of the work of Rutledge and Hobbs (1983; 1984) and Ziegler (1985) to non-steady convective clouds.

2 Derivation

Assume a set of observations over the time interval (t_0, t_1), and a numerical model describing the process observed. A model solution is sought that will fit the observations 'the best'. Courtier and Talagrand (1990) suggest that in view of the complexity of the minimization problem, the only practical way to numerically determine the minimizing solution is to take the model initial conditions as the control variables of the problem. To define the problem it is necessary to define a distance function (the cost) between the model state and the observations, and then to determine the gradient of that distance function with respect to the control variables.

Assume the observations are of some general function $z = z(\mathbf{x})$ of the control variables $\mathbf{x}$. Boldface lowercase letters are used to indicate vectors, uppercase indicate matrices. The observations are indicated by the vector $\mathbf{o} = \mathbf{o}^j$, where the superscript j indicate time. For simplicity it is assumed that observations are available for every time step of the model. The model solution at each time step is indicated by $\mathbf{x}^j$, $j = 0, \ldots, N$. Define the cost function as

$$E(\mathbf{x}^o) = \frac{1}{2}\sum_{j=0}^{N} \left[\mathbf{z}(\mathbf{x}^j) - \mathbf{o}^j\right]^T \mathbf{W} \left[\mathbf{z}(\mathbf{x}^j) - \mathbf{o}^j\right] \tag{1}$$

where $\mathbf{W}$ is a constant weight matrix and superscript T denotes a transpose. The gradient of the cost function with respect to the initial conditions is

$$\nabla_{\mathbf{x}^o} E(\mathbf{x}^o) = \sum_{j=0}^{N} \left[\nabla_{\mathbf{x}^j}\mathbf{z}(\mathbf{x}^j)\nabla_{\mathbf{x}^o}\mathbf{x}^j\right]^T \mathbf{W} \left[\mathbf{z}(\mathbf{x}^j) - \mathbf{o}^j\right] \tag{2}$$

since $\nabla_{\mathbf{x}^o}\mathbf{o}^j = 0$. To get a usable expression for $\nabla_{\mathbf{x}^o}\mathbf{x}^j$ the chain rule must be applied backwards to the forward operator of the model, which in this case is just a simple forward upstream operator

$$\mathbf{x}^j = \mathbf{x}^{j-1} + \delta t\ \mathbf{f}(\mathbf{x}^{j-1}). \tag{3}$$

Taking the Jacobian of Eq (3) gives

$$\begin{aligned} \nabla_{\mathbf{x}^o}\mathbf{x}^j &= \left[\mathbf{I} + \delta t\ \nabla_{\mathbf{x}^{j-1}}\mathbf{f}(\mathbf{x}^{j-1})\right] \nabla_{\mathbf{x}^o}\mathbf{x}^{j-1} \\ &= \mathbf{T}_{j-1}\nabla_{\mathbf{x}^o}\mathbf{x}^{j-1} \end{aligned} \tag{4}$$

Realizing that $\nabla_{\mathbf{x}^o}\mathbf{x}^o = \mathbf{I}$, the identity matrix, Eq (4) can be written as

$$\nabla_{\mathbf{x}^o}\mathbf{x}^j = \mathbf{T}_{j-1}\mathbf{T}_{j-2}\ldots\mathbf{T}_1\mathbf{T}_0. \tag{5}$$

Eq (2) can then be written as

$$\begin{aligned} \nabla_{\mathbf{x}^o} E(\mathbf{x}^o) = \ & \mathbf{W}\left[\mathbf{z}(\mathbf{x}^o) - \mathbf{o}^o\right] + \\ & \mathbf{T}_0^T\left\{\left[\nabla_{\mathbf{x}^1}\mathbf{z}(\mathbf{x}^1)\right]^T \mathbf{W}\left[\mathbf{z}(\mathbf{x}^1) - \mathbf{o}^1\right] + \right. \\ & \mathbf{T}_1^T\left\{\left[\nabla_{\mathbf{x}^2}\mathbf{z}(\mathbf{x}^2)\right]^T \mathbf{W}\left[\mathbf{z}(\mathbf{x}^2) - \mathbf{o}^2\right] + \ldots \right. \\ & \mathbf{T}_{N-1}^T\left\{\left[\nabla_{\mathbf{x}^N}\mathbf{z}(\mathbf{x}^N)\right]^T \mathbf{W}\left[\mathbf{z}(\mathbf{x}^N) - \mathbf{o}^N\right]\right\} \\ & \ldots\}\}. \end{aligned} \tag{6}$$

Defining $\mathbf{y}^j = \left[\nabla_{\mathbf{x}^j}\mathbf{z}(\mathbf{x}^j)\right]^T \mathbf{W}\left[\mathbf{z}(\mathbf{x}^j) - \mathbf{o}^j\right]$ and $\mathbf{A}_{j-1} = \mathbf{T}_{j-1}^T$, Eq (6) can be written in shorthand notation as

$$\begin{aligned} \nabla_{\mathbf{x}^o} E(\mathbf{x}^o) = \ & \mathbf{y}^o + \mathbf{A}_0\{\mathbf{y}^1 + \mathbf{A}_1\{\mathbf{y}^2 + \\ & \ldots\{\mathbf{y}^{N-1} + \mathbf{A}_{N-1}\mathbf{y}^N\}\ldots\}\}. \end{aligned} \tag{7}$$

Thus, it can be seen that the gradient of the cost function can be expressed as a linear operator. *This operator has been called the adjoint model.* The unknowns are the matrices $\mathbf{T}_j$ and $\nabla_{\mathbf{x}^j}\mathbf{z}(\mathbf{x}^j)$.

3 A simple example

To illustrate how the adjoint model is computed, a simple example will be shown. Assume a single grid-point model which describes the evolution of a raindrop distribution through prognostic equations for two bulk parameters of the distribution, number concentration n and mixing ratio r. The rain drops are distributed according to the gamma distribution

$$f(D) = \frac{1}{\Gamma(\nu)}\left(\frac{D}{D_n}\right)^{\nu-1}\frac{1}{D_n}\exp\left(-\frac{D}{D_n}\right) \tag{8}$$

where D_n is the characteristic diameter of the distribution and Γ is the complete gamma function. The relationship between the characteristic diameter and the prognostic variables of the model can be determined from the definition of r,

$$\begin{aligned} r &= \int_0^\infty \frac{\pi}{6}\frac{\rho_l}{\rho_a}D^6 n f(D)dD \\ &= C_2 n D_n^3, \end{aligned} \tag{9}$$

where C_2 is a constant.

Assume that the reflectivity of this distribution is observed. The functional relation between the model prognostic variables and the observed function is given by

* Current Affiliation: South African Weather Bureau

$$Z = \int_0^\infty D^6 n f(D) dD = C_1 n D_n^6, \tag{10}$$

where C_1 is another constant.

The forward model can be described by

$$n^i = n^{i-1} + \delta t \ f_n(n^{i-1}, r^{i-1}) \tag{11}$$

$$r^i = r^{i-1} + \delta t \ f_r(n^{i-1}, r^{i-1}) \tag{12}$$

where f_n is the tendency equation for n and f_r for r. The matrices $\mathbf{T}_i$ are then given by

$$\mathbf{T}_i = \mathbf{I} + \delta t \ \nabla_{\mathbf{X}^i}\mathbf{f}(\mathbf{x}^i) = \begin{pmatrix} 1 & 0 \\ 0 & 1 \end{pmatrix} + \delta t \begin{pmatrix} \frac{\partial f_n}{\partial n} & \frac{\partial f_n}{\partial r} \\ \frac{\partial f_r}{\partial n} & \frac{\partial f_r}{\partial r} \end{pmatrix} \tag{13}$$

where all the derivatives are evaluated at time $t = i$. Next the Jacobian $\nabla_{\mathbf{X}^i}\mathbf{z}(\mathbf{x}^i)$ needs to be determined. Since there is only a single observation, for this simple example this will in fact be a vector. It can be shown that

$$\nabla_{\mathbf{X}} Z = \left(\frac{\partial Z}{\partial n}, \frac{\partial Z}{\partial r}\right) = C_1 D_n^6(-1, 2). \tag{14}$$

With these terms defined a single step of the adjoint model can then be written as

$$\begin{pmatrix} n_*^i \\ r_*^i \end{pmatrix} = C_1 D_n^6 (Z_{mod} - Z_{obs}) \times \begin{pmatrix} 1 + \delta t \ \frac{\partial f_n}{\partial n} & \delta t \ \frac{\partial f_r}{\partial n} \\ \delta t \ \frac{\partial f_n}{\partial r} & 1 + \delta t \ \frac{\partial f_r}{\partial r} \end{pmatrix} \begin{pmatrix} -1 \\ 2 \end{pmatrix} \begin{pmatrix} w_n & 0 \\ 0 & w_r \end{pmatrix} + \begin{pmatrix} n_*^{i+1} \\ r_*^{i+1} \end{pmatrix} \tag{15}$$

where all terms on the right hand side are evaluated at time $t = i$

4 Procedure

With the forward model and the adjoint model defined, the procedure to fit the model to the observations can be described. An initial guess for the initial conditions is chosen — generally some state that is close to the observations at the initial time. The forward model is integrated till the time of the last observation, and the cost function is calculated. If the cost is below ϵ, convergence has occurred, if not, the adjoint model is integrated to determine the gradient. The cost function value and the gradient are then passed to an optimization routine which determine new minimizing values of the control variables.

This technique was applied to three different models. First, a positive definite advections scheme. Second, a simple 1-D model with a bulk microphysics, and thirdly, to a 2-D model with bulk microphysics. The first two models was used to perform cheap tests on certain properties of the algorithm.

5 Models and results

The advection model converged to the correct solution in as little as 4 iterations, and generally in less than 10 iterations. It was found that an overdetermination of the degrees of freedom by the observations resulted in good model fits, even when random perturbations were added to the observations. The construction of the adjoint model for 2- or 3-D models becomes increasingly complex, and though possible, it becomes unpractical and very costly to compute.

The 1-D microphysical model had three prognostic variables, liquid water potential temperature, total water mixing ratio and rain water mixing ratio. Temperature, saturation mixing ratio and cloud water mixing ratio were then diagnosed from the prognostic variables (Tripoli and Cotton, 1981). Constant wind and pressure fields were prescribed as 'observables'. The physical processes included in the microphysical parameterization were autoconversion of cloud water to rain water (Kessler, 1969), collection of cloud water by rain water (accretion equation) and the sedimentation of rain (through Lagrangian advection with subsequent redistribution). For simplicity it was assumed that the prognostic variables were observed.

The control variables for this problem are the initial fields of the three prognostic variables. These variables are of greatly different magnitude. The cost function will therefore be flat in certain directions. Consequently, the descent algorithm will soon fall into a long flat valley, with a slow rate of convergence. Ideally one would like the gradient to be such that all variables converge to the solution at about the same rate. This can be accomplished by scaling with the Hessian matrix (Thacker, 1989), but it is prohibitively expensive to calculate the Hessian matrix for this problem. Moore (1991) has suggested that the gradient should be scaled by the relative magnitude of the variables, while Kapitza (1991) suggested that there is no *a priori* way of knowing the correct scaling factors. As an extension from linear theory, the scaling factors are often chosen as a function of the variance of the measurement errors (e.g. Courtier and Talagrand, 1990).

Various experiments indicated that scaling by the relative magnitude of the variables lead to bad convergence rates, while scaling with a function of the variance of the measurement errors results in good convergence rates. These results disagree with Kapitza's (1991) suggestion. It further was found that longer assimilation periods lead to slower convergence rates. This model was also used to investigate the necessity of having information (observations) of all the prognostic variables. It was found that the algorithm was able to retrieve to a satisfactory degree all the variables even when there were no observations of one of the prognostic variables. The convergence rate was slow ($\sim$ 150 iterations) compared to when observations of all variables were available ($\sim$ 30 iterations). When two spot observations were added for the otherwise not observed variable, only 75 iterations were needed for the same accuracy. Thus, even small amounts of information will greatly help the fitting process. From the simple example it can be seen that when observations of functions of the prognostic variables are taken, information spread immediately to all the variables related to the observations. It is thus likely that with real observations information about all the prognostic variables will exist, if not, it would be wise to make a special effort in any field project to get at least some information (like flying a plane through the cloud) of all the variables.

The algorithm was able to improve the error statistics for all times during the assimilation period when randomly perturbed observations were used. Greater overdetermination of the variables gave better error statistics. When the model was integrated beyond the time of the final observations (after assimilation) the errors increase again, but did not get up to the level of the errors in the observations after twice the assimilation period.

The 2-D microphysical model had as prognostic variables liquid water potential temperature, total water mixing ratio, rain water mixing ratio and rain water number concentration. Temperature, saturation mixing ratio, cloud water mixing ratio and mean diameters for both the cloud and the rain distributions were diagnosed. The physical processes allowed were autoconversion of cloud water to rain water (Berry and Reinhardt, 1974; Ziegler, 1985), collection of cloud water by rainwater (accretion equation, but with a sharp drop-off in the collection efficiency for smaller cloud droplets), self-collection/breakup by rain (Verlinde et al, 1990), and sedimentation of rain (Lagrangian advection and subsequent redistribution). This microphysical parameterization was added to the non-hydrostatic version of the RAMS cloud model (Tripoli and Cotton, 1982; Tripoli 1986). This model was used to simulate a vigorous convective cloud. All model fields were written to file at every time step. The retrieval model was a kinematic model, using the time-varying wind and pressure fields as observables (Kapitza, 1991; Sun et al., 1991).

This model was much more sensitive to the scaling factors. It may in part be explained by the introduction of the number concentration variable — since mks units were used this number was on the order of thousands — which further increased the relative magnitude differences between the variables. The explosive physics played a further part. The mathematical formulation of processes like breakup can lead to very steep gradients, especially when the optimization code returns slightly unrealistic initial conditions to the model. It was found that scaling by the relative magnitude of the variables gave no convergence at all. Only when scaling factors related to the error variance were used did convergence occur. The sensitivity of the model to zeroth order discontinuities were tested by making the drop-off in the collection efficiency in the accretion equation a step function. With the discontinuity the algorithm did not converge. It was necessary to fit a spline over a wide interval around the discontinuity in order to get good convergence. This model was also used to investigate the impact of the neglect of certain physical processes in the retrieval model. It was found that the neglect of any of the processes, without compensation elsewhere in the model, greatly inhibited the algorithms ability to retrieve the correct initial conditions.

6 Discussion

This study has shown that the adjoint technique of data assimilation can be applied to numerical models of complex physical processes. This study was a preliminary study into a technique, it must now be applied to real problems. One important question in numerical cloud modelling is what the necessary complexity of microphysical parameterization for realistic simulation of cloud processes is. This technique can address that question. The derivation can easily be modified to include parameterization coefficients in the control vector. Simulations can then be done with highly detailed models, followed by an assimilation process of that data into simpler parameterized model where the control variables are the (constant) parameterization coefficients. The reduction in the cost function is a measure of the ability of the parameterized model to produce the results of the more detailed, and numerically much more expensive, model. At the least, one application for such simplified models would be to perform the assimilation phase for a forecasting model, producing initial conditions for the more detailed forecasting model. Other applications could be for sensitivity studies. The adjoint model can be integrated to reveal where and how much changes in the prognostic variables at earlier times would impact a result at a specific position at a later stage (Errico and Vukicevic, 1992). This can give insight in the necessary accuracy required in the observations of certain variables in order to obtain accurate forecasts. The dependence of 'constant' parameterization coefficients on different situations and locations can be investigated when extensive observational data sets are available. One serious problem, general to all assimilation problems, remains, namely, how can the transformation function (z in the derivation), from the model variables to the observation, be defined. In some cases it is easy to find simple good relationships, like reflectivity of a water distribution used in the example, but for of the remotely sensed observations, especially when ice is involved, it is not al all clear what the proper transformation should be. This issue needs to be addressed.

Acknowledgements

The author JV was supported by the South-African Weather Bureau. Dr G Taylor from the Dept. of Mathematics at CSU contributed greatly through many discussions and suggestions. His continued encouragement and optimism contributed greatly. Piotr Flatau stimulated many discussions on the subject, and he introduced JV to symbolic algebra, which eased the pain of the construction of the adjoint model considerably. Dr Errico from NCAR helped in the early stages. The research was sponsored by the National Science Foundation under Grant ATM-8814913 and the Army Research Office under grant DAAL03-86-K-0175.

References

Berry, E. X. and R. L. Reinhardt, 1974: Analysis of cloud drop growth by collection: Part II. Single initial distributions. *J. Atmos. Sci.*, **31**, 1825—1831.

Courtier, P. and O. Talagrand, 1990: Variational assimilation of meteorological observations with the direct and adjoint shallow-water equations. *Tellus*, **42A**, 531—549.

Errico, R. M. and T. Vukicevic, 1991: Sensitivity analysis using an adjoint of the PSU/NCAR mesoscale model. Submitted to *Mon. Wea. Rev.*

Kapitza, H., 1991: Numerical experiments with the adjoint of a nonhydrostatic mesoscale model. *Mon. Wea. Rev.*, **119**, 2993—3011.

Moore, A. M., 1991: Data assimilation in a quasi-geostrophic open-ocean model of the Gulf Stream region using the adjoint method. *J. Phys. Ocean.*, **21**, 398—427.

Rutledge, S. A. and P. V. Hobbs, 1983: The mesoscale and microscale structure and organization of clouds and precipitation in midlatitude cyclones. VIII: A model for the "seeder-feeder" process in warm-frontal rainbands. *J. Atmos. Sci.*, **40**, 1185—1206.

Rutledge, S. A. and P. V. Hobbs, 1984: The mesoscale and microscale structure and organization of clouds and precipitation in midlatitude cyclones. XII: A diagnostic modeling study of precipitation development in narrow cold-frontal rainbands. *J. Atmos. Sci.*, **41**, 2949—2972.

Sun, J., D. W. Flicker, and D. K. Lilly, 1991: Recovery of three-dimensional wind and temperature fields from simulated single-Doppler radar data. *J. Atmos. Sci.*, **48**, 876—890.

Thacker, W. C., 1989: The role of the Hessian matrix in fitting models to measurements. *J. Geophys. Res.*, **94**, 6177—6196.

Tripoli, G. J., 1986: *A numerical investigation of an orogenic mesoscale convective system.* PhD thesis, Colorado State Univ., Fort Collins CO 80523, 290 pp.

Tripoli, G. J. and W. R. Cotton, 1981: The use of ice-liquid water potential temperature as a thermodynamic variable in deep atmospheric models. *Mon. Wea. Rev.*, **109**, 1094—1102.

Tripoli, G. J. and W. R. Cotton, 1982: The Colorado State University three-dimensional cloud/mesoscale model - 1981. Part I: General theoretical framework and sensitivity experiments. *J. Rech. Atmos.*, **16**, 185—220.

Verlinde, J., P. J. Flatau, and W. R. Cotton, 1990: Analytical solutions to the collection growth equation: Comparison with approximate methods and application to cloud microphysics parameterization schemes. *J. Atmos. Sci.*, **47**, 2871—2880.

Ziegler, C. L., 1985: Retrieval of thermal and microphysical variables in observed convective storms. Part I: Model development and preliminary testing. *J. Atmos. Sci.*, **42**, 1487—1509.

THE ROLE OF SOLID PRECIPATION ELEMENT MELTING ON THERMODYNAMICS AND DYNAMICS BELOW MELTING LEVEL

M. Ćurić and D. Janc

Institute of Meteorology, Dobračina 16, YU-11000 Belgrade, Yugoslavia

1. INTRODUCTION

The main purpose of our article is the investigation of ice particles transformation below zero isotherm level and their effect on thermodynamic structure of melting layer and propagation velocity of isothermal layer of 0^{0}C. The problem of melting of ice crystals takes care of scientists more than thirty years. So, Mason (1956) considered that the all melted water concentrically recovers the solid ice core with no internal circulation. Later, many authors as Rasmussen et al. (1984a) enriched the hailstone melting theory with more experimental and theoretical results. The special group of papers as that of Matsuo and Sasyo (1981) treat the problem of snowflake melting following the kinematic ice particle growth model. In most papers, insufficient coution is dedicated to thermodynamic structure of an ambient air and propagation valocity of isothermal layer of 0^{0}C which may be formed for great amounts of solid particles and enough long residential time below melting level.

2. MODEL EQUATIONS

The model used is the combination of microphysical model which describes the melting process of ice particles and simple 1-D time-dependent model. The microphysical model uses the main results of Farley hail category model (1987). In this study, we employ 20 logarithmically spaced mass size categories to represent the precipitation ice specter at the melting level. According to Farley (1987), the representative mass and mass interval per category comprising this fixed mass scale may be written as

$$m_j = m_0 \exp[\frac{3}{J_0}(j-1)]; \quad dm_j = \frac{3}{J_0} m_j \qquad (1)$$

where $J_0=3.05$ and $m_0=2.8*10^{-7}$g.

The number concentration of ice particles is assumed to be:

$$N_{ij} = \frac{1}{\rho} n_{0i} \exp(-2\lambda_i r_{ij}) dr_{ij}/dm_j \qquad (2)$$

where subscript j is related to corresponding size category; n_{0i} is the intercept parameter taken to be $0.3\mathrm{cm}^{-4}$; λ_i is the slope of the modified Marshall-Palmer distribution; r_{ij} and dr_{ij}, the radius of a ice particle of mass m_j and its corresponding radius interval, are given by:

$$r_{ij} = (\frac{3m_i}{4\pi\rho_i})^{1/3} \; ; \; dr_{ij} = \frac{r_{ij}}{J_0} \qquad (3)$$

where ρ_i is the ice particle density assumed to be variable in the melting regime contrary to Matsuo and Sasyo (1981) and in agreement with Mason's concept (1956) as

$$\rho_i = \rho_{ci}(\frac{r_{ci}}{r_i})^3 + \rho_l[1 - (\frac{r_c}{r_i})^3] \qquad (4)$$

where ρ_{ci} is the solid ice core density taken to be $0.3\mathrm{gcm}^{-3}$ according to Farley(1987); r_{ci} the solid ice core radius and ρ_l the liquid water density.

The heat-balance equation for an ice particle in the melting regime is taken according to Ćurić and Janc (1991) as:

$$\frac{dm_t}{dt}[L_f + c_w(T-T_s)] + \delta \frac{dm_w}{dt} c_w(T-T_s) = -4\pi r_i f L_v D(\rho_v - \rho_{vi}(T_s)) - 4\pi r_i K_a f(T-T_s) = -4\pi r_i r_{ci} K_w \frac{T_s - T_0}{r_i - r_{ci}} \qquad (5)$$

where m_t and m_w are masses of solid ice core and water shell; L_f and L_v latent heats of fusion and condensation; c_w specific heat of water; f ventilation coefficient; K_a and K_w thermal conductivities of air and water; D coefficient of water vapour diffusion; ρ_v and ρ_{vi} water vapour density of an ambient air and saturation vapour density over water; T_s and T_0 temperature of ice particle surface and 273.15^{0}K respectively. The parameter δ is one inside a cloud and zero outside it. The surface temperature calculates iteratively using the Newton-Raphson method. In model calculations we suppose that the zero isotherm and cloud base are closed one to another.

Numerical techniques used is described by Wisner et al. (1972)

3. EXPERIMENTS

In calculations we assume that the height of isothermal layer is z_0=400m and that the subcloud layer is devided into 20 layers. The initial temperature of ice particles is taken to be 0^0C and the air temperature is changed only due to melting effects. The analyzed ice particle categories correspond to interval of their radii from 100µm to 1.5cm. The initial temperature profile is shown in Figure 1(curve 1). Temperature of ambient air as function of time and height is presented by curves 2-5 in Figure 1. We observe that propagation of ice crystals towards the ground level increase the vertical temperature gradient while this tendency has the opposite sign towards the ground level. In Figure 2, it is shown the procentage of each particular category to melting rate. The calculated time needed for zero isothermal layer formation is 1.6h.

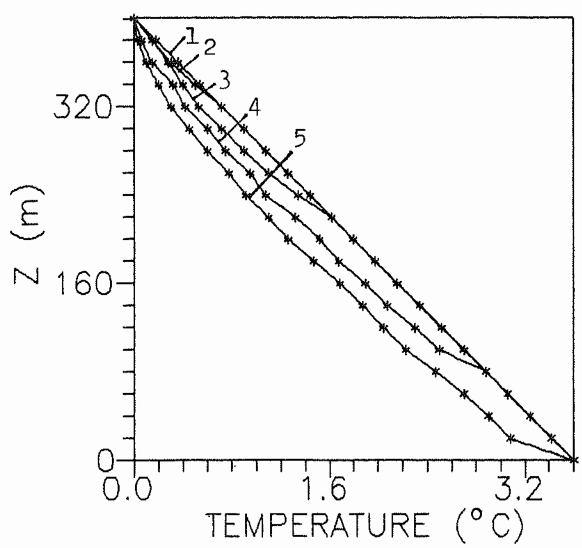

Figure 1.: Temperature as function of height and time. Curves 1-5 are related to t=0,1,2,3,4 min.

4. CONCLUSION

The microphisical model with simple 1-D time-dependent model is applied to simulate the behaviour of , ice crystals below melting level. The primar interest was to show the effect of melting to thermodynamical structure of subcloud environment and ice particle specter transformation under melting conditions. Also, we calculate the time needed for formation of zero isotherm level. The melting of ice particles causes the increase of vertical temperature gradient with time while this tendency has the opposite sign towards the ground level. The melting process modified the size specter of ice particles to be narrowed.

REFERENCES:

Ćurić, M., and D. Janc, 1991: Graupel Growth and Trajectories in a Shallow Cb Cloud Determined by a Forced 1-D Model, Atmosphere-Ocean, 29, 462-478.

Farley, R. D., 1987: Numerical Modeling of Hailstorms and Hailstone Growth. Part II: The Role of Low-Density Riming Growth in Hail Production, J. Climate Appl. Meteor., 26, 234-254.

Mason, B. J., 1956: On the melting of hailstones. Quart. J. Roy. Meteor. Soc., 82, 209-216.

Matsuo, T., Y. Sasyo, 1981: Melting of Snowflakes below Freezing Level in the Atmosphere, J. Met. Soc. Japon, 59, 10-25.

Rasmussen, R. M., V. Levizzani, and H. R. Pruppacherr, 1984a: A wind tunnel and theoretical study of the melting behaviour of atmospheric ice particles. II: A theoretical study for frozen drops of radius <500µm. J. Atmos. Sci., 41, 374-380.

Wisner, C., Orville, H. D., Myers, C., 1972: A numericaal model of a hailbearing cloud. J. Atmos. Sci., 29, 1160-1181.

ON THE NUMERICAL SIMULATION OF MICROPHYSICAL PROCESSES IN THE 22 JUNE 1976 CENTRAL HIGH PLAINS AND 2 AUGUST 1982 CCOPE STORMS USING THE WISCONSIN DYNAMICAL/MICROPHYSICAL MODEL

Daniel E. Johnson and Pao K. Wang

Department of Atmospheric and Oceanic Sciences
University of Wisconsin
Madison, WI 53706
U.S.A.

1. INTRODUCTION

A primary factor for inadequately understanding the microphysical processes in severe storms has been the difficulty in obtaining direct observations of airborne hydrometeors by platforms such as aircraft and radar. In recent years, sophisticated three-dimensional numerical models have provided an alternative means of studying cloud microphysical processes in great detail and at a cost many orders of magnitude less than that required by field experiments. With increasing computer storage and speed, considerable progress has been made in improving the microphysical parameterizations used in the models. For example, inclusion of ice physics in the microphysical scheme (e.g. Farley and Orville, 1986) has resulted in simulations which exhibit more realistic dynamical and microphysical features than do those with liquid water microphysics only. One major contribution of the ice phase is the significant release of latent heat associated with the freezing of water drops and the deposition of water vapor onto ice particles. The net result is a much warmer cloud and greater enhanced cloud growth than without ice processes. The inclusion of ice physics in three dimensional models is especially crucial in simulations of severe storms of the High Plains which are highly glaciated. Graupel and hail have been shown to be the main sources of precipitation for storms in these regions (Knight et al., 1974).

The microphysical processes of a supercell storm from the 2 August 1981 Cooperative Convective Precipitation Experiment (CCOPE), and a multicell storm from the 22 June 1976 National hail Research Experiment (NHRE) have been simulated with the Wisconsin Dynamical/Microphysical Model (WISCDYMM). The simulations are shown to exhibit dynamical and microphysical features characteristic of the observed storms, including maximum updraft velocities, locations of the weak echo region and hook echo, and distributions of cloud water, cloud ice, rain, snow, and hail.

2. METHODOLOGY

The three-dimensional time-dependent WISCDYMM was developed by Jerry M. Straka and Pao K. Wang at the University of Wisconsin with the intention of providing a more complete understanding of the microphysical processes in convective storms than had been offered by previous numerical models and observations. Detailed equations for the dynamics and microphysics of the WISCDYMM can be found in Straka (1989). The WISCDYMM incorporates energy-conserving, non-hydrostatic primitive equations cast in quasi-compressible form (Anderson et al., 1985). The model uses a conserving "box" method finite difference scheme (Matsuno, 1966; and Kurihara and Holloway, 1967) on all prognostic variables. Boundary conditions developed by Klemp and Wilhelmson (1978a) are incorporated at the lateral boundaries while at the top boundary, all variables are held at their base state values. The atmosphere is represented by a staggered Arakawa C-grid mesh (Arakawa and lamb, 1977), in which the thermodynamic variables are placed at the center of the grid box and velocity variables are located at the edges.

The WISCDYMM incorporates six different types of water substance: water vapor, cloud droplets, cloud ice crystals, cloud snow crystals and aggregates, rain drops, and hail/graupel. Equations for the model microphysics are primarily based on those of Lin et al. (1983), Farley et al. (1986), and Farley (1987a, 1987b). The model uses an exponential size distribution for rain and snow, a mono-dispersed size distribution for cloud water and ice, and a discretized size distribution for hail. Number concentrations for graupel/hail are predicted for 21 different size bins which increase exponentially in size from 100 μ to 7.3 cm in diameter. There are a total of 37 microphysical processes incorporated in the model including condensation, evaporation, freezing, melting, sublimation, deposition, aggregation, riming, and drop-drop collisions.

The CCOPE simulation was carried out to 7200 s using a horizontal grid spacing of 1 km over a 54 x 54 km domain and a vertical grid spacing of 0.5 km over a 19 km depth. The NHRE simulation was carried out to 6000 s using a horizontal grid spacing of 0.9 km over a 38 x 38 km domain and a vertical grid spacing of 0.6 km over a 16.2 km depth. To keep each storm near the center of the domain, a constant and spatially uniform horizontal wind vector was added to the wind profiles. Convection was initiated by a warm thermal bubble which was superimposed on soundings taken to the east of each storm. These soundings can be found in Fankhauser (1982) for the NHRE case and Miller et al. (1988) for CCOPE. Both simulations had similar storm structures and hydrometeor distributions, and only the results of the CCOPE simulation will be presented below. More detailed descriptions of the NHRE and CCOPE simulations can be found in Straka (1989) and Johnson (1991) respectively.

3. RESULTS

Fig. 1 shows the XZ cross-section of cloud water mixing ratio and storm-relative wind vectors at 75 minutes. Cloud water forms by condensation of water vapor and is located in a 10 km wide band mainly in regions of updraft. The maximum cloud water mixing ratio is 4.5 g/kg and is located at a height of 5 km AGL (all heights are vertical distances above ground level; AGL) where temperatures are approximately -13 °C. In the model, both cloud water and cloud ice are allowed to exist simultaneously between 0 °C (3.6 km) and -40 °C (8.6 km). Cloud water mixing ratios greater than 3 g/kg are located in a cyclonically rotating mid-level updraft in the Bounded Weak Echo Region (BWER) of the storm. The BWER is depicted on the eastern flank of the updraft on the vertical cross-section of radar reflectivity at 75 minutes (Fig. 2). The simulated cloud water mixing ratios agree with observations of cloud liquid water contents by T-28 aircraft near the BWER (Musil et al., 1986). The average simulated cloud water droplet diameter was approximately 4-5 μ in the BWER region, indicating that there was little time for any kind of particle growth due to the intense updrafts. T-28 measurements also indicated cloud droplet diameters of 4 to 10 μ in the BWER (Musil et al., 1986). Cloud water mixing ratios of 0.5 g/kg are located as low as 1.5 km, corresponding well with the observed cloud base of 1.6 km. The eastward extension of cloud water at this level corresponds to the shelf cloud while the notch in the cloud water field on the western flank is associated with falling precipitation.

Fig. 3 shows the XZ cross-section of cloud ice mixing ratio and storm-relative wind vectors at 75 minutes. The largest mixing ratios of cloud ice are located at and above the region of strongest vertical motion. The maximum cloud ice mixing ratio is 1.9 g/kg and is located at 11 km. Growth of ice particles in these regions is mainly by water vapor deposition as the collection efficiency of ice crystals by ice particles at this height is minimal due to the cold temperatures (< -40 °C). Since the number concentration of cloud ice exponentially approaches zero as temperatures increase from -40 °C to 0 °C (Straka, 1989), cloud ice exists only down to 4.5 km or 1 km above the ambient freezing level. Little cloud ice exists outside of the updraft, except in the eastward extending anvil, since ice particles sublimate rapidly in the drier air away from the updraft.

Snow exists mainly above the -10 °C level (4.7 km), with maximum snow mixing ratios of 1.0 g/kg in the eastern downwind anvil at approximately 9 to 10 km (Fig. 4). Snow forms primarily by the freezing of very small raindrops in the lower portion of the updraft, the Bergeron-Findeisen mechanism in the lower to middle levels, and aggregation in the middle to upper levels of the storm. Snow serves an important role in the production and growth of small hail, graupel, and ice particles. This is especially true below 5.5 km (-17 °C), where significant riming of snow occurs due to high cloud liquid water accretion rates. An extensive anvil of snow which is being exhausted from the updraft extends downshear to the east, and can be considered to be representative of the observed storm anvil. Also, an overshooting snow top extends up to approximately 14.5 km, and can be considered to correspond to the observed cloud top dome of 14 to 15 km (Miller et al., 1988).

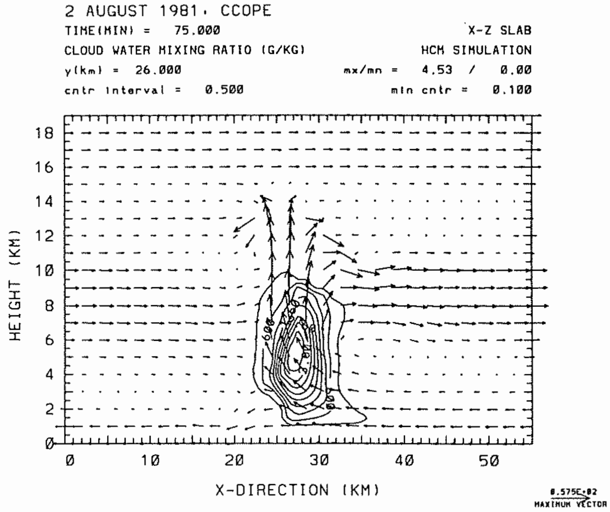

Fig. 1. XZ cross-section of cloud water at 75 minutes.

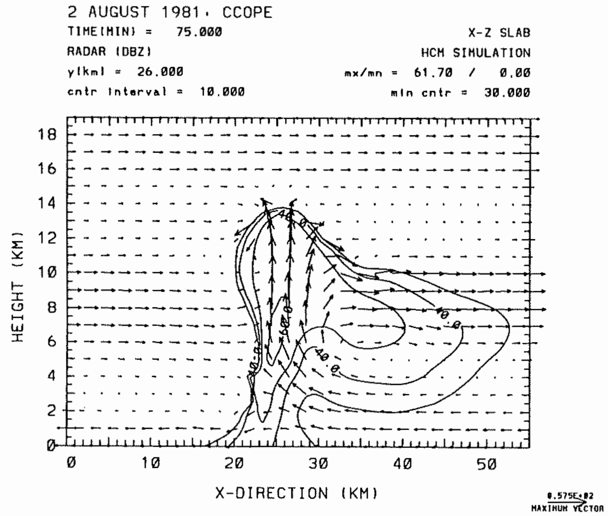

Fig. 2. XZ cross-section of radar reflectivity at 75 minutes.

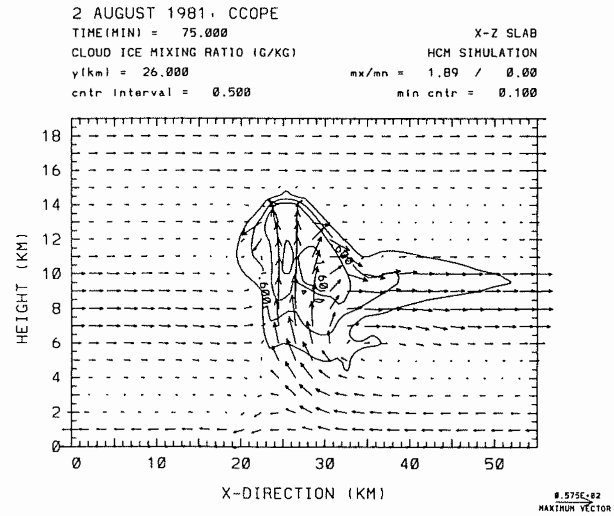

Fig. 3. XZ cross-section of cloud ice at 75 minutes.

The simulation produces copious amounts of graupel and hail (Fig. 5). Maximum total hail mixing ratios of 8.8 g/kg are located at heights of approximately 8.5 km (-40°C). This region of the storm contains a large number of graupel and small hailstones which develop from heavily rimed snow aggregates and the freezing of small raindrops in the lower regions of the updraft. These particles quickly grow to larger sizes in the updraft core where there is a plentiful supply of supercooled liquid water and rimed snow. Graupel and small hail falling from the overhanging anvil can also grow to large sizes (D > 25 mm) if they are advected back into the storm and pass through spiraling trajectories around the updraft.

Evident in Fig. 5 is the BWER, which is embedded in a region of total hail mixing ratio less than 1.0 g/kg and is characterized by very steep gradients of hail to the west. The steep gradient in hail was also noted by Musil et al. (1986) in observations of the storm by T-28 aircraft. The rapid movement of air upward and into the downstream anvil reduces the resident time of hail embryos in the BWER, thus preventing many large hailstones from forming. The large number of graupel and small hailstones being advected into the anvils by the intense updraft is also resulting in a net reduction of precipitation at the surface. Many of these ice particles melt and sublimate as they fall below the anvil, and most of the shed water evaporates in the drier air below.

The XZ cross-section of rain water at 75 minutes is presented in Fig. 6. Rain water exists primarily below the freezing level (3.6 km) with maximum mixing ratios of 1.9 g/kg at the surface. An eastward extension of rain exists below the anvil which does not reach the ground due to evaporation into the drier air below. Nearly all of the rain water below the freezing level forms from the melting and shedding of hail and graupel as it falls to the surface. A quick glance at Fig. 5 shows that there is a very good correlation between heavy hailfall and heavy rainfall. The low-level XY cross-section of rain water at 120 minutes (Fig. 7) shows that the heaviest rainfall is occurring approximately 9 km northwest of the mid-level updraft core in a region of anticyclonic downward moving air. A hook echo is evident on the southern flank of the rain water field, as cyclonic vorticity with the low-level winds is bringing cooler but very moist air from the rain induced downdraft into the low-level updraft. The hook echo is commonly associated with tornadic storms (Doswell, 1985), and indeed a similar hook echo was observed on the 2 August supercell for more than two hours (Miller et al., 1988).

Finally it is worth mentioning that the inclusion of ice physics not only resulted in a storm which had a similar structure to the observed supercell (e.g. storm top heights in the simulated and observed storm), but also played a large role in the dynamics of the storm. As an example, Fig. 8 shows the results of maximum updraft velocities for simulations of the CCOPE storm with and without ice physics. The simulated storm with ice physics was not only more intense, but remained in a quasi-steady state for a longer period of time.

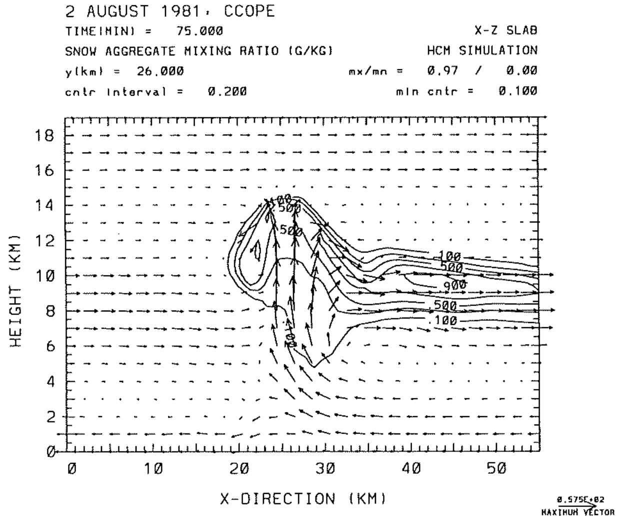

Fig. 4. XZ cross-section of snow aggregates at 75 minutes.

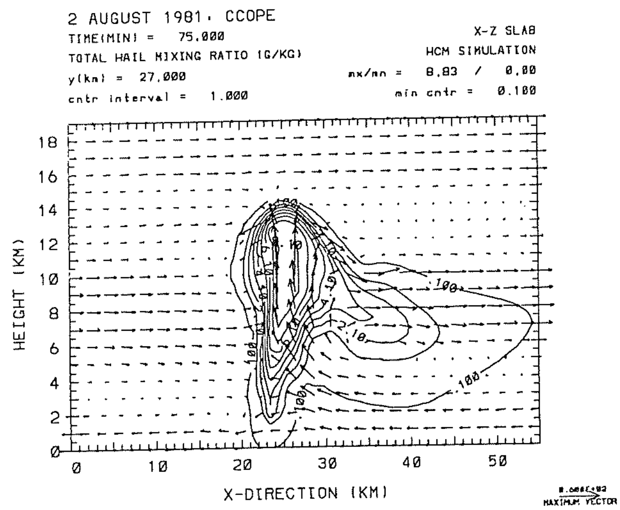

Fig. 5. XZ cross-section of total hail at 75 minutes.

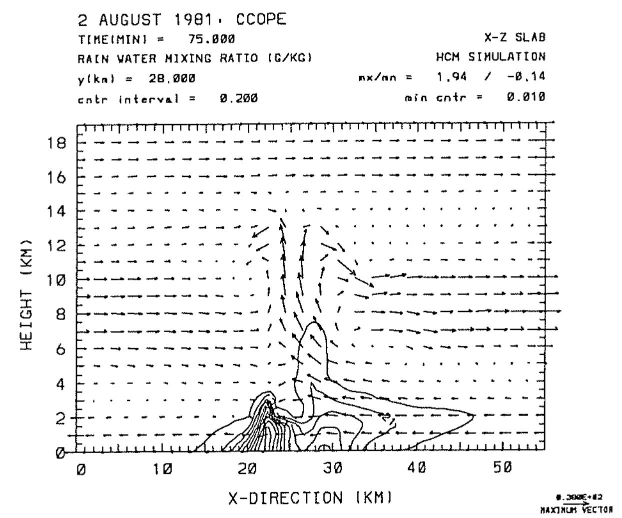

Fig. 6. XZ cross-section of rain water at 75 minutes.

4. CONCLUSIONS

Simulations of the 2 August 1981 CCOPE supercell and 22 June 1976 NHRE multicell storms have been carried out with the WISCDYMM using ice microphysics. A description of the production, distribution and concentration of the hydrometeor types has been presented for the CCOPE case only, as these features are qualitatively similar for both storms. The results of the simulations show that the WISCDYMM has the capability to simulate highly glaciated storms in a manner which is realistic and consistent with observations. Data from the simulations have filled in many of the gaps from observational data due to inadequate instrumentation and poor resolution. This has led to a better understanding of the microphysical processes which occur in severe storms of the High Plains.

5. ACKNOWLEDGMENTS

The simulations were performed on the CRAY-2 at the National Center for Supercomputing Applications (NCSA) at the University of Illinois at Urbana-Champaign. This work was sponsored in part by the National Science Foundation under the grants ATM-8718221 and ATM-9002299. We thank Jerry M. Straka at the University of Oklahoma for his assistance in this work.

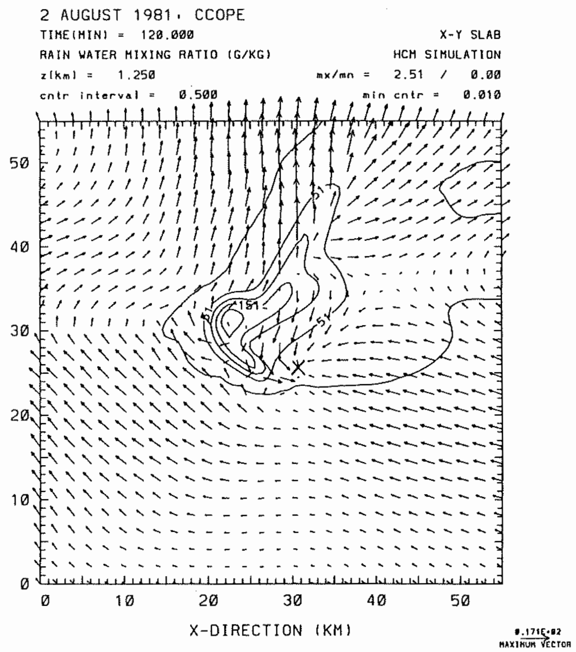

Fig. 7. XY cross-section of rain water at 120 minutes.

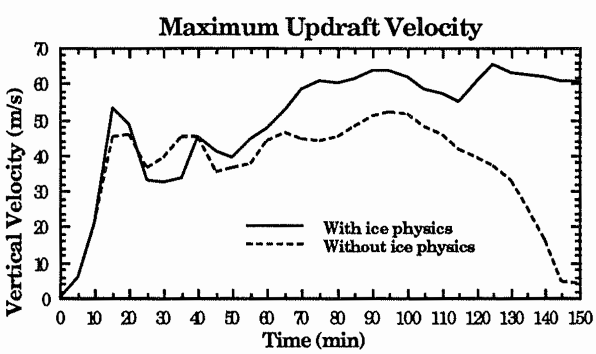

Fig. 8. Maximum vertical veloctiy vs. time

6. REFERENCES

Anderson, J. R., K. K. Droegemeier and R. B. Wilhelmson, 1985: Simulation of the thunderstorm subcloud environment. Preprints, *14th conf. on Severe Local Storms.* Indianapolis, IN., Amer. Meteor. Soc., 147-150.

Arakawa, A., and V. R. Lamb, 1977: Computational design of the basic dynamical processes of the UCLA general circulation model. *Methods in Computational Physics*, **17**, Academic Press, 174-265, 337 pp.

Doswell, C. A., III, 1985: The Operational Meteorology of Convective Weather. Vol. II, Storm Scale Analysis. NOAA Technical Memorandum ERL ESG-15.

Fankhauser, J. C., 1982: The June 22, 1976 case study: Large scale influences, radar structure, and mesoscale circulations. *Hailstorms of the central High Plains, Vol II: Case Studies of the National Hail Research Experiment*, Knight, C. A., and P. Squires, Eds., Colorado Associated Universities Press, Boulder, CO., 1-34.

Farley, R. D., 1987a: Numerical modeling of hailstorms and hailstone growth. Part II: The role of low density riming growth in hail production. *J. Climate Appl. Meteor.*, **26**, 234-254.

Farley, R. D., 1987b: Numerical modeling of hailstorms and hailstone growth. Part III: Simulation of an Alberta hailstorm-natural and seeded cases. *J. Climate Appl. Meteor.*, **26**, 789-802.

Farley, R. D., and H. D. Orville, 1986: Numerical modeling of hailstorms and hailstone growth. Part I: Preliminary model verification and sensitivity tests. *J. Climate Appl. Meteor.*, **25**, 2014-2035.

Johnson, D. E., 1991: A study of the 2 August 1981 CCOPE supercell storm using the Wisconsin Dynamical/Microphysical Model. M. S. Thesis, Department of Meteorology, University of Wisconsin, 157 pp.

Klemp, J. B., and R. B. Wilhelmson, 1978a: The simulation of three-dimensional convective storm dynamics. *J. Atmos. Sci.*, **35**, 1070-1096.

Knight, C.A., N. C. Knight, J. E. Dye and V. Toutenhoofd, 1974: The mechanism of precipitation formation in northeastern Colorado cumulus. I. Observations of the precipitation itself. *J. Atmos. Sci.*, **31**, 2142-2147.

Kurihara, Y., and J. L. Holloway Jr., 1967: Numerical integration of a nine-level global primitive equations model formulated by the box method. *Mon. Wea. Rev.*, **95**, 509-530.

Lin, Y. L., R. D. Farley and H. D. Orville, 1983: Bulk parameterization of the snow field in a cloud model. *J. Climate Appl. Meteor.*, **22**, 1065-1092.

Matsuno, T., 1966: Numerical integrations of the primitive equations by a simulated backward difference method. *J. Meteor. Soc. Japan*, **44**, 76-83.

Miller, L. J., J. D. Tuttle and C. A. Knight, 1988: Airflow and hail growth in a severe northern High Plains supercell. *J. Atmos. Sci.*, **45**, 736-762.

Musil, D. J., A. J. Heymsfield and P. L. Smith, 1986: Microphysical characteristics of a well-developed weak echo region in a High Plains supercell thunderstorm. *J. Climate Appl. Meteor.*, **25**, 1037-1051.

Straka, J. M., 1989: Hail growth in a highly glaciated central High Plains multi-cellular hailstorm. Ph. D. dissertation, Department of Meteorology, University of Wisconsin-Madison.

APPLICATION OF A ONE DIMENSIONAL CLOUD MODEL TO THE STUDY OF INVERSION CHARACTERISTICS OVER THE ARABIAN SEA

Ahmet Aksakal and Gandikota V. Rao

Department of Earth and Atmospheric Sciences
Saint Louis University
St. Louis, Missouri 63103-2010

1. INTRODUCTION

One-dimensional cloud models can be useful in studying the characteristics of inversion and stable layers, particularly, over the oceans where cloud data are lacking. Given the moisture and temperature fields, it is possible employing the One Dimensional Steady State (IDSS) models to estimate the cloud top and infer the inversion characteristics. It is well known that the cloud radius, which is one of the input parameters in the IDSS model, plays an important role in the cloud top estimation. In unsaturated environments model clouds of a certain radius may not exist at all. Thus IDSS cloud models would reveal many interesting aspects of the structure of the atmosphere unavailable through the convectional means.

The kinematics and thermodynamics of the flow over the Arabian Sea are increasingly being studied as a result of the 1979 Summer Monsoon Experiment (SMONEX). While the overall aspects of the inversion and flow characteristics over the Arabian sea are well documented (See Hasternrath, 1992 for a recent bibliography), it is still not clear how the temporal and spatial variation of the inversion occurs over different portions of the Arabian sea.

In the following are discussed, some results of a IDSS cloud model study of convection over the Arabian sea. The top of the cloud estimates the inversion height. With the help of the neighboring dropwindsonde data, vertical velocity is estimated at some key locations over the Arabian sea using the Bellamy technique. The large scale wind field obtained through the conventional upper air data and satellite cloud tracked wind data at 850 mbs provides a picture of the horizontal flow in the vicinity of the inversion. Thus a comprehensive conceptual model of the inversion is constructed over different parts of the Arabian sea. This model illustrates how the advection of warm air from the Saudi Arabian peninsula inhibits the growth of convection in the western Arabian sea. The structure of convection appears to be different depending on the phase of monsoon (pre-onset, onset and post-onset) and the location (west, central and eastern Arabian sea). The model deduced results are compared to the observed.

2. CLOUD MODEL

A steady state cumulus cloud model developed by Simpson and Wiggert (1969) was chosen because of its long track record. Many scientists (e.g., Cotton, 1975) believe this model reasonably predicts the cloud top, but may overestimate the liquid water content.

The governing equation is the vertical component of the equation of motion:

$$\frac{d}{dt}\left(\frac{w^2}{2}\right) = \frac{gB}{1+\alpha} - gQ_{1w} - \mu w^2 \qquad (1)$$

where B is buoyancy, α is the virtual mass coefficient (0.5), Q_{1w} total liquid water content and μ the entrainment rate.

The cloud model as employed by us (See Aksakal, 1991) consists of 321 levels with a 50 m vertical separation through a 16 km depth. The cloud base is set at the Lifting Condensation Level (LCL). The LCL is determined from the surface and the dewpoint temperatures. The cloud radius is defined as 500, 1000, 1500 or 2000 m. Equation 1 is integrated upward. Cloud temperature and mixing ratios are modified by entrainment. The vertical velocity is set at 1 m s^{-1} at the cloud base. The top is reached when the vertical velocity is very small.

It must be commented that the cloud model does not consider the effect of the ambient wind or its vertical shear. On the other hand the cloud model estimates the mean eddy viscosity coefficient for the free atmospheric region by using the mean calculated vertical velocities (Cotton, 1975).

3. DATA SOURCES

The Arabian sea (0°-20°N) was divided into three parts in this research: western (59°E to 63°E), central (63°E to 67°E),and eastern (67°E to 75°E). The time period also, was divided into three phases. The pre-onset period was between June 1 to 10, the onset between June 10 to 18, and the post-onset between June 18 to 28, 1979.

The data set used in this research was collected by the three U.S. aircraft: NCAR Electra, NOAA-P3 and NASA-CV 990 during May-June 1979. Research ship data also were available.

4. SYNOPTIC RESULTS

The Skew-T Log p diagrams of the ship thermodynamic data indicated, that during the pre-onset phase the western Arabian sea and central Arabian sea showed deep conditionally unstable stratification, while the eastern Arabian sea experienced a low-level inversion. It is possible, that although climatologically the western Arabian sea experiences inversion more often than the eastern Arabian sea, during the pre-onset season the moist southwesterly flow from the southern hemisphere causes convection in the western Arabian sea. This convection appears short lived, however.

When the onset of monsoon over India started, the eastern and the central Arabian seas showed deep convection, whereas, shallow convection capped by a modest low-level inversion formed in the western Arabian sea. A similar situation also, prevailed during the post-onset phase, but the intensity of convection was slightly diminished. The convection over the Arabian sea was studied analytically by Roadcap and Rao (1992) and observationally by Rao and Hor (1991).

The cloud model was set to run for the pre-onset, onset and post-onset phases. Only some of these runs are given in Tables 1, 2, and 3. The cloud core radius varied at each run. The parameters W_{max}, LWC_{max} and K_m represent the maximum upward vertical velocity, the maximum liquid water content and mean eddy viscosity coefficient, respectively.

TABLE 1. *The cloud model results for the pre-onset phase.*

Core (m)	C-Base (m)	C-Top (m)	W_{max} (m/s)	Level (m)of W_{max}	LW C_{max} (g/kg)	Level (m)of LW C_{max}	K_m m^2/s
PRE-ONSET (WESTERN ARABIAN SEA)							
500	500	4000	7.97	2650	3.77	3050	27.97
2000	500	6550	16.72	3800	7.26	5050	233.70
PRE-ONSET (CENTRAL ARABIAN SEA)							
500	550	4450	8.82	2050	3.35	2600	20.12
2000	550	6950	13.03	4250	6.57	4900	180.11
PRE-ONSET (EASTERN ARABIAN SEA)							
500	500	650	0.92	550	0.22	650	32.73
2000	500	650	0.89	550	0.45	650	209.27

From this table, it can be seen that the cloud top reached almost 7.0 km over the central and western Arabian sea during the pre-onset phase. But over eastern Arabian sea the cloud remained shallow.

Tables 2 and 3 show the results for the onset phase.

TABLES 2. *The cloud model results for the onset phase.*

ONSET (CENTRAL ARABIAN SEA)							
500	300	1500	4.33	1100	2.68	1500	44.30
2000	300	6900	9.85	4700	5.03	5250	174.61
ONSET (EASTERN ARABIAN SEA)							
500	100	6000	13.71	1350	5.96	2900	30.89
2000	100	9200	24.66	4700	10.68	6250	234.00

TABLE 3. *The cloud model results for the post-onset phase.*

POST-ONSET (CENTRAL ARABIAN SEA)							
500	750	2700	7.09	1650	3.00	2500	44.70
2000	750	5750	10.05	4000	5.87	4500	158.89
POST-ONSET (EASTERN ARABIAN SEA)							
500	600	3600	7.47	2100	3.63	2850	31.88
2000	600	6500	13.92	3700	6.90	4850	199.96

During the onset phase, the growth of cloud suddenly increased over the eastern Arabian sea and decreased over the western Arabian sea (not shown). The strongest vertical motion (w = 24.66 m/s) was obtained from the cloud model for the eastern Arabian sea for a 2000 m core radius. This phase showed a very shallow 50 m thick cloudiness over the west and deep, intense growth over the east. Thus, the cloud top increased from west to east dramatically.

During the post-onset the conditionally unstable stratification had become somewhat neutralized. Moderately, deep convection ensued. The west Arabian sea did not have data during this phase.

Our model results indicate that core radius plays an important role in cloud growth. However, when there is initially no cloud or very shallow cloud, the cloud core radius in cloud growth is insignificant.

The cloud model results, together with synoptic observations would provide a better picture to understand the relationship between convection and inversion during the monsoon season. Figure 1. shows such a picture. Here WAA represents the warm air advection from Saudi Arabian desert. The subsiding air reaches its maximum during the onset phase. The strong warm air advection (WAA) and subsidence maintain the inversion layer during onset and post-onset phases over the west Arabian sea.

During the pre-onset low-level ascent is taking place in the western Arabian sea. Consequently, cloud tops are high (6 km) although descent still exists above 6 km. During the onset and post-onset periods, pronounced descent takes place in the western Arabian sea reinforced by warm air advection. It is possible that some of the descent in the upper levels (over WAS) is due to convection occurring in the eastern Arabian sea. The conceptual picture drawn here appears in agreement with that proposed by Pant (1978).

ACKNOWLEDGMENT

Dr. Ahmet Aksakal's graduate studies at Saint Louis University were sponsored by the Ministry of Education, Government of Turkey. Both authors benefitted from discussions with Dr. John Roadcap.

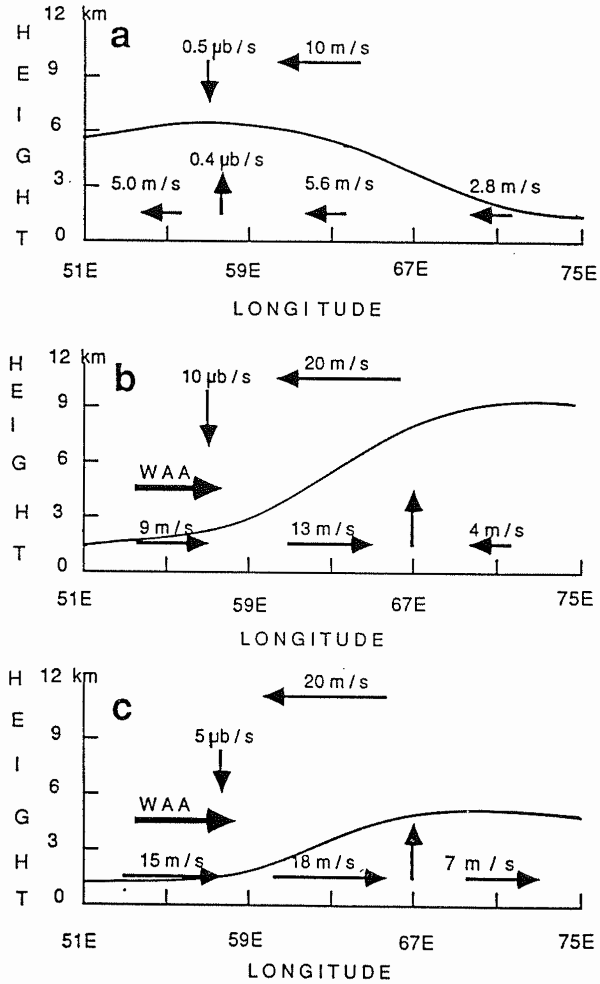

FIGURE 1. *Estimated cloud top (thin solid line), vertical and horizontal wind field during a) pre-onset, b) onset, c) post-onset phases.*

REFERENCES

Aksakal, A., 1991: Some physical processes that govern inversion and analytically modeled convection over the Arabian sea. Ph.D. dissertation, Saint Louis University, 187 pp.

Cotton, W. R., 1975: On parametrization of turbulent transport in cumulus clouds. *J. Atmos. Sci.*, **32**, 548-566.

Hasternrath, S., 1988: Climate and circulation over the tropics. Reidel, Boston, 455 pp.

Pant, M. C., 1978: Vertical structure of the planetary boundary layer in the west Indian ocean during the Indian summer monsoon as revealed by ISMEX data. *Indian J. Met. Hydrol. Geophys.* **29**, 88-98.

Rao, G. V., and T. H. Hor, 1991: Observed momentum transport in monsoon convective cloud bands. *Mon. Wea. Rev.*, **119**, 1075-1087.

Roadcap, J. R., and G. V. Rao, 1992: An analytical study of the dependence of orientation and propagation of the Arabian sea convection bands on wind shear and static stability (manuscript under preparation).

Simpson, J., and V. Wiggert, 1969: Models of precipitating cumulus towers. *Mon. Wea. Rev.*, **97** 471-489.

THREE-DIMENSIONAL NUMERICAL SIMULATIONS OF THE EFFECTS OF ICE PHASE PROCESSES ON EVOLUTION OF CONVECTIVE STORMS

Kong Fanyou Huang Meiyuan Xu Huaying
(*Institute of Atmospheric Physics, Chinese Academy of Sciences, Beijing 100029, PRC*)

In this paper, a fully elastic three-dimensional numerical cloud model with more detail ice phase microphysics processes is used to investigate the sensitivity of two types of convective storms to ice phase processes.Their influences on storm structure,life cycle, precipitation distribution and intensity, latent heat contribution, and in-cloud microphysical properties are widely analysed. Moreover, attempt is made to go into the mechanisms and principles of these effects.

1. CLOUD MODEL

The model's dynamic framework and parameterization scheme for microphysics processes have been described in detail in papers authored by Kong et al.(1990,1991)[1-3]. The model governing equations consist of the compressible form primitive equations, thermodynamic equation, and water substance conservation equations,with ten prognostic variables. The time-split scheme used by Klemp & Wilhelmson(1978)[4] is adopted to process acoustic wave.The bulk-water technique is adopted in parameterizing microphysical processes. Four warm rain microphysics processes are considered based on the Kessler parameterization scheme. In order to include most ice phase influences in clouds, 17 important ice phase microphysics processes are also parameterized in the model. Considering two ice multiplication processes is a unique feature in microphysics in this model.

2. SIMULATING CASES

Two sets of sounding data are used as model input in order to investigate the sensitivity of different types of convective storms to ice phase microphysics. For each data set, two cases are runned, denoted as AW,AI and BW,BI, respectively. Here W refers pure liquid water cloud and I refers ice phase contained cloud. Sounding data A is similar to that in [2], which is suitable for developing a moderate isolated thunderstorm, with lifetime of about one hour, cloud top no more than 9 km, maximum vertical velocity about 20 m/s, and cloud base temperature about 12°C. Data set B is based on a quasi-steady intensive thunderstorm's environment on July 19, 1977 in SPACE[5], in which a strong wind shear($8\times10^{-3}s^{-1}$) appears in the lowest 2.5 km layer. The maximum updraft speed of the modeling hailstorm is larger than 35 m/s, cloud top higher than 15 km, cloud base temperature about 7°C, and lifetime longer than 2 h.

3. SIMULATION RESULTS AND ANALYSES

3.1 Ice Phase Effects on Isolate Storms

This group of cases(AW and AI) are runned for 80 min, till storms decay. Before 20 min, the two modeling clouds have the same development. After that, ice substance appear significantly in mid and upper level of the AI cloud. The two clouds reach their peak values of updraft speed at 26 min, and then begin to weaken gradually. Till 80 min the water cloud totally disappear, but in case AI an 18 km wide ice-crystal-made anvil still remain in 4-8 km layer.

The ice phase microphysics processes in the model result in that the simulating total accumulative ground precipitation amount increases by 23.1%, and that the total net released latent heat within the model domain increases by 29.1%. For the case AI, the dominant precipitation is liquid, with only 16.9% of solid component.

It is seen from Figure 1a that the two w_{max}-t curves have very similar tendencies with little deviation from each other, the peak value for AI is only slightly larger than that for AW. In addition, the differences of the two storms' flow structures and morphology are not great, except that the anvil of the cold cloud stretches downwind some wider and the low level outflow is more intensive.

3.2 Effects of Ice Phase for Steady Storms

The cases in Group B (BW and BI) are simulated for 112 minutes. The maximum updraft velocity in the water cloud (BW case) reaches the peak value of 30.5 m/s at 30 min, when that in the cold cloud (BI case) is 31.6 m/s (Figure 1b). By 40 min, the cold cloud top reaches 13 km and begins to stretch out horizontally to form a distinct anvil. In contrast, the top of the water cloud stretches weakly during the entire evolution period, especially along the lateral direction.The liquid water cloud weakens rapidly after 60 min,entering dissipation stage. The gust front of the storm moves downshear and laterally fast, going further and further away from the main storm(Figure 2a). The cold cloud, however, is in vigorous stage during this period: The maximum updraft speed is kept to about 30 m/s, the cloud top still rises, the continuous development of the vortical motion promotes the storm splitting. At 64 min, the two splitting updraft cores are 7-8 km away along the north-south direction. The ground gust front centers are quasi-stationary relative to the two splitting updraft shafts, located just at the northeast and southeast flanks of them respectively (Figure 2b), so that

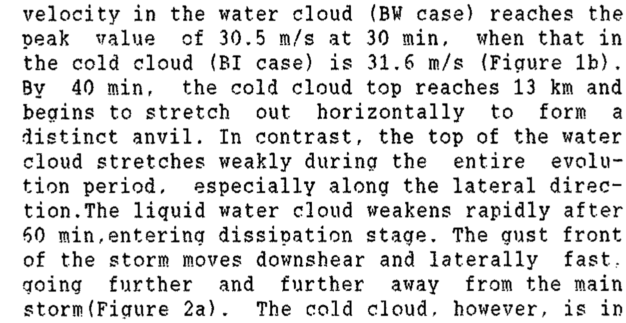

Figure 1. Time variation of maximum updraft speed for: (a) Group A cases and (b) Group B cases. Solid lines denote ice phase cases and dashed lines denote non-ice cases

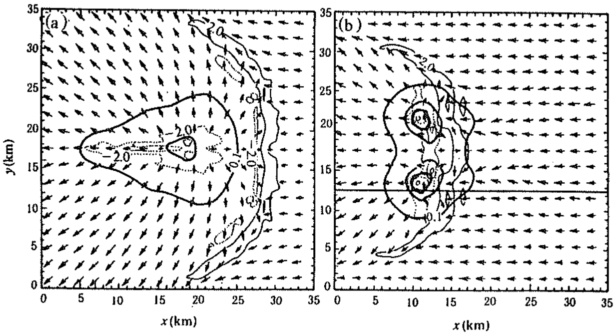

Figure 2. Horizontal cross section(z=0.25 km) at 80min for case BW(a) and BI(b). The thick solid lines for hydrometerors with an interval of 2g/kg and the outmost one is 0.1 g/kg; the thin solid lines for w≥2 m/s with an interval of 4 m/s; the dashed lines for w≤-2 m/s with 2 m/s interval

the splitting cells can undergo a quite long period of developing stage.

Similar to the Group A cases, the inclusion of ice phase processes promotes, in general, the development of convection, but with much more significant degree. The total cumulative precipitation amount and the total latent heat released during 112 minutes simulation increase 3 and 7.6 times, respectively. In the Group B simulating, however, the inclusion of ice phase not only increases the storm's intensity and precipitation amount, but largely modifies the evolution process of the storm—causing the convective storm to undergo a longer quasi-steady stage. This is evident in Figure 1b, which shows that the modeling storm in BW case does not evolve into such a quasi-steady stage.

Distinct differences also exist between the spacial distribution features of the hydrometerors in the BW and BI modeling clouds. In Figure 3, the vertical echo structure of the modeling hailstorm(BI) is quite similar to the radar observation result of the actual storm[6]. In addition, the rainfall distributions of the two cases are totally different: The rainfall area produced from the full-liquid-water cloud distributes mainly along the ambient wind direction, with less lateral widening. On the other hand, the most remarkable feature of the hailstorm rainfall area is the very strong lateral development.

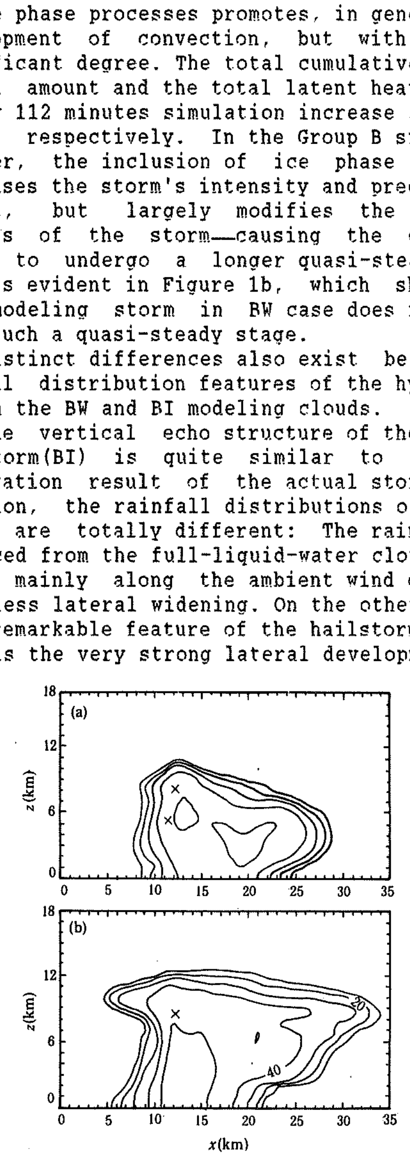

Figure 3. Vertical echo distribution (y=17.5 km) for: (a) BW case, (b) BI case, at 48 min. Contour interval is 10 dBZ with the starting contour of 10 dBZ. 'X' denotes the location of maximum updraft speed

3.3 The Mechanisms of Ice Phase Effects

In theory, the storm type can usually be determined by the *convective Richardson number* R_i, defined as[6] R_i=CAPE/(½ U^2). Here, CAPE is the convective available potential energy, U is the low level inflow speed relative to storms, Storm dynamics and most field observations point out that the most favourable condition to develop a supercell storm is that an optimum balance must be reached between low level wind shear and convective available potential energy. This balance is affected by many sophisticated factors such as large- and meso-scale forcing, horizontal inhomogeneity of underlying surface, and terrain etc. However, the research results of this paper further show that the change of microphysical processes within clouds is another innegligible factor to modify the balance.The inclusion of ice phase microphysics processes in the model increases the buoyancy in clouds, which is equivalent to the increase of the magnitude of numerator in the formula of R_i. The field observations made by Knupp et al. (1982)[6] show that a severe quasi-steady storm was actually developed in the environment similar to that in Group B experiments, which has low R_i value because of strong low level shear and quite small lifting index (3.5°C). In Group B cases, the modeling storm in BI case is quite coincident in life cycle, structure and intensity with the actual observed storm. Bearing in mind that ice particles actually exist in most storms. it can be thought of that, it is for lack of ice phase microphysics in BW case that the buoyancy in cloud decreases to a greater degree, so as to deviate from the *buoyancy-shear* optimum balance area, and consequently the severe long-lasting splitting storm like in BI case can not be formed.

This effect of ice phase processes has also some closer relation, in degree, to environmental conditions, especially to vertical profile of temperature. In Group B cases, for example, the decrease of buoyancy in cloud, caused by the removal of ice phase processes from the model (like in BW), is strong enough to destroy the *buoyancy-shear* optimum balance required to maintain a quasi-steady storm structure. On the other hand, since the environment in Group A cases is relatively warmer, the latent heat contribution of ice substance is much smaller than that in Group B cases. The influence, resulted from the microphysics difference of AW and AI cases, is not significant enough to modify this feature. therefore the two modeling clouds have no substantial difference in structure and life cycle, and the removal of ice phase processes (AW case) only decreases to some degree the convection intensity and precipitation amount.

REFERENCES

[1] Kong,F.Y., 1991: Three-dimensional numerical simulations of hailstorms, Ph.D dissertation, Institute of Atmospheric Physics, 155p.

[2] Kong,F.Y. et al., 1990: *Chinese J.Atmos.Sci.*, **14**,437-450.

[3] Kong,F.Y. et al., 1991: *Chinese J.Atmos.Sci.*, **15**,78-88.

[4] Klemp,J.B. and Wilhelmson,R.B.,1978: *J.Atmos. Sci.*, **35**, 1070-1096.

[5] Tripoli,G.J. and Cotton,W.R., 1982: *J. Rech. Atmos.*, **16**, 185-219.

[6] Knupp,K.K. and Cotton,W.R., 1982: *J. Atmos. Sci.*, **39**, 343-358.

THE EVOLUTION OF SATURATION RATIO

Jen-Ping Chen and Dennis Lamb

Department of Meteorology
Pennsylvania State University
University Park, PA 16802, U.S.A.

1. INTRODUCTION

Saturation ratio represents the amount of water in the gas-phase that constantly interacts with the condensed-phase particles in the cloud. It not only reflects the details of ongoing microphysical processes but also governs the nucleation and subsequent growth of both cloud droplets and ice particles, and ultimately determines the formation of precipitation. Simple cloud models that cannot properly resolve the change of the saturation ratio will not be able to accurately simulate the cloud processes, especially when ice-phase microphysics are involved. For instance, rapid glaciation with ice number concentrations of over several hundreds per liter has been frequently observed to exist in the tops of cumuliform cloud (Coons and Gunn, 1951; Koenig, 1963; Hallett et al., 1978; and Hobbs and Rangno, 1990). Rangno and Hobbs (1991) suggested that such phenomena could be result from the enhanced ice-nucleation activity at very high water saturations. Thus, any factor that controls the saturation ratio may have a strong influence on the ice nucleation process. Extensive studies have demonstrated the effect of updraft speeds and CCN distribution on the development of supersaturation (e.g., Howell, 1949; Squires, 1952; Lee et al., 1980). Some attention has also been paid to the effect of the liquid-phase hydrodynamic interactions (e.g., Young, 1974; Ochs, 1978). Little work, however, has been done in examining other factors that are strongly related to the development of saturation ratio. In this paper we use a detailed microphysical cloud model to study the evolution of the saturation ratio and the factors that control it. Several scenarios are designed to investigate the sensitivity of the saturation ratio to each of the controlling factors. Some emphasis will also be placed on the effect of the liquid-phase microphysics on the formation of ice particles through the development of supersaturation.

2. THEORY

The two basic factors that control the saturation ratio in an air parcel are: (1) the intensity of the upward motion that causes the adiabatic cooling of air and acts as the source of excess water vapor; and (2) the available surface area of cloud particles that water vapor may deposit onto. Squires (1952) derived the *supersaturation development equation*:

$$\frac{ds}{dt} = A_1 W - A_2 \frac{dm}{dt}. \qquad (1)$$

Here, s is the supersaturation ratio, W the updraft velocity, A_1 and A_2 are functions of air properties (temperature and pressure), and dm/dt the overall rate of vapor deposition onto cloud particles. In liquid-phase clouds, the deposition rate is controlled by the initial cloud condensation nuclei (CCN) distribution and the microphysical processes that affect the drop size distribution and hence the total surface area. We can thus categorize the controlling factors of the supersaturation development into: (1) microphysics, (2) updraft velocity, (3) CCN distribution, and (4) air properties, which will be examined separately in the first part of our model simulation.

The presence of ice particles in the mixed-phase clouds can provide more surface area for a more effective rate of vapor deposition than cloud drops do. On the other hand, it also reduces the total surface area through the hydrodynamic collection of droplets. To study ice-phase processes, it is essential to know the mechanisms of ice generation. Among the various modes of ice nucleation, the heterogeneous deposition-nucleation is usually the most effective in the updraft region of clouds. In his experimental studies, Fletcher (1962, pp 241-242) measured the ice number concentration as a function of temperature in a water-saturated environment and gave the empirical relationship:

$$N = N_o \exp(\beta\, \Delta T), \qquad (2)$$

where N is the number concentration of ice nuclei active at a supercooling of ΔT, N_o and β are constant. However, Huffman (1973) suggested that this temperature dependence is merely reflecting the temperature dependence of the ice saturation ratio at 100% liquid water-saturated environment. The number concentration of ice particles actually depends on the supersaturation over ice according to the power-law relationship:

$$N = c\, s_i^{\alpha}, \qquad (3)$$

where c and α are constants, and s_i is the supersaturation over ice. The second part of our model simulation will emphasize the effect of ice-phase microphysics on the saturation ratio, as well as the effect of saturation ratio on the ice nucleation according to the power-law relationship (3).

3. MODEL DESCRIPTION

To properly simulate the physical and chemical changes of cloud particles, a multi-component particle framework is developed which categorizes cloud particles into different bins according to several major properties of the particles. The liquid-phase particle framework is two-dimensional with 45 bins in the water-mass component and 20 bins in the solute-mass component. An extra component, the aspect ratio, with 10 bins is applied to the ice-phase particle framework. The transfer of particles between bins for the growth in various bin-components is calculated with a "*method of moments*" type scheme that conserves both the number and the component value. Other particle properties, such as temperature and ice particle density, are preserved without the detailed categorization treatment.

In the present study, ammonium-sulfate is used as the solute component. An initially log-normal distribution (dry size) is assumed for the sulfate particles, which act as cloud condensation nuclei. Liquid-phase microphysics considered are the nucleation, condensation, and stochastic collision-coalescence/breakup of droplets. Detailed ice-phase microphysics are also included with the shapes of ice particles approximated by oblate and prolate spheroids. Ice nucleation mechanisms included are the heterogeneous deposition-nucleation, the homogeneous and heterogeneous freezing, the contact freezing, as well as the secondary ice generation by rime-splintering. Diffusional growth of ice particles is computed using the electrostatic analogy for both mass and heat transfer. The treatment of the linear growth rates on the prism and basal faces is based on both theoretical and experimental results, but the details will not be addressed here. The growth of ice particles by accreting droplets is calculated with the stochastic approach with collision efficiencies based on experimental studies.

4. SIMULATIONS AND DISCUSSIONS

To analyze the various factors that determine the saturation ratio, a parcel model with constant updraft speed is used to simplify the basic physics. The first four sensitivity tests on the evolution of the saturation ratio in warm clouds will be done by varying the following parameters: (1) liquid-phase microphysics, (2) updraft speed, (3) CCN number concentration (N_{CCN}), and (4) air properties. For the purpose of comparison, a standard scenario will be appearing throughout each sensitivity study with $W = 2$ m s^{-1}; $N_{CCN} = 500$ cm^{-3}, and cloud base at $T = 5$ °C and $P = 990$ mb. One parameter will be allowed to vary in each case. The role of ice-phase microphysics will be demonstrated in the fifth case. By varying the CCN concentration and checking its effect on the number concentration of ice particles, we will also show the inter-connections between the liquid- and ice-phase processes through the saturation ratio.

Case a: Liquid-phase microphysical factors

Before the activation of CCN in an ascending air parcel, the saturation ratio increases monotonically as the saturation vapor pressure is depressed upon the cooling of air by expansion. At this stage, the source term in (1) dominates the change of s. Once saturation is reached, large CCN particles activate and form cloud drops, which then continuously provide more surface area for further water vapor deposition. Thus, during the early nucleation stage, more and more CCN are nucleated as the saturation ratio builds up. The sink term in (1) increases rapidly while the source term remains fairly constant. As indicated by the point **A** in Figure 1, the saturation ratio reaches a maximum once the effect of increasing surface area surpasses that of expansion cooling. When the saturation ratio starts to decrease, the activation of more CCN ceases to occur so that the total number of cloud droplets stays fairly constant. After point **A**, the depositional growth of drops increases the total surface area while depressing the saturation ratio. The net effect is that the sink term in (1) gradually reduces to a value approaching that of the source term. Without other microphysical processes involved, the saturation ratio will tend to reach an equilibrium value as shown by the curve **a** in Figure 1. However, as cloud drops reach certain sizes (the Hocking limit), coalescence starts to occur as droplets collide with each other due to differential fall velocity. Curve **b** shows the evolution of the saturation ratio when the collision-coalescence process is included. The saturation ratio starts to rise at point **B** when the droplets grow large enough by deposition to coalesce. This is due to the decrease of total surface area as droplets coalesce with each other. Since the ability of collecting smaller drops increases as droplets grow larger, the effect of coalescence is cumulative once it is started. This can be seen from the exponential increase of the saturation ratio. Curve **c** shows the evolution of the saturation ratio when the collision-breakup process is allowed. The breakup process tends to offset the effect of coalescence, but it will not occur until the colliding drops exceed several hundred μm in size. Thus, the effect of breakup on the saturation ratio will not be significant until a later time. The results up to this point are similar to those in Young (1974) and Ochs (1978). Note that the temperature curve in Figure 1 can be applied to all events except those in Case *b* with updraft velocities other than 2 m s^{-1} and those in Case *d* with different cloud-base temperatures. Also, curve **c** in the first four figures is the same curve from the standard run.

Case b: Effect of updraft velocity

Upward motion in the atmosphere causes the air to cool by expansion. The cooling of air directly leads to the increase of the saturation ratio as shown in equation (1). Thus, a stronger updraft means a stronger source term in the *supersaturation development equation*. Consequently, the balancing point between the source and sink terms will be greater with stronger updraft. This is reflected by the higher maximum saturation ratio for larger W in Figure 2 (note the change in scale). Also, the saturation ratio is higher throughout the time so that the droplets always grow faster in stronger updrafts. The deposition growth rate is very important in determining the timing of the onset of the hydrodynamic interactions. As shown in Figure 2, the hydrodynamic interactions start earlier with $W = 4$ m s^{-1} (curve **d**) than the standard run with $W = 2$ m s^{-1} (curve **c**). When the updraft speed is small, the coalescence process might not start in time (curve **a**, **b**). Note that the kink in curve **d**, as indicated by the point **A**, results from the re-enabled nucleation of the previously inactivated CCN as the saturation ratio exceeds the initial maximum. The newly activated drops produce more surface area that reduces the rate increase of the saturation ratio.

Case c: Effect of CCN number concentration

The magnitude of the sink term in (1) is directly related to the CCN number concentration during the nucleation stage. Higher N_{CCN} means more drops will be nucleated at the same updraft speed and supersaturation. As shown in Figure 3, the maximum saturation ratio increases with lowered N_{CCN}. With fewer cloud drops formed, the equilibrium saturation ratio is higher when other parameters are kept the same. Therefore, those fewer droplets grow faster due to the higher supersaturation. Similar to the previous case, faster deposition growth will initiate the hydrodynamic interactions earlier. With only 20 cm^{-3} N_{CCN}, the hydrodynamic interactions start about 10 min earlier than the one with 100 cm^{-3} (curve **b**), and 20 min earlier than the standard case (curve **c**). For N_{CCN} of 2500 cm^{-3}, the droplets do not grow large enough to initiate the hydrodynamic interactions until a much later time. The re-enabled nucleation also shows up at point A of curve **b**. However, such a kink in the curve

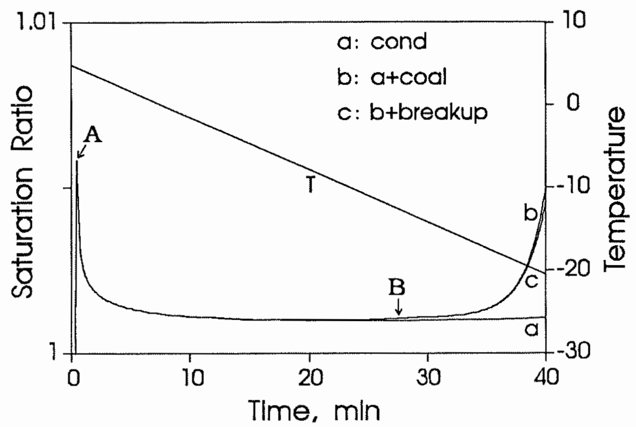

Figure 1: Evolution of saturation ratio with various microphysics. (**a**) nucleation and condensation, (**b**) additional coalescence, and (**c**) additional breakup. Curve T denotes the corresponding temperature at each time.

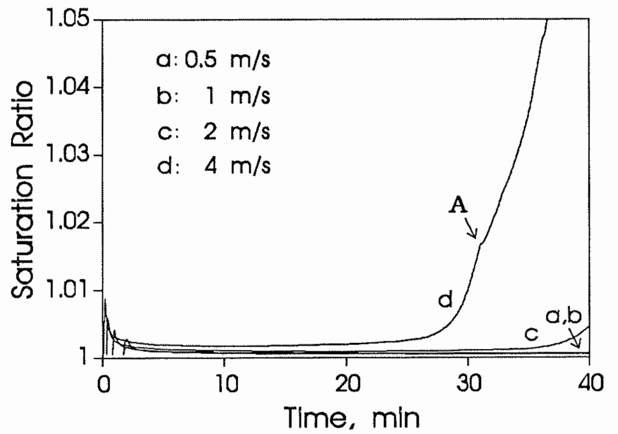

Figure 2: Evolution of saturation ratio with updraft speed of (**a**) 0.5 m s^{-1}, (**b**) 1 m s^{-1}, (**c**) 2 m s^{-1}, and (**d**) 4 m s^{-1}.

does not occur further down the curve, and does not show up in curve **a** at all due to the availability of residue CCN. With very few CCN left, not much new surface area could be created to have any significant effect on the existing trend.

Case d: Effect of air properties

The effect of air properties shows up in the coefficients A_1 and A_2 in (1). Figure 4 (with vertical scale the same as Figure 1) shows the evolution of saturation ratio in air parcels with cloud-base temperatures of 25 °C (curve **a**), 15 °C (curve **b**), 5 °C (curve **c**), and -5 °C (curve **d**). Clouds formed at higher temperatures will have lower saturation ratio maxima. This means fewer CCN are activated in warmer clouds. The saturation ratios for colder clouds are generally higher. However, this higher saturation ratio does not readily translate into a faster growth rate since the deposition growth rate also depends on temperature. In fact, the growth rate is directly proportional to the vapor density difference between drop surface and air, which tends to be larger at warmer temperature according to the Clausius-Clapeyron equation. Therefore, the hydrodynamic interactions start sooner in warmer clouds as shown by the earlier increase of saturation ratio in curves of higher cloud-base temperatures. The re-enabled nucleation (point **A** and **B**) is even more distinct in this case than in the previous cases because more interstitial CCN are available.

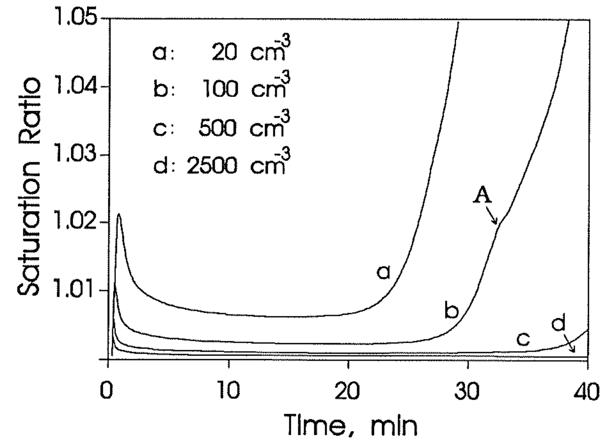

Figure 3: Evolution of saturation ratio with varying CCN number concentration of (a) 20 cm^{-3}, (b) 100 cm^{-3}, (c) 500 cm^{-3}, and (d) 2500 cm^{-3}.

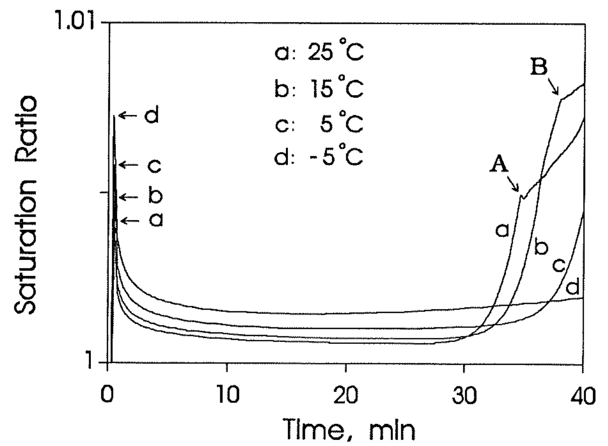

Figure 4: Evolution of saturation ratio with various cloud-base temperatures of 25 °C (curve **a**), 15 °C (curve **b**), 5 °C (curve **c**), and -5 °C (curve **d**). The four arrows to the left point to the saturation maxima of each curve.

Case e: Ice-phase microphysical factors

Ice particles are more efficient in growing by either vapor deposition or hydrodynamic interactions than droplets. The liquid-phase effects on the evolution of saturation ratio discussed previously will be even stronger for ice-phase processes. Figure 5 shows the saturation ratio profile for only depositional growth of droplets and ice particles (curve **a**), adding the liquid-phase hydrodynamic interactions (curve **b**), and with the additional riming process (curve **c**). With only depositional growth, as shown in curve **a** of the upper graph, the saturation ratio evolves in a similar way to the 'condensation only' scenario in case *a*, except for a lower saturation ratio toward the end (not obvious in the graph owing to the small scale). These lowered saturation ratios result in a slower condensational growth of droplets so that the initiation of liquid-phase hydrodynamics is delayed, as can be seen from curve **b**. The bottom graph of Figure 5 demonstrates the number concentrations of ice particles corresponding to the upper graph. The number concentration of ice particles follows the power-law dependence on the *ice supersaturation* in equation (3). The freezing-nucleation modes are insignificant here partly due to the depletion of droplets by riming. The number concentrations in scenarios **a** and **b** are just slightly more than what can be provided by the "basic" ice-supersaturation corresponding to the 100% water saturation. It reaches about 200 mol^{-1} (about 6 per liter) at -20 °C. The hydrodynamic interactions start too late to give significant enhancement in the ice nucleation. The riming process, however, is very effective in reducing the total surface area and enhancing the supersaturation, as shown by the curve **c** in the upper graph. The few ice particles that nucleated under the "basic" supersaturation can grow to a size that is effective in accreting droplets in a very short time through the *Bergeron-Findiesen process*. The saturation ratio,

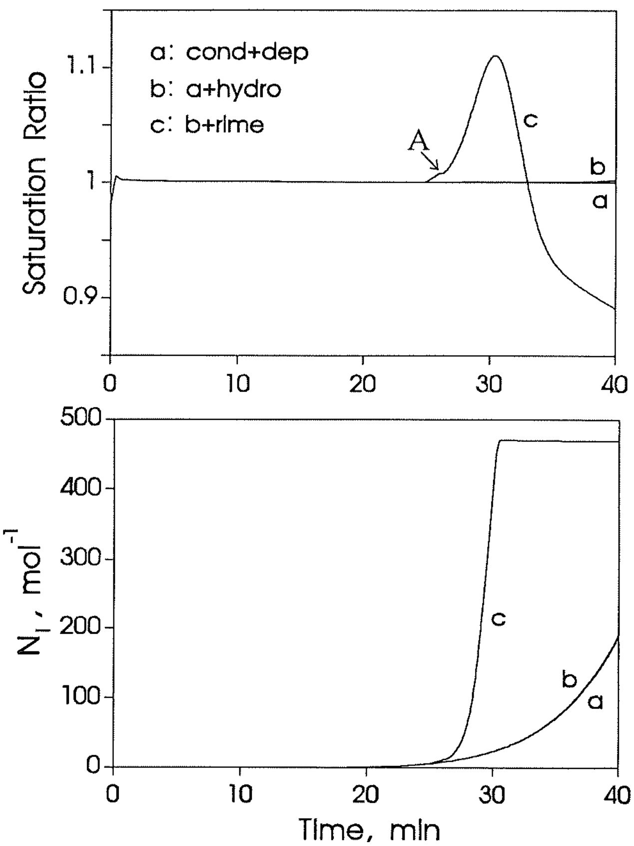

Figure 5: Evolution of saturation ratio (top) and the number concentration of ice particles (bottom) for (a) liquid- and ice-phase deposition growth, (b) additional liquid-phase hydrodynamic interactions, and (c) additional riming.

at first, increases as the ice particles deplete cloud drops. The increase in the saturation ratio, in turn, helps to nucleate even more ice particles. This multiplying process is eventually self-terminated due to the overwhelming production of new surface area of ice particles. The saturation ratio then decreases and approaches the 100% *ice saturation ratio*. Again, notice the re-enabled CCN nucleation at point **A**. Curve **c** in the bottom graph shows that the number concentration of ice particles stops to increase when the saturation ratio reaches a second maximum, a situation similar to that of the drop number concentration after the first saturation ratio maximum. The number concentration of ice particles is more than doubled when riming is included.

Case f: Effect of CCN on ice nucleation

The previous case demonstrated that ice nucleation will occur naturally in the cold regions of supercooled clouds as the ice supersaturation increases with decreasing temperature in a water-saturated environment. However, it is possible to initiate ice nucleation at higher temperatures by enhancing the saturation ratio through the controlling factors mentioned earlier. Here, we use CCN number concentration as an example to demonstrate this effect. Figure 6 gives the evolution of the saturation ratio with various N_{CCN} and full microphysics. Note that curves **c**'s are the same as those in Figure 5. We can see that air with lower N_{CCN} can initiate ice nucleation earlier and obtain higher number concentrations of ice particles. However, for N_{CCN} near or above 500 cm^{-3}, there is not much difference in the ice nucleation due to the limited enhancement of supersaturation. The efficiency of ice accreting droplets is apparently similar for those with high N_{CCN}. By comparing curves **c** and **d**, one may find that the one with higher N_{CCN} is even slightly more efficient in riming than that with lower N_{CCN}. This might result from the larger fall-speed difference between the collector ice and the droplets that are smaller with respect to the higher N_{CCN}.

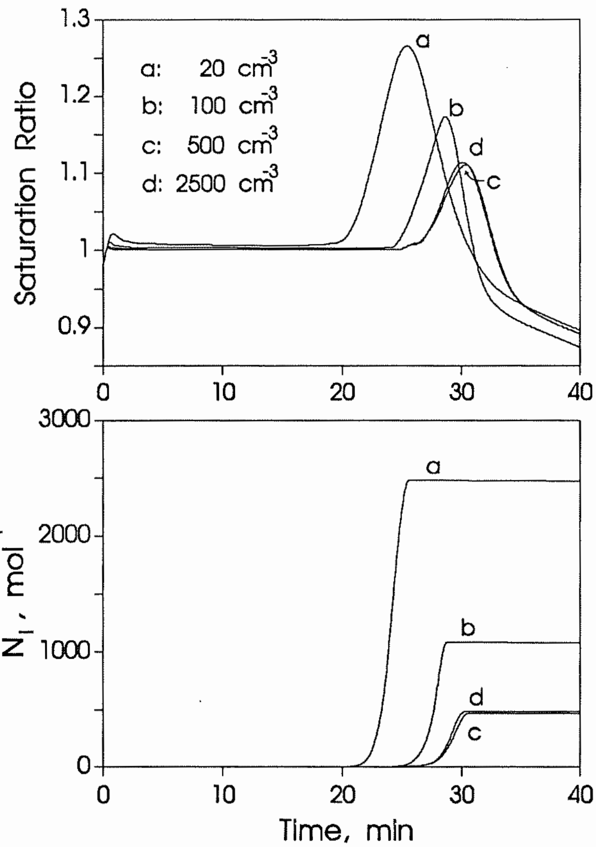

Figure 6: Evolution of saturation ratio (top) and the number concentration of ice particles (bottom) with full microphysics and various CCN number concentrations.

5. CONCLUSIONS

Although neither entrainment nor sedimentation is considered, an air parcel model with detailed microphysics provides a systematic examination of the evolution of saturation ratio and the factors that control it. Cloud drops need to grow by vapor deposition to a certain size before they are capable of growing by coalescence and forming precipitation. The development of supersaturation is very important to the timing of the growth-mode transition from vapor deposition to hydrodynamic collection. Updraft speed, CCN number concentration, cloud-base temperature and other parameters that can influence the saturation ratio in clouds are all controlling factors of precipitation formation. From the evolution of the saturation ratio, the signatures of the ongoing microphysics are reviewed. Saturation ratio is also crucial to the ice nucleation. The enhancement of supersaturation through various microphysical processes may be partly responsible for the observed high number concentrations of ice particles in the relatively warm region of mixed-phase clouds.

6. ACKNOWLEDGMENTS

This work was sponsored in part by the U. S. National Science Foundation under Grant No. ATM-8919837 and the Department of Energy under Grant No. DE-FG02-90ER 61071.

7. REFERENCES

Coons, R. D., and R. Gunn, 1951: Relation of Artificial Cloud-Modification to the Production of Precipitation. In *Compendium of Meteorology*, American Meteorological Society, Boston, 235-241.

Fletcher, N. H., 1962: *The Physics of Rainclouds*, Cambridge University Press.

Hallett, J., R. I. Sax, D. L. Lamb, and A. S. Ramachandra Murty, 1978: Aircraft Measurements of ice in Florida Cumuli. *Q. J. R. Meteorol. Soc.*, **104**, 631-651.

Hobbs, P. V., and A. L. Rangno, 1990: Rapid Development of High Ice Particle Concentrations in Small Polar Maritime Cumuliform Clouds. *J. Atmos. Sci.*, **47**, 2710-2722.

Howell, W. E., 1949: The Growth of Cloud Drops in Uniformly Cooled Air. *J. Meteorol.*, **6**, 134-149.

Huffman, P. J., 1973: Supersaturation Spectra of AgI and Natural Ice Nuclei. *J. Appl. Meteor.*, **12**, 1080-1082.

Koenig, L. R., 1963: The Glaciating Behavior of Small Cumulonimbus Clouds. *J. Atmos. Sci.*, **20**, 29-47.

Lee, I.-Y., G. Hänel, and H.R. Pruppacher, 1980: A Numerical Determination of the Evolution of Cloud Drop Spectra due to Condensation on Natural Aerosol Particles. *J. Atmos. Sci.*, **37**, 1839-1853.

Ochs, H. T. III, 1978: Moment-Conserving Techniques for Warm Cloud Microphysical Computations. Part II: Model Testing and Results. *J. Atmos. Sci.*, **35**, 1959-1973.

Rango, A. L., and P. V. Hobbs, 1991: Ice Particle Concentrations and Precipitation Development in Small Polar Maritime Cumuliform Clouds. *Q. J. R. Meteorol. Soc.*, **117**, 207-241.

Squires, P., 1952: The Growth of Cloud Drops by Condensation. Part I: General Characteristics. *Aust. J. Sci. Res.*, **A5**, 59-86.

Young, K. C., 1974: The Evolution of Drop Spectra through Condensation, Coalescence and Breakup. *Preprints*. AMS Conf. Cloud Phys., Oct 21-24, Tucson Arizonza, 95-98.

METEOROLOGICAL CHARACTERISTICS OF THE PO VALLEY FOG

Wolfram Wobrock

Zentrum für Umweltforschung, Johann Wolfgang Goethe-Universität
Robert Mayer-Str. 7-9, D-6000 Frankfurt a.M. (F.R.G.)

1. INTRODUCTION

In November 1989 a joint fog field campaign was performed in the Po-valley in Italy by various research groups working together in the EUROTRAC subproject GCE (=ground based cloud experiment). The main objective of this experiment was the study of the physico-chemical properties in ground fogs with respect to gas phase and liquid water chemistry and cloud and aerosol microphysics. Also meteorological observations were performed at a 51 m tower, by radiosoundings, and by a Doppler sodar system. The tower observations included next to wind, temperature and humidity also the LWC as a function of height. Additionally satellite pictures of NOAA-10 and 11 were available four times a day. The NOAA satellite data gave a ground resolution of 1.1 x 1.1 km^2. The binary fog masks presented in the following figures were calculated from the differences in brightness temperature of channel 4 and 3 using the method of Bendix and Bachmann (1991). Consequently, only fogs with a vertical thickness exceeding 20 m were registered. In the course of one week five fog events were observed at the observational site (44.66°N, 11.61°E). These fogs varied significantly in vertical and horizontal extension, in lifetime, and in their evolution history.

2. OBSERVATIONS

During the period from 10.-17.Nov.1989 a huge, blocking anticyclone developed and persisted over Central Europe and due to a cloud free atmosphere the radiative cooling in the nights caused a temperature inversion favoring fog formation especially in the moist Po river valley. Figure 1 illustrates the time evolution of the fog field at the observational site for the night of Nov.10/11 between 1.5 and 51 m heights. The LWC measurements were performed with one FSSP-100 which was attached to the tower elevator and a second remaining at 1.5 m. The elevator ascended the tower every hour on the hour and descended again. At the beginning of this night only a very shallow ground fog formed. The fog formation in this period was caused by radiative cooling of the surface and the adjacent layers. The formation process was favoured by calm winds and, as the sodar observations indicate, by a nearly turbulence free boundary layer. This dynamic condition, however, lasted only until 23:00 when the fog dissipated. The wind increase and the strong wind shear in the first 120 m were probably resulting in the mixing in of warmer and drier air. At 3:00 new fog appeared. As the increase of the LWC up to about 150 mg m^{-3} in the first 30 m took place within only a few minutes and we can assume

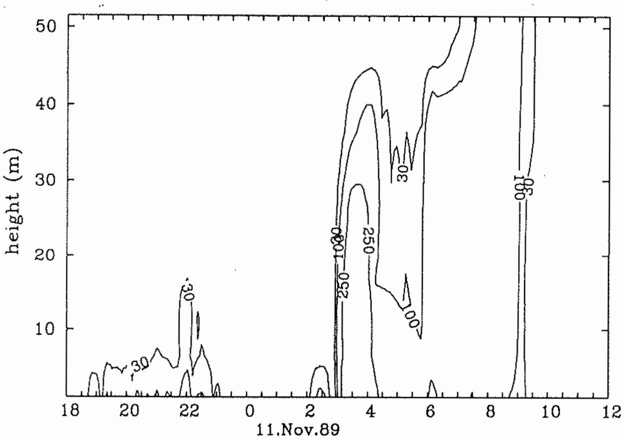

Fig.1: Time evolution of the LWC as a function of height on Nov. 10/11, 1989. The values used are 10 min averages in time and 5m averages in height. The con-tour lines display the LWC in mg m^{-3}.

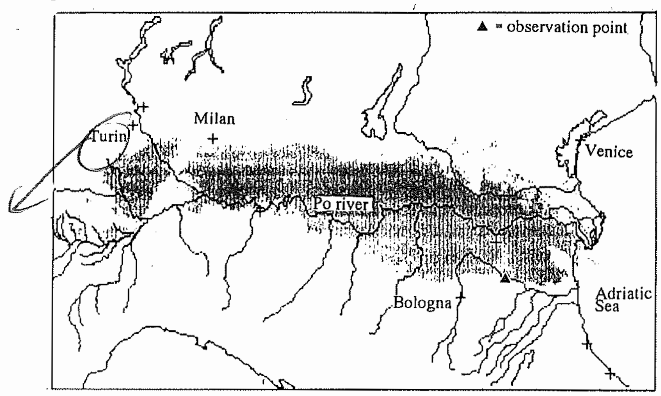

Fig.2: Satellite pictures of NOAA-11; Nov.11 at 2:35 local time. Shaded areas represent areas covered with fog. The gaps in the fog field do not represent fog free areas; they are caused by a band of cirrus clouds in the higher troposphere.

that this fog had formed elsewhere and was transported to the observational site. This is confirmed by the satellite picture (Fig.2) at 2:35. We can see that a huge fog field had formed covering nearly the entire Po-valley, however, the observation point is accordingly to Fig.1 still fog free. A characteristic of this and other advected fog fields observed in the following days is that vertical gradients of temperature, mixing ratio, and LWC disappeared nearly completely, i.e. the fog layer showed a well mixed structure.

The fog intensified in height up to about 120 m in the morning hours and dissipated at 9:00. This dissipation process took place nearly at the same time over all heights. The satellite pictures at 8:58 (Nov.11) (not illustrated here) indicate that we were again just at the edge of a seemingly eastward drifting fog field. During daytime the fog field thinned out so that satellite images at 14:06 (Nov.11) showed fog only for isolated areas in the center of the Po valley. Most responsible for the shrinking seemed to be the warming of the air at the edges of the fog field and the subsequent mixing processes.

On the other hand, also the dynamics in the valley have an important influence on the fog formation and dissipation. Due to the large scale situation winds in the free atmosphere came from north-east directions. Observations in the first 150 m, however, registered continuously western and north-western directions with wind speeds up to 7 m s^{-1} in 30 m. This channelling of the wind in a valley is a well known phenomenon (Wippermann, 1984) and its appearance was already observed during fog experiments in the Hudson river valley (Fitzjarrald and Lala, 1989).

In the evening of Nov.11 an enormous fog field developed again covering the entire Po valley with an extension over 350 km in west-east and up to 100 km in north-south direction. This fog field persisted at the observational point for about 63 hours. Only during daytime the fog field shrunk at its eastern rim. This is illustrated by the satellite picture at 13:49 Nov.13 in Fig.3. However, the fog intensified again during the night even extending several ten kilometers into the Adriatic sea. The fog field appeared at the observational side by advection. The LWC exceeded 300 mg m^{-3} in the early evening and decreased during daytime to 30 mg m^{-3}. The vertical extension of the fog constantly reached up to 200m. We suspect that the following facts are responsible for this persistent and dense type of fog: during the night of Nov. 10/11 a ground temperature inversion developed up to 450 m. This inversion persisted the entire following day since the solar radiation only generated a boundary layer of 250 m. In this well mixed layer the warm air was loaded with water vapour from the open water surfaces and the moist soil in the valley.

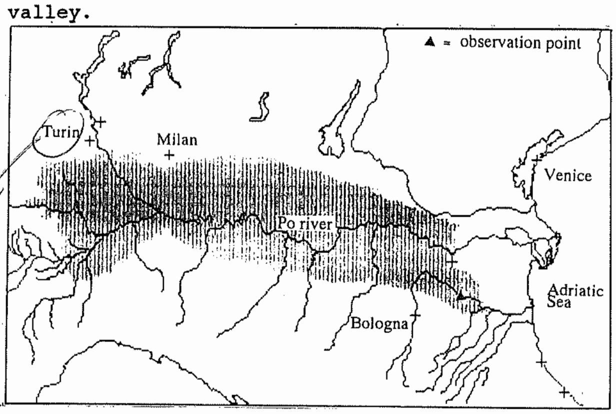

Fig.3: Satellite pictures of NOAA-11 on Nov.13, 1989 at 13:49 local time

In the period from Nov. 14 until 15, however, the subsidence of warm and dry air from the high pressure system into the boundary layer became effective and consequently the inversion and the fog field decreased and finally disappeared. The fogs which developed in the following three nights displayed different characteristics from those described above. Fig. 4 illustrates the time evolution of the LWC for Nov. 15/16. The fog formation started relatively late at 22:45 as the rel. humidity was around 55% in the afternoon. From the observation of the water vapor mixing ratio it was found that this fog formation was caused by moisture advection. This advection took place over all observed heights, however, due to the relatively high temperatures above 30 m supersaturation was only caused in the lower layers. During this type of fog the growth in LWC took place very slowly and significant vertical gradients in LWC developed. The moisture advection lasted only 30 minutes, thereafter the fog started to weaken and finally disappeared at 1:00. The new LWC observed at 3:00 (Fig.4) corresponded again to an advected fog.

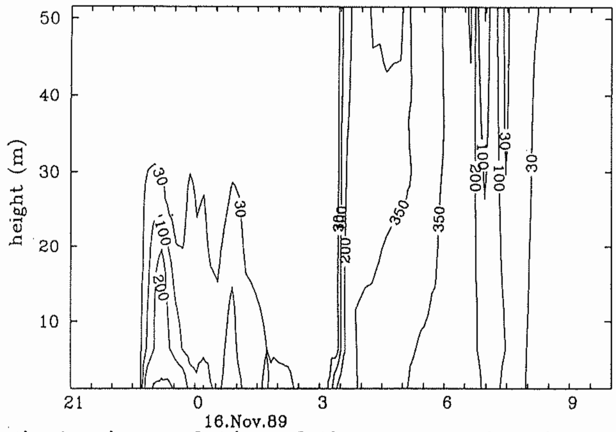

Fig.4: Time evolution of the LWC as a function of height on Nov. 15/16, 1989.

3. CONCLUSION

Our observational results show that there is a clear difference between the height of an advected fog field and the height of fogs which formed due radiative cooling or due to the advection of moisture or cold air. The advected fogs reached up to 200m, the others were lower than 20-30m. Fitzjarrald and Lala (1989) also found this difference for the Hudson river valley fog and therefore proposed to distinguish between boundary layer and surface layer fogs. Boundary layer fogs extend up to 200-250m and their formation is mainly determined by the dynamics of the nocturnal boundary layer. Surface layer fogs form in very stable conditions when the surface layer is decoupled from the boundary layer. But also here dynamical processes like moisture or cold air advection play an important for the formation of dense fog. The observations have shown that pure radiative cooling of the surface and the adjacent layers can only result in a very shallow and non persistent ground fog.

4. ACKNOWLEDGEMENT

The observations of the LWC were performed by the Netherlands Energy Research Foundation (ECN), Petten. Sodar observations and radiosoundings were done by ENEL, Milan (Italy). The field experiment was organized and hosted by FISBAT/CNR, Bologna (Italy).

5. REFERENCES

Bendix, J. and M. Bachmann, 1991: Ein operationelles einsetzbares Verfahren zur Nebelerkennung auf der Basis von AHVRR-Daten der NOAA-Satelliten. Meteor. Rundsch. 43; 169-178.

Fitzjarrald, D.R., and G.G. Lala, 1989: Hudson Valley Fog Environments, J. Appl. Meteor., 28, 1303-1328.

Wippermann, F., 1984: Air flow over and in broad valleys: Channelling and Counter-current, Contrib. Phys. Atmos., 57, 92-105.

ON THE FORMATION OF BIMODAL DROPLET SIZE DISTRIBUTIONS IN STRATIFORM CLOUDS

Alexei V. Korolev

Central Aerological Observatory, Dolgoprudny, 141700, Russia

1. INTRODUCTION

This paper presents some experimental results of bimodal droplet spectra observations in stratiform clouds and possible mechanisms of their formation.

2. INSTRUMENTATION

The cloud droplet spectra were measured with the FSSP on the IL-18 aircraft. Sampling of droplet spectra was done at 0.1s (10m) intervals. Data were collected during 1982-1984 over the USSR. Measurements were made in *St*, *Sc*, *As*, *Ac*, *Ns* in height and temperature ranges of 0.5-6km and of -20°- $+5^{\circ}$C, respectively. A total length of incloud flight was 2502km.

The modal droplet size was defined as

$$d_m = \frac{d_{i-1}N_{i-1} + d_iN_i + d_{i+1}N_{i+1}}{N_{i-1} + N_i + N_{i+1}} . \qquad (1)$$

Here N_i is the number of particles counted in a channel d_i corresponding to a local maximum in droplet size spectrum.

The local maximum N_{max} was rejected if

$$N_{max} - max(N_{min1}, N_{min2}) < \sqrt{N_{max}} \qquad (2)$$

here N_{min1}, N_{min2} are the numbers of particles counted in local minima from left- and right-hand-sides of the local maximum N_{max}. When data processing corrections on droplet sizes, dead time, air velocity were taken into account.

For further consideration we define d_{m1}, d_{m2} to be modal sizes of a bimodal droplet spectrum, n_{m1}, n_{m1} to be their modes, respectively. Always $d_{m1} < d_{m2}$.

3. EXPERIMENTAL RESULTS

In stratiform clouds, zones with bimodal spectra are distributed extremely sporadically. On the one hand, clouds were encountered where the length of a zone with bimodal spectra exceeds several tens of kilometers. On the other hand, there are a lot of cloud layers without bimodal spectra at all. Zones with bimodal spectra occupy on average, about 14% of stratiform cloud volume. Occurence of bimodal spectra practically does not depend on total droplet concentration n.

3.1 *Mode relation.*

Let us define bimodal spectra with $n_{m1} > n_{m2}$ as the type 1 and with $n_{m1} < n_{m2}$ as the type 2.

Data analysis shows that bimodal spectra of 1st type occur more frequently: in 76% cases of all bimodal spectra.

Fig.1 presents distribution functions $F_o(\eta)$, $F_1(\eta)$, $F_2(\eta)$ for all bimodal spectra and for bimodal spectra of the 1st and the 2nd types, respectively; here $\eta = n_{min}/n_{max}$, $n_{min} = min(n_{m1}, n_{m2})$, $n_{max} = max(n_{m1}, n_{m2})$.

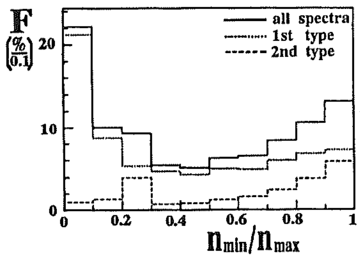

Fig.1. Distribution of mode relation in bimodal droplet size spectra.

It is seen from Fig.1 that most probable forms of bimodal spectra have $n_{m1} \simeq n_{m2}$ or $n_{m1} \gg n_{m2}$ (Korolev, 1991).

3.2 *Modal size difference.*

The statistics of modal size difference $\Delta d_m = d_{m2} - d_{m1}$ have been examined. Fig.2 shows distribution functions $F_o(\Delta d_m)$, $F_1(\Delta d_m)$, $F_2(\Delta d_m)$ for all bimodal spectra and for bimodal spectra of the 1st and the 2nd types, respectively. Average modal size difference for all bimodal spectra is $\overline{\Delta d_m} = 8\mu m$, that for the 1st type is $\overline{\Delta d_m} = 8.5\mu m$, and that for the 2nd type is $\overline{\Delta d_m} = 6.5\mu m$. Approximately for 50% of all bimodal spectra $\overline{\Delta d_m} \leqslant 7\mu m$.

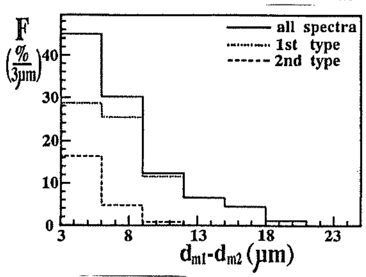

Fig.2. Distributions of modal size difference in bimodal droplet size spectra.

For bimodal spectra of the 1st type maximum modal size difference as found was $\Delta d_m = 21\mu m$, and that for the 2nd type was $\Delta d_m = 12\mu m$.

3.3 *Lengths of bimodal spectra zones.*

We define the zones with continuous bimodal spectra as zones where each next spectrum, measured by the *probe*, is bimodal one.

One of the main features of bimodal zones is their frequent discontinuity by unimodal spectra. As the length of zone with discontinuous bimodal spectra may reach tens of kilometers, the typical length of zones with continuous bimodal spectra is dozens of meters.

Fig.3 shows distribution function of horizontal length of the zones with continuous bimodal spectra. Approximately in 70% of cases, lengths of continuous bimo-

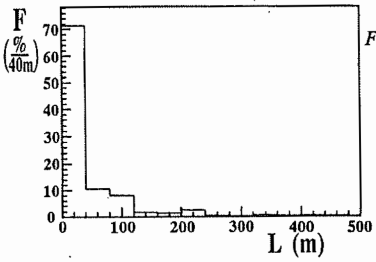

Fig.3. Distribution of length of zones with continuous bimodal droplet size spectra.

dal spectra zones do not exceed 40 meters. The maximum measured length is about 5km, the minimum one being 10m. The latter coincides with spatial resolution of the FSSP. Statistical errors do not allow us to use data collected with spatial resolution of FSSP less than 10m in bimodal spectra analysis. So, characteristic length of bimodal zones may be of the order of meters or even centimeters.

3.4 *Spectra spatial variations.*

We distinguish three types of spatial variation of bimodal spectra: "transitional", "local", "chaotic".

When the transitional zone is penetrated the following succession is observed. While entering the zone of unimodal spectrum with modal size (for example) d_{m1}, the second mode with modal size d_{m2} emerges. Proceeding further in the zone, first mode n_{m1} decreases, while second one n_{m2} increases. On leaving the bimodal zone the first mode disappears and droplet spectra become unimodal with modal size d_{m2} (Fig.4).

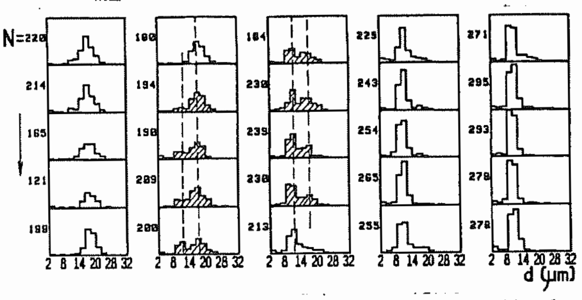

Fig.4. The spatial variation of droplet size spectra in transitional zone. Figures denote number of particles in each sample. Time of averaging 0.25s (25m). St-Sc, 25.01.84, Borispole Region, H=2150m, T=-7°C.

The length of transition zones may vary from meters up to hundreds of meters. Typical lengths of the zones are several tens of meters.

"Local" type of spatial variation is characterized by absence of variations in unimodal spectra outside bimodal spectra zone. In another words there is no "source" of second mode as in the case of transitional bimodal spectra zones. Typical lengths of local type zones are about tens of meters.

Within "chaotic" zones there is no distinct structure of modal size variations. Usually there are several stable modal sizes which in various combinations, form two- and threemodal spectra (Fig.5).

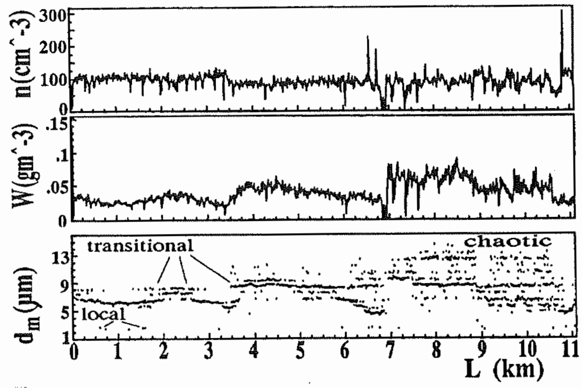

Fig.5. The spatial variations of droplet concentration, LWC, and modal diameter in St-Sc. Time of averaging 0.1s (10m). 03.02.84, Borispole Region, H=2100m, T=-4°C.

The length of chaotic zones may reach several dozens of kilometers. This is one of the most wide-spread type of spatial variation in stratiform clouds.

4.MECHANISMS OF BIMODAL SPECTRA FORMATION

Up to now there has been no clear understanding of mechanisms of bimodal spectra formation. In papers (Warner, 1969; Telford et. al.,1984; Baker and Lathem, 1985) one may find some hypothesis of bimodal spectra formation in convective clouds. As to bimodal spectra formation in stratiform clouds, this question is poorly examined. Below we discuss three possible mechanisms.

4.1 *Mixing*

For bimodal spectra formation due to turbulent mixing to be possible, the characteristic mixing time τ_t should be greater than the characteristic lifetime of bimodal spectra τ_b, i.e. $\tau_b \gg \tau_t$.

The characteristic time of turbulent mixing of a parcel with size l_o is of the order of $\tau_t \sim (l_o^2/\varepsilon)^{1/3}$, where ε is the turbulent energy dissipation rate. Assuming l_o=100m, $\varepsilon=10^{-4}m^2/s^3$, we obtain $\tau=5\times10^2$s.

A bimodal spectrum with modal sizes r_{m1} and r_{m2} will transfer into unimodal one if droplets of smallest modal size r_{m1} evaporate, or two modes merge into one due to condensational growth .

Let us estimate τ_b, assuming that two modes merge into one if $\Delta r_m=r_{m2}-r_{m1}\leq 1\mu m$. Time required for the modal size difference becomes equal to Δr_m, (if initial modal sizes are r_{m10} and r_{m20}) may be expressed as

$$t=\frac{1}{8AS}\left(\frac{(r_{m20}^2-r_{m10}^2)^2}{\Delta r^2}-2(r_{m20}^2+r_{m10}^2)+\Delta r_m^2\right), \quad (3)$$

where S is supersaturation of water vapor, A is a known coefficient ($A\simeq 6\times 10^{-11}$ m^2/s, when $T=0^oC$). Supposing $r_{m1o}=4\mu m$, $r_{m2o}=8\mu m$, $\Delta r_m=1\mu m$, $S=0.01\%$, and using Eq.(3), we find time interval $\tau_b=4.5\times 10^4 s$. Thus, in stratiform clouds bimodal spectra are quite stable ($\tau_b \gg \tau_t$) and may have lifetimes about several hours.

Another question arises: how are unimodal spectra with different modal sizes formed at one and the same level in stratiform clouds?

One of the reasons may be the vertical motion of cloud parcels. It is known that some cloud parcels may ascend or descend due to turbulence within cloud layers. Assuming motion to be adiabatic, we find

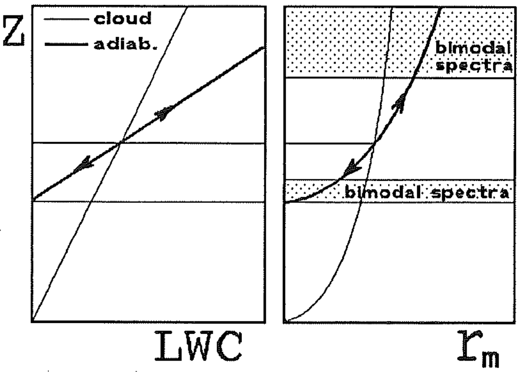

Fig.6. Scheme of bimodal droplet size spectra formation due to vertical adiabatic motions of cloud parcels.

height variation of droplet size of monodisperse spectra equals to

$$\left(\frac{dr}{dz}\right)_{ad}=\frac{d}{dz}\left(\frac{3\rho_a}{4\pi\rho_l}\frac{W}{n}\right)^{1/3}=\frac{\rho_o}{4\pi\rho_l}\frac{\beta_{ad}}{nr^2}, \quad (4)$$

where ρ_l is liquid water density, ρ_a is air density, n droplet concentration, W is the specific LWC, $\beta_{ad}=(dW/dz)_{ad}$ is vertical adiabatic gradient of LWC, ($\beta_{ad}=1.5\times 10^3$ g/kg/m, when $T=0^oC$, P=900mb).

In real stratiform clouds vertical gradient of modal size dr_m/dz is usually less than the one found from Eq.(4). Hence, if vertical displacement Δz is so large that modal sizes within a cloud parcel and those in surrounding environment differ enough, mixing will lead to bimodal spectra formation (Fig.6).

Let us estimate vertical displacement Δz of a cloud parcel required for bimodal spectra to be formed. Experimental data collected by CAO have shown that dr_m/dz usually varies in the range of 0.5×10^{-2}-$2\times 10^{-2}\mu m/m$. On the other hand we know from sect.3.3 that average modal size difference $\overline{\Delta r}_m=4\mu m$. Assuming $n=100cm^{-3}$, $r_{mo}=4\mu m$, $\Delta r_m=4\mu m$, $dr_m/dz=2\times 10^{-2}\mu m/m$, we find from Eq.(4) that vertical displacement required for bimodal spectra formation is equal to $\Delta z\simeq\pm 40$-$80m$. Turbulent pulsations on scale of 40-80m are typical of stratiform clouds.

4.2 *Activation*

If supersaturation in a cloud parcel exceeds critical value

$$S^*=2\left(\frac{B}{3r_e^*}\right)^{3/2}, \quad (5)$$

interstitial condensation nuclei (ICN) $r_e<r_e^*$ are activated and a second mode may arise in droplet size spectrum. Here r_e is effective radius of ICN.

Supersaturation increase may occur within an isolated cloud parcel due to adiabatic cooling during ascent. The supersaturation rises if the rate of increase of moisture excess due to adiabatic ascent

$$\left(\frac{dW}{dt}\right)_{ad}=\beta_{ad}u_z \quad (6)$$

exceeds the rate of moisture decrease due to droplet condensation growth

$$\frac{dW}{dt}=\frac{4\pi\rho_l n}{\rho_a}\int_0^\infty f(r)r^2\dot{r}dr, \quad (7)$$

Here $f(r)$ is droplet size spectrum, u_z is the velocity of cloud parcel ascent, $\dot{r}=AS/r$ is the rate of a droplet condensation growth, n is droplet concentration. Substituting Eq.(5), Eq.(6) into Eq.(7), we find the velocity of ascent u_z^* which gives rise to activation of ICN r_e^* in cloud parcel containing droplets of concentration n and average radius $\bar{r}$.

$$u_z^*=\frac{Gn\bar{r}}{\beta_{ad}(r_e^*)^{3/2}}, \quad (8)$$

here $G=8\pi A(B/3)^{3/2}\rho_l/\rho_a$

Experimental studies (Hudson and Rogers, 1982) have shown that in stratiform clouds supersaturation increase up to 0.5%-1% may cause additional activation of ICN of tens or hundreds per cubic centimeter.

Assume that cloud droplets were condensed on soluble CCN having Junge's size distribution $\varphi(r_e)=dr_e^{-\gamma}$. Then we may find threshold size of wettered CCN which have not yet transformed into droplets

$$r_{en}=\left(\frac{n(\gamma-1)}{\alpha}\right)^{\frac{1}{(1-\gamma)}} \quad (9)$$

Substituting Eq.(9) into Eq.(8) we have

$$u_z^*=\frac{Gn^\delta\,\bar{r}}{a\,\beta_{ad}}, \quad (10)$$

where $a=((\gamma-1)/\alpha)^{\frac{3}{2(\gamma-1)}}$, $\delta=(2\gamma+1)/(2\gamma-1)$

Thus, if upward velocity $u_z>u_z^*$, activation of ICN begins. As can be seen from Fig.7 u_z^* is of the order of tenths of meter and meters per second for typical $n\bar{r}$. Turbulent pulsations with such velo-

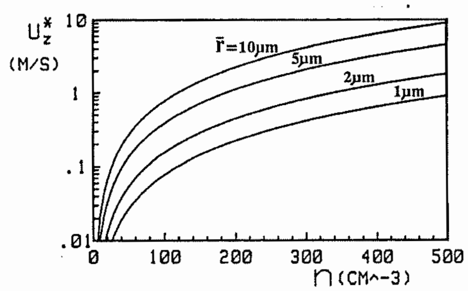

Fig.7. Threshold vertical velocity required for ICN activation versus n for various droplet radii r. Droplet size spectrum is formed on soluble CCN which have Junge's size distribution (γ=-3.8, α=8.54 10^-13).

cities are typical in stratiform clouds.

In deriving Eq.(8) and Eq.(10), we have made some simplifications. A more thorough study of ICN activation and bimodal spectra formation was carried out with the help of computational model of droplet spectra evolution (Korolev and Mazin, 1992). Modelling of parcel verti-

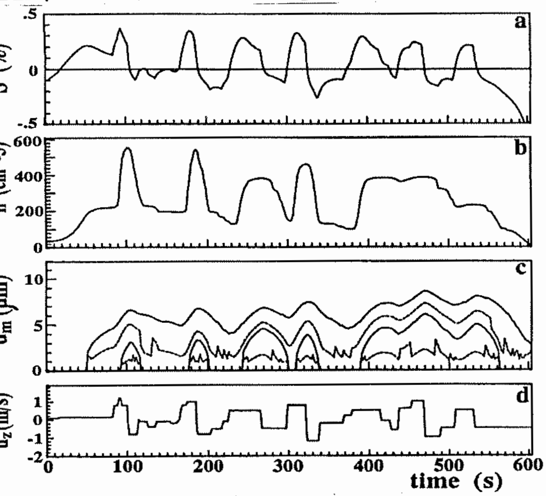

Fig.8. Numerical simulation of the droplet size spectrum in an adiabatic volume when the vertical velocity varies randomly. (a) supersaturation; (b) concentration; (c) modal size, dashed line denotes spectrum local minimum; (d) vertical velocity.

cal velocity was supplied by generator of random numbers and ranged from -1m/s up to +1m/s.

The time evolutions of S, n, d_{m1}, d_{m2}, u_z are presented in Fig.8. Bimodal spectra form during ascent and disappear during descent. Modelled sectra are very close to those observed with FSSP in clouds.

Comparison of u_z^* value calculated from Eq.(8) with that, obtained from the model, shows that the results are in a good agreement and differ by no more than 15%-

4.3 *Averaging*

Bimodal spectra may result from spatial averaging of unimodal spectra (Fig.10). Scale of spatial averaging varies from tens of meters to kilometers.

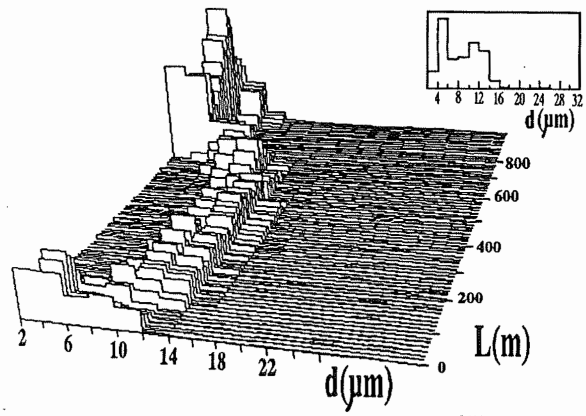

Fig.9. Spatial averaging over the zone with unimodal spectra resulting in bimodal spectra (in the upper right corner). St-Sc, 03.02.84, Borispol Region, H=2100m, T=-4°C.

Averaging interval choice procedure is rather artificial. Variations of interval length of 10%-40% may result in disappearance of bimodal spectra. An opposite situation is also possible: averaging over the interval with bimodal spectra may result in unimodal spectrum.

5. CONCLUSION

We would like to emphasize two points resulting from the above discussion. First, bimodal spectra in stratiform clouds are quite time stable. Their lifetime may reach several hours. Second, the formation of bimodal spectra is closely connected to turbulence which exists now, or may have been existed in bimodal spectra zone previously. Characteristic scales of turbulent pulsations are tens of meters, and that of vertical velocities are from tenths of meter to meters per second.

REFERENCES

Baker M.B., and J.Lathem, 1985: An airborne study of vertical structure and microphysical variations within a small cumulus. Q.J.R.Meteor.Soc, 111, pp.773-792

Hudson J.G., and C.F. Rogers, 1982: Interstitial CCN measurements. Conf. Cloud Phys., Illinois, Chicago, pp. 79-82.

Korolev A.V., and I.P.Mazin, 1992: Zones of increased and decreased droplet concentration in stratiform clouds., J. Appl.Meteor., (in press).

Korolev A.V., 1991: Study of bimodal spectra in stratiform clouds. Izv. AN SSSR, Fizika Atmos. i Okeana, N5, pp.511-518.

Telford J.W., T.S.Keck, and S.K.Chai 1984: Entrainment at cloud tops and the droplet spectra. J.Atmos.Sci., 41, pp.3170-3179.

Warner J., 1969: The microstructure of cumulus clouds. P.1. General features of droplet spectrum. J.Atmos.Sci., 26, pp.1049-1059.

PHASE STRUCTURE OF STRATIFORM CLOUDS

Mazin I.P., Nevzorov A.N., Shugaev V.F. and Korolev A.V.

Central Aerological Observatory, Dolgoprudny, Moscow Region, 141700, Russia

1. INTRODUCTION

The cloud phase structure (CPS) is the key problem in the cloud physics. Further we will refer to it as the CPS problem. Without solving this problem we are not able to judge about the degree of reliability of many cloud numerical models or parameterization of clouds in atmospheric radiation or climate models. Many applications of cloud physics also need solving this key problem.

The new aircraft instrumentation and techniques developed by A.N.Nevzorov and his colleagues in the Cloud Physics Laboratory (CPL) of the Central Aerological Observatory (CAO) which we called ACMC (aircraft cloud microphysical complex) permit us to advance in solving the CPS problem. Presented in this paper is a technique of CPS determination and main physical and statistical results.

2. INSTRUMENTS AND METHODS OF MEASUREMENTS

The ACMC consists of 5 instruments listed in Tab.1. Here we will confine ourselves to the brief comments.

2.1 *Measurement of LWC and IWC*

Both the total water content (TWC) and liquid water content (LWC) meters are based on the calorimetric technique improved as compared with J-W and King's meters. They differ only in the shapes of the in-flow probes each consisting of two

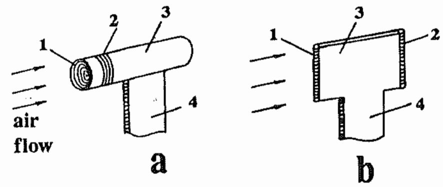

Fig.1. In-flow sensors of TWC (a) and LWC (b) meters: 1-collector, 2-water- protected sensing element, 3-base, 4-pillar with anti-icing heater.

differential sensors (Fig.1) kept at the same temperature (90°C). Both the meters are calibrated against the LWC. Denoting the readings of the TWC meter by *W1* and these of the LWCM by *W2*, we may write:

$$W_1 = C_1(LWC) + \eta C_3(IWC), \quad (1)$$

$$W_2 = C_2(LWC) + \delta C_4(IWC). \quad (2)$$

Here C_i are effective collision efficiencies for droplets (C_1 and C_2) and for ice crystals (C_3 and C_4), $\eta \simeq 1.12$ is the correction for the difference in ice and water heat of evaporation, δ is a factor of residual effect of ice crystals on the LWC probe. Actually, $C_2 > C_1$. In ice clouds $\beta = C_4/\eta C_3$ is of the order of a unity and $W_2/W_1 \simeq \delta \ll 1$. Experimental estimations have shown that $\delta < 0.03$. Assuming $\delta = 0$ we may rewrite Eqs.(1) and (2):

$$LWC \simeq W_2, \quad (3)$$

$$IWC = 0.89\ (W_1 - \frac{C_1}{C_2} W_2). \quad (4)$$

Table 1. ACMC instrumentation

Instrument	Parameter to measure	Range	Max. error	Sampl. area	References
Particle phase/sise analyser PPSA	Drop diameter Crystal eff.dia. Concentration	30-180 μm 20-120 μm $10-10^4$ l^{-1}	5% 20% -	16 mm^2	Loba et al.(1985) Kosarev et al.(1986)
Large particle spectrometer LPS	Particle size Concentration	0.2-6 mm $1-10^4$ m^{-3}	10% -	7 cm^2	Borovikov et al.(1968) Nevzorov (1973)
Water content meters: -liquid - LWCM	LWC	0.003-4 gm^{-3}	10%	0.25 cm^2	Nevzorov (1980) Kosarev et al.(1986)
-total - TWCM	LWC equivalent	0.003-2 gm^{-3}	10%	0.5 cm^2	Nevzorov et al.(1992)
Cloud transparency meter RP	Extinction coef. (via Bourger law)	1-200 km^{-1}	30% (range edges)	-	Kosarev et al.(1976) --"- -"-- (1986)

Measurements in warm clouds ($T>0^oC$) allow us to determine using (1), (2)

$$C_1/C_2 = W_1/W_2 \qquad (5)$$

Ratio C_1/C_2 dependends on drop effective diameter d_{23} (see Fig.2).

2.2 *Measurement of the extinction coefficient (EC)*

If ε_m is the EC value as measured with RP, ε_l and ε_i are true values of EC contributed by correspondingly liquid and ice cloud fractions, then

$$\varepsilon_m = G_l\varepsilon_l + G_i\varepsilon_i . \qquad (6)$$

Factors G_l and G_i account for the instrument distortion and diminish from 1 through 0.5 with particle size increasing, from 0 through $\geqslant 80\mu m$ (Nevzorov, 1971).

2.3 *Particle phase and size determination*

The particle phase and size analyzer PPSA is based on the analysis of orthogonally polarized components of light scattered at 90^o by single particles from S-polarized beam. The signals of initially polarized S-component are processed by the 5-channel pulse height analyzer with size thresholds d_k (drop diameter) and a_k (ice particle effective cross-sectional diameter) presented in Table 2.

Table 2. The channel size thresholds d_k and a_k of PPSA (Kosarev et al., 1986)

k	1	2	3	4	5
d_k (μm)	30	50	80	120	180
a_k (μm)	20	33	53	80	120

In a general case, each channel provides the sum concentration N_k of both IP with $a>a_k$ and drops with $d>d_k$ without distinguishing between them:

$$N_k = N_i(a_k) + N_l(d_k) \qquad (7)$$

In the polarized p-component channel the sum concentration $N_p = N_i(a_p) + N_l(d_p)$ of crystals with $a>a_p$, and drops with $d>d_p$ is measured where $a_p \simeq 25\text{-}30\mu m$, $d_p \simeq 100\mu m$. It follows from Table 2 that the concentration of IP in the range of $a_p < a < a_3$ must be no less than

$$N^* = N_p - N_3 \qquad (8)$$

Thus the inequality $N^* > 0$ may be used as a sufficient criterion of the presence of ice crystals in a cloud.

The large particle spectrometer LPS measures the sizes of drops d and crystals a^* ($a^* \simeq a$, Kosarev et al., 1986). Measurement range is 200 to 6000 μm.

3. THE CPS DETERMINATION

It has been just mentioned that $N^*>0$ implies the presence of crystals with $a>25\mu m$ in a cloud. If such crystals were absent, i.e. $N_p=N_3=0$, we deemed that smaller ice crystals ($a<a_p$) occured in cloud when:

$$\frac{W_1}{W_2} > f_{max} = \left(\frac{C_1}{C_2}\right)_{max} . \qquad (9)$$

(Nevzorov and Shugaev, 1992). Here $(C_1/C_2)_{max}$ is the upper limit on a scatter plot in Fig.2: $f_{max}=1.15f$, where $f = f(d_{23})$ is the mean curve in Fig.2.

The existence of liquid water in a cloud was determined by $W_2=LWC>0$.

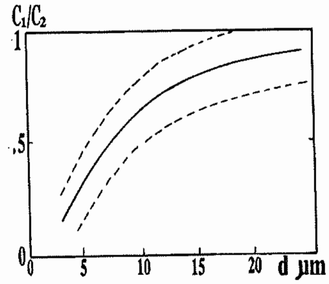

Fig.2. Experimental dependence of C_1/C_2 ratio on d_{23} in warm clouds. The dash lines are the limits of the dots spread.

4. THE DROP SIZE ESTIMATION

The characteristic drop diameter d_{23} is defined as $d_{23} = \overline{d^3}/\overline{d^2}$ where the overbared letter means the mean value. For liquid clouds

$$d_{23} = 3\, LWC/\rho_w\varepsilon_l \qquad (10)$$

According to Eq.(6) $\varepsilon_l = \varepsilon_m/G_l$. Using the factor G_l in a function of d_{23} (Nevzorov, 1971), from Eq.(10) the value of d_{23} can be found.

In the cases where $W_2>0$ and $N^*>0$ the following inequality is fair because $0.5<G_l<1$ and $\varepsilon_l<2\varepsilon_m$:

$$d_{23} > \frac{3LWC}{2\rho_w\varepsilon_m} = D. \qquad (11)$$

In clouds with $N^*>0$, experimental D values varied between units and tens of microns which implies the true d_{23} values to be correspondingly larger. In certain cases more accurate estimation of d_{23} may be made. Let ε_c to be a calculated "instrumental" value of EC for particle spectrum measured by PPSA, $G_o\varepsilon_o$ the true contribution of small particles (most possible drops) into ε_m, then

$$\varepsilon_m - \varepsilon_c \simeq G_o\varepsilon_o \simeq G_l\varepsilon_l . \qquad (12)$$

Substituting $\varepsilon_l = (\varepsilon_m - \varepsilon_c)/G_l$ into Eq.(10)

as for liquid clouds, we may estimate the effective drop diameter d_{23}. If d_{23}<30μm, the technique employed proves this value. If $\varepsilon_m - \varepsilon_c \leqslant 0$ or d_{23}>30μm with W_2>0, it means only that d_{23}>30μm, but we do not know the exact value.

5. THE TYPES OF CLOUD PHASE STRUCTURE

All cloud situations were divided into 5 categories according to their CPS types: liquid (L), ice (I) and three types of mixed (M) structures.

To (L) type we referred the cases with $W_2=LWC>0$ and with no evidence of ice crystals, that is, with $N^*=0$ and $W_1/W_2<1.15C_1/C_2$ (i.e. $IWC=0$). In all (L) type cases there was d_{23}<30μm.

Type (I) included the cases in which $N^*=N_p-N_3>0$, but $W_2=LWC=0$.

To mixed clouds (M) referred were all the cases where ice and liquid phases were simultaneously observed divided to dispersion types as follows:

-(M1) type - $N_p=0$ and $W_1>1.15W_2$. This means that all the IP are less than 25μm.

-(M2) type - $N^*>0$ and d_{23}<30μm. The last condition implies that the main shares of the LWC and ε_l are contributed by small enough droplets.

- (M3) type - $N^*>0$ and d_{23}>30μm i.e. with large drops contribution prevailing in the LWC value.

6. EXPERIMENTAL RESULTS

The research flights were performed in 1988 over the Uzbekistan (Middle Asia) and in 1989 over Bulgaria (Plovdiv region). Flight levels were between 1 and 10 km, temperatures from 0°C to -55°C. Total length of flights in stratiform clouds for 50 days exceeded 20,000 km. Each cloud penetration was divided into homogeneous sections about 1 to 50 km long for which the CPS types have been determined. The frequency of occurrence of all types of CPS in each 5°C interval was analyzed. The diagram in Fig.3 shows and the examples of Fig.4 illustrate some of the obtained results arranged below.

- The mixed CPS occurred much more often than it was thought before (Borovikov, 1968). In the overwhelming majority of clouds at T<0°C water particles of liquid and solid phases were co-existing. Liquid water was usually observed in clouds at very low temperatures down to at least -55°C. In the majority of clouds, in any case in these of (M3) type (Fig.3), drops larger than 30μm exist and contribute noticeably into the LWC.
- The typical IP concentrations are 10^2-10^3 l^{-1}, the maximum values reaching (maybe exceeding) 10^4 l^{-1}, and display no marked correlation with the cloud temperature.
- The proportion between LWC and IWC varies in wide limits even within the same cloud. But at short enough scales (units of km) the strong positive correlation between them prevails. Mean TWC is approximately twice as large as LWC (for example, their mean values are correspondingly 16 and 8 mg m^{-3} at -50°C as well as 26 and 12 mg m^{-3} at -40°C).
- The modal IP effective diameters ranged from <20 μm through about 50μm.

7. CONCLUSION

The obtained results are unexpected and unusual in many respects. Surely they are to some extent preliminary and need to be confirmed and statistically ensured. Nevertheless, we may say that:
- The existent ideas on the phase structure of clouds need to be revised today. The CPS problem involving the problems of IP generation in the atmosphere and liquid water at T<0°C is the main problem of cloud microphysics. Until it is solved, nobody can judge about the adequacy of the numerical cloud models to the real clouds. The same may be said about the parameterization scheme of cloud structure in climate models and in other applications.
- Numerical modelers have to be ready to revise their results. And it is time to investigate the dependence of their results on the scheme of parameterization of cold cloud processes.

A field experiment with well-instrumented aircraft including ACMC, PMS probes, RICE probe, etc., seems to give the possibility of clarifying many of the rising questions.

REFERENCES

Borovikov A.M., 1968: Supercooling of water in the atmosphere and phase of various types of cloud. Proc. Intern. Confer. on Cloud Phys., Toronto, Canada, 290-294.

Borovikov A.M., Mazin I.P., Nevzorov A.N., 1968: Large particles in cloud (experimental data). *Ibid.*, 356-363.

Kosarev A.L., Mazin I.P., Nevzorov A.N., Shugaev V.F., 1976: Optical density of clouds. Trudy CAO, Issue 124, 167 p.

Kosarev A.L., Mazin I.P., Nevzorov A.N., Shugaev V.F., 1986: Microstructure of cirrus clouds. In: Some problems of cloud physics (Coll.Papers), Leningrad, Gidrometeoizdat, 160-186.

Loba T.A., Nevzorov A.N., Potyomkin V.G., 1985: Aircraft polarizing analyzer of cloud particles. Trudy CAO, issue 158, 24-31.

Mazin I.P., Khrgian A.Kh. (ed.), 1989: Clouds and cloudy atmosphere. Leningrad, Gidrometeoizdat, 647 p.

Nevzorov A.N., 1971: An estimation of the light scattering effect in cloud transparency measurement. Trudy CAO, Issue 102, 102-117.

Nevzorov A.N., 1973: Large particle spectrometer for high-altitude pressurized airplane. Trudy GGO, Issue 276, 189-195.
Nevzorov A.N., 1980: Aircraft cloud water content meter. Proc. of the 8th Intern. Cloud Phys. Confer., Clermont-Ferrand, France, v.2, 701-703.
Nevzorov A.N., Shugaev V.F., 1992. Observations of the initial stage of ice phase evolution in supercooled clouds. Meteorology and Gydrology, N 1, 84-92.

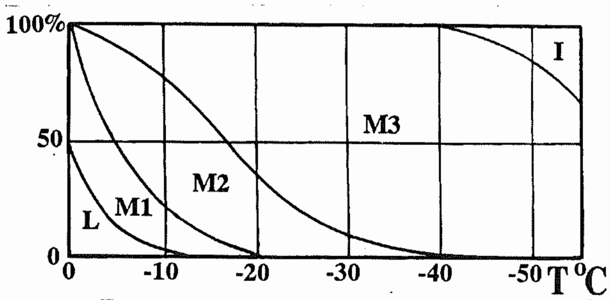

Fig.3. Temperature diagram of cloud phase structure.

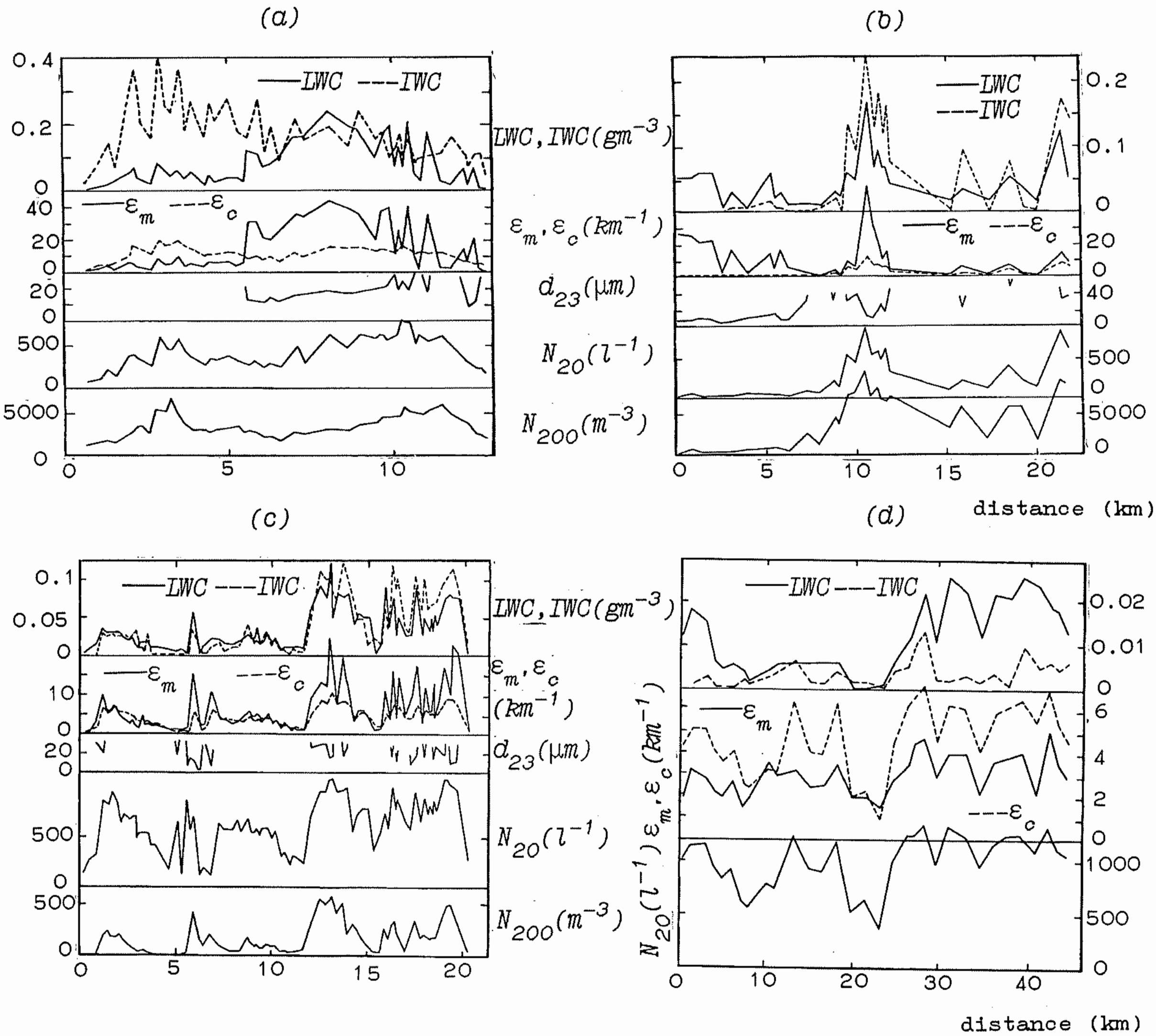

Fig.4 Some examples of cloud penetrations:
(a) Bulgaria, 13.04.1989, Ac, 3200 m, -7°C;
(b) Uzbekistan, 21.03.1988, As, 5000 m, -17°C;
(c) Uzbekistan, 13.03.1988, Cs, 7800 m, -44°C;
(d) Uzbekistan, 21.03.1988, Cs, 9650 m, -52°C.
These examples illustrate that the liquid phase exists in clouds at any negative temperatures even at <-40°C (c,d) with LWC values comparable with IWC. Drop sizes are very variable and zones with $d_{25} > 30\mu m$ are not infrequent. On short distances the positive correlation between LWC and IWC is seen.

MODELING ENTRAINMENT AND MIXING IN STRATUS CLOUDS

Steven K. Krueger and Patrick A. McMurtry
University of Utah, Salt Lake City, Utah USA 84112

1 Introduction

The goal of our research is to increase our understanding of entrainment and mixing in stratus clouds. In particular, we would like to determine if cloud-top entrainment instability (CEI) is possible in marine subtropical stratus clouds. CEI has long been viewed as the most likely mechanism to explain the stratus-to-cumulus transition that occurs over the subtopical oceans. However, stable stratus layers have been observed where theory (Randall 1980; Deardorff 1980a) predicted they should be unstable to CEI (Kuo and Schubert 1988).

One possible mechanism for CEI is "buoyancy reversal", a situation in which a mixture can be denser than its constituents. For buoyancy reversal to occur in clouds, cloud droplets must be mixed with unsaturated air on very small scales. The details of the mixing process in stratus clouds are poorly understood—primarily because of the tremendous range of scales between the large eddies and the Kolmogorov microscale.

The net buoyancy of entrained (and subsequently mixed) air will determine the dynamic effect of the mixing. Complete mixing (resulting in a homogenous mixture) will always produce the minimum buoyancy. The minumum buoyancy is obtained once no further evaporation can occur. This is the case if all mixtures are either saturated, or unsaturated with no liquid water.

Our direct knowledge of stratus entrainment and mixing is extremely limited, due to the difficulties in measuring temperature and water content in clouds, and to the very high sampling rates ($\sim 10^5 s^{-1}$) that must be used by aircraft to resolve the small-scale structures. In addition, laboratory studies are not directly applicable to atmospheric flows (Broadwell and Breidenthal 1982; Siems et al. 1990). As a result of our poor understanding, nearly all approaches to modeling entrainment in stratus clouds have made unjustified assumptions about the nature of the small-scale mixing process.

Even in the most detailed numerical models of stratus clouds—those which use the large-eddy simulation (LES) approach—the small-scale mixing process is subgrid-scale (SGS) since it occurs at scales near the Kolmogorov microscale (about 1 mm). For this reason, all simulations of stratus must parameterize this small-scale mixing. The horizontal grid size used in published LES stratus simulations (Deardorff 1980b; Moeng 1986; Tag and Payne 1987) ranges from 50 to 100 m. In all three of the above models, condensation is based on volume-averaged values of conserved variables. This is equivalent to complete mixing at the scale of the grid-box volume, and therefore results in the minimum possible volume-averaged buoyancy. This may explain why simulations done with LES codes have exhibited CEI under atmospheric conditions for which CEI is apparently not observed in nature.

There is a recently developed modeling approach for mixing in turbulent flows that may prove useful for studies of mixing in stratus clouds. The basic concepts were advanced by Kerstein (1988), who recognized the need to account for and distinguish between the effects of turbulent motion and molecular diffusion, particularly at the smaller scales. The result is the "linear eddy model" which separately treats the turbulent advection and molecular diffusion processes. Applications of this model show that it is capable of accurately describing many features of turbulent mixing (Kerstein 1991). In the next section, we present a brief description of the linear eddy model. We then describe how we are using it to study the mixing of entrained air in stratus clouds.

2 Linear Eddy Model

The development of the linear eddy model has been described in detail elsewhere (Kerstein 1991) and is only briefly outlined here. This approach has a number of unique features that distinguish it from other more commonly used mixing models (e.g., eddy diffusivity models). In particular, the distinction between molecular diffusion and turbulent advection is retained at *all* scales of the flow in a computationally affordable simulation by reducing the description of the scalar field to one spatial dimension. Diffusion and advection have very different effects on scalar field evolution; accounting for these differences is crucial to accurately describe the species field, especially when evaporation is involved. This distinction has not been achieved by any previously proposed mixing model.

Velocity field statistics are inputs into the model, although no explicit velocity field appears. The required model parameters that describe the flow field include the turbulent diffusivity (D_T), the largest eddy size (L), and the nominal Reynolds number, Re_S (which determines the Kolmogorov scale, η). Thus, the flow field properties are inputs to the linear eddy model, not predictions of the model.

The first mechanism acting on a scalar field ϕ, molecular diffusion, is simply implemented by the numerical solution of the diffusion equation,

$$\frac{\partial \phi}{\partial t} = D_M \frac{\partial^2 \phi}{\partial x^2},$$

over the linear domain. Here, D_M is the molecular diffusivity.

The key feature of the model is the manner in which turbulent advection is treated. This is implemented by random rearrangements of the scalar field along a line. The frequency of these rearrangements is determined by requiring that the stochastic rearrangement events result in a turbulent diffusivity consistent with accepted scalings for high-Re turbulent flows. Each rearrangement event involves spatial redistribution of the species field within a randomly selected spatial domain. The size of the selected domain, representing the eddy size, is sampled from a distribution of eddy sizes that is obtained by applying Kolmogorov scaling laws. In this model, the spatial redistribution of a segment of length l represents the action of an eddy of size l. A rearrangement event is illustrated and described in Fig. 1.

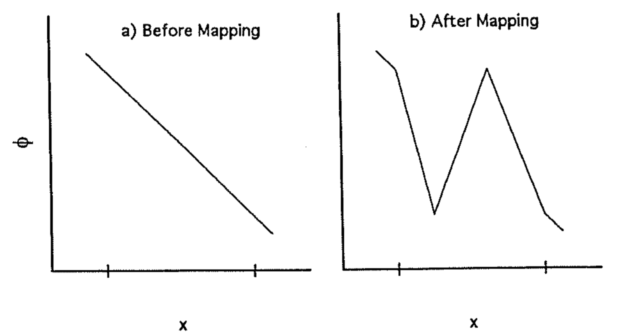

Fig. 1. The scalar rearrangement process is carried out by the use of the "triplet" map. The triplet map makes three compressed copies of the scalar field in the selected segment, replaces the original field with the three copies, and inverts the center copy. a) Illustrative initial scalar field. b) Scalar field after rearrangement.

The rearrangement process is governed by two parameters: λ, which is a rate parameter with dimensions $[L^{-1}T^{-1}]$, and $f(l)$, a pdf describing the segment length distribution. These parameters are determined by recognizing that the rearrangement events induce a random walk of a marker particle on the linear domain. Equating the diffusivity of the random process with the turbulent diffusivity provides the necessary relationships to determine λ and $f(l)$. For high-Re turbulent flow,

$$f(l) = \begin{cases} \frac{5}{3}\frac{l^{-8/3}}{\eta^{-5/3}-L^{-5/3}}, & \eta \leq l \leq L; \\ 0 & \text{otherwise} \end{cases}$$

$$\lambda = \frac{54}{5}\frac{D_T}{L^3}\left(\frac{L}{\eta}\right)^{5/3}.$$

The evolution of the scalar field is thus governed by the molecular diffusion process, punctuated by the random rearrangement events parameterized by $f(l)$ and λ.

3 Linear Eddy Simulations

We are using the linear eddy model to simulate entrainment and mixing in a convective boundary layer (CBL). The model is used in a Lagrangian manner; it simulates the mixing that takes place in a horizontal slab of fluid of width z_i as it travels from the top of the CBL down to the surface in the descending branch of a large convective eddy. This is assumed to occur during one large-eddy time interval z_i/w_*; this time interval is supported by composite plume analyses in clear and cloud-topped LES CBLs which indicate that w_* is the average plume downdraft velocity (Schmidt and Schumann 1989; Moeng and Schumann 1991). Laboratory and LES studies of CBLs clearly show that entrainment occurs as "wisps" or curtains of warm air are drawn downwards at the sides of penetrating updrafts (domes) in the stable layer (Stull 1973; Willis and Deardorff 1979; Schmidt and Schumann 1989; Moeng and Schumann 1991). These studies also indicate that the dome separation is $\sim z_i$. We therefore take z_i as the width of the linear eddy domain. We must also specify the size of the wisp or curtain of entrained air; we assume it can be modeled as a thin sheet of fluid of width $w_e/w_* z_i$, where w_e is the entrainment rate. This estimate is also supported by the laboratory and LES studies referred to previously. Reported values of w_e/w_* in CBLs range from 0.005 to 0.05. We will use 0.05 for this set of simulations.

We performed three simulations. The simulations differed only in resolution. We set the nominal Reynolds number, $Re_S \equiv (L/\eta)^{4/3}$, to 375 for the control run (A). This run resolves 85 wavenumbers. McMurtry et al. (1992) showed that scalar mixing statistics are independent of Reynolds number for $Re_S > 100$. Thus, run A will produce a high-Reynolds number solution. Run B's resolution is similar to that of a LES with 25 m grid spacing and $z_i = 1000$ m: it resolves only 20 wavenumbers with wavelength less than or equal to z_i. For run B, $Re_S = 59$; therefore, it is expected to exhibit departures from high-Re mixing behavior. Run C resolves only 10 wavenumbers with wavelength less than or equal to z_i; this resolution is typical of many LES CBL simulations. For run C, $Re_S = 23$. We set the Schmidt number to its value in air, 0.7 for all three runs.

For all three cases we ran the simulations for a time interval of $0.1\tau_{LE}$; this is equivalent to $1.5z_i/w_*$ (Krueger 1992). We collected 200-bin pdfs at 31 observation times during a series of 100 realizations for each case. Cases B and C used 4 and 8 adjacent domains, respectively, of length z_i for computational efficiency.

The evolution of the pdfs for these three cases (see Fig. 2) is qualitatively similar. The initial pdf in all three cases consists of two spikes: one at $\chi = 0$ representing 95% of the original, unmixed fluid; and one at $\chi = 1$ representing the remaining 5%. As time proceeds, the two consituents mix under the combined action of the rearrangement events, which represent the effects of turbulent eddies (and exactly conserve grid-point scalar concentrations), and molecular diffusion. After only one large-eddy turnover time, the fluid is yet not homogenized. After several large-eddy turnover times, the pdf becomes a spike at the mixture fraction, 0.05 (not shown). The lower-Re cases show that spatial resolution comparable to that of a LES leads to more rapid mixing than in the high-Re case.

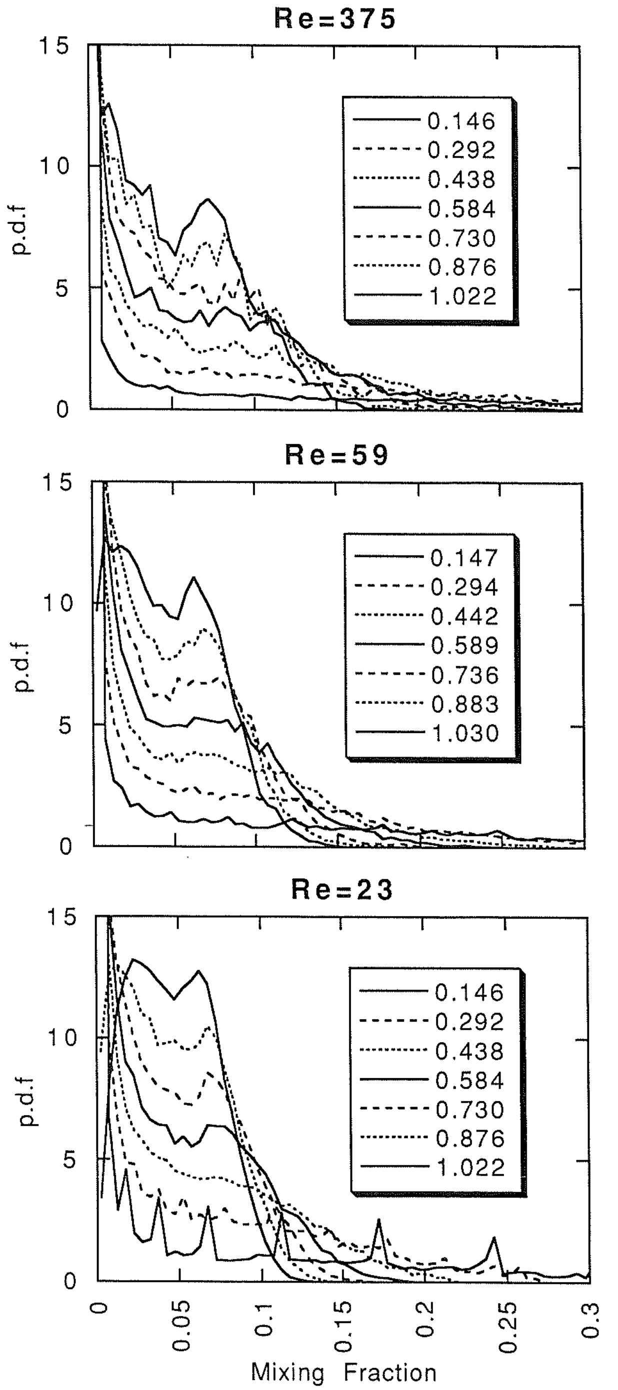

Fig. 2. Time evolution of the pdfs of χ for (a) $Re_S = 375$, (b) $Re_S = 59$, and (c) $Re_S = 23$. The times (indicated in the legends) are scaled by the large-eddy turnover time, z_i/w_*.

4 Calculation of Mean Buoyancy

Once the evolution with time (or height) of the pdf is calculated, we can determine the mean buoyancy of the mixture. In the case we are considering, we begin with two distinct air masses: the entrained air, which has properties of the non-turbulent air immediately above the boundary layer top, and the boundary layer air, which is assumed to be characterized by the mean properties of the boundary layer. The density of a mixture at a height z consisting of a mass fraction χ of entrained air and mass fraction $1-\chi$ of boundary layer air is denoted $\rho(\chi, z)$. We define the buoyancy $b(\chi, z)$ of such a mixture relative to the unmixed boundary layer air as

$$b(\chi, z) \equiv g \frac{\rho(0,z) - \rho(\chi, z)}{\rho(0,z)}.$$

In the atmosphere, $b(\chi, z)$ has the following piece-wise linear form (Siems et al. 1990):

$$b(\chi, z) = \left\{ \begin{array}{ll} b_2 \chi & \text{if } \chi \le \chi^*(z) \\ b_1 \chi + (b_2 - b_1)\chi^* & \text{otherwise} \end{array} \right\}$$

where χ^* is the just-saturated mixing fraction. An example is shown in Fig. 3. If both air masses are unsaturated (and remain unsaturated during mixing) $b(\chi, z)$ is simply a linear function of the mixing fraction, and the mean buoyancy, $\bar{b}(z)$, is the just the buoyancy of the mean mixing fraction: $\bar{b}(z) = b(\bar{\chi}, z)$. In this case, knowledge of the details of the mixing process (i.e., the pdf evolution) is not needed to calculate $\bar{b}$. However, when some mixtures are saturated (i.e., when $\chi^* > 0$), $\bar{b}$ can no longer be determined from $\bar{\chi}$ alone. The mixing fraction of the most negatively-buoyant mixture is denoted $b^*(z) = b(\chi^*, z)$; its mixing fraction is $\chi^*(z)$.

5 Results

We have calculated the evolution of the mean buoyancy using several buoyancy functions and the pdfs shown in Fig. 2. The results are presented in Figs. 4-8. In these figures, the profiles are plotted versus z/z_B by assuming that the Lagrangian slab descends at a constant rate w^*. The mean buoyancy profiles thus obtained do not in themselves allow a criterion for CEI to be established since the turbulence dynamics are prescribed. However, they do allow a quantitative evaluation of the assumptions used in previous studies of CEI regarding the small-scale mixing process.

Our control case (the solid profile in Figs. 4-8) uses the high-*Re* pdfs and the buoyancy function $b(\chi, z)$ used by Siems et al. (1990) for their experiment "CLD". The parameters chosen for this case correspond to a cloud with 0.24 g/kg liquid water, a 3.76 K jump in buoyancy across cloud top, 0.2 K maximum negative buoyancy available from mixing at cloud top, cloud top at 500 m, and cloud depth of 167 m.

Fig. 4 compares two extreme mixing scenarios with the control case (CLD). The "instant mixing" case reproduces the situation addressed by Randall (1980). The "no mixing" case illustrates the opposite extreme. CLD is more similar to the no mixing case than the instant mixing case.

Fig. 5 compares profiles obtained by varying $\chi_B^* \equiv \chi^*(z_B)$ but keeping $D \equiv -b^*(z_B)/b(1, z_B)$ constant at 0.0532. The larger value of χ_B^* results in less mean buoyancy in the cloud layer.

Fig. 6 shows that a deeper cloud layer allows greater mean buoyancy reductions to occur in the cloud layer for the same χ_B^* and D. Figs. 5 and 6 suggest that D may not be the only non-dimensional parameter relevant to CEI.

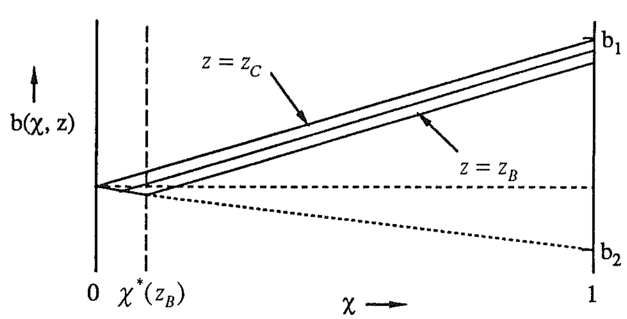

Fig. 3. The mixing curve $b(\chi, z)$ (after Siems et al. 1990).

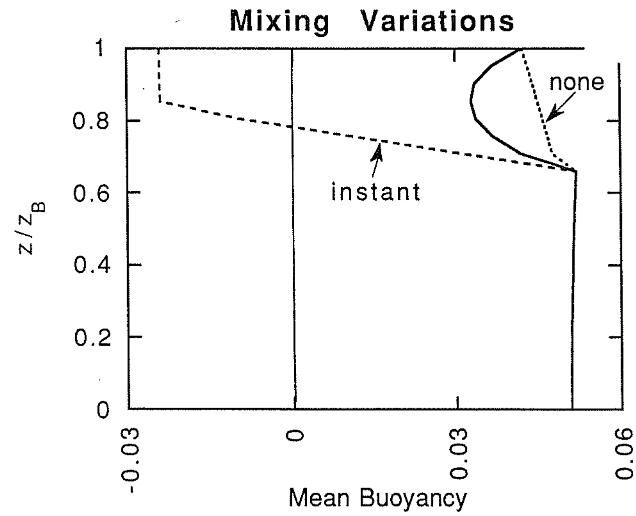

Fig. 4. Mean buoyancy profiles for three mixing scenarios.

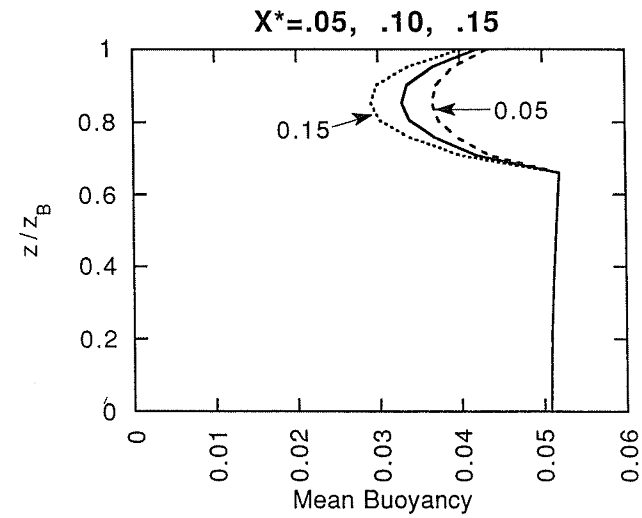

Fig. 5. Mean buoyancy profiles for three values of $\chi^*(z_B)$.

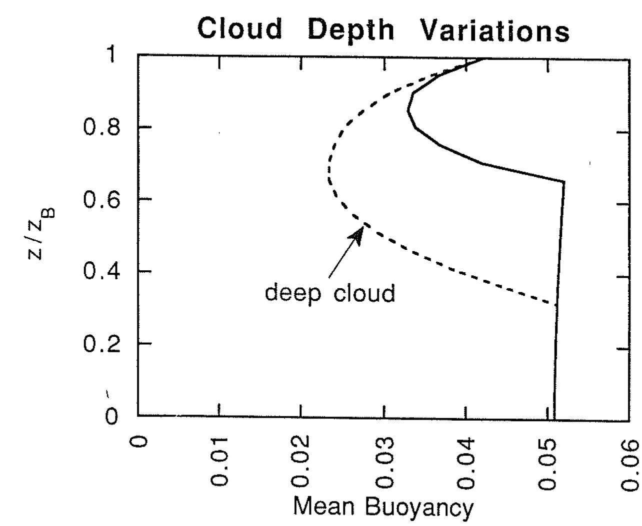

Fig. 6. Mean buoyancy profiles for two cloud depths.

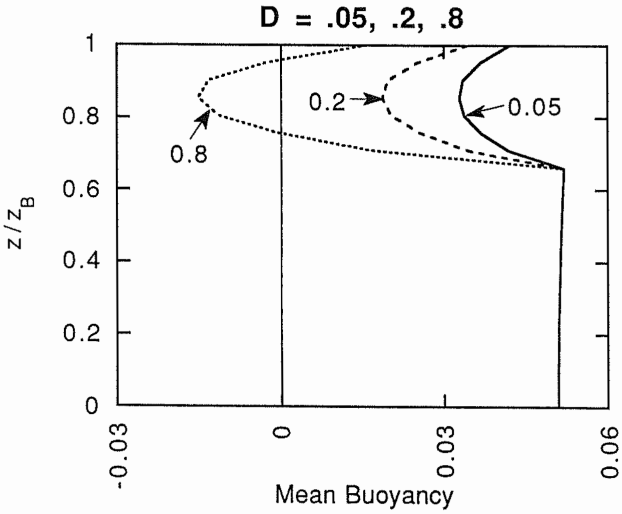

Fig. 7. Mean buoyancy profiles for three values of D.

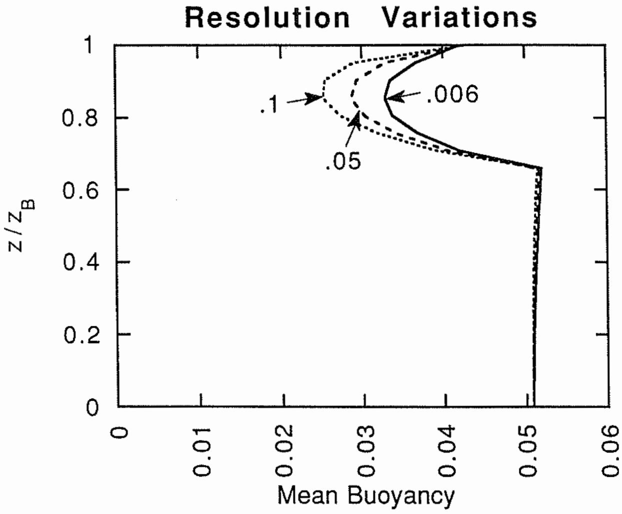

Fig. 8. Mean buoyancy profiles for three different spatial resolutions. Labels indicate grid size scaled by z_B.

Siems et al. (1990) report that $0 < D < 0.2$ in stratus clouds. Fig. 7 compares profiles obtained by varying D while maintaining χ_B^* at 0.1. Only for D greater than about 0.5 does the mean buoyancy ever become negative in this case.

Fig. 8 shows that the decreased resolution of a typical LES significantly reduces the mean buoyancy in the cloud layer. As noted in the introduction, this may explain why low-resolution LES simulations have exhibited CEI under conditions for which CEI is not observed in the atmosphere.

Acknowledgements. This research was supported by ONR grant N00014-91-J-1175. A grant of computer time from the Utah Supercomputer Institute, which is funded by the State of Utah and the IBM Corporation, is gratefully acknowledged.

REFERENCES

Baker, M. B., R. E. Breidenthal, T. W. Choularton, and J. Latham, 1984: The effects of turbulent mixing in clouds. *J. Atmos. Sci.*, **41**, 299-304.

Broadwell, J. E., and R.E. Briedenthal, 1982: A simple model of mixing and chemical reaction in a turbulent shear layer. *J. Fluid Mech.*, **125**, 397-410.

Deardorff, J. W., 1980a: Cloud top entrainment instability. *J. Atmos. Sci.*, **37**, 131-147.

Deardorff, J. W., 1980b: Stratocumulus-capped mixed layers derived from a three-dimensional model. *Bound.-Layer Meteor.*, **18**, 495-527.

Kerstein, A. R., 1988: Linear eddy modeling of turbulent scalar transport and mixing. *Comb. Sci. and Technol.*, **60**, 391-421.

Kerstein, A. R., 1991: Linear-eddy modelling of turbulent transport. Part 6. Microstructure of diffusive scalar mixing fields. *J. Fluid Mech.*, **231**, 361-394.

Krueger, S. K., 1992: Entrainment and mixing in stratus clouds. *J. Atmos. Sci.*, (submitted).

Kuo, H.-C., and W. H. Schubert, 1988: Stability of cloud-topped boundary layers. *Quart. J. Roy. Meteor. Soc.*, **114**, 887-916.

McMurtry, P. A., T. C. Gansauge, A. R. Kerstein, and S. K. Krueger, 1992: Linear eddy simulations of mixing in a homogenous turbulent flow. *Phys. Fluids*, (submitted).

Moeng, C.-H., 1986: Large-eddy simulation of a stratus-topped boundary layer. Part I: Structure and budgets. *J. Atmos. Sci.*, **43**, 2886-2900.

Moeng, C.-H., and U. Schumann, 1991: Composite structure of plumes in stratus-topped boundary layers. *J. Atmos. Sci.*, **48**, 2280-2291.

Randall, D. A., 1980: Conditional instability of the first kind, upside-down. *J. Atmos. Sci.*, **37**, 125-130.

Schmidt, H., and U. Schumann, 1989: Coherent structure of the convective boundary layer derived from large-eddy simulations. *J. Fluid Mech.*, **200**, 511-562.

Siems, S. T., C. S. Bretherton, M. B. Baker, S. Shy, and R. T. Breidenthal, 1990: Buoyancy reversal and cloudtop entrainment instability. *Quart. J. Roy. Meteor. Soc.*, **116**, 705-739.

Stull, R. D., 1973: Inversion rise model based on penetrative convection. *J. Atmos. Sci.*, **30**, 1092-1099.

Tag, P. M., and S. W. Payne, 1987: An examination of the breakup of marine stratus: A three-dimensional numerical investigation. *J. Atmos. Sci.*, **44**, 208-223.

Willis, G. E., and J. W. Deardorff, 1979: Laboratory observations of turbulent penetrative- convection planforms. *J. Geophys. Res.*, **84**, 295-301.

A 3-D large-eddy simulation model of a stratocumulus cloud layer with explicit formulation of microphysical and radiative processes

Yefim L. Kogan, Douglas K. Lilly, Zinaida N. Kogan, and Victor V. Filyushkin

Cooperative Institute for Mesoscale Meteorological Studies
University of Oklahoma, Norman OK

1. Introduction

The climatic significance of the marine stratocumulus cloud layers is well established. Because they usually lie within a km of the ocean surface, the temperature of their tops is only a few degrees lower than that of the ocean surface, so that their greenhouse warming effect is nearly negligible. Thus they contribute substantially to oceanic and global cooling. It is estimated (Ramanathan, 1989; FIRE 1989) that an increase of a few percent of low cloud cover, or a comparable increase in its albedo, would counter the anticipated greenhouse warming of the next century, while similar decreases would double the warming. The conclusion is based on the work of Twomey (1977) who pointed out that cloud albedo is dependent on drop size distributions which, in turn, depend on cloud condensation nuclei (CCN).

Many theoretical and numerical studies have shown that spatial and temporal changes in cloud microstructure significantly affect the cloud radiative characteristics. Stephens (1984) showed that both solar heating and IR cooling within cloud layers are very sensitive to liquid water content, and somewhat less so to drop size distribution. Cloud albedo, however, is highly dependent on drop-size distribution for a given liquid water content. The importance of cloud microphysics is further emphasized by studies showing the apparent sensitivity of stratocumulus clouds to anthropogenic addition of heat, smoke, and water vapor by steamship passages. Ship condensation trails are commonly observed by satellite, and may last for hundreds of km and many hours. These trails are reported (Radke et al, 1988) to be visually thickened and brightened parts of otherwise translucent cloud layers. One might expect this to be the result of a large increase in condensation nuclei in a region relatively devoid of them, thereby producing a more reflective cloud of many small droplets.

Aerosols also can significantly affect the precipitation efficiency of the stratocumulus cloud layers due to their high sensitivity to the drizzle process (Albrecht, 1989). The increase in the CCN concentrations will reduce the dispersion of cloud drop spectra and increase the clouds colloidal stability, thereby resulting in increased cloud cover and longevity.

The complex interactions between different physical processes in cloud formation and evolution on a wide range of scales make the development of accurate cloud parameterizations for global climate and GCM models quite a difficult task. One tool that can improve our understanding of the complex interactions between all these processes and serve as a basis for the development of more accurate parameterizations is a high-resolution model that explicitly formulates microphysical and radiative processes on a physical rather than empirical ground.

In this paper, after describing the model developed along the above mentioned lines, we show the early results from a numerical simulation, primarily to demonstrate its potential. More detailed study of stratocumulus cloud layer evolution will be presented in the future.

2. Model description

The dynamical framework of our model is taken from the 3-D LES model developed by Moeng (1984). It computes the horizontal derivatives by means of pseudospectral discretization in the horizontal and central finite differences in the vertical. The subgrid-scale eddies are parameterized through Deardorff's (1980) turbulence energy closure model and the long wave radiation is parameterized according to Herman and Goody (1976).

The cloud physics formulation follows that of Kogan (1978, 1991) and includes processes of nucleation, condensation, evaporation, and coalescence. Two distribution functions considered in the model- one for cloud condensation nuclei (19 categories from 0.0076 to 7.6 micron) and another for cloud drops (22 categories on a logarithmic scale from 1 to 128 microns) - allow prediction of the aerosol and drop spectra starting from activation up to drizzle formation. The simulation presented here has been made with 40^3 grid points covering the $(2\text{km})^3$ domain. The initial mean environment had the top of the PBL at 1 km and a temperature jump of 12 K over an inversion layer 400 m deep. Following Moeng (1976) we specify initially a uniform cloud at the inversion base with LWC= 0.1 g/m^{-3}. The cloud layer is 200 m deep and is formed by cloud droplet spectra defined according to the Khrgian-Mazin distribution with a mean radius of 3.5 micron. Initially, a small amount of random noise was applied to the temperature field near the surface to initiate the turbulent motion.

3. Results

To demonstrate the model performance and potential we show the results from a simulation of a cloud-topped boundary layer (CTBL) during its transition from convective to a well-mixed quasi stationary stage. Fig. 1 shows a cross-section of the velocity field at 5 and 15 min from the beginning of cloud formation. The small scale structures in the stably stratified layer above the cloud top, ~ 0.8 km, are the internal gravity waves excited by the updrafts interacting with the inversion layer (Moeng, 1976). The size of thermal elements at this time is from 200 to 600 m and the subgrid scale turbulent energy is comparable to that of the resolvable large eddies. Fig. 2 illustrates the process of breakup of the initially homogeneous cloud layer. The understanding of cloud breakup mechanisms is especially important for radiation parameterization in global climate models and will require a thorough analysis of each individual physical processes involved.

The isolines of CCN concentrations and supersaturation shown on Figs. 3 and 4 demonstrate that the activation zones at 300 sec are located at cloud base, ~ 0.55 km. At later times, however, most of the new droplet growth is near the cloud top. This is indicated by the shifting of the maximum values of supersaturation and minimum of CCN concentration towards the cloud top. As Fig. 3 indicates, at 900 sec rather large regions near the cloud top contain very small number of cloud condensation nuclei. The prime cause of this is strong radiative cooling near the cloud top. It results in large supersaturations and, consequently, CCN sink through droplet activation and growth. On the other hand, droplets activated near cloud top will easily evaporate and regenerate CCN. Our results indicate that the mechanism of CCN regeneration after evaporation process may be quite crucial in the physical formulation of the stratocumulus cloud layers. We plan to test several

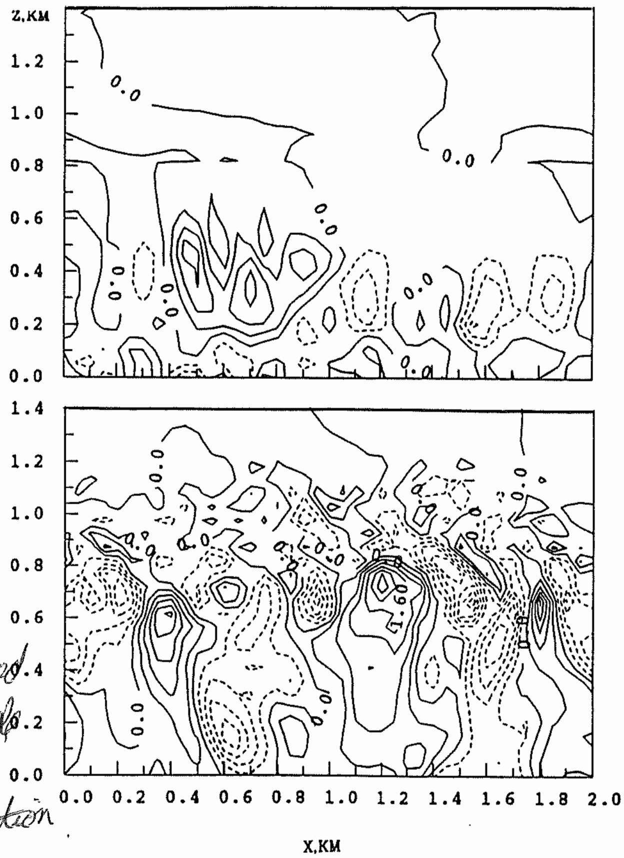

Fig. 1. Isolines of vertical velocity in the x-z cross-section at y=0.45 km. Top panel is for 300 sec, bottom panel - 900 sec. Contour interval is 0.4 m/s.

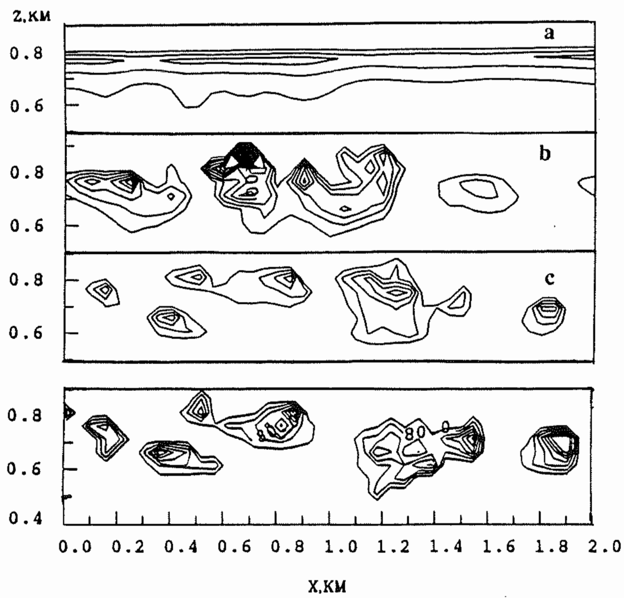

Fig. 2. Top-isolines of LWC in the x-z cross-section at y=0.45 km. a- 300 sec, b-600 sec, c- 900 sec. Contour interval is 0.1g m $^{-3}$. Bottom - isolines of concentration of cloud droplets at the same cross-section at 900 sec.

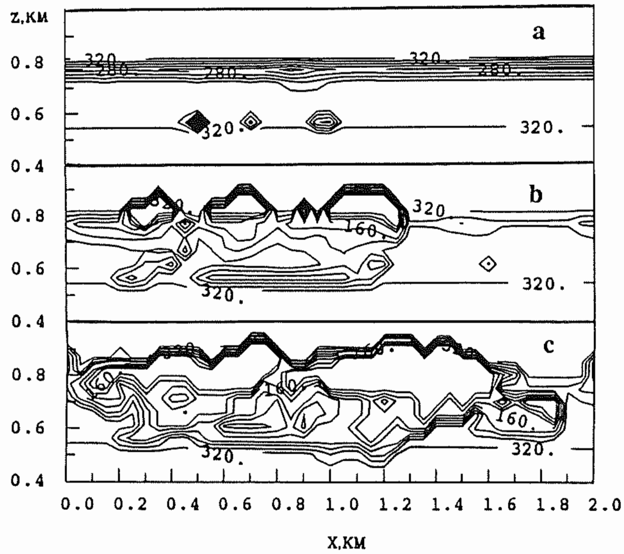

Fig. 3. Isolines of CCN concentration in the x-z cross-section at y=0.45 km at: a- 300 sec, b-600 sec, c- 900 sec. Contour interval is 10 cm $^{-3}$ for plot a, and 40 cm $^{-3}$ for b and c.

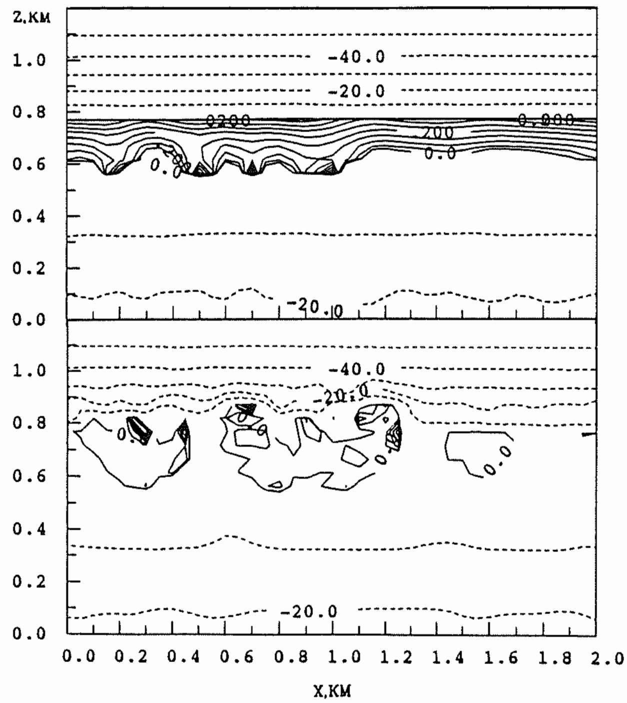

Fig. 4. Isolines of supersaturation at 300 sec (top), and 600 sec (bottom). Contour interval is 10% for negative values; for positive values it is 0.05% on the top plot and 0.2% on the bottom.

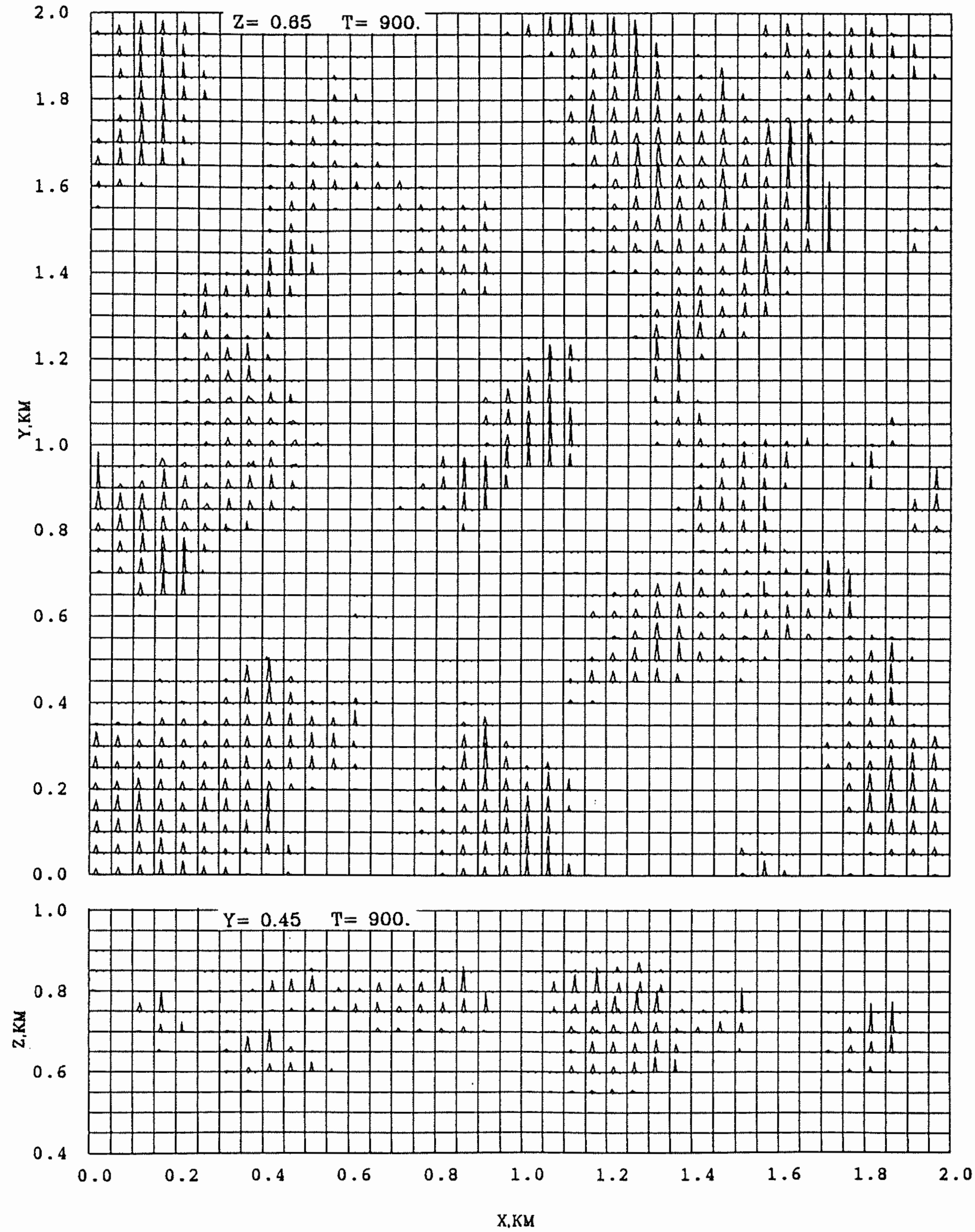

Fig. 5. Cloud droplet distribution functions are shown at cross-sections identified in the plot. At each grid point the square box represents the plot the droplet mass distribution function Vs log r.

computer code

parameterization of CCN regeneration and their effect on the aerosol balance in the nearest future.

Examples of cloud droplet spectra predicted by the model are shown in Fig. 5. Bimodal distributions of drop spectra are seen at certain points in cloud. As coagulation was turned off in the present simulation, the effect is entirely due to repeated activation and mixing. Evidently the assumption sometimes used in simplified cloud models that nucleation occurs only at cloud base may result in large error in cloud microphysics. The highly variable character of cloud microphysics evident from Fig. 5 leads to significant scatter in effective radius, which is of crucial importance in assessments of the cloud radiative properties in global climate models (Fig. 6). The large variation in the value of the effective radius may, however, be partially due to the rather small size of the simulated clouds and, evidently, greater impact of mixing with environmental dry air. In the case of a continuous stratocumulus cloud layer, the microphysics may be more uniform and easier to parameterize.

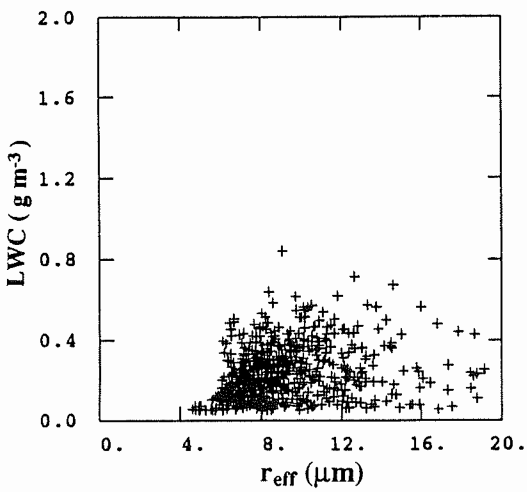

Fig. 6. The variation of effective radius and liquid water content at height 0.65 km and time 900 sec.

4. Conclusions

Preliminary results for a new model that includes 3-D LES dynamical framework and explicit formulation of cloud microphysics have been presented primarily to demonstrate the model's performance and potential. We are planning a more extensive set of experiments to study the effects of atmospheric aerosol on cloud thermodynamic, microphysical and radiative parameters.

Acknowledgments. The help of Jeff Castle in preparing the plots is gratefully acknowledged. Support for this research was provided by NOAA's Climate and Global Change Program under the Grant NA16RC0117.

References

Albrecht, B. A., 1989: Aerosols, cloud microphysics, and fractional cloudiness. *Science,* **245**, 1227-1230.

Deardorff, J. W., 1980: Stratocumulus-capped mixed layers derived from a three-dimensional model. *Bound. Layer Meteorol.*, **18**, 495-527.

Herman, G.F., and R. Goody, 1976: Formation and persistance of summertime Arctic stratus clouds. *J. Atmos. Sci.,* **33**, 1537-1553.

Kogan, Y. L., 1978: A three-dimensional numerical model of a liquid-drop cumulus cloud that takes account of microphysical processes. *Izv. Akad. Sci. USSR, Atmos. Ocean. Phys.*, **14**, 617-623.

Kogan, Y. L., 1991: The simulation of a convective cloud in a 3-D model with explicit microphysics. Part I: Model description and sensitivity experiments. *J. Atmos. Sci.,* **48**, 1160-1189.

Moeng, C.-H., 1984: A large-eddy simulation model for the study of planetary boundary layer turbulence., *J. Atmos. Sci.* , **41**, 2052-2062.

Moeng, C.-H., 1986: Large-eddy simulation of a stratus-topped boundary layer. Part I: Structure and budgets. *J. Atmos. Sci.* , **43**, 2886-2900.

Nicholls, S., 1984: The dynamics of stratocumulus: Aircraft observations and comparisons with a mixed-layer model. *Q. J. R. Meteor. Soc.*, **110**, 783-820

Radke, L. F., J. H. Lyons, P. V. Hobbs, and J. E. Coakley, 1988: In situ measurements of "ship tracks" . Preprints for 10-th Intern. Cloud Phisics Conf., Bad Homburg, FRG, August 15-20, 1988. pp. 121-123, (vol. 1).

Ramanathan, V., R. D. Cess, E. F. Harrison, P. Minnis, B. R. Barkstorm, E. Ahmad, D. Hartman, 1989: Cloud-radiative forcing and climate: Results from the earth radiation budget experiment. Science, 243, 57-63.

Stephens, G. L., 1984: The parameterization of radiation for numerical weather prediction and climate models. *Mon. Wea. Rev.*, **112**, 826-867

Twomey, S., 1977: The influence of pollution on the shortwave albedo of clouds. *J. Atmos. Sci.*, **34**, 1149-1152.

A FOG-TO-CLOUD TRANSITION

James W. Telford and Steven K. Chai
Atmospheric Sciences Center, Desert Research Institute
Reno, Nevada 89506-0220
USA

1. INTRODUCTION

The importance of marine stratus clouds in determining the albedo of the earth in its response to global climate change is now well recognized. However the models of these processes have been hampered by two constraints: (1) the insufficient recognition of the need for trustworthy observational data, and (2) the flourishing development of computer programs based on unfounded conjectures about the physics and the role of horizontal averages (Telford, 1992).

Models are an essential part of science in the sense that conceptual structures, which include the known facts, allow us to predict the future state of a physical system beginning at a known state. However our experience shows, until the physics is understood, little progress can occur.

2. MARINE STRATUS CLOUDS AND FOG

Radiation has been conjectured as an essential element in the formation of marine stratus clouds since Petterson (1938). He postulated that, since a warm off-shore wind in southern California often later resulted in a fog drifting on-shore, thermal driven convection was needed to cool the warm air and increase its water mixing ratio. The essential missing element in this argument is the cooling of the air once saturated parcels form with condensed water. Mixing of subsaturated warmer air with these drops can cool the dry air to its wet bulb temperature, which when it is cooler than the sea, as it often is, drives convective mixing.

Furthermore, until the surface air is saturated in fog, the water vapor itself creates buoyant parcels at the surface. Thus the water can cool a layer to sea surface temperature if the wet bulb potential temperature is lower than the sea temperature, even when the actual temperature of the air is ten degrees or more warmer than the water (Telford and Chai, 1984). If, at less than a few hundred meters altitude, the wet bulb potential temperature of the air is the same as the sea surface temperature only a shallow layer needs to become saturated to form fog.

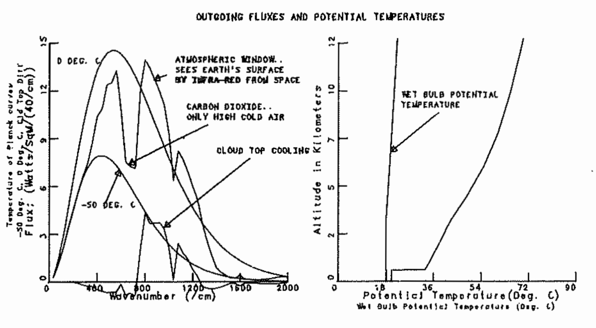

Figure 1.This shows the total radiation emitted to space, and the heat loss from the top 11 m of marine stratus cloud. Two black body emission curves are icluded, and the vertical thermal structure. Cloud top is near 600 m and it is about 200 m thick. The total heát loss fron 700 to 1200 cm⁻¹ comes mostly from the cloud.

Thus radiation is not an essential component of sea fog or stratus formation as the simple argument maintains, and the question becomes one of determining the role of radiation. Measurements showing these conditions are given below.

3. RADIATION THEORY

The radiation exchange between parcels of clear air is mostly dominated by the exchange over distances of many hundreds of meters where subsaturated temperature differences exist in the vertical. Very highly absorbent wavelengths, including most of the CO_2 bands, are ineffective because the return radiation comes from short distances where the returning radiation originates in molecules of almost the same temperature, and hence the quantity of heat returned is almost the same as that lost. Similarly, where the air is transparent, in the atmospheric window, the air does not radiate, and hence loses heat. The effective heat transfer between air parcels is mostly from water vapor at intermediate absorption.

Two exceptions to these general arguments occur at the top of marine stratus clouds. First the very high temperature gradients, say 10°C in 10 m, make the cooling of the warm air just above clouds very large because of the highly absorbing bands, such as some water bands and CO_2. Second, the water drops in the cloud, if they behave as a

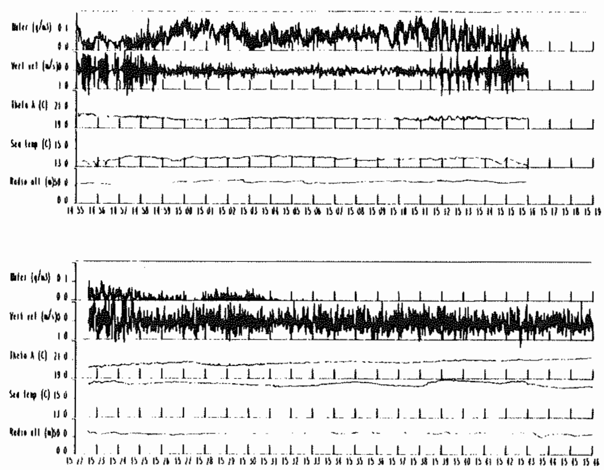

Fig. 2. Time series including fog over cooler water, and the clearing region beyond. The data traces, from the top in each segment, represent liquid water mixing ratio, vertical motion, absolute potential temperature, sea surface temperature and altitude.

black substance like bulk water, will radiate strongly where the air is transparent. These rays are lost directly into space with no return heat; producing strong cooling. Fig. 1 shows the radiation loss from a marine stratus cloud top through the window, and the total upwelling radiation at the top of the atmosphere. The net heat loss from the top of the atmosphere exceeds 100 W m^{-2}.

The surface flux of convective heat from dry land at mid latitudes in early summer is typically about 250 W m^{-2}, and this produces vigorous turbulent convection. Thus 100 W m^{-2}. Cooling at fog top would similarly produce vigorous convection if it occurred.

4. OBSERVATIONS OF MARINE FOG AND CLOUD

The observations were obtained on September 25, 1981 over the ocean west of San Francisco using an NCAR Queen Air aircraft. The aircraft flew due west from the coastline for about 200 miles over the ocean, at about 60 m above the water. The coastal water for about 120 miles has a surface temperature of about 14°C, whereafter, proceeding west, the surface water temperature increases by about 3°C over a few hundred feet.

A satellite photo shows that the cloud or fog extends from the coast to a mile or so before the 126°W meridian of longitude. The cloud tops show a higher visible brightness from 124°W to the western edge with the foggy region next to the shore not so bright. The aircraft flew to beyond the cloud edge before returning.

There was a slight easterly wind in the fog and the cloud descended to the surface a few miles off shore. The air was well mixed vertically below cloud or fog top with a temperature increase of about 6°C at the inversion and an increase in wet bulb potential temperature of 2°C. At higher levels the wet bulb potential temperature was variable, reflecting the previous addition of moisture over land to the levels above the inversion.

Most of the flight was at constant level in fog and the liquid water mixing ratios and the vertical velocities are shown in Fig. 2.

When the fog descends to the surface, as encountered at 1449 LST, the variations in vertical velocity become about 0.1 m s^{-1}, which is about system noise. Convective transfer effectively stops, while the liquid water mixing ratio remains highly variable. At about 1513 LST the turbulence in the vertical velocity becomes more prominent and increases to 1515 LST and remains at about 0.5 m s^{-1} average until the end of the record at 1546 LST.

The liquid water mixing ratio begins decreasing at 1515 LST and decreases to zero at 1534 LST as the fog rises and the cloud soon totally evaporates. The sea surface temperature is about 14°C until 1516 LST, but has increased to 17°C by 1523 LST where the liquid water content begins reducing to zero. Here there was very little wind.

The mean drop size and the drop concentrations are shown in Fig. 3a. As is typical for marine stratus clouds the mean drop size is not very variable, around 10 lm, compared to the variation in drop concentrations from a few cm^{-3} to 300 cm^{-3}

This is the result of the entity type entrainment mixing (ETEM) at cloud top (probably before the fog reached the surface). Fig. 3b shows how the more diluted cloud contains more warm air from above cloud top.

5. DISCUSSION

There is no overlaying cloud so the radiative cooling above cloud top is essentially similar between the fog and the cloud. There is effectively no turbulence in fog but the approach to the warm water shows how this produces turbulence and a rising fog with a cloud base increasing upwards until all the cloud evaporates.

a. The fog is over the cooler water where the cloud base descends to the surface.

b. The large theoretical cooling due to radiation does not produce vertical stirring and so is not occurring here. Either the sun exactly balances the cooling or some other unknown process prevents heat removal.

c. The convection begins to stir the air when the warm water is reached and the main effect
is to increase the entrainment of dry air at cloud tops. This evaporates the cloud eventually although the albedo increases at first.

Thus the common conjectures that radiative cooling creates fog is not supported by the evidence.

6. REFERENCES

Petterssen, S., 1938: On the causes and the forecasting of the California fog. *Bull. Amer. Meteor. Soc.*, *19*, 49-55.

Telford, J.W. and S.K. Chai, 1984: Inversions, and fog, stratus and cumulus formation in warm air over cooler water. *Boundary-Layer Meteorol.*, *29*, 109-137.

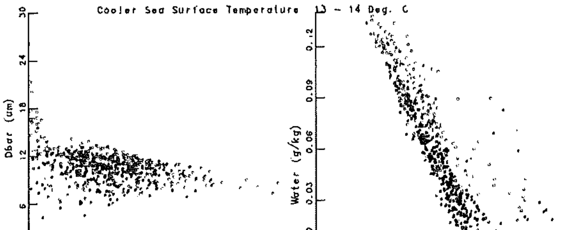

Figure 3. The mean drop size is relatively constant and does not correlate with the large variations in drop concentration. The liquid water mixing ratio decreases as absolute potential temperature (constant in a well mixed cloud) increases. This shows that more subsaturated air from above cloud top with a higher temperature, both dilutes the cloud more, and increases its temperature. The ETEM ensures that the cloud dilution reduces drop numbers but not sizes.

A NUMERICAL STUDY OF STRATUS CLOUDS:
RADIATIVE AND PRECIPITATION SENSITIVITY TO MICROPHYSICS

Jean-Pierre Pinty and Peter Bechtold

Laboratoire d'Aérologie
Université Paul Sabatier
118, route de Narbonne
31062 Toulouse Cedex, France

1. INTRODUCTION

The stability of stratocumulus decks can be altered by the simple fact of changing the cloud droplet concentration (N_{cw}). Clearly, the sensitivity of these shallow clouds to N_{cw} is twofold. First, the cloud droplets are efficient scatter sites and thus increasing their number concentration reduces the net solar radiative fluxes. When radiative absorption is strong enough, a stratus layer can be sufficiently heated to become thermodynamically decoupled from its subcloud layer. Besides, considering cloud physics processes, one can also expect a great sensitivity of the long-term stability of these boundary-layer clouds depending on their efficiency to drizzle out. As the cloud droplet to rain drop conversion is a delicate mechanism which depends primarily on the cloud droplet spectrum, one can speculate a complex turbulence-cloud physics interaction.

This study describes some improvement made in a 1D version of the cloud topped boundary layer (CTBL) model of Bechtold et al. (1992, hereafter BFP92) for simulating both radiative and precipitating processes in stratus clouds. To account for the cloud-radiation interactions, an effective radius (and so the optical thickness) is computed on each vertical level of the cloud. Furthermore, the microphysical scheme of Richard and Chaumerliac (1989, hereafter RC89) has been incorporated in the CTBL model to simulate the effect of drizzle. Compared to the widely used Kessler's scheme, this scheme seems more suitable to describe shallow low-precipitating clouds as both rain water contents and rain drop concentrations are predicted. The main assumptions of this scheme are the steadiness of the vertically homogeneous N_{cw} and also the constraint that the cloud droplet size distribution follows a log-normal density function.

A short summary of the model content is presented in Section 2. Then several cases of diurnal radiative evolution of a stratus deck, obtained by varying the initial cloud droplet concentrations for a single sounding, are analysed in Section 3. In Section 4, we discuss a case of drizzle formation and the consequent modification of the stratus cloud properties. Finally, a conclusion is drawn on the importance of these two processes in CTBL modelling. Further possible refinements of the model are also suggested.

2. MODEL DESCRIPTION

2.1 Basic equations

The basic model comes from the work of BFP92. Reversible processes such as condensation and evaporation of cloud water, are solved implicitly from the prediction of two quasi conservative thermodynamical variables which are the liquid water potential temperature θ_l, and the total moisture mixing ratio q_w, defined as:

$$\theta_l = \theta(1 - \frac{Lq_l}{C_pT}) = \theta_e - \theta\frac{Lq_w}{C_pT} \quad (1)$$

$$q_w = q_v + q_l = q_v + q_{cw} + q_{rw} \quad (2).$$

All the notations are classical, the subscript l stands for the total condensed phase (cloud water with $_{cw}$ and rain water with $_{rw}$) while v stands for the water vapor phase.

The basic equations of the model are:

$$\frac{\partial u}{\partial t} = -w\frac{\partial u}{\partial z} + f(v - v_g) - \frac{\partial}{\partial z}\overline{w'u'} \quad (3)$$

$$\frac{\partial v}{\partial t} = -w\frac{\partial v}{\partial z} - f(u - u_g) - \frac{\partial}{\partial z}\overline{w'v'} \quad (4)$$

$$\frac{\partial \theta_l}{\partial t} = -w\frac{\partial \theta_l}{\partial z} + \frac{\partial \theta_l}{\partial t}|_{rad} + \frac{\partial \theta_l}{\partial t}|_{rain} - \frac{\partial}{\partial z}\overline{w'\theta_l'} \quad (5)$$

$$\frac{\partial q_w}{\partial t} = -w\frac{\partial q_w}{\partial z} - \frac{\partial q_w}{\partial t}|_{rain} - \frac{\partial}{\partial z}\overline{w'q_w'}. \quad (6)$$

The diabatic term, $\frac{\partial \theta_l}{\partial t}|_{rad}$ in (5), includes both longwave and shortwave radiative processes. The drizzle sedimentation terms, labelled $\frac{\partial \theta_l}{\partial t}|_{rain}$ in (5) and $\frac{\partial q_w}{\partial t}|_{rain}$ in (6), are a heat source for θ_l but a moisture sink for q_w. The turbulent fluxes $\overline{w'\chi'}$, where χ is any of the prognostic variables in Eqs. (3) to (6), are calculated with the classical K-closure mixing coefficient :

$$\overline{w'\chi'} = -K\frac{\partial \chi}{\partial z} \quad (7)$$

$$K = c_K l_K e^{1/2}. \quad (8)$$

l_K is a characteristic mixing length and e is the prognosed turbulent kinetic energy :

$$\frac{\partial e}{\partial t} = -w\frac{\partial e}{\partial z} - g\frac{\overline{w'\theta_{vl}'}}{\theta_0} - \overline{w'u'}\frac{\partial u}{\partial z} - \overline{w'v'}\frac{\partial v}{\partial z} - \frac{\partial}{\partial z}(\overline{w'e} - \frac{\overline{w'p'}}{\rho}) - c_\epsilon\frac{e^{3/2}}{l_\epsilon}, \quad (9)$$

with l_ϵ, the dissipation length and $\theta_{vl} = \theta\,(1 + 0.61\,q_w - 1.61\,q_l)$, the virtual potential temperature defining the buoyancy flux in (9).

The model has also a gaussian subgrid scale condensation scheme to allow for a fractional cloudiness N and its associated mean cloud water content $\overline{q_{cw}}$. All the details concerning the turbulent closure and the computation of the length scales are available in BFP92.

2.2 Radiative scheme

Due to infrared cooling in the upper part of the cloud (and a slight heating in the lower part) and also due to shortwave diurnal absorption, radiation processes strongly interact with the clouds (Fravalo et al., 1981) and so affect the dynamics of the CTBL. In the model, accurate radiative computations are performed with the ECMWF radiation scheme, based upon earlier works of Fouquart and Bonnel (1980) and Morcrette and Fouquart (1985). The only departure from the original ECMWF scheme (Morcrette, 1989) is that an effective radius r_e, proportionnal to the ratio of the total volume to the total surface of the droplet distribution, is defined as:

$$r_e = (\frac{3\,\rho_a\,q_{cw}}{4\pi\,\rho_w\,N_{cw}})^{1/3} exp(\sigma_{cw}^2), \quad (10)$$

where ρ_a (ρ_w) is the density of the air (liquid water) and σ_{cw}, a variance parameter of the cloud droplet distribution with a value of 0.2775 for typical maritime clouds as recommended by RC89. Thus the optical thickness δ, given by:

$$\delta = \frac{3\,W}{2\,r_e}, \quad (11)$$

with W being the liquid water path, is used to compute the radiative properties of the cloud along its depth.

2.3 Microphysical scheme

The complete description and some properties of the microphysical scheme are exposed in RC89. As for the cloud droplets, the rain drops are assumed to fit with a log-normal distribution provided an extra value for the variance parameter σ_{rw}. Here, we only recall the microphysical processes involved in the parameterization:

$$\frac{\partial q_{rw}}{\partial t} = -w\frac{\partial q_{rw}}{\partial z} + \frac{\partial q_{rw}}{\partial t}|_{auto} + \frac{\partial q_{rw}}{\partial t}|_{accr} - \frac{\partial q_{rw}}{\partial t}|_{evap} + \frac{\partial q_{rw}}{\partial t}|_{sedi} \quad (12)$$

$$\frac{\partial N_{rw}}{\partial t} = -w\frac{\partial N_{rw}}{\partial z} + \frac{\partial N_{rw}}{\partial t}|_{auto} - \frac{\partial N_{rw}}{\partial t}|_{self} - \frac{\partial N_{rw}}{\partial t}|_{evap} + \frac{\partial N_{rw}}{\partial t}|_{sedi}. \quad (13)$$

In (12), the rain water mixing ratio evolves through autoconversion, accretion, evaporation and sedimentation, respectively. Simultaneously, (13) shows that the rain drop concentration of the drizzle is sensitive to autoconversion, self-collection, evaporation and sedimentation, respectively. Each term in (12) and (13) contains parameters (autoconversion coefficients, collection kernels, drop terminal velocity) with complex expressions involving q_{cw} and N_{cw}, which cannot be repeated here. Notice also that subgrid scale microphysical processes, as introduced by Chen and Cotton (1987) or Redelsperger and Sommeria (1982) but in the case of the Kessler's scheme, are not accounted for in this model version.

2.4. Numerical aspects

An accurate representation of radiative exchanges and turbulent entrainment, at both cloud top and cloud base, necessitates a high vertical resolution. The uniform vertical grid spacing of 50 m is a reasonable compromise between numerical accuracy and computational cost. The model time step is set to 10 s while the numerically expensive calculations of radiation and turbulent length scales are made every 360 s and 60 s, respectively. The vertical advection term in (3) to (6) is discretized with a first-order upstream scheme to avoid negative humidity fluxes at boundary layer top. All the turbulent transport terms in (3), (4), (5), (6) and (9) are integrated with a fully implicit scheme.

2.4. Initial conditions

The initial sounding, shown in Fig. 1, has been already used by BFP92 in their study of buoyancy-driven CTBL. It corresponds to an idealized case of North Sea stratocumulus layer observed during JASIN (Nicholls and Leigthon, 1986). The liquid water content q_{cw}, increases linearly from the cloud base (500 m) up to 1100 m where a maximal value of 0.82 g/kg is found. The geostrophic wind has a north-south component of 7 m/s. A positive divergence of 3×10^{-6} s^{-1} is applied to the model leading to a subsidence of $w \sim 3.5$ mm/s at the top of the inversion level (1150 m). The surface pressure is 1020 hPa. The sea surface temperature is 284.5 K, so the surface fluxes are in the range of 15 W/m^2 (sensible heat) and of 45 W/m^2 (latent heat). The numerical experiments are made for 1 July to maximize the diurnal radiative solar flux. All the simulations start at 00:00 LST.

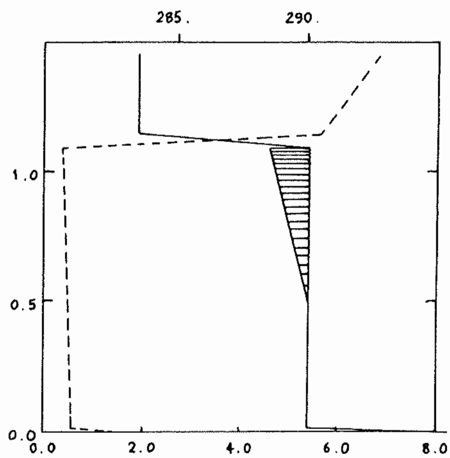

Fig. 1: Initial sounding θ_l (dashed line), q_w (solid line) and q_{cw} (corresponding to the hatched area), used in the numerical experiments.

3. DIURNAL RADIATIVE DECOUPLING CASES

In this section, we only test the sensitivity of the stratocumulus to the solar radiative warming. First, the behaviour of the stratus deck is illustrated in Figs 2 and 3 where the time-height evolutions of the turbulent kinetic energy and of the nebulosity are plotted. For this experiment, N_{cw} is set to 200 droplets per cm^{-3}. One can clearly see that the cloud experiences a strong diurnal cycle with a minimal turbulence ($e < 0.5$ m^2s^{-2}) in the cloud, around noon. The lowering of the turbulence production by buoyancy in the cloud is

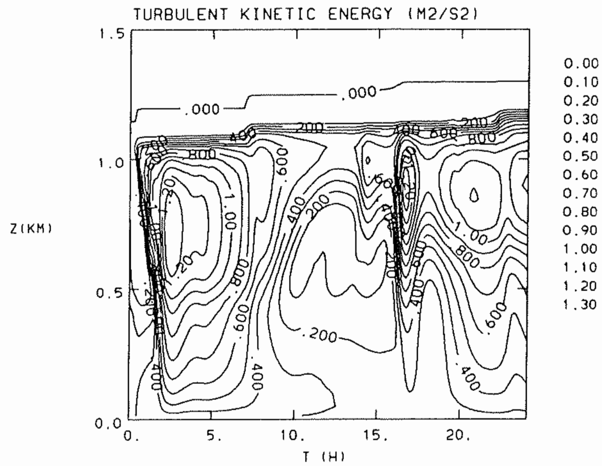

Fig. 2: Time-height section of the turbulent kinetic energy e. The isocontours are drawn for each 0.1 m^2s^{-2}.

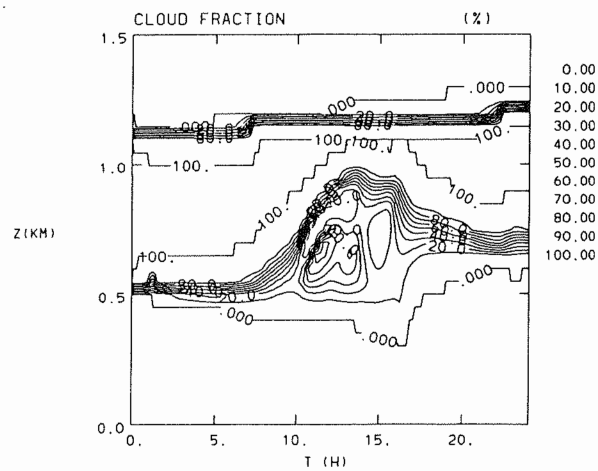

Fig. 3: Time-height section of the nebulosity (cloud fraction predicted with the gaussian scheme of subgrid condensation). The isocontours are drawn for each 10 % of cloud fraction.

due to significant solar radiative absorption which counteracts the infrared cooling at the cloud top. This effect tends to erode the cloud from below with an overall reduction of the cloud water mixing ratio (not shown) as the condensation level is higher (Fig. 3). The main cloud being warmer, it tends to be decoupled from its subcloud mixed layer. The thermodynamical insulation of the cloud by a thin stable layer favors the formation of a second cloud layer which is fed by the surface latent heat flux. Finally, the reconnection of the main cloud deck with the subcloud layer at 17:00 LST is accompagnied by a burst of turbulence (see Fig. 2) due to an intensification of the $\overline{w'q'_w}$ flux.

We now consider the optical properties of the stratus related to the cloud microphysical composition. Holding q_{cw} constant (as usually done, see Charlson et al., 1987), any increase of the cloud droplet number concentration N_{cw} reduces the effective radius r_e and thus leads to an increase of the cloud albedo as the total surface of the droplets is larger. But as the cloud water mixing ratio presents large diurnal fluctuations due to the solar warming, no definitive conclusion can be drawn on the sensitivity of the cloud albedo with respect to N_{cw}. So, a series of 24-hour experiments have been performed by setting N_{cw} equal to 25, 50, 100, 200, 400 and 800 droplets per cm^{-3}, successively. In Fig. 4, are plotted the diurnal evolutions of the cloud albedo for each case with the different cloud water concentrations. The diurnal course of the solar zenithal angle is mainly responsible for the large variation of the cloud albedos. At sunrise, the albedos are high and increase with N_{cw}, from 0.793 (25 cm^{-3}) up to 0.844 (800 cm^{-3}) (at 5:00 LST). Despite the diurnal trend in the morning, the highest N_{cw} still gives the highest albedo however, the situation reverses between 12:00 LST and 16:00 LST. Because the cloud is more heated by solar radiations when N_{cw} is high, the liquid water path W is reduced and so is the optical thickness (see Eq. 11). As a consequence, the lowest albedo (0.441) is now attained with N_{cw}=800 cm^{-3}. Notice also that in either case, there is roughly a delay of 2 hours between the maximal diurnal heating and the time when the minimal albedo is found. At the end of the day, the model retrieves the early situation that is the positive correlation between the cloud albedo and the cloud droplet concentration.

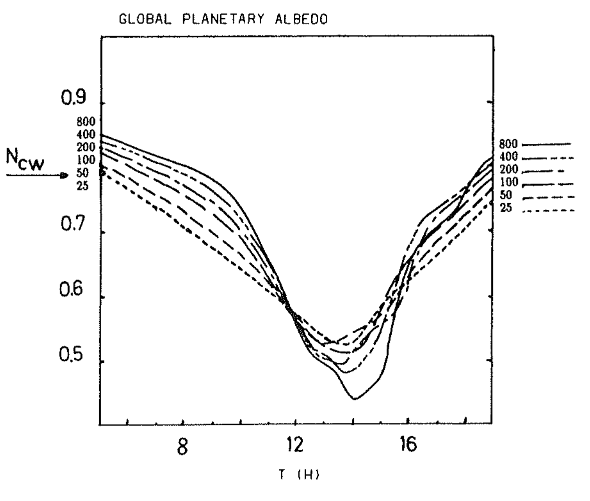

Fig. 4: Time evolution of the planetary albedo (visible and near-infrared bands) for several cloud droplet concentrations N_{cw} given in cm^{-3}.

4. PRECIPITATING CASE

To isolate the effects of precipitation, we have performed numerical experiments in which the solar radiative forcing has been suppressed. Furthermore, as the model possesses some spin-up to adapt the turbulent fields, we decided to slowly incorporate the generation of precipitating drops by linearly increasing the autoconversion rates ($\frac{\partial q_{rw}}{\partial t}|_{auto}$ and $\frac{\partial N_{rw}}{\partial t}|_{auto}$) from zero to the nominal values during the first hour of the simulation. The model is run for 6 hours only, as it reaches a quasi steady state after this period of time.

For the first experiment, the cloud number concentration N_{cw} is fixed to value of 25 cm^{-3} giving a surface precipitation rate of 0.04 mm per hour at the end of the simulation. Fig. 5 shows the time-height evolution of the cloudiness with the main cloud thinning and the formation of an underlying cumulus layer. At 3:30 LST, the two cloudy layers thicken and reconnect into a single precipitating cloud. The formation of the subcloud layer is also a consequence of the decoupling between the main cloud and the mixed sublayer (Albrecht, 1989). The loss of liquid water by microphysical conversion in the stratus deck leads to a global warming inside the cloud and an evaporative cooling in the sublayer.

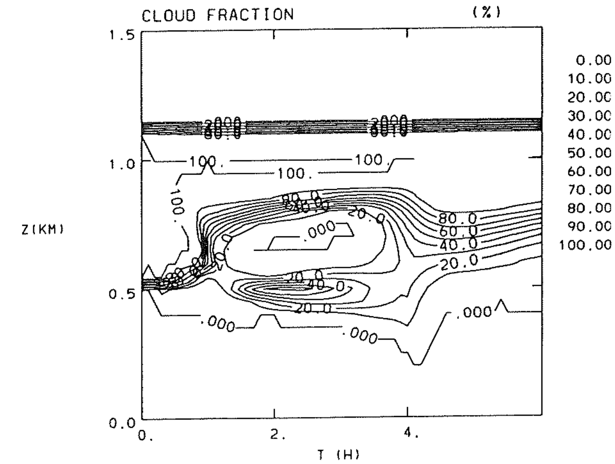

Fig. 5: Time-height section of the cloudiness for the precipitating cloud deck with N_{cw}=25 cm^{-3}. The isocontours are drawn for each 10 % of cloud fraction.

In order to test the sensitivity of the precipitating cloud to the microphysical processes and to the turbulent fluxes, two other experiments have been performed by inhibiting the raindrops evaporation (Fig. 6) and then by removing the surface heat fluxes (Fig. 7).

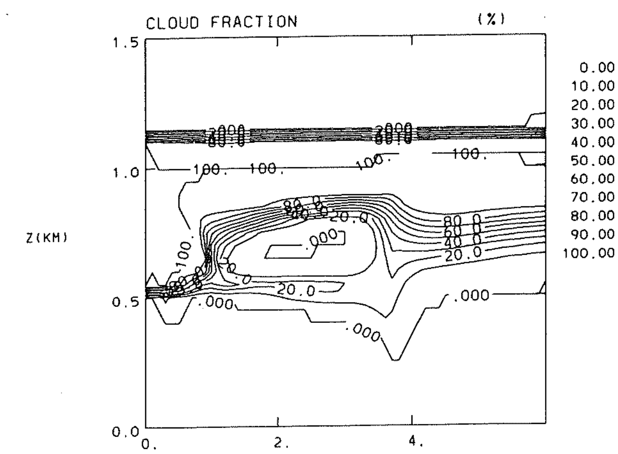

Fig. 6: As in Fig. 5, but when the evaporation of raindrops is suppressed.

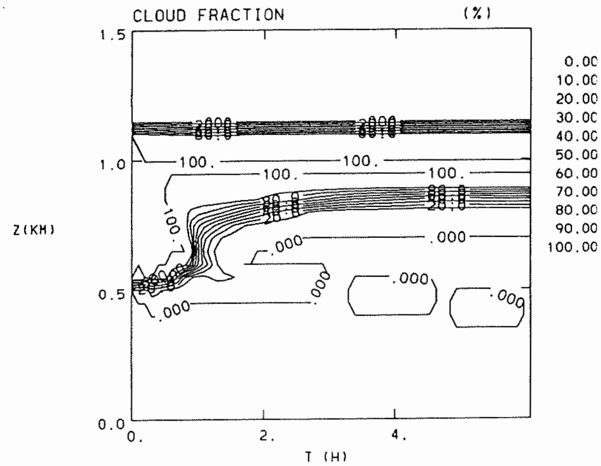

Fig. 7: As in Fig. 5, but when the surface sensible and latent heat fluxes are suppressed.

In the first case, the absence of cooling and moistening by rain drop evaporation gives a lesser amont of cloudiness in the secondary cloud layer. Comparing Figs 5 and 6 indicates that due to a reduced degree of decoupling between the main cloud and the cumulus layer below, the two cloud layers mix slightly more rapidly.

The importance of the surface fluxes is illustrated in Fig. 7. When no surface fluxes are allowed at the sea level, the turbulent decoupling persists in the CTBL during the 6 hours of simulation. The cumulus layer is now very shallow with an apparent cycle of formation/dissipation. On the contrary, the upper main cloud reaches an approximate steady state (Fig.7) in spite of continuous precipitations. It seems that the maintenance of the cloud is favored by a partial recirculation (turbulent transport) of water at the cloud base.

For the last numerical experiment, a value of 100 cm^{-3} has been prescribed to the cloud number concentration N_{cw}. The corresponding plot of cloudiness in Fig. 8 shows that a transient decoupling only occurs in that case. It should be noted that the precipitation rate (not shown) attains a steady state value of 0.02 mm per hour after the two first hours of simulation.

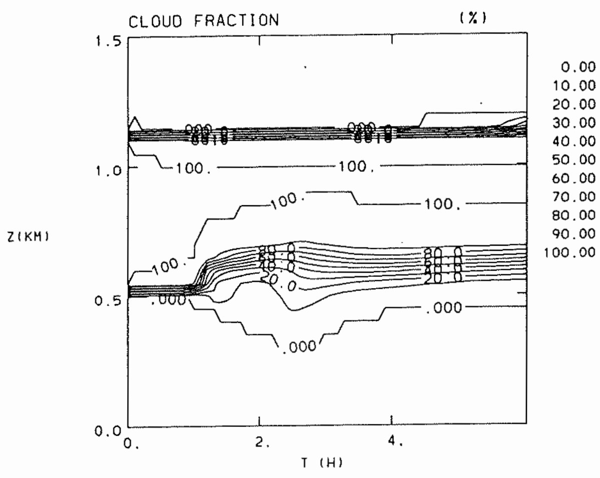

Fig. 8: As in Fig. 5, but for $N_{cw} = 100\ \mathrm{cm}^{-3}$.

5. CONCLUSION

This preliminary study aimed to illustrate the complex role of the cloud droplet concentrations in modulating some diabatic forcings (solar radiations and precipitation) in a CTBL. As expected both effects tend to produce a decoupled structure between the upper stratus layer and the subcloud layer and so may have a considerable impact on the life cycle of extended stratus decks. The cloud-radiation interaction is certainly more intense for 'polluted' clouds where N_{cw} is enhanced (Charlson et al., 1987). On the contrary, 'clean' clouds with low droplet concentrations are more likely to drizzle (Albrecht, 1989). Some of the results shown here need to be confirmed with other model refinements, such as non-linear effects of broken cloudiness on the radiation fields and on the precipitation efficiency. Another intriguing point to explore concerns the growth of subcloud cumuli rising into the main stratus layer (Nicholls, 1985) and its relation with the surface fluxes. This phenomenon, although connected to the diurnal cycle of non-precipitating clouds, possesses a more unexpected timescale in the case of drizzling cloud. Finally, this study is going to gain more interest in the next future as soon as unambiguous observations of cloud decoupling through radiation and/or precipitation will be available.

6. ACKNOLEDGEMENTS

The authors are pleased to acknowledge Drs Ph. Bougeault and Ch. Fravalo for some very stimulating discussions. This research program is supported by the CNRS (ATP PAMOS). Computations were made at the CCVR (Centre de Calcul Vectoriel pour la Recherche in Palaiseau, France).

7. REFERENCES

Albrecht, B., 1989: Modulation of boundary layer cloudiness by precipitation processes. *Proceedings of the 69th AMS Annual Meeting,* Anaheim, California, Jan.29-Feb.3.

Bechtold, P., C. Fravalo and J.-P. Pinty, 1992: A model of marine boundary layer cloudiness for mesoscale applications. *J. Atmos. Sci.,* to appear.

Charlson, R. J., J. E. Lovelock, M. O. Andreae and S. G. Warren, 1987: Oceanic phytoplankton, atmospheric sulfur, cloud albedo and climate. *Nature,* 326, 655-661.

Chen, C. and W. Cotton, 1987: The physics of the marine stratocumulus-capped mixed layer. *J. Atmos. Sci.,* 44, 2951-2977.

Fouquart, Y. and B. Bonnel, 1980: Computations of solar heating of the earth's atmosphere: A new parameterization. *Beitr. Phys. Atmosph.,* 53, 35-62.

Fravalo, C., Y. Fouquart and R. Rosset, 1981: The sensitivity of a model of low stratiform clouds to radiation. *J. Atmos. Sci.,* 38, 35-62.

Morcrette, J.-J., 1989: Impact of changes to the radiation transfer parameterizations plus cloud optical properties in the ECMWF model. *Mon. Wea. Rev.,* 118, 847-873.

——— and Y. Fouquart, 1985: On systematic errors in parameterized calculations of longwave radiation transfer. *Quart. J. Roy. Meteor. Soc.,* 111, 691-708.

Nicholls, S., 1984: The dynamics of stratocumulus: aircraft observations and comparisons with a mixed layer model. *Quart. J. Roy. Meteor. Soc.,* 110, 783-820.

——— and J. Leighton, 1986: An observational study of the structure of stratiform cloud sheets. Part I: structure. *Quart. J. Roy. Meteor. Soc.,* 112, 431-460.

Redelsperger, J.-L. and G. Sommeria, 1982: Methode de representation de la turbulence associee aux precipitations dans un nuage tri-dimensionnel de conection nuageuse. *Bound. Layer Meteor.,* 24, 231-252.

Richard, E. and N. Chaumerliac, 1989: Effects of different rain parameterizations on the simulation of mesoscale orographic precipitation. *J. Appl. Meteor.,* 28, 1197-1212.

STABILITY OF CLOUD TOP TO ENTRAINMENT

Peter G. Duynkerke
Utrecht University, IMAU, 3584 CC Utrecht, The Netherlands

1. INTRODUCTION

Under dry adiabatic conditions only the case of a statically unstable interface can permit the entrainment to generate turbulent kinetic energy. For cloudy conditions this process can furthermore be influenced by radiative cooling and evaporative effects. Radiative effects are thought to have a small effect on the entrainment directly. The importance of the radiation is mainly indirect, it drives the convection and thus produces turbulence, which will finally promote the entrainment (Nicholls and Turton, 1986; Nicholls,1989). Lilly (1968) pointed out that the evaporative cooling of unsaturated air which has been entrained into the cloud can, under some conditions, cause the entrained air to sink unstably as a convective downdraft. The process is referred to as cloud top entrainment instability CTEI (Randall, 1980; Deardorff, 1980; Hanson, 1984; Kuo and Schubert, 1988; Siems et al., 1990; MacVean and Mason, 1990; Weaver and Pearson, 1990).

In the cloud free case the stability can be characterized by the jump in virtual potential temperature across the interface. Lilly (1968) constructed a simple model for the stratocumulus-topped boundary layer. He argued that for stability of the interface between the cloud layer and the overlying air the temperature inversion must be strong enough that the equivalent potential temperature remains constant or increases at cloud top. The deficiency of Lilly's stability parameter was that it did not include the effects of water vapor and liquid water on buoyancy. These additional effects were taken into account by Randall (1980) and Deardorff (1980). However they restricted themselves to the case in which after mixing a parcel just remained saturated. This results in a stability criterion which states that the thermodynamic properties across the interface have to be unstable with respect to the wet adiabat.

In this paper we will give the thermodynamic theory of cloud top evaporative instability. We will follow arguments similar to those given by Nicholls and Turton (1986) and Albrecht et al. (1985). It will be shown that this process can be depicted in a simple diagram and that all stability criteria discussed in the literature can simply be pointed out in this diagram. The limitations of all the criteria will be discussed and a new stability criterion will be presented. The new stability criterion treats all cases with a smooth transition from the cloud free to the cloudy case. Besides the instability criterion this theory also gives a stability parameter if the interface is stable, and as such can be used in entrainment studies.

2. THEORY

We consider a turbulent uniformly saturated cloud layer separated from an overlying non-turbulent unsaturated layer by a thin transition layer. In the analysis we will assume that this transition layer (the inversion) is infinitesimally thin. Across this transition layer the temperature, specific humidity, liquid water content and turbulence properties change sharply. The upper layer will be denoted by 1 and the lower layer by 2.

The entrainment of a parcel with mass m_1 and consequent mixing of a parcel with mass m_2 will be considered. The mixed parcel with mass $m_1 + m_2$, with m_1 constant and m_2 a function of time, has a virtual potential temperature $\delta\theta_m$ higher than its surroundings. Moreover, if the parcel 2 has no initial momentum (no entrainment of momentum is considered) then the simplified momentum equation can be written as

$$\frac{d\, w(m_1+m_2)}{d\,t} = \frac{g}{T}(m_1+m_2)\ \delta\theta_m\,. \qquad (2.1)$$

Normalizing the masses with m_1 we obtain

$$\frac{d\, w/\chi}{d\,t} = \frac{g}{T}\ \delta\theta_m/\chi \qquad (2.2)$$

in which $\chi = m_1/(m_1 + m_2)$ is the mass mixing ratio. The important quantity to consider is thus the total buoyancy of the parcel $((m_1 + m_2)\ \delta\theta_m)$ per unit mass of the entrained air (m_1). This contrasts with the buoyancy per unit mass $(\delta\theta_m)$ as has been considered by most previous investigators (Nicholls and Turton, 1986; Siems et al., 1990). It is not fully clear what process they had in mind but $\delta\theta_m$ is the important quantity to consider when the initial momentum (w_2) of the surrounding air is the same as that of the parcel under consideration, because in that case the relevant momentum equation can be written

$$(m_1+m_2)\frac{d\,w}{d\,t} = \frac{g}{T}(m_1+m_2)\ \delta\theta_m\,. \qquad (2.3)$$

However we are interested in how the momentum of an entrained and mixed parcel changes relative to its environment; therefore (2.1) and (2.2) are the relevant momentum equations. Integration of (2.2) with time gives

$$(\, m_1+m_2(t)\,)\ w(t) = m_1\ w(0) + m_1 \int_0^t \frac{g}{T}\ \delta\theta_m/\chi\ dt \quad (2.4)$$

so that the important quantity to consider is the integral of the total buoyancy excess of the parcel $(m_1 + m_2)\ \delta\theta_m$ per unit mass of entrained air (m_1) with respect to time.

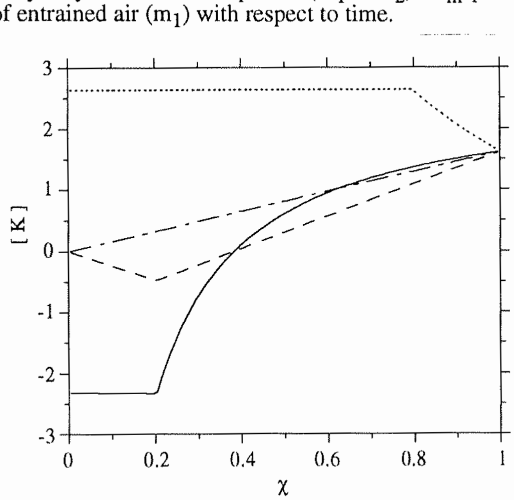

Fig. 1 Virtual potential temperature difference as a function of the mass mixing ratio χ for $\Delta\theta_e$ = - 5 K, q_{l2} = 0.5 g/kg and Δq = -2.8 g/kg (T_2 = 273 K and p_2 = 900 hPa): $\chi\Delta\theta_v$ (dash-dotted), $\delta\theta_{v2}$ (dashed) , $\delta\theta_{v2}/\chi$ (full line) and $\delta\theta_{v1}/\chi$ (dotted).

2.a. STABILITY DIAGRAM

For the case in which both layers consist of moist air, without any liquid water, and no condensation is occurring during the mixing ($\delta\theta_{vm} = \chi\ \Delta\theta_v$, where the operator Δ stands for the value above, minus the value below the inversion) it is immediately clear from (2.2) that there is no buoyancy change due to the mixing, so the only buoyancy change we have to account for is due to the entrainment.

In the general case where phase changes are occurring it is obvious that there is a buoyancy change due to the mixing. This is because the virtual potential temperature of the mixture (θ_{vm}) is not just a mass weighted average of the virtual potential temperature above and below the inversion. A derivation of θ_{vm} and $\delta\theta_{v2}$, for the case that the lower layer is saturated and the upper layer contains no liquid water, is given in Duynkerke (1992). In Figure 1 we have shown $\chi\ \Delta\theta_v$, $\delta\theta_{v2}$ and $\delta\theta_{v2}/\chi$ as a function of χ for the case that $\Delta\theta_e = -5$ K, $q_{l2} = 0.5$ g/kg and $\Delta q = -2.8$ g/kg ($T_2 = 273$ K and $p_2 = 900$ hPa). All three curves pass through the point $\chi = 1$, $\Delta\theta_v$ because in this case $m_2 << m_1$ and the mixed parcel will retain its original properties from above the inversion. The buoyancy excess is therefore simply $\Delta\theta_v$. For $\chi = 0$ it can be shown that

$$\left(\frac{\delta\theta_{v2}}{\chi}\right)_{\chi=0} = \Delta_2 = \frac{\Gamma_m}{\Gamma_d}\Delta\theta_e - \theta_{e2}\,\Delta q_T \qquad (2.5)$$

where, Γ_m is the wet adiabatic lapse rate at T_m, Γ_d is the dry adiabatic lapse rate and q_T is the total water specific humidity ($q_T = q + q_l$). Randall (1980) and Deardorff (1980) assumed that instability would occur if

$$\Delta_2 < 0 \qquad (2.6)$$

The values $\delta\theta_{v2}/\chi$ for small values of χ (up to about 0.2 in Figure 1) are nearly independent of χ because the ratio of the wet and dry adiabat is nearly independent of temperature, in this case the temperature of the mixed parcel (T_m). In this range of mass mixing ratios the mixed parcel remains saturated ($q_{lm} > 0$). It can be seen that the stability parameter (Δ_2) represents the stability for only a small range of mass mixing ratios. Therefore it is not surprising that this criterion is not sufficient to explain cloud top entrainment instability. In the next section we will discuss how this is done.

2.b. STABILITY PARAMETER

The lines for $\chi\ \Delta\theta_v$ and $\delta\theta_{v2}$ have already been shown by Nicholls and Turton (1986). It is clear from Figure 1 that any indicator of cloud top interfacial stability should take into account the density fluctuations as a result from evaporative cooling during mixing. And as discussed in section 2.a the range of possible values can not be well represented by just two points on the curve, $\Delta\theta_v$ and Δ_2, which correspond to only two special circumstances - no mixing and mixing which maintains saturation.

Turton and Nicholls (1986) now assumed that all values of χ are equally likely to happen within the entrainment interface layer (EIL). On the basis that all values of χ are equally important in determining the interfacial stability, they defined

$$\Delta_m = 2\int_0^1 \delta\theta_{v2}\, d\chi \ . \qquad (2.7)$$

The numerical factor 2 ensures that $\Delta_m = \Delta\theta_v$ in the cloud free case. A disadvantage of Δ_m is that even in the cloudy case its value is very close to $\Delta\theta_v$. Which means that a cloud top entrainment instability criterion based on Δ_m will predict instability to occur close to that for static stability of a moist but unsaturated atmosphere.

As discussed above $\delta\theta_{v2}/\chi$ (rather than $\delta\theta_{v2}$) is the important quantity, we will define a new stability parameter:

$$\Delta_a = \int_0^1 \delta\theta_{v2}/\chi\, d\chi \ . \qquad (2.8)$$

This can be interpreted as follows. We entrain a parcel with mass m_1. At this time no mixing has taken place ($\chi = 1$). As soon as mixing takes place, χ decreases until so much surrounding air has mixed with the parcel that χ approaches zero. During the whole mixing process the buoyancy excess of the parcel per unit mass of entrained air (m_1) is given by $\delta\theta_{v2}/\chi$. The stability parameter Δ_a represents therefore the 'time' integral of the buoyancy excess during the life time of the parcel from its unmixed state to a state in which its properties are overwhelmed by the properties of the surrounding air.

The criterion $\Delta_a < 0$ states that under these conditions the net effect of entrainment and evaporative mixing together promotes convection. If $\Delta_a < 0$ typically the parcel still needs energy in order to be entrained as given by (2.3). The cloud layer therefore has to be turbulent to deliver this energy. After the entrainment the mixing (due to turbulence) gives way to evaporative cooling and the potential energy can be converted to kinetic energy and thus to convection. The condition $\Delta_a < 0$ thus states that there is a net conversion of potential energy into kinetic energy over the full transformation, as the parcel is entrained and then proceeds from its unmixed to its completely mixed state. Typically, some level of active turbulence is necessary to maintain entrainment and mixing. However, once $\Delta_a < 0$ the entrainment and mixing can increase spontaneously.

2.c. COMPARISON WITH OTHER CTEI's

MacVean and Mason (1990) also studied the cloud top entrainment instability mechanism. They were not so much interested in the general stability of the interface but more in the conditions under which cloud top entrainment instability would occur. They didn't as such consider entrainment to happen but investigated under which conditions free mixing would occur at an interface with different thermodynamical properties. Their criterion for instability is that there is a net conversion of potential energy to kinetic energy.

The difference with our approach is that they investigated what I would call free mixing. They assumed that not only a parcel with mass fraction χ from layer 1 is

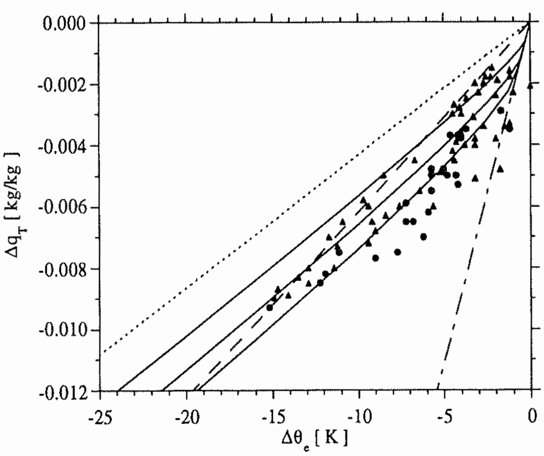

Fig. 2 Observations of Δq_T and $\Delta\theta_e$ made in solid stratocumulus from Weaver (1987): soundings (circles) and horizontal legs (triangles). The lines represent the different stability criteria: dry adiabat $\Delta\theta_v = 0$ (dotted); wet adiabat $\Delta_2 = 0$ (dash-dotted); stability criterion of MacVean and Mason (1990) (short dashed) and $\Delta_a = 0$ (full lines) for $q_{l2} = 0.5$, 1.0 and 1.5 g/kg, from left to right respectively.

exchanged across the interface with layer 2, but also a parcel with mass fraction χ from layer 2 is exchanged with layer 1. This process is not typical for entrainment in which only a parcel from the overlying layer is pulled downwards into the lower layer 2. The entrainment process depends upon the turbulence which delivers the kinetic energy to overcome the potential energy necessary to pull down the parcel across the interface.

The process which MacVean and Mason (1990) studied can be depicted in Figure 1 as well. The curve $\delta\theta_{v2}/\chi$ is for the the parcel which is entrained and mixed from the upper layer into the cloud layer. For the parcel which is 'entrained' and mixed from the cloud layer into the overlying layer a similar expression can be obtained ($\delta\theta_{v1} = \theta_{v1} - \theta_{vm}$). The derivation of this expression is given in Duynkerke (1992) and $\delta\theta_{v1}/\chi$ is shown in Figure 1. MacVean and Mason (1990) now considered the limit of χ --> 0 and assumed that CTEI would happen if there were be a net conversion of potential energy into kinetic energy if (for their $H_1 = H_2$ case)

$$\left(\delta\theta_{v2}/\chi\right)_{\chi=0} + \left(\delta\theta_{v1}/\chi\right)_{\chi=0} < 0 \ , \qquad (2.9)$$

which can with $q_{l1} = 0$ be rewritten as

$$\Delta\theta_e < \Delta q_T \frac{\left[1 + \frac{l_v}{c_p}\left(\frac{\partial q_s}{\partial T}\right)_m\right]\left[\frac{l_v}{c_p} + \theta_{e2} - \psi\theta_{e1}\right]}{2 + \left(\frac{\partial q_s}{\partial T}\right)_m \left[\frac{l_v}{c_p} + (1+\psi)\,\theta_{e2}\right]} \, . \qquad (2.10)$$

This is equation (13) of MacVean and Mason (1990).

The result of MacVean and Mason (1990) is thus based on exchanging small mass fractions. It does not cover all the χ values which can and will occur in reality. Moreover they assume that a parcel is exchanged from the cloud layer into the overlying layer, a process which has nothing to do with entrainment. Therefore it is not possible to derive a general stability parameter from their analysis to describe entrainment. Even if according to their criterion (2.9) the inversion would be unstable it would require energy to get the parcel from the cloud layer into the overlying air, and the parcel would never return any energy for this. Moreover once the parcel is in the overlying layer there will be no process which can take care of mixing the parcel with the surrounding air, as there is no turbulence in the overlying layer as there is in the turbulent cloud layer.

The most likely process to describe CTEI thus seems to be entrainment (in contrast with free mixing) in which parcels of air are pulled into the cloud. This costs energy, but due to the evaporative cooling of the parcel there are situations under which the parcel can return more energy than was needed to entrain the parcel.

In Figure 2 we have shown the criteria of MacVean and Mason (1990) and $\Delta_a < 0$ for q_{l2} = 0.5, 1.0 and 1.5 g/kg. For $q_{l2} = 0$ the criterion $\Delta_a = 0$ reduces to the dry adiabat (dotted line in Figure 2). As q_{l2} increases the stability line moves further to the right in the diagram. In the upper right corner the instability line collapses with the wet adiabat ($\Delta_2 = 0$) because under these conditions ($\Delta\theta_e$, Δq_T) also the upper layer is saturated. If the liquid water in the lower layer would approach large values (q_{l2} --> ∞) the new stability criterion would reduces to that for the wet adiabat ($\Delta_2 = 0$). The new stability criterion is thus able to describe the stability of the interface under all conditions (cloudy and cloud-free) and provides a smooth transition between all the different states.

3. OBSERVATIONS

The stability criterion divides the $\Delta\theta_e$, Δq_T plane as shown in Figure 2. If (2.8) is the right stability condition, we should find that all observations taken under persistent stratocumulus conditions lie to the right of the dividing line. In order to give an idea of where the data are typically situated we have plotted the data of Weaver (1987) in Figure 2. These data are all made in solid stratocumulus , the data are grouped into two categories: soundings (circles) and horizontal legs (triangles). In the first case the aircraft flew soundings at constant heading. High 'vertical' resolution profiles were obtained, and the data were plotted in a mixing diagram (to find the jumps a mixing line analysis was used). The second method of obtaining the vertical structure is to consider horizontal legs at cloud top. The plane skips in and out of the cloud and provides multiple samples of the EIL.

It is now tempting to plot all observational data in the diagram and check whether we have found the right stability criterion (Kuo and Schubert, 1988; MacVean and Mason, 1990). However we should be very careful doing this because there are many other mechanisms which can cause the cloud to dissipate. One mechanism is subsidence, which, if sufficiently strong, can lower cloud top below the lifting condensation level (LCL) and make the cloud disappear (Weaver and Pearson, 1990). Another mechanism is the solar absorption in the cloud which can cause a diurnal variation in cloud thickness (Bougeault, 1985; Duynkerke, 1989; Betts, 1990, Hignett, 1991; Blaskovic et al., 1991). Therefore the existence or dissipation of a stratocumulus cloud can not simply be related to whether the CTEI criterion is met or not.

4. CONCLUSIONS

By considering the simplified momentum equation for a parcel which is entrained and consequently mixed with the surrounding air we have defined a buoyancy parameter which is relevant for this process. This buoyancy parameter is the total buoyancy of the parcel per unit mass of entrained air ($\delta\theta_{vm}/\chi$). This is different from what most investigators have considered until now: the buoyancy per unit mass ($\delta\theta_{vm}$).

Using the new buoyancy parameter ($\delta\theta_{vm}/\chi$) the process of evaporative cooling of an entrained parcel is studied as a function of the mass mixing ratio. All the other parameters discussed in the literature can be shown to be simplifications of this more general parameter.

By assuming that all mass mixing ratios are equally likely to happen, a new stability parameter for the interface is proposed. In the case that the lower layer contains no liquid water the stability criterion reduces to that for the moist but unsaturated case, the dry adiabat. If the liquid water content in the lower layer is infinitely large (q_{l2} --> ∞) the stability criterion reduces to that found by Randall (1980) and Deardorff (1980) ($\Delta_2 < 0$), the wet adiabat. Thus as the liquid water content of the lower layer increases from zero upwards there is a smooth transition of the cloud top entrainment instability criterion from the dry adiabatic to the wet adiabatic criterion.

From the analysis given in section 2 it is clear that the total buoyancy conversion is given by the integral of $\delta\theta_{vm}/\chi$ with time (2.4). The outcome of this integral will probably depend upon the mixing speed and thus upon the turbulence intensity and scales within the boundary layer. It is not clear how all these details can be incorporated in the relative simple criteria discussed in this paper. Also for a model it might be difficult to describe these processes. The model should at least resolve scales which are one (or perhaps several) orders of magnitude smaller than those of the entrained parcel. Because at these scales there will be probably be the most effective mixing. So one would need a Large Eddy Simulation (LES) model with a high resolution.

Checking the instability criterion with data should be done very carefully. Stratocumulus clouds can dissipate due to a variety of mechanisms: subsidence, diurnal variation and decoupling. Using data from the transition zone between the stratocumulus and cumulus region should be done with caution, because other processes such as boundary layer mixing might cause this transition (Albrecht, 1991). It is apparently insufficient to relate cloud type and amount to the thermodynamical structure at the inversion only.

There is clearly a need for more definitive observational data to which the different criteria should be evaluated. I think that we should not only try to unfold the instability problem, but we should be looking for the stability parameters (in terms of dimensionless Richardson numbers) which describe the stability of the interface and as such control the entrainment and evaporative cooling (Nicholls and Turton, 1986), especially when the interface is stable. This will probably give the instability criterion as the stability parameter approaches a certain value. Also from an observational point of view it will be a lot easier to make measurements under these (nearly) stable conditions rather than looking for the single case in which cloud top entrainment instability is actually happening.

5. REFERENCES

Albrecht, B.A., 1991: Fractional cloudiness and cloud-top entrainment instability. *J. Atmos. Sci.*, **48**, 1519-1525.

Albrecht, B.A., R.S. Penc and W.H. Schubert, 1985: An observational study of cloud-topped mixed layers. *J. Atmos. Sci.*, **42**, 800-822.

Betts, A.K., 1990: Diurnal variation of California coastal stratocumulus from two days of boundary layer soundings. *Tellus*, **42A**, 302-304.

Blaskovic, M., R. Davies and J.B. Snider, 1991: Diurnal variation of marine stratocumulus over San Nicholas Island during July 1987. *Mon. Wea. Rev.*, **119**, 1469-1478.

Bougeault, P., 1985: The diurnal cycle of the marine stratocumulus layer: A higher-order model study. *J. Atmos. Sci.*, **42**, 2826-2843.

Deardorff, J.W., 1980: Cloud-top entrainment instability. *J. Atmos. Sci.*, **37**, 131-147.

Duynkerke, P.G., 1992: The stability of cloud top to entrainment: amendment of the cloud top entrainment instability mechanism, *submitted to J. Atmos. Sci.*

Duynkerke, P.G., 1989: The diurnal variation of a marine stratocumulus layer: a model sensitivity study, *Mon. Wea. Rev.*, **117**, 1710-1725.

Hanson, H.P., 1984: Stratocumulus instability reconsidered: a search for physical mechanisms. Tellus, **36A**, 355-368.

Hignett, P., 1991: Observations of diurnal variation in a cloud-capped marine boundary layer, *J. Atmos. Sci.*, **48**, 1474-1482.

Kuo, H. and W.H. Schubert, 1988: Stability of cloud-topped boundary layers. *Quart. J. Roy. Met. Soc.*, **114**, 887-916.

Lilly, D.K., 1968: Models of cloud-topped mixed layers under a strong inversion. *Quart. J. Roy. Met. Soc.*, **94**, 292-309.

MacVean, M.K. and P.J. Mason, 1990: Cloud-top entrainment instability through small-scale mixing and its parameterization in numerical models. *J. Atmos. Sci.*, **47**, 1012-1030.

Nicholls, S. and J.D. Turton, 1986: An observational study of the structure of stratiform cloud sheets: Part II. Entrainment. *Quart. J. Roy. Met. Soc.*, **112**, 461-480.

Nicholls, S. 1989: The structure of radiatively driven convection in stratocumulus. *Quart. J. Roy. Met. Soc.*, **115**, 487-511.

Randall, D.A., 1980: Conditional instability of the first kind upside-down. *J. Atmos. Sci.*, **37**, 125-130.

Siems, S.T., C.S. Bretherton, M.B. Baker, S. Shy and R.E. Breidenthal, 1990: Buoyancy reversal and cloud top entrainment instability. *Quart. J. Roy. Met. Soc.*, **116**, 705-739.

Turton, J.D. and S. Nicholls, 1987: A study of the diurnal variation of stratocumulus using a mixed layer model. *Quart. J. Roy. Met. Soc.*, **113**, 969-1009.

Weaver, C.J., 1987: Observational analysis of cumulus clouds and stratocumulus entrainment using ozone. Colorado State University, Atmospheric Science Paper No. 422, Fort Collins, CO 80523, 114 pp.

Weaver, C.J. and R. Pearson jr., 1990: Entrainment instability and vertical motion as causes of stratocumulus breakup. *Quart. J. Roy. Met. Soc.*, **116**, 1359-1388.

NUMERICAL MODEL STUDY ON CONVECTIVE CLOUD PRECIPITATION IN STRATIFORM CLOUD

Hong Yanchao, Hu Zhaoxia, Wang Angsheng

Institute of Atmospheric Physics, Academia Sinica, Beijing, 100029, China

The heavy rains in China are often caused by the mixed cloud system which consists of stratiform cloud and cumulus clouds embeded in it. Precipitation amount from the cumulus cloud in this system is much larger than that from the isolated cumulus cloud and contributes more to the precipitation of the mixed cloud system (Hong etc., 1987; Li, 1982). The observations indicate that convective cloud in stratiform cloud is very easy to produce rainfall with high intensity. In this paper, we regard the stratiform cloud as saturated air that includes cloud water, rain water and updraft, and ignore its dynamic processes and micro-physics processes. This kind of stratiform cloud is regarded as cumulus developing environment. And we use one dimensional time-dependent cold cumulus model (Hong etc.,1989) to simulate convective cloud and its developing in the stratiform cloud to inquire into its precipitation principle.

I. CALCULATION

Assuming that the stratiform cloud is located in layer between 1.0 and 7.0 km,i.e.,the thickness is 6.0 KM, and with cloud water content Qce of $0.2 g/m^3$, rain water content Qre of $0.5 g/m^3$, and relative humidity fe of 1.0; and meso-scale updraft velocity we of 0.2m/s. It is supposed that when the stratification in the stratiform cloud is stable, the convergence lift in lower level can result in cumulus development, and the parameters of the environmental

Table 1. Predicted Cloud Parameters Under Different Conditions

parameters		H (km)	Sp (mm)	Tp (min)	Tc (min)	Pa (mm/h)	W (m/s)	Qc (g/m^3)	Qr (g/m^3)	Qi (g/m^3)	η (%)	
Qce	0.0	13.0	90.1	216	276	240.4	26.2	4.4	13.2	9.2	18.5	
(g/m^3)	0.2	13.0	90.0	216	276	251.6	25.9	4.4	13.9	8.8	19.7	Qre=0.0
	0.4	13.0	88.8	220	276	302.1	25.7	4.4	14.0	9.1	20.8	
fe	100	13.0	90.0	216	276	251.6	25.9	4.4	13.9	8.8	19.7	
(%)	95	12.8	62.9	128	276	205.7	25.0	4.4	13.7	8.7	16.3	Qre=0.0
	90	12.5	56.0	96	172	136.6	13.9	4.4	13.5	8.5	16.5	
Qre	0.0	13.0	90.0	216	276	251.6	25.9	4.4	13.9	8.8	19.7	
(g/m^3)	0.1	12.8	111.1	276	276	261.2	24.3	3.6	10.5	7.5	37.1	
	0.3	12.5	134.4	276	276	319.5	23.4	2.8	12.5	7.8	53.4	
	0.5	12.3	154.2	276	276	256.8	22.1	2.6	12.1	7.6	70.7	
thick-	3	12.0	105.6	104	100	285.1	21.4	3.1	12.1	7.3	61.3	cloud base
ness	6	12.3	154.2	276	276	256.8	22.1	3.6	12.1	7.6	70.7	height
(km)	9	12.5	164.9	276	276	279.4	21.8	2.6	12.8	7.7	72.6	is 1.0km
posi-	1-4	12.0	105.6	104	100	285.1	21.4	3.1	12.1	7.3	61.3	
tion	4-7	11.8	66.1	224	276	136.2	20.4	4.2	12.0	7.2	23.6	
(km)	7-10	11.5	35.0	100	276	143.4	19.1	4.3	11.1	7.8	14.3	
w'	0.5	7.0	36.3	∞	∞	14.2	0.4	0.6	0.5	0.1	95.0	
(m/s)	1.0	7.3	83.1	∞	∞	32.9	0.8	0.6	1.1	0.4	98.0	*
	1.5	7.5	94.6	∞	∞	54.1	1.5	2.0	2.6	0.9	97.3	
clear cloud		11.5	30.4	52	108	144.5	19.2	4.3	11.3	7.6	12.8	

* Sp and η are taken as values at Tc=184min.

stratiform cloud (ESC) effecting on cumulus cloud are taken as Qce, Qre, fe, thinckness and position of ESC and intensity w' of convergence lift. The parameters of cumulus and its precipitation are radar echo height H, cumulus rainfall amount Sp, rainfall lasting time Tp, cloud life cycle Tc, rainfall intensity Pa, rainfall efficiency η and updraft velocity w. Pa and w are maxium values in the cloud life cycle. We use respectively the radiosonde data at 07 AM (Beijing time) on September 3, 1977(instable stratification) and 08 AM on May 30, 1990(stable stratus) at Shanghai Station to calculate. The results are shown in table 1.

II. THE INFLUENCE OF ESC ON CUMULUS DEVELOPMENT AND ITS PRECIPITATION

1. THE INFLUENCE OF SINGLE PARAMETER OF ESC

(1) When Qce ranges from 0.0 to $0.4g/m^3$, the values of cumulus parameters chang no distinctly, so the influence of Qce on cumulus development may be neglected.

(2) When fe decreases from 100% to 90%, Sp, Tp and Tc decreases tremendoudly; It's obvious that the increase of fe prolonges cumulus life cycle and rises intensify of cumulus precipitation, so the effects of fe is very distinct.

(3) Qre is main control factor to increase cumulus precipitation intensity and precipitation efficiency. These can be found from increase of the cumulus parameters when Qre is increased from 0.0 to $0.5g/m^3$. Analysis shows that effects of Qre on the cumulus development are as following: (a) the radar echo from cumulus cloud appears earlier; (b) the initial time of cumulus precipitation is advanced greatly (see Fig.3); (c) the high refectivity region of radar echo appears early, and have larger vertical range, faster descend, and its low part maintains longer time. From above analysis, it can be concluded that although cumulus cloud rain water content is not added under the condition of existing rain water in ESC, the region of radar echo with high refectivity has been enlarged greatly and the time of rainfall with high rate prolonged enormously.

(4) Increase of thickness of ESC is very beneficial for the cumulus development and its precipitation, especially for the later.

(5) Influence of position of ESC on the cumulus is very explicit, for example, the lower stratiform cloud (ranging between 1.0 and 4.0 KM above the ground) is very favorable for the cumulus development, but the higher stratiform cloud (ranging from 7 to 10 KM) almost has no effect on the cumulus cloud (compared with isolated cumulus clouds).

2. THE INFLUENCE OF WHOLE STRATIFORM CLOUD

Above analyses about the single parameter indicate that fe, Qre, the thickness and the position are all main control factors which influence the cumulus development. In table 1 the stratiform cloud to be located between 1.0 and 7.0 KM above the ground is defined as the typical case, in which fe=1.0, $Qce=0.2g/m^3$, $Qre=0.5g/m^3$. By comparing the cumulus cloud in the mixed cloud system with the isolated cumulus cloud (Table 1, Fig.1 and Fig.2), we find that because of the existing of stratiform cloud , height of the radar echo increases from 11.5KM to 12.3KM, the rainfall amount from 30.4mm to 154.2mm, the cloud life cycle from 52 minutes to 276 minutes, the precipitation efficiency from 12.8% to 70.7%. So we can conclude that the existing of stratiform cloud not only reinforces cumulus cloud development but also promotes formation of its precipitation and rises precipitation efficiency. The above conclusion can be explained as following:

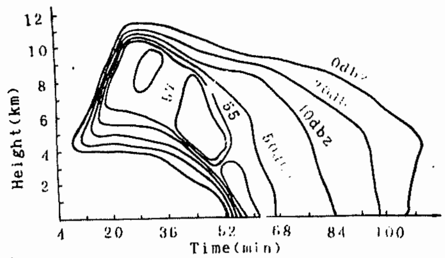

Fig.1 Time cross-section of clear cumulus radar echo intensity Z(dbz)

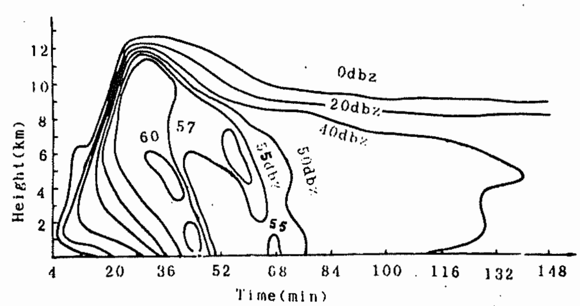

Fig.2 Time cross-section of cumulus radar echo intensity Z(dbz) in ESC ($Qce=0.2g/m^3$, $Qre=0.5g/m^3$)

Firstly, because the cumulus cloud embeded in the stratiform cloud is located in saturated air, the boundary turbulent exchange and dynamic entrainment can not deplete water vapor and heat energy in the cumulus cloud, evaporation amount of cloud water at the cloud top is also decreased; secondly, because the air entering the cumulus cloud from the stratiform cloud is saturate, condensation amount and condense latent heat are enlarged so updraft in the cumulus cloud is strengthened; finally, the saturated environment is also beneficial to rain formation. When effect of rain water content in the stratiform cloud is not considered, rainfall amount of the cumulus cloud in it is about 90mm, as three times as that (about 30.4mm) in the isolated cumulus cloud. If rain water content in the stratiform cloud is from $0.1g/m^3$ to $0.5g/m^3$, rainfall amount of the cumulus cloud increases from 111.1 to 154.2 mm. It can be seen that rain water in the stratiform cloud promotes greatly formation and development of precipitation in the cumulus cloud, the reasons are as following: (a) the rain water entering the cumulus cloud from the stratiform cloud quicken the processes of collecting cloud water and that makes cloud water change to rain water fastly; (b) In the initial period of cumulus life cycle, dynamic effect caused by the high rain water content region restraining the updraft makes rainfall in advanced. Furthermore, by comparing Fig. 1 to Fig.2, it can be seen that the radar echo structure of cumulus cloud in the mixed cloud system is quite different from that in the isolated cumulus. In the mixed cloud system, the intensive radar echo of cumulus sustains long time, and the two intensive radar echo reach the ground one by one. Correspondently, the precipitation on ground appears the second maxium rainfall rate (see Fig. 3).

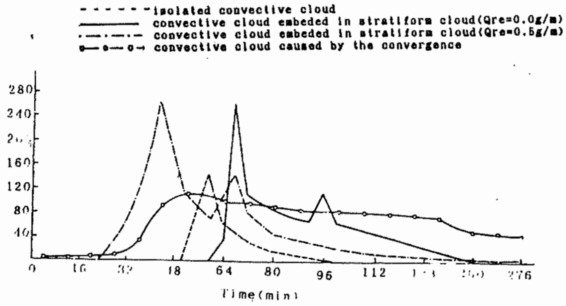

Fig.3 The timedistributions of rainfall rate of various cumulus cloud

III. THE INFLUENCE OF CONVERGENCE LIFT IN ESC

Even in stratiform cloud system with stable stratification, the cumulus clouds often develope, too. Their occurrence and developing rely on the energy of convergence lift motion occured in lower lever of the stratiform cloud . The observations indicate that a meso-scale convergence system is easy distinguished from the radar echo system, in which vertical extent of the cumulus cloud is not large, the radar echo intensity is lower, the severe radar echo region is always located in the mid and lower body of the cloud, and the gradient of echo intensity is small, but the cloud life cycle is persistent and rainfall lasting time is long, too. Although rainfall rate is small, accumulated rainfall amount often reaches the intensity of heavy rain. Now we take numerical simulation on this kind of cumulus.

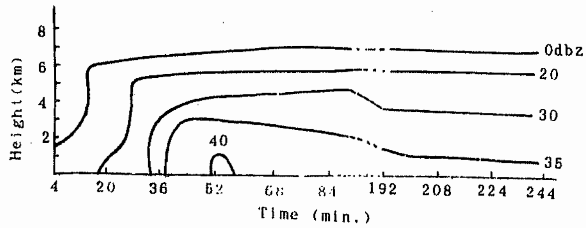

Fig.4 Time cross-section of concergence lift cumulus radar echo intensity Z(dbz)

We assume that updraft (speed w') from 1.0 to 7.0 KM levels, is not change with height and time. When the vertical motion equation is differenced in time forward different scheme, the w at first time is substituted by the w'. So in the cumulus there is always updraft with speed of w' to simulate the lift motion. In table 1, the cumulus parameter values are given when w' equals to 0.5, 1.0, and 1.5 m/s. The results show that with the strengthening of convergence (i.e. w' increases), the rainfall rate and precipitation amount all become larger obviously. For example, at 184th minute, corresponding w' of 0.5, 1.0 and 1.5 m/s, Pa and Sp are 14.2 mm/h and 36.3mm, 32.9 mm/h and 83.1mm, 54.1 mm/h and 94.6 mm respectively. Fig.4 is the reflectivity-time cross-section diagram of cumulus echo caused by the convergence. Compare Fig.1, Fig.2 with Fig.4, this kind of cumulus echo intensity is lower, vertical gradient of the reflectivity smaller, the position of severe echo range (35 dbz) is located in lower part of the cloud. So in terms of echo structure, convergence lift cumulus cloud is very different from the cumulus cloud embeded in ESC with instable stratification. Extra, convergence lift cumulus's life cycle and the rainfall lasting time are very long. If lower level convergence exists, the cloud will never disappear and rainfall never stop. Although rainfall rate is not large, rainfall preserves long, so accumulated precipitation amount is very large. It often reaches to the degree of heavy rain. Convergence lift cumulus cloud has stable echo structure and its echo intensity almost no changing. correspondently, the cumulus cloud's rainfall rate chang little. Another obvious feature of convergence lift cumulus cloud is that the cloud's precipitation efficiency is great (95% or more), i.e., almost all condense water change into rainfall water. This indicates, in vast and deep stratiform cloud system (there is enough vapor), if the convergence reaches to some degree, the cumulus cloud with lower radar echo intensity, long life period and precipitation time, stable precipitation rate and high rainfall efficiency will be produced, and heavy rain will be occured frequently. All above features correspond with the observations. In the fact, the cumulus cloud echo reflectivity often is not high in heavy rain-mixed cloud. According to statistics from 68 composited echo pictures collected in 11 heavy rain processes in 1983, 84% of the cumulus cloud echoes are of less than mid-level (Du, 1985).

IV. CONCLUSIONS

From fact of radar observation, echo and precipitation features of two kinds of convective cloud in ESC system are simulated to explaine the physical reasons why deep and thick mixed cloud system produce heavy rain easily. The cumulus cloud in ESC which contains saturated air rain water and cloud water is a good machine to produce rain. Saturature environment promote greatly developing of cumulus and its precipitation and prolong cumulus's life cycle, but the rain water in ESC promote further developing of the cumulus precipitation and increase rainfall amount and rainfall efficiency. Under the conditions of stable stratification, meso-scale convergence lift in the low level may result in cumulus cloud which could engender heavy rain. This kind of cloud has a long life cycle, rainfall rate lower than other cumulus, but much higher than stratiform cloud, and because of longer precipitation time, the rainfall amount is very large. The numerical model study on these two kinds of cumulus clouds have explained the physical principles why the mixed clouds system to be composed of cumulus and stratiform cloud often engender heavy rain.

REFERENCES

[1] Hong Yanchao, 1987, Echo structure of mesoscale systems in the Mei-Yu frontal cloud system and their relations with the heavy rainfall, ACTA METEOROLOGICA SINICA, Vol.45, No.1, 64-64.

[2] Li Zihua, 1982, The precipitation echo featuresin the Mei-Yu frontal cloud system in Jiang-Huai Valley, Collected Papers on Cloud Physics and Artifical Rainfall in the South Part of China, Meteorological Press, Beijing, 55-59.

[3] Hong Yanchao, Wang Angsheng, 1989, A model for predicting intense cumulus rainfall and experiments on its sensibility, Journal of Nanjing Institute of Meteorology, Vol.12, No.3, 11-15.

[4] Du Bingyu,1985, Radar echo features of heavy rain in Mei-Yu front, Journal of Nanjing Institute of Meteorology, Vol.8, No.3.

PHYSICAL-CHEMICAL FEATURES OF THE CHONGQING WINTER FOG AND THE PROCESS OF ITS FORMATION

Li Zihua Zhang Limin
(Nanjing Institute of Meteorology, China)

Zhang Qinghong Dai Anguo
(Chongqing Weather Bureau, China)

Chongqing is a very famous foggy metropolis in China. Composite observations including fog physics and chemistry were conducted in the Chongqing metropolitan area at 13 ground meteorological posts, 3 captive aeronaut sounding sites and 10 fog water collection points as well as at aerosol and fog droplet spectrum observation, radiation and heat budget component measurement, atmospheric quality monitoring, and wind and temperature pultar detection systems during the period of Dec.15, 1989 to Jan.15, 1990. In addition, some supplementary observations were made from Dec.7, 1990 to Jan.7, 1991.

1.Physical-Chemical Features of the Chongqing Fog

The Chongqing fog shows vigorous vertical development with its top at the height of about 400 meters. As shown in Table 1, in the Chongqing urban area (except on the Shapingba Flatland) the number density of fog droplets is great, varying in most cases between 400 and 1100 cm^{-3} while its water content is quite low, generally no more than 0.1gm^{-3} and the size of fog droplets is very small, averaging 3.8-4.8 μm in diameter. As can be seen, there are two factors responsible for such features of the Chongqing fog microstructure. One is the existence of the urban heat island. The air is thus not cooled enough for the droplets to grow sufficiently by condensation. As a result, the water content is low and the size of the droplets is small. The other is the serious air pollution, which causes an increase of both the atmospheric condensation nuclei and number density of the fog droplets.

Table 1 Comparison between the microphysical structures of winter fog in Chongqing and in other places

Loction	Date	Number density (cm-3)	Mean diameter (μm)	Mean square root diameter (μm)	Mean cubrc rootdiameter (μm)	Water content (gm-3)
Shapingba	90.01.02	560	4.6	6.0	8.3	0.01
	90.12.09	160	8.4	9.7	11.3	0.14
	90.12.24	77	11.1	12.5	14.1	0.02
	90.12.20	87	10.4	12.2	14.3	0.03
Shabanpo	89.12.30	110	7.4	9.5	11.0	0.03
	90.01.02	613	3.0	4.0	4.4	0.03
Chenjiaping	90.01.23	1114	3.8	3.9	4.1	
	90.12.09	439	4.8	6.1	8.4	0.12
Liziba	90.12.09	40	12.0	14.3	17.5	0.08
	90.12.24	219	7.0	9.0	10.7	0.09
	90.12.28	159	7.6	8.9	10.6	0.04
Shanghai	89.01.07	195	5.5	8.3	12.9	0.33

The fog water in the Chongqing urban area is all acid, with its PH value ranging between 4.5 and 5.5 (averaging 5.19). Its major chemical components are SO_4^{2-}, Ca^{2+}, NO_3^-, NH_4^+ and Cl^-. The total ion concentration is, on the average, 3.3×10^4 μmol/L, accounting for 0.97% of the fog water weight. In comparison, the components Cl^-, NO_3^-, SO_4^{2-} and NH_4^+ in Chongqing are 1.4 times those in Los Angeles, the United States and 5.9 times those in Akagisan, Japan. Its H^+ ion concentration is 8.5 times that of Shanghai. they come from the burning coal, and the sulphide, chloride and halogenide discharged into the atmosphere bacome sulphuric acid, nitric acid, Hcl and HF by multi-phase catalysis or hydrolysis, thus resulting in the acidification of the fog water.

2.Local Circulation Features

The boundary layer in urban Chongqing has pronounced heat and humidity island structures, which play an important part in the development and dispersal of fog. When night falls, the city center and the Changjiang River are shrouded in a domed layer of warm, humid air. Within the lowest 400 m above the ground, the air temperature and specific humidity are considerably higher than on both sides of the city (Fig.1). In addition, the mean temperature field shows good correspondence with the specific humidity field. Not only does the extent of the warm air is on the whole in agreement with that of the humid air, but also the isolines of temperture (isotherms) and specific humidity on the border of the city both wedge in the warm humid zone, indicating that in the mountains there is an outlet of cold air. In the lower layer the relative humidity is considerably higher in the central part of the city than in its suburbs. In contrast, many other cities have just the opposite effect owing to the existence of the heat island.

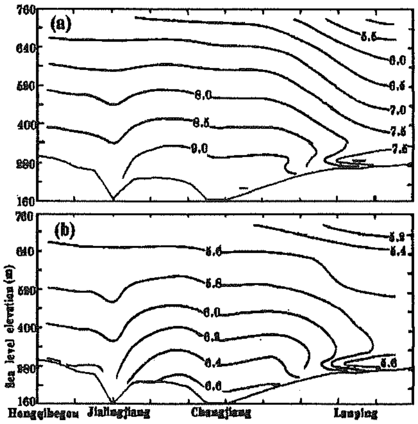

Fig.1. Mean temperature (a) and mean specific humidity (b) at 0200

The city of Chongqing is situated in the valleys. Its central part is enclosed by the Changjiang and Jialingjiang Rivers with a northeast-southwest parallel mountain range on its east and west sides. Modeling of the wind field in the boundary layer shows that at night two air flows drain down the south slope of the Changjiang River and the north slope of Jinlingjing River respectively under the combined action of the topography, heat island and two rivers. They meet in the urban area and converge upward. A clockwise circulation is observed above the south slope of the Changjiang River and a counterclockwise circulation above the Jialingjiang River and its north bank (Fig.2).

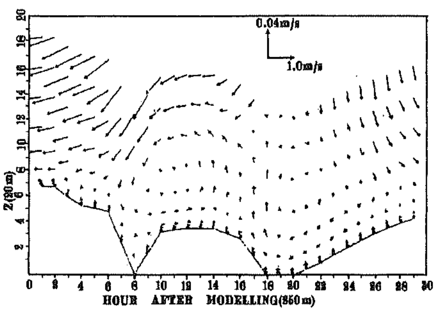

Fig.2. Modeling of the wind field for six hours after 2000

The converging updraft carries with it the moisture upward over the two rivers and transports it to the city center through diverging air. As a consequence, the humidity island is formed.

3.The Physical Process of the Chongqing Fog Formation

3.1 Fog formed and developed under the action of the mountain wind

Take the dense fog on Jan.2, 1990 for example. On the night of Jan.1, clear skies were experienced in the suburbs and clear with cloudy conditions in the urban area. As seen from the map for 0200 Jan.2(omitted), the low-level air flow descending in the mountains on both sides converged in the city center ,while the warm, humid air was thus lifted and mixed with the cold air above, causing a decrease of air temperature and an increase of specific humidity and relative humidity. As shown in Fig. 3, at the height of about 150m (the Shahuba Flatland is 170 m above sea level),a zone of high value f≥94% was observed. From the observation on the Loquats hill in the city center (328 m above sea level),the visibility had been reduced to less than 1 km.Then under the action of gravity settling and turbulent diffusion the air reached the ground in the form of fog at 0500.

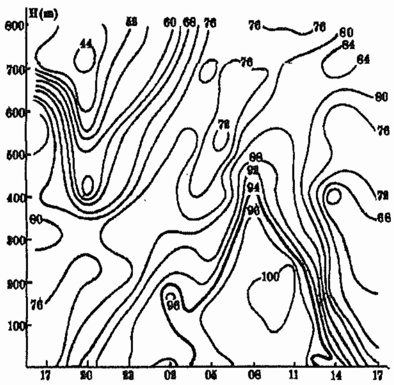

Fig.3. Time-height cross section of relative humidity on the Shahuba Flatlad on Jan.2.

At 0500-0800,the fog developed rapidly, its top leaping up to the height of 400m and a zone of dense fog(f=100%) was experienced at the height of 150 m above the Changjiang River (see Fig.3).Besides the intense radiation cooling at the fog top, which was beneficial to its upward extension, the development of the fog was mainly due to the intensified radiation cooling in the mountains and the increased mountain wind during this period of time. As a result, the air temperture decreased considerably in the fog zone and the upward motion became intensified over the two rivers and urban area, causing plenty of moisture over the water surface to move up to greater heights of the fog layer.

At 1100,the fog began to dissipate.Its top decreased rapidly first and meanwhile its base lifted. After 1400,the fog was all dispersed. this was due to the change of the air flow field. The convergence field originally over the Changjiang River became the divergence field and the diverging flow originally at the fog top became the converging flow, that is, the mountain wind at the lower level became the valley wind.

3.2 Fog formed by radiation cooling and then developed under the action of mountain wind

Take the dense fog on Dec.9,1990 for example. On the night of Dec.8, the urban area experienced clear, calm conditions with intense effective radiation and abrupt temperature drop (the rate exceeded 1℃/hr). The relative humidity increased rapidly and at 0052 fog resulted first on the Shapingba Flatland. As seen from Fig.4(a),in the boundary layer there were two inversion layers in the process of fog formation, one within the lowest layer of 20m, very near the ground and the other at the height of 180-360 m. As the top extended upward, radiation cooling became intensified. The surface inversion disappeared while the inversion structure at the top emerged and combined with the low-level inversion. At 0200-0500, the fog top developed rapidly and lifted 120m. Meantime, the inversion layer at the top increased its depth of 500 m and intensity of 1℃/100m.This situation was entirely different from the fog on Jan.2,in which no obvious inversion structure was observed. Comparison between 4(a) and 4(b) shows that the fog in Fig.4(a) was in a closed cold core and its top was covered with warm air, its temperature being even higher than the surface temperature, whereas the fog in Fig. 4(b) was roughly in the cold trough and the temperature in the boundary layer as a whole decreased steadily upward.

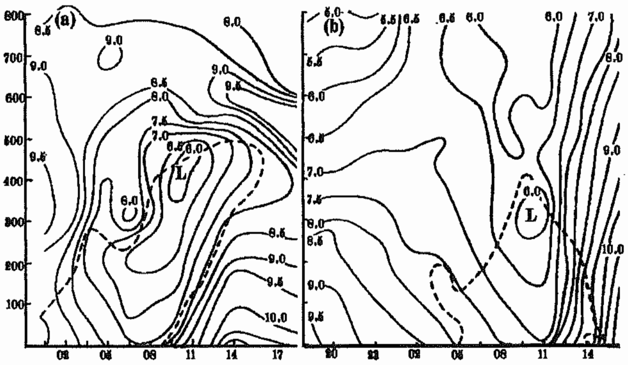

Fig.4.Time-height cross section of air temperature on Dec.9(a) and Jan. 2(b). The fog distribution was within the dotted line.

It is seen too from Fig.4(a) that as radiation heating started from the surface ground after sunrise and gradually developed upward, the fog dissipated upward from the ground surface and became low clouds, which lifted slowly. This situation was also different from the fog on Jan.2.

Although this fog resulted from radiation cooling, the mountain wind played an important role in its development. Analysis indicates that in the fog formation the descending air let out in the mountains on both sides converged in the city center, causing an increase of the fog top.

4.Conclusion

Radiation is not the only factor responsible for the production of the Chongqing fog. Besides, the topography, mountain wind,two major rivers across the city, urban heat and humidity islands and air pollutants all exert a great influence on its formation and development.

PRECIPITATION MEASUREMENTS OF WINTER STRATIFORM CLOUD ALONG TIAN SAN MOUNTAINS IN XINJIANG, CHINA

Gao Ziyi and Li Jinyu

Xinjiang Meteorological Bureau, Wulumuqi, Xinjiang, China, 830002

1. INTRODUCTION

Since 1980, surface precipitation intensity measurements of winter stratiform clouds have been done along Tian San Mountains in nortnern Xinjiang , China. About thirty sampling sites were distributed over an area of 600Km long and 50Km wide. Sampling instrumentation was a wooden collector with a 3600cm^2 opening which was paved with plastic film. Samples 20 minutes in duration were taken consecutively from the begin of snowfall to the end, and were weighed with a balance to determine the average snowfall intensity during the collection period.

In this paper, based on data collected from 58 integrated snowfall processes, statistical characteristics of the snowfall and evolution patterns of snowfall intensity with time under six main synoptic situations that affett Xinjiang area are analysed. Evidence suggested that precipitation property of stratiform cloud in arid region had significant difference from general theory and observation results in the past.

2. STATISICAL CHARACTERISTICS

Main synoptic systems affected Xingiang include long-wave trough, short-wave trough, frontal-zone trough, frontal-zone small wave and low-vortex. In addition, a special weather type by name "dark-cloud-fog" which occurred within Zhunger Basin during wintertime and under control of high-pressure system also has been considered. According to different weather types and strengths, average and Maximum of snowfall intensities , as well as average durations of the snowfall are given by Table 1.

From Table 1, it is clear that, in general, the amount and intensity of the precipitation of winter stratiform clouds in Xinjiang were little, and the duration of precipitation was short . The range of the precipitation

TABLE 1. Statistical characteristics of snowfall

Synoptic situation	Weather strength	Snowfall intensity(mm/hr.)		Precipitation amount(mm)	Precipitation duration(hour)
		mean	max.	mean	mean
Long-wave trough	Heavy	0.43	2.66	10.97	21.5
	Moderate	0.18	1.80	5.48	27.4
	Lighter	0.16	0.42	1.44	9.1
	All	0.22	2.66	4.65	19.8
Short-wave trough	Moderate	0.25	2.41	4.39	17.3
	Lighter	0.15	1.19	1.63	10.7
	Lightest	0.03	0.13	0.05	1.4
	All	0.18	2.41	1.86	10.2
Frontal-zone trough	Moderate	0.17	3.10	8.96	10.4
	Lighter	0.14	1.48	1.87	13.5
	All	0.15	3.10	2.57	12.5
Forntal-zone small wave	Moderate	0.27	1.67	5.80	19.4
	Lighter	0.14	2.06	1.59	10.5
	Lightest	0.02	0.12	0.09	5.7
	All	0.15	2.06	1.55	9.7
Low-vortex	Lighter	0.05	0.35	1.10	23.9
	Lightest	0.01	0.06	0.07	16.1
	All	0.04	0.35	0.75	21.3
Dark-cloud-fog	Lighter	0.02	0.13	0.42	15.5
	Lightest	0.01	0.02	0.02	2.0
	All	0.02	0.13	0.29	11.0
All		0.14	3.10	1.96	12.0

intensities were $10^{-2} \sim 10^{1}$mm/hour that were less than observed results of $10^{1} \sim 10^{2}$mm/hour in some regions of China (Zhenchao Gu, 1980).

3. EVOLUTION PATTERNS

The evolution patterns of snowfall intensity with time were found to be many and varied. Fig.1 show typical patterns which respond to six synoptic situations presented in the above section.

A general property displayed by Fig.1 is that snowfall intensity fluctuates within a wide range. Particularly in the cases of short-wave trough and frontal-zone trough, snowfall intensity can increased or decreased rapidly by factor of a few to above ten within 20 minutes. It is different from results measured in northern Colorado during wintertime storms(Rauber, 1987).

Evidence suggested that the evolution of sonwfall intensity with time was related to both the lower narrow cloud band near the front and the higher level cloud band.

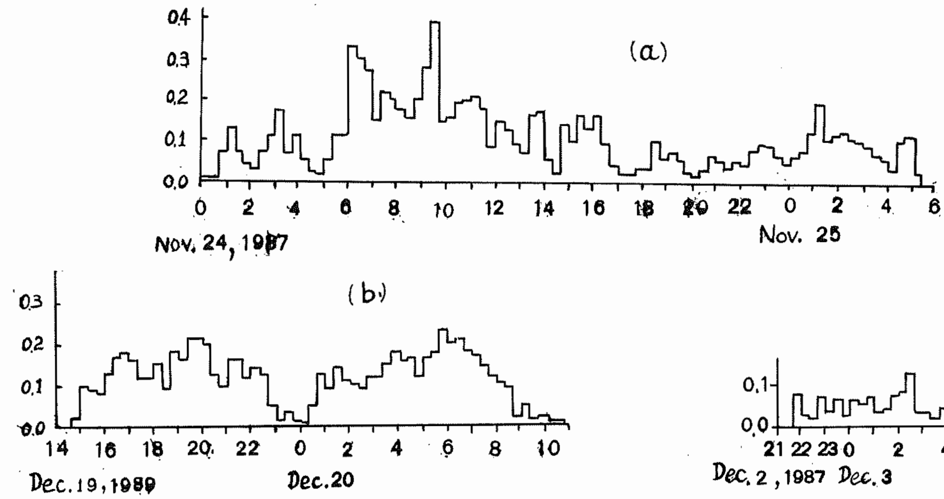

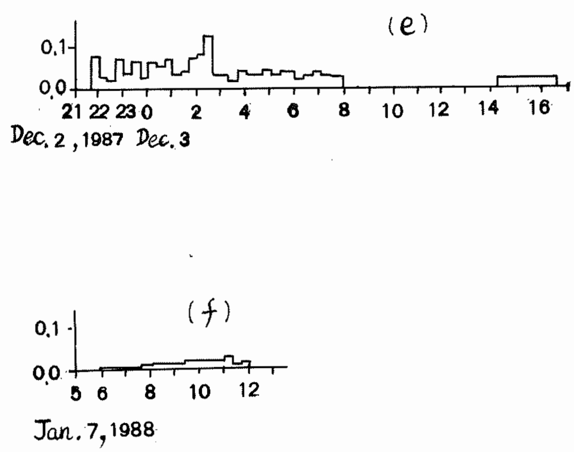

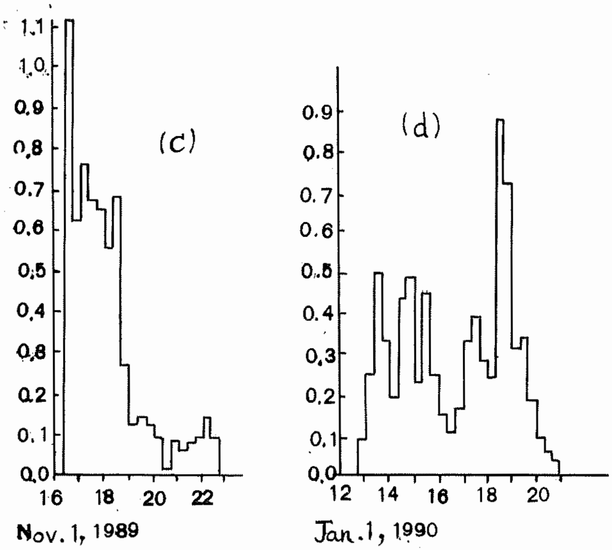

Fig 1. Typical evolution patterns of sonwfall intensity with time.
All abscissas show time (Beijing Time).
All ordinates show snowfall intensity (mm/hour).
(a) long-wave trough. (b) frontal-zone small wave. (c) short-wave trough. (d) frontal-zone trough. (e) low-vortex. (f) "dark-cloud-fog".

4. SUMMARY

The results of this study are summarized below.

1) The amount and intensity of the precipitation from winter stratiform clouds in Xinjiang were little, intensities ranged from 10^{-2} to 10^{1}mm/hour and, moreover the large majority of the precipitation in one storm process falled concentratively within a few hours. This is a distinguishing feature in arid region.

2) The evolution of the precipitation intensity was closed relevant to both type and strength of the storms. In some storms, changed patterns of precipitation intensity were very similar to the cumuliform cloud precipitation during summertime. This is different from grneral concept on stratiform cloud precipitation.

REFERENCES

Gu zhenchao, 1980: Physical basis of cloud and precipitation. China Scientific Press, 28~~29.

Rauber, R.M., 1987:Characteristics of cloud and precipitation during wintertime storms over the Mountains of northern Colorado, J. Climate and Appl. Meteor., 26 , 488~~524.

Lagrangian Observations of Marine Stratocumulus Evolution and Breakup

Robert Pincus,[+] Marcia Baker,[+] and Chris Bretherton[✧]

[+]Geophysics Program AK-50 [✧]Department of Applied Mathematics FS-10
University of Washington, Seattle WA 91895 USA

1. Introduction

Interest in marine stratocumulus clouds has exploded in the last 25 years. This activity is in part the result of satellite observations which have emphasized the very large areal extent and long lifetime of these clouds. Models (Lilly, 1968; Schubert et al., 1979), in-situ measurements (e.g. Nicholls, 1984, Paluch and Lenschow 1991) and satellite observations (Minnis et al. 1992) have led to a good understanding of the processes which sustain homogeneous cloud decks, but the physical mechanisms which cause these decks to change to other regimes (such as trade cumuli or clear sky) remain unclear.

Modelling studies have suggested that cloud decks are not in equilibrium with either their local environment (Wakefield and Schubert 1981; Wang et al. 1992) or the instantaneous radiative forcing (Bougeault 1985). In order to understand the evolution of the clouds, then, we need to account for time dependent changes in the forcings to which the clouds are subject. This is a straightforward addition to most models but a difficult task when making observations, not least because of the geographical remoteness of the clouds.

We have developed a technique for observing the Lagrangian evolution of mesoscale parcels of marine stratocumulus clouds. By combining the large scale view available from geostationary satellites with information about the spatially and temporally varying environment from NMC analyses, we are able to follow the life histories of individual cloud parcels, and relate the clouds' responses to the environment in which they have evolved. We focus on cloud parcels which break up, changing from homogeneous decks to clear air in the course of a 24 hours period.

2. Methodology

2.1 Data Sources

We focus on the time and region observed during the FIRE Intensive Field Operations during 1987. We consider the region of the Eastern Pacific ocean bounded by 135 W and115 W longitude, 23 N and 40 N latitude, during the time period June 27 to July 19, 1987.

a. Environmental Parameters

We use the 1000 mb wind fields from the NMC gridded analyses to compute the trajectory of the boundary layer clouds. From these wind fields we compute a large scale divergence field on a staggered grid. These fields are available every 12 hours at 2.5 degree spacing. The sea surface temperature field is a weekly composite of clear sky measurements from the AVHRR (McClain et al., 1985) at 18 km resolution.

b. Satellite Images

We use full resolution broadband infrared and visible images from the GOES-6 geostationary satellite. The images are reported every half hour, with a spatial resolution of 1 km in for the visible data and 4 x 8 km for the infrared data.

2.2 Computation of Trajectories

We use the NMC wind fields to calculate the trajectory of mesoscale-sized cloud parcels. At hourly intervals we obtain a 128 km square IR and visible images centered on the parcel. We determine the values of wind speed, divergence and sea surface temperature at each hour by linear interpolation in space and time.

We estimate the cloud top height for each IR pixel using the relation $z_i = (SST - T_{zi})/7.1$, where SST is the environmental value and T_{zi} is the radiometric temperature from the GOES IR image. At this time we make no correction for cloud emissivity.

We convert the visible data to reflectance values using the calibration of Minnis et al. (1992). We estimate the optical depth of the cloudy pixels using the technique of Gu et al., (1992). At this time a pixel is determined to be cloudy if its reflectance exceeds a threshold value (typically 0.2). Similarly, we determine a rough estimate of cloud fraction for daytime hours by dividing the number of pixels whose reflectance value exceeds the threshold by the total number of pixels in each image.

3. An Example of Breakup

3.1 Regional View

Figures 1a and 1b show the large scale view at 1515 PDT on June 26, 1987 and 1415 PDT on June 27. The image covers 25 square degrees, from 25 to 30N and 120 to 125W. Superimposed on the images (though perhaps not well reproduced) are the NMC wind and divergence fields from the analysis closest in time to the image.

On June 26th the region is covered by a stratocumulus deck with large scale cellular structure. The deck is brighter and thicker to the northwest. The divergence field increases from $2.5 \times 10^{-6}\ s^{-1}$ in the northern section of the region to 6.5×10^{-6} at the southern edge. The winds are weak (about 2 m/s) everywhere. Typical cloud top temperature is about 282 K, which corresponds to a cloud top height of 1.4 km, given the average sea surface temperature of 292 K in the region.

By mid-afternoon the next day a large fraction of

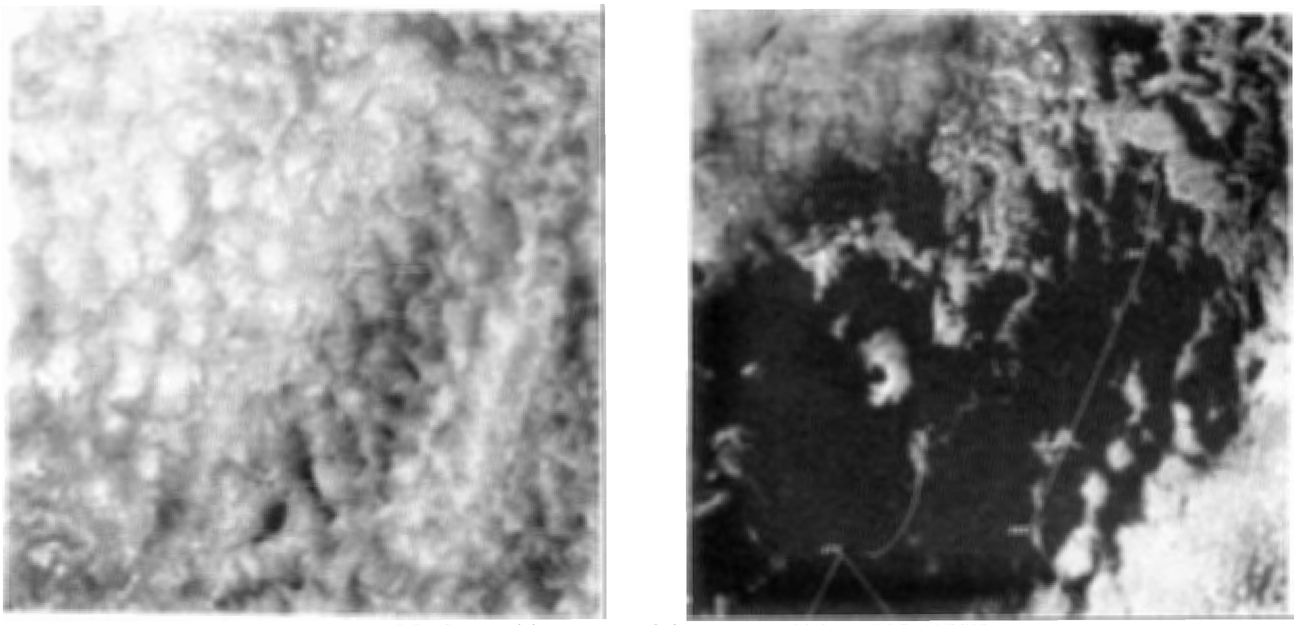

a. Figure 1: GOES-6 visible images of the region 25 N to 30 N, 125 W to 120 W, at1 515 PDT on June 26, 1987, and 1415 PDT on June 27. Also shown are NMC divergence and wind fields and the path of our parcel. b.

the region is devoid of clouds. The divergence field is similar in magnitude to the previous day but the gradient is now oriented east-west. The winds are even lighter. Some clouds with tops about 1.4 km remain in the northwest corners of the image, but a patch of brighter, lower clouds is now evident in the southeastern corner, with cloud tops at roughly 850 m, and structure on a smaller scale.

3.2 Trajectory Analysis

We will investigate this clearing episode by following a trajectory beginning at 26.1 N, 123.6 W at the time of the first image. The parcel moves slowly north and west along the path shown in figure 1. The wind velocity is quite low along the trajectory, averaging about 1.5 m/s and never exceeding 2.5 m/s. The sea surface temperature and large scale divergence vary little from their average values of 291.5 K and 6×10^{-6} s^{-1}, respectively.

Figure 2 shows the time evolution of cloud fraction and of the estimated cloud top height, based on the lowest quartile of radiant temperatures. Figure 3 shows the time evolution of the histograms of radiant temperature and optical depth. The gray scale indicates the number of pixels with a given temperature or optical depth (the vertical axis) at a given time (the horizontal axis). Every six hours the water vapor channel is recorded, and the radiant temperatures are not available.

On the first afternoon cloud top temperature is relatively uniform at 282 K. The mode optical depth is $\tau = 7$, corresponding to a liquid water path of about 37 g/m^2, or a cloud roughly 200 m thick with adiabatic liquid water content. The mode optical depth decreases to $\tau = 2$ with decreasing variability at sunset, as the cloud fraction drops to 0.8. Cloud top temperature remains uniform and cold until just before midnight, when both the temperature and the variability increase for 7 hours. This is also evident in the estimated cloud top height, which shows a drop of 300 m in 6 hours. Taken at face value, this indicates both cloud top and cloud base decreasing by 1.3 cm/s. We offer another explanation in the next section.

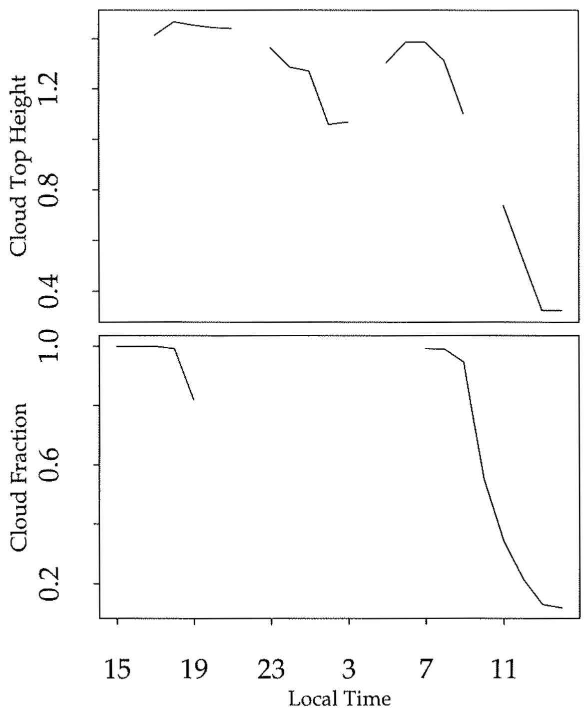

Figure 2: Estimates of cloud fraction and cloud top height z_i. The apparent nighttime decrease in z_i is due to thinning.

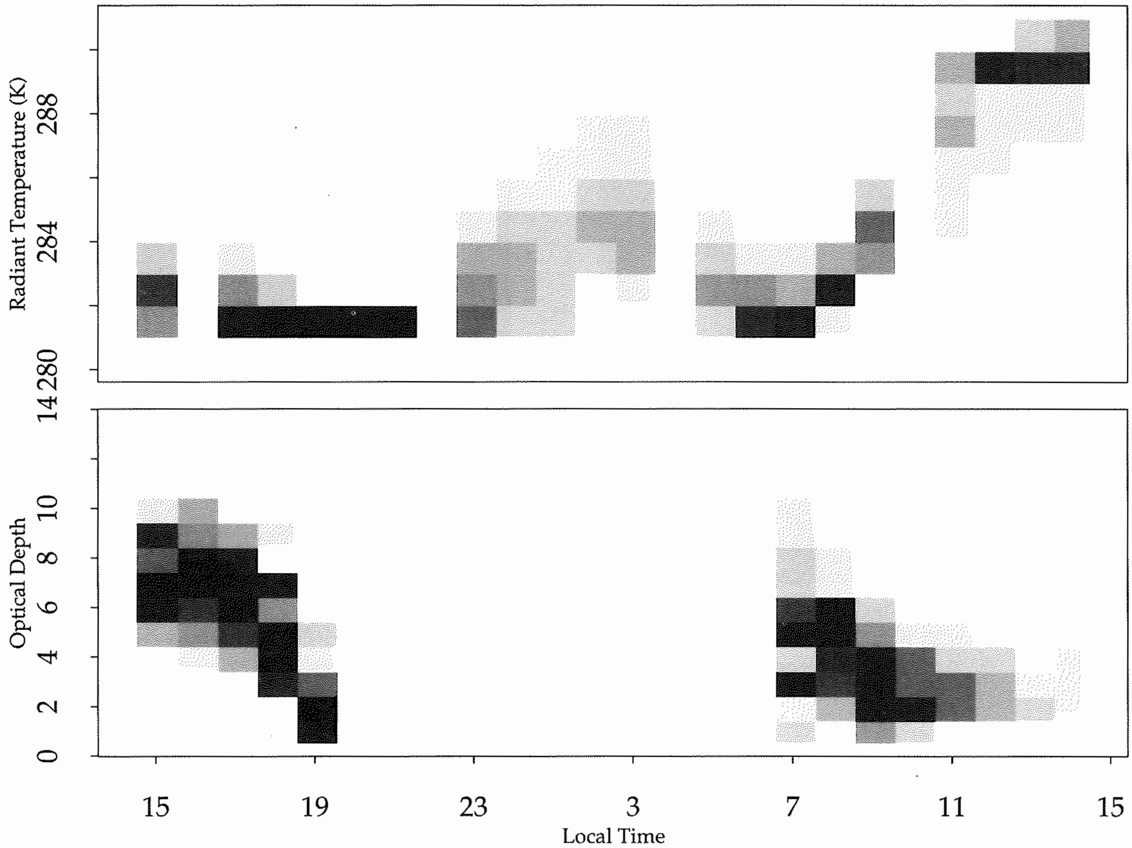

Figure 3: Time evolution of radiant temperature and optical depth. The gray scale indicates the number of pixels at a given temperature or optical depth at a given time.

At sunrise the cloud top temperature is again cold, though more variable than on the previous afternoon, and the cloud optical depth has increased to a mean of $\tau = 6$. As the sun rises in the sky the temperature increases while the optical depth, estimated cloud top height and cloud fraction all decrease precipitously, until by 2:15 PDT there are only a few thin wisps of cloud in the study region.

4. Discussion

The low wind speed and consequent low surface flux of moisture appears to be the leading cause of breakup in this case, although the diurnal cycle also modulates cloud thickness. We believe the data are consistent with the following story:

When we first observe the clouds they are uncoupled from the surface layer, and they continue to thin until midnight due to entrainment and, before dusk, absorption of solar radiation. The increasing mean and variability in temperature between local midnight and early morning indicate that the cloud deck is becoming thin and patchy, with holes smaller than the resolution of the satellite sensor. This is confirmed by inspection of the IR images for this time. Were the wind speeds higher, larger surface fluxes would act in concert with the radiative cooling to mix water into the cloud layer and thicken the cloud.

In the early morning the cloud reconnects with the subcloud layer and becomes thicker and more uniform with the addition of moisture from the sea surface. The moisture fluxes from the sea surface are limited by the low wind speed, however, so that after the sun comes up the solar absorption quickly overwhelms the additional moistening, and the cloud evaporates.

Discussion of stratocumulus cloud breakup often focuses on physical mechanisms, such as cloud top entrainment instability (CTEI, Randall 1980) or decoupling (Paluch and Lenschow, 1991). In our case study, however, we see that processes as mundane as solar absorption in concert with low surface fluxes, can be responsible for clearing over large regions.

5. Summary

We have described a technique we use to observe the Lagrangian evolution of marine stratocumulus clouds in remote regions of the ocean. We have show the results of one case study, and concluded that absorption of solar radiation, combined with low surface fluxes due to decoupling and low wind speeds, led to the breakup of the clouds.

6. Acknowledgments

The GOES data were graciously provided by the

NASA Climate Data System at NASA Goddard Space Flight Center. The sea surface temperature observations come from the National Ocean Data System at the Jet Propulsion Laboratory. The NMC analyses were made available by the Data Support Section of the Scientific Computing Division at NCAR. We would like to thank Scott Katz and Marc Michelsen for development and maintenance of the satellite image software. This work was supported by a NASA Graduate Fellowship in Global Change Research and by grant number N0014-90-J-1162 from the Office of Naval Research.

7. References

Bougeault, P., 1985: The diurnal cycle of the marine stratocumulus layer: A higher-order closure model study. J. Atmos. Sci., 42, 2826-2843

Gu, J., R. Pincus, P. Austin and M. Szczodrak, 1992: Cloud optical depth estimates from satellite measurements. Proceedings of the 11th International Conference on Clouds and Precipitation. Montreal, Canada.

Lilly, D. K., 1968: Models of cloud-topped mixed layers under a strong inversion. Quart. J. Roy. Met. Soc., 77, 598-626.

McClain, E. P., W. G. Pichel, and C. C. Walton, 1985: Comparitive performance of AVHRR-based miltichannel sea surface temperatures. *J. Geophys. Res.*, **90**, 11587-11601.

Minnis, P., P. W. Heck, D. F. Young, C. W. Fairall and . B. Snider, 1992: Stratocumulus cloud properties derived from simultaneous satellite and island-based instrumentation during FIRE. J. App. Met., 31, 319-339.

Nicholls, S, 1984: The dynamics of stratocumulus: aircraft observations and comparisons with a mixed layer model. Quart. J. Roy. Met. Soc., 110, 783-820.

Paluch, I. R. and D. H. Lenschow, 1991: Stratiform cloud formation in the marine boundary layer. J. Atmos. Sci., 48, 2148-2158.

Randall, D. A., 1980: Conditional instability of the first kind upside-down. *J. Atmos. Sci.*, **37**, 125-130.

Schubert, W. H., J. S. Wakefield, E. J. Steiner and S. K. Cox, 1979: Marine stratocumulus convection: Part II: Horizontally inhomogeneous solutions. J. Atmos. Sci., 6, 1308-1307.

Wakefield, J. S. and W. H. Schubert, 1981: Mixed-layer model simulation of Eastern North Pacific stratocumulus. Mon Wea. Rev., 109, 1952-1968.

Wang, S., B. A. Albrecht and P. Minnis, 1992: Regional modeling of marine boundary layer clouds. Atmos Sci., in press.

Measurements of the Radiative and Microphysical Properties of Stratocumulus Over the South Atlantic and Around the British Isles.

J. P. Taylor
UK Meteorological Office, Meteorological Research Flight,
RAE Farnborough, Hampshire, England.

1 Introduction

During November 1991 the Meteorological Office Research Flight C130 took part in a series of flights off the West Coast of Africa at a latitude of around 10^oS as part of the First ATSR (Along Track Scanning Radiometer) Tropical Experiment, FATE. Several flights were made over the extensive stratocumulus sheets found to the south east of Ascension Island (8^oS, 14.5^oW) at this time of year. Climatological data suggests that this region of the South Atlantic (SA) has between 80% and 90% frequency of occurrence of stratus and stratocumulus during the period September through November (based on 1952 - 1981 data), and that the coverage when cloud is present is between 80 and 95%. This, combined with the probability that the air would be relatively unpolluted and hence the stratocumulus would be truly maritime, made this an interesting area to study the radiative and microphysical properties of maritime stratocumulus to contrast with stratocumulus measurements around the British Isles (BI).

In this report data from one flight on the 11 November 1991 in the South Atlantic will be compared with that from a flight around the British Isles on 28 June 1990.

2 Instrumentation

The UK C130 aircraft is extensively equipped for the study of atmospheric processes. The radiation instrumentation flown during the FATE detachment included the Multi - Channel Radiometer, MCR, (Rawlins and Foot 1990). The MCR measures radiances in many narrow spectral bands between $0.55\mu m$ and $12\mu m$. Broad band hemisphere viewing Eppley pyranometers and pyrgeometers were also flown on the C130 which measured upwelling and downwelling fluxes in the wavelength ranges: $0.3 - 3.0\mu m$, from now on referred to as clear flux, $0.7 - 3.0\mu m$, from now on referred to as red flux and $4 - 50\mu m$, from now on referred to as infra red (IR) flux. The visible flux $0.3 - 0.7\mu m$ can also be calculated as the difference between the clear and red fluxes. Also flown during the experiment, although the data is not presented here, was a two channel microwave radiometer measuring zenith and nadir views at 89GHz and 157GHz.

Figure 1: A146 11 November 1991, profiles of (a) Liquid water content and (b) cloud droplet effective radius. 101436 - 102354 GMT

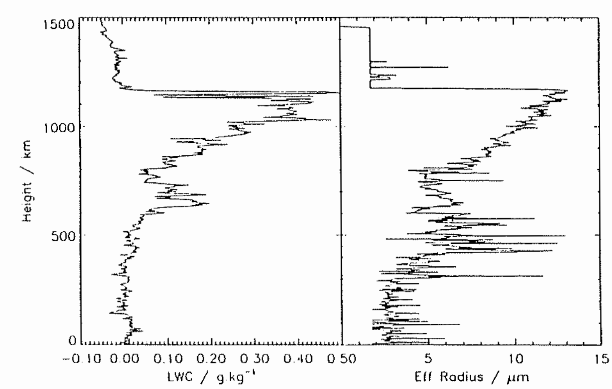

Aerosol concentrations were measured using a Particle Measuring Systems (PMS) Passive Cavity Aerosol Spectrometer Probe (PCASP) which measures aerosol in the range $0.3 - 3.0\mu m$, droplet size and concentration were measured using a PMS Forward Scattering Spectrometer Probe (FSSP) for droplet radii from $0.5 - 25\mu m$. The FSSP was calibrated with glass beads of known size and the estimated accuracy of the measured radius is $\pm 1\mu m$. The liquid water content of the clouds was obtained from measurements made by a Johnson Williams hot wire probe. Cloud condensation nuclei were also measured using an MRF developed static diffusion chamber.

3 Flight A146 on 11 November 1991.

This flight was over an extensive sheet of stratocumulus to the south east of Ascension Island. Figure 1 shows profiles of the Johnson Williams cloud liquid water content and FSSP measured cloud droplet effective radius. The cloud base was at 0.6km and the tops at 1.18km. The effective radius at cloud top was a maximum of $13.2\mu m$. A run below the cloud showed the mean PCASP aerosol concentration to be $125 cm^{-3}$, the CCN concentration below the cloud was also measured and found to be low, both indicating a maritime airmass. There is evidence in the profiles of figure 1 that lower in the cloud the aircraft passed through the remains of some convective cloud that had intruded into the stratocumulus deck; the effective radius increases slightly and there is a small increase in liquid water content. There was no visible evidence of cumulus below the stratocumulus sheet so one must infer that this is the remains of an older cumulus turret.

Figure 2: A146 11 November 1991, Straight and level run (a) Liquid water content, (b) cloud droplet effective radius and (c) cloud droplet concentration. 103556 - 104058 GMT

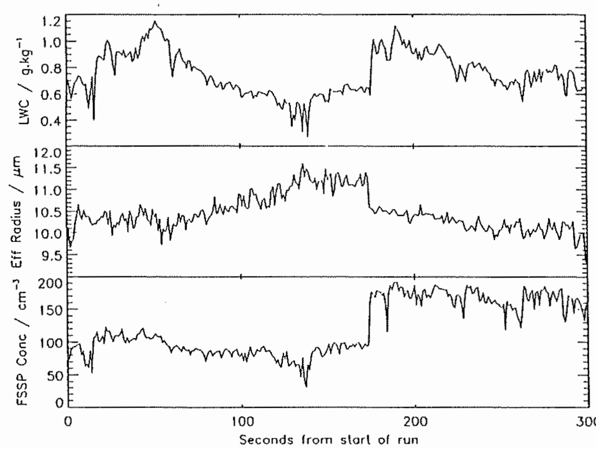

Straight and level runs in the tops of the stratocumulus, figure 2, showed variations in liquid water content from $0.4g.kg^{-1}$ to $1.1g.kg^{-1}$ and changes in droplet concentration from $50cm^{-3}$ to $180cm^{-3}$. The maximum liquid water content observed being very close to the adiabatic liquid water content for this cloud layer of $1.15g.kg^{-1}$. This is further evidence that the stratocumulus sheet has been modified in the recent past by cumulus intrusion. The variations in effective radius along the run in cloud tops, as measured by the FSSP, are considerably smaller from around $10.2\mu m$ to $11.2\mu m$.

Figure 3: A019 28 June 1990, profiles of (a) Liquid water content and (b) cloud droplet effective radius. 130130 - 130738 GMT

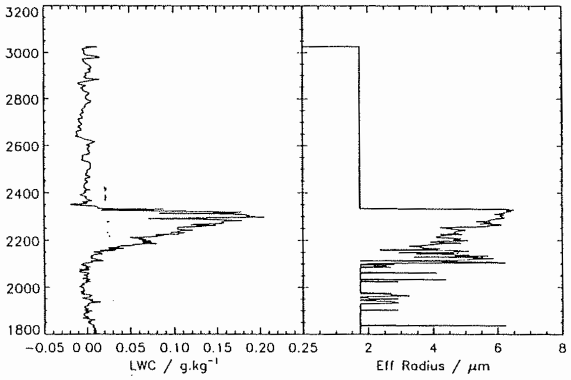

4 Flight A019 on 28 June 1990

This flight was over a region of stratocumulus to the South West of the British Isles. Figure 3 shows the liquid water content and effective radius during a profile. The stratocumulus during this flight was thinner than that found in the SA, tops 2.33km base 2.1km. Figure 4 shows the effective radius, liquid water content and droplet concentration for a run skimming through the cloud tops. During the run the droplet concentration remains relatively constant between 60 and $80cm^{-3}$ and the effective radius changes from $6.5\mu m$ to $5.5\mu m$. The liquid water also decreases along the run from $0.2g.kg^{-1}$ to $0.14g.kg^{-1}$. The regions where droplet concentration falls to zero is where the aircraft temporarily left the cloud. The liquid water content observed is always significantly less than the adiabatic liquid water content of the cloud, $0.394g.kg^{-1}$.

A run below the cloud showed PCASP aerosol concentrations of only $130cm^{-3}$ which indicates that this airmass was also maritime. The PCASP aerosol concentrations measured here are very similar to those found in the South Atlantic, flight A146, however the droplet concentrations and effective radii for the two flights are significantly

Figure 4: A019 28 June 1990, Straight and level run (a) Liquid water content, (b) cloud droplet effective radius and (c) cloud droplet concentration. 133303 - 134257 GMT

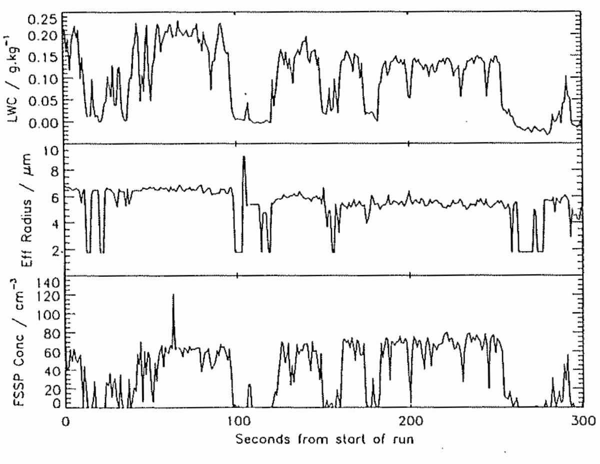

different. The synoptic situation for the 28 June 1990 showed a weak high over Northern France. The airmass being sampled is likely therefore to have at some time in its past been over continental Europe. The droplet concentrations observed during the BI flight A019 were nearly always less than those observed in the SA, flight A146. This suggests that the fraction of aerosol that could act as CCN in the SA was higher than that in the BI so activating more drops. This is understandable since the SA aerosol are likely to be largely sea salt which are a good hygroscopic CCN.

These two stratocumulus sheets represent the extremes in terms of cloud microphysics. In one case we have high liquid water content and large effective radii, in the other we have low liquid water content and low effective radius. Since the microphysical properties of these two stratocumulus sheets are so different it is worth studying their radiative properties both in narrow spectral bands and in terms of broad band fluxes.

5 Narrow Spectral Band Measurements.

Figure 5 shows the reflectance of the BI cloud sheet and figure 6 the SA sheet at 0.55, 1.25, 1.55 and $2.26\mu m$. The solar zenith angles for the BI and SA flights are 31.8^o and 26.2^o respectively. The cloud sheet in the BI case is optically thinner than the SA case and the reflectivity of the sheet is lower at all four wavelengths than the optically thick SA case. It should also be noted that the reflectance of the BI cloud case is almost the same for all four wavelengths where as for the tropical cloud it is a strong function of wavelength.

This suggests that as we move to optically thinner cloud the changes in reflectance and hence optical depth and effective radius will become imperceptible and any scheme which uses reflectance to derive effective radius or optical depth will no longer work. For flight A146 the variation in reflectance along a run is largest for the lowest wavelengths which suggests that variations in liquid water path are greater than variations in effective radius, as observed in-situ. However for flight A019 the large variations in reflectance are common for all wavelengths which suggests that the cloud is less homogeneous and that the liquid water content, effective radius and cloud structure are changing along the run.

The radiative properties of a plane parallel homogeneous stratocumulus cloud sheet can be characterised in terms of the cloud droplet effective radius, r_e, and the cloud optical depth, τ, (Slingo and Schrecker 1982). Using the MCR on the C130 it is possible to retrieve these two properties of a stratocumulus sheet, (Rawlins and Foot 1990, Taylor 1992).

Figure 5: A019 28 June 1990, Reflectance of stratocumulus at specified MCR wavelengths.

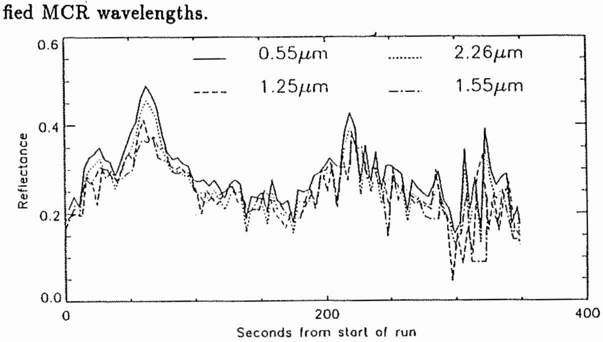

Figure 6: A146 11 November 1991, Reflectance of stratocumulus at specified MCR wavelengths.

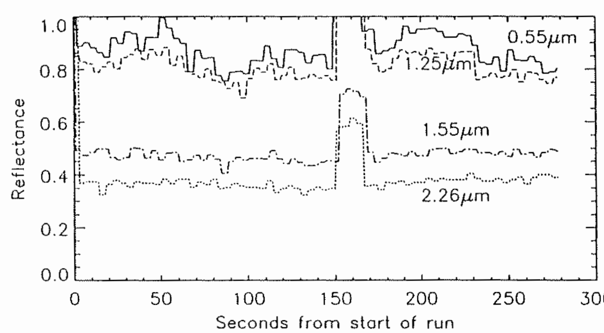

Figure 7: A019 28 June 1990, (a) Retrieval of effective radius at $2.01\mu m$ and (b) Retrieval of optical depth at $1.25\mu m$

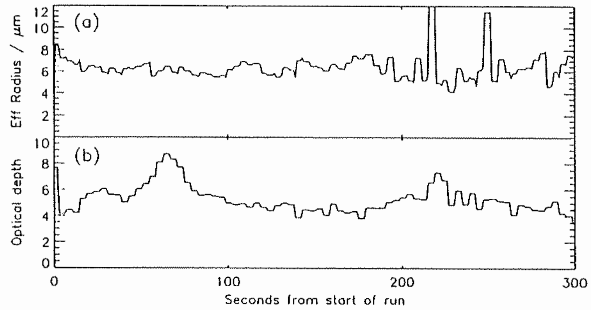

The retrieval scheme works by measuring the reflectivity of the cloud sheet in two narrow wavelength bands. The reflectivity in a spectral region of weak liquid water absorption is relatively insensitive to changes in r_e but increases monotonically with increasing τ. This reflectivity measurement is used to retrieve an optical depth for the cloud which is used in turn to retrieve effective radius by measuring the reflectivity in a wavelength region of strong liquid water absorption where reflectivity is a strong function of r_e and relatively insensitive to optical depth.

In this paper the optical depth of both stratocumulus cloud decks has been retrieved using the MCR $1.25\mu m$ channel and the effective radius retrieved at wavelengths of $2.26\mu m$ and $2.01\mu m$. Rawlins and Foot 1990 and Taylor 1992 detail this retrieval scheme and discuss the depth into the cloud to which the retrieved effective radius refers.

The optical depth, retrieved at $1.25\mu m$, and the effective radius, retrieved at $2.26\mu m$ for the BI flight A019 are shown in figure 7, and for the SA flight in figure 8. In both cases the retrieved effective radius is in good agreement with that measured in-situ with the FSSP, (figures 2 and 4).

Figure 8: A146 11 November 1991, (a) Retrieval of effective radius at $2.26\mu m$ and (b) Retrieval of optical depth at $1.25\mu m$

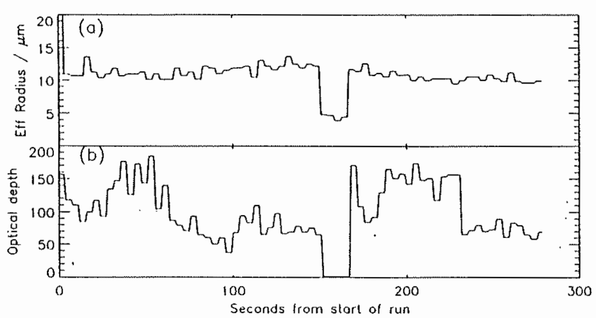

The optical depth of the SA stratocumulus field is very large with a mean optical depth of 90 as opposed to 5 for the BI flight. There is considerable variation in the optical depth for the SA flight whilst the effective radius only changes slowly from around $11\mu m$ at the beginning of the run to $12\mu m$ in the middle of the run, then back to $10\mu m$ at the end. This shows that in this case the effective radius is largely independent of the optical depth which varies as the liquid water content, as seen in-situ. The reduction in optical depth and effective radius at 150 seconds from start of run is an instrument problem and not real. The retrievals of optical depth for the flight around the BI shows considerably less variation, the effective radius for the BI flight shows more variation along the run with sudden changes of the order of $1.5\mu m$ occuring within a few seconds.

The retrieval of r_e at the very low optical depths, found in flight A019, is less satisfactory for a number of reasons including more significant departures from the plane parallel assumption, also as we move to very low optical depths there arises the problem of multiple values of effective radius that can give the same reflectance.

6 Broad Band Spectral Measurements.

Broad band hemispherical fluxes, downwelling and upwelling, were measured for both flights at levels above, within and below the cloud. The clear and red fluxes are measured directly and the visible fluxes calculated from their difference. Following the method of Rawlins (1989) the absorptance of the cloud layer is calculated as:

$$A \;=\; \overline{A} - E \tag{1}$$

where $A =$ absorptance of cloud layer, $\overline{A} =$ directly measured absorptance, and $E =$ the net energy gained or lost through sides of cloud.

In any practical application of equation 1, the term E will include both edge effects and sampling errors. Rawlins (1989) corrected for cloud edge effects and sampling errors by assuming that the divergence of visible radiation within the cloudy layer is very small and that the loss through edges to be approximately the same in different spectral regions, which is realistic in view of the scattering properties of clouds only changing slowly with wavelength. The term E can therefore be equated to the apparent absorption at visible wavelengths, if the absorption at visible wavelengths $(0.3 - 0.7\mu m)$ can be assumed to be negligible. By calculating the absorptance of a cloud layer using equation 1 it is therefore possible to remove sampling errors and errors associated with in-homogeneous cloud fields and allows the direct comparison of the absorptance of different cloud sheets.

Figure 9: The bulk radiative properties of the stratocumulus clouds for (a) the BI flight A019, and (b) the SA flight A146.

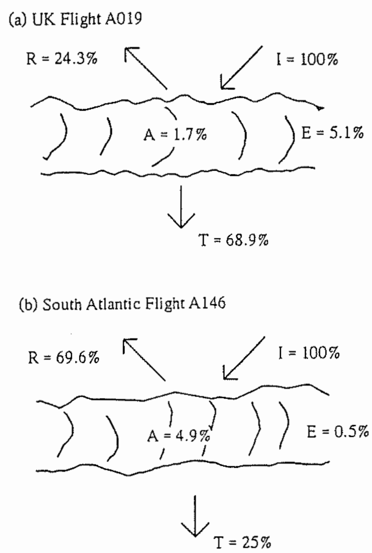

Using run means of legs of at least 5 minutes endurance above and below both cloud sheets the results shown in figure 9 are obtained.

The broad band data for flight A019 have been normalised to a solar zenith angle of 31.8^o and in flight A146 have been normalised to 26.2^o. In figure 9, I is the incident radiation (100 units) and the albedo (R), absorptance (A), transmittance (T) and visible absorptance (E) are expressed as a percentage of the incident flux. The visible absorptance should be zero, any deviation from this is assumed to be due to sampling errors, ie the problems of assuming that the run below cloud is vertically stacked underneath the run above and that the same cloud is being observed. The BI flight A019 was optically thinner and more inhomogeneous than the flight in the

Figure 10: The albedo and albedo ratios of the stratocumulus clouds for both the BI and SA flight.

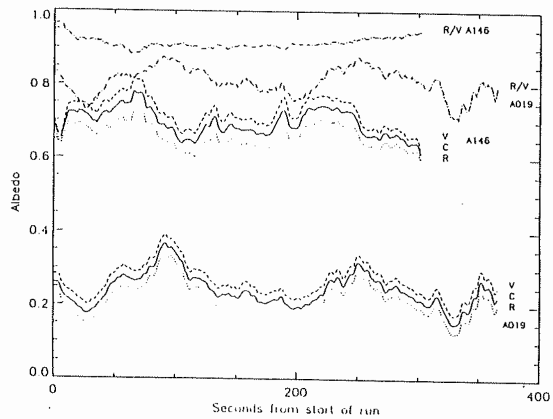

SA, this is self evident from the two values of E, 5.1% for A019 and 0.5% for A146. This highlights the need for caution when analysing the radiative properties of optically thin or broken cloud fields. The measurement of solar absorption ($0.3 - 3.0\mu m$) in clouds is difficult since it requires a small residual to be found from the subtraction of pyranometric observations made at different times and from different instruments. If the errors due to sampling and cloud edges associated with the inherent non-uniformity of clouds are not accounted for in the analysis of the observations then large errors in the perceived cloud absorption can occur. The absorptance in the tropical cloud (4.9%) is almost three times as great as that around the BI (1.7%).

Figure 10 shows the clear (C), red (R) and visible (V) albedo for both flights and the ratio of red albedo to visible albedo (R/V). This figure shows that the variation in broad band albedo along a run for both flights is quite large and comparable in magnitude to the variations in reflectance at the shorter wavelength MCR channels ($0.55\mu m$ and $1.25\mu m$ figure 5 and 6). The ratio of red albedo to visible albedo was found, by Hignett (1986), to be relatively insensitive to variations in liquid water path, which is contrary to the work of DeVault and Katsaros (1983) who offer this ratio as a means of determining liquid water path. The reflectance measured at narrow wavelength bands with the MCR lead to the conclusion that for flight A146 the variations in liquid water were large as the changes in reflectance at low wavelengths were large. In figure 10 we see that there is little change in the albedo ratio for flight A146 suggesting that the ratio of red albedo to visible albedo has little variation with liquid water path, in support of Hignett's results. The variations in the albedo ratio for flight A019 are a combination of the clouds low optical depth and increased inhomogeneity.

7 Conclusions

The two cases considered represent two extremes in the microphysics of stratocumulus. Both have similar aerosol concentrations below the cloud yet have very different microphysical properties. In the BI case the cloud had lower liquid water content and lower effective radius than the cloud in the South Atlantic. The difference in droplet concentration between the two flights suggests that the fraction of aerosol in the SA that can act as CCN is larger than that around the BI which is consistent with the SA aerosol being predominantly hygroscopic salt nuclei.

Retrievals of cloud optical depth and effective radius have been carried out for both cases, the BI case suggesting that a lower bound in terms of optical depth may be reached for $\tau < 5$ where the retrieval scheme may no longer work. For both cases the retrieval of effective radius is in good agreement with in-situ FSSP measurements giving confidence in the possibility of using this scheme more widely in a future satellite retrieval.

Broad band measurements of albedo, reflectivity, transmissivity and absorptance have shown the SA cloud sheet to have a larger albedo and absorptance with a correspondingly lower transmittance than the BI case. A combination of narrow band and broad band measurements have thrown some light onto the causes of variability in reflectance and albedo and have shown that it does not appear possible to retrieve cloud liquid water path by using a ratio of the red albedo to the visible albedo.

Further studies will use these two stratocumulus sheets to look at the behaviour of various radiation codes in the two contrasting conditions.

8 References

Barrowcliffe, R., K.J. Dewey and J.S. Foot 1988: The Multi Channel Radiometer Fitted To MRF's C130. Description and Calibration methods before and during FIRE 87 Experiment. MRF Internal Note No.42. Available from National Meteorological Library, Bracknell, England.

DeVault, J.E. and K.B. Katsaros 1983: Remote determination of cloud liquid water path from bandwidth limited shortwave measurements. J. Atmos. Sci., **40**, 665-685

Hignett, P. 1986: A study of the shortwave radiative properties of marine stratus: Aircraft measurements and model comparisons. MRF Internal Note No. 29. Available from National Meteorological Library, Bracknell, England.

Rawlins, F. 1989: Aircraft measurements of the solar absorption by broken cloud fields: A case study. Quart. J. Roy. Meteor. Soc. **115** pp 365-382

Rawlins F. and J.S. Foot (1990): Remotely sensed measurements of stratocumulus properties during FIRE using the C130 aircraft Multi-channel Radiometer. J. Atmos. Sci. **47**,2488-2503

Slingo A. and H.M. Schrecker (1982): On the shortwave radiative properties of stratiform water clouds. Quart J. Roy. Meteor. Soc. **108**pp. 407-426

Taylor J.P. (1992): Sensitivity of remotely sensed effective radius of cloud droplets to changes in LOWTRAN version. Accepted for J. Atmos. Sci.

The Effects of Radiation Exchange on the Entrainment Stability of Boundary Layer Stratiform Clouds

Steven T. Siems[1], Donald H. Lenschow[1] and Christopher S. Bretherton[2]

[1]National Center for Atmospheric Research*, Boulder, CO, USA 80307-3000
[2]University of Washington, Applied Mathematics, Seattle, WA 98195

I. Introduction

Mixed layer models (MLMs) have been used for nearly a quarter of a century in the investigation of stratocumulus clouds (SC) (Lilly, 1968). Although the limitations of such a simple one-dimensional approach are substantial and well-noted, this method continues to be a fundamental tool in investigating stratocumulus clouds because of its conceptual simplicity and computational efficiency. With the continuing increase in computational capabilities, mixed layer models may become practical for parameterization schemes of the marine boundary layer in general circulation models.

Simple MLMs approximate the nature of the mixed layer fluid and the overlying fluid to first order only. Many enhancements have been introduced to MLMs in an effort to gain further insight. Examples include a decoupling of the primary cloud layer from the underlying boundary layer (Turton & Nicholls; 1987) and Lagrangian effects (Wakefield & Schubert, 1980; hereafter WS). Most of these enhancements have dealt with the actual mixed layer while largely neglecting the structure of the air being entrained. It is common to assume that at a given location the air entrained into the mixed layer (also referred to as overlying air) has a linear profile in height for moisture and moist static energy (WS). When compared to actual soundings (Figure 1) a linear profile is often only a crude approximation. (This sounding was taken during FIRE phase I off the coast of California and kindly provided by Ilga Paluch.)

While the nature of the overlying air may not be of primary interest in studying SC, it has a direct impact on SC evolution through the strength of the inversion and entrainment. Indeed, current parameterization schemes for the marine boundary layer (Betts & Albrecht, 1987) depend directly on overlying parcels. The nature of this air also influences the radiation exchange and the level of buoyancy reversal through evaporative cooling across the inversion; both processes remain unresolved.

In this paper we develop a simple one-dimensional model for the investigation of the coupled mixed layer and overlying system. We then investigate nature of the overlying air as it approaches the inversion and the impact of radiational processes.

II. Description of Model

Rather than prescribing the temperature of the overlying air our goal is to allow it to evolve freely. The free atmosphere from cloud-top to 3000 meters is divided into over 100 layers or parcels. Each layer subsides at the rate $D_{sub} \cdot z$, where D_{sub} is the divergence and z is the height above the ocean. The Slingo & Schrecker (1982) short-wave (SW) and Roach & Slingo (1980) long-wave (LW) algorithms are used to compute the radiative divergence for each layer. Thus, following a given parcel, it is cooled at the rate

$$\partial T/\partial t = LW + SW + (g \cdot D_{sub} \cdot z)/Cp,$$

where T is the parcel temperature. The last term allows for the adiabatic adjustment of the air.

To isolate the impact of the overlying air on the radiative properties of the SC we begin by prescribing a cloud of depth 150m at the top of a homogenous mixed layer with an inversion at 800m. The individual layers within the mixed layer are set at 20m. Above the inversion, layers begin at 10m thickness and are graduated to roughly 40m at the 3km level to account for the linear increase in subsidence velocity. Above 4km, the atmosphere is prescribed to 100km on a sparse mesh according to the mid-latitude, summer sounding of McClatchey, et al. (1972). The atmosphere is linearized between 3 and 4km with the air at 3km prescribed from the sounding of Figure 1. We use climate variables suitable for this time region as required by the radiation schemes and MLM.

For these fixed mixed layer simulations, only air

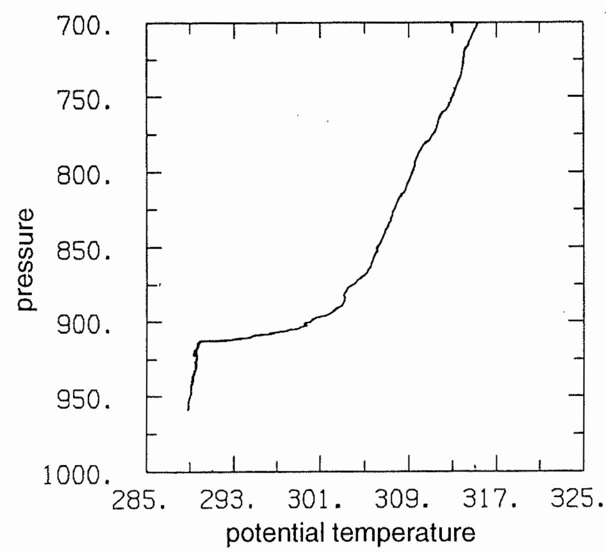

Figure 1. A sounding of potential temperature against pressure taken from the NCAR Electra during FIRE on July 2nd, 1987.

*The National Center for Atmospheric Research is sponsored by the National Science Foundation.

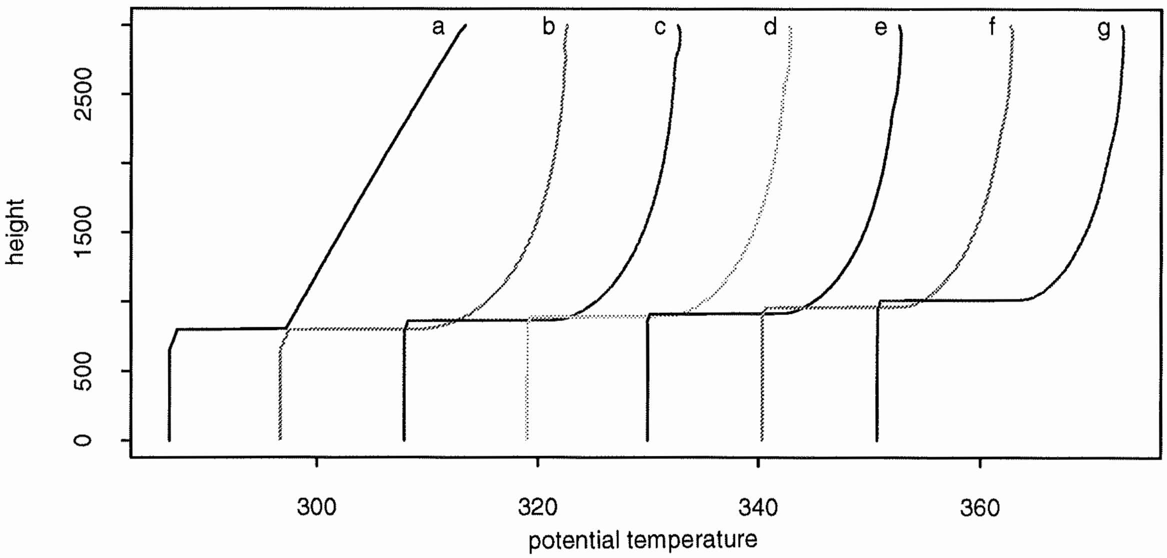

Figure 2(a-g). Profiles of the potential temperature versus height; 2a) linear profile typical of mixed layer models, 2b) near steady-state profile of the OLM, 2c-g) profiles at 6, 12, 18, 24 and 30 hours of the ML-OLM. Profiles have been successively offset by 10 degrees.

within the range of the inversion to 3000m is followed by the grid as it subsides. As a grid point falls below the inversion, the parcel is assumed to be entrained into the mixed layer and another layer is introduced at the 3km level at the prescribed state. Thus entrainment perfectly matches the subsidence velocity at cloud-top, an unrealistic assumption. However, by not allowing a cloud feedback at this time, we isolate the impact of the overlying air on the cloud-top. We refer to this as the overlying Lagrangian model or OLM.

The inversion of the mixed layer is not one-dimensional (Lenschow, 1990) and cannot be modelled within such a frame work. In hopes of bounding the true effect of the entrainment zone above the inversion, we have chosen two extremes: one an infinitely thin entrainment zone and the other a 50 meter entrainment zone in which air is mixed linearly in the moist static energy and total water content between the cloud-top and overlying air immediately above the 50 meter zone.

Next we couple the OLM to a traditional MLM for the boundary layer (ML-OLM). The MLM is based on the Lagrangian scheme of WS and developed by Bretherton (1990). The model assumes a well-mixed boundary layer defined by prognostic equations for the mixed-layer total water content, moist static energy, and the inversion level. We use the entrainment closure of WS in which the negative buoyancy flux of the entrained air is fixed at a fraction of the positive buoyancy flux of the mixed layer. The fraction of 1/10 has been chosen for work presented here. This closure is relatively simple since the buoyancy flux at intermediate levels may be calculated directly. On occasion the SW heating within the cloud overwhelms the LW cooling and there is not a net positive buoyancy flux within the cloud. At this point, decoupling of the primary cloud layer is likely and the entrainment assumption is no longer valid. We set the entrainment velocity equal to zero in these cases. The division of radiation between the mixed layer and the overlying air may be done directly and does not require an ad-hoc assumption as for simpler MLMs (Randall, 1984). The flux divergence at the top of the entrainment zone is directly introduced into the mixed layer. The entrained parcel is taken from the air immediately above the entrainment zone.

III. Discussion

Initially, the OLM simulations were run for ten days in hourly time steps providing a nearly steady-state profile for the overlying air. This profile (Figure 2b) agrees well with the sounding of Figure 1 and varies considerably from the linear profile initially assumed (Figure 2a). For this simulation we assumed a divergence of 3×10^{-6} s^{-1} as based on the data in WS. The vapor content of the overlying air is fixed at 0.10 *g/kg*. Initially no entrainment zone is considered.

Given that the entire mixed layer is fixed, we find that there is virtually no direct diurnal variation in the overlying air. The high noon SW heating rate is typically an order of magnitude less than the LW rates. Even these rates are rather modest, on the scale of 0.1 K/hour. However, given the many days required for a parcel to subside to the inversion, variations in the LW divergence can have a great impact on the nature of the entrained air and inversion strength.

The LW divergence is found to be dependent on the divergence D_{sub} and the vapor content of the overlying air q_{en}. To understand their impact, simulations have been run over the range $q_{en} \in$ (0.02, 0.10, 0.40, 1.00, 2.50, 5.00 *g/kg*) and $D_{sub} \in$ (1, 2, 3, 4, 5, 6×10^{-6} s^{-1}). While 5 g/kg is an extremely large value for q_{en} near the 3km level, this is quite modest for an upper limit within a couple hundred meters of the inversion possibly due to horizontal advection (Kloessel, 1989).

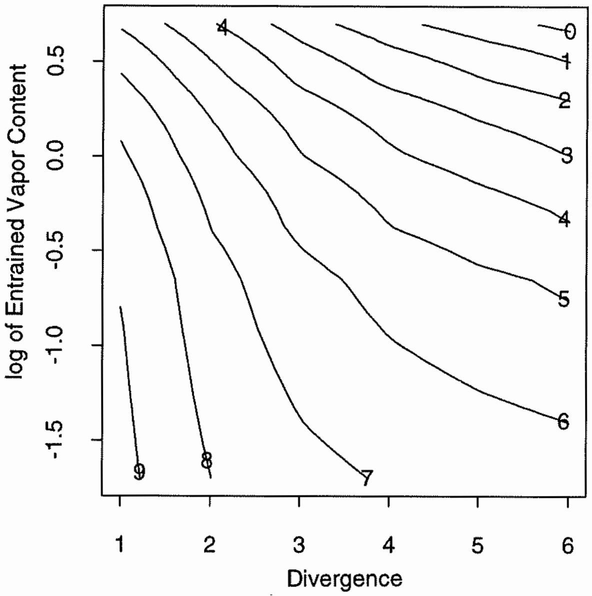

Figure 3. Contours of LW cooling (K/hour) across the top 20 meters of cloud for the OLM simulations with no entrainment zone. The x-axis denotes the divergence D_{sub}; the y-axis denotes the log of the overlying vapor content, q_{en}.

In investigating the impact the overlying air has on the flux divergence across the inversion, we measure the LW cooling across the top 20 meters of the cloud. Contours of LW cooling in Figure 3 show that cooling rates can change drastically from 9 *K/hour* to virtually none. The no-cooling cloud-top occurs with large D_{sub} and q_{en}. Since the overlying air is pushed to the inversion quickly, it produces a large buoyancy jump across the inversion. Given that this air is both warm (since it has had relatively little time to cool) and moist, it too emits a considerable LW flux which actually balances the flux from cloud-top. As q_{en} and D_{sub} are reduced, the air immediately above the inversion emits less LW flux into the cloud. The cooling rates do vary with cloud thickness but there is no change in the overall pattern. When the 50m linear entrainment zone is added, a buffer is placed between the cloud and the overlying air. The range of cloud-top cooling falls along similar contours but with a spread of 4 to 10 *K/hour*.

In reducing the LW cooling at cloud-top, the convective energy in the mixed layer is largely shut-off; entrainment is correspondingly weakened. This would suggest that when moist blobs are pushed down on the inversion, they may resist being easily entrained and eventually push the cloud-top below the inversion, forcing breakup as suggest by Kloessel (1989).

Given the steady-state OLM solutions as an initial condition, we next turn to the coupled ML-OLM. We maintain the same q_{en} and D_{sub} domain. Randall & Suarez (1984) have noted that MLMs are sensitive with respect to the large scale divergence. The mixed layers variables are marched forward with a Runge-Kutta scheme with the radiative conditions updated every 15 minutes. We begin the simulations at midnight to allow for the mixed layer to adjust to the initial conditions without the additional complication of SW heating. Any rapid adjustment was largely complete within three hours. Simulations were run for two days or until the cloud layer shrank to 20m, at which point the mixed layer assumption is certainly invalid.

Contrary to what was suggested by the steady-state simulations, dry overlying air with large D_{sub} was most successful in causing cloud breakup. While the entrainment was reduced when moist overlying air was used, the amount of moisture entrained dropped

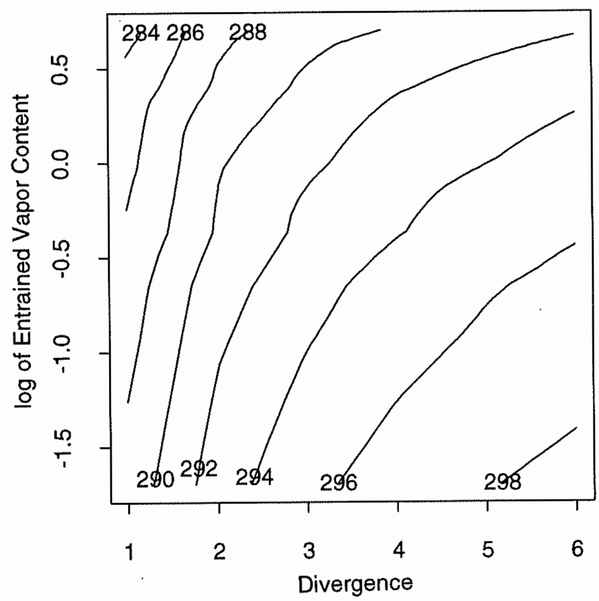

Figure 4. Contours of the entrained air temperature after 6 hours of simulation time with no entrainment zone.

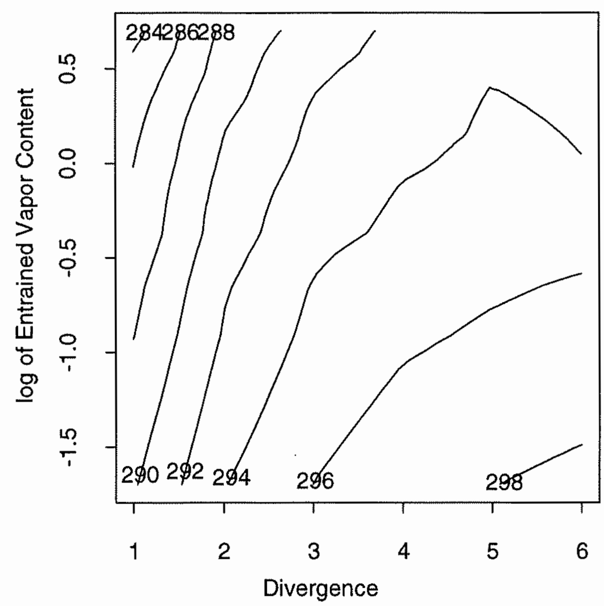

Figure 5. Contours of the entrained air temperature after 30 hours with no entrainment zone.

the lifting condensation level sufficiently to resist breakup through the extent of the simulation.

Perhaps the most intriguing result pertains to the temperature of the air immediately entrained into the mixed layer. MLMs typically assume that the equivalent potential temperature increases linearly with the height of the inversion (WS). Thus as the inversion rises the entrained air has a greater potential temperature. WS suggest a rate of less than 2°/*km* for this latitude. This was not observed. Figures 4 and 5 present contour diagrams of the entrained air temperature at 6am of the first and second day. In some of these weak subsidence simulations the cloud-top has risen nearly 500m over the 24 hours yet the temperature of the entrained air remains very steady. Similarly, a fall in cloud-top under strong subsidence does not significantly change the temperature of the air entrained. Thus as the inversion rises or falls the potential temperature of the actual air being entrained changes at a rate of nearly 9.8°/*km*. This would suggest that the inversion is stronger at great heights than assumed by traditional MLMs and thus more stable. Figure 2 presents the evolution of the potential temperature profile over the first 30 hours in 6 hour intervals.

The figures and discussion for this coupled model have been for simulations with no entrainment zone. The conclusions reached here hold when a 50m entrainment zone is maintained. The most immediate impact observed with the entrainment zone is an increase in the strength of the jump across the inversion (Figure 6). Here, the temperature of the entrained air is still found to not vary in time. The most immediate impact of the entrainment zone is that the cloud-top is found to rise less quickly. A stronger inversion weakens entrainment. Averaged over the domain of 36 runs, the cloud-top was found to increase 40 meters or 33% less than without an entrainment zone.

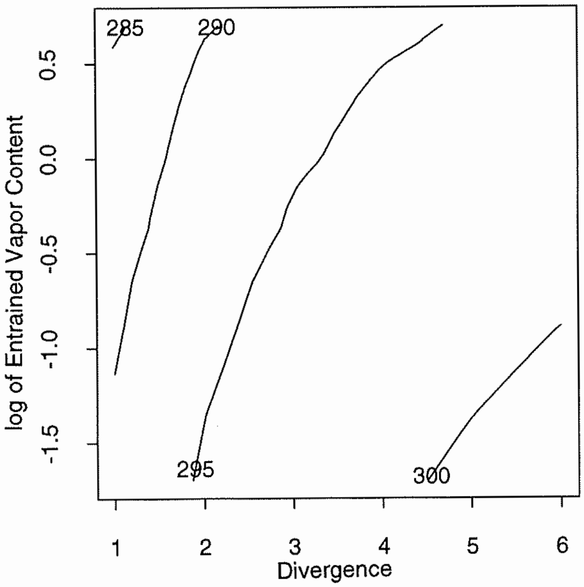

Figure 6. Contours of the entrained air temperature after 30 hours time with a 50 meter entrainment zone.

IV. Conclusions

We have developed a one-dimensional model to examine the structure of the air overlying the inversion. Our results suggest that the vapor content of this air and the rate of subsidence will have a large impact on the LW radiative fluxes and thus the evolution of the cloud. The simulations suggest that clouds will have large LW divergence when the subsidence is weak and the overlying air is quite dry. When we couple the overlying Lagrangian scheme to a mixed layer model, we note that the temperature immediately above the inversion remains nearly constant in spite changes in the inversion height. This has important implications with respect to the modelling and parameterization of the SC deck.

Acknowledgments

The authors have benefitted from the insight and aid of Dr. Ilga Paluch, Mr. Robert Pincus and Ms. Hope Hamilton.

References

Betts, A. K., and B. A. Albrecht, 1987: Conserved variable analysis of the convective boundary layer thermodynamic structure over the tropical oceans. *J. Atmos. Sci.*, 44, 83-89.

Bretherton, C. S., 1990: Lagrangian development of a cloud topped boundary layer in a turbulent closure model. Preprint Volume of the Conference on Cloud Physics, San Francisco, Amer. Meteor. Soc., 48-55.

Kloessel, K. A., 1989: Observational Study of the above-inversion structure and marine stratocumulus cloud-clearing episodes during FIRE. Ph.D. Thesis, Penn State University.

Lenschow, D. H., 1990: Factors affecting the structure and stability of boundary layer clouds, Preprint Volume of the Conference on Cloud Physics, San Francisco, Amer. Meteor. Soc., 37-42.

Lilly, D.K., 1968: Models of cloud topped mixed layers. *Quart J. Roy. Meteor. Soc.*, 94, 292-309.

McClatchey, *et al.*, 1972: AFCRL Optical properties of the atmosphere, Environmental research paper No. 411.

Randall D. A., 1984: Buoyant production and consumption of turbulence kinetic energy in cloud-topped mixed layers. *J. Atmos. Sci.*, 41, 402-413.

Randall, D. A., and M. J. Suarez,1984:On the dynamics of stratocumulus formation and dissipation. *J. Atmos. Sci.*, 41, 3052-3057.

Roach, W. T., and A. Slingo, 1980: A high resolution infrared radiative transfer scheme to study the interaction of radiation with cloud. *Quart. J. Roy. Meteor. Soc.*, 105, 603-614.

Slingo, A., and H. M. Schrecker, 1982: On the shortwave radiative properties of stratiform water clouds. *Quart. J. Roy. Meteor. Soc.*, 108, 407-426.

Turton, J. D., and S. & Nicholls, 1987: A study of the diurnal variation of stratocumulus using a multiple mixed layer model. *Quart. J. Roy. Meteor. Soc.*, 113, 969-1009.

Wakefield, J. S., and W. H. Schubert, 1980: Mixed-layer model simulation of eastern north pacific stratocumulus, *Mon. Wea. Rev.*, 109, 1952-1968.

A CONCEPTUAL MODEL OF THE STRATOCUMULUS-TRADE-CUMULUS TRANSITION IN THE SUBTROPICAL OCEANS

Christopher S. Bretherton

Applied Mathematics Department, FS-20, University of Washington, Seattle, WA 98195, USA

1. INTRODUCTION

Over the cool water off the west coasts of the Americas and Africa east of the subtropical highs, extensive regions of the oceans which are blanketed by nearly solid stratocumulus for much of the year. As this air advects westward and equatorward in the trade winds, there is a climatological transition to trade cumulus clouds with lower fractional cloud cover and a deeper boundary layer ; the STT (*S*tratocumulus to *T*rade cumulus *T*ransition.)

There is a qualitative change in the boundary layer structure and dynamics between the two endpoints of this transition. Stratocumulus layers over the cold upwelled water in the subtropics near the west coasts of the continents are often observed to be well mixed due to convective circulations which extend continuously through the entire depth of the layer. Trade cumulus layers, on the other hand, are not well mixed. They consist of a fairly well-mixed convecting subcloud layer, a transition layer at cloud base generally marked by a weak inversion and a decrease in mixing ratio, and a cloud layer in which the mean mixing ratio decreases with height, the mean relative humidity tends to remain between 80-95%, and the stratification lies between dry and moist adiabatic (Augstein *et al* 1974). The cloud layer contains cumuliform, cloudy updrafts, which only fill a small volume fraction of the cloud layer, and weak dry compensating downdrafts made up of mixtures of detrained updraft air and air originating from above the trade inversion. The trade cumulus boundary layer is topped by a trade inversion, which is generally 100-400 m thick.

The thesis of this paper, presented more fully by Bretherton (1992), is that the transition in cloudiness occurs in two steps, which get somewhat intertwined by diurnal decoupling and recoupling, but which follow inexorably from the systematic downwind increase in SST relative to temperatures at a given level above the inversion, following boundary layer air parcel trajectories. Other processes such as precipitation , the diurnal cycle, systematic changes in solar radiation or mean upper level mixing ratio, the changing amount of mean subsidence at the inversion height, and changing surface winds are important in actually determining fractional cloudiness as a function of position, but are not crucial to the dynamics of the transition. Figure 1 is a schematic illustration of the essential feedbacks involved in the two-step conceptual model of the STT.

The first step is a change from mixed layer dynamics (with some diurnal decoupling) to a regime in which even at night, the stratus cloud and subcloud layers are dynamically separate, and are connected by cumulus clouds that. develop atop the subcloud layer and rise through a conditionally unstable layer up to the stratus base. We suggest that much or most of the high fractional cloudiness subtropical stratocumulus regime may consist of this intermediate cloud type, $C_L 8$, or cumulus rising into stratocumulus, over the entire diurnal cycle.

The second step is the evaporation of the upper stratocumulus layer, which we suggest is a necessary consequence of the continued deepening of the boundary layer, and we attribute to increasingly vigorous entrainment drying by cumulus clouds rising through the stratocumulus layer. This process is gradual and involve the formation of mesoscale and smaller scale holes in an thinning cloud sheet to reveal the cumulus cloud field below. Satellite photos of the STT are consistent with such a view. Mesoscale stratus patches persist as far southwest as Hawaii even though cloud fraction decreases gradually downstream.

This hypothetical view of the dynamics of the STT is to be contrasted with cloud top entrainment instability (CTEI) (Randall 1980; Deardorff 1980). CTEI predicts a rapid increase in entrainment and entrainment drying, inducing a transition in a matter of an hour or two from stratocumulus to scattered cumulus. CTEI depends mainly on the jumps of temperature and mixing ratio across the inversion, which can be combined into a parameter Δ_2, which must be negative for mixing-induced buoyancy reversal and CTEI. In this view, the observed gradual STT is a consequence of time and space variations in Δ_2 due to different boundary layer trajectories and upper air conditions. Climatologically, the borders of the region of maximum fractional cloudiness in the northeastern Pacific marine stratocumulus are not grossly inconsistent with the climatological boundary $\Delta_2 = 0$ predicted by CTEI, according to the extremely scanty upper-air data we have over this part of the ocean (Neiburger *et al* 1961). However, persistent stratocumulus decks with $\Delta_2 < 0$ are commonly observed (Kuo and Schubert 1988) and both numerical models and laboratory analogues to evaporative cooling (Siems *et al*, 1990; Siems

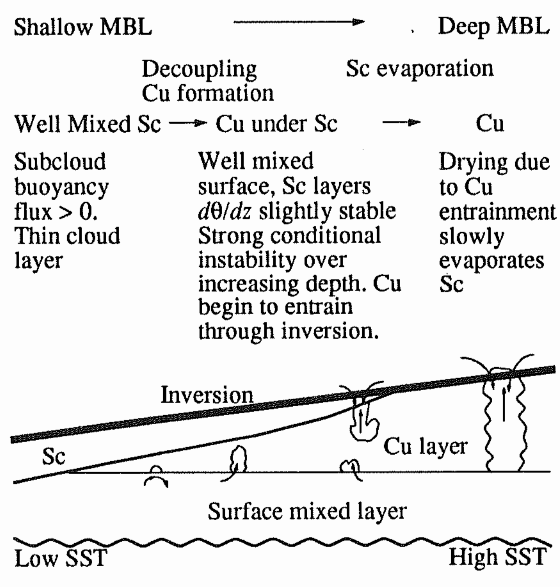

Figure 1. A conceptual diagram of the STT.

and Bretherton, 1992) suggest that CTEI can occur only in clouds of much higher liquid water content (2 g kg^{-1} or more) than typical marine stratocumulus clouds. Hence it seems unlikely that the STT is primarily a result of CTEI.

Section 2 discusses decoupling, its relation to increasing SST. This is discussed in more detail in paper P7.16 by Wyant and Bretherton. It also discusses how persistent decoupling leads to a C_L8 (cumulus rising into stratus) cloud field. Section 3 presents modelling results for Lagrangian boundary layer evolution from a turbulence closure model. Section 4 examines the thermodynamics structure in the cumulus layer in which the cumulus rise into optically thick stratocumulus layer , and how it relates to the need to maintain a near radiative-convective balance . In this lies the seed for the ultimate evaporation of the the stratocumulus cap.

2. DECOUPLING

In the past few years, observations have shown that during the day, near-neutral (i.e. surface buoyancy fluxes of 0-30 W m^2) MBL's capped by solid stratocumulus layers are frequently decoupled into two separate mixed layers (Nicholls and Leighton, 1986). Multiple-mixed layer (Turton and Nicholls, 1987) and turbulence closure models (e. g. Bougeault, 1985) reproduce this behavior quite well, and indicate that decoupling is intimately connected to the formation of a region of negative buoyancy fluxes below the stratus base of a well-mixed boundary layer.

These studies show that diurnal decoupling is a consequence of absorption of shortwave radiation within the cloud. The buoyancy flux just below cloud base is determined primarily by a competition between radiative cooling and entrainment warming. Only the net (longwave minus shortwave) flux divergence in the cloud layer helps drive buoyancy fluxes below the cloud. Below cloudbase, entrainment acts to decrease buoyancy fluxes. The entrained air has higher potential temperature, so entrainment contributes to positive buoyancy of descending air parcels below cloud base (i. e. negative buoyancy fluxes) in proportion to the mixing fraction of entrained air. During the day, the net radiative flux divergence of the cloud layer becomes small or even negative, while the entrainment contribution decreases less rapidly, so the subcloud buoyancy flux plummets, leading to decoupling. Drizzle and surface fluxes affect but are not vital to the diurnal decoupling process.

The thesis of paper P7.16 is that further downstream, diurnal decoupling is replace by *permanent* decoupling due to the rising inversion height and cloud layer thickness produced by higher SST's. It is argued that were the MBL to remain well mixed, the deeper cloud layer and larger surface latent heat fluxes associated with the higher SST would create more vigorous convective circulations and more entrainment for a given amount of cloud layer radiative cooling. More entrainment drives subcloud buoyancy fluxes negative, creating decoupling. The diurnal cycle strongly modulates this process, but ultimately the nocturnal increase in cooling is not sufficient to recouple the layer before the next morning. Typically, if the cloud layer thickness predicted by the mixed layer model exceeded 400 m, negative diurnally averaged buoyancy fluxes were found just below cloud base. It is an interesting coincidence that drizzle also becomes a significant contributor to decoupling for clouds of about 400 m or thicker because of its impact on moisture fluxes.

In both observations and models, diurnal decoupling leads to a rapid drying and slight warming of the cloud layer and a rapid moistening of the surface layer. The intervening layer is typically conditionally unstable. After a few hours of decoupling, cumulus scud are observed to form atop the surface layer. In his study of the diurnal cycle of North Sea stratocumulus, Bougeault (1985) found that the scud cumulus did not produce a significant vertical flux of moisture or heat between the decoupled layers. However, if decoupling persisted for longer, such cumulus would be the only connection between the two layers. Modelling results presented in the next section suggest that these cumuli are capable of maintaining the upper stratus layer for days. The cloudiness transition then occurs gradually as the upper stratus deck dissipates, exposing the underlying cumulus clouds.

3. MODELLING RESULTS

The intermediate regime in which cumulus rise into stratocumulus may well be one of the most common cloud types over the oceans. Nicholls (1984) found that this cloud type (C_L8) accounted for 25-35% of all daytime observations in May-August at a typical UK station. Unfortunately, nighttime observations which would distinguish a diurnally decoupled from a persistently decoupled MBL are not available.

Similar observations do not appear to be available for a subtropical station in a region of high mean MBL cloudiness with a typical inversion height of 1000-1500 m, greater than during FIRE. However, indirect support for the existence of substantial areas of C_L8 comes from a Lagrangian modelling study based on a turbulence closure model reported on in more detail in Bretherton (1992).

This study used a second-order turbulence closure model including parameterized drizzle microphysics, long and shortwave radiation, and fractional cloudiness and condensation at each height. The fractional cloudiness was interactive with the radiation scheme; the radiative flux profile used a weighted average of separate computations for clear and cloudy columns. Lagrangian boundary conditions were specified as follows. Mean July COADS climatology was used for the surface winds, divergence D and SST. The geostrophic wind was also taken from COADS data; vertical shear of the geostrophic wind was ignored. The vertical motion was assumed equal to -Dz. A climatology of 850 mb temperature from ECMWF analysis and a specified lapse rate of $d\theta^+/dz = 6$ K km^{-1} was applied as an upper boundary condition at all gridpoints 200 m and more above the model-predicted inversion. Since both NMC and ECMWF climatologies overpredict above-inversion mixing ratio in the stratus regimes (Minnis, *et al* 1992) a constant above-inversion mixing ratio of 6 g kg^{-1} was enforced. Trajectories were calculated based on the mean COADS surface winds. These boundary conditions are similar to those used in the mixed layer model of paper P7.16. Trajectories were started one day upstream of the initial analysis time (t = 0) to minimize the effect of initialization transients on the analysis. Figure 2 shows a typical five-day trajectory starting at 40 N, 130 W at local midnight, superimposed on the climatological SST. The temperatures at 2 km also change along this trajectory, but at only slightly under 1 K day^{-1}, roughly half the rate of surface temperature increase. It is the difference between SST and upper-level temperature which drives MBL deepening. In addition the lessening low-level horizontal divergence leads to lower subsidence rates at cloud-top downstream. For the discussion that follows, the important point is that increasing SST - $\theta_{2\ km}$, assisted in this case (but not necessarily in general) by decreasing low-level divergence, deepens the MBL downstream. In what follows,we will use 'increasing SST' as a proxy for this complex of effects.

Fig. 3 shows the instantaneous liquid water profile and upward flux of total water every two hours In this simulation, drizzle was negligible due to the small thickness of the solid cloud layer. The boundary layer deepens substantially during the five days. There is a fairly well mixed surface-coupled layer extending up to about 400 m. The moisture flux becomes intermittent in a layer extending from about 400 m above sea level up into the solid cloud layer. This indicates a failure of the turbulence closure in a manner suggestive of cumulus convection. A more detailed examination shows that mean mixing ratio builds up nearly to saturation at the top of the surface mixed layer, setting off the partial condensation parameterization and making a 'cloud' which then rises up into the upper cloud layer. Thus while the mean liquid water content is too small to show up on figure 3, there is cloud within this layer, with a fairly constant cloud base of 400 m. In reality, cumulus convection is spatially intermittent, which violates some closure assumptions of second-order turbulence closure model. The apparent result is that spatial intermittency aliases into temporal intermittency. Nevertheless, the mean profiles in the model do recreate some features of a trade-cumulus sounding, and we will calll this layer of intermittent fluxes the cumulus layer. Lastly, the diurnal cycle in the thickness of the upper solid cloud layer is quite apparent.

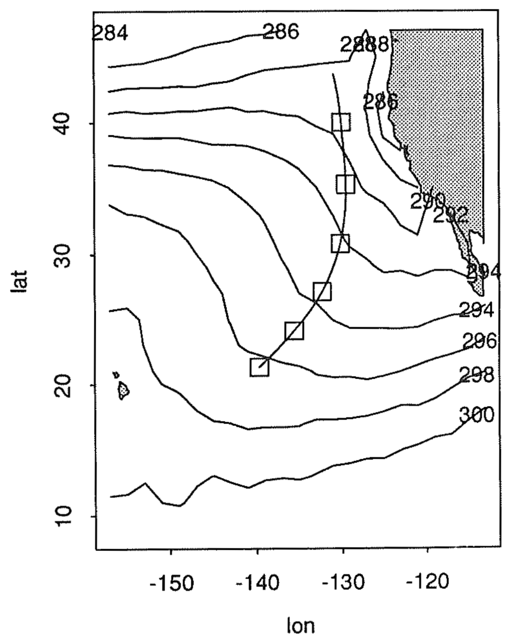

Figure 2. The climatological trajectory . Each square corresponds to one day.

In this simulation, the stratus layer does not break up. Although with some tuning of parameters it is not too difficult to engineer a breakup of the upper cloud layer in this model, neither the nature of the breakup nor the structure of the cumulus cloud field after breakup appear entirely realistic for reasons to be addressed in the next section. However, downstream decoupling and cumulus-under-stratus (CUS) regimes are very robust features of this type of simulation (and of two-dimensional Lagrangian LES simulations we have done), with or without a diurnal cycle. Note that the cumulus cloud base does not rise nearly as fast as the inversion and the cloud layer thickens rapidly downstream as SST increases, in accordance with Betts and Ridgway (1988).

At time zero (after one day of time integrated along the trajectory) the layer is well mixed with uniform moisture fluxes with height and slightly positive buoyancy fluxes below cloud base. Diurnal decoupling is visible on the first day, and the nocturnal recoupling is only partial (the moisture fluxes never attain a linear profile). After this the layer is persistently decoupled. Figure 4 shows a midnight sounding at the end of the simulation in the cumulus-coupled Sc regime. The sounding is dry-adiabatic below the cumulus layer, slightly stably stratified in the cumulus layer, and close to moist-adiabatic in the solid cloud layer. There is a substantial gradient of mixing ratio in the cumulus layer. This sounding is quite similar to typical trade-cumulus soundings except that the stability in the cumuls layer is rather low. In the next section, we argue that this is a radiative consequence of the overlying stratus and show how it might lead to a breakup not predicted by the turbulence closure model.

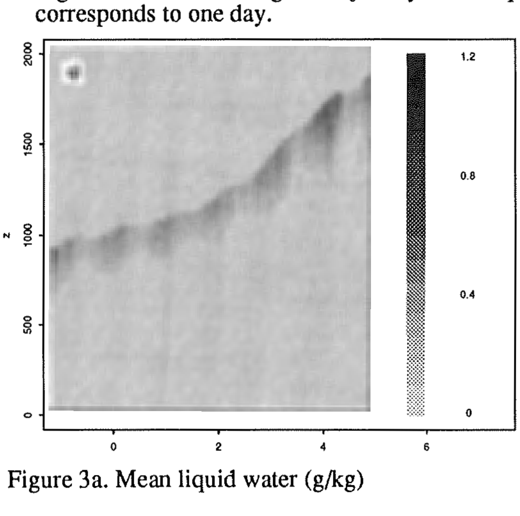

Figure 3a. Mean liquid water (g/kg)

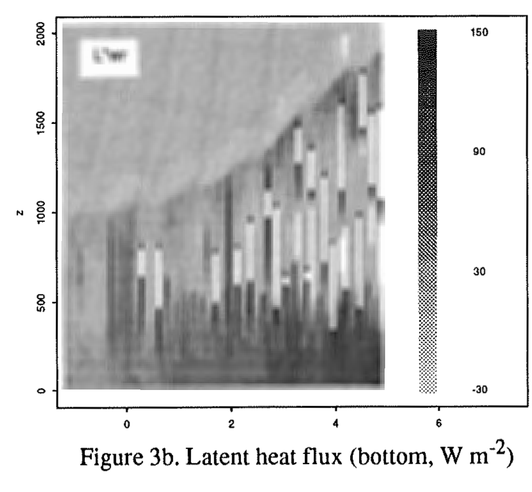

Figure 3b. Latent heat flux (bottom, W m^{-2})

4. THE CUMULUS BELOW STRATUS REGIME

Weak stratification in the cumulus layer is a fundamental feature of the CUS regime, reflecting the radiative-convective balance that occurs beneath the stratus. It arises as follows: to carry the moisture flux that sustains the overlying stratus, there must be a significant cumulus mass flux and hence significant compensating subsidence in the environment. In a trade-cumulus regime, the adiabatic warming due to this subsidence compensates the clear-air radiative cooling that occurs at all heights in the MBL. However, in the CUS regime, the overlying Sc blanket leads to negligible radiative cooling below the Sc base, so subsidence warming is uncompensated and must therefore be small (just large enough to produce the 1-2 K/day downstream warming required for the MBL to keep up with the downstream increase in SST. This reflects itself in a weak stratification in the cumulus layer.

In this regime the Sc cloud layer is still dynamically as well as radiatively active. The strong cloud-top cooling drives circulations that penetrate downward part way into the cumulus layer, and can still be responsible for much of the entrainment into the MBL However, the weak stratification is strongly conditionally unstable and leads to increasingly vigorous Cu convection as SST increases and the MBL deepens. The strong entrainment and entrainment drying created by these energetic cumuli sets the stage for the second part of the STT, the evaporation of the overlying Sc. This is not robustly predicted by the turbulence closure model because it models transport of kinetic energy is purely by downgradient diffusion and does not correctly transport kinetic energy in cumulus clouds up to the inversion where it can lead to entrainment . Hence entrainment requires stratiform cloud, which more efficiently (in the turbulent closure model) entrains via layer convection driven by radiative cooling.

To test some of these ideas, we have performed two-dimensional Lagrangian large-eddy simulations using the radiation parameterization, no drizzle fluxes, fixed upper-level conditions and SST increasing by 2 K/day. As the MBL deepens, the CUS structure develops in a manner similar to that inferred from the turbulence closure model, except that the stratus cloud cover dissipates with a sufficient increase in SST. While there is insufficient space to report on these preliminary results here, we hope to report on them at the presentation.

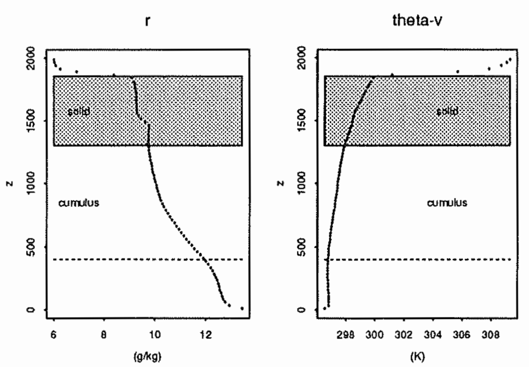

Figure 4. Soundings of mixing ratio r and θ_v at 5 days.

Acknowledgements

This research has been supported by ONR grant N0014-90-J-1136, NSF grant ATM8806789 and a grant from the Digital Equipment Corporation External Research Program.

REFERENCES

Augstein, E., H. Schmidt, and F. Ostapoff, 1974: The vertical structure of the atmospheric planetary boundary layer in undisturbed trade winds over the Atlantic Ocean. *Bound.-Layer Meteor.*, **6**, 129-150.

Betts, A. K., 1989: The diurnal variation of California coastal stratocumulus from two days of boundary layer soundings. *Tellus*, **42A**, 302-304.

------, P. Minnis, W. Ridgway, and D. F. Young, 1992: Integration of satellite and surface data using a radiatve-convective oceanic boundary-layer model. *J. Appl. Meteor.*, **31**, 340-350.

------,and W. Ridgway, 1988: Coupling of the radiative, convective and surface fluxes over the equatorial Pacific. *J. Atmos. Sci.*, **45**, 522-536.

Bougeault, P., 1985: The diurnal cycle of the marine stratocumulus layer: A higher-order model study. *J. Atmos. Sci.*, **42**, 2826-2843.

Bretherton, C. S. , 1992: The Lagrangian evolution of cloud-topped boundary layers. *J. Atmos. Sci.*, submitted.

Deardorff, J. W., 1980. Cloud Top Entrainment Instability. *J. Atmos. Sci.*, **37**, 131-147.

Kuo, H.-C. and W. H. Schubert, 1988: Stability of cloud-topped mixed layers. *Quart. J. Roy. Meteor. Soc.*, **114**, 887-916.

Minnis, P., P. W. Heck and D. F. Young, 1992: Stratocumulus cloud properties derived from simultaneous satellite and island-based instrumentation during FIRE. *J. Appl. Meteor.*, in press.

Neiburger, M., D. S. Johnson, and C. W. Chien, 1961: Studies of the structure of the atmosphere over the eastern Pacific Ocean in summer. I: The inversion over the eastern north Pacific Ocean. *Univ. Calif. Publ. Meteor.*, **1**, 1-94.

Nicholls, S., 1984: The dynamics of stratocumulus: aircraft observations and comparisons with a mixed layer model. *Quart. J. Roy. Meteor. Soc.*, **110**, 783-820.

------, and J. Leighton, 1986: An observational study of the structure of stratiform cloud layers: Part I. Structure. *Quart. J. Roy. Meteor. Soc.*, **112**, 431-460.

Randall, D. A., 1980: Conditional instability of the first kind upside-down. *J. Atmos. Sci.*, **37**, 125-130.

Siems, S. T., C. S. Bretherton, M. B. Baker, S. Shy and R. T. Breidenthal, 1990: Buoyancy reversal and cloudtop entrainment instability. *Quart. J. Roy. Meteor. Soc.*, **116**, 705-739.

Siems, S. T., and C. S. Bretherton, 1992: A numerical investigation of cloud-top entrainment instability and related experiments. *Quart. J. Roy. Meteor. Soc.*, to appear.

Turton, J. D., and S. Nicholls, 1987: Diurnal variation of stratocumulus. *Quart. J. Roy. Meteor. Soc.*, **113**, 969-1009.

NUMERICAL MODELLING OF THE STRATOCUMULUS-TOPPED MARINE BOUNDARY LAYER

Andrew S. Ackerman[1], Owen B. Toon[2], and Peter V. Hobbs[1]

[1]Atmospheric Sciences Department, University of Washington, Seattle, WA
[2]NASA Ames Research Center, Moffett Field, CA

1. INTRODUCTION

Marine stratocumulus clouds overlie about ~25% of the earth's surface. They therefore play an important role in the earth's radiation budget. The albedo of these clouds depends on the cloud droplet spectrum and therefore, in part at least, on the population of cloud condensation nuclei – CCN (Twomey et al., 1984). This is illustrated by the so called "ship track" phenomenon, in which marine stratus clouds affected by emissions from ships appear brighter in satellite imagery than adjacent cloud regions (Conover, 1966). In the ship-track affected clouds studied by Radke et al. (1989) both droplet concentrations and liquid water contents were higher than in adjacent clouds. The higher liquid water content could have been due to suppression of drizzle by the high droplet concentrations (Albrecht, 1989). The production of drizzle is not only regulated by, but may also regulate, aerosol populations. Investigation of this feedback loop led Baker and Charlson (1990) to postulate that the cloud-topped boundary layer is a bistable system with respect to CCN concentrations, with two stable CCN and cloud droplet number concentration regimes each controlled by a different sink.

Here we will briefly describe a numerical model that we have developed to investigate these and related issues. We then describe the results of the application of this model to the ship track phenomenon and to the hypothesis of a bistable cloud-topped boundary layer.

2. DESCRIPTION OF THE MODEL

We have developed a one-dimensional, Eulerian model for marine stratocumulus clouds. It consists of three coupled modules that treat cloud microphysics, turbulent mixing, and radiative transfer. The vertical grid is resolved into 50 layers of variable thickness, ranging from 30 m near the surface to 10 m at the height of a temperature inversion that caps the boundary layer (which is typically between 500 and 1000 m above the ocean surface).

The cloud microphysical module is based upon that of Toon et al. (1988). It resolves the size distributions of haze particles and droplets into 50 logarithmically spaced size intervals, ranging in radius from 0.005 to 500 μm. It treats the physical processes of droplet activation, condensational growth and evaporation of water, coalescence of drops due to thermal coagulation and gravitational collection, and vertical transport due turbulent diffusion, sedimentation, and advection. By treating the exchange of water between droplets and vapor, the model calculates the average supersaturation at each vertical level. A time invariant source of particles in the boundary layer, roughly representing gas-to-particle conversion, is prescribed by a log-normal size distribution. The effect of radiative transfer on droplet growth (Davies, 1985) is also included in the model.

The mixing module uses turbulent kinetic energy closure to calculate gradient transfer coefficients. The method is based upon the work of Duynkerke and Driedonks (1987), who applied E-ε turbulence closure to the stratocumulus topped marine boundary layer. Using profiles of liquid water and water vapor from the microphysical model, the model solves continuity equations for horizontal winds, temperature, turbulent kinetic energy, and the dissipation rate of turbulent kinetic energy. Vertical winds are prescribed, and are evaluated by assuming a time-invariant subsidence rate to be constant over the depth of the boundary layer. Radiative heating rates are taken from the radiative transfer module. Although Duynkerke and Driedonks (1987) used "all or nothing" condensation, we have incorporated a treatment of fractional cloudiness (Bougeault, 1981) for use in the buoyancy fluxes.

The radiative transfer scheme is the same as that described by Toon et al (1989). It treats multiple scattering in twenty-six solar wavelength bands (between 0.26 and 4.3 μm), and emission over fourteen infrared wavelength bands (4.4 and 62 μm). Two-stream methods are applied to both wavelength regimes. An exponential sum formulation is used to treat gaseous absorption coefficients. The optical properties of particles are determined through Mie calculations.

3. APPLICATION TO "SHIP TRACKS" IN CLOUDS

To investigate ship tracks in clouds with our model, we initialized a simulation with a cloudless marine boundary layer. Due to the upward mixing of water vapor from the ocean surface, a cloud forms 2 hours into the simulation. This "shocks" the model, which then takes another 8 hours to equilibrate. At 10 hours, the simulation is split into a control run, which is allowed to run unperturbed for another 70 hours, and a ship track run. In the ship track run a pulse of particles (representing pollution from a ship) is released into a grid point 100 m above the surface. The source strength of this input is inferred from the measurements by Radke et al. (1989), and the particles are instantaneously spread over a horizontal width of 25 km.

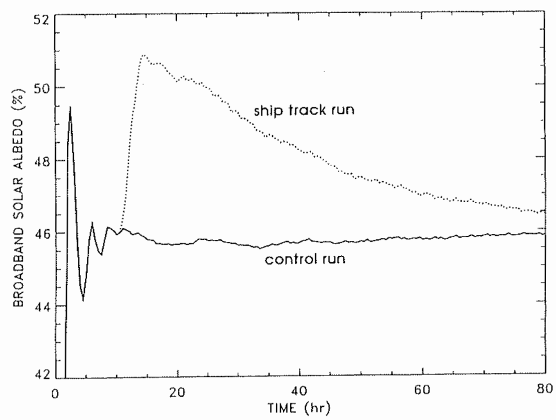

Figure 1. The evolution of the broadband solar albedo of marine stratocumulus clouds for a control run (solid line) and a ship-track run (dotted line) in which a pulse of 10^7 cm^{-2} of CCN is injected at 10 hours into the simulation at an altitude of 100 m above the ocean.

A comparison of the control and ship track runs reveals that in the latter case the cloud droplet concentration, liquid water content and albedo (the latter is shown in Figure 1) respond to the pulse of particles (CCN) in ~2-4 hours, with the delay depending on the depth of the boundary layer (500 and 830 m). This response is followed by a slow decay back to the original state, with an e-folding time of about 30 hours. Although the drizzle rate is reduced by the pulse of particles, the mass of particles in each drizzle drop that reaches the surface is increased. Hence, drizzle flushes the particles from the system. Although the boundary conditions that we used for these simulations, such as sea surface temperature and geostrophic wind, were taken from observations in the North Sea (Nicholls, 1984), the agreements between our model results and the observations of Radke et al. (1989) are encouraging.

To study the stability of the system to particle injections, we analyzed the perturbations in cloud properties as a function of particle pulse strength up to 16 times the strength of the ship source inferred by Radke et al. No signs of instability were found. In fact the perturbations in cloud droplet concentration (shown in Figure 2), liquid water content, and optical depth, were less than linearly related to the particle pulse strength. Doubling the pulse strength increased the e-folding time for the decay of the effects from ~30 to ~55 hours.

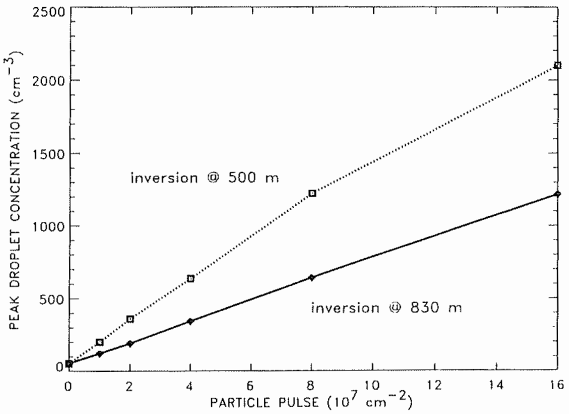

Figure 2. Peak cloud droplet concentrations reached following the injection of a pulse of CCN as a function of the pulse strength. The pulse strength is measured in multiples of the pulse strength for the base case (10^7 cm^{-2}). Results for initial inversion heights of 500 and 830 m are shown.

4. BISTABILITY OF THE CLOUD-TOPPED BOUNDARY LAYER WITH RESPECT TO CLOUD CONDENSATION NUCLEI

Baker and Charlson (1990) suggested that the cloud-topped boundary layer is bistable with respect to CCN populations. In their model, when the source strength of CCN is low enough, drizzle production – via droplet activation, coalescence and gravitational removal – maintains low CCN concentrations. They identify this stable state in their model with a very clean marine boundary layer, in which the production of CCN is assumed to be below 0.002 cm^{-3} s^{-1} and CCN concentrations are ~10 cm^{-3}. When the production of CCN was slightly higher Baker and Charlson found that drizzle ceased. They suggested that under these conditions the main sink of CCN is dry particle coagulation; the CCN concentrations then stabilized at ~1000 cm^{-3}.

We have begun to explore the relations between CCN production rates, CCN concentration and drizzle production with our more sophisticated model. Baker and Charlson's single layer model assumes the boundary layer to be well mixed. This is not necessarily the case, since evaporation of drizzle below cloud base can contribute to a decoupling of vertical mixing between the cloud and subcloud layer. This shortcoming, combined with a prescribed boundary layer thickness, prevented Baker and Charlson from addressing time evolution issues. Our model predicts the evolution of boundary-layer mixing. The Baker-Charlson model assumes that all cloud droplets are the same size, and their precipitation parameterization is correspondingly crude. Our explicit treatment of particle size distributions allows us to simulate microphysical processes more realistically. Finally, our radiative transfer scheme is coupled into the turbulent transfer and microphysics modules, thereby allowing examination of the effects of the absorption of solar radiation by the cloud on the decoupling of boundary layer mixing, as well as the sensitivities of the cloud optical properties to microphysical and mixing processes.

As discussed in the previous section, our model does not exhibit any instability to a *pulse* of CCN. We have also investigated the sensitivity of the cloud-topped boundary layer to a *constant* source of CCN, equivalent to that considered by Baker and Charlson. In this case, there is an instability. As shown in Fig. 3a, our model reaches a steady state droplet

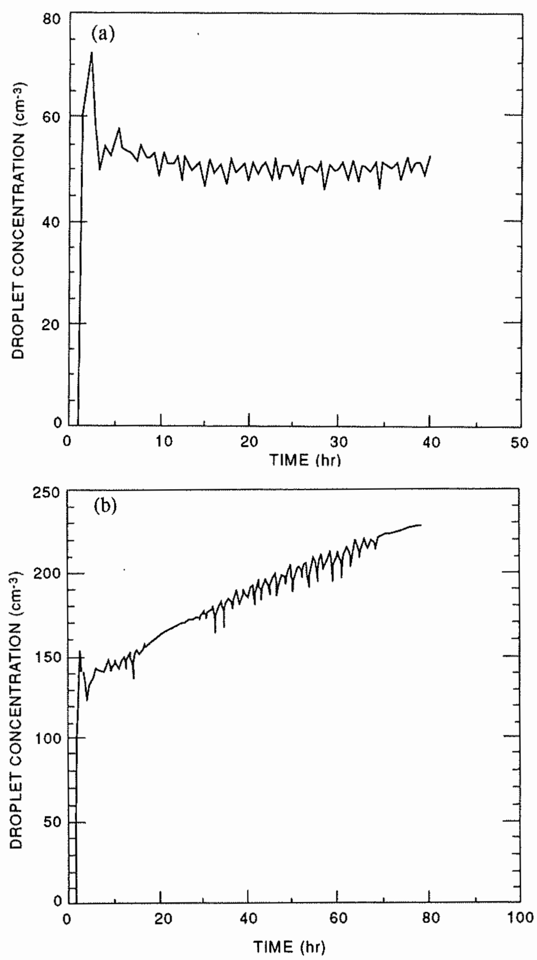

Figure 3. Comparison of the evolution of droplet concentration at cloud top for steady CCN production rates of (a) 0.002 cm^{-3} s^{-1} and (b) 0.004 cm^{-3} s^{-1}. The initial CCN concentrations were (a) 75 cm^{-3} and (b) 150 cm^{-3}.

concentration of 50 cm^{-3} in about 10 hours when we use a CCN production rate (0.002 cm^{-3} s^{-1}) corresponding to the upper limit for which Baker and Charlson's model was able to maintain a low equilibrium CCN concentration. When we double the CCN production rate, a steady state is not achieved even after 80 hours of simulated time, at which time the cloud top droplet concentration is 230 cm^{-3} (Fig. 3b). About 120 hours would be required for dry particle coagulation to become a significant sink even for particle number concentrations as high as 1000 cm^{-3}. It seems likely that the model is moving on a similar time scale toward a balance between CCN production and dry particle coagulation. However, on such long time scales, dry deposition will be a significant sink for CCN.

Our results are consistent with the steady state results of Baker and Charlson. However, the application of these ideas to marine stratiform clouds may be limited by the long time scales needed for equilibrium to be reached, at least for the case of high CCN concentrations. If marine clouds require five or more days to establish equilibrium under high CCN production rates, it is unlikely that such a balance will ever be reached in nature. Atmospheric processes that operate on shorter time scales, such as advection of CCN or frontal passages, will tend to disrupt evolution toward a steady state. Finally, it should be noted that these model simulations do not take into account that clouds are not only sinks but probably also sources of CCN (e.g. Hoppel et al., 1990; Hegg et al., 1990). Inclusion of this additional source, which is time dependent, may prevent the system from ever reaching a steady state.

Acknowledgments. This research was supported by NASA University Consortium agreement NCA2-623 with the University of Washington.

5. REFERENCES

Albrecht, B. A., 1989: Aerosols, cloud microphysics, and fractional cloudiness. Science, 245, 1227–1230.

Baker, M. B., and R. J. Charlson, 1990: Bistability of CCN concentrations and thermodynamics in the cloud-topped boundary layer. Nature, 345, 142–145.

Bougeault, Ph., 1981: Modeling the trade-wind cumulus boundary layer. Part I: Testing the ensemble cloud relations against numerical data. J. Atmos. Sci., 38, 2414–2428.

Conover, J.H., 1966: Anomalous cloud lines. J. Atmos. Sci., 23, 778–785.

Davies, R. G., 1985: Response of cloud supersaturation to radiative forcing. J. Atmos. Sci., 42, 2820–2825.

Dyunkerke, P. G., and A. G. M. Driedonks, 1987: A model for the turbulent structure of the stratocumulus-topped atmospheric boundary layer. J. Atmos. Sci., 45, 43–64.

Hegg, D. A., L. F. Radke, and P. V. Hobbs, 1990: Particle production associated with marine clouds. J. Geophys. Res., 95, 13,917–13,926.

Hoppel, W. A., J. W. Fitzgerald, G. M. Frick, R. E. Larson, and E. J. Mack, 1990: Aerosol size distributions and optical properties found in the marine boundary layer over the Atlantic Ocean. J. Geophys. Res., 95, 3659–3686.

Nicholls, S., 1984: The dynamics of stratocumulus: aircraft observations and comparisons with a mixed layer model. Quart. J. Roy. Meteorol. Soc., 110, 783–820.

Radke, L. F., J. A. Coakley, Jr., and M. D. King, 1989: Direct and remote sensing observations of the effects of ships on clouds. Science, 246, 1146–1149.

Toon, O. B., R. P. Turco, D. Westphal, R. Malone, and M. S. Liu, 1988: A multi-dimensional model for aerosols: description of computational analogs. J. Atmos. Sci., 45, 2123–2143.

Toon, O. B., C. P. McKay, T. P. Ackerman, and K. Santhanam, 1989: Rapid calculations of radiative heating rates and photodissociation rates in inhomogeneous multiple scattering atmospheres. J. Geophys. Res., 94, 16,287–16,301.

Twomey, S. A., M.Piepgrass, and T. L. Wolfe, 1984: An assessment of the impact of pollution on global cloud albedo. Tellus, 36B, 356–366.

A NUMERICAL SIMULATION OF MARITIME STRATUS CLOUDS BY AN ENSEMBLE CLOUD MODEL

Tetsuji Yamada[1] and Takashi Sasamori[2]

[1]Yamada Science & Art Corporation, Los Alamos, NM USA 87544
[2]University of Illinois, Urbana, IL USA 61801

1. INTRODUCTION

Mesoscale models with a horizontal grid spacing of 5–10 km cannot simulate horizontal distributions of cumulus clouds whose diameters are less than a few kilometers. A conventional approach is a parameterization where condensation is assumed to occur at the value less than the saturation point. This is in agreement with the fact that the grid volume averaged water vapor mixing ratio is always less than the saturation value unless the grid volume is fully contained in clouds. This parameterization is simple, but suffers considerable ambiguity in determining the "ad hoc" saturation value. The results are obviously very sensitive to the value selected. It is necessary to "optimize" or "tune" the value so that modeled cloud amounts agree with observations.

An alternative approach is an ensemble cloud model (Sommeria and Deardorff, 1977; Mellor, 1977) where the ensemble of condensation is considered. In other words, microstructure of clouds are not explicitly modeled, but statistic representation of condensation, such as mean values variances, and cloud volumes are modeled.

2. MODEL DESCRIPTION

The model equations are for horizontal wind components, liquid water potential temperature (Betts, 1973), and mixing ratio for water contents (vapor and cloud water). Turbulence fluxes are modeled based on the Level 2.5 turbulence closure model of Mellor and Yamada (1982). This ensemble cloud model had been used successfully (Yamada and Mellor, 1979; Yamada, 1979; Yamada and Kao, 1986; Kao and Yamada, 1989; Koracin and Rogers, 1990) to simulate clouds, interaction between condensation and turbulence, interaction between clouds and longwave radiation. Recently, a shortwave radiation parameterization scheme developed by Hanson and Derr (1987) was added to model shortwave radiation heating of clouds. The longwave radiation flux in the liquid water potential temperature equation was computed according to Sasamori (1968).

The model was further advanced by adopting a precipitation microphysics model developed by Nickerson et al. (1986). Nickerson's model parameterizes autoconversion of raindrops from the cloud droplets, accretion of cloud droplets by the falling raindrops, self-collection of small raindrops by the falling large drops, sedimentation of raindrops by gravity and the evaporation of raindrops in the unsaturated atmospheric layer.

3. RESULTS AND DISCUSSIONS

A numerical simulation was conducted to investigate complex interactions among clouds, turbulence, and atmospheric radiation. Maritime stratus clouds were simulated by using a one-dimensional version of a three-dimensional mesoscale model HOTMAC, Higher Order Turbulence Model for Atmospheric Circulation (Yamada and Bunker, 1989).

Integration initiated at 0000 LT (Local Time). Clouds began to form almost immediately and occupied the layer between 1200 m and 1600 m above the sea surface (Fig. 1). As the shortwave radiative heating increased, clouds dissipated from the top and clouds became as thin as 100 m deep by 1800 LT. As the solar heating subsided the cloud depth increased again.

Figures 2 and 3 show, respectively, shortwave radiation heating rate (C/day) and longwave radiation cooling rate (C/day). The shortwave radiation heating was maximum at the cloud top and decreased exponentially within the cloud (Hanson and Derr, 1987). Shortwave radiation heating (Fig 2) was partially offset by longwave radiation cooling at the cloud top (Fig. 3). Figure 3 also indicates longwave radiation warming at the cloud base.

Finally diurnal variations of mixing ratio of rain are shown in Fig. 4. Rain was produced in the cloud but evaporated before it reached the surface.

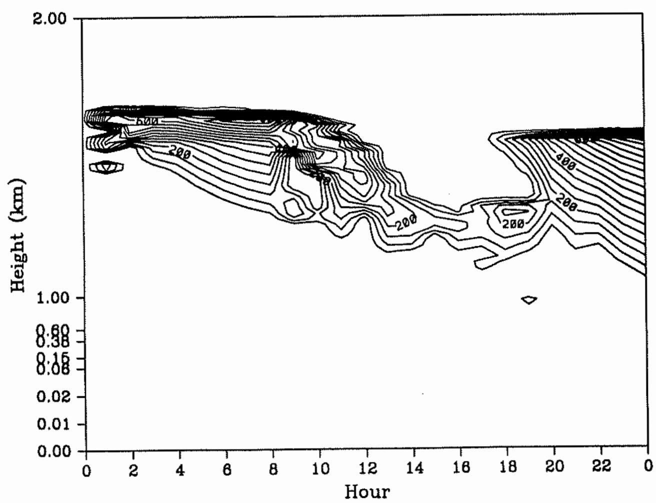

Fig. 1 Diurnal variation of cloud water mixing ratio.

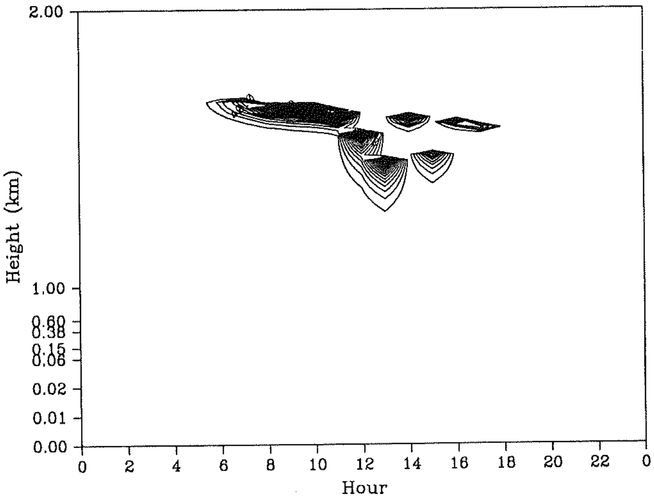

Fig. 2 Diurnal variation of shortwave radiation heating rate.

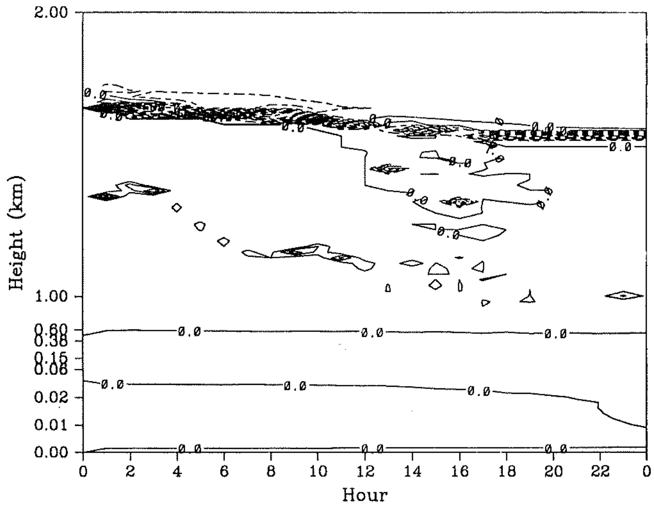

Fig. 3 Diurnal variation of longwave radiation cooling rate.

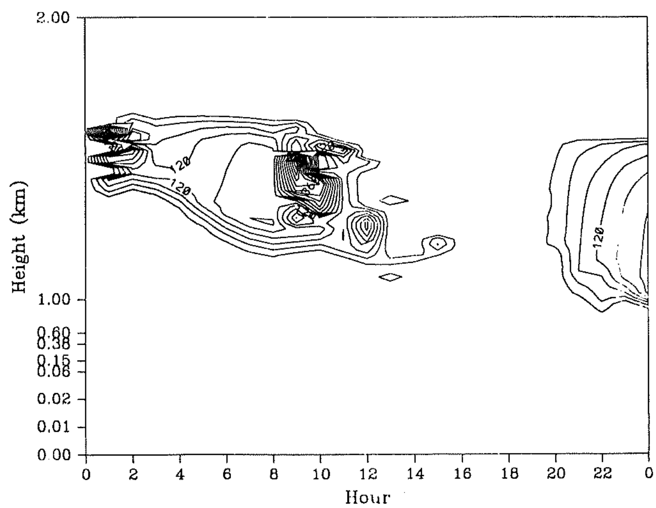

Fig. 4 Diurnal variation of rain water mixing ratio.

REFERENCE

Betts, A. K. 1973. Non-precipitating cumulus convection and its parameterization. *Quart. J. Roy. Meteor. Soc.* **99:** 178–179.

Hanson, H. P. and V. E Derr. 1987. Parameterization of radiative flux profiles within layer clouds. *J. Climate. Appl. Meteor.* **11:** 1511–1521.

Kao, C.-Y. J. and T. Yamada. 1989. Numerical simulations of a stratocumulus-capped boundary layer over land using a turbulence closure model. *J. Atmos. Sci.* **46:** 832–848.

Koracin, D. and D. P. Rodgers. 1990. Numerical Simulation of the Response of the Marine Atmosphere to Ocean Forcing. J. Atmos. Sci. **47:** 592–611.

Mellor, G. L., 1977. The Gaussian cloud model relations. *J. Atmos. Sci.* **34:** 356–358.

Mellor, G. L. and T. Yamada. 1982. Development of a turbulence closure model for geophysical fluid problems. *Rev. Geophys. Space Phys.* **20:** 851–875.

Nickerson, E. C., E. Richard, R. Rosset and D. R. Smith. 1986. The numerical simulation of clouds, rain, and airflow over the Vosges and Black Forest Mountains: a meso-β model with parameterized microphysics. *Mon. Wea. Rev.* **114:** 398–414.

Sasamori, T. 1968. The radiative cooling calculation for application to general circulation experiments. *J. Appl. Meteor.* **7:** 721–729.

Sommeria, G. and J. W. Deardorff. 1977. Subgrid-scale condensation in models of non-precipitation clouds. *J. Atmos. Sci.* **34:** 344–355.

Yamada, T. 1979. An application of a three-dimensional simplified second-moment closure numerical model to study atmospheric effects of a large cooling-pond. *J. Atmos. Environ.* **13:** 693–704.

Yamada, T. and S. Bunker. 1989. A numerical model study of nocturnal drainage flows with strong wind and temperature gradients. *J. Appl. Meteo.* **28:** 545–554.

Yamada, T. and C.-Y. J. Kao. 1986. A modeling study on the fair weather marine boundary layer of the GATE. *J. Atmos. Sci.* **43:** 3186-3199.

Yamada, T. and G. L. Mellor. 1979. A numerical simulation of the BOMEX data using a turbulence closure model coupled with ensemble cloud relations. *Quart. J. Roy. Meteor. Soc.* **105:** 915–944.

A REGIONAL SIMULATION OF MARINE BOUNDARY LAYER CLOUDS

Shouping Wang[1], Bruce Albrecht[2] and Patrick Minnis[3]

[1]University Space Research Association
[2]Pennsylvania State University
[3]NASA/Langley

1. Introduction

There have been many modeling efforts for understanding and parameterizing marine boundary layer cloud systems. These efforts have mainly involved one-dimensional models that are usually verified against observational data from field experiments, However, to verify the parameterization of some cloud parameters such as fractional cloudiness, it is necessary to compare horizontal distribution of these parameters with those derived from satellite data. Thus, the regional modeling approach is preferred to verify the parameterization of cloudiness that can be used in a large-scale meteorological model. Furthermore, the regional modeling approach also provides a framework for defining detailed boundary layer structure from coarse resolution global analyses and satellite data.

In this work, we develop a regional model of marine boundary layer model based on the one-dimensional two-layer model developed by Albrecht et al. (1979) and Wang (1992). We then use this model with the large-scale conditions provided by the ECMWF analyses to simulate the boundary layer clouds in the eastern North Pacific observed during FIRE. The model results are compared with those derived from satellite data from GOES. The sensitivity of the simulated cloudiness to the specification of large-scale divergence and drizzle are also evaluated.

2. The model description

The model used in this study was originally developed by Albrecht et al. (1979) and modified by Wang (1990). It assumes a mixed-layer structure in the subcloud layer and linear variation for the cloud layer structure for any conserved thermodynamic variable. the cloud base height is determined by the saturation level of a surface air parcel. The discontinuities in thermodynamic variables at cloud base regulate the decoupling between the cloud and the subcloud layer in the model.

The grid size is 0.4° x 0.4° latitude-longitude for the model. The simple lateral boundary condition applied is: the horizontal gradient of variables normal to the boundary are zero except for the coastline where the derivatives along longitudes are zero. A daily mean value for zenith angle is used for the solar radiation calculation. All results presented below are steady-state solutions after 200 hours of integration of the model with a time step of 6 minutes.

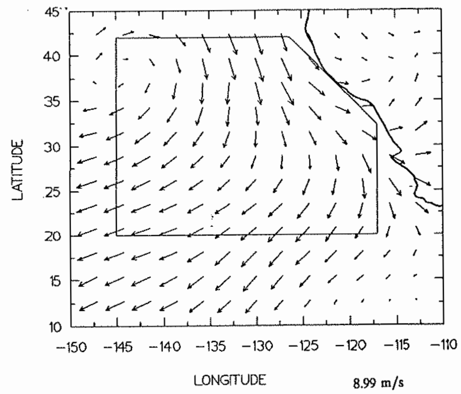

Figure 1. a: Mean wind at 1000 mb over June 29 - July 20, 1987 (the FIRE period) defined from the ECMWF analyses. The inner area is the area simulated with the model.

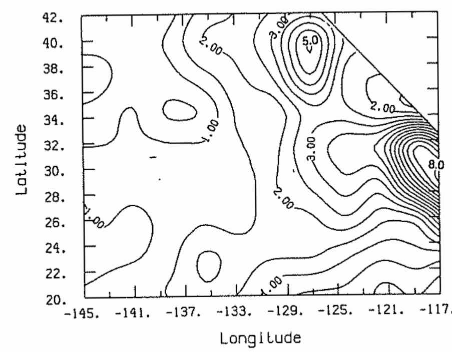

Figure 2. large-scale divergence field ($x10^{-6}s^{-1}$) calculated from large-scale velocities from the ECMWF analyses.

3. Large-scale conditions for the simulations

The boundary layer model is applied to the region of 20°N-42°N and 117°W-145°W for June 29 - July 19, 1987, the period of FIRE marine stratocumulus intensive field observation. In this study, the land area is neglected. Averaged large-scale fields over this period from the ECMWF analyses are used to provide upper and lower boundary conditions for the model. The wind at 1000 mb and the simulated domain are shown in Figure 1. The wind field at 1000 mb is used for calculations of the horizontal advection for both the cloud and subcloud layers. The conditions just above the boundary layer top are derived by interpolation or extrapolation of input at the layers of 700 mb and 850 mb.

The July mean sea surface temperature (SST) used in this study are obtained from COADS. The mean large-scale divergence (Figure 2) is calculated from ECMWF analyses. For convenience, the divergence field shown in Figure 2 is designated as the reference divergence $\boldsymbol{D}_r$.

4. Mean fields

Away from cold ocean surfaces near the coast, cloud-base height rises to the southwest (Figure 3a), in accordance with the warmer and more moist subcloud layer associated with increasing SST. The cloud-top height shown in Figure 3b is a function of the large-scale divergence and entrainment velocity. The divergence maximum near the eastern border leads to a shallow boundary layer ($z_i \approx$ 700 m). Cloud-top heights increase rapidly to the west and reach 2.7 *km* at the southwest corner of the domain where the large-scale divergence is only about $10^{-6} s^{-1}$.

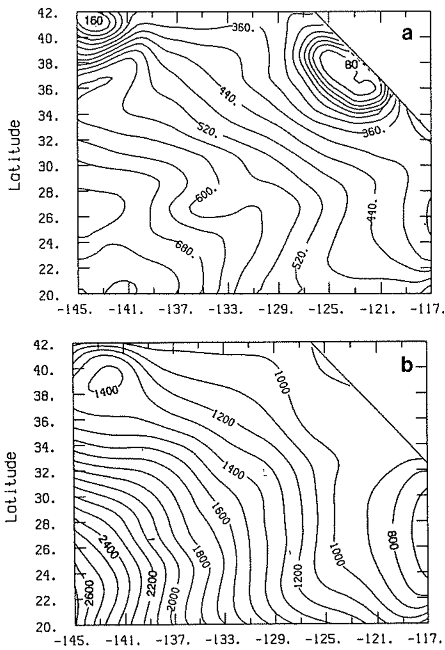

Figure 3. a: The simulated cloud-base heights (m) and b: cloud-top heights (m).

The simulated cloud cover is shown in Figure 4a. The cloud cover is close to unity over low SST areas along the northern border and the coast. It decreases southward and has a local maximum located at 27°N-135°W. Toward the east it decreases to a minimum value of 0.5. This cloud cover pattern is closely related to the fields of large-scale divergence, drizzle and entrainment. Divergence increases from the west to the east and reaches the maximum near the eastern border, thus the cloud cover is minimized there. Drizzle rates (Figure 4b) and entrainment velocity (Figure 4c) increase to the southwest from the coastline, which tends to reduce cloud cover toward southwest.

Mean low-cloud-top heights and low-cloud cover (Figure 5) for the FIRE IFO (1-19 July, 1987) were derived on a 2.5° x 2.5° latitude-longitude grid using a

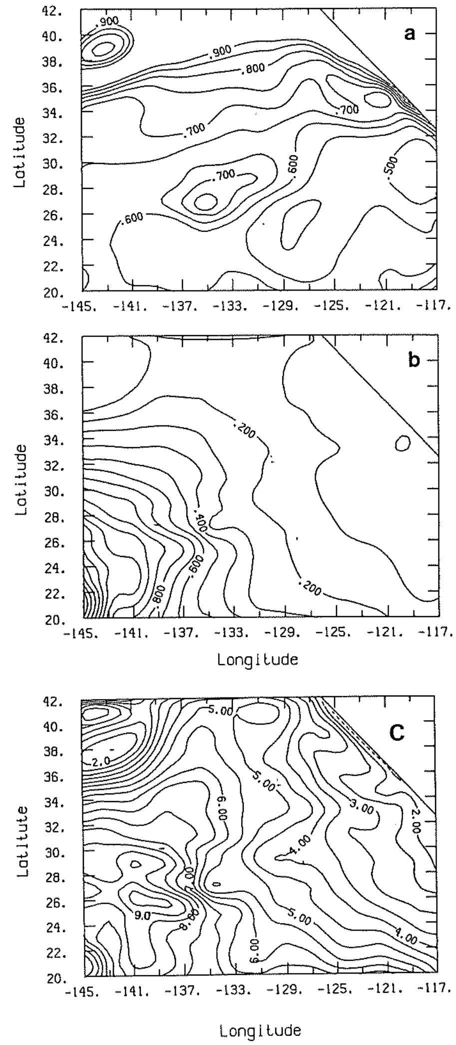

Figure 4. Simulated cloud cover (a); drizzle rate (mm day^{-1}) (b) and entrainment velocity (c).

3-hourly GOES West 8-km resolution visible and infrared data set and the analysis procedures described by Minnis et al. (1987) and Minnis et al. (1992). The basic patterns of both simulated and satellite-derived cloud-top heights are qualitatively consistent. Both have relatively low values near the coast and the eastern border and increase toward the southwest. The large discrepancies in the southwest suggest that either the model entrains excessively or large-scale subsidence is too weak.

The simulated (Figure 4a) and satellite-derived (Figure 5b) cloud cover also show some qualitative agreement. A relative minimum is seen in the northwestern corner of both domains although the satellite-derived minimum extends further to the east. The satellite-derived cloud amounts reach the maximum of 0.9 at 36°N- 138°W corresponding to unity in the simulated results near the northern border. The domain average from the simulation is 0.68 compared with 0.74 of that derived from satellite data.

Differences between the two cloud cover fields may arise from a number of sources. The simulation may not capture fluctuations in cloudiness due to

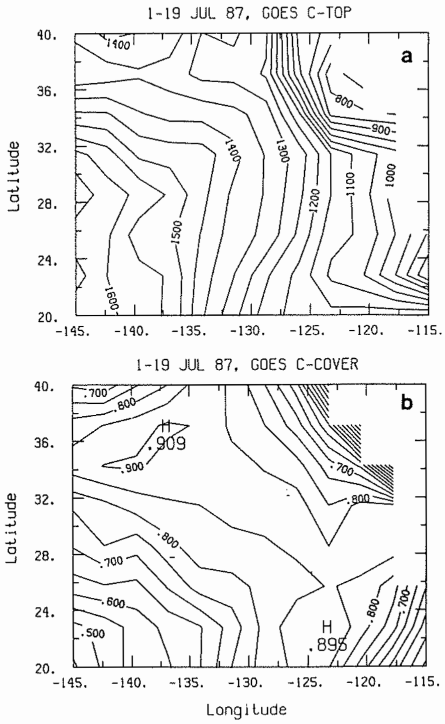

Figure 5. Mean cloud properties derived from GOES for 1 - 19 of July, 1987. a: Mean cloud-top heights (m); b: mean low-cloud cover.

variable large-scale conditions and diurnal variation.Errors in the large-scale conditions may also be an source for the simulated versus observed cloud cover and cloud-top height differences. Thus, the sensitivity to large-scale subsidence is explored in the next section.

5. Sensitivity tests

In this section, we show that large-scale subsidence may influence the simulated MBL clouds. Three model runs will be made in this section. In the case of DIV, we uniformly increase the large-scale divergence by $2x10^{-6}$ s^{-1} over the entire domain. In the case of NDRZ, drizzle is suppressed; in the case NDRZ-DIV, drizzle is suppressed and the large-scale divergence is uniformly increased by $2x10^{-6}$ s^{-1} over the entire domain. The conditions for these runs are listed in Table 1.

Figure 6 presents the results from DIV. It is seen that cloud top height decreases substantially due to the increase of the large-scale divergence compared that of CNTRL. The maximum z_i at the southwest from DIV is 1800 m, 900 m lower than that from CNTRL, while it is 450 m from DIV compared with 700 m from CNTRL for the minimum at the east boundary. The overall pattern of z_i does not change. The cloud cover decreases for the entire domain owing to the stronger divergence.The averaged cloud cover over the entire domain decreases by 20% from 0.67 (CNTRL) to 0.54 (DIV) as shown in Table 2.

Table 1: The conditions and results for sensitivity tests.

	CNTRL	DIV	NDRZ	NDR-DIV
Conditions	$D=D_r$ drizzle	$D=D_r$ + $2x10^{-6}$ s^{-1} drizzle	$D=D_r$ No drizzle	D=Dr+ $2x10^{-6}$ s^{-1} No drizzle
Mean cloud cover	0.67	0.54	0.86	0.66
Mean drzl. rate (mm day^{-1})	0.35	0.1	0.0	0.0

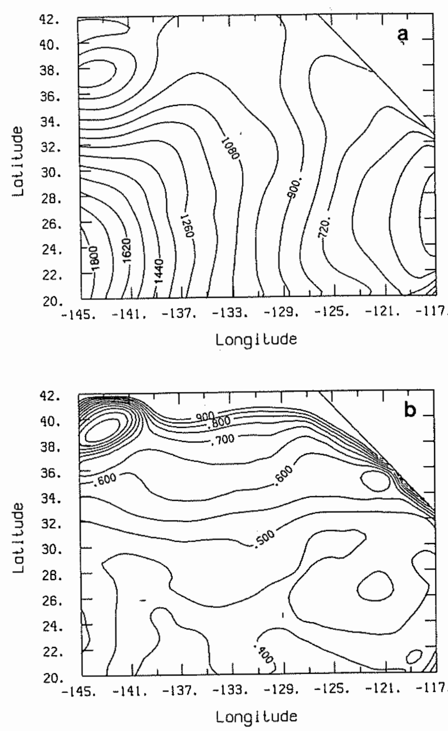

Figure 6. Results from sensitivity test DIV. a: Cloud-top heights (m); b: cloud cover.

Comparison of results from NDRZ and NDRZ-DIV (not shown here) indicates that the increase in large-scale divergence significantly decreases cloud-top height and cloud cover. The averaged cloud cover is reduced from 0.86 in NDRZ to 0.66 in NDRZ-DIV (23%) as shown in Table 1. It is seen that for these cases, the cloud cover is sensitive to large-scale divergence in the model. This sensitivity is due to the sensitivity of cloud-top height to subsidence, since a stronger subsidence may force cloud-top height well below the saturation level of the environment. It is known, however, that large-scale divergence or vertical motion over tropics is difficult to predict in a climate model. Therefore one should consider this sensitivity in evaluating the various schemes for shallow cloud cover used in climate models.

It also should be mentioned that drizzle may have strong impact on the cloud cover as demonstrated by one-dimensional version of the model (Albrecht, 1989; Wang, 1992). One can recognize this sensitivity by comparing Figure 4a and Figure 7. The cloud cover pattern is significantly changed by drizzle and the average cloud cover is increased by 22% from 0.67 in CNTRL to 0.86 in NDRZ as shown in Table 1. Clearly more studies are needed on the effects of drizzle on boundary layer structure and cloud cover.

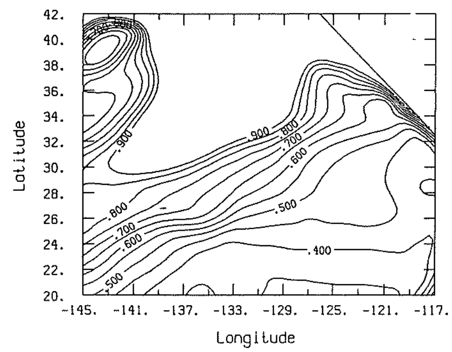

Figure 7. Cloud cover from sensitivity test NDRZ run.

6. Summary

In this study, the simulated distribution of cloud-top height and cloud cover show some qualitative agreement with available satellite data. The cloud cover is shown to be sensitive to large-scale divergence since it changes the boundary layer thickness, and thus the thickness of the solid clouds.

The steady-state solutions presented in this paper are difficult to verify. A time-dependent solution could provide the transient MBL structure needed to study diurnal variations as well as to define a time-mean structure that is more compatible with averaged satellite data. In a future study, we will simulate the time-dependent behavior of MBL clouds using time-dependent large-scale conditions provided by the ECMWF analysis and study the diurnal variation of fractional cloudiness and its influences on the surface turbulent fluxes.

Acknowledgments

Shouping Wang was supported by NASA Grant NAS-8-37130. Bruce Albrecht was supported by NSF Grant ATM 89-09947. The satellite analyses were supported in part by the Office of Naval Research Grant USN-N000149IMP24011.

References

Albrecht, B.A., 1989: Aerosols, cloud microphysics, and fractional cloudiness. *Science*, **245**, 1227-1230.

Albrecht, B.A., 1981: Parameterization of trade-cumulus cloud amounts. *J. Atmos. Sci.*, **38**, 97-105.

Albrecht, B.A., A.K. Betts, W.H. Schubert and S.K. Cox, 1979: A model of the thermodynamic structure of the trade wind boundary layer. Part I: Theoretical development and sensitivity tests. *J. Atmos. Sci.*, **36**, 73-89.

Albrecht, B.A., D.A. Randall, and S. Nicholls, 1988: Observations of marine stratocumulus clouds during FIRE. *Bull. Amer. Meteor. Soc.*, **69**, 618-626.

Betts, A.K., P. Minnis, W. Ridgway, and D.F. Young, 1992: Integration of satellite and surface data using a radiative convective oceanic boundary layer model. *J. Appl. Meteo.*, .

Minnis, P. and E.F. Harrison, 1984: Diurnal variability of regional cloud and clear-sky radiative parameters derived from GOES data. Part II: November 1978 cloud distributions. *J. Climate Appl. Meteor.*, **23**, 1012-1031.

Minnis, P., P.W. Heck, D. Young, C.W. Fairall, and J.B. Snider, 1992: Stratocumulus cloud properties derived from simultaneous satellite and island-based instrumentation during FIRE. *J. Appl. Meteo.* (in press).

Nicholls, S.H., 1984: The dynamics of stratocumulus: Aircraft observations and comparison with a mixed-layer model. *Quart. J. Roy. Meteor. Soc.*, **110**, 783-820.

Wakefield, J.S., and W.H. Schubert, 1981: Mixed-layer modeling of eastern North Pacific stratocumulus. *Mon. Wea. Rev.*, **109**, 1952-1968.

Wang, S, 1991: The breakup of marine stratocumulus clouds in a two-layer boundary layer model. (submitted to *J. Atmos. Sci.*)

TRANSPORT AND MIXING ABOVE THE MARINE STRATUS OVER THE EASTERN PACIFIC OCEAN

I. R. Paluch and D. H. Lenschow
National Center for Atmospheric Research, Boulder, Colorado *

R. Pearson, Jr.
NASA Ames Research Center, Moffet Field, California

We examine aircraft observations in the lower troposphere over the eastern Pacific Ocean in summer $\geq$ 400 km off the southern California coast (Fig. 1). The location of the research area and the season were chosen to observe the marine boundary layer and the overlying troposphere in a nearly pristine state, away from known pollution sources. In the summer the winds over the eastern Pacific Ocean are usually from the northeast, and the air has previously traveled over the ocean for weeks. This region is in the southeastern part of the subtropical high, which is a very stably stratified subsiding region with a relatively shallow stratiform-capped boundary layer (Riehl, 1978).

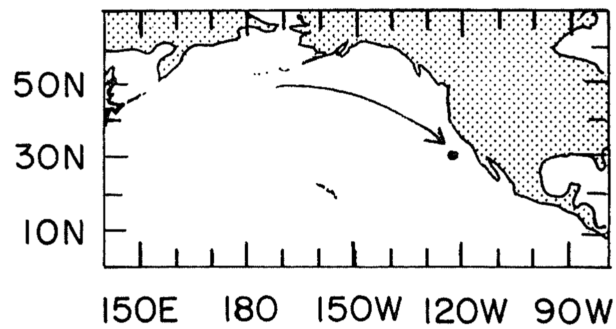

Fig. 1. The location of the research area is indicated by the dot near the southern California coast. The arrow shows the approximate path of typical air-parcel trajectories that arrive in the research area.

The data were collected from the National Center for Atmospheric Research (NCAR) Electra aircraft during the First ISCCP (International Satellite Cloud Climatology Project) Regional Experiment (FIRE). We use fast response ozone data (Pearson, 1990) at 20 samples per second, which corresponds to a flight distance of about 5 m per sample. To correct for time lag due to the transit time of the air going through the inlet duct to the sensor, the O_3 data have been shifted forward in time by 0.2 s. Other aircraft measurements with the above resolution include air temperature, liquid water from the FSSP, and moisture measured by a fast-response Lyman-alpha hygrometer, which is calibrated against a dew-point hygrometer for each flight. In the following analysis we focus on two quasi–conserved variables: ozone (O_3) and total-water (liquid plus vapor) mixing ratio (Q_T).

Figure 2 shows vertical profiles of O_3 and Q_T, followed by a plot of O_3 versus Q_T. Abrupt changes in the O_3 and Q_T profiles occur at the temperature inversion (at 925 mb). In the O_3 versus Q_T plot, point A represents data from the well-mixed boundary layer, points forming line A–B come from data at the inversion, whereas points on line B–C come from data above the inversion. Here B–C is a continuation of A–B, implying that the same two sources of air are

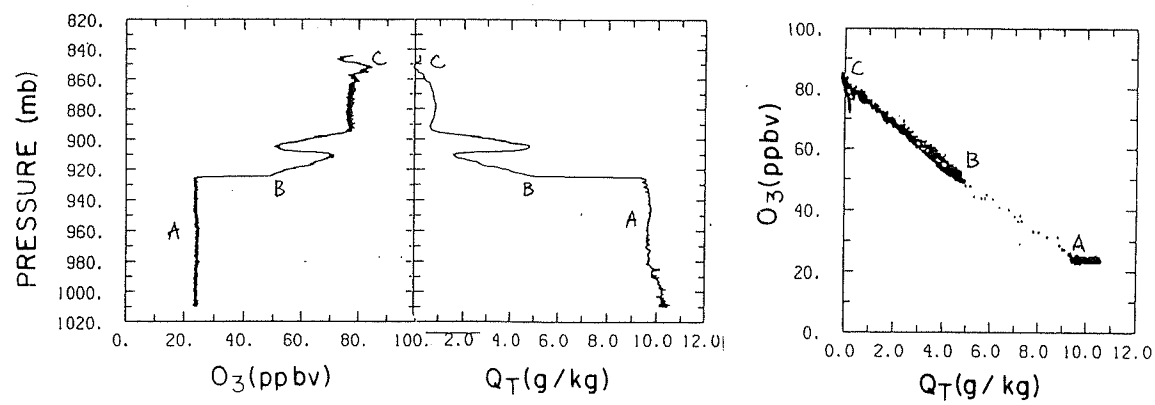

Fig. 2. Profiles of ozone mixing ratio (O_3) and total-water mixing ratio (Q_T), and O_3 versus Q_T. The letters are added to facilitate comparisons between O_3 vs. Q_T plots, and O_3 and Q_T profiles. The data are from the usual research area $\geq$ 400 km offshore (flight 5, 21:54–22:00 UT, local time is 7 hrs less).

* The National Center for Atmospheric Research is sponsored by the National Science Foundation.

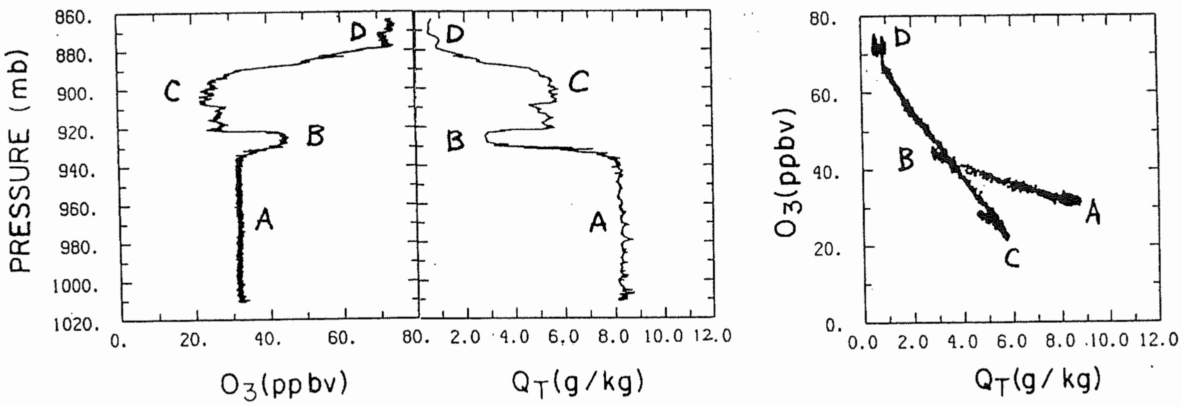

Fig. 3. same format as Fig. 2. The data are from the usual research area $\geq$ 400 km offshore (flight 4, 17:43–18:00 UT).

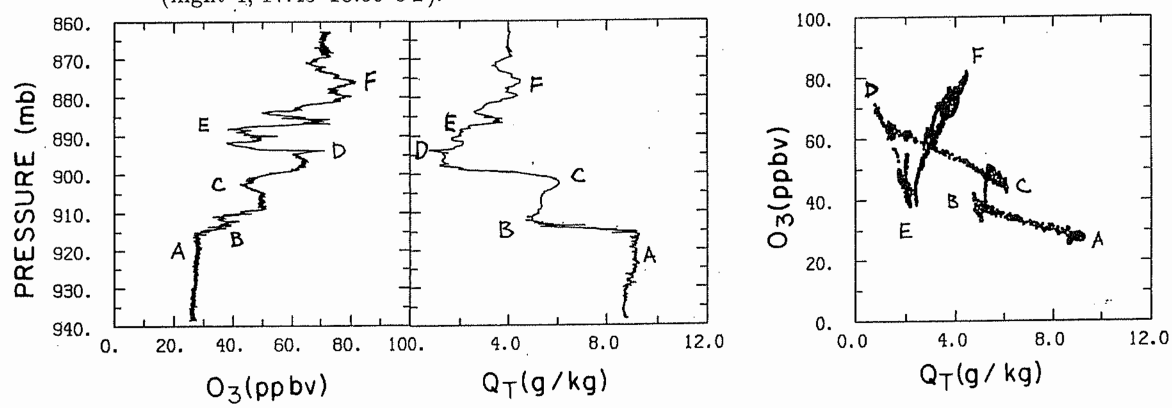

Fig. 4. same format as Fig. 2. The data are from the usual research area $\geq$ 400 km offshore (flight 2, 21:20–21:25 UT).

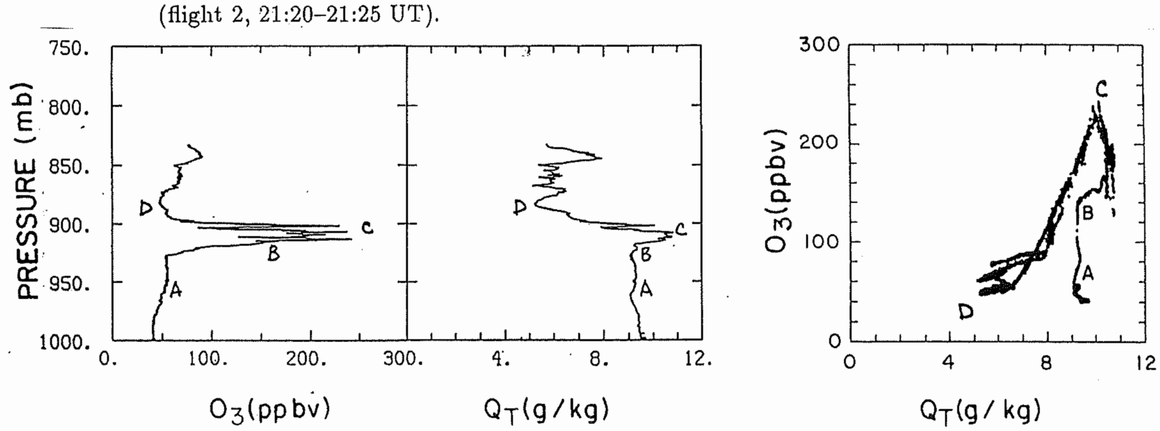

Fig. 5. same format as Fig. 2. The data are from a polluted layer about 100–150 km off the California coast (flight 9, 19:00–19:09 UT).

involved: moist, ozone depleted boundary-layer air (A) and dry, ozone-rich air (C) that probably originated in the middle or upper troposphere.

Soundings with single mixing lines similar to that in Fig. 2 are quite rare (except over a narrow altitude range). A sounding that forms two well-defined mixing lines is shown in Fig. 3. Here besides the boundary-layer air (A) two other sources of air are involved: one of the sources is dry, ozone-rich air (D), while the other is moderately moist, ozone-depleted air (C).

Figure 4 shows a sounding that produces a complex mixing-line pattern, which is about the most complex encountered in the FIRE data. Successive aircraft penetrations indicate that the characteristic mixing-line patterns persist for hours or longer, but they vary over distances of the order of tens of kilometers (Paluch et al., 1992). The unique "signatures" formed by the mixing lines could have a potential use for identifying air-masses in Lagrangian field experiments.

Very different mixing-line patterns result from soundings 100–150 km off the Los Angeles–San Diego coast (Fig. 5). Above the inversion (at 925 mb) there is a layer with unusually high concentrations of O_3 and Q_T. (It also contains very high concentrations of aerosols, see Hudson and Frisbie, 1991, and Paluch et al., 1992.) This layer probably represents a direct intrusion of polluted air from the coast, which could have been the result of baroclinic flow associated with boundary-layer warming over land. The mixing-line pattern through this layer is highly irregular and we see large increases in O_3 (note change in scale) that are not accompanied by a decrease in Q_T, as is typical of soundings in the usual research area farther offshore.

Observations from FIRE indicate that the lower free troposphere consists of horizontal layers that travel with different velocities. Above the boundary layer the horizontal wind typically changes with altitude (Paluch et al., 1992), which tends to stretch an air-mass horizontally. The stretching can be quite rapid: for instance, a wind-shear of 1 m $s^{-1}km^{-1}$ will stretch a 1 km by 1 km square into a 7.2 km by 0.14 km band in only 2 hrs.

How the mixing-line patterns may have formed and why there is a tendency for the mixed points to form lines rather than cover areas on the O_3–Q_T plots may be explained from the following considerations. Let points A, B, and C represent three air masses on an O_3–Q_T plot. If the mixing eddies extend to scales that are equal to or larger than the air-mass size, then mixing will take place between all three air masses, and the mixed air properties will lie within the area of the triangle ABC.

If the mixing eddies are small compared to the air-mass size then mixing takes place only at the boundaries of adjacent air masses, and if there are common

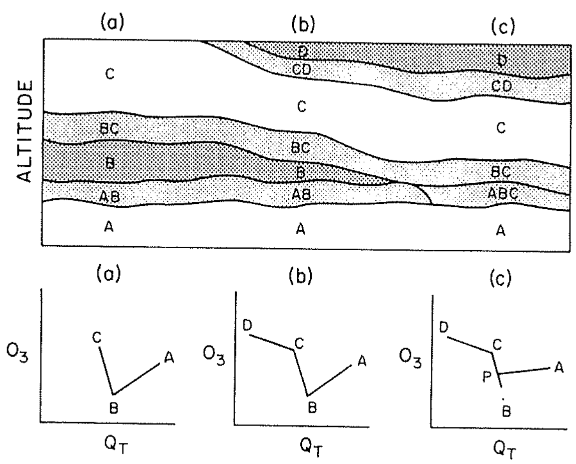

Fig. 6. Sketches of different arrangements of layers with height (top), and the corresponding mixing lines (bottom). (a) mixing between three stratified adjacent layers A, B, and C; AB and BC represent mixed regions; (b) mixing between four layers; (c) part of the mixed layer BC with local properties P in contact with layer A.

boundaries between each pair, then the properties of the mixed air will lie on lines forming the triangle ABC.

In a stable atmosphere the buoyancy stratification will tend to suppress the formation of large-scale eddies, and the air masses will be layered according to their buoyancy, say in the order A, B, C. In this case A and C have no boundaries in common, and thus the mixed air properties will lie on lines AB and BC only, as sketched in (a) in Fig. 6.

In a sounding the aircraft may sample a number of different, nonuniformly mixed layers and these will produce mixing-line patterns consisting of a number of connected lines, as sketched in (b) in Fig. 6. The lines will be straight if mixing involves adjacent layers only, but they need not always extend from an endpoint. For example, differential advection may bring layer A into contact with a mixed region with properties P on the B-C mixing line. At this boundary we will observe the mixing line A-P, and in its neighborhood a portion of the mixing line B-C that includes P, as sketched in (c) in Fig. 6, and observed in the sounding in Fig. 3.

The tendency for the mixing lines to be straight imply that two processes are operating: large–scale differential advection, which transports air masses from different sources while stretching them into horizontal layers, and small–scale turbulent mixing between the adjacent layers.

Figure 7 shows a composite plot of mixing lines from FIRE that involve ozone with maximum concentrations above 70 ppbv (this limit was chosen to avoid clutter; our conclusions do not depend on it). The mixing lines are numbered according to the aircraft flight day. For comparison, boundary-layer values are also shown. These form a cluster of points in the shaded area on lower right. Segments of mixing lines involving unusually high ozone concentrations (9) are from the polluted layer about 100 km offshore. The rest are from the usual research area $\geq$ 400 km offshore.

In the FIRE research area away from the coast the mixing lines tend to point to zero moisture and high concentrations of ozone, which suggests that this ozone has come from the middle or upper troposphere where the air is very cold and dry. The ozone could have originated in the stratosphere and been mixed into the upper and middle troposphere during a tropospheric folding event as described e.g. by Danielson (1968), and Shapiro (1980). Alternatively, the ozone could be of anthropogenic origin, having been carried to the middle or upper troposphere by deep convection at some earlier time.

At the other end the mixing lines terminate at low ozone and variable moisture contents. There the O_3– Q_T values are lower than what could be produced by mixing of boundary-layer air with mid- or upper-tropospheric air, which suggests the presence of ozone and/or moisture sinks. In the troposphere ozone can be lost through photochemical reactions with a time scale of about 90 days (Fishman et al., 1991), while the boundary-layer air can lose moisture through lifting and

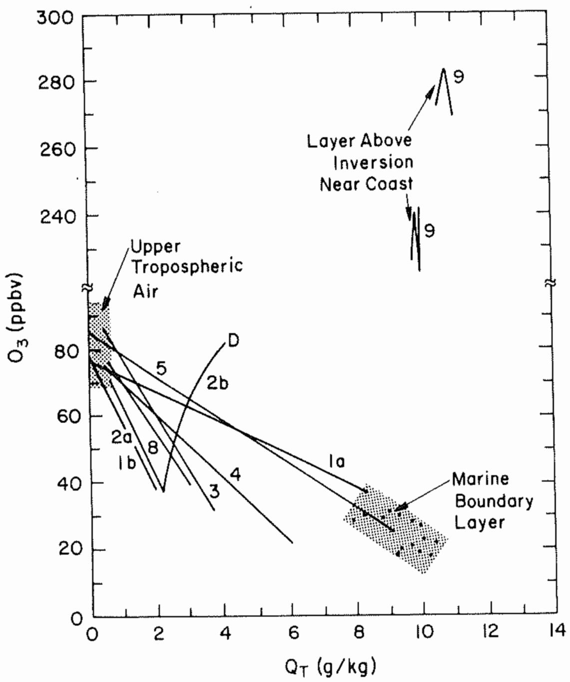

Fig. 7. Mixing lines from FIRE soundings that involve O_3 maxima above 70 ppbv. Boundary layer O_3– Q_T values from all flights form a cluster of points in the shaded lower right area. The data are from the research area $\geq$ 400 km offshore, except for (9) which is from a polluted area about 100 km off the southern California coast.

precipitation within a fraction of an hour. The present data do not allow us to distinguish between ozone loss and moisture loss (for this we need a third tracer), but the loss of moisture through precipitation seems a likely candidate, because of its shorter time scale. The loss of several g/kg of moisture should involve convection that penetrates well above the inversion in the present soundings. Typically, in the research area the inversion was too strong to allow such penetration (and indeed, no convective clouds were observed above the inversion), but upstream, to the northwest of the research area the inversion is expected to be higher and less sharply defined (Riehl, 1979). There convective clouds could have formed earlier through cyclonic activity (Kloesel, 1990) or as unorganized convection, and their residues transported to the research area within days.

Mixing line 2b (ending at F), which comes from Fig. 4, differs from other mixing lines in the usual research area. Here increases in ozone are associated with increases in humidity. The formation of point F may have involved local ozone production through photochemical reactions, or the mixing of boundary-layer air with traces of ozone-rich polluted air or upper-tropospheric air that contained unusually high concentrations of ozone. Alternatively, F may represent typical mid- or upper-tropospheric air that has gained moisture through the evaporation of precipitation falling through it. Aside from this particular case, which has several interpretations, we see no evidence that ozone is being produced in the lower marine troposphere.

The mixing process in the troposphere is sensitive to its temperature stratification. In regions of relative hydrodynamic instability, deep cumulus convection can rapidly transport and mix boundary-layer air with mid- and upper-tropospheric air, while in relatively stable regions, discrete horizontal layers with differing flow velocities transport air over long distances with little vertical mixing. The latter is typical of conditions over the eastern Pacific Ocean in summer, where the subtropical high results in stably-stratified, subsiding air. The mixing process is started by localized large-scale flows (such as tropospheric folding, deep convection, or baroclinic flow from the coast) that "inject" air of different properties into the troposphere. This air is then subject to buoyancy sorting and differential advection. When the troposphere is very stably stratified, the mixing eddies are small compared to the air-mass size and small-scale turbulent diffusion is slow, but mixing is enhanced by wind-shear, which stretches and thins the different layers horizontally until small-scale diffusion completes the mixing process.

Acknowledgments. We would like to thank the NCAR Research Aviation Facility for providing the aircraft and processing the FIRE data. Part of this research was supported by NASA (NAG-11-113) and the Office of Naval Research under Interagency Agreement (IA) No. 89-12.

REFERENCES

Danielsen, E. F., 1968: Stratospheric–tropospheric exchange based on radioactivity, ozone, and potentia vorticity. *J. Atmos. Sci.*, **25**, 502–518.

Fishman, J., K. Fakhruzzaman, B. Cross, and D. Nganga, 1991: Identification of widespread pollution in the southern hemisphere deduced from satellite analyses. *Science*, **252**, 1693–1696.

Hudson, J. G. and P. R. Frisbie, 1991: Cloud condensation nuclei near marine stratus. *J. Geophys.Res.*, **96**, 20,795–20,808.

Kloesel, K. A.,1990: Observational study of the above-inversion structure and marine stratocumulus cloud clearing episodes during FIRE. Ph.D. dissertation, 124 pp., Dept. of Meteorology, Penn State Univ., University Park, PA 16802.

Paluch, I. R., D. H. Lenschow, J. H. Hudson, and R. Pearson, Jr., 1992: Transport and mixing processes in the lower troposphere over the ocean. *J. Geophys. Res.*, in press.

Pearson, R., Jr., 1990: Measuring ambient ozone with high sensitivity and bandwidth. *Rev. Sci. Instrum.*, **61**, 907–916.

Riehl, H., 1979: Climate and weather in the tropics. Academic Press, San Diego, California.

Shapiro, M. A., 1980: Turbulent mixing within tropopause folds as a mechanism for the exchange of chemical constituents between the stratosphere and troposphere. *J. Atmos. Sci.*, **37**, 994–1004.

MARINE STRATOCUMULUS RADIATIVE FEEDBACK DERIVED FROM ERBE

Lazaros Oreopoulos and Roger Davies

Department of Atmospheric and Oceanic Sciences, McGill University, Montreal, PQ, CANADA, H3A 2K6

1. Introduction

The importance of the marine stratocumulus (mSc) decks forming at the east coasts of the Atlantic and Pacific Oceans in the Earth's Radiation Budget has been stated often in climate literature (e.g. see Randall et al., 1984 and Slingo, 1990). Their variability over times longer than a few days, and space scales larger than those of a well-planned surface-based experiment, has, however, hardly been addressed (Hanson, 1991).

We have examined the annual variability of several top of the atmosphere (TOA) radiation budget components in the tropics, as measured by the ERBS satellite of the ERBE experiment. One thing we noticed is that two of the regions with very strong annual albedo and minimal outgoing longwave radiation (OLR) variability are those off the west coasts of S. America and Africa, dominated by mSc clouds. The Warren et al. (1988) cloud climatology confirms that this albedo variability is mainly due to the seasonal change of mSc clouds. Moreover, sea surface temperature (SST) climatologies (e.g., Bottomley et al.,1990) show a strong seasonal cycle of SST (of the order of 5° C) almost out of phase with that of cloud amount, i.e., warmer temperatures during the low cloud amount seasons and vice-versa. We examine the anticorrelation between SST and cloud amount using albedo as a cloud amount estimator in order to explore the existence of any direct feedback mechanism.

2. Dataset used

We use 5 years (December 84-November 89) of ERBE (in particular ERBS satellite) albedo and Climate Analysis Center SST data (Reynolds, 1988). Both are monthly averaged values binned in a spatially coincidental 2.5°x2.5° grid. To achieve that we had to degrade the resolution of the SST field (which is 2.0°x2.0°) using a bilinear interpolation scheme. Hereafter, we refer to the region 95-75W, 5-30S (for S. America Sc) as Region 1 and to the region 15W-15E, 5-20S (for Africa Sc) as Region 2. Regions 1 and 2 consist respectively of 74 and 64 2.5°x2.5° gridpoints with ocean as the underlying surface.

3. Annual variability

The seasonal cycle of the spatially averaged SST is almost sinusoidal with an approximate amplitude of $5\,^{\circ}$C in both regions as figures 1 and 2 indicate. The value for each month is the average of the 5 monthly averages available. Plotted in the same figures are the corresponding albedos. It is evident that the warmer months have lower albedos and the colder months have higher albedos in both regions. The month of maximum albedo is September, also a month of minimum SST, for both regions, whereas the month of minimum albedo for Region 1 is March, and February for Region 2, with maxima of SST occurring in March in both cases. Figure 3 depicts the coefficients of the SST-albedo cross-correlation for spatially averaged values and different time lags (one month step) for both S. America and Africa mSc. The seasonality of the anticorrelation is obvious: absolute maxima occur every six months. However, there is a difference in the two curves: the one for Region 2 is almost symmetric around 0 lag (contemporaneous correlation) while the one for Region 1 around the -1 lag, implying that albedos may influence SST one month later. Due to the large thermal stability of the oceans it is very unlikely that in either region the clouds are driving the SST and it seems more reasonable to expect clouds responding to SST changes.

Figures 4 and 5 show the fields of the cross-correlation coefficients for lag 0 and -1 month for Region 1 (contour interval 0.05) and Region 2 (contour interval 0.04) respectively. The high density of contours on the right edge of the figures occurs over the land gridpoints because of the correlation breakdown as we move over land surface. We observe that Region 1 has maxima close to the coast with values decreasing southward, indicating that the validity of the anticorrelation is restricted spatially in only part of the total area. Region 2 shows a more homogeneous field, although there is a decreasing tendency as one goes to the south or away from the coast. The results are consistent with the observation that the mSc covered areas are well-defined relatively close to the coast of the continents. Figure 6 has the contours (interval 0.2) of the derivative $\partial a/\partial SST \times 100$ (a=albedo) calculated using the seasonal variations. The fields resemble those of the correlation coefficients for 0 lag as expected and are useful if one wants to perform the task of predicting albedo changes when a temperature perturbation is given. For example for the center of Region 2 a 1°C SST decrease would increase (in absolute value) the albedo by approximately 4%.

We would like to make the following comments on the results presented so far. First, the fact that maximum correlations appear for a lag of -1 month for Region 1 may just be an artifact due to the small length of the time series used

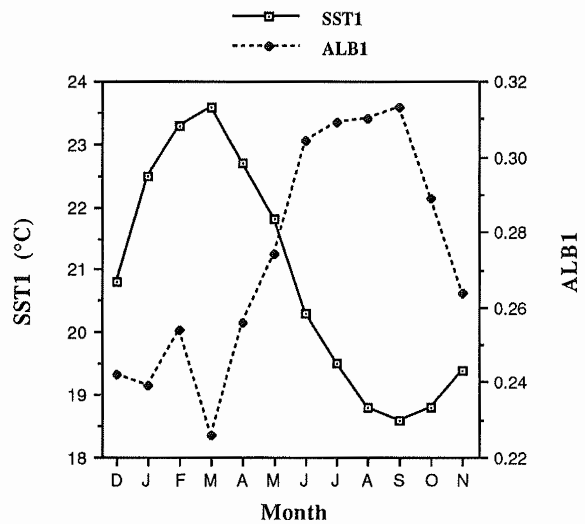

Figure 1 5 year monthly averages of SST and albedo for region 1

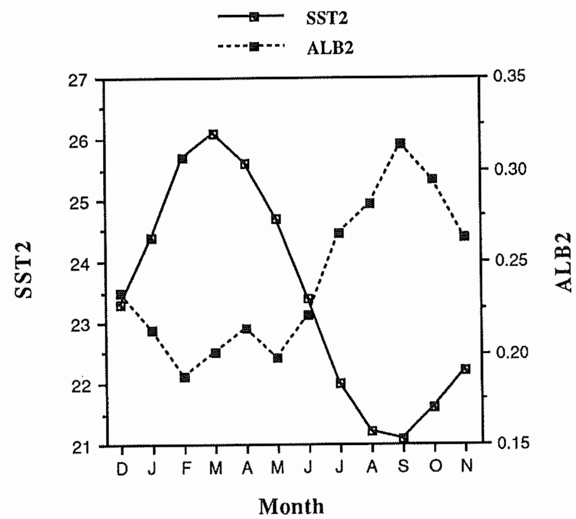

Figure 2 As in figure 1, for region 2

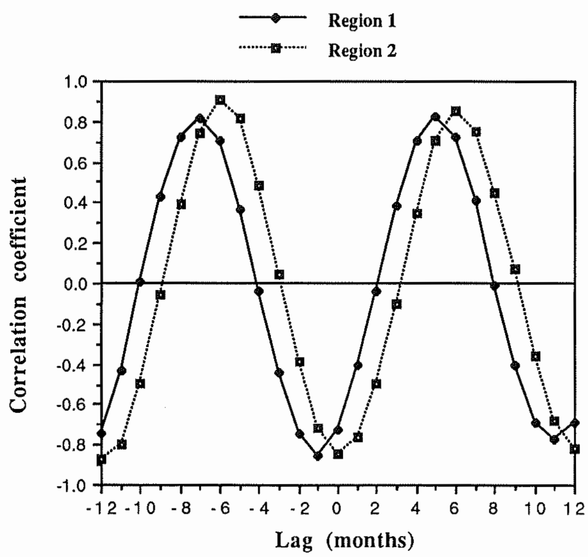

Figure 3 Cross correlation analysis for various time lags of the spatial averages of albedo and SST (60 months used for both regions).

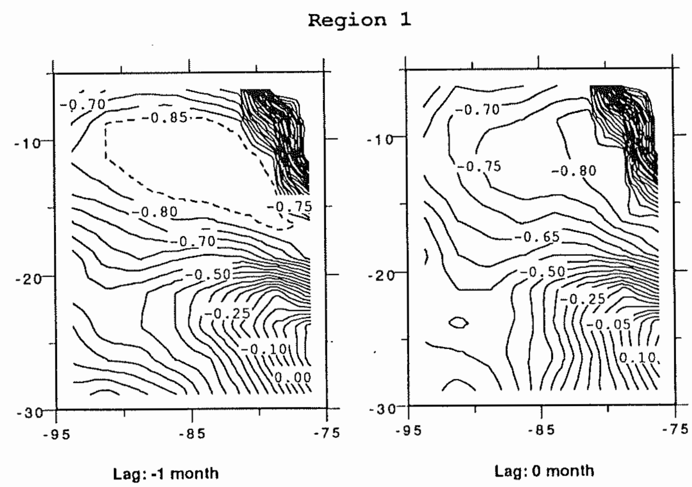

Figure 4 Patterns of cross-correlations at 0 and -1 lag for region 1. Contours smaller than -0.8 are dashed. The (-) sign is for south and west.

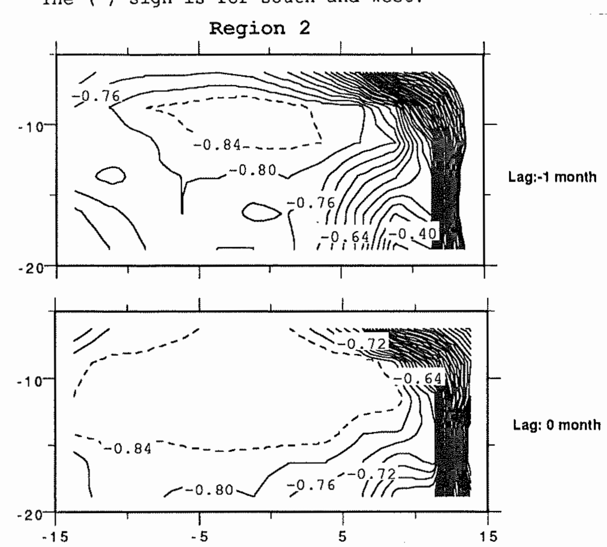

Figure 5 As in figure 4, for region 2

and might have been 0 lag had a sufficiently longer series been used. Second, no direct cause and effect relationship between SST and albedo has been proven with this type of analysis because both can be driven seasonally by a third unknown factor (seasonal change in the location of the subsidence branch of the Hadley cell or current induced seasonal changes in upwelling, to name a few). Third, the effect of the seasonal change of solar zenith angle, which is small, however, for the tropics, has not been removed. Thus, we have to explore the anticorrelation further.

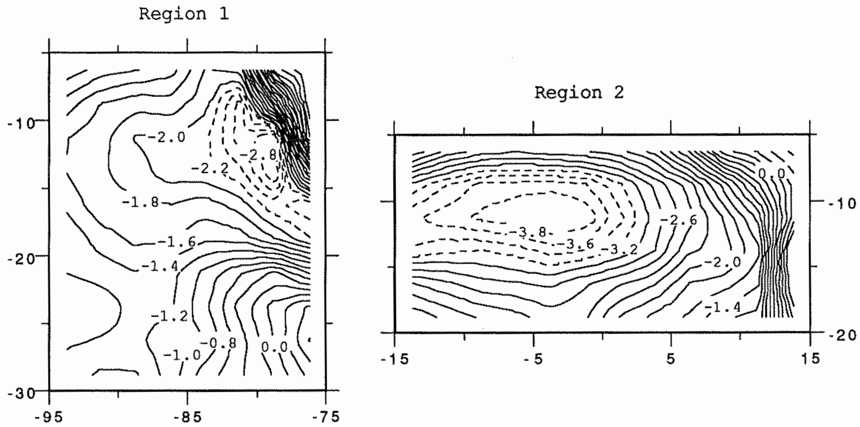

Figure 6 Patterns of the feedback component $\partial a/\partial SST$ (x100) for both regions. The maxima are shown with the dashed contours.

4. Interannual variability

In order to study the interannual variability we form 5-year climatologies of SST and albedo for each month and for each gridpoint in both regions. Then we subtract the monthly values, forming this way 60 anomaly fields for each variable and for each region. We select from those anomaly fields all gridpoints that have an SST anomaly larger than 0.5°C in absolute value and an albedo anomaly larger than 0.05 for Region 1 and 0.025 for Region 2, also in absolute value. The thresholds chosen are arbitrary but this is one way to exclude a large number of points where the anomalies can be attributed to measurement uncertainties and nonsignificant natural variability. The smaller albedo threshold for Region 2 was chosen because of the smaller interannual variability of albedo in that region. It is, however, a relatively high value (a bit less than 10% of the mean albedo). The gridpoints extracted this way are plotted in figures 7 and 8. It is evident that the number of points lying on the 1st and 3rd quadrants in both figures is far more than those lying on the 2nd and 4th. More specifically there are 103 out of a total of 113 points for Region 1 and 114 out of 124 for Region 2. The 1st and 3rd quadrants are the ones where the correlation is negative: lower-than-average albedos with higher-than-average SST's for the 1st and lower-than-average SST's with higher-than-average albedos for the 3rd quadrant. Similar interpretation applies for the other two quadrants. We should, however, point out that especially for Region 1 about 50% of the points (52/103) which satisfy the anticorrelation come from only four months, suggesting that synoptic conditions favored the creation of "correct" anomalies. For Region 2 38/114 i.e. 1/3 of points in 1st and 3rd quadrant come from four months but in general they are distributed over more months compared to Region 1. Thus, the interannual variability is, at least statistically, working in the same direction as the annual variability, showing negative albedo responses to positive SST perturbations and vice-versa.

5. Spatial variability

One more way to examine the SST-albedo relation is to check if there are any significant correlations at the "gridpoint level", i.e, if

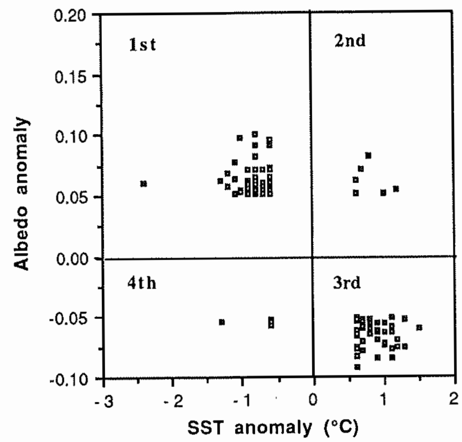

Figure 7 Gridpoints with abs(anomalb)> 0.05 and abs(anomSST)>0.5 °C for region 1

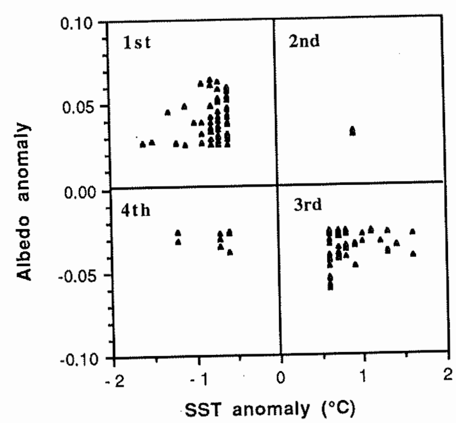

Figure 8 Gridpoints with abs(anomalb)> 0.025 and abs(anomSST)>0.5 °C for region 2

colder or warmer gridpoints, compared to the spatial average, have higher or lower than average albedos, respectively. This is done for all 60 months and for both regions. For Region 1 we use 74 pairs and for Region 2 64. The time series of those "spatial" correlation coefficients is given in figures 9 and 10. As you can see they are negative with very few exceptions. Bear in mind that the number of **independent** pairs is smaller than the total number of gridpoints in each region. This should be taken into account if significance levels are to be put in figures 9 and 10. A spatial autocorrelation analysis indicates that about 20 pairs for Region 1 and 18 pairs for

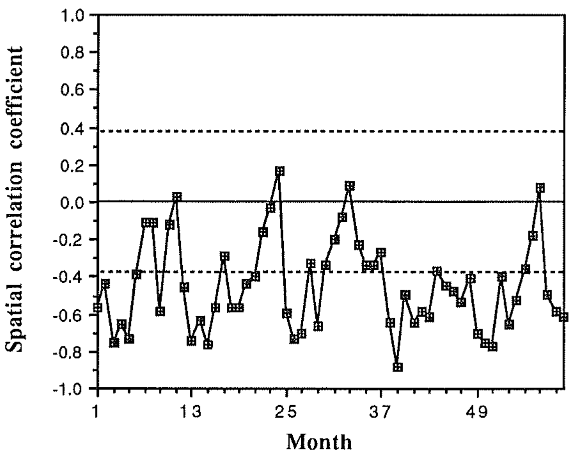

Figure 9 Coefficient of spatial correlation for the period Dec84-Nov89, for region 1. The significance levels are approximate.

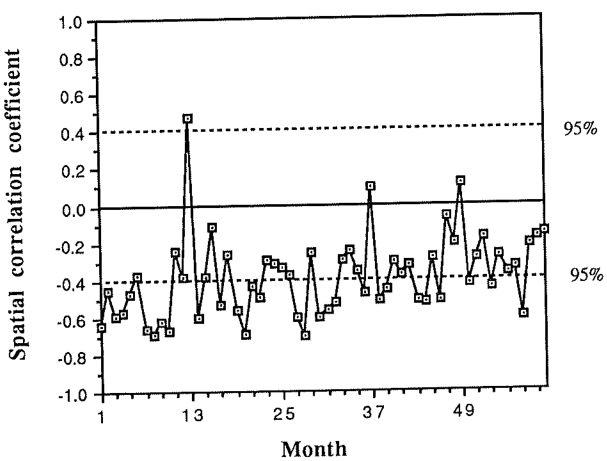

Figure 10 As in fig. 9 for region 2

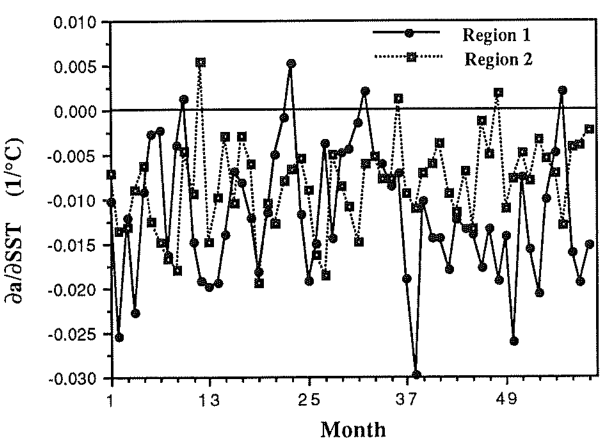

Figure 11 ∂a/∂SST from the regression line of the spatial variability for both regions and for the period Dec84-Nov89.

Region 2 can be considered independent. A Student's t-test with corrected degrees of freedom gives that the correlation coefficients with absolute value> 0.38 for Region 1 and 0.40 for Region 2 are statistically significant at the 95% level. More than half the months in Region 1 and about half in Region 2 satisfy this criterion. Some degrees of freedom are probably also lost if the temporal autocorrelation is considered. Nevertheless, the fact that the correlation coefficients lie in vast majority under the zero line strongly indicates that an anticorrelation exists. We plot the time series of the slopes of the regression lines that are calculated for each month in figure 11 (both regions included). This is essentially a time series of the feedback term ∂a/∂SST. There is large variability but most of the values are negative, as expected. The numbers for Region 1 are, in general, slightly more negative compared to Region 2.

6. Conclusions.

The mSc clouds are known to be controlled by small scale processes, but as Hanson (1991) points out "it seems reasonable to expect that there exist globally coherent relationships among clouds and other climate variables". An obvious choice for such a variable is SST. Our results indicate that a local relationship between mSc albedo and SST is consistent with the observed variability when examined spatially, annually and interannually. The feedback estimate depends on the way the anticorrelation is viewed. The annual variability will provide on average -0.02/°C for Region 1 and -0.03/°C for Region 2 (fig. 6) and the spatial variability about -0.01/°C in both cases. If no additional meteorological variables significantly affect this relationship, such clouds would change so as to locally amplify the effects of increased greenhouse forcing. The search for such additional factors is likely in the realm of General Circulation Modelling, for which our results should provide a useful diagnostic test of model performance, as far as mSc feedback is concerned.

References

Bottomley, M., C. K. Folland, J. Hsiung, R.E.Newell and D. E. Parker, 1990: *Global Surface Temperature Atlas "GOSTA"*, 20pp. and 313 plates, U.K. Meteorol. Off., Bracknell, 1990.

Hanson, H. P ,1991: Marine Stratocumulus Climatologies. *Int.J. Climat.*, **11**, 147-164.

Randall, D. A., J. A. Coakley, C. W. Fairall, R. A. Kropfli, and D. H. Lenschow, 1984: Outlook for research on subtropical marine stratiform clouds. *Bull. Am. Meteorol. Soc.*, **65**, 1290-1301.

Reynolds, R. W., 1988: A real-time global sea surface temperature analysis. *J. Climate*, **1**, 75-86.

Slingo, A. 1990: Sensitivity of the Earth's radiation budget to changes in low clouds. *Nature*, **343**, 49-51.

Warren, S. G., C. J. Hahn, J. London, R. M. Chervin and R. L. Jenne, 1986: *Global Distribution of Total Cloud Cover and Cloud Type Amounts Over Ocean*. NCAR Tech. Note NCAR/TN-317+STR, National Center for Atmospheric Research, 42 pp. plus 170 maps.

MICROPHYSICAL CHARACTERISTICS OF A STRATIFORM CLOUD
OBTAINED FROM LIDAR AND IN SITU MEASUREMENTS

J-F Gayet[1], G. Febvre [1], P. Personne[1]
G. Brogniez [2] and P. Moerl[3]

[1] LaMP, CNRS, University Blaise Pascal, Clermont-F^{d}, France
[2] LOA, University Lille I, Villeneuve d'Ascq, France
[3] DLR, Oberpfaffenhofen, FRG

1. INTRODUCTION

From a climate perspective, the stratocumulus clouds of the marine boundary layer are especially important because they nearly cover 25% of the Earth's surface, their contrast with the very low surface albedo of the oceans is the largest and their greenhouse effect is small. The propensity for drizzle development (via CCN concentration) and subsequent lifetimes of marine stratocumulus is part of the effects which constitute a potentially important feedback to global warming (Vali, 1991). We present in this communication a marine stratocumulus case study from data simultaneously obtained with two aircraft (in situ and airborne Lidar measurements). These data were performed during the International Cirrus Experiment (ICE) (Raschke *et al.*, 1990), a regional experiment within the scope of the International Satellite Cloud Climatology Project (ISCCP).

2. METEOROLOGICAL DESCRIPTION AND PROCEDURES

The experiment below described was carried out in the southern part of the North Sea on 23 September 1989. The meteorological situation was characterized by a low center pressure located over the Irish Sea. An associated cold front passed over the experiment site just before the aircraft operation. The low levels vertical sounding displayed on Figure 1 shows a wet layer between the 800 m/10°C and 2700 m/2°C levels and a dry layer above. Two aircraft were involved in the present study. The Merlin aircraft (operated by the Centre d'Aviation Météorologique / French Weather Service) performed microphysical in situ measurements from Johnson-Williams, PMS FSSP and 2D-C probes. The DLR Do228 remotly sensed the cloud with the ALEX-F Lidar (upward oriented). This Lidar operated with a 1.06 μm wavelength. Basically, the horizontal sampling resolution was 100 m for both aircraft measurements and Lidar vertical profiles resolution was around 6 m. Figure 2 exemplifies time-series of the attenuated backscatter profile obtained by the Do228/Lidar. Examination of the results reveals that the marine boundary layer is characterized by multiple stratiform cloud layers (mainly two but sometimes three depending on the sampling

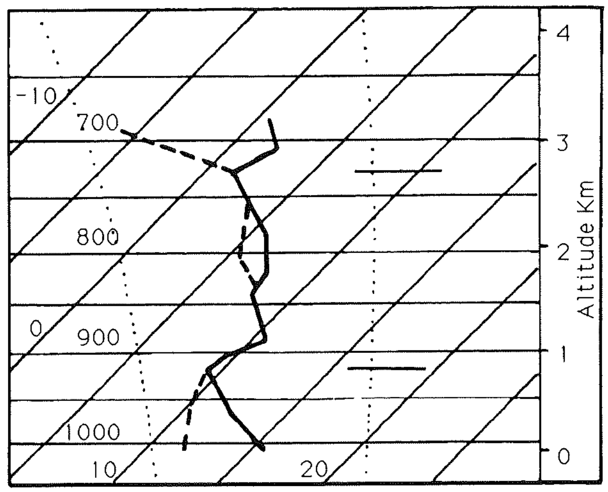

Figure 1 : *Vertical sounding of air temperature (full line) and dew-point temperature (dotted line).*

location). Figure 2 also reveals the presence of precipitating zones of around 10 km of horizontal extent. As for the cover of each layer, it was found to be not homogeneous, but the fractional cloudiness could be quantified from Lidar measurements due to the strong attenuation of the Lidar signal by the lower droplet cloud layer. The Merlin aircraft flew in the two main cloud layers at the 1650 and 2500 m levels and visual observations have revealed that each layer was not deeper than around 500 m.

3. MICROPHYSICAL ANALYSIS

In the two cloud layers, analysis of time-series of microphysical parameters obtained from the Merlin aircraft evidenced two main regions :
(i) Cloud regions characterized by the presence of small droplets, the concentration of particles > 50 μm in diameter (C50) being very small (the threshold value chosen in this study was 1 l^{-1}).
(ii) Precipitating regions containing mostly drizzle particles with C50 > 1 l^{-1}.

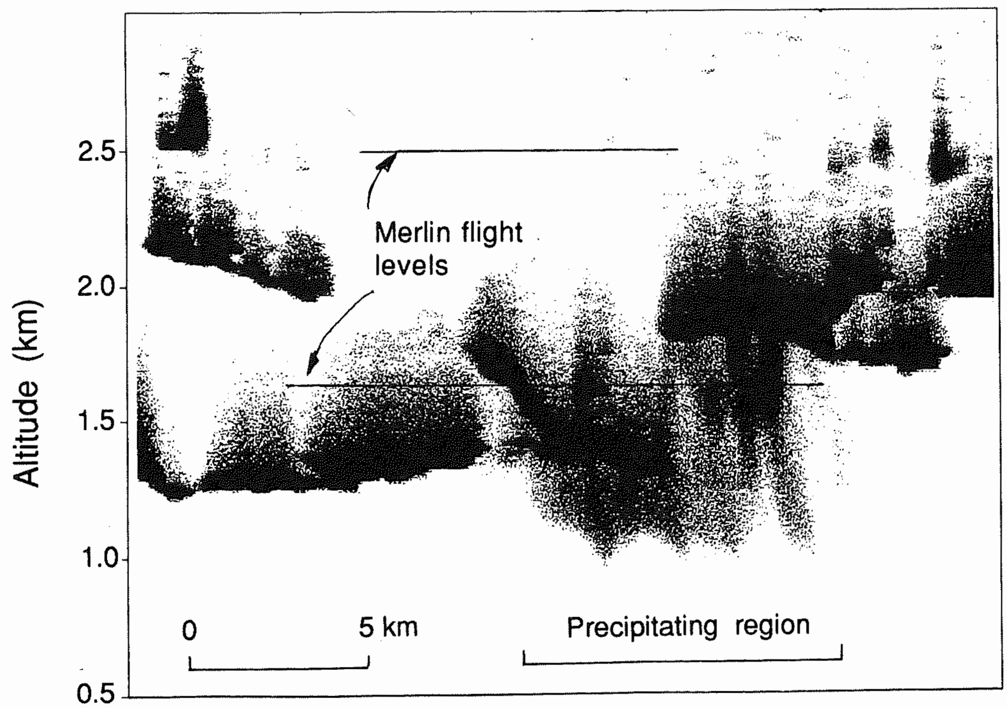

Figure 2 : Vertical cross-section of the attenuated backscatter profile obtained from the Do228/ALEX-F Lidar (scale in arbitrary units).

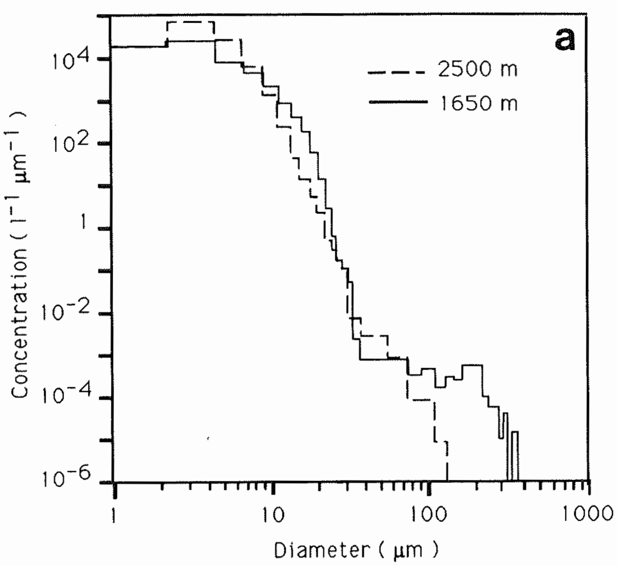

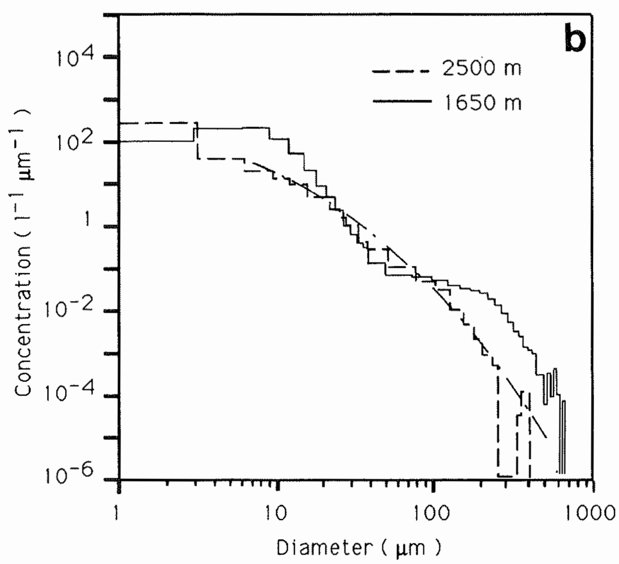

Figures 3.a & b : Mean drop size spectra obtained in cloud regions (a) and in precipitating regions (b). Dotted and full lines correspond to data sampled at the 2500 and 1650 m levels respectively.

Figures 3 displays the mean size distribution of droplets measured simultaneously by the FSSP and 2D-C instruments in the two cloud layers above mentionned. Figs. 3.a and 3.b refer to cloud regions and precipitating regions respectively. Table 1 summarizes the corresponding microphysical charateristics.

	Level (m)	LWC (mgm^{-3})	LWCmax (mgm^{-3})	RE (μm)	CF (cm^{-3})	C50 (l^{-1})	Dmax (μm)
Cloud regions	2500	50	80	7	210	.1	150
	1650	40	175	10	110	.1	500
Precip. regions	2500	3	25	70	10	3.7	375
	1650	25	200	140	10	6.0	650

Table 1 : Mean values of liquid water content (LWC) and maximum observed value, effective radius (RE), FSSP concentration (CF), concentration of drops > 50μm (C50) and maximum diameter measured.

Analysis of results show that in cloud regions at the higher level, the drops are characterized by a single-mode size distribution and drops up to 150 μm are detected (Fig. 3.a). The presence of such large drops suggests that precipitating particles primarily form near the top of the higher cloud layer probably due to the presence of large hygroscopic CCN particles at this level. The drop size distribution of cloud regions at the lower level is quite different. As a matter of fact, this distribution is characterized by a secondary mode near 300 μm and the largest drops detected are 500 μm in diameter. Two distinct particle populations may therefore characterize the cloud: small condensation droplets ($\approx$ 10 μm) and larger drops ($\approx$ 300 μm) being hypothesized to be precipitating from the cloud layer above.

As for the precipitating regions (Fig. 3.b), large differences in size distributions are also evidenced when comparing the results obtained at 1650 and 2500 m. In the higher cloud layer, the droplet size distribution is roughly semi-exponential (the Figs. 3.a & b are in log-log scales and the best fit of data point assuming such a size distribution is also reported). This feature strongly contrasts with the lower cloud characteristics. At 1650 m the excess of drops larger than 100 μm (about the semi-exponential curve) may also be attributed to precipitating particles issued from the above cloud layer.

The higher flight level was performed around 100 m below the cloud top and about 50% of the total cloud length sampled was characterized by the presence of drops >50 μm in excess of 1 l^{-1}. We have evidenced that precipitating regions are significantly different with the clouds regions from a microphysical point of view, particularly on drop concentration (10 and 210 cm^{-3} respectively, see Table 1) and effective radius (70 and 7 μm respectively). These differences may have a significant interaction with the radiative properties of the cloud. As a matter of fact, droplet size have a direct and strong effect on cloud albedo (Fouquart *et al.*, 1990).

4. STRUCTURE OF THE PRECIPITATING DRIZZLE ZONES

a. Lidar calibration procedure

Several methods of Lidar data inversion are used to calculate the extinction coefficient profile. In this study we used the "Shadow Technique" proposed by Ruppersberg and Renger (1991) because of the multi-layers behaviour of the studied clouds. This method allows to determine the Lidar signal inversion factor $A.\beta/\sigma$ to within an accuracy of around 20%. A is the Lidar system constant (*a priori* unknown), σ is the extinction coefficient and β the backward value of the scattering function. It should be noticed that the ratio β/σ has a quasi-constant value ($0.053\ Sr^{-1}$) in the range of drop diameter above mentionned.

The extinction profile can therefore derived using the solution of the following equation in linear form :

$$\sigma(d) = (P.d^2/A.\beta/\sigma)\ 2\int_0^d \sigma(d').d(d') \quad (1)$$

with d the distance and P the Lidar power.

b. Relation between Liquid water content and extinction coefficient for drizzle particles

The liquid water content (LWC) and the visible extinction coefficient (σ) are obtained from the following relations :

$$LWC = \pi/6\ \rho \sum_i N_i\ D_i^3 \quad (2)$$

$$\sigma = \beta \sum_i N_i\ D_i^2 \quad (3)$$

with ρ the water density, N_i the concentration of droplets, D_i the diameter and β the extinction efficiency which is assumed to have a constant value (= 2) in the range of observed drop diameter.

Figure 4 represents the values of LWC versus σ, both parameters being obtained from FSSP and 2D-C probes measurements. Each data points are 5-second averages and correspond to precipitating regions at the two flight levels above described. Despite the apparent scattering of data points (the correlation coefficient is 0.92), a simple relationship between the two parameters may be proposed such as : LWC = $\alpha\ \sigma$, with α = 55 for LWC in $g\ m^{-3}$ and σ in km^{-1}. The dispersion of data points is due to the change of the mean diameter of the drizzle size distribution. The value of α is the greater as the mean diameter is large.

c. Structure of the precipitating drizzle zones

From the relation LWC/σ above proposed, the extinction profiles obtained from the Lidar data may be converted in terms of precipitating liquid water content. Figure 5 displays one example of the vertical cross-section of liquid water content of a precipitating zone of about 10 km of horizontal extent. The dark areas correspond to cloud regions where the Lidar signal is attenuated in few hundred meters. The relation LWC/σ cannot obviously be applied in

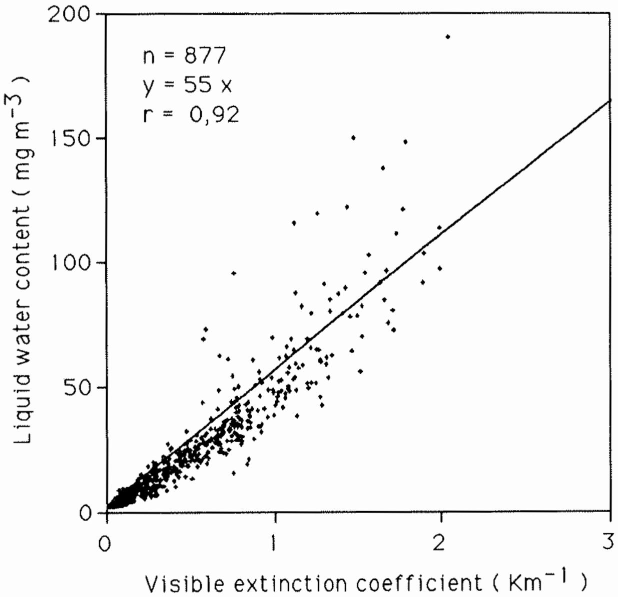

Figure 4 : Experimental relation between the liquid water content and the visible extinction coefficient. The data were obtained in precipitating regions (drizzle particles). The best-fit line is also reported.

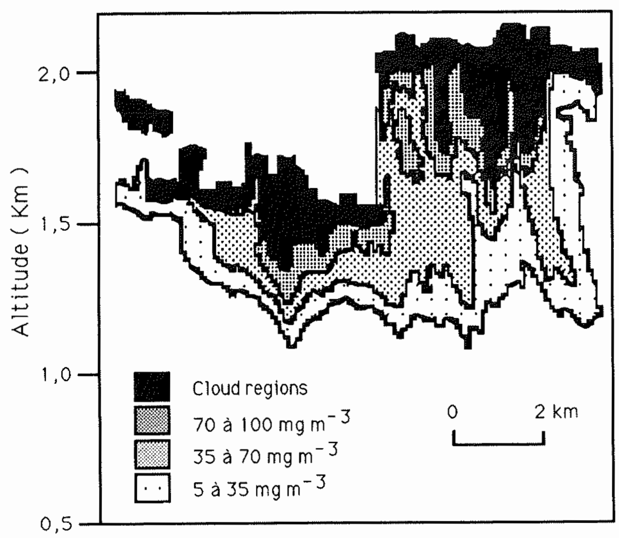

Figure 5 : Vertical Lidar cross-section of the precipitating regions calibrated in terms of liquid water content. The grey-scale is also indicated on the Figure.

these regions. On the other hands, the structure of precipitating regions are clearly evidenced below the cloud. They are vertically extended on around 1500 m and maximum values ($\approx$ 100 mg m^{-3}) are found near the cloud base.

5. CONCLUSIONS

The results presented in this study shows an efficient drizzle particles formation in very thin marine stratiform layers which primarily occurs near the top of the cloud. Around 50% of the total cloud length are characterized by precipitating regions. The differences in microphysical properties between these regions and cloud regions are clearly evidenced and may have a strong influence on cloud albedo. The calibration of the Lidar data we proposed leads to describe the vertical structure of the precipitating drizzle regions.

6. ACKNOLEDGEMENTS

These works were supported by grants from CNRS/PNEDC n°88/50/N/5080, DRET/Université Blaise Pascal n°89 1183 and EPOCH/EUCREX-0002-C (MB).

7. REFERENCES

Fouquart, Y., J. C. Buriez, M. Herman and R. S. Kandel, 1990: The influence of clouds on radiation: A climate-modeling perspective. Rev. Geophys., 28, 145-166.

Vali, G., 1991: Report of the Experts Meeting on Interaction between Aerosols and Clouds. Hampton, USA, 5-7 Feb. 1991. WMO/TD-No. 423.

Raschke, E. *et al*, 1990: The International Cirrus Experiment (ICE). A joint European Effort. ESA Journal, 14, 193-199.

Ruppersberg, G. H. and W. Renger, 1991: Shadow Technique for improved inversion of Lidar data to cirrus optical depth. 3rd ICE Workshop, Lille, France, 3-6 December 1990.

Identification of Icing Water Clouds by NOAA AVHRR Satellite Data

K.P. Schickel, H.E. Hoffmann, K.T. Kriebel.

DLR, Institute for Atmospheric Physics, Post Wessling
D 8031 Oberpfaffenhofen, Germany

1. Introduction

Icing of aircraft happens within clouds containing supercooled water droplets. Forecasting of icing conditions is possible with only very little accuracy. Therefore, aircrafts without 'icing clearance' are already not allowed to take off when there is a little chance of icing. The risk of a wrong forecast is taken into account. This problem is well known since about 70 years [3]. On the other hand, supercooled water clouds occur quite frequently during winter time. Therefore, the use of satellite data to increase the forecasting accuracy has been tried [4].

The effect of supercooled water clouds on aircraft consists in a reduced lift by icing of exposed parts [1]. The amount of icing is given in four steps: trace, light, moderate, severe; the assignment is made by subjective as well as by objective criteria. Hoffmann et al. [2] have shown that a water cloud

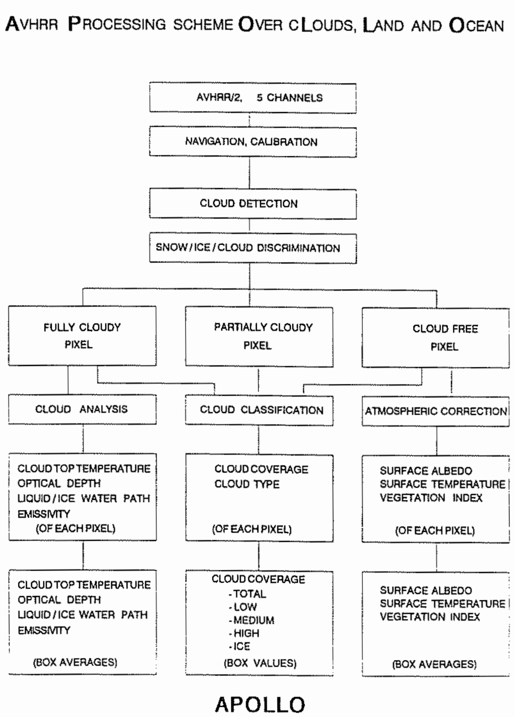

Figure 1. Flow chart of the multispectral algorithm package for satellite data processing, APOLLO

gives rise to icing if it is supercooled in the range of 0 °C to -13 °C, with a liquid water content of 0.02 gm^{-3} to 0.8 gm^{-3} and a median volume diameter from 9 µm to 300 µm. However, these are approximate ranges. (The median volume diameter divides the liquid water content into two equal halves).

2. Identification of stratiform water clouds by APOLLO

The algorithm package APOLLO ("AVHRR Processing Scheme Over CLouds, Land, and Ocean") is used to analyze AVHRR data (cf. Figure 1). It consists of a set of threshold tests which are applied pixelwise. This yields a cloud mask indicating for each pixel whether it is cloud free, fully cloudy or partially cloudy.

In this paper, only fully cloudy pixels are used. From the reflectance at 3.7 μm (i. e. AVHRR channel 3) the phase of the cloud can be derived. If the reflectance is more than 8 %, the phase has to be considered as liquid. If the reflectance is below 8 %, the phase is ice. In Figure 2, to all pixels with a reflectance in channel 3 (3.7 μm) > 8 %, a grey value of 200 is assigned to separate them from all other pixels, which are represented by the grey value 0.

3. Comparison of the APOLLO analysis with airborne measurements.

In 21 cases, satellite and aircraft data have been taken close enough in time to be compared. The satellite data have been analysed along the flight path of the aircraft (cf. Figure 2) which is about 100 pixels. The satellite data comprise the temperature of the cloud top, the cloud phase and the liquid water path. These data are compared with the in situ-airborne measurements of temperature within the cloud, cloud phase and liquid water content. The cloud phase is the same in all data sets. However, the temperature of the cloud top varies much more than the temperature range of 0 °C to -13 °C where icing should occur. This means that cloud top temperature is not a good indicator of icing conditions, but the cloud phase is. So far, icing conditions are overestimated because all liquid phase clouds bear the risk of icing because the cloud top temperature is not very indicative. Further, clouds which are found to consist of ice particles may contain supercooled water droplets, at least in lower parts of the clouds. These icing conditions are missed by a scheme depending solely on the cloud phase. An additional information which could reduce these uncertainties is the cloud liquid water content. This can be derived from satellite data provided the relative vertical profile of the liquid water content is known. This will be studied in the future, in particular whether it could be parametrized for stratiform clouds.

Figure 2. Identification of icing water clouds in the NOAA image by means of the reflectance in AVHRR channel 3 (3.7 μm): bright indicates fully cloudy pixels with a reflectance in channel 3 (3.7 μm) > 8 %. All other pixels are shown dark. The area is represented by the river Danube and the cities Munich (M), Stuttgart (S), Nuremberg (N) and Amberg (AM). The flight route starts and ends in Oberpfaffenhofen between the lakes Starnberger See and Ammersee, as indicated. The squares indicate the areas where vertical profiles of the liquid water content have been measured.

4. Discussion

Supercooled water clouds can be visualized in the satellite image during winter, provided there are no ice clouds on top of the water clouds. The analysis of AVHRR data has the potential to yield cloud physical information which is related to icing conditions, in a spatially continuous manner and cheaper than could be obtained from aircraft data. These data are cloud top temperature, cloud liquid water path, cloud phase and, possibly, geometrical thickness. Herefrom, the icing conditions can be derived, provided the geometrical thickness can be derived from a parametrization of the vertical distribution of the liquid water content in stratiform clouds. Only the size distribution of the cloud droplets, represented e. g. by the median volume diameter, can not be derived from AVHRR data so far.

5. Conclusions

From NOAA-AVHRR data several parameters to describe icing conditions can be derived if an appropriate data processing package is used. Cloud top temperature and cloud phase can easily be used, however, they are not enough to give a unique identification. The additional use of the cloud liquid water content will certainly improve the method, however it still has to be shown that it can be derived from AVHRR data, at least in case of stratiform clouds.

Though there are still some open questions, an improvement of an icing warning system by using satellite data seems to be possible.

6. Bibliography

[1] Hoffmann, H.E.: *The icing of the wing and of the elevator of an aircraft.* Proceedings of 5th International Workshop on Atmospheric Icing of Structure (IWAIS '90), Tokyo, Japan, pp. B1-1-(1) - B1-1-(4), 1990.

[2] Hoffmann, H.E.; Demmel, J.: *A. Icing and cloudphysical parameters. B. Icing relevant cloudphysical parameters and synoptic (Some aspects of an icing atmosphere).* DLR, Institute of Atmospheric Physics, Oberpfaffenhofen, Germany, Presented on Society of Automotive Engineers, Aircraft Committee-9 "Aircraft Environment System" and Subcommittee Aircraft Committee-9C "Aircraft Icing Technology" in Orlando, Florida, USA, 1991.

[3] Schickel, K.P.; Fuchs, W.: *Bibliographie zur Vereisung von Luftfahrzeugen (Stand 1987).* DLR, Institut fuer Physik der Atmosphaere, Oberpfaffenhofen DFVLR-Mitt. 87-18, 1987.

[4] Schickel, K.P.; Hoffmann, H.E.; Kriebel, K.T.: *Identifikation von vereisenden Wasserwolken mittels NOAA-AVHRR-Satellitendaten.* DLR, Institut fuer Physik der Atmosphaere, Oberpfaffenhofen, DLR-FB 92-11, 1992.

Modeling the Trade-Wind Boundary Layer

Alain Bergeron and Steven K. Krueger

University of Utah
Salt Lake City, UT, USA 84112

1. Introduction

In this study, we have performed simulations of the trade-wind boundary layer using a two-dimensional cumulus ensemble model (CEM) with third-moment turbulence closure (Krueger, 1988), an approach similar to that of Soong & Ogura (1980). The CEM covers a large horizontal domain but is capable of resolving individual clouds. Thus, it enables us to analyze in detail the cloud-scale dynamics and finely resolve the thermodynamic structure of the boundary layer. We are using the output from the CEM simulations to evaluate bulk thermodynamic models of the trade-wind boundary layer. In particular, we are testing the critical assumptions in the model developed by Albrecht *et al.* (1979).

At this stage, we are particularly concerned with the specification of the turbulent length scale. In this paper, we compare the results of two simulations with differing length scale specifications to gauge its impact on the cloud dynamics.

2. Description of the numerical simulations

In many higher-order turbulence closure models, the dissipation rate, ϵ, is modeled using an inviscid estimate of the rate of the kinetic energy cascade from large to small eddies that occurs in the inertial range. The time scale for this cascade is $\sim l/e^{1/2}$, where l is the largest eddy size, and e is the turbulent kinetic energy. Then it follows that $\epsilon \sim e^{3/2}/l$. The problem faced by the numerical modeler is specifying l to accurately estimate ϵ.

In general, $l \sim$ the depth or width of the turbulent region since the largest eddies are limited to this size. Thus, in the sub-cloud mixed layer, $l \sim$ the mixed layer depth, h. However, near the surface, we expect $l \sim z$; for this reason, we use Blackadar's interpolation formula

$$l(z) = \frac{1}{C_1}\frac{\kappa z}{1 + \kappa z/l_\infty},$$

(where $C_1 = 0.07$, $\kappa = 0.35$ and $l_\infty = 0.15h$) in the mixed layer. In the cloud layer, we expect $l \sim$ the widths of the clouds themselves. This specification of l is appropriate in a one-dimensional turbulence closure model since in such a model, the cloud circulations are treated as turbulence. However, in a two-dimensional numerical model in which the cloud circulations are intended to be explicitly simulated and therefore *not* to be considered turbulence, l should be reduced. Otherwise, the cloud circulations will be treated as turbulence and will not tend to appear in the simulation as explicit cloud-scale motions.

We have performed two simulations, T21 and T22. In T21, we have set l to one half of that used in Bougeault's (1981) trade cumulus boundary layer simulation using a third-moment turbulence closure model. Thus, $l = 450$ m at $z = 600$ m $\sim h$, and $l = 125$ m in the cloud layer ($z > h$). In T22, we set l to one eighth of Bougeault's value in the mixed layer, so that $l = 112$ m at $z = 600$. In the cloud layer, l increases continuously with height from $l = 112$ m at $z = 600$ m to $l = 142$ m at $z = 2000$ m; there is no jump at $z = h$, but otherwise the cloud layer values of l are similar to those in T21. The length scale specification used in T22 is similar to that used by Soong and Ogura (1980) in their two-dimensional trade cumulus simulation; they used a constant value of $l = 143$ m.

3. Results and Discussion

3.1. Fluxes

The partition between cloud-scale and turbulent-scale fluxes differs significantly between the two simulations.

In experiment T21, the buoyancy flux in the boundary layer is dominated by the turbulent fluxes, while in T22, the turbulent component is much smaller (see Fig. 1). In T22, cloud-scale motion is larger much closer to the surface. The diffences are much less prominent in the cloud layer, although the minima of the fluxes near cloud base are shifted some 10-15 mb lower in T22. The fluxes in the lower part of the cloud layer are mostly turbulent; the cloud-scale contribution increases considerably above $p*$=100 mb ($p*$ is defined as $(p - p_0)$, where p is pressure, p_0 is surface pressure), while the turbulent fluxes remain constant in T21 and increase slightly in T22. The negative peak above the inversion occurs higher in T22. At that level, the turbulent component becomes zero. The cloud-scale fluxes above that threshold display similar profiles in both experiments; however, they extend higher in T22.

The moisture flux profiles, shown in Fig. 2, display similar features. Turbulence is responsible for the main contribution to the flux in the lower 50 mb in T21. In T22, cloud-scale motions dominate the mixed-layer flux. The negative fluxes near $p*$=200 mb may be an artifact caused by the advection scheme used in the model. The profile of moisture with height is highly non-linear near that level, possibly resulting in truncation errors.

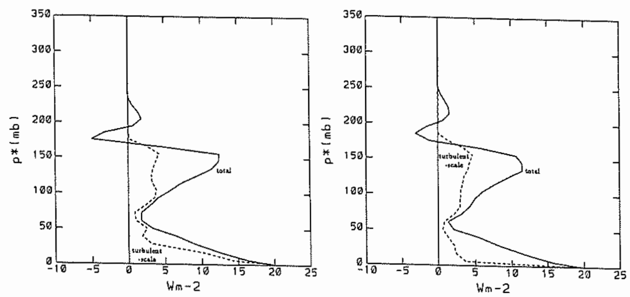

Fig. 1. Vertical profiles of buoyancy fluxes for simulations T21 (left) and T22 (right). The total convective flux and the turbulent component are shown.

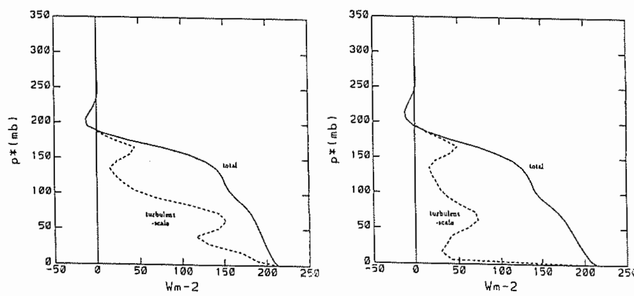

Fig. 2. Same as Fig. 1 except for moisture fluxes (F_{q_w}).

While the relative magnitudes of the cloud-scale and turbulent-scale terms are expected to be different in each experiment, the total fluxes should not be significantly affected. This has been verified for the fluxes discussed above. The buoyancy flux profiles are very similar, with a surface value of 20 W m^{-2} in both cases. The total moisture flux in the cloud layer is larger in T21. However, this difference is small and localized; the moisture flux profiles differ only slightly. Therefore it appears that the total fluxes are not sensitive to the specification of the turbulent length scale in the model.

3.2. Heat and moisture budgets

The transport of sensible and latent heat from the warm sea surface into the sub-cloud layer by cloud-scale and turbulent motion is nearly compensated by the specified radiative cooling (see Fig. 3). Within the cloud layer, a different balance prevails. Cloud-scale motions produce a cooling comparable in magnitude to the radiative cooling. There is considerable condensational heating, which is evenly distributed vertically in simulation T21, but peaks just above the cloud base in T22. We also find a lesser contribution to warming from the large-scale subsidence. The slight net warming extending through the lowest 150 mb of the atmosphere is expected, since there was no horizontal temperature advection in these model runs. Evaporation at the top of the cloud layer results in a strong cooling, particularly in T21, where it exceeds 15 K day^{-1}. Despite the warming effects of both the subsidence and small-scale transports, there is some residual cooling. This is also observed above the inversion layer, where the subsidence warming does not quite balance the radiative cooling. In steady-state conditions, the horizontal advection contributes some warming at these levels.

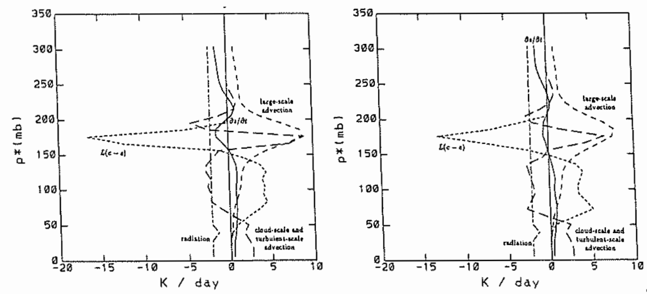

Fig. 3. Budgets of dry static energy (s/c_p) for the two cases in Fig. 1.

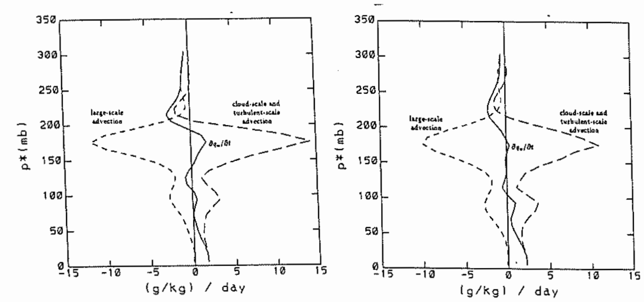

Fig. 4. Budgets of total water for the two cases in Fig. 1.

The total water budget shows a balance between the large-scale and the cloud-scale and turbulent-scale advection terms. (see Fig. 4). In the mixed layer, however, there is a net moistening due to the transport of water vapour from the sea surface. This effect should be opposed by the horizontal advection of cooler, drier air by the trade winds. The residual is much smaller in the cloud layer in both experiments, and is near zero in T22 in the upper part of the cloud layer. In T21, the cloud-scale and turbulent transports are stronger in the latter region, reaching a peak of nearly 15 g kg^{-1} day^{-1} at the top of the cloud layer. This is not entirely compensated by the large-scale advection (although it is slightly larger than in T22); this results in a net moistening. Both experiments also show some drying above $p*$=200 mb, resulting in a strenghtening of the inversion, particularly in T21, where it is coupled with the moistening below.

It is reassuring that the budgets are rather insensitive to the turbulent length scale specification. At this time, it is not clear which specification produced more realistic clouds. This is currently being investigated.

3.3. Cloud-environment differences

We have computed the averaged values of potential temperature and water vapour in "cloudy" and "clear" grid cells. The clouds were defined as points having a cloud fraction larger than 0.5, and a positive vertical velocity. This corresponds to cloudy updrafts, which are present in the active phase of cloud development. The cloud-environment temperature differences should yield a measure of the buoyancy of the clouds. However, profiles of potential temperature show that the clouds are actually cooler than the environment. In this situation, it is critical to include the effects of the water vapour (mixing ratio q_v), which enhances buoyancy, as well as the loading from cloud water droplets (mixing ratio q_c). Therefore, we define virtual potential temperature θ_v, as follows:

$$\theta_v \equiv \theta(1 + 0.609q_v - q_c)$$

Indeed, we find that θ_v is slightly higher in the clouds, highlighting the importance of the virtual effects in this case (see Fig. 5). The cloud-environment difference of θ_v (defined as $\theta_v' \equiv \theta_{v_c} - \theta_{v_e}$) reaches a maximum of ~ 0.1 K. The T22 profile is nearly linear in the lower 50 mb of the cloud layer, where θ_v' increases slightly with height. Above the maximum, it decreases more sharply. The clouds become cooler than the environment just below the $p*$=150-mb level. The cloud base in T21 is higher, and θ_v' is much smaller in the lower cloud layer, where it remains near 0.02 K. Above $p*$=100 mb, its profile is highly non-linear: θ_v' reaches a maximum comparable to that in T22, then decreases rapidly to a zero value near $p*$=150 mb.

We also investigated the updraft velocities of the clouds in our simulations. The averaged profiles are shown in Fig. 6. The updrafts in T22 are twice as strong as in T21 near cloud base. In both simulations, a maximum slightly exceeding 1 m s^{-1} is reached near the $p*$=125-mb level. Near the cloud top, the velocities are again larger in T22, and the updrafts also extend higher.

The dynamics of the mixed layer have a crucial impact on cloud development. The specification of the turbulent length scale allows greater turbulent mixing in experiment T21. On the other hand, cloud-scale motions prevail in T22, allowing more variation in the thermodynamic properties of parcels rising to the top of the mixed layer. Therefore, although the mean distribution of temperature and moisture is similar in both cases, the base of the cloud layer is lower in T22, since the parcels of air with properties deviating from the average (in particular, the parcels with a lower LCL) remain less mixed. In other words, stronger cloud "roots" are present in the latter simulation. This results in a lower cloud base, and also explains the larger cloud-environment differences in θ_v and the stronger updrafts in the lower part of the cloud layer, as discussed above.

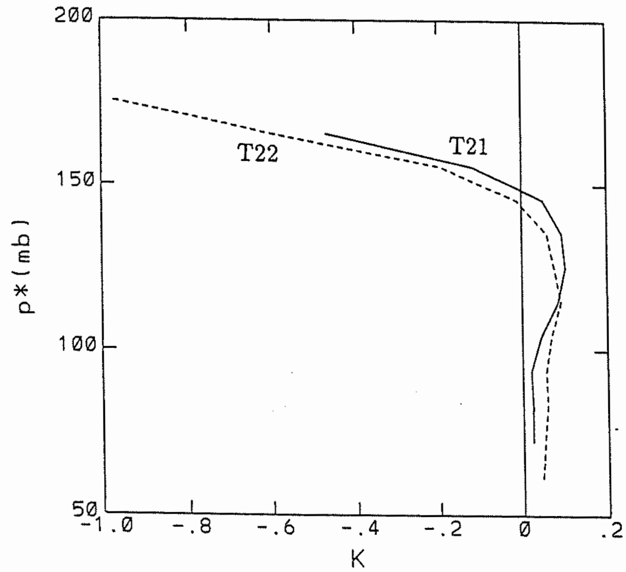

Fig. 5. Cloud-environment difference of virtual potential temperature.

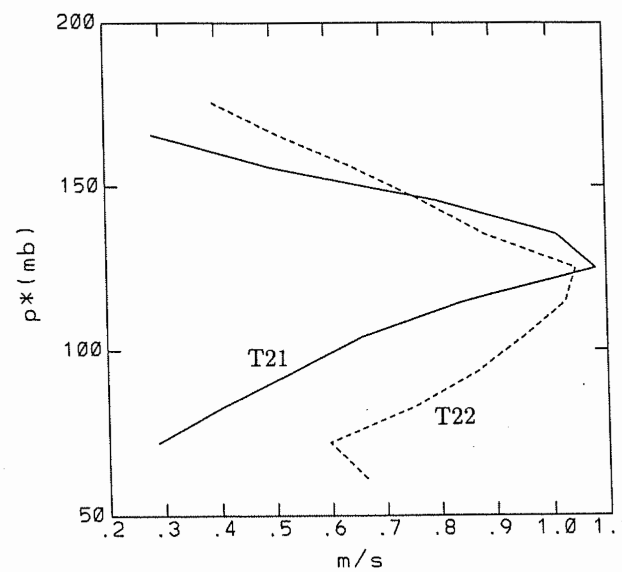

Fig. 6. Average vertical velocity of cloudy updrafts.

4. Implications for Albrecht's model

The results from the CEM can shed some light on the critical assumptions in bulk models such as the one developed by Albrecht *et al.* (1979). For instance, in that model, the cloud-environment differences in both h and q were assumed to vary linearly with pressure. However, in the CEM, the relationship between these quantities deviates significantly from linearity. This will affect the parameterization of the heat and moisture fluxes within the cloud layer.

An important assumption made by Albrecht was that all the clouds reach the inversion at some point in their lifetime. This is equivalent to considering a single cloud type. Indeed, preliminary results indicate a significant number of clouds reaching the inversion in the CEM simulations. However, we found that shallower clouds are also present. Thus, it becomes difficult to accurately represent the total contribution of different entrainment profiles across the entire spectrum of cloud types.

5. Conclusion

Further research is under way to confirm these hypotheses and study more parameters which are relevant in the evaluation of Albrecht's model. The visualization of individual clouds and their evolution over time is of particular interest for this purpose. We are currently investigating the distribution of the properties of individual clouds, and the possibility of dividing them into cloud types with specific entrainment profiles. We shall also attempt to establish a relationship between the lifetime of the clouds and the fractional area covered by the active updrafts. The assumed linearity of this relationship was crucial in the specification of a fixed parameter governing mass flux in Albrecht's model.

Acknowledgements. This research was supported by ONR grant N00014-91-J-1175. We would like to thank S. Esbensen and C. Bretherton for their valuable help in this projet.

References

Albrecht, B. A., 1979: A model of the thermodynamic structure of the trade-wind boundary layer: Part II. Applications. *J. Atmos. Sci.,* **36,** 90-98.

——, A.K.Betts, W.H.Schubert and S.K.Cox, 1979: A model of the thermodynamic structure of the trade-wind boundary layer: Part I. Theoretical development and sensitivity tests. *J. Atmos. Sci.,* **36,** 73-89.

Betts, A. K., 1975: Parametric interpretation of trade-wind cumulus budget studies. *J. Atmos. Sci.,* **32,** 1934-1945.

Bougeault, P., 1981: Modeling the trade-wind cumulus boundary layer. Part I: Testing the ensemble cloud relations against numerical data. *J. Atmos. Sci.,* **38,** 2414-2428.

Bretherton, C. S., 1991: Understanding Albrecht's model of trade cumulus cloud fields. Submitted to *J. Atmos. Sci.*

Esbensen, S., 1975: An analysis of subcloud-layer heat and moisture budgets in the western Atlantic trades. *J. Atmos. Sci.,* **32,** 1921-1933.

Krueger, S. K., 1988: Numerical simulation of tropical cumulus clouds and their interaction with the subcloud layer. *J. Atmos. Sci.,* **45,** 2221-2250.

Nitta, T., and S. Esbensen, 1974: Heat and moisture budget analyses using BOMEX data. *Mon. Wea. Rev.,* **102,** 17-28.

Soong, S.-T., and Y. Ogura, 1980: Response of tradewind cumuli to large-scale processes. *J. Atmos. Sci.,* **37,** 2035-2050.

STRATOCUMULUS CLOUD PROPERTIES DERIVED FROM SATELLITE
AND CORRELATIVE OBSERVATIONS DURING THE ASTEX

Patrick W. Heck[1], Patrick Minnis[2], David R. Doelling[1], William L. Smith, Jr.[1], and David F. Young[1]

[1]Lockheed Engineering and Sciences Co., Hampton, VA, USA 23666
[2]NASA Langley Research Center, Hampton, VA, USA 23665-5225

1. INTRODUCTION

The Atlantic Stratocumulus Transition Experiment (ASTEX) will be performed during June 1992 over the northeastern Atlantic Ocean in the vicinity of the Azores Islands (McDougal and Suttles, 1992). This experiment is designed to comprehensively examine the variation in marine stratocumulus properties and processes as the air mass giving rise to the clouds passes from colder to warmer seas. Observations such as cloud base, cloud fraction, cloud-top height, liquid water path, radiative fluxes, and moisture and wind fields will be taken from ship and surface instruments. Similar properties will be derived from satellite data. To gain some perspective of this experiment in relationship to the larger spatial scale and to long-term variability, a climatology of June clouds in the vicinity of the Azores was developed using Meteosat data. This paper shows the initial results of that study. Preliminary satellite results for the field experiment will be presented at the meeting.

2. DATA

Total and low (tops lower than 2 km) cloud amounts, low cloud-top heights, and equivalent visible (VIS, 0.65 µm) optical depths, τ, were derived from 3-hourly, 10-km Meteosat VIS and IR (infrared, 11.5 µm) data using the techniques described by Minnis et al. (1987) and Minnis et al., (1992). The data were analyzed on 2.5° grid covering the area between 10°N and 45°N and between 5°W and 40°W. The ASTEX analysis triangle (Fig. 1) has Santa Maria, Azores at its northwestern apex, Porto Santo, Madeiras at the eastern apex, and a meteorological research ship at its southwestern corner. The Meteosat VIS channel covers a relatively broad spectrum (0.4 - 1.1 µm). It was calibrated here by normalizing it through the GOES-East (Geostationary Operational Environmental Satellite) to the 1987 GOES-West VIS sensor which has a much narrower bandwidth (0.55 - 0.75 µm). Thus, the Meteosat reflectance here is an equivalent VIS reflectance. The GOES-East was normalized to the GOES-West satellite. The calibration for the latter was given by Minnis et al. (1992). In practice, the Meteosat VIS brightness count D_m (0-255),

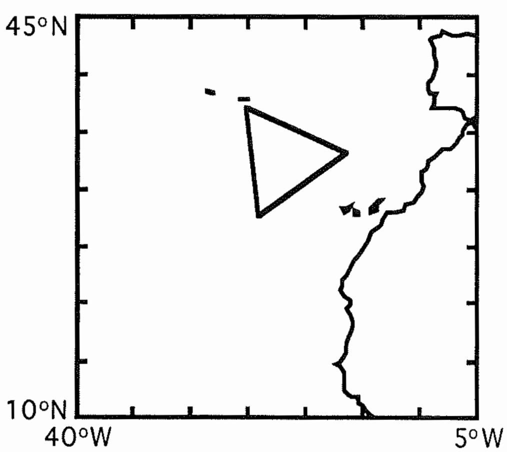

Fig. 1. Map of the ASTEX analysis area.

which is linear in radiance, is converted to an equivalent 1987 GOES-West count D (0-63) that is related linearly to radiance by its square. Thus,

$$D^2 = aD_m + b. \qquad (1)$$

and the reflectance $\rho = (0.16D^2 - 8)/526.9\delta_o\mu_o$, where δ_o is the earth-sun distance correction factor and μ_o is the cosine of the solar zenith angle. Interannual calibrations for Meteosat were approximated by assuming that the minimum reflectance over certain ocean and desert regions was invariant from year to year. Thus, the 1987 Meteosat data for those regions could be used to normalize the other years to the July 1987 GOES-West calibration. The resulting coefficients for (1) are given in Table 1. The Meteosat IR channel was calibrated by normalizing its brightness counts to the July 1987 GOES-East IR data. The resulting conversion is

$$T = 3.5\,I + 6.0,$$

where T is the equivalent blackbody temperature and I is the Meteosat IR brightness count. It was assumed that the July 1987 normalization was valid for all of the years. Sea-surface temperatures were taken from the Comprehensive Oceanic and Atmospheric Data Set (COADS; Woodruff et al., 1987). Climatological soundings from Oort (1983) provide the moisture data to correct the IR radiances for water vapor attenuation.

3. RESULTS

Means and standard deviations for total cloud cover, low cloud cover, and low-cloud visible optical depth for 1984-1989 are shown in Figs. 2 through 4, respectively. Areas with large total cloud amount in the northern and southeastern parts of the marine domain are composed of multiple layer clouds although clearly, low clouds are the predominant type. Frontal passages in the north and convective activity in the southeast are responsible for the higher clouds. Over the remainder of the grid, middle and upper level cloudiness is less important. Interannual variability in the cloud cover (Fig. 2b), except in the northwestern areas, is primarily due to fluctuations in low clouds (Fig. 3b). The axis of maximum low clouds follows the mean northeasterly boundary-layer winds and the relatively cold Canary Current. The largest year-to-year changes in cloudiness occur along this axis. The break in the maximum low cloudiness around 27°N is probably due to the barrier formed by the Canary Islands. Their altitude and

Table 1. Coefficients for Meteosat-to-GOES-West normalization

Year	a	b
1984	15.7	-39.6
1985	15.2	-8.0
1986	15.2	-8.4
1987	13.0	1.2
1988	13.8	-29.7
1989	14.2	-42.6

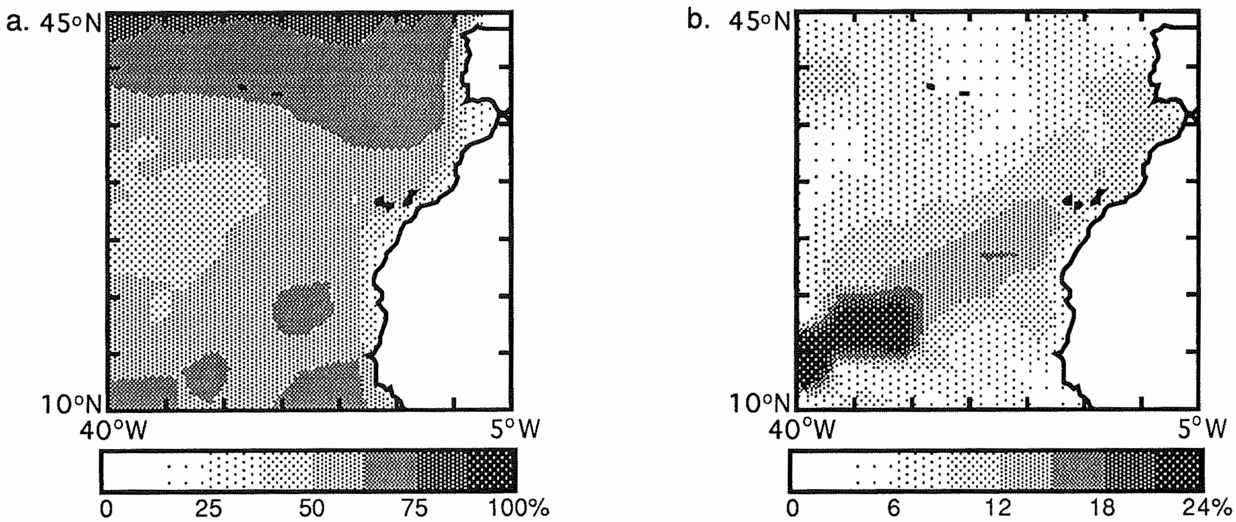

Fig. 2. Mean (a) and standard deviation (b) of total cloud cover for 1984-1989.

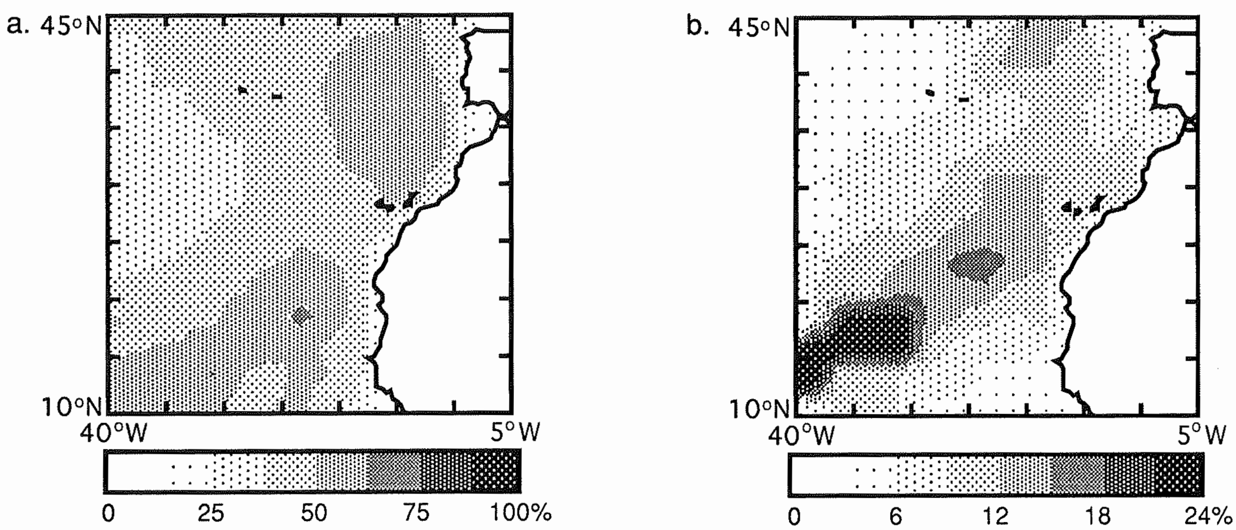

Fig. 3. Same as Fig. 2, but for low cloud amount.

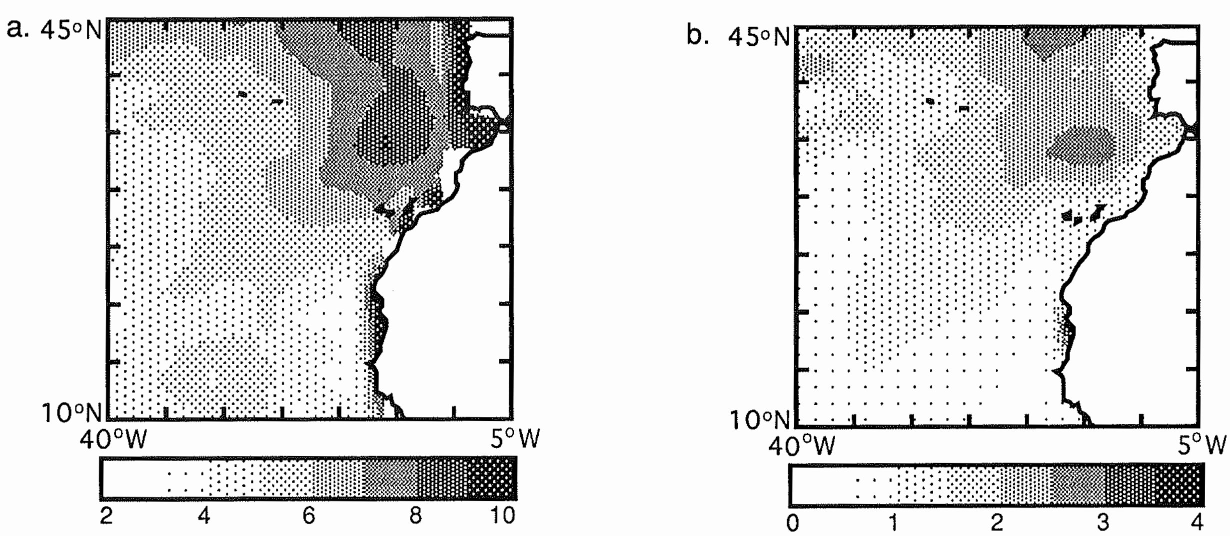

Fig. 4. Same as Fig. 2, but for low cloud optical depth.

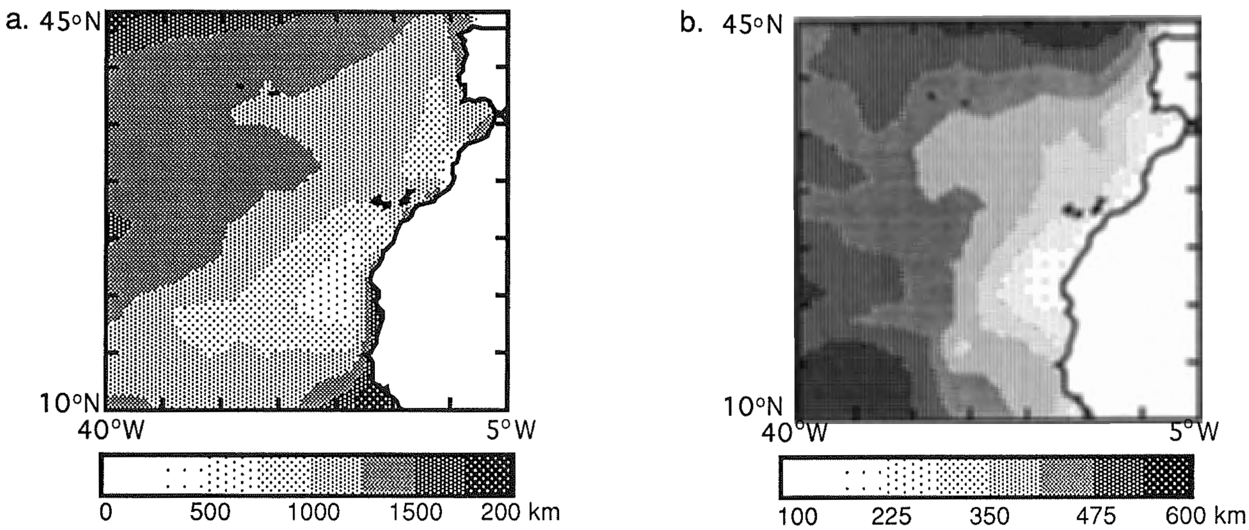

Fig. 5. Same as Fig. 2, but for low cloud heights.

horizontal extent are sufficient to induce a lee effect frequently evident in the satellite imagery as an abrupt clearing south of the islands or as arced wake clouds trailing downstream of the islands. Porto Santo is located near the northern low-cloud maximum. The low cloudiness decreases to the west by more than 10% at Santa Maria and to the southwestern apex (Fig. 1) by 10%. The northern area of minimum low cloudiness roughly corresponds to the climatological center of the Azores high.

Generally, the clouds north of the Canaries are much denser ($\tau > 6$) than those to the west and south (Fig. 4a). Cloud optical depth is also much more variable from one year to the next (Fig. 4b) in the north than elsewhere. The ASTEX triangle includes areas near the maximum optical depth. The triangle also includes an east-west gradient in low-cloud altitude (Fig. 5) from lower clouds near Porto Santo (~1150 m) to higher clouds (~ 1400 m) near the center of its western edge. Lowest clouds are found along the coast. The heights gradually increase toward the northwest. The interannual variability in the heights is relatively large and may arise from uncertainties introduced by the use of a constant IR calibration and climatological soundings.

The diurnal variations in cloud properties are significant over most of the ASTEX area. Figure 6 shows the 5-year, 3-hourly means of each cloud parameter for the region including Porto Santo. All of the quantities follow a similar pattern, maximum near sunrise and a minimum during the midafternoon. Similar results, found for the region southeast of Santa Maria (Fig. 7), reflect the parameter gradients seen in the previous figures. Mean cloud-top height over Santa Maria shows a larger dip in the afternoon than seen over Porto Santo. Part of this decrease results from the thinning of the clouds during the afternoon as seen in the optical depth data. Correction for the semitransparency of the clouds would raise the Santa Maria cloud heights at 1530 Local Time, relative to the other hours, because the lowest optical depths are observed then. The emissivity correction was not applied because there were no optical depth data at night.

4. DISCUSSION

These data show a significant amount of variability at several time and space scales. To verify the spatial variability in cloudiness, the 1984-1988 mean Meteosat cloud amounts were compared to the corresponding COADS ship-observed cloud amounts. The 5-year means plotted in Fig. 8 show remarkable consistency confirming the large-scale patterns observed using the Meteosat data. As expected, the satellite results show more detail since the COADS sampling is irregular and sparsely sampled in some areas. Overall, the satellite results yield a 5-year mean total cloud amount of 60.2% over all 147 marine regions compared to 61.7% obtained from COADS. The rms regional difference for the 5-year means is 5.0% indicating the magnitude of the satellite cloud amounts is also quite reasonable.

Very little data exist on cloud-top heights for the greater ASTEX area. However, the results in Fig. 5a are consistent in both pattern and magnitude with the boundary-layer inversion heights taken by von Ficker (1936) and replotted by Heck et al. (1990). The uncertainty in the heights are probably much less than those suggested by the standard deviations in Fig. 5b for the reasons noted earlier. In situ measurements taken during the ASTEX will help to alleviate the paucity of cloud-height data in this part of the Atlantic. The cloud optical depths seem relatively low compared to the northeastern Pacific (e.g., Heck et al., 1990). Errors in the optical depth could arise from a number of sources. The parameterization used to derive the clouds is based on plane-parallel radiative transfer calculations using an effective water-droplet radius of 8 µm. Broken clouds, stratus with irregular tops, or a different water-droplet size could all affect the value of the retrieved optical depth. Aerosols from Saharan dust storms could also impact those calculations. The use of an equivalent VIS calibration may cause some errors because it ignores the differences between the Meteosat and GOES spectral bands. The diurnal cycles in the cloud parameters are significant and similar to those observed over the northeastern Pacific by Minnis et al. (1992), giving further support to a general model of subtropical marine stratocumulus clouds.

5. CONCLUDING REMARKS

The results shown here give a preview of the ASTEX arena. While the experiment will focus on the triangular area, there will some measurements taken over other parts of the grid used here to help validate satellite retrievals like those shown here. The averages presented in this paper only tell part of the story. Correlation of individual measurements with some of the surface and aircraft data taken during ASTEX will be extremely useful for understanding and modeling the processes governing clouds in the subtropical marine boundary layer.

Acknowledgments. Funding for part of the Meteosat satellite analyses was provided by the Office of Naval Research under Grant USN-N0001491IMP24011.

REFERENCES

Heck , P. W., B. J. Byars, D. F. Young, P. Minnis, and E. F. Harrison, 1990: A climatology of satellite-derived cloud properties over marine stratocumulus regions. *AMS 1990 Conf. Cloud Physics.*, San Francisco, CA, July 23-27, J1-J7.

McDougal, J. S. and J. T. Suttles, 1992: FIRE Cirrus and ASTEX field experiments. *Proc. 11th Intl. Conf. Clouds and Precip.*, Montreal, Canada, August 17-21.

Minnis, P., E. F. Harrison and G. G. Gibson, 1987: Cloud cover over the eastern equatorial Pacific derived from July 1983 ISCCP data using a hybrid bispectral threshold method. *J. Geophys. Res.*, **92**, 4051-4073.

Minnis, P., P. W. Heck, D. F. Young, C. W. Fairall, and J. B. Snider, 1992: Stratocumulus cloud properties derived from simultaneous satellite and island-based instrumentation during FIRE. *J. Appl. Meteorol,*, **31**, 317-339.

Oort, A. H., 1983: Global atmospheric circulation statistics, 1958-1973. *NOAA Professional Paper No. 14*, U.S. Gov. Printing Office, Washington, D.C., 180pp.

von Ficker, H., 1936: Die passatinversion. *Veroffentlichungen Meteorol. Institut, Univ. Berlin*, **1**, 4, 1239-1250.

Woodruff, S. D., R. J. Slutz, R. L. Jenne, and R. M. Steurer, 1987: A comprehensive ocean-atmosphere data set. *Bull. Amer. Meteor. Soc.*, **68**, 1239-1250.

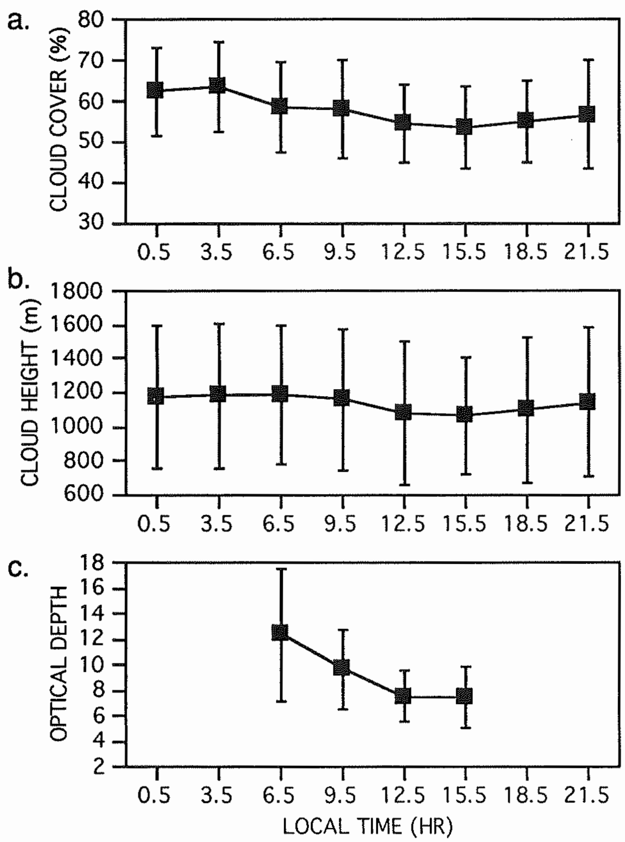

Fig. 6. Diurnal variability of low cloud cover (a), cloud-top height (b), and visible optical depth (c) over Porto Santo.

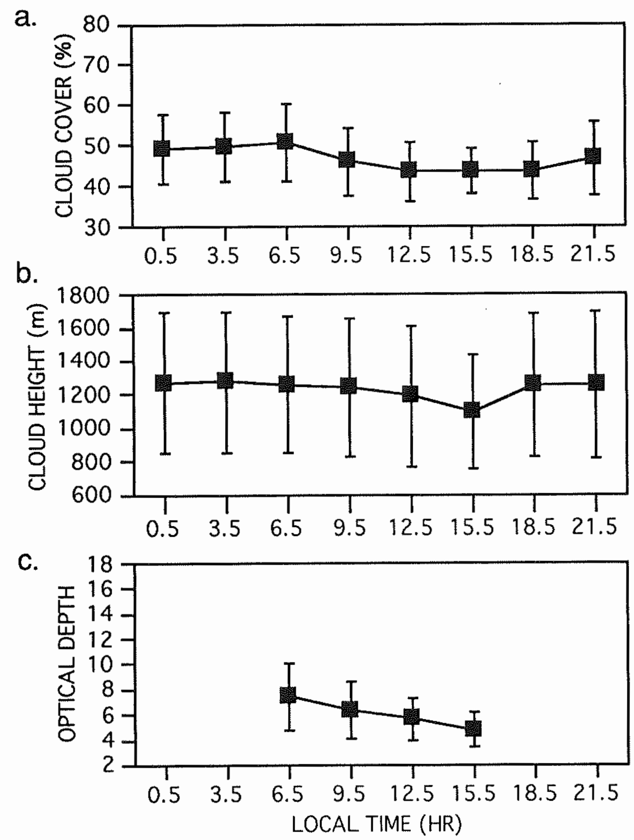

Fig. 7. Same as Fig. 6 for Santa Maria.

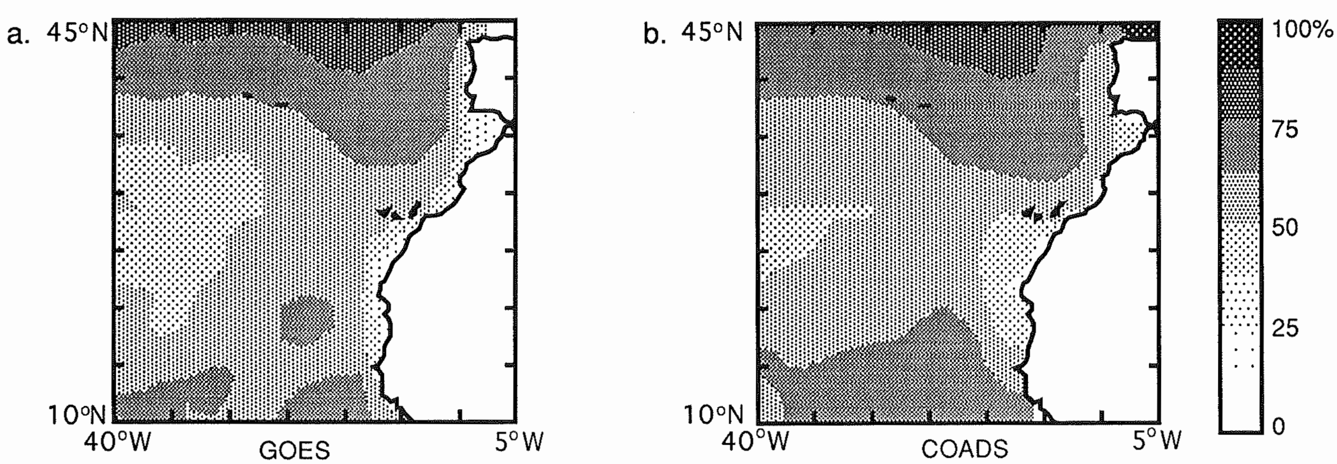

Fig. 8. GOES-derived (a) and COADS (b) total cloud cover for 1984-1988.

Doppler Radar Observation on the Kelvin-Helmholtz Billows in Stratiform Rainfall

Nobuhiro Takahashi, Hiroshi Uyeda and Katsuhiro Kikuchi
Department of Geophysics, Faculty of Science, Hokkaido University, Sapporo 060, Japan

1. Introduction

It is well known that the Kelvin-Helmholtz (K-H) instability occurs within a hydrostatic stable flow wherever there is a strong vertical shear. It appears as amplifying billows oriented perpendicular to the shear vector. These shear instability waves occur under a condition in which the Richardson number (Ri) is less than 0.25. The K-H billows were observed from the upper troposphere to the planetary boundary layer with different wave lengths. Several radar observations were carried out using high power FM-CW radars in order to understand the CAT (Clear Air Turbulence) mechanisms (Browning,1971; Browning et al., 1973; Hardy et al.,1973) and using multiple Doppler radars to clarify the structure of thunderstorm outflows (Weckerth and Wakimoto,1991). The K-H billows observed in the latter study are induced by the well known gravity current head, which is realized by a laboratory experiment (Simpson,1969) and a numerical simulation (Droegemeier and Whilhelmson, 1987). On the other hand, the observational studies on the K-H billows in the stratiform light rainfall are rare. Because the K-H billows are not observed by naked eyes in the rainfall and it is considered that the K-H billows do not occur in the rainfall with weak stability. Since Doppler radars can obtain the information not only from reflectivity but also by Doppler velocity of the rain echoes, it is possible to detect the K-H billows in the stratiform light rainfall with a Doppler radar.

In this study, we describe a result of single Doppler radar (Hokkaido University X-band Doppler radar) observation on the K-H billows in the stratiform light rain echoes from 0500 to 0700 JST(Japan Standard Time) on 6 September 1989 during an observation period of the mountain effect on precipitation enhancement around the isolated Mt. Yotei, Hokkaido, Japan. In this case, since the K-H billows occurred in the stratiform weak rainfall, we were able to observe the wind profiles at 15 min interval by using the VAD (Velocity Azimuth Display; Browning and Wexler, 1968) method. Furthermore, we were able to obtain the Doppler velocity data of the vertical cross section of the K-H billows which render it very easy to understand the dynamics of the billows. This study is focused on the billow formation mechanism related to the variation of the wind profile which is derived from VAD analysis and on the influence of the K-H instability on the enhancement of precipitation clouds (echo intensity).

2. Observation and analysis method

A Doppler radar observation was performed on purpose to verify the isolated mountain (Mt. Yotei; 1893m in Fig.1) effect on the precipitation enhancement from 26 August to 6 September in 1989. Figure 1 shows the observation area and the topography with the 500m height contour. Doppler radar was situated beside Lake Toya. The Doppler radar data were collected within 63.5km in radius with a 250m range resolution. The reflectivity, Doppler velocity and width of Doppler velocity data were obtained in PPI and RHI scans. Data were collected about 15 min intervals. Using high elevation angle(10°) PPI scan data, we calculated the vertical wind profiles with VAD method. Analyses on the mountain effects (lee wave and down slope wind) were performed by Uyeda et al.(1991). In this paper, therefore, our attention was focused on dynamically induced wave.

The K-H billows were determined as a series of relatively strong echo lines or a series of lines with the anomaly of the Doppler velocity. Then the reflectivity data of PPI and RHI scans were utilized to determine the wave length and orientation of the billows. The Doppler velocity data of RHI scan were utilized to describe the micro-structure of the billows.

Routine radio-sounding data of Sapporo District Meteorological Observatory (about 70km northeast of radar site) by JMA(Japan Meteorological Agency) at 0900 JST were utilized for analysis. The validity of using these sounding data was evaluated by the fact that the wind profile of Sapporo was almost the same as that of VAD method.

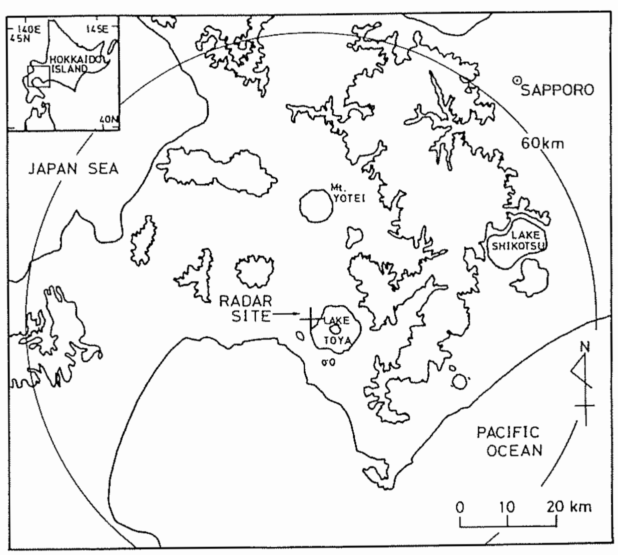

Fig. 1. Map of the observation area with topography of 500m contour. Radar site is depicted by cross with 60km range circle.

Since we were able to obtain the vertical wind profiles at every 15 min, Richardson number (Ri) was calculated at every 15 min by fixing the vertical structure of potential temperature as that of the soundings at 0900JST.

3. Results

Synoptic situations are shown in Fig. 2 as surface and 500mb weather maps at 2100JST on 5 September 1989. From the surface map at 2100JST on 5 September, it is understood that the northern part of Japan Islands was situated behind the stationary front which was associated with a cyclone. The observation area, therefore, was dominated by a relatively weak wind speed near the ground surface. Actually the wind speed at the radar site was less than $1ms^{-1}$ during the appearance of the K-H billows (0500~0700JST on 6 September). However, the 500mb weather map shows that a short wave trough was approaching Japan. Because of the northern part of Japan is located in front of the short wave trough, it was considered that the wind speed was accelerated at this region. This tendency of strong wind speed existed actually on 700mb map at 2100JST on 5 September. This synoptic situation, therefore, would cause a strong vertical shear.

Figure 3 shows the PPI(6°) displays of the typical K-H billows at 0548JST on 6 September. From Fig.3, the K-H billows appeared at the height between 3 and 4km with a wavelength about 3.5km and oriented perpendicular to the shear vector between 3 and 4km as clearly from the wind hodograph which is shown in Fig.4. Doppler velocity field at the same scan in Fig. 3 shows that an anomaly of Doppler velocity had a similar feature with the wavelength and orientation in the reflectivity display. Vertical cross sections of the K-H billows by RHI scan indicate the same wavelength in Fig.3.

Figure 5 represents the vertical wind profiles at 0620JST at the radar site and the sounding data at 0900JST at Sapporo. From the sounding data, we know that a stable layer is present between 3 and 4km. The height of $0°C$ level was at about 3.5km at Sapporo. The right hand panel in Fig.5 shows the vertical profile of Ri in every 200m obtained by using sounding data at 0900JST at Sapporo and VAD wind data at 0620JST. The vertical profile of Ri indicates that the value below critical Ri(0.25) is present at around 3.5km height(from 3.2 to 3.6km). The height of the wave pattern of reflectivity, therefore, coincided with the low Ri

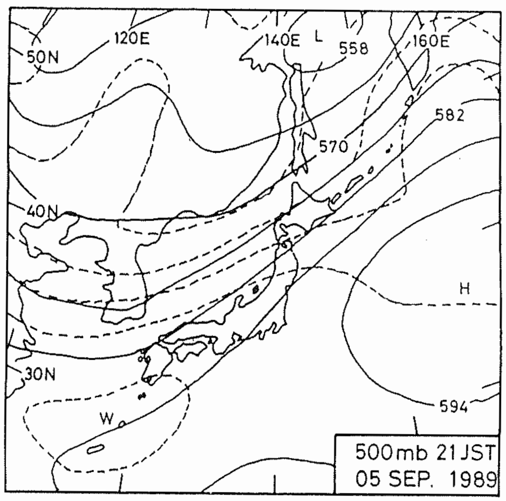

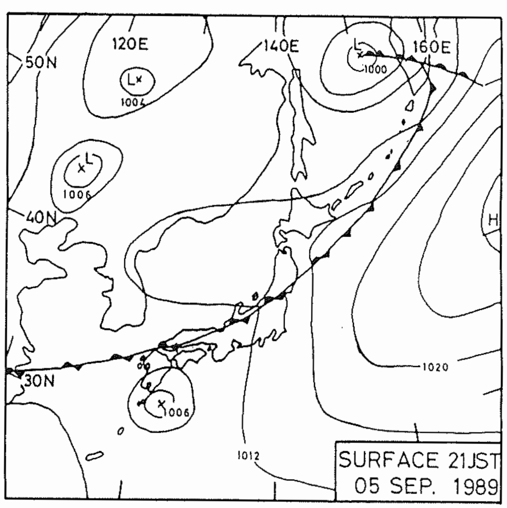

Fig. 2. Surface and 500mb weather charts at 21 JST on 5 September, 1989.

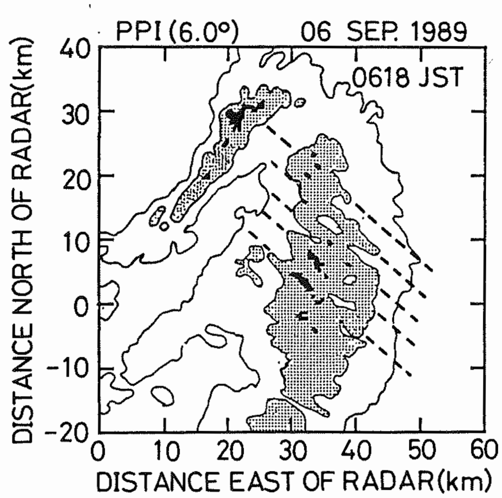

Fig. 3. Reflectivity display of PPI scan (elevation = 6°) at 0618 JST. Contours are presented at 5 dBZ intervals, beginning with 18 dBZ. Dashed lines indicate the Kelvin-Helmholtz billows.

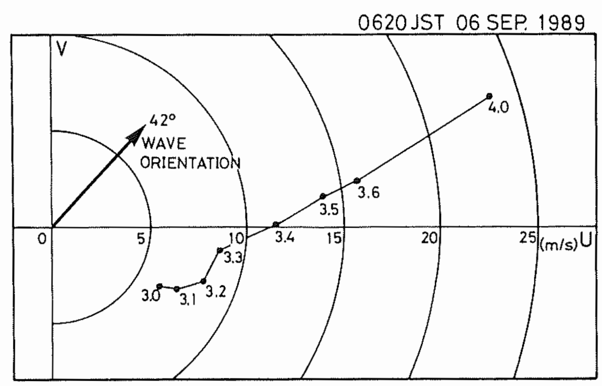

Fig. 4. Wind hodograph at 0620 JST derived from VAD method. Arrow indicates the orientation of the Kelvin-Helmholtz billows.

region. Furthermore, from Fig. 5, the thickness of effective shear layer was estimated to be 400∼600m. Figure 6 shows a time-height cross section of Ri obtained from the time series of wind profiles derived by VAD method and sounding data at 0900JST at Sapporo. Two cores of low value of Ri(minimum value = 0.14) are recognized at the height of 3.3km between 0548 and 0620JST. From the reflectivity pattern, the K-H billows were identified from 0540 to 0630JST. In particular, a predominant wave structure was observed around 0548 and 0620JST.

The micro-structure of the K-H billows was clarified by the analysis of Doppler velocity data of RHI scan. Figure 7 shows the Doppler velocity field of the RHI scan. Here, the positive value indicates the receding wind component from the radar. In the region between 3 and 4km in height and

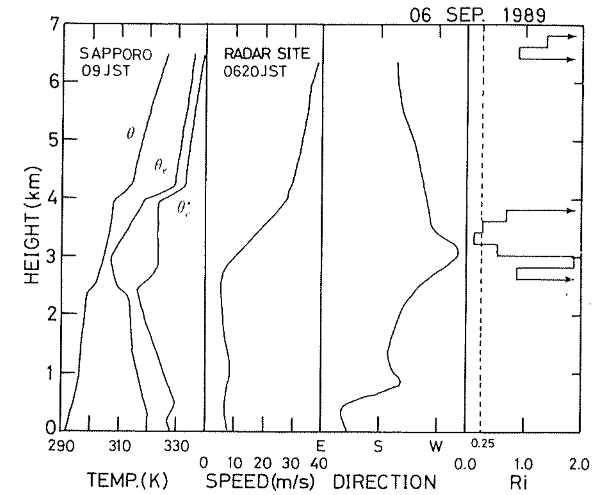

Fig. 5. Vertical profiles of potential temperature, equivalent potential temperature and saturated equivalent potential temperature at 0900JST at Sapporo, wind profile which is derived from VAD method at 0620JST at radar site, and vertical profile of Richardson number.

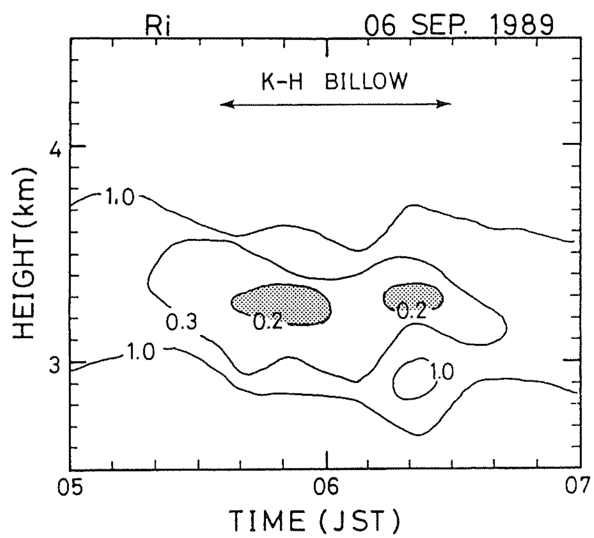

Fig. 6. Time height cross section of Richardson number from 05 to 07 JST. Stippled areas indicate the Ri less than 0.2. Arrow indicates the regime of the Kelvin-Helmholtz billows determined by reflectivity and Doppler velocity patterns.

21, 25 and 29 km from the radar site, isotachs concentrated vertically. It showed that the isotach of Doppler velocity undulated with the wave length of 4∼5km. And further the strong reflectivity cores coincided with the horizontally concentrated zone of isotachs except the region of 29km.

4. Discussion

Compared with the previous studies, the observed K-H billows were reasonably consistent with the previous studies in wave length, orientation and critical value of Ri. From the linear theory, the relationship between wavelength and the thickness of the shear layer is $\lambda = 7.5\Delta Z$ (Miles and Howard,1964) and $\lambda = 4.4\Delta Z$ (Drazin, 1958). In this case study, the effective thickness is almost 400 to 600m, so $\lambda = 5.8{\sim}8.75\Delta Z$. Considering the synoptic situation in this case, not the thermal stability but the vertical shear played an important role for the generation of the wave. Because the wave structure sensitively varies with the variation of Ri. And the wave generation was under the condition of Ri<0.25. This value agrees with the theoretical ones. We assumed that the temporal fluctuation of Ri may be related to gravity wave, however, there is no proof to clarify this assumption.

Next, we compared with numerical simulations concerning the micro-structure (e.g. Tanaka, 1975; Patnaik et al., 1976; Klaassen and Peltier, 1985). From the result of numerical simulations, it is considered that in the early or middle stage of the K-H billows, the isentropic contours begin to undulate and increase the amplitude, therefore, the wave reaches its maximum amplitude, and consequently the structure disintegrates. Compared with their results, if the isotachs of Doppler velocity correspond to the isentropic line(this assumption may be valid in the stratiform light rain, because the vertical mixing is not active in the stratiform rain compared with the convective one), the result of Fig. 7 coincides with the amplifying stage of the numerical simulations.

Also, the formation mechanism of the reflectivity core is considered. Returning to Fig.7, and if we consider the

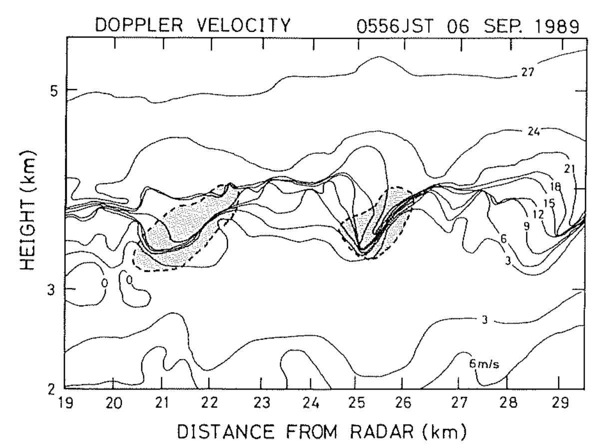

Fig. 7. Doppler velocity field of RHI at 0556 JST (azimuth = 30.5°). Stippled areas indicate the reflectivity cores(>24dBZ). Contours are presented at 3 ms^{-1} intervals, and the positive value indicates the receding wind component from the radar.

stratiform rain as in this case, it is reasonable that the isotachs of Doppler velocity correspond to the isentropics. If we consider that the $0°C$ level is at 3.5km height, the correspondence between reflectivity core and undulation of Doppler velocity field shows that the thermal instability caused to enhance the bright band formation, because precipitation particles originating above the shear layer($0°C$ level in this case) melted effectively at these undulated regions. One of the reasons for the existence of the undulated region without reflectivity core (29km from the radar site in Fig.7), we assume that there were not enough precipitation sources to form the bright band above this region.

This case study using Doppler radar clarified the dynamical and thermodynamical structure of the K-H billows displayed by PPI and RHI echoes. The condition of stratiform light rain made it possible to detect the K-H billows by X-band Doppler radar, and to deduce the thermodynamical characteristics. In particular, since the shear layer coincided with the $0°C$ level, the thermodynamic characteristic of the K-H billows was clarified as intense echoes in the bright band. It is assumed that the K-H billows rarely occur and are rarely detected by Doppler radar at the condition of moderate or heavy rainfalls.

5. Conclusions

The K-H billows were observed in the stratiform light rainfall during the Doppler radar observations of mountain effect on precipitation enhancement near Mt. Yotei, Hokkaido, Japan on 6 September 1989. Wave patterns were recognized both in reflectivity and Doppler velocity fields. The K-H billows appeared at the height between 3 and 4km, and had about a 3.5km wave length and was oriented almost perpendicular to the shear vector from 3.0 to 4.0km in height. This billow occurred under the condition of the Ri less than 0.30, especially a clear wave structure was originated when the Ri was less than critical value of Ri(Ric = 0.25). Here, a vertical structure of potential temperature was calculated from 0900JST sounding data at Sapporo, and a vertical wind profile was obtained at every 15 min with VAD method. In this case, a variation of the Ri was caused by the variation of vertical wind profiles.

Micro-structures of these K-H billows were revealed by Doppler velocity field of RHI scan. The K-H billows were identified as an undulated structure of Doppler velocity fields. Reflectivity cores coincided with the horizontally concentrated zone of isotachs of Doppler velocity. If the vertical structure of Doppler velocity in RHI is related to potential temperature, this wave structure resembles the early or developing stage of the K-H billows derived by numerical simulations (Tanaka,1975; Patnaik et al.,1976; Klaassen and Peltier,1985). The precipitation cores situated at the thermally unstable region, because of the effective melting of ice particles around the $0°C$ level.

Acknowledgments. The authors would like to express their thanks to students in their laboratory for their support in this field observation.

REFERENCES

Browning, K. A.,1971:Structure of the atmosphere in the vicinity of finite-amplitude Kelvin-Helmholtz billows. *Quart. J. Roy. Meteor. Soc.*,**97**,283-299.

——, G. W. Bryant, J. R. Starr and D. N. Axford, 1973: Air motion within Kelvin-Helmholtz billows determined from simultaneous Doppler radar and aircraft measurements. *Quart. J. Roy. Meteor. Soc.*,**99**,606-618.

—— and R. Wexler, 1968: The determination of kinematic properties of a wind field using Doppler radar. *J. Appl. Meteor.*,**7**,105-113.

Drazin, P. G., 1958:The stability of a shear layer in an unbounded heterogeneous inviscid fluid. *J. Fluid Mech.*,**4**,214-224.

Drogemeier, K. K. and R. B. Wilhelmson, 1987: Numerical simulation of thunderstorm outflow dynamics. Part I: Outflow sensitivity experiments and turbulence dynamics. *J. Atmos. Sci.*,**44**,1180-1210.

Hardy, K. R., R. J. Reed and G. K. Mather, 1973: Observation of Kelvin-Helmholtz billows and their mesoscale environment by radar, instrumented aircraft, and a dense radiosonde network. *Quart. J. Roy. Meteor. Soc.*,**99**,279-293.

Klaassen, G. P. and W. R. Peltier, 1985: Evolution of finite amplitude Kelvin-Helmholtz billows in two spatial dimensions. *J. Atmos. Sci.*,**42**,1321-1339.

Miles, J. M. and L. N. Howard, 1964: Note on a heterogeneous shear flow. *J. Fluid Mech.*, **20**, 331-336.

Patnaik, P. C., F. S. Sherman and G. M. Corcos, 1976: A numerical simulation of Kelvin-Helmholtz waves of finite amplitude. *J. Fluid. Mech.*,**73**,215-240.

Simpson, J. E., 1969: A comparison between laboratory and atmospheric density currents. *Quart. J. Roy. Met. Soc.*,**95**,758-765.

Tanaka, H.,1975: Quasi-linear and non-linear interactions of finite amplitude perturbations in a stably stratified fluid with hyperbolic tangent shear. *J. Meteor. Soc. Japan*,**53**,1-32.

Uyeda, H., N. Koizumi, K. Iwanami, R. Shirooka, N. Takahashi and K. Kikuchi, 1991: Structure of wind field and precipitation system around an isolated mountain observed with a Doppler radar during the passage of a typhoon. *Preprints, 25th Int. Conf. on Radar Meteor., Paris, Amer. Meteor. Soc.*,686- 689.

Weckerth, T. M. and R. M. Wakimoto, 1991 : Convection initiation associated with a gust front and Kelvin-Helmholtz instability. *Preprints, 25th Int. Conf. on Radar Meteor., Paris, Amer. Meteor. Soc.*,454-457.

Microphysical variability and drizzle formation in FIRE clouds

Philip Austin, Yinong Wang, and Malgorzata Szczodrak

Programme in Atmospheric Science, #217 Geography, 1984 West Mall, University of British Columbia, Vancouver, British Columbia V6T 1Z2 Canada

1. Introduction

Drizzle is a principal sink for stratocumulus cloud liquid water and cloud condensation nuclei. Simple boundary layer models (Albrecht, 1989; Baker and Charlson, 1989; Turton and Nicholls, 1986) indicate that precipitation may play a role in controlling cloud fraction, setting the equilibrium cloud droplet number and, through evaporative cooling, aid in decoupling a well mixed boundary layer.

A limited number of measurements, and the inherent sizing and sampling uncertainties that accompany aircraft observations of low droplet concentrations, has made it difficult to provide even order of magnitude estimates for the dependence of the precipitation rate on cloud properties. For example, Turton and Nicholls (1986), using data from 6 flights in North Atlantic stratocumulus layers, found that the in-cloud rainfall rate was approximately proportional to cloud thickness for clouds with droplet populations with mean radii > 10 μm. In contrast, Nicholls (1987) found a more sensitive dependence in a study which used a one-dimension microphysical model to track the growth of drizzle droplets. In his model, doubling the liquid water path (from 143 g m^{-2} and 283 g m^{-2}) produced a factor of 10 change in the precipitation rate (from 7 x 10^{-6} and 7 x 10^{-5} m s^{-1}). This result suggests that the precipitation flux might increase as the fifth power of cloud thickness, given a linear increase of liquid water content with height.

Below we look at measurements of precipitation flux made by the NCAR Electra as part of the First ISCCP Regional Experiment (FIRE, Albrecht et al., 1988) which appear to demonstrate both high and low sensitivity to cloud thickness. On July 14, 1987, the Electra made an extended level penetration through nearly adiabatic cloud with liquid water paths of more that 250 g m^{-2}, and found precipitation rates exceeding 5 x 10^{-5} m s^{-1} for 10 — 20 km sections, with relative variations in the precipitation flux of a factor of 5 across the cloud. Two days later, on July 16, the cloud was thinner and the Electra flew across a clear-cloud transition in which the precipitation rate increased approximately linearly with liquid water content. Below we discuss the Electra microphysical measurements and examine vertical and horizontal microphysical profiles for theses two days.

2. Electra data reduction

a. Definitions

Given the dropsize distribution n(r) (#/m^{-3} μm^{-1}) as a function of the dropsize radius r, the precipitation rate is defined as:

$$f_{precip} = \frac{4}{3}\pi\frac{\rho_w}{\rho}\int_0^\infty w_T(r)r^3n(r)dr \quad (kg\, kg^{-1}\, m\, s^{-1}) \qquad (1)$$

where $w_T(r)$ is the droplet fall speed for droplets of radius r and ρ and ρ_w are the densities of air and water. A measure of the cloud water available for coalescence is given by the liquid water path between cloud bottom and top: $lwp = \int_{z_{bot}}^{z_{top}} lwc\, dz$ where the liquid water content, lwc, integrated over the drop size distribution is $lwc = \frac{4}{3}\pi\rho_w\int_0^\infty r^3n(r)dr$.

We will also present estimates of the visible optical depth, τ, obtained from GOES satellite and aircraft data. At visible wavelengths the cloud optical depth is well approximated by:

$$\tau = \frac{3}{2\rho_w}\int_{z_{bot}}^{z_{top}}\frac{lwc(z')}{r_e(z')}dz' \qquad (2)$$

with the effective radius, r_e given by the ratio of the second and third moments of the distribution:

$$r_e = \int_0^\infty r^3n(r)dr / \int_0^\infty r^2n(r)dr \qquad (3)$$

A relation between lwp and τ requires profiles of the effective radius and liquid water content. If we assume an adiabatic liquid water profile and a number concentration between 120–150 cm^{-3} (rough approximations that apply to portions of these cloud layers), then over a limited optical depth range

$$lwp = C\tau \qquad (4)$$

Where, for 20 < τ < 40, C ranges from 7 to 9 g m^{-2}.

b. Instrumentation

Droplet size concentrations n(r) were measured by three Particle Measuring System (PMS) microphysical probes: a Forward Scattering Spectrometer Probe (FSSP) set on these flights to size particles with diameters in 15 bins between 2 and 47 μm, the 260X, with a diameter size range from 40 to 620 μm spaced in 10 μm increments, and the 200Y, with diameters from 300 to 4500 μm in 300 μm increments. We have applied the corrections of Baumgardner and Spowart (1990) to each of these probes. These consist of a response time correction, which reduces the effective sample volume of some of the size bins in all three probes, and a correction for the inhomogeneous beam intensity of the FSSP laser.

The impact of the corrections is substantial. Figure 1 shows a July 14 sounding of FSSP liquid water mixing ratio and number mixing ratio with and without these corrections. The straight, dashed lines indicate adiabatic liquid water profiles. Without the corrections the estimated liquid water path is 108 g m^{-2} (38% of adiabatic) and the mean number mixing ratio is 71 mg^{-1}. The application of the corrections increases the liquid water path to 252 g m^{-2} (91% of adiabatic), primarily by increasing the number concentration: mean radius increases from 8.9 – 9.5 μm while

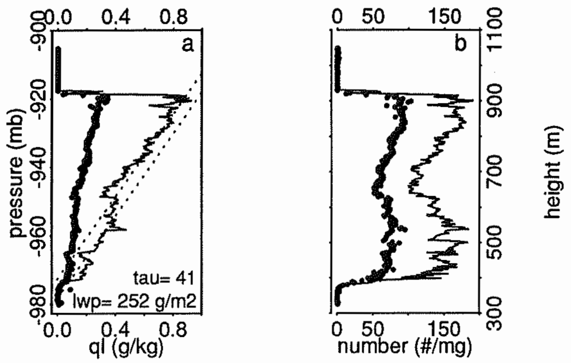

Figure 1 July 14 sounding (18:09 — 18:15 PDT) of (a) FSSP liquid water mixing ratio (g/kg) and (b) number mixing ratio (#/mg). Dots: uncorrected FSSP values, Solid line: with correction. The straight dotted line shows the adiabatic liquid water profile.

the mean droplet mixing ratio is increased to 138 mg^{-1}. The local maxima in liquid water and number concentration appear to be the product of the long horizontal descent used for this sounding and are discussed in Section 3.1 below.

Although the inhomogeneous beam correction can produce artifacts (principally, bimodal spectra due to the coarse mapping of the laser inhomogeneity pattern ((Baumgardner, personal communication) see Figure 5 below) the correction produces liquid water profiles much closer to adiabatic values, in agreement with measurements made by both British Met. Office C130 and the University of Washington C131 aircraft. Comparing simultaneous penetrations made by the three aircraft on July 14 and July 16, the C130 measured a mean droplet concentration of 144 cm^{-3} and mean liquid water content (measured by the Johnson-Williams probe) of 0.4 g m^{-3} in level flight at 730 m. Corrected FSSP values for the Electra at this time give a concentration of 160 cm^{-3} and a liquid water content of 0.5 g m^{-3} at 700 m. Similarly, measurements made on July 16 University of Washington C131 show mean droplet concentrations of 120 cm^{-3} , which is within 5% of the corrected FSSP number concentrations measured by the Electra in the same boundary layer.

The impact of the response time correction on the 260X and 200Y probes is to decrease the sample volume, and increase the concentration in probe bins with radii at the lower end of the probe size range. The correction reduces the sample volume of the first 3 200Y size categories (r= 150, 300, 450 μm) to zero, and produces changes in the 260X concentration for drops with 25 $\mu m < r < 100$ μm of as much as a factor of two. The correction results in an increase in the precipitation flux of 30 — 40% at drizzle rates of 2 x 10^{-5} m s^{-1}; we will show both corrected and uncorrected 260X measurements in the figures below. A sampling length of 60 seconds is sufficient to resolve all drizzle drops present in concentrations > 1 m^{-3}. We choose shorter sampling lengths in the figures below, but require that at least five raw counts are present in all size bins that contain droplets in the longer sixty second sample.

3. Observations

a. Vertical structure

Figure 2 shows histograms of optical depth estimated from GOES visible images made using the procedure outlined in Gu et al. (1992). Each image is centered at the time and location of the in-cloud Electra flight legs for July 14 (11:45 PDT) and July 16 (10:45 PDT) and covers an approximately 300 x 200 km^2 box. Both the mode and extreme optical depths for July 14 indicate that it is a substantially thicker cloud. July 14 also showed a more organized reflectivity pattern, with optical depth maxima spaced roughly 10 km apart in mesoscale cells. Optical depths vary from values of 20 at the edges to 40 in the center of these closed cells.

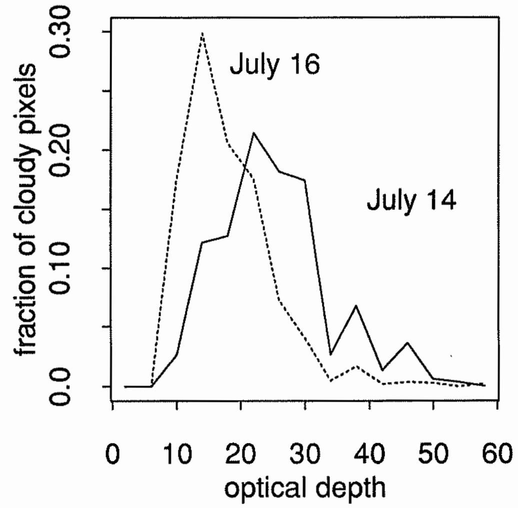

Figure 2 Histograms of optical depth estimates using GOES satellite imagery. Solid line: July 14. Dashed line: July 16.

The effect of these horizontal cloud inhomogeneities is apparent in the July 14 sounding of Figure 1. The Electra traversed a horizontal distance of 21 km between cloud top and cloud base during this sounding; this is roughly double the length scale of the mesoscale cloud optical depth features. We have inserted two adiabats to suggest that the profile separation at 950 mb is consistent with an aircraft sample across a region with 5 – 8 mb variation in cloud base. Independent liquid water measurements by a hot wire liquid water probe (PMS/CSIRO King), although unsatisfactory for quantitative liquid water content estimates due to offset and gain problems, show this same local maximum in several in-cloud soundings with low angles of descent/ascent. The mid-cloud maximum is absent in steeper soundings which cover a horizontal distance of less than 7 km (cf. Figure 3.b below).

Figure 3 presents two additional soundings from July 14 (3.a and 3.b) and two from July 16 (3.c and 3.d) which are representative of the 7–8 soundings taken over the 4–5 hour flights on each day. The cloud top height measured by aircraft stayed between 919 — 925 mb, and a lidar mapping run on July 16th (10:36 — 11:04 PDT) showed 100 m cloud top variations on 50 km scales. Satellite temperature measurements show a larger variation in the mean temperature on July 14th than on July 16th (c.f. Gu et al. 1992) with 1 K variations across 50 km scales. Given a mean lapse rate of 7 K/km this would indicate 150 m variations in cloud top height on the 14th. For adiabatic, 400 m thick clouds, thickness changes of 100 m produce 80 g m^{-2} changes in lwp.

The soundings in Figures 1 and 3 indicate possible 20 mb variations in cloud base height. The evaporation of falling drizzle prohibits the determination of horizontal cloud base variations from sub-cloud measurements using the lifting condensation level, but horizontal liquid water fluctuations of 0.3 g/kg measured in mid-cloud penetrations (see Figure 4.c), if produced by changes in cloud base height, would indicate 150 m thickness changes and lwp variations of 120 g m^{-2} in adiabatic cloud.

b. Horizontal measurements: July 14

Figure 4 shows an extended (55 minute, 11:18–12:13 PDT) Electra penetration through the July 14 stratocumulus layer, in which the aircraft flew a figure-8 pattern at a constant altitude of 700 m (940 mb) approximately 20 mb below cloud top. The solid line in Figure 4b is the corrected precipitation rate (20 second or 2 km average). There are three 20–30 km portions of the leg in which the precipitation rate exceeds 4 x 10^{-5} m s^{-1} and a number of others where it exceeds 2 x 10^{-5}. Measurements of the mean vapor flux at cloud base, calculated using the 20 Hz Lyman-α vapor values and the uncorrected pressure-gust probe, are roughly 1 x 10^{-5} m s^{-s} and may be an overestimate (Paluch and Lenschow, 1991). Two thirds of the precipitation flux measurements exceed the 1 x 10^{-5} m s^{-1} level which would represent a liquid water steady-state for the layer.

There is a clear correlation between precipitation flux and the small droplet population as measured by the FSSP. The central maximum, labeled B in Figure 4.a corresponds to a reduction in small droplet concentration and liquid water mixing ratio to 33% and 40% of the mean values. The corresponding spectra averaged over 30 seconds surrounding the points labeled A and B in Figure 4.a are shown in Figure 5. For spectrum a) the FSSP and 260X size ranges contribute an equal 8 x 10^{-6} m s^{-1} to the drizzle flux. Spectrum b) shows the FSSP concentration reduced from 176 to 50 cm^{-3} The drizzle flux measured by the 260X for Spectrum b) is 5.45 x10^{-5} m s_{-1}.

c. Horizontal measurements: July 16

As indicated by the optical depth measurements of Figure 2 and the vertical soundings, liquid water paths on July 16 are smaller than on July 14. Mean vapor fluxes at cloud base are also lower, ranging between 5 x 10^{-6} and 1 x 10^{-5} m s^{-1}. The

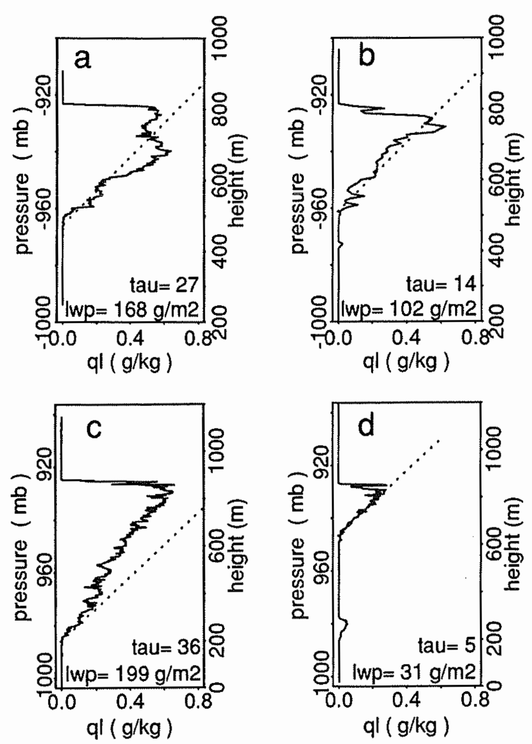

Figure 3 Liquid water mixing ratio (g kg^{-1}) for July 14 (a and b) and July 16 (c and d) Dashed line indicates adiabatic profile. Each sounding is labeled with its optical depth τ and liquid water path. a) 7/14 12:23 PDT b) 7/14 15:09 PDT c) 7/16 16:45 PDT, d) 7/16 19:00 PDT.

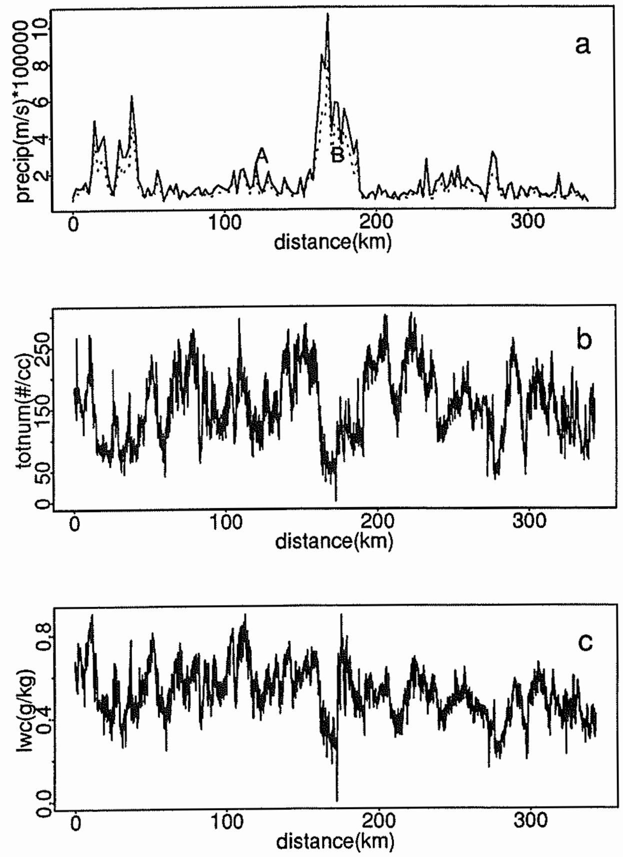

Figure 4 Horizontal sounding for July 14 (11:18 — 12:13 PDT). a) Precipitation rate (m s^{-1} x 10^{-5} m s^{-1}). Dots show uncorrected values. b) FSSP number concentration (# cm^{-3}) c) FSSP liquid water content (g kg^{-1}).

Electra made two cloud penetrations at 940 mb (roughly 20 mb below the mean cloud-top) on July 16; plots of precipitation rate, liquid water content and number concentration from both penetrations are shown Figure 6. Each penetration crossed a region of increasing liquid water content, the 0.3 g m^{-3} increase is consistent with a cloud thickness change of 150 m for an adiabatic cloud. Although the in-cloud flight legs were short, Figure 6a indicates that the drizzle rate is not affected by the liquid water concentration change. One possible reason for this lack of sensitivity is the corresponding increase in the number concentration shown in Figure 6.b Aerosol spectrometer measurements taken on a sub-cloud leg preceding 6b show a doubling in the condensation nuclei concentration below cloud. The additional activated

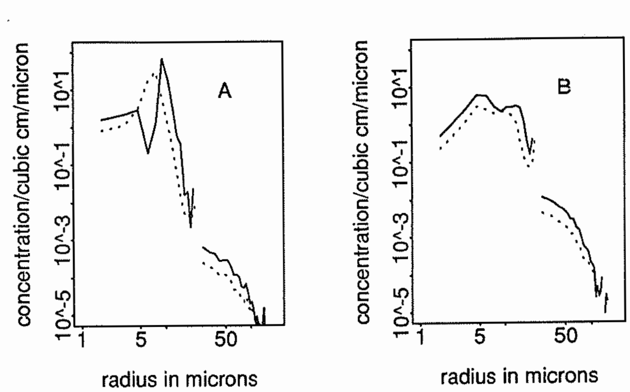

Figure 5 Droplet spectra for the points labeled A and B in Figure 4. Solid line, corrected. Dashed line, uncorrected. Note the minimum at $r \approx$ 10 μm produced by the discrete map of the FSSP laser inhomogeneities

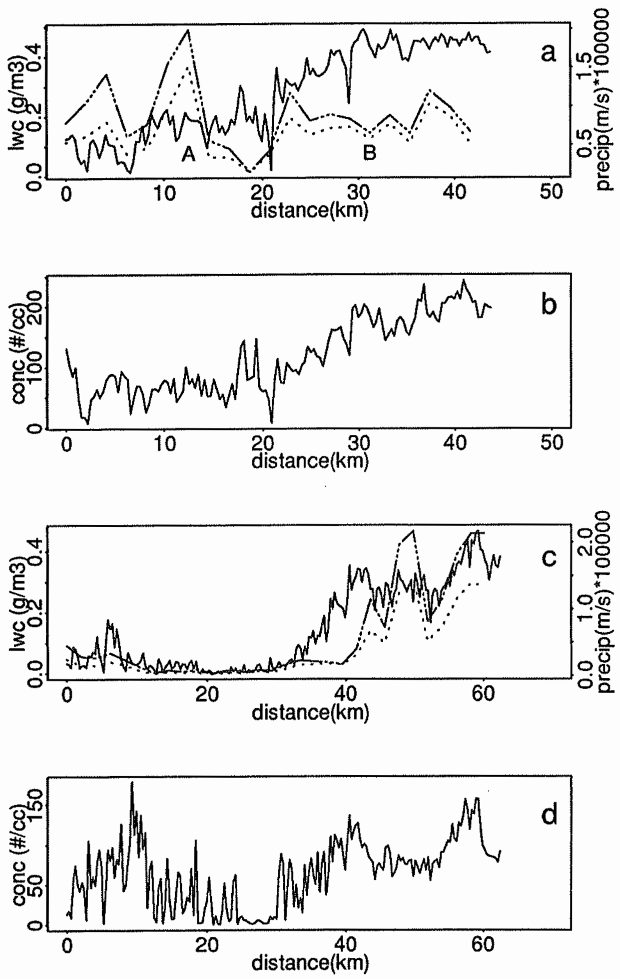

Figure 6 Horizontal sounding for two 940 mb in-cloud penetrations, July 16. a) 10:17 — 10:24 PDT. Solid line: FSSP liquid water content (g m^{-3}). Dot-dashed line: corrected precip. rate x 10^5 ms^{-1}. Dotted line: uncorrected precip rate x 10^5 m s^{-5}. b) 10:17 – 10:24 PDT. FSSP number concentration (#/cm^{-3}. c) 11:19 — 11:29 PDT. Variables as in 6a. d) 11:19 – 11:29 PDT. Variables as in 6b.

droplets produce a decrease in the volume mean radius measured by the FSSP from 10 to 8 μm, and could make coalescence less effective, despite the larger liquid water path.

Drizzle rates reach a similar maximum of 2 x 10^{-5} m s^{-1} in the second 940 mb leg shown in Figure 6c. Here the number concentration stays below 150 cm^{-3} and the 0.4 g m^{-3} increase in liquid water content is accompanied by the initiation of precipitation. Figure 7 shows corrected and uncorrected droplet spectra for 30 second averages about the points labeled A and B in Figure

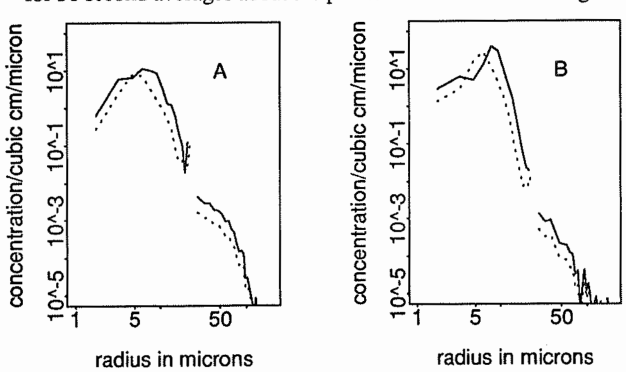

Figure 7 Droplet spectra for the points labeled A and B in Figure 6. Solid line, corrected. Dashed line, uncorrected.

6.a For 7a the number concentration is 75 cm^{-3} and the drizzle rate is 2 x 10^{-5} m s^{-1}, while for 7b the number concentration has increased to 170 cm^{-3} while the precipitation rate has dropped to 0.7 x 10^{-5} m s^{-1}.

4. Summary

Data from the two FIRE case studies with the largest drizzle fluxes present different pictures of the organization of precipitation in thick marine stratocumulus clouds. On July 14 the Electra measured peak precipitation values of more than 8 x 10^{-5} m s^{-1}, with 20 —30 km sections of the extended in-cloud flight leg with drizzle rates which were a factor of four greater than the background values of 1 - 2 x 10^{-5} m s^{-1}. Cloud thickness estimates from satellite optical depths, cloud top heights, and in-cloud liquid water measurements indicate liquid water path variations of roughly a factor of two, suggesting that the precipitation rate may be a fairly sensitive function of cloud thickness for the July 14 boundary layer.

Shorter flight legs on July 16 show maximum drizzle rates of 2 x 10^{-5} m s^{-1}, with some evidence for a lower sensitivity and the suppression of drizzle in a region of increasing droplet concentration.

An examination of cloud soundings on both July 14 and July 16, and a comparison with in-cloud measurements made by two other aircraft indicate that FSSP corrections designed to account for sample time delays and inhomogeneities in the FSSP laser produce liquid water and droplet number concentrations in agreement with the other estimates, with observed drizzle rates and with satellite retrievals of cloud optical depth

5. Acknowledgments

We would like to thank the NCAR Research Aviation Facility for providing the Electra aircraft and processing the FIRE data, Darrel Baumgardner for the probe correction software and helpful discussions and Keith Bower and Mike King for providing the C130 and C131 data. We are grateful to Robert Pincus for the optical depth retrievals and to the NASA Climate Data System for the GOES imagery. This work was supported by the National and Science and Engineering Research Council of Canada and the Atmospheric Environment Service.

6. References

Albrecht, B. A,. 1989: Aerosols, cloud microphysics, and fractional cloudiness. *Science*, **245**, 1227–1230.

Baker, M. B. and R. J. Charlson, 1990: Bistability of CCN concentrations and thermodynamics in the cloud-topped boundary layer, *Nature*, **345** p. 142–145.

Baumgardner, D. and Michael Spowart, 1990: Evaluation of the Forward Scattering Spectrometer Probe. Part III: Time response and laser inhomogeneity limitations. *J. Atmos. and Ocean. Tech.*, **7**, 666–672

Gu, J., R. Pincus, P. Austin and M. Szczodrak, 1992: Cloud optical depth estimates from satellite measurements. *Proceedings of the 11th International Conference of Clouds and Precipitation.* Montreal, Canada, 1992.

Nicholls, S., 1987: A model of drizzle growth in warm, turbulent, stratiform clouds.*Q. J. R. Met. Soc.*, **113**, 1141–1170.

Nicholls, S. and J. Leighton, 1986: An observational study of the structure of stratiform cloud sheets: Part I. Structure. *Q. J. R. Met. Soc.*, **112**, 431–460.

Paluch, I. R. and D. H. Lenschow, 1991: Stratiform cloud formation in the marine boundary layer. *J. Atmos. Sci.*, **48**, 2141–2158.

Turton, J. D. and S. Nicholls, 1987: A study of the diurnal variation of stratocumulus using a multiple mixed layer model. *Quart. J. of the Roy. Meteor. Soc.*, **113**, 969–1009

THE DYNAMICS OF DECOUPLING IN A CLOUD-TOPPED BOUNDARY LAYER

Matthew C. Wyant[1] and Christopher S. Bretherton[2]

[1] Department of Atmospheric Sciences, AK-40
[2] Department of Applied Mathematics, FS-20
University of Washington, Seattle, WA, USA 98195

Introduction

The phenomenon of decoupling in cloud topped boundary layers has been documented both in observations (Nicholls, 1984, Betts, 1989) and in modelling studies (Turton and Nicholls, 1987, Bougeault, 1986, Chen and Cotton, 1987). Decoupling in stratocumulus is defined as the vertical separation of the mixed layer into two well mixed layers separated by a small inversion. Physically, decoupling results when the maintenance of well-mixed conditions throughout the depth of the cloud-topped boundary layer (CTBL) would require large negative buoyancy fluxes in some range of heights in the interior of the layer.

The boundary layer convection in a stratocumulus cloud regime is primarily driven by longwave (LW) cooling at cloud top and secondarily by surface latent heat fluxes. Entrainment of warm, dry air from above the inversion reduces the buoyancy fluxes below cloud base, but has much less impact on in-cloud buoyancy fluxes. Thus, more entrainment promotes decoupling. After decoupling, the upper layer, cut off from the surface moistening and no longer moderated in temperature by the sea surface, becomes warmer and dryer than the lower layer.

Definitive observations of decoupling have been made only during the daytime. Modelling studies suggest that decoupling during the daytime is largely a result of the stabilization of the upper part of the boundary layer due to shortwave (SW) heating in the cloud. This heating tends to reduce the cloud thickness and reduce net radiative cooling, resulting in diminished in-cloud buoyancy fluxes and ultimately decoupling of the boundary layer. When nighttime conditions are reestablished, a decoupled layer can recouple, provided that the buoyancy fluxes generated by the cloud-top LW cooling generate enough turbulent kinetic energy (TKE) to overcome the weak stratification between the layers. The diurnal cycle consisting of daytime decoupling followed by nighttime reconnection is known as diurnal decoupling. Nicholls and Turton (1987) modelled this process using a one dimensional mixed-layer model which was allowed to switch between a mixed-layer state and a two-mixed-layer state based on parameterized diagnoses of the turbulent fluxes.

Drizzle is also a factor contributing to decoupling. As pointed out by Nicholls (1984), drizzle plays a significant role in the moisture budget of stratocumulus. Drizzle depletion of the cloud layer of water dries out the cloud layer and promotes decoupling. There is no parameterization for drizzle in this model, though drizzle can be incorporated into a mixed-layer framework.

In this study, the value of the buoyancy flux just below cloudbase in a mixed-layer model is used as an indicator of the tendency for decoupling. Decoupling is predicted when the buoyancy flux at this level becomes negative. In typical cloud-topped mixed layers, a large positive jump in buoyancy flux is found at the cloud base. This jump is driven by the differential latent heating effects connected with the different saturation vapor pressure of updrafts and downdrafts. The minimum buoyancy flux typically lies just below this jump in the upper subcloud layer. When the buoyancy flux just below cloudbase is less than zero, a finite layer of negative buoyancy fluxes, which consumes TKE, is present indicating likely decoupling.

To use a mixed-layer model to predict decoupling, the manner in which the entrainment velocity, w_e, is specified is crucial. For example the Lilly (1968) maximum entrainment condition, on which many entrainment parameterizations are based, actually uses the constraint that the buoyancy flux just below cloudbase is zero in order to predict the entrainment. This effectively pins the mixed layer (according to the hypothesis presented here) to a barely decoupled state. Instead, what is needed to predict decoupling is a w_e related to some eddy convective velocity w_*. Such a formulation is described below.

The predictions of the buoyancy flux criterion are examined here using a Lagrangian mixed-layer model following July climatological trajectories in the subtropical East Pacific near California. The results indicate that along most trajectories, the CTBL decouples as it progresses southwestward even in the absence of drizzle or of a diurnal radiation cycle because of the increasing SST.

The Mixed-Layer Model

The mixed layer prognostic equations (Lilly, 1968, Schubert *et.al.*, 1979) of moist static energy, h_M, total water mixing ratio, q_M, and inversion height, z_I, are

$$\rho_{ref}\frac{dh_M}{dt} = -\frac{(F_h)_{I-} - (F_h)_0 - \Delta F_{RM}}{z_I}$$

$$\rho_{ref}\frac{dq_M}{dt} = -\frac{(F_q)_{I-} - (F_q)_0}{z_I}$$

$$\frac{dz_I}{dt} = -Dz_I + w_e$$

where the $(F)_I$ and $(F)_0$ terms represent turbulent fluxes at the inversion and at the surface and ΔF_{RM} is the radiative flux divergence in the mixed layer. It is assumed that large-scale vertical velocity increases linearly with height proportional to a specified large-scale horizontal divergence, D.

This set of equations can be used to model a one dimensional column of air, well-mixed below the inversion, as it follows a Lagrangian trajectory determined by a specified large scale velocity, $\vec{\mathbf{V}}$. The absence of vertical shear in $\vec{\mathbf{V}}$ is fully justified as long as the layer remains well mixed. The other boundary conditions specified along the trajectories are the sea surface temperature (SST) and the above inversion profiles moist static energy and mixing ratio, $h_{I+}(z)$ and $q_{I+}(z)$.

The fluxes of h and q at the surface are given by the bulk relations

$$(F_h)_0 = -\rho_0 C_T V \Delta h_0$$

$$(F_q)_0 = -\rho_0 C_T V \Delta q_0$$

where $\Delta h_0 = h_M - h^*_{SST}$, $\Delta q_0 = q_M - q^*_{SST}$, h^*_{SST} and q^*_{SST} are the saturation moist static energy and the saturation mixing ratio computed at the sea surface temperature, and C_T is the bulk transfer coefficient.

The turbulent fluxes of h and q just below the inversion, as derived from heat and moisture budget equations in the inversion layer, are

$$(F_h)_{I-} = \rho_I(\overline{w'h'})_{I-} = -\rho_I w_e \Delta h_I - \Delta F_{RI}$$

$$(F_q)_{I-} = \rho_I(\overline{w'q'})_{I-} = -\rho_I w_e \Delta q_I$$

in which $\Delta h_I = h_{I+} - h_M$ and $\Delta q_I = q_{I+} - q_M$ are the jumps in h and q across the inversion, and ΔF_{RI} is the radiative flux divergence in the inversion.

The radiative fluxes in the mixed layer and the inversion are determined using two-stream radiative schemes for both the SW and LW radiation calculations.

To close the model equations, w_e must be parameterized based on assumptions about the turbulent structure of the mixed layer. As mentioned in the introduction, decoupling will only be predicted if w_e is determined directly in terms of w_*. Therefore we use a modified version of the entrainment parameterization of Turton and Nicholls (1987). This formulation, based upon aircraft measurements, has the same Richardson number dependence as many dry entrainment formulations:

$$\frac{w_e}{w_*} = \frac{A}{Ri}$$

The convective velocity scale, w_*, and the Richardson number are given by

$$w_*^3 = \frac{g}{z_I s_{vref}} \int_0^{z_I} \overline{w's_v'}dz$$

$$Ri = \frac{g z_I \Delta s_{vI}}{w_*^2 s_{vref}}$$

where s_v is the virtual dry static energy and s_{vref} is a reference s_v. Combining the above equations yields the entrainment velocity in terms of the integrated buoyancy flux:

$$w_e = \frac{A}{z_i \Delta s_{vI}} \int_0^{z_I} \overline{w's_v'}dz$$

For dry entrainment the constant A is usually set to 0.5 . Turton and Nicholls multiply A by a factor which parameterizes the entrainment-enhancing effects of evaporative cooling in cloud-top mixtures of dry above-inversion air and cloudy air. In this study we use a constant value $A = 2.5$.

Mixed-layer Experiments

In this study, the evolution of the boundary layer off the southern California coast following mean July climatological trajectories is modelled and analyzed. To concentrate on the downstream evolution of buoyancy fluxes, we have used a diurnally-averaged insolation, i.e. a solar zenith angle which produces the same insolation as the diurnal average. Since our radiation scheme treats the solar beam as diffuse, the low resultant zenith angle has no effect on the efficiency of the SW absorption.

The COADS 2° latitude x 2° longitude monthly data set, based on ship observations, is used for surface u and v velocities and SST. The divergence is derived from the u and v velocities. All of the COADS data is linearly interpolated for the model runs. The temperature above the inversion is estimated from ECMWF 850 mb July climatology with a specified lapse rate of

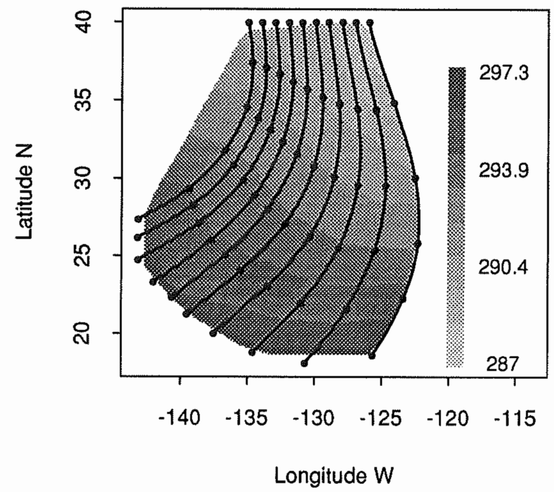

Figure 1: The ten climatological trajectories, starting at 40°N, are indicated by solid lines, with black dots indicating 24 hour periods. The COADS July SST is shaded.

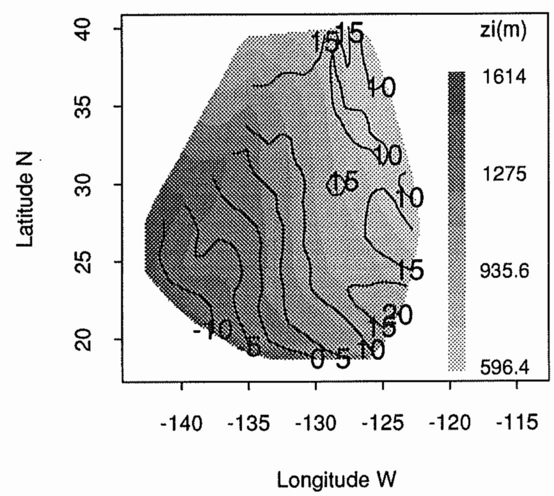

Figure 2: Cloud-top height, z_I, is shaded (m) and $(\overline{w's_v'})_{z_{B-}}$ is contoured (W/m^2)

6° K/km. The above-inversion mixing ratio is set to 4.0 g/kg based on observations from Riehl *et.al.* (1951).

The ten trajectories studied are started at latitude 40° N and longitudes varying from 126°W to 135°W. Each trajectory is initialized by computing a one-day back trajectory and letting the model evolve for one day, back to the starting position. This procedure allows the mixed layer to come into dynamical balance with its time-varying boundary conditions. Once initialized, all mixed-layer trajectories are followed for a five-day period. The trajectories and the COADS SST are plotted in Figure 1. All of the trajectories experience rising SST, and the easternmost trajectories, which start in the relatively cold water near the coast of California experience the fastest rise in SST.

Figure 2 shows the cloudtop height, z_I, shaded over the evolution of the ten trajectories. The general trend is for the cloudtop to rise as the layer evolves. This is a direct result of the fact that the SST is increasing at a faster rate than the temperature of air above the inversion, T_+. The gradual

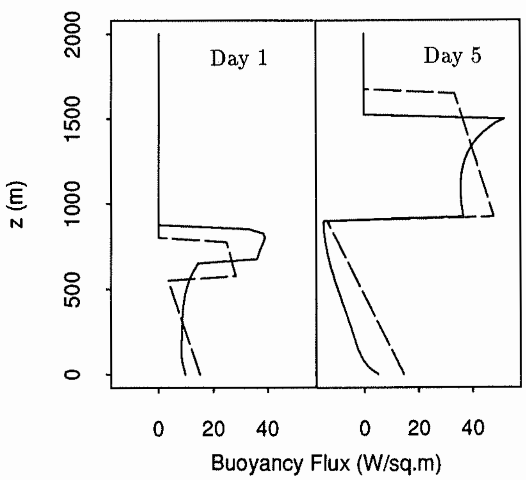

Figure 3: The profiles of $\overline{w's'_v}$ (W/m^2) at day 1 and day 5. The solid lines represent the full-radiation case and the dashed lines represent the idealized-radiation case.

destabilization of the lower atmosphere causes the cloudtop to rise. The prescribed large scale divergence also influences the cloud-top height. Most notably, the high divergence and accompanying subsidence covering the northeast part of the figure suppresses the growth of the layer in the first few days of the easternmost trajectories.

Cloudbase height, z_B, also rises along most trajectories, though about half as fast as z_I. The behavior of z_B, which is just the LCL for air at the surface, is determined by jumps in θ and q at the ocean surface. Since the rate of rise of the LCL is slower than that of z_I, the cloud is thickening with time as the model CTBL evolves downstream.

The contoured buoyancy flux just below cloudbase is also shown in Figure 2. The buoyancy flux at this level diminishes with time, and decoupling is diagnosed on the line $(\overline{w's'_v})_{z_{B-}} = 0$. For two of the easternmost trajectories decoupling is not predicted within the 5 day simulation time, while the westernmost trajectories decouple 3 days into the simulation. Decoupling in these trajectories is well correlated with cloud-top height and even more strongly correlated with the cloud thickness; In particular, the decoupling line is encountered at about $z_I - z_B = 400$m. It is noteworthy that the decoupling line coincides quite well with a region of rapid downstream decrease in mean cloudiness deduced from satellite climatologies (Betts *et.al.*, 1992). When $(\overline{w's'_v})_{z_{B-}} < 0$, the mixed-layer model is no longer valid. In fact, diurnal decoupling would render use of a mixed-layer model questionable during midday even much closer to the coast. One might hope that the nocturnal recoupling may allow the diurnally averaged mixed-layer dynamics to still represent the mean trends over a day, but this is an open question.

To help illustrate the evolution of $(\overline{w's'_v})_{z_{B-}}$ and its relation to z_I and z_B, we will consider a single trajectory starting at 40°N, 130°W. For simplicity an idealized radiation profile is used with a constant net upward radiative flux of 40 W/m^2 at cloud top and 0 W/m^2 below cloud top. The results are qualitatively similar to the diurnally averaged radiation scheme, indicating that systematic changes in radiative heating and cooling are relatively unimportant in producing the downstream decrease in $(\overline{w's'_v})_{z_{B-}}$.

Figure 3 shows the buoyancy flux profile at the end of days 1 and 5 for both the idealized and the interactive radiation runs started at at 40°N, 130°W. The cloud is demarcated by the large flux discontinuities at cloudbase and cloudtop. The idealized case has a piecewise-linear buoyancy flux profile because of the absence of radiative flux divergence except at cloudtop, but otherwise, the fluxes are qualitatively similar. In both cases the cloud rises and becomes thicker with time and the day 5 profiles indicate decoupling because $(\overline{w's'_v})_{z_{B-}} < 0$.

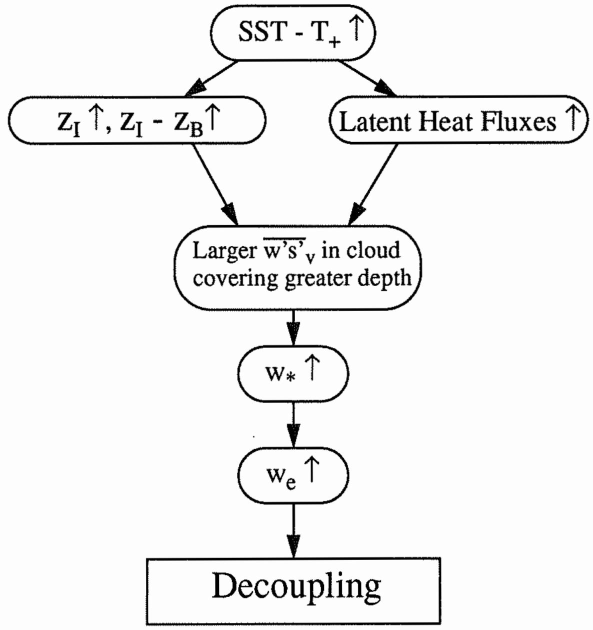

Figure 4: Conceptual model of decoupling due to the rise in SST.

The tendency for decoupling is driven by the rise in SST. A conceptual model for decoupling is depicted in Figure 4. As noted previously, the increase in SST relative to the temperature above the inversion tends to increase the cloud thickness by pushing up the inversion while the cloud base rises more slowly. At the same time q^*_{SST} rapidly increases, while q_+ is constant. This causes the jumps in q at the surface and at the inversion to increase, and the moisture fluxes in the mixed layer to increase. The increasing moisture fluxes increase the size of the positive in-cloud buoyancy flux due to a larger cloudbase jump in buoyancy flux.

Larger and deeper positive in-cloud buoyancy fluxes increase the vigor of convection, thus increasing w_* and driving more entrainment across the inversion. Increased entrainment decreases the subcloud buoyancy fluxes and promotes decoupling. Thus the increasing SST as well as the consequent rise of SST relative to T_+ drives the tendency towards decoupling. Increasing cloud thickness will also lead to increased SW heating in the cloud. This stabilizing heating will also promote decoupling, but even without such effects, the CTBL will decouple because of the rising SST, as demonstrated by the idealized-radiation case.

It is interesting to compare the results to a steady-state calculation based on the instantaneous boundary conditions. An idealized-radiation simulation with boundary conditions fixed to those corresponding to the end of day 3 is run out to a near steady-state at day 10 using the idealized radiation profile (Figure 5). The steady-state solution is fully decoupled with $(\overline{w's'_v})_{z_{B-}}$ well below zero. The tendency toward decoupling

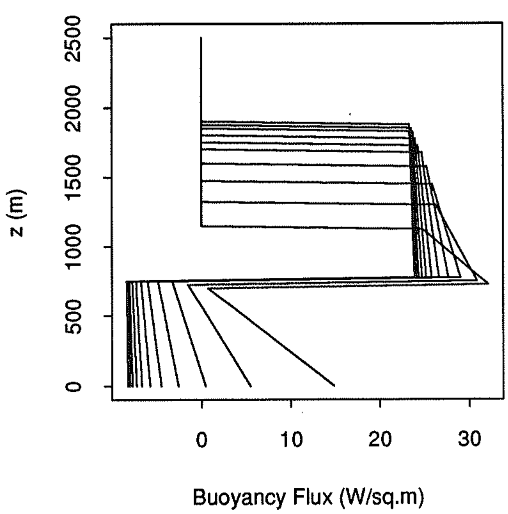

Figure 5: The $\overline{w's'_v}$ profiles for an idealized-radiation simulation with boundary conditions fixed at 27°N 132°W, corresponding to day 3 for the Lagrangian simulation started at 40°N 130°W. Simulation days 0-10 are plotted.

can be understood as primarily due to thickening of the cloud in the steady state and secondarily a reduction in surface buoyancy fluxes. As pointed out by Schubert *et.al.* (1979, Part II), the timescale for inversion height to adjust to changes in the CTBL is $O(D^{-1})$, which is several days. Thus the Lagrangian inversion height always lies significantly below the steady-state inversion height. This also points to the importance of a Lagrangian perspective to cloud-topped boundary layers. For example, a layer carried more slowly to warmer SST's would track more closely to the steady-state solution and tend to decouple geographically (but not necessarily temporally) sooner.

Conclusions

The criterion $(\overline{w's'_v})_{z_{B-}} = 0$ is presented as an indicator of the onset of decoupling in a Lagrangian mixed-layer model. Using July climatological data of coastal California, a set of ten mixed layers are simulated for 5 day trajectories following the climatological surface winds. Decoupling is indicated for the western trajectories after 3 days and takes progressively longer toward the east. Two of the mixed layers do not decouple within the 5 day simulation period. The decoupling correlates most closely with cloud thickness. The cloud thickness increases with time because of the rise in cloud top due to increasing SST, and the relatively slower rise of cloudbase. The relative thickness of the cloud modifies the buoyancy flux profile causing the buoyancy fluxes below cloudbase to become negative and decoupling to occur.

The effects of the diurnal cycle and drizzle depletion of the cloud layer substantially modify the timing and physics of decoupling, but are not necessary to produce decoupling. The fundamental effect is the downstream increase in SST, which forces a downstream rise in inversion height and cloud layer thickness, as well as large downstream latent heat fluxes. Both of these effects promote decoupling due purely to the internal convective dynamics of a mixed layer.

In a companion presentation, the role of a decoupled cloud layer as a intermediate state in the transition of stratocumulus to trade cumulus is examined.

Acknowledgements: This material is based upon work supported under a National Science Foundation Graduate Fellowship and has been partially supported through ONR grant N0014-90-J-1136 and NSF grants ATM8806789 and ATM8858846.

References

Betts, A. K., 1989: The diurnal variation of California coastal stratocumulus from two days of boundary layer soundings. *Tellus*, **42A**, 302-304.

Betts, A. K., P. Minnis, W. Ridgway, and D. F. Young, 1992: Integration of satellite and surface data using a radiative-convective oceanic boundary-layer model. *J. App. Meteor.*,**31**, 340-350.

Bougeault, P., 1985: The diurnal cycle of the marine stratocumulus layer: A higher-order model study. *J. Atmos. Sci.*, **42**, 2826-2843.

Chen, C., and W. R. Cotton, 1987: The physics of the marine stratocumulus-capped mixed layer. *J. Atmos. Sci.*, **44**, 2951-2977.

Lilly, D. K., 1968: Models of cloud-topped mixed layers under a strong inversion. *Quart. J. Roy. Meteor. Soc.*, **94**, 292-309.

Nicholls, S., 1984: The dynamics of stratocumulus: Aircraft observations and comparisons with a mixed layer model. *Quart. J. Roy. Meteor. Soc.*, **110**, 783-820.

—, and J. D. Turton, 1986: An observational study of the structure of stratiform cloud sheets: Part II. Entrainment. *Quart. J. Roy. Meteor. Soc.*, **112**, 461-480.

Riehl, H., T. C. Yeh, J. S. Malkus, and N. E. LaSeur, 1951: The north-east trade of the Pacific Ocean. *Quart. J. Roy. Meteor. Soc.*, **77**, 598-626.

Schubert, W. H., J. S. Wakefield, E. J. Steiner, and S. K. Cox, 1979: Marine stratocumulus convection. Part I: Governing equations and horizontally homogeneous solutions. *J. Atmos. Sci.*, **36**, 1286-1307.

—, —, —, and —, 1979: Marine stratocumulus convection. Part II: Horizontally inhomogeneous solutions. *J. Atmos. Sci.*, **36**, 1308-1324.

Turton, J. D., and S. Nicholls, 1987: A study of the diurnal variation of stratocumulus using a multiple mixed layer model. *Quart. J. Roy. Meteor. Soc.*, **113**, 969-1009.

CONVECTIVE MIXING IN STRATOCUMULUS-TOPPED BOUNDARY LAYERS OBSERVED DURING FIRE

Qing Wang and Bruce A. Albrecht

Meteorology Department, Penn State University
University Park, PA 16802

1. INTRODUCTION

The decoupling of the cloud layer and the subcloud layer has been the focus of many stratocumulus boundary layer studies. One detailed observational study on this subject was conducted over the North Sea near the UK (Nicholls, 1984). Hignett (1991) also documented a decoupled case using tethered balloon data observed over the San Nicolas Island during the First International Satellite Cloud Climatology Project Regional Experiment (FIRE). Both of these studies found a solid stratocumulus deck below the capping inversion, although conditions that influence the cloud layer may differ for these two studies. In this study we analyze aircraft data from the NCAR Electra obtained during the FIRE intensive marine stratocumulus observations off the coast of California (Albrecht *et al*, 1988). The study focuses on the analysis of the mixing processes inside the boundary layer, both for decoupled and well mixed cases. In the decoupled case the cloud cover was broken and patchy, typical of the cloud pattern observed during FIRE. Turbulent statistics and the turbulent kinetic energy (TKE) budget are analyzed and compared with previous studies. The effects of drizzle on decoupling are also discussed.

2. GENERAL CONDITIONS, INSTRUMENT AND DATA PROCESSING

Data collected from the NCAR Electra on two days are analyzed. On June, 30 (Flight 2), the upper one third of the boundary layer was occupied by a mixture of thin, broken and solid clouds, below which scattered cumulus were observed to extend up to the main cloud deck. Drizzle and showers were also numerous. Mixing extended from the cloud top to about 270 meters above the sea surface. The lower boundary of the mixed layer was marked by a discontinuity in the profiles of q_T and Θ_e. Flight 3 (July, 3) began after sunset in patchy solid/broken clouds that gradually became more and more solid. No obvious lower cumuli or drizzle were evident during this flight. Mixing extended from the cloud top down to the surface. Flight information and surface meteorological conditions are listed in Table 1.

Turbulent quantities were calculated from data that were sampled at 50 Hz and then filtered to give 20 Hz data. Temperature was measured by a Rosemount sensor located on the nose boom. It is found to be less affected by wetting in the cloud layer (Betts, 1990) than other temperature sensors on the aircraft. The absolute humidity was measured with a fast-response Lyman-alpha hygrometer calibrated against a dewpoint sensor. Fast-response liquid water was measured using both a King liquid water probe and a Knollenberg Forward Scattering Spectrometer Probe (FSSP). Unfortunately, neither instrument provided accurate liquid water measurements. The King probe showed signs of malfunctioning, and the FSSP was in need of recalibration (Paluch and Lenschow, 1991). All 20 Hz Data were highpass filtered before calculating the turbulent statistics. This filtering eliminates influence of scales larger than 3 km.

3. CLOUD BASE HEIGHT vs. THE LIFTING CONDENSATION LEVEL (LCL)

The sounding legs of a flight usually cover a horizontal distance of about 100 km. This makes it very difficult to obtain an accurate vertical profile at a fixed point. By computing the lifting condensation level (LCL) using observations obtained near the surface and comparing it with the observed cloud base height, we can exam the extent of mixing. This method avoids the ambiguities of the aircraft soundings. If the boundary layer is perfectly mell mixed, the LCL would agree well with the cloud base height. In a decoupled boundary layer, however, a difference in the two heights is expected.

Temperature and dewpoint at 1 Hz from the lowest turbulence legs (~50 m above the sea surface) are used to calculate the LCL. The cloud base height was measured by an upward-looking lidar. A comparison between the two heights is shown in Fig.1. In Fig.1a, the actual cloud base height is about 200-400 meters higher than the calculated LCL, suggesting a very decoupled boundary layer in Flight 2. Close agreement is seen in Fig.1b. Flight 3 is therefore believed to be a well mixed case. These results are consistent with our previous observations from the sounding data, where the discontinuity in Θ_e and q_T marked the cloud mixed layer base.

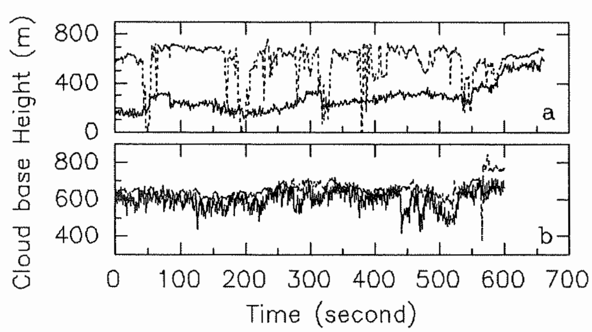

Fig. 1. Time series for the lidar observed cloud base heights (dashed line) and the calculated LCL (solid line). Observations were made from 21:40:00 to 21:51:00 (UTC) in Flight 2 (a), and from 01:35:00 to 01:45:00 (UTC) in Flight 3 (b).

4. BUOYANCY AND MOISTURE FLUXES

Table 1. Flight information and surface conditions.

Flight No.	Start Time (UTC)	End Time (UTC)	Z_i (m)	Cloud base(m)	Mixing layer depth(m)	Sea Surface Temp.(K)	Surface Relative Humid.(%)	Surface Wind Speed (m/s)	Surface wind Dir. (deg.)
2	18:54	23:48	920	610	670	17.7	89.3	4.1	300
3	01:16	06:04	860	630	860	17.1	76.4	10.1	322

The buoyancy and moisture flux profiles as functions of the normalized height are shown in Fig.2. These are calculated by the eddy correlation method using highpass-filtered 20 Hz data. The liquid water effect was not included in the estimation of Θ_v flux because of the uncertainties in the liquid water sensors. The drizzle flux and the liquid water flux are not calculated for the same reason. From the results of previous observations in the same area (Broast *et al*, 1982), the average liquid water flux is about 5 Wm^{-2}. The drizzle flux changes considerably with individual cases, its magnitude is usually smaller than 10 Wm^{-2}, although in some extreme cases it may reach 50 Wm^{-2}.

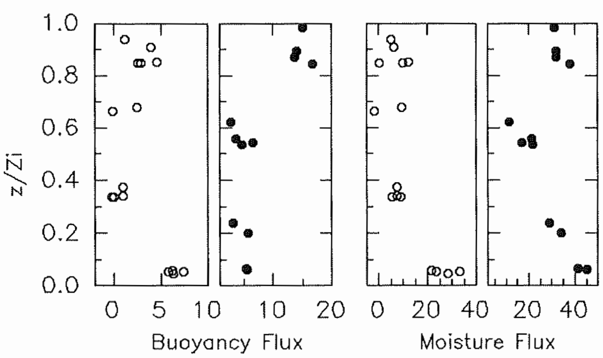

Fig. 2. Buoyancy and moisture flux profiles for Flight 2 (∘) and Flight 3 (•).

One noticeable feature in Fig.2 is the maximum buoyancy flux below the cloud top in both flights, indicating a turbulent field that is driven by the in-cloud buoyancy. However, the magnitudes of the maxima for the two flights differ significantly. Another maximum is usually found near the surface, with the exception of Flight 3. The surface buoyancy flux for Flight 3 is about 5 Wm^{-2}. In fact it is smaller than any other observed surface buoyancy flux during FIRE. The air-sea temperature difference is about -2°C in Flight 2, while in Flight 3 it is only about -0.5°C, which will cause the surface sensible heat flux in Flight 2 to be 4 times as large as that in Flight 3.

The largest moisture flux is seen near the surface in both flights. The behavior of this quantity inside the cloud layer is not certain, due to the exclusion of the liquid water flux and the drizzle flux and the uncertainties associated with the response of the velocity sensors and the Lyman-alpha hygrometer in the presence of intermittent clouds (Paluch and Lenschow, 1991), such as in the broken cloud of Flight 2 and the ragged cloud top of Flight 3 .

5. TURBULENT KINETIC ENERGY (TKE) BUDGET

The balance between the production and the dissipation of turbulent kinetic energy (TKE) is very important in controlling the internal mixing processes in the boundary layer. For a horizontally homogeneous situation the TKE balance may be written as:

$$\frac{\partial E}{\partial t} = \underbrace{\frac{g}{\Theta_v}\overline{w'\theta'}_v}_{B} - \underbrace{\frac{\partial \overline{w'E}}{\partial z}}_{T} - \underbrace{\frac{\partial \overline{w'p'}}{\partial z}}_{P} + \underbrace{\left[\overline{w'u'}\frac{\partial \overline{U}}{\partial z} + \overline{w'v'}\frac{\partial \overline{V}}{\partial z}\right]}_{S} - \underbrace{\epsilon}_{D} ,$$

where B, T, P, S and ε are the buoyancy production, turbulent transport, pressure transport, shear production and the dissipation rate, respectively. E is the total turbulent kinetic energy. For the convective boundary layer, the time change for TKE is usually negligible, leaving a balance among the terms on the right hand side of the equation. All but the pressure term can be deduced directly from the data. The dissipation rate is estimated from the spectra in the inertial subrange. The residual term I is defined as -(B+S+T-ϵ) and is the pressure transport term (P) plus the error.

There are some limitations in using the aircraft data to define the TKE budget. Since the vertical gradients of the observed variables are needed in order to obtain T and S, uncertainties are inevitable because of ambiguities in the vertical profiles due to the coarse vertical resolution of the data. Despite this, a broad picture can still provide us with some useful information. Fig.3 shows the terms of TKE budget from Flight 2 and 3. These terms are averages for the entire data set for each flight. One outstanding feature shown here is the balance between the buoyancy and dissipation term and between the turbulent transport and pressure scrambling term (the residual term). This is especially true in

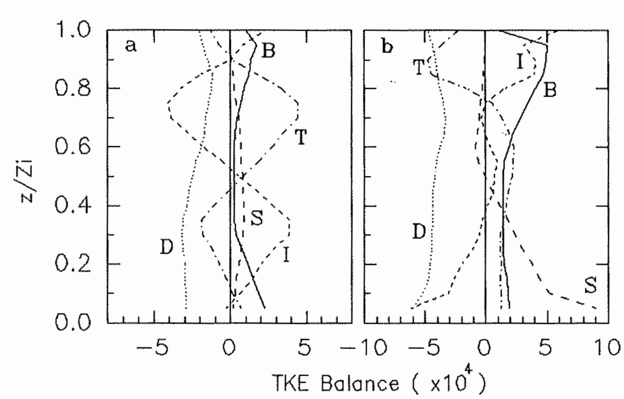

Fig. 3. The TKE balance. The terms are described in the text. (a) Results from Flight 2. (b) As (a), but for Flight 3.

the cloud layer, where shear production is negligibly small.

In Flight 3, turbulence near the surface is largely generated by shear, while surface buoyancy plays a secondary role. The shear effect extends up to about 0.2Zi as estimated from the value of -L/Zi in Table 2, where L is the Monin-Obukhov length obtained from the surface layer quantities. In the cloud layer, however, buoyancy provides the main TKE source. The turbulent transport term acts as a sink of TKE in the cloud layer, while the pressure term increases TKE, possibly a direct effect of the strong capping inversion. All terms are small in the region between 0.2Zi to 0.7Zi. In Flight 2, we see a weaker turbulence field than that in Flight 3. All the terms in the budget equation are small and in delicate balance. In the upper part of the cloud layer, where buoyancy is relatively large, turbulent transport moves TKE downward to the layer below and the T term remains a source until about 0.5Zi. Ambiguities exist in the middle of the boundary layer as to where the cloud mixing layer extends. This will be discussed in the next section.

The findings in this study are similar to those of Nicholls (1989) in the cloud mixed layer, if we neglect the lower part of the observations from Flight 3 where the shear effect is relatively large. In the Nicholls' cases, the in-cloud buoyancy was very large, about twice that of Flight 2 and about the same magnitude as in Flight 3. The cloud mixed layer in his cases extended to about 480 m below the cloud top. In Flight 3, however, the surface shear effect extends upward to 0.2Zi (Table 2). Consequently, the cloud buoyancy driven mixed layer would at least extend from the cloud top downward to 0.2Zi above the surface, since the entire boundary layer is well mixed. Therefore the cloud mixed layer would have a depth of at least 0.8Zi (about 690 m). However, since Nicholls' observations were made during the day, solar warming of the cloud layer and drizzle may both act to stabilize the boundary layer and thus prevent mixing. A comparison between the cloud mixed layer depth of Flight 3 and that of Nicholls' indicates that the thermodynamic stratification is equally as important as the in-cloud buoyancy in determining the vertical extent of mixing.

6. Discussion

a. Mixed Layer Scaling

As we can see from the results presented earlier in this paper, buoyancy driven convection is characteristic of the stratocumulus-topped boundary layer, especially in the cloud mixed layer. Mixed layer scaling for the dry convective boundary layer, in which the layer integrated buoyancy plays the major role, is a favorable candidate to scale the cloud topped boundary layer. The w_* used here is defined in the same way as in Nicholls (1989). The scaling parameters thus calculated are listed in Table 2.

The scaled vertical velocity variance from the two flights studied here are plotted together against the distance from the cloud top scaled with the cloud mixed layer depth (Fig.4). Also plotted in Fig.4 are results from Hignett (1991)

Table 2. Mixed layer and surface layer scaling parameters.

Flt. No.	w_* (m/s)	Θ_* (K)	q_* (g/kg)	u_* (m/s)	$-L/Z_i$
2	0.50	0.011	0.010	0.06	0.0
3	0.85	0.025	0.016	0.21	0.21

and the fitted curve from Lenschow and Stephens (1980) for the dry convective boundary layer (plotted upside down). Although the data show considerable scatter, the dashed line is still a fairly good description, except near the mixed layer base where there are large excursions. These excursions may arise because of the different boundary conditions between the cloud and dry convective boundary layers. The similarity of all these cases indicate the convective nature of the cloud-topped boundary layer, whether it is well mixed or decoupled, and regardless if it is covered by solid or broken clouds.

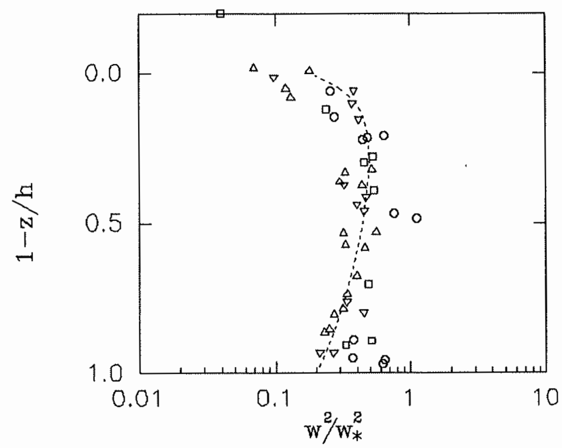

Fig. 4. Vertical velocity variance (scaled by the convective velocity) against distance from cloud top normalized by the cloud mixed layer depth. (o — Flight 2; ▽— Flight 3; □— decoupled case from Hignett (1991); △— well-mixed case from Hignett (1991); Dashed line— from Lenschow and Stephens (1980) for dry convective boundary layer, plotted upside down.

b. Horizontal and Vertical Complications Observed During FIRE

The effects of fractional cloud cover are clearly evident in the time series. Fig.5 shows observations from one horizontal flight leg at about 80 m below the averaged cloud top. The liquid water content from the King probe is used to show the intermittency of the cloud cover. Comparing time (and therefore space, since the aircraft was flying at 100 ms^{-1}) variations of w, Θ_v, and q to that of liquid water content, we notice there are correlations with the presence and absence of the cloud patches. Furthermore, less intense vertical velocity fluctuations, higher Θ_v and lower q are observed in the clear patches and illustrate the influence of the above inversion air on the structure of these clear patches. Differences in the turbulence structure are then expected between the cloudy and the clear

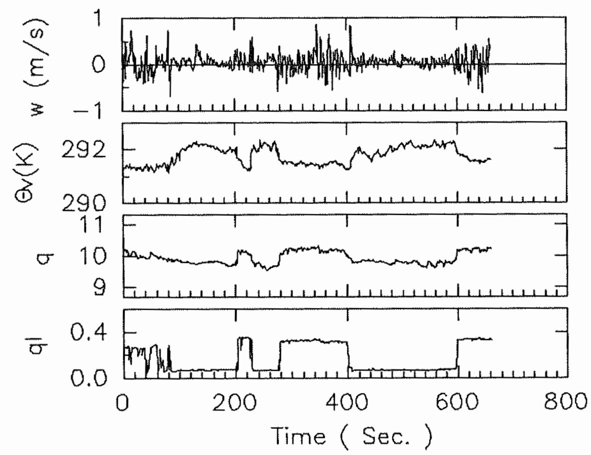

Fig. 5. Time series from Flight 2 (from 20:21:00 to 20:32:00 UTC). q and q_l are absolute humidity and the liquid water content (in unit of gm^3), respectively.

patches. This large horizontal variability would impose requirement of longer turbulence legs in order to obtain the same accuracy on the turbulent statistics compared with a horizontally more homogeneous situation (Lenschow and Stankov, 1986). The intermittent cloud also cause malfunctions in the velocity sensor, thus casting more doubt on the leg averaged statistics. The scattered points in the cloud layer of Flight 2 is an example of the effect of the broken cloud. A similar pattern is also seen on a lower leg at about 150 m below the cloud top.

Drizzle was frequently observed during Flight 2. In addition to its effects on the cloud microphysical structure, drizzle stabilizes the boundary layer by cooling the subcloud layer through evaporation. This effect results in the decoupling of the boundary layer that inhibits the internal mixing processes (Broast, *et al*, 1982; Nicholls, 1984). Our sounding profiles penetrated through drizzle events also demonstrate this decoupling effect.

If the extent of vertical mixing is affected by the presence of drizzle , large horizontal variations in vertical mixing are then expected due to the sporadic horizontal distribution of drizzle. This is illustrated in Fig.6., where the LCL estimated from observations at 310 m above the

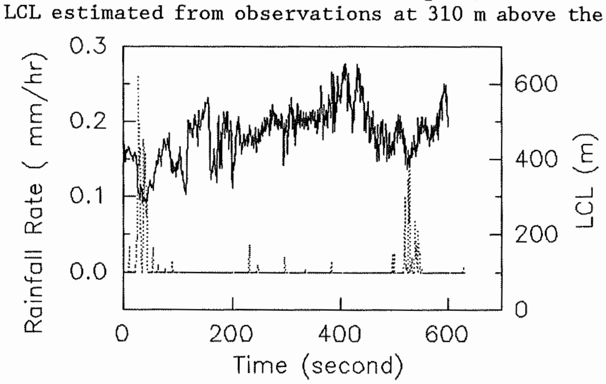

Fig. 6. Time series of rainfall rate (dotted line) and the LCL calculated from observations between 19:40:00 and 19:50:00 UTC of June 30 at about 310 m above the sea surface (solid line).

surface is plotted together with the drizzle rate (courtesy of Mark A. Miller). Since the average cloud base is about 610 m, the boundary layer is generally not well mixed down to this flight level. If we use the difference between the cloud base height and the LCL to diagnose the extent of mixing qualitatively, then the weakest mixing appears to be related to relatively significant drizzle rates. This is seen in Fig.6 at about 50 seconds and 550 seconds into the time series. The strongest coupling appears to coincide with negligible drizzle at about 430 second. The drizzle, however, is not the only mechanism that affects the extent of mixing. The availability of TKE generation, is also a crucial factor (as seen in the buoyancy flux difference between Flights 2 and 3 in Fig.2). Horizontal variations in the buoyancy generating processes can not be separated from the drizzle effects in our measurements. Nevertheless, the extremely low LCL at the two locations are clearly the effect of drizzle.

7. SUMMARY

Two cases from the 1987 FIRE experiment were discussed in this study. We focused on defining the likelihood and the intensity of the internal mixing, rather than describing the individual physical mechanisms that drive this mixing. Conditional sampling studies currently in progress will be used to study the mechanisms. The horizontal inhomogeneity induced by the broken cloud cover and drizzle requires that special care be taken in analysis of the data as well as in formulation of model parameterizations.

8. ACKNOWLEDGMENTS

This work was supported by the National Science Foundation Grant ATM-8909947.

9. REFERENCE

Albrecht, B. A., D. A. Randall and S. Nicholls, 1988: Observations of marine stratocumulus during FIRE. *Bull. Amer. Meteor. Soc.*, **69**, 618-626.

Betts, A. K., 1990: A cloudiness transition in a marine boundary layer. *J. Atmos. Sci.*, **47**, 1480-1497.

Broast, R. A., J. C. Wyngaard and D. H. Lenschow, 1982: Marine stratocumulus layers. Part II: Turbulence budgets. *J. Atmos. Sci.*, **39**, 818-836.

Hignett P., 1991: Observations of the Diurnal Variation in a cloud-capped marine Boundary layer, *J. Atmos. Sci.*, **48**, 1474-1482.

Lenschow, D.H., and B. Boda Stankov, 1986: Length scales in the convective boundary layer. *J. Atmos. Sci.*, **43**, 1198-1209.

———, and P. L. Stephens, 1980: The role of thermals in the convective boundary layer. *Bound.-Layer Meteor.*, **19**, 509-532.

Nicholls, S., 1984: The dynamics of stratocumulus: aircraft observations and comparisons with a well-mixed model. *Quart. J. Roy. Meteor. Soc.* **111**, 391-426.

———, 1989: The structure of radiatively driven convection in stratocumulus. *Quart. J. Roy. Meteor. Soc.* **115**, 487-512.

Paluch, I.R., and D.H. Lenschow, 1991: Stratiform cloud formation in the marine boundary layer. *J. Atmos. Sci.*, **48**, 2141-2158.

HIGH-FREQUENCY VARIABILITY OF TROPICAL CONVECTION OVER THE MARITIME CONTINENT

Ryuichi Kawamura and Atsushi Takeda

National Research Institute for Earth Science and Disaster Prevention
Tsukuba, Ibaraki 305, Japan

1. Introduction

High-frequency variations of tropical convection around the maritime continent are investigated utilizing brightness temperature (TBB) by the Geostationary Meteorological Satellite (GMS). The TBB provides a useful measure of active convection in tropical regions since low values correspond to large amounts of high cloud cover, indicating the dominance of tropical convection. One of the largest regions of convective heat source in the tropics is the maritime continent, and the variations of large-scale convective heating influence the east-west circulation in the tropics and further extratropical atmospheric circulation. However, notable powers of the intraseasonal variations are not found there. It is confirmed in this study that this is because the intraseasonal variations are strongly modified by an effect of a dominance of diurnal variation.

2. Dominant high-frequency variations

Figure 1 shows power spectra of TBB over regions A and B during March to May 1986. Here region A is located in the Borneo island, whereas region B is located in the tropical western Pacific. It is clear that high-frequency variations shorter than synoptic scale are dominant over the island within the maritime continent, while low-frequency (intraseasonal) variations occupy a large part of total variance of TBB over the tropical western Pacific region. The diurnal variation dominates over the entire maritime continent and the ratio of 1 day period variance to the total variance is greater than 20%. A 2-3 day variation is also observed over the maritime continent and the western Pacific. The 3-5 day (synoptic scale) variation dominates over the western Pacific from the east of the Philippines to the date line and is not very clear over the maritime continent. This variation seems to correspond to the easterly waves.

3. Relationship with orographic effect

Figure 2 shows the dependence of the integrated power spectra of TBB for high-frequency ranges on the horizontal and vertical scales of the islands located within the maritime continent. The power of diurnal variation tends to be small over islands within a horizontal scale of about 300 km. It is little seen, however, that the amplitudes of the 2-3 day and the 3-5 day variations depend on the spatial scale of the islands located within the maritime continent. The variations with 5-10 day (and 7-12 day) scale, which are rather quasi-periodic phenomena, tend to be suppressed over the islands beyond a scale of about 700-900 km. These quasi-periodic variations reflect the behavior of super cloud cluster (SCC) with a scale of 1000-2000 km and of tropical depression. It is inferred that these disturbances are strongly modified when they move over the land greater than a scale of 700-900 km. The 15-30 day variation on the intraseasonal time scale is not dominant over the entire maritime continent and thus independent of the spatial scale of the islands.

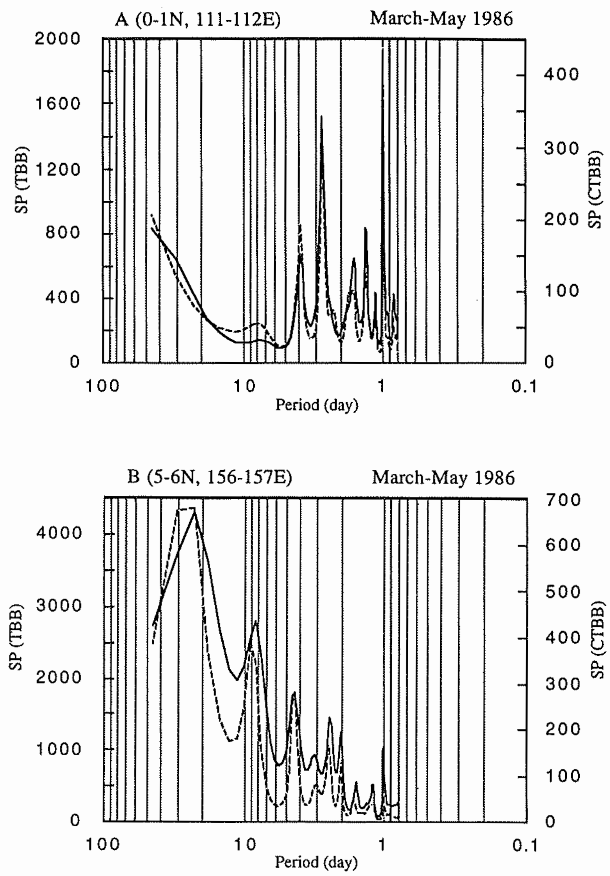

Fig. 1 Power spectra of TBB over region A (0-1°N,111-112°E) and region B (5-6°N,156-157°E) during the period from March to May 1986.

It is suggested that although a hierarchy structure of the SCC group is composed of the SCC and cloud cluster, the spatial scale of the land over which the disturbances are modified by orographic effect varies with an individual structure having a corresponding time scale, and as a consequence a modification of internal structure of the SCC group occurs over the maritime continent.

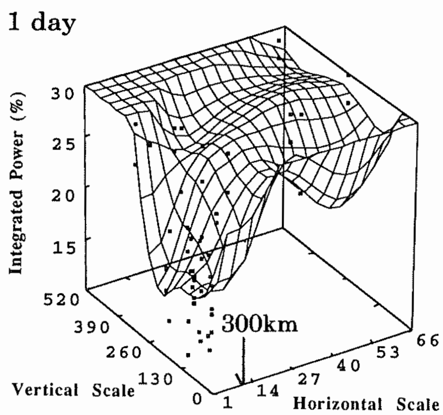

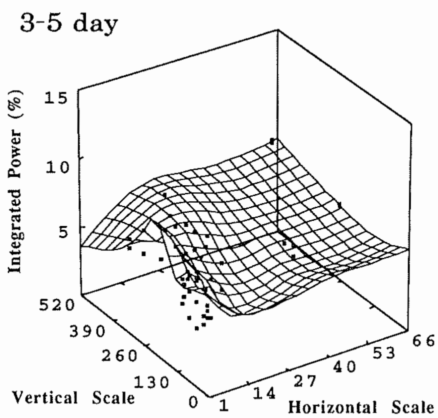

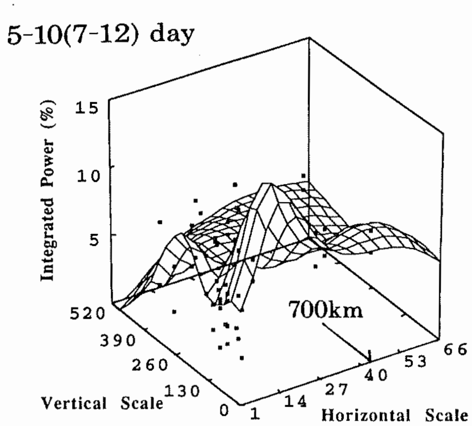

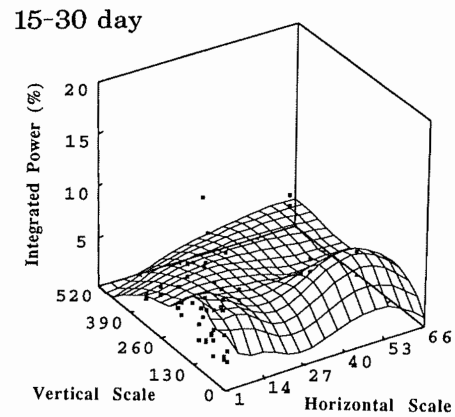

Fig. 2 Three dimensional surface diagrams representing the dependence of integrated power spectra of TBB for high-frequency ranges on the horizontal and vertical scales of the islands within the maritime continent.

GRAVITY WAVES DETERMINING MESOSCALE STRUCTURES OF CLOUD CONVECTION

Jerzy M. Radziwill

Institute of Geophysics, University of Warsaw
Pasteura 7, 02-093 Warsaw, Poland

1. INTRODUCTION

Convective clouds often develop in wave-like patterns, visible for example in satellite images. They can be bands of convective clouds originating from a localized source, with a length scale of a few tenths kilometers (Erickson and Whitney, 1973; Radziwill, 1990), homogeneous fields of wave-like cloud convection with the scale of few kilometers (Radziwill, 1988), narrow wave trains propagating on a long distance (Stobie et al., 1983), clouds patterns generated by orographic effects. Generally, these wave patterns are perpendicular to the wind or wind shear direction, as opposite to the cloud streets. There are several hypothetical mechanisms explaining development of such a wave patterns in relation to gravity waves, e.g.: convection waves (Hauf, 1989), wave-CISK (Lindzen, 1974), and other.

In the following, very general rules are offered concerning gravity wave propagation for typical atmospheric conditions in relation to the wind speed and direction. Propagation of gravity waves is affected by the presence of wind in a way similar to the Doppler effect for acoustic waves. However, for gravity waves the effect is more complicated. The results are based on linear theory and can be useful in analyzing and predicting development of wave-like cloud patterns, despite the specific mechanism of the gravity wave - clouds interaction.

2. THEORETICAL BACKGROUND

In the linear theory the vertical distribution of amplitude of a plane, monochromatic gravity wave is described by the Taylor-Goldstein equation:

$$\tilde{W}'' + \left[\left(\frac{N^2}{\tilde{\omega}^2} - 1 \right) \tilde{k}^2 - \frac{\tilde{\omega}''}{\tilde{\omega}} \right] \tilde{W} = 0 \qquad (1)$$

$$\tilde{\omega} = c - u\,\tilde{k} = (c-u)\,k - i\,u\,\kappa \qquad (2)$$

where $\tilde{W} = (\rho_0/\rho_s)^{1/2}\,\tilde{w}$, w(z) - amplitude of the vertical velocity, $\rho_0(z)$ - density, ρ_s - constant, N(z) - Brunt-Väisälä frequency, $\tilde{k} = k + i\,\kappa$ - complex wave number, $\tilde{\omega}(z)$ - intrinsic frequency, c - phase velocity, u(z) - wind projection in the direction of wave propagation, z - height, prim (') - differentiation in respect to height, and tilde (~) - potentially complex variable. Derivation of this equation can be found in various textbooks, (e.g. Gossard and Hook, 1975).

Consider gravity waves with real frequency and phase velocity, but a potentially complex wave number. This means that wave can decay in horizontal because of energy radiation upward into the upper layers of atmosphere. The rate of decay can be best characterized by the relative decay coefficient d (rate of decay per 1 wave length) defined as: $d=\lambda/l=2\pi\kappa/k$, where $\lambda=2\pi k^{-1}$ - wave length, and $l=\kappa^{-1}$ - e-folding distance.

The zero-amplitude lower boundary condition is assumed at the ground level, and a radiative condition is assumed at the top of model domain (zero amplitude of the solution component corresponding to the downward energy flux). With these boundary conditions, solutions of (1) exist only for combinations of wave parameters (σ-k or c-k) fulfilling specific dispersive relation. The dispersive relation, and corresponding solution of (1), can be found as a function of σ or c. It can be done for any vertical profile of wind and temperature with a numerical procedure similar to the shooting method. For the model atmosphere consisting of layers where coefficients of (1) are constant it can be done by solving numerically an appropriate algebraic equation. Appropriate numerical codes have been developed and used in the present study. It was verified empirically, that in most circumstances results are not sensitive to the choice of the upper boundary level.

3. RESULTS FOR MODEL ATMOSPHERE

The model atmosphere consists of 3 layers and inversion as indicated in Fig. 1. Basic calculations were done for the Brunt-Väisälä frequencies: $N_1 = 0.00\ s^{-1}$, $N_2 = 0.01\ s^{-1}$, $N_3 = 0.02\ s^{-1}$ and inversion $\Delta T = 3^{o}C$. Wind is constant with height. A plane, monochromatic gravity wave is generated by a point source (e.g. dissipating storm or convective cloud), and can propagate horizontally in various directions.

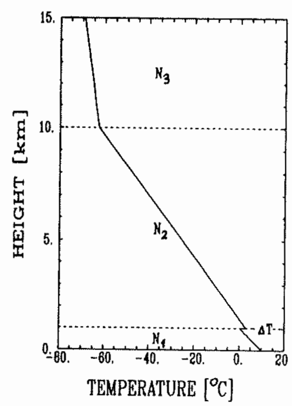

Fig. 1. *Model atmosphere*

For the direction perpendicular to the wind vector, the wind projection is zero, and results are similar to these discussed by Gossard (1962). There is a characteristic set of wave parameters (c_*, ν_*, k_*) clearly defined as the transition point between zero and non-zero decay coefficient in Fig. 2. It was verified experimentally that these parameters are not

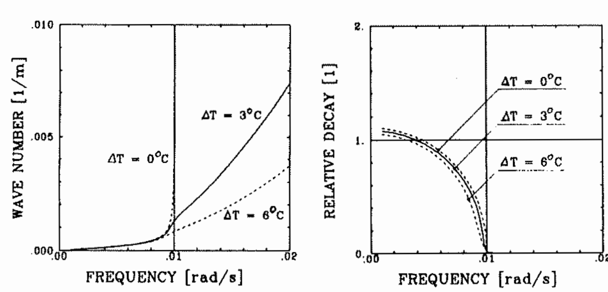

Fig. 2. *Dispersive relation for various inversions (ΔT), for the zero-wind case.*

sensitive to the stratification (N_3) in the stratosphere. Phase velocity (c^*) and wave number (k^*) at the characteristic point depend on the strength of inversion, whereas the characteristic frequency is not sensitive to it, and equal approximately to the average Brunt-Väisälä frequency in the troposphere (N_2). For the typical stratification considered in this study $c^* = 7.92$ m/s, $\nu^* \simeq N_* = 0.01$ s^{-1}, ($T^* \simeq 10$ min), and $k^* = 1.26$ km^{-1}, ($\lambda^* \simeq 5$ km).

Equation (1) depends on the wind speed in the direction of wave propagation only through the complex intrinsic frequency defined in (4). It means that fragments of solutions for k(c), where $\kappa(c) = 0$, are simply shifted by the wind vector, and $\nu(c)$ is modified appropriately as in the classical Doppler effect. For waves propagating downwind slower than the wind, and for waves propagating upwind, the resulting characteristic frequency is lower, and consequently lower frequency sources are able to produce non-decaying waves. It might be important, since typical characteristic frequency corresponds to the period of about 10 min, whereas time scale of potential sources (e.g. dissipating storms or convective clouds) is usually longer.

For decaying fragments of dispersive relation ($\kappa \neq 0$) the situation is more complicated. In addition to the Doppler effect, the rate of decay is modified by the wind. Results for the wave propagating upwind faster than wind, and downwind are presented in Figs 3 and 4, respectively. Stretching along the x-axis reflects generally the Doppler effect, which is kinematic in nature. However, in addition to this, the value of decay coefficient is modified by presence of the wind, as a result of dynamic interaction between the source and air flow. For the wave propagating upwind (Fig. 3.) the decay coefficient is bigger, and the wave will radiate most of its energy at a distance much shorter than a single wavelength. In the downwind direction, the decay coefficient is lower, and the wave can keep its energy on a distance longer than a single wavelength. It is important, since then an amplification effect in a feedback interaction with cloud convection is likely to occur.

4. CONCLUSIONS

For any vertical distribution of the temperature, there is a unique characteristic wave length (λ^*) determining the radiative properties of gravity waves. Waves longer than λ^* radiate their energy upward into the upper layers of atmosphere, and consequently decay horizontally. Shorter waves do not radiate energy, and can propagate on long distances without any supporting feedback mechanism.

For typical model atmosphere considered in this study, with midtropospheric inversion of $\Delta T = 3^oC$, the corresponding characteristic wavelength (λ^*) is about 5 km. Without inversion it tends to $\lambda^* = 0$, and with stronger inversions it became longer. The characteristic wave length can be found for any real atmosphere from the dispersive relation calculated for (1) with an appropriate numerical code.

The characteristic wave length does not depend on the wind speed or direction. However, the corresponding characteristic frequency (ν^*) can be shifted by the Doppler effect, if there is a non-zero flow in relation to the wave source. For waves propagating downwind, slower than the wind or upwind, this shifting is towards lower frequencies. It is important, since the typical characteristic frequency without wind is usually higher than the typical frequency of cloud convection, which potentially may generate or maintain the gravity wave.

For waves longer than the characteristic wave length, there is a dynamic effect of wind in addition to the kinematic Doppler effect. As the result of this effect the rate of decay becomes higher (or very high) for waves propagating upwind, and lower for waves propagating downwind. Even slight changes of the relative decay coefficient (d) might be important, since it can decide about amplification effect of the feedback mechanism between waves and cloud convection. Generally, long gravity waves are likely to propagate downwind, whereas in the upwind direction they radiate their energy upward at distances shorter than a single wave length. It is a very general role, which still has to be verified for various specific mechanisms of gravity wave - cloud convection structures.

In the present study only the wind constant with height was considered. Results are valid in real situations with non-constant wind, for gravity waves propagating slower or faster than wind at any level. The case of a gravity wave propagating with the phase velocity equal to the wind speed at any level involves special problems like wave behavior around the critical level, and was not investigated in this study.

5. REFERENCES

Erickson, C.O., and L.E. Whitney, Jr., 1973: Picture of the Month: Gravity Waves Following Severe Thunderstorms. *MWR*, 101, 708-711.

Gossard, E.E., 1962: Vertical flux of energy into the lower ionosphere from internal gravity waves generated in the troposphere. *JGR*, 67, 745-757.

Gossard E.E., and W.H. Hooke, 1975: *Waves in the Atmosphere*. Elsev.

Hauf T., and T.L. Clark, 1989: Three-dimensional n umerical experiments on convectively forced internal gravity waves. *QJMRS*, 115, 309-333.

Lindzen R.S., 1974: Wave-CISK in the tropics. *JAS*, 31, 156-179.

Radziwill J.M., 1988: Organization of cloud convection by gravity waves in the lower troposphere. *Prep. 10 Int. Cloud Phy. Conf., Bad Homburg, August 15-20*, 606-608.

Radziwill, J.M., 1990: Organization of cloud convection by spatially decaying modes of gravity waves. *Prep. of the Conference on Cloud Physics, July 2-27, 1990, San Francisco, Calif.*, AMS, 561-563.

Stobie, J.G., F. Einaudi, and L.W. Uccellini, 1983: A case study of Gravity Waves - Convective Storms Interaction: 9 May 1979. *JAS*, 40, 2804-2830.

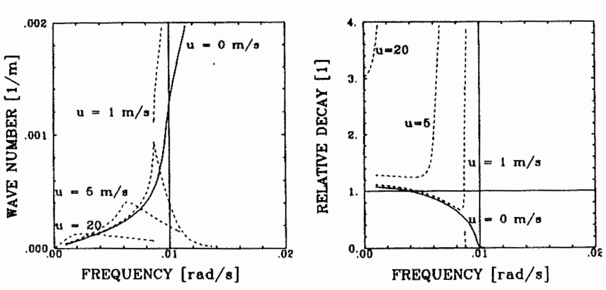

Fig. 3. *Dispersive relation for various wind speeds (u), for a wave propagating upwind.*

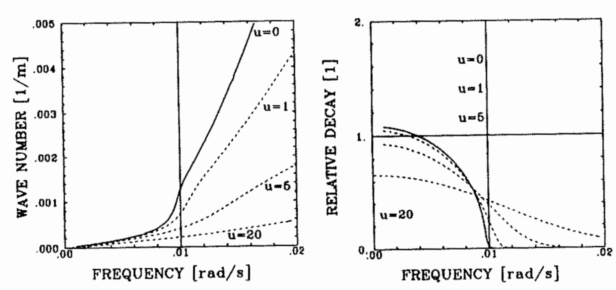

Fig. 4. *Same as in Fig. 3., except for a wave propagating downwind, faster then wind.*

DUAL-WAVELENGTH STUDY OF EARLY CUMULUS IN FLORIDA

Charles A. Knight, L. J. Miller, and Nancy C. Knight

NCAR, PO Box 3000, Boulder, CO, USA 80307

1. INTRODUCTION

This work continues an effort to extend radar first-echo studies toward the onset of coalescence or accretion in cumulus clouds (Knight et al., 1983). Studies with a 5-cm-wavelength radar in North Dakota (Knight and Miller, 1990) and Hawaii (unpublished) revealed that all clouds visible to the eye--even less than one minute old--are also visible on the 5-cm radar at the -20 dBZ_e level or above. Bragg scattering was the suspected mechanism of radar return, not backscattering from hydrometeors. The 1991 CaPE experiment in Florida included the CP-2 radar, which is dual wavelength, 10 and 3 cm, and studies there confirm the strong Bragg scattering. The two wavelengths probably allow the Rayleigh scattering component to be deduced with some confidence, and together the data make accessible new information on cloud water content distribution, an earlier stage of precipitation formation than has been studied using radar, and entrainment. Reported here are the method (very briefly) and early results.

2. METHOD

Bragg scattering comes from index-of-refraction gradients at half the radar wavelength, usually from turbulent mixing of air with different values of humidity and temperature. In a cloud, liquid water content fluctuations also may contribute, but the CaPE data show that the Bragg radar echo takes several minutes to dissipate after the visual cloud disappears, so humidity fluctuations resulting from entrainment and mixing are probably the scatterers within cloud as well. The theory for Bragg scattering uses an assumed spectrum of inhomogeneities that obeys the -5/3 power law of turbulence in the inertial subrange. A 19 dB difference between 10-cm and 3-cm return (stronger at 10 cm: this is a 19 dB ratio of the equivalent reflectivity factors) is the result from ideal Bragg scattering alone when the radar echoes are expressed as dBZ_e, as they all are herein. Given data at two wavelengths, the Rayleigh and Bragg components are easily separated if the theory is correct. Rayleigh scattering values deduced here rely upon this assumption and the further assumption that ratios greater than 19 dB represent Bragg scattering at both wavelengths while those less than 19 dB imply Rayleigh contributions. Actually, the data suggest strongly that the ratio for Bragg scattering in clouds is often substantially greater than 19dB, indicating a slope steeper than -5/3 for the index of refraction variations. Errors from assuming a 19 dB ratio are usually not serious. There is much more to be said about method and assumptions, but the limited space is better spent on results.

The radars have 1 degree beams and 150 m pulse lengths, giving 150 m or better resolution within 10 km range, where the sensitivity is about -30dBZ_e or better.

Since the main purpose has been to examine the onset of precipitation, three sources of radar return need to be distinguished: (1) Bragg scatter, as noted above, (2) Rayleigh scatter from cloud droplets, and (3) Rayleigh scatter from precipitation--meaning here droplet sizes that must have grown by coalescence. Operationally, it is convenient to define cloud as everything detected by the FSSP: diameters up to 45mm.

3. RAYLEIGH SCATTERING FROM CLOUD DROPLETS

The CaPE project included many aircraft penetrations within clouds of different sizes, and the Rayleigh radar reflectivity factors, ΣD^6, in mm^6/m^{-3}, have been calculated for several flights using the 1-second data from the FSSP (diameter range 1 to 45 μm) and the 260-X (50 to 600μm) probes on the NCAR King-Air, as well as the FSSP on the University of Wyoming King-Air. Figure 1 shows scatter plots derived entirely from FSSP data, of calculated dBZ *vs* liquid water content, mean droplet diameter and droplet concentration. This includes all of the 1-sec data from 15 successive penetrations through small clouds (3 in all) at 3 km altitude (cloud base was about 1 km). The cloud droplets produce Z values commonly up to -10dB at this elevation, so in view of radar sensitivities to -30dBZ_e or better, this is a very important source of radar return. It can be important even quite close to cloud base in these warm clouds.

(It is interesting in itself that correlations this good or nearly so between liquid water content and dBZ at a constant altitude are almost without exception in the CaPE data. The implication in general terms is that variability of the smaller droplets, that contribute little to either lwc or dBZ, dominates the scatter in the plots of concentration and mean diameter versus dBZ. This in turn suggests inhomogeneous mixing, as well as an important and very general role for the formation of new cloud droplets well above cloud base.)

The radar can be used as a remote sensor of liquid water content in clouds at 100-200 meter scales, before enough precipitation-sized hydrometeors form to obscure the return from the cloud droplets, and when Bragg scattering does

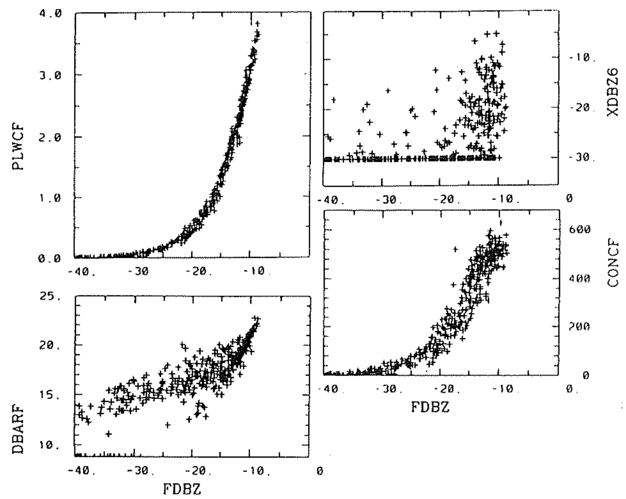

Fig. 1. Scatter plots of all 1-sec, FSSP data from 15 penetrations (3 different clouds) in CaPE, time and date shown. Abscissa is dBZ, ordinates are liquid water content (top left, g cm^{-3}), mean diameter (lower left, mm), concentration (lower right, cm^{-3}), and dBZ from 260-X data (50-600 μm diam., top right).

not interfere. In order for this to be used in practice, one needs to know the temperature and droplet concentration at cloud base.

The 260-X probe provides data on larger sizes, and the liquid water content from its size range is only very rarely above 0.5 g m^{-3} at the early cloud stages studied. The last panel in Fig. 1 is a scatter plot for the same period, of dBZ from one probe against that from the other, showing that nearly always the reflectivity from the cloud droplets dominates that from the precipitation sizes--at this altitude, from these clouds. This too is a quite general result from clouds no more that about 2 km deep, which also tend to be rather short-lived.

4. RADAR RESULTS

The early radar return from cumulus is dominated by Bragg scatter at 10-cm wavelength and by Rayleigh scatter from the cloud droplets at 3 cm. Figure 2 shows radar data of a vertical slice through a cloud about 2 km deep at 9 km range. (Cloud base is between 0.8 and 1 km, about +21C, and the freezing level in CaPE was 4.4 km within 0.4 km.) The 10-cm view is typical of the CaPE early-cloud echoes: a strong mantle around cloud top and sides, to Z_e values above 0dB (often above +5, never above +10), with a prominent weak-echo hole beneath. The echo minimum, here centered at about cloud base, is as ubiquitous a feature as the mantle-shaped maximum, and presumably results from rapid dissipation of the turbulent index of refraction variations

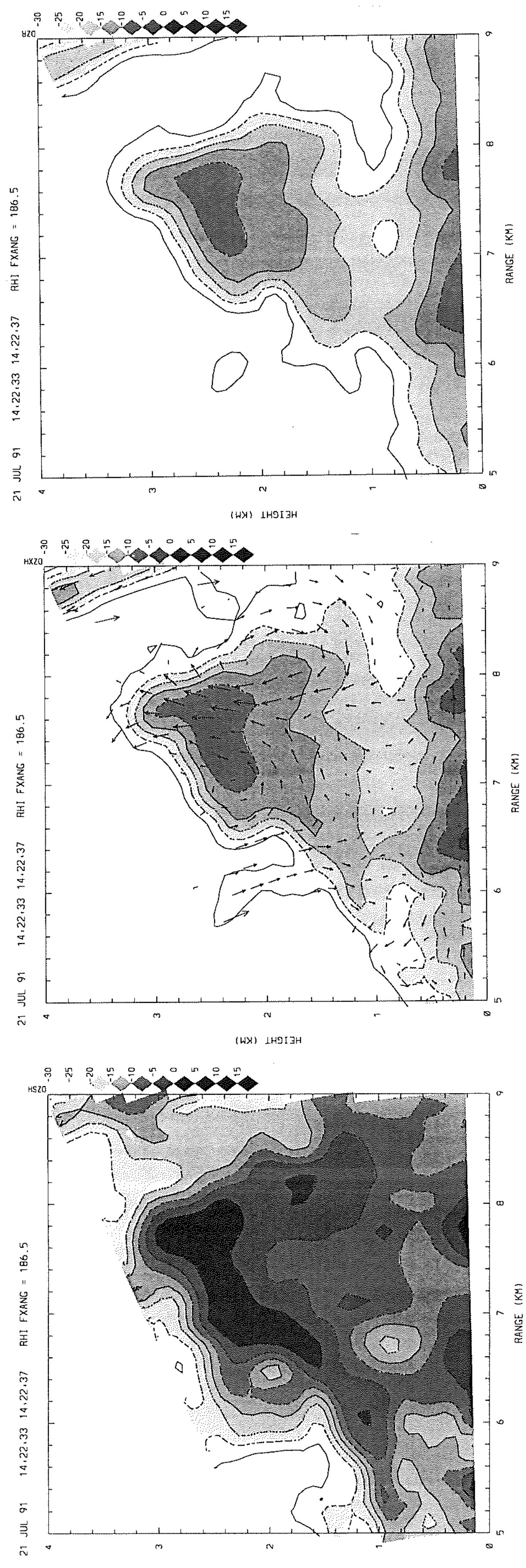

Fig. 2. Vertical slices of reflectivity factor in a small cloud: from left, 10-cm wavelength, 3-cm wavelength with velocity arrows, and deduced Rayleigh signal.

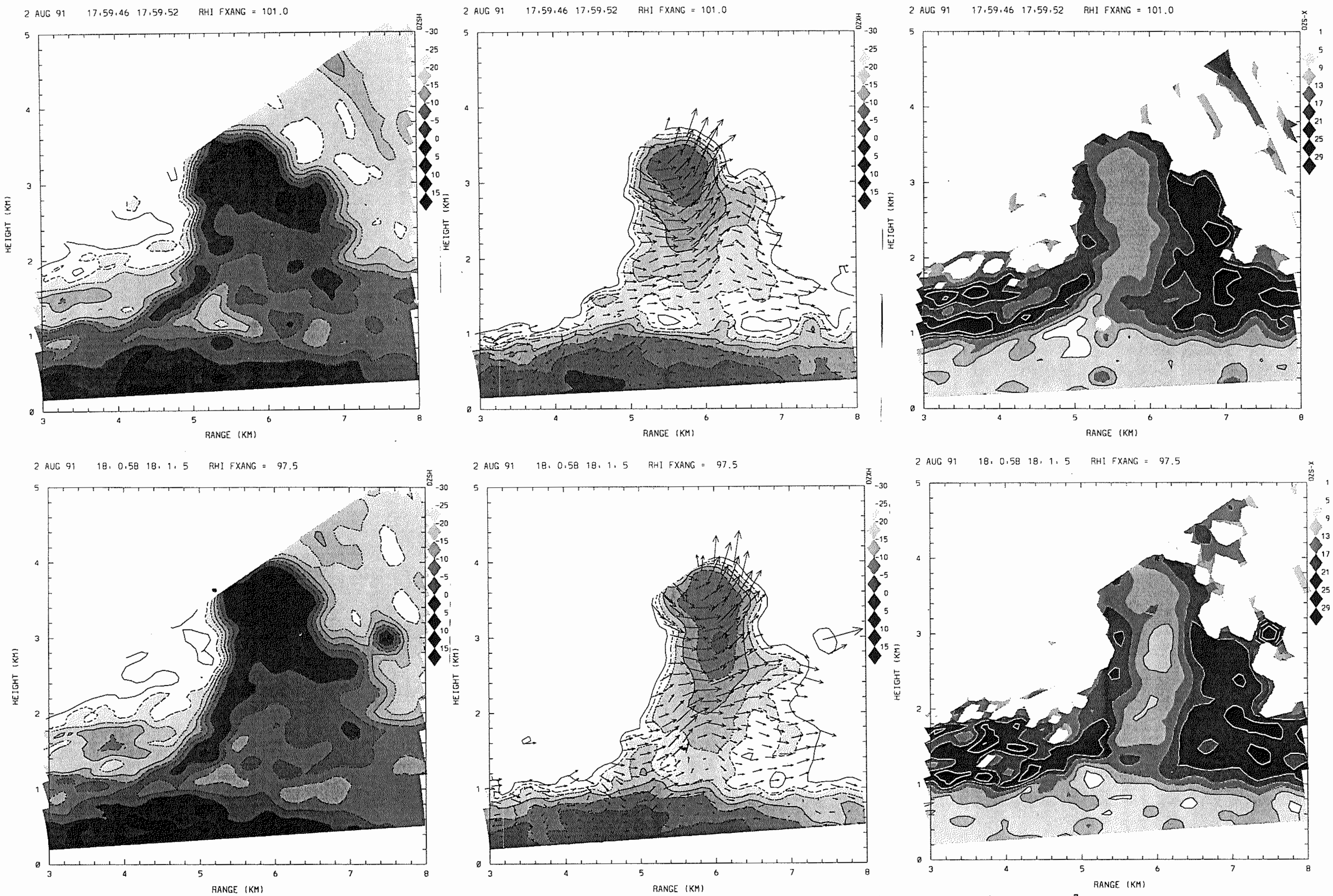

Fig. 3. Vertical slices of (left to right) 10-cm, 3-cm and reflectivity ratio for two successive scans of a rapidly-growing turret, for which the time-height diagram is shown in Fig. 4.

in the region of accelerating flow. Both the 3-cm and the deduced Rayleigh echo patterns show flat, horizontal lower boundaries of the echo contours. These are interpreted as representing adiabatic cloud water content, following the kind of data represented in Fig. 1. This interpretation proves to be quantitatively reasonable.

The greater horizontal extent of the flat lower contours in the 3-cm than in the Rayleigh interpretation probably results from inapplicability of the theoretical 19dB reflectivity ratio used in the interpretation. This is especially important near the cloud edges, where the observed ratio is close to 19 dB. The parts of the flat lower contours in the 3-cm data that are deleted in the Rayleigh version are where the observed reflectivity ratio is close to 19 dB, and if the Bragg ratio were several dB higher than 19, they would be restored. This would be well-justified, because observed ratios up to 25dB and more are common near cloud edges. Since the 3-cm-wavelength radar senses inhomogeneities at the 1.5 cm scale, this is close to the dissipation range and slopes steeper than -5/3 might well be anticipated.

The motivation has been to examine the onset of precipitation. There is no evidence of precipitation in Fig. 2, but the Rayleigh return is ambiguous. An objective way to detect precipitation would be to identify echo that is significantly stronger than that which would arise from adiabatic cloud at every level. This would not be the "very first" precipitation, or perhaps even very close to it at these reflectivity values, but it is the best that can be done.

Figure 3 shows some vertical slices through the center of a rapidly-rising turret that does produce unequivocal precipitation, illustrating the kind of data that are available from the CP-2.The winds were derived from the Doppler radial velocity measurements, assuming 2-D flow, integrating the radial convergence to obtain tangential velocity.

Figure 4 is a radar reflectivity time-height diagram for this case, showing the vertical extent of the reflectivity factor values over the observed time. The first evidence of coalescence in the radar data is at about 17:59:30, since the reflectivity factor cannot increase much above -10 dBZ from cloud droplets alone . Up to about that time the lower -25 to -15 dBZ_e contours are quite flat, again suggesting adiabatic cloud water values (and again reasonably so, according to the aircraft data). After about that time, they slope distinctly but gradually downward. Reflectivity growth occurs at about 3 km, at the surprisingly fast rate of nearly 10 dBZ per minute.

5. CONCLUSIONS

The CaPE data are not yet completely analysed. The purpose is to relate first-detectable coalescence growth to cloud

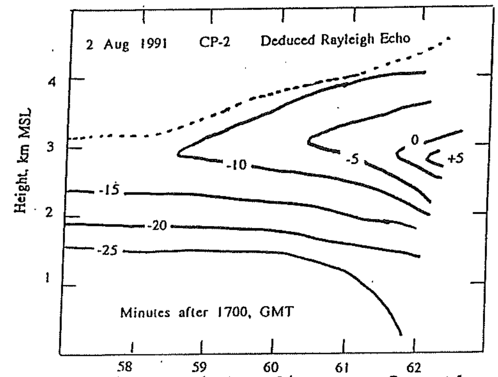

Fig. 4. Time-height diagram for the cloud illustrated in Fig. 3. The solid contours represent the bottom and top levels for the dBZ_e values indicated by the numbers. Cloud top (visual and radar) is shown by the dotted line, and the top levels of -15, -20, and -25 would all crowd along the top. The data are from 6, 1-minute scans.

size and to elapsed time, using all available cases, and generalizations are not as yet warranted. However, evidence of coalescence growth appears to be very rare in clouds less than 2 km deep, even with deduced Rayleigh reflectivity from cloud droplets to -15 dBZ and higher. Time is a more elusive factor, especially because the smaller clouds tend to be very short-lived thermals, while the deeper ones have more plume-like, long-lasting updrafts. With the aircraft data providing evidence that the early, Rayleigh reflectivity values are a remarkably good measure of cloud water content, the onset of coalescence growth detectable by radar appears to require several grams per cubic meter cloud water content. So far, the onset of detectable coalescence seems to occur in the regions with highest liquid water content, rather than in entrained regions.

Finally, dual-wavelength radar combined with aircraft data on clouds within about 20 km radar range appears to be a powerful means of studying both entrainment and the early evolution of precipitation in cumulus.

7. ACKNOWLEDGMENTS

We thank NCAR FOF personnel for superb field support, and Joanne Parrish, John Tuttle and Bill Anderson for invaluable assistance with data processing. The National Center for Atmospheric Research is sponsored by the National Science Foundation.

REFERENCES

Knight, C. A., W. D. Hall, and P.M. Roskowski, 1983: Visual cloud histories related to first radar echo formation in Northeast Colorado Cumulus. J. Appl. Met., 22, 1022-1040.

Knight, C. A., and L. J. Miller, 1990: First 5-cm radar echoes at low dBZ values in convective clouds. Preprints, AMS 1990 Conference on Cloud Physics, San Francisco. 716-721.

CLOUD – ENVIRONMENT INTERFACE INSTABILITY AND THE DYNAMICS OF CUMULUS ENTRAINMENT

Wojciech W. Grabowski and Terry L. Clark

NCAR*, Boulder, CO 80307, USA

1. INTRODUCTION

High resolution numerical simulations of small cumulus clouds reported by Klaassen and Clark (1985), Clark *et al.* (1988) and Grabowski (1989) suggested that entrainment in convective clouds results from the instability of the cloud-environment interface. However, details of the process leading to onset of the instability as well as factors involved in the scale selection and growth rate of unstable modes were unclear. To study the instability, Grabowski and Clark (1991, hereinafter GC91) and Grabowski and Clark (1992, hereinafter GC92) considered two-dimensional (2D) and three-dimensional (3D) moist thermals rising in a stably stratified environment. The underlying assumption was that the thermal's leading edge mimics the dynamics of the upper part of a cumulus cloud in the case of environment without shear provided that the Reynolds number is sufficiently large. Direct numerical simulation approach was adopted and resulted in physical regime similar to laboratory experiments with thermals in liquids (e.g., Scorer 1958). Twin experiments were performed, with and without small amplitude random perturbations in the temperature field that provided excitation for the instability, see GC91 for details. This paper discusses physics of the instability as revealed by rising thermal experiments and suggests some implications for the cumulus entrainment problem.

2. NUMERICAL EXPERIMENTS WITH RISING THERMALS

Numerical model of Clark was used to study evolution of moist thermals from rest in the stably stratified environment. The thermal diameter was about 500 m and relative density excess over the environment was around 1/300. Nesting technique (i.e., use of several computational domains with increasing spatial and temporal resolution while zooming into part of the outermost domain) was essential in these experiments. It allowed use of very high spatial resolution for the thermal (i.e., few hundred gridpoints across thermal diameter in 2D and more than a hundred in 3D) and at the same time allow to chose the outermost computational domain large enough to provide rise of the thermal with negligible effects of horizontal and vertical boundaries.

Temporal evolution of the base state, i.e., the laminar flow near the interface in the case without excitation, was very similar in both 2D and 3D experiments. The fundamental feature of the base state was a shear layer tangential to the interface. The shear near the interface develops as the thermal rises and it is associated with the baroclinic production of vorticity. Temporal evolution of the interfacial shear layer was studied in GC91. Using analytical model a limiting or long time solution for the product of the shear layer depth and average shear layer vorticity was found. The product was named shearing velocity and it approximates velocity change across the interfacial shear layer. In the long time solution (valid after few minutes in a typical atmospheric situation), the shearing velocity becomes constant and it depends only on thermal buoyancy and radius, and it *does not* depend on the mixing coefficient. In the effectively inviscid case, the depth of the shear layer exponentially decreases with time and interfacial shear exponentially increases. The e-folding time of this process τ is of the order of 100 s for a typical atmospheric situation. In the viscid case, both the depth and shear magnitude approach asymptotic values which depend upon the mixing coefficient. The asymptotic depth is an effect of the balance between baroclinic generation of shear and viscous dissipation. These analytical results agreed well with results of numerical experiments.

Once excitation is provided, unstable modes develop at the interface of the rising thermal. Example of results is shown in Figure 1. The scale selection and growth rate of unstable modes are related to the parameters of the tangential shear layer much in line with the classical linear theory developed for the plane shear layer with unstable stratification (e.g., Asai 1970). The estimated nondimensional wavenumber of unstable modes was around 2 and 1.3 for 2D and 3D experiments respectively, and nondimensional growth rate was around 0.4 (2D) and 0.5 (3D). Shear layer depth and shearing velocity was used to scale wavenumber and growth rate of unstable modes. Analysis of the kinetic energy (KE) associated with unstable modes showed that both buoyancy and shear production terms contributed, with buoyancy source dominating near

* NCAR is sponsored by the NSF

thermal top and shear source dominating near thermal side.

Large amplitude development of the instability differed considerably between 2D and 3D cases. In the 2D case vortex pairing was observed and this process corresponds to upscale transport of KE associated with the instability. Evolution of large amplitude eddies in the 3D experiments seem to result in secondary instabilities and generation of small scale motions. Analysis presented in GC92 suggests that this process was associated with the transition to turbulence which, in 3D case, corresponds to downscale transfer of KE associated with unstable modes.

Although these experiments were characterized by Reynolds number orders of magnitude smaller than in a typical atmospheric situation, they suggested some clues for the cumulus entrainment problem. This is discussed in the next section.

3. CUMULUS ENTRAINMENT

In rising thermal experiments, development and further evolution of interfacial instabilities together with the transition from a motionless spherical bubble into rising vortex ring influenced almost the whole volume of the rising thermal. Unlike thermals, convective clouds have a clearly defined cloud base which continuously

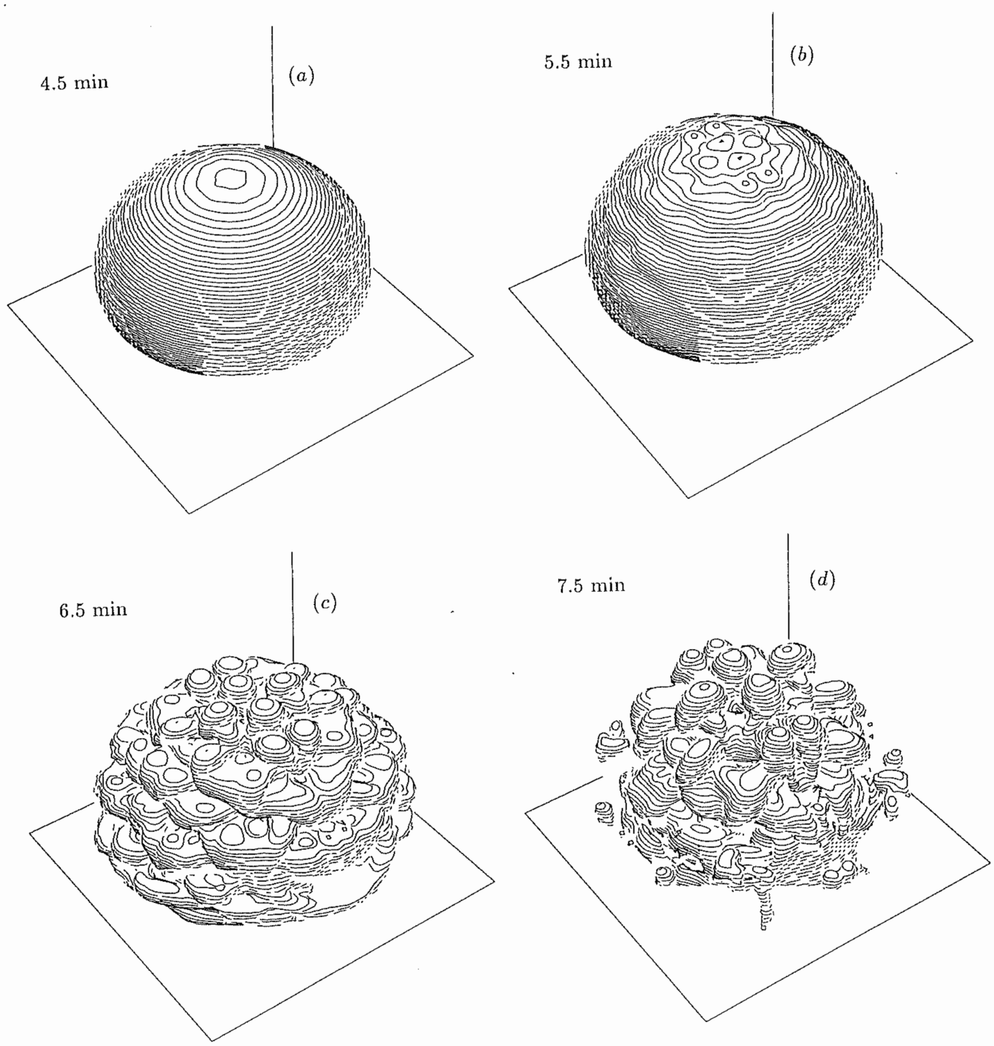

Figure 1. Three-dimensional perspective of the cloud water field greater than 0.01 g kg^{-1} for the 3D simulation of the rising moist thermal at t = 4.5 (*a*), 5.5 (*b*), 6.5 (*c*) and 7.5 min (*d*). Excitation was provided at t = 3 min. Only quarter of the thermal was actually resolved in this experiment and the whole thermal was plotted using symmetries as assumed in the experimental setup.

supplies the cloud with boundary layer air. While the cloud top continues to rise, cloud base usually remains at the initial height. This suggests that development of instabilities in the case of a small cumulus results in formation of the mixing (or entraining) region which separates undiluted fluid inside the core from the environmental air above and around. Such a structure seems to be suggested by at least some cloud observations as well. Inside the mixing region, kinetic energy associated with large eddies developed due to the instability is transferred toward smaller scales and dissipated when the Kolmogorov microscale is reached. Scale selection of new large scale instabilities which develop as the cloud continues to rise, should depend not only on the parameters of large scale flow (like average buoyancy and velocity profiles across the mixing region), but also on the nonlinear interaction between different scales of motion in the mixing region. This aspect is probably the most important from the point of view of further evolution of the upper interface of a rising cloud. An intriguing problem is to determine the dominant scale of the instability after time long compared to the lifetime of the largest eddy, i.e., after a number of cycles of the instability have occurred. Below, a simple model is suggested to provide an estimate of the dominant scale.

Large scale instabilities developing in the upper part of a rising cloud decay and transfer energy into smaller eddies. In this process of turbulent mixing, gradients of thermodynamic fields and momentum between the cloud and environment are smeared out. At the same time, however, the continuous rise of the cloud tends to sharpen these gradients by decreasing the depth of the mixing region in the manner described in last section. If, at a certain stage of cloud development, these two effects are in balance, the mean depth of the mixing region (i.e., depth averaged over time long compared to the lifetime of a large scale eddy) should become constant. This is the quasi-equilibrium assumption. It is interesting to note that quasi-equilibrium should be fairly typical in the cumulus case since the lifetime of a single cloud is large compared to the e-folding time scale of the inviscid interfacial shear layer, τ. The second assumption is that the average depth of the mixing region plays a similar role in the scale selection process as the depth of the laminar shear layer discussed in the rising thermal experiments. This is a very strong assumption since the role of existing modes within the mixing region is neglected. With the two assumptions, the quasi-equilibrium depth, l_{eq}, may be estimated as (see GC92 for details):

$$l_{eq} \sim \frac{R}{10} , \tag{1}$$

where R is the (average) radius of the upper interface which may be approximated as the radius of the cloud. The eddy size that corresponds to the quasi-equilibrium state would be a few tenths of the thermal radius.

There are several interesting features associated with (1). First of all, (1) states that the quasi-equilibrium depth of the mixing region (or the scale of large eddies) should scale with the thermal radius. This, however, is not surprising, since the thermal radius is the only length scale in the problem, at least in the unstratified dry case. The quasi-equilibrium depth of the shear layer as predicted by (1) is close to the limiting depth for rising thermal experiments discussed in the previous section. It follows that the effective mixing coefficient associated with turbulent processes inside the mixing region of the real cloud is of the same order of magnitude as the mixing coefficient assumed in rising thermal experiments. This seems to provide some justification for studying extremely high Reynolds number atmospheric processes using techniques allowing only moderate Reynolds number flow regimes (e.g., using tank experiments or numerical simulations). Eq. (1) also suggests that entrainment in high Reynolds number buoyancy driven flows for which quasi-equilibrium is feasible, should be dominated by large structures, with tangential scales comparable to R. This point seems to be supported by the appearance of convective clouds and high Reynolds number laboratory thermals (e.g., Scorer 1958). It should be stressed, however, that arguments that lead to (1) are heuristic and more rigorous theoretical work is required to refine these concepts.

4. REFERENCES

Asai, T., 1970: Stability of a plane parallel flow with variable vertical shear and unstable stratification. *J. Meteor. Soc. Japan*, **48**, 129-138.

Clark T. L., P. K. Smolarkiewicz and W. D. Hall, 1988: Three-dimensional cumulus entrainment studies. *Preprints, 10th Int. Cloud Physics Conf.*, Bad Homburg (FRG), 88-90.

Grabowski W. W., 1989: Numerical experiments on the dynamics of the cloud-environment interface: Small cumulus in a shear-free environment. *J. Atmos. Sci.*, **46**, 3513-3541.

Grabowski, W. W., and T. L. Clark, 1991: Cloud-environment interface instability: Rising thermal calculations in two spatial dimensions. *J. Atmos. Sci.*, **48**, 527-546.

Grabowski W. W. and T. L. Clark, 1992: Cloud-environment interface instability. Part II: Extension to three spatial dimensions. *J. Atmos. Sci.* (in press)

Klaassen G. P. and T. L. Clark, 1985: Dynamics of the cloud-environment interface and entrainment in small cumuli: Two-dimensional simulations in the absence of ambient shear. *J. Atmos. Sci.*, **42**, 2621-2642.

Scorer, R. S., 1958: *Natural aerodynamics.* Pergamon Press, 312 pp.

CLOUD AND HYDROMETEOR MICROPHYSICS AT -3°C IN A VIGOROUS FLORIDA CONVECTIVE UPDRAFT

P. Willis[1], John Hallett[2] and R. Black[1]

[1] NOAA/AOML/Hurricane Research Division, Miami, Florida
[2] Desert Research Institute, Reno, Nevada

1.0 INTRODUCTION

During the **C**onvection **a**nd **P**recipitation **E**lectrification **E**xperiment (**CaPE**) the NOAA P-3 aircraft was used to make a series of radar and microphysical measurements in support of the primary objectives of the experiment. This and a companion paper (Hallett, et al., 1992 - this volume), describe an analysis of three cloud penetrations of typical south Florida convective clouds near Kennedy Space Center. The subject cloud of this article is a developing Cb system, that was already complex. The other paper describes two penetrations of a smaller, younger, single convective cell that was developing on the south end of this cloud complex. By that time the main cloud had become very well developed.

2.0 STRUCTURE OF THE CLOUD SYSTEM

On 11 August 1991 a well-developed convective cloud was penetrated with the NOAA P-3 instrumented aircraft on a SE - NW track at 1909/12 UTC. New growth was visually observed on the S - SE side of the vigorously growing cloud, or cloud system. From an examination of rawinsondes from the Cape Canaveral (XMR), West Palm Beach (PBI), and Tampa (TBW) it appears that the overall shear controlling the structure of the cloud was from the SE - NW, so that this pass was from the upshear side to the downshear side of the cloud.

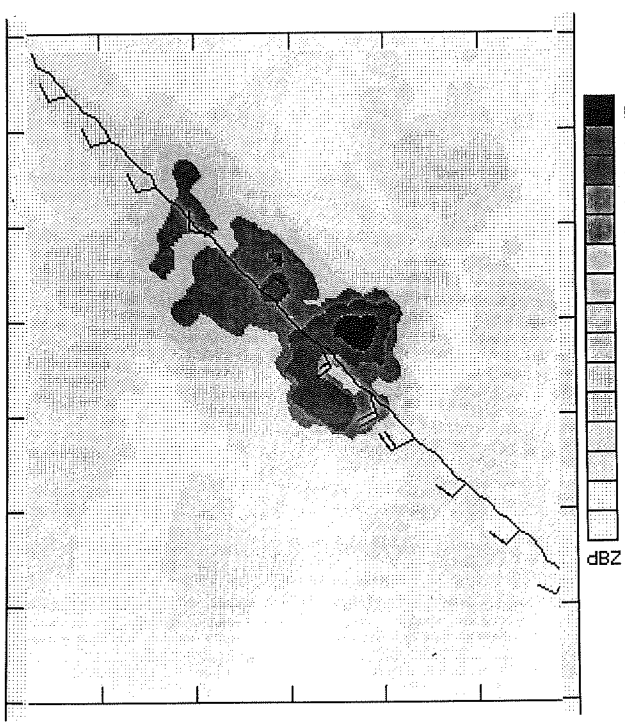

Fig. 1 Lower fuselage 5 cm radar PPI scan at 190754 Z with flight track superimposed. the tick marks on the borders are 3 km apart.

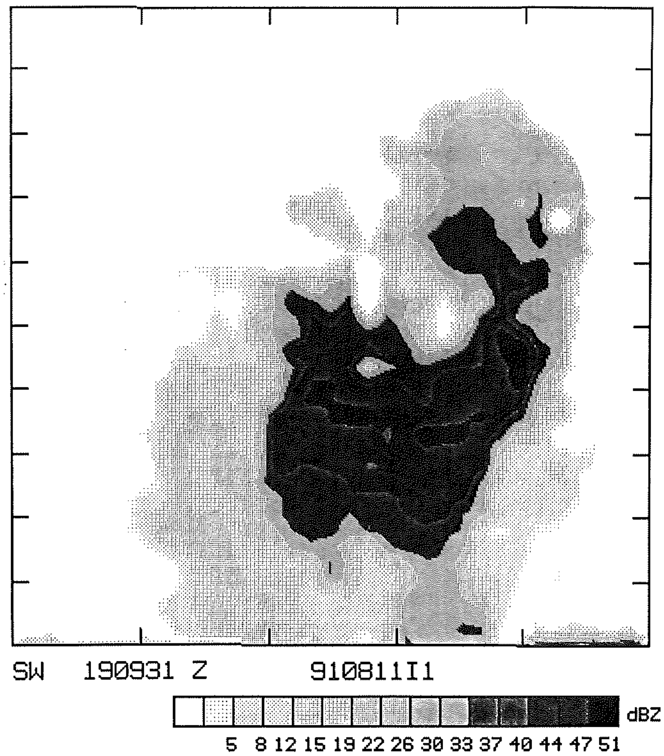

Fig. 2 Tail 3 cm radar RHI scan from within the cloud at 1909/31 Z.. The vertical axis spans 12 km (tics 1.2 km), the horizontal 10 km (tics 2.0 km). The aircraft is at 5.43 km and the holes, immediately to the left above and below, are artifacts.

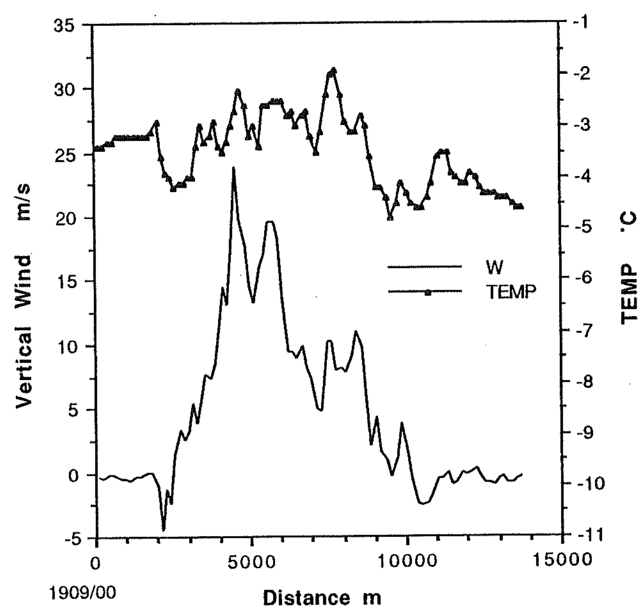

Fig. 3 Plot of the Rosemount total temperature and 1 s mean vertical winds (updraft velocities) through the cloud pass versus distance from 1909/00 Z.

Fig 1 is a 5-cm aircraft radar PPI taken just prior to cloud entry. The radar echo is spreading, or elongating, to the NW in response to the vertical shear of the horizontal wind. The radar echo pattern at this time is ~4.5 km wide and ~10-12 km long. The vertical structure of part of the cloud can be seen in Fig. 2, which is a 3-cm tail radar RHI scan, a vertical slice approximately orthogonal to the flight track, from within the cloud. (Because of an experimental antenna being tested it is actually a cone 23° forward of the orthogonal plane.) Part of the cloud extends to ~10 km, or 4.5 km above the flight level. There was very little precipitation reaching the surface, indicating that the cloud is still fairly young. Fig. 3 is a plot of the measured vertical wind (w) and the temperature measured by the Rosemount temperature sensor. The mean temperature through the cloud was -3.5°C and the peak 1-s updraft velocity was nearly 24 m/s. A very large fraction of the entire cloud pass was characterized by significant updraft velocity. No significant downdraft was measured at this level at this time.

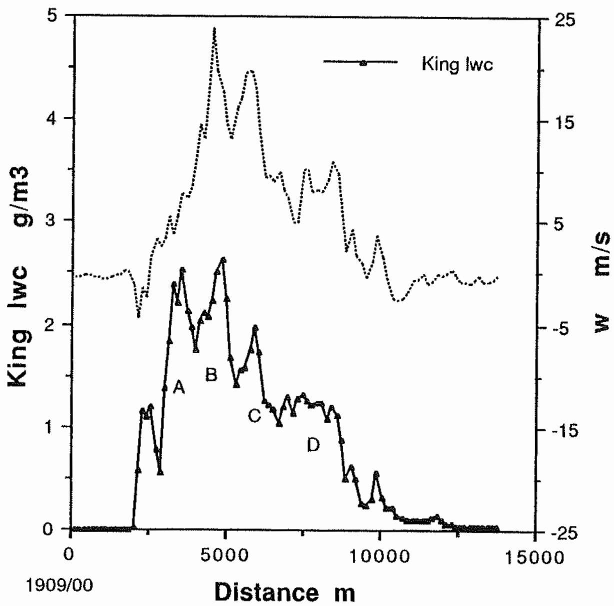

Fig. 4 Plot of the CSIRO/King liquid water content versus distance. The vertical velocity trace of Fig. 3 is overlain as a dashed line for reference. The letters mark the locations of the FSSP spectra of Fig. 5.

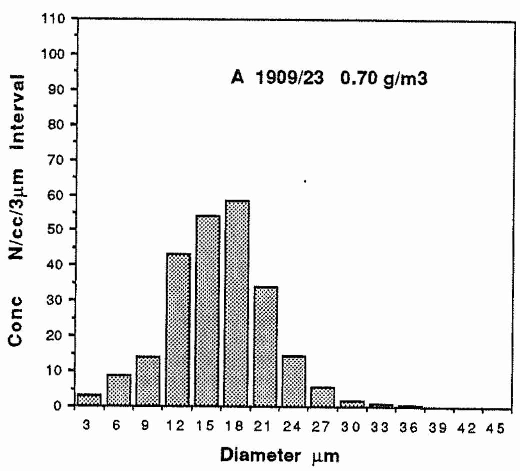

Fig 5a FSSP cloud droplet size distributions for 2 s ending at 1909/23.Z

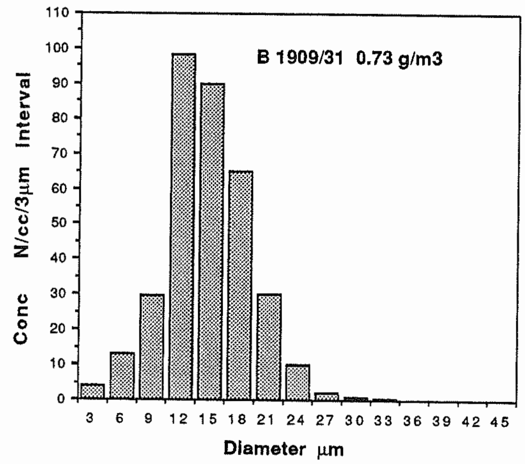

Fig 5b FSSP cloud droplet size distributions for 2 s ending at 1909/31.Z

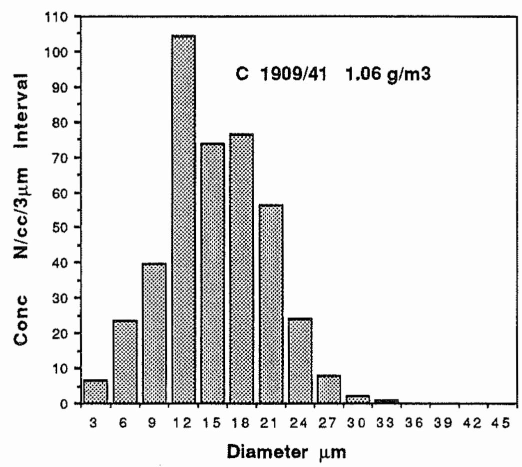

Fig 5c FSSP cloud droplet size distributions for 2 s ending at 1909/41.Z

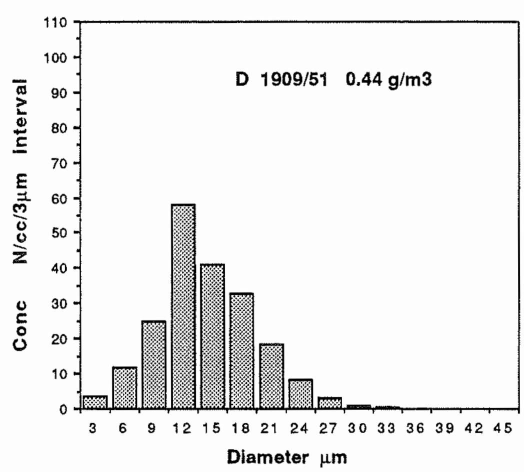

Fig 5d FSSP cloud droplet size distributions for 2 s ending at 1909/51.Z

3.0 MICROPHYSICS AT -3°C

Fig. 4 is a plot of the liquid water content (lwc) measured by the CSIRO/King liquid water probe. The lwc that was measured correlates well (positively) with the measured updraft velocities, showing a large extent of > 2 g/m3. The droplet spectra measured by the FSSP are shown in Fig. 5 for four locations marked on the King probe profile (Fig. 4). Although the absolute concen-trations are in question here due to the high true air speeds (> 150 m/s), the relative spectral shifts are meaningful. The entire spectrum is probably undersampled and the small droplet sizes nearly truncated. The lwc integrated from the droplet spectra, and indicated on the figures, is systematically less than that measured by the King probe. The water contents from an integration of the droplet concentrations on the formvar replica are discussed for pass 2 in the companion paper.

The PMS 2D image data for each 5 s of track were reduced by letting the maximum orthogonal dimension (x or y) be the diameter of a water sphere. Data reduced in this way will slightly overestimate the precipitation water contents. The precipitation water contents computed from the 2D-P probe, only, are plotted in Fig. 6, which has been overlain on the vertical velocity plot for reference. A selected sample of hydrometeor spectra taken at the locations marked is shown in Fig. 7 a-d. The spectra show deviations from exponentiality, but the sample size is probably too low for these differences to be significant.

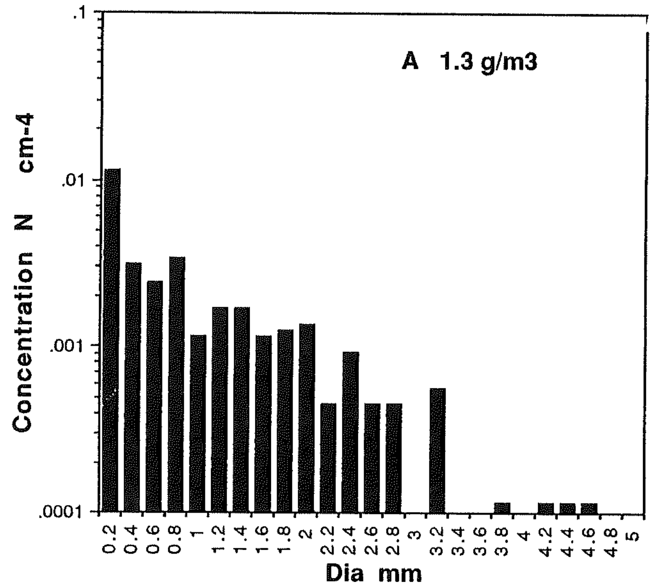

Fig. 7a Hydrometeor spectra from a 5 s summation of. PMS 2D-P precipitation probe data ending at 1909/22Z. Water contents computed assuming water spheres are shown.

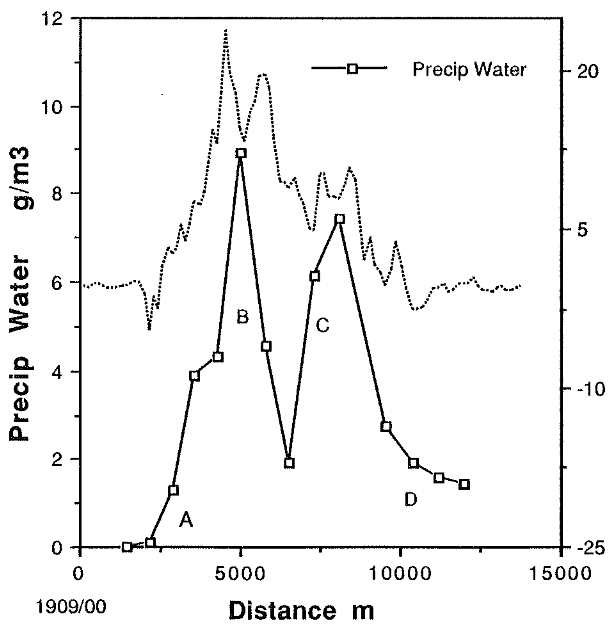

Fig. 6 Precipitation water content computed from PMS 2D-P data. Vertical velocity shown as a dashed line for reference. The capital letters mark the locations of the hydrometeor distributions presented in Fig.7.

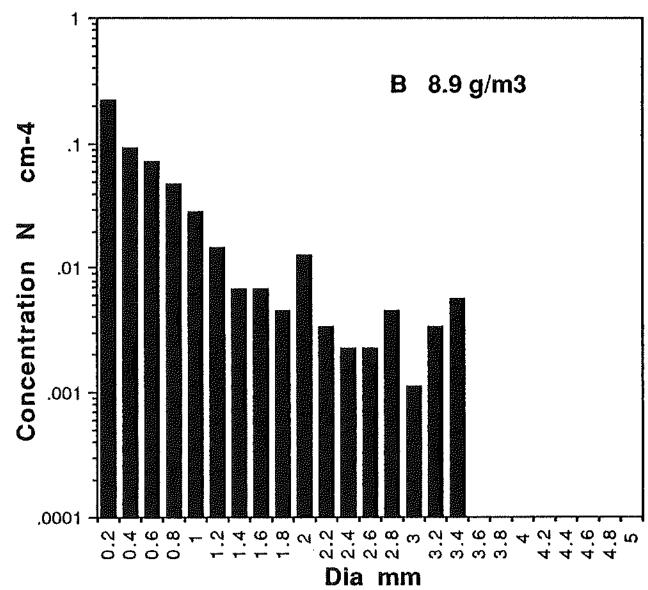

Fig. 7b Hydrometeor spectra from a 5 s summation of. PMS 2D-P precipitation probe data ending at 1909/37Z. Water contents computed assuming water spheres are shown.

A sampling of PMS 2D cloud probe images ordered by distance along the cloud pass is shown in Fig. 8. The distance after 1909/00 is shown so the images can be keyed to other figures. The canting evident in some cloud probe images provides a sure indication of liquid hydrometeors, because graupel does not cant (Black and Hallett, 1986). In the strongest updrafts (> 10 m/s and before 5621 m) the hydrometeors at -3°C appear to be exclusively liquid. The strip at d = 5621 m (and 6849 m) shows clear evidence of the coexistence of the coexistence of hydrometeors in both the frozen and liquid states. This coexistence of water and ice in close spatial proximity occurs , particularly, where the updraft weakens immediately downshear of the strongest updraft velocities. Further downshear (at 7468 m, and beyond) the hydrometeors become exclusively ice.

4.0 CLOUD ELECTRIFICATION

This cloud exhibited well-developed electrification on this penetration. Fig. 9 is a plot of the measured vertical component of the electrical field, with the vertical velocity again included as a point of reference. The aircraft charge has been subtracted from the measured field. This profile indicates a positive charge center below and a negative charge center above the flight level of the aircraft. The significant electrification does not occur until the aircraft is just downshear of the strongest updraft. This is in the region where a mixture of liquid and frozen precipitation-size hydrometeors was first observed. The slow return to zero field on the NW side of the cloud, which occurred outside of the cloud at flight level, is not due to the aircraft charge. The charge on the aircraft (not shown here) returned to zero quickly after exiting the cloud. We probably were flying under the anvil on this downshear part of the track.

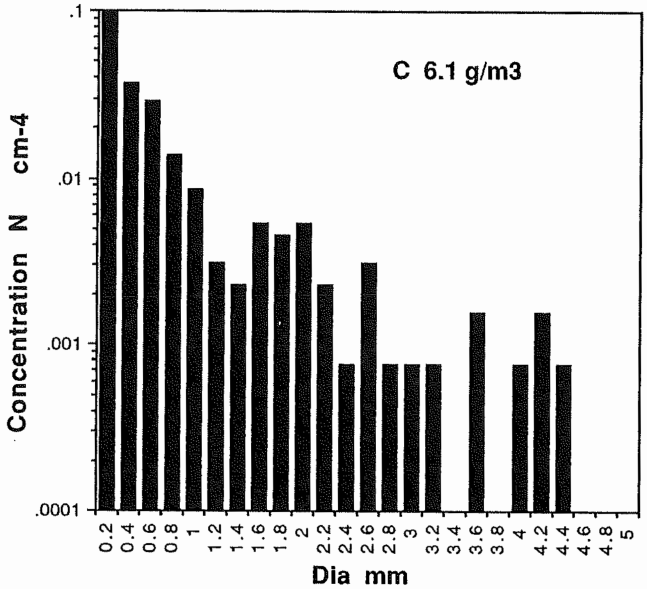

Fig. 7c Hydrometeor spectra from a 5 s summation of. PMS 2D-P precipitation probe data ending at 1909/52Z. Water contents computed assuming water spheres are shown.

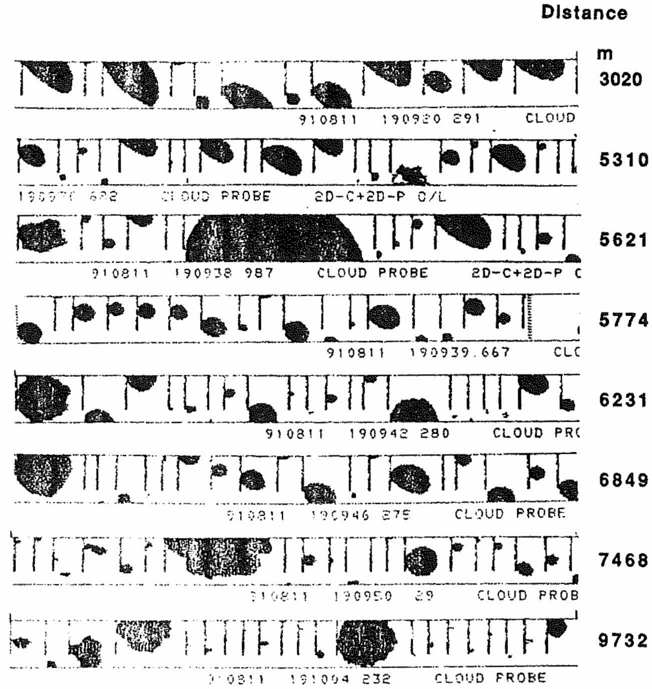

Fig. 8 A sequence of selected representative PMS 2D-C cloud probe images along the cloud pass. The distance is given for each record strip so they can be keyed to other figures. The distance between the thin lines at the top and bottom of each strip is 1.6 mm.

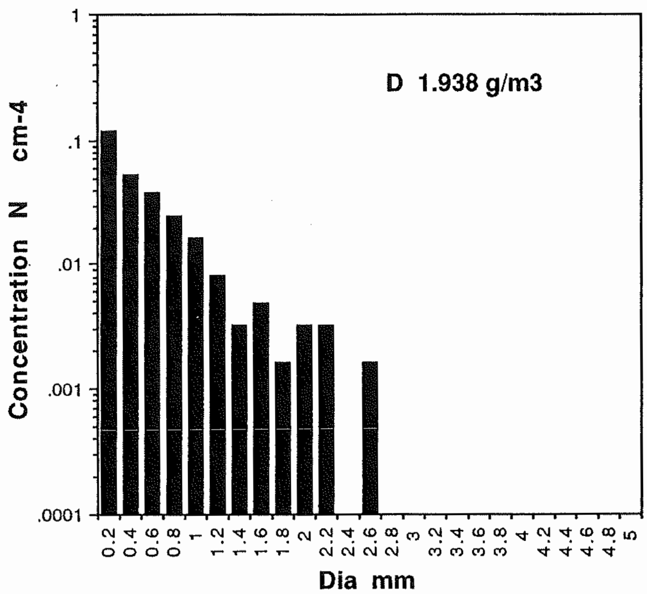

Fig. 7d Hydrometeor spectra from a 5 s summation of. PMS 2D-P precipitation probe data ending at 1910/10Z. Water contents computed assuming water spheres are shown.

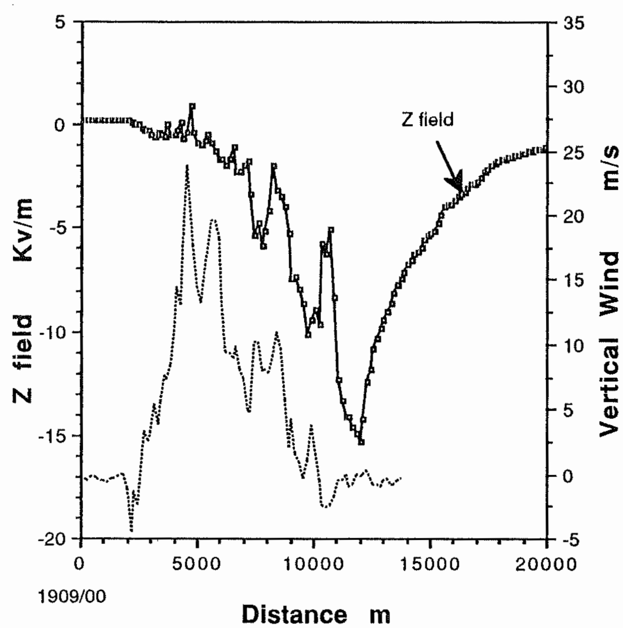

Fig. 9 Vertical component of the electrical field versus distance

5.0 SUMMARY AND CONCLUSIONS

- The cloud at the stage sampled along the shear vector consisted exclusively of updraft.
- At the 3.5°C level the strongest updrafts contained only water hydrometeors. Where the updrafts weakened slightly, a mixture of ice and water hydrometeors was present. This content changed to predominantly ice on the downshear edge of the cloud.
- The cloud electrification was not observed until the region of mixed hydrometeors was encountered.

References:

Black, R. A., and J. Hallett, 1986: Observations of the distribution of ice in hurricanes. *J. Atmos. Sci.* **43**, 802-822.

The evolution of cumulus congestus in a low shear, high instability environment: CaPE aircraft analyses

Gary M. Barnes and Wesley D. Browning
University of Hawaii, Honolulu, Hawaii

and

James C. Fankhauser
NCAR, Boulder, Colorado

1. Introduction

Successful parameterization and forecasting of convection depends upon the degree of our understanding of updraft-downdraft structure and entrainment-detrainment. Unfortunately our knowledge of mixing, whether it be at cloud top or side, remains a contested issue. The thermodynamic measurements in-cloud are suspect; Lawson (1990) demonstrates that conclusions using total water and pseudo-equivalent potential temperatures (Paluch, 1979) may undergo significant modification when the typical errors due to sensor wetting are considered. Reuter and Yau (1987) remind us that the scheme cannot be employed once raindrops form and fall out of the parcel which leaves us unable to examine mixing processes for the latter stages of the cloud. The development of a comprehensive theory of mixing also suffers from the difficulties inherent in marshalling the critical resources to observe the entire rapid evolution of a convective cloud. We are left with a plethora of schematics that make the cloud the result of a bubble, a series of bubbles, plume, starting plume or thermal. Surprisingly, many of these schematics of the airflow are not based on high frequency airflow sampling in-cloud.

Blyth et al. (1988) provide a review of the evidence supporting either top or side entrainment. The top of the cloud is the favored location for entrainment since it provides the best explanation for the "top-hat" cross-sections of liquid water that are most often observed (e.g. Squires 1958, Warner 1955, 1977). Mixing diagrams have been used by Paluch (1979), Jensen et al. (1985), and Pontikis et al. (1987) to show that most parcels within cloud are a blend of cloud base and cloud top air.

NCAR is partially funded by NSF.

Stommel (1947) argued effectively for clouds being similar to plumes; if this is a reasonable assumption then lateral entrainment should dominate mixing processes. The continuous nature of the updraft (e.g. Byers and Hull 1949, Malkus 1954, Fankhauser et al. 1983) would seemingly lend credence to the plume model and thus the importance of lateral mixing. Saturation point analyses made by Betts (1982a,b) show that lateral entrainment is necessary for at least some of the air mixing into the cloud.

Finally, the schematic of Blyth et al. (1988) emphasizes environmental air entering the top, descending around the heart of a thermal, and eventually entering into the sides on the trailing portions of the thermal. Such a model incorporates aspects of both the "top" and "side" schools of thought.

2. Goals

During the summer of 1991 the Convection and Precipitation/Electrification Experiment (CaPE) was conducted in the vicinity of Cape Canaveral. One of the goals of this experiment was to identify the relationships between the evolving wind, water, thermodynamic, and electrical fields within convective clouds. Our specific interest is to examine the evolution of a number of cumulus and cumulus congestus with nearly simultaneous penetrations by the two King Airs operated by the University of Wyoming (2UW) and the NCAR Research Aviation Facility (312D). Our hope is to examine the issue of entrainment primarily through the use of wind measurements in an effort to compliment the thermodynamic-based studies that represent the majority of the mixing research done for convective clouds. In this limited space we will discuss only a few of the preliminary findings from the study of 5 isolated cumulus congestus.

3. Data and sampling strategy

Figs. 1 and 2 display the flight patterns for the two King Airs in plan view and vertical cross-section, respectively. The rosette pattern in Fig. 1 offers numerous passes through the cloud and the near environment over a short period; it also provides information normal and parallel to the mean wind direction and the wind shear. A modification of the rosette is the bow-tie pattern where the two aircraft take reciprocal headings in order to sample essentially the same vertical cross-section of the target cloud.

All clouds were chosen by their appearance and were intercepted by the two aircraft as the cloud grew to their respective altitudes. Normally the lower aircraft maintained visual contact with the upper aircraft resulting in near-simultaneous penetration of the cloud. Typical altitude separation was 600 to 900 m. The clouds were flown until there was little or no visible cloud present or when the electric fields reached a magnitude where the threat of a lightning strike to the aircraft was a distinct possibility.

On every mission the two aircraft did a wing to wing intercomparison on the ferry to the target clouds. Biases in the wind and thermodynamic data were identified in this manner; tower fly-bys were used to check the absolute accuracy of the aircraft temperature, dew point, pressure, and mean horizontal wind. Biases were small (e.g. 0.3 ms^{-1} for the vertical velocity and 0.5 degrees for the dew-point temperature). The true airspeed of the King Airs and the 1Hz sampling rate yield a horizontal resolution of 100m.

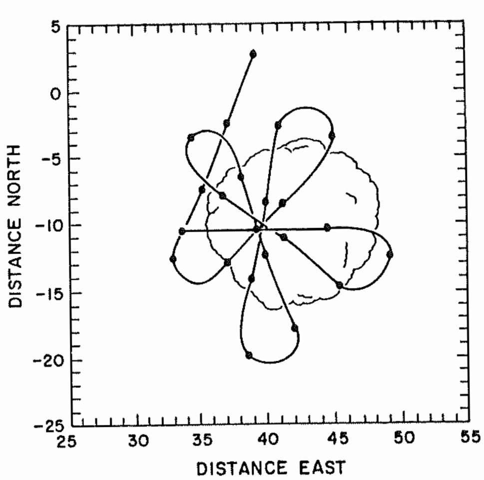

Fig. 1: A plan view of the aircraft pattern known as the rosette. Tic marks denote each min. of flight time.

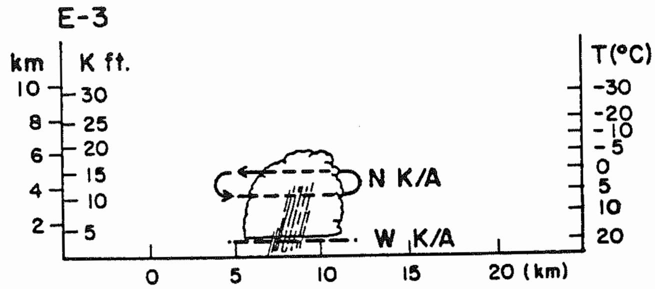

Fig. 2: A vertical cross-section view of the flight pattern. For many of our cases the lower aircraft was 600-900m below the upper aircraft and in cloud.

The two aircraft completed nearly 600 passes through cumulus and cumulus congestus. Over 25 clouds were sampled ten or more times by 2UW and 312D providing us the opportunity to explore the evolutionary aspects of convective clouds. Most of the target clouds had tops from 3000 to 8000 m.

Almost all of the cloud studies were conducted over the CaPE mesonet array and in range of one of the three NCAR radars. Soundings and the mesonet provide the information to assess the shear, instability, and triggering mechanism for the clouds under scrutiny. In most cases the clouds had a diameter less than two km negating the possibility of any dual-Doppler analysis. Additionally, the dual-Doppler technique would not be able to show the near environment where there are no scatterers.

The surface mesonet and the soundings launched within 1-2 hours of each of the 5 target clouds have been used to define the environment. Convective available potential energies were between 1600 and 2700 m^2s^{-2} for the periods when these clouds were observed. Shear of the horizontal wind was generally less than 1.0 ms^{-1} per km for the layer bounded by the base and top of the cloud. The mesonet shows that these 5 target clouds were not located above or near any significant gradients in wind, temperature, and moisture. This suggests that the clouds were not triggered by an outflow or a sea-breeze front, but were more aptly described as airmass convection.

4. Preliminary results

Fig. 3 is an example of the type of updraft structure and evolution that seems typical. Cloud edge is determined from the FSSP and verified by the nose camera. Each aircraft samples the cloud five times, and each aircraft shows no updraft by pass 4 or 8 minutes after the first pass. Neither this example or any other isolated cumulus or cumulus congestus shows evidence of a series of ascending bubbles separated by regions of little or no positive vertical velocity. A plume conceptual model much better describes the observations. These observations are for the upper third of the cloud. Both aircraft observe similar structure and evolution with the updraft suddenly being replaced by a downdraft.

Attempting to predict the updraft magnitude at the altitude of the upper aircraft for a given pass based on the observations of W from the lower aircraft for the previous pass met with complete failure. Generally the vertical velocities observed at the upper level were much lower than that predicted by a modified parcel method that included water loading effects. We calculated the difference in buoyancy between the two aircraft from a sounding close in time and space to the target cloud and estimated the water loading from the FSSP, 2D-C, and 2D-P sensors. Pressure perturbations due to the interaction of the updraft with the shear were estimated using the approximation of LeMone et al. (1988) and found to be negligible. At first glance Fig. 3 suggests that a steady state assumption may work but careful examination shows that this fails too, especially for the latter stages of the cloud when the updraft is replaced quickly by a downdraft.

Fig. 4 shows the correlation between the magnitude of the vertical velocity, normalized by the maximum value observed for each pass, and the liquid water content, also normalized by the maximum value for that pass. In the core of the updraft the weaker portions of the updraft are regions of low liquid water content as seen by the FSSP. The other particle measuring sensors show that these weaker W regions are not regions where there are larger drops. This suggests that the weaker updraft regions are due to entrainment directly into the core, not the edges of the draft.

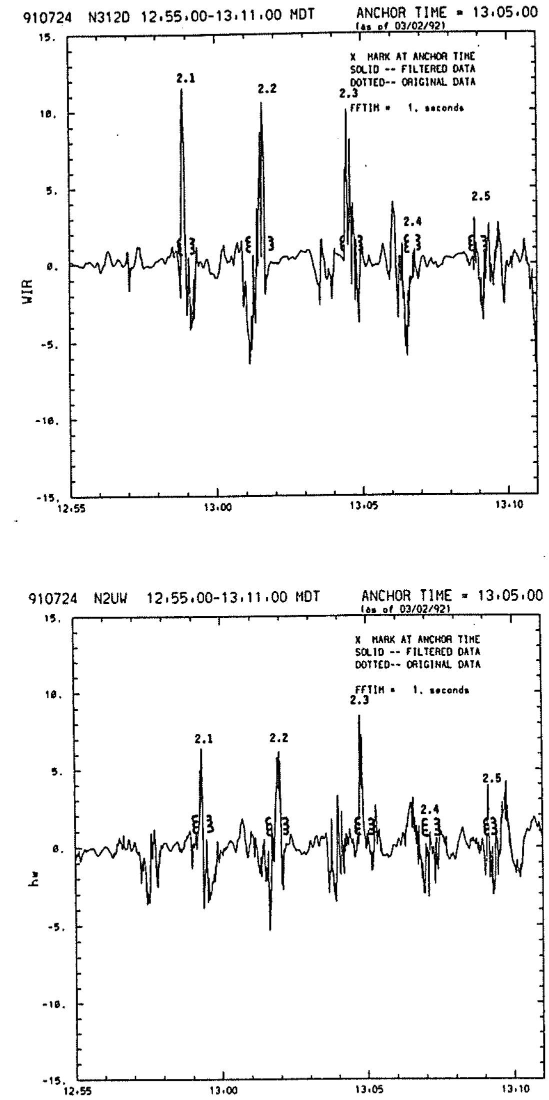

Fig. 3: Overview of the vertical velocity sampled by the two King Airs from 1417 to 1429 LT on 7/26/91, cloud 2. Cloud edges denoted by scalloped lines. 312D is at 3660m and 2UW is at 2740m. Altitudes above MSL.

Fig. 4: Correlation of W and liquid water content for the core of the updraft. Values normalized by the maximum value of each variable for each pass. →

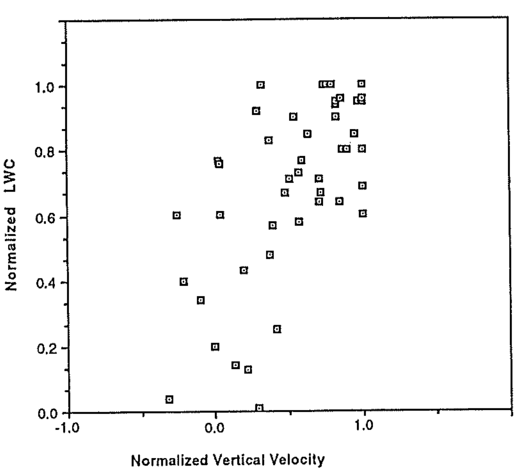

5. Discussion

To date, we have examined 43 passes made through five towering cumulus clouds with the two King Airs during the CaPE experiment. These clouds are 1-2 km wide and about 4-5 km in maximum vertical extent. They barely reached the freezing level, were not electrified, and were not triggered by an outflow boundary or the sea-breeze front. They did exist in a high instability, low shear environment indicative of typical summertime Florida conditions.

Analyses at this time support the following: 1) the updraft is a continuous feature, not a series of bubbles, 2) the updraft core rapidly weakens and its variance increases with time, 3) the regions in the core with weaker upward velocities are correlated with lower liquid water content, and 4) lateral entrainment occurs only 40% of the time at cloud edge, is unsteady at a given level, and varies widely for modest vertical displacements (~600m).

These early results support a conceptual model that includes the ingestion of small parcels (scales < 100m) of environmental air at cloud-top, much like those simulated in the high resolution two-dimensional model by Klassen and Clark (1985).

Analyses are currently continuing on larger congestus clouds that do grow beyond the freezing level and do develop an electric field.

6. References

Betts, A.K.,1982a: Saturation point analysis of moist convective overturning. *J. Atmos. Sci.*, **38**, 1484-1505.

______, 1982b: Cloud thermodynamic models in saturation point coordinates. *J. Atmos. Sci.*, **39**, 2182-2191.

Blyth, A.M., W.A. Cooper, and J.B. Jensen, 1988: A study of the source of entrained air in Montana cumuli. *J. Atmos. Sci.*,**45**, 3944-3964.

Byers, G.R., and E. C. Hull, 1949: Inflow patterns of thunderstorms as shown by winds aloft. *Bull. Amer. Meteor, Soc.*,**30**,90-96.

Fankhauser, J.C., G.M. Barnes, D.W. Breed, C. Biter, and M.A. LeMone, 1983: Summary of Queen Air measurements beneath cumuli in CCOPE. NCAR Tech. Note 207+STR. {avail. from NCAR, P.O. Box 3000, Boulder, CO 80307}.

Jensen, J.B., P.H. Austin, M.B. Baker, and A.M. Blyth, 1985: Turbulent mixing, spectral evolution and dynamics in a warm cumulus cloud. *J. Atmos. Sci.*, **42**, 173-192.

Klassen, G.P., and T.L. Clark, 1985: Dynamics of the cloud-environment interface and entrainment in small cumuli: two dimensional simulations in the absence of ambient shear. *J. Atmos. Sci.*, **42**, 2621-2642.

Lawson, R.P., 1990: Thermodynamic analyses of buoyancy and entrainment in cumuli using measurements from a radiometric thermometer. AMS Preprints from 1990 Conf. on Cloud Physics, July 23-27, San Francisco, 685-691.

LeMone, M.A., L. F. Tarleton, and G. M. Barnes, 1988: Perturbation pressure at the base of cumulus clouds in low shear. *Mon. Wea. Rev.*, **116**, 2062-2068.

Malkus, J.S., 1954: Some results of a trade cumulus cloud investigation. *J. Meteor.*, **11**, 220-237.

Paluch, I.R., 1979: The entrainment mechanisms in Colorado cumuli. *J. Atmos. Sci.*, **36**, 2467-2478.

Pontikis, C., A. Rigaud, and E. Hicks, 1987: Entrainment and mixing as related to the microphysical properties of shallow, warm, cumulus clouds. *J. Atmos. Sci.*, **44**, 2150-2165.

Reuter, G.W., and M.K. Yau, 1987: Mixing mechanisms in cumulus congestus clouds. Part I: Observations. *J. Atmos. Sci.*, **44**, 781-797.

Squires, P., 1958: Penetrative downdrafts in cumuli. *Tellus*, **10**, 381-389.

Stommel, H., 1947: Entrainment of air into a cumulus cloud. *J. Meteor.*, **4**, 91-94.

Warner, J., 1955: The water content of cumuliform cloud. *Tellus*, **7**, 449-457.

______, 1977: Time variation of updraft and water content in small cumulus clouds. *J. Atmos. Sci.*, **34**, 1306-1312.

COORDINATED AIRCRAFT AND MULTI-PARAMETER RADAR OBSERVATIONS OF CaPE WARM BASED CLOUDS

Paul L. Smith, Andrew G. Detwiler and Dennis J. Musil
Institute of Atmospheric Sciences
South Dakota School of Mines & Technology
501 E. St. Joseph Street
Rapid City, SD 57701-3995

and

V. Chandrasekar and V. N Bringi
Colorado State University
Fort Collins, CO 80523

1. INTRODUCTION

The Convection and Precipitation/Electrification experiment (CaPE) was carried out in the region around the Kennedy Space Center in Florida during July and August 1991. CaPE had a variety of scientific objectives, one of which was to compare polarimetric radar measurements with *in situ* microphysical observations in order to help validate retrievals based on the radar observations. This paper reports on the preliminary results of one such comparison.

The basic approach was to scan the cloud of interest with the CP-2 multi-parameter radar, usually in an RHI mode, while the T-28 research aircraft penetrated the same cloud. The general objective was to penetrate regions of the clouds that had an active precipitation process and displayed multi-parameter signatures of scientific interest. The T-28 penetrations were directed from the ground, on the basis of CP-4 C-band Doppler radar PPI observations with overlaid flight tracks of the aircraft plus verbal information relayed from the CP-2. Figure 1 provides a map showing the layout of the radars.

The CP-2 radar operates at both S-band and X-band, with reasonably well-matched 1° beam patterns; it obtains reflectivity and Doppler data at both wavelengths as well as differential reflectivity (ZDR) measurements at S-band and linear depolarization (LDR) measurements at X-band. The T-28 obtains microphysical observations across the entire hydrometeor spectrum from cloud droplets to hailstones. We present here one example of the correlated observations, obtained on the afternoon of 9 August 1991. In this example, the T-28 appears to have passed near a "positive ZDR column" on a westbound penetration and then a region of high LDR on a returning eastbound penetration.

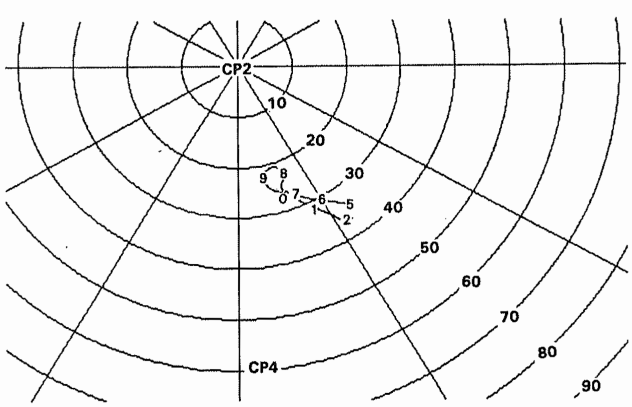

Figure 1: A spider web centered on CP-2 shows relative locations of the CP-2 and CP-4 radars. GPS flight tracks of the T-28 storm penetrations discussed are superimposed. Range rings are labeled in kilometers.

2. OVERVIEW OF AIRCRAFT OBSERVATIONS

On this day, the T-28 made a series of penetrations at about 4.9 km MSL altitude, corresponding to a temperature of about -4°C. At the same time, the CP-2 scanned the sector using a mix of RHI and PPI scans. The storm of particular interest here had a maximum reflectivity factor approaching 60 dBz at the time of the initial penetration, and decreased in intensity as time progressed.

The cloud was penetrated three times over the period 1415-1429 EDT (Eastern Daylight Time), generally along a track lying west-northwest to east-southeast. Each penetration found weak to moderate updrafts, the strongest being about 10 m s^{-1}, and cloud liquid water concentrations (LWC) up to about 1.5 g m^{-3} as measured by the Johnson-William sensor. (As this instrument is not generally sensitive to droplets larger than about 30 μm, the actual LWC's were probably greater.)

Images obtained by a Particle Measuring Systems (PMS) OAP-2D-P probe showed the precipitation particles to be predominantly graupel, as far as this can be established from the images. The Cannon particle camera photographed a few liquid raindrops during the penetration at 1416, but otherwise found only graupel. Particles up to 3-4 mm in size were observed on each penetration; the larger particles would have been falling against the updraft in each case. A puzzling feature is the apparent absence of significant numbers of raindrops; with typical cloud-base temperatures in Florida being around 20°C and the penetration levels at -4°C, one would expect to find drops developing by coalescence appearing in at least the stronger updrafts. However, there is very little evidence of this in any of the microphysical observations obtained.

3. COMPARISONS WITH RADAR DATA

We present here only the comparisons for the first two aircraft penetrations. The penetrations passed diagonally across the CP-2 radar beam at angles of about 30° - 40° and distances of 28-33 km. At this range, the (3 dB) width of the radar beam is about 0.6 km. Given the geometry of the flight track with respect to the radar, the beam in effect averages over about 0.8 km of flight path, or roughly 9 s of flight time.

3.1 First Penetration (1416 EDT)

On this westbound penetration, the T-28 apparently passed near a "positive ZDR column" (Fig. 2). The penetration track was at an angle of about 40° to the radial along which the RHI was taken; the track shown is a projection of the actual path onto the plane of the RHI. The ZDR values reached about 2 dB at the penetration level, and over 4 dB lower down in the storm. The region of higher ZDR was located between a pair of small updrafts, each a little more than 1 km wide and separated by about 3 km (Fig. 3). The T-28 observed a region of mixed-phase precipitation (graupel and rain) a few hundred meters across, where the particle camera photographed a few supercooled raindrops, shortly after exiting the eastern updraft.

The location where the T-28 crossed the 153° radial at 141620 was characterized by updrafts of 6-9 m s^{-1} in a region a little over 1 km wide, cloud LWC of over 1 g m^{-3}, and essentially no precipitation particles (Fig. 3). However, both the 2D-P probe and the Cannon camera showed graupel in the region just to the east of that updraft (Fig. 4). The largest observed particles were about 3 mm in diameter. This region had at most very weak updrafts, and there was no cloud water present. Consequently, the graupel must have been falling in a dry growth environment (*Musil and Smith,* 1989).

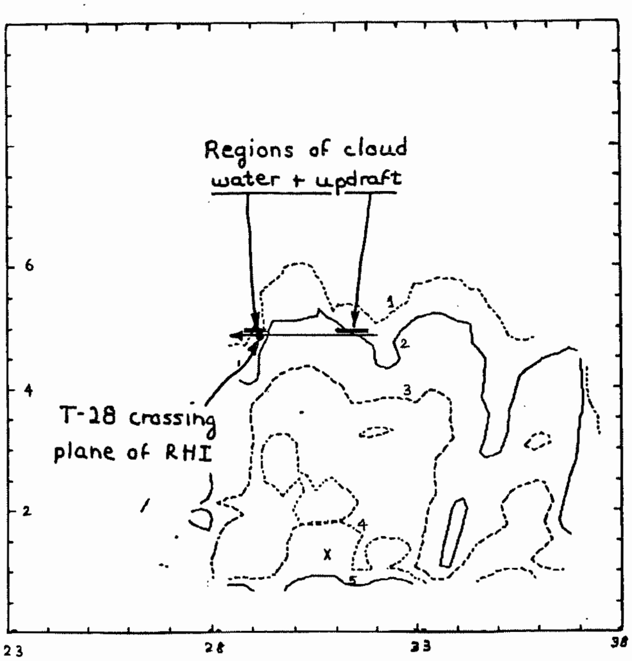

Figure 2: Portion of RHI section from CP-2 along the 153° radial at about 181355 UTC, showing contoured ZDR values in dB. T-28 flight track for the 1416 EDT penetration is projected onto the plane of the RHI scan. Range and height scales in km.

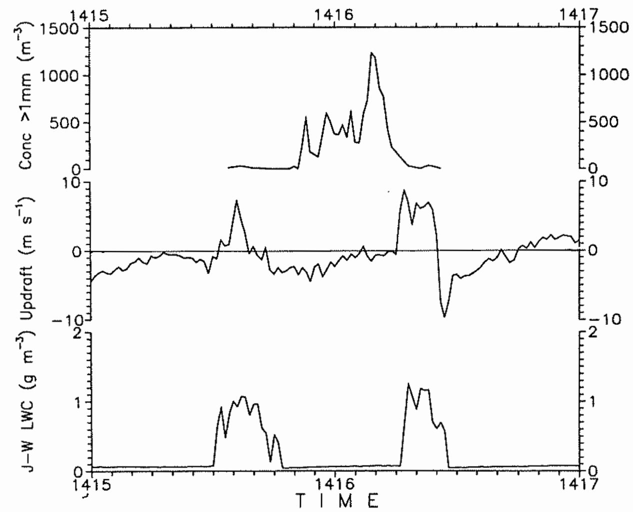

Figure 3: Plot of selected variables measured by the T-28 during the 1416 penetration. Top: concentration of precipitation particles larger than 1 mm (m^{-3}). Middle: updraft speed (m s^{-1}). Bottom: cloud LWC (g m^{-3}). Time scale is EDT (HHMM).

3.2 Second Penetration (1421 EDT)

In the initial segment of the second, return penetration, the cloud LWC reached a maximum of about 1.5 g m^{-3} in an updraft up to 5 m s^{-1} (Fig. 5). At the same time, precipitation particles were found in moderate number concentrations, although the presence of "streaker" artifacts in the image data may lead to an underestimate of these concentrations. The average number concentration of particles larger than 1 mm was around 500 m^{-3}. Particles as large as 4 mm in size appeared in the image data (Fig. 6). The precipitation mass concentration averaged a few grams per cubic meter over this portion of the penetration.

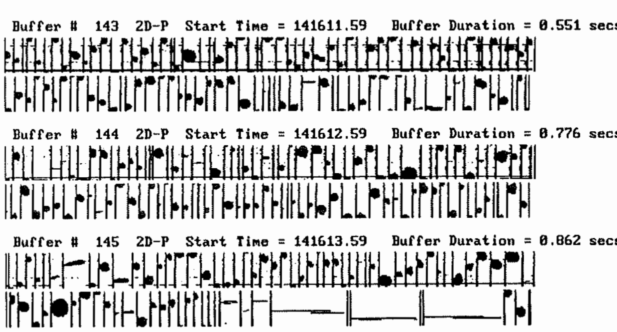

Figure 4: Examples of PMS 2D-P images from about 141613 EDT during the first penetration. Vertical bars represent 6.4 mm.

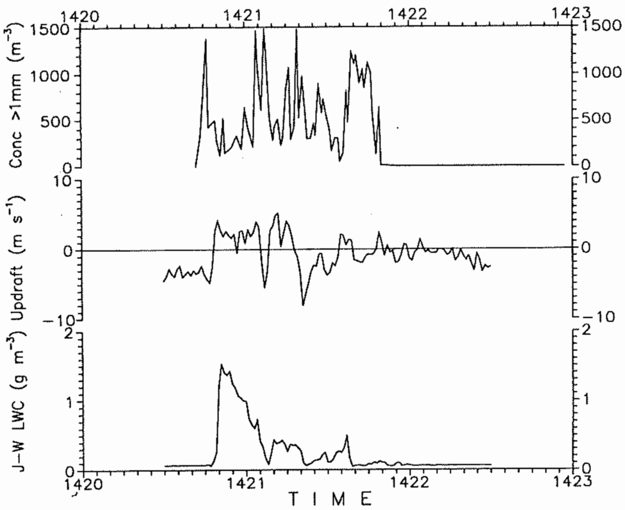

Figure 5: As Fig. 3, but for the 1421 penetration.

The LDR signature in this region (Fig. 7) approaches -20 dB and is suggestive of the presence of wet graupel. A few of the particle images might have represented liquid raindrops, but most of them were irregular and indicated the presence of graupel, as illustrated by the examples in Fig. 6. The presence of "streaker" images in the data substantiates the presence of liquid water at the penetration level. In view of the substantial amounts of cloud water present, it is clear that the particles must have been in a wet growth mode (*Musil and Smith,* 1989). Thus, an interpretation of wet graupel is consistent with the microphysical data.

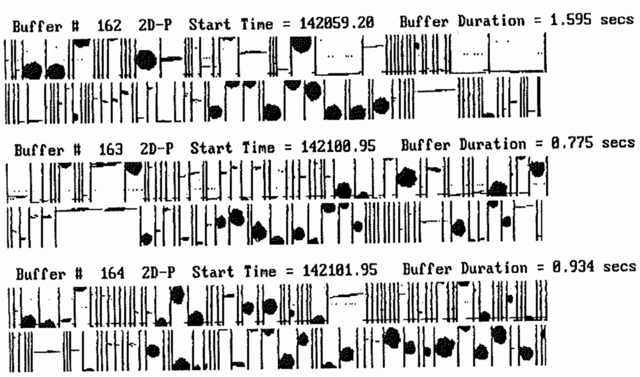

Figure 6: As Fig. 4, but for times around 142101 during the second penetration.

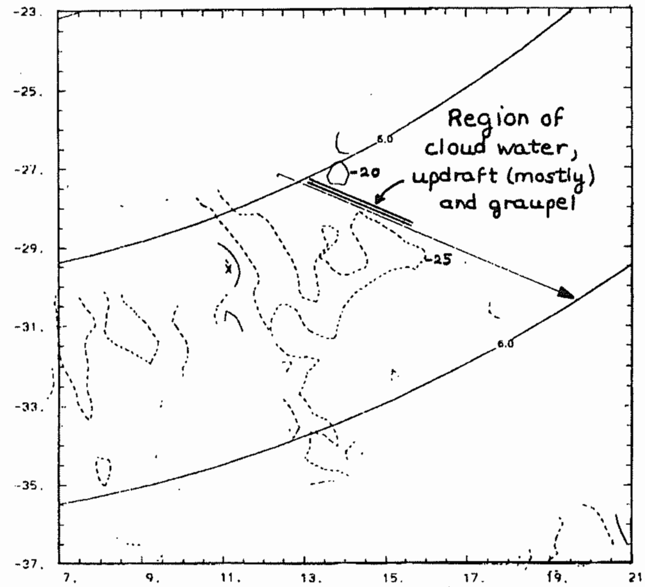

Figure 7: PPI sector scan from CP-2 at 9.3° elevation at about 182045 UTC, showing contoured LDR values in dB. Rings show where beam crossed altitudes of 5.0 and 6.0 km MSL. T-28 flight track for the 1421 EDT penetration is superimposed. Scales for x and y in km, from CP-2.

4. DISCUSSION

These are preliminary findings from a detailed comparison of the aircraft and radar data that is continuing. Both sets of data contain interesting signatures, and the major task is to find observations that are well-correlated in time and space for the comparisons. Accurate navigation of the independent data sets is also necessary to obtain valid comparisons.

ACKNOWLEDGMENTS

The research reported here was supported by the National Science Foundation under Cooperative Agreement No. ATM-9104474 and Grants No. ATM-9022846 and No. ATM-9014600.

REFERENCES

Musil, D. J., and P. L. Smith, 1989: Hail growth processes in an Alberta hailstorm. *J. Wea. Modif.*, **21**, 65-72.

CASE STUDIES OF OBSERVED BOUNDARY LAYER CLOUDINESS PHENOMENA

P. Bechtold

Laboratoire d'Aérologie
Université Paul Sabatier, 31062 Toulouse, France

1. INTRODUCTION

The cloud-topped boundary layer (CTBL) is one of the most important climate relevant factors. Over the ocean, large sheets of stratocumulus clouds regularly occur over cold water near the ouest coasts of the continents in the presence of high pressure systems. Marine cumulus clouds are preferably found over warm ocean water in the trade-wind zone. Another important source of boundary cloudiness are cold air oubreak events which frequently can be observed off the east cost of the continents. The large temperature difference between the sea and the air leads to strong convection and to a more or less partially covered sky. Numerous experimental campaigns (AMTEX, JASIN, GALE, MASEX, FIRE,...) have been cunducted in order to investigate the turbulent structure of the marine CTBL. However, the continental CTBL, where cloudiness phenomena are less persistant, has experienced much weaker attention.

Here, our aim is the simulation of some selected marine and continental CTBL cases, where particular cloudiness phenomena were present.

2. THE MODEL

The numerical simulations are done with the aid of one-, two- and three-dimensional versions of a hydrostatic mesoscale model (Bechtold et al., 1992a). The model contains prognostic equations for the horizontal wind speeds, the liquid potential temperature, the total water content and the turbulent kinetic energy. It further includes the recent ECMWF radiation package (Morcrette, 1989) and a statistical partial condensation scheme (Mellor, 1977) with parameterized second-order thermodynamic moments (Bechtold et al., 1992b). Microphysical processes are neglected in the present version, so the effectif drop radius, necessary for the radiation calculations, is simply expressed as a function of the liquid water content. As another important feature, the model also contains a detailed surface scheme to calculate the exchanges betwen the soil, the vegetation and the atmosphere. The model runs are done with horizontal and vertical resolutions of 10 km and 50 m, respectively, the model time step is 10 s.

3. CASE STUDIES

a. *North Atlantic stratocumulus clouds, 1D case*

We use aircraft observations made on 16 november 1983 off the north west coast of Scotland as reported by Nicholls and Leighton (1986). The simulation is made for 1 July in order to test the diurnal variation of the CTBL under summertime radiation conditions, when solar absorption in the cloud deck is strong enough to induce a stable zone with cumulus clouds appearing just near the condensation level. Figure 1 shows the 48 hours evolution of the the partial cloudiness. One clearly observes the strong diurnal oscillation of the cloud deck and

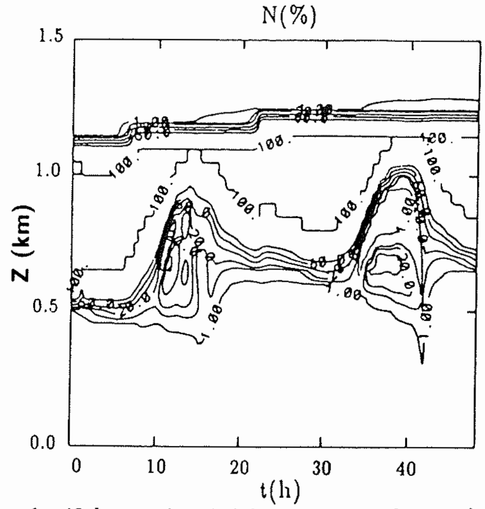

Figure 1. 48 hours time-height section of the partial cloudiness.

the formation of a secondary cloud layer during the afternoon. This secondary cloud layer forms at the top of a stable layer which decouples the primary cloud layer from the surface moisture and heat fluxes. Although the short wave heating (0.3 K h^{-1}) is much weaker than the longwave cooling (-5 K h^{-1}), it acts more efficiently in the interior of the cloud because it is not compensated by turbulent processes.

b. Cloudiness transition, 2D case

The second case study is devoted to the simulation of a two-dimensional cloudiness transition observed during a cold air outbreak event off the Carolina coast (Boers and Melfi, 1987). A discussion of this case is given in Bechtold et al. (1992b). Strong surface heat fluxes of the order of 200 and 300 W m^{-2} rapidly heat and moisten the dry and cold continental air as it streams over the ocean. A slope in boundary layer height develops, resulting in a continuous cloudiness transition with cloudiness varying between 0% near the coast and 100% at some distance over the ocean. Figure 2 shows the simulated horizontal distribution of the cloud cover (i.e. the vertically integrated partial cloudiness) after 3, 6, and 9 hours of simulation. First cumulus clouds develop after 3 hours. Finally, after 9 hours a cloudiness transition zone of about 100 km is established. The observed cloudy patches are displayed by the horizontal line. There is quite good agreement between the simulated and observed cloudiness transition zone.

c. Continental CTBL, 3D case

The last case we consider is a continental CTBL observed June 16, 1986 during the HAPEX-MOBILHY campaign (André et al., 1986) over the south- west of France. This day can be caracterized as a fair summer day with maximum surface teperatures attaining 30 °C. However, the satellite image for

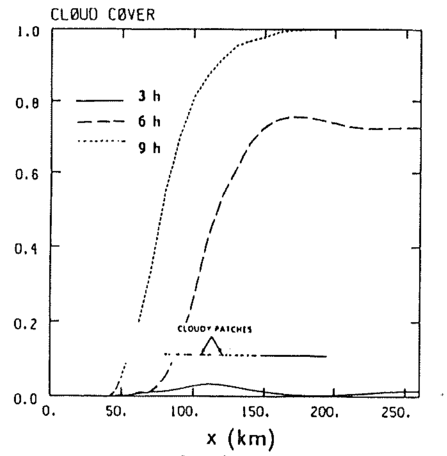

Figure 2. Distribution of the simulated cloud cover after 3, 6 and 9 hours of simulation. The horizontal line displays the observed cloudy patches (from Boers and Melfi, 1987).

1300 UTC (Figure 3a) shows convectif clouds over the Pyrhenees mountain range (south of the domain) and some cloudiness over the Masif Central (east of the domain). But the most interesting feature in Figure 3a is the existance of a thin convectif cloud band which is associated to a meso-front built up by the inland penetration of fresh and humid maritime air.

The model is initialized with the analyzes of the French Weather Service and the detailed surface observations (soil and vegetation properties) made during HAPEX-MOBILHY. The simulated cloud cover is shown in Figure 3b. The model reproduces quite well the cloudiness over the Pyrenees but unfortunately could not resolve the convectif cloud band near the Atlantic coast. The failure of the model does not question the partial cloudiness scheme used but reflects a general problem which poses the simulation of the continental CTBL. Two main difficulties can be mentioned.

- Surface inhomogeneities lead to small scale and mesoscale variations in the continental CTBL structure
- The inversion at boundary layer top, and so the second-order thermodynamic moments, are much weaker for the continental CTBL than for the marine CTBL. It is therefore much more difficult to produce continental boundary layer cloudiness with the partial cloudiness scheme at low values for the relative humidity.

4. CONCLUSION

The used mesoscale model including a performant radiation scheme and a statistical partial cloudiness scheme with parameterized second-order moments simulates quite well different cases of marine boundary layer cloudiness. However, problems have been encountered in simulating small cumulus clouds in the continental CTBL. This is due to the fact the the inversion at the top of the continental CTBL is weak, so the turbulent moments necessary to produce cloudiness with a partial cloudiness scheme are not strong enough. In the case of a continental CTBL, an improved expression for the second-order thermodynamic moments including meso- and small-scale variations in boundary layer structure might be necessary.

Figure 3a. Visible satellite image from NOAA-9 AVHRR data, showing the south-ouest of France and the north-east of Spain for Juin 16, 1986 1300 UT.

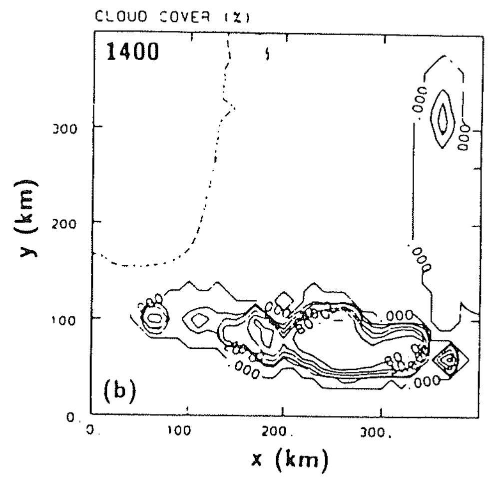

Figure 3b. Corresponding simulated cloud cover.

REFERENCES

André, J.-C., J.-P. Goutorbe et A. Perrier, 1986: A Hydrologic Atmospheric Experiment for the Study of Water Budget and Evaporation Flux at the Climatic Scale. *Bull. Amer. Meteor. Soc.*, **67 (2)**, 138-144.

Bechtold, C. Fravalo and J. P. Pinty, 1992a: A model of marine boundary layer cloudiness for mesoscale applications. *J. Atmos. Sci., in press (July issue)*

———, C. Fravalo and J. P. Pinty, 1992b: A two-dimensional cloudiness study during a cold air outbreak event. *Bound. Layer Meteor., in press*

Boers, R. et S. H. Melfi, 1987: Cold air outbreak during MASEX: Lidar observations and boundary-layer model test. *Bound. Layer Meteor.*, **39**, 41-51.

Mellor, G. L., 1977: The gaussian cloud model relations. *J. Atmos. Sci.*, **34** , 356-358.

Morcrette, J.-J., 1989: Impact of changes to the radiation transfer parameterizations plus cloud optical properties in the ECMWF model. *Mon. Wea. Rev.*, **118**, 847-873.

Nicholls and J. Leighton, 1986: An observational study of the structure of stratiform cloud sheets: Part I: Structure. *Quart. J. Roy. Meteor. Soc.*, **112**, 431-460.

LARGE EDDY SIMULATION OF CUMULUS DEVELOPMENT UNDER SHEARED AND CONVECTIVE CONDITIONS

J.W.M. Cuijpers *) and P.G. Duynkerke **)

*) Royal Netherlands Meteorological Institute, P.O. Box 201,
3730 AE DE BILT, The Netherlands

**) Institute for Marine and Atmospheric Research Utrecht, Utrecht University
P.O. Box 80 000, 3508 TA UTRECHT, The Netherlands

1. INTRODUCTION

Large areas of cumulus clouds are found in the trade wind regions in each hemisphere and over the midlatitude continents in summer. In the tropical region cumulus is often the most frequently occurring cloud type and, moreover the cloud type contributing most to the total cloud cover. Because of these distributions in space and time and the influence of this cloud type on the turbulent exchange between the convective boundary layer and the free atmosphere above, cumulus cloud fields are important in daily weather and in climate. However, in regional and global models cumulus convection is a subgrid proces and has to be parameterized.

In order to investigate the processes that are important in cumulus convection we extended an existing large eddy simulation model (Nieuwstadt and Brost, 1986) with an equation for the specific humidity and a condensation scheme. With this model two simulations have been made. The first one (Cuijpers and Duynkerke, 1991) is based on the observations gathered near Puerto Rico (Pennell and LeMone, 1974). During the observations there was a high wind speed of about 15 m/s. The second simulation is based on the observations gathered during GATE (Nicholls and LeMone, 1980). During the day that is simulated the wind speed was 2-3 m/s. So, while in the first simulation shear production is an important production term in the turbulent kinetic energy budget, in the second simulation the buoyancy production is more important.

2. MODEL DESCRIPTION

In the model we use the liquid water potential temperature θ_l and the total water specific humidity q_t as conserved variables in the thermodynamical equations. Radiational cooling is fixed to a constant, which is chosen such that it balances the heat input at the surface.

The condensation scheme of Sommeria and Deardorff (1977) is used to determine whether or not a gridbox contains liquid water. It is assumed that a gridbox is either entirely saturated or entirely unsaturated.

The model domain is 5 x 5 km^2 horizontally (with a 125 m grid interval), and it extends vertically from the surface up to a height of 2 km (with a 50 m interval).

3. RESULTS

To initiate the model the profiles of potential temperature, specific humidity and horizontal velocity are chosen such as to reproduce the observed conditions during GATE day 253 (10 September 1974).

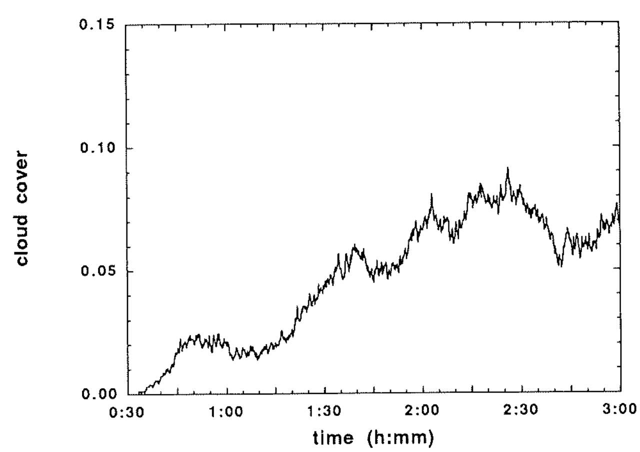

Fig. 1 The temporal evolution of cloud cover.

The first clouds form after about half an hour. Hereafter the cloud cover gradually increases to reach a quasi-steady state after 2 hours (Figure 1). Cloud cover thereafter varies between 5 - 10 %, about the same as during the observations. The mean cloud base height is at 600 m, the highest cloud tops reach up to 1000 m. The latter is slightly lower than observed.

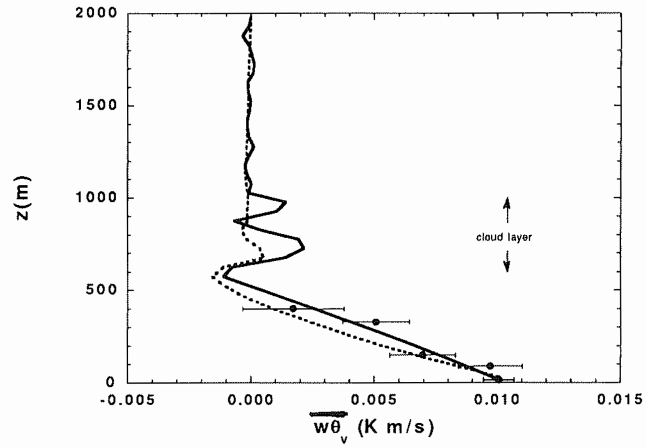

Fig. 2 The horizontally averaged virtual potential temperature flux at $t=1^h00^m$ (broken line) and $t=2^h30^m$ (full line). The dots with error bars are the observations.

In Figure 2 we show the profile of the virtual potential temperature flux at $t = 1^h00^m$ and $t = 2^h30^m$. In the subcloud layer the flux decreases linearly with height and shows no variations with cloud cover. In the cloud layer the release of latent heat enhances the buoyancy. In this layer the virtual potential temperature flux depends on cloud cover.

The vertical flux of total water varies with cloud cover in the mixed layer as well as in the cloud layer (Figure 3). Note that the profile at $t = 2^h30^m$ is almost constant with height from the surface up to the cloud base, which means that all vapor is transported from the ocean surface into the cloud layer.

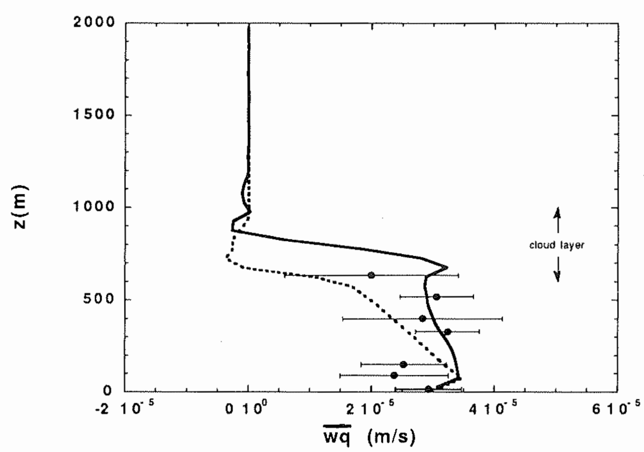

Fig. 3 The horizontally averaged total water flux at $t=1^h00^m$ (broken line) and $t=2^h30^m$ (full line). The dots with error bars are the observations.

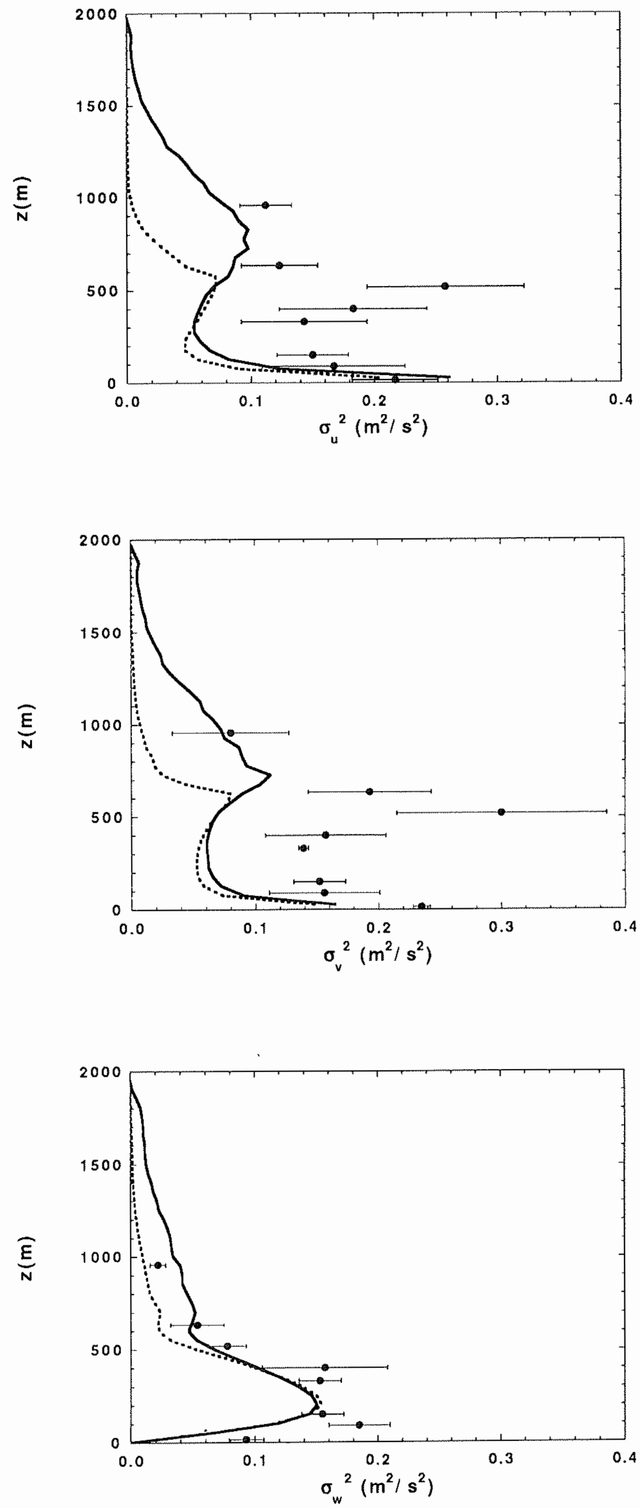

Fig. 4 Profiles of the horizontally averaged variances of u, v and w at $t = 1^h00^m$ (broken line) and $t = 2^h30^m$ (full line) compared with observations (dots with error bars).

Figure 4 shows the variances of the u, v and w velocity components. The model seems to underestimate the variances of the horizontal velocity components. However, the spectra of the observed u and v velocities show considerable contributions from scales larger than the model domain. The spectrum of the w velocity peaks at about 700 m. The observed and modeled vertical velocity variances compare well.

4. DISCUSSION

Both simulations (based on Puerto Rico and GATE) seem to reproduce the observed situations fairly well. It is therefore interesting to compare both cases. In Figure 5 we show the profiles of the shear and buoyancy production term of the turbulent kinetic energy equation. As expected shear production dominates over buoyancy in the Puerto Rico case in the lower part of the mixed layer and in the cloud layer. In the GATE simulation buoyancy production exceeds shear production in the subcloud layer, while they are comparable in the upper half of the cloud layer.

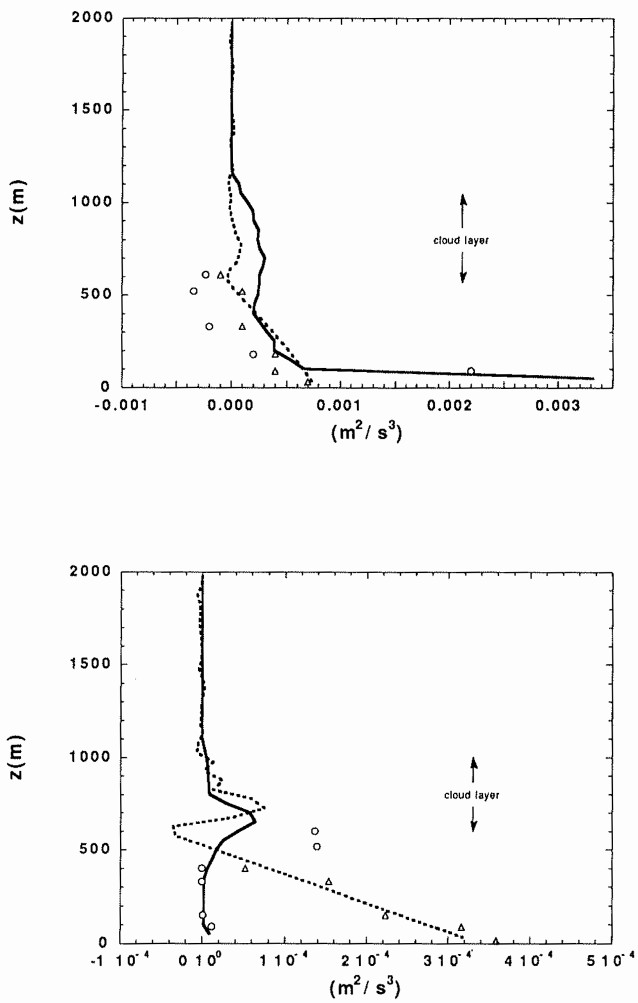

Fig. 5 Shear (full line) and buoyancy production (broken line) for Puerto Rico (upper panel) and GATE (lower panel). Observed shear and buoyancy is indicated by circles and triangles, respectively

The different circumstances have a clear influence on the air motions inside the clouds. In Table 1 we show the results of an analysis of scatterplots in which we plotted the virtual potential temperature θ_v as a function of the vertical velocity w for all grid points in a horizontal plane, i.e. at a certain height. We then calculated the percentage of cloud grid points with:

$\theta_v^{cloud} > \langle\theta_v\rangle$ and $w^{cloud} > 0$ (Warm Updrafts WU),

$\theta_v^{cloud} < \langle\theta_v\rangle$ and $w^{cloud} > 0$ (Cold Updrafts CU),

$\theta_v^{cloud} > \langle\theta_v\rangle$ and $w^{cloud} < 0$ (Warm Downdrafts WD), and

$\theta_v^{cloud} < \langle\theta_v\rangle$ and $w^{cloud} < 0$ (Cold Downdrafts CD),

where $\langle\theta_v\rangle$ is the horizontally averaged virtual potential temperature, θ_v^{cloud} is the virtual potential temperature at a cloud grid point and w^{cloud} the vertical velocity at a cloud grid point.

Puerto Rico 1972

z(m)	WU	CU	WD	CD	n
1000	13	53		33	15
950	10	65		25	20
900	18	56		26	50
850	15	46	1	38	82
800	17	56	1	26	119
750	27	47	1	24	135
700	31	40	3	26	148
650	51	35	4	10	114
600	69	28	3		36

GATE 1974

z(m)	WU	CU	WD	CD	n
850	50	50			4
800	56	33		11	9
750	64	23		14	22
700	55	28	3	14	58
650	38	36	6	20	66
600		75	25		4

Table 1 The number of cloud grid points (n) at height z and the percentage of warm updrafts (WU), cold updrafts (CU), warm downdrafts (WD), and cold downdrafts (CD).

In the Puerto Rico case WU's are dominant near cloud base but only a hundred meters higher CU's are most important. However, in the WU-section there are a few points with θ_v much larger than $\langle\theta_v\rangle$ and w^{cloud} much larger than 0. These points contribute much to the buoyancy flux.
Furthermore, about 25 - 30 % of the incloud motions is in cold downdrafts. So, both upward and downward motions are found inside clouds.

In the GATE simulation warm and cold updrafts are equally present near cloud base. The release of latent heat enhances the buoyancy and warm updrafts become the most important. Downdrafts are only a minor portion of the motions, so in this case upward motions are mostly inside clouds and downward motions are found in the environment.

ACKNOWLEDGEMENT

The authors like to thank Dr. M.A. LeMone for providing the data of the Puerto Rico experiment and GATE. The first author acknowledges financial support by the Netherlands organisation for scientific research (NWO) under contract # 752-365-031.

REFERENCES

Cuijpers, J.W.M., and P.G. Duynkerke, 1991: Large eddy simulation of cumulus clouds. *Eighth symposium on turbulent shear flows*, Munich, Germany, II-4-1 & II-4-2.

Nicholls, S., and M.A. LeMone, 1980: The fair weather boundary layer in GATE: The relationship of subcloud fluxes and structure to the distribution and enhancement of cumulus clouds. *J. Atmos. Sci.*, **37**, 2051-2067.

Nieuwstadt, F.T.M., and R.A. Brost, 1986: The decay of convective turbulence. *J. Atmos. Sci.*, **43**, 532-546.

Pennell, W.T., and M.A. LeMone, 1974: An experimental study of turbulence structure in the fair-weather trade wind boundary layer. *J. Atmos. Sci.*, **31**, 1308-1323.

Sommeria, G., and J.W. Deardorff, 1977: Subgrid-Scale Condensation in Models of Nonprecipitating Clouds. *J. Atmos. Sci.*, **34**, 344-355.

DYNAMICS OF NON-ACTIVE PARTS OF CONVECTIVE CLOUDS

Krzysztof E. Haman and Hanna Pawłowska

Institute of Geophysics, University of Warsaw, Poland
ul. Pasteura 7, PL-02-093 Warszawa, Poland.

1. INTRODUCTION

It is a well known empirical fact that the prevailing part of a visible Cumulus cloud (except perhaps of very early stages of its development) is dynamically inactive, i.e. is void of organized updrafts and downdrafts on the scale comparable with the size of the cloud. The motions observed there resemble typical unordered turbulence with rather not too frequent intrusions of relatively small scale vertical drafts. Records of temperature or liquid water content (LWC) taken in these regions have strongly fluctuating character and presence of pockets of unsaturated air is often detected. Even in the case of conditionally unstable environment, these parts often do not reveal tendency to develop downdrafts (what should have place according to the simple "parcel theory") but decay slowly; the cloud in this stage has characteristic ragged edges. One may speculate, that this relative stability is due to the presence of small scale turbulence, which may stabilize the whole cloud as does molecular diffusion of heat and momentum in the case of classical cellular convection at low Rayleigh numbers, but this seems not very likely. Precise quantitative estimates of these effects for clouds are not known to the authors, but application of bulk Priestley criterion suggests that the object of size of a Cumulus cloud should not be too sensitive to them.

In the present paper another possibility is being investigated. On the grounds of increasing observational evidence (Blyth et al., 1988; Doroure and Guillemet, 1990) it is hypothetically assumed that that the inactive part of the cloud is not thermodynamically homogeneous, but consists of a coarse mixture in form of filaments of saturated and droplet containing air entangled with filaments of air free from LWC and even unsaturated with water vapor; the scale of inhomogeneities may be of order of meters or less. In order to avoid cumbersome descriptions we shall refer to these components as to "dry" and "wet" air in the cloud, with quotation-marks emphasizing the atypical use of these terms. During vertical adiabatic motions the "dry" and "wet" filaments change their buoyancy according to dry and wet adiabate respectively but being entangled with each other they cannot develop separate vertical drafts. A bulk buoyant draft can develop only if the bulk resultant buoyancy appears. **Thus the hydrostatic stability criterion for such a coarse mixture is the environmental virtual temperature lapse rate being somewhere between the dry and wet adiabatic value, depending on the ratio between the "dry" and "wet" volume of the cloud.** This may explain the absence of bulk drafts despite of conditionally unstable stratification. The ratio of "dry" to "wet" air as well as the bulk buoyancy is permanently evolving under the processes of internal homogenizing mixing and bulk scale motions. The interaction between these two processes to high extent determines the speed and character of cloud evolution and decay. In the nature, the mixing process is due to the turbulence generated by inertial decay of toroidal vortices formed during the development of active drafts as well as by local small scale baroclinicity. Since such turbulence has usually scaling properties, we can expect that the boundary between the "wet" and "dry" volume may be conveniently described in terms of fractal theory, while distributions of LWC and subsaturation may be of a multifractal nature.

In the following we shall present some results of a preliminary study of relations between the internal homogenizing mixing and bulk dynamics of a thermodynamically inhomogeneous cloud, with particular attention paid to the persistence and decay of inactive clouds in conditionally unstable atmosphere.

2. THE ROLE OF INTERNAL MIXING

The air mass consisting of coarse mixture of "wet" and "dry" air may be changing its bulk density (and hence buoyancy) not only due to bulk adiabatic vertical displacements but also due to the heat and moisture fluxes from outside (e.g. radiation and/or entrainment) as well as internal mixing. The external fluxes, which are important mostly close to the cloud edges, will be disregarded in this study. In the mixing two physical processes can be distinguished:

a) homogenizing mixing i.e. formation of thermodynamically homogeneous fluid, either "wet"or "dry";

b) gravitational sedimentation of cloud droplets from one volume to another, and their evaporation in "dry" air.

Both these processes may change not only the bulk buoyancy but also the ratio between "dry" and "wet" air mass and hence the character of hydrostatic stability. For instance, if the resulting variation of buoyancy is positive, the parcel will start to move upwards and may eventually become totally saturated, becoming an organized updraft (in the case of conditionally unstable environment). In the opposite case the parcel will start to sink, with net loss of liquid water, possible relative decrease of "wet" component and eventual loss or even reversal of downward directed net buoyancy. In the first case the developing updraft has unstable character; in the second, the bulk motion becomes rather a quasisteady subsidence with permanent adjustment to the local equilibrium conditions. The latter process is of main interest in the present study.

It is easy to show that in the course of any isobaric process, net condensation should lead to a decrease of density (increase of buoyancy) and net evaporation should give an opposite result. Thus sedimentation of cloud droplets into unsaturated air always leads to net evaporation and hence to decrease of net buoyancy of the inhomogeneous air mass. Homogenizing mixing may give various results but usually, unless the "dry" component is fairly close to saturation, the net buoyancy decreases.

3. BIFRACTAL AND MULTIFRACTAL MODELS OF NONACTIVE CLOUDS

In order to get better understanding of the complex behavior of dynamically inactive parts of convective clouds in the course of their dissipation it may be useful to consider some simple models, perhaps not very realistic but with clear physics refelecting the basic properties of the investigated processes. In the first model we shall assume that the cloud consists of "dry" and "wet" component each of them being thermodynamically homogeneous (though evolving in time) and filling volume of fractal geometrical structure; the name "bifractal" seems thus appropriate for this model. In more complex models, which are out of the scope of the present study, thermodynamical properties of "dry" and "wet" component may differ from point to point and we shall refer to them as to "multifractal models".

4. PRELIMINARY RESULTS OF CLOUD SIMULATIONS

In the preliminary study several series of computer simulations has been performed by means of a simple model of 1D Lagrangian buoyant parcel with bifractal internal structure characterized with the following parameters: ; α - fraction of the "wet" air mass in the total; β - fraction of total mass being exchanged in a unit time between "dry" and "wet" component during homogenizing mixing; γ - LWC sedimentation coefficient being of the order of ratio of average sedimentation speed of cloud droplets to average thickness of "dry" filaments. Environmental stratification is given by surface data, parameter k = (environ. lapse rate - wet adiab. lapse rate)/(dry adiab. lapse rate - wet adiab. lapse rate) and relative humidity f. General conclusion from these simulations (two examples of which for constant values of all parameters are presented below) is that even for relatively high degree of conditional instability the model cloud parcel may subside slowly finally decaying by evaporation of LWC in the "wet" part. This behavior can be achieved with fairly realistic values of the model parameters, although requires fairly precise adjustment between α and β; otherwise intensive bulk drafts can develop after some time. The latter might be an artifact following from simplifications of the model, since in nature some feedbacks leading to adjustment of α and β can be present. Numerical experiments with different variants of bifractal model as well as works on development of multifractal model and its implementation in 3D models of convective clouds are continued.

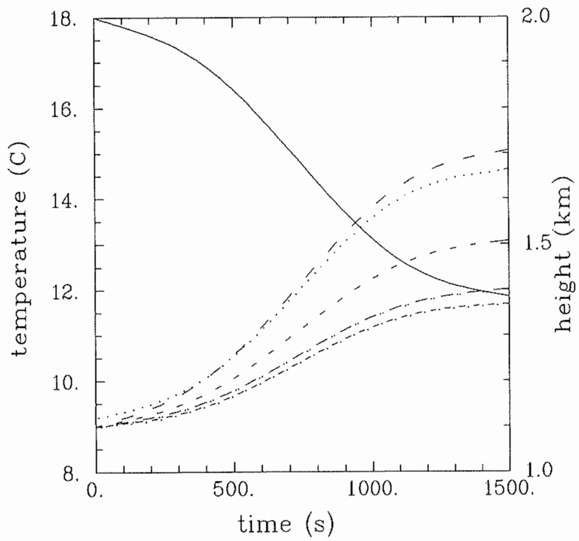

Fig.1. Motion of a "bifractal" parcel under internal mixing. k=0.3; f=0.7; α=0.55; $\beta=4\cdot10^{-5}$; γ= 0; ——— height of the parcel (right scale); temperatures along the trajectory (left scale): ---- environmental, ········ "dry" component, -·-·- "wet" component; -··-··- wet adiabate; — — dry adiabate.

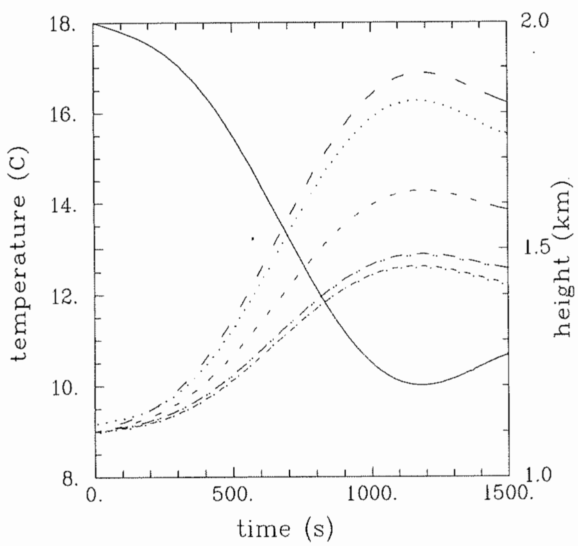

Fig 2. The same as Fig.1 with $\gamma = 1\cdot10^{-4}$.

REFERENCES

Blyth, A.M., W.A.Cooper and J.B.Jensen, 1988: A study of source of entrained air in Montana cumuli. *J.Atmos.Sci.*, **45**, 3944-3964.

Duroure, C., and B.Guillemet, 1990: Analyse des hétérogénéités spatiales des stratocumulus et cumulus. *Atmos.Research.* **25**, 331-350.

Three-Dimensional Analytical Mesoscale Dynamic and thermodynamic Structure of the Stratiform Part of a Squall Line Retrieved from Airborne Doppler Radar Data Obtained during the Experience CaPE

X.K Dou, G.Scialom, and Y.Lemaître

38-40, rue Général Leclerc
CNET-CNRS/CRPE Issy-les-Moulineaux, France

1. INTRODUCTION

The technique of airborne meteorological Doppler radar is progressively used and demonstrates a promising interest in meteorological studies(Hildebrand, 1990). The evident advantages of airborne facilities are that they allow to scan meteorological systems (squall lines, cloud clusters, fronts,...) in places where ground-based systems are not easy to operate (i. e. oceans) and/or to follow them during a significant part of their life time. In this context, in 1990, the CNET/CRPE (France) decided to cooperate with the NCAR (United States) to develop an airborne system called "ASTRAIA/ELDORA" carrying a dual-beam antenna for dual wind and reflectivity estimation. In order to test the capabilities of this antenna, a similar one was installed on the P-3 aircraft of the NOAA, instead of the single-beam antenna of this airborne radar system. The Convection and Precipitation/Electrification (CaPE) Experiment, carried out in Summer 1991 in Florida, USA, was the first experiment involving a dual-beam antenna on an airborne radar facility. On 9 August 1991, from 20h30 to 21h45 (UTC), five legs were flown around a squall line located near (80°.90"W, 28°.75"N). The aim of this paper is to present a general overview concerning the dynamics and the evolution of the squall line with particular emphasis on the interaction between the convective and the stratiform parts of this system. This aspect may be scrutinized thanks to the recently developed MANDOP analysis (Scialom and Lemaître, 1990). This study is presently under progress and will be detailed in the poster session.

2. SCANNING SYSTEM AND RADAR DATA

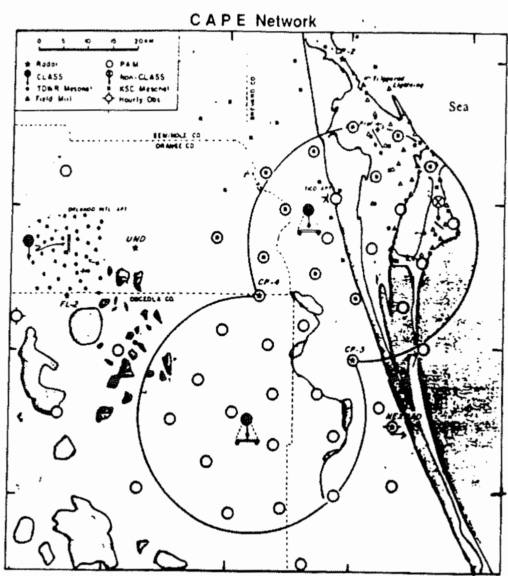

Fig.1

Fig. 1 gives a general scheme of the facilities involved in the CAPE experiment, in particular radiosonde, surface stations, ground-based radars (CP-2, CP-3 and CP-4), and the P-3 aircraft. This latter radar operates in the X-band with the French-made dual-beam antenna mounted in the tail of the aircraft. The antenna is turning about an axis parallel to the plane movement direction. The two beams are directed respectively 18.3^0 forward and backward with respect to the plane perpendicular to the rotation axis. Fig.2 depicts the scanning geometry.

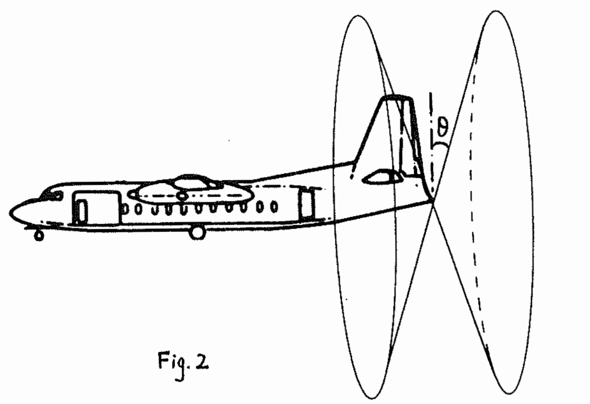

Fig. 2

Each antenna consists of a DOPPLER radar carrying out a sampling of the radial air velocity along the antenna's observation direction. The plane's movement in association with the antenna rotation makes a complete sampling in the observation volume.

The following figure (Fig3) shows a typical sampling in a cross-section parallel to the plane's trajectory:

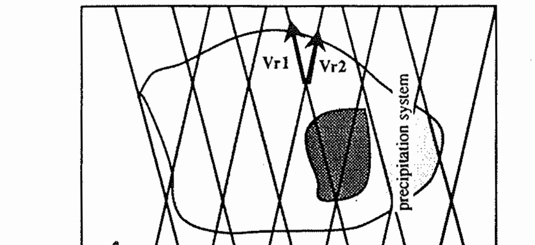

Fig.3

The antenna rotation time is of about 6s, which produces an effective horizontal data spacing of ~ 1km at the typical P-3 ground speed (about 600 km/h).

3. WIND SYNTHESIS

a. Methodology

The MANDOP analysis (Scialom and Lemaître, 1990) was used for the wind field retrieval.

With the hypothesis that the three components of the wind may be expanded as orthogonal functions series, the method allows to obtain these components and thus the measured radial wind under an analytical form. The seeked coefficients of this analytical form are obtained through a least-square minimization process with additional constraints also expressed analytically and simultaneously satisfied in a variational procedure. These constraints are the mass conservation and a lower boundary condition (vertical velocity null at ground).

The interests of this approach are:

- the method is applicable to any number (at least two) of Doppler radars , of any type (ground-based or airborne);
- the order of development and the base for orthogonal functions necessary to retrieve each component may be adapted to the type of observed meteorological event and very easily changed in the software;
- the analytical form of the wind allows to obtain the physical parameters related to it, such as vorticity, divergence, pressure and temperature perturbations in the same form.

b. Tests of qualification of the method

Scialom and Lemaître (1990) have essentially examined the case of ground-based radar data. Dou et al (1991) have qualified the method in the case of airborne radar data by means of simulations. They have solved the problems encountered on the wind retrieval from airborne radar data, in particular the effects linked to:

- a nonlinear trajectory of the aircraft;
- the noise;
- errors on the radar angles;
- errors on the estimation of the terminal fall velocity of the hydrometeors;
- the lobe width;
- last but not least, the correction for advection. This point is crucial for airborne radar data, since in order to obtain the 3D wind field at the scale of the system, a sampling time of 15 minutes is necessary.

One of the aims of the present study is to qualify the analysis on real airborne radar data.

4. DESCRIPTION OF THE SQUALL LINE

a. Lower fuselage radar reflectivity images

Squall lines in both tropics and middle latitudes generally consist of two cloud and precipitation zones: a leading convective part and a trailing stratiform region. Within the convective region, which is typically a few tens of kilometers, the vertical air motions are violent and the precipitation is generally strong. Contrarily, in the stratiform region, which can extend behind the leading convective at several hundreds kilometers, the vertical air motions are much smaller (a few tens of cm) and the precipitation is much lighter and horizontally uniform. These two zones are separated by a reflectivity minimum or 'trough' with no or very light precipitation.

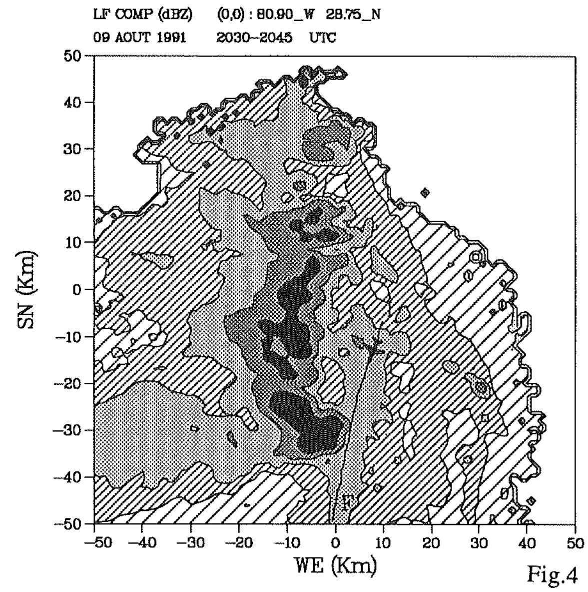

Fig.4

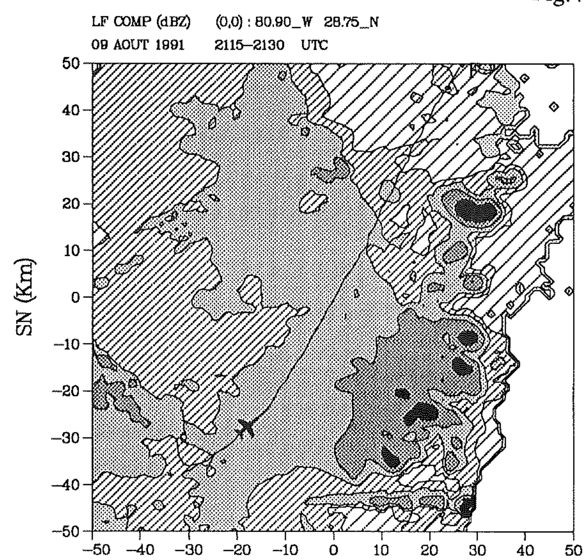

Fig.5

The two reflectivity patterns presented in Figs.4 and 5 were observed by the lower-fuselage (LF) radar during the aircraft passages named leg1 (from 2030 to 2045 UTC) and leg4 (from 2115 to 2130 UTC) respectively. The aircraft P-3 flew in front of the convective part during the leg1, behind the convective part (in the stratiform part) during leg 4. As for the reflectivity structure of leg4, two regions, the one convective in the southeast corner, the other stratiform spreading to the northwest, are well distinct. But compared with the reflectivity structure of leg 1, the reflectivity became less high, the scale in the propagation direction became larger for the convective part, and the orientation of the convective part moves from North-South to Northeast-Southwest about parallel to the coast. We can assume that the squall line during the passsage of leg 4 is at mature stage. The reflectivity structure of leg 5 from 2130 to 2145 UTC (not shown here) shows that the system began to dissipate when it reaches the coast, suggesting a sea-land contrast effect.

The system moves from the Northwest to the Southeast at a mean speed of about 13 m/s for the leading convective part during the period of analysis.

b. Application of MANDOP to the squall line of 09.08.91

Dual-Doppler synthesized wind and reflectivity fields constructed from the C-P3 radar data collected during leg 4 are depicted at 500m et 4km (Figs.6 and 7). The reflectivity structure is in good agreement with that of LF radar as shown in Fig.5, in particular the structuration into convective, stratiform and reflectivity trough. The horizontal flow within the system appears as highly three-dimensional. On the contrary, the environmental inflow observed on the East side of the convective part shows a quasi-two-dimensional structure perpendicular to the leading edge of the squall line. This 3-D aspect appears clearly on the vertical cross-section given in Fig.8 (CD) along the convective line direction. If we look in more detail the southern part of the squall line in the region of maximal reflectivity noted R in Fig. 8, a more classical circulation is observed in the cross-frontal direction (given Fig. 9). In this region of the squall line, the mature stage may be described in terms of an inflow and a rear-to-front outflow interacting with each other in the convective leading edge, leading to the convective updraft. A front-to-rear flow is also evidenced in the first two kilometers to the rear in the stratiform. These last two flows appear linked to the mesoscale downdraft initiated in the 4-6 km layer, 60 km to the rear of the leading edge. Microphysical processes (melting and evaporation) could contribute to the observed mesoscale downdraft which reinforces the convective updraft and maintains the system. Indeed, the freezing level evidenced from the reflectivity bright band, was located in the source layer of the mesoscale downdraft, about 4.5 km, fed by the southwesterly flow observed in Fig. 7

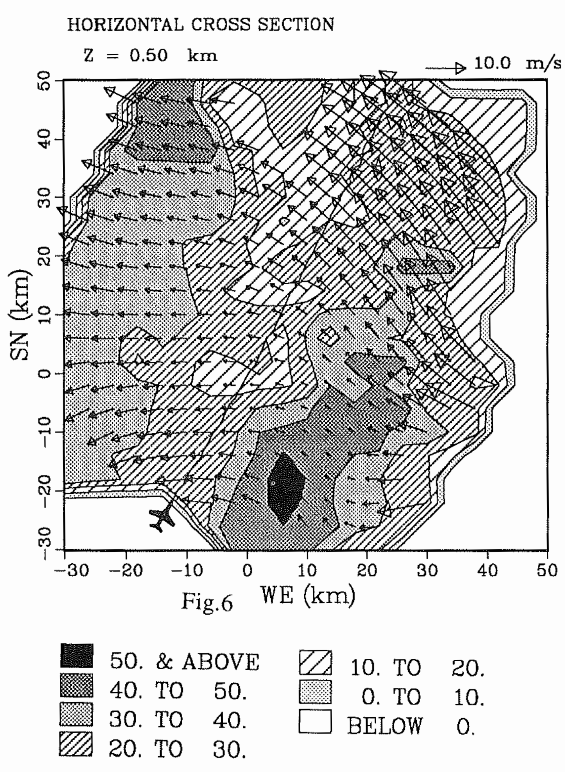

Fig.6

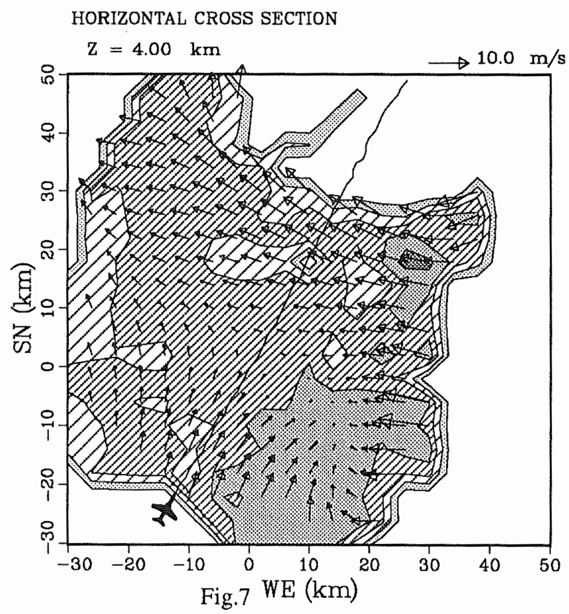

Fig.7

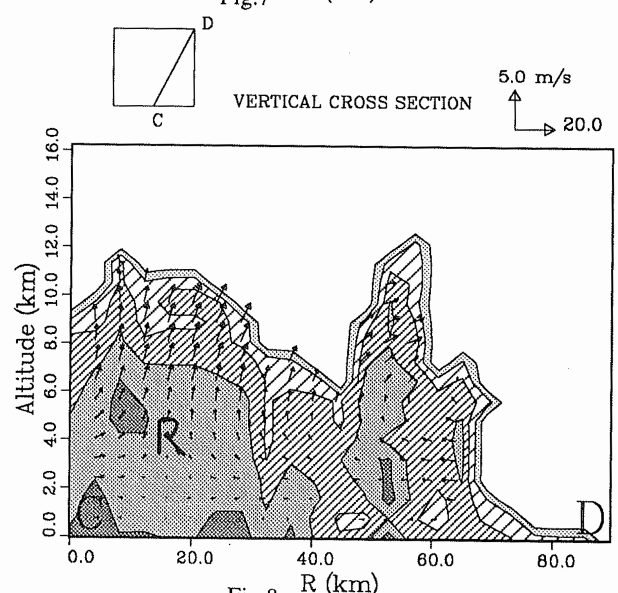

Fig.8

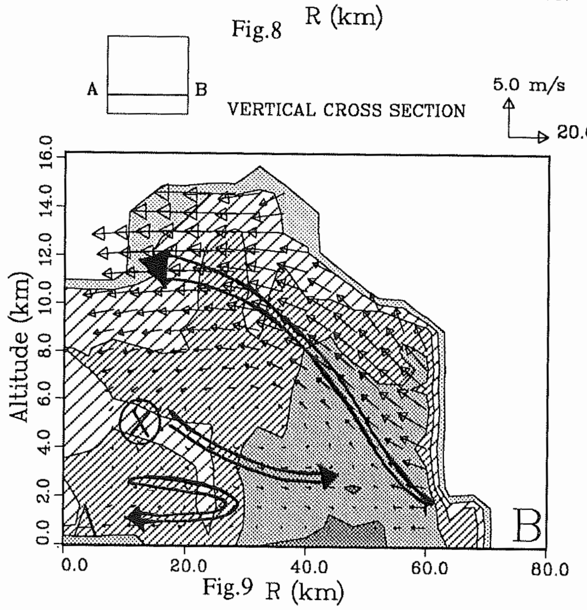

Fig.9

6. CONCLUSION AND PERSPECTIVES

The description outlined before is in good agreement with what is generally known about squall lines. This first application of the MANDOP analysis to data obtained from airborne Doppler radar is indeed encouraging. These results will have to be confirmed in the future, using other measurements such as radiosoundings (not available at the time of the study).

This study must be pursued into several directions:

- 1) in this study a domain of 80km x 80km x 12km was selected, and the order of expansion of the wind on the orthogonal function was chosen to be 4, leading to horizontal and vertical scales of 13 km and of 2 km resolved by the method, respectively. If we want to study the dynamic structure at smaller scale, in order to attain the convective scale, we must either decrease the domain width, or increase the development order.
- 2) the determination of the circulation within the squall line is very sensible to the chosen advection speed. In particular, the system rotates when it approaches to the coast. This point will be carefully examined.
- 3) in this paper, only the leg 4 was analysed (because it was the only one available).The other legs will be investigated in order to understand the evolution of this squall line. Moreover, the ground-based radar data of CP-2 obtained in the same site and during the same period will also be exploited with MANDOP processing to cross-validate the two kinds of results.This point is the main advantage of MANDOP processing.
- 4) the particle trajectories will be determined in order to better understand the dynamics of this squall line.
- 5) the thermodynamic structure of the squall line will be deduced from the MANDOP wind under the form of pressure and temperature perturbations.
- 6) the energy and vorticity budget will be performed at the scale of the squall line.

ACKNOWLEDGEMENTS

Special thank to D.P. Jorgensen of NOAA/NSSL/MRD for providing us the radar data. Thanks also to M.Trost and F. Roux for providing us the software of band lecture and the software of drawing the LF reflectivity pattern.

References:

Dou X. K., G. Scialom and Y. Lemaître, 1991: Three-dimensional analytical mesoscale wind field retrieval from airborne Doppler radar data.
Preprints, 25th Conf. on radar Meteorology. Paris, 490-492.

Hildebrand P., R. K. Moore, 1990: Meteorological Radar observations from mobile platforms. *Radar in meteorology* (edited by David ATLAS). 287-314.

Scialom G., Lemaître Y., 1990: A new analysis for the retrieval of three-dimensional mesoscale wind fields from multiple Doppler radar. *J. Atm. and Oceanic Technol.*,7, 640-665.

COMPARISON OF NUMERICAL ENTRAINMENT WITH THE RAYMOND AND BLYTH MODEL

David Stevens and Chris Bretherton

Department of Applied Mathematics, University of Washington, Seattle, Washington

April 29, 1992

Introduction

Most cumulus parameterizations use thermodynamic ideas and empirical observations to parameterize the behavior of cumulus clouds. A major shortcoming of these parameterizations is the lack of understanding about the dynamics of entrainment and mixing. Often these dynamics are seen as a mechanism used to equilibrate the thermodynamics. This paper compares a preliminary 2D numerical simulation of a Hawaiian trade cumulus cloud with a simple buoyancy sorting model, due to Raymond and Blyth [1]. The buoyancy sorting model treats cumulus convection as a mechanism for creating turbulently mixed parcels which then drift to their level of neutral buoyancy. In this model, the dynamics lie entirely in specifying the mixing profile at each height level after which buoyancy thermodynamics determines the entire behavior of the cloud. Critically examining the relationship of the dynamics to the thermodynamics of entrainment in a model cumulus cloud is the goal of this paper.

An example of other possible interactions between dynamics and thermodynamics is illustrated by the linear gravity wave model postulated by Bretherton and Smolarkiewicz [2]. They proposed that there is a feedback between gravity waves and the detrainment that produces them. Detrainment creates a strong gravity wave response, which by mass continuity causes strong horizontal flows around the cloud. These gravity waves adjust the buoyancy of the environment in a widening region around the cloud that in turn alters the levels at which mixed air detrains. Gravity waves also alter the environmental air that cloudy air parcels are exposed to in their mixing events. Given these complications, can a buoyancy sorting model adequately describe the vertical fluxes in a cumulus cloud.

Raymond and Blyth [1] (hereafter RB) in their analysis of continental cumulus clouds proposed a simple model. Their model parameterizes a cumulus cloud on the basis of mixing of cloud base air with environmental air at different levels and allowing the resultant parcels to detrain at their level of neutral buoyancy. The dynamical assumptions made in this model concern the formation of mixed parcels and their ensuing trajectories. The RB cloud is assumed to be composed initially of an updraft of homogeneous air originating from below cloud base in a conditionally unstable environment. This air is adiabatically raised to its lifting condensation level (cloud base) where it proceeds to become mixed. At each level between cloud base and cloud top, a uniform amount of cloudy air is mixed in a uniform spectrum. Once a parcel has been mixed, it is assumed to not mix again and drift to its level of neutral buoyancy. This paper will compare results from the RB model with results from a numerical model.

Analysis

For consistency, the same thermodynamics were used in both models. The environment in both models was broken down into, a base state $\bar{\psi}$, the hydrostatic environmental perturbation from that base state, $\psi_e = \bar{\psi} + \psi'$ and the time dependant spatially varying component $\psi''(x, y, z, t)$ as in Klaassen and Clark [3]. The relative deviations $\psi^* = (\psi - \bar{\psi})/\bar{\psi}$ and $\psi_e^* = (\psi - \psi_e)/\psi_e$ were also useful quantities. The thermodynamics were formulated in terms of

$$\theta_l = \theta - \frac{L\theta_e}{C_{pd}T_e} \quad \text{and} \quad Q_t = Q_v + Q_c$$

which are conserved under moist and dry adiabatic processes. These quantities along with the vertical position of a parcel in the environment determine the saturation of a parcel. Saturation is computed by solving an implicit relation that is obtained by using the definitions of Q_t and θ_l and the Clausius-Clapeyron relation relation. Virtual potential temperature,

$$\theta_v = \theta\left(1 + \delta Q_v - Q_c\right),$$

where $\delta = 0.608$, is used to determine the relative buoyancy of a parcel of air to the environment. The perturbation in virtual potential temperature relative to the environment determines the parcel's buoyancy. This is expressed as

$$\theta_{ve}^* = \frac{\theta''}{\bar{\theta}} + \delta Q_v'' - Q_c''.$$

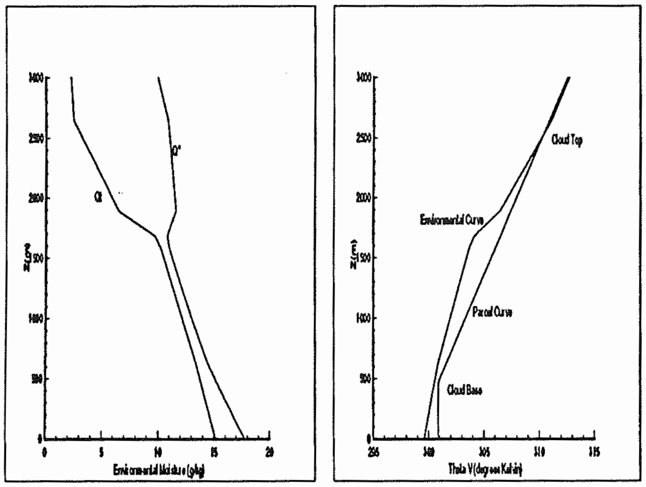

Figure 1: Hawaiian Trade Sounding

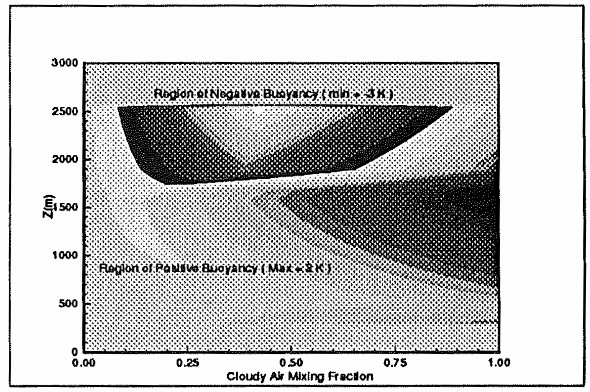

Figure 2: Parcel Buoyancies

These thermodynamic relations, although simplified, contain the relevant thermodynamics effects required to make a comparison between the two models.

The models were compared by simulating a cloud in a typical trade cumulus sounding from Hawaii (Raga et. al. [6]) with a trade inversion at 2 km. This sounding was chosen because we intend in the future to compare these results with data from the 1990 Hawaiian Rain Bands Project (HARP). The sounding used is shown in Figure 1 along with the adiabatic trajectory of a parcel of environmental air from 300 m that has been perturbed .5 K and moistened 1 g/kg. This figure indicates that the parcel is positively buoyant in the lower part of the sounding up to about 2500 m. This indicates that if a cloud is determined solely by its thermodynamic properties, that a cloud of this air will range from a cloud base of 500 m to a cloud top at 2500 m.

The Raymond and Blyth Model

This model is concerned with mixing parcels of environmental air from some subcloud level that might be slightly perturbed in both θ_l and Q_t with parcels of environmental air at some higher altitude. In particular, the 1 g/kg moistened and .5 K heated air in Figure 1 was chosen. Since the linearly mixing quantities Q_t and θ_l are adiabatically conserved, they will determine the thermodynamic properties of the parcel at levels inside the cloud. We have neglected possible effects of precipitation here, though the formulation can be generalized to include percipitation if a microphysical model is added. By following the sign of θ^*_{ve}, we are able to determine the progress of a parcel. When the sign of θ^*_{ve} changes, the mixed parcel is said to have neutral buoyancy and be detrained at the level prior to that level. Figure 2 shows a contour plot of θ''_v. The abscissa is a mixing fraction of updraft air and the ordinate is the mixing level of the parcel. Figure 2 shows the strong effect of evaporative cooling in causing buoyancy reversal for moist mixtures (shaded region at upper left) at higher levels. The plot (shaded region at lower right) indicates that most of the positively buoyant parcels will occur between 600 m and 1800 m and that above this level only relatively undilute parcels are still positively buoyant. Another consequence of this plot is that small differences in mixing fraction can cause large differences in the final destination of a parcel.

The convection properties of the RB cloud are determined by assuming that each parcel has a mixing fraction f of updraft air and a uniform mass m. Profiles of entrainment are computed by assigning a negative sign to entrained air and a positive sign to detrained air. Hence a parcel is assumed to remove updraft mass fm from cloud base and deposit this mass eventually at its detrainment level. The initial updraft of homogenous air is assumed to be entrained at cloud base. This generates a mass source profile, $S_m(k)$, of all the air entering or leaving a level defined by

$$S_m(k) = m \left(\sum f_{\text{detrained}} - \sum f_{\text{entrained}} \right)$$

This profile has the nice property that it preserves mass continuity, in that the cloud serves only to rearrange air according to its thermodynamic properties. This is seen by calculating the mass flux as

$$M(k) = \sum_{i=k_{cb}}^{k} S_m(i)$$

The mass flux is zero at the top of the cloud, indicating that there is no unaccounted mass in this cloud as shown in Figure 3. Note that although they make it look like mass is merely being moved from the bottom to the top of the cloud, the contour plot of the parcel buoyancies shows that this is actually the numerical average of an assortment of mixed parcels undergoing buoyancy sorting. The other important point of

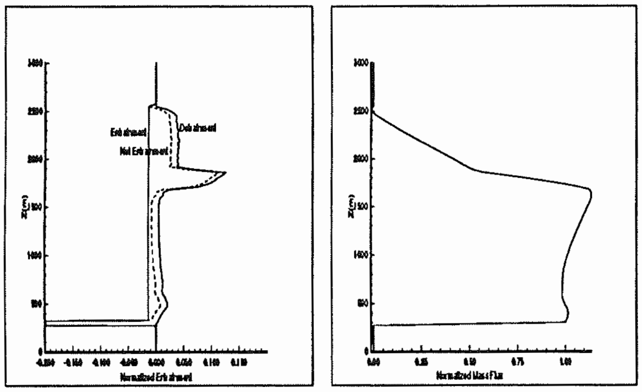

Figure 3: Entrainment Profiles

this figure is that it illustrates that the uniform entrainment profile produces a nonuniform detrainment profile as mixed parcels preferentially tend to detrain at the bottom of statically stable layers.

Numerical Model

The numerical model integrates the 3D anelastic equations of Ogura and Phillips [5] forward in time. The anelastic continuity equation, $\nabla \bullet (\bar{\rho}\vec{U}) = 0$, is formulated about a hydrostatically balanced isentropic base state. One of the major benefits of the anelastic equations is that they allow us to define an Exner function $\phi = C_{pd}\theta_o p''/\bar{\rho}$ and write conservation of momentum as

$$\frac{D\vec{U}}{Dt} = -\nabla\phi + g\theta^*_{ve}\vec{k}.$$

The thermodynamic equations are given by

$$\frac{D\theta^*_l}{Dt} = 0 \quad and \quad \frac{DQ_t}{Dt} = 0.$$

To numerically integrate this system of equations forward in time, we use the semi-Lagrangian algorithm as described in Smolarkiewicz et. al. [7]. This algorithm contains no explicit smoothing or diffusion.

The numerically simulated Hawaiian cloud was initiallized as a warm bubble with central temperature and moisture 0.5 K and 1g/kg higher than the environmental air at 300m as shown in Figure 1. The bubble rose and eventually equilibrated to the sounding. The bubble had an initial radius of 500 m and was in a domain 4 km high by 7 km with a resolution of 50 m per grid box. The boundary conditions were periodic and there was no initial motion. The calculation described here is two-dimensional; three-dimensional calculations are being analyzed.

In order to numerically evaluate entrainment and mixing, additional tracers were implemented, the initial position (ξ, ζ) and a parabolic profile $h = \zeta^2$. The horizontal tracer of initial position was useful for diagnosing the vertical divergence that had occured as mass was vertically transported by the thermal, see Bretherton and Smolarkiewicz [2]. Using two vertical tracers, we computed a mixing field based on a conserved variable analysis introduced to cloud physics by Paluch [4] and described in [2],

$$D_{mix} = \min\left((\zeta - \zeta_e)^2 + (h - h_e)^2\right)^{\frac{1}{2}}.$$

The quantity D_{mix} is the minimum distance of a point $(h(x,z,t), \zeta(x,z,t))$ from the environmental curve (h_e, ζ_e) on a mixing diagram of (h, ζ). Air is said to be irreversibly mixed, if this field achieves a threshold of 1 % of the maximum amount of the run. Figures 4 and 5 show that at times 6 and 10 minutes the mixing field extends substantially farther than the borders of the Q_c field indicating that mixing is going on in air that has not been saturated due to the presence of the cloud. The mixing level extends above cloud top indicating that mixing has gone on in air that is no longer part ot the rapidly decaying cloud. The divergent flow due to the cloud is especially clear in Figure 6 where the lines are bowed out where divergence has taken place and bowed in for convergent regions.

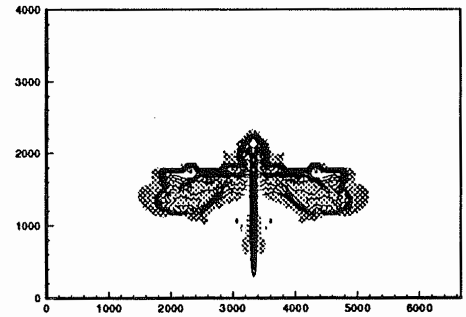

Figure 4: Domain after 6 minutes, the mixing field is the flooded contour and the lines represent values of Q_c.

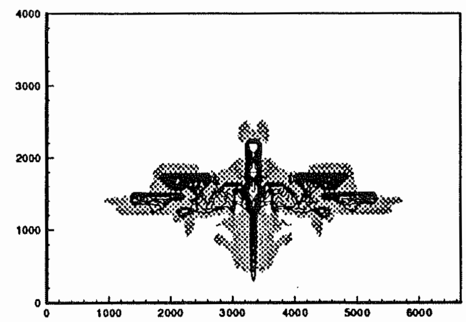

Figure 5: Domain after 10 minutes.

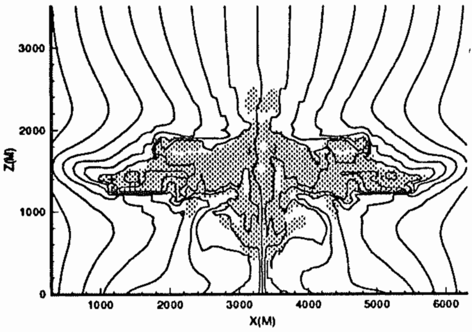

Figure 6: Horizontal Tracer after 10 minutes

The use of tracers facilitates creating profiles of the rates of entrainment and of the cloud affected region (CAR) which is defined as the region diagnosed as saturated or mixed. The amount of cloud and the cloud vertical mass flux at height z are defined as

$$M_c = \int_c \bar{\rho} dA \quad \text{and} \quad M_{mf} = \int_c \bar{\rho} w dA$$

where $\int_c dA$ is the horizontal integral of all points in the CAR. It is also possible to define an entrainment rate which is a combination of increased cloudy area and convergence of the cloudy vertical mass flux.

$$\dot{M}_e = \frac{\partial M_{mf}}{\partial z} + \frac{\partial M_c}{\partial t}$$

$M_e(z,t)dz$, the time integral of $\dot{M}_e$, is then the total mass entrained up to some final time t from heights z to $z + dz$. An analogous quantitiy that uses only information at time t but requires horizontal tracers is

$$M_{jac} = \int_c \bar{\rho} \frac{\partial \xi}{\partial x} dA.$$

The integrated Jacobian of the horizontal initial position tracers results in a profile of how the mixed region has entrained mass. This is the analogous profile to the profile in Bretherton and Smolarkiewicz [2] in which a horizontal tracer of initial position was used to diagnose entrainment. The profiles of these quantities are in figure 7. According to Figure 2, only relatively undilute parcels can rise above 2000 m as most other mixtures will be negatively buoyant by evaporative cooling. This result is seen in the entrainment profiles for the time, $t = 10$ minutes, where all three peaks fall off sharply at 1800 m. The small part of the curves above 1800 m results from the undilute core of the thermal that was shielded from the entraining eddy.

Conclusions

In the initial stages of the run, mixing occured at the edges of the entraining eddy as environmental air

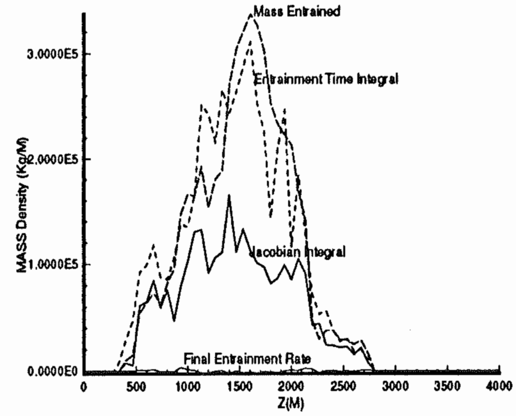

Figure 7: Numerical Simulated Entrainment

on the outside of the eddy was wrapped around and into the eddy tongue. It appears that entrainment proceeds by the process of this eddy mixing. This eddy will determine the types and concentrations of mixed parcels and to some extent their trajectory.

Acknowledgements This research was sponsored by NSF grants ATM891054 and ATM8858846.

References

[1] Blyth, A. M., and D. J. Raymond, 1988: Comparisons between observations of entrainment in Montana and a simple model. *J. Atmos. Sci.*, **45**, 1965-1969.

[2] Bretherton, C. S., and P. K. Smolarkiewicz, 1989: Gravity Waves, compensating subsidence and detrainment around cumulus clouds. *J. Atmos. Sci.*, **46**, 740-759.

[3] Klaassen, G. P., and T. L. Clark, 1985: Dynamics of the cloud-environment interface and entrainment in small cumuli: Two-dimensional simulations in the absence of ambient shear. *J. Atmos. Sci.*, **42**, 2621-2642.

[4] Paluch, I. R., 1979: The entrainment mechanism in Colorado cumuli. *J. Atmos. Sci.*, **36**, 2467-2478.

[5] Ogura, Y., and Phillips, N., 1962: Scale analysis of deep and shallow convection in the atmosphere. *J. Atmos. Sci.*, **19**, 173-179.

[6] Raga, G. B. , Jensen J. B., and Baker, M. B., 1990: Characteristics of cumulus band clouds off the coast of Hawaii. *J. Atmos. Sci.*, **47**, 338-355.

[7] Smolarkiewicz, P. K., and Pudykiewicz, J. A., 1992: A class of semi-Lagrangian approximations for fluids. *J. Atmos. Sci.* (to be submitted).

A STUDY OF THE TURBULENT FLUXES IN A FIELD OF CUMULUS CLOUDS.

S A Smith and P R Jonas

Pure and Applied Physics Department, UMIST, PO Box 88, Manchester, United Kingdom

1. BACKGROUND

The structure of the atmospheric boundary layer is dependent on the turbulent fluxes of heat, moisture and momentum. However, while there have been many studies of these fluxes in horizontally uniform, either cloud free or stratocumulus capped, boundary layers, little attention has been paid to the problem of the fluxes in cumulus capped boundary layers. In this paper we report experimental observations of the fluxes in cumulus clouds and in the clear air between the clouds from which the *mean* fluxes may be determined. The fluxes are also compared with the values found under horizontally uniform conditions.

Observations were made in fields of cumulus clouds over the North Sea during two daytime flights of the MRF Hercules aircraft.The flight plan consisted of L-patterns orientated N-S and E-W with a nominal 30 km leg length, flown above cloud tops, below cloud base, and a few levels in cloud. A number of cumulus cells were penetrated on each leg. The majority of the instrumentation and its performance have been described in previous papers (Nicholls 1978).

(a) *Flight A067*

An occluding frontal system was present to the south of the UK with a ridge of high pressure over the west of Scotland. An extensive area of cumulus developed in the light northerly flow over the North Sea.

The average temperature inversion height was approximately 3000 m. However, on this day, the maximum height reached by the clouds was around 2200 m. A relatively dry layer apparent at about this height was sufficient to prevent further development. Typical cloud depth varied from 700 m to 1300 m.

(b) *Flight A119*

A cold front was moving south across the North Sea, with an unstable north-north westerly flow behind. The average inversion height was 2500 m, and the clouds reached this level, being typically 1500 m deep. Cloud base was variable, with decaying remnants below the base of the mature clouds.

3. VERTICAL VELOCITY ANALYSIS

In order to facilitate subsequent analysis, the records for the horizontal flight legs were divided into in-cloud and between-cloud regions on the basis of the observed (FSSP) droplet concentrations. Vertical velocities during flight A067 reached ±2 m s^{-1}, while values of up to 4 m s^{-1} were observed during flight A119 in the much deeper clouds.

Average vertical velocity power spectra were calculated for cloudy and clear parts of each level run, examples of which are given in

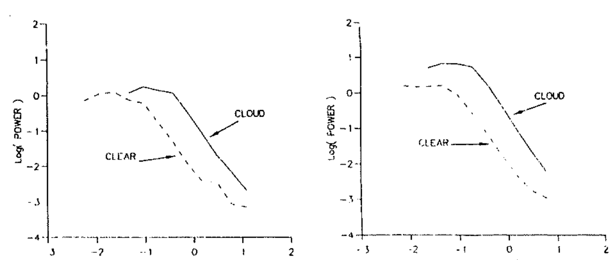

Figure 1 (a)Average vertical velocity power spectra at a height of 1070m (mid-cloud level) for in and between clouds as observed during flight A067. (b)As before, but at a height of 1800m in flight A119.

figure 1. The peaks of the in-cloud spectra were at approximately 0.1 Hz (wavelength 1 km), which corresponds to the scale of the main updraughts. At higher frequencies the spectra fall off with a gradient of -5/3 on a logarithmic plot. Between clouds, the spectral peak occured at lower frequencies, corresponding to distance between the clouds, and showed the same -5/3 slope at high frequencies.

It was evident that in-cloud energy densities for high frequencies were larger than those in clear air, due to the increase in turbulence in cloud. When the energy variation with height was plotted for each frequency band, both flights showed, for most frequencies, an increase in energy with height in cloud until just below cloud top. Then energy density decreased across cloud top. In contrast, energy densities between clouds decreased with increasing height for all frequencies. Also, a shift in the spectral peak towards higher frequencies was observed as cloud top was approached, due to the influence of the capping inversion.

The spectra were integrated to obtain the total turbulent kinetic energy (TKE) at each flight level, and the variation of TKE with height in cloud (normalised by the depth of the cloud layer) is shown in figure 2(a). In flight A119, turbulent kinetic energy increased with height through the sub-cloud layer and up through the cloud layer, reaching a maximum just below cloud top. Across cloud top, energy decreased almost to zero, as the overlying stable layer is entered and turbulence is suppressed. The TKE profile for flight A067 differs from this in that the the energy is a maximum at mid-cloud level rather than at cloud top.

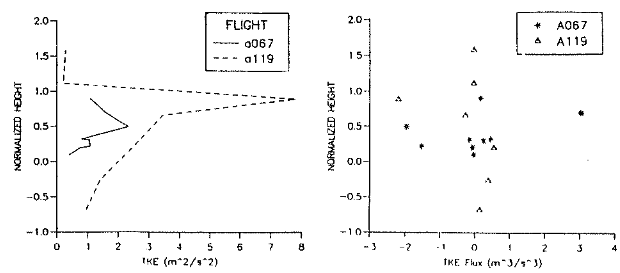

Figure 2 (a)In-cloud turbulent kinetic energy (TKE) for both flights, plotted against the height normalized by the cloud layer depth, i.e. height above cloud base divided by cloud layer depth. (b)Comparison between flights A067 and A119 of the vertical transport of TKE.

Cloud top entrainment leads to the generation of TKE if the entrained air is sufficiently dry for the subsequent evaporative cooling to cause the resulting mixture to be negatively buoyant (Randall,1980; Deardorff,1980). As an approximation, the condition to be met is as follows.

$$0.6\,\Delta\theta_e < \theta\,\Delta q_T$$

$\Delta\theta_e$ and Δq_T are the cloud top jumps in equivalent potential temperature and total water mixing ratio respectively. θ is the potential temperature.

In flight A119, cloud tops reached the inversion. Thus entrainment at cloud top will entrain warm, dry air from the overlying inversion, satisfying the entrainment instability criterion and thus producing TKE. In flight A067, the clouds did not reach the inversion. The entrainment instability criterion is not met and the process consumes TKE. In this case the major source of TKE is lower in the cloud, where condensation produces positively buoyant updraughts. No secondary maximum is evident near cloud base for flight A119, but this may be due to the very low vertical resolution of the in-cloud data.

4. TURBULENT FLUXES

Average values of fluxes of sensible heat, liquid water and turbulent kinetic energy (TKE) were calculated for in-cloud and clear sections and profiles were obtained for each flight.

The in-cloud profiles of the TKE flux for both flights are shown in figure 2(b). The profile for flight A119 shows a positive flux of TKE in the lower part of the cloud layer, away from any region of production at cloud base. This confirms the suggestion that the lack of evidence of a TKE maximum at cloud base is due to the low vertical resolution of the data. The energy flux becomes negative around mid-cloud level, with a large negative flux just below cloud top, corresponding to the downward transport of TKE away from cloud top within the downdraughts. Thus, energy is being transported from regions of production into the body of the cloud. Flight A067 has no negative energy flux at cloud top. Instead, TKE is being transported away from the region of maximum energy at mid-cloud level.

The flux of liquid water in cloud increases with height from zero at cloud base as seen in figure 3(a). It reaches a maximum at cloud top for flight A119. For flight A067, the cloud top flux is reduced by the absence of dry downdraughts, and the maximum is in the upper half of the cloud.

When averaged over the whole cloud layer, the profile is as shown in figure 3(b). The flux increases with height, with a maximum of 4×10^{-5} m s^{-1} in the upper half of the layer. This resembles the profiles obtained by Nicholls and Leighton (1986) for stratocumulus clouds over the North Sea.

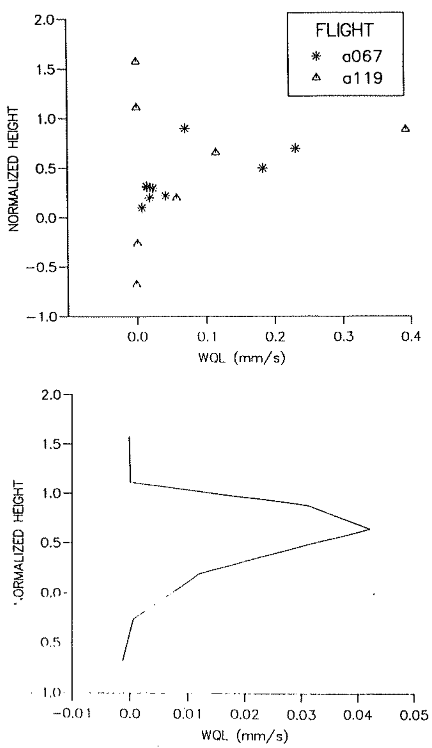

Figure 3 (a)Comparison of the vertical liquid water fluxes in cloud for flights A067 and A119, plotted against normalized height. (b)Layer averaged vertical flux of liquid water from flight A119.

The profiles of sensible heat flux in cloud are shown in figure 4. The data from the Rosemount resistance thermometer is used. Vertical sensible heat flux increases with height in cloud. The maximum flux in flight A119 is at cloud top, where cool downdraughts carry much of the upward heat flux. This is in agreement with the shape of the heat flux profile observed by Nicholls (1984). The heat flux in case A067, however, has a maximum at mid-cloud level, with very small fluxes at cloud top. Here, the upward heat flux is carried by the updraughts from

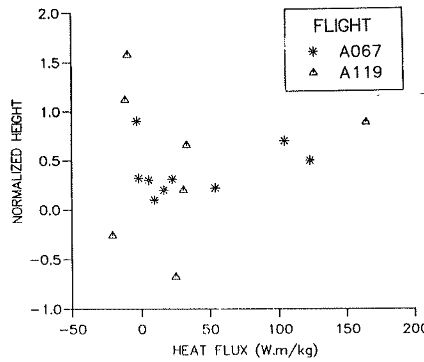

Figure 4 (a)Comparison of the in-cloud vertical fluxes of sensible heat for flights A067 and A119, plotted against normaliozed height. Data from the Rosemount resistance thermometer is used in both cases.

cloud base, which accelerate in the lower half of the cloud, but decelerate towards cloud top as their buoyancy decreases.

All the clear air transports are small in comparison. In flight A119, TKE transport only had a small value between cloud tops and there was a small negative heat flux there, both due to the displacement of the warm, stable layer air from aloft. Flight A067 showed evidence of small negative values of TKE flux between cloud tops due to mixed layer air being displaced from above the clouds.

5. CONCLUSIONS

Data from two daytime flights in fields of cumulus clouds over UK coastal waters have been analyzed, and turbulent flux profiles examined.

In general, maximum turbulent kinetic energy is found in the regions of production at cloud base and cloud top, and it is then transported into the body of the cloud. This is similar to the cases of marine stratocumulus examined by Nicholls and Leighton (1986). Clear air fluxes are small and positive between cloud tops, due to the displacement of stable air.

Sensible heat and liquid water fluxes are positive in cloud and increase with height, with maxima at cloud top. They are carried by the warm/moist updraughts from cloud base and by the cool/dry downdraughts from cloud top. There is a small negative sensible heat flux between cloud tops. Layer averaged liquid water fluxes resemble those found for marine stratocumulus.

In the absence of significant evaporative cooling at cloud top, as in the case of flight A067, in which the cloud tops do not reach the inversion, the formation of downdraughts and the generation of TKE are reduced and an important transport mechanism in cumulus clouds is lost. Cloud top fluxes are small, with maxima at mid-cloud level. Turbulent kinetic energy has a maximum at mid-cloud level, and is transported away from this region.

6. REFERENCES

Deardorff, J. W: *J. Atmos. Sci.*, **37 (1980)**, p.131-147
Randall, D. A: *J. Atmos. Sci.*, **37 (1980)**, p.125-130
Nicholls, S: *Q. J. R. Met. Soc.*, **104 (1978)**, p.653-676
Nicholls, S: *Q. J. R. Meteorol. Soc.*, **110 (1984)**, p.783-820.
Nicholls, S;Leighton, J: *Q. J. R. Meteorol. Soc.*, **112 (1986)**, p.431-460.

MESOSCALE BOUNDARY LAYER STRUCTURE OVER THERMALLY INHOMOGENEOUS SURFACE AND ITS EFFECT ON CONVECTIVE CLOUD DEVELOPMENT.

A. A. Postnov and E. A. Stulov

Central Aerological Observatory.
Dolgoprudny, Moscow region, 141700 Russia

1. INTRODUCTION

The spatial variability of thermodynamical parameters in atmospheric boundary layer(ABL) is known to contribute much into mesoscale structure of convective cloud fields. The variability is often determined by the emergence of so called heat islands(HI), which are due to thermal inhomogenity of the underlying surface.

This paper offers the experimental quantative assessments of amplitudes and localization of meteorological field perturbations in the ABL, emerging over mid-latitude peninsula and effecting convection.

The study is based on the data of airborne measurements and observations from IL-18DC aircraft in 14 flights in the summer seasons of 1986-87 over Onegsky peninsula in the White sea(appr. 63 N, 38 E). The dimensions of the peninsula are 60x120 km. The flights were taken in the midday, when the thermal perturbations and convection reached their maxima.

The vertical temperature gradient over the sea(γ_0) was convectively stable.

2. AIR TEMPERATURE STRATIFICATION

In the middle of a summer day an air thermal disturbance(heat island - HI) was formed over the peninsula(Fig.1). The value of γ within HI either surpassed or was close to dry adiabatic. So, the vertical extension of the HI (H) characterized the depth of unstable layer, where vertical temperature stratification facilitated convection(at least, dry).

The values of H over the peninsula varied from 0.5 to 1.2 km, as H was found to be linked to a combination of Δ Trs, γ_0, U

$$H/\Delta Trs = a[(\gamma - \gamma_0)U]^{-1/2} \qquad (1)$$

where a= 100 $c^{-1/2}$ m/$°C^{1/2}$

ΔTrs- sea-land IR temperature contrast

U- large-scale flow speed

The (1) shows that if Δ Trs is constant, the vertical extension of HI and the unstable layer decrease with the growth of the large-scale flow speed and ABL stability over the sea.

A disturbance of the vertical temperature gradient in the HI as compared to that over the sea($\Delta\gamma$) is related to vertical extension of HI and air temperature perturbation at the Z level [ΔT(z)] in the following way

$$\Delta\gamma = \Delta T(z)/(H-z) \qquad (2)$$

Depending on the profiles within and out of HI two types of cases may be distiguished. The first type is characterized by large values of ΔT at 0.2 km level (3.7-5.0° C), while $\gamma_0 \leq$ 0.6 C/100 m (Fig. 2). The second type implied that ΔT did not exceed 2-2.5°C; it was observed when γ_0 >0.6 C/100 m.

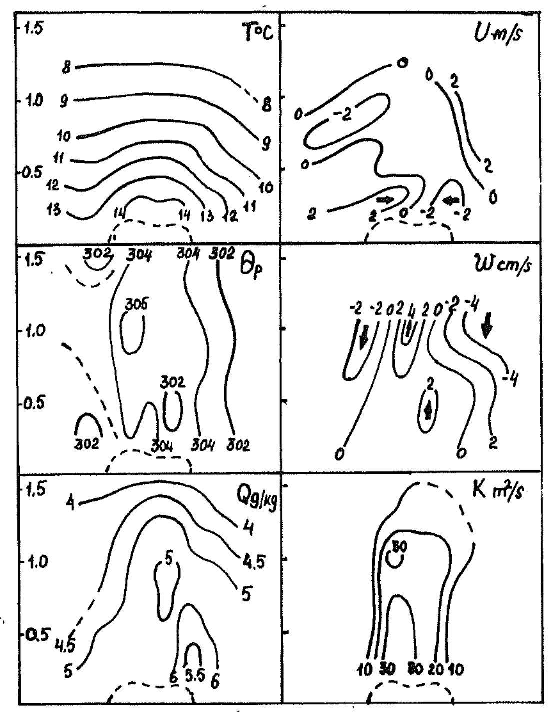

Fig 1. Vertical cross-sections of meteorological fields over Onegsky peninsula on July 23,1986

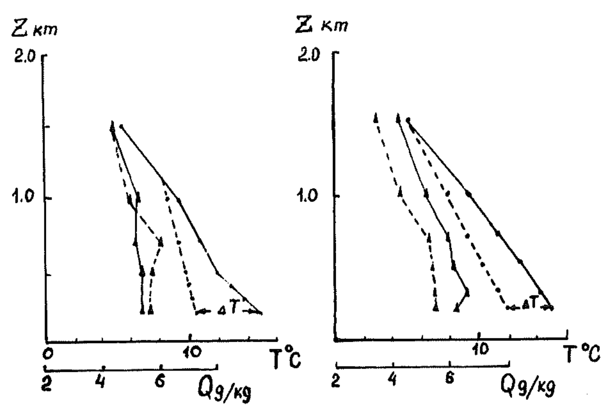

Fig 2. Vertical profiles of temperature(dots) and vapour mixing ratio(triangles) in ABL over Onegsky peninsula and sea on July 16 (a) and 23 (b), 1986

The localization of the HI and the zone with $\gamma > \gamma_{da}$ in relation to the peninsula depended on the large-scale flow speed(U). When U<2 m/s the HI centre and maximum of γ located approximately over the axis of the peninsula. As U encreased by every 1 m/s the local maximum of γ shifted to the downwind coast by 5-6 km.

3. HUMIDITY FIELD STRUCTURE AND CONDENSATION LEVEL VARIATIONS

The relative humidity in ABL is known to affect the condensation level height. The convective clouds can develop only if the condensation level is not higher than the top of the unstable layer.

The departure of the relative humidity over the peninsula from that over the sea was determined by a) a stronger evaporation from a warmer surface of peninsula, b) enhanced upward turbulent vapor transfer, c) low level vapor convergence due to breeze circulation.

These factors caused an encrease of vapor mixing ratio Q over peninsula by 0.5-1.5 g/kg (as compared to ABL over the sea). A moisture dome was formed over peninsula, although it was not as clearly defined as the HI. An encrease in Q within HI did not compensate for the fall of relative humidity (f) resulting from temperature growth(and hence, the saturation mixing ratio) towards the centre of HI. This led to a decline in f below 0.5-0.7 km by about 10%, which produced a growth of condensation level height (h) in HI, comparing to that over the sea. Using Ferrel's formula, h spatial changes (Δ h) may be estimated by

$$\Delta h = 122(\Delta T - \Delta \tau) \qquad (3)$$

where $\Delta \tau$ is a departure of dew point temperature in HI

Formula (1) puts Δ h over peninsula at 0.2-0.5 km.

The realization of potential instability (indicated by $\partial\theta/\partial z$ <0, where θ is pseudopotential temperature) is one of feasible mechanisms for convection enhancement. Perturbation of Q over peninsula extended much higher than the top of the HI (about 500-600 m for July 23, 1986 - Fig.1). As a result, a zone of potential instability was found above 1.5 km level.

4. WIDESPREAD VERTICAL MOTION AND TURBULENCE

Convection is strongly modulated by vertical motion on the top of ABL, since uplifting facilitates and subsidence hinders reaching of condensation level by rising air parcels.

Widespread vertical motion (W) over peninsula was formed by breeze circulation. The upward motion was localizated near the centre of the heat island as subsidence occured on its flanks. In cases, in which the large scale flow was weak, W reached 8-10 cm/s at 1.0-1.2 km level. When U>2 m/s the zone with upward motion joined HI in shifting to downwind coast, and the absolute values of W decreased to 1-2 cm/s.

Almost in all cases, strong thermal turbulence was observed over peninsula. The turbulence coefficient values over peninsula were 20-30 m^2/s in excess of those over the sea. The top of the turbulent layer coinsided with the HI top(Fig.1).

The effects of turbulence on convection are multiform. The strong turbulence in the ABL a) can produce a primary impetus for convection development, with large turbulent eddies serving as thermics; b) is mixing up the turbulent layer and facilitates γ reaching dry adiabatic value; c) encreases turbulent entrainment into dry thermics, hindering convection.

5. CONVECTIVE DAYS PECULIARITIES

Convective clouds were observed only in 3 of 14 cases studied. In 2 of them clouds developed over peninsula and lacked over the sea, while in the third one the Cb cells passed both over sea and land.

The cases with exlusive cloud development over peninsula were marked by the following peculiarities:

- large heat island depth (1.0-1.2 km)
- small low level temperature excess(Δ T = = 2.0 - 2.5° C)
- high relative humidity over sea(60-70%)
- condensation level exceeding the top of unstable layer by only 0.2 km
- strong uplifting (W = 4-8 cm/s)
- strong turbulence over peninsula(k=25-30 m^2/s)

The bands of Cu med clouds, observed over peninsula were oriented along the peninsula axis and coinsided with maximum of γ in the subcloud layer (Fig.3).

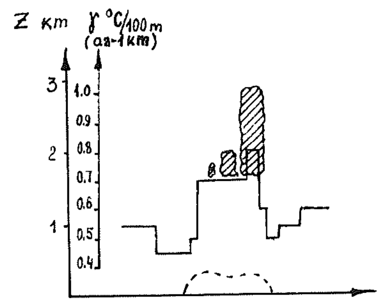

Fig 3. Horizontal profile of γ within 0.2-- 2.0 km layer and location of Cu med bands over Onegsky penin. on 23.07.86

COMPARISONS BETWEEN OBSERVATIONS AND NUMERICAL SIMULATIONS OF A WINTERSTORM EPISODE OVER COMPLEX TERRAIN

by

R.T.Bruintjes, T.L.Clark*, and W.D. Hall*
Dept. of Atmospheric Science, University of Arizona, Tucson, AZ
*NCAR, P.O.Box 3000, Boulder, Co. 80307

1. INTRODUCTION

Since the first conceptual models to increase winter snowpack on mountain ranges by seeding clouds numerous field projects have been conducted worldwide, including a large number of weather modification projects (Elliott (1986), Reynolds (1988)). More recent experiments include those conducted over the Tushar mountains in Utah (Sassen et al., 1990), and in the Sierra Nevada of California (Deshler et al. 1990).

There still are, however, major gaps in our understanding of both the natural and modified evolution of winter orographic cloud systems. Some of the key areas where scientific knowledge is lacking or inadequate are the evolution of the three-dimensional flow fields over mountainous terrain and its effect on cloud and precipitation development. This in turn determines the extent and timing of areas of cloud liquid water (CLW) regions and the specific microphysical processes that are active in the precipitation formation process.

Understanding of the complex interactions between the mesoscale and the cloud environment and between microphysical and dynamical processes in winterstorms in mountainous regions can be substantially increased by a combined modeling and field measurements approach. Modeling of flows and their effects on cloud and precipitation development over mountainous terrain has in the past been primarily conducted with models using two spatial dimensions. This approach might be useful in situations where the relevant orographic barrier can be viewed as an approximate two-dimensional inclined plane like the Sierra Nevada. However, this approach is inadequate for more complex terrain. At least three spatial dimensions are required to adequately simulate the flow and cloud and precipitation development over such regions. In a series of numerical experiments studying the effects that gravity waves have on orographic precipitation along the west coast of Wales, Bradley (1985) came to the following conclusion. The gravity waves primarily produce regions of enhanced upward motion with high liquid water contents which are poorly explained by simple orographic lifting models. Microphysically, enhanced precipitation growth occur in these regions which should result in higher amounts of surface precipitation.

The purpose of this paper is to describe and explain the interaction between the air flow and cloud and precipitation development during the passage of a winterstorm system over the Mogollon Rim area in northern Arizona on 15 and 16 March 1987. Observational data as well as results from a modeling study will be presented to specifically document the gravity waves that develop as a result of the the interaction between the flow and the the topography and the effect on precipitation formation processes.

2. OBSERVATIONS AND NUMERICAL MODEL

The data discussed in this paper were collected as part of the Arizona Snowpack Augmentation Program (Super et al., 1989), conducted during part of the winters (January to March) of 1987 and 1988. During the winter of 1987 measurements were concentrated at Happy Jack, south of Flagstaff, on the crest of the Mogollon Rim. The principal observational systems used during this period were described by Super et al.,1989.

The observational data collected on March 15, 1987 will be discussed in this paper. This was one of the major winterstorms of the season. A wave developed on a pacific polar cold front and as it approached the California coast the wave developed into a well defined low pressure system at the surface and in the upper air. At 500 mb a cut-off low was situated over central California during the morning of March 15. The center of the surface low pressure moved towards the east and passed just to the north of the area along the Arizona-Utah border with a well developed cold front bringing in moisture from the Pacific and the golf of California. Initially scattered low and middle level clouds with some cirrus were evident over the area with isolated patches of precipitation during the early morning until a well defined cloud band moved over the area from about 09h00 to 15h00 MST. This cloud band brought with it large amounts of moisture through a deep layer of the atmosphere and substantial amounts (> 25 mm in many mountainous areas) of precipitation. The passage of the cold front coincided with the passage of the rear of the cloud band. In the post-frontal airmass areas of convection were observed resulting in scattered areas of precipitation which lasted until the morning of March 16. The front passed over Happy Jack around 13h00 MST. In general the flow was from the South-Southwest in the lower layers turning to Southwest in the upper layers. After the passage of the front the winds were more south-westerly to westerly and increased in speed in the lower layers.

The purpose of the modeling studies is to assess certain aspects of the physical chain of events of cloud and precipitation development. Physically accurate dynamics is essential to the success of such a study since the dynamics to a large extent drives the microphysics. The model has to be able to simulate the initiation, organization and complete life cycle of orographic clouds over complex terrain. For this reason the three-dimensional, time-dependant, non-hydrostatic, anelastic model developed by Clark (1977), and Clark and Hall (1991) which employs a terrain following coordinate transformation was chosen to conduct the modeling studies. The model has interactive nesting capabilities allowing one to focus in on the area of interest. The capability to simulate the transport and dispersion of tracer or seeding plumes was added to the model. The area covered in Fig. 1 represents a three–dimensional perspective of the topography of the outer domain of a 240 by 240 km horizontal area used in the modeling study (looking from the southeast). The depth of the outer domain was 26 km using a 4 km horizontal and 500 m vertical resolution. The horizontal and vertical

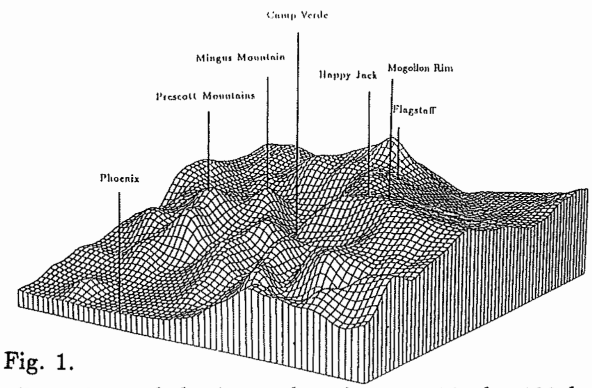

Fig. 1.

dimensions of the inner domain were 160 by 120 km by 16 km using a 2 km horizontal and 250 m vertical resolution. The complexity of the terrain is clearly evident from Fig. 1.

The model was initialized using a composite sounding constructed from rawinsonde data collected at Tucson and Camp Verde, and thermodynamic and wind data collected by a research aircraft during the passage of the main frontal cloud band.

3. RESULTS

Figures 2a and b show horizontal cross–sections of the vertical velocity field just above the surface and at 4 km MSL for the inner domain while Figs. 3a and b display the accompanying CLW fields for the same heights. Both the vertical velocity and CLW fields exhibit a complex three–dimensional structure. While the upward vertical velocities associated with the mountain ridges close to the surface were generally less than 1 ms^{-1} (Fig. 2a), the peak upward vertical velocities in the gravity waves reached values larger than 5 ms^{-1} (Fig. 2b). It is evident that most of the CLW at the lower levels were associated with the mountain ridges (see Fig. 3a) while at higher levels above 3 km MSL it is mostly associated with the gravity waves (Fig. 3b). The CLW regions are for this reason highly space dependant. In addition, simulations for other experiments showed that when the general flow changes

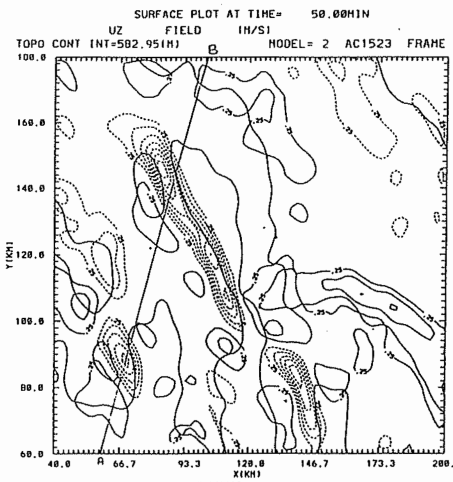

Fig. 2a.

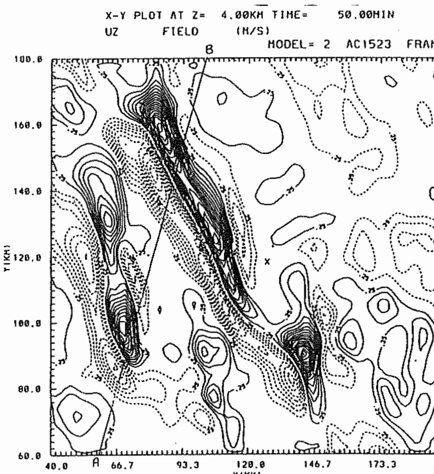

Fig. 2b.

direction substantial changes also occur in the flow over the area making flow patterns and cloud water regions also time-dependant. After the passage of the cold front much weaker vertical velocities were evident from the model simulations in the waves and the wavelengths were smaller. This was primarily due to the weaker horizontal windspeeds and the more westerly direction of the wind in the post–frontal period.

Figures 4a and b displays the vertical cross-sections through the lines A-B (approximately parallel to the wind direction) marked in Figs. 2 and 3 of the vertical velocities and the cloud water mixing ratio respectively. They clearly show the gravity waves excited by the mountains (Prescott Mountains and Black Hills) upwind of the Mogollon Rim. The simulations indicated vertical velocities of more than 3 ms^{-1} in some of the waves and CLW amounts up to 1 gkg^{-1}. Note the vertical extent of the gravity waves with the peak vertical velocities reached between 3 and 4 km MSL. It is evident from Fig. 4b that the amounts of CLW associated with the waves were higher than that associated with the ridges. In addition, the CLW in the waves were distributed through a deeper layer of the atmosphere (Fig. 4b). In the Arizona case the CLW associated with gravity waves may provide an additional source of CLW for precipitation development not previously considered in cloud seeding experiments.

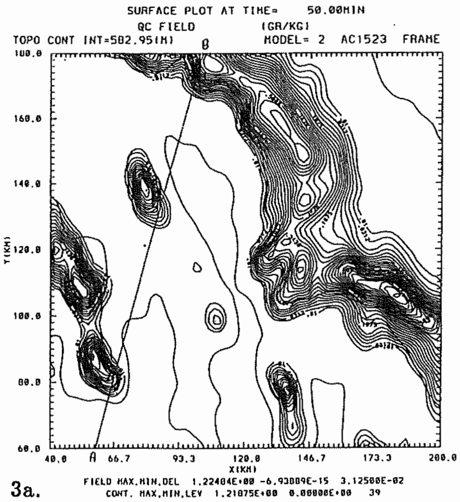

Fig. 3a.

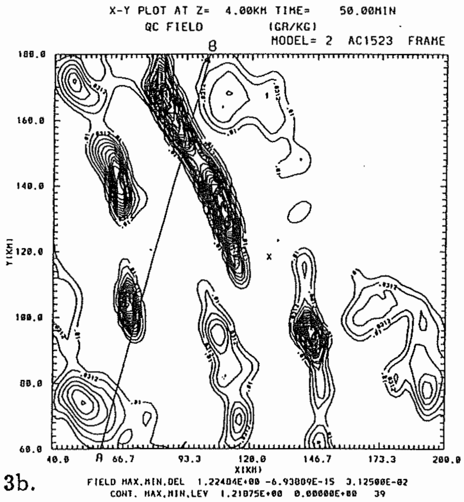

Fig. 3b.

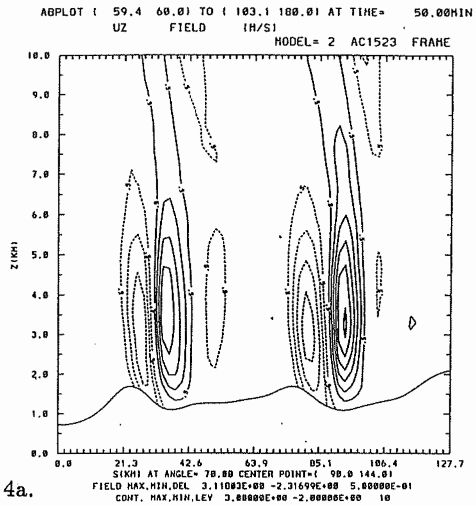

Fig. 4a.

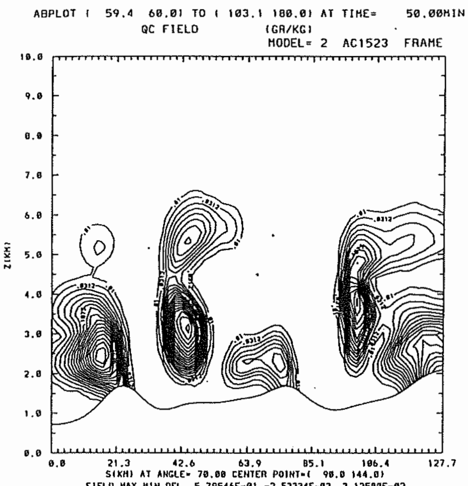

Fig. 4b.

It was clearly evident from the ice fields (not shown here) that the distribution of both the ice mixing ratios and the particle concentrations throughout the troposphere is strongly dependant on the gravity wave activity. These results seem to confirm the results from the aircraft microphysical data. The concentrations predicted by the model agree fairly good with the concentrations observed in-situ by the aircraft in the absence of an active ice multiplication process (usually active during the pre-frontal situation). However, when ice multiplication is active the difference between the observed and model predicted ice concentrations can be as much as a few orders of magnitude. We hope to parameterize ice multiplication in the model in the near future to take care of this problem.

The peak concentrations of ice particles occur between 5 and 7 km MSL in the region where primary ice nucleation is very efficient. The gravity waves provide for regions of enhanced and depleted particle concentrations depending on the location of the up and downward motions associated with the waves. Therefore in complex terrain like the present case precipitation development and the distribution of precipitation on the ground will certainly be dependent on the amount and magnitude of wave activity.

In an effort to verify the modeling results the aircraft data for the 1987 field program was retrieved to look if the aircraft ever unintentionally penetrated some of these wave regions. During the 1987 field program the research aircraft was located at Prescott airport. Whenever the aircraft took off on or returned from a mission to the Happy Jack area an aircraft sounding was conducted. The most direct route to Happy Jack took the aircraft directly over Mingus Mountain. By the time the aircraft crossed Mingus Mountain it was usually close to the top of the sounding between 4 and 5 km MSL during most of the missions flown. Two missions were flown on March 15, one in the morning and one in the afternoon. There were thus four passes over Mingus Mountain, two leaving from and two returning to Prescott.

Figures 5 show the flight tracks for the incoming leg of the morning flight to Prescott for the morning flight. The vertical velocities (ms^{-1}) as measured by the aircraft are plotted on the track and the topography is displayed at the bottom of the graph. Note Mingus Mountain on the left side of the graph. The inset picture shows the horizontal flight track of the aircraft as it passed over Mingus Mountain. The times indicated on the flight track are all in Mountain Standard Time (MST).

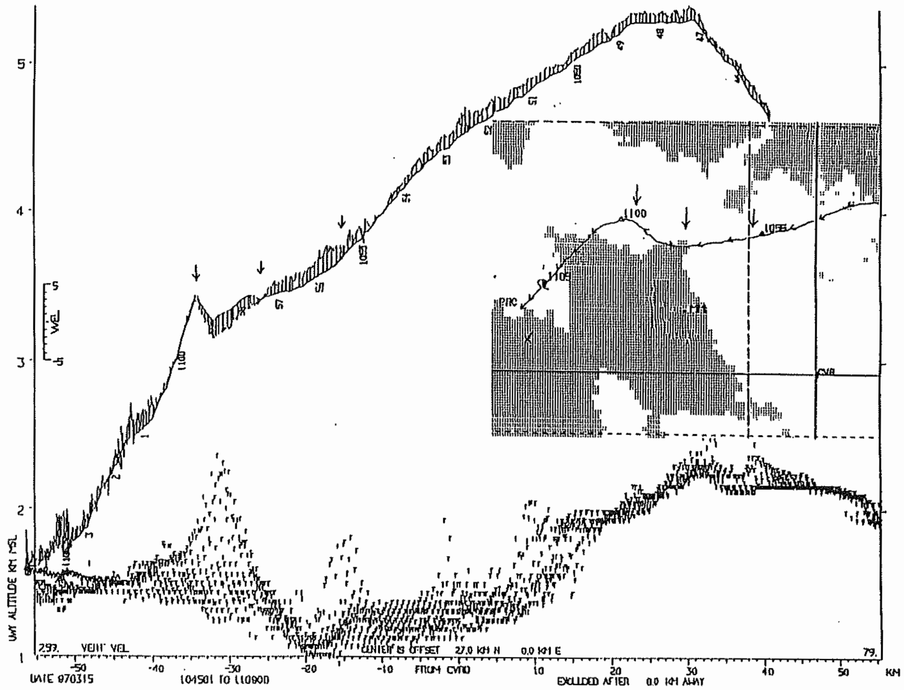

Fig. 5.

Although the aircraft did not concentrate on detecting the gravity wave over Mingus Mountain, the data indicates that gravity wave excited by Mingus Mountain was detected. This was also the case for the other legs not shown here with sinking motions over the peak and just downwind of the peak and upward motions more downwind of the mountain over the Verde Valley. Supercooled liquid water was detected on all four occasions in the regions of upward motion in the wave accompanied with increased particle concentrations. It is interesting to note that during the afternoon flight the highest amount of SLW ($> 0.3gm^{-3}$) was detected in the wave over Mingus Mountain. In three of the four flight legs the SLW was detected above 4 km MSL while during the return flight in the morning (Fig. 5) SLW was detected at about 3.5 to 3.6 km.

The existence of SLW in these winter storm systems over complex terrain was in the past usually associated with the ridges and it was assumed that the SLW is only present in the lower layers of the atmosphere close to the ridge. However, the data presented here indicate that apart from SLW associated with the mountain ridges substantial amounts of SLW can also occur at higher levels in the troposphere due to upward motions induced by gravity waves excited by the mountains upwind from the Mogollon Rim. This was further confirmed by one pass over Happy Jack when the aircraft extended the upwind leg well into the Verde Valley at an altitude of 4km when high amounts of SLW ($> .2gm^{-3}$) were detected during the upwind turn on the extended leg over the Verde Valley at 4.4 km MSL. The SLW in this region was again associated with gravity waves excited by the Black Hills and Mazatzal mountains.

The modeling results indicated that the atmospheric structure and flow on March 15, 1987 was conducive to the development of vertically propagating trapped gravity waves. Especially Mingus Mountain was identified as an obstacle producing strong waves due to its high relief and steep lee slope. The magnitude of model simulated vertical velocities and CLW agreed well with the aircraft observed velocities and CLW. The aircraft calculated wavelengths of the gravity waves also agree well with the model calculated wavelengths with both being between 20 km and 24 km.

4. REFERENCES

Bradley, M.M., 1985: The numerical simulation of orographic storms. Ph.D. dissertation, Univ. of Illinois, Urbana–Champaign, 263pp.

Clark, T.L., 1977: A small scale numerical model using a terrain following coordinate transformation. *J. Comput. Phys.*, **24**, 186 – 215.

Clark, Terry L. and William D. Hall, 1991: Multi-domain simulations of the time dependent Navier Stokes equation: Benchmark Error analyses of nesting procedures. *J. Comp. Phys.*, **92**, 456–481.

Deshler, Terry, D.W. Reynolds and A.W. Huggins, 1990: Physical response of winter orographic clouds over the Sierra Nevada to airborne seeding using dry ice or silver iodide. *J. Appl. Meteor.*, **29**, 288–330.

Elliott Robert D., 1986: Review of wintertime orographic cloud seeding. *Meteor. Monogr.*, **21, No. 43**, Am. Meteor. Soc., Boston, pp. 87 – 103.

Reynolds, D.W., 1988: A report on winter snowpack-augmentation. *Bull. Amer. Meteor. Soc.*, **69**, 1291 – 1300.

Sassen, K., A.W. Huggins, A.B. Long, J.B. Snider and R.J. Meitin, 1990: Investigations of a winter mountain storm in Utah. Part II: Mesoscale structure, supercooled liquid water development, and precipitation processes. *J. Atmos. Sci.*, **47**, 1323–1350.

Super Arlin, B. and E.W. Holroyd, 1989: Temporal variations of cloud liquid water during winter storms over the Mogollon Rim of Arizona. *J. Weather Mod.*, **21**, 35–40.

CVI MEASUREMENTS ON SMALL CRYSTALS IN CIRRUS CLOUDS.

J. Ström[1], J. Heintzenberg[1], K. J., Noone[2], K. B., Noone[2], J. A. Ogren[3], F. Albers[4], M. Quante[4]

[1] Dept. of Meteorology (MISU), Stockholm University, S-10691 Stockholm, Sweden
[2] NOAA, Climate Monitoring and Diagnostics Laboratory, 325 Broadway R/E/CG1, Boulder, CO 80303, USA
[3] Atmos. Chemistry Dept., School of Oceanography, University of Rhode Island, Narragansett, RI 02882, USA
[4] Institute Fur Physic, GKSS, D-2054 Geesthacht, Germany

1. INTRODUCTION

During the ICE89 campaign over the North Sea in September and October of 1989, in-situ measurements in cirrus clouds were conducted with an airborne counterflow virtual impactor (CVI). The CVI is a device that inertially separates particles larger than a certain aerodynamic size (about 4 µm in diameter) from the surrounding air into a warm, dry and particlefree air (Ogren et al., 1985) (Noone et al., 1988). The evaporated crystals/droplets leave behind non-volatile residues that can be sensed downstream of the impactor by other instruments working in conjunction with the CVI.

The payload during this campaign consisted of: a TSI 3760 condensation nucleus counter (CNC) to count the total number of residual particles, a PMS ASASP-X optical particle counter (OPC) to determine the residue size distribution and two Lyman-α hygrometers (Zuber and Witt, 1987) to measure the cloud water content (CWC) in the condensed phase. For some flights a PMS 2D-probe was mounted providing information about crystal habit and size distribution of large ice crystals. Wind structure was measured during cloud sampling, by a 5-hole probe, together with standard meteorological parameters. All instruments were mounted onboard the DLR (German Aerospace Research Establishment) research aircraft Falcon.

We shall present results from four flights conducted on the 15, 16, 17 and 18 of October. The synoptic weather during the sampling period was characterized by a warmfront passing the sampling area between the 15th and 16th, moving rapidly from the west to the east. From the 16th to the 18th the sampling area were under the influence of a moderate anticyclonic airflow. Thus the cirrus clouds entering the sampling area from the north-west were partly dissolved due to subsidence. Although the vertical extent of the clouds was of several kilometers between 7km to 12km altitude, they were optically very thin. The surface could often be seen from the airplane even at the highest altitudes.

2. RESULTS AND DISCUSSIONS

The results presented in this paper represent almost 3 hours of in-cloud measurements over four days and the values reported are reduced to standard temperature and pressure (STP; 0^{o}C,1 atm).

We assume that there is a 1:1 ratio between the number of residue particles and the number of crystals sampled. Thus the number concentration of residuals is equivalent to the number concentration of ice crystals above 4µm Stokes diameter. Due to the fact that different instruments have different time responses and time constants, we use a 90s averages comparing different quantities. The average number concentrations have a median value of 16 L^{-1} (as counted by the OPC) with a peak value of 455 L^{-1}. The CWC median value was 1.8 mg m^{-3} with a maximum value of 15.5 mg m^{-3}. From these primary measurements we can calculate secondary parameters such as the diameter of mean mass (DMM). The median of the DMM over all flights was 58 µm and differed only slightly from day to day. This is in the lower range of the detection limit for the 2D-probe. During the 17th and 18th the DMM

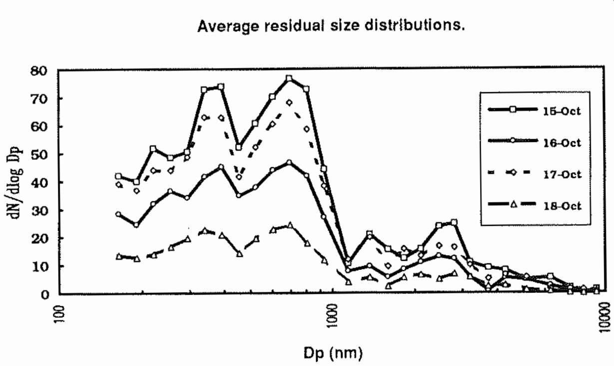

Figure 1. The average number size distribution for ice crystal residues from four flights, where Dp is the diameter of the particle in nanometer. The total sampling time for each flight is between 30 to 45 min.

was at times larger than 200μm, but at the same time the number concentrations were very low and thus associated with large statistical uncertainties.

In Figure. 1 the average residual size distribution is plotted for each day. Although the average integral number differs from day to day, the overall shape of the distributions show very similar characteristics. The most pronounced feature is the bimodal structure with maxima at about 350nm and 700nm in diameter. A minor mode is also suggested for residual particles of 2500nm in diameter but it is not very distinct. Time series for the evolution of the size distributions reveal that the two modes often appear exclusive of each other. Thus the flight average is not representative for a distribution at a given time. Due to the low number concentrations of aerosols at cirrus levels, the scavenging of interstitial aerosol particles by ice crystals alone is not very likely to explain the structure seen in the distribution. We are certainly dealing with particles that have gone through more than one cloud passage. Furthermore, the sampling took place in air where the cloud had reached different stages in its life cycle. This composite picture leaves us with no simple explanation for these intriguing measured size distributions. Several alternative hypothesis will discussed. We will also suggest experiments that will test these hypotheses to shed more light on this problem. It is our intention to merge the additional information provided by the 2D-probe and the wind measurements to incorporate the implicit dynamics of the cloud to the microphysical measurements.

REFERENCES

Noone, K.J., Ogren, J.A., Heintzenberg, J., Charlson, R.J., Covert, D.S.,1988., Design and calibration of a counterflow virtual impactor for sampling of atmospheric fog and cloud droplets. Aerosol Sci. Tech., 8: 235-244.

Ogren, J.A., Heintzenberg, J., Charlson, R.J., 1985., In-situ sampling of clouds with a droplet to aerosol converter. Geophys. Res. Lett., 12: 121-124.

Zuber, A., Witt, G., 1987., Optical hygrometer using differential absorption of hydrogen lyman-α radiation., 26: 3083-3089

Homogeneous Ice Nucleation and Supercooled Liquid Water in Orographic Wave Clouds

Andrew Heymsfield and Larry Miloshevich
National Center for Atmospheric Research, Boulder, Colorado*

1. Introduction

In recent years increasing attention has been focused on mid- and upper- tropospheric ice clouds, through such field campaigns as the First ISCCP Research Experiment (FIRE; Cox et al. 1987) and the International Cirrus Experiment (ICE; Raschke 1988), as the meteorological community has become more aware of the potential importance of these clouds to the radiative properties of the atmosphere and to global climate. The radiative properties of these clouds depend strongly on their microphysical composition, particularly hydrometeor size spectra and shape. Ice size spectra are strongly influenced by ice production rates and ice nucleation mechanisms. The ice nucleation process therefore indirectly plays an important role in determining the radiative properties of ice clouds, and an understanding of this process is necessary for the proper treatment of cirrus clouds in numerical models.

It is difficult to observationally investigate ice nucleation mechanisms in cirrus, since conditions when sampled crystals are produced may not be known, and instrumentation to measure hydrometeor size distributions, crystal shapes, and relative humidity may be inadequate. In our study, we consider the relatively simple and quasi–steady–state dynamical and microphysical framework of orographically–formed lenticular wave clouds to gain an understanding of the ice nucleation process at temperatures below −30°C. Our approach combines in-situ measurements and numerical modeling calculations.

2. Aircraft instrumentation

The measurements to be presented in Section 3 employed the National Center for Atmospheric Research (NCAR) Sabreliner and King Air aircraft, whose performance characteristics and instrumentation are described in detail in RAF Bulletins No. 2 and 3 (available from NCAR).

Droplet size distributions were measured in fifteen size categories with Particle Measuring Systems (PMS) forward scattering spectrometer probes (FSSP), nominally sizing between 2 and 32 μm or 3 and 45 μm depending on the size range selected. A Rosemount icing probe (RICE) provided an indication of the presence of liquid water (LW) and an estimate of the liquid water content (LWC) above its approximately 0.002 g m^{-3} detection threshold for the conditions studied here (Heymsfield and Miloshevich 1989). Saturation ratio measurements are derived from the cryogenic frost–point hygrometer (Spyers–Duran 1991) on the Sabreliner, and are inferred from the Lyman–alpha device on the King Air following the technique given by Heymsfield et al. (1991).

3. Aircraft measurements

The NCAR Sabreliner flew five research missions in orographic wave clouds along the Front Range of the Rocky Mountains during November and December of 1989. The flights included 5 cloud penetrations between −25 and −30°C, 19 penetrations between −30 and −40°C, and 6 penetrations below −40°C. We also considered one research flight of the NCAR King Air on 8 Dec. (courtesy of W. Cooper, NCAR), consisting of 18 cloud penetrations between −30 and −41°C, in the same cloud sampled by the Sabreliner two hours earlier on this day. The aircraft flew legs parallel to the wind direction from the leading (upwind) to trailing (downwind) edge of the cloud at constant altitude. Since sampling occurred across streamlines, changes in individual parcel properties were not observed; the resulting effects will not be discussed here.

The examples below show the salient features observed in the data set.

Penetration 1–S (Fig. 1), with minimum temperature $T_{min} \approx -29.2$°C, shows characteristics expected of droplet growth and evaporation in a wave, but shows no evidence of significant ice production. The RICE and FSSP signals are above their detection thresholds over approximately the same region, indicating that LW exists throughout the cloud width, and these signals coincide with the region of high saturation ratio (panel A). Concentrations of particles detected by the 2D–C (not shown) were less than 0.3 L^{-1}, suggesting that few ice particles formed since the relative humidity in the downdraft is highly ice–supersaturated, and any ice crystals present would grow to 25 μm in approximately 50 s or 1 km horizontal distance. Furthermore, the RICE, FSSP, and saturation ratio signals are centered on and are roughly symmetric about the wave crest (i.e. the minimum temperature, or the beginning of the downdraft), as expected for droplet growth and evaporation under conditions of adiabatic ascent and descent.

Penetration 2–S (Fig. 2), with $T_{min} \approx -36.0$°C, shows a complement of instrument signals which indicate the presence of droplets in an updraft followed by an abrupt transition to ice. The RICE and FSSP first show signals which exceed their detection thresholds in the updraft when the saturation ratio is approximately 1.0 (panel B, at distance coordinate x=15 km), suggesting these cloud particles are droplets. The FSSP continues to detect cloud particles throughout the penetration, but the RICE ceases to detect LW at approximately the location where the saturation ratio drops below 1.0 (panel B, x=18 km). Since the updraft speed is near its maximum of 2 m s^{-1} (panel A, x=18 km), it appears that droplets have frozen rather than evaporated. Simultaneously, FSSP–detected mean particle diameter increases abruptly (panel C, x=18 km), and particles are detected successively with the 2D–C and 2D–P probes.

Penetration 4–K (Fig. 3), with $T_{min} \approx -40.7$°C, is similar to 3–S in that FSSP particles are first detected in the midst of a relatively strong updraft (4.5 m s^{-1}) at the location where the saturation ratio rapidly decreases and the temperature ceases its rapid decline (panel A, x=7 km). The Lyman–alpha data suggest that the peak saturation ratio is below 1.0. No liquid water is measured by the RICE.

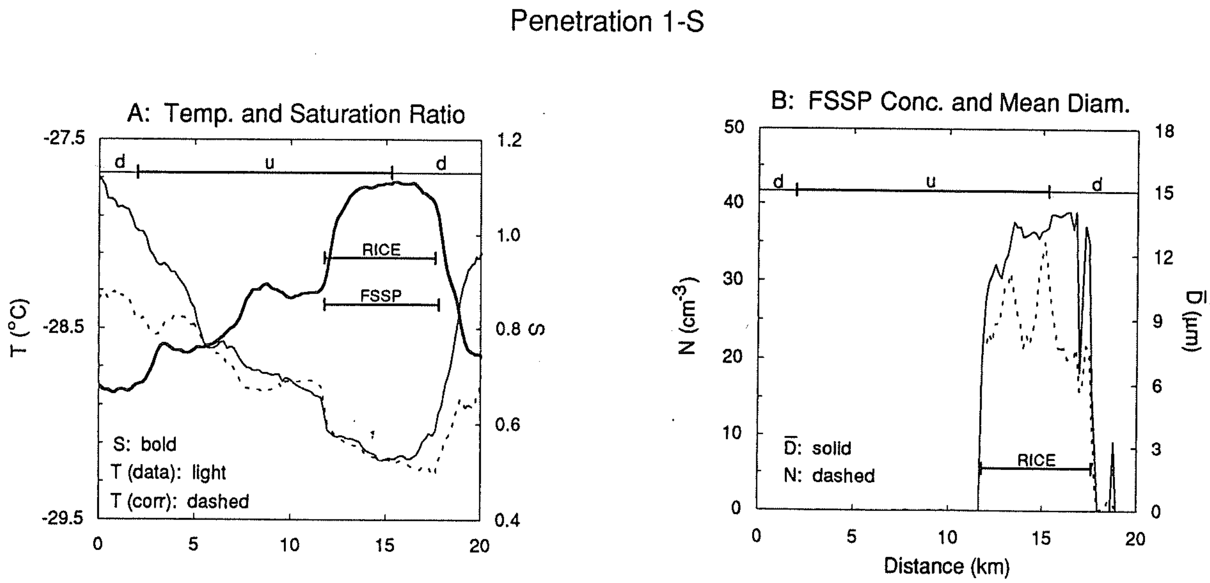

Figure 1: Measurements from the Sabreliner taken on 9 Nov. 1989, during the time period 110857–111059 MST. Panel A: Saturation ratio (S) from the cryogenic hygrometer, and temperature (T). A derived temperature curve which corrects for variation in aircraft altitude (labeled "T(corr)") is shown for reference, where a reasonable mean between the ice-saturated and dry adiabatic lapse rates of -9°C km^{-1} was assumed. This correction was negligible for the King Air penetrations. Labeled horizontal bars indicate regions of: detection of LW by the RICE, detection of cloud particles (droplets or ice) by the FSSP (in concentrations ≥ 1 cm^{-3}), and regions of updraft or downdraft (labeled "u" or "d," relative to W=0 m s^{-1}). Panel B: total particle concentration (N) and mean diameter ($\overline{D}$) from the FSSP.

4. Discussion

To investigate the instrument signals expected to be characteristic of homogeneous ice nucleation, we draw upon modeling of this process in a wave cloud for making qualitative comparisons with the observations. The physics of the 1–D numerical model employed in this study is based on Heymsfield and Sabin (1989).

We will first show a synthesis of several runs of the model to give the reader an overview of the changes in microstructure which might be expected in a wave cloud in the critical temperature range -30 to -40C. Model results of the phase of condensed water are shown schematically and summarized in Fig. 4, for a vertical cross–section parallel to the wind direction along several streamlines. Each model run (i.e. each streamline) was initialized at the start of uplift (distance = 0 km) at relative humidity 85%,[1] assuming homogeneous freezing to be the only ice nucleation mechanism. Additional model parameters, based in part on the aircraft measurements presented earlier, are an upwind environmental lapse rate of −6.5°C km^{-1}, a sinusoidal vertical velocity profile of peak magnitude 280 cm s^{-1} and wavelength 25.6 km with no wind shear, and a horizontal windspeed of 20 m s^{-1} everywhere. Note that the left ordinate (T_0) represents *initial* parcel temperatures at 85% relative humidity, and since subsequent parcel temperature changes in the vertical are adiabatic, *temperature at a given altitude across the cloud is not constant.*

In Fig. 4, the model suggests that LW should exist at the leading edge and lower levels of the cloud; however, the start of condensation at a given level in the cloud depends on the assumed upstream humidity profile. The increase in ice nucleation rate with decreasing temperature is apparent in the decreasing widths of the liquid–phase and mixed–phase regions with altitude.

The model results in Fig. 4 and inspection of the microphysical and thermodynamic data (not shown) were examined. These model results agree both qualitatively and quantitatively (to +/- 1C) with the observations. The model results also show the following instrument responses: abrupt disappearance of liquid water; decrease in relative humidity from near water–saturation to ice–saturation; increase in mean particle diameter and change in particle concentration; and indication of latent heat release. Inspection of the data in Figs. 1–3 reveals the same characteristic signatures are noted in the measurements.

5. Summary and Conclusions

A 1–D numerical model of droplet and ice particle growth and homogeneous ice nucleation has been used to aid in interpretation of aircraft microphysical measurements taken in lenticular wave clouds in the temperature range −29 to −41°C.

The rationale for proposing that homogeneous ice nucleation is the primary mechanism producing the ice observed in this study is summarized as follows.

1. The absence of ice at a temperature of −29°C under conditions of water–supersaturation is consistent with the low homogeneous ice nucleation rate expected at this

[1] The model runs are initialized at 85% relative humidity rather than at "cloudbase" (i.e. approximately 100% relative humidity) for several reasons: (1) 85% relative humidity is near the deliquescence point of ammonium sulfate CCN, (2) the rate at which droplets freeze homogeneously depends on the droplet diameter, which would be significantly overestimated if "equilibrium diameters" at cloudbase were assumed initially, and (3) homogeneous freezing at cold temperatures (e.g. <−40°C) can occur in unactivated droplets at relative humidities below 100%.

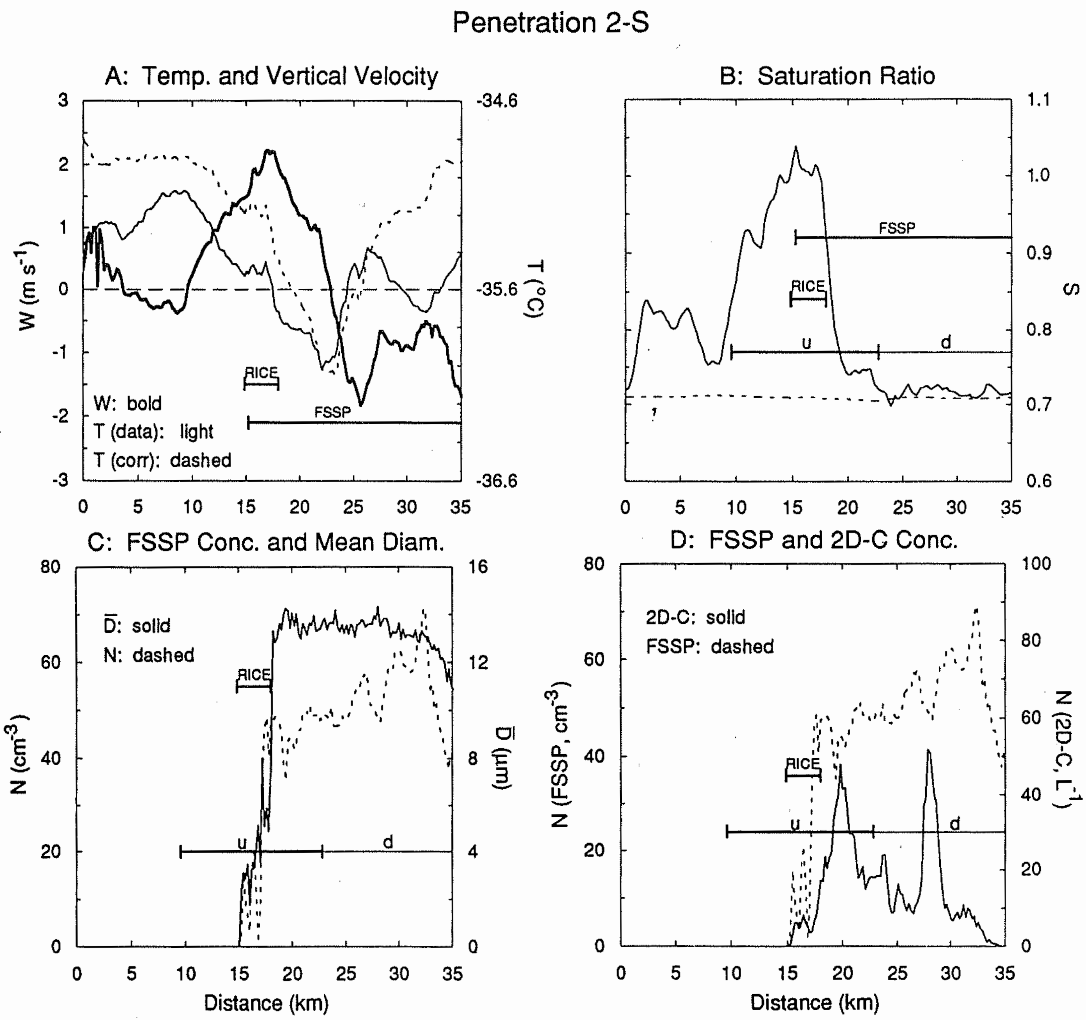

Figure 2: Measurements from the Sabreliner taken on 9 Nov. 1989, during the time period 120040–120338 MST. Labeled horizontal bars are defined as in Fig. 2. Panel A: vertical velocity (W) and temperature (T). Panel B: saturation ratio (S) from the cryogenic hygrometer. Dashed reference curve is the saturation ratio which corresponds to ice-saturated conditions. Panel C: total particle concentration (N) and mean diameter ($\overline{D}$) from the FSSP. Panel D: total particle concentrations from the FSSP and the 2D-C.

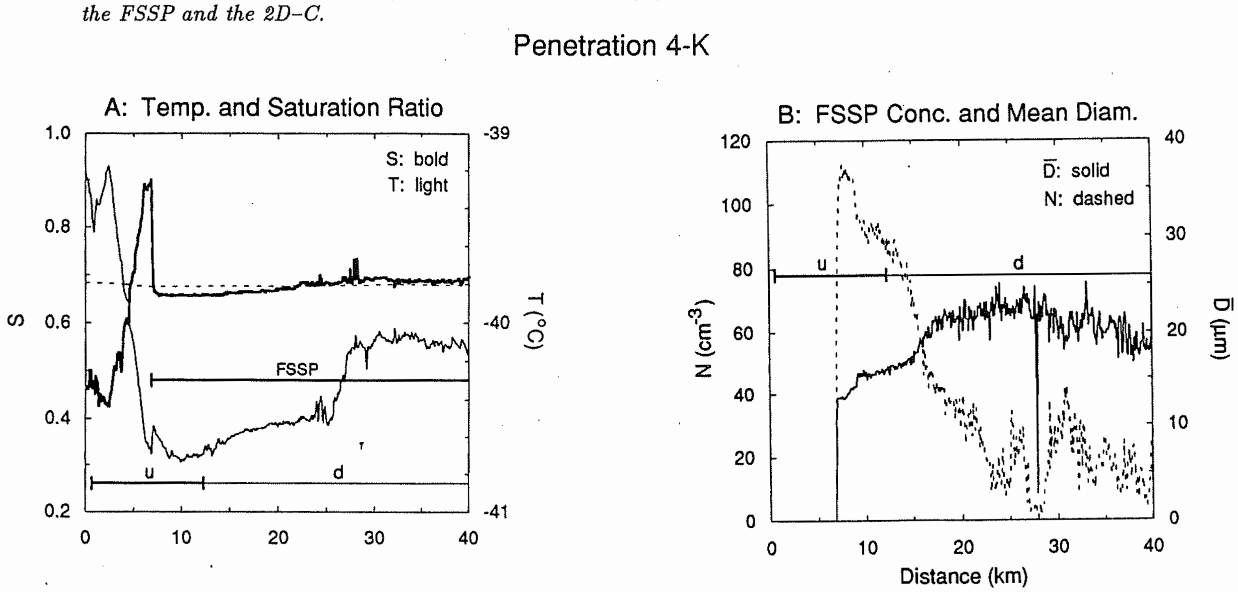

Figure 3: Measurements from the Sabreliner taken on 8 Dec. 1989, during the time period 131500–132102 MST. All curves and symbols are the same as in Fig. 2. Also shown in panel A is the location of the peak saturation ratio taken from panel B (labeled "S_{max}").

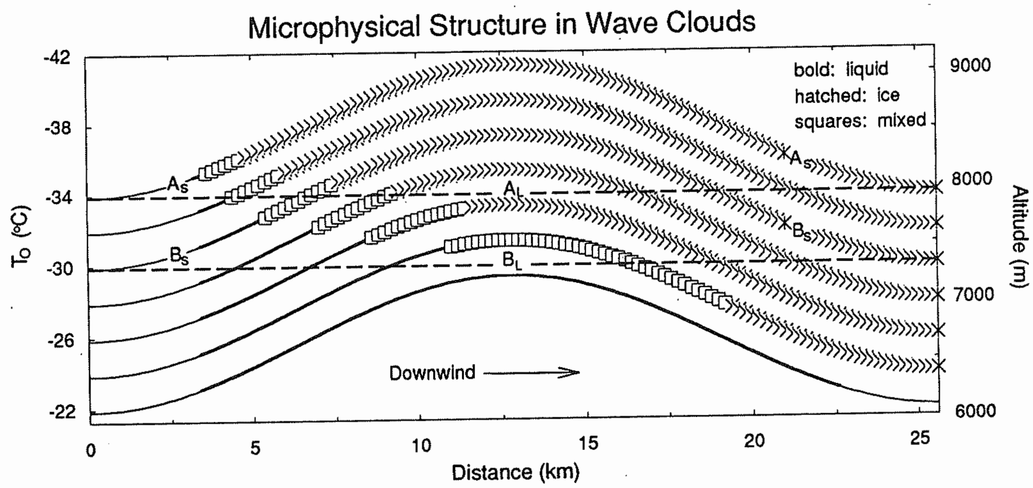

Figure 4: Measurements from the King Air taken on 8 Dec. 1989, during the time period 105700–110700 MST. All curves and symbols are the same as in Fig. 1, except saturation ratio is derived from the Lyman–alpha measuremenmts. Data courtesy of W. (Al) Cooper, NCAR.

temperature, and is suggestive that neither deposition nor immersion nuclei are important to the ice formation process at this and presumably warmer temperatures in these clouds.

2. Insignificant ice concentrations are observed when the relative humidity exceeds saturation with respect to ice, yet is below that required to cause droplets to form and subsequently freeze homogeneously, at temperatures at least as low as −40.7°C. This observation and (1) above suggest that ice formation on deposition nuclei was unimportant at all temperatures sampled in this study.

3. The measurements from various instruments show the abrupt transition from droplets to ice crystals in the characteristic manner suggested by the modeling calculations.

4. The measured sizes at which droplets freeze show a temperature–dependence which is consistent with the modeling calculations. [The relative humidity data are also consistent with the temperature–dependence of the peak saturation ratio expected theoretically from the homogeneous nucleation of solution droplets.

5. The temperature–dependence of the observed magnitude of change in FSSP–detected particle concentrations across the phase transition region shows general agreement with that expected from the modeled homogeneous ice nucleation process.

- Supercooled liquid water was observed conclusively at a temperature of −40.7°C and possibly even at −47.5°C, considerably lower than previously documented measurements. There is apparently no fundamental low–temperature physical limit around −40°C to the existence of cloud droplets; modeling results and the measurements suggest that small, unactivated solution droplets merely freeze at smaller sizes and lower relative humidities as temperature decreases, and can exist for a time following droplet deliquescence as a result of depression of the homogeneous ice nucleation rate by the dissolved solute. Furthermore, unactivated droplets will freeze homogeneously before reaching liquid–saturated conditions at temperatures below about −40°C.

The following results are also interpreted from the data.

- The theoretically–based, temperature–dependent ice nucleation rates employed by the model (Eq. 1) appear to fit the experimental data well.

- Consideration must be given to instrument detection thresholds in interpretation of these and prior measurements in cold clouds. For example, direct interpretation of only the RICE and FSSP measurements in this study would have implied a total absence of the liquid phase at temperatures colder than about −36°C, as was likely the case in results reported by Sassen and Dodd (1988) and Heymsfield and Sabin (1989).

ACKNOWLEDGEMENTS

We gratefully acknowledge W. (Al) Cooper (NCAR), Charlie Knight (NCAR) and Don Hagen (University of Missouri at Rolla) for their helpful discussions. The support of the NCAR research aviation facility (RAF) was instrumental to this study, especially Ed Brown for coordinating aircraft logistics, and Paul Spyers–Duran for developing the airborne cryogenic hygrometer. This work was supported in part by FIRE NASA (grant no. 1–98100–B), and by NSF (grant no. ATM 88–20708 to Don Hagen). **The National Center for Atmospheric Research is sponsored by the National Science Foundation.*

REFERENCES

Cox, S. K., D. S. McDougal, D. A. Randall, and R. A. Schiffer, 1987: FIRE—the First ISCCP Regional Experiment. *Bull. Amer. Meteor. Soc.*, **88**, 114–118.

Heymsfield, A. J. and L. M. Miloshevich, 1989: Evaluation of liquid water measuring instruments in cold clouds sampled during FIRE. *J. Oc. Atmos. Tech.*, **6**, 378–388.

Heymsfield, A. J., and R. M. Sabin, 1989: Cirrus crystal nucleation by homogeneous freezing of solution droplets. *J. Atmos. Sci.*, **46**, 2252–2264.

Heymsfield, A. J., L. M. Miloshevich, A. Slingo, K. Sassen, and D. Starr, 1991: An observational and theoretical study of highly supercooled altocumulus. *J. Atmos. Sci.*, **48**, 923–945.

Raschke, E., 1988: The international satellite cloud climatology project, ISCCP, and its European regional experiment ICE (International Cirrus Experiment). *Atmos. Res.*, **21**, 191–201.

Sassen, K., and G. C. Dodd, 1988: Homogeneous nucleation rate for highly supercooled cirrus cloud droplets. *J. Atmos. Sci.*, **45**, 1357–1369.

Spyers–Duran, P., 1991: An airborne cryogenic frost–point hygrometer. *Proc. AMS seventh symposium on meteorological observations and instrumentation*, New Orleans, La., 303–306.

THREE DIMENSIONAL MICROPHYSICAL MODELING OF CIRRUS CLOUDS DURING THE 1991 FIRE IFO

Eric J. Jensen, Douglas L. Westphal, Owen B. Toon, and Stephan Kinne

NASA Ames Research Center, Moffett Field, California

1. Introduction

Considerable effort has been directed at simulating and understanding our current climate and the potential for future climate change. One of the primary shortcomings of the climate models is the oversimplified representations of clouds. These deficiencies can be attributed both to a lack of understanding of cloud formation processes and to the computational speed limitations. Perhaps the best way to improve cloud parameterizations is to use a hierarchy of cloud models. Comparisons between the results from computationally efficient cloud parameterizations, detailed cloud simulations, and observations from field experiments can be used to develop improved parameterizations efficient enough for use in large-scale models.

During the 1992 FIRE IFO, we used a hierarchy of cloud models within a mesoscale model to simulate the formation of cirrus, including a simple semi-prognostic relative humdity scheme and a bulk water parameterization. At the most detailed level, we used an explicit microphysical model which included resolved CN solution drop and ice crystal size distributions over a 600 km x 600 km subgrid of the mesoscale model domain. Within this subgrid, condensation nuclei (CN), solution drop, and ice crystal size distributions were explicitly resolved and predicted. Several processes were included such as homogeneous freezing nucleation, deposition growth, sublimation, coagulation, and transport. Wind velocities, diffusion coefficients, and temperatures were taken from the MM4 mesoscale model simulations. Results from different cloud models and remote sensing observations are compared below for the the cirrus observed on Nov. 26, 1991.

2. Cloud Models

Within the PSU/NCAR mesoscale model, three different schemes were used to represent cloud processes. At the simplest level, a semi-prognostic relative humidity method (RH) was used. In this scheme, ice water content (IWC) is simply defined as vapor in excess of saturation. The IWC is carried along with the vapor; sedimentation and latent heat release are not treated. At the next level of complexity, the PSU/NCAR bulk water prognostic parameterization (BW) was used. This scheme distinguishes between non-precipitating hydrometer classes (cloud water and ice) and precipitating classes (rain and snow). Analytic expressions for the size distributions of the hydrometers are assumed [Zhang, 1989].

The most detailed cirrus model (EC) used includes explicit microphysics, radiative transfer, and a turbulent kinetic energy closure scheme. Three distinct aerosol types are treated in the model: condensation nuclei (CN), solution drops, and ice crystals. Size distribution for each aerosol type are resolved in 40 size bins, with radii ranging from 0.01 to 600 μm. Water vapor is also treated as a fully interactive element in the model. For each size bin in each aerosol type and water vapor, the continuity equation is solved at each time step, including sources and sinks due to nucleation, condensation/deposition growth, evaporation/sublimation, coagulation, sedimentation, advection, and diffusion. The numerical algorithms used are described by Toon et al. [1988], and the analytic expressions for microphysical processes are described by Toon et al. [1989].

We have assumed that nucleation of ice crystals in midlatitude cirrus clouds occurs primarily by homogeneous freezing of either deliquescent sulfate CN or activated solution drops. At temperatures below about -40°C, supersaturations larger than about 25% are required for homogeneous freezing nucleation of CN. Once nucleated in a supersaturated environment, the ice crystals grow rapidly by deposition of water vapor. Ice crystals larger than about 50 μm fall rapidly, and the largest ice crystals appear to be formed by coagulation. One dimensional simulations suggest that the cloud radiative properties are most sensitive to the vertical wind speed (cooling rate), turbulence, and the height at which the clouds form.

3. 1991 FIRE Simulations: Initial Conditions

During the 1991 FIRE experiment, we ran the PSU/NCAR mesoscale model, using analyses from NOAA's Forecast Systems Laboratory for initial conditions and boundary conditions. The mesoscale model (RH and BW) predicted temperature, wind velocities, and relative humidity over a domain encompassing the entire United States for the period 03–21z of each day..

The explicit microphysics scheme was not computationally efficient enough for use in the entire mesoscale model grid. Hence, we used the model on a 10 x 10 subrid (600 km x 600 km), centered on Kansas and including most of Kansas, Oklahoma, and Coffeyville, Kansas where the remote sensing observations were made.

The explicit microphysical model requires initial conditions (including water vapor concentration, temperature, and CN concentration), and meteorological conditions such as wind speeds and temperature throughout the simulation. At the beginning of the simulation (15z), temperature and relative humidity were taken from the mesoscale model simulation (RH version). During the EC simulation, the redistribution of water among vapor, liquid drops, and ice crystals, and transport of hydrometers were calculated with the explicit model. Wind speeds and temperature were taken from the mesoscale model throughout the simulation. Eventually, we plan to include full interaction between the models, such that cloud radiative properties calculated with the microphysical model are used in the mesoscale simulation and can affect the dynamics.

4. Simulation Results: November 26, 1991

For this paper, we will focus on simulations of the cirrus observed on November 26, 1991. A sample of the detailed microphysical results is given in Figure 1. The concentration of ice crystals is plotted as a function of equivalent volume radius and height for a vertical column over Coffeyville at 20z. Nucleation of ice crystals primarily occurs at the top of the cloud (above 10 km). When the ice crystals get larger than about 20 μm, they fall rapidly. The largest crystals form by coagulation in the lower portion of the cloud. The sublimation of ice crystals at the bottom of the cloud shows up as a tail extending down to small radii.

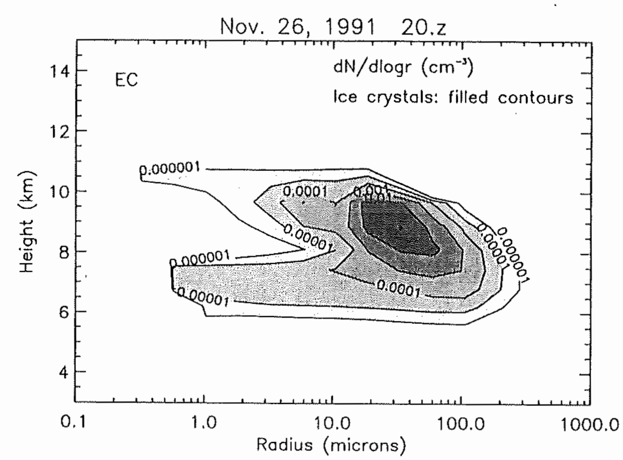

Figure 1. Simulated microphysical cloud properties over Coffeyville (from the EC simulation). The contours show concentration of ice crystals versus equivalent volume radius and height. The nucleation region (10–11 km), ice crystal growth region (7–10 km), and the ice crystal sublimation region (6–7 km) are all clearly evident.

Time-height displays of ice water content over Coffeyville are shown in Figure 2 from simulations with (a) the bulk cloud water scheme (BW) and (b) the explicit microphysical model (EC). The general features of the simulated clouds are similar, and the ice water contents calculated with the two models are similar. The primary difference is that the cirrus ice crystals seem to sediment more rapidly in the explicit microphysics model than in the bulk scheme. This problem may be a result of the cuttoff between cloud ice and snow in the bulk scheme.

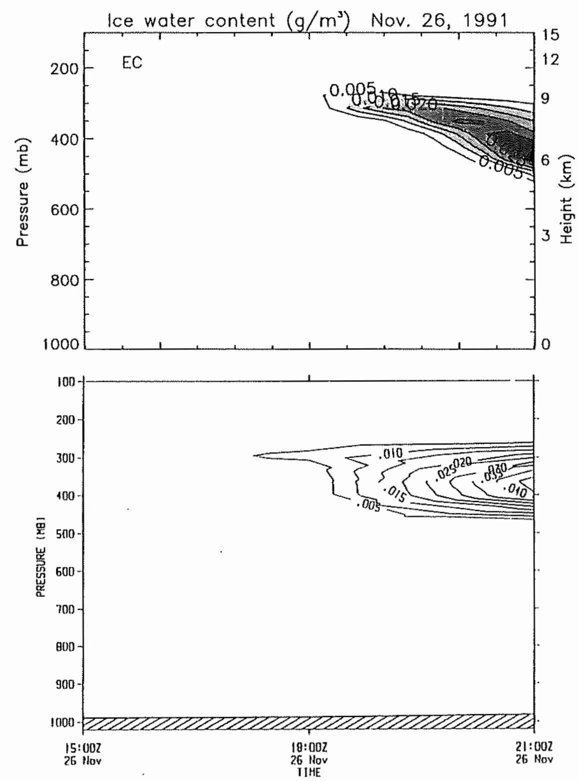

Figure 2. Time series of ice water content from the (a) EC model and (b) BW model over Coffeyville. The Clouds appear at about the same time and height in the two simulations, but the EC model predicts more ice crystal sedimentation.

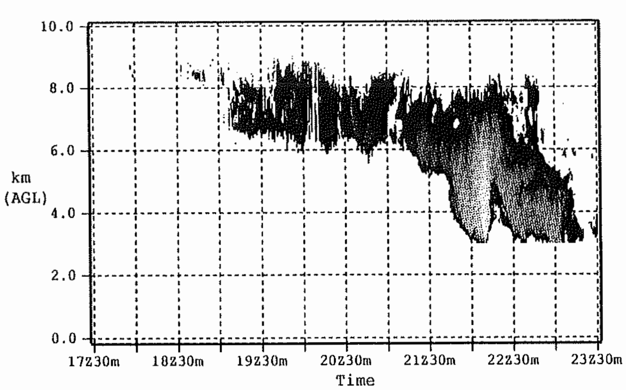

Figure 3. Penn State 94 GHz cloud radar backscatter for 15–21z, on the same day. This data suggests qualitatively that the model correctly predicted the time of appearance and the time variation in cloud height.

The backscatter from the Penn State 94 GHz cloud radar over the same time period is shown in Figure 3. Comparison between Figures 2 and 3 suggests that the model did a reasonable job of simulating the cirrus, at least in terms of when the cloud appeared over Coffeyville and the decrease in cloud height with time. The explicit microphysical model (EC) did a better job of representing the observed decrease in cloud height with time over Coffeyville. This is probably a result of the BW scheme incorrectly treating the cirrus crystals as nonprecipitating cloud ice.

Several extensions of this work are necessary. We intend to implement the explicit microphysics over the entire mesoscale model domain, and include full interaction between the dynamical model and the microphysics. As aircraft and remote sensing data from the FIRE experiment become available, we will use it to validate the cirrus microphysical and radiative properties calculated with the cloud models. Our underlying goal is to use the explicit microphysics scheme as a benchmark for development and improvement of bulk parameterizations.

Acknowledgments. Eric Jensen is a National Research Council associate. Partial support was provided by NASA's Climate Research program, directed by Dr. John Suttles.

References

Toon, O. B., R. P. Turco, D. Westphal, R. Malone, and M. S. Liu, A multidimensional model for aerosols: Description of computational analogs, *J. Atmos. Sci.*, **45**, 2123–2143, 1988.

Toon, O. B., R. P. Turco, J. Jordan, J. Goodman, and G. Ferry, Physical processes in polar stratospheric ice clouds, *J. Geophys. Res.*, **94**, 11359–11380, 1989.

Zhang, D.-L., The effect of parameterized ice microphysics on the simulation of vortex circulation with a mesoscale hydrostatic model, *Tellus*, **41A**, 132–147, 1989.

SATELLITE ANALYSES OF CIRRUS CLOUD PROPERTIES
DURING THE FIRE PHASE-II CIRRUS INTENSIVE FIELD OBSERVATIONS OVER KANSAS

Patrick Minnis[1], David F. Young[2], Patrick W. Heck[2], Kuo-Nan Liou[3], and Yoshihide Takano[3]

[1]NASA Langley Research Center, Hampton, VA, USA 23665-5225
[2]Lockheed Engineering and Sciences Co., Hampton, VA, USA 23666
[3]University of Utah, Salt Lake City, UT, USA 84112

1. INTRODUCTION

The First ISCCP (International Satellite Cloud Climatology Project) Regional Experiment (FIRE) Phase II Intensive Field Observations (IFO) were taken over southeastern Kansas between November 13 and December 7, 1991, to determine cirrus cloud properties. The observations include in situ microphysical data; surface, aircraft, and satellite remote sensing; and measurements of divergence over meso- and smaller-scale areas using wind profilers. Satellite remote sensing of cloud characteristics is an essential aspect for understanding and predicting the role of clouds in climate variations. The objectives of the satellite cloud analysis during FIRE are to validate cloud property retrievals, develop advanced methods for extracting cloud information from satellite-measured radiances, and provide multiscale cloud data for cloud process studies and for verification of cloud generation models. This paper presents the initial results of cloud property analyses during FIRE-II using Geostationary Operational Environmental Satellite (GOES) data and NOAA Advanced Very High Resolution Radiometer (AVHRR) radiances.

2. DATA

GOES visible (VIS, 0.65 µm) data taken every half hour at the nominal 1-km resolution were averaged to obtain an effective 4-km resolution to match the corresponding 4-km x 8-km infrared window (IR, 11.2 µm) radiances. Each scan line of the IR data was duplicated to achieve an effective 4-km resolution. Radiances at 12.7 µm (channel 7) were also taken each half hour at a 14-km resolution using the GOES multispectral imager (MSI). Data from the MSI channel 12 (3.94 µm) were taken with the VIS, IR and channel 7 radiances at 20 minutes after the hour at 3-hour intervals. The MSI data were duplicated to obtain the same resolution as the IR data. AVHRR channels 1 (0.67 µm, VIS), 3 (3.73 µm), 4 (10.8 µm, IR), and 5 (12.0 µm) were also taken at a 1-km resolution from the NOAA-11 and NOAA-12. These satellites have ascending nodes at 1430 and 0730 local time (LT), respectively.

In addition to standard 12-hourly soundings at the National Weather Service (NWS) stations, temperature and humidity profiles were taken from hourly Cross-Chain Loran Atmospheric Sounding System (CLASS) soundings at several sites in the vicinity of Coffeyville, KS, the hub of the experiment (Fig. 1). Cloud-top heights were derived from lidar backscattering profiles. Surface lidars were located at the hub; Parsons, KS; and in northeastern Oklahoma. A down-looking lidar was flown on the NASA ER-2 at various times during FIRE-II.

3. METHODOLOGY

a. *Visible and infrared retrievals*

During the daytime, cloud amount and height are derived with several techniques. One method uses the VIS and IR channels in a manner similar to that used to analyze the ISCCP data. The VIS reflectance, ρ_V, is interpreted with a parameterization of radiative transfer calculations using the scattering characteristics of a specified particle size distribution. Only two distributions are considered here, a water-droplet distribution having an effective radius of 10 µm and an effective variance of 0.05, and a cirrostratus (CS) hexagonal ice-crystal distribution (Takano and Liou, 1989). The water-droplet (WD) distribution, close to that used by the ISCCP, was used to compute a Mie-scattering phase function. The CS phase function was derived from ray tracing. An optical depth, τ_V, is derived with the parameterization from a given reflectance observation using one of the two models. In addition to the cloud reflectance, the parameterization accounts for the surface reflectance, Rayleigh scattering, and ozone absorption. The VIS optical depth is then used to compute IR emissivity of the cirrus cloud which is then used to correct the observed equivalent blackbody temperature, T_{IR}, to obtain a better estimate of the true radiating temperature of the cloud, T_c. The value of T_c is then converted to cloud height, z_c, using the nearest available sounding. Estimates of the clear-sky temperature, T_s, and clear-sky reflectance, ρ_{VS}, are needed to perform this analysis. The clear-sky reflectance map was developed from minimum reflectances taken during November 1986. Clear-sky temperature was derived as described by Minnis et al. (1987). Details of the technique, the parameterizations, and the models are given by Minnis (1991).

For intercomparison with the surface and aircraft data, only data within a small area around the sensor are extracted from the image. To provide a larger scale cloud-parameter dataset for model intercomparison, the data are analyzed half-hourly on a 0.5° grid covering the area between 32°N and 42°N and between 93°W and 103°W. The VIS and IR data are converted to two-dimensional histograms following the methods of Minnis et al. (1990).

b. *Multispectral infrared retrievals*

Another technique applicable both day and night uses

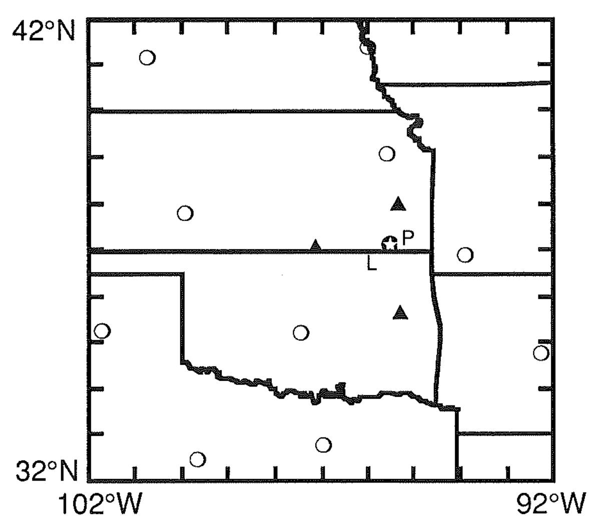

Fig. 1. Locations of Coffeyville (✪), Parsons (P), University of Wisconsin lidar (L), NWS sites (O), and CLASS sites (▲).

brightness temperature differences that arise from variations of cloud optical properties with wavelength and the nonlinearity of the Planck function with wavelength. Estimates of cloud emissivity, cloud height, and cloud microphysics can be derived theoretically from an analysis of multispectral infrared data [IR and channels 7 and 12 (GOES) or channels 3, 4, and 5 (AVHRR)] by taking advantage of the observed temperature differences. These differences have been examined both theoretically and with observations in attempts to derive various cloud properties from the satellite data (e.g., Allen et al., 1990; Stone et al., 1990; Parol et al., 1991). As in the earlier methods, the technique used here attempts to find the best match between the observations and theoretical calculations.

Radiative transfer calculations using an adding doubling model were performed for a range of particle sizes and shapes. Cirrus clouds were modeled using ice spheres with effective radii, r = 4, 8, 16, 32, and 64 μm, and hexagonal crystals having the CS and cirrus uncinus (CU) distributions (Takano and Liou, 1989). Surface temperatures, Tg, were varied from 260 K to 320 K. Cloud temperatures ranged from 210 K to 270 K. Atmospheric attenuation of the IR radiances was estimated in the same manner used by Minnis (1991). The channel-7 and -12 atmospheric absorption optical depths were 2 and 0.75 times the corresponding IR values, respectively. The channel-3 and -5 optical depths were set at 1.25 and 0.75 times the channel-4 values, respectively. The computations were performed for both a wet and dry atmosphere.

The results were parameterized as

$$\varepsilon_i = \sum_{n=0}^{3} a_n \ln(\tau_v / \mu)^n + a_4 \ln(\Delta T_{sc}) + a_5 \mu, \quad (1)$$

where ε_i is the effective emittance for channel i, $\Delta T_{sc} = T_s - T_c$, and $\mu = \cos\theta$, and θ is the satellite zenith angle. Two sets of coefficients, a_i, were determined for each channel, one for $\Delta T_{sc} \geq$ 5K and another for $\Delta T_{sc} <$ 5K. The effective emittance includes both the absorption and scattering effects of the cloud. The parameterization fits the radiative transfer results with an rms error of $\pm$ 0.02 and $\pm$ 0.03 for large and small ΔT_{sc}'s, respectively. The VIS optical depth is $\tau_v = Q_{exv}\,\tau_i / Q_{exi}$, where Q_{ex} is the extinction efficiency and τ_i is the extinction optical depth for channel i.

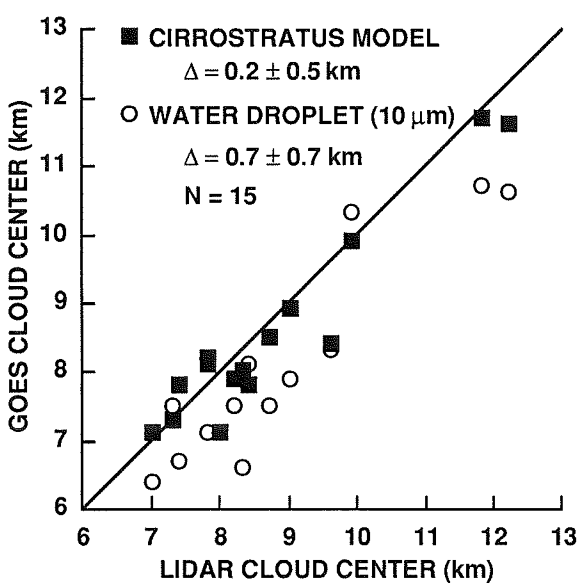

Fig. 2. Comparison of surface lidar and satellite-derived cloud-center heights over Parsons, KS.

A given radiance observation is modeled as

$$B_i(T) = (1 - C)\,B_i(T_{si}) + C[\varepsilon_i B_i(T_c) + (1 - \varepsilon_i)B_i(T_{si})], \quad (2)$$

where B_i is the Planck function at the center of channel i and C is the cloud fraction.

Similarly, calculations were performed for solar reflectance in the VIS and GOES channel 12 for the CS and CU distributions and for Mie-scattering water droplet distributions having an effective variance of 0.1 and r = 2, 4, 6, 8, 12, 16, 32, and 64 μm. The results were used to develop a set of bidirectional reflectance models, $\rho_i(k_i,\tau_i,\theta_o,\theta,\psi)$, where k_i is the microphysical model, θ_o is the solar zenith angle, and ψ is the relative azimuth angle. Thus, in the daytime, for channels 12 (GOES) or 3 (AVHRR), the observed radiance is approximated as

$$B_i(T') = B_i(T) + \mu_o E_i[\rho_i C + (1 - C)\rho_{si}], \quad (3)$$

where $\mu_o = \cos\theta_o$, E_i is the solar constant at the central wavelength of channel i, and ρ_{si} is the clear-sky reflectance for channel i. Values for ρ_{si} are estimated at 0.05 and 0.10 over land and water, respectively. The non-unit emittance of these surfaces is included in the clear-sky measurements of T_s at night. The separate modeling of the emission and reflectance for these channels accounts for the diffuse surface source and the beam solar source.

4. RESULTS

a. *Preliminary VIS-IR results*

An initial comparison of weighted cloud-center heights from the NASA Langley lidar (J. M. Alvarez, personal communication) with the cloud heights derived using VIS and IR GOES data over a small area surrounding Parsons, KS, is shown in Fig. 2. These data were taken at various times during FIRE-II. As in Minnis (1991), the CS model produces cloud center heights which are within 0.2 km of the lidar-derived values. The WD model yields underestimates of the cloud heights. Additional data covering more hours and sites are being analyzed.

The prime case study day for FIRE-II is November 26, 1991. During this day, thin cirrus replaced clear skies over the hub around noon and produced a halo around the Sun. A broken cirrus layer had developed around 2000 UTC (Universal Time Coordinated) centered near 9 km. The surface lidars also indicated a lower deck at 6.5 km with multiple levels reported by surface observers to the north and west. Multilayered clouds prevailed with a low-level cloud deck moving in from the south. Both a large-scale network and an inner network of frequent (3-6 hr) rawinsonde launches and extensive wind profiler, aircraft, and surface measurements provide an exceptional dataset for defining and monitoring the dynamics of this developing cyclone over the south-central Great Plains.

Figures 3 and 4 show sequences of cloud height and optical depth, respectively, resulting from the gridded analyses for four times during November 26. A clear zone around the hub at 1600 UTC filled in by 1900 UTC and remained overcast through 2100 UTC. High clouds predominate over Kansas and Oklahoma at 1600 UTC followed by a mix of cloud layers which give rise to the lower cloud heights during the afternoon. Low clouds ($z_c \leq$ 2 km), evident over north Texas in the morning, spread northward during the day. They are probably obscured by the higher clouds over southeastern Kansas. Thin cirrus clouds ($\tau_v <$ 4; $z_c >$ 7 km) are seen over part of eastern Kansas and much of Oklahoma at 1600 UTC while denser, high-level clouds are found over northern and central Kansas. By 1900 UTC, the thin cirrus clouds are mainly over southeastern Kansas with average cloud top heights over 7 km. At 2030 UTC, thin cirrus clouds with mean heights over 9 km pervade over eastern Kansas, Missouri, and central Arkansas.

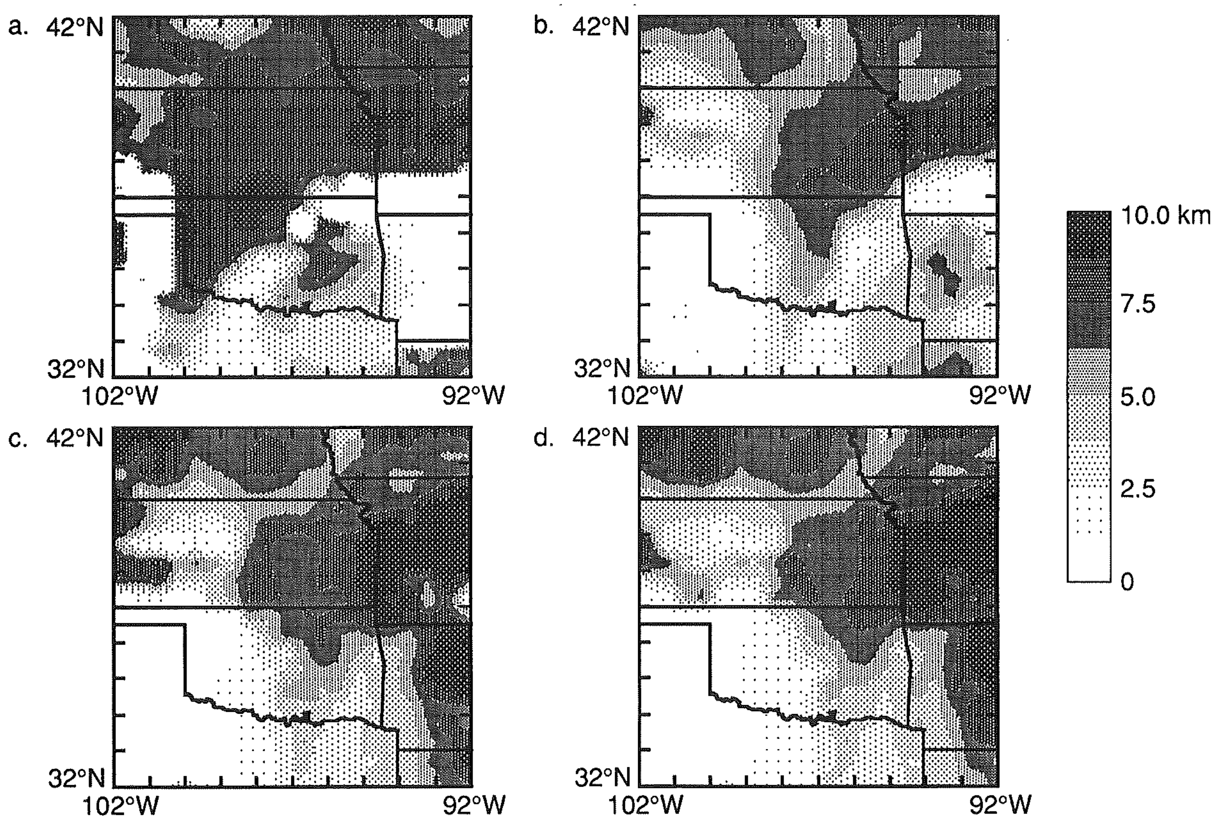

Fig. 3. GOES-derived cloud-center height (km) from November 26, 1991 at a) 1600 UTC, b) 1900 UTC, c) 2030 UTC, and d) 2100 UTC.

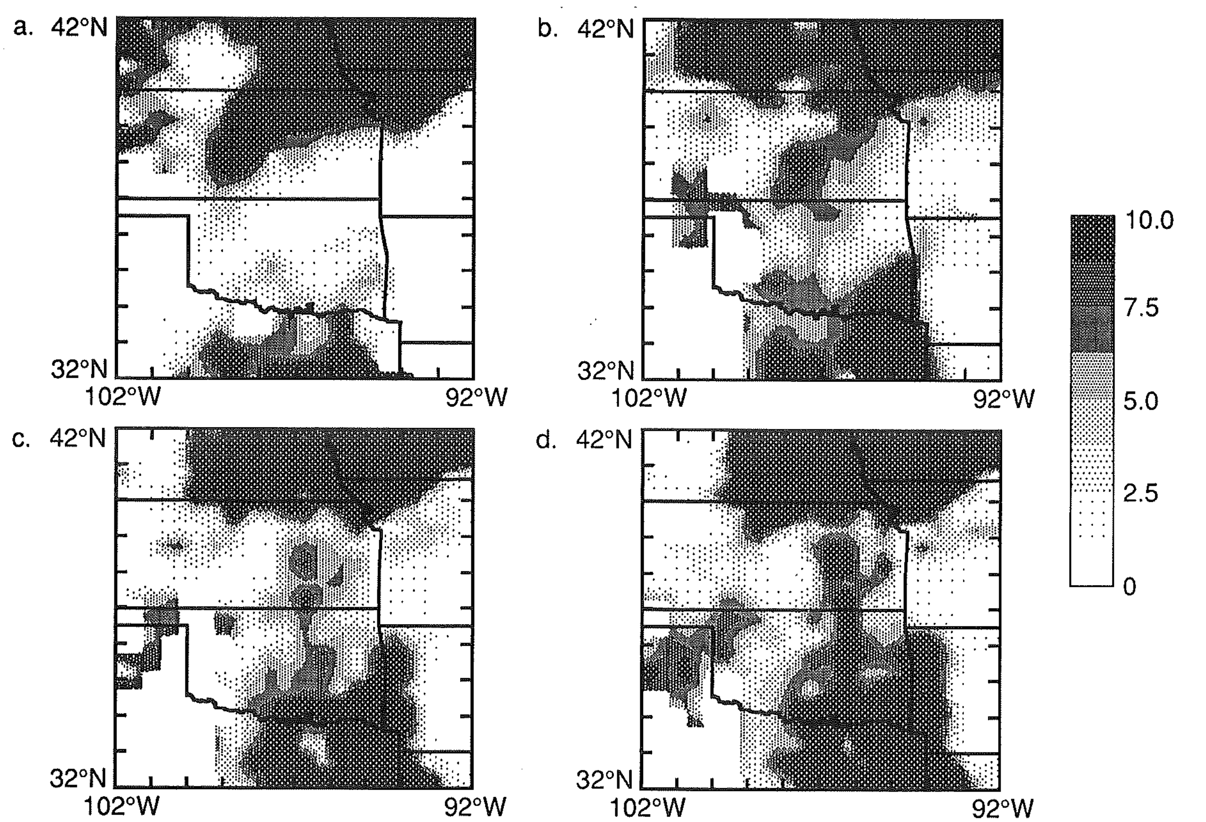

Fig. 4. GOES-derived visible optical depth from November 26, 1991 at a) 1600 UTC, b) 1900 UTC, c) 2030 UTC, and d) 2100 UTC.

These preliminary satellite analyses produce results that qualitatively agree with the observers' notes and quantitatively match the surface lidar reports. Figures 3 and 4 depict just a few of the products which are derived on a half-hourly basis from GOES VIS-IR data. Since the gridded analyses yield values for parameters that can be produced with mesoscale or larger scale models, they will be also useful for model development and validation. Therefore, such results should greatly enhance our capability to understand the complex dynamics and energetics involved in the development and dissipation of cirrus clouds.

b. *Preliminary IR multispectral results*

Cirrus was observed during the night of December 5, 1991 over Coffeyville, KS at ~ 9 km (K. Sassen, personal communication) which corresponds to a temperature of 234 K. Figure 5 shows a histogram of temperature differences between channel 7 and 12 from the GOES versus the channel-7 brightness temperatures. The heavy dark lines delineate the variation of these differences with τ_V and C computed with the parameterizations for an ice-sphere distribution having r = 16 µm. Assuming that the cirrus particles had this distribution, this plot indicates that most of the clouds passing over the lidar site were thin (τ_V < 3) and broken (C ~ 50%). Overall, this model encompasses these data better than those for the larger and smaller effective radii. Using a third channel, it should be possible determine particle size, cloud temperature, and cloud fraction without the aid of the surface data.

5. CONCLUDING REMARKS

Initial results from studying cirrus clouds using multispectral GOES data have been presented. Other comparisons using simultaneous GOES and AVHRR data are in progress. The cloud parameters that can be derived using these datasets will be used in process studies of cirrus clouds and validation of modeling efforts.

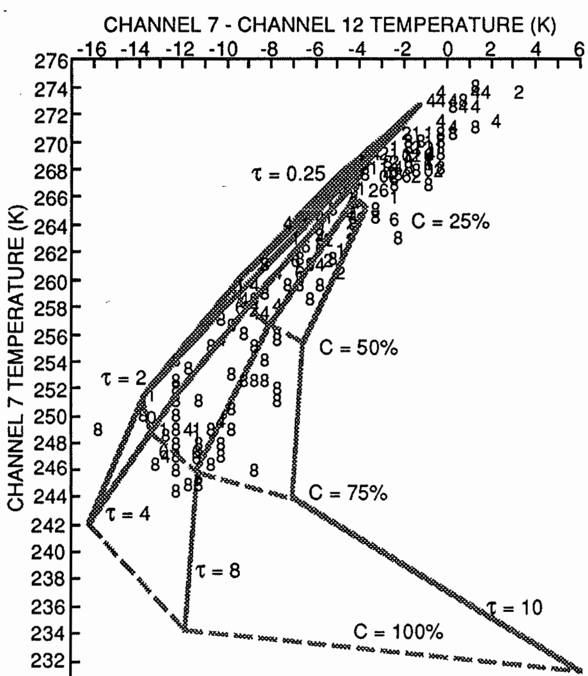

Fig 5. IR multispectral histogram for data over Coffeyville at 0920 UTC on December 5, 1991. The heavy lines represent model results for effective ice particle radius of 16 µm.

REFERENCES

Allen, Jr., P. A. Durkee, and C. H. Wash, 1990: Snow/Cloud discrimination with multispectral satellite measurements. *J. Appl. Meteorol.*, **29**, 994-1004.

Minnis, P, 1991: Inference of cirrus cloud properties from satellite-observed visible and infrared radiances. PhD dissertation, University of Utah, Salt Lake City, 161 pp.

Minnis, P., E. F. Harrison and G. G. Gibson, 1987: Cloud cover over the eastern equatorial Pacific derived from July 1983 ISCCP data using a hybrid bispectral threshold method. *J. Geophys. Res.*, **92**, 4051-4073.

Minnis, P., P. W. Heck, and E. F. Harrison, 1990: The 27-28 October 1986 FIRE IFO Cirrus Case Study: Cloud parameter fields derived from satellite and lidar data. *Mon Wea. Rev.*, **118**, 2426-2446.

Parol, F., J. C. Buriez, G. Brogniez, and Y. Fouquart, 1991: Information content of AVHRR channels 4 and 5 with respect to the effective radius of cirrus cloud particles. *J. Appl. Meteorol..*, **30**, 973-984.

Stone, R. S., G. L. Stephens, C. M. R. Platt, and S. Banks, 1990: The remote sensing of thin cirrus cloud using satellites, lidar, and radiative transfer theory. *J. Appl. Meteorol.*, **29**, 353-366.

Takano, Y. and K. N. Liou, 1989: Radiative transfer in cirrus clouds: I. Single scattering and optical properties of oriented hexagonal ice crystals. *J. Atmos. Sci.*, **46**, 3-19.

TWO-DIMENSIONAL NUMERICAL SIMULATION OF THE DEVELOPMENT FOR OROGRAPHIC-CONVECTIVE CLOUD

Gu Guojun, Wang Angsheng

(Institute of Atmospheric Physics, Academia Sinica, Beijing 100029)

Xu Huanbin

(Beijing Institute of Applied Meteorology, Beijing 100088)

1. INTRODUCTION.

The precipitation of orographic-convective cloud holds a large proportion in summer precipitation. Many authors have studied it by means of numerical simulation[1,2,3,4]. In 60's, Orville[1] studied and simulatied the development of convective-cloud over an upslope. Recently, Ogura etc. have applied their 2-D and 3-D moist cloud models to simulate: <1>. the orographic-convective precipitation over the Eastern Arabian Sea and the Ghat Mountain during the summer Monsoon[2], <2>. the Big Thompson storm occurred on 31 July- 1 August 1976 over Big Thompson Cayon, Colorado[3].

The paper presented here simulates the development of orographic-convective cloud over an upslope in ambient wind, and mainly discusses the effect of ambient wind on the intensity, structure, precipitation of orographic-convective cloud.

2. BRIEF DESCRIPTION OF THE MODEL.

The numerical model we use in the study is a two-dimensional compressible, moist cloud model[5,6] in a terrain-following coordinate system[2,7,8].

(1). TERRAIN-FOLLOWING COORDINATE SYSTEM($\bar{X}$, $\bar{Z}$).

$$\bar{x} = x, \bar{z} = H(z - zs(x)) / (H - zs(x)).$$

H is the height of the simulating domain, zs(x) is the elevation of terrain surface above the base of the simulating domain.

$$G1(x,\bar{z}) = \frac{H}{H - zs(x)}\left[\frac{\bar{z}}{H} - 1\right]\frac{\partial zs(x)}{\partial x}$$

$$G2(x) = H / (H - zs(x)).$$

(2). GOVERNING EQUATION IN(X, $\bar{Z}$).

$$\frac{\partial u}{\partial t} + u\frac{\partial u}{\partial x} + w\frac{\partial u}{\partial \bar{z}} = -\frac{1}{\bar{\rho}}\frac{\partial P'}{\partial x} - \frac{1}{\bar{\rho}}G1(x,\bar{z}) \cdot \frac{\partial p'}{\partial \bar{z}} + D_u,$$

$$\frac{\partial w}{\partial t} + u\frac{\partial w}{\partial x} + \bar{w}\frac{\partial w}{\partial \bar{z}} = -\frac{1}{\bar{\rho}}G2(x)\frac{\partial P'}{\partial \bar{z}} + \left[\frac{T_v'}{T_{vo}} - \frac{P'}{P_o} - q_l\right]g + D_w$$

$$\frac{\partial P'}{\partial t} + u\frac{P'}{\partial x} + \bar{w}\frac{\partial P'}{\partial \bar{z}} + P_o \cdot \left[\frac{\partial u}{\partial x} + G1(x,\bar{z}) \cdot \frac{\partial u}{\partial \bar{z}} + G2(x) \cdot \frac{\partial w}{\partial \bar{z}}\right] + w \cdot G2(x) \cdot \frac{\partial P_o}{\partial \bar{z}}$$
$$= \frac{P_o}{T_{vo}} \cdot \left[\frac{\partial T_v}{\partial t} + u\frac{\partial T_v}{\partial x} + \bar{w}\frac{\partial T_v}{\partial \bar{z}}\right] + D_p,$$

$$\frac{\partial T}{\partial t} + u\frac{\partial T}{\partial x} + \bar{w}\frac{\partial T}{\partial \bar{z}} = \frac{1}{\rho_v C_p}\left[\frac{\partial p'}{\partial t} + u\frac{\partial p'}{\partial x} + \bar{w}\frac{\partial p'}{\partial \bar{z}}\right] - r_d \cdot w$$
$$+ \frac{L_v C}{Cp} + D_T,$$

$$\frac{\partial q_v}{\partial t} + u\frac{\partial q_v}{\partial x} + \bar{w}\frac{q_v}{\partial \bar{z}} = -C_1 + C_2 + P_3 + D_{qv},$$

$$\frac{\partial q_c}{\partial t} + u\frac{\partial q_c}{\partial x} + \bar{w}\frac{q_c}{\partial \bar{z}} = C_1 - C_2 - P_1 - P_2 + D_{qc},$$

$$\frac{\partial q_r}{\partial t} + u\frac{\partial q_r}{\partial x} + \bar{w}\frac{\partial q_r}{\partial \bar{z}} = \frac{1}{\bar{\rho}} \cdot G2(x) \cdot \frac{\partial}{\partial \bar{z}}(\bar{\rho} V_T q_r) + P_1 + P_2 - P_3 + D_{qr}.$$

$$\bar{w} = uG1(x,\bar{z}) + wG2(x)$$

(3). MICRO-PHYSICS PARAMETERIZATION[6].

Ice precesses are not included, Kessler warm rain parameterization is applied, water is divided into three forms: water vapor, cloud water and rain water.

$$P_1 = 0.001 \cdot (q_c - 0.001)(\frac{g}{g} \cdot s^{-1}),$$

$$p_2 = 2.2 \cdot q_c q_r^{0.875}(\frac{g}{g} \cdot s^{-1}),$$

$$P_3 = \frac{1}{\bar{\rho}}\frac{(1 - \frac{q_v}{q_{vs}}) \cdot c \cdot (\bar{\rho} q_r)^{0.525}}{5.4 \times 10^5 + 2.55 \times 10^6 / (\bar{\rho} q_{vs})},$$

$$c = 1.6 + 12.49(\bar{\rho} q_r)^{0.2046}.$$

$$V_T = 3634 \cdot (\bar{\rho} q_r)^{0.1346}(\frac{\bar{\rho}}{\rho_o})^{-0.5}(cm.s^{-1}).$$

(4). SUBGRID SCALE PARAMETERIZATION[7].

$$D_u = \frac{\partial}{\partial x}(K_m A) + G1.\frac{\partial}{\partial \bar{z}}(K_m A) + G2.\frac{\partial}{\partial \bar{z}}(K_m B),$$

$$D_w = \frac{\partial}{\partial x}(K_m B) + G1.\frac{\partial}{\partial \bar{z}}(K_m B) - G2.\frac{\partial}{\partial \bar{z}}(K_m A).$$

$$D_\varphi = \frac{\partial}{\partial x}[K_H(\partial\varphi / \partial x + G1.\partial\varphi / \partial \bar{z})] + G1.\frac{\partial}{\partial \bar{z}}[K_H(\partial\varphi / \partial x + G1.\partial\varphi / \partial \bar{z})]$$
$$+ G2.\frac{\partial}{\partial \bar{z}}\left[K_H.G2.\frac{\partial\varphi}{\partial \bar{z}}\right].$$

$(\varphi \sim T、q_v、q_c、q_r)$.

$$A = \frac{\partial u'}{\partial x} + G1(x,\bar{z}).\partial u' / \partial \bar{z} - G2(x).\frac{\partial w'}{\partial \bar{z}},$$

$$B = \frac{\partial u'}{\partial \bar{z}} G2(x) + \frac{\partial w'}{\partial x} + G1(x,z).\frac{\partial w'}{\partial \bar{z}}.$$

$$u' = u - \bar{u}, w' = w$$

$$Def^2 = A^2 + B^2,$$

$$R_i = \left[-\frac{\partial T'}{\partial \bar{z}} / T_{vo} + \frac{\partial p'}{\partial \bar{z}} / P_o + \frac{\partial q_l}{\partial \bar{z}}\right].g.G2(x) / Def^2,$$

$$K_m = (0.21)^2.\Delta x.\Delta \bar{z}.Def.[max(0,(1 - 3Ri))]^{0.5},$$

$$K_H = 3.K_m.$$

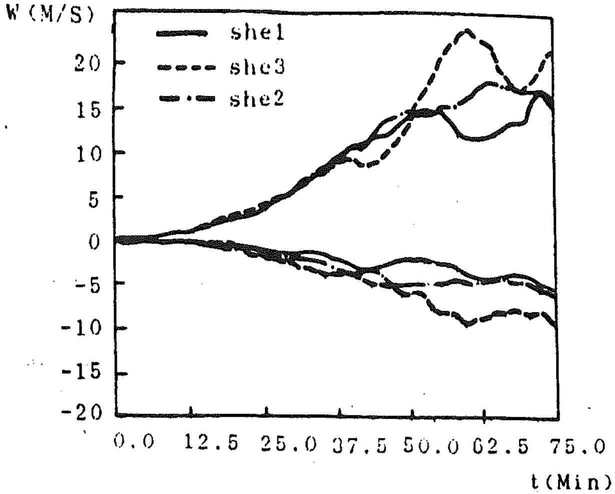

Fig.1. Time variations of updraft and downdraft peaks for case she1, she2, she3 respectively.

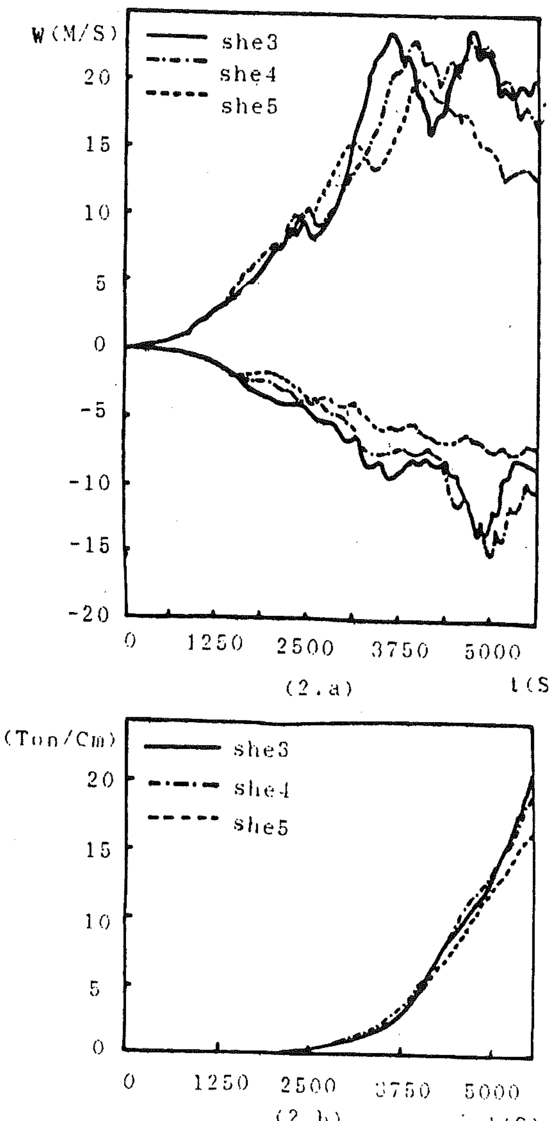

Fig.2. Time variations of updraft and downdraft peaks (2.a), total ground precipitation (2.b) for case she3, she4, she5 respectively.

3. SIMULATING RESULTS.

(1). INITIAL FIELDS.

There are 60 and 35 grid points in the x- and ž - directions, recpectively and the model domain is 120 km X 17.5 km (a upper friction layer of 2.5 km depth is included). The splitting time precedure proposed by Klemp and Wilhelmson[5] is applied. The small time step is 2.5 sec, while the larger time step is 12.5 sec.

zs(x):

When x> or = xo(40 km), zs(x)=2.0 km;

When x< xo(40 km), zs(x)=h*a*a/((x-xo)*(x-xo)+a*a),

h=2.0 km, a=10.0 km.

The initial distribution of temperature and moist, wind is assumed to be uniform horizontally in (x,z), the part parameters of temperature and dew temperature is in Table 1.

Table 1. The part parameters of the initial temperature and dew temperature:

Average lapse rate(0–12km) (℃ / km)	7.15
Temperature on the ground (℃)	25.0
Dew temperature on the ground (℃)	20.0
Temperature on the top of terrain (℃)	23.4
Dew temperature on the top of terrain (℃)	21.4

The building of the initial flow is accomplished in 12.5 minutes.

The purpose of the paper is to study the effect of ambient wind over the terrain peak (higher than 2.0 km) on the orographic-convective cloud. Till the accomplishment of the mean flow, the lower lever wind can produce an maximum vertical velocity about 80 cm/s along the upslope.

The ambient wind is divided into seven forms, seen in Table 2.

Table 2. The part parameters of ambient wind (higher than 2.0 km).

Name	she1	she2	she3	she4	she5	she6	she7
Shear range (km)	2–4.5	2–4.5	2–4.5	2–7.0	2–9.5	2–4.5	2–4.5
Shear (10^{-3}1 / s)	–0.8	–4	–8	–4	–2	0.8	4
Maximum upper wind (m / s)	–2.0	–10.0	–20.0	–20.0	–20.0	2.0	10.0

"–" implies middle–upper wind and upslope wind are in the reverse direction.

(2). SIMULATING RESULTS.

<1>. THE MIDDLE-UPPER WIND (HINGER THAN 2.0 KM, THE FOLLOWING IS THE SAME) AND LOWER UPSLOPE WIND ARE IN THE REVERSE DIRECTION.

Fig.1 comparies the time variations of peak updraft, peak downdraft for case she1, she2, she3, they have different shear intensity and identical shear range. Fig.2 comparies the time variations of peak updraft, peak downdraft and total ground precipition for case she3, she4, she5, they have different shear intensity and range but identical upper wind. From Fig.1 and Fig.2, we can find , with the increase of wind shear, the peak values of the maximum vertical velocity and minimum vertical velocity are enhanced, and the total ground precipitation increases too.

Fig.3 shows the distributions of cloud and rain water, wind vectors at 62.5 minutes for case she3, she4, she5. It can be seen, with the decrease of wind shear , the upper body and updraft region of orographic-convective cloud incline against wind.

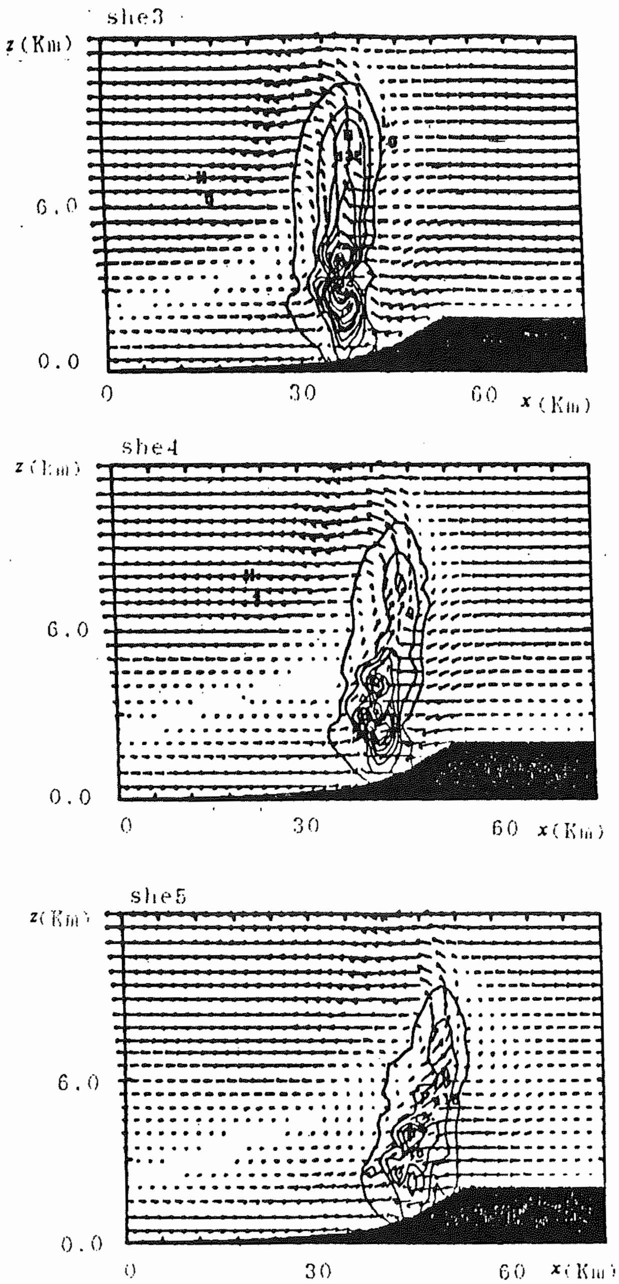

Fig.3. The distributions of cloud and rain water,wind vector at 62.5 minutes for she3, she4, she5 respectively.

Fig.4 compares the time variations of peak updraft, peak downdraft between case she2 and she4, they have identical shear intensity but different range and upper layer wind, it shows, with the increase of the middle-upper level wind, the peak values of maximum vertical velocity, minimum vertical velocity have increased.

<2>. THE DIRECTIONS OF MIDDLE-UPPER LEVEL WIND AND LOWER UPSLOPE WIND ARE IDENTICAL.

Fig.5 compares the time variations of peak updraft, peak downdraft between case she6 and she7. It can be seen, the increase of middle-upper wind shear restains the peak values of convection. It is similar to that on plain.

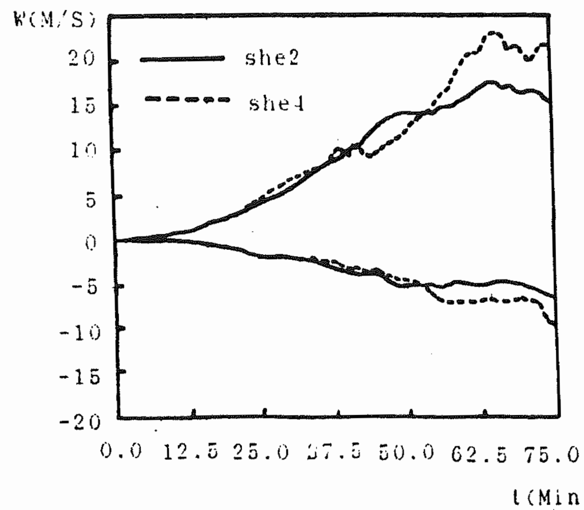

Fig.4. Time variations of updraft and downdraft peaks for case she2, she4 respectively.

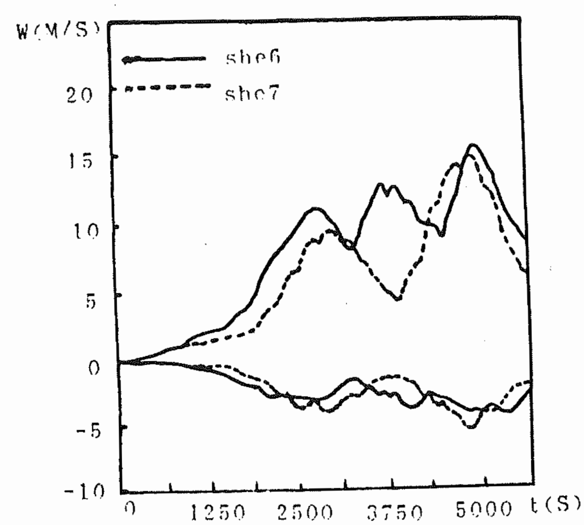

Fig.5. Time variations of updraft and downdraft peaks for case she6, she7 respectively.

(3). DISCUSSES.

From the upper simulating results, we obtain: the direction, shear and velocity value of middle-upper wind are very important for the development of orographic-convective cloud.

When the middle-upper wind and lower wind are in the reverse direction, convective cloud is produced near the upslope top, the ambient wind and wind shear of middle-upper level compel the cloud move towards the bottom of the slope, the larger the ambient wind value or wind shear, the greater the compel force, and the moist air of the lower level on the bottom of upslope become its ideal inflow at its head. So the increase of the wind shear or value cannot weaken the development of orographic-convective cloud, instead, promote its development.

When the directions of middle-upper wind and lower wind are identical, the effect of ambient wind on the development of convective cloud is similar to that on plain, that is, the wind shear weakens the maximum intensity of convection.

So the first and most important influence of ambient wind on the development of orographic-convective cloud is the wind direction relative to the upslope wind direction, the second influence is its vertical structure. When the initial humidity is uniform horizonally, the heavy precipitation location of orographic-convective cloud depends on the wind direction and shear.

REFERENCES:

[1] Orville, H. D., J. Atmos. Sci., 22(1965), 684-699

[2] Ogura, Y., and M. Yoshizaki, J.Atmos.Sci., 45(1988), 2097-2122

[3] Yoshizaki, M., and Y., Ogura, J.Atmos.Sci., 45(1988), 3700-3722

[4] Cocho, Y., J.Meteor.Soc. Japan, 56(1978), 405-423

[5] Klemp, J.B. and Wihelmson, R.B., J.Atmos.Sci., 35(1978), 1070-1096

[6] Xu Huanbin and Wang Siwei, Acta Meteorologica sinica of China, 48(1990),80-90

[7] Durran, D.R. and J.B., Klemp, Mon.Wea.Rev, 111(1983), 2341-2361

[8] Clark, T.L., J.Comput.Physi., 24(1977), 186-215

MICROSTRUCTURE OF CIRRUS CLOUDS OBSERVED BY HYVIS

H. Mizuno, T. Matsuo, M. Murakami and Y. Yamada

Meteorological Research Institute, Tsukuba, Ibaraki 305, Japan

1. INTRODUCTION

It is well known that cirrus clouds are closely related to radiative energy balance in the atmosphere (Liou, 1986). They control reflection of solar radiation and also absorption of infrared radiation emitted by the earth's surface and lower clouds. Infrared radiation emitted by the earth is decreased by the presence of cirrus clouds, because they are high clouds with temperatures appreciably colder than the earth's surface. Furthermore, since cirrus clouds cover about 20% of the globe (Barton, 1983), they are considered to have important effect on climate.

The optical properties of cirrus clouds are highly dependent on their microphysical properties such as types and sizes of ice crystals. For example, halos formed in cirrostratus are attributed to the refraction of the light in hexagonal ice crystals (Wallace and Hobbs, 1977). The information of the composition and structure of cirrus clouds is needed for estimation of their optical and also radiative properties.

Composition and structure of cirrus clouds are observed by two different methods: one remote sensing, the other in situ observations. Satellite, lidar and radar are remote sensing measurements. Satellite can observe cirrus clouds over global scale area (Curran and Wu, 1982; Barton, 1983). The advantage of lidar is continuous observation of vertical structure of clouds (Platt, 1973; Uchino et al., 1988; Imasu and Iwasaka, 1991). However, remote sensing could not grasp crystal types and size distribution of ice particles.

The types and size distribution have been observed by aircraft observations (Braham and Spyers-Duran, 1967; Knollenberg, 1972; Heymsfield and Knollenberg, 1972; Heymsfield, 1975 and 1986; Heymsfield et al., 1990). However, it is well known that the measurements for small particle less than about 100 μm in size by Knollenberg 2-D probe are not enough to discern phase and types of particles from its shadow image (Heymsfield and Baumgardner, 1985). In order to overcome these difficulties, recently Tanaka et al.(1989) and Murakami and Matsuo(1990) have developed an airborne video-microscope for measuring cloud particles (AVIOM-C) and a special sonde, the hydrometeor videosonde (HYVIS), for cloud and precipitation particles, respectively.

The HYVIS can provide direct images of hydrometeors from 7 μm to 1 cm with two TV cameras by wireless, and observe a vertical distribution of hydrometeor as well as meteorological elements. With the HYVIS Murakami et al.(1988) and Mizuno and Murakami(1989) observed successfully microphysical structures of warm-frontal clouds and winter monsoon snow clouds, respectively.

Using the HYVIS the in situ observations of cirrus clouds were made in June 1989 at Tsukuba, Japan. The purpose of this paper is to present the results of the cirrus cloud observations and to describe the microstructure.

2. SYNOPTIC CONDITION

The HYVIS observations were made of three cirrostratus clouds: one cirrostratus cloud extended northward portion from the surface stationary front on 22 June 1989, the other two clouds extended northeastward from the surface warm front on 30 June 1989. Here only results of a detailed case study for 22 June will be described, because this case was observed intensively by 3-hourly soundings over a 18-hour period. The other cases had a similar characteristics in microstructure.

Figure 1 shows a satellite picture around the Japanese Islands on the observation day. A surface stationary front (heavy line), Baiu front, is located about 300 km south of the site (closed triangle), Tsukuba, and a 20 kPa jet core (broken line) to the north of the site parallels the Baiu front. These situation indicate that there exists a frontal zone toward the cold air with increasing height. A wide cloud band system in Fig.1 is associated with the Baiu front overrunning to the north. The Baiu front moved slowly northward, and the cloud layer over the site changed from upper clouds at 0830 LST to middle cloud at 1130 LST. The HYVIS observation was carried out at 1105 LST in the course of the movement of the large scale system.

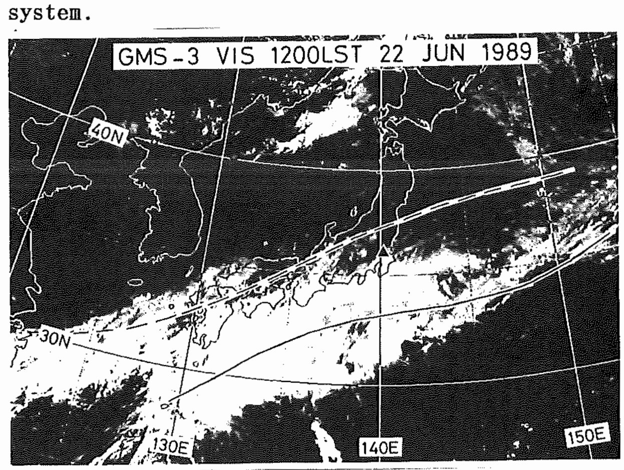

Fig. 1 Visible GMS-3 image at 1200LST 22 June 1989. Heavy line and broken line denote a surface stationary front (Baiu front) and 20 kPa jet core, respectively. A closed triangle represents an observation site. (Meteorological Satellite Center, JMA photo)

3. MICROSTRUCTURE

a. Sounding

Figure 2 shows temperature and relative humidity profiles observed with the HYVIS. From Fig. 2 cloud base was determined to be about 7 km (-20 °C) and cloud top was estimated to reach the tropopause level at about 13 km (-60 °C), although the measurement of humidity becomes unreliable as temperature decreases. Below the cloud base air was very dry, and air inside cloud layer was considered to be almost ice-saturated (82% at -20 °C and 75 % at -30 °C).

b. Types of Cloud Particles

The images observed by the HYVIS were those of single ice crystals. Cloud droplets and aggregates were not observed. Figure 3 shows images taken through a close-up and microscope TV cameras at 9.8 km (-34 °C) in the middle of the cloud layer. The close-up image shows a large ice crystal with a background of a portion of 22 ° halo and a balloon (dark circle in center). The microscope image shows a solid bullet (240 μm in length and 64 μm in width). The columnar crystal occurrence is consistent with the halo appearance, in accordance with the crystal habit expected from ice crystal diagram of Magono and Lee(1966). Most of ice particles in the cirrostratus were identified to be column or bullet types from the microscope images.

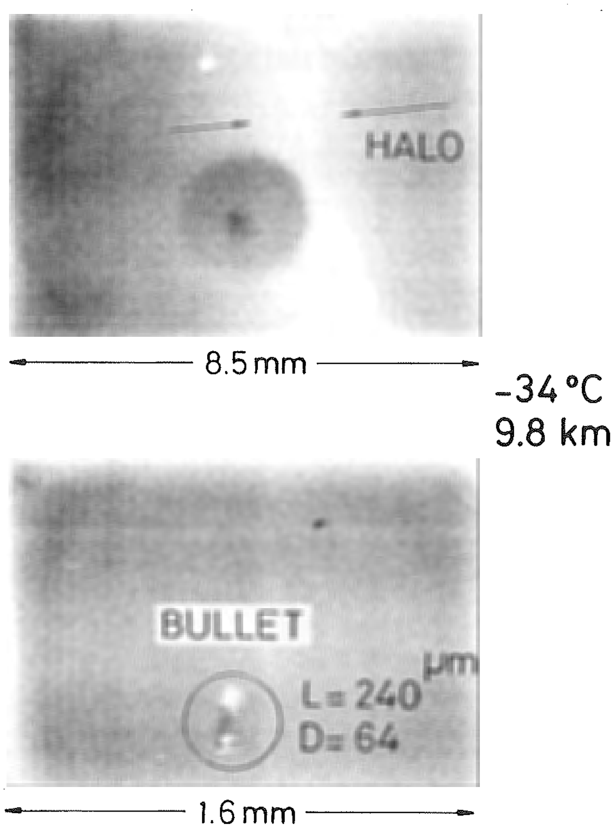

Fig. 3 Ice crystal images observed at 9.8km MSL (-34°C). A top image shows a large ice crystal, a 22° halo, and a balloon taken through a close-up TV camera. A bottom shows a solid bullet taken through a microscope TV camera.

Figure 4 shows a vertical distribution of close-up images of the HYVIS having not only large ice crystals but also a portion of halo. In Fig. 4 halos appeared in the layer between 8.5 km and 11.5 km. In that layer, column or bullet types were detected by the microscope images.

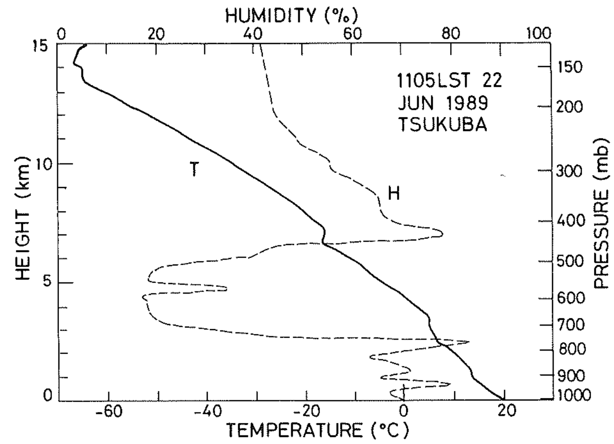

Fig. 2 Temperature and humidity profiles for 1105LST 22 June 1989.

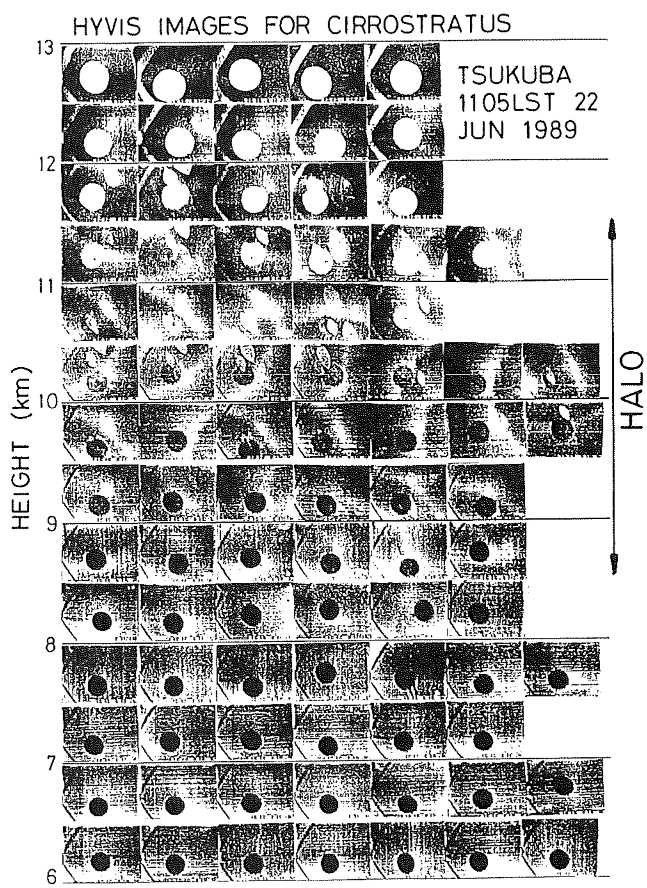

Fig. 4 Vertical distribution of HYVIS images showing 22° halos for 1105LST 22 June 1989.

c. Size Distribution

Figure 5 shows a vertical change in size distribution of ice crystals obtained from the micrographs. In the upper and middle part of the cloud, ice crystals are composed of about 10 μm to 240 μm in size and the large ice crystals are seen in the middle part. The total concentrations are about 10^5 m^{-3} and the number concentration generally decreases with size. In the lower part of the cloud, the concentration decrease. The size distribution obtained from the close-up images showed that the ice crystals up to 1.5 mm were found in the middle part of the cloud layer and that the concentration decreased in the lower part. Considering no droplets and the vertical change in size distribution of ice crystals, it is inferred that the ice crystals grew by deposition and fell in the cirrostratus.

d. Vertical Velocity

Estimation of vertical velocity profile was made using the isentropic method according to Starr and Wylie (1990). The updrafts up to 10 cm s^{-1} was analyzed in the region between the cloud base and 11 km level. This is illustrated on the left of Fig. 6.

In order to examine the relationship between the updraft profile and the observed microstructure, a critical vertical velocity (W_C) was defined and was calculated according to Jiusto(1971). It was defined as the vertical velocity which allows all ice crystals grow by deposition in water-satureted without producing any droplets. If the analyzed vertical velocity (W_{ANL}) is higher than W_C, cloud droplets will be expected. Since W_{ANL} on the left of Fig. 6 is lower than W_C on the right through the middle and upper part of the cloud, it is considered that no cloud droplets are produced and ice crystals grow by depositional process. These are consistent with the observed microstructure. A comparison between W_{ANL} and W_C suggests that the true upward velocity may exist between 10 and 50 cm s^{-1}, say a few ten centimeters per second.

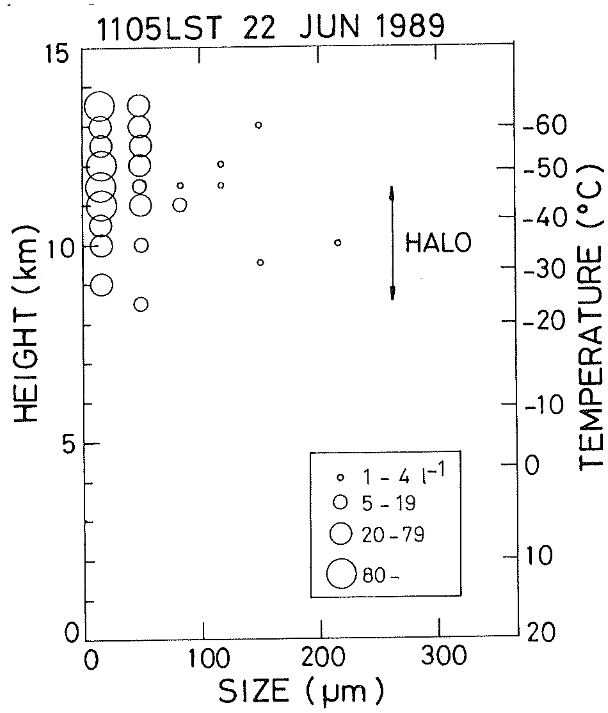

Fig. 5 Vertical change in size distribution of ice crystals. The number concentration of ice crystals in each 500 m layer is indicated.

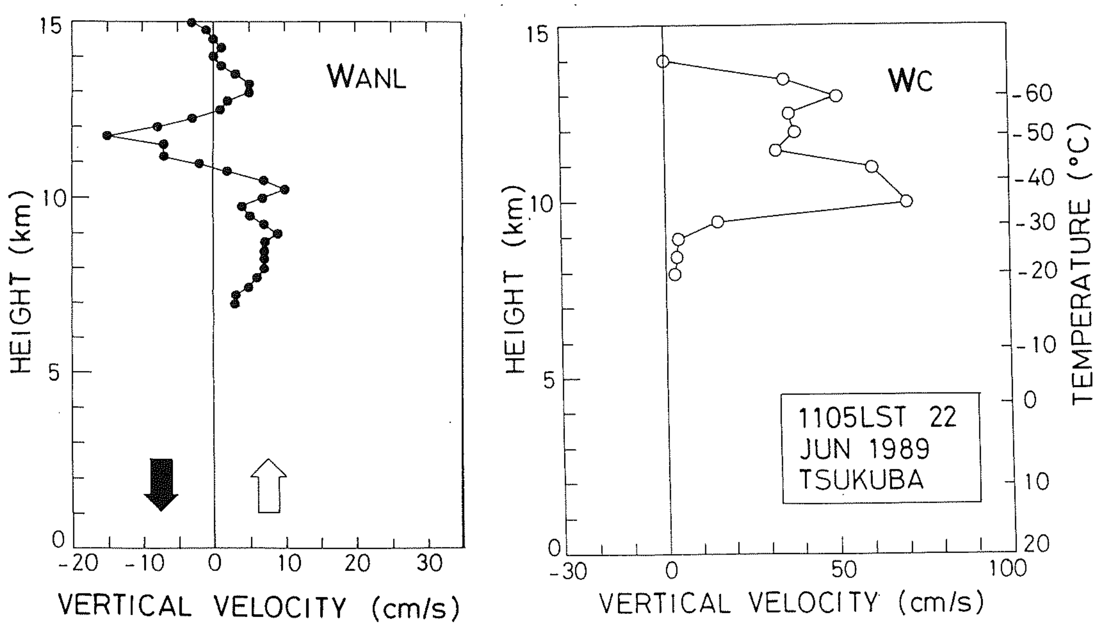

Fig. 6 Vertical velocity (W_{ANL}) and critical vertical velocity (W_C) are indicated. W_{ANL} is estimated from the ascent rate of contours of equivalent potential temperature at 1130LST and 1430LST on 22 June 1989. W_C is calculated using the data of ice crystal concentration observed on the assumption that ice crystals grow by deposition in water saturated condition in the absence of cloud droplets.

4. CONCLUSIONS

Cirrostratus clouds extended northward from the surface stationary front and warm front were observed by the HYVIS. The microstructure of the cirrostratus clouds is schematically represented in Fig. 7. The main results are summarized as follows:

1) Updraft up to 10 cm s^{-1} associated with a large-scale frontal overrunning was analyzed in the clouds.

2) The clouds had no cloud droplets included and were composed of single ice crystals of about 10 μm to 1.5 mm which grew by deposition.

3) The dominant types of ice crystals were column and bullet types and were consistent with a 22° halo in the middle part of the clouds.

4) In the upper and middle parts of the clouds, the total concentrations were about 10^5 m^{-3} and the number concentration generally decreased with size. The large ice crystals were found in the middle part.

5) In the lower part of the clouds, the concentration of ice crystals decreased.

These results provide an useful information on the composition and structure of cirrus clouds.

Acknowledgements. This work was done as a part of the WCRP/MRI program entitled "Field Experiments and Theoretical Modeling of Cloud-Radiation Processes" (FY1987-1990). We would like to thank every colleagues who contributed to this experiment. We would also like to acknowledge the contribution of the Aerological Observatory in providing special rawinsonde data. The computations were made with the HITAC M280D Computer Systems of the MRI.

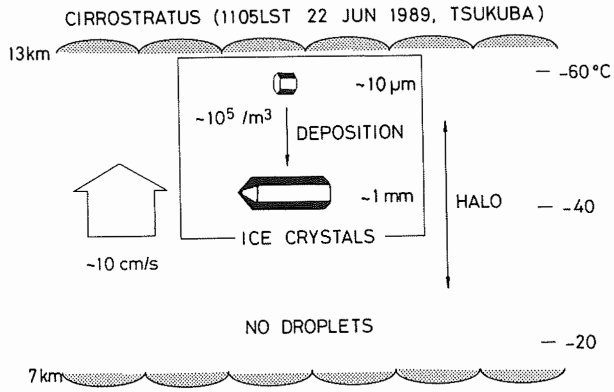

Fig. 7 Schematic drawing of vertical structure in the cirrostratus clouds.

REFERENCES

Barton, I. J., 1983: Upper level cloud climatology from an orbiting satellite. *J. Atmos. Sci.*, 40, 435-447.

Braham, R. R. and P. Spyers-Duran, 1967: Survival of cirrus crystals in clear air. *J. Atmos. Meteor.* 6, 1053-1061.

Curran, R. J. and M. L. C. Wu, 1982: Skylab near-infrared observations of clouds indicating supercooled liquid water droplets. *J. Atmos. Sci.*, 39, 635-647.

Heymsfield, A. J. and R. G. Knollenberg, 1972: Properties of cirrus generating cells. *J. Atmos. Sci.*, 29, 1358-1366.

Heymsfield, A. J., 1975: Cirrus uncinus generating cells and the evolution of cirriform clouds. part I: Aircraft observations of the growth of the ice phase. *J. Atmos. Sci.*, 32, 799-808.

Heymsfield, A. J. and D. Baumgardner, 1985: Summary of a workshop on proceeding 2-D probe data. *Bull. Amer. Meteor. Soc.*, 66, 437-440.

Heymsfield, A. J., 1986: Ice particles observed in a cirriform clouds at -83°C and implications for polar stratospheric clouds. *J. Atmos. Sci.*, 43, 851-855.

Heymsfield, A. J., K. M. Miller and J. D. Spinhirne,1990: The 27-28 October 1986 FIRE IFO cirrus case study: Cloud microstructure. *Mon. Wea. Rev.*, 118, 2313-2328.

Imasu, R. and Y. Iwasaka, 1991: Characteristics of cirrus clouds observed by laser radar (lidar) during the spring of 1987 and the winter of 1987/88. *J. Meteor. Soc. Japan*, 69, 401-411.

Jiusto, J. E., 1971: Crystal development and glaciation of a supercooled cloud. *J. Rech. Atmos.*, 5, 69-85.

Liou, K. N., 1986: Influence of cirrus clouds on weather and climate processes: A global perspective. *Mon. Wea. Rev.*, 114, 1167-1199.

Magono, C. and C. W. Lee, 1966: Meteorological classification of natural snow crystals. *J. Fac. Sci., Hokkaido Univ.*, Ser. VII, 2, 321-335.

Mizuno, H. and M. Murakami, 1989: Microstructure of winter monsoon snow clouds over the Sea of Japan observed with HYVIS. *WMO/TD*-No.269, 69-72.

Murakami, M., T. Matsuo, H. Mizuno and Y. Yamada, 1988: Microphysical structures of Japanese warm-frontal clouds observed with a new type sonde (HYVIS). *Preprint 10th International Cloud Physics Conference*, Bad Homburg, FRG, 1988, 144-147.

Murakami, M. and T. Matsuo, 1990: Development of the Hydrometeor Videosonde. *J. Atmos. Ocean. Tech.* 7, 613-620.

Platt, C. M. R., 1973: Lidar and radiometric observations of cirrus clouds. *J. Atmos. Sci.*, 30, 1191-1204.

Starr, D. O'C. and D. P. Wylie, 1990: The 27-28 October 1986 FIRE cirrus case study: Meteorology and clouds. *Mon. Wea. Rev.*, 118, 2259-2287.

Tanaka, T., T. Matsuo, K. Okada, I. Ichimura, S. Ichikawa and A. Tokuda, 1989: An airborne video-microscope for measuring cloud particles. *Atmospheric Research*, 24, 71-80.

Uchino, O., I. Tabata, K. Kai and Y. Okada, 1988: Polarization properties of middle and high level clouds observed by lidar. *J. Meteor. Soc. Japan*, 66, 607-616.

Wallace, J. M. and P. V. Hobbs, 1977: *Atmospheric Sciences*. Academic Press, New York, 224-226.

NUMERICAL MODEL SIMULATIONS OF CIRRUS CLOUDS INCLUDING HOMOGENEOUS AND HETEROGENEOUS ICE NUCLEATION

Paul J. DeMott, Michael P. Meyers, and William R. Cotton

Colorado State University
Fort Collins, CO

1. INTRODUCTION

An effort is described herein to improve the microphysics of numerical simulations of cirrus clouds using CSU Regional Atmospheric Modeling System (CSU RAMS). This is done by deriving practical and accurate parametizations of the process of ice initiation by homogeneous freezing of cloud and haze (CCN) particles in the atmosphere. Heterogeneous nucleation processes are already parameterized in CSU RAMS. This paper develops homogeneous freezing formulations for use with generalized distributions of cloud water and CCN, and initiates investigations of the impact of nulceation on simulations of cirrus clouds.

2. THEORETICAL CONSIDERATIONS

In this initial study, cloud water and unactivated particles are treated as separate populations. In reality the CCN concentrations, sizes, and compositions will determine the populations of both cloud droplets and haze particles for given atmospheric conditions. Our current treatment is satisfactory for RAMS because an explicit routine for cloud droplet activation is not yet in place. Neither are conservation equations yet formulated for cloud species.

2.1 Homogeneous Freezing of Supercooled Liquid Water

The total concentration of cloud droplets freezing per time step may be formulated as:

$$N_f = \int (1-\exp(-J_{ls}V_l\Delta t))n(D)dD \quad [cm^{-3}] \quad (1)$$

with, $J_{ls} = J_{ls}(0) \quad [cm^{-3}\ s^{-1}]$

and, $V_l = \pi\ D_l^3/6 \quad [cm^3]$

In (1), Δt is the time step. The concentration of droplets freezing is determined by the spectral density function of cloud droplets **n(D)**, the volume of the drops V_l , and a formulation for the nucleation rate of pure water $J_{ls}(0)$. Since $J_{ls}(0)$ is primarily a function of droplet temperature (T_l) and is not a function of droplet diameter **D**, (1) is easily integrable for a generalized distribution of cloud droplets. We use a gamma function to describe cloud drop distributions.

There are a number of approaches to obtaining $J_{ls}(0)$. One method is to use a classical theoretical calculation, assuming equilibrium conditions of a spherical ice embryo in water and using the steady state approximation of the number of embryos passing critical size. In using this approach, one is faced with selecting values for quantities, the true values of which are uncertain, but the impact of which on the calculation can be large. Most critical is the value chosen for σ_{l-w}, the interfacial surface tension at the ice water interface. The primary recourse for determining this value has been to use actual experimental data on the freezing of pure water or highly dilute solution droplets. DeMott and Rogers (1990) found a value of σ_{l-w} = 27 erg cm^{-2} to characterize their data on the freezing of droplets nucleated and freely grown on three types of CCN. DeMott and Rogers used the classical equation, as presented in Pruppacher and Klett (1978), and assumed constant values for the latent heat of fusion and the activation energy for self diffusion of water as given by Taborek (1985) to obtain this value. Values of $J_{ls}(0)$ as given by this result are compared with the experimental data in Fig. 1.

Also shown in Fig. 1 are the Sassen and Dodd (1988) estimates for $J_{ls}(0)$ made by combining numerical calculations with aircraft measurements in high altitude clouds. They suggested that values for $J_{ls}(0)$ versus temperature were well described as being about 10^6 times the theoretical values given by Pruppacher and Klett (1978). Such a curve is in good agreement with the curve suggested by DeMott and Rogers. In a theoretical study of homogeneous freezing nucleation and its effect on cirrus ice crystal formation, Heymsfield and Sabin (1989) used the temperature dependence for $J_{ls}(0)$ given by Eadie's (1971) statistical thermodynamic model for water. This formulation for $J_{ls}(0)$ is given by the dashed line in Fig. 1 (courtesy of A. Heymsfield). This result is also

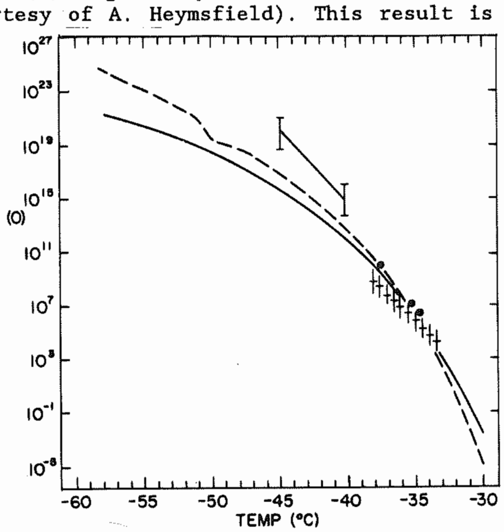

Figure 1. Homogeneous freezing nucleation rate of pure water (cm^{-3}) versus temperature. Various estimates shown include experimental data from DeMott and Rogers (1990) (crosses) and Hagen et al. (1981) (bars), field data from Sassen and Dodd (1988) (•), and theoretical approximations from DeMott and Rogers (1990) (solid line) and Heymsfield and Sabin (1989) (---).

in excellent agreement with DeMott and Rogers (1990) and Sassen and Dodd (1988) over the temperature range of their measurements, and lends support to these. However, Eadie's curve diverges to higher values than the others at temperatures below -45°C. In this sense, it is in better agreement with the rapid expansion experiments quantified by Hagen et al. (1981), which provide data for pure water droplets below -40°C. The Heymsfield and Sabin expression is used for pure water in this numerical study since it can be expressed as a simple function of temperature.

2.2 Homogeneous Freezing of CCN Solution Droplets

In many cases, cirrus clouds may form at temperatures below about -38°C where freezing can actually occur before cloud droplets are activated on CCN particles. In this case, J_{ls} replaces $J_{ls}(0)$ in (1), where J_{ls} is now a function of both dry particle size (D_s) and the water vapor saturation ratio (S_{vw}) with respect to water, in addition to temperature. Also, V_l is now $\pi D_a^3/6$, where D_a is the solution droplet diameter.

The theoretical approach to calculating J_{ls} is straightforward, but is not discussed here for the sake of space. Ultimately, a purely theoretical approach is not entirely satisfactory because these methods underpredict the effects of the solution concentrations on homogeneous freezing rates (see Pruppacher and Klett, 1978, p.280-281). Due to nonideal ionic interactions between the solute and condensed water, the freezing point is depressed an amount in addition to the amount obtained by considering curvature (Kelvin) and equilibrium solution (Raoult) effects. Sassen and Dodd (1988) therefore formulated an effective freezing temperature as:

$$T^* = T_l + (1.7\Delta T_m) \qquad (2)$$

where ΔT_m (°C) is the bulk freezing point depression. Values of ΔT_m can be obtained as a function of solution droplet molality M from tabular data for different salts. We assumed a CCN composition of ammonium sulfate ($(NH_4)_2SO_4$) for this study. Then, based on Weast (1981):

$$\Delta T_m = 0.102453 + 3.48484M \qquad (3)$$

valid from $M = 0.038$ to 3.716 ($r^2 = 0.9996$). Molality is evaluated as:

$$M = 1000m_s/(M_s((\pi D_a^3 \rho_l''/6) - m_s)) \qquad (4)$$

where ρ_l'' is solution density and m_s the dry solute mass. The factor 1.7 in (2) was based on Rassmussen's (1982) observations of the relationship between the depression of nucleation temperature and the melting point depression for a variety of salt solutions. The slope factor is an average for the materials tested, the actual value differing for each salt over a range from about 1.3 to 2.1. Ammonium sulfate was not one of the salts tested. Nevertheless, we will assume the validity of the average relationship for ammonium sulfate in this study. We note, however, that neglect of these nonideal effects can lead to serious potential overestimates of homogeneous freezing nucleation rates of solution droplets.

Substituting T^* for T_l in the theoretical expression for $J_{ls}(0)$ (DeMott and Rogers, 1990) gives the results of J_{ls} versus temperature as a function of M shown in Fig. 2. We should note that no one has yet directly verified such results in the laboratory.

The last pieces of information necessary to complete the calculation of homogeneous freezing of haze solution droplets are unique values for D_a, M, and ρ_l''. These may be obtained by way of the Kohler equation:

$$\ln S_{vw} = \frac{4M_w\sigma_{l\text{-}a}}{RT_l\rho_w D_a} - \frac{\nu\phi_s m_s M_w/M_s}{((\pi D_a^3 \rho_l''/6) - m_s)} \qquad (5)$$

which expresses equilibrium growth conditions for a dry solute particle at a given S_{vw}. Both the interfacial surface tension of the solution-air interface $\sigma_{l\text{-}a}$ and ρ_l'' depend on molality and the particular salt. Empirical relationships for these quantities with ammonium sulfate as the soluble component are obtained from Pruppacher and Klett (1978) and Weast (1981), respectively, as:

$$\sigma_{l\text{-}a} = 76.10 - 0.155(T_l - 273.15) + 2.17M \qquad (6)$$

$$\rho_l'' = 1.0054 + 0.062075M \qquad (7)$$

Equation 5 must be solved implicitly. If the haze particles are mixtures of specific soluble and insoluble components, m_s is replaced in (5) by $\epsilon_m m_n$, where ϵ_m is the soluble mass fraction and m_n is the mixed particle mass. We assume pure CCN.

It is possible to develop approximate relations for D_a and M to substitute into the equations for explicitly evaluating (1) for haze particles within RAMS. However, what is sought for these initial simulations is a simple relation describing the formation of ice from a distribution of CCN. Therefore, the explicit equations were solved for unit mass particles in order to seek a parameterization of N_f. The solid curves in Fig. 3 show the computed fractions freezing s^{-1} (F) of haze particles containing given masses m_s of dry CCN at three temperatures. These results are quite consistent with Sassen and Dodd's (1989) estimated minimum saturation ratio required for ice initiation. Curves of F at constant dry CCN mass (g) appear approximately

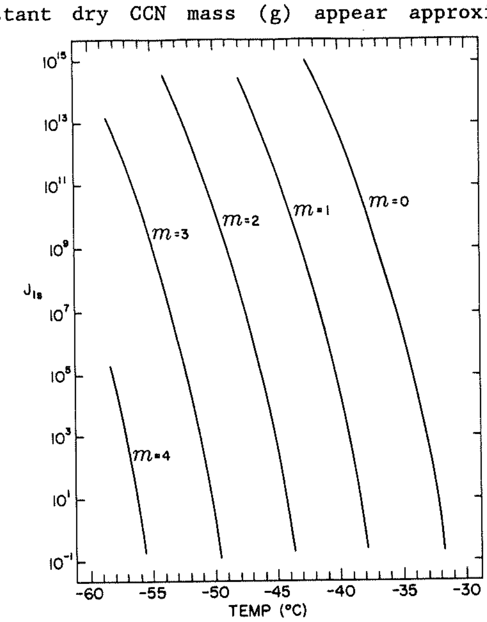

Figure 2. Homogeneous freezing rate of solution droplets versus temperature as a function of droplet molality (M).

linear over a wide range of Log (F). However, they asymptotically approach F = 0 at low humidity and F = 1 at high humidity. The equation derived to approximate the equilibrium behavior of F as a function of S_{vw}, D_s, and T_1 is:

$$F = 1 - \exp(-a((\pi \rho_s/6)^2)D_s^5) \quad (8)$$

where,

$$a = c1(S_{vw})^{c2} \quad (9)$$

with, $c1 = \exp(-23.3-(2.12(T_1-273.16)))$

and, $c2 = 3110+94.6(T_1-273.16)+0.8((T_1-273.16)^2)$.

The parameterized results are plotted as dashed curves in Fig. 3. Alhough exact agreement could not be obtained for all sets of conditions, (8) quite adequately describes homogeneous freezing nucleation by a distribution of CCN.

One factor not yet considered in this parameterization is that only the smaller nuclei for cloud condensation achieve their equilibrium radii as relative humidity approaches 100%. It is clear upon considering typical cirrus cloud

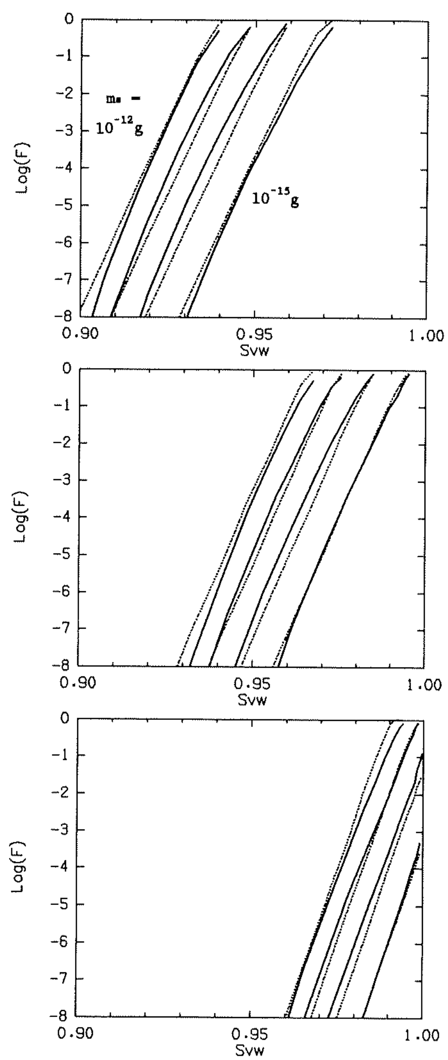

Figure 3. Logarithms of the fractions of unit mass, pure ammonium sulfate aerosols nucleating ice as a function of saturation ratio at -50°C (a), -45°C (b), and -40°C (c). Solid lines are exact and dotted lines parameterized results.

vertical velocities that nonequilibrium considerations are important for soluble particles with mass larger than about 10^{-13} g. We are in the process of including nonequilibrium effects in the parameterization based on explicit calculations. This effect will enter the parameterization as an adjustment to the equilibrium saturation ratio which is dependent on D_s and vertical velocity.

The results given by (8) are in a form which may be integrated over a generalized CCN size distribution. We do this numerically. A gamma distribution of dry CCN was chosen for the simulations which follow. Geometric mean diameter and Γ coefficients were selected by fitting to the dry particle size distribution determined from CCN supersaturation spectra reported by Heymsfield (1973). This CCN spectra was also used in the theoretical study of Heymsfield and Sabin (1989). Freezing nucleation is only permitted above the deliquescence point (82% relative humidity).

3. NUMERICAL SIMULATIONS

The CSU RAMS numerical model is a modified version of the model described by Tripoli and Cotton (1982) and Cotton et al. (1982, 1986). A comprehensive overview of the model microphysics is given in Flatau et al. (1990). Heterogeneous ice formation occurs in the model by deposition/condensation freezing and contact freezing nucleation as parameterized by Cotton et al. (1986) and modified by Meyers et al. (1992).

For the preliminary simulations reported in this paper, the model was run in a one-dimensional mode to facilitate comparison of the ranges of effect of the different homogeneous and heterogeneous ice formation processes at cirrus cloud altitudes. A one-dimensional simulation is performed by running the model over a large horizontal domain (1000 km) with only 8 grid points. A cyclic boundary condition is applied in the x-direction. The vertical grid spacing is stretched from 10 m at 10km MSL to 100 m at the surface. Separate simulations using an idealized humidity profile were performed to isolate each nucleation parameterization. The results for ice crystals formed versus height and temperature are shown together in Fig. 4. The model was initialized with low humidity to -32°C and either a constant 100% (Fig. 4a) or 95% (Fig. 4b) relative humidity from -32 to -50°C. The results presented are for the instantaneous ice initiation that such conditions would produce and should not be taken to be representative of longer time integration results that will be produced in simulations initialized with a realistic atmospheric sounding. We show Fig. 4 simply to demonstrate features of the parameterizations.

There are three factors to note in Fig. 4 which will be the focus of more realistic simulations to follow. First, the parameterized heterogeneous ice formation process produces substantial amounts of ice which will compete for water vapor and may effectively shut off the homogeneous process. While the heterogeneous process will be important, its magnitude is probably not well represented at cirrus temperatures by a formulation which extrapolates from data collected on lower level aerosols at T > -20°C. The second effect shown in Fig. 4 is the strength of the onset of homogeneous processes. Very high potential numbers of ice crystals may be produced in certain conditions. Vertical motion will be important in realistic cases. Finally, Fig. 4 shows the desired response of the haze nucleation parameterization to lower humidities. Namely, the onset of nucleation occurs at lower temperatures as humidity lowers. This response to humidity and temperature should help in simulating layered cirrus cloud structures.

4. SUMMARY AND CONCLUSIONS

A parameterization for homogeneous ice formation processes has been described for use in a mesoscale cloud model. The parameterization includes most essential dependencies on time, temperature, humidity, and CCN characteristics. Improvements are underway to include variable soluble fraction of CCN, nonequilibrium growth of larger CCN, and differing CCN characteristics. In future simulations which include the combined effects of all nucleation processes, tests will be run to examine the sensitivity of modifying the vertical ice nucleus concentration profile. Numerical simulations planned include 2-D sensitivity tests using a composite sounding and a 3-D resimulation of a specific cirrus cloud event.

5. ACKNOWLEGEMENTS

This research was conducted with the support of the National Science Foundation (Grants ATM8813345 and ATM-9103748) and the Air Force Office of Scientific Research (Grant AFOSR-91-0269). The authors would also like to thank Mr. Piotr Flatau and Mr. Louis Grasso for many helpful discussions.

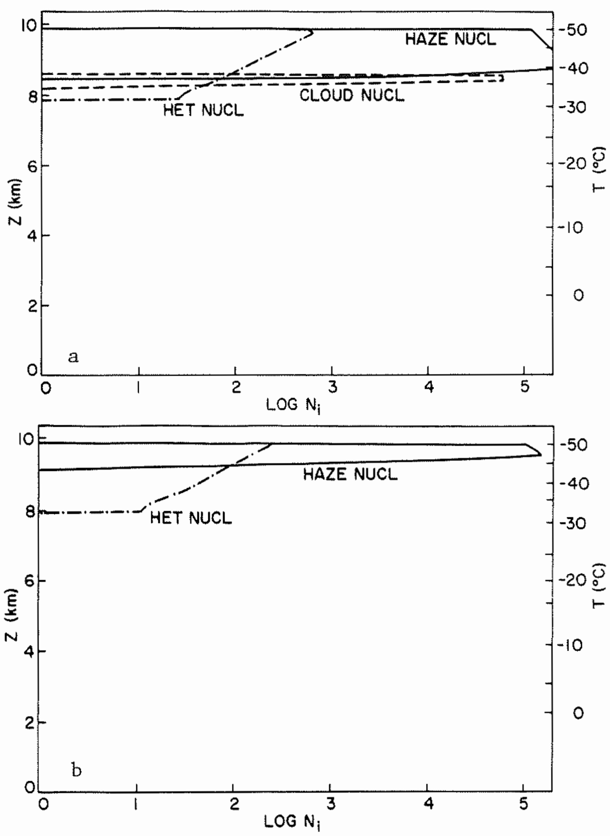

Figure 4. Instantaneous ice formation response of parameterizations of homogeneous freezing of cloud droplets, homogeneous freezing of haze particles, and heterogeneous ice nucleation to 100% (a) and 95% (b) uniform relative humidity soundings in 1-D sensitivity simulations.

6. REFERENCES

Cotton, W.R., G.J. Tripoli, R.M. Rauber, and E.A. Mulvehill, 1986: Numerical simulation of the effects of varying ice crystal nucleation rates and aggregation processes on orographic snowfall. *J. Clim. Appl. Meteor.*, **25**, 1658-1680.

Cotton, W.R., M.A. Stevens, T. Nehrkorn and G.J. Tripoli, 1982: The Colorado State University Three-Dimensional Cloud/Mesoscale Model-1982. Part II: An ice phase parameterization *J. Rech. Atmos.*, **16**, 295-320.

DeMott, P.J. and D.C. Rogers, 1990: Freezing nucleation rates of dilute solution droplets measured between -30 and -40C in laboratory simulations of natural clouds. *J. Atmos. Sci.*, **47**, 1056-1064.

Eadie, W.J., 1971: A molecular theory of the homogeneous nucleation of ice from supercooled water. Ph.D. Dissertation, Univ. of Chicago, Cloud Physics Lab., Tech. Note 40, 117pp.

Flatau, P.J., G.J. Tripoli, J. Verlinde, and W.R. Cotton, 1990: The CSU-RAMS cloud microphysical module: General theory and code documentation. Atmos. Sci. Paper No. 451, Dept. of Atmos. Sci., Colorado State University, Ft. Collins, 88p.

Hagen, D.E., R.J. Anderson and J. L. Kassner, Jr., 1981: Homogeneous condensation freezing measurements for small water droplets in an expansion cloud chamber. *J. Atmos. Sci.*, **38**, 1236-1243.

Heymsfield, A.J. and R.M. Sabin, 1989: Cirrus crystal nucleation by homogeneous freezing of solution droplets. *J. Atmos. Sci.*, **46**, 2252-2264.

Heymsfield, A.J., 1973: The cirrus uncinus generating cell and the evolution of cirroform clouds. Ph.D. Dissertation, University of Chicago, 269 pp.

Meyers, M.P., P.J. DeMott, and W.R. Cotton, 1992: New primary ice nucleation parameterizations in an explicit cloud model. *J. Appl. Meteor.*, in press.

Pruppacher, H.R. and J.D. Klett, 1978: *Microphysics of Clouds and Precipitation*. D. Reidel, Boston, 714 pp.

Rasmussen, D.H., 1982: Thermodynamic and nucleation phenomena - A set of experimental observations. *J. Crystal Growth*, **56**, 56-66.

Sassen, K. and G.C. Dodd, 1988: Homogeneous nucleation rate for highly supercooled cirrus cloud droplets. *J. Atmos. Sci.*, **45**, 1357-1369.

Sassen, K. and G.C. Dodd, 1989: Haze particle nucleation simulations in cirrus clouds, and applications or numerical and lidar studies. *J. Atmos. Sci.*, **46**, 3005-3014.

Taborek, P., 1985: Nucleation in emulsified supercooled water. *Phys. Rev.*, **32**, 5902-5906.

Tripoli, G.J. and W.R. Cotton, 1982: The Colorado State University Three-Dimensional Cloud/Mesoscale Model-1982. Part I: General theoretical framework and sensitivity experiments. *J. Rech. Atmos.*, **16**, 186-219.

Weast, R.C., Editor, 1981: *CRC Handbook of Chemistry and Physics: 61st Edition*. CRC Press, Inc., Boca Raton, Florida.

Precipitation development in the 30-31 March 1988 Front Range snowstorm: Model simulations including detailed microphysics

Douglas A. Wesley and Roger A. Pielke
Colorado State University, Dept. of Atmospheric Science, Fort Collins, CO 80523

1. Introduction

A series of mesoscale model simulations designed to assess the role of topography in the production of snowfall during the evolution of a deep, cyclonic storm system which crossed the southern Rockies during late March 1988 are presented. Wesley and Pielke (1990) investigated this upslope event in detail from an observational standpoint. In the present modeling study, the CSU RAMS (Regional Atmospheric Modeling System) nonhydrostatic cloud model is utilized to further examine precipitation development in this storm. It includes a standard NMC-grid initialization, including radiosonde and surface observations over a domain extending from eastern Missouri to the central Pacific Ocean, and from central Mexico to southern Canada (see Fig. 1). The inner grid of the two-way, telescopic nest is centered over north-central Colorado (see Fig. 2). The dynamical and microphysical model output is extensively compared to dense surface, radar and sounding observations along the northern Colorado Front Range for this storm. The role of direct orographic forcing is assessed in the simulations.

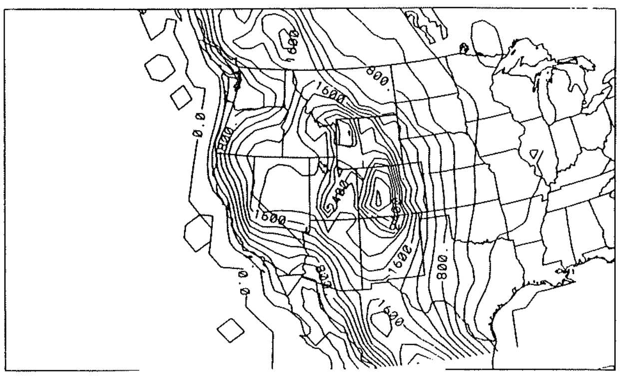

Figure 1: Model topography for grid 1.

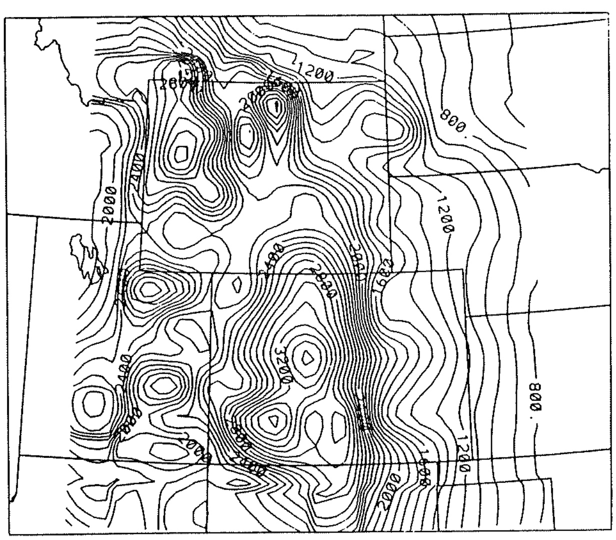

Figure 2: Model topography for grid 2.

The development and evolution of blocking-induced convergence over and just east of the foothills, and its influence on upward motion and snow production, are examined. This has been documented previous storms (Dunn, 1987 and Schultz *et.al.*, 1985). As shown in the observational study (Wesley and Pielke 1990), portions of a low-level layer of strong easterly flow were unable to completely rise over the barrier in this storm due to stable low-level lapse rates. Mesoscale high pressure developed in the low levels over and just east of the foothills. As the upstream easterly flow strengthened, overrunning occured since the lowest layers near the foothills were essentially stagnant. This coexisted with larger-scale deep ascent as the cyclone approached the region. The local convergence led to enhanced upward motion in a moisture-rich environment, concentrating snowfall in a north-south band over and just east of the foothills. An extreme case of this type of blocked structure is the barrier jet (Wesley, 1991).

The aims of this investigation are to successfully simulate the precipitation development, and subsequently analyze the relative importance of the nature of the upstream low-level winds to the resulting vertical motion field. The minimum horizontal and vertical resolution of the model required to capture this blocking-induced flow scenario are also discussed.

2. 30-31 March 1988 simulations

A three-dimensional simulation was produced using RAMS (Note: for a more detailed model description, see Walko and Tremback, 1991). This model has been utilized previously in studies of Colorado winter storms (Peterson *et.al.*, 1991; Cotton *et.al.*, 1986). Model equations include short- and long-wave radiation parameterizations, and the production of cloud and rain water, graupel, pristine crystals, aggregates and frozen precipitation. An improved ice nucleation scheme, introduced by Meyers *et.al.* (1991) was included in the prediction of pristine ice crystal concentrations. This scheme provides more realistic concentrations, based on laboratory measurements, than the Marshall-Palmer distributions utilized in previous model versions. The model topography, calculated using a silhouette average (Bossert, 1990), retains the major terrain features including the effective barrier height at the Continental Divide and shallow east-west oriented ridges in eastern Colorado. Elevations for the coarse and fine grids (horizontal grid spacing 110 and 22 km) are shown in Figs. 1 and 2, respectively.

Table 1 presents the basic options employed in the mesoscale model simulation for the March 30-31 1988 storm. The model was initialized with an objective analysis of NMC grids, radiosondes and surface observations over the coarse grid domain for 1200 GMT, 30 March 1988 (see Fig. 3). At this time, the storm was well to the west of the Front Range, and intensifying. Precipitation

Table 1

Model category	Option
initialization	NMC grids + sfc. obs. + radiosondes, 1200 GMT 30 March 1988
dimensions	3-dimensional lat-lon
top boundary condition	Rayleigh friction
height of model top	16 km
lateral boundary conditions	radiative, with Davies nudging to analysis files
thermodynamics	full microphysics
radiation	longwave and shortwave parameterizations
horizontal grid, spacing, size	coarse grid: 110 km, fine grid: 22 km, approx. 35 and 55 grid points, resp.
vertical grid, spacing	1 grid, 10 m near surface stretched to 500 m above 10 km MSL, 37 levels
topography	silhouette-averaged from 30 sec data
time step	coarse grid: 90 sec, fine grid: 18 sec

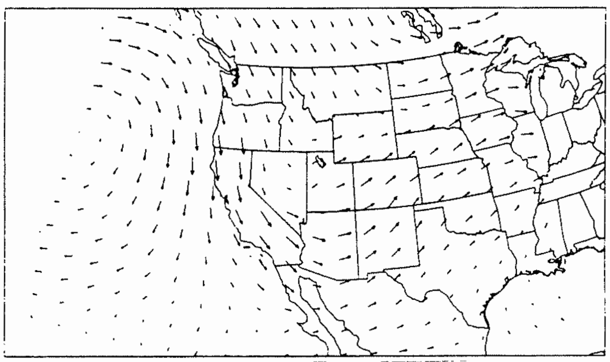

Figure 3: Model initial field at 1200 GMT 30 March 1988. Vectors indicate wind direction and speed on the 2.65 km terrain-following model surface.

had not yet begun over eastern Colorado. The model was run with only the coarse grid for four hours; the second grid was added at that time. Until 1800 GMT only cloud water was included in the model equations. The simulation after this time included the full parameterized microphysics.

A cross-section of the predicted w field at 18 hours of simulation (or at 0600 GMT 31 March) is shown in Figure 4. The latitude of this x-z slice is 40.6°. Strong easterly flow over the eastern slopes is generating 10 to 40 cm/s updrafts. Even above the easterly flow, deep upward motion is apparent over the same area, apparently due to convective processes. Figs. 5-7 present model-predicted precipitation fields at 18 hours of simulation (12 hours after the parameterized microphysics were initiated in the model). As shown, significant aggregate precipitation (maximum 5.4 mm) is accumulating over the foothills of northeastern Colorado and southeastern Wyoming. Graupel and rain are predicted in lesser amounts mainly just east of the foothills, from southeastern Wyoming to the Palmer Divide. Maximum total precipitation accumulation over the 12 hour period occurs over the foothills near the Colorado/Wyoming border, and totals 12 mm.

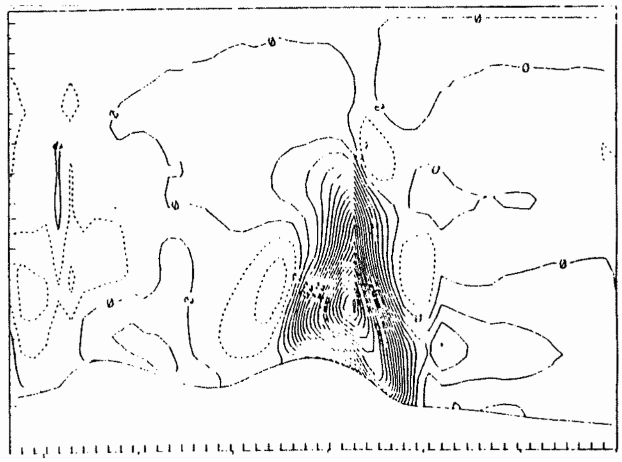

Figure 4: Model-predicted vertical motion, m/s, for grid 2, at 0600 GMT 31 March 1988.

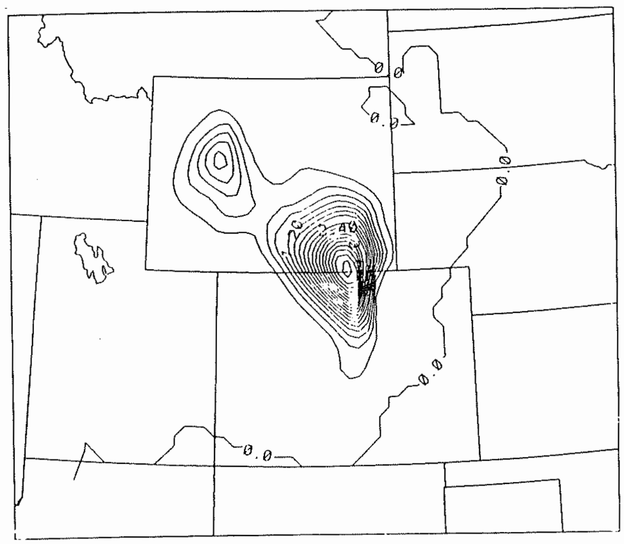

Figure 5: Model-predicted accumulated aggregate precipitation, mm, for grid 2, at 0600 GMT 31 March 1988 (after 12 hours microphysics).

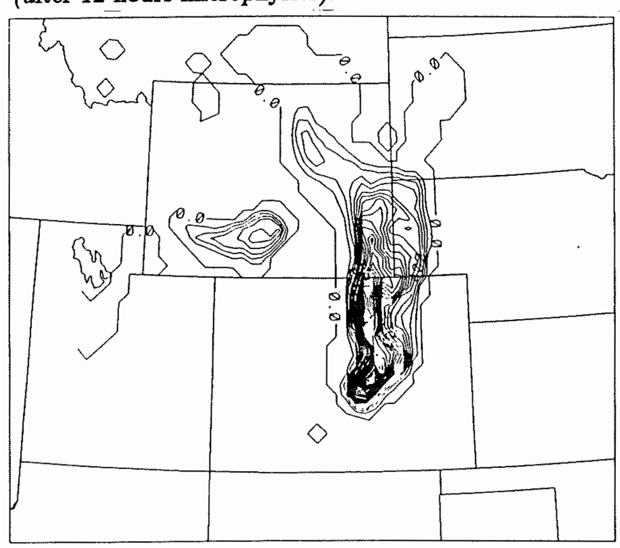

Figure 6: Model-predicted accumulated graupel precipitation, mm, for grid 2, at 0600 GMT 31 March 1988.

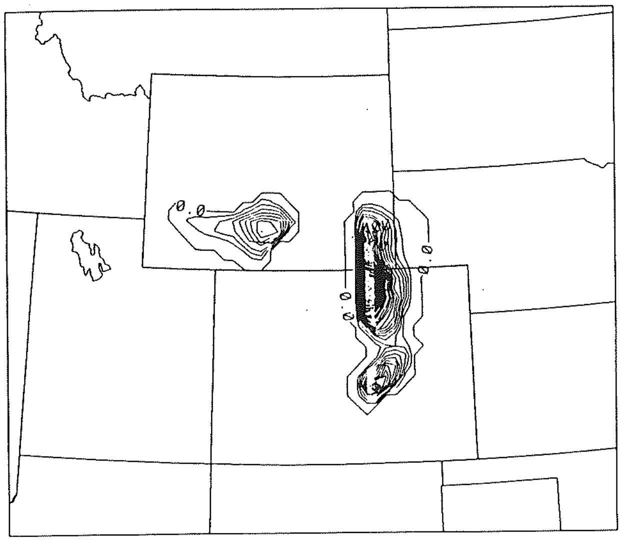

Figure 7: Model-predicted accumulated liquid precipitation, mm, for grid 2, at 0600 GMT 31 March 1988.

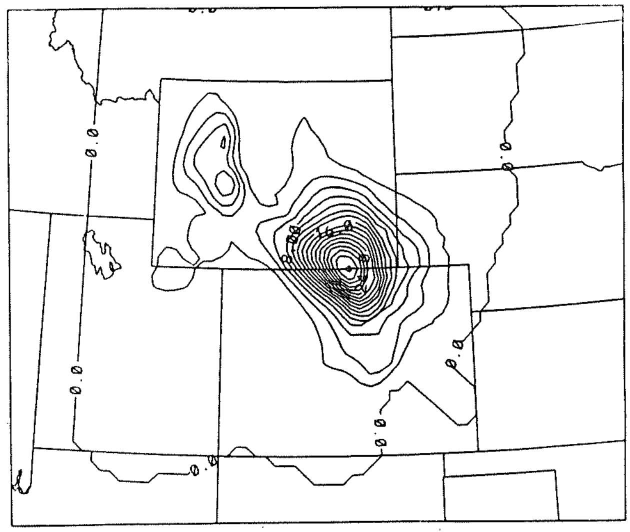

Figure 8: Model-predicted total precipitation, at 1200 GMT 31 March 1988.

At the termination of the simulation, 1200 GMT 31 March 1988, the accumulated precipitation distribution (Fig. 8) indicates a maximum of 34 mm near the WY/CO border just northwest of FCL. Most of this precipitation fell in the form of aggregates, in agreement with observations in the foothills. Note the persistence of the eastward extension of precipitation onto the plains in northeastern CO and southeastern WY and the strong east-west gradient in precipitation over the foothills. This compares well with the observed snowfall gradient with the exception of significant underprediction between the I-25 corridor and the foothills. Examination of the u-component at this time (Fig. 9) reveals that the maximum easterly component has propagated down the slope over the last several hours of simulation, and that west of the easternmost foothills, the upslope is actually decelerating, and thus creating strong convergence over the foothills. Also contributing to this convergence is the north-south component of low-level winds. The result is deep tropospheric upward motion over the area, as shown in Fig. 10, portions of which are contributing to the eastward extent of precipitation. The upward portion of the terrain-induced gravity wave over the lee side of the barrier is also contributing to the upper section of this updraft.

A significant fraction of the precipitation east of the foothills continued to fall as graupel and rain in the model (Fig. 11), as 50 m temperatures in this region remained above freezing. Maximum accumulated quantities, located just east of the foothills by about 50 km, were 6.4 mm and 15.3 mm for graupel and rain, respectively.

These precipitation fields agree well with observed amounts over the foothills (see Wesley and Pielke, 1990), but underestimate snow accumulation east of that region. The model winds in the mid- and upper-levels also compare well to measurements, but there are serious problems in the lowest 2 km of the atmosphere over northeastern Colorado. The model has failed to predict the observed southward propagation and intensification of the Dakotas anticyclone (and the associated northeasterly surface flow over the Front Range). As a result, surface tempera-

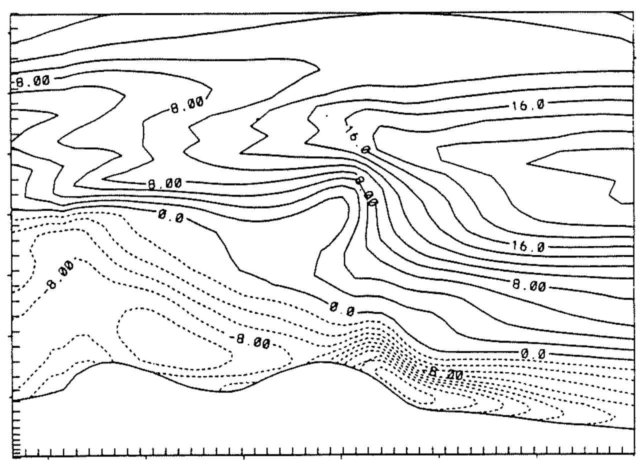

Figure 9: Model u-component (m/s) for an x-z cros section at 40.6 latitude, for 1200 GMT 31 March 1988.

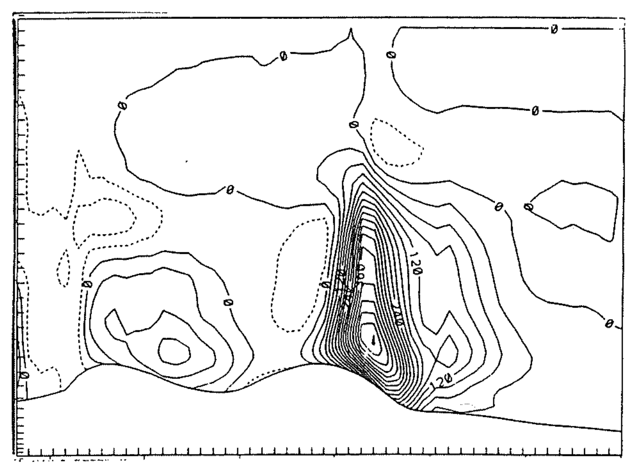

Figure 10: As in Fig. 9, w-component (mm/s).

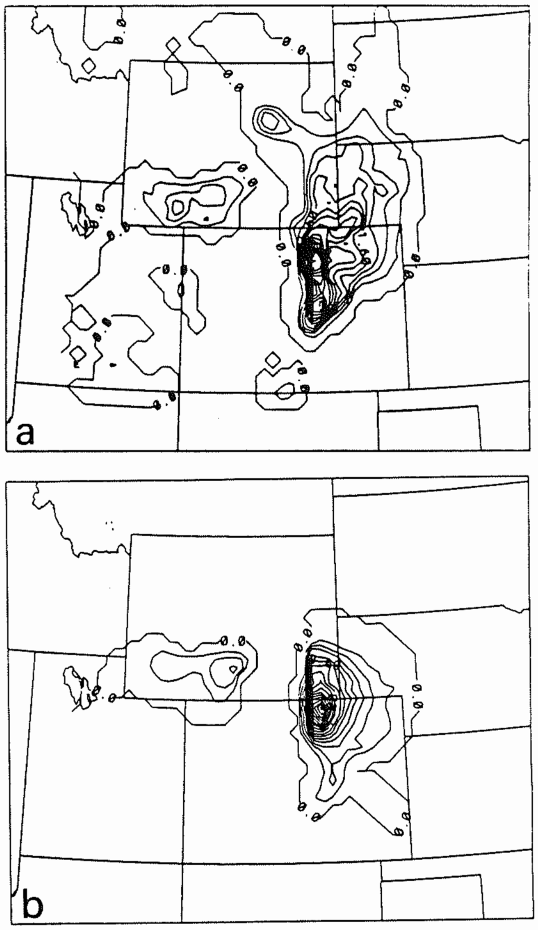

Figure 11: As in Fig. 8, (a) graupel, and (b) rain.

tures are much too warm over the Colorado northeastern plains, and lapse rates do not exhibit the low-level stability observed near the foothills. Though orographically-induced vertical motions appear to be handled well, low-level blocking is underpredicted. This shortcoming also leads to incorrect prediction of dominant precipitation phase (ie. liquid vs. solid) over the plains.

3. Discussion

Large orographic- and synoptically-forced precipitation amounts are successfully predicted in this case by the three-dimensional RAMS; the model precipitation fields for this storm compare well with observations of snowfall over the foothills. However, it does not correctly simulate the low-level blocked structure observed along the Front Range. A subjective summary of the performance of the NGM and RAMS for 24-hour predictions of this storm is given Table 2. As shown, the main advantage of the RAMS simulations is the orographic effect on precipitation. We are currently addressing the problems with these simulations; they appear to originate in the objective analyses of NMC, radiosonde and surface observations utilized by the model at 0, 12 and 24 hours of simulation. The model is very sensitive to both the initial fields and the objective analysis at the model boundaries at intermediate simulation times. We are currently rerunning RAMS with improved input at these times. Results of simulations which included a third grid, which has a horizontal spacing of 5.5 km, are in the making. Preliminary results indicate that the 2-grid structure reported on in this paper does not have sufficient resolution to capture the small-scale details of the blocked flow.

Table 2

Observed Feature	Overall Degree of Accuracy in Simulations	
	NGM	RAMS
Topography	moderate	high
Initial + 12 hr fields	high	moderate
Large-scale general features	high	moderate
Strength/location of cutoff	high	moderate
Development of upslope flow	high	high
Low-level cold advection	moderate	low
Orographic effect on precip.	low	high
Blocking-induced convergence	low	moderate
Precipitation type	N/A	moderate

References

Bossert, J.E., 1990: Regional-scale flows in complex terrain: an observational and numerical investigation. Paper no. 472, Department of Atmospheric Science, Colorado State University, Fort Collins, CO 80523, 254 pp.

Cotton, W.R., G.J. Tripoli, R.M. Rauber and E.A. Mulvihill, 1986: Numerical simulation of the effects of varying ice crystal nucleation rates and aggregation processes on orographic snowfall. *J. Clim. Appl. Meteor.*, **25**, 1658-1680.

Dunn, L., 1987: Cold air damming by the Front Range of the Colorado Rockies and its relationship to locally heavy snows. *Wea. Forecasting*, **2**, 177-189.

Meyers, M.P., P.J. DeMott, 1991: New primary ice nucleation parameterizations in an explicit cloud model. *J. Appl. Meteor.*, **31**, In Press.

Peterson, T.C., L.O. Grant, W.R. Cotton and D.C. Rogers, 1991: The effect of decoupled low-level flow on winter orographic clouds and precipitation in the Yampa River valley. *J. Appl. Meteor.*, **30**, 368-386.

Schultz, P., M.C. McCoy, R.W. McGowan, and J.S. Wakefield, 1985: The first experiment in forecasting cool-season weather with the PROFS system. *NOAA Tech. Memo.*, ERL ESG-16, April 1985.

Walko, R.L. and C.J. Tremback, 1991: *The RAMS Version 2c, User's Guide.* ASTeR Inc., PO Box 466, Fort Collins, CO 80521.

Wesley, D.A., 1991: An investigation of the effects of topography on Colorado Front Range winter storms. Paper No. 489, Department of Atmospheric Science, CSU, 197 pp.

Wesley, D.A. and R.A. Pielke, 1990: Observations of blocking-induced convergence zones and effects on precipitation in complex terrain. *Atmos. Res.*, **25**, 235-276.

PRECIPITATION MODIFICATION OF SURFACE PRESSURE GRADIENTS

James Toth, John Marwitz and Yulan Wei
University of Wyoming, Laramie 82071

1. INTRODUCTION

A cutoff low which developed in the Four Corners area of the Southwestern United States during the period 5–7 March 1990 produced very heavy rain and snow along the Front Range of northeast Colorado in the Winter Icing and Storms Project (WISP) area. A narrow barrier jet with northerly winds behind a mesoscale front developed concurrently with the heavy precipitation. Marwitz and Toth (1992) have hypothesized that the front resulted from the diabatic process of melting (Wexler et al, 1954). Previous studies of the Front Range area (e. g., Dunn, 1987) have noted that the development of this mesoscale front contributes to a narrow band of heavy precipitation due to enhanced upslope lifting. This paper emphasizes how the diabatic cooling by the melting precipitation provided dynamic support for the northerly barrier jet.

2. ANALYSES

In addition to the normal surface data, 40 mesonet stations in the WISP area provided data across northeast Colorado. The mesonet winds and temperatures on 6 March at 0600Z and 1500Z are shown in Fig. 1. Initially only a narrow northerly barrier jet developed. Cold air advection did not cause this jet; in fact at 06/0600Z there was warm air advection (WAA) along the northern border of Colorado (CO). It was not until 06/1500Z that a broad area of north–northeasterly winds and cold air advection developed in the area.

The mesoscale surface horizontal pressure gradients were analyzed based on a technique developed by Weaver and Toth (1990). The results of this analysis for northern CO, southern Wyoming (WY) and western Nebraska (NB) are shown in Fig. 2. The evolution of the surface pressure field was consistent with the winds. Viewing the earliest time in Fig. 2 and moving from west to east we can see that there are weak pressure gradients over the highest terrain, a narrow zone of north–northeasterly geostrophic winds just east of the Front Range, and a broad area of southeasterly geostrophic winds over eastern CO. A narrow inverted trough lies roughly along the location of the mesoscale fronts in Fig. 1. Shortly before 06/1500Z a cold surge developed in the northeast corner of the mesonetwork. This cold air spread rapidly southward, and the narrow trough near DEN and FCL was replaced by a broad trough covering all of eastern CO by 06/1800Z.

3. GENERATION OF THE NARROW BARRIER JET

At 06/0600Z there was a cutoff pocket of cold air near FCL (Fig. 2). This cold air was located southeast of a region of WAA (Fig. 1). There had been several hours of heavy precipitation near FCL. Therefore, we hypothesize that the cold air was generated by the diabatic process of melting. The dynamic effects of this cold air are enhanced by terrain. Near FCL the terrain height increases by approximately 1 km in a horizontal distance of 50 km. A cooling of 4 °C, combined with this terrain slope, results in the tight packing of adjusted altimeter setting contours that is analyzed in Fig. 2. This analyzed gradient (0.05 in. Hg / 50 km) corresponds to a north–northeasterly geostrophic wind of 27 m s^{-1}. Since this gradient persisted for over ten hours, it provided a mechanism for developing and supporting the narrow barrier jet. The Palmer Divide south of DEN appeared to block and pool the cold air behind the mesoscale front. Consequently, the mesoscale front south of DEN progressed slowly eastward into an area of less steep terrain, while the portion north of DEN remained stationary.

The Colorado State University Regional Atmospheric Modeling System (RAMS) was used to test the effects of melting precipitation. A two–dimensional simulation was initialized with a southeasterly surface upslope wind as observed over eastern CO. The east–west cross–section in Fig. 3 shows that after six hours surface westerlies developed between –110 km and –100 km. Between –100 km and –75 km the winds were northwesterly. Between –75 km and –60 km the winds were light. The east–west component of the surface horizontal pressure gradient force at –105 km was approximately two–thirds of the gradient analyzed near FCL at 0600 Z in Fig. 2. An identical simulation but without ice and snow microphysics (no melting) produced a much weaker pressure gradient and did not develop surface westerly winds.

Acknowledgement: The authors were funded under NSF grant ATM–9014763.

4. REFERENCES

Dunn, L., 1987: Cold air damming by the Front Range of the Colorado Rockies and its relationship to locally heavy snows. *Wea. and Forecasting,* **2,** 177–189.

Marwitz, J., and J. Toth, 1992: The Denver blizzard of 1990, Part I: Surface and sounding data. Submitted to Monthly Weather Review.

Weaver, J., and J. Toth, 1990: The use of satellite imagery and surface pressure gradient analysis modified for sloping terrain to analyze the mesoscale events preceding the severe hailstorms of 2 August 1986. *Wea. and Forecasting,* **5,** 279–298.

Wexler, R., R. Reed and J. Honig, 1954: Atmospheric cooling by melting snow. *Bull. Amer. Meteor. Soc.,* **35,** 48–51.

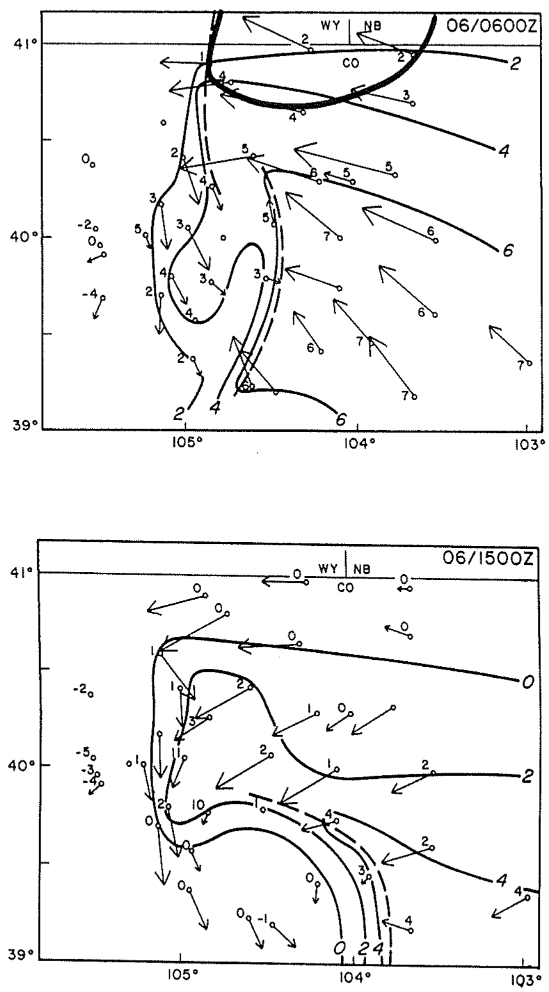

Fig. 1. Mesonet surface data for the times indicated. The wind vector is scaled to 20 m s^{-1} = 1° of longitude and the number beside each site is T °C (NOTE: the heavy, wet snow caused some erroneous temperature data). Within the broad line is WAA > 1 C h^{-1}, solid thin lines are isotherms, and dashed lines are mesoscale fronts.

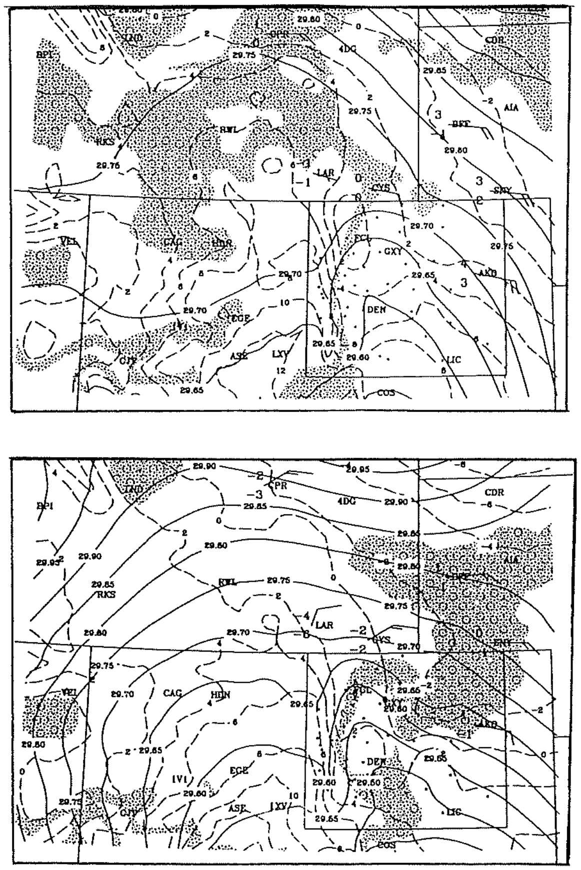

Fig. 2. Surface pressure and potential temperature analysis for the same times as in Fig. 1. Solid contours are altimeter setting (interval 0.05 in. Hg) adjusted to 1600 m. Dashed contours are temperature (interval 2 °C) adjusted by the difference (Station elevation –1600 m) multiplied by 9.8 °C m^{-1}. Box indicates area shown in Fig. 1; small dots are locations of mesonet stations. Shading indicates surface temperature 0 ± 1 °C. Temperature, dewpoint, and wind barbs (full barb = 5 m s^{-1}) plotted at selected stations north and east of the surface mesonet.

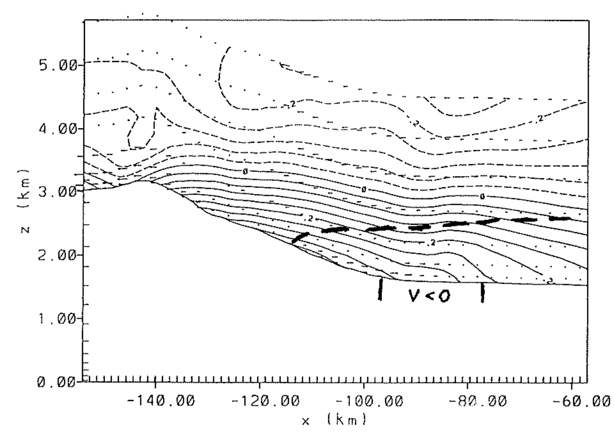

Fig. 3. Model generated perturbation Exner function after six hours. Heavy dashed line is the 0 °C isotherm.

MODELING ICE PHYSICAL PROCESSES OVER A MOUNTAIN BARRIER

WILLIAM D. HALL
National Center for Atmospheric Research [1]
Boulder, Colorado 80307

The formation of ice phase precipitation in wintertime clouds formed by flow over mountain barriers has continued to have considerable interest by the weather modification community. These wintertime clouds are known to produce significant quantities of supercooled liquid water which may be suitable for precipitation enhancement, Heggli and Rauber, 1988. It is critically important to understand the relative roles and time scales of the physical processes of precipitation formation in order to assess any weather modification potential. The present study uses the three dimensional small scale dynamical model of Clark with parameterized warm rain and ice physics to numerically investigate a shallow orographic cloud system formed by forced ascent of moist air over the Sierra Nevada Mountains that was observed during the 1986/1987 Sierra Cooperative Pilot Project (SCPP).

The present study presents preliminary results of 2 simulations of the morning of 18 December 1986 that correspond to a case study that has been reported by Deshler et. al. 1990, (DRH). On this day a weak split-front passed through the area with seeding taking place between the passage of an upper level cold surge/humidity front and a surface kata-cold front. The topography used in the model is shown in Figure 1. The domain of the model extended 300 Km in the north-south and east-west directions and was centered over Blue Canyon Weather Station. The horizontal grid spacing was 5 Km and the vertical grid employed a stretched grid ranging from 200 m at the surface to 500 m at 14 Km and extending to 24 km with a constant grind spacing of 500 m.

The crosses (X) mark the positions of the surface weather stations at Sacramento, Sheridan, and Blue Canyon. The long line A-B indicate where the cross-section plots that will follow are located. The short line just south of Blue Canyon indicates the initial position of the seeding material.

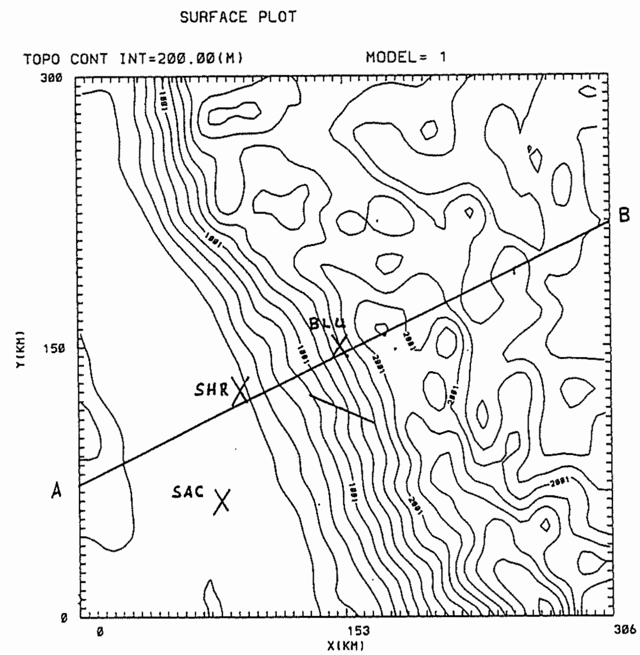

Figure 1.

The model was initialized by using the sounding data from Sheridan at 18 UZT. Two numerical experiments were conducted, one case without and one where seeding was activated simulating silver iodide seeding.

No seed case:

The parameterized ice microphysics applied in the model follow closely the works of Koenig and Murray (1976), (KM). The background nuclei are assumed to be activated as a function of temperature,

$$N = a10^{(max(To-T,+20)/b)}$$

where:

$a = 4.642\ 10^{-4}$ number of nuclei/(cm$^{3)}$

and

$b = 12°K$

$To = 273.15°K$

[1] The National Center for Atmospheric Research is sponsored by the National Science Foundation.

This activity prescription was used by KM and corresponds to ice-particle generation in accordance with observations suggesting the activity of a process strongly augmenting ice production at relatively warm temperatures (multiplication, splintering, or perhaps contact nucleation processes) similar to observations of Mossop et al. (1970).

Seeded Case:

In addition to the background ice nucleation, a line source 40 Km long at the 3 Km msl level was released 2 hours into the integration. The amount of seeding agent released was .4gm/km with the activity of 10^{13} particles/gm and having an activation time lag of 5 min. No attempt was made to explicitly simulate the specific processes of ice nucleation such as sorption, contact, or immersion nucleation.

All of the following figures are at the same time of 40 min after the seedline was introduced. Figures 2a and 2b show the vertical velocity near 2km (msl) for the nonseeded and seeded cases. The field show a week upward motions over Blue Canyon site and that there is very little dynamical response in the seeded event. Figures 3a,b, 4a,b, and 5a,b show cross-sections that intersect the seeded plume along the line A-B in Fig. 1. These figures are respectively plots of the cloud droplet water mixing ratio, the number concentration of ice particles and the ice mass mixing ratio for the non seeded and seeded case. The ice particle number concentration field indicates a strong seeding signature. In the region of high ice particle number concentrations the cloud droplet mixing ratio has been completely converted to ice particle mass with very little change to the dynamical fields.

Future work will emphasize the upwind airflow and cloud structure along with the precipitation formation and sedimentation characteristics. Model results will be compared with aircraft, radar, and surface precipitation field data taken during both non-seeding and seeding conditions in order to assess the suitability of the microphysical parameterizations used by the model and to assess the potential of precipitation enhancement by cloud seeding. Problems associated with the targeting and timing of the seeded material will also be discussed.

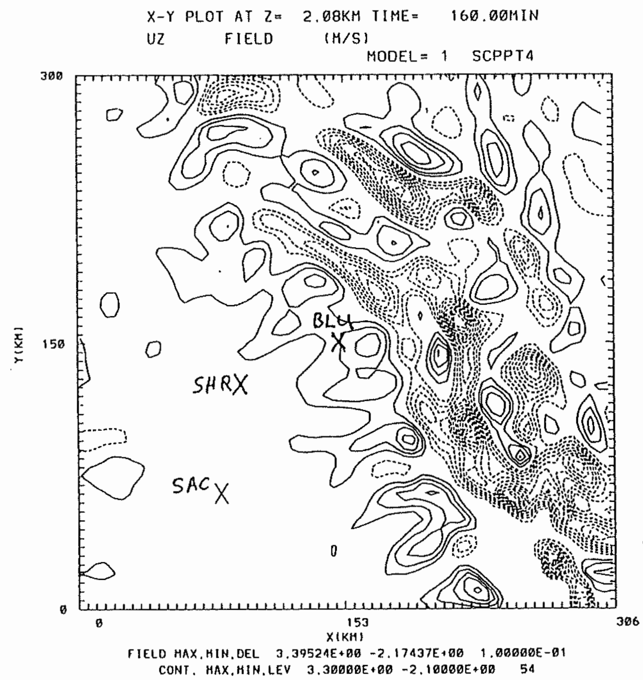

Figure 2a.

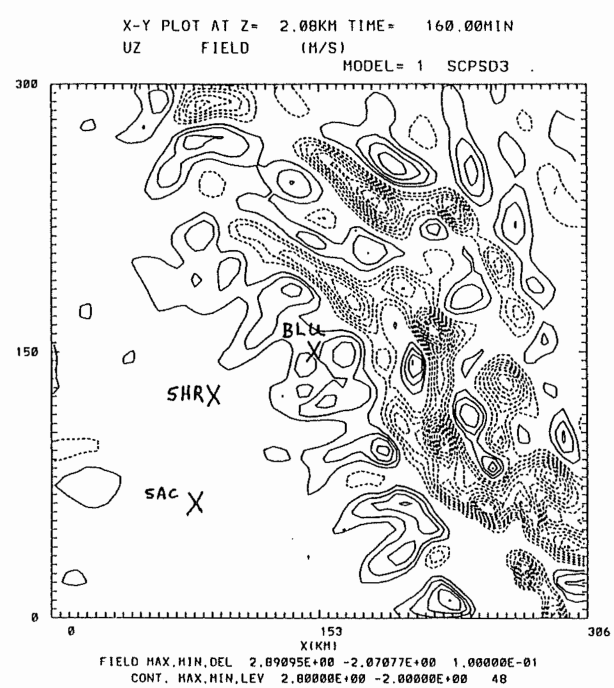

Figure 2b.

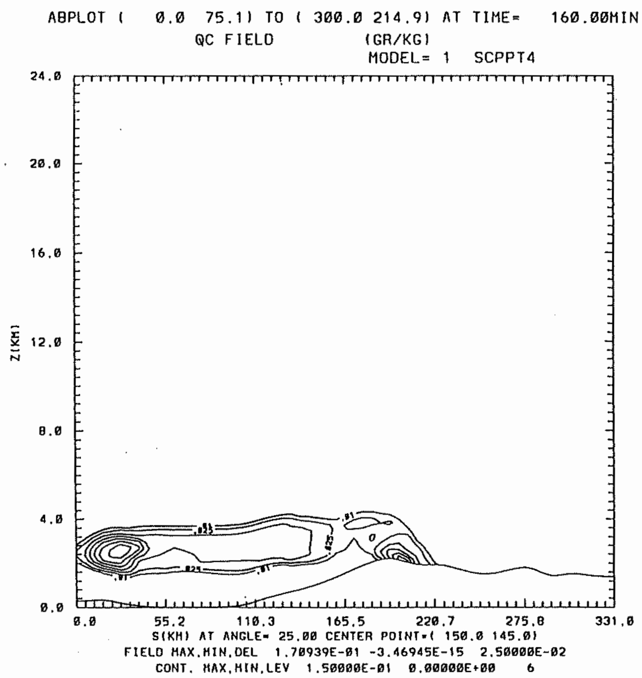

Figure 3a.

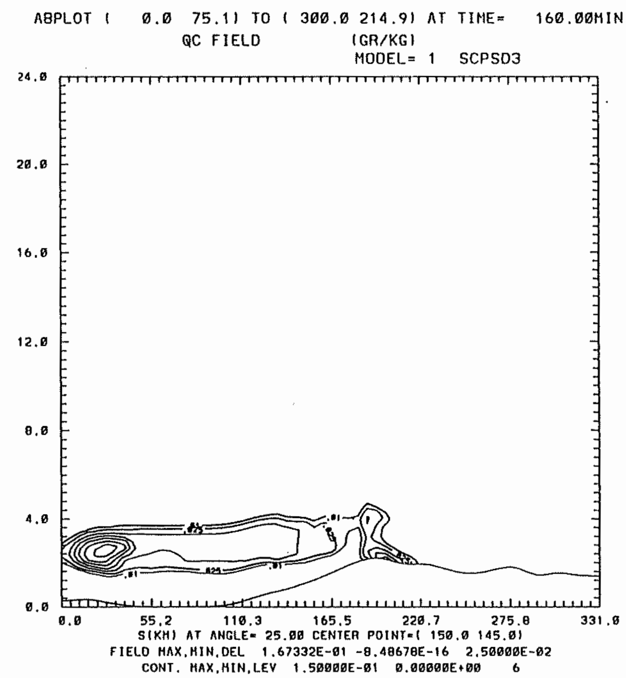

Figure 3b.

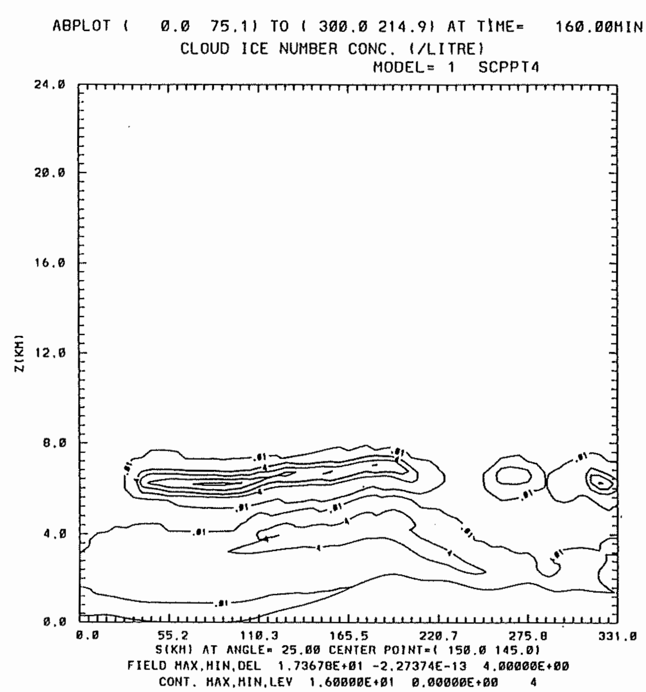

Figure 4a.

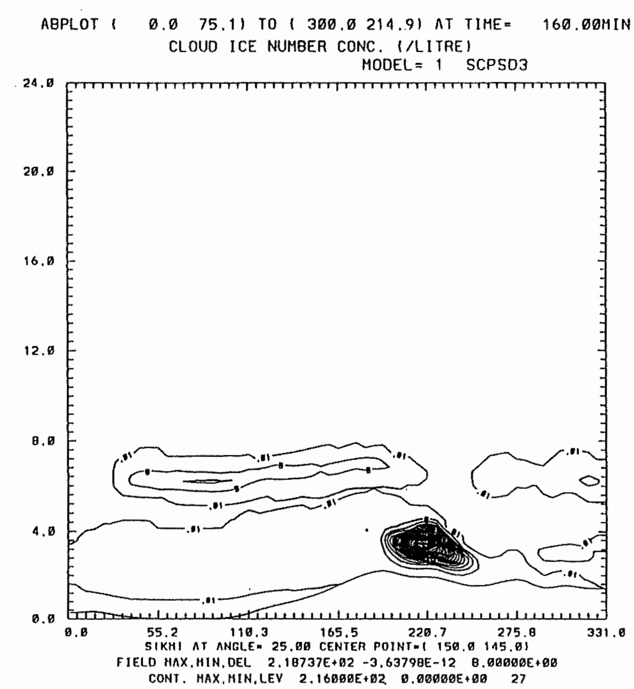

Figure 4b.

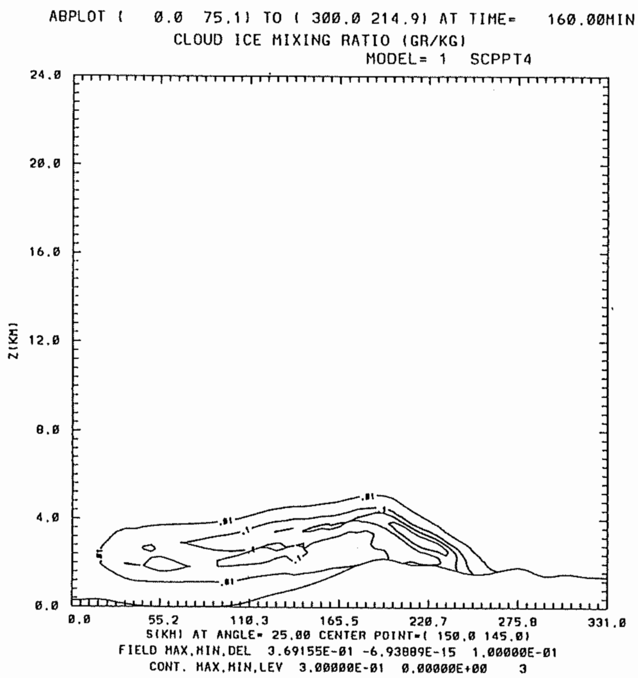

Figure 5a.

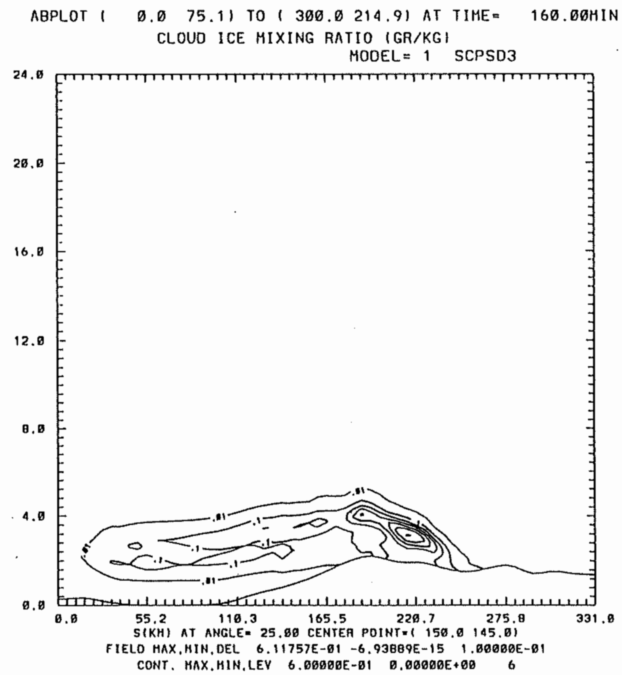

Figure 5b.

REFERENCES

Heggli, M.F., and R.M. Rauber, 1988: The Characteristics and Evolution of Supercooled Water in Wintertime Storms over the Sierra Nevada: A Summary of Microwave Radiometric measurements taken during the Sierra Cooperative Pilot Project. *J. Appl. Met*, **27**, 989-1015.

Deshler, T., D.W. Reynolds and A.W. Huggins, 1990: Physical Response of Winter Orographic Clouds over the Sierra Nevada to Airborne Seeding using Dry Ice or Silver Iodide. *J. Appli. Met*, **29**, 288-330.

Mossop, S.C., A. Ono, and E.R. Wishart, 1970: Ice Particles in Maritime Clouds over Tasmonia. *Quart. J. Roy. Meteor. Soc.*, **96**, 407-508.

A TECHNIQUE TO ESTIMATE CIRRUS CLOUD PARTICLE SIZES AND CONCENTRATIONS FROM IR RADIOMETER AND RADAR MEASUREMENTS

S.Y. Matrosov[1], T. Uttal[2], J.B. Snider[2], and R.A. Kropfli[2]

[1] Cooperative Institute for Research in Environmental Sciences
University of Colorado/NOAA/WPL, Boulder, CO, USA 80309
[2] NOAA/ERL/Wave Propagation Laboratory, Boulder, CO, USA 80303

1. INTRODUCTION

It is recognized that clouds are an important part of the climatic system. Cirrus clouds composed predominantly of ice particles are the most temporally persistent and spatially extensive cloud type with a high frequency of occurrence. To parameterize cirrus clouds in the climate general circulation models one needs to have information on their microstructure. Effective particle sizes and concentrations are among the most important parameters characterizing cloud microstructure.

Cirrus clouds are often optically semi-transparent at infrared "window" wavelengths (10 - 12 μm) and their thermal radiation depends not only on the temperature distribution within the cloud but also on details of the microstructure. Knowing the temperature profile, we can obtain estimations of cloud optical thickness τ_0 from ground-based infrared measurements of downwelling radiation. Values of τ_0 depend on both particle sizes and concentrations, and it is impossible to distinguish between effects of these two factors from only radiometric measurements.

Radar reflectivities also depend on scatterer size and scatterer concentration, however, in a different way that infrared brightness temperatures (i.e. optical thicknesses τ_0). Therefore, by combining the radar and infrared radiometer measurements it is possible to obtain closure and simultaneously solve two equations, for two unknowns, the particle size and concentration.

2. THEORY

a. *The Two Stream Model*

Radiative transfer within clouds is a complex process involving absorption, emission and multiple scattering of radiation. A simple and commonly used approach to describe this rather complicated process is the two-stream approximation which is usually used for plane-parallel models. Different versions of this approximation assume different angular distribution of the radiation intensity inside scattering media. The general solution for upward $F^{\uparrow}$ and downward $F^{\downarrow}$ fluxes are (Toon et al. 1989):

$$F^{\uparrow}(\tau) = k_1\exp(\Lambda\tau) + \Gamma k_2\exp(-\Lambda\tau) + C^{\uparrow}(\tau)$$
$$F^{\downarrow}(\tau) = \Gamma k_1\exp(\Lambda\tau) + k_2\exp(-\Lambda\tau) + C^{\downarrow}(\tau) \quad (1)$$

where $C^{\uparrow}(\tau)$ and $C^{\downarrow}(\tau)$ describe the thermal source of radiation, the coefficients k_1 and k_2 are determined by boundary conditions, and coefficients Λ and Γ can be given in terms of γ_1 and γ_2:

$$\Lambda = (\gamma_1^2 - \gamma_2^2)^{1/2}$$
$$\Gamma = \gamma_2/(\gamma_1 + \Lambda). \quad (2)$$

γ_1 and γ_2 depend on a version of the two-stream approximation. For the quadrature version chosen here,

$$\gamma_1 = 0.866[2 - \omega(1 + g)]$$
$$\gamma_2 = 0.866\omega(1 - g) \quad (3)$$

where ω and g are the single scattering albedo and the scattering asymmetry factor, respectively.

The radiation intensities $[I^{\uparrow(\downarrow)}(\tau)]$ can be obtained from the fluxes:

$$I^{\uparrow(\downarrow)}(\tau) = (2\pi\mu_0)^{-1}F^{\uparrow(\downarrow)}(\tau) \quad (4)$$

where μ_0 is the mean value of the zenith angle cosine ($\mu_0 = 0.577$). The thermal source terms for a non-isothermal cloud are (Toon et al. 1989):

$$C^{\uparrow}(\tau) = 2\pi\mu_0\{B_0 + B_1[\tau + 1/(\gamma_1 + \gamma_2)]\}$$
$$C^{\downarrow}(\tau) = 2\pi\mu_0\{B_0 + B_1[\tau - 1/(\gamma_1 + \gamma_2)]\} \quad (5)$$

where $B_0 = B(T_t)$, $B_1 = [B(T_b) - B(T_t)]/\tau_0$, $B(\ldots)$ is the Planck function, and T_t and T_b are the cloud top and bottom temperatures. The total optical thickness of a vertically homogeneous cloud τ_0 counting from the top relates to its geometrical thickness h_c by means of the extinction coefficient, α_e : $\tau_0 = \alpha_e h_c$.

Boundary conditions for finding coefficients k_1 and k_2 assume that the atmosphere above the cloud top does not emit significant amounts of thermal radiation and the upwelling flux at the cloud bottom is due to the emission of the surface and the intervening water vapor continuum:

$$F^{\downarrow}(0) = 0$$
$$F^{\uparrow}(\tau_0) = 2\pi\mu_0[B(T_s)P_a + I_a^{\uparrow}] \quad (6)$$

where T_s and P_a are the surface temperature and the atmospheric transmittance, and $I_a^{\uparrow}$ is the atmospheric radiation due to the water vapor.

Equations (1)-(5) with boundary conditions (6) allow calculations of the thermal radiation intensities $I^{\uparrow(\downarrow)}(\tau)$ within the cloud if we know the temperature profile, cloud optical thickness τ_0, water vapor amount and scattering parameters ω and g. Infrared radiometers measure brightness temperatures of thermal radiation. The brightness temperature at the cloud bottom $T_{bc}^{\downarrow}$ level relates to the respective intensity by means of the Planck function:

$$I^{\downarrow}(\tau_0) = B(T_{bc}^{\downarrow}) \quad (7)$$

The ground-level thermal radiation intensity is

$$I_g^{\downarrow} = I^{\downarrow}(\tau_0)P_a + I_a^{\downarrow}. \quad (8)$$

It can be shown that downwelling and upwelling atmospheric radiation intensities close to each other and

$$I_a^{\uparrow} \approx I_a^{\downarrow} \approx B(T^*)\,(1 - P_a) \qquad (9)$$

where T^* is the effective temperature of the atmosphere which is close to the thermodynamic temperature at an altitude of about 1.1 - 1.4 km. More precise estimations of T^* can be made for particular vertical profiles of temperature and water vapor.

We used the described two-stream model to calculate brightness temperatures of downwelling radiation for several observed cirrus clouds. Theoretical and observed values of downwelling brightness temperatures compared favorably.

b. Microphysical and Measurable Parameters

Cloud particles were modeled as solid ice spheres. The size distribution $N(D)$ was assumed to be the gamma function of the first order because of this function satisfactorily describes experimental data (Kosarev and Mazin 1989)

$$N(D) = N_0 \exp(-4.67D/D_m) \qquad (10)$$

where D_m is the median diameter.

Calculations of extinction and absorption efficiencies of ice spheres at the "window" wavelengths show that beginning from approximately $D \approx 20$ µm these efficiencies approach 2 and 1 respectively. Similarly, the asymmetry factor approaches 1 which shows the dominant role of forward scattering. This justifies the use of the Mie theory for describing the radiative transfer because this theory is a reasonable approximation for the forward scattering processes.

Assuming asymptotic value of extinction efficiency we can carry out integration with respect to size distribution (10) and get the asymptotic value of the extinction coefficient

$$\alpha_e^{\circ} \approx 0.02\, N_0 D_m^4 \quad [\mathrm{cm^{-1}}]. \qquad (11)$$

Our calculations show that extinction coefficients obtained from the full Mie theory and those obtained from (11) do not differ significantly. For D_m = 20 µm the difference is about 8%,' and it swiftly diminishes as D_m increases. It means that (11) is a reasonable approximation for the extinction coefficient.

In a similar manner we can obtain simple equations for radar reflectivity Z_i, cloud ice mass content w_i and cirrus particle concentration C

$$Z_i \approx 0.0223\, N_0 D_m^8 \ [\mathrm{cm^3}] \qquad (12a)$$

$$w_i \approx 5090\, N_0 D_m^5 \quad [\mathrm{g/m^3}] \qquad (12b)$$

$$C \approx 0.0458\, N_0 D_m^2 \ [\mathrm{cm^{-3}}] \qquad (12c)$$

where N_0 is in $\mathrm{cm^{-5}}$, D_m is in cm, and the ice density $\rho_i = 0.9$ g/cm³.

3. RETRIEVAL OF CLOUD MICROSTRUCTURE PARAMETERS

a. Model Calculations

Curve 1 in Fig.1 shows how the brightness temperature of the downwelling thermal radiation (λ in the region from 10.0 to 11.4 µm) at a cloud bottom level depends on the optical thickness τ_0 as calculated by the two-stream model. It was assumed that particle median diameter D_m = 40 µm and the temperature and cloud boundary input conditions were taken from averages for a two hour period on October 4, 1989 during the CLARET-I experiment described in (Intrieri et al.,1991).

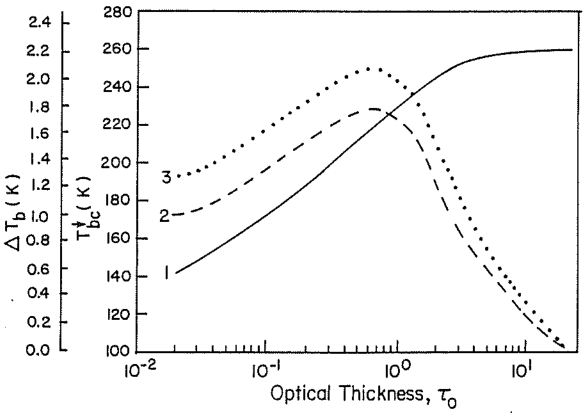

Figure 1. Brightness temperatures $T_{bc}^{\downarrow}$ and brightness temperature differences ΔT_b versus ice cloud optical thickness at different cirrus particle median sizes: (1) $T_{bc}^{\downarrow}(D_m{=}40\mu m)$; (2) $\Delta T_b = T_{bc}^{\downarrow}(D_m{=}40\mu m) - T_{bc}^{\downarrow}(D_m{=}300\mu m)$; (3) $\Delta T_b = T_{bc}^{\downarrow}(D_m{=}40\mu m) - T_{bc}^{\downarrow}(D_m{=}600\mu m)$.

Curves 2 and 3 in Fig.1 show how the brightness temperatures for D_m = 300 µm and D_m = 600 µm differ from those for D_m = 40 µm at the same values of τ_0. One can see that the differences are generally less than 2 K for this considerably large range of median sizes. This indicates that the brightness temperatures are primarily determined by the cloud optical thickness. However, the same value of the optical thickness can be achieved with different combinations of particle concentrations and characteristic sizes.

b. A Technique for Cloud Parameter Estimation

From Fig. 1, one can see that brightness temperatures of the downwelling radiation approach an asymptotic value as optical thickness τ_0 increases. This asymptotic value equals the thermodynamic temperature of the cloud bottom T_b. Exponential behavior of brightness temperatures $T_{bc}^{\downarrow}$ as a function of τ_0 suggests a means to match this function by an equation

$$B(T_{bo}^{\downarrow}) = B(T_b)\,[1 - \exp(-a_0\tau_0)] \qquad (13)$$

where the Planck function B is calculated in the middle of the considered "window" region.

For a predominantly absorbing medium $a_0 \approx 1$. In cirrus clouds, processes of scattering are important and the single scattering albedo is close to 0.5. From the model calculations with wide variations of parameters describing cloud microstructure, we found that for the atmospheric "window" frequencies the best fit for the coefficient a_0 in (13) is 0.7. The differences between the brightness temperatures $T_{bc}^{\downarrow}$ obtained from the two-stream model and those $T_{bo}^{\downarrow}$ obtained from (13) are generally within ±3 K over the wide range of values assigned to microphysical parameters.

Equation (13) is very simple which gives us an opportunity to estimate the optical thickness of a semitransparent ice cloud in a very simple way if the cloud brightness and thermodynamic temperatures are known. If we also know the geometrical cloud thickness, h_c, we can estimate the product $N_0 D_m^4$ from (11) and (13)

$$N_0 D_m^4 \approx -72\, \ln[1 - B(T_{bc}^{\downarrow})/B(T_b)]/h_c. \qquad (14)$$

The brightness temperature at the cloud bottom level, $T_{bc}^{\downarrow}$, can be obtained from the measured brightness temperature at the ground, $T_{bg}^{\downarrow}$, if we know the brightness temperature of the intervening atmosphere, $T_{ba}^{\downarrow}$, and the atmosphere transmittance P_a:

$$B(T_{bc}^{\downarrow}) = [B(T_{bg}^{\downarrow}) - B(T_{ba}^{\downarrow})(1 - P_a)]/P_a. \quad (15)$$

If IR radiometer measurements of the clear sky are not available, $T_{ba}^{\downarrow}$ and P_a can be estimated from data about the water vapor amount in the atmosphere. Infrared measurements are integral in their nature, and retrieved product $N_0 D_m^4$ will refer to the effective average values characterizing the whole cloud layer.

Information about parameters N_0 and D_m can be obtained independently from radar measurements. Equation (12a) provides

$$N_0 D_m^8 \approx 8.1\ Z_e \quad (16)$$

where the usually measured effective reflectivity Z_e relates to the reflectivity with respect to ice Z_i as follows: $Z_i \approx 5.28 Z_e$. Note that h_c in (14) can also be measured with radar.

By combining radar and IR radiometer measurements, we can obtain an estimate of the vertically averaged cirrus particle median size:

$$D_m \approx 1.35\{-\bar{Z}_e h_c/\ln[1 - B(T_{bc}^{\downarrow})/B(T_b)]\}^{1/4} \quad (17)$$

where the overbar means the value of radar reflectivity averaged through the cloud's vertical extent. Knowing D_m, one can obtain an estimate of the mean cirrus particle concentration C from (12c) and (14) or (16).

4. EXPERIMENTAL ESTIMATION OF CIRRUS PARAMETERS

a. Estimation of Sizes and Concentrations

Measurements of cirrus clouds chosen here to illustrate the proposed technique were taken on October 4, 1989 during the CLARET-I experiment. During this experiment simultaneous vertically pointed radar and IR radiometer measurements were performed. Microwave radiometer data were used to identify cases when liquid water was present in clouds.

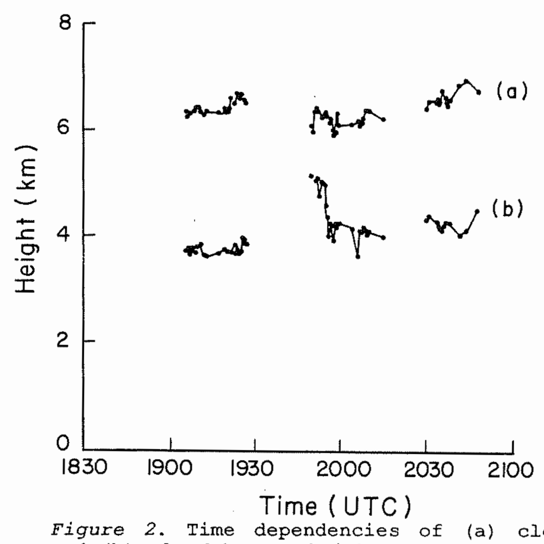

Figure 2. Time dependencies of (a) cloud top, and (b) cloud bottom heights.

Figure 2 shows the geometrical boundaries of the observed cirrus cloud. Data gaps occurred when the radar performed other types of measurements. This case was interesting because the almost pure ice cloud with relatively stable geometrical boundaries produced a broad range of infrared brightness temperatures and radar reflectivities.

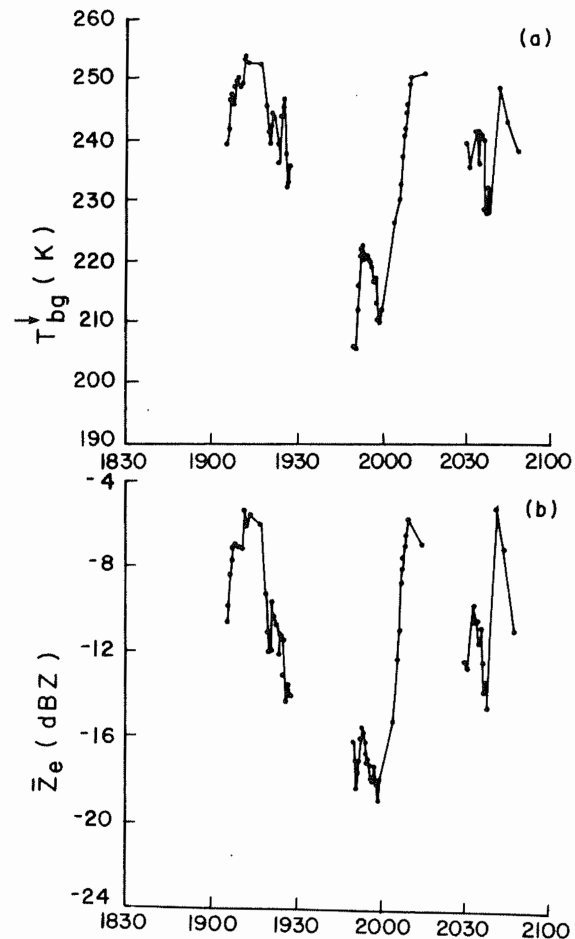

Figure 3. Time dependencies of (a) measured IR brightness temperatures and (b) radar reflectivities averaged through the cloud.

The IR brightness temperatures were measured every 30 seconds by the WPL IR radiometer with a narrow view angle (2°) and a band width from 9.95 µm to 11.43 µm. These temperatures shown in Fig. 3a varied from 206 K to 255 K and were significantly colder than the thermodynamic temperature of the cloud bottom given by the radiosonde data. Knowing the vertical profiles of temperature and humidity we found for the effective atmospheric temperature $T^* \approx 283$ K.

At 1928 UTC the cloud nearly disappeared for a short period of time and then reappeared. From this short clear sky interval we estimated the atmospheric radiation $I_a^{\downarrow}$ and the atmospheric transmittance P_a. The brightness temperature $T_{ba}^{\downarrow}$ corresponding to $I_a^{\downarrow}$ was 199 K and P_a was 0.87. Regions of higher values of the measured brightness temperature (e.g., between 1900 and 1927 UTC) corresponded to relatively dense cloud with optical thickness τ_0 from 0.6 to 1.9. The cloud was more transparent between 1950 and 2006 UTC with corresponding values of τ_0 in the region from 0.1 to 0.6.

Figure 3b shows vertically averaged values of radar reflectivity Z_e measured by the NOAA/WPL X-band radar. These values varied from -19 dBZ to -5 dBZ during two hours of observation. The radar data were also averaged over 30 seconds. The data collected between 1990 and 2100 UTC were filtered to satisfy the criteria that 1) both the radar and the IR radiometer were operating and 2) the integrated liquid water detected by the microwave radiometer did not exceed 0.01 mm. This resulted in 75 data points which represented a pure ice cloud.

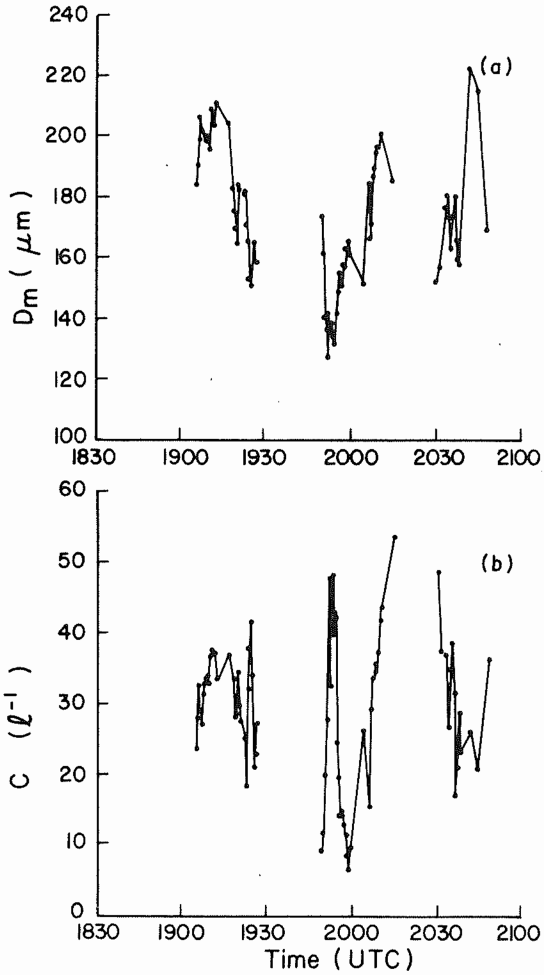

Figure 4. Time dependencies of (a) retrieved particle median size, D_m, and (b) particle concentration, C.

Retrieved values of the cirrus particle median size D_m and their concentration C are shown in Fig. 4. Values of D_m, characterizing the whole vertical extent of the cloud, vary between 125 μm and 225 μm. The mean value of the particle median size during the observational period is about 170 μm. The retrieved sizes are within a reasonable range for cirrus clouds particles (Kosarev and Mazin, 1989). There were no direct in situ measurements that could be compared to our data.

However, we were able to compare retrieved particle sizes to those obtained by another technique based on the comparison of lidar and radar backscattering coefficients (Intrieri et al. 1991). For 2035 UTC our technique gives $D_m \approx 180$ μm and the lidar/radar technique provides $D_m \approx 300$ μm. The difference between these results can be attributed to errors inherent to both techniques, and, in particular, to the attenuation of lidar signals in clouds leading to an overestimation of particle sizes in the upper part of the cloud.

The retrieved values of particle concentration vary over a large range. The peaks of C at 1925, 1953 and 2015 UTC resulted from the increase of the measured brightness temperatures when the radar reflectivities did not change notably. This can be explained by the growing number of small particles that did not significantly contribute to the radar echoes but did increase the cloud optical thickness. We note also that retrieved values of particle concentrations are in the reasonable range for cirrus clouds (Kosarev and Masin 1989).

b. Estimation of Ice Water Path

Ice water path (IWP) is an important cloud parameter, and it is defined as a vertical path integral of ice water content w_i (see (12b)). Knowing the particle median size, particle concentration and cloud boundaries from IR radiometer/radar measurements, we can calculate IWP. IWP values were obtained for all 75 data points of the experimental case discussed above.

Figure 5 shows IWP data retrieved by the proposed technique and those (IWP_s) obtained from the empirical equation proposed by Sassen (1987):

$$w_i = 0.037\ Z_i^{0.696} \tag{18}$$

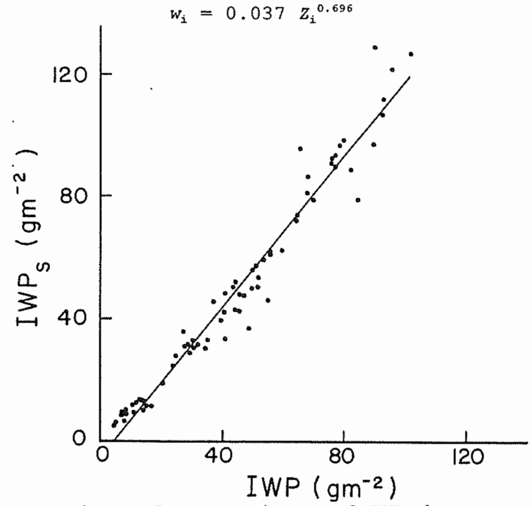

Figure 5. Comparisons of IWP data.

One can see that both techniques give close results for this experimental case. The corresponding linear regression equation is

$$IWP_s = 1.2\ IWP - 5.4 \tag{19}$$

The agreement is surprisingly good given the fact that our technique uses individual values of particle characteristic sizes and concentrations to obtain values of IWP in contrast to (18) which is just an empirical relationship. We can expect many other experimental situations where agreement probably will not be so good because (18) represents only an average relationship without taking into account independent variations of particle sizes and concentrations.

5. CONCLUSIONS

A technique is proposed to retrieve vertically averaged cirrus cloud particle characteristic sizes and concentrations from combined ground-based IR radiometer and radar measurements. An example of the retrieval is presented for an experimental case of the CLARET-I experiment.

REFERENCES

Intrieri, J.M., W.L. Eberhard, and T. Uttal, 1991: Determination of cirrus cloud particle effective radii using radar and lidar backscattering data, in *Proceedings of the 25th Conference on Radar Meteorology*, AMS, Boston, Mass., 809-812.

Kosarev, A.L., and I.P. Mazin, 1989: Empirical model of physical structure of the upper-level clouds of middle latitudes, in *Radiation Properties of Cirrus Clouds*, Nauka, Moscow, 39-53 (in Russian).

Sassen, K., 1987: Ice cloud content from radar reflectivity, *J. Clim. and Appl. Meteorol.*, **26**, 105-1053.

Toon, O.B., C.P. Mckay, T.P.Ackerman, and K. Santhanam, 1989: Rapid calculation of radiative heating rates and photodissociation rates in inhomogeneous multiple scattering atmospheres, *J. Geophys. Res.*, **94**, 16287-16301.

TURBULENCE CHARACTERISTICS FOR DIFFERENT TYPES OF CIRRUS CLOUDS

M. Quante[1] and P.R.A. Brown[2]

[1] *GKSS Research Center, Institute for Physics, D-2054 Geesthacht, F.R.G.*
[2] *D.R.A.(Aerospace), Meteorological Research Flight, Farnborough, UK*

1. INTRODUCTION

Clouds play a major role in the radiation budget of the earth and thus are relevant to climate. In a recent study Cess et al. (1990) intercompared climate feedback processes in 19 atmospheric general circulation models. Their most important conclusion is that variations between the models are mainly due to their depiction of cloud feedbacks. They further emphasize that cloud feedback is related to all interacting physical and dynamical processes in a model. There is a need to improve the understanding of the influence of microphysics, radiation and dynamics on the life cycle of clouds in order to develop better, physically based representation in climate models. This is especially true for cirrus clouds, which have only recently gathered attention by larger observational programs like the First ISCCP Regional Experiment (FIRE; Starr, 1987) or the International Cirrus Experiment (ICE; Raschke, 1988).

As observations show, one of the most striking features of cirrus clouds is the great deal of structure in the horizontal and vertical direction. These clouds often appear patchy and multilayered. Dynamical processes, i.e. small-scale turbulence, have an important influence on the cloud structure and therefore on the spatial distribution of optical properties. Through internal mixing and entrainment processes turbulence is directly linked to the life cycles of the clouds.

The major information expected from turbulence measurements in cirrus may be summarized as follows: 1. How does the typical flow field look like for different types of cirrus (frontal, jet stream etc.); 2. What are the typical scales of turbulence?; 3. Is there a link between mesoscale and microscale structure of the clouds and the observed dynamics? 4. How does the interaction of turbulence, microphysics and radiation look like? Answers to these questions are important for the identification of dominant processes and are directly related to process-oriented modelling.

Here we will report on aircraft measurements of turbulence in different types of cirrus obtained during the ICE field campaigns. In this extended abstract only a few general results will be discussed. Not all points listed above can be answered satisfactory on the basis of our or other published results.

2. TURBULENCE IN THE VICINITY OF CIRRUS CLOUDS

Since cirrus clouds are located in the upper troposphere, they are embedded in a flow field, which typically is characterized by stable stratification and a vertical shear of the horizontal wind. In such an environment the coexistance and interaction of nonlinear internal gravity waves and turbulence on different time- and space-scales is most likely (e.g. Fritts and Rastogi, 1985; Hopfinger, 1987). Distinguishing between those two dynamical regimes, which is not an easy task, is of crucial importance for the interpretation of measurements, in particular, if vertical fluxes of energy, heat and moisture are of interest.

Possible sources of turbulence in stratified shear flows are instabilities associated with internal gravity waves and wind shear. Since the generation processes are not continous in time and spacially inhomogeneous, turbulence in the free atmosphere occurres intermittent. Thermal stratification counteracts the production processes and leads to permanent decay of turbulent kinetic energy. If clouds are present turbulence is generated by the energy release through condensation and radiative cooling or heating. While on the mesoscale vortical modes or gravity waves are likely to dominate the cloud morphology, on the microscale the interaction between microphysics, radiation and turbulence determines local structure of the cloud and influences their life cycle. For cirrus clouds, at present not much is known about this interaction (Jonas, 1989), mainly due to a lack of extensive observational studies. For turbulence the separation of that induced by clouds and the more sporadic turbulence of the background flow is quite complicated, i.e. for aircraft measurements, where only samples along a line through the flow field are collected.

Up to now only a few studies dealt with dynamical aspects of cirrus clouds. Heymsfield (1975) investigated the formation and maintenance of uncinus and explained the observed data as a result of wind shear effects and those of small convective cells, possibly generated by wave motion. In a modelling study Starr and Cox (1985) investigated the interaction of microphysics, radiation and turbulence in a thin cirrus layer, they found considerable generation of turbulent kinetic energy during the development of the cloud. The dynamical structure in the persistent cloud layer was controlled by radiative processes. Some authors applied mixed layer models for the investigation of cirrus. Lilly

(1988) discussed cirrus outflow plumes from deep convection and found, that in these quite dense clouds strong radiative heat flux curvature leads to the maintenance or generation of turbulence, which again maintains a mixed layer. Flatau et al. (1989) used the mixed layer framework for a cirrus case study. They stated that their entrainment constants and turbulent fluxes were educated guess and pointed out the need for more observational studies.

Measurements of turbulence in cirrus are rare, some early measurements are documented in Vinnichenko et al. (1980). Dimitriev et al. (1984) reported on aircraft observations in jet stream cirrus, Quante (1989) analysed in situ measurements in frontal cirrus, Flatau et al. (1990) evaluated measurements performed during the FIRE and GASP experiment. All observational studies point out the patchy occurrence of turbulence and the anisotropy in the velocity field, resulting in a two-dimensional character of the flow. Turbulence in general was found to be weak, apart from patches in regions of strong wind shear.

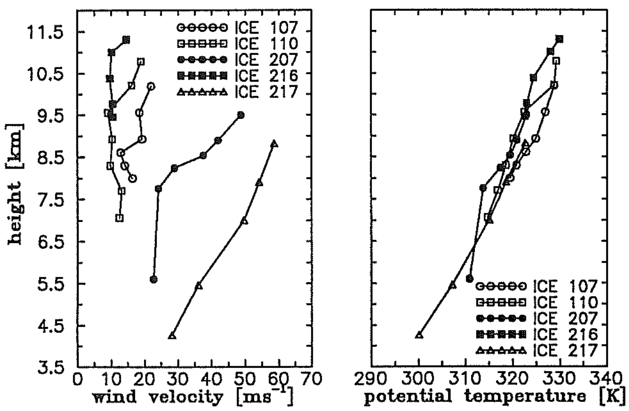

Figure 1: Vertical profiles of horizontal wind velocity and potential temperature in the cloud region for five different cirrus missions during ICE'87 and ICE'89. Values represent averages for several horizontal flight legs.

3. MEASUREMENTS

Measurements of turbulence in cirrus clouds have been obtained during the pilot field phase of ICE in 1987 and the intensive field observation phase in 1989 (Hennings et al., 1990). Three high-flying aircraft equiped with turbulence instrumentation were available during ICE. High resolution measurements of the wind components were made by the DLR-Falcon (five hole pressure probe, 100 Hz), the MRF- C 130 (potentiometric wind vane, 32 Hz) and the CAM-Merlin (five hole radome, 25 Hz). Aircraft attitude angles were in all three cases delivered by an inertial navigation system. Temperatures were measured using Rosemount fast total temperature sensors.

Up to now measurements obtained during five case studies have been analysed. The cirrus encountered during ICE missions 107 and 110 of the pilot field phase can be classified as frontal cirrus with medium wind speeds. A general description of these case studies is given in Quante (1989) and Quante et al. (1990). During mission ICE 207 the cloud field was associated with a branch of a splitted jet stream. No considerable large scale lifting was present. Thin cirrus at high altitude was found during ICE 216 in a region under high pressure influence. The cloud field on this day was filled with contrails, which were a major source of humidity. A deep cirrus layer ahead of a warm front, rapidly moving eastward, was target of mission ICE 217. The system was characterized by a strong wind shear. The cloud in contrast to the other cases was quite uniform in horizontal extend over the entire flight pattern. During all missions measurements were made at several altitudes.

4. SOME RESULTS

In this section a few examples of measurements during the above mentioned case studies will be given, in order to illustrate some characteristics of turbulence in cirrus. More detailed results will be presented during the conference.

In order to examine the turbulence structure time series, variances and turbulent fluxes (of unfiltered and filtered data), power- and cross-spectra of the three wind components (u, v, w) and the static- and potential temperature have been analysed. For relatively long data segments power- and cross-spectra were computed applying a method proposed by Welch using a FFT-routine. For shorter data segments the spectra were calculated employing the maximum entropy method. It should be mentioned that the large scale inhomogeneity, or patchiness, of the energy containing turbulence, also called "global intermittency" (Mahrt, 1989), makes it particularly difficult to calculate reliable statistics for stably stratified flows.

Figure 1 shows vertical profiles of the horizontal wind and the potential temperature for five case studies. The values represent averages over several flight legs for the corresponding height levels. The profiles for ICE 207 are composed of measurements made by three aircraft. In all cases the thermal stratification of the flow is quite obvious. Except for mission ICE 216 vertical wind shear was present in at least a part of the cloud layer. As expected the wind shear was most pronounced during ICE 207, the jet stream case, were values around 10 m/s/km were found, but also in the frontal cirrus of mission ICE 217 values around 7 m/s/km are typical. Bulk Richardson numbers calculated for entire layers between flight legs were in general larger than the critical value of 0.25. But the Ri-number profile calculated from composed aircraft ascents, which are only available for ICE 207, show quite a variation with height and values lower than 0.25, indicating the possible existence of several turbulent layers in the cloud field.

Examples of time series of the vertical wind component measured during ICE 207 for two different alitudes are shown in figure 2. The upper time series corresponds to an altitude of 9.5 km, this flight leg was flown just above cloud top and close to the tropopause. Most obvious are wavelike features in the first third of the leg and the extremely weak turbulence. The power spectrum (number 1 in figure 3) rolls

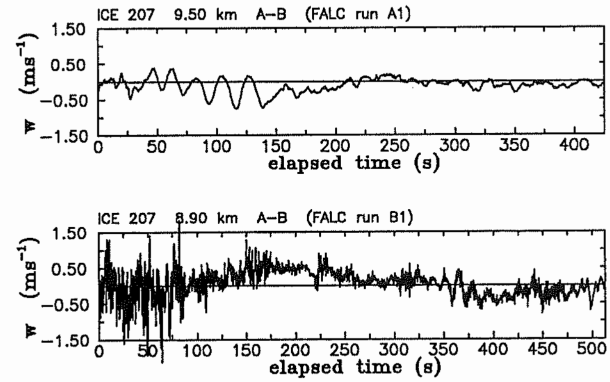

Figure 2: Time series of vertical velocity w along flight leg A-B at 9.5 km height (upper graph) and at 8.9 km height (lower graph) for mission ICE 207, 28.09.89. The length of the flight legs was about 100 km.

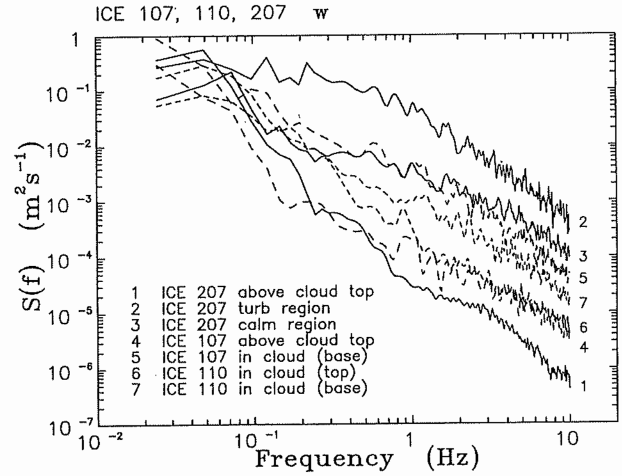

Figure 3: Typical power spectra of the vertical velocity component for different regions in frontal cirrus (ICE 107, ICE 110) and jet stream cirrus (ICE 207).

off with a slope of around -3 down to scales below 190 m. Much more shortwave variability in the vertical wind (this is also true for horizonl components) occurred at lower levels inside and below the cloud field. The lower graph in figure 2 shows the w-time series for leg A-B at 8.9 km height, flown in the cloud top region. This is a good example for the high complexity of the flow. Very active regions appear together with less intense ones and segments, where wavelike behaviour occured. Turbulence is definitly not homogeneous. Sometimes the transition from very weak to stronger turbulence was found to be very abrupt. This was especially pronounced in the cases with strong wind shear.

In figure 3 typical power spectra of the vertical velocity for different regions in frontal and jet-stream cirrus are compared. The velocity variance at some locations in the jet stream cirrus was quite intense and compared with intense regions in frontal cirrus at least one order of magnitude higher over a large wavelength interval. Curve 2 in figure 3 shows a w-spectrum for a turbulent region, whose general shape and amplitude is comparable to spectra for CAT regions, encountered in the neighborhood of the cloud field. Curve 3 is an example for a more quiet region at the same altitude. When samples could be obtained above the cloud tops, turbulence was extremely weak or quasi non existent, curve 1 is a corresponding example for ICE 207. The region just below the tropopause behaves like a lid and is responsible for well marked cloud tops. Turbulence in frontal cirrus (curves 4 to 7) and in "still air" cirrus (ICE 216 , not shown here) was found to be weak. The spectra indicate that typical length scales for turbulence vary substancially between different cases, but also between different locations or altitudes in one case study. Also the degree of anisotropy in the velocity field varies from turbulent to calm regions. In general vertical motions were suppressed, due to buoyancy, leading to a two-dimensional character of the flow. Scales of energy containing eddies vary between a few tens of meters to a few hundreds of meters.

In order to determine the existence of linear gravity waves, cross-spectra of vertical velocity and temperature were

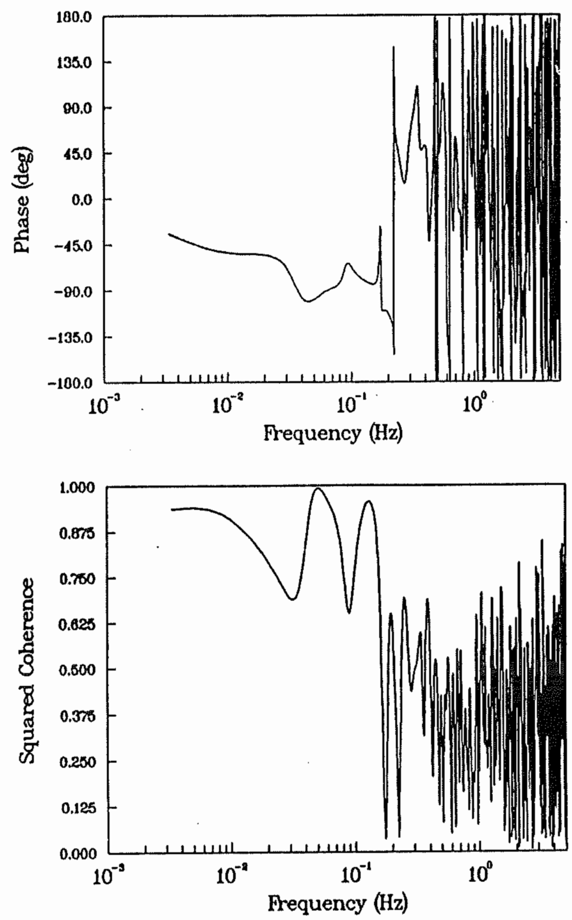

Figure 4: Phase- (upper graph) and squared coherence spectra (lower graph) for vertical velocity and potential temperature for a segment of flight leg D-A at 9.5 km height (just above cloud top) for mission ICE 207.

calculated. If linear waves are present w and T cross-spectra are expected to show a 90 degree phase relation and high coherence. This conditions were met for several flight segments in jet stream and in frontal cirrus. As a very clear example figure 4 shows a phase and coherence spectrum for w and T for a segment of leg D-A at 9.5 km height, mission ICE 207. At the frequency of 0.05 Hz a phase of 90 degree goes along with high coherence and a large contribution to the amplitude spectrum (not shown here). The frequency of 0.05 Hz translates to a wavelength of about 3.8 km. For this case study wavelike structures can also be seen on photographs taken during the flight mission. A study looking for a direct relation between scales seen in turbulence data and in cloud microphysical data has been started.

Variances and turbulent fluxes were calculated from high-pass filtered data. The results are of course very sensitive to the choice of the cutoff-wavelength and the location of the analysed segment along the horizontal flight leg. Typical standard deviations for horizontal wind components, $s_{u,v}$, (cutoff-wavelength: 500 m) were around 0.4 m/s in turbulent regions for jet stream cirrus, the ratio of s_w to $s_{u,v}$ was about 0.8. Standard deviations in calm regions were found to be about 0.1 m/s, here the ratio of horizontal to vertical values was about 0.5 for scales smaller than 500 m. Dissipation rates calculated from w-spectra in regions, where an inertial subrange was established, were around $2 * 10^{-4}$ m^2s^{-3} for turbulent and about one magnitude lower for calmer segments. The corresponding values for frontal cirrus with moderate wind shear were in general much lower.

5. CONCLUSIONS

Cirrus clouds are imbedded in the upper tropospheric flow field, which often is characterized by stable stratification and a vertical shear of the horizontal wind. In this kind of flow internal waves, quasi-two-dimensional turbulence and mostly weak three-dimensional turbulence on small scales coexist. Sporadic generation processes, nonlinear wave-turbulence interactions and the influence of buoancy lead to a complex flow field, for which the calculation of representative turbulence statistics is quite difficult.

During ICE turbulence measurements could be obtained in frontal cirrus, in cirrus associated with the jet stream and in thin cirrus under high pressure influence. The turbulence measurement systems have shown to be capable of resolving different types of behaviour in the observed wind and temperature data. The observations show that in general turbulence in cirrus was quite weak, with the exception of patches in jet stream cirrus and in frontal cirrus with strong wind shear. The turbulence occurred intermittent and showed a two-dimensional character. The observed cirrus clouds appeared often multilayered and exhibited a significant horizontal and vertical variability, which partly can be explained by the patchy occurrence of turbulence and the limited vertical mixing, due to suppressed vertical motions by buoyancy. Typical scales of energy containing eddies vary between a few tens to a few hundreds of meters. Since many of the results contain usefull information for process-oriented cirrus modelling, the collaboration with modelling groups will be intensified (at GKSS a non-hydrostatic mesoscale model is used for cirrus cloud simulations).

REFERENCES

Cess, R.D. et al., 1990: Intercomparision and interpretation of climate feedback processes in nineteen atmospheric general circulation models. *J. Geophys. Res.*, Vol. 95, No. D10, 16601-16615.

Dmitriev, V.K., T.P. Kapitanova, V.D. Litvinova, N.G. Pinus, G.A. Potertikova, G.N. Shur, 1984: Meso- and microscale structure of wind and temperature fields in jet stream cirrus clouds. The 9th International Cloud Physics Conference, Vol. II, Tallinn, 347-350.

Flatau, P.J., G.A. Dalu, W.R. Cotton, G.L. Stephens, A.J. Heymsfield, 1989: Mixed layer model of cirrus clouds: growth and dissipation mechanisms. *Symposium on the role of clouds in atmospheric chemnistry and global climate*, Ameri. Meteor. Soc., 151-156.

Flatau, P.J., I. Gultepe, W.R. Cotton, A.J. Heymsfield, G.D. Nastrom, 1990: Cirrus cloud spectra and layers observed during the FIRE and GASP projects. *Conference on Cloud Physics*, San Francisco, Ameri. Meteor. Soc., 200-206.

Fritts, D.C., P.K. Rastogi, 1985: Convective and dynamical instabilities due to gravity wave motions in the lower and middle atmosphere: Theory and observations. *Radio Science*, **Vol. 20**, 1247-1277.

Hennings, D., M. Quante, R. Sefzig, (ed.) 1989: International cirrus experiment, 1989 field phase report. Institut für Geophysik und Meteorologie, Universität zu Köln, 110pp.

Heymsfield, A.J., 1975: Cirrus uncinus generating cells and the evolution of cirriform clouds. Part II: The structure and circulation of the cirrus uncinus generating head. *J. Atmos. Sci., 4,* 809-819.

Hopfinger, E.J., 1987: Turbulence in stratified fluids: A review. *J. Geophys. Research, 92 (C5)*, 5287-5303.

Jonas, P.R., 1989: Effects of radiation on clouds. *Atmos. Research, 23,* 259-286.

Lilly, D.K., 1988: Cirrus outflow dynamics. *J. Atmos. Sci., 45,* 1594-1605.

Mahrt, L., 1989: Intermittency of atmospheric turbulence. *J. Atmos. Sci., 46*, 79-94.

Quante, M., 1989: Flugzeugmessungen der Turbulenzstruktur in Cirruswolken. Mitteilungen, Heft 65, Institut für Geophysik und Meteorologie, Universität zu Köln, 121pp.

Quante, M., E. Raschke, F. Albers, A. Gratzki, P. Scheidgen, Y. Zhang, 1990: The International Cirrus Experiment (ICE) - Results from the pilot experiment 1987-. Preprints Seventh Conference on Atmospheric Radiation, San Francisco, Calif., Americ. Meteorol. Soc., Boston, 30-37.

Raschke, E., 1988: The international satellite cloud climatology project, ISCCP, and its european regional experiment ICE (International Cirrus Experiment). *Atmos. Res., 21,* 191-201.

Starr, D.O´C., 1987: A cirrus-cloud experiment: Intensive field observations planned for FIRE. *Bull. Amer. Meteor. Soc., 68*, 119-124.

Starr, D.O´C., S.K. Cox, 1985: Cirrus Cloud. Part I: A cirrus cloud model. *J. Atmos. Sci., 42,* 2663-2681.

Vinnichenko, N.K., N.Z. Pinus, S.M. Shmeter, G.N. Shur, 1980: *Turbulence in the free atmosphere.* Consultans Bureau, New York, 310pp.

ACKNOWLEDGMENTS: The authors would like to thank B. Guillemet, Clermont-Ferrand, for providing data obtained by the Merlin aircraft during ICE´89. This work is supported by the BMFT, Bonn, within the German Climate Research Programme and by the CEC, Brussels.

3-D NUMERICAL SIMULATION OF CIRRUS CLOUDS

L. Levkov, B. Rockel, E. Raschke

GKSS Forschungszentrum Geesthacht, Institit für Physik

Postfach 1160 D-2054 Geesthacht Fed. Rep. Germany

1. BASIC FRAMEWORK OF THE MODEL AND CLOUD SCHEME

This study uses the three-dimensional non-hydrostatic model GESIMA (GEesthacht SImulation Model of the Atmosphere). The governing equations are the Boussinesq approximated, anelastically filtered equations of motion in flux-conserving form. A detailed derivation of the equations is given by Kapitza (1987).

Both liquid water and ice phase microphysics is developed and incorporated. The predicted model variables are the three velocity components (u, v, w), potential temperature (θ), pressure (p), the mixing ratio for water vapor (q_V), and the mixing ratios and the number concentration for cloud water $(q_W; N_W)$, rain$(q_R; N_R)$, ice$(q_I; N_I)$ and snow$(q_S; N_S)$. The shapes of all hydrometeors are assumed to be spherical and the total number of cloud particles is taken into account in the radiation code for more precise calculation of the optical characteristics of clouds.

The continuity equations for the time-dependent water species and potential temperature can be written as follows:

$$\frac{\partial q_X}{\partial t} = ADV(q_X) + DIF(q_X) + \frac{\partial}{\partial z}(q_X U_X) + Q_{qx} \quad (1)$$

$$\frac{\partial \Theta'}{\partial t} = ADV(\Theta') + DIF(\Theta') + Q_{\Theta'} \quad (2)$$

where q_X is the grid volume average mixing ratio of a species X of water. The variable Θ is split into a background $\bar{\Theta}$ and deviation Θ'. The cloud code (Levkov et al., 1987) is extended by prognostic equations for the grid volume average number concentration (N_X) of cloud particle formulated as follows:

$$\frac{\partial N_X}{\partial t} = ADV(N_X) + DIF(N_X) + \frac{\partial}{\partial z}(N_X U_X) + Q_{N_X} \quad (3)$$

Equation (2) is integrated in time by a predictor-corrector scheme and the advection ("ADV") is calculated by McCormacks's scheme. All water species are integrated in time by a forward step, and the advection is calculated by use of an algorithm by Smolarkiewicz (1984). The eddy diffusion term ("DIF") is calculated by a first order closure and the turbulent diffusion coefficient is assumed to be function of turbulent kinetic energy. U_X is the mass weighted mean terminal velocity for precipitating particles and Q_{q_X}, Q_{N_X} and $Q_{\Theta'}$ denotes the change of the water species and temperature due to microphysical and radiative processes. The cloud microphysical processes simulated in the model are illustrated in Figure 1. The algorithms allowing for an explicit calculation of the species are based upon a modified combination of those proposed by Levkov et al. (1987), Nickerson et al. (1989) and Flatau et al. (1989).

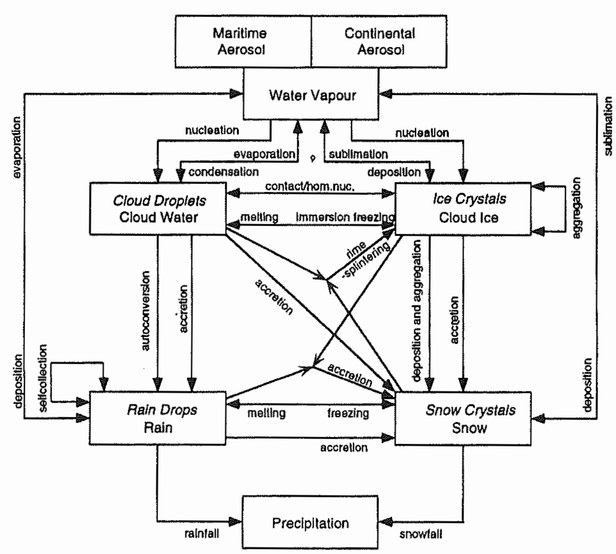

Fig. 1 Cloud physical processes considered in the GESIMA cloud scheme.

2. INITIALIZATION

The horizontal domain of the model is 26 km in X and 9 km in Y direction with a 1000 m grid interval. The vertical domain is 11.5 km with variable resolution ranging from about 40 m near the surface to about 250 m near 11.5 km. The model grid is place in the region where mission ICE207 (28 September 1989) was flown during the field phase of the International Cirrus Experiment. The cirrus on this day was associated with the jet stream and appeared multilayered, showing a band structure aligned with the wind. Cirrus cloud top were observed to reach 9.2 km (-46^0C) and low cloud area of cumulus and stratocumulus was reported to be situated between 950 and 800 hPa.

Nonperiodical rectangular wave generator (CASE A), impuls (CASE B) and random number generator (CASE C) are used as thermal perturbation in order to cause a cloud to form.

3. RESULTS OF NUMERICAL SIMULATIONS

The model was run for two and a half hours simulation time (12:00 - 14:30 UTC). Fig. 2a shows sum of ice and snow content (solid lines) and cloud water (dashed lines) in a vertical section at $y = 2.5$ km after 24 min simulation time in CASE A. Two cloud layers have been formed and still are developing: a cirrus layer between 7 and 9 km and a stratus layer between 0.5 and 2 km. Maximum ice content produced at this time of simulation at cirrus height is about $0.040gkg^{-1}$. Maximum cloud water at stratus height is $0.023gkg^{-1}$. Fig. 2b shows the location of the model clouds after 56 min simulation time. There is a tendency to develop multi-layered structure in the vertical with lower ice mixing ratio of $0.009gkg^{-1}$. The initial perturbation is supressed, but the circulations triggered by cloud activity are strong enough to maintain some form of moist convection. During the next hour of simulation a quasi-steady value of q_I is reached showing that cirrus cloud layers may exist at high altitudes for a long periods of time. With time the formed stratus cloud shows sign of weakening and at 56 min simulation time is disappeared.

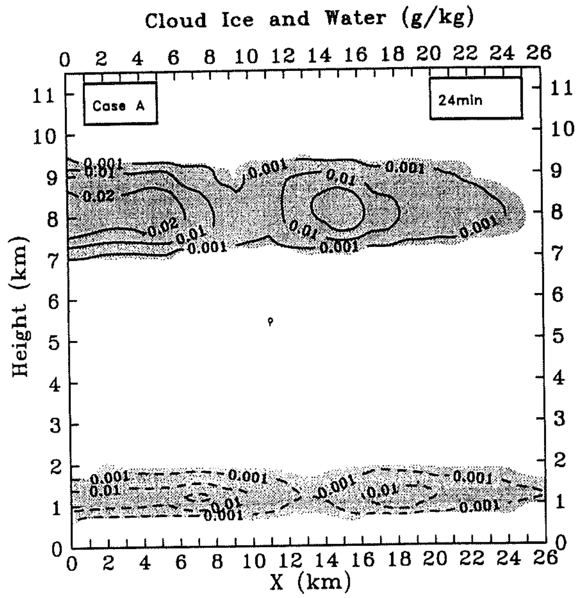

Fig. 2a Contour plot of the sum of cloud ice water and snow field (solid) and cloud liquid water (dashed) of "CASE A" after 24 minutes simulation time for a xz-slice at gridpoint 3km in y-direction. Shaded areas represent areas for values higher than $10^{-4}gkg^{-1}$.

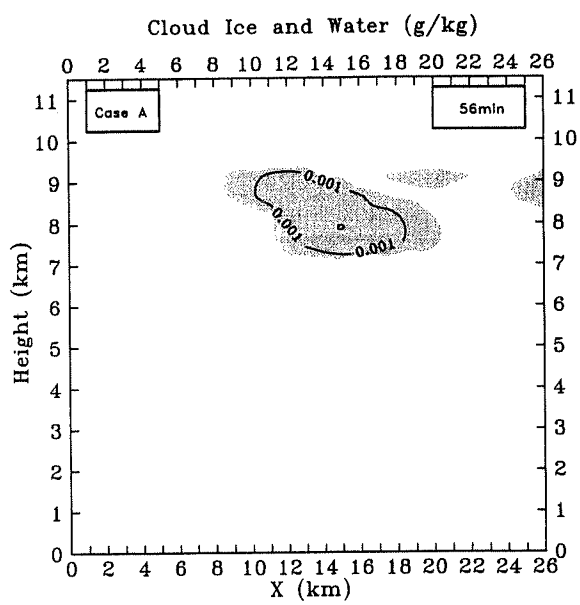

Fig. 2b As Figure 2a but after 56 minutes simulation time.

The time evolution of the cloud layers by the different temperature perturbations is shown in Fig. 3 in terms of ice and water content summed up over the whole model domain. It is obvious that the cirrus cloud "CASE B" has the same stages in the simulation time, but is likely to be weaker than if the perturbation "CASE A" is activated. By "CASE C" the whole live cycle of the model clouds are replaced in the time. Fig. 4 shows the time evolution of total horizontal cloud cover in the computation area for "CASE C".

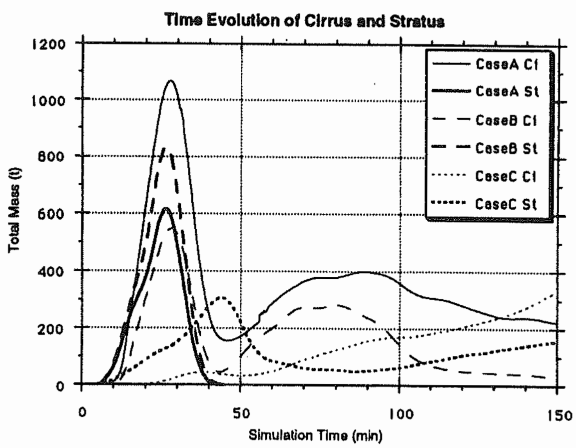

Fig. 3 Time evolution of cirrus and stratus cloud for the three different initial temperature disturbances.

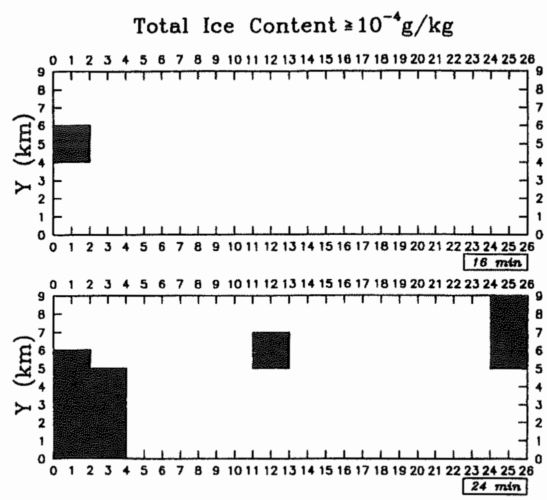

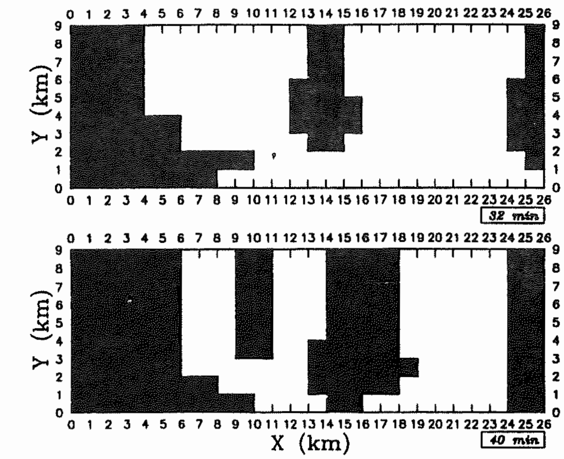

Fig. 4 Horizontal cloud cover for "CASE C" after 16, 24, 32, and 40 minutes simulation time. Grid boxes with at least one layer in the vertical containing more than $10^{-4} gkg^{-1}$ total ice content are painted black.Θ

4. CONCLUSIONS

The general features of the double cloud layer (cirrus cloud with stratus cloud below) show encouraging results concerning the computed mixing ratios as well as the total number concentration of cloud particles. Once the phenomena have been plausibly simulated we have done sensitivity model runs showing that the life cycle of cloud may be attributed to the way in which the large-scale heat flux is comming into the model domain. However, the used atmospheric profile leads to a spatial and a temporal probleme. In order to get comparable simulation runs a larger number of atmospheric profiles has to be measured at different places of the measurement area, the more structured cirrus clouds are the more atmospheric profiles are necessary. The model starts with the given atmospheric sounding as initial profile. After that the model is no longer coupled to the "real atmosphere" and begins to live his own life. In order to achieve a more realistic coupling the model has to be adjusted with actual atmospheric profiles after certain times.

5. REFERENCESS

Flatau, P. J., G. J. Tripoli, J. Verlinde, W. R. Cotton, 1989: The CSU-RAMS Cloud Microphysics Module: General Theory and Code Documentation, Colorado State University, Department of Atmospheric Science, Paper No 451, 88 pp.

Kapitza, H., 1987: Das dynamische Gerüst eines nichthydrostatischen mesoscalen-Modells der atmosphärischen Zirkulation. Ph. D. Thesis, University of Hamburg, 104 pp, available from Research Center Geesthacht, 2054 Geesthacht, F.R.G., External Report GKSS 87/E/35.

Levkov, L., D. Eppel, H. Graßl, 1987: Parameterization of phase change of water in a mesoscale model. External Report GKSS 87/E/44, 45 pp, available from Research Center Geesthacht, 2054 Geesthacht, F.R.G.

Nickerson, E. C., E. Richard, R. Rosset, and D. R. Smith, 1986: The numerical simulation of clouds, rain, and airflow over the Vosges and Black Forest Mountains: A meso-model with parameterized microphysics, Mon. Wea. Rev., 114, 398 - 414.

Smolarkiewicz, P. K., 1984: A fully multidimensional positive definite advection transport algorithm with small implicit diffusion, J. Comp. Phys., 54, 325 - 362.

EXTINCTION CHARACTERISTICS OF TROPICAL HIGH CLOUDS AS OBSERVED BY THE SAGE II SATELLITE INSTRUMENT

Pi-Huan Wang,[1] M. P. McCormick,[2] L. R. Poole,[2]
W. P. Chu,[2] G. K. Yue,[2] and G. S. Kent[1]

1. Science and Technology Corp., 101 Research Dr., Hampton, VA 23666
2. Atmospheric Sciences Division, NASA Langley Research Center, Hampton, VA 23665

1. Introduction

The purpose of this study is to describe the extinction characteristics of tropical high clouds based on aerosol extinction measurements from Stratospheric Aerosol and Gas Experiment (SAGE II) and the temperature analyses of the National Meteorological Center (NMC).

SAGE II is the latest of a series of NASA solar occultation satellite sensors, which include also the Stratospheric Aerosol Measurement (SAM II) on Nimbus 7 and SAGE I on the Application Explorer Mission 2 satellite. The ability of solor occulation satellite instruments to monitor high clouds is well demonstrated by the discovery of the polar stratospheric clouds (PSC) based on the SAM II observations [*McCormick et al.*, 1982]. In addition, aerosol extinction measurements obtained by SAGE I and SAGE II have been used to study cirrus occurrence frequency [*Woodbury* and *McCormick*, 1983; *Woodbury* and *McCormick*, 1986; and *Chiou et al.*, 1990]. Additional efforts have been devoted to separate the aerosol data from cloud data for study of the tropospheric aerosol climatology [*Kent and McCormick*, 1991].

2. SAGE II Satellite Instrument

The SAGE II satellite instrument provides aerosol extinction measurements at 0.385-, 0.453-, 0.525-, and 1.02-μm wavelengths [*McCormick*, 1987]. The field of view of the instrument is 0.5 arc-min in elevation by 2.5 arc-min in azimuth. At the orbit altitude of 610 km this field of view corresponds to a viewing cross section of 0.5 km in the vertical by 2.5 km in the horizontal at the limb tangent point. The SAGE II measurements are averaged to give a 1-km vertical resolution. The horizontal path length, corresponding to a 1-km thick spherical atmospheric shell, is about 200 km at a tangent height of 20 km. This sampling resolution is comparable to the typical spatial scale of tropical cirrus, which is approximately 1 km in the vertical with a horizontal coverage roughly 200 (km)$\times$200 (km) [*e.g., Ackerman et al.*, 1988].

The respective upper and lower limits of the SAGE II extinction measurements are approximately 2×10^{-2} and 2×10^{-6} (km^{-1}). For a 1-km thick layer, these limits correspond to the upper and lower limits of the optical depth of 2×10^{-2} and 2×10^{-6}, respectively. Based on polarization lidar measurements, and the shortwave radiation flux and solar corona observations, *Sassen et al.* [1989] defined a threshold cloud optical thickness $\tau_c \sim 3\times10^{-2}$ for visible-versus-invisible cirrus. Therefore, the cloud data in the SAGE II aerosol extinction measurements correspond generally to subvisible or thin cirrus, given that a well developed cloud visible to the human eye is likely to be opaque to the SAGE II instrument. As noted by *Sassen et al.* [1989], the visible cirrus clouds are enhanced concentrations of particles that are commonly distributed over extended regions. At low particle concentrations or smaller sizes, these regions may seem to be cloudless. Recently based on the Mie theory calculation, *Wang et al.*, [1989] have investigated the particulate size distribution information content of the SAGE II multiwavelength aerosol extinctions. Their results indicate that the SAGE II aerosol size information is between approximately 0.1- and 1.0-μm radii with the instrument most sensitive to particle radii between 0.25 and 0.80 μm.

3. Data and Analysis

The data of this study consist of the spring (March-April-May) 1991 SAGE II multiwavelength aerosol extinctions. Under cloud free conditions, the SAGE II channel at 1.02 μm obtains data deep into the troposphere, as illustrated in Figure 1a. The value of the 1.02-μm aerosol extinction is roughly on the order of 10^{-4} km^{-1} between 5- and 25-km altitudes. The cloud signatures are revealed by sharp vertical gradients of the extinction profile with distinct enhanced extinction values. Figure 1b shows three events of typical layer clouds as observed by the SAGE II instrument. Three cases of typical heavy clouds encountered by SAGE II are displayed in Figure 1c.

Because temperature plays an important role in cloud evolution, it is essential to examine the temperature dependence of SAGE II aerosol extinction measurements. The 1.02-μm aerosol extinctions of the SAGE II spring 1991 measurements at altitudes of 16.5, 17.5, and 18.5 km are plotted against the associated temperature data in Figure 2. Only the data with an uncertainty less than 40% of the extinction value are employed. Two distinct branches of data distribution are apparent. They can be separated fairly well by the extinction value $\sim 3\times10^{-4}$ km^{-1}. In the first branch, the data points have large extinctions, and are distributed in a narrow temperature range between approximately 197 and 200 K, while in the second branch the data points have smaller extinctions, and are distributed in a wide range of temperature from 197 to 227 K. Note in Figure 2 the SAGE II data that are associated with values less than 2.0 of the ratio of the extinction at 0.525 μm to that at 1.02 μm are labeled by solid squares. For SAGE II data with this extinction ratio greater than 2.0, a plus sign is used. As indicated in Figure 2, the low temperature data with extinction values larger than 3×10^{-4} km^{-1} are characterized generally by extinction ratios less than 2.0, and the high temperature data by extinction ratios greater than 2.0. According to *Yue and Deepak* [1983], aerosol measurements with larger extinction ratios are usually associated with smaller size particles, and smaller extinction

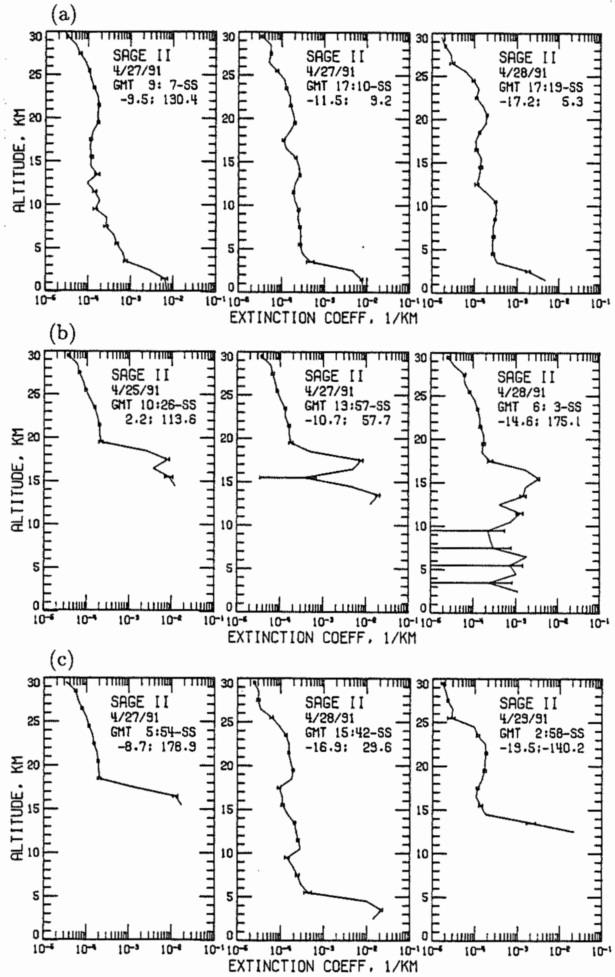

Fig. 1. Typical SAGE II extinction profiles at 1.02-μm wavelength: (a) cloud free measurements; (b) cloud with layer structure; (c) thick cloud.

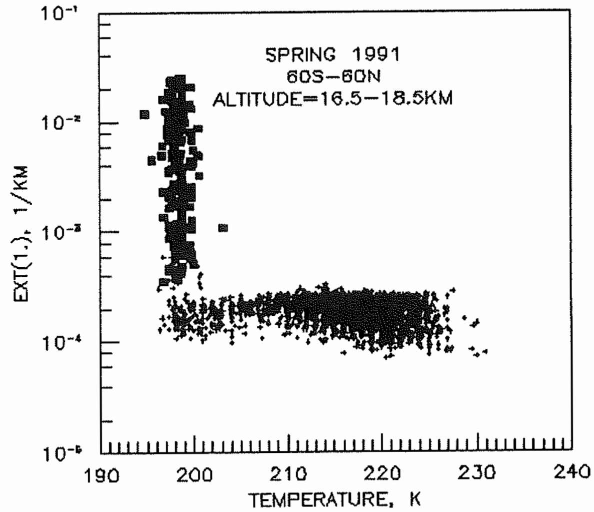

Fig. 2. Temperature dependence of SAGE II aerosol extinction (1.02 μm) measurements obtained in March-May 1991 at altitudes 16.5, 17.5 and 18.5 km. Solid squares represent the SAGE II data with the ratio of the extinction at 0.525 μm to that at 1.02 μm less than 2.0. The plus signs are for the data with the ratio greater than 2.0.

ratios are the characteristics of larger size particles. Because the SAGE II data of smaller ratio values ($\leq$2.0) exhibit enhanced extinctions and are associated with large size particles at low temperatures, clearly these data are the SAGE II measurements with the presence of clouds. In light of the measurement characteristics of the SAGE II instrument described in the previous section, these clouds are referred as subvisible or thin cirrus clouds.

The geographic distribution of the spring 1991 SAGE II thin cirrus is illustrated in Figures 3 and 4. In Figure 3,

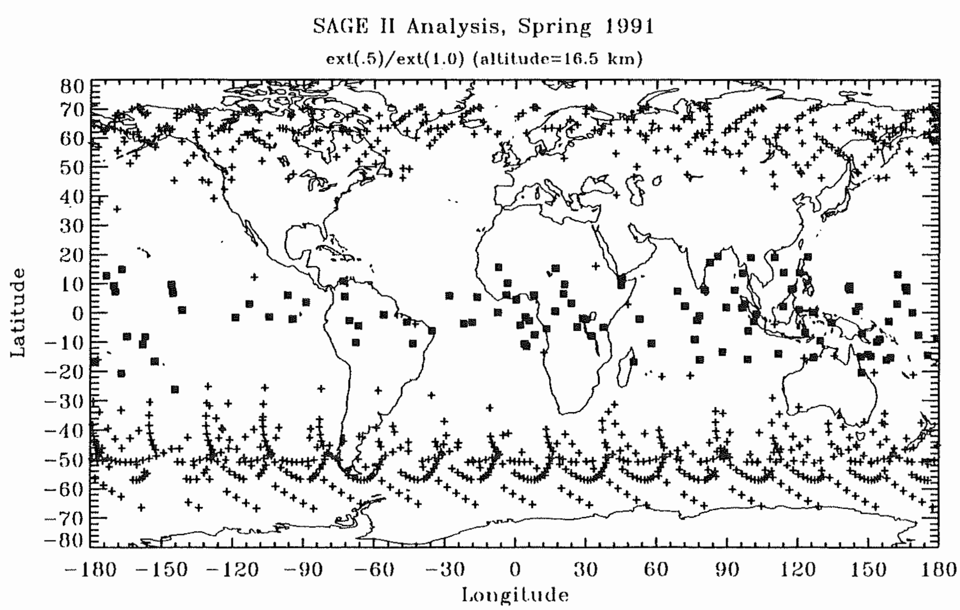

Figure 3. Longitude-latitude distribution of the March-May 1991 SAGE II data at an altitude of 16.5 km (labeled in the same manner as Figure 2).

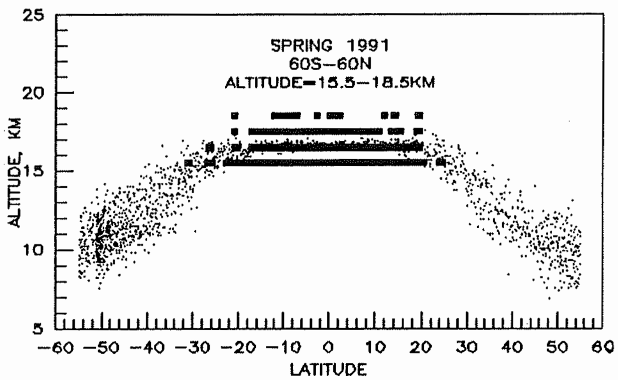

Fig. 4. Latitudinal distribution of the March-May 1991 cloud data (solid squares) at altitudes from 15.5 to 18.5 km. Dots represent the tropopause of the SAGE II measurements.

the latitude-longitude distribution of the SAGE II data at an altitude of 16.5 km are shown. Again, the solid square is for extinction ratio less than 2.0 and the plus sign for the ratio greater than 2.0 as in Figure 2. Generally, most of the high cloud data are measurements made in the eastern sector of the tropic region, especially in areas around Indonesia. In Figure 4, the altitude and latitude of each of the SAGE II data with the extinction ratio less than 2.0 are indicated. Shown also in Figure 4 are tropopause heights associated with each of the spring SAGE II measurements, indicated by dots. As seen from Figure 4 these cloud data are distributed in the tropics near the tropopause region. This is not surprising given that the tropical tropopause is the coldest region year round in the atmosphere.

To further examine the SAGE II measurements, the extinction data at 1.02 μm are plotted against the associated data at 0.525 μm in Figure 5. Again, the data are labeled

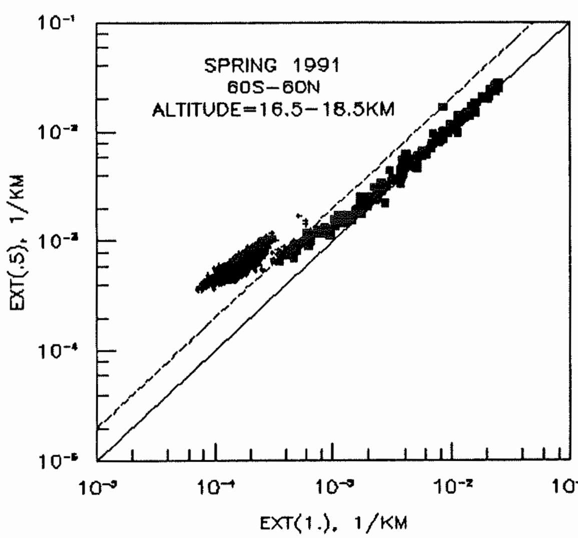

Fig. 5. Distribution of the March-May 1991 extinction data in the 1.02-μm extinction to 0.525-μm extinction space (labeled in the same manner as Figure 2).

according to the associated extinction ratio, either greater or less than 2.0 as in Figures 2 and 3. Clearly, Figure 5 shows that the data points with extinction ratios greater than 2.0 are close together in one dense cluster, while the data points with ratios less than 2.0 are distributed tightly along a curve extending from the skirt of the cluster previously mentioned and approach asymptotically the straight line of the extinction ratio of one. Thus, Figure 5 further illustrates the distinctly different optical behavior of the particles, i.e., ordinary aerosols and cirrus particles, in the SAGE II multiwavelength extinction measurements and their ability to be separated by the threshold extinction ratio 2.0.

The results of the wavelength dependence of cirrus extinctions are presented in Figure 6, in which the ratio of particulate extinction at 0.525 to that at 1.02 μm, Ext(.5)/Ext(1.), is plotted against the extinction ratio at 0.385 to 0.525 μm, Ext(.3)/Ext(.5). Note, only the cloud data are included. In general, Figure 6 indicates that, as the ratios Ext(.5)/Ext(1.) changes from a large value ($\sim$ 2.0) to smaller ones, the corresponding ratio Ext(.3)/Ext(.5) reduces its magnitude from approximately 1.6 to about 1. This feature is indicative of changes in the particle size distribution during the evolution of cirrus clouds.

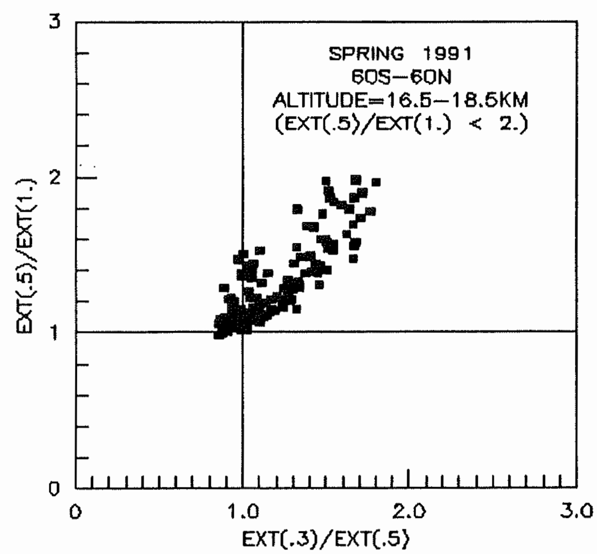

Fig. 6. Wavelength dependence of the March-May 1991 extinction data at altitudes from 16.5 to 18.5 km (only measurements with the ratio Ext(.5)/Ext(1.) greater than 2.0 are included).

Recent investigations indicate that cirrus clouds are likely to be controlled by homogeneous nucleation processes [*Sassen and Dodd*, 1988; *Heymsfield and Sabin*, 1989]. Furthermore, stratospheric aerosols are suggested to be important cloud condensation nuclei (CCN) of cirrus [*Mohnen*, 1990]. Based on these findings, a model study of the observed cirrus extinction characteristics was proposed. Currently this modeling study is in progress, and model results will be reported subsequently.

4. Summary

Results from this analysis indicate that (1) the SAGE II instrument is capable of detecting subvisible cirrus clouds with extinction up to 2×10^{-2} km^{-1} corresponding to an optical depth of 2×10^{-2} for a 1-km thick cirrus; (2) the cirrus data can be distinguished from aerosol data by using the ratio of the extinction at 0.525 μm to that at 1.02 μm as an indicator; (3) the cirrus data are characterized by the extinction ratios less than 2; and (4) SAGE II cloud extinction data reveal various degrees of wavelength dependency indicating particle growth during cirrus evolution.

Acknowledgments

P.-H. Wang and G. S. Kent are supported by NASA contract NAS1-18676.

References

Ackerman, T. P., K.-N. Liou, F. P. J. Valero, and L. Pfister: Heating rates in tropical anvils. *J. Atmos. Sci., 45*, 1606-1623, 1988.

Chiou, E. W., M. P. McCormick, W. P. Chu, and G. Y. Yue: Global distributions of cirrus determined from SAGE II occultation measurements between November 1984 and October 1988. Paper presented at Conference on Cloud Physics. *Am. Meteorol. Soc.*, San Francisco, July 23-27, 1990.

Heymsfield, A. J., and R. M. Sabin: Cirrus crystal nucleation by homogeneous freezing of solution droplets. *J. Atmos. Sci., 46*, 2254-2264, 1989.

Kent, G., and M. P. McCormick: Separation of cloud and aerosol in two-wavelength satellite occultation data. *Geophys. Res. Lett., 18*, 428-431, 1991.

McCormick, M. P.: SAGE II: An overview. *Adv. Space Res., 7*, 319-326, 1987.

McCormick, M. P., H. M. Steele, P. Hamill, W. P. Chu, T. J. Swissler: Polar stratospheric cloud sightings by SAM II. *J. Atmos. Sci., 39*, 1387-1394, 1982.

Mohnen, V. A.: Stratospheric ion and aerosol chemistry and possible links with cirrus cloud microphysics–A critical assessment. *J. Atmos. Sci., 47*, 1933-1948, 1990.

Sassen, K., and G. C. Dodd: Homogenerous Nucleation rate for highly supercooled cirrus cloud droplets. *J. Atmos. Sci., 45*, 1357-1369, 1988.

Sassen, K., M. K. Griffin, and G. C. Dodd: Optical scattering and microphysical properties of subvisual cirrus clouds, and climatic implications. *J. Appl. Meteor., 28*, 91-98, 1989.

Wang, Pi-Huan, M. P. McCormick,T. J. Swissler, M. T. Osborn, W. H. Fuller, and G. K. Yue: Inference of stratospheric aerosol composition and size distribution from SAGE II satellite measurements. *J. Geophys. Res., 94*, 8435-8446, 1989.

Woodbury, G. E., and M. P. McCormick: Global distributions of cirrus clouds determined from SAGE data. *Geophys. Res. Lett., 10*, 1180-1183, 1983.

Woodbury, G. E., and M. P. McCormick: Zonal and geographical distribution of cirrus clouds determined from SAGE data. *J. Geophys. Res., 91*, 2775-2785, 1986.

Yue, G. K., and A. Deepak: Retrievals of stratospheric aerosol size distribution from atmospheric extinction of solar radiation at two wavelengths. *Appl. Opt., 22*, 1639-1645, 1983.

THE PERSISTENCE OF VERY THIN CIRRUS NEAR THE COLD TROPICAL TROPOPAUSE

Henry B. Selkirk[1] and Eric J. Jensen[2]

[1]Space Physics Research Institute, Sunnyvale, CA 94087
[2]NASA Ames Research Center, Moffett Field, CA 94035

1. Introduction

The dehydration of air entering the stratosphere through the tropical tropopause to the global observed value of 3.5-4 ppmv requires, at minimum, a global average stratospheric entry temperature equivalent to 191 K at 100 hPa. This minimum requirement obtains only if there is nearly complete sedimentation of tropopause ice crystal mass; if substantial ice crystal mass remains in nascent stratospheric air then the temperature on entry must be colder in order to account for rehydration occurring during radiative heating in the lower stratosphere. Aircraft measurements of water content and ice particle populations from the NASA STEP experiment in Darwin, Australia in January and February 1987 have shown that monsoonal cumulonimbus anvils in that region can produce near-tropopause ice particle populations with a non-negligible fraction of mass in the size range under 10 microns, at times equivalent to several ppmv of water vapor upon sublimation. Given the slow sedimentation rate of these particles (less than 1 $\mathrm{cm\,s^{-1}}$), these particles are potential candidates for sublimation before settling out of the vicinity of the tropopause. This "residual" cirrus was occasionally observed outside of active convection.

Here we examine the processes of growth, evaporation, sedimentation and radiative heating which influence the ice water budget of a thin cirrus layer in the tropical tropopause environment using a one-dimensional numerical model with size-dependent microphysics and radiation and a high resolution in the vertical. The present case study was motivated by the upper tropospheric ice water structure observed during the STEP flight of 23 January. In this instance a residual cirrus layer overlying an otherwise clear troposphere was encountered at 15.5 km. At this level the ice water mixing ratio was on the order of 15 ppmv. The lack of an underlying deep convective cloud suggests that this thin layer of ice water was the remainder from previous convective activity. But when was this activity? Was it local or was it at some great distance? In this study we examine the evolution of such a layer over approximately a 10 hour time period. The results suggest that the thin cirrus observed in the STEP flight may well have been the result of injection at a remote location, perhaps hundreds of kilometers and tens of hours earlier.

2. The cirrus model and initial data

The one-dimensional model used in this study has previously been employed by Jensen *et al.* (1992) to study the evolution of middle latitude cirrus. The model calculates radiative heating rates and explicitly resolves and predicts the size distributions of condensation nuclei, solution drops and cirrus ice crystals. Each of these three aerosol types is subdivided into 40 size bins for a total partcle size range from 0.01 to 600 μm. At each time step the model solves the continuity equation for each aerosol size bin; for ice crystals the processes of interest here are condensation and evaporation, sedimentation and coagulation. The radiative transfer code is described by Toon *et al.* (1989) and uses a generalized two-stream technique for visible wavelengths and direct integration of the radiative transfer equation for the infrared. The 30 layers in the model extend from the ground to 22 km although the gridding is concentrated in the height region near the tropopause: the region between 19 km and 14.25 km is divided into 23 layers 250 m in depth. This high resolution permits a high degree of precision in the calculation of particle bin accumulation rates.

The initial temperature profile for the present model run is the 22 UT sounding at Darwin on 22 January 1987 which is shown in Fig. 1. In the upper tropospheric region of interest above 10 km it is assumed that the air at the outset is saturated (with respect to ice) Above the temperature minimum the initial water vapor content is set to a constant 4 ppmv. Near the tropopause little or no vertical motion is present initially, although a moderate

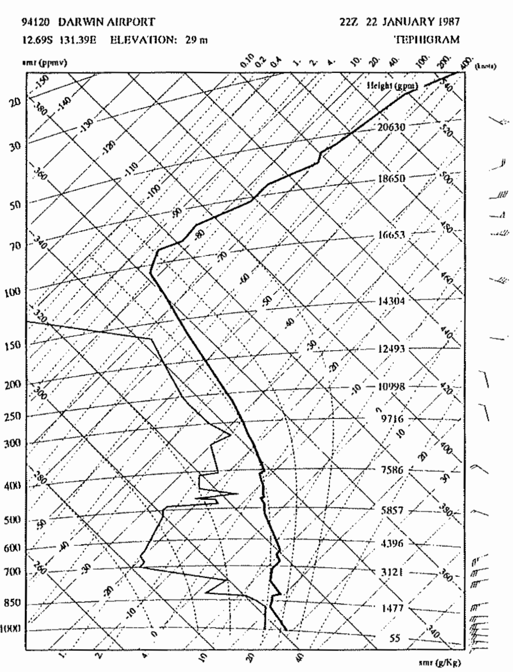

Fig. 1. Darwin sounding used as initial temperature profile.

amount of sinking (order 1 $cm\,s^{-1}$) is specified at 10 km which somewhat balances mid-tropospheric cooling.

An initial ice mass was introduced in a 3 km layer between 17 and 14 km. A log-normal distribution of ice particles was chosen with a mode radius at 15 μm. The integrated initial total ice water content was equivalent to 15 ppmv water vapor. This amount of ice is roughly equal to that seen at 15.25 km, the first ER-2 leg in STEP flight 006.

3. Results

Fig. 2 shows the evolution of the integrated ice crystal concentration for four times during the run: 0, 1.5, 5 and 10 hours. The initial cloud begins to spread both upward and downward almost immediately. The former may be due in part to a somewhat unrealistically large vertical eddy diffusion for the lower stratosphere, whereas the latter is due to the descent of larger particles. By 10 hours the lower edge of the cloud has descended to 9.5 km, a descent rate of 30 $cm\,s^{-1}$.

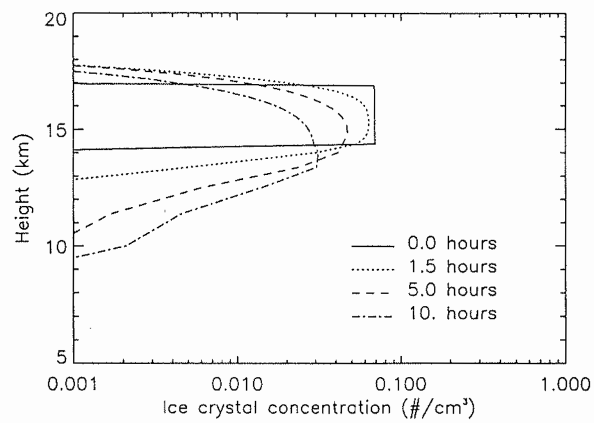

Fig. 2. Evolution of ice crystal concentration during 10-hour run.

The cloud produces substantial heating compared with the clear air values $\sim$ 0.5 K d^{-1}. The evolution of the heating profile is depicted in Fig. 3. The instantaneous heating rate at the initial time is over 10 K d^{-1}. As this

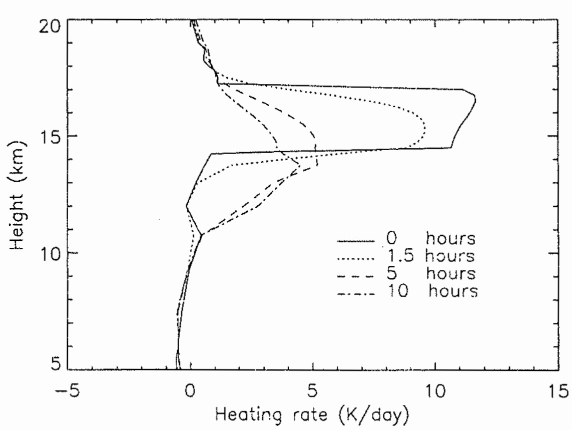

Fig. 3. Heating rate changes during run.

model atmosphere has a fixed vertical wind, the consequent warming tends to produce a negative feedback on the instantaneous heating. The consequent drying also enhances the sublimation of ice crystals in the strato-

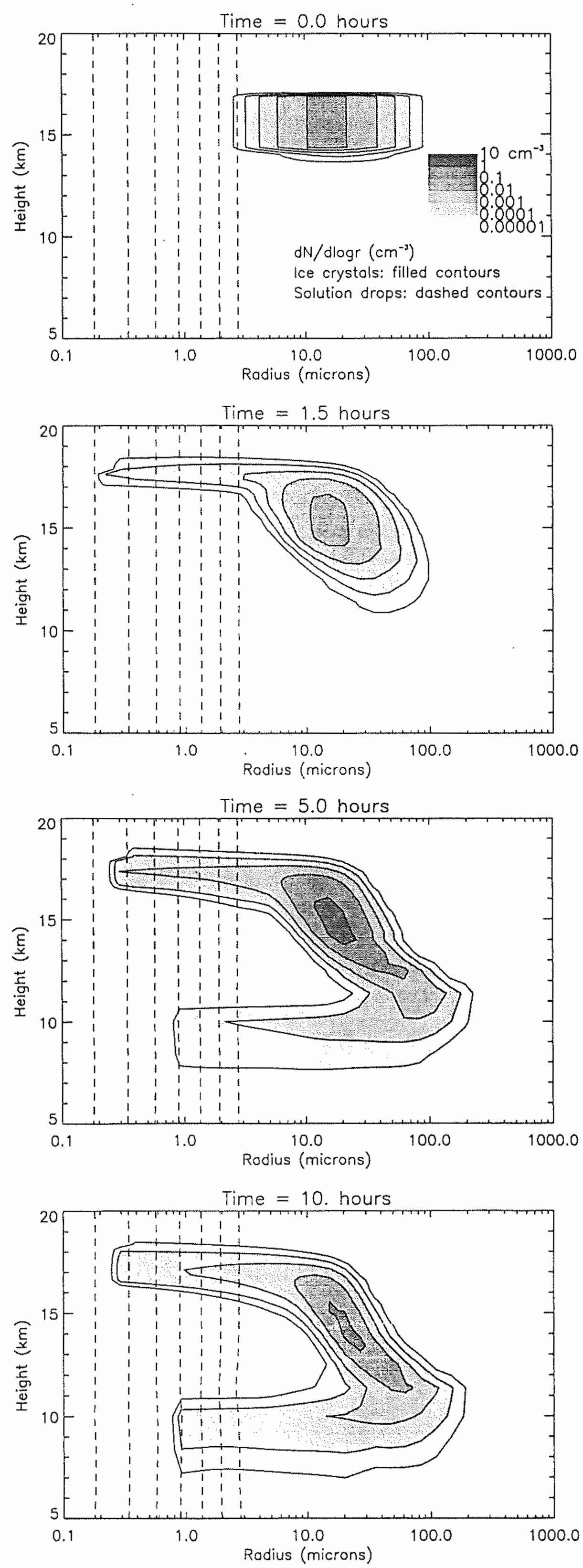

Fig. 4. Height-dependent evolution of ice crystal distribution during run.

spheric part of the cloud where it is substantially subsaturated initially. Despite the negative feedback however, the heating rate is still as large as 5 K/day at center of the sinking cloud by 10 hrs.

Fig. 4 shows the evolution of the ice water distribution over the course of the 10-hour run in height and size phase space. By 1.5 hours, the largest particles, i.e. those over 30 μm radius, have fallen between 1 and 2 km, a rate on the order of 100 cm s^{-1}. Nonetheless the particle density mode remains relatively stationary near 15 μm for the first 5 hours of the run. At 1.5 hours there is significant sublimation in evidence above the initial cloud top as particles are diffused upward, heated and slowly sublimated to smaller sizes. A similar processes has appeared below 10 km by 5 hours, reversing the growth of the falling particles above that level. The growth was caused by the particles encountering increasing water vapor in their descent.

4. Discussion

The primary idealization in the present model formulation is the specification of the vertical motion; there is no coupling of the vertical motion field to the diabatic heating resulting from the the presence of this rather thin cloud. In the vicinity of the real tropical tropopause, there is some stabilization evident as one passes from mesoscale convective regions out into relatively clear air, but the amount of warming here is excessive. Despite this shortcoming, the model demonstrates a remarkable persistence of very thin clouds near the tropical tropopause. If there is any substantial upward diffusion of ice particles into the stratosphere, these would rapidly sublimate and lead to a hydration of the lower stratosphere.

Acknowledgments: The first author is supported through a Cooperative Agreement between NASA Ames Research Center and the Space Physics Research Institute. Support for the second author at NASA Ames is provided through the Associateship Programs of the National Research Council.

References

Jensen, E.J., O.B. Toon, D.L. Westphal, S. Kinne and A.J. Heymsfield, 1992: Microphysical modelling of cirrus: Comparison with 1986 FIRE IFO measurements. Manuscript in preparation.

Toon, O.B., C.P. McKay and T.P. Ackerman, 1989: Rapid calculation of radiative heating rates and photodissociation rates in inhomogeneous multiple scattering atmospheres. *J. Geophys. Res.*, **94**, 16,287-16,301.

MICROPHYSICAL MEASUREMENTS IN CIRRUS CLOUDS FROM ICE CRYSTAL REPLICATOR SONDES LAUNCHED DURING FIRE II

Larry M. Miloshevich and Andrew J. Heymsfield
National Center for Atmospheric Research[1]
Boulder, Colorado 80307

and

Peter M. Norris
Scripps Institution of Oceanography, University of California, San Diego
La Jolla, California 92093

1. INTRODUCTION

The potential importance of cirrus clouds to the radiative properties of the atmosphere and to the global climate is becoming increasingly apparent (e.g. Ramanathan and Collins 1991). In response to the need for a better understanding of cirrus clouds, FIRE II (the First ISCCP Research Experiment, Phase II), conducted in southern Kansas during Nov. and Dec. 1991, employed a variety of aircraft, satellites, and ground–based remote sensors in an intensive study of cirrus cloud systems and their microphysical and radiative properties. One of the scientific goals of FIRE II is to improve the ability to retrieve cirrus cloud microphysical properties from remote sensors, which requires calibration of the remote measurements with simultaneous in–situ measurements. A related scientific problem concerns the so–called "small particle anomaly," wherein the small ice crystal sizes inferred from satellite measurements are not detected by in–situ aircraft instrumentation. Knowledge of cirrus ice crystal habits and size spectra are also necessary for cirrus cloud numerical modeling, especially radiative transfer calculations.

Balloon–borne formvar ice crystal replicators were launched during FIRE II to measure "vertical profiles" (in a Lagrangian sense) of cirrus microphysical properties, with emphasis on the detection of small ice particles. Replicator launches were timed to coincide with satellite overpasses, and during time periods when ground–based remote sensors and aircraft were operating. This paper will describe the design and operation of the ice crystal replicators, then present samples of replicator data for the purpose of assessing instrument performance in cirrus clouds.

2. INSTRUMENT PRINCIPLES AND DESIGN

Schaefer (1941) developed the formvar replication technique to capture and preserve detailed features of snowflakes, using a solution of formvar (polyvinyl formal) dissolved in ethylene dichloride. Particles falling onto a solution–coated slide or filmstrip are enveloped by the fluid, forming a detailed replica of the particle when the solvent evaporates and the plastic hardens. Several effective combinations of plastics and solvents have been investigated by Takahashi and Fukuta (1988). The use of formvar replication on a balloon–borne instrument (i.e. a "replicator sonde") was developed by Magono and Tazawa (1966) to study the vertical distribution of snow crystals up to the 500 mb level in a snow cloud. The fundamental design of our ice crystal replicator is based on that of Magono and Tazawa, with modifications to improve data quality and to allow the instrument to collect data at the high altitudes and low temperatures of cirrus clouds.

The replicator (Fig. 1) consists of an aluminum framework supporting a continuous 5 m loop of transparent 35 mm film, driven by a motor (labeled "A") at a rate of approximately 0.13 cm s^{-1}. The film is pre–coated with a 4% solution of formvar dissolved in chloroform, as discussed in Spyers–Duran and Braham (1967) in connection with an aircraft–mounted formvar replicator. During ascent on a balloon, chloroform is slowly released from a container ("B") onto the film, softening the formvar just prior to the exposure opening ("C") such that cloud particles entering the opening fall into the solution. The solvent subsequently evaporates, preserving a 3–D formvar replica of the cloud particle. A calibrated pressure switch ("D") activates the tape motion at a pre–determined level. The instrument is powered by a 9 V lithium battery which is encased in a water blanket and several layers of insulation ("E"), allowing the battery to supply power even at tropopause temperatures.

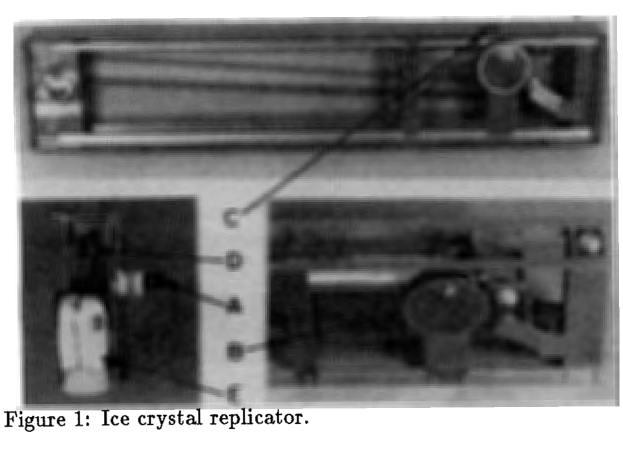

Figure 1: Ice crystal replicator.

[1] The National Center for Atmospheric Research (NCAR) is sponsored by the National Science Foundation.

3. INSTRUMENT DEPLOYMENT AND RETRIEVAL

The replicators were launched as part of a sounding "train" (Fig. 2), then tracked and retrieved by automobile using radio direction–finding (RDF) equipment. The balloon size and inflation were chosen to deliver an ascent rate of about 5 m s^{-1} and to burst at 11–13 km altitude, after which the train descends on a parachute. High resolution radiosonde data and position coordinates were obtained from the NCAR CLASS (Cross–chain LORAN Atmospheric Sounding System) facility.

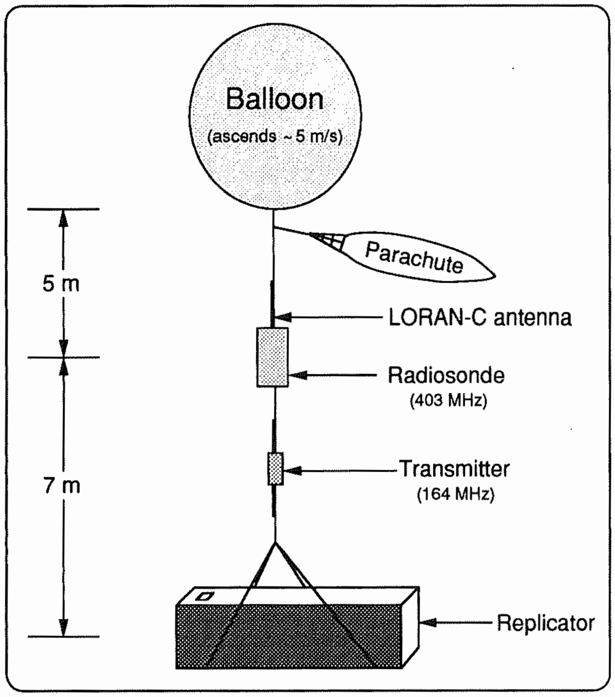

Figure 2: Schematic diagram of replicator sounding system.

Several means of tracking and locating the replicators were employed. The LORAN navigational capabilities of the radiosonde allowed the replicator landing position to be estimated within 2–4 km if the signal could be followed down to the horizon; however, frequent failure of the LORAN receiving antenna when the balloon burst often required a crude estimation of the landing position based on the wind profile measured during the ascent. At close range, detection of the radiosonde signal using RDF equipment aided in triangulation of the replicator position; however, this signal was often ineffective for tracking due to the limited useful lifespan of the radiosonde battery ($\leq$3 hours) and a tendency for the transmitted frequency to drift, as well as interference from other airborne radiosondes. An additional transmitter/receiver system was employed, of the type commonly used in the wildlife biology field to track animals in "capture and release" wildlife studies. This system uses transmitters with a battery life of several months and a very stable transmitted frequency, as well as an exceptionally sensitive receiver. These transmitters necessarily operate at low power and are therefore detectable only within 2–4 km of the replicator, although the signal is detectable over much larger distances if the transmitter is suspended even 1 m above the ground. The combination of these tracking techniques allowed us to recover all of the seven replicators which were launched for this research study.

4. MEASUREMENTS

An overview of the replicator data has thus far been performed for two of the seven research days using photomicroscopy. The replicators experienced no significant mechanical problems during the field experiment.

The general character and quality of the replicator data are seen in Fig. 3. Ice crystal habits are readily identifiable, and ice crystal structure is preserved in detail. The 3–D geometry of the rosette crystals is suggested even in the photographs (panel A), and can be seen in greater detail from the original data by finely adjusting the microscope focus to view different planes through a crystal. Ice crystal breakup upon impact with the filmstrip appears not to be a significant problem, even for the relatively large and fragile rosettes.

The replicator sondes provide a *continuous vertical record* of the cloud microphysics, in contrast to methods of obtaining similar microphysical measurements from aircraft (e.g. optical imaging devices such as the Particle Measuring Systems 2D–C probe, exposures of oil–coated slides, aircraft–mounted formvar replicators, or the new Video Ice Particle Sampler developed for FIRE II). The importance of obtaining measurements in the vertical is suggested by Fig. 4, which shows a distinct vertical variation in ice crystal properties measured near cloud top (panel A), in mid–cloud (panel B), and near cloud base (panel C). The 30–50 μm quasi–spherical cloud top particles are easily resolved against the "background noise" (which consists mainly of dust particles, scratches, and frost growth). Few of these particles are large enough to be imaged by a 2D–C probe. Ice crystal habit and structure are well defined in the mid–cloud replicas in Panel B. The 200 μm rosettes, if imaged by a 2D–C probe, would provide a poorly resolved and ambiguous picture of the ice crystal structure, and these rosettes would likely be crushed upon impact with an aircraft–mounted collection device. The resolution of the replication technique is sufficient to show the rounded corners of the cloud base particles in Panel C, which is clearly important in identifying these as partially sublimated ice crystals.

Neither the maximum resolution of the replicator sondes nor the minimum collectable particle size can be definitively stated, in part because all seven cases have not yet been evaluated. Examination of positions in the cloud above that represented by Fig. 4A (not shown) suggest that the smallest conclusively identifiable cloud particles collected by the replicator are approximately equal in size to the background noise, generally about 5 μm. Fig. 5, a microphysically more complex case where small ice crystals coexist with larger, partially sublimated ice crystals, shows that particles *at least* as small as 15 μm are collected and can easily be resolved against the background noise.

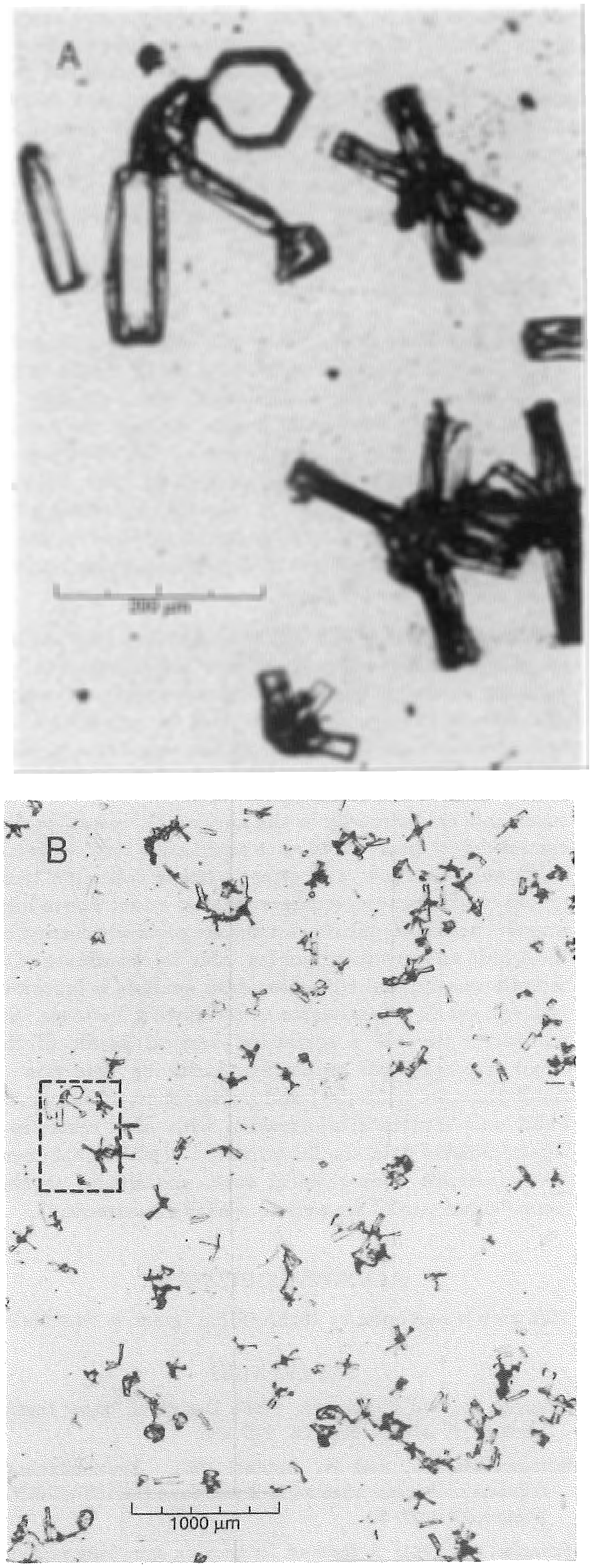

Figure 3: Photomicrographs of cirrus ice crystal replicas from Nov. 25, 1991. Panel A is a higher-magnification view of the dashed-box region in panel B.

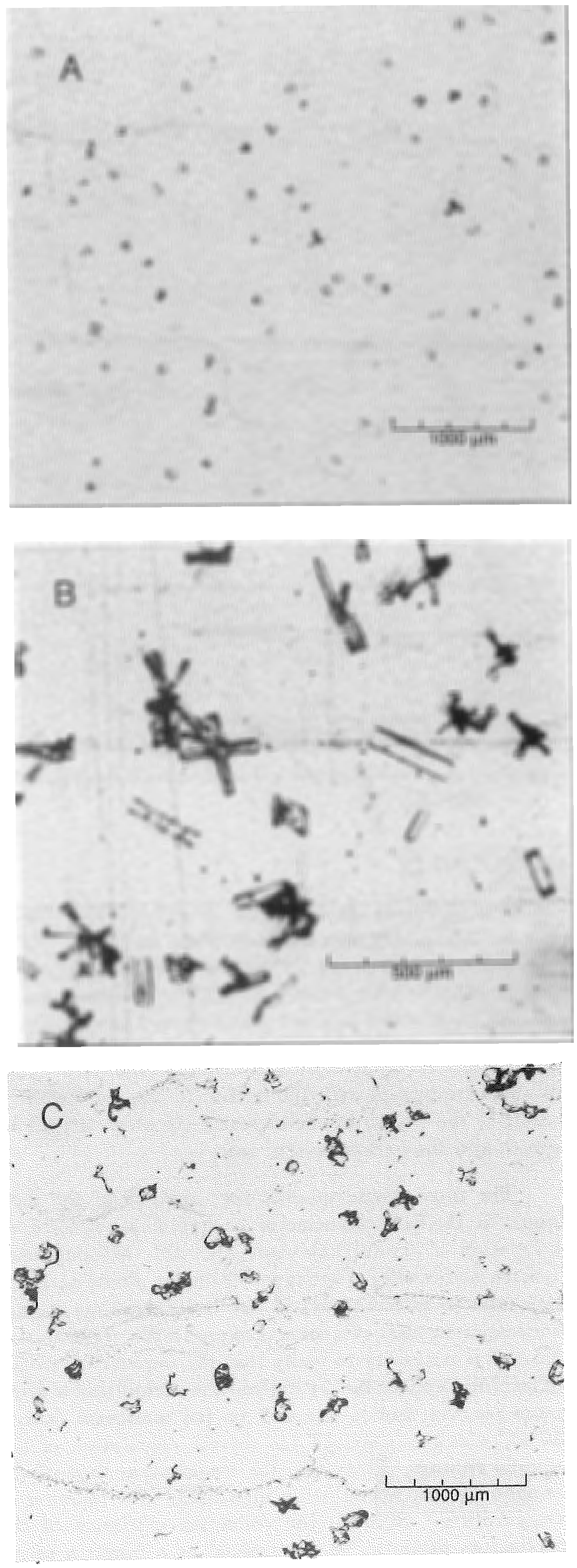

Figure 4: Photomicrographs of cirrus ice crystal replicas from Nov. 25, 1991.

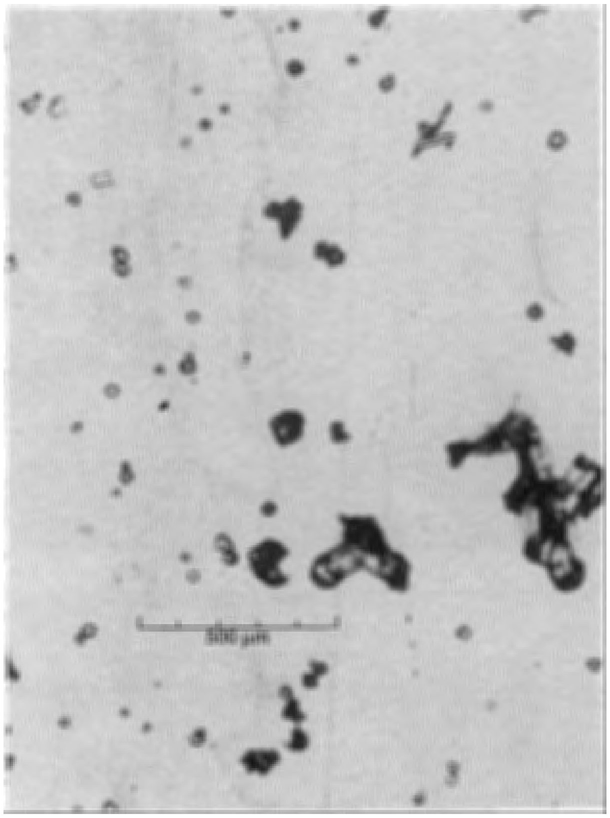

Figure 5: Photomicrograph of cirrus ice crystal replicas from Nov. 26, 1991.

5. DISCUSSION

The replicator data will be recorded onto videotape to facilitate more complete data analyses. The radiosonde measurements will then be correlated with the microphysical measurements, based on experimental determination of the replicator motor speed as a function of temperature. The microphysical measurements at a given position on the replicator film represent an average of cloud properties over 100–150 m in the vertical, as a result of the length of the exposure opening, the motor speed, and the balloon ascent rate.

The most useful quantitative analysis of the data would be the determination of ice crystal size spectra, as a function of crystal habit and altitude. Although size spectra are readily determined from the data, accurate estimates of uncertainties in the concentrations require addressing at least two aspects of replicator performance. First, it is necessary to verify that the formvar is capable of forming replicas for the entire time period that a given point on the film is exposed to the airstream (about 30 s), which is required for correct calculation of the sample volume. Therefore, the evaporation time of the applied solvent needs to be quantified as a function of temperature. Second, the collection efficiency of the replicators needs to be determined as a function of ice crystal size, which is a difficult task to consider theoretically given the complexity and turbulent nature of airflow through the instrument. Detailed measurements in a wind tunnel of the flow field near the replicator film are an important first step in quantitatively evaluating the collection efficiency. However, the demonstrated ability of the instrument to collect significant concentrations of *small* particles (e.g. about 400 L^{-1} of 30–50 μm particles in Fig. 4A) implies some non–zero, non–trivial collection efficiency for those sizes. Since collection efficiency increases with increasing particle size, it might be reasonable to assume a high collection efficiency for those cloud regions containing significantly *larger* particles.

6. CONCLUSIONS

The replicator data appear well suited to contribute to the scientific inquiries concerning cirrus clouds cited in the Introduction. Qualitatively, the data give a vertical record of ice crystal habits through the cirrus cloud layers sampled in this study, and the variation of microphysical properties with altitude in these clouds is apparent. Quantitatively, it may also be possible to determine vertical profiles of ice crystal size spectra from the replicator data if sources of measurement uncertainty can be adequately addressed.

The performance and utility of the replicator sondes can be judged by comparison with other methods of obtaining similar microphysical measurements. Aircraft have the advantages that they can be positioned in regions of particular interest, they can coordinate closely with ground–based remote sensors, and their data are readily processed by computer; however, aircraft measurements are primarily in the horizontal, optical probes cannot detect small particles or adequately resolve crystal habit and structure, and direct particle collection techniques may not preserve larger crystals intact due to high impact speeds. Replicator sondes are passively carried by the winds and are therefore less able to coordinate with remote sensors, and replicator data analysis is laborious and subject to quantitative uncertainties; however, the replicators provide a somewhat vertical profile of the cloud microphysical properties, including detection of small particles (<15 μm) and preservation of ice crystal habit and structure information with high resolution. The replicator data should provide a useful complement to the aircraft microphysical data, and should provide some "cloud truth" for remote sensor measurements.

ACKNOWLEDGEMENT

This work is supported by NASA/FIRE (grant # 1-98100-B).

REFERENCES

Magono, C., and S. Tazawa, 1966: Design of "snow crystal sondes." *J. Atmos. Sci.*, **23**, 618–625.

Ramanathan, V., and W. Collins, 1991: Thermodynamic regulation of ocean warming deduced from the 1987 El Niño. *Nature*, **351**, 27–32.

Schaefer, V., 1941: A method for making snowflake replicas. *Science*, **93**, 239–40.

Spyers–Duran, P., and Braham, R., 1967: An airborne continuous cloud particle replicator. *J. Appl. Meteor.*, **6**, 1108–13.

Takahashi, T, and N. Fukuta, 1988: Ice crystal replication with common plastic solutions. *J. Atmos. Oc. Tech.*, **5**, 129–135.

MODELING THE MICROPHYSICAL AND RADIATIVE PROPERTIES OF CIRRUS CLOUDS

David L. Mitchell

Desert Research Institute, Reno, NV, USA 89506

1. INTRODUCTION

Cirrus clouds are probably the least understood type of cloud in terms of their microphysics and life cycle. As stated in Stephens et al. (1990): "Characterization of the shape and size of ice crystals in terms of their environmental parameters continues to be a subject of extensive research in cloud physics and is a topic that, through the dependence of both cloud albedo and emittance on microphysical parameters, is also crucial to the cloud-climate problem." This article is intended to highlight some recent results where the microphysical properties predicted for a cirrus cloud case study are compared with the observed properties, namely maximum ice particle size and mean concentration. The second part of this article describes how the size distribution parameters predicted from the microphysical model are incorporated into analytical formulations for the extinction and absorption coefficients, and the single scatter albedo. These radiative properties are expressed as functions of wavelength, refractive index, size distribution parameters and ice crystal habit. A new formulation for the absorption coefficient is presented, based on both projected ice crystal area and mass, which predicts less absorption and greater single scatter albedos in the near infrared than standard treatments using equivalent area spheres.

2. MICROPHYSICAL MODEL AND CASE STUDY COMPARISON

The microphysical equations for a Lagrangian, time dependent, 3-dimensional snow growth model are described in Mitchell (1992), the first in a two part series on cirrus clouds, hereafter referred to as Part I. Part I builds upon the model of Mitchell (1991). The model predicts the evolution of ice particle size spectra in cirrus clouds in terms of the growth processes of vapor diffusion and aggregation, as well as the cloud updraft profile. This was done by deriving moment conservation equations from a form of the stochastic collection equation, and parameterizing the moment conservation equations. Size distributions were parameterized by the form

$$N(D) = N_o D^{\nu} \exp(-\lambda D), \qquad (1)$$

where λ and N_o are functions of the growth processes. Growth by diffusion and aggregation were formulated to depend on the percentages of spatial and columnar crystal habits at a given level in the cloud. When run in the 1-dimensional height dependent mode, model inputs consist of the vertical distribution of the ice water content (IWC), the temperature and pressure profiles and mean diameter at cloud top. Mass- and fallspeed-dimensional relationships for ice crystals were used to parameterize the moment conservation equations. Due to space limitations, the reader is referred to Part I and Mitchell (1991) for a description of the model.

The ice particle growth model was run in the steady state, height dependent mode in order to compare model predictions with the measured microphysical properties of a case study in Heymsfield (1975). Measured microphysical properties were transcribed from Fig. 10 in Heymsfield (1975), and were obtained during a downward spiral through a cirrostratus deck capping a winter cyclone. Ice particle sizes and concentrations were determined from an optical-array particle size spectrometer developed by Knollenberg (1970), where the minimum detectable size was about 140 μm and bin widths were 100 μm. Unfortunately, information on crystal habits was not given for this case study.

The cirrus cloud was assumed to consist of column and bullet ice crystals, and the corresponding mass-dimensional expression was taken from Heymsfield and Knollenberg (1972), having a coefficient and exponent of 0.000907 and 1.74 in cgs units. The fallspeed-dimensional relationship appropriate for cirrus clouds was taken from Kajikawa and Heymsfield (1989), with a coefficient and exponent of 172 and 0.25 in cgs units. Since size distributions were not plotted for this case study, the choice for the distribution dispersion parameter ν was ambiguous and a value of $\nu = 1$ was assigned to all spectra. The mean dimension $\bar{D}$ at cloud top was 0.016 cm, and cloud base and cloud top temperatures were -20°C and -45°C.

The vertical distribution of the IWC measured for this case study is shown by the dashed line in Fig. 1. The solid line is a curve fit used as model input. Although the lower three peaks of the curve fit coincide with the data, the upper two peaks of the curve fit do not coincide with the three smaller peaks in the data. Thus, correlation between model predictions and observations should not be expected in the upper cloud.

The measured maximum ice particle size is depicted by the short dashed line in Fig. 2. The solid line is predicted by the model and the long dashed line is for diffusional growth only, without aggregation. Maximum dimensions were predicted by the model as described in Mitchell (1991), where $[\lambda_e D_{max}]_o = 5$. Over the region where the IWC curve fit and data coincide, their is a good correspondence between predicted and observed values. Predicted and observed ice particle concentrations are compared in Fig. 3 by the solid and short dashed lines, respectively. The long dashed line is for individual ice crystals only (no aggregates). Again, correspondence between measured and predicted peaks in the upper cloud is not expected via Fig. 1. Ice crystal concentrations would be higher in the upper cloud if $\nu < 1$, which often occurs in regions with greater convection and higher ice crystal production rates (Herzegh and Hobbs 1985; Mitchell 1991). Enhanced convection and numerous small ice crystals impacted on replicators were reported in the upper cloud.

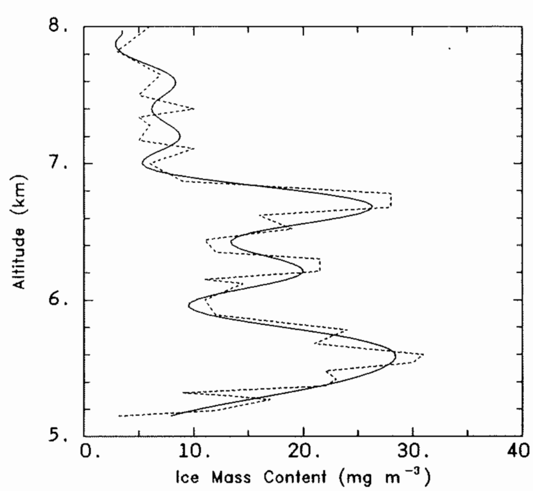

FIG. 1. Vertical distribution of the ice mass content for the cirrostratus case study in Heymsfield (1975). The short dashed line gives measured values. The solid line is a curve fit to the data, and serves as the primary model input.

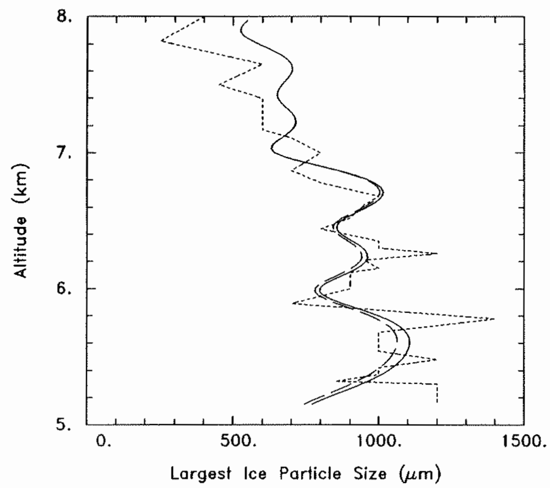

FIG. 2. Height dependence of the maximum ice particle size for the case study. The short dashed line is from aircraft measurements, the solid line is predicted by the model and the long dashed line is predicted for diffusional growth only.

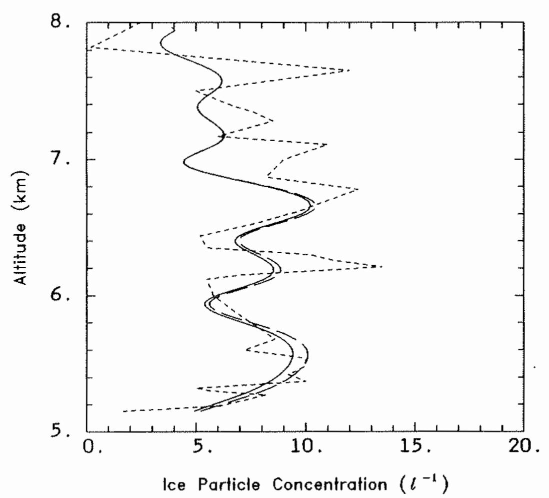

FIG. 3. Ice particle concentration profiles for the case study. The short dashed line indicates measured concentrations, the solid line is predicted by the model and the long dashed line is predicted for diffusional growth only, giving ice crystal concentrations (no aggregates).

3. MODEL SIMULATION

In this section, the potential effects of ice crystal habit on the evolution of ice particle size spectra is investigated. As discussed extensively in Part I, a transition in ice crystal habit often occurs in cirrus clouds between -40°C and -50°C, with T < -50°C characterized primarily by columns and bullets, and T > -40°C by bullet rosettes, side planes and other spatial crystal habits (Heymsfield and Platt 1984). Changes in crystal habit and their effect on the evolution of ice particle size spectra can be modeled using mass-dimensional relationships for various habits as described in Part I. Based on mass-dimensional expressions for spatial habits (Mitchell et al. 1990; Personne et al. 1991), a m-D exponent value of 2.6 was selected for spatial habits.

In Fig. 4 and 5, the case study is simulated by allowing only spatial crystal habits, such as bullet rosettes, to form below the -40°C level. This is shown by the long dashed line. The solid line is the same as the earlier simulation when only columnar crystals were allowed to form. Other than the change in crystal habit, all other conditions and parameters are identical between simulations. It is seen that in the mid-to-lower cloud, mean ice particle sizes in Fig. 4 are about 30% smaller when spatial habits dominate. The same region exhibits number concentrations in Fig. 5 which are over three times greater for the spatial habit simulation than the column simulation.

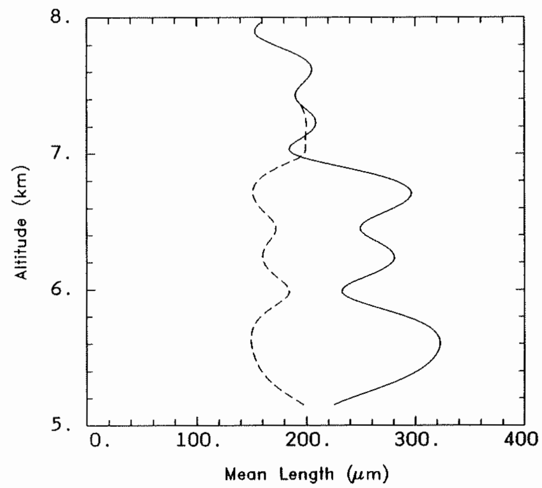

FIG. 4. Simulations of the case study. The simulation for when only columns form is given by the solid line, while the simulation for when only spatial crystal habits form below the -40°C level is given by the dashed line. Both lines are predicted mean sizes for ice particles, which include aggregates.

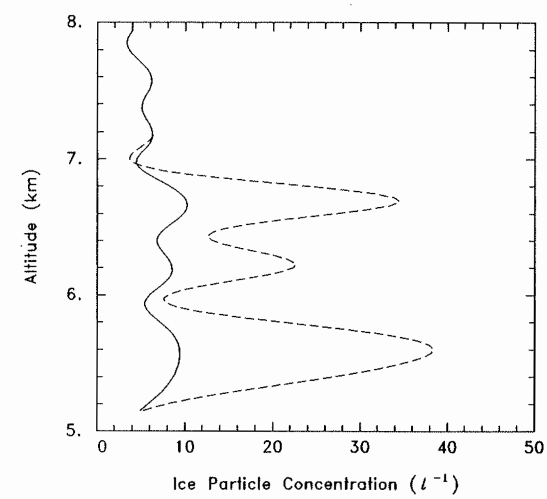

FIG. 5. Same as Fig. 4, except showing the predicted number concentrations for ice particles, which include aggregates.

4. CALCULATION OF RADIATIVE PROPERTIES

The formulations for the extinction and absorption coefficients described in this section are derived in the second of a two part series on cirrus clouds (Mitchell and Arnott 1992), hereafter referred to as Part II. The predicted ice particle size distribution parameters can be transformed into parameters for equivalent mass spheres as described in Part II, where the total number concentration remains constant. When the size parameter is >> 1 and the refractive index is near 1, anomalous diffraction theory (van de Hulst 1981) can be used to estimate the extinction coefficient for a distribution of equivalent mass spheres in terms of their size distribution parameters as

$$\beta_{ext,s} = \frac{\pi N_o \Gamma(\nu+3)}{2\lambda^{\nu+3}} + \mathrm{Re}\{\frac{\pi N_o \Gamma(\nu+2)}{q(\lambda+q)^{\nu+2}} + \frac{\pi N_o \Gamma(\nu+1)}{q^2}[(\lambda+q)^{-(\nu+1)} - \lambda^{-(\nu+1)}]\} \quad , \qquad (2)$$

where Γ denotes the gamma function, $q = i2\pi(n-1)/\Lambda$, n = complex index of refraction, Λ = wavelength and $i = (-1)^{1/2}$. Re indicates only the real part of the complex function is used. The s on β refers to equivalent mass spheres.

The projected area of a size distribution can be estimated as a function of crystal habit as follows. The projected area for a size distribution of columns is given in Part II as

$$A_{col} = \frac{0.0512 N_{o*}\Gamma(\nu_* + 2.414)}{\lambda_*^{\nu_*+2.414}} \quad , \tag{3}$$

and the projected area of a size distribution of bullet or column rosettes with 4 to 5 branches is estimated as

$$A_{ros} = \frac{0.00192 N_{o*}\Gamma(\nu_* + 1.828)}{\lambda_*^{\nu_*+1.828}} + \frac{0.0549 N_{o*}\Gamma(\nu_* + 2.414)}{\lambda_*^{\nu_*+2.414}} \quad , \tag{4}$$

where * denotes the actual size distribution for ice particles is used and units are cgs. Length-width relationships for columns (Auer and Veal 1970) and the fact that the average projected area of randomly oriented convex particles is 1/4 their total surface area was used in deriving (3) and (4). The overall projected area at a given level is weighted by the concentrations of columns and rosettes predicted in the model, giving

$$A_c = A_{col}\left(\frac{N_{col}}{N_c}\right) + A_{ros}\left(\frac{N_{ros}}{N_c}\right) \quad , \tag{5}$$

where N_c refers to the total concentration of ice crystals.

Once A_c is known, the extinction coefficient can be determined from the projected area ratio for distributions of ice particles and equivalent mass spheres. Thus, at a given level,

$$\beta_{ext} = \frac{A_c}{A_s}\,\beta_{ext,s} \quad , \tag{6}$$

where s refers to spheres and A_s is equal to the value of the first term in (1). This operation effectively transforms the extinction coefficient for a size distribution of equivalent mass spheres to the extinction coefficient appropriate for a corresponding ice crystal size distribution.

The absorption coefficient may also be formulated using anomalous diffraction theory, size distribution parameters, and the area ratio in (6), but in such a way that it depends on both the mass and projected area of an ice crystal size distribution. The latter is particularly important, since previous methods of calculating radiative properties in ice clouds generally assume equivalent area spheres, which overestimate the ice particle masses. If a wavelength exhibits strong absorption, absorption depends on projected area and equivalent area spheres are adequate. But in the near infrared, absorption is generally weak or moderate, and absorption depends mostly on particle mass. Thus, the use of equivalent area spheres will overestimate absorption in the near IR. As discussed in Pollack and Cuzzi (1980), when $\gamma n_i x < 1$ where x = size parameter = $\pi D/\Lambda$, n_i is the imaginary part of refractive index and γ is a constant to be determined (Pollack and Cuzzi assumed $\gamma = 2$), then absorption is proportional to the particles mass. When $\gamma n_i x > 1$, then the absorption coefficient, β_{abs}, is proportional to particle area. The quantity $\exp(-\gamma n_i x)$ is an indication of the amount of light transmitted through the particle. When most light can pass through the particle, $\exp(-\gamma n_i x) \to 1$. When little radiation can pass through the particle, $\exp(-\gamma n_i x) \to 0$. This functional behavior can be used to predict when absorption depends on either particle mass, particle area or both. As described in Part II, this relationship was combined with anomalous diffraction theory to formulate the absorption coefficient as

$$\beta_{abs} = \frac{\pi}{2} N_o\left[I_2 + \frac{A_c}{A_s}(I_1 - I_2)\right] \quad , \tag{7}$$

where

$$I_1 = \frac{\Gamma(\nu+3)}{2\lambda^{\nu+3}} + \frac{\Gamma(\nu+2)}{\epsilon g(\lambda+\epsilon g)^{\nu+2}} + \frac{\Gamma(\nu+1)}{(\epsilon g)^2}\left[(\lambda+\epsilon g)^{-(\nu+1)} - \lambda^{-(\nu+1)}\right] \quad , \tag{8}$$

$$I_2 = \frac{\Gamma(\nu+3)}{2(\lambda+g)^{\nu+3}} + \frac{\Gamma(\nu+2)}{\epsilon g[\lambda+g(1+\epsilon)]^{\nu+2}} + \frac{\Gamma(\nu+1)}{(\epsilon g)^2}\left\{[\lambda+g(1+\epsilon)]^{-(\nu+1)} - (\lambda+g)^{-(\nu+1)}\right\} \quad , \tag{9}$$

and where $g = \gamma\pi n_i/\Lambda$ and $\epsilon = 4/\gamma = 3.5714$. If we define $\beta_{abs,s}$ as the absorption coefficient for a distribution of equivalent mass spheres, then for strong absorption g >> 1, $I_2 \to 0$ and $\beta_{abs} \to (A_c/A_s)\beta_{abs,s}$. When g << 1, $I_2 \to I_1$ and $\beta_{abs} \to \beta_{abs,s}$. Absorption cross-sections calculated for columns using this new formulation were compared with those determined from an exact solution using anomalous diffraction theory in Part II. Using $\gamma = 1.12$, the relative error of the new formulation was < 1.4%.

The single scatter albedo can now be calculated as

$$\tilde{\omega}_o = 1 - \frac{\beta_{abs}}{\beta_{ext}} \quad . \tag{10}$$

6. RADIATIVE PROPERTIES OF CIRRUS CASE STUDY

a. Absorption and Single Scatter Albedo

Optical properties were calculated for the case study and were based on a wavelength of 2.2 μm, since it is a spectral band on the Landsat satellite, exhibits moderate absorption and has been used to infer particle sizes in cirrus clouds (Wielicki et al. 1990). Absorption coefficients are plotted in Fig. 6. The solid line is predicted by the new method described by (7). The dashed line gives β_{abs} for equivalent area spheres, $\beta_{abs,a}$, where $\beta_{abs,a} = \beta_{abs,s} \times A_c/A_s$. Recall $\beta_{abs,s}$ depends only on particle mass. It is seen that the equivalent area sphere (EAS) approach overestimates β_{abs} to a large degree when radiation is not strongly absorbed by ice.

Single scatter albedos are plotted in Fig. 7. The solid line gives $\tilde{\omega}_o$ for the new method, while the dashed line gives $\tilde{\omega}_o$ for equivalent area spheres. Differences in $\tilde{\omega}_o$ values are about 0.03 in the upper cloud and about 0.040 to 0.045 in the mid-to-lower cloud. Since radiation models are sensitive to $\tilde{\omega}_o$, these differences indicate the results from radiation models may depend considerably on what method is used to calculate $\tilde{\omega}_o$.

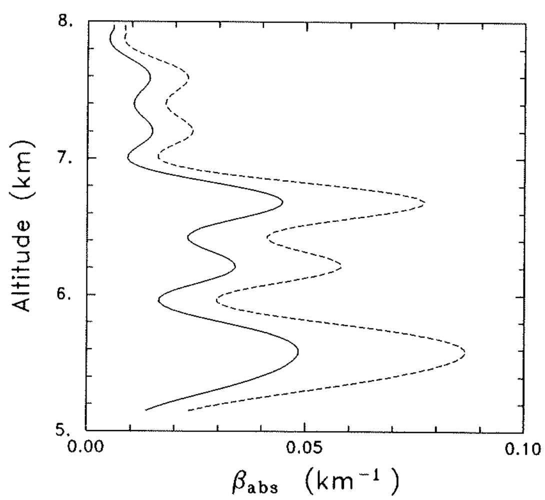

Figure 6. Vertical profiles of the absorption coefficient for the case study. The solid line is predicted by the new formulation. The dashed line is predicted for corresponding size distributions of equivalent area spheres.

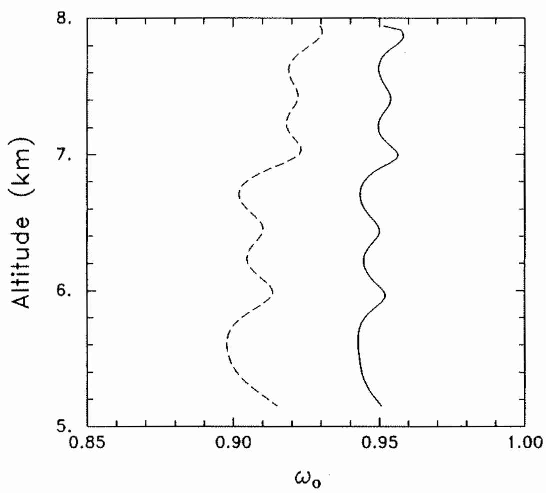

Figure 7. Vertical profiles of the single scatter albedo for the case study. The solid line is predicted by the new formulation. The dashed line is predicted for corresponding size distributions of equivalent area spheres.

b. Dependence of Extinction on Crystal Habit

Extinction for geometric optics depends on the projected area of a size distribution. As shown in Figs. 4 and 5, changes in crystal habit can change the evolution of size spectra, which results in changes in projected area. A shift toward smaller but more numerous ice crystals in the case study simulation, brought about by a transition to spatial habits, increased the projected area below the -40°C level relative to the simulation where only columns formed. Another factor which increased projected area was the crystal habits themselves, since (3) and (4) confirm the expectation that rosettes have more area per unit length than do columns.

Extinction coefficients for the case study are shown in Fig. 8. The simulation for column crystals only is described by the solid line, and the simulation with rosettes introduced below the -40°C level (about 7.3 km) is described by the dashed line. All other conditions are the same in both simulations. It is seen that the introduction of rosettes approximately doubled β_{ext} in the mid-to-lower cloud, giving a cloud optical depth of 2.07. When only columns were present, the optical depth was 1.27. Thus, the introduction of rosettes below the -40°C level increased the optical depth by 63%. Note that the IWC was not changed. Also, the single scatter albedo for the rosette simulation was considerably > $\tilde{\omega}_o$ when only columns form. Changes in crystal habit may evidently affect both b_{ext} and $\tilde{\omega}_o$ substantially.

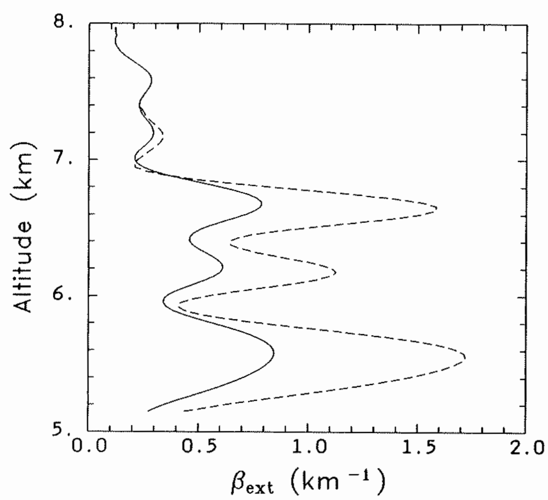

Figure 8. Vertical profiles of the extinction coefficient for the simulations shown in Figs. 4 and 5. The solid line gives extinction when only columnar crystals exist. The dashed line gives extinction when only bullet or column rosette crystals are produced below the -40°C level.

7. CLOSING COMMENTS

Since these results indicate that the optical properties of cirrus clouds depend on what type of crystal habits form in the cloud, more research is needed to determine what conditions promote different crystal habits. The treatment of absorption here differs substantially from the approach taken in other studies (i.e. Wielicki et al. 1990). If this approach were used in radiative transfer models, predicted reflectances in the near IR and solar albedos, based on observed ice particle size spectra, might yield better agreement with reflectances and albedos measured remotely.

Acknowledgments. This work was supported by NOAA grant NA16-RC0118-01, and this institution is thanked for its support. Suggestions from Dr. Pat Arnott regarding the formulation of the absorption coefficient are deeply appreciated.

REFERENCES

Auer, A. and D. Veal, 1970: The dimensions of ice crystals in natural clouds. **J. Atmos. Sci.**, 27, 919-926.

Herzegh, P.H. and P.V. Hobbs, 1985: Size spectra of ice particles in frontal clouds: Correlations between spectrum shape and cloud conditions. Q.J.R. **Met. Soc.**, **111**, 463-477.

Heymsfield, A.J., 1975: Cirrus uncinus generating cells and the evolution of cirriform clouds. Part I: Aircraft observations of the growth of the ice phase. **J. Atmos. Sci.**, 32, 799-808.

Heymsfield, A.J., and R.G. Knollenberg, 1972: Properties of cirrus generating cells. **J. Atmos. Sci.**, 29, 1358-1366.

Heymsfield, A.J., and C.M.R. Platt, 1984: A parameterization of the particle size spectrum of ice clouds in terms of the ambient temperature and the ice water content. **J. Atmos. Sci.**, 41, 846-855.

Kajikawa, M., and A.J. Heymsfield, 1989: Aggregation of ice crystals in cirrus. **J. Atmos. Sci.**, 46, 3108-3121.

Knollenberg, R.G., 1970: The optical array: An alternative to scattering or extinction for airborne particle size determination. **J. Appl. Meteor.**, 9, 86-103.

Mitchell, D.L., 1991: Evolution of snow-size spectra in cyclonic storms. II: Deviations from the exponential form. **J. Atmos. Sci.**, 48, 1885-1899.

Mitchell, D.L., 1992: A model predicting the evolution of ice particle size spectra and the radiative properties of cirrus clouds. Part I: Microphysics. Submitted in May to **J. Atmos. Sci.**

Mitchell, D.L., R. Zhang, and R.L. Pitter, 1990: Mass-dimensional relationships for ice particles and the influence of riming on snowfall rates. **J. Appl. Meteor.**, 29, 153-163.

Mitchell, D.L. and P.W. Arnott, 1992: A model predicting the evolution of ice particle size spectra and the radiative properties of cirrus clouds. Part II: Radiation. Submitted in May to **J. Atmos. Sci.**

Personne, P., Ch. Duroure, C. Isaka and H. Isaka, 1991: Geometrical Characteristics of bullet-rosette ice crystals. XX General Assembly IUGG Vienna, Austria, 11-24 August 1991. IAMAP Program and Abstracts, p.39.

Pollack, J.B. and J.N. Cuzzi, 1980: Scattering by non-spherical particles of size comparable to a wavelength: A new semi-empirical theory and its application to tropospheric aerosols. **J. Atmos. Sci.**, 37, 868-881.

Stephens, G.L., S. Tsay, P.W. Stackhouse, Jr. and P.J. Flatau, 1990: The relevance of the microphysical and radiative properties of cirrus clouds to climate and climate feedback. **J. Atmos. Sci.**, 47, 1742-1753.

van de Hulst, H., 1981: **Light Scattering by Small Particles.** Dover, 470 pp.

Wielicki, B.A., J.T. Suttles, A.J. Heymsfield, R.M. Welch, J.D. Spinhirne, M.C. Wu, D. O'C. Starr, L. Parker and R.F. Arduini, 1990: The 27-28 October 1986 FIRE IFO cirrus case study: Comparison of radiative transfer theory with observations by satellite and aircraft.

Doppler Radar Measurements of Ice Water Path and Vertical Velocities in Optically Thin Clouds: CLARET I and FIRE II Results

Taneil Uttal[1], Sergey Y. Matrosov[2], Jack B. Snider[1], Robert A. Kropfli[1]

[1]National Oceanic and Atmospheric Administration
Environmental Research Laboratories/WPL
325 Broadway
Boulder, Colorado 80303

[2]Cooperative Institute for Research on Environmental Science
University of Colorado/NOAA/WPL
Boulder, Colorado 80303

1. INTRODUCTION

Since 1989 the NOAA Wave Propagation Laboratory (WPL) has been using cloud radars to detect and measure optically thin clouds that have significant effects on the global radiation budget. Studies that have traditionally been addressed with optical lidars can often be significantly augmented by the use of microwave radars. Two field experiments are good examples of this: The Cloud Lidar and Radar Exploratory Tests (CLARET I, Eberhard et al., 1990) and the First ISCPP Regional Experiment II (FIRE II, NASA, 1991).

This paper will highlight the observational results of radar-derived ice water path (IWP) and its effect on downward infrared fluxes. These observations are then compared to theoretical calculations of this relationship for different mean ice particle diameters. We will also present some preliminary measurements of vertical velocities [w (air motion) - v_t (particle terminal velocity)] obtained with a Doppler radar with a theoretical accuracy of ± 2 cm s^{-1}. Companion papers in these proceedings that also document radar results from the CLARET and FIRE projects are Matrosov et al. 1992, and Intrieri et al., 1992.

2. BACKGROUND

The ice water path is a radiatively important parameter of cirrus clouds that has been difficult to measure. This quantity is of considerable importance as modeling and observational work has determined that ice mass content (IMC) is a critical ingredient in parameterizing cloud absorption, optical depth, albedo, and emissivity. IMC has been shown to be an highly variable quantity, which typically ranges over four orders of magnitude in cirrus clouds (Dowling and Radke, 1990), with correspondingly large variations in IWP.

One of the simplest methods for measuring IWP involves the development of an empirical relationship between IMC and a second more easily observed quantity such as radar reflectivities (Heymsfield, 1977 and Sassen, 1987). This paper utilizes the empirical relationship developed by Sassen which is the reflectivity-mass (Z-IMC) relationship tailored most specifically for all-ice cirrus type clouds.

3. THE EXPERIMENTS

In fall 1989 the WPL conducted the CLARET experiment near Boulder, Colorado. The purpose of this experiment was to observe cirrus clouds with vertically pointing remote sensors operating simultaneously at different wavelengths. This study utilized data from a 3.2 cm radar, a three-channel radiometer (20.6, 31.65, 90.0 GHz) and a narrow field-of-view infrared (IR) radiometer (PRT-5) with a 9.95-11.43 µm narrow band filter. The nearest rawinsonde site was the Denver NWS office (35 km south) with the normal 12 hour release schedule. A primary goal of the experiment was to improve and expand techniques for observing cirrus cloud properties using remote sensors singly and in combination. In particular, we were testing radar data processed with long dwells to improve our ability to detect non-precipitating optically thin cirrus clouds.

The most recent cirrus experiment, FIRE II, was coordinated by NASA and was conducted in Coffeyville, Kansas during the winter of 1991. This large multi-agency program included numerous ground-based remote sensors, instrumented aircraft and satellite observations. WPL provided an 8 mm (35 GHz) wavelength cloud sensing Doppler radar, a 10.6 µm Doppler lidar, a three channel microwave radiometer, a PRT-5, a RASS system and wind profilers. Although a large fraction of the time was spent with all instruments pointed vertically, off-vertical scans were routinely performed by the radar and lidar to provide wind profiles and vertical cross-sections of the nearby cirrus clouds. The 8 mm radar (Kropfli, et al., 1990) operates at a wavelength which provides of optimum observations of cirrus type clouds and an excellent data set was collected. Operating characteristics are summarized in Table 1.

FREQUENCY	34.6 GHz (Wavelength=8.7mm)
PEAK POWER	85 KW
SENSITIVITY	-30 dBZ at 10 Km range
BEAM WIDTH	.5 deg
PULSE WIDTH	.25 µs (37 m)
PULSE PERIOD	Period between pulse pairs variable: 625 to 2500 µs
RANGE GATES: NO. AND SPACING	328, (n*37.5) meters where n=1,2,3...
PARAMETERS MEASURED	Reflectivity, Doppler Velocity, Spectral Width, Depolarization Ratio, Normalized Coherent Power

Table 1. WPL Cloud Radar Characteristics

4. IWP CALCULATIONS

a. Calculation of IMC from radar reflectivity

Sassen (1987) has developed an equation relating radar reflectivities to IMC. Ice mass contents and radar reflectivities were calculated based on the size spectra and concentrations of the particles precipitating to the ground from polar ice clouds. The resulting Z_i (gm^{-3}) - IMC (mm^6m^{-3}) relationship

$$IMC = 0.037 Z_i^{0.696} \qquad (1)$$

was considered to be applicable to cirrus clouds based on the thermodynamic similarities between the two types of clouds. Since radar reflectivities are traditionally calculated using the dielectric constant for water, we have corrected our equivalent reflectivity factors to utilize the dielectric constant for ice ($Z_i = 5.3Z_e$) as is appropriate for the observation of predominantly ice clouds. Heymsfield (1977) has also developed a Z_i - IMC relationship for ice clouds based on data collected by aircraft and radar, and both Z_i - IMC relationships are shown in Figure 1. The relationships show good agreement, especially for ranges of Z_e between -25 and -5 dBZ which are within typical observed values for cirrus clouds.

Values of IMC are integrated through the cloud depth to obtain IWP.

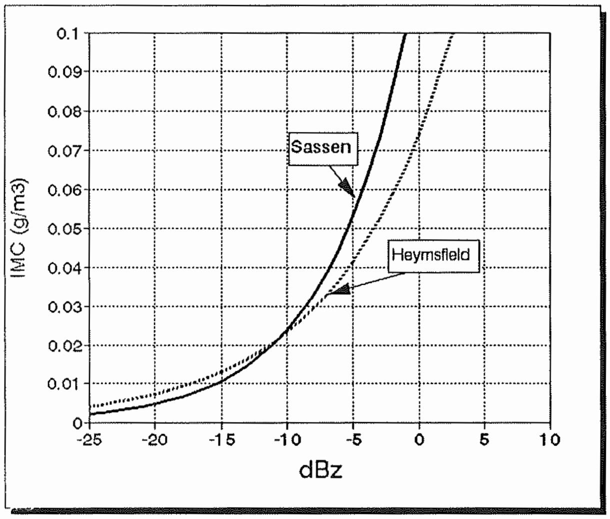

Figure 1. Z_e-IMC relationships from Sassen (1987) and Heymsfield (1977).

b. Theoretical calculations of IWP-Brightness Temperature Relationships.

A two-stream radiative transfer model was used to calculate brightness temperatures of cloud thermal radiation in the λ = 10-11.5 μm region. The details of this model are described by Matrosov et al., 1992. The model treats cirrus particles as equal-volume spheres and used Mie theory for calculations of absorption and scattering characteristics of the cloud. This approach is justified in part because cloud particles scatter radiation mostly in the forward direction when particle sizes are small compared to the wavelength of the incident radiation, and Mie theory is a reasonable approximation for the forward scattering processes (Bohren, 1991).

Atmospheric transmittance and background clear sky radiation were used to correct cloud base brightness temperatures to surface values. Boundary conditions were specified by cloud base and surface temperatures measured with rawinsonde. In the direct solution of this equations, IWP is the independent variable with values being adjusted by changing particle concentrations for different fixed values of mean particle size.

5. RESULTS

a. October 4 1900-2130, 1989 (CLARET I) IWP - IR Relationships

Figure 2 shows a time series plot of cloud boundaries from radar (2a), integrated water vapor from three-channel radiometer (2b), integrated liquid water from three-channel radiometer (LWP) (2c), IWP from radar (2d), and IR cloud brightness temperatures from PRT-5 (2e). Gaps occurred in the radar data when the radar was performing other kinds of scans. Radiometric integrated liquid was quite variable in this cloud, varying from 0 to 0.16 mm. IWP parameterized by radar reflectivity was also variable, ranging from 10 to 170 gm^{-2}. Scatter plots of cloud brightness temperature vs. cloud base height and cloud thickness show large scatter.

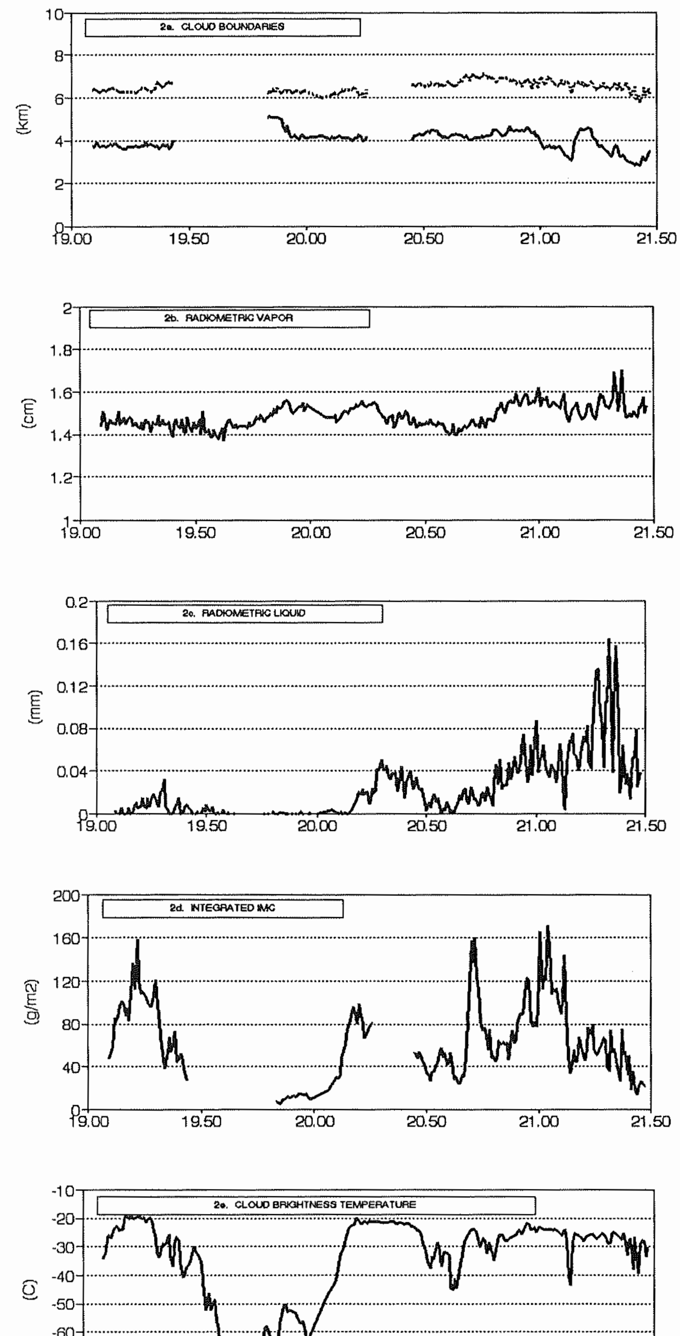

Figure 2. Time series plot of cloud boundaries from radar (2a), integrated water vapor from three-channel radiometer (2b), integrated liquid water from three-channel radiometer (LWP) (2c), IWP from radar (2d), and IR cloud brightness temperatures from PRT-5 (2e).

Figure 3, however, shows a plot of cloud IR brightness temperature vs. the IWP parameter calculated from radar reflectivities using (1). All time periods with LWP > 0.01 mm have been removed from this data set, therefore the remaining data points show the relationship between cloud brightness temperature and IWP when the cloud was strictly ice. Figure 3 also has curves from the theoretical calculations of cloud IR brightness temperature vs. IWP for three different values of median particle diameter, 120 µm, 170 µm and 200 µm. This result, combined with the observations, would suggest that the particles in this cloud had median diameters of about 170 µm.

The most difficult aspect of the radar vertical velocity estimates is that measurements combine effects of w and V_t. We are presently devising methods to correct the vertical velocity measurements for V_t using radar reflectivities.

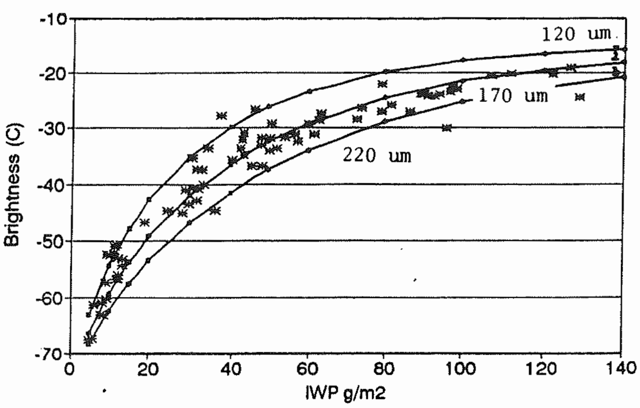

Figure 3. Observed cloud brightness temperatures vs. IWP (*) overlayed with theoretical curves of cloud brightness temperature vs. IWP for median particle diameters of 120 µm, 170 µm, and 200 µm (solid lines).

b. *November 17 1604-1630 1991 (FIRE II) Measurements of Vertical Velocities*

During the FIRE experiment the 8.66 mm radar pointed vertically for extended observations of cirrus clouds with the antenna fixed and a pulse-pair estimate of the Doppler velocity was performed. For strong signal-to-noise ratios that we observed in FIRE, the uncertainties of the Doppler velocity estimate can be expressed as

$$sd(\hat{v}) = \sqrt{\frac{\sigma_v \lambda}{(8MT_s\sqrt{\pi})}}$$

(Doviak and Zrnic, 1984)

where σ_v = Doppler velocity spectrum width, λ = radar wavelength, M = # of samples, and T_s = Pulse Repetition Time. For the FIRE processing we have used 3000 samples, and T_s = 1000 µs (resulting in a dwell of 3 s). We can assume σ_v = 1 ms^{-1} as an upper bound for most cirrus clouds which results in a standard deviation of the velocity estimate of less than 2 cm s^{-1}. A time series of velocities at a single range gate within a cirrus cloud is shown in Figure 4. This figure indicates high frequency oscillations with periods on the order of 1-2 minutes, with a suggestion of a lower frequency oscillation with a period of about 18 minutes. It will be necessary to look at longer time series with Fast Fourier Transform analysis to quantitatively define the observed periodicities.

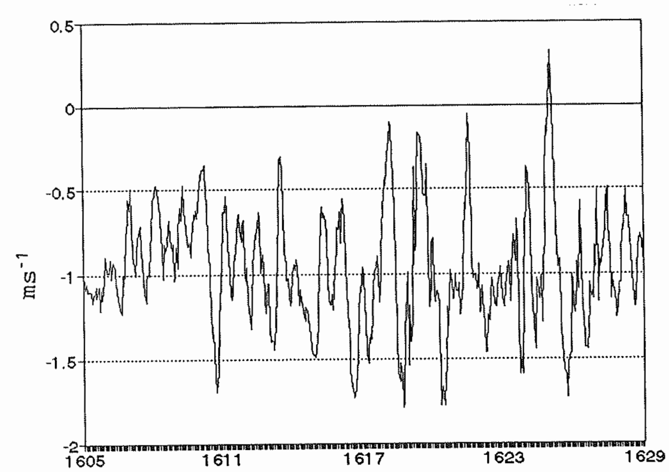

Figure 4. 24 minute time series of radar measured Doppler velocities (w - V_t) at one range gate within a cirrus cloud on November 17, 1991.

6. CONCLUDING REMARKS

These results demonstrate that radar is useful tool in the observation of optically thin clouds. Integrated radar reflectivities have been interpreted as a measure of cloud IWP through an empirical Z_i-IMC relationship developed by Sassen, 1987. In the observed cloud, this measured quantity appears to be the primary control on the downwelling IR radiation measured at the ground dominating the effects of cloud geometrical thickness or cloud base height.

This result has been also suggested by Ebert and Curry (1992), who examined the effects of particle size and IWP on shortwave reflectivity and longwave fluxes. Their modeling results indicate that reflectivity, transmissivity and emissivity all vary significantly as a function of IWP and ice crystal effective size. However, changes in ice crystal effective size were more dominant in altering the shortwave reflectivity, while changes in total IWP were the primary control in determining the values of longwave fluxes. It is also of note that over a relatively short time, the cloud demonstrated a wide variation of IWP values and resulting values of downward IR fluxes, despite the fact that cloud boundaries were quite stable.

Radar measurements of vertical velocities from the FIRE II data sets show interesting periodicities, indicating that it will be possible to determine high resolution temporal and spatial characteristics of the cloud dynamics with great precision.

7. ACKNOWLEDGEMENTS

The authors wish to thank the many people involved with the collection and processing of the data for the FIRE and CLARET projects. These include C. Clark, J. Gibson, B. Bartram, E. Ash, M. Jacobson, L. Church, B. Martner, and B. Orr. W. Eberhard coordinated the CLARET I project and D. McDougal and D. Starr coordinated the FIRE II project. Partial funding for CLARET I was provided by DOE/ARM under grant DE-AI06-91RL12089 Earth Science and Applications Division and partially by NASA #4020-CL-378. FIRE was partially funded by the NOAA Climate and Global Change program.

8. REFERENCES

Bohren, C.F., and S.B. Singham, 1991: Backscattering by Nonsperhical Particles: A Review of Methods and Suggested New Approaches, J. Geophys. Res., 96, No.D3, 5267-5277.

Doviak, R.J. and D.S. Zrnic, 1984: Doppler Radar and Weather Observations, Academic Press, Inc.

Dowling, D.R. and L.F. Radke, 1990: A Summary of the Physical Properties of Cirrus Clouds, J. Appl. Meteor., 29, 970-978.

Eberhard, W.L., T. Uttal, J.M. Intrieri, and R.J. Willis, 1990: Cloud Parameters from IR Lidar and other Instruments, CLARET Design and Preliminary Results, Preprints of the 7th Conf. of Atmos. Radiation, July 23-27, Amer. Met. Soc., San Francisco, California.

Ebert, E.E., and J.A. Curry, 1992: A Parameterization of Ice Cloud Optical Properties for Climate Models, J. of Geophy. Res., 97, 3831-3836.

Heymsfield, A.J., 1977: Precipitation Development in Stratiform Ice Clouds: A Microphysical and Dynamic Study, J. Atmos. Sci., 34, 367-381.

Intrieri, J.M., W.L. Eberhard, J.B. Snider and T. Uttal, 1992: Multi-Wavelength Observations of a Cirrus Cloud Event from FIRE II: Preliminary Lidar, Radar and Radiometer Measurements (these proceedings).

Kropfli, R.A., B.W. Bartram, and S.Y. Matrosov, 1990: The Upgraded WPL Dual-Polarization 8.6 mm Doppler Radar for Microphysical and Climate Research. Preprints of the Conf. on Cloud Physics, July 23-27, Amer. Met. Soc., San Francisco, California.

Matrosov, S.Y., T. Uttal, J.B. Snider, R.A. Kropfli, 1992: A Technique to Estimate Cirrus Cloud Particle Sizes and Concentrations from IR Radiometer and Radar Measurements (these proceedings).

NASA, 1991: FIRE Cirrus Intensive Field Observations -II: Operations Plan, FIRE Project Office and FIRE Cirrus Working Group, NASA/LARC, 116 pp.

Sassen, K., 1987: Ice Cloud Content from Radar Reflectivity, J. Atmos. Sci., 26, 1050-1053.

Multi-Wavelength Observations of a Cirrus Cloud Event from FIRE II: Preliminary Lidar, Radar, and Radiometer Measurements

J. M. Intrieri[1], W.L. Eberhard[2], J. B. Snider[2], and T. Uttal[2]

[1]Cooperative Institute for Research in Environmental Sciences, Boulder, CO, USA 80309

[2]NOAA/Wave Propagation Laboratory, Boulder, CO, USA 80303

1. INTRODUCTION

Cirrus clouds present a tough problem for modelers. They are difficult to understand theoretically because they are composed of ice crystals in a myriad of sizes and complex shapes. Insitu measurements are expensive and problematic because cirrus reside at high altitudes, typically 7 to 11 km above the surface. Because cirrus can both trap outgoing IR (infrared) radiation and reflect incoming shortwave radiation, they act to significantly modulate atmospheric radiation. Thus, knowledge of cirrus characteristics is important to understanding any cloud feedback mechanisms during a climatic variation (Stephens et al., 1990).

In the First ISSCP Regional Experiment - phase II (FIRE II) a unique and comprehensive data set was collected on the radiative, dynamical, and microphysical properties of cirrus clouds. FIRE II, held in Coffeyville, Kansas from 13 November to 8 December 1991, focused on obtaining multi-wavelength ground-based remote sensor observations of continental cirrus clouds supported by aircraft and satellite. In this paper, an example of measurements obtained by four remote sensors from NOAA's Wave Propagation Laboratory (WPL) is presented to illustrate how multiparameter information can be utilized to study the radiative forcing of cirrus clouds. This particular event progressed from clear sky in the morning, to high, thin cirrus, which advected in from the southwest. The end of the case study was characterized by middle and low clouds .

2. REMOTE SENSORS

Pertinent specifications for the remote sensors used in this study are listed in Table 1. The majority of data taken during FIRE II were obtained with the sensors staring vertically in order to observe the clouds advecting overhead and to establish a long and consistent time series of measurements. Ground-based remote sensor measurements have many advantages for observing the radiative properties of clouds. They are not hindered by satellite-related problems such as contaminated and partially filled pixels or the inability to unambiguously detect optically thin clouds. The lidar and radar provide range-gated information. Virtually unlimited operating lengths provide statistical information that is easily obtained unlike radiation measurements from aircraft which are temporally and spatially limited.

3. OBSERVATIONS

On 26 November 1991, three distinct periods of cirrus cloud backscatter were observed from the CO_2 lidar and the K_a-band radar returns:

1. Lidar backscatter returns with no corresponding radar returns.
2. Lidar and radar backscatter returns in agreement on cloud boundaries.
3. Radar returns with significant lidar signal attenuation.

Representative examples of measurements from each period are illustrated in Figs. 1-3, respectively. Each figure corresponds to an 8.5 min time series showing (a) the 8.66 mm radar reflectivity field (dBZ_e), (b) the CO_2 lidar signal backscatter field (dB), (c) cloud brightness temperature (°C) and integrated liquid water amounts (mm) from the IR and microwave radiometer, respectively, and (d) effective radius (μm) estimates (not shown for period 1) from a synthesis of the lidar and radar backscatter values.

Effective radii are estimated from Mie theory scattering calculations of radar and lidar backscatter returns computed for a cirrus cloud composed of ice spheres in a modified gamma distribution. These are then compared to the observed backscatter returns from each instrument to yield estimates of effective radius (Intrieri et al. 1991).

Table 1.

Instrument	Wavelength	Temporal/Spatial Averaging	Comments
CO_2 lidar	10.6 μm	4 s, 75 m	backscatter, velocity, .005° beamwidth
K_a radar	8.66 mm	3 s, 37.5 m	reflectivity, velocity, .8° beamwidth
Infrared radiometer	10.7 μm bandwidth	30 s, column integrated	brightness temperature, 2.5° FOV*
Microwave radiometer	20,31,90 Ghz	30 s, column integrated	liquid water, precipitable water, vapor, 2.5° FOV*

(* Field of View)

The lidar/radar method is currently the only technique that produces range-resolved (75 m) estimates of cloud particle sizes.

Period 1. At 1500 UTC the skies over the experiment site were visually clear, no corresponding lidar or radar cloud returns were observed. The first cloud return was detected at approximately 1615 UTC, was seen only by the lidar at 10 km AGL, and was approximately 200 m deep. Inspection of an all-sky camera video taken between 1600 and 1730 UTC, revealed that the clouds were clearly visible and extensive but appeared thin with the blue sky visible behind them. At 1708 UTC the cirrus cloud was located between 8.9 and 9.75 km (Fig. 1b) with no corresponding radar returns (Fig. 1a), thus no effective radius time series could be computed. The IR radiometer indicated a temperature response of ~ -72.5° (Fig. 1c), 1.5° warmer than the clear sky reading taken earlier. However, this warming may also be a result from the air temperature warming as the day progressed.

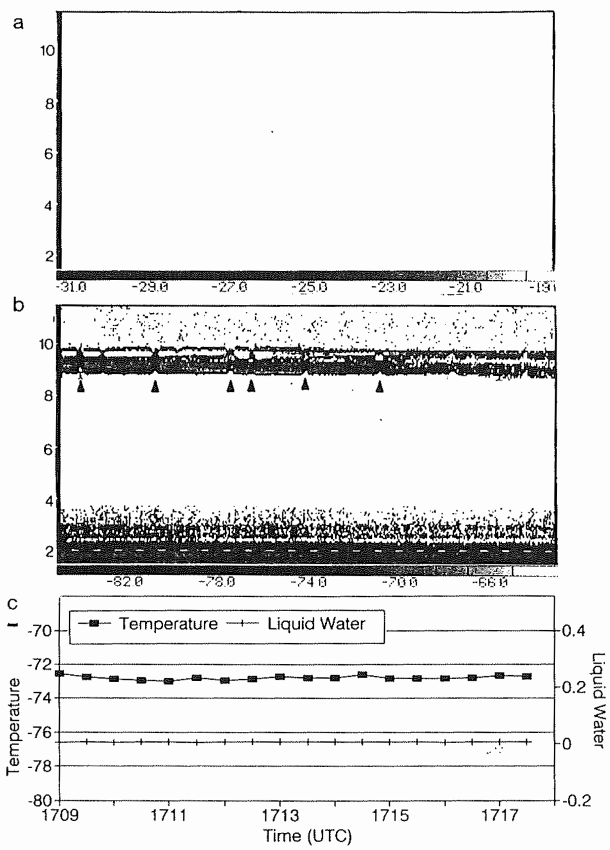

Fig. 1. 8.5 min time-height series from 1708 to 1717 UTC of (a) K_a band radar reflectivity (dBZ_e), (b) CO_2 lidar backscatter (dB), (c) radiometer brightness temperature (°C) and liquid water (mm) for period 1. All heights in km above ground level. Arrows in panel (b) indicate times when laser scanned off-vertical.

The enhanced region of backscatter in the early part of the lidar time series is due to specular reflection caused by aerodynamically oriented hexagonal plates or needles acting as tiny mirrors producing greater backscatter returns when the lidar beam is pointed vertically (Eberhard and Post, 1991). During the FIRE II experiment the laser beam was "rocked" off-vertical by 10° in order to discern times when specular reflection occurred. The off-angle instances are labeled with arrows in Fig. 1b. It is evident that the backscatter increases by ~ 6 dB between 89° and vertical. Specular reflection is not as strong in the latter half of this time series; however, it does reappear sporadically throughout all periods of this case study.

Period 2. The first cirrus cloud return detected by the radar occurred at 1735 UTC between 9 and 10 km AGL. The cirrus base gradually lowered to 8.25 km AGL by 1815 UTC as shown in Figs. 2a and b. There is fair correspondence between the radar and lidar backscatter fields at this time with the lidar detecting a higher cloud top and intra-cloud regions presumably containing particle regions where the radar shows no return signal. Specular reflection is still apparent especially at the end of the time series. The IR radiometer indicates a brightness temperature of -70 to -66°C (Fig. 2c) which is an average of 5 °C greater than the temperatures observed during period 1.

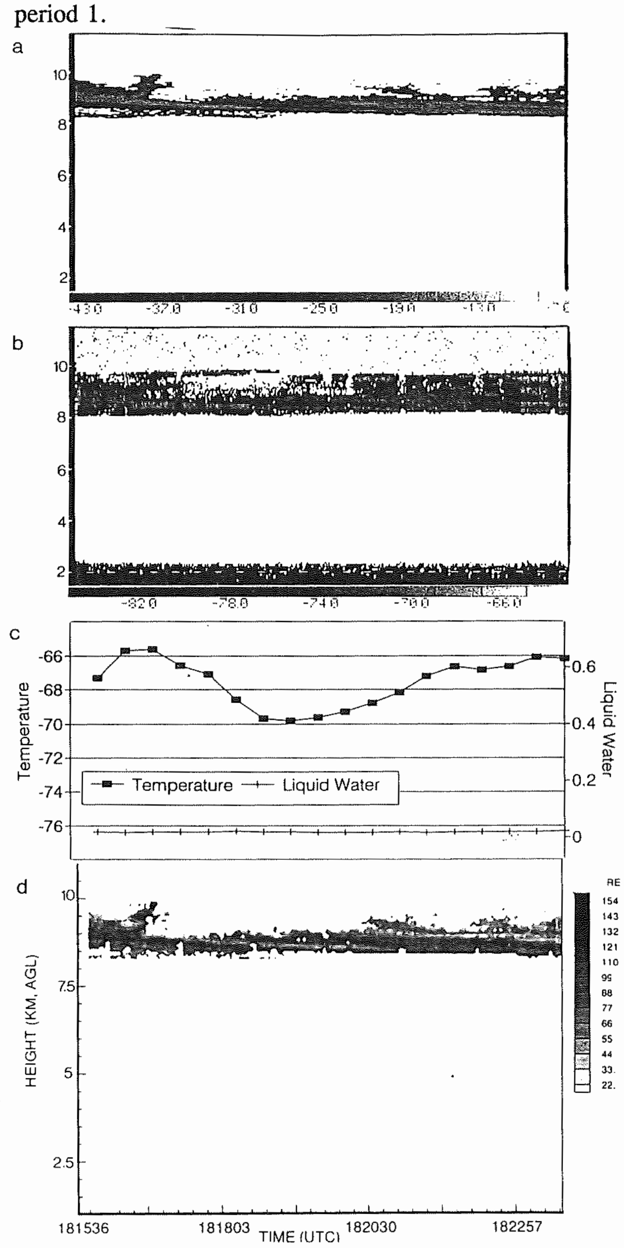

Fig. 2. As in Fig. 1 with (d) derived effective radius (μm) for 1815 to 1824 UTC, period 2.

Period 3. In the 2 h that elapse between periods 2 and 3, the cirrus cloud visually becomes optically thick and no blue sky is visible through the cloud. As shown in Fig. 3a the cloud is now located between 6 and 9 km AGL. Although there is excellent correspondence between the radar and lidar observed cloud base, the lidar signal becomes attenuated (Fig. 3b) between 7 and 8 km. The IR radiometer now detects a more typically observed cirrus cloud base temperature that ranges from -40 to -30°C (Fig. 3c).

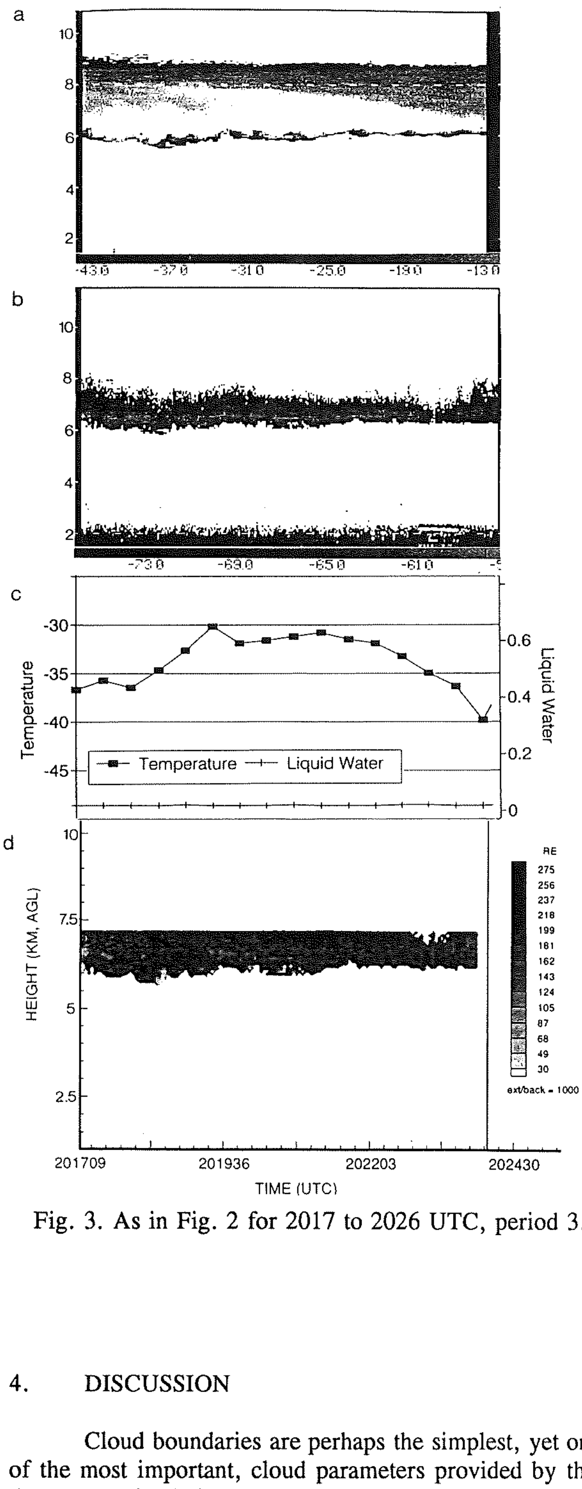

Fig. 3. As in Fig. 2 for 2017 to 2026 UTC, period 3.

4. DISCUSSION

Cloud boundaries are perhaps the simplest, yet one of the most important, cloud parameters provided by this data set. It is obvious that in this case both the radar and lidar observations are needed in order to assess correctly where the cirrus are located. In period 1 the lidar backscatter field provides the only indication of cloud top and bottom heights. During periods 2 and 3 the lidar and radar observations agree on the cloud base heights; however, the cloud top boundaries are determined best by the lidar for period 2 and by the radar for period 3.

Other equally important parameters necessary to model cirrus are size and concentration of the particles. Cirrus cloud particle size estimates can be derived using the combination of radar and lidar measurements. The absence of radar returns (Period 1) allows the qualitative judgement that this cloud is most likely composed of small ice crystals in low concentrations. Using the method from Eberhard and Post (1991) to determine particle diameter from specular returns, we can refine this estimate to conclude that the cloud is composed of plates and needles approximately 110μm in effective diameter.

Although the cirrus cloud in period 1 is spatially uniform and expansive, its high altitude and low optical depth suggest an insignificant impact on downwelling IR radiation. Because shortwave reflectance is driven by smaller particles, and this cloud exhibits oriented crystals, the upward reflection of shortwave radiation dominated the radiative effects of this cloud. Planned comparisons with satellite data will allow the examination of the cloud top radiation budget.

In period 2, the lidar and radar observe the same cirrus cloud base altitude. However, the lidar detects the cloud top at a higher altitude because it receives backscatter from the smaller particles. Size estimates from the lidar/radar method indicate that larger particles are located in the turret-like feature at ~ 1817 UTC as well as the lowest portion of the cloud from ~ 1821 to 1823 UTC where settling may have occurred (Fig. 2d).

During period 3 we determined that the lidar signal becomes attenuated due to the high concentration of ice particles since there is no liquid water as observed by the radiometer. During this period the cloud becomes optically thick and the IR radiometer begins to observe typical cirrus cloud brightness temperatures. This time period also corresponds to the larger particle size estimates (only calculated up to 7.4 km due to the loss of lidar signal).

5. SUMMARY

This case study is presented to illustrate the synergistic utility of multi-wavelength observations. The combination of lidar, radar, and radiometer measurements yield information not attainable by any one of these instruments alone. For example, the combination of radar and lidar yields estimates of size and concentration. In addition, specular reflection signatures from the lidar provide information that suggest the cirrus are composed of small, horizontally oriented plates or needles. Although specular reflection has been recorded by many lidar studies in all parts of the world, not every cirrus cloud exhibits this characteristic and, as shown above, even the same cloud will not consistently show specular reflection from one minute to the next.

Radiative information as a function of cloud height, depth, particle size and concentration can be obtained from integration of the radar, lidar, and radiometer data. For example, although this high, thin cirrus may have a small influence on the IR energy reradiated back to the surface, small, oriented plates and needles will have a more significant impact on reflection and albedo observed from space. Satellites, in general, have difficulty observing these types of tenuous and thin cirrus clouds and consequently little information has been gathered about them. Therefore, the information on low optical depth cloud particle sizes, heights, concentrations, and IR budget produced by ground-based remote sensors is crucial input for models. In general, with a knowledge of cirrus top and base height, thickness, particle size, and concentration from the lidar and radar, as well as radiative data from the radiometers and satellites, the radiative forcing of cirrus clouds can be better understood and modeled.

Acknowledgements. The authors thank all of those who operated and maintained the instruments during FIRE II, especially R. Cupp, R. Willis, M. Jacobson, B. Bartram, B. Orr, B. Martner, L. Olivier, C. Grund, M.J. Post, R. Beeler, B. Madsen, and A. Francavilla. Also, many thanks to K. Healy for all of the specialized programming and processing of the effective radius data. This research was sponsored by the Atmospheric and Land Surface Processes component of NOAA and through a subcontract from the University of Utah.

References

Eberhard, W.L., and M.J. Post, 1991: CO_2 lidar techniques for observing characteristic particle size of selected cloud types. Preprints, Lower Tropospheric Profiling: Needs and Technologies, 10-13 September, 1991, Boulder, CO, American Meteorological Society, Boston, MA, 7-8.

Intrieri, J.M., W.L. Eberhard, and T. Uttal, 1991: Determination of cirrus cloud particle effective radii using radar and lidar backscattering data. Preprints, 25th International Conf. on Radar Meteor., 24-28 June, 1991, Paris, France, American Meteorological Society, Boston, MA, 867-870.

Stephens G.L., S.C. Tsay, P.W. Stackhouse, Jr., and P.J. Flatau, 1990: The relevance of the microphysical and radiative properties of cirrus clouds to climate and climatic feedback. J. Atmos. Sci., 47, 1742-1753.

Large Scale Forcing of Middle and Upper Level Clouds: Preliminary Results from a FIRE Cirrus Case Study

Gerald G. Mace and Thomas P. Ackerman

Department of Meteorology
The Pennsylvania State University
University Park, PA 16801

1. Introduction

In recent years, a major goal of atmospheric research has been directed toward understanding the role clouds play in the global climate system. Numerous published papers have pointed to the fact that clouds significantly impact the global climate system. However, the magnitude and even the sign of the impact which clouds exert is, however, still a subject of scientific debate. Cess et al. (1990) concluded that the major source of disparity in the sensitivity of 17 GCM simulations forced by a common climate perturbation rested almost entirely on the way in which clouds were parameterized in the models.

Cirrus clouds, in particular, represent a unique challenge in the parameterization problem. The large scale dynamical forcing of cirrus cloud systems tends to be complicated by the dynamical structure of the upper troposphere. The present knowledge of upper tropospheric dynamics has been largely determined from highly idealized models with little observational verification (Keyser and Shapiro, 1986). This deficiency in observational evidence results in a lack of knowledge in the relationship between the cirrus clouds and the environment in which they exist. This environment is characterized by small water vapor concentrations in which vertical motions are forced by small imbalances in the large scale atmospheric flow. It is necessary, therefore, to acquire thermodynamic and dynamic observations of high precision to adequately resolve the relevant mechanisms which lead to cirrus cloud development. Furthermore, the microphysical properties of the cirrus, which in turn govern its radiative impacts are strongly coupled to the dynamical and thermodynamical fields. The presence of the cirrus itself, however, alters these fields through radiative heating and vapor condensation. It is precisely this coupling between large-scale environment and small scale cloud properties that must be diagnosed if the parameterization problem it to be solved.

This connection between scales is one of the reasons the First International Satellite Cloud Climatology Project (ISCCP) Regional Experiment (FIRE Cirrus II) was conducted in Coffeyville, Kansas in November and December, 1991. This location was chosen, in large part, because of the presence of the NOAA wind profiler demonstration array. These 404 Mhz wind profilers were located in a mesoscale array around Coffeyville (Fig. 1) and provided continuous horizontal and vertical wind information at high temporal resolution from approximately 1 Km above mean sea level (msl) to 16 Km msl with vertical resolution ranging from 250 m to 900 m. This data was supplemented by spatially and temporally enhanced radiosonde information. Consequently, the mesoscale characteristics of the cirrus environment were characterized quite well. A dataset of unprecedented resolution and detail was obtained by combining this information with detailed microphysical and radiative measurements from both surface based and aircraft based sensors.

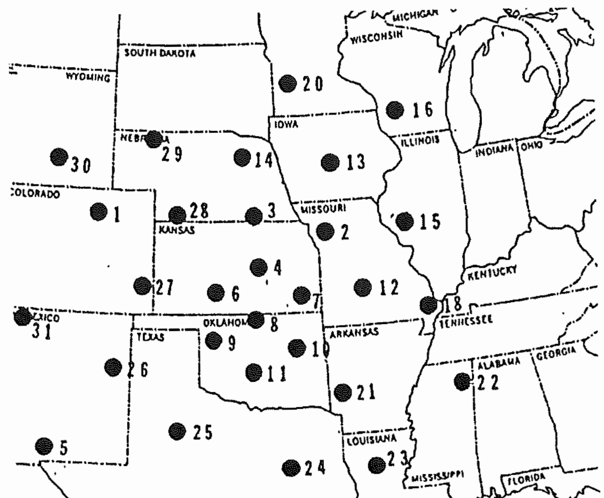

Fig 1. A portion of the NOAA Demonstration Array of 404 Mhz wind profilers. The sites used in the calculations presented in the text were 8, 9, 6, 4, 7, and 10.

This dataset will be exploited to present preliminary results from one case study conducted during FIRE Cirrus II, concentrating mainly on the mesoscale dynamical forcing of the upper cloud system.

2. Diagnostic Methods

Zamora et al. (1987) presented a method whereby the linear kinematic properties of the atmospheric flow could be determined from three non-colinear wind profiler observations. They noted that the primary drawback of their method was that it required the wind field to vary in a linear fashion. Nonlinear variations in the flow would then lead to erroneous results. The method outlined here takes advantage of the number of wind profilers in the region and is a logical extension of the method described by Zamora et al. (1987).

By using a second order Taylor Series expansion in two dimensions, a scalar variable, $\alpha(x,y)$, can be expanded about a point in space, (x_0, y_0),

$$\alpha(x, y) = \alpha_0 + \frac{\partial\alpha}{\partial x}\delta x + \frac{\partial\alpha}{\partial y}\delta y + \frac{\partial^2\alpha}{\partial x^2}\frac{\delta x^2}{2} + \frac{\partial^2\alpha}{\partial x\partial y}\frac{\delta x\delta y}{2} + \frac{\partial^2\alpha}{\partial y^2}\frac{\delta y^2}{2} \qquad (1)$$

Here the LHS is a measured quantity at a profiler location denoted by (x, y). The point (x_0, y_0) is the location to which we would like to interpolate the observed values. The distance constants on the RHS are determined by the location to which we are interpolating and the geometry of the observational network. Our goal is to determine the value of α as well as the first and second order differentials at the point (x_0, y_0). Solving for these six unknowns requires six independent measurements of α. If these observations exist, then the six unknowns can be written as the vector,

$$\mathbf{D} = \left(\alpha(x_0, y_0), \frac{\partial\alpha}{\partial x}, \frac{\partial\alpha}{\partial y}, \frac{\partial^2\alpha}{\partial x^2}, \frac{\partial^2\alpha}{\partial x\partial y}, \frac{\partial^2\alpha}{\partial y^2}\right) \qquad (2)$$

The observations on the LHS can be expressed as the vector,

$$\mathbf{U} = (\alpha_1, \alpha_2, \alpha_3, \alpha_4, \alpha_5, \alpha_6) \qquad (3)$$

and the system of equations can be written

$$\mathbf{DX=U} \qquad (4)$$

where **X** is the 6x6 matrix of distance constants. Calculation of the kinematic properties of the variable α then reduces to solving the linear system for the vector **D**.

When Eq 4 is solved successively for orthogonal wind components, the method permits the calculation of quantities such as the horizontal divergence, the vertical component of vorticity and the deformation properties of the atmospheric flow. In addition to being more accurate due to its higher order determination, expanding the series out to second order allows the determination of spatial cross sections of the differential quantities and the variables which depend on them, such as vertical velocity and ageostrophic wind. It is then possible to examine the forcing of the three-dimensional vertical circulations by the large scale flow using methods developed to diagnose frontal circulations (e.g., Keyser and Shapiro (1987)). Time height cross sections of the applicable variables can also be interpolated directly to Coffeyville for a direct correlation of the large scale forcing with the observed cirrus cloud properties.

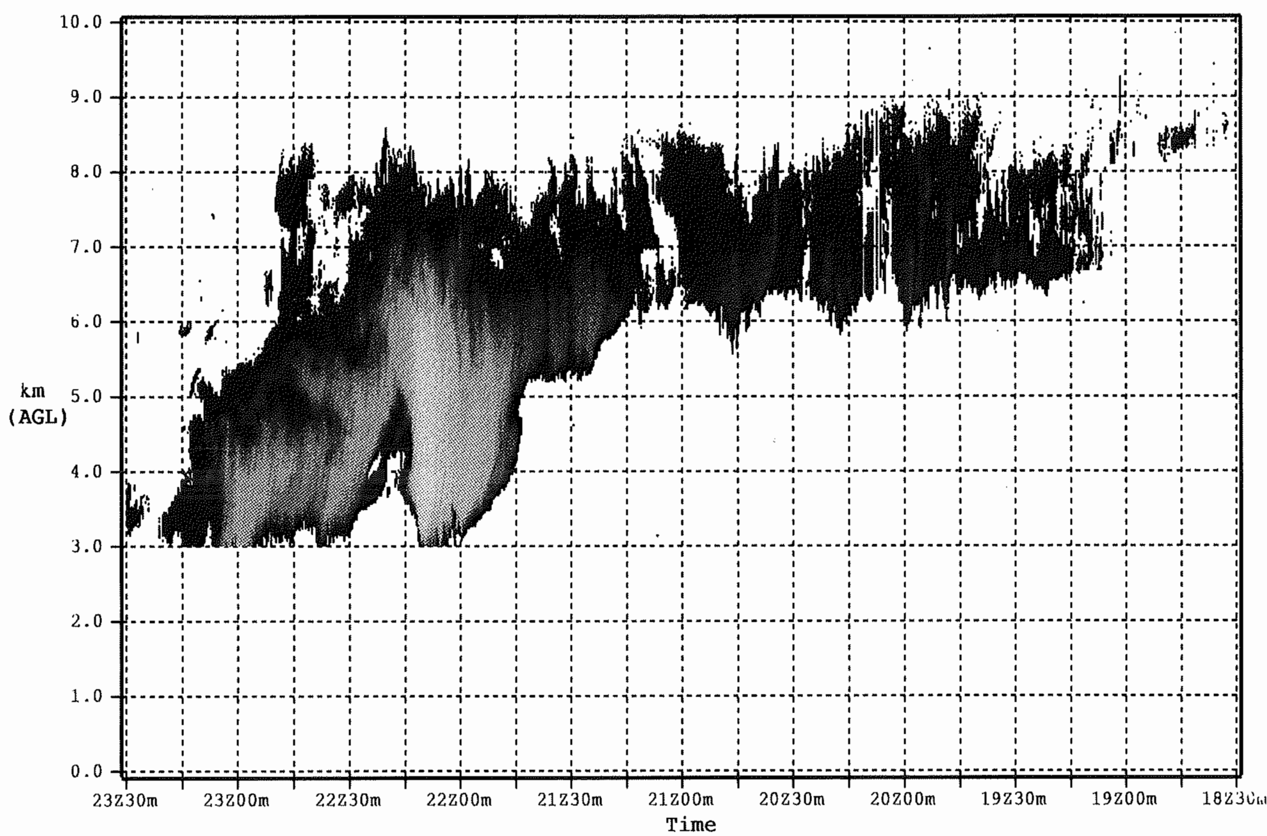

Fig. 2. Time height series of uncorrected reflectivities measured by the Penn State 94 Ghz cloud Radar. Note time increases from right to left.

3. Case Study

During the afternoon of 26 November, 1991, a small amplitude trough axis was moving slowly eastward over the central United States. The surface analysis revealed a low pressure center in northwestern Nebraska with a trough of low pressure extending into central Kansas. Associated with this trough of low pressure was a north-south band of cloudiness. This band gives the appearance of being associated with a warm front, although surface reports indicate the band contained mainly non-precipitating middle and upper-level clouds.

Tenuous cirrus clouds at a height of 8.5 Km were first observed over Coffeyville at 1830z. Soundings from the surrounding region indicated a continual moistening of the upper troposphere during the late morning hours. Fig. 2 shows a time-height cross section of radar reflectivities observed with the Penn State 94 Ghz cloud radar (Peters et al., this issue). As can be seen from this figure, cloud base quickly lowered to 7.25 Km and the layer thickened with tops extending to near 9 Km. The reflectivity pattern indicates convective instability within this layer. Fig 3 shows the 2025z sounding over Coffeyville. This profile clearly shows the moist layer associated with the cirrus deck just below 7 Km. The cloud tops were well below the tropopause, which was located at 10.25 Km. The dew point profile does not show a well defined cloud top.

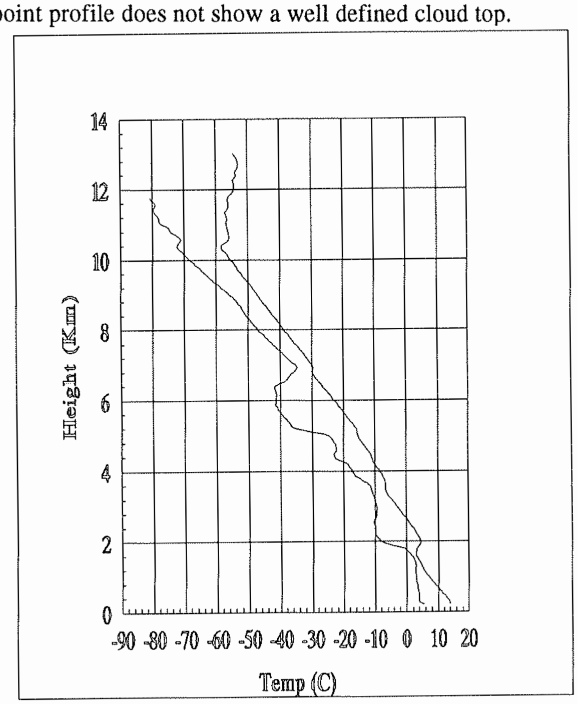

Fig 3. Radiosonde profile recorded at Coffeyville, Kansas. Instrument was launched at 2025z, 26 Nov, 1991.

The cloud deck remained nearly continuous until 2115z when a significant lowering of the cloud base was observed. By 2200z, cloud base was near 3 Km and cloud top extended to 8 Km. Enhanced reflectivities were observed after this time as the cloud developed a more mid-level appearance. By 2300z, cloud top had lowered rapidly to near 5.25 Km and nearly complete dissipation of the deck occurred by 2330z.

The forcing of the large scale vertical motions can be seen in Fig. 4. This figure shows divergence values interpolated to Coffeyville using the six wind profilers indicated in Fig 1.

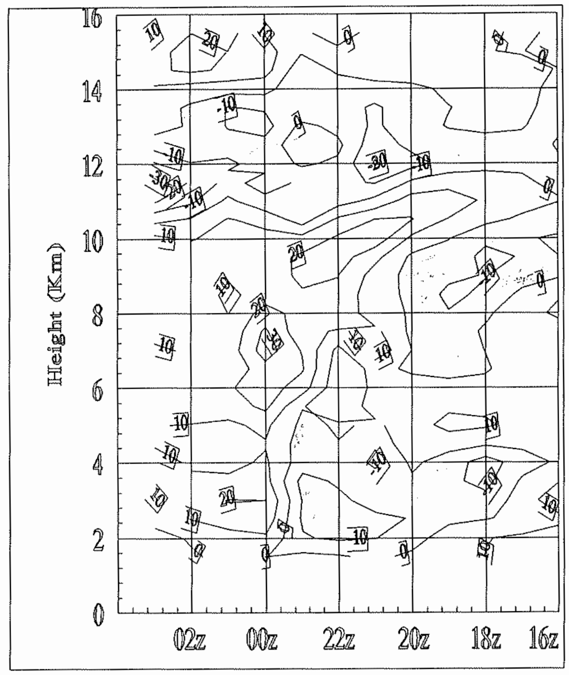

Fig. 4 Divergence values in units of 10^{-5} s^{-1} interpolated to Coffeyville using the method described above. Values of convergence are shaded. Note that time increases from right to left.

The most prominent feature of this profile is the region of upper level divergence which first appeared at 1800z at 11 Km. This divergent layer appeared to strengthen and deepen with the main axis of divergence descending with time. Coupled with this layer of divergence were two layers of convergence. A convergent layer first appeared over Coffeyville at 10z, 26 November and remained at 9 Km throughout the morning hours. Of particular interest is the manner in which upper level clouds first appeared as the convergence-divergence couplet organized over the site. The layer of upper convergence vanished over Coffeyville by 2000z. Vertical motions then appeared to be forced by the lower convergent layer between 2 and 4 Km. This layer reached its maximum intensity near the time of the lowering of cloud based mentioned earlier. This lower convergent layer decreased in intensity and became divergent by 0000z, 27 November. This is in line with the dissipation of the cloud layer and the passage of an upper level trough. It then appears that subsidence was initiated due to the strong convergent layer above 10 Km.

Mesoscale vertical motions were determined using the hourly averaged profiler measured vertical velocities at the six sites. These values were then interpolated to Coffeyville using the method described above. Problems are known to exist with profiler vertical beam measurements due to contamination by any small off zenith component in the beams. Under light wind conditions,

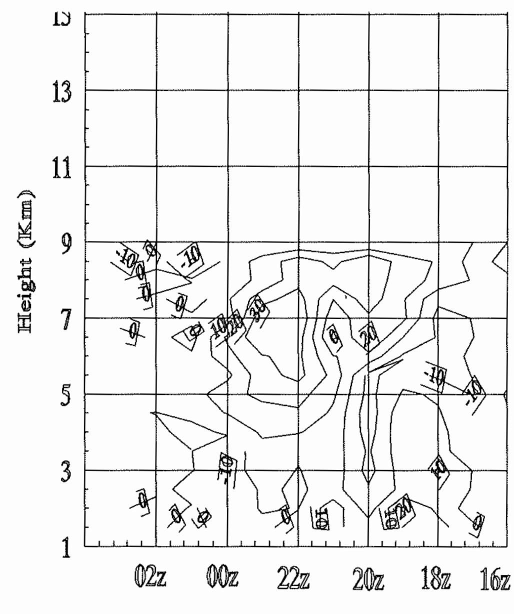

Fig. 5 Observed vertical velocities in units of cm s^{-1}. Data was available only to 9 Km.

contamination of the vertical beam measurements by the horizontal wind should be minimized. Wind speeds at cloud level generally remained less than 20 ms^{-1} during the afternoon of 26 November. Absolute accuracy is not claimed here, however by comparing the vertical velocity with the divergence and cloud patterns it would appear that the measurements are qualitatively correct. Significant upward motion appeared in conjunction with the upper convergence-divergence couplet mentioned above. This layer of upward motion deepened and descended and reached its maximum value at the same time as the maximum refelctivities were measured over Coffeyville. The significant uplift ceases with the trough passage at 0000z, 27 Nov and correlates well with the dissipation of cloudiness over Coffeyville.

4. Summary

The discussion presented above represents an initial analysis of the large scale forcing of the cirrus clouds observed during this particular case study. It appears that the vertical motions which contributed to upper cloud formation, maintenance and dissipation were the result of varying influences throughout the troposphere. Of significance is the appearance that the middle and upper tropospheric clouds were initially forced by features which resided above 8 Km but eventually were maintained by the coupling of middle and lower tropospheric convergence. Dissipation was initiated after the upper trough passage when strong convergence was initiated near the tropopause.

While this type of analysis is illuminating, it does not necessarily help solve the parameterization problem. Since upper cloud formation is closely coupled with small changes in water vapor concentration, this factor needs to be examined closely. Additionally, the mesoscale vertical motions can be visualized as the result of imbalances in the larger scale flow pattern. Identifying these imbalances and then diagnosing the resulting vertical circulations on regional scales will be necessary to carry forward the linkage of cirrus cloud formation with large scale forcing. It will then be necessary to test the ability of meso and larger scale models to accurately model the imbalances in the wind and thermal fields which are important to cirrus cloud formation and maintenance. This is the direction future research will take.

Acknowledgments: We are indebted to R. Peters, S. Williams, R. Thompson and T. Treaster for their invaluable assistance with the intrument development and data collection. This research was supported under NASA Grant NAG-1-1095 and DOE ARM Grant DE-FG02-90ER61071

References:

Cess ,R. D., G.L. Potter, J. P. Blanchet, G J. Boer, M. Deque, W. L. Gates, S. J. Ghan,J. T. Kiehl, H. Le Treut, Z. X. Li, X. Z. Liang, B. J. McAvaney, V. P. Meleshko, J. F. B. Mitchell, J. J. Morcrette, D. A. RAndall, L. Rikus, E. Roeckner, J. F. Royer, U. Schlese, D. A. Sheinin, A. Slingo, A. P. Sokolov, K. E. Taylor, W. M. Washington, R. T. Wetherald, and I. Yagai, 1990: Intercomparison and interpretation of climate feedback processes in seventeen atmospheric general circulation models. *J Geophys Res.*, **95,** 16601-16701.

Keyser R. F., M. A. Shapiro, and C. A. Doswell III, 1987: The diagnosis of upper tropospheric divergence and ageostrophic wind using profiler wind observations. *Mon Wea Rev.*, **115,** 871-884.

----- and M. A. Shapiro, 1986: A review of the structure and dynamics of upper-level frontal zones. *Mon Wea Rev.*, **114,** 452-499.

Peters, M. P., B. A. Albrecht, M. A. Miller, J. T. Treaster, 1992: Automated cloud profiling with a 94 GHz radar. Preprints, 11th International Conference on Clouds and Precipitation, Montreal, 17-21 August, 1992, American Meteorlogical Society.

MICROPHYSICAL AND RADIATIVE DEVELOPMENT OF A CIRRUS CLOUD DURING FIRE: IMPLICATIONS FOR DYNAMIC EFFECTS

I. GULTEPE and D. STARR
NASA Goddard Space Flight Center,
Code 913, Greenbelt, MD 20771.

1. INTRODUCTION

Cirrus clouds play an important role in the upper troposphere water and heat budgets and may significantly affect the earth's climate and atmospheric general circulation. Recent studies indicate that cirrus clouds often exhibit complex structure (Sassen et al., 1989; Starr and Wylie, 1990). The purpose of this study is to show how physical and radiative processes may generate dynamical changes in cirrus clouds that could contribute to the development of the complex physical structures that are observed.

2. AIRCRAFT MEASUREMENTS AND SYNOPTIC CONDITIONS

Data for this study were collected over Minnesota on 19 October, 1986 during the First International Satellite Cloud Climatology Project (ISCCP) Regional Experiment (FIRE) cirrus field campaign. Measurements used in this study were obtained from instruments mounted on the NCAR King Air and Saberliner. Measurements included infrared (IR) and shortwave (SW) irradiances, particle concentration and size, and temperature and pressure. Both aircraft collected data along constant altitude flight legs ($\simeq$60 km long) over a 1.5-hour time period at altitudes from 6 to 12 km. The sampling rate was 1 Hz.

The SW and IR irradiance measurements were averaged over each of the flight legs. Fig. 1 shows averaged IR upwelling (a) and downwelling (b) irradiance profiles versus altitude. Arrows indicate flight leg altitude and time is also noted. King Air measurements are indicated with **K**. The dashed curve shows the best fit. **C** signifies the clear air legs before entering and after leaving the cloud. Fig. 2 is similar to Fig. 1 except for SW irradiances. Although cloud top occurred at about 11.5 km with cloud base at about 6.5 km, it is very evident from the radiative flux profiles that an optically dense layer was located just above 8 km within the much deeper cirrus cloud. Ice particle data were collected by a 2D-C probe mounted under the aircraft wing. Measurements from the 2D-C probe are not useful for particles less than 75 μm in size. Particle concentration was therefore extrapolated for the small particle sizes, using an exponential distribution.

Temperature measurements from both aircraft indicate that the cirrus formed in statically-stable atmospheric conditions. Cloud formation was associated with an upper level shortwave propagating to the SE with little low level development.

3. CALCULATION TECHNIQUES

Our approach is to quantify various physical processes in terms of an effective vertical velocity required to balance a particular budget equation subject to some assumptions. The calculations are briefly discussed here.

a. Calculation from Mass Conservation

The total water mass conservation equation for an air parcel within a cloud may be expressed (Fletcher, 1962) as:

$$\frac{dS_i}{dt} = \phi_1 w - \phi_2 \frac{d\omega_w}{dt} - \phi_3 \frac{d\omega_i}{dt} \tag{1}$$

where S_i is the supersaturation with respect to ice, t the time, ϕ_1, ϕ_2, and ϕ_3 the thermodynamic constants for given environmental conditions, w the vertical velocity, and $d\omega_{w,i}/dt$ the growth rate of liquid or ice particles. Assuming that S_i is maintained at a constant value and that no liquid is present, Eq. 1 may be solved following Heymsfield (1977) as:

$$\overline{w}_{DIF} = \frac{\phi_3}{\phi_1} \frac{d\omega_i}{dt} \tag{2}$$

where

$$\frac{d\omega_i}{dt} = 4\pi S_i \sum_{i=1}^{m} N(i)C(i)F(i)G(i)\rho_i(i) \tag{3}$$

represents diffusional growth of ice crystals (Fletcher, 1962), N is the ice crystal concentration, C the shape factor, F the ventilation coefficiency, G the modified diffusion factor, and ρ_i the ice density. The m represent the number of sizes. Thus, $\overline{w}_{DIF}$ is the vertical motion required to balance the total water budget subject to the thermodynamical and microphysical constraints associated with diffusional growth at constant S_i.

b. Calculation from Heat Conservation

Neglecting turbulent processes, heat conservation may be expressed as:

$$\left(\frac{d\theta}{dt}\right)_{LOC,ADV} = \left(\frac{\partial\theta}{\partial t}\right)_{IR,SW} + \frac{L_s}{\rho_a C_p}\left(\frac{\partial\omega_i}{\partial t}\right)_{DIF} \tag{4}$$

where θ is potential temperature, L_s the latent heat of sublimation, and C_p the specific heat at constant pressure. It is useful to express the radiative heating in terms of the adiabatic vertical motion required to compensate (balance) the radiative heating, i.e.,

$$\overline{w}_{RAD}\frac{\partial\theta}{\partial z} = \left(\frac{\partial\theta}{\partial t}\right)_{IR,SW}, \tag{5}$$

where

$$\left(\frac{\partial\theta}{dt}(z)\right)_{RAD} = -\frac{1}{\rho_a C_p \pi_a}\left(\frac{dF}{dz}\right)_{IR,SW}. \tag{6}$$

Here ρ_a is the air density, π_a the Exner function, and F the measured radiative fluxes (positive upward). Thus,

$$\overline{w}_{RAD} = -\frac{1}{\rho_a C_p \pi_a}\left(\frac{dF}{dz}\right)_{IR,SW} / \left(\frac{\partial\theta}{dz}\right). \tag{7}$$

4. RESULTS

a. *Cirrus Radiative and Physical Characteristics*

Following the method of Paltridge and Platt (1981), the infrared emittance, ϵ, calculated from data shown in Fig. 1 ranges between 0.1 and 0.30 for individual cloudy layers of about 500 m in depth. The most optically thick cloud layer is found at about 8.3 km (ϵ=0.30). Integrated emmitance for the entire cloud is about 0.64.

The cirrus optical depth at visible wavelengths may be estimated from the particle data as:

$$\tau_{vis} = 2\Delta z\left(\frac{0.94}{r_e}\right) IWC, \tag{8}$$

where Δz the layer thickness, r_e the radius of a spherical ice particle of equivalent cross-sectional area, and IWC the ice water content. The factor 2 results from the large-particle approximation (Foot, 1988). Optical thickness for the IR region may be estimated using $\tau_{ir}=\tau_{vis}/2$ (Sassen et al., 1990). Using r_e=25 μm, the mean value of τ_{ir} is found to be about 0.32 for the 500-m layers between about 9 and 11 km. The layer at about 8.3 km, where r_e is found to be approximately 70 μm, is more optically dense ($\tau_{ir} \approx$1.13). The corresponding estimated value of ϵ for the entire cloud is 0.91 which is significantly greater than that derived from the observed flux profiles.

Following Paldridge and Platt (1981), the albedo of cloudy layers are derived from the observed SW flux profiles (Fig. 2). A maximum value of 11% was found for the layer around 8.7 km with values of less than 5% for the overlying layers (above 9 km). The integrated SW albedo for the entire cirrus deck is approximately 30%.

IR and SW heating rate profiles calculated from Eq. (6) are shown in Fig. 3. The net SW+IR heating rate (dash) in the cloud layer reaches a maximum of about 150 K day^{-1} at 8.3 km. IR heating contributes more than half of the total radiative heating at this level. Above 8.5 km, IR cooling ranges between 18 and 43 K day^{-1}. However, solar warming yields a net warming of 25 K day^{-1}.

Integrated ice crystal growth rate is estimated using Eq. (3). In the calculation, we assumed cloud layers are slightly supersaturated with respect to ice (S_i=1.01). Size spectra are taken from the 2D-C probe measurements. Growth rate of the ice crystals below 8.3 km is much larger (10^{-8} g cm^{-3} s^{-1}) than these found in the upper layers ($\simeq 10^{-10}$ g cm^{-3} s^{-1}).

b. *Effective Vertical Motion Profiles*

Based on conservation of total water mass (Eq. 2), the determined profile of w_{DIF} is shown in Fig. 4. A maximum value of about 0.15 m s^{-1} is found approximately at about 8.3 km. Above 9 km, w_{DIF} is approximately 0.02-0.03 m s^{-1}. The w_{RAD} calculated from Eq. (6) is also shown in Fig. 4. The small dashed line is based on IR irradiance measurements and a temperature gradient of approximately 0.4 K (100 m)$^{-1}$. The large dashed line is for the net radiative heating rate. Maximum w_{RAD} (0.6 m s^{-1}) occurs at about 8.3 km. w_{RAD} is about 0.05-0.15 m s^{-1} above 8.7 km. These values are comparable to those found by Gultepe *et al.* 1990. Overall, w_{RAD} is larger than w_{DIF}. This shows that, although adiabatic temperature changes (ascent) generally act to partially compensate for the effects of net radiative heating (and latent heat release) in this cirrus cloud, radiative processes are predominant. Thus, the radiative temperature changes will actually be realized to a significant extent. Consequent changes in static stability structure will likely influence the dynamical and physical development of the cloud.

c. *Potential Temperature Profile Changes*

In order to illustrate how radiative heating/cooling can affect the static stability structure within cirrus, we computed a new vertical profile of θ assuming a steady radiative heating profile. Fig. 5 shows the θ profile obtained from aircraft measurements (small dash) and the new θ profile after a 1-hour integration (large dash). It can be seen from Fig. 5 that a thermally unstable layer developed just above 8 km after only a one-hour time period. Development of unstable layers through radiative heating/cooling will likely result in convection, mixing (with outside dry air) and turbulence. Conversly, radiative stabilization, as seen just below the 8 km level, may help support gravity wave activity.

d. *Error in the Calculations*

Because of deviations from the horizontal plane, the irradiance measurements are corrected for aircraft pitch and roll angles, and solar zenith angle. Error in SW irradiance measurements due to temporal change (zenith angle effect) can be as large as 15 %. Downwelling SW irradiance may also include an error of about 20-30 W m^{-2} due to direct/diffuse partition at each level. This error is somewhat mitigated in the radiative heating rate calculations because net radiative flux is computed from the difference between two flight levels.

Errors in the w_{DIF} calculations arise from the steady-state assumption, the uncertainty in the concentration of small particles, and assumed value of supersaturation with respect to ice. Total error in w_{DIF} and w_{RAD} calculations based upon the above error sources can be as high as 20-40%.

e. Comparisons of Radiative, Physical, and Dynamical processes

The magnitudes of different processes are qualified using the terms in Eq. 4. The value for each process at three different altitudes is shown in Table 1.

The results show that at the level of maximum radiative heating (139 $K day^{-1}$) at about 8.3 km, the cooling rate diagnosed from water mass conservation (w_{DIF}) is about 52 $K day^{-1}$. This shows that adiabatic cooling due to ascent may partially neutralize the effects of radiative and latent heating. The magnitude of latent heating is small (column 2) compared to other terms. The cooling rate due to large scale vertical ascent, assuming w_{LAR} of about 0.02 m s^{-1} (Starr and Wylie, 1990) and using $d\theta/dz$=0.4 K (100 $m)^{-1}$, is estimated to be approximately 7 $K day^{-1}$. Cirrus clouds may easily form due to this amount of cooling if the environment holds enough moisture. However, w_{DIF} may correspond to a mesoscale circulation representing a much stronger forcing of cloud formation than evident on the synoptic scale.

5. CONCLUSIONS

In this study, cirrus cloud characteristics were studied using the calculations based on the radiation, temperature, and particle measurements. Errors in the measurements and calculations may significantly affect the results.

Radiative effects can change cirrus dynamical and thermodynamical structure. The coupling between radiation and physical processes (e.g., particle growth) is important to generate *in-situ vertical velocities*, intensifying vertical circulation. Comparisons between radiative and advective heating rates in the cloud and large scale can be used to understand cirrus cloud formation, maintenance, and decay. Additional high resolution data set from the FIRE II field project will help us to understand the various processes in cirrus clouds, including turbulence and entrainment.

ACKNOWLEDGMENT

This work was done while first author held a National Research Council Research Associateship at Climate and Radiation Branch of the NASA Goddard Space Flight Center in Greenbelt Maryland.

REFERENCES

Fletcher, N. H., 1962: *The physics of rain clouds*, Cambridge University Press, 386 pp.

Foot, J. S., 1988: Some observations of the optical properties of clouds. II: Cirrus. *Q. J. R. Meteor. Soc.*, 114, 145-164.

Gultepe, I., A. J. Heymsfield, and D. H. Lenschow, 1990: A comparison of vertical velocity in cirrus obtained from aircraft and lidar measurements during FIRE. *J. Atmos. Ocean. Tech.*,7, 58-67

Heymsfield, A. J., 1977: Precipitation development in stratiform ice clouds: A microphysical and dynamical study. *J. Atmos.Sci.*, 34, 367-381.

Sassen, K., D. O'C . Starr, and T. Uttal, 1989: Mesoscale and microscale structure of cirrus clouds: Three case studies. *J. Atmos. Sci.*, 46, 371-396.

Sassen, K., A. J. Heymsfield, and D. O'C. Starr, 1990: Is there a cirrus small particle anomaly ? Preprint Vol., Conf. on Cloud Phys., July 23-27, San Fransisco, Amer. Meteor. Soc., J91-J95.

Starr, D. O'C., and D. P. Wylie, 1990: The 27-28 October 1986 FIRE cirrus case study: Meteorology and Clouds. *Month. Wea. Rew.*, 118, 2259-2287.

Paltridge, G. W., and C. M. R. Platt, 1981: Aircraft measurements of solar and infrared radiation and microphysics of cirrus cloud. *Quart. J. R. Met. Soc.*, 107, 367-380.

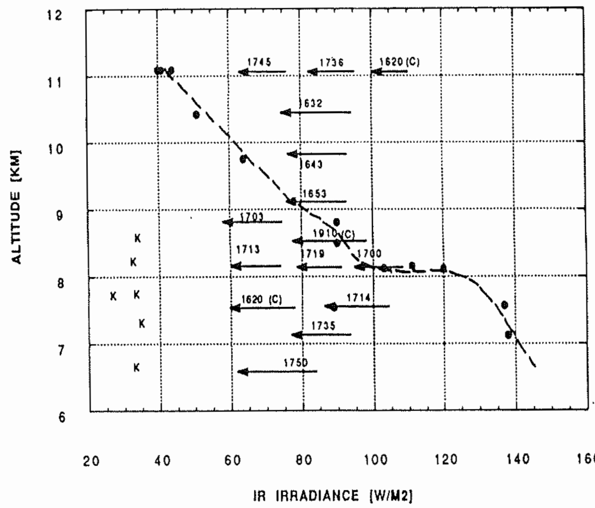

Fig. 1a: Vertical profile of leg-averaged, broadband, upwelling IR irradiance measurements.

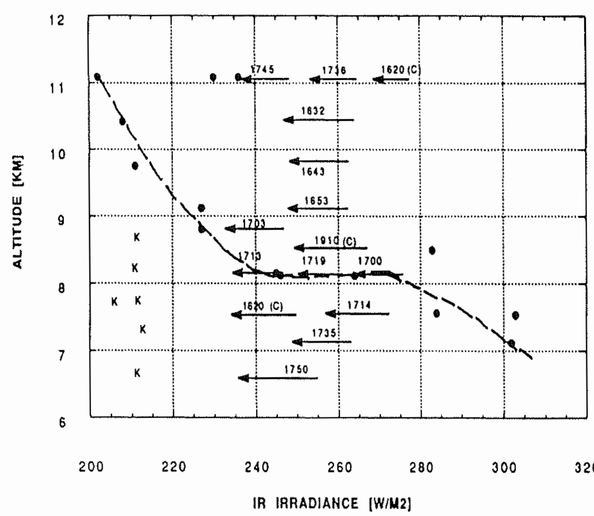

Fig. 1b: Vertical profile of leg-averaged, broadband, downwelling IR irradiance measurements.

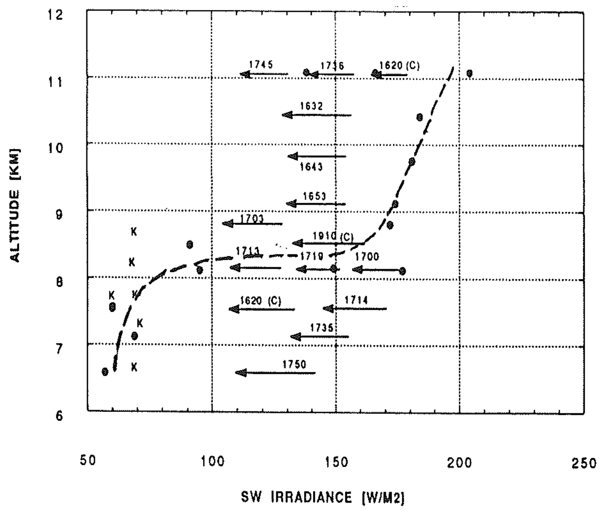

Fig. 2a: Vertical profile of leg-averaged, broadband, upwelling SW irradiance measurements.

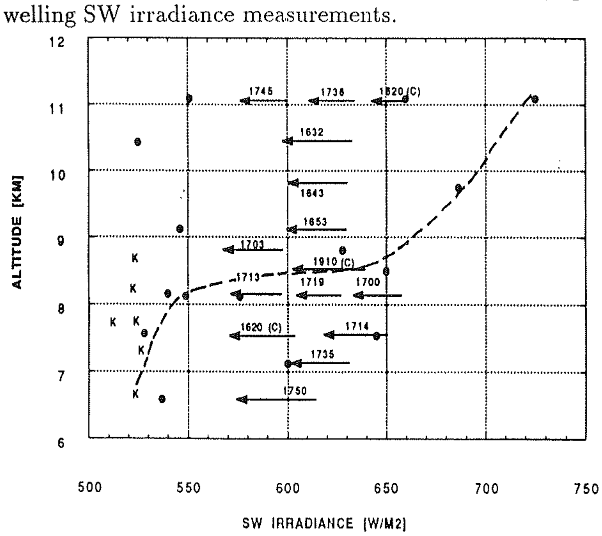

Fig. 2b: Vertical profile of leg-averaged, broadband, downwelling SW irradiance measurements.

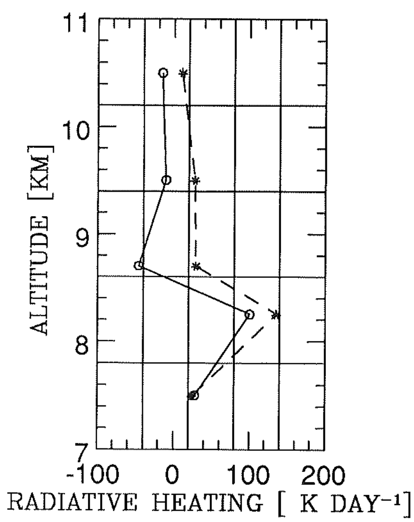

Fig. 3: Vertical profile of radiative heating rate: line with stars is for net radiation (SW+IR) and line with circles is for IR radiation.

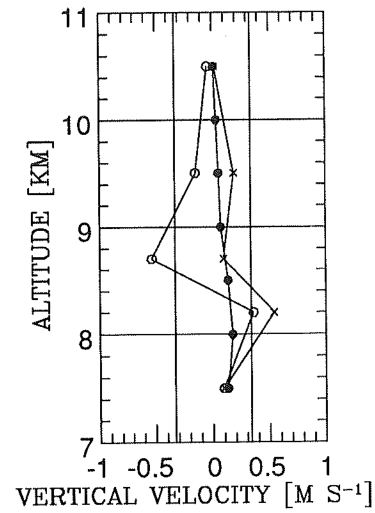

Fig. 4: Profiles of w_{IR} (with blank circle), w_{DIF} (with solid circle), and w_{RAD} (with cross).

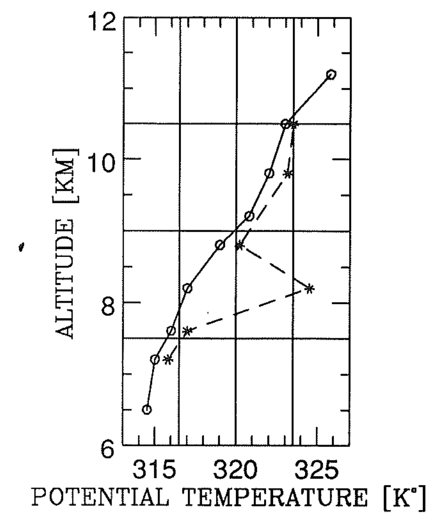

Fig. 5: Profiles of potential temperature: initial θ profile is shown by blank circles. New θ profile is shown by line with stars.

Table 1: Heating rates because of radiative, thermodynamical, and dynamical processes within cirrus layers.

Altitude km	LHR $K day^{-1}$	NRH $K day^{-1}$	IRH $K day^{-1}$	AHWD $K day^{-1}$	AHWL $K day^{-1}$
7.5	4.2	28	28	-18	-7
8.3	1.0	139	100	-52	-7
10.5	0.1	8	-15	-4	-4

LHR: Latent heat release

NRH: Net radiative heating

IRH: Infrared heating

AHWD: Adiabatic heating based on w_{DIF}

AHWL: Adiabatic heating based on w_{LAR}

PRECIPITATION PROCESSES WITHIN STABLE OROGRAPHIC STORMS

Larry D. Oolman
University of Wyoming
Laramie, WY 82071

1. INTRODUCTION

Much of the precipitation in the western United States is from orographically induced storms. There have been a number of theoretical and field studies conducted to study these storms. A numerical cloud model, which uses parameterized particle spectra, has been developed at the University of Wyoming to study the formation of precipitation. This model was applied to a deep stable orographic storm over the Sierra Nevada.

2. MODEL

The cloud model utilizes parameterized bulk microphysics. The condensate is partitioned into three classes: cloud water, rain, and ice. The spectra for each class of particles is characterized by two or more parameters which may be calculated from physical properties such as number concentration and mixing ratio.

The cloud water is constrained to fit a gamma distribution as described by Berry and Reinhardt (1974). The distribution of droplet mass is given by

$$n(m) = m^{\nu_w} e^{-\lambda_w m}. \tag{1}$$

The parameter, ν_w, which determines the dispersion in the drop spectra is set. The remaining two parameters are determined from the number concentration and the mixing ratio.

The rain drop spectra is given by

$$n(r) = \begin{cases} n_r\, e^{-\lambda_r r} & \text{for } r > 50\mu\text{m} \\ 0 & \text{for } r < 50\mu\text{m} \end{cases} \tag{2}$$

A gamma distribution was also selected for the ice spectra

$$n(r) = n_i\, r^{\nu_i} e^{-\lambda_i r}. \tag{3}$$

Gordon (1986) showed that this distribution fit the observed aircraft data well and that ν_i was negative most of the time.

Processes which involve individual particles are parameterized in such a way that they may be integrated over the entire size range of the particle class. These processes include diffusional growth, activation of cloud condensation nuclei, freezing of supercooled water, melting, coalescence, riming, aggregation, and secondary ice crystal production.

3. CASE STUDY

The cloud model was used to simulate the 30 March 1982 case study from the Sierra Cooperative Pilot Study (SCPP). This case study is described in detail by Marwitz (1987a, 1987b). This storm was a deep, stable orographic storm which produced heavy precipitation in the Sierra Nevada. The storm appeared to be quasi-steady during the period when the University of Wyoming King Air was in flight. The ascent and decent soundings showed few differences. It was necessary to find such a case since the model is assumed to be steady state.

The temperature and vapor fields were initialized from the Sheridan sounding taken at 0000 UCT on 31 March 1982. The sounding was adjusted upstream since Sheridan is located at the foot of the Sierra Nevada. This air is already modified by the uplifting over the barrier. The sounding used is near saturation in the lowest 7 km and except for the boundary layer, is stable. The 0 °C isotherm (Fig. 1) intersects the barrier near the midpoint. The temperature at the crest line is –7 °C.

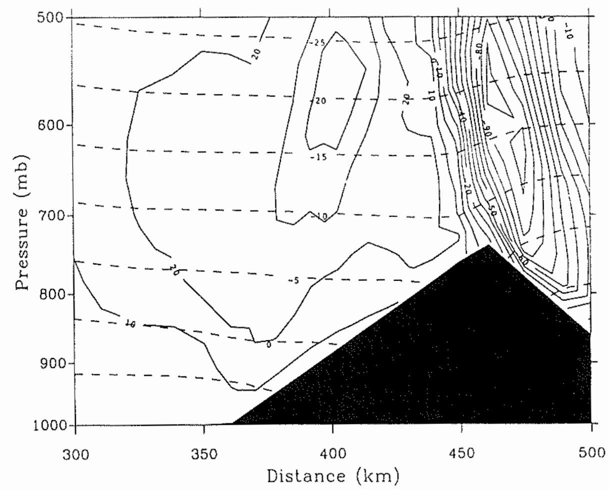

Figure 1. Vertical velocities (cm s^{-1}) and temperature (°C) for a portion of the model domain.

The kinematic field for the region over and upstream of the barrier was obtained from the King Air data and from the NCAR CP–3 Doppler radar data. The horizontal velocities for the remainder of the domain were taken from the results of Waight (1984). A subjective analysis of these data sets was used to set the horizontal velocity at each point. The vertical velocities (Fig. 1) were obtained from the continuity equation. The vertical velocity reaches a maximum of 45 cm s^{-1} above the upper half of the barrier. Downward velocites reach 1 m s^{-1} in the lee of the barrier.

The model was integrated for four hours. By this time steady state was reached.

The predicted mixing ratios for cloud water and for ice are shown in Fig. 2. The cloud water mixing ratio increases for the first 25 km of the cloud. It reaches a maximum value of 0.20 g cm^{-3}. The cloud water mixing ratio begins decreasing once the ice mixing ratio exceeds 0.1 g cm^{-3}.

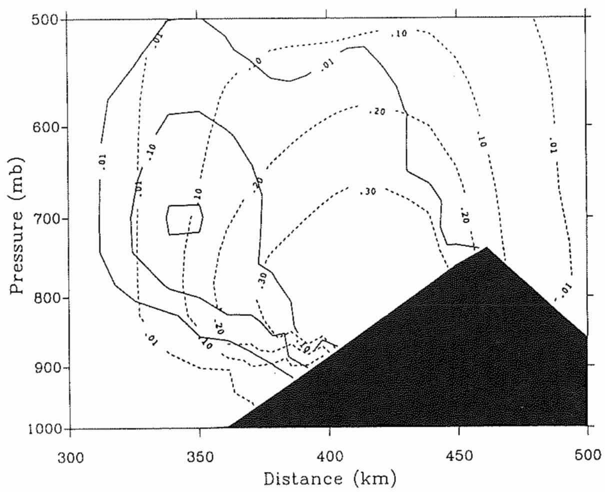

Figure 2. Mixing ratios for cloud water (solid) and ice (dotted). The units are in g m^{-3}.

The ice mixing ratio tends to increase both downward in the cloud and downwind. The high ice mixing ratios, which exceed 0.37 g cm^{-3}, are in the plume of ice particles produced by splintering during riming. These splinters have small fall speeds and low aggregation efficiencies so they grow slowly and remain with the cloud rather than precipitate out.

The rates for various precipitation processes are presented in Figs. 3–6. The odd units of g cm^{-3} / 1000 s were chosen for two reasons: it gives convenient values to work with and 1000 s is approximately the time scale at which these processes operate.

The diffusional growth rate of cloud water is presented in Fig. 3. The highest values for this process process occur low in the cloud at warmer temperatures, where the difference between the vapor pressure of water and ice is small, and in the region of maximum lifting, where the condensation supply rate exceeds the growth rate of the ice particles.

The deposition growth rate for vapor to ice is presented in Fig. 4. Even though the supersaturation with respect to ice is much greater than the supersaturation with respect to water, the depositional growth rate of vapor to ice reaches a value of only half of that reached by the diffusion of vapor to water. The diffusional growth rate depends primarily on two factors: the supersaturation and the size of the particles. Since the cloud water is distributed among many more smaller particles, it is able to take up the excess vapor at a much faster rate. At temperatures warmer the –5 °C, the difference between the vapor pressures of water and ice is small. Most of the diffusion of vapor is to the cloud water. Deposition of vapor to ice exceeds 0.1 g cm^{-3} / 1000 s only at temperatures colder than –5 °C.

The growth rate of ice by the accretion of cloud water is presented in Fig. 5. This is a mixed phase process which requires the presence of both water and ice. This is confined primarily below the –15 °C level. Cloud droplets above this level are more likely to freeze to form new ice crystals. The accretion of cloud water by ice is also relatively unimportant in the first 25 km of the cloud. This is where the liquid water content reaches its maximum. Few ice particles are in this region. Once the riming rate by the ice particles, falling from the colder regions of the cloud, exceed the diffusional growth rate of the cloud droplets, the liquid water content decreases.

Beyond the region of maximum lifting above the upper part of the barrier, the riming rate shows the same trend as the diffusional growth rate for water. The concentration of ice particles is high enough that cloud droplets which grow larger than 5 μm in radius are quickly rimed.

The aggregation rate for the ice is presented in Fig. 6. Aggregation does not produce ice but merely transfers the mass to larger particles. The aggregation rate is similar to the ice mixing ratio shown in Fig. 2. It increases as the ice mixing ratio increases. It also increases towards warmer temperatures where the aggregation efficiency is larger.

The maximum precipitation rate of 4 mm hr^{-1} occurs near the middle of the barrier (Fig. 7a). This agrees well with observations. This is a sign of an efficient storm, since most of the condensate falls out before reaching the crest line. Very little of the condensate is advected over the barrier. Storms with the maximum precipitation rate near the crest line also advect more condensate over the barrier. The precipitation efficiency, defined as the accumulative ratio of the precipitate to condensate, is 90% at the crest line.

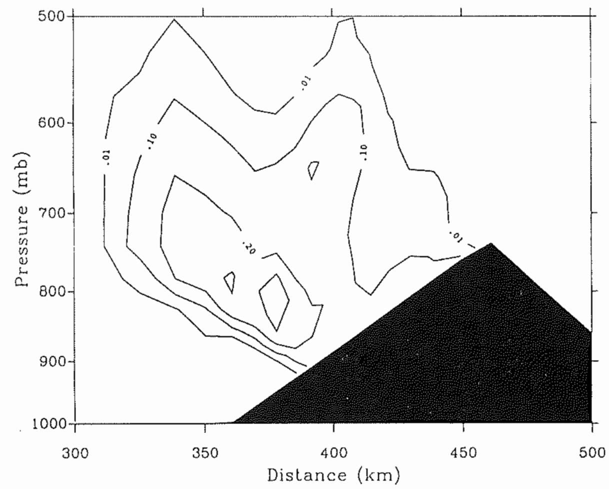

Figure 3. The diffusional growth rate for cloud water. The units are in g m^{-3} / 1000 s.

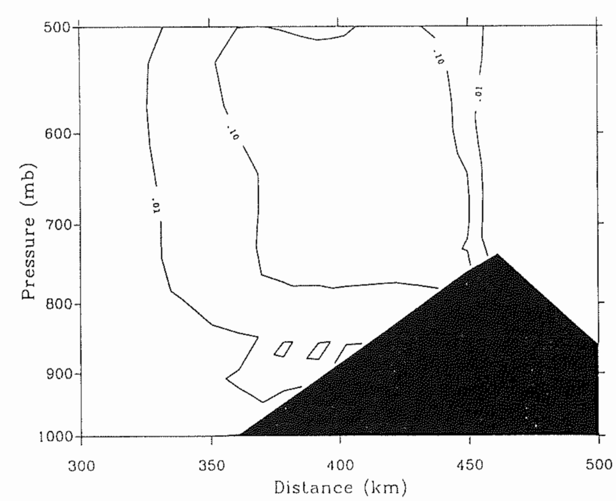

Figure 4. The depositional growth rate for ice. The units are in g m^{-3} / 1000 s.

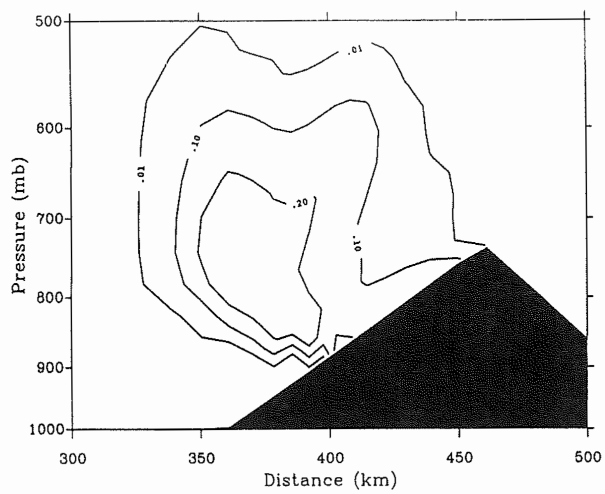

Figure 5. Growth rate of ice by the accretion of cloud water. The units are in g m^{-3} / 1000 s.

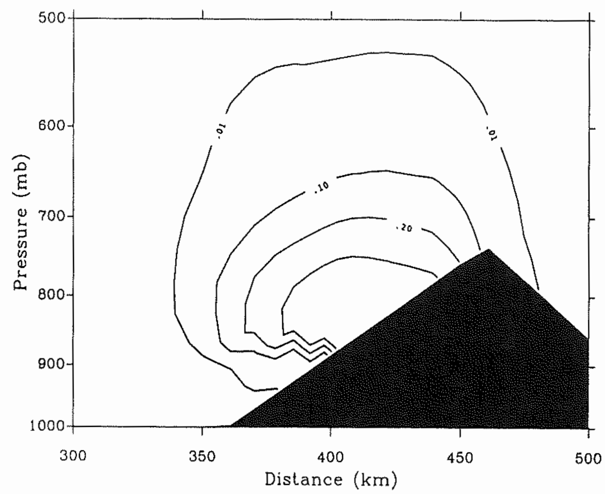

Figure 6. Aggregation rate for ice. The units are in g m^{-3} / 1000 s.

Over the entire spatial extent of the storm, the growth of ice is nearly evenly divided between the accretion of cloud water and the deposition of vapor to ice (Fig. 7b). Accretion of cloud water dominates in the upwind half of the cloud where the concentration of the particles is small and the concentration of water droplets is high. Most of the available vapor goes into growing the cloud droplets (Fig. 7c). The ice particles fall through these regions of high liquid water content and rime. After most of the cloud water has been accreted and the ice particles increase in size and concentration, deposition to ice becomes the dominant process in the downwind half of the cloud.

All of the condensate over the crest line is ice. Ice which is advected over the barrier either falls out in the lee of the mountain or it sublimates. The amount which sublimates is shown by the negative portion of the trace for the deposition of vapor to ice in Fig. 7c. About 10% of the total condensate formed in the storm is advected over the barrier. Of this, only 20% reaches the surface.

4. CONCLUSIONS

Deep orographically induced storms over a long barrier are very efficient. The transport time for a parcel to traverse the barrier is sufficiently long for precipitation processes to be active. Very little liquid water is able to pass over the crest line. This type of storm presents little seeding potential.

ACKNOWLEDGEMENTS

This research was supported by the Division of Atmospheric Water Resources Management, Bureau of Reclamation, Department of the Interior, Contract #2–07–81–V0256. I would like to thank all the participants of SCPP for the invaluable data set which they provided.

REFERENCES

Berry, E. X., and R. L. Reinhardt, 1974: An analysis of cloud drop growth by collection: Part I. Double distributions. *J. Atmos. Sci.*, **31**, 1814–1824.

Gordon, G. L., 1986: Using the gamma function to represent hydrometeor distributions. Cloud Physics Studies in SCPP, Interim Progress Report 1985–1986. Dept. of Atmos. Sci., AS–155, University of Wyoming, Laramie, WY, 104–121.

Marwitz, J. D.: 1987a: Deep orographic storms over the Sierra Nevada. Part I: Thermodynamic and kinematic structure. *J. Atmos. Sci.*, **44**, 159–173.

———, 1987b: Deep orographic storms over the Sierra Nevada Part II: The precipitation processes. *J. Atmos. Sci.*, **44** 174–185.

Waight. K. T., 1984: A numerical study of the Sierra Nevada barrier jet. M.S. thesis, Dept. of Atmos. Sci., AS–148, University of Wyoming, Laramie, WY, 119 pp.

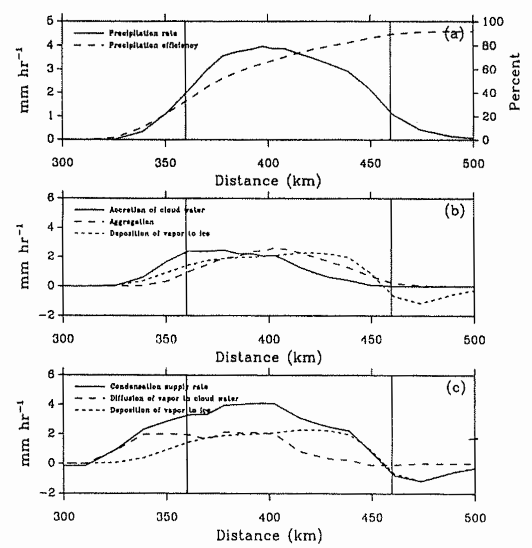

Figure 7. (a) The precipitation rate (mm hr^{-1}) and the accumulated precipitation efficiency (%). (b) Vertically integrated ice processes: accretion of cloud water (solid), aggregation (dashed), and deposition of vapor to ice (dotted). (c) Vertically integrated vapor processes: condensation supply rate (solid), diffusion of vapor to cloud water (dashed), and deposition of vapor to ice (dotted). The vertical lines indicate the base and crest of the barrier.

PRECIPITATION VARIABILITY IN THE DIFERENT TYPES
OF CYCLONES IN THE EUROPEAN RUSSIA

N.A. Bezrukova

Central Aerological Observatory, Moscow Region, Russia

INTRODUCTION

According to climatological studies the amount of solid precipitation (in the form of snowfall) contributes about 1/5 to annual precipitation amount at the latitude of Moscow and already about 1/4 at the latitude of St.Petersburg. However, the spatial and temporal variability of frontal snowfall intensity remains poorly investigated. An estimation of contribution of various intensity into total snowfall as well as an assessment of fraction of area covered by precipitation of various intensity are of particular interest, since they indicate relative importance of convective updrafts and widespread frontal lifting in precipitation development.

This paper presents the results of radar observations of various snow intensity contributions into the total snowfall and precipitation area.

The observational data cover 27 frontal cases, which occurred in the region of Moscow in winter 1985-86.

METHODOLOGY

The data were taken from the Central Aerological Observatory Meteorological digital radar, located 20 km to the north of Moscow centre. The 3 cm radar scans an area within 100 km radius and measures precipitation intensity, averaged over 3x3 or 10x10 km and 20 min or 1 hour. Area-averaged error of precipitation intensity radar measurements is less than 10%.

Only cases with snow-form precipitation were taken. The temperature of -5°C at 1 km level was the main criterion of these cases.

Light/heavy precipitation was suppo sed to be of stratiform/convective origin. The threshold between stratiform and convective snowfall was taken to be 0,3 mm/hr (as it is generally accepted for the European Russia).

Relative contribution (in percent) of stratiform precipitation (SP) was determined for each front case. Since convective precipitation (CP) contribution may be found as a mere complementary to 100%, given below are the contributions of stratiform precipitation only.

CONTRIBUTIONS IN TOTAL SNOWFALL AMOUNT

Usually, in winter the stratiform precipitation contribution (SPC) in total snowfall amount prevails, with the exception of cases with southern and south-western warm advection.

It has been found that relative contribution of CP ($I>0,3$ mm/hr) and SP ($I<=0,3$mm/hr) to the total snowfall to some degree depends on a type of front. Fig.1 shows SPC in the total snowfall. In winter SP contributes 90-100% in

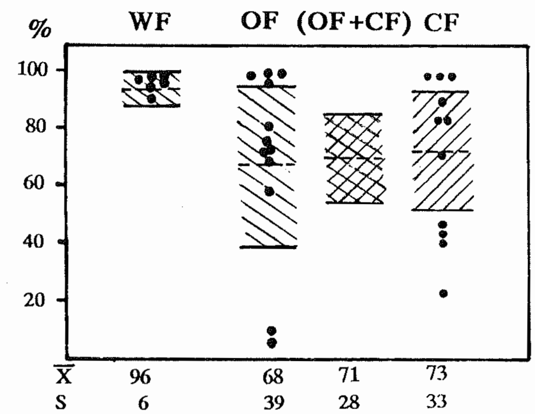

Fig.1 Contribution (%) of stratiform snowfall fraction ($I=<0,3$mm/hr) into total precipitation amount for diferent types of fronts, warm fronts, cold fronts and occlusion fronts.

warm frontal snowfall. Occlusions and cold fronts show simular SPC average values and confidence limits. That is why SPC in cold fronts and occlusions are united. The united SPC is 70%, which is less than that in the warm fronts .

It has been found that SPC strongly depends on the type of cyclone. Fig.2 depicts the cumulative snowfall intensity distribution function, averaged over the bulk of frontal precipitation area during its passage within the radar range (by analogy to the Area Time Integral method of Doneaud et al. (1984)). The curves on Fig.2 fall into three categories which correspond to 3 typical cyclone trajectories: a) from N and NW (or from Arctics), b) from W (or from Atlantics), and, at last, c) from SW and S (or from Mediterranean Sea).

STRATIFORM PRECIPITATION FRACTION OF TOTAL SNOWFALL AREA

Also derived were the fractions of total snowfall area, covered by stratiform precipitation in 3 types of cyclones.

The frontal precipitation areas produced by N and NW (Arctic) cyclones are made up entirely of stratiform precipitation. Moreover, in 90% of total snowfall area, precipitation intensity does not exceed 0.2 mm/hr.

On average stratiform snowfall covers 80-90% of precipitation area in the W (Atlantic) cyclones, remaining 10-20% of the area being filled up by convective snowfall.

The S and SW cyclones usually bear warm airmass from Mediterranean, rich in moisture and unstable. Instability at 850-700 hPa levels forms layers with embedded convection and heavy precipitation. Stratiform precipita-

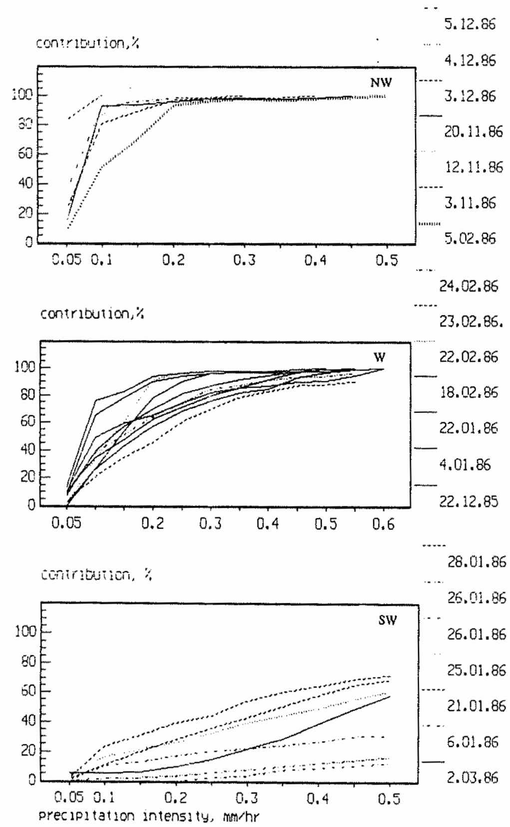

Fig.2 Percent of total frontal snowfall as a function of snowfall intensity for a) northern and northwestern (Arctic), b) western (Atlantic), c) south and south-western (Mediterranean) cyclone trajectories.

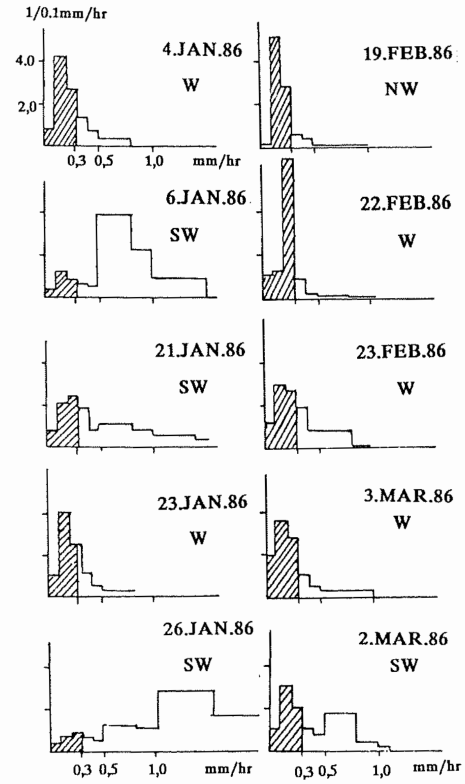

Fig.3 Probability density distribution (PDD) of area covered by snowfall of various intensity for a number of frontal cases.

tion covers only 30-40% of total precipitation area. Remaining 60-70% of the area are filled up by convective precipitation of various intensity.

It is worth noting, that in S and SW cyclone frontal systems SP contribution both in total snowfall and total precipitation area experience large case-to-case variability. The likely reasons for that are both lack of statistics and a variety of thermal and especially higrometric parameters of precipitation-bearing warm airmasses.

According to Popova et al.(1975) a mixed character of Mediterranean cyclone cloud system is caused by synoptic scale deferential temperature advection. Its type and intensity subject to vertical variations, facilitating the emergence of multilayered cloud systems with a variety of cloud forms. The latter broadens the precipitation rate spectrum, producing a pronounced convectively generated component.

Aforesaid features of diferent types of cyclones are well demonstrated on Fig.3, which shows examples of Probability Density Distribution (PDD) of area covered by snowfall of various intensity. The relative contribution of stratiform snowfall is shaded.

In the frontal zones of N, NW and W cyclones where stratiform snowfall prevails, areal SPC is formed mainly by snowfall rates of 0,1-0,2 mm/hr.

In the frontal zones of S and SW cyclones, where convective snowfall prevails the majority of area is covered by convective snowfall rates of 0,5-1,0 mm/hr. Remark that area covered by stratiform snowfall in these cases is also formed by intensity of 0,1-0,2 mm/hr.

Thus, there are two maxima in two intensity ranges, one of them being in the range of SP and another in the range of CP.

The Table gives area-averaged snowfall rates for three types of cyclones and 50-percentile of intensity.

Cyclones trajectory (number of cases)	I, mm/hr	S mm/hr	I-50% mm/hr
N, NW (6)	0,08	0,02	0,1
W (13)	0,14	0,03	0,2
S, SW (8)	0,6	0,3	0,4

Here N is the number of cases, S is standard deviation, which shows considerable variations

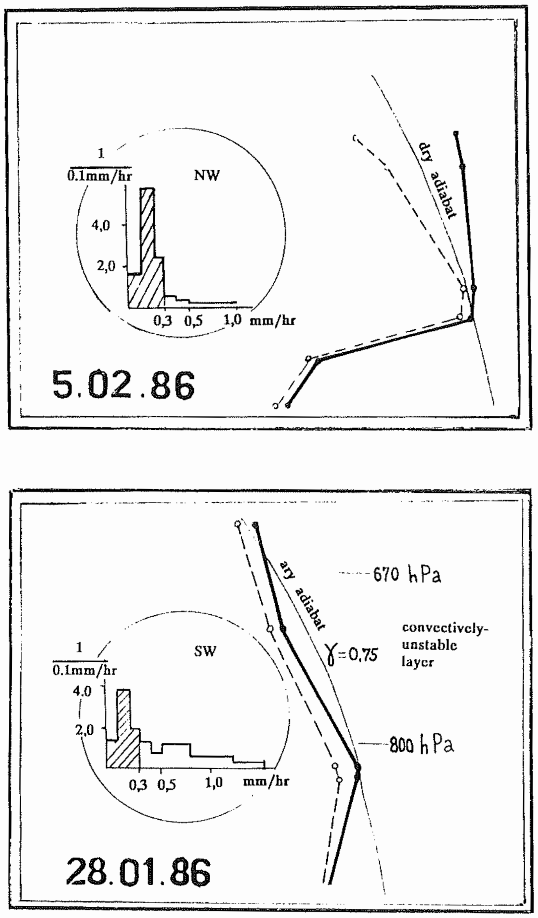

Fig.4 Fragments of aerological diagramms for precipitation-bearing warm airmasses in two cyclones of diferent types: Arctic and Mediterranean. Window shows examples of PDD, respectively.

in the last group. According to the table only 50% of the total snowfall area in south-western (Mediterranean) cyclones is covered by rates of less than 0,4 mm/h, while in Atlantic and Arctic cyclones - by rates of less, than 0,1 mm/hr and 0,2 mm/hr respectively.

Fig.3 shows fragments of aerological diagramms which support the existance of unstable or conditionally unstable layers within the S and SW cyclone frontal zones. The circles show PDD of area covered by snowfall of various intensity in Arctic and Mediterranean cyclones. The latter are characterized by well manifested second mode in the distribution of precipitation intensity.

CONCLUSION

The paper examines 27 cases of winter time frontal precipitation in various types of cyclones. It has been found, that in nothern, north-western and western cyclones 90% of frontal precipitation is stratiform. By contrast, in south and south-western cyclones stratiform precipitation covers no more than 30-40% of the total area.

The largest fraction of snowfall is contributed by the stratiform precipitation of 0,01-0,02 mm/hr and by convective precipitation of 0,5-1,0 mm/hr. Thus, precipitation intensity distribution in south and south-western cyclones may be bimodal, unlike that in western and north-western cyclones, which fits the lognormal law.

REFERENCES

Doneaud, A. A, S. Ionescu-Niscov, D. L. Priegnitz, and P. L. Smith, 1984: The area-time integral as an indicator for convective rain volumes. J. Clim. Appl. Meteor., 23, 555-561.

Mediterranean cyclones in the field of cloud. (Edited by T. P. Popova), 1975, Leningrad, Gidrometeoizdat, 205.

2-D MESOSCALE AGEOSTROPHIC WIND CIRCULATION IN A COLD FRONT

Mathieu NURET, Michel CHONG and Geneviève JAUBERT

Centre National de Recherches Météorologiques (METEO-FRANCE and CNRS)
31057 Toulouse Cedex, France

1. Introduction

On 11 November 1987, a cold-front system was observed during the FRONTS 87 experiment in western Europe, which involved a wide range of observing techniques (aircrafts, radars, radiosondes, dropsondes and ground stations). Details on the mesoscale structure of this system have been discussed by Chong *et al.*(1991) and Jaubert *et al.*(1991). Doppler radar observations revealed a mesoscale organization of precipitation into narrow and wide rainbands, associated with convective-scale and mesoscale updrafts from converging transverse airflows. This transverse circulation resulted from mesoscale and synoptic-scale dynamical constraints which were forcing frontogenesis.

The aim of this paper is to compare the observed cross-frontal airflow to the ageostrophic circulation that can be predicted from the frontogenesis theory based upon the assumption that the atmosphere constantly tends to maintain the thermal wind balance. In other words, the diagnostic two-dimensionnal equation of Sawyer (1956) and Eliassen (1962) will be solved numerically, using data from soundings, Doppler radars and from the French mesoscale operational data assimilation system PERIDOT designed for the analysis of conventional (soundings, ...) as well as non-conventional (satellite, ...) observations (Durand and Bougeault, 1987).

2. The Sawyer-Eliassen (S-E) equation

The diagnostic S-E equation that is used in this study is the unapproximate version, referred to as the primitive equation form (Keyser and Pecnick, 1985). It is expressed in terms of the pressure-dependent pseudo-height Z (Hoskins and Bretherton, 1972),

$$Z = Z_a(1-(p/p_0)^{R/C_p})$$

where $Z_a = Cp\theta_0/g$ is the pseudo-height at the top of the atmosphere, θ_0 and p_0 are reference values of potential temperature and pressure.

Considering x and y as the cross-front and along-front coordinates, and defining a streamfunction ψ from the transverse ageostrophic wind (u_a, w) as

$$ru_a = \partial\psi/\partial Z \qquad (1a)$$

$$rw = -\partial\psi/\partial x \qquad (1b)$$

with the pseudo-density r defined as:

$$r = \rho_0(1-Z/Z_a)^{C_v/R}$$

the primitive equation version of the diagnostic equation for ψ (Keyser and Pecnick, 1985) takes the following form, for a moist atmosphere and in the absence of diabatic and frictional forcing and of unbalanced effects such as inertia-gravity waves:

$$N^2\frac{\partial^2\psi}{\partial x^2} - 2S^2\frac{\partial^2\psi}{\partial x\partial Z} + F^2\frac{\partial^2\psi}{\partial Z^2} + (\mu f\frac{\partial v}{\partial Z})\frac{\partial\psi}{\partial x}$$

$$-\mu F^2\frac{\partial\psi}{\partial Z} = -Q_g - Q_{ag} \qquad (2)$$

where

$$N^2 = \frac{g}{\theta_0}\frac{\partial\theta_v}{\partial Z}$$

$$S^2 = (\frac{f}{2})(\frac{\partial v}{\partial Z} + \frac{\partial v_g}{\partial Z})$$

$$F^2 = f(f+\frac{\partial v}{\partial x})$$

$$\mu = r^{-1}\partial r/\partial Z$$

$$Q_g = -2r\frac{g}{\theta_0}(\frac{\partial u_g}{\partial x}\frac{\partial\theta_v}{\partial x} + \frac{\partial v_g}{\partial x}\frac{\partial\theta_v}{\partial y}) \qquad (3)$$

$$Q_{ag} = -rf\frac{\partial v_{ag}}{\partial Z}\frac{\partial u_g}{\partial x} - 2r\frac{g}{\theta_0}\frac{\partial v_{ag}}{\partial x}\frac{\partial\theta_v}{\partial y} \qquad (4)$$

f is the Coriolis parameter, θ_v is the virtual potential temperature, u_g is the transverse geostrophic wind, v_a and v_g are the ageostrophic and geostrophic components of the along-front wind. Q_g and Q_{ag} define the geostrophic and ageostrophic forcings, respectively. The first and second terms in (3) and (4) represent the effects of confluence and horizontal shear. All the terms involved in (2) can be deduced from the observations and a numerical resolution of (2) will give a diagnosed ageostrophic circulation.

3. The 11 november 1987 cold-front system

a) Synoptic meteorological context

At 0000 UTC, an intense zonal flow was well-established over the Atlantic Ocean with a baroclinic zone lying between 48N and 50N, south of a geopotential low centered on the south-west of Ireland. Between 0000 and 0600, a wave developed and moved toward the British Isles. The associated cold front reached Brittany at 1900 and its passage over the experimental site of Brest was observed at 1940. The surface chart at 1800 shows that the surface cold front (SCF) was oriented at 40 degrees clockwise from the North, with a marked undulation.

Figure 1 shows two composite pictures of reflectivity from a network of French and British conventional radars, at 1830 and 2030 respectively. The SCF is associated with the marked narrow rainband (black area), elongated from northeast to south-west and with an apparent discontinuity over the Channel at 1830, related to the above-mentioned undulation. Comparison of the two pictures also shows that the SCF underwent rotation in its northern part and horizontal translation in its southernmost part when it passed over the experimental area in Brest. This south portion had a cross-frontal propagation speed of 11 $m\ s^{-1}$ (Chong *et al.*, 1991).

b) Thermodynamic structure

Figure 2 shows the virtual potential temperature (θ_v) in a time-height cross-section from the long series of soundings launched at Brest between 0540 on 11 November and 1130 on 12 November. The height coordinate in this figure and in the next ones refers to the pseudo-height Z, except in Fig.4 where it refers to the altitude above ground level. The time coordinate is

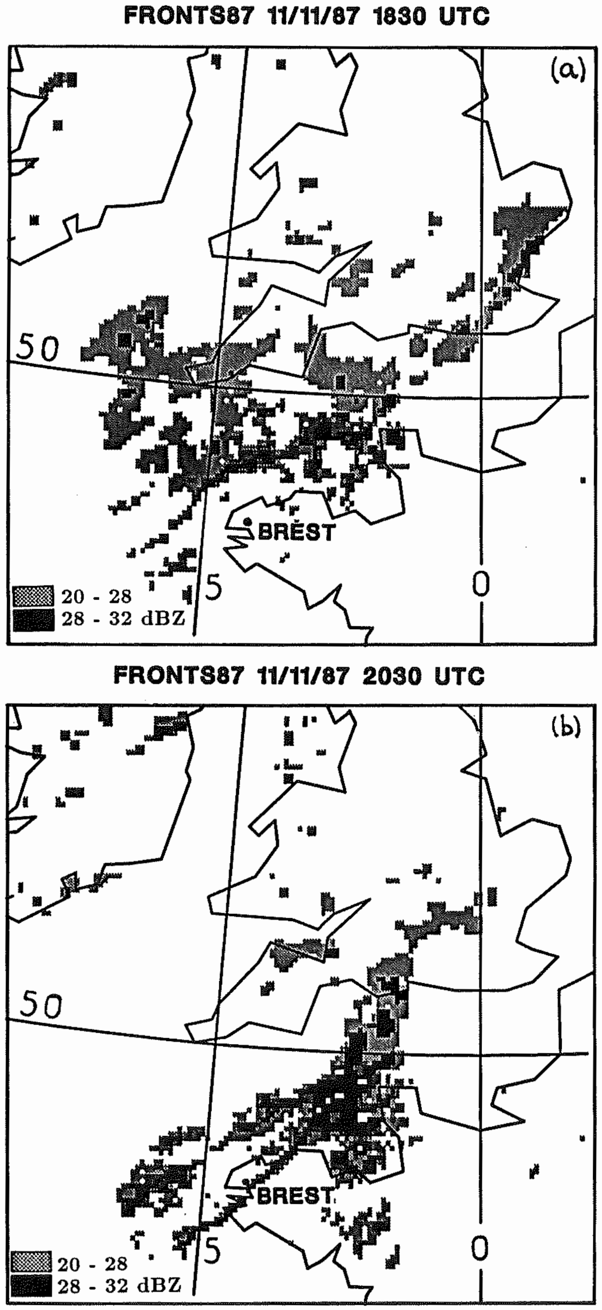

Fig. 1: Composite radar reflectivity (dBZ) observed at (a) 1830 and (b) 2030 UTC.

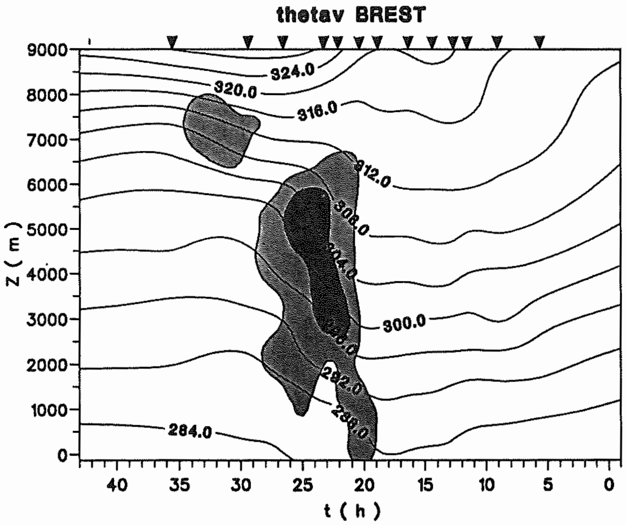

Fig. 2: Time-height section of virtual potential temperature (K) from soundings launched at Brest (upper marks). Shaded regions denote cross-front gradients in excess of 2 and 4 K (100 km)$^{-1}$.

running from right to left (zero refers to 0000 on 11 November) as one progresses toward the front system. The time-interval between soundings was of 2-3 hours as the southern part of the frontal discontinuity passed over the site. Fig. 2 reveals two relatively homogeneous warm and cold air masses before and after 2000 with a well-defined transition. This transition is materialized by the shaded areas superposed to the temperature contours, which delimit regions of cross-frontal horizontal gradients in excess of 2 and 4 K (100 km)$^{-1}$. Evaluation of these gradients has been performed from the time observations by considering a time-distance conversion in a steady-state context. Maximum temperature contrast occurred above 2.5 km altitude and behind the surface contrast at 2000. The along-front gradient of θ_v (not shown) deduced from PERIDOT analyses (see Sec. 4) is relatively uniform and reaches -0.5 K (100 km)$^{-1}$ within the frontal discontinuity zone. Behind this zone and at low levels, a local region of positive gradient is observed.

c) Along-front wind component

The along-front wind component v derived from soundings, is presented in Fig.3 in the same cross-section as in Fig.2. Two well-marked jets characterize this along-front flow: a low-level jet at 1 km altitude ahead of a sharp zone of strong horizontal cyclonic shear and an upper-level jet at 9 km, above this frontal zone. In order to verify how much this parallel flow is geostrophic, i.e., how much the thermal wind balance is verified, the vertical shear in the v-component is also reported in Fig.3 (shaded areas of vertical shear in excess of 10 and 15 $m\ s^{-1}\ km^{-1}$). Comparison of Figs. 2 and 3 reveals that, at very low levels ahead of the frontal discontinuity and at upper levels, the cross-frontal thermal contrast was not perfectly coinciding with the vertical v-shear. This suggests that the ageostrophic component of the flow in the along-front direction can be a non-negligible feature of the observed frontal system. We will see later how this imbalance contributes to the increase/decrease of the frontogenetic forcing terms in the S-E equation.

d) Cross-front circulation

The mesoscale cross-front circulation deduced from VAD analysis of Doppler radar observations between 1200 and 2400 was discussed in Jaubert *et al.*(1991). This description was however incomplete, due to some unappropriate radar scan sequences. In order to get a more complete view of the air circulation, a composite was done from these radar-derived winds and those deduced from soundings. Fig. 4 is this composite wind representation: the vectors visualize the cross-front projection (transverse flow) while the contours represent the along-front component.

The transverse circulation appears to be organized into three updraft cores of 10 to 30 $cm\ s^{-1}$: in the warm air region well ahead of the SCF, near the SCF, and above the frontal surface revealed by the sharp zone of along-front wind shear. They correspond to the observed bands of precipitation discussed in Chong *et al.*(1991). Globally, the visualized vectors reveal a thermally direct circulation in the regions of the frontal discontinuity and an indirect circulation ahead. Using a steady-state approach, Jaubert *et al.*(1991) evaluated the temporal evolution of the cross-front gradient of the equivalent potential temperature, and found that frontogenetic forcing may account for the observed transverse flow.

4. Geostrophic wind components

The frontogenesis theory leading to the S-E equation (2) is based upon the knowledge of the geostrophic wind field. Fig. 5 shows the time-height cross-sections of the transverse and along-front components above the experimental site of Brest. Their evaluation has required 6-hours analyses of geopotential fields deduced from observed mass fields, through the French operational assimilation system. This system is based on a 3-D multivariate optimal interpolation onto grid points over 15 σ-levels with a horizontal resolution of 35 km. Extraction of these components at Brest was performed by using an elaborate software designed to provide pertinent meteorological variables at any spatial locations.

The along-front component presents an upper-level jet centered at 8 km altitude which overhangs a well-defined zone of horizontal cyclonic shear. This jet has a non-negligible transverse component which presents a maximum behind the along-front one. This transverse geostrophic flow is converging within

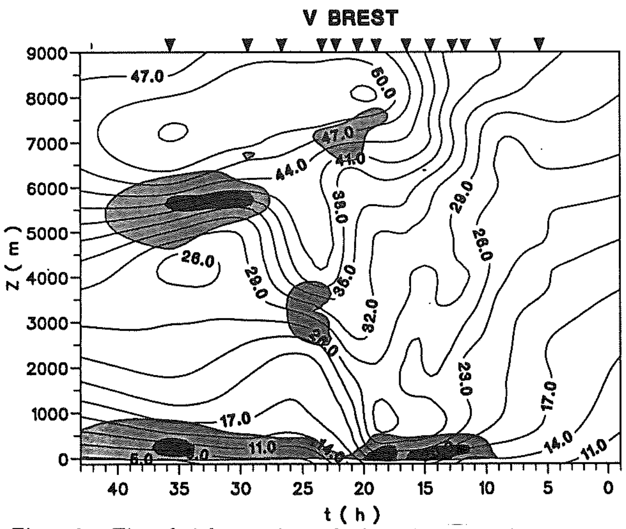

Fig. 3: Time-height section of along-front wind component ($m\ s^{-1}$) above Brest. Vertical shears greater than 10 and 15 $m\ s^{-1}\ km^{-1}$ are shaded.

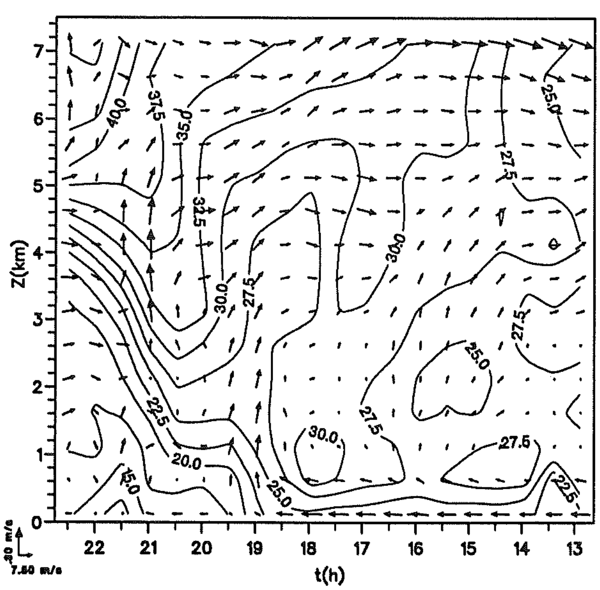

Fig. 4: Composite cross-front circulation (arrows) and along-front velocity (contours) deduced from Doppler radar observations and soundings between 1300 and 2300 UTC.

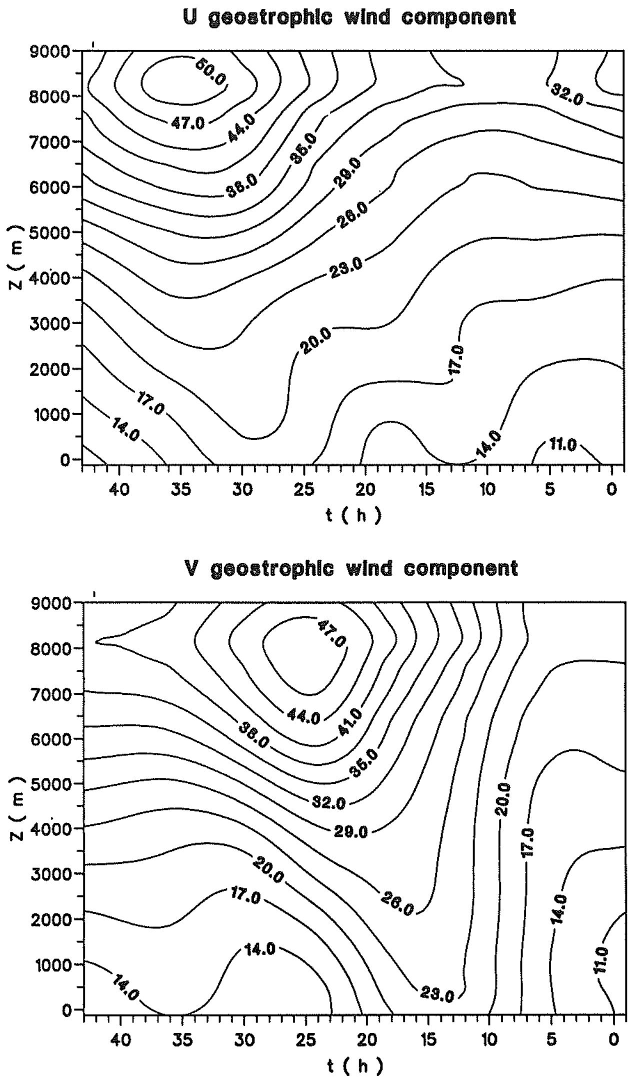

Fig. 5: Geostrophic wind components (u_g and v_g) deduced from PERIDOT analysis performed every 6 hours.

the sheared zone. In most respects, the along-front geostrophic wind resembles the observed wind (see Fig. 3) although sensible differences expressing the thermal imbalance can be noted. The major differences concern the low-level jet and the intensity of the horizontal shear which is about half of the observed shear. This justifies the use of the primitive equation version of the S-E equation in the diagnosis of the transverse ageostrophic circulation.

5. Diagnosed ageostrophic circulation

The above-discussed fields of virtual potential temperature and along-front wind components (total and geostrophic) have been used to compute all terms involved in Eq. (2), in order to diagnose the ageostrophic flow. Fig. 6 shows the time-height sections of the geostrophic (Q_g) and total ($Q_g + Q_{ag}$) forcings. The geostrophic forcing (Fig. 6a) has two maxima within the frontal zone, in the lowest and mid levels, respectively. Both confluence and horizontal shear forcings positively contribute to them, with a dominance of the confluence term. This results from the larger cross-front virtual potential temperature gradient with respect to the along-front gradient (see Sec. 3b). In regions ahead of the frontal zone, negative val-

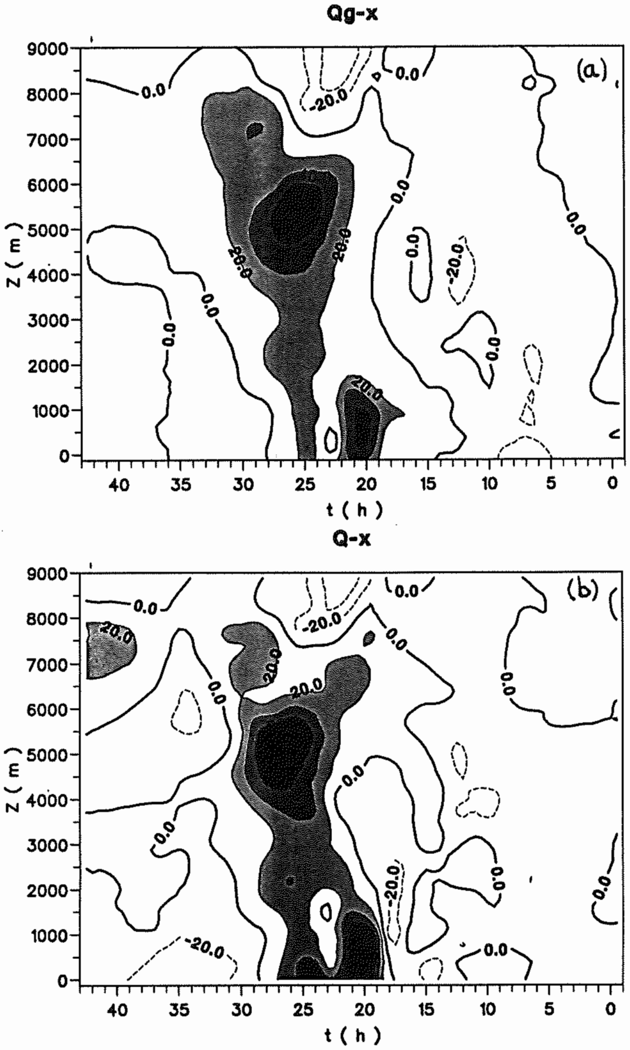

Fig. 6: (a) Geostrophic and (b) total forcings (units are 10^{-12} kg m^{-3} s^{-3}). Regions with values greater than 20, 40 ... units are shaded.

ues of Q_g are effects of the horizontal shear. Contribution of the ageostrophic forcing to the total Q is evident from Fig. 6b. The net effects of the thermal wind imbalance are to enhance the low-level maximum and to reduce (opposed contribution) the horizontal extension of the low-to-mid level positive forcing just ahead of the local maxima. The horizontal shear mainly contributes to the ageostrophic forcing.

The response of the atmosphere to the total forcing is presented in Fig. 7, which results from the numerical resolution of (2) where upper and lower boundary conditions are set to impose zero vertical velocity at these limits. Contour lines in Fig. 7 are streamfunctions ψ and vectors are the derived transverse ageostrophic flow (Eqs. 1). Shaded regions represent the vertical velocity in excess of 2 and 4 $cm\ s^{-1}$. The diagnosed flow is qualitatively consistent with that observed (Fig. 4), and it is characterized by a thermally direct circulation in the region of positive forcing and indirect circulation ahead of this region. However, the observed updrafts are not fully reproduced, in particular the low-level updraft core associated with the SCF. This suggests that mesoscale and synoptic-scale dynamical constraints partly contribute to force ageostrophic circulation, and that diabatic and frictional forcing which has been neglected in this study, should be taken into account.

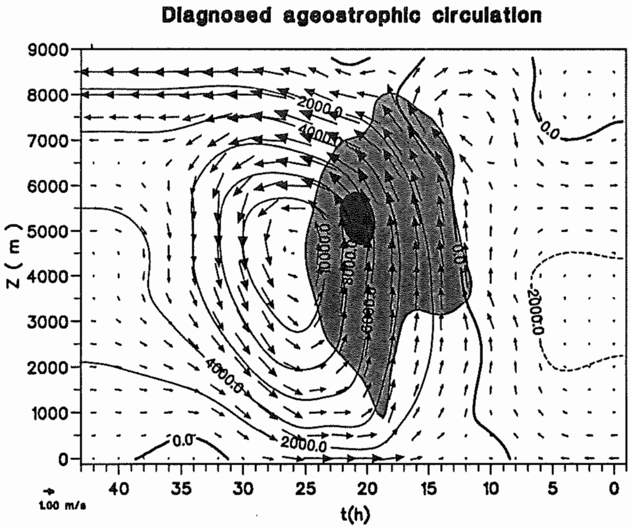

Fig. 7: Diagnosed cross-front circulation (arrows) corresponding to the total forcing in Fig. 6b, and derived from the S-E equation for streamfunction ψ (contour lines). Vertical velocities greater than 2 and 4 cm s^{-1} are shaded.

6. Summary

This paper has investigated the frontogenesis theory in order to predict the forced ageostrophic circulation within a cold front. Only forcings due to geostrophic and ageostrophic along-front wind have been considered. A good agreement has been found between the diagnosed flow and the observed one, although this comparison strongly suggests that improvement should be realized if small-scale processes are included.

Acknowledgements. FRONTS 87 was a cooperative field project in which the Institut National des Sciences de l'Univers (INSU) and french participating research laboratories contributed to its financial support.This work was partly supported by INSU, under Grants ATP 803615. Special thanks to S. Sénési who provided analysis software of PERIDOT outputs, and to J. Périé for his assistance in the realization of the illustrations.

REFERENCES

Chong, M., G. Jaubert and M. Nuret, 1991: Small mesoscale structure of a cold-frontal rainband. *Preprints 25th Intern. Conf. on Radar Meteor.*, Paris, Amer. Meteor. Soc., 181-184.

Durand, Y. and P. Bougeault, 1987: L'analyse objective PERIDOT. *Note de travail de l'E.E.R.M.*, 193, 71pp.

Eliassen, A., 1962: On the vertical circulation in frontal zones. *Geophys. Publ.*, 24, 147-160.

Hoskins, B.J. and F.P. Bretherton, 1972: Atmospheric frontogenesis models: Mathematical formulation and solution. *J. Atmos. Sci.*, 29, 11-37.

Jaubert, G., M. Nuret and M. Chong, 1991: A case study of cold-frontal rainbands. *Preprints 25th Intern. Conf. on Radar Meteor.*, Paris, Amer. Meteor. Soc., 185-188.

Keyser, D. and M. J. Pecnick, 1985: Diagnosis of ageostrophic circulation in a two-dimensional primitive equation model of frontogenesis. *J. Atmos. Sci.*, 42, 1283-1305.

Sawyer, J.S., 1956: The vertical circulation at meteorological fronts and its relation to frontogenesis. *Proc. Roy. Soc. London*, A234, 346-362.

NON-HYDROSTATIC SIMULATIONS OF FRONTAL SYSTEMS OBSERVED DURING THE EUROPEAN MFDP/FRONTS 87 EXPERIMENT

Jean-Luc Redelsperger and Jean-Philipe Lafore

Centre National de Recherches Météorologiques
(Météo-France and CNRS)
42 Ave Coriolis, 31057 Toulouse Cedex
France

1 Introduction

A non-hydrostatic model is used to simulate a cold front at a grid resolution of 5 km. The case studied corresponds to the second Intensive Observing Period (IOP 2) of the MFDP / FRONTS 87 experiment. This European field observation project was conducted in western Europe, and involved a wide range of observating technics, including aircrafts, Doppler radars and dropsondes. An overview of the project can be found in Browning *et al.*(1986) and Clough and Testud (1988). One specific scientific objective of the FRONTS 87 project is to obtain an improved dynamical understanding of synoptic, meso- and smaller scale interactions in active cold fronts. As part of this project explicitly simulations of both the convective and large scale flow are performed to reproduce the great variety of observed rainbands and to allow a study of the scale interactions.

Before to simulate FRONTS 87 cases, a series of numerical moist experiment with high resolution (5 km) have been performed with an analytical solution to the Eady problem as initial condition (Benard *et al.*, 1992 a and b). These experiments have shown the ability of models working at cloud scale, to reproduce most of mesoscale features, observed in the frontal systems.

2 Model and Initialization

The model used in this study is the anelastic model of Redelsperger and Sommeria (1986). Prognostic equations for momentum, potential temperature θ and moisture variables, are resolved on a finite difference mesh, together with a diagnostic equation for pressure derived from the anelastic continuity equation. Condensation effects are treated in a bulk microphysical parameterization of warm rain physics. Subgrid-scale effects are treated in the turbulence parameterization of Redelsperger and Sommeria (1986). Momentum, heat and moisture transfer at the ground are treated with a parameterization of the surface boundary layer. Details are to be found in the references above.

In the present work, a two-dimensional version of the model was used in order to look at the relationship of rainband occurences and mechanisms with the large scale forcings (namely the along front deformation and baroclinicity). The 2D model domain was 3000km $\times$ 15km with a stretched vertical coordinate going from 60 m near the ground to 500 m above the cloud layer. The model uses open boundary conditions in x (cross-front) but using a method suggested by Carpenter (1982), to monitor the large scale forcings. More details on this method may be found in Redelsperger and Lafore (1988).

The IOP2 case was first simulated using the French forecast hydrostatic "Peridot" model with horizontal resolution of 35 km. The "Peridot" fields at 18 h on the 11 september 1987 are used both to initialize the non-hydrostatic model and to monitor the large scale forcings through a one-way coupling between the two models. The "Peridot" fields were first interpolated on a cartesian domain (2000 km x 1200 km) and averaged on a y-slice (along-front) of 300 km where the observed front was nearly two-dimensional.

Fig. 1 shows the two-dimensional initial fields as computed from the "Peridot" model. The cold and warm sectors are easily identified on the cross-section of the virtual potential temperature deviation θ'_{vl}. The main region of baroclinicity across the front is localized between 2 and 6 km height. The obtained structure of along-front wind component allows to identify the two horizontal jets (Fig. 1b), namely the low-level jet ahead the surface cold front (SCF) (maximum 21 $m\ s^{-1}$) and the upper-level jet (maximum 35 $m\ s^{-1}$). The vertical circulation in "Peridot" model (Fig. 1d) is caracterized by a main ascent in phase with the SCF and a wide band (350 km wide) in the warm sector.

The along-front large scale forcings (the deformation $\frac{\partial v}{\partial y}$ and the baroclinicity $\frac{\partial \theta_{vl}}{\partial y}$) show maxima in altitude. The baroclinicity is the most important with values up to $-2\ K\ /\ 100\ km$ around 5 km. A stationary state is assumed for these large scale forcings in the system moving-frame (11 $m\ s^{-1}$ and 15 $m\ s^{-1}$ in the cross and along-front directions respectively).

3 Simulations and Comparisons with Observations

Results of the first experiment (REF) are shown on (Fig. 2) after 4 hours of simulation. A first result is the ability of the model to reproduce a large variety of frontal bands, starting from only the knowledge of β-mesoscale fields. The Narrow Cold-Frontal Rainband (NCFR) is identified at the SCF with a maximum of vertical velocity of 1.4 $m\ s^{-1}$. Two classes of wide bands are also observed : Wide Cold-Frontal Rainbands and Warm Sector Wide Rainbands (WCFR and WSWR respectively, hereafter) producing less precipitation and with weak vertical velocities around .15 $m\ s^{-1}$.

As indicated by the time-history of the vertical velocity maximum and the ground precipitation (Fig. 5), the REF simulation needs around 3 hours to reach a nearly steady state, comparable with Doppler radar observations (Fig. 3) performed in the VAD mode, as the cold front reached the french coast (Jaubert *et al.*, 1991). Wavelengths shorter than 40 km have been removed from the simulation fields to be able to compare with observations. The localization, intensity and width of different bands are well reproduced by the model. The downdraugths seem a little underestimated in the simulation, may be due to the non-representation of the ice phase in the model.

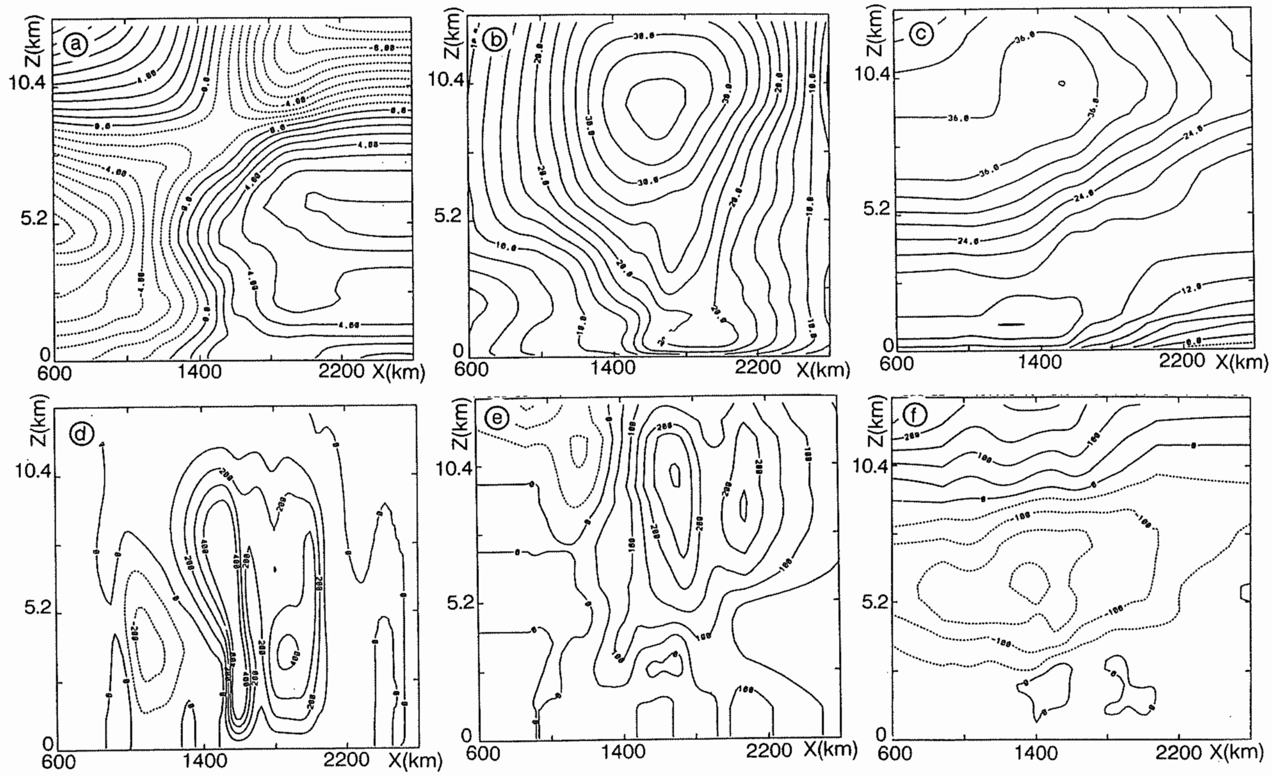

Figure 1: Cross sections of initial fields; a) Virtual potential temperature (contour interval 1 K) b) Along-front wind (contour interval 2.5 $m\ s^{-1}$) c) Relative cross-front wind (contour interval 3 $m\ s^{-1}$) d) Vertical velocity (contour interval 1 $cm\ s^{-1}$) e) Deformation $\frac{\partial v}{\partial y}$ (contour interval .5 $m\ s^{-1}$ / $100km$) f) Baroclinicity $\frac{\partial \theta_{vl}}{\partial y}$ (contour interval .5 K / $100km$)

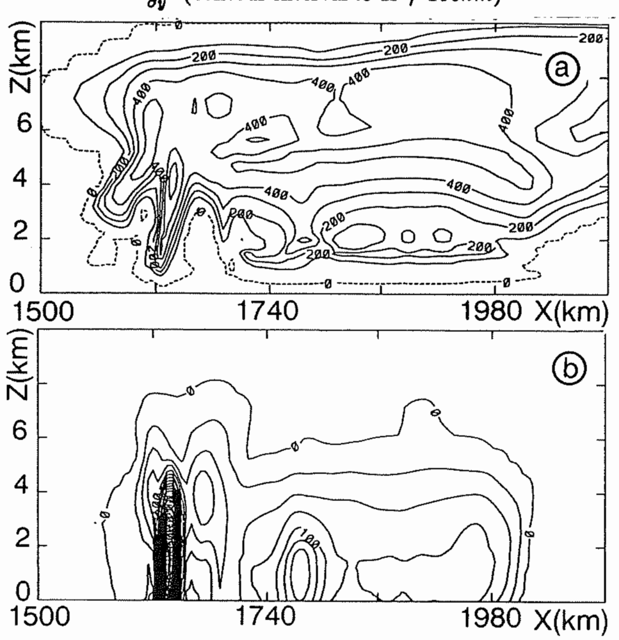

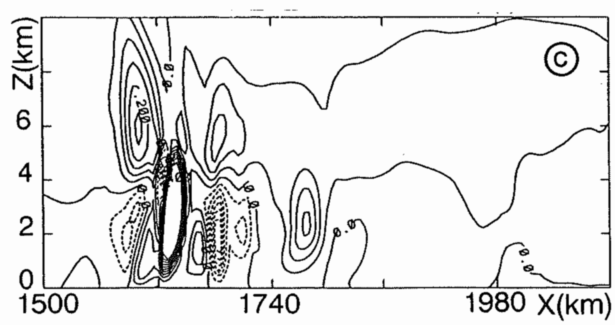

Figure 2: Cross sections for experiment REF at t = 4h; a) Cloud water mixing (contour interval .1 $g\ kg^{-1}$) b) Rain water mixing ratio (contour interval .025 $g\ kg^{-1}$) c) Vertical velocity (contour interval 5 $cm\ s^{-1}$)

In order to assess the importance of the initial ageostrophic part on the simulation success, a second simulation (NOAG) was performed, in starting the model without ageostrophic wind (namely, $u_{ag} = w = 0$). The simulated vertical velocity field after 5 hours (Fig. 4a) is noteworthy similar to the one obtained in simulation REF after 4 hours (Fig. 2). A 90 min lag time of the simulation NOAG may be more precisely viewed on the time history of both ground precipitation and vertical velocity maximum ((Fig. 5)). The consequences of the strong similiarities between experiments REF and NOAG are twofold:

- The knowledge of the ageostrophic part is not neccessary to start a simulation. That means for example it is possible to initialize the model from the analyzed fields of mesoscale model (instead forecasted fields). Indeed, it well known that the divergent part of analyzed fields of such models is generally noisy, though the other analyzed fields are closer of the observations than the forecasted fields.

- It is possible to modify the large scale forcings to study their influences on the rainband occurence. Indeed, it is impossible to modify the deformation field in the case where a complete initialization scheme is used, as the divergence is modified in the same time.

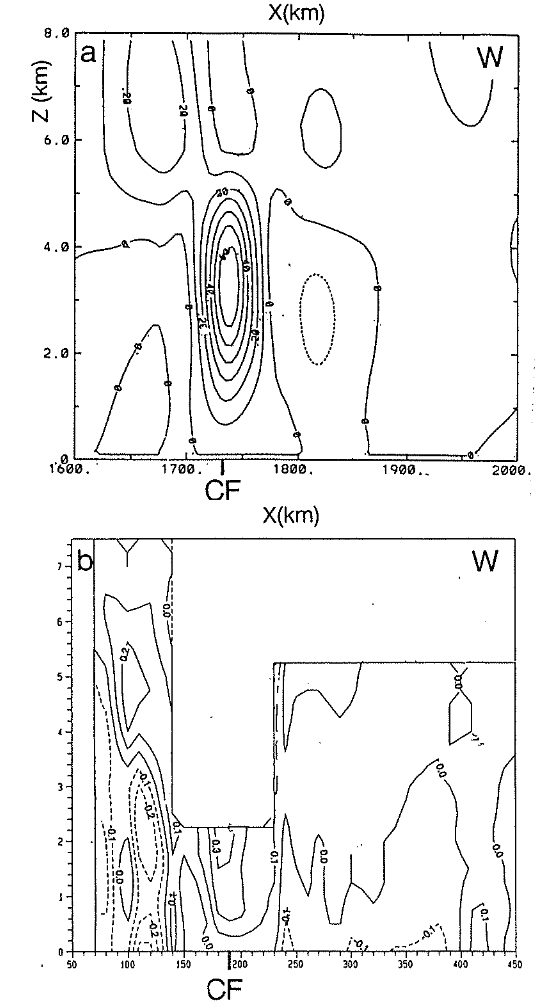

Figure 3: Comparisons for the vertical velocity (contour interval .1 $m\ s^{-1}$) between a) simulation REF and b) VAD Doppler radar observations. The model fields are filtered (40 km wavelength cut–off).

4 Relationship between Bands and Large Scale Forcings

As a first step in the understanding of the simulated frontal rainband mechanisms, we performed two other simulations starting without initial ageostrophic part. The first one (DEF) is started as the simulation NOAG but with the deformation term $\frac{\partial v}{\partial y}$ set to zero. (Figs. 4a nd b) indicates a very little sensitivity of results to this large scale forcing. The vertical velocity intensity in the WSWR is sligthly reduced, though the localization and the structure of bands are similar.

To look at the importance of the baroclinicity term, it is not possible to modify it alone, as in the case of the deformation. Instead, in a second simulation (BARO), both the deformation $\frac{\partial v}{\partial y}$ and the baroclinicity $\frac{\partial \theta_{vl}}{\partial y}$ were reduced by a factor 3. As the simulation DEF has shown the deformation term was not important, the simulation BARO may be considered as an experiment of sensitivity to the baroclinicity $\frac{\partial \theta_{vl}}{\partial y}$. In this experiment, results ((Fig. 4c) show large departures from the results of the NOAG simulation. Indeed, the NCFR is the only band that may be identified on the simulation BARO, with similar intensity. The wide bands have almost disappeared and did not produced precipitation.

The time history as represented on (Fig. 6) for experiments NOAG, BARO and DEF confirms these findings. The ground precipitation in the simulation BARO is smaller by a factor 3 than in the simulations DEF and NOAG. The maxima of vertical velocity are similar for all the simulations, as they correspond to the NCFR.

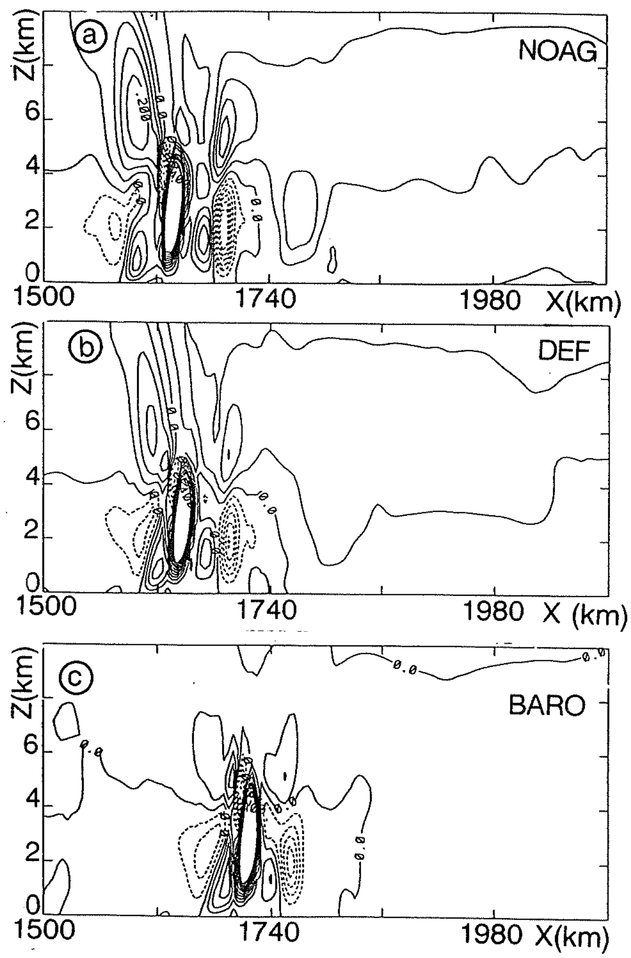

Figure 4: Cross section of vertical velocity at t = 5h (contour interval 5 $cm\ s^{-1}$) for experiment: a) NOAG, b) DEF and c)BARO

5 Conclusions

These simulations have shown the capability of a non-hydrostatic model to simulate fine scale structures of frontal systems. The results are promising in that those structures show strong similarities with the observed ones. Particularly, the vertical velocity fields exhibit similar banded features in both simulations and Doppler radar observations. In the simulated case (IOP2 of the FRONTS 87 experiment), we have shown that the initial ageostrophic part was not neccessary to the success of the simulation. A 90 min lag time was founded in the simulations with no initial ageostrophic part, corresponding to the time neccessary for the model to build this ageostrophic part. This finding together with the two-dimensional framework, enable to study the relationships between rainband and large scale forcings (namely the along-front deformation and baroclinicity). The main conclusions of these sensitivities studies are for the IOP2 case:

- The deformation term is not important
- The baroclinicity term is important for the structure of wide bands (WCFR and WSWR).
- The NCFR structure and intensity is weekly dependant on these forcings, as well for the ground precipitation produced by this band as for the amplitude of the vertical velocity

In order to increase the realism of our simulations, two future works will be realized. Using grid nesting technics implemented in our model, we plan to perform three-dimensional simulations with higher horizontal resolution (1 km). As recently outlined by Clough and Franks (1991), evaporation of precipitation is important in frontal systems under the ice phase during the FRONTS 87 experiment. For this reason, the ice phase parameterization should be activated in our future frontal simulations, as we did for squall line simulations (Lafore and Redelsperger, 1992).

Besides the aim to increase the realism of our simulations, our main goal will be the understanding of rainband mechanisms. As we did in previous academic works (Benard *et al.*, 1992b), numerical tools associated to our model will be used, as the full potential vorticity budget and diagnostic equations as the Sawyer–Elliassen equation.

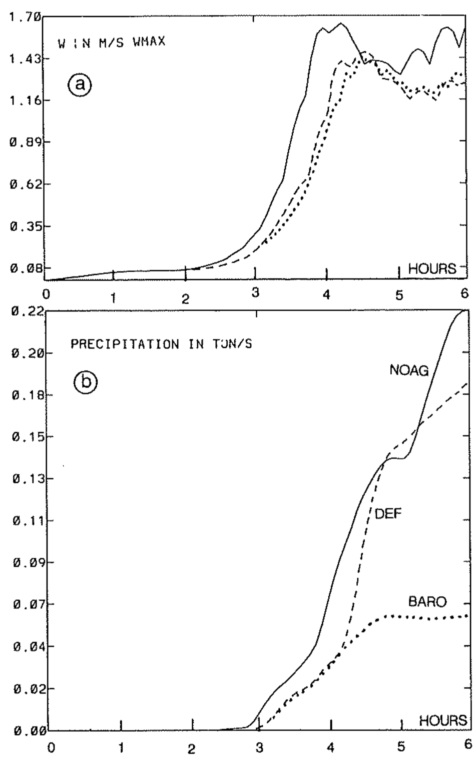

Figure 5: Time evolution for simulations REF and NOAG (a) Vertical velocity maximum and (b) Ground precipitation

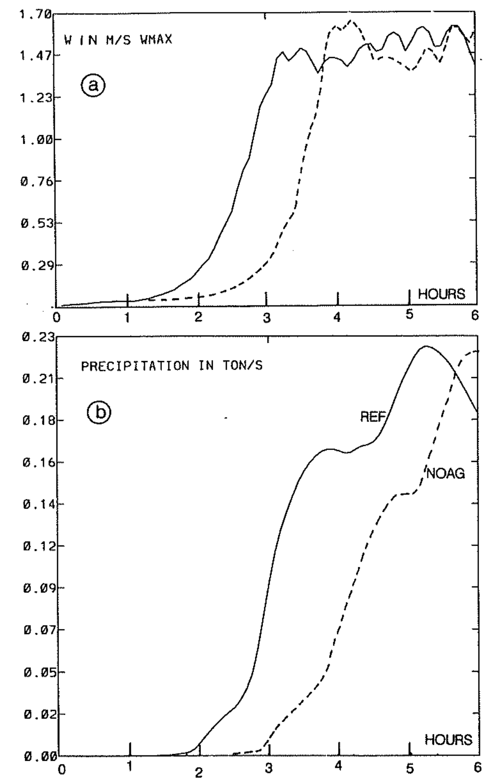

Figure 6: Time evolution for simulations NOAG, DEF and BARO (a) Vertical velocity maximum and (b) Ground precipitation

6 References

Benard P., J.-L. Redelsperger and J.-P. Lafore, 1992: Non-hydrostatic simulation of frontogenesis in a moist atmosphere. Part I : General description and narrow frontal bands. Accepted by *J. Atmos. Sci.*.

Benard P., J.-P. Lafore and J.-L. Redelsperger, 1991: Non-hydrostatic simulation of frontogenesis in a moist atmosphere. Part II : equivalent potentiel vorticity budget and wide bands. Accepted by *J. Atmos. Sci.*.

Browning, K.A., B.J. Hoskins, P.R. Jonas and A.J. Thorpe, 1986: European collaboration on atmospheric fronts *Nature*, **322**, 114-115.

Carpenter, K.M., 1982: Note on the paper "radiation conditions for the lateral boundaties of limited area numerical models". *Q. J. R. Meteorol Soc.*, **108**, 717–719

Clough, S.A. and J. Testud, 1988: The FRONTS87 experiment and mesoscale frontal dynamics project *WMO Bull*, **37**, 276-281.

Clough, S.A. and R. A. A. Franks: The evaporation of frontal and other stratiform precipitation *Q. J. R. Meteorol Soc.*, **117**, 1057–1080

Jaubert, G., M. Nuret and M. Chong, 1991: A case study of cold-frontal rainbands. *Preprints 25th Int. Conf. on Radar Meteor, AMS*, 185–188.

Lafore, J.-P. and J.-L. Redelsperger, 1992: Relationship between mass, pressure and momentum fields in the stratiform region of a fast-moving tropical squall line. (*in this preprint volume*)

Redelsperger, J-L. and G. Sommeria, 1986: Three-dimensional simulation of a convective storm: Sensitvity studies on subgrid parameterizationand spatial resolution. *J. Atmos. Sci.* **43**, 2619-2635.

Redelsperger, J-L. and J.-P. Lafore, 1988: A three-dimensional simulation of a tropical squall line: Convective organization and Thermodynamic Vertical Transport. *J. Atmos. Sci.* **45** 1334-1356.

THE FORM OF CYCLONIC PRECIPITATION AND ITS THERMAL IMPACT

Stanley David Gedzelman and Robert Arnold

Department of Earth and Atmospheric Sciences
City College of New York, New York, NY USA 10031

1. INTRODUCTION

The form of precipitation becomes difficult to predict whenever the temperature at or near the surface approaches 0°C (Stewart, 1992). In problematic situations the most common techniques for forecasting precipitation form involve using statistical properties of the sounding (Bocchieri, 1980). If, for example, surface temperature is below 0°C but a thick melting layer is forecast aloft, freezing rain will be recorded at the surface. However, in borderline situations several complications arise that reduce the value and accuracy of the statistical techniques. For example, many cases of freezing drizzle are produced in shallow, supercooled clouds. Furthermore, if the melting layer aloft is less than about 250 m thick or if the surface layer of cold air is very thick and cold, ice pellets rather than freezing rain will form. In these and other similar cases, replacement of the statistical techniques with physically compelling models for predicting precipitation form would be greatly welcome.

Falling precipitation can also have an important impact on the atmosphere's thermal structure. When falling precipitation undergoes phase changes, it changes the air temperature. The changed temperature field can, in turn have a significant impact both on the dynamics and on the form of subsequent precipitation. As an example, when falling snow melts it may eventually cool the air enough so that the 0°C isotherm approaches the ground. Once this happens snow will reach the ground without melting (Wexler, et. al., 1954).

The purpose of this preprint is to show how a bulk microphysical model can be used to predict the form of cyclonic precipitation in a range of problematic situations and also capture the thermal impact of changing precipitation form. The model and results are briefly described below; further details are presented in Gedzelman and Arnold (1992).

2. THE MODEL

The model is a bulk microphysical model modified from Lin, et. al. (1983). It includes six species of water and most of the important microphysical interactions between these species. The principal modifications were to represent ice pellets rather than hail, and to include the thermal impact of sublimation of ice pellets and snow. As an example, the collision of a large snowflake with a smaller raindrop at temperatures below 0°C will result in a wet snowflake, but the collision of a small snowflake with a larger raindrop will collapse the snowflake and freeze the drop to an ice pellet.

The model uses an imposed wind field, and therefore cannot evaluate the interactions between the dynamics and the thermal field. All fields are advected using a fourth order scheme modified from Crowley (1968). This scheme includes an ad hoc correction technique designed to reduce the spurious ripples in all fields that invariably form at or near cloud boundaries. The correction technique works in a manner similar to that of the monotone positive definite advection transport algorithm of Smolarkiewicz and Grabowski (1990). It smooths the fields without diffusing them, prevents upwind transport or downwind transport faster than the wind, and replaces the countergradient flux sometimes demanded by a high order advection scheme with downgradient flux.

3. RESULTS

Idealized versions of three common winter storm situations are now presented. The first situation consists of a strong warm or stationary front with a pronounced frontal inversion aloft. This leads to a geographical pattern of rain, freezing rain, ice pellets, and snow. The second situation has been called a warm snowstorm (Gedzelman and Lewis, 1990). In warm snowstorms, all surface temperatures are above 0°C and precipitation begins as rain but as the air is cooled by falling precipitation, the rain at the ground changes to snow in a core region. The third situation consists of a shallow cloud whose top is ony a few degrees below 0°C and in which supercooled freezing rain or drizzle form.

Results of all model runs are calculated and displayed using 2-dimensional cross-sections. All runs were conducted with a time step, $\delta t = 20$ s and were run for 2000 time steps or about 12 h of real time. The model uses a horizontal gridpoint spacing, $\delta y = 20$ km, and has 20 gridpoints in the horizontal. For the strong front and the warm snowstorm there are 30 gridpoints in the vertical spaced a distance $\delta z = 250$ m, while for the shallow supercooled cloud there are only 15 gridpoints in the vertical spaced a distance $\delta z = 200$ m.

A frontal boundary slopes upward to the right from the lower left corner. Air enters the grid on the left and slides up over the frontal surface while air with different temperature and humidity enters the grid on the right below the front. The temperature and humidity contrasts at the front are represented by hyperbolic tangent functions while the differences are varied from case to case. A background lapse rate of 7°C km^{-1} is superimposed on the temperature fields of the strong front and warm snowstorm while the background lapse rate for the shallow supercooled cloud is 4°C km^{-1}. The relative humidity field includes a slow decrease with height to avoid supersaturation with respect to ice.

a. The Strong Front

For the strong front, air enters the grid from the left with a surface temperature of 11°C and a relative humidity of 90% while air beneath the front enters from the right with a surface temperature of 0°C and a relative humidity of 70%. The wind field was chosen parallel to the frontal surface to keep the front stationary. The largest vertical velocities (0.08 m s^{-1}) occur on the left and about 2 km above the surface front. Vertical velocity for the subfrontal air is 0.

The temperature field is shown after 2000 times steps in Fig. 1. It closely resembles the initial temperature field but the gradient at the frontal surface slowly increased with time as a result of the confluent wind field and evaporative cooling. Beyond about $y = 50$ km the near-surface air is below 0°C. A melting zone up to $z = 2$ km overlies the cold air and extends across the grid but becomes progressively thinner toward the right. This zone is thick and warm enough to melt all snow falling through it on the left but is so thin on the right that snow melts so little it retains its crystalline form.

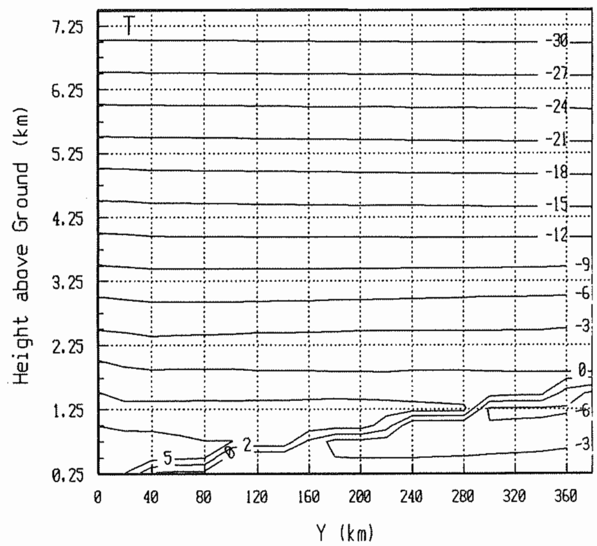

Fig. 1. Temperature field (°C) for the strong front after 2000 time steps.

The total accumulations of rain, snow and ice pellets reaching the ground are shown in Fig. 2. The model does not include freezing rain per se, but where the surface temperature is below 0°C any rain would be classified as freezing rain. Precipitation totals are small on the left side of the grid where the slantwise ascent of humid but unsaturated air entering from the left boundary of the grid has just begun and also on the right side, where vertical velocities are smallest. The maximum accumulated precipitation occurs between y = 80 km and y = 100 km, and closely agrees with elementary calculations of the water that would condense in a moist adiabatic process. However, the small variation of precipitation totals between y = 220 km and y = 280 km has no physical cause and is merely an artifact of the numerics.

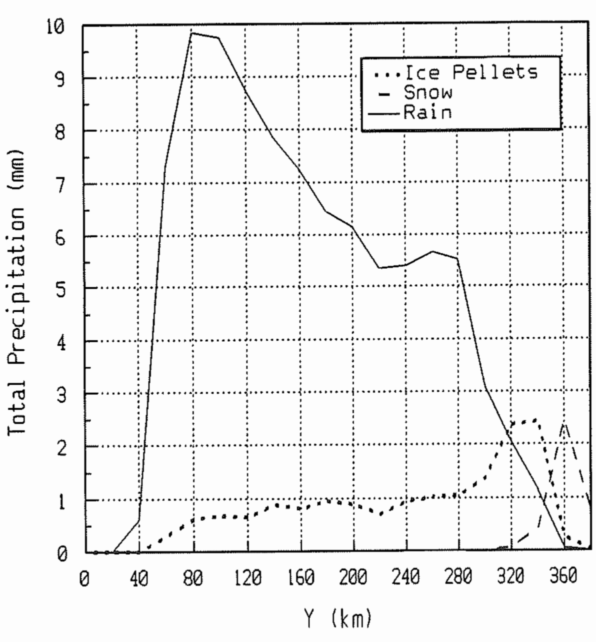

Fig. 2. Accumulated rain, snow and ice pellets at the ground after 2000 time steps for the strong front.

The model produces the classical pattern of precipitation form. Rain is the sole form of precipitation on the extreme left side where the region of warm air extends from the surface to about 2 km. The central region of the grid up to y = 290 km is dominated by freezing rain. Snow dominates only on the extreme right, where the melting layer is too thin to melt the flakes substantially. Ice pellets dominate in the small belt between the regions of freezing rain and snow. The melting zone in this region is about 250 m thick with a maximum temperature of about 1°C. Snowflakes in this region melt just enough to collapse into slushy mixtures of ice and rain that quickly freeze when they fall into the cold zone below. The dominant ice pellet producing process in the model is the collapse of snow into a mixture of ice and rain. Where the snow melts entirely, only a few raindrops are able to freeze to ice pellets in the cold layer below.

b. The Warm Snowstorm

In warm snowstorms, advection is so weak that the effects of evaporation and/or melting of falling precipitation on both the thermal structure and dynamic behavior of the atmosphere become quite conspicuous. All runs for the warm snowstorm were initialized with a horizontally uniform temperature field with a surface value of 5°C and a constant lapse rate of 7°C km^{-1}. The relative humidity of the surface air entering from the left was fixed at 90% but two different values of relative humidity (RH_r = 70% and 90%) were used for the air entering from the lower right to determine the impact of evaporative cooling on the temperature field and on the form of precipitation reaching the ground. The model was run again with a horizontal wind field increased by 50% (u_{fac} = 1.5) to assess the impact of enhanced warm air advection on the temperature and precipitation fields.

The change in the temperature field over the first 1000 time steps is shown in Fig. 3 for the case of RH_r = 70%. Warming has taken place just above the front as a result of moist adiabatic ascent in a conditionally stable atmosphere and also at the extreme right as a result of dry adiabatic sinking. Cooling has taken place between these two warming regions and results in the formation of a cold air core sometimes seen in warm snowstorms. The cooling is greatest near the surface in the core of the region of precipitation as a result of evaporation and melting of the falling hydrometeors. There is no cooling at the surface outside the precipitation region.

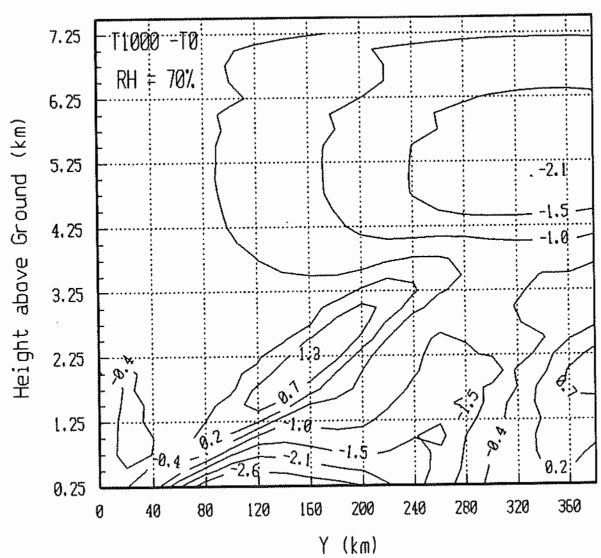

Fig. 3. Total temperature change during the first 1000 time steps for the warm snowstorm with RH_r = 70%.

As a result of the cooling, an isothermal layer, shown in Fig. 4, forms beneath the cloud near the 0°C line. In saturated air the temperature of the isothermal layer would be 0°C but because of evaporation it is -1.5°C.

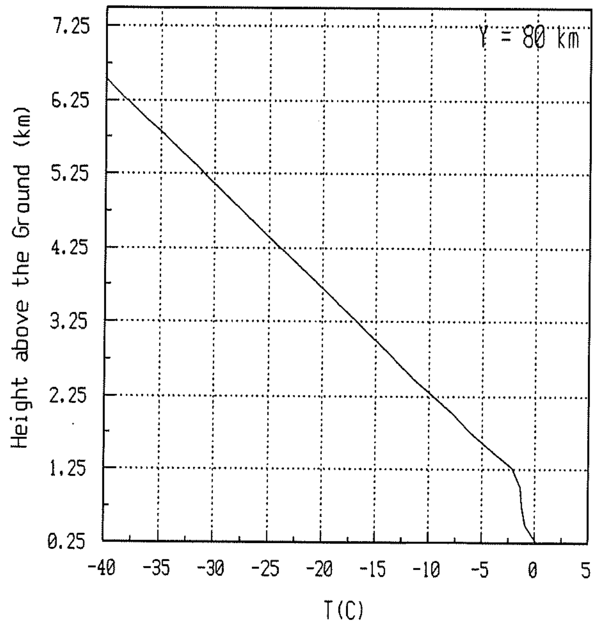

Fig. 4. Temperature sounding at y = 80 km for the warm snowstorm with RH_r = 70%.

In all runs, precipitation initially reaches the ground as rain but changes to snow or some mixture of rain and snow in a core region once the air is cooled by melting and evaporation (Fig. 5).

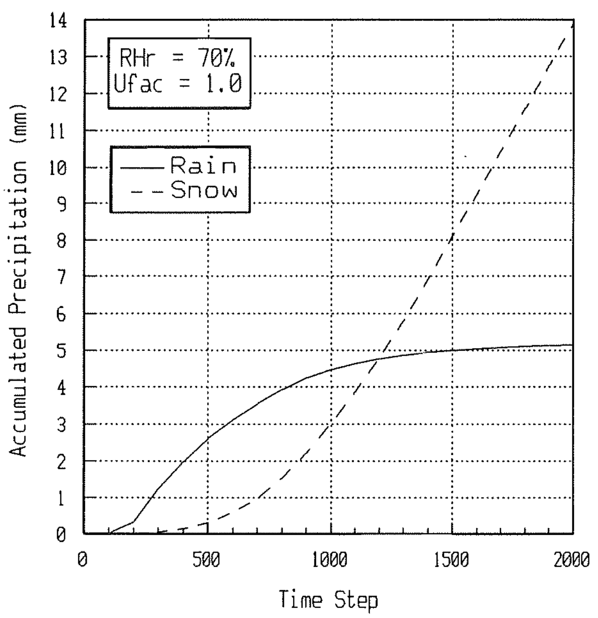

Fig. 5. Accumulated rain and snow as a function of time at y = 100 km for RH_r = 70%.

The change to snow occurs sooner and covers a larger area when RH_r is lower (compare Fig. 6 and Fig. 7) and also when the winds are weaker. As a result, in potential warm snow situations the change from rain to snow is much more likely and occurs much sooner when dry air is advected beneath cloud base.

Rain never changes to snow at the periphery of the precipitation shield since surface air converges from each side without having undergone any prior cooling. This rather unusual pattern of a core region of snow surrounded by a ring of rain is one of the classical signatures of a warm snowstorm (Gedzelman and Paluszek, 1992).

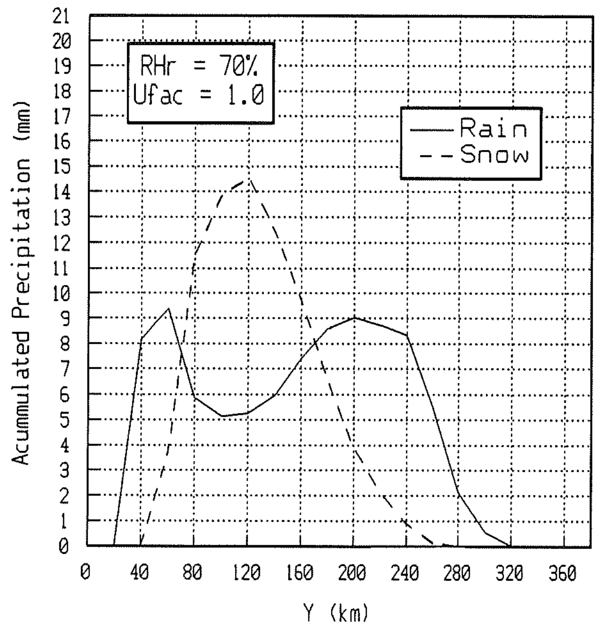

Fig. 6. Accumulated rain and snow along the ground after 2000 time steps for the warm snowstorm with RH_r = 70%.

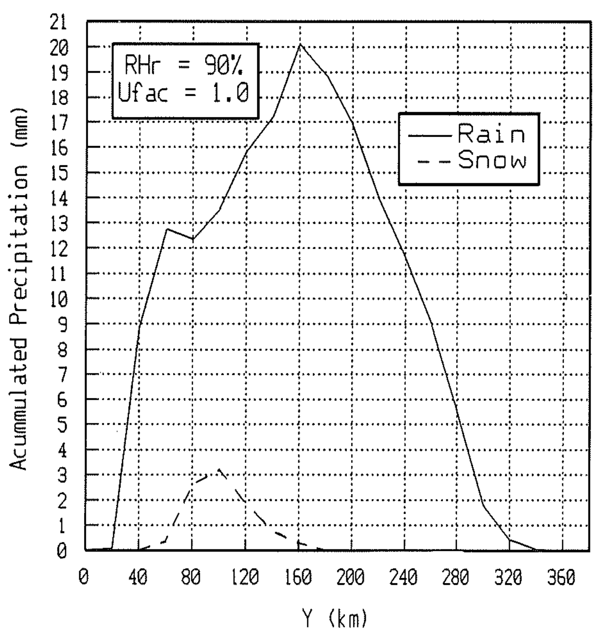

Fig. 7. Same as for Fig. 6. but with RH_r = 90%.

c. Supercooled Freezing Drizzle

A surprisingly large number of cases of freezing drizzle occur in soundings that remain below 0°C at all heights. The clouds in such cases are generally quite shallow, with tops warmer than about -10°C so that ice crystal nucleation remains unlikely unless the cloud is seeded from above.

All parameterized cloud microphysical models include some expression for the dispensation of condensed vapor among ice crystals and water droplets at temperatures below 0°C. Our model distributes condensed vapor between cloud water and cloud ice according to the temperature if the total mixing ratio of cloud particles remains below a threshold value of 10^{-5} kg m^{-3}. Then the percentage of vapor condensing as water, PctW, is

$$PctW = \frac{1+\tanh\left(\frac{T-T_{glac}}{3}\right)}{2}$$

where T_{glac} is the effective freezing or glaciation temperature. For this case we set T_{glac} = -15°C so that most vapor condensed as water rather than ice.

Once the total mixing ratio of cloud particles exceeds the threshold value, the vapor is is assumed to condense onto already existing particles in the proportion they are present in the cloud. In effect, this converts the supercooled liquid regions of stratiform clouds to ice once snow begins falling through them.

The temperature field for the shallow, supercooled cloud was initially set warmer than -10°C and remained above -12°C after 2000 time steps. Because the bulk of the cloud remained significantly warmer than T_{glac}, most vapor condensed as liquid and remained in liquid form. Significant amounts of ice formed in the lower parts of the cloud where mixing ratios were larger. The model generated small amounts of snow but most of this was accreted by larger raindrops which then readily froze to form ice pellets. As a result, although freezing rain dominated, precipitation reached the ground as a mixture of rain, snow and ice pellets (Fig. 8).

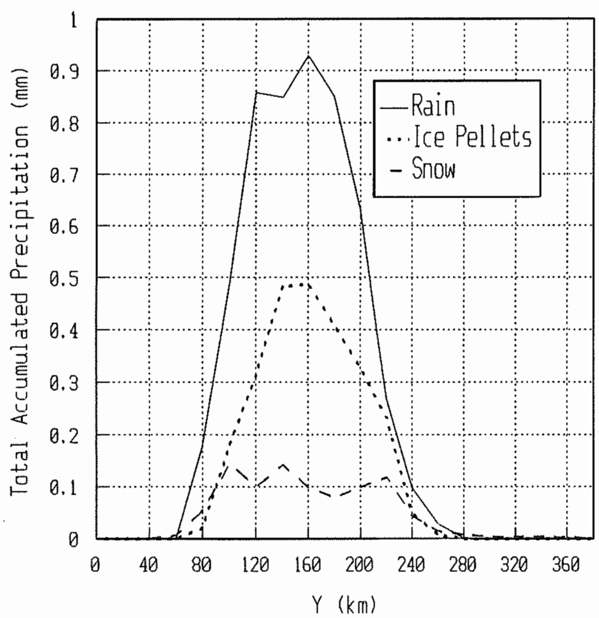

Fig. 8. Accumulated precipitation along the ground after 2000 time steps for the shallow, supercooled cloud.

4. CONCLUSIONS

A kinematic, bulk parameterized cloud microphysics model was developed and applied to several winter storm situations to simulate the form of precipitation and the thermal impact of melting and evaporation of hydrometeors beneath cloud base. In all situations, model results were physically compelling and constitute a strong argument for the inclusion of at least some parameterized microphysics both in general circulation models and in operational forecasting models.

5. REFERENCES

Bocchieri, J. R., 1980: The objective use of upper air soundings to specify precipitation type. *Mon. Wea. Rev.*, **108**, 596-603.

Crowley, W. P., 1968: Numerical advection experiments. *Mon. Wea. Rev.*, **96**, 1-11.

Gedzelman, S. D., and R. Arnold, 1992: The form of cyclonic precipitation and its thermal impact. Submitted to *Mon. Wea. Rev.*

Gedzelman, S. D., and E. Lewis, 1990: Warm snowstorms. *Weatherwise*, **43**, 265-270.

Gedzelman, S. D., and J. Paluszek, 1992: The structure and climatology of warm snowstorms. Submitted to *Weather and Forecasting*.

Lin, Y., R. D. Farley, and H. D. Orville, 1983: Bulk parameterization of the snow field in a cloud model. *J. Clim. Appl. Meteor.*, **22**, 1065-1092.

Smolarkiewicz, P. K., and W. W. Grabowski, 1990: The multidimensional positive definite advection transport algorithm. *J. Comp. Phys.*, **86**, 355-375.

Stewart, R. E., 1992: Precipitation types in the transition regions of winter storms. *Bull. Amer. Meteor. Soc.*, **73**, 287-296.

Wexler, H. R., R. J. Reed, and J. Honig, 1954: Atmospheric cooling by melting snow. *Bull. Amer. Meteor. Soc.*, **35**, 48-51.

THE INTERACTION OF FRONTS WITH TOPOGRAPHY: A COMPARISON OF FRONTAL AND POST-FRONTAL ORGANIZATION AND MICROPHYSICAL CONDITIONS.

Jørgen B. Jensen and Sunhee Lee.
CSIRO Division of Atmospheric Research.
Private Bag 1, Mordialloc, Victoria 3195, Australia.

1. INTRODUCTION

During the 1990 Australian Winter Storms Experiment (AWSE) the CSIRO F-27 research aircraft flew 15 missions in frontal and post-frontal conditions. The study area was centered around Mt. Baw Baw (1500 m maximum height) in the extreme southwestern end of the Great Dividing Range. In this study we use flight observations from one day to compare the highly continental cloud associated with the pre-frontal and frontal bands (north-westerly wind) to the more marine post-frontal clouds (south-westerly wind).

The purpose of the study is to investigate to what extent the airmass and organization of the clouds affect the ability of the clouds to develop precipitation, what the predominant precipitation habits are, and how efficient the clouds are at converting the available liquid water and water vapor to precipitation water.

Mt. Baw Baw is an elongated mountain ridge oriented in a NW-SE direction. The deep frontal clouds are investigated both in the low lying areas to the west on Mt. Baw Baw and in the region over and downstream of the mountain top. The frontal cloud bands are highly organized in the area west of the mountain due to synoptic and mesoscale effects. In contrast, the post-frontal clouds are often shallow stratocumulus clouds, which do not become highly organized until they are forced up over the mountain. They thus form a cap cloud, which may persist for extended periods, on some occasions even days after the frontal passage.

2. METHODOLOGY

The present study utilizes a combination of aircraft observations and theoretical calculations of growth rates of of precipitation to evaluate time scales for conversion of cloud liquid water to precipitation water. The conversion is calculated for both collection and vapor deposition growth. We note that vapor depositional growth of ice particles in the presence of cloud drops (i.e. saturated air) will be at the expense of cloud liquid water. Hence, we can calculate time scales for the depletion of cloud water by both collection and deposition.

a. Observation Platform

The CSIRO F-27 aircraft for observing thermodynamic properties, wind and microphysical parameters. Using multiple aircraft legs we are able to follow some of the major cloud features as the air is advected towards and up over Mt. Baw Baw.

A airborne PMS 2D-C probe was used for observing precipitation particles. Individual particles were sized and classified according to habit using the procedures given in Heymsfield and Parrish (1979). The precipitation particles were characterized as graupel, dendrites, aggregates of dendrites, columns, and small particles assumed to be plates. Expressions for size-mass relations ships have been adapted from Ono (1970) for columns/needles, and from Heymsfield and Parrish (1979) for all other habits.

The aircraft PMS FSSP probe was used for observing cloud drop spectra and liquid water content. Extensive thermodynamic measurements were available, but horizontal winds are only reliable in straight and level flight. No measurement of vertical wind speed was available.

b. Procedures for Calculation of Precipitation Growth

The growth rate of individual 1-second precipitation spectra has been calculated assuming vapor deposition and collection growth. The calculation is only done for samples containing liquid water; accordingly we have assumed saturation with respect to liquid water in the selected samples.

Vapor depositional growth of precipitation particles is calculated using the ice growth equation applied to 5 habit classes, each with particles in 80 size classes. We have used the formulation of the ice growth equation as described by King (1986), which includes the Hall and Pruppacher (1976) correction due to ventilation. Particle terminal velocity is calculated using expressions from Heymsfield and Parrish (1979) for graupel, rimed dendrites, rimed plates, and aggregates of rimed particles. Expressions for rimed columns have been taken from Locatelli and Hobbs (1974), corrected to different pressure and temperatures using procedures from Pruppacher and Klett (1979). The deposition calculation is done assuming saturation with respect to liquid water; i.e. only samples containing cloud drops are included.

Collection growth (or equivalently, riming growth) is calculated assuming precipitation particle terminal velocities as detailed above, and cloud drop terminal velocities were calculated using Stokes law. Collection efficiencies for graupel-drop interactions are assumed to be unity. Collection efficiencies for columns were interpolated from data in Schlamp *et al.* (1975), and for plates the values in Pitter (1977) were interpolated.

By summing over all habits and all size classes we can thus calculate the changes in precipitation particle mixing ratio due to vapor deposition and collection as:

$$\frac{dq_{p\ dep}}{dt} \quad \text{and} \quad \frac{dq_{p\ col}}{dt}$$

3. FRONTAL STRATUS DECKS

In the early morning of 22 August 1990 a cold front approached the study area. The F-27 made several penetrations of the prefrontal and frontal bands in the low lying area west of Mt. Baw Baw. The flight legs extended up to 100 km west of the mountains and were likely not much affected by the topography at this stage Radar PPI scans showed two main rain bands, which together were about 75 km wide. The bands were first penetrated by the F-27 during the ferry towards Mt. Baw Baw. At this stage the bands were over the low terrain west of the mountains, and they had extensive regions of uniform character with precipitation rates of 1-10 mm h^{-1}.

These extensive stratiform decks did only contain significant liquid water in small isolated pockets near the upper part of the clouds. Everywhere below the clouds were essentially glaciated with typical liquid water contents being 0.05 g m^{-3}. Fig. 1 shows selected time series of cloud liquid water content and 2-D particle concentration. A typical 2-D particle image sample is shown in Fig. 2. It can be seen that the particles are mainly columns and dendrites, with some evidence of riming and aggregation. The main impression is, however, that the observed particles have grown by vapor deposition.

We have calculated the growth rates of precipitation due to collection and vapor deposition for individual 1-second particle spectra. These are shown in Fig. 3; it can be seen that collection growth far exceeds vapor deposition growth, in some cases by two orders of magnitude.

It is possible that the small liquid water content shown in Fig. 3 is not real, the error being introduced due to splintering of ice particles on probe arms (Gardiner and Hallett, 1985); both the CSIRO hotwire liquid water sensor and the FSSP show small liquid water contents (typically 0.05-0.1 g m^{-3}). However, the magnitude of a possible error can not be directly estimated. Given that the EG&G dewpoint sensor shows a dewpoint temperature almost identical to the reverse flow temperature, we will proceed by assuming that the cloudy samples are at saturation.

We have furthermore calculated time constants for the removal of cloud water by precipitation growth as:

$$\tau_{dep} = \frac{L}{\rho_a \left[\frac{dq_{p\ dep}}{dt}\right]} \tag{1}$$

and

$$\tau_{col} = \frac{L}{\rho_a \left[\frac{dq_{p\ col}}{dt}\right]} \tag{2}$$

where τ_{dep} and τ_{col} are the time constants for depositional and collectional removal of liquid water, respec-

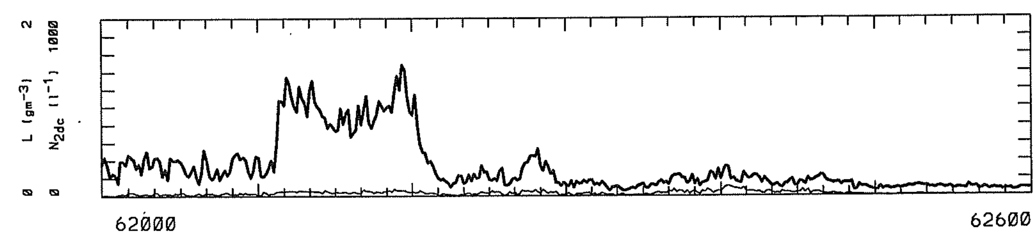

Fig. 1. Time series of cloud liquid water content (L, thin curve) as determined from the CSIRO hotwire probe, and 2-D particle concentration (N_{2dc}, bold curve) for the time interval 6:20 to 6:26 AM on 22 August 1990.

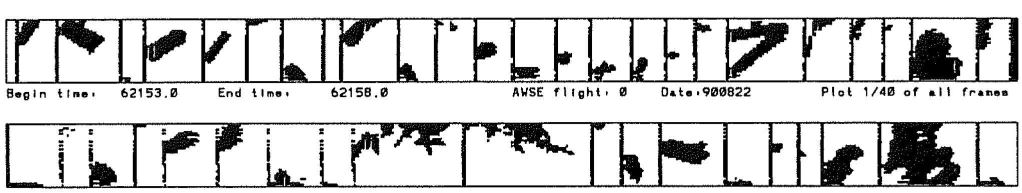

Fig. 2. 2-D particle images for 6:21:58 AM. The vertical distance represent 800 μm.

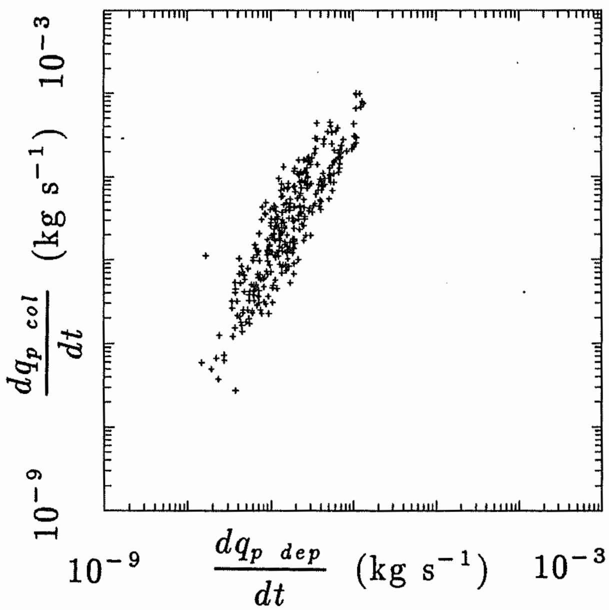

Fig. 3. Values of precipitation growth rate due to collection as a function of the growth rate due to vapor deposition for the time interval 6:20 to 6:26 AM.

tively. L is the liquid water content, and ρ_a is the air density.

Fig. 4 shows time series of τ_{col} and τ_{dep} for the same time interval as in Fig. 3. It can be seen that both time constants are small, implying that the water condensed out due to uplift is very quickly taken up by growing precipitation.

The following hypothetical situation may aid in estimating the likely changes in the cloud microphysical field, should the precipitation from the stratiform bands subsequently fall into a liquid water rich orographic cloud over Mt. Baw Baw. The time constant for depositional growth would remain essentially unchanged, given that vapor growth of ice particles in liquid water clouds depend solely on the fact that the drops provide saturation with respect to liquid water, and not on how much liquid water is present. For an increase in liquid water content, L, in eq. (2) it is therefore clear than τ_{dep} will *decrease*. By contrast, the time constant for removal of liquid water due to collectional growth will remain approximately *unchanged*. This is because the denominator in eq. (2) is approximately proportional to L, assuming large cloud drops with near unity collection efficiency.

Consider the case of the stratiform precipitation particles falling into a airstream with rapid generation of liquid water due to strong updraft. From the above approximate arguments, it is clear that the falling precipitation can *not* take up all the condensed water; some higher 'equilibrium' liquid water content may be approached. This increased liquid water will partly evaporate in the downdraft on the rear side of the mountain. Hence not all the liquid water condensed on the upstream side will be available for precipitation growth on the upstream side; part of it will evaporate on the down-

Fig. 5. 2-D image for prefrontal conditions 1200 m above Mt. Baw Baw, 9:02 AM.

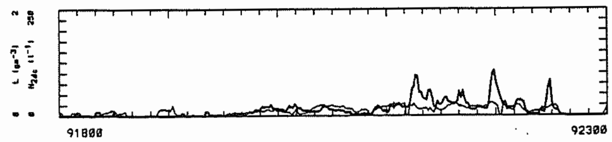

Fig. 6. Time series of liquid water content and 2-D particle concentration for 9:18:00 to 9:23:00 AM. The aircraft flew from southwest to northeast during this time segment. The cloud free stretch in the last part of the leg is located immediately downwind of Mt. Baw Baw.

stream side. Given the normal increase in wind speed on the down-stream side of a mountain (e.g. Queney, 1947), it is therefore likely that a significant amount of condensed liquid water will evaporate during the descent on the down-stream side.

This situation of stratiform precipitation falling into an orographic cloud may possibly be further examined by means of numerical modeling.

4. POST-FRONTAL LOW LEVEL OROGRAPHIC CLOUD

Shortly after 9 AM did the surface coldfront pass over Mt. Baw Baw; this determination was primarily due to low level wind change as observed from the aircraft. At 9:02 was the F-27 flying in northwesterly winds (pre-frontal conditions) immediately over Mt. Baw Baw at 2700 m altitude. Here the aircraft observed uniform stratiform precipitation, with 2-D concentrations of up to 40 l^{-1}, precipitation rates of 1-3 mm h^{-1}-1 and ice water contents as high as 1 g m^{-3}. Liquid water (if at all present) was below 0.05 g m^{-3}. An example of typical observed 2-D images is shown in Fig. 5. The images show predominantly large aggregates of vapor grown particles.

At 9:22 AM the aircraft flew over the top of Mt. Baw Baw at 2100 m altitude in westerly winds (post-frontal conditions). At this time the aircraft observed a modest liquid water containing cloud, which stretched from foothills 25 km west of Mt. Baw Baw. East of Mt. Baw Baw there was a small cloud free stretch, possibly associated with strong descending motions. The liquid water content and 2-D particle concentration for the cloud over Mt. Baw Baw is shown in Fig. 6. Even for this relatively low liquid water content, there is strong evidence of coalescence growth in most parts of the cloud. Examples of coalescence drops of a few hundred micron diameter are shown in Fig. 7. This strong development of coalescence is surprising in view of low droplet concentrations (≈ 50 cm^{-3} maximum) and modest liquid water content. In some segments there were also observations of much larger heavily rimed particles

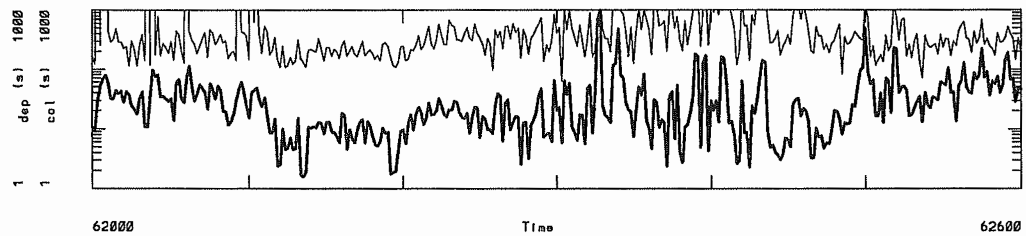

Fig. 4. Time series of liquid water depletion rates due to depositional growth (thin curve) and collection growth (bold line).

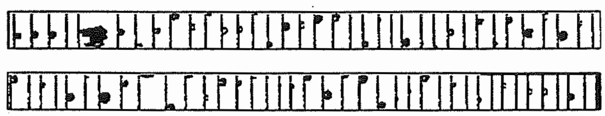

Fig. 7. 2-D image for post-frontal conditions 600 m above Mt. Baw Baw, 9:21 AM. The figure shows many coalescence drops of a few hundrede micron diameter.

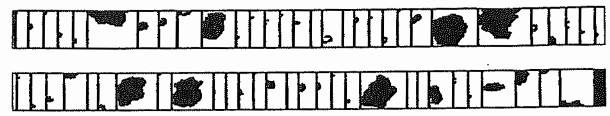

Fig. 8. 2-D image for post-frontal conditions 600 m above Mt. Baw Baw, 9:21 AM. Large heavily rimed particles are apparent.

(Fig. 8); these are possibly remnants of the extensive overlying stratus decks observed earlier.

5. SUMMARY

Microphysical and dynamical aspects of frontal clouds and and of post-frontal clouds from immediately after the frontal passage have been discussed. The frontal clouds are nearly glaciated, with lightly or only moderately rimed particles. This is likely due to the low liquid water content in these clouds.

After the front pasage the clouds were observed to be of post-frontal origin at low levels. These clouds still have low to modest liquid water content - though higher than the frontal clouds -, and coalescence appears to be very active. This vigor of the coalescence is somewhat surprising given liquid water contents of about 0.3 g m^{-3} and drop concentrations of only about 50 cm^{-3}.

Growth rates due to vapor deposition and collection in the frontal clouds appear to be dominated by collection. The possibility of some error in the determination of liquid water content may contribute to this conclusion; however, given that both liquid water sensors and thermometers point towards saturated conditions, then the present procedure appear justified.

Arguments are presented for the likely behavior of precipitation development in orographic clouds, which are "seeded" from above by natural precipitation originating in widespread stratiform decks.

ACKNOWLEDGMENTS

The present study was carried out with assistance of a grant from Melbourne Water Corporation.

Gardiner, B. A., and J. Hallett, 1985: Degradation of ic-cloud forward scattering spectrometer probe measurements in the presence of ice particles. J. Atmos. and Ocean. tech., 2, 171-180.

Hall, W. D. and H. R. Pruppacher, 1976: The survival of ice particles falling from cirrus clouds in subsaturated air. J. Atmos. Sci., 33, 1995-2006.

Heymsfield, A.J. and Parrish J. R., 1979. Techniques employed in the processing of particle size spectra and state parameter data obtained with the T-28 aircraft platform. NCAR technical note NCAR/TN-137+1A.

King, W. D., 1984. Seeding stratiform clouds: The effects of cloud parameters on aiming., J. Cli. Appl. Meteo., 23, 1265-1272.

Locatelli, J. D. and Hobbs P. V., 1974: Fall speeds and masses of solid precipitation particles. J. Geophys. Res., 79, 2185-2197.

Ono, A., 1970: Growth mode of ice crystals in natural clouds. J. Atmos. Sci., 27, 649-658.

Pitter, R. L., 1977: A reexamination of riming on thin ice plates. J. Atmos. Sci., 34, 684-685

Pruppacher, H. R. and Klett, J. D., 1978: Microphysics of clouds and precipitation. Reidel, 741pp.

Queney, P., 1947: Theory of perturbations in stratified currents with applications to flow over mountain barriers. Misc. Repts. No. 23, Dept. of Geophys. Sci., The University of Chicago.

Schlamp, R. J., Pruppacher, H. R. and Hamielec, A. E., 1975: A numerical investigation of the efficiency with which simple columnar ice crystal collide with supercooled water drops. J. Atmos. Sci., 32, 2330-2337.

NUMERICAL SIMULATION OF DEPENDENCE OF FRONTAL CLOUD AND PRECIPITATION MESOSTRUCTURE ON BACKGROUND LARGE SCALE FLOW PARAMETER

B.N.Sergeev
Central Aerological Observatory,
Dolgoprudny, Moscow Region, 141700 Russia

1. INTRODUCTION

Atmospheric front development and evolution are controlled by background large-scale temperature and wind fields. Numerical simulation of warm and cold front dynamics and their cloud system development has been performed using various values of large-scale flow parameters, such as 1) temperature lapserate, 2) frontal temperature difference, 3) wind field deformation and 4) vertical wind shear.

2. NUMERICAL MODEL

Two-dimensional numerical model of atmospheric front, which describes frontal dynamics and cloud and precipitation development (MIRONOVA, SERGEEV,1984) is used. Background large-scale wind field is determined in the form of linear deformation field with vertical shear and boundary layer. The equations of motion are written in terms of vorticity - stream function. Conditions of zero velocity and given heat andmoisture flux are applied for theground surface. We implemented thewave extinction upper boundary condition in order to eliminate wavereflection. Open boundary conditionsare used for side boundaries.

Bergeron mechanism of precipitation development is included in a parameterized way.

In this simulation, we used a 60s time interval with 257x65 grid point covering a domain 2560 km x 12,8 km.

3. RESULTS

The results have shown a considerable dependence of mesoscale structure of frontal cloud and precipitation on large-scale flow parameters.

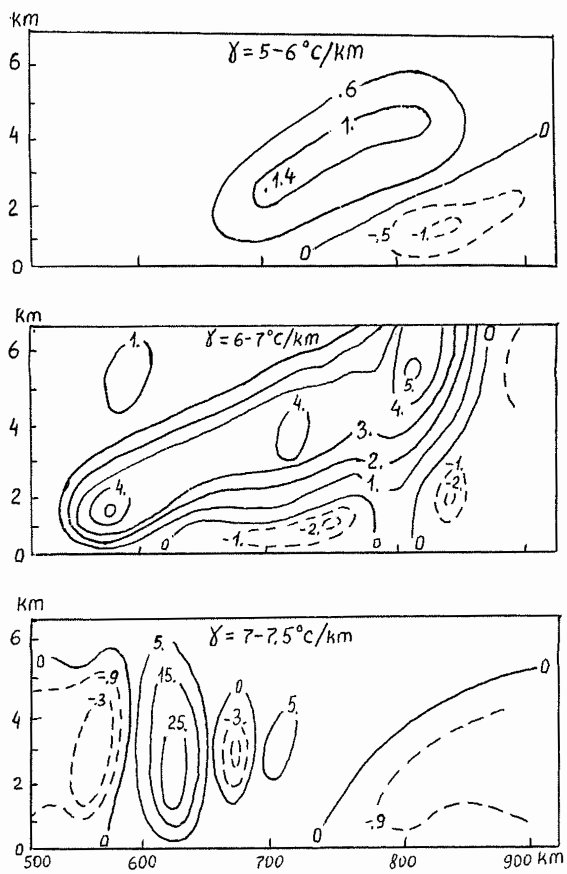

Fig.1. Vertical velocity field (cm/s) for the warm front. Temperature lapserates a) 5-6 C/km, (b) 6-7 C/km, (c) 7-7,5 C/km.

As large-scale flow static stability is decreasing, vertical motions are strengthening and mesostructure of the vertical velocity field is changing substantionally (Fig. 1). The field is uniform if stratifica-tion is very stable (Fig.1a). Convec-tive cells are developed if convec- tively unstable layer exists in the warm air mass (Fig.1c). In case of low stability (Fig.1b) a gravity wave develops in the frontal zone, with wave length being 70-130 km. Some 3 or 4 cellsof increased upward motion appear in the normal-to-front plane. Disturbances, causing waves, are formed by oscillating latent heat release due to sublimation. Wave length increases as frontal temperature difference becomes larger.

Weak large-scale flow deformation of contraction or deformation of dilatation (which causes frontolyse) lead to layer-like structyre of frontal zone. In that case severallayers, stretching along frontal surface, with alternatively upward and downward vertical motion appear (Fig.2).

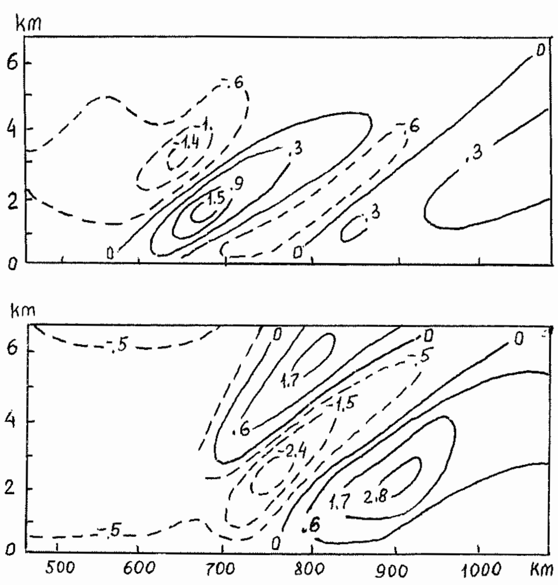

Fig.2. Vertical velocity field (cm/s)for the warm front under thecondi-tion of large-scale flowdilatation.Times are (a) 19 hour, (b)33 hour.

Such a structure may be responsible for layer-like structure of frontal cloud systems at the stage of decay. Vertical wind shear in the normal-to-front plane brings about strengthening of vertical motions in the frontal zone and more active cloud and precipitation development (Fig.3).

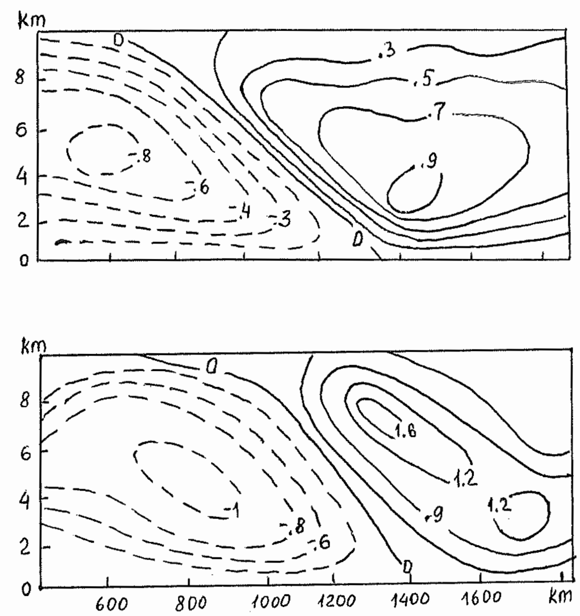

Fig.3. Vertical velocity field (cm/s) for the "dry" cold front. Wind shear is absent (a) and equals 10 s (b).

This effect is accounted for different ent horizontal advection of temperature ture and wind fields. The wind shear effect is especially pronounced in the middle troposphere on the downwind side of frontal zone. Because of that vertical wind shear has a special impact on cold frontal clouds and precipitation.

REFERENCES

MIRONOVA G.A., SERGEEV B.N.:Two-dimensional numerical model of frontal-clouds and precipitation. 9th Int.Cloud Physics Conference, Tallinn,1984. Proceedings, v.11, 633-636.

REMOTE SENSING INVESTIGATION OF CLOUD LIQUID WATER SPACE DISTRIBUTION

A.V.Koldaev[1], Yu.V.Melnichuk[1], A.F.Mironov[1]

[1] Central Aerological Observotory, Pervomayskaya 3, Dolgoprudny, Moscow Reg., Russia

1. Introduction.

Untill now, in the cases the information on clouds' Liquid Water Content (LWC) at different heights is important, very expensive experiments are carried out (as the GATE experiment), in which two or more aircrafts provide simultaneous "in situ" measurements. Nevertheless 8 years ago it was pointed on the principal possibility of remote measurements of spatial distribution of liquid water in vertical crossections of clouds (Warner et al, 1984). This possibility is based on the well known method of remote microwave radiometric measurements of the integral LWC in clouds and precipitation (Westwater et al, 1978). The value of LWC in every point of cloud crossection can be derived from the integral data by computer tomography technique (Navarra et al, 1981).

In the following paper we shall consider some of problems concerning utilization of cloud microwave tomography, but the main aim of the article is to present statistically meaningful results of cloud LWC space distribution obtained by this method.

2. Experimental technique.

Microwave tomography measurements of LWC space distribution in vertical crossection of clouds is carried out by aircraft with flight level under the bottom of clouds or through clouds. Aircraft microwave system permits to receive radiation from two directions arranged in vertical plane.

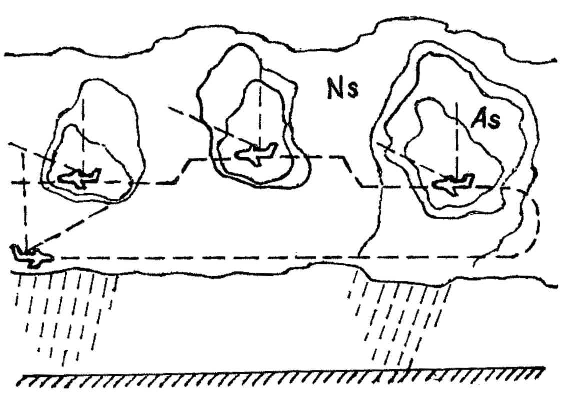

Fig.1. Standard flight track in experimental work.

Theoretical review of two-beam microwave tomography possibility was made by means of numerical simulation (Koldaev et al, 1990).

For experimental work we have chosen microwave system, which have included two identical modulative radiometers each receiving radiation from definite direction by appropriate antenna. The main parameters of the radiometer in use are shown in Table 1.

Parameters	Values
operating frequency	37.5 GHz
measured values	5K - 400K ± 0.15K
sensitivity, 1 sec	0.15 K
time stability	1 K/h
temperat. stability	2.5 K / 10 K
modulation frequency	1.2 - 1.6 kHz
external power	+27 V +7/-4 V
consumed power	45 W
weight	10 kg

Table 1. Experimental radiometer parameters.

Radiometers were installed on board the aircraft laboratory of Central Aerological Observatory "IL-18".

The radiation is received by two antennas from zenith and from the second direction along the aircraft flight track with the angle of 30 degrees. Fig.2 shows open radom on the top side of aircraft, under which horn lenses of microwave system are installed. Besides that, the aircraft was equipped with weather radar and "in situ" LWC test system including "King sensor" and FSSP OAP 2D PMS sensors. All information was recorded by board computer center.

Fig.2. Horn-lenses under open radom on the top side of aircraft "IL-18".

While flight planning we have taken into account the necessivity to compare remote and "in situ" LWC data. Warner et al (Warner et al,1988) used two-aircraft experiment for the same task, where one aircraft with "in situ" probe penetrated cloud at the time the second one with microwave system passed under the bottom of this cloud. It was shown, that such flight scheme permited to make comparison only in statistical form while immediate comparison was impossible.

For this reason our flight technique concerned in passing at 100-200 m upper the bottom of the clouds and quick defining by microwave sensing of the height of LWC maxima in clouds' vertical crossection. After that aircraft changes its height and penetrates the clouds through the maximal LWC zones, which were localized before (Fig.1). At this time simultaneous measurements by remote and "in situ" sensors, are carried out, which permit us to compare immediate "in situ" data with remote ones derived from the lowest level of reconstructed matrix .

Two-dimension microwave measurements were used in a set of experimental flight programs: in Moldavia 1979, Cuba 1986, Bulgaria 1989, Vietnam 1990. Mostly statistically essential results have been obtained in flight experiment on investigation of frontal cloud systems in Bulgaria, and the following discussion is concerned to the analysis of data of this program. In this program all measurements were carried at heights upper the height of 0 C, so the data correspond to zones of supercooled liquid water.

3. Comparison of "in situ" and remote LWC measurements.

In flight experiments LWC field in vertical crossection of clouds was retrieved with resolution 350 m through hight and 600 m through horizont from microwave radiometric data. The nearest to the flight level LWC data elements of retrieved matrix were compared with LWC data of "King sensor". The example of direct comparison is presented on Fig.3.

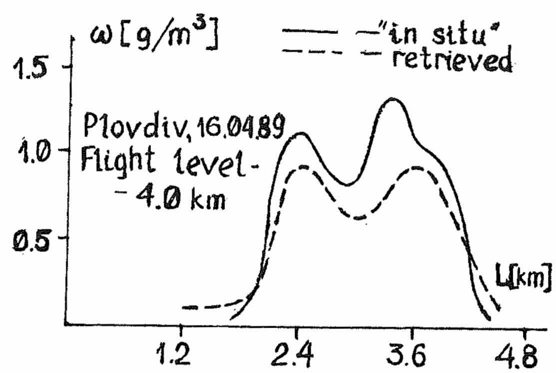

Fig.3. Simultaneous microwave and "in situ" LWC data in Ns-Ac cloud.

Though 38 vertical crossections were reconstructed, only 14 clouds were chosen for comparison after checking of the quality of information. In 11 cases among them cross-correlation between "in situ" and remote data was found, and 3 cases gave negative result. Fig.4 shows regression between LWC data measured "in situ" and ones by microwave tomography technique for 11 selected cases.

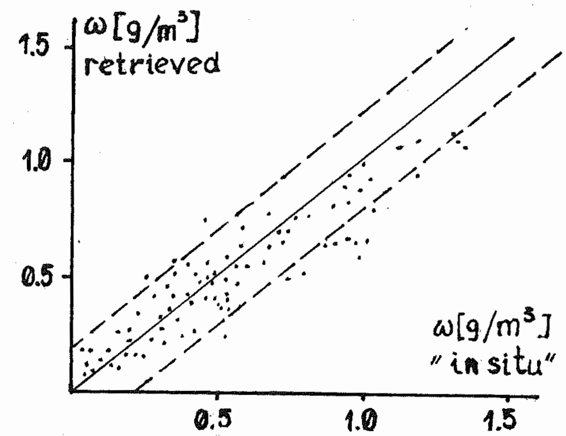

Fig.4. Regression between retrieved and "in situ" LWC data.

More than 100 combined "in situ" and microwave values of LWC were used in correlation analysis, and correlation coefficient was found to be equal 0.87. Meansquare (MSQ) deviation from direct dependence is equal 0.18 g/m^3. The MSQ value pointed here is the real accuracy of microwave tomography retrieval of cloud LWC obtained in direct comparison at the first time.

4. Cloud Liquid Water space distribution in frontal systems.

All experimental results presented here relate to flight investigation program performed on CAO aircraft laboratory "IL-18" in Bulgaria in April 1989. At this period a set of frontal situations was observed in Bulgaria, which were presented by Ns-Ac cloud systems. In the course of experiment 7 flights were conducted, in which characteristics of 52 LWC zones in clouds were measured. The distinguishing of each LWC zone was made, if the level of integral LWC in vertical direction was more than 0.05 kg/m^2. Among 52 measured zones together quality of two-beam information allowed us to reconstruct 38 vertical crossections of LWC in clouds. For this reason statistic set in presented below clouds' characteristics is different, namely for horizontal characteristics it is 52 units and for vertical one 38 units.

4.1. Horizontal characteristics.

Differential distribution of horizontal size LWC zones observed in 7 flights is presented on Fig.5 by solid line. As can be seen, this distribution is rather wide with maximum at length 15-20 km. Zones with horizontal size less than 7 km and more than 20 km were observed two times rarely.

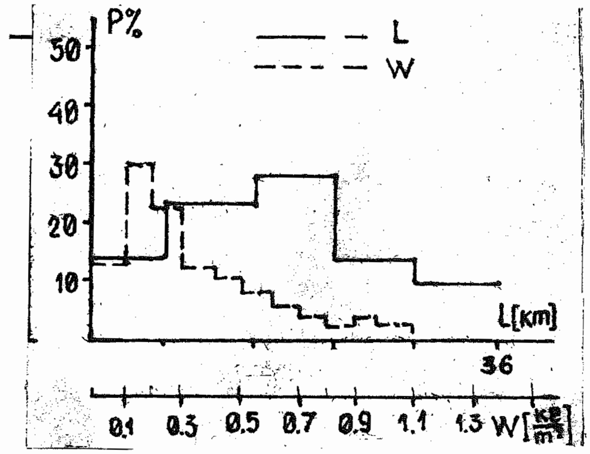

Fig.5. Distribution of horizontal size and integral LWC in frontal clouds' supercooled water zones.

This fact indicates, that supercooled liquid water in frontal cloud systems is contained in regions with size more close to convective form of clouds and a few times lower than horizontal scale of own cloud system.

On Fig.5 differential distribution of integral LWC is presented by dotted line. The maximum of distribution is relatively narrow and corresponds to the value 0.1 kg/m^2, and the probability of integral LWC with value more than 0.5 kg/m^2 is very small. With respect to integral LWC in Cu clouds (Koloskov et al,1992) the value presented here is approximately one order lower. Together analysis of size and integral LWC distribution allows us to understand supercooled LWC zones' origination in frontal systems as a special type of internal convection. More detailed characteristics of this convection can be obtained in the analysis of vertical structure of supercooled LWC zones.

4.2. Vertical structure.

Characteristics of vertical structure of supercooled LWC zones in frontal clouds are presented in Fig.6.

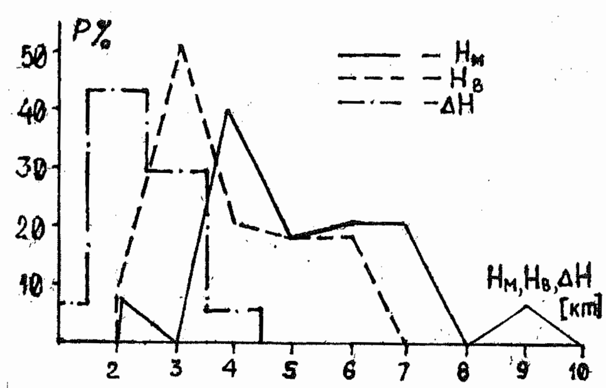

Fig.6. Distribution of top height, medium height and thickness of supercooled LWC zones in frontal clouds.

Solid line in the figure shows distribution of the top levels of LWC zones. Maximum of distribution lies at the height about 4 km, and this height corresponds to the temperature -15 C at the experimental period. It is interesting, that LWC zones' with top at the height 5-7 km were observed twice rarely. Dotted line shows distribution of the height, on which maxima of supercooled LWC were observed. This distribution has a sharp maximum at the height of 3 km (corresponding temperature -7 C), and this height of LWC zones' center was observed practically in the half from all cases.

Two previous graphics are accomplished by the graphic of thickness of supercooled LWC zones presented on the figure by point-dotted line. In accordance with the heights of LWC zones' tops and with the heights of maxima in LWC zones this distribution has a maximum at value of 2 km.

Together analysis permits us to suggest, that supercooled LWC zones in frontal cloud systems frequently lie in the space from zero isotherm up to the height of -10-15 C isotherm with medium height of 3 km (-7 C).

Experimental data presented are illustration of the method, but we are sure, that it is the first step in regular use of microwave tomography technique in cloud physics.

References:

Koldaev, A.V., Melnichuk, Yu.V., Mironov, A.F., Agapov, Yu.V., Dmitriev, V.V., Nikolski, A.N., 1990: The application of aircraft microwave radiometric tomography in weather modification experiments. Proc 20-th European Microwave Conf, Budapest, Vol 2, pp 1402-1407

Koloskov, B.P., Koldaev, A.V., Batista, L., Perez, C., 1992: Spatial and microphysical investigation of tropical convective storms by remote sensing techniques. Proc 11-th Int Cloud Physics Conf, Montreal

Navarro, A.P., Parev, K., Dunlap, J.L., 1981: Two dimensional spatial distribution of volume emission from line integral data. Rev Sci Instrum, Vol 52

Warner, J., Drake, J.F., Krehbiel, P.R., 1984: Microwave tomography as a means of determining liquid water profiles in cloud. Proc 9-th Int Cloud Physics Conf, Tallin, Vol III, pp 823-826

Warner, J., Drake, J.F., 1988: Field tests of an airborne remote sensing technique for measuring the distribution of liquid water in convective cloud. J Atmoth and Oceanic Tech, Vol 5, N 6, pp 833-

Westwater, E.R., 1978: The accuracy of water vapor and cloud liquid determination by dual frequency ground-based microwave radiometry. Rad Sci, Vol 13, N 4

ROLL FLOW-FIELD CHARACTERISTICS AND FORMATION MECHANISMS IN LAKE-EFFECT SNOW STORMS

David A. R. Kristovich

Cloud Physics Laboratory, University of Chicago
5734 S. Ellis Ave., Chicago, IL 60637

1. INTRODUCTION

The mesoscale flow-field structures of boundary layer (BL) rolls and possible mechanisms for their development, were explored using aircraft and dual-Doppler radar data taken over southern Lake Michigan during the 1983/1984 field operations of Project Lake Snow (Braham and Kelly, 1982). The findings discussed here are given in more detail in Kristovich (1991, 1992).

Rolls were evidenced by wind-parallel bands of effective radar reflectivity factor. An example is given in Fig. 1. The high-reflectivity bands were oriented near 130°-310° with spacings of 7.6 to 9.8 km. Similar patterns were frequently observed during the Project, usually in conditions of strong surface thermal forcing, strong winds and snow.

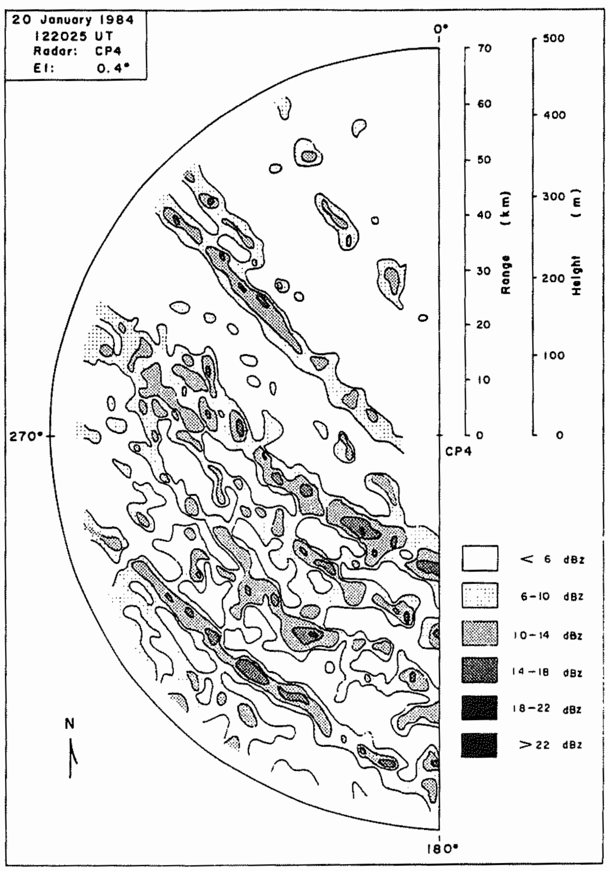

Fig. 1. Plan view of radar reflectivity taken on 20 January 1984.

It is often difficult, or impossible, to determine how rolls formed in a particular case. However, since rolls are very common in the atmospheric BL and can form by a number of mechanisms, it is a topic worth pursuing. In this study, measured atmospheric conditions are compared with those required by several previously-proposed roll formation mechanisms in order to determine which may be responsible for the rolls.

Four dates were chosen for detailed study (17, 18, 29 Dec 1983 and 20 Jan 1984) based on the presence of near wind-parallel bands of high-reflectivity and on data availability. Roll-mean characteristics were derived from measurements taken by NCAR radars CP3 and CP4. Roll-mean flow fields were found by averaging along-roll (U_r) and cross-roll (V_r) wind components along the roll axes. Vertical wind components were derived using the continuity equation. Wind profiles and atmospheric conditions were determined from balloon soundings taken at Muskegon, Michigan and from aircraft (NCAR Queen Air) measurements.

2. ATMOSPHERIC CONDITIONS

The rolls were observed within boundary layer depths (Z_i) of 1.0 to 1.5 km. There was strong surface thermal forcing (air-lake temperature differences were 11 to 21°C) and strong winds (near 10 m s^{-1}). The ratio of Z_i to Monin-Obukhov length (L) was -136 to -359; values that are often thought to favor three-dimensional, rather than two-dimensional, convection (Grossman, 1982).

Fig. 2 gives profiles of U_r and V_r on each of the four dates under study. There were along-roll wind speed maxima at or below 0.5 Z_i and minima between 0.6 and 1.0 Z_i on each date. Cross-roll winds varied less and tended to become more positive with height. Strong wind shear was observed below 0.2 Z_i with weak shear above.

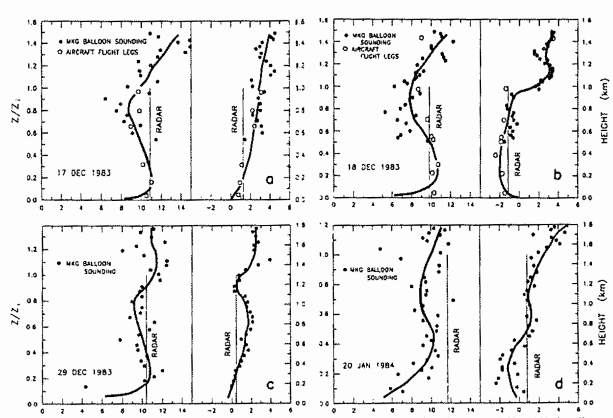

Fig. 2. Profiles of along- (U_r, left panels) and cross-roll (V_r, right panels) winds for four dates. Radar measured winds are also given.

3. ROLL CHARACTERISTICS

The observed rolls had wavelengths of 2.0 to 6.7 Z_i and were oriented within 10° of the wind shear below 0.2 Z_i and the mean-BL wind direction. No consistent pattern was obvious between roll orientations and mean-BL shear, shear between 0.9 and 1.1 Z_i. Fig. 3 gives the roll-mean (a) cross-roll and vertical winds and (b) along-roll wind speed deviations measured on 17 Dec. Counter-rotating roll circulations are evident in Fig. 3a. Roll-updraft zones coincide with the high-reflectivity bands. Peak cross-roll wind speeds were up to 1.3 m s^{-1} and peak vertical velocities were somewhat weaker (up to 0.5 m s^{-1}). These values are near those previously observed and predicted by past numerical studies.

Along-roll winds (Fig. 3b) were found to be 0.5 to 1.4 m s^{-1} stronger in the roll-updraft zones than in the roll-downdraft zones on each date. Aircraft measurements on 17 Dec tended to confirm this pattern. Since there was a low-level wind speed maxima in these cases (Fig. 2), these observations support the conclusions of Brown (1970) and others that U_r variations may result from vertical advection of momentum by the rolls. However, other reasons for these variations should be explored.

4. ROLL-FORMATION MECHANISMS

Observed atmospheric conditions were compared to those required by three commonly-accepted roll-formation mechanisms. Kuettner (1971) argued that along-roll wind shear curvature favored wind-parallel bands of convection if that curvature was at least 10^{-7} cm^{-1} s^{-1}. Only one of these cases had BL-mean curvature (0.48 to 1.1 x 10^{-7} cm^{-1} s^{-1}) that met Kuettner's criteria. However, Kuettner's criteria was met on all cases below 0.2 Z_i, where the greatest shear was observed. If BL convection can be organized at the lowest levels (as found by Sykes and Henn (1989)), then Kuettner's mechanism may explain the observed rolls. It should be noted that the rolls consistently oriented within 10° of the low-level shear, supporting this conclusion.

Brown (1970) found that cross-roll wind shear could result in rolls when an inflection point is present in the V_r wind profile. In three of these four roll cases, no such inflection point was obvious (Fig. 2). In addition, V_r wind shear was an order of magnitude weaker than U_r wind shear in these cases, suggesting rolls formed by this mechanism would have much different orientations.

Clark, et al. (1986) found that gravity waves initiated in the entrainment zone could subsequently organize BL convection into rolls. This mechanism could not be fully tested with our data. It should be noted, however, that the direction of the wind shear in the entrainment zone changed considerably with fetch on 17 Dec (Kristovich 1991). Satellite photos generally show only gradual changes of roll orientation with fetch. Therefore, it was concluded that gravity waves were probably not responsible for the wind-parallel bands in these cases, but could have influenced convection along the rolls. Further study on this topic is required to determine the role of gravity waves in these cases.

5. CONCLUSIONS

An observational study of roll flow fields and an exploration of possible roll formation mechanisms was conducted using data collected on four dates during Project Lake Snow. It was found that

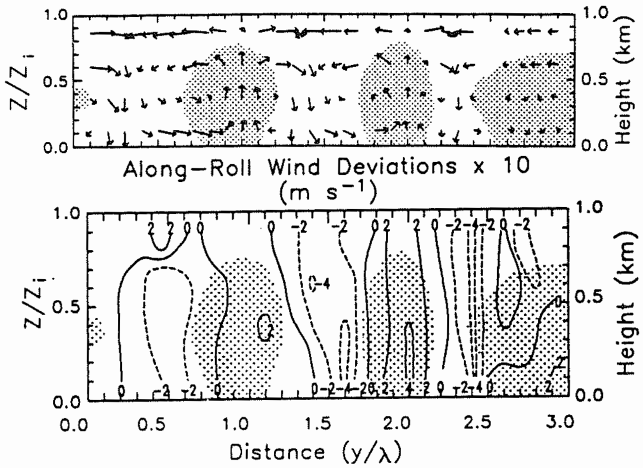

Fig. 3. Roll-mean cross sections of (a) cross-roll (V_r) and vertical winds and (b) along-roll (U_r) component winds on 17 Dec 1983.

vertical and cross-roll wind components were consistent with those previously predicted and reported. This is the first study to the author's knowledge to observe consistent U_r speed variations related to the rolls. These were probably due to vertical advection of the along-roll wind profile by the rolls, as predicted by past models.

Criteria required by a number of roll-formation mechanisms was compared to those observed in these cases. Although no criterion was strictly met, it was suggested that strong along-roll wind shear at low levels was responsible for organizing the convection into linear patterns. If this is so, then the decrease of surface friction over water areas may increase the chances of roll development by allowing for larger gradients of wind speed near the surface.

6. REFERENCES

Braham, R.R., Jr. and R.D. Kelly, 1982: Lake effect snow storms over Lake Michigan. In *Cloud Dynamics*, E.M. Agee and T. Asai, eds., Boston: D. Reidel, 432 pp.

Brown, R.A., 1970: A secondary flow model for the planetary boundary layer, **J. Atmos. Sci.**, **27**, 742-757.

Clark, T.L., T. Hauf, and J.P. Kuettner, 1986: Convectively forced internal gravity waves: Results from two-dimensional numerical experiments. **Quart. J. Roy. Meteor. Soc.**, **112**, 899-925.

Grossman, R.L., 1982: An analysis of vertical velocity spectra obtained in the BOMEX fair-weather, trade-wind boundary layer. **Bound.-Lay. Meteor.**, **23**, 323-357.

Kristovich, D.A.R., 1991: *The three-dimensional flow fields of boundary layer rolls observed during lake-effect snow storms*. Ph.D. Thesis, The University of Chicago, 182 pp.

Kristovich, D.A.R., 1992: Mean circulations of boundary-layer rolls in lake-effect snow storms. **Bound.-Lay. Meteor.**, accepted for publication.

Kuettner, J.P., 1971: Cloud bands in the Earth's atmosphere -- observations and theory. **Tellus**, 23, 404-425.

Acknowledgements: The author gratefully acknowledges the guidance from Roscoe R. Braham, Jr., members of my advisory committee, and Cloud Physics Laboratory members. This work was supported by NSF ATM-86-17177 and NSF ATM-89-221202.

THE ROLE OF CONVECTIVE CLOUDS IN THE DEEPENING OF THE EXTRATROPICAL CYCLONES IN THE ARGENTINE LITORAL

María Elena Saluzzi

Departamento de Ciencias de la Atmósfera
UBA - CONICET

1. INTRODUCTION

The southern region of the Atlantic Ocean which borders the American continent from 20°S latitude to 40°S latitude approximately, is known as one of the cyclogenetic zones with most activity.

Several investigators have done a statistic recount of their occurrences (Chung, 1977; Necco, 1982) and have marked the regions of maximum frequency. One of them is the mouth of the Río de la Plata.

In the statistic recounts (Necco, 1982), winter appears as the season where the greatest number of cases is registered considering all the zone, but for cyclones originated in the argentine litoral, the equinox seasons and summer are the time with most frequency.

These cyclones recognize a determinant orographic influence (Palmen and Newton, 1963), they are in reality lee cyclones, and over the argentine litoral they form preferently and generally in the latitute which corresponds with the greatest mid roof of the Andes. Likewise and according to Necco (1982) the mountains in southern Brazil seem to have influence in the formation of the ones which affect the North of this cyclogenetic region.

The trajectory which the cyclones follow until they emerge over the ocean and which the cyclone will then follow over it, also acknowledges studied patterns as a consequence of its origin, though it admits exceptions.

2. THE CONVECTIVE CLOUDS

Observation has shown that the most important cyclogeneses in the argentine litoral are accompanied by important convective events. The deep convective clouds, which sometimes give origin to great storms, present themselves over all the cyclogenetic area and three stages may be considered in their presentation:

a) In this first stage they appear sweeping all the cyclogenetic area, preceeding the cyclonic development.

b) In the second stage they group in the region where the cyclon will manifest and they extend over the zone of the cyclone's future trajectory, i.e they accompany the cyclone in all the formation stage and at least during the first phase of development.

c) As the deepening of the cyclone progresses, the convective clouds weaken until they disappear.

2.1 The experimental evidence

The resources available to illustrate the behaviour of the convective clouds are: the analyzed synoptic maps (with the exception that, though the synoptic network marks the convective events which it detects, these may be more and may have been filtered); the study of the precipitation fallen and its character (in the present study the 24 hours accumulated precipitation maps were available); the third and most important observed data are the satellite photographs provided by the APTHR belonging to the argentine National Meteorological Service which have permited a continuous and detailed observation of the numerous cyclogenetic developments.

2.1.1 Cyclogenesis. May 1984

The satellite photograph shows the cyclone's position, already mature and ready to start its Atlantic stage (Fig. 1).

Fig. 1. Satellite photograph 30/5/84 00 UTC. Shows great development and the anomalous trajectory following the atlantic coast upto 40°S.

The synoptic maps for the situation which took place at the end of May 1984 are presented in correlation with the isohyet maps for the same situation.

The cyclogenesis of the end of May 1984 answers to the typification of the cyclones of the argentine litoral: it starts in the south of the Mesopotamia, advances over the Uruguaian territory, develops over the external coast of the Río de la Plata and continues southwards reaching its greatest deepening over the ocean, but heading always southwards coasting the province of Buenos Aires. It reaches its complete maturity over the ocean at 40°S and goes on south to higher latitudes. All the evolution has been typic, except its trajectory and its here and in the beginning of the cyclogenesis where the role of the convective clouds is visualized. In effect, with their presence they accompanied the first stages of the formation and they preannounced their trajectory with their manifestations over the uruguaian coast and their exit onto the estuary heading directly southwards, road which would be later followed by the cylcone. The synoptic maps (Figs. 2 and 3) and in the map of 24 hours accumulated precipitation

(Fig.4) clearly evidence this process.

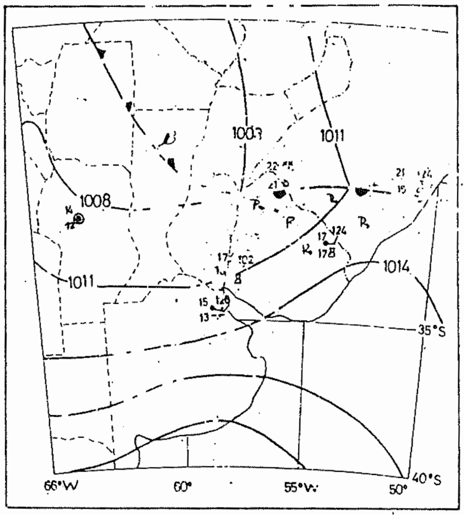

Fig. 2. Synoptic Situation for 27-5-84 at 12UTC

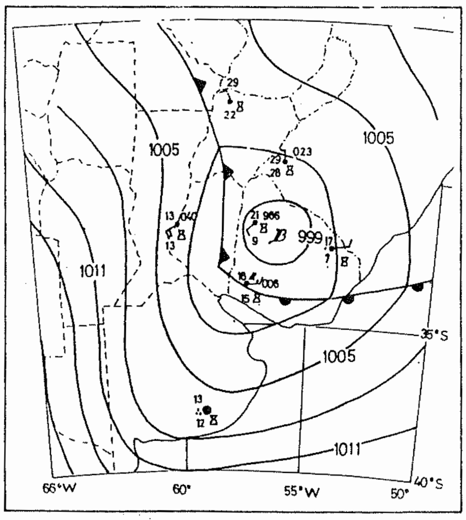

Fig. 3. Synoptic Situation for 28-5-84 at 18UTC

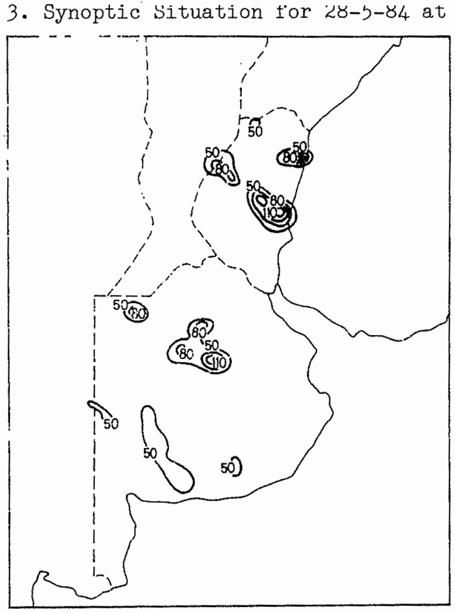

Fig.4. 24 hour accumulated precipitation (mm) for 27-5-84

The litoral cyclones, dependant of their trajectory, occasion a very adverse weather over the Río de la Plata and its coasts characterized by very strong winds which cause the typical "sudestada" (storm from the southeast) which brings floods to the shores and consequently evacuations take place.

2.1.2 Cyclogenesis during november 1989

This cyclone is another typical case of cyclogenetic formation over the argentine litoral. In a similar way to the former one, it forms over the Mesopotamia, but somewhat more to the north, and following a trajectory which may be foretold, heads quickly towards Uruguay. The cyclone crosses the country latitudinally and emerges over the Atlantic ocean following the classic path.

Maturity and the beginning of the deepening is reached over the coast. The cyclone deepens until it reaches less than 990 Hpa descending over 15 Hpa since the first stage.

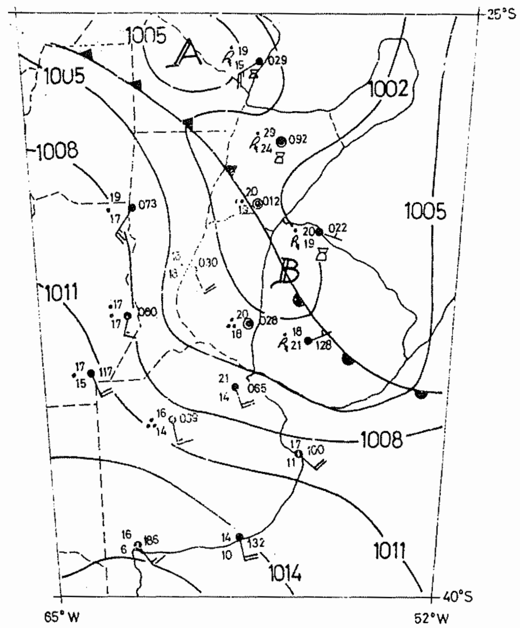

Fig. 5. Synoptic Situation for 11-11-89 at 18UTC

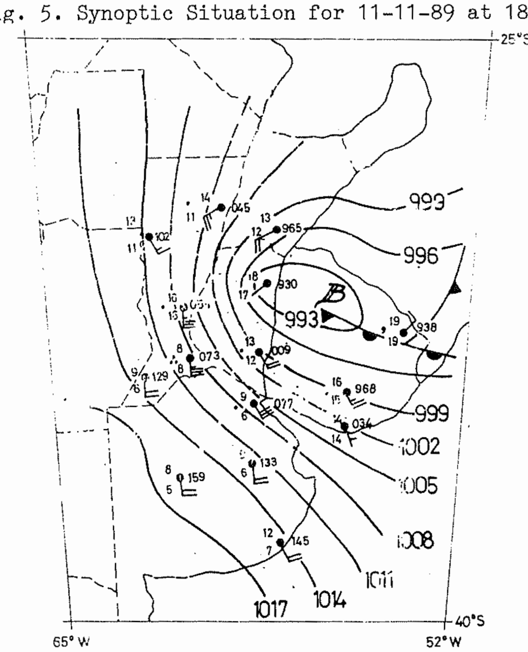

Fig. 6. Synoptic Situation for 12-11-89 at 9UTC

Fig. 5, the synoptic map for november 11th 1989 at 18UTC, shows the beginning of the cyclogenesis and the grouping of the convective activity. The map for november 12th at 9UTC shows the start of the cyclogenetic development, its rapid maturity and the beginning of its deepening (Fig. 6).

The maps clearly show that this cyclone, due to its position, generated strong winds from the ESE over the Río de la Plata estuary giving origin to an intense and persistent "sudestada" which caused important floods over all the coast up to the exterior region of the Río de la Plata.

2.2 Surface circulation

The convective clouds modify the surface circulation locally, but with great intensity. With the object of measuring the importance of this modification the surface vorticity and divergence was measured through the application of an objective analysis method which considers satellite information (Saluzzi 1992) and uses a synoptic grid of 328 km between grid points. If some alteration is observed specially in the vorticity field, which cannot be attributed to the synoptic systems, and considering the scale, this fact itself will account for the importance of the modification.

2.2.1 Divergence and vorticity

The divergence and vorticity maps for the situation of May 1984, which correspond with the surface maps already shown, are presented. The divergence map for 27-5-84 shows the most important convergent nucleus in the cyclogenetic zone, extending along the cold front and over the region which the cyclone will follow.

The same affirmation may be done with respect to the relative cyclonic vorticity map which also marks the coincidence between the cyclonic centres and the systems (Figs. 7 and 8).

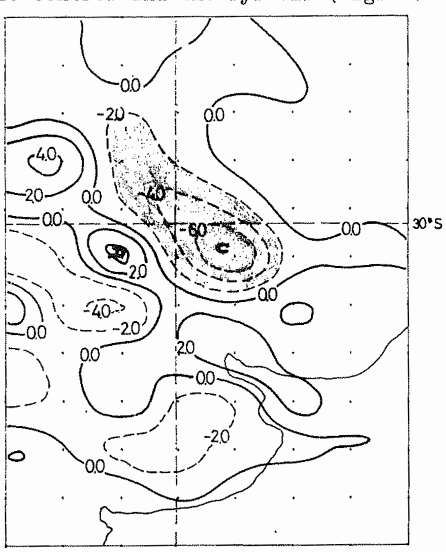

Fig. 7. Divergence map for 27/5/84 at 9UTC. Units 10^{-5} sec^{-1}.

The analysis done permits to show the modification which the convective nucleus introduce in the surface circulation.

A wee displacement in the position of the divergence and vorticity nucleus with respect to

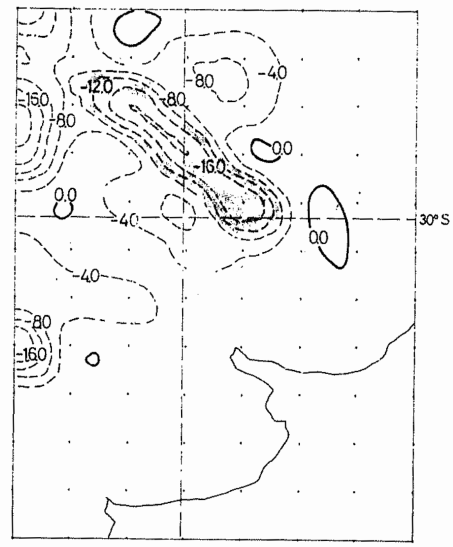

Fig. 8. Vorticity map for 27/5/84 at 9UTC. Values 10^{-5}.

the synoptic systems is observed. This is due to the difference between the map projections used in the synoptic maps and the one used by the computer.

The situation of november 1989 was studied analogously.

The divergence map which corresponds to 11/11/89 at 18UTC shows the convergent nucleus which coincides with the position of the cyclogenetic zone and extends southwards marking the zone of convective activity (Fig.9).

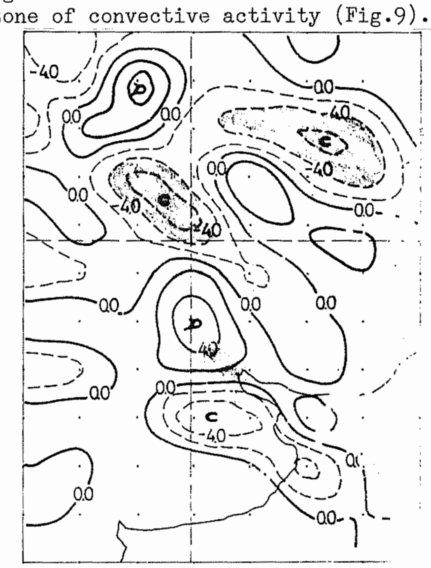

Fig. 9. Divergence map for 11/11/89 at 18UTC. Units 10^{-5} sec^{-1}.

3. THE ROLE OF THE CONVECTIVE CLOUDS AND THEIR CHARACTERISTICS

If the conditions for the self-development of the cyclone (Eliassen, 1959) are given and are only controled by the S stability term, when the vertical instability and the surface humid advection are such that favour the formation of great convective clouds, these will cause the change of the lapse rate (increasing it) in such a way that the influence of the S term lessens and the dam~~pening~~ of the troposphere is obtained. The deepening of the cyclone is reached in this way and the deep convective clouds play their role.

The resource used to study the characteristics of the clouds has been the application of a deep convective cloud numeric model (Saluzzi, 1988) adapted to the geographic characteristics and to the synoptic network of the country.

As the clouds considered have formed over the litoral or the Río de la Plata zone, the initial data used was the radiosonde of Ezeiza (International Airport of the city of Buenos Aires).

To illustrate the way in which the convective clouds act and to study their characteristics a summer cyclogenesis was chosen.

3.1 Cyclogenesis of January 15 and 16, 1986

The model calculates the temperature in the cloud, which permits showing the conditions of the saturated ascent in the cloud. Its drawing (Fig. 10) evidences, comparing with the real lapse rate, how and upto what level the humidification of the troposphere is reached, within the error limits of the numeric model (Squires, 1976). This dampening favours the deepening of the cyclone.

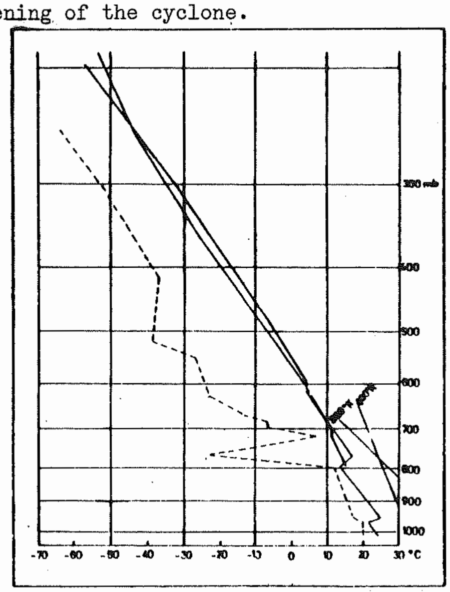

Fig. 10. Radiosonde for Ezeiza 15/1/86 and saturated sounding in the simulated cloud

With the application of the model, the characteristics attributed to the convective clouds which characterize the intense activity registered on 15/1/86, previous day to the deepening stage, were studied. The cloud obtained was over 12000 m high, the maximum value of the updraft is over 25 m/s at 10600 m height and the cloud has a maximum amount of total water Q equal to 6.06 g/kg at 7820 m; it produces 34mm of rain and is capable of producing hale.

Figure 11 shows the values reached by the cloud parameters and accounts for the importance of the cloud reached.

The evolution and development of this cyclone is typical and takes place in the mouth of the Río de la Plata, which has been pointed out by Chung as being one of the zones of maximum relative frequency of occurrence.

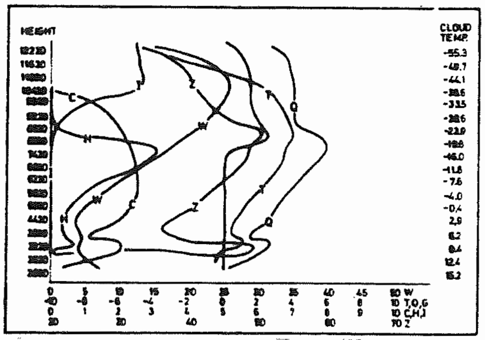

Fig. 11. Graphic of the values reached by the different parameters in the development of the simulated convective cloud for 15/1/86.W(m/s): updraft veloc. Q(g/kg): total liquid water. G(g/kg): Graupel water. T(°C): cloud temperature. C(g/kg): Cloud water. H(g/kg): Hidrometeor water. I(g/kg): Cloud Ice. Z(DBZ): Reflectivity.

4. CONCLUSIONS

It has been shown, from the experimental evidence and through the application of a deep convective cloud numeric model, that convective clouds accompany all the development stage and the first part of the deepening stage of the cyclones of the argentine litoral, favouring it through the humidification of the lapse rate and its increase and therefore diminishing the stability term S, which favours the cyclonic self-development.

5. REFERENCES

Chung, 1977: On the orographic influence and lee cyclogenesis in the Andes, Rockies and the east asian mountains. Archiv. Meteor. Geophys. Biokl., Ser A 26.

Eliassen, 1959: On the formation of fronts in the atmosphere. The atmosphere and sea in motion. B. Bolin, Ed. Rockefeller Institute Press, 277-288.

Necco, 1982a: Comportamiento de vórtices ciclónicos en el área sudamericana durante el FGGE: Ciclogénesis. Meteor., 13, 7-19

Palmen y Newton, 1969: Atmospheric circulation systems: their structure and physical interpretation. Academic Press, New York, 603 pp.

Saluzzi, 1988: Experiments with a one-dimensional deep convection model. Report of the second international cloud modeling workshop. Toulouse 8-12 August, 1988. 237.

Saluzzi, 1991: Resultados de la aplicación de un método de análisis objetivo que considera la información satelitaria. Geoacta (en prensa).

Squires, 1976: Evolution of cloud droplet spectra: The effect of nuclei spectra. 29 Bull. Amer. Meteor. Society. Jan. 1977.

Troup, 1972: Satellite observed Southern hemisphere cloud vortices in relation to conventional observations. J. Appl. Met., 11, 909-917.

DEVELOPMENT OF WINTERTIME PRECIPITATION

D.R. Hudak[1] and Roland List

Department of Physics, University of Toronto
Toronto, Ontario, CANADA M5S 1A7

1. INTRODUCTION

The Toronto Winter Storms Program was a pilot study by the University of Toronto into wintertime precipitation occurring in the Toronto area during the winter of 1990/91. The area is directly affected by most major storms that move across North America in the winter and experiences a great variety of weather and a diversity of precipitation types. Lake Ontario, on whose shores Toronto is situated, remains ice free all year and has a significant influence on the winter storms which pass through the area. As a result almost one-half of the precipitation in the winter occurs as rainfall (Thomas and Hare, 1974).

The main emphasis in this study is to provide descriptions of the microphysical processes in the clouds of these systems in the form of typical footprints. In this way the role of readily observable microphysical quantities can be related to the precipitation and synoptic-scale characteristics.

2. DATA ACQUISITION AND ANALYSIS PROCEDURES

The main means of investigating the storms was with an X-band Doppler radar operating at the University of Toronto. It has the following features: transmitted power 25 KW; beamwidth 2.5°; pulse width 0.4 μs; and the PRF 2000 s^{-1}. The Nyquist velocity is 16.0 m s^{-1} but dual PRF techniques were employed when appropriate to increase the unambiguous velocity up to 48.0 m s^{-1}. Normal operating procedure, repeated every 10 min, involved volume scans and RHIs on selected azimuths to document the storm morphology, precipitation intensity, and wind field information. The range resolution was 250 m out to a maximum range of 18.25 km. This scanning strategy was interrupted about every hour to operate the radar in a vertically pointing mode in order to collect the full Doppler spectral power density information. In this mode the vertical resolution was increased to 125 m. The range bins were stepped through sequentially from 0.25 km to echo top, recording the full Doppler spectrum. This cycle was repeated usually from three to five times before returning to the regular scanning mode.

The radar data were analyzed in the two ways. The first technique derived the horizontal winds over the radar by Volume Velocity Processing (VVP) using the volume scan data (Siggia and Holmes, 1991).

The second, and far more comprehensive technique in assessing the microphysics, involved the use of the radar in a vertically pointing mode. In this case, the Doppler power spectral density data were obtained by the discrete Fourier transform of the complex returned signal using Von Hahn windowing. The spectrum was smoothed with a five point weighted average. Then the noise level was objectively determined by the method of Hildebrand and Sekhon (1974). The procedure for determining acceptable parts of the spectra for analysis recognized that some regions of the storm systems contained mixed particle types with large variations in the nature of the particles and their terminal velocity. As a result, the interval over which valid points were accepted in subsequent calculations required that the data points exceeded the noise level in sequences corresponding to Doppler shifted velocities of at least a 0.5 m s^{-1} interval. Furthermore, adjacent intervals could be separated by gaps of up to 0.5 m s^{-1}. Afterwards, regions in which there were sharp discontinuities in the valid spectral bounds were examined manually in order to remove anomalies. In this way, spectral artifacts were filtered and multi-modal spectra more easily identified. The first three moments were then calculated directly to give the radar reflectivity, radial velocity, and velocity spectrum (see Keeler and Passarelli, 1990). The moments at the various range bins were averaged for all the cycles performed while the radar was pointing vertically to arrive at the mean profiles of equivalent reflectivity (Ze), fall velocity (V), and spectrum width (W).

Interpretation of the Doppler spectral density data is not straightforward in wintertime situations. As discussed in Stewart (1992) terminal velocities of the different types of precipitation vary substantially. Snow aggregates have terminal velocities which vary with habit and degree of riming, and there is no single relationship between aggregate size or mass and its fall velocity. Regions with melting or freezing result in pronounced terminal velocity changes and a corresponding large spread in the fall velocities of the particles in the sample volume of the radar. Other complicating factors contributing to the spread of the Doppler spectrum include wind shear and turbulence. However, an examination of the spectral moments and their variation in height and time can allow the establishment of conceptual scenarios of the microphysical processes.

Additional sources of data for the study included a radiosonde release performed most

1. present affiliation: Atmospheric Environment Service, Downsview, Ontario.

mornings at 0700 LST at the Atmospheric Environment Service building in Toronto, located about 15 km north of the radar. Also, hourly surface observations were taken from 0700 to 2200 LST at the Toronto Island airport, located about 3 km south of the radar on the lakeshore.

Although precipitation was below normal in the winter of 1990/91 (Environment Canada, 1991), there were several major winter storms which impacted upon the area. As a result, the Toronto Winter Storms Program is comprised of 23 precipitation events, of which 10 could be considered long lived. In 10 of the 23 events the predominant surface precipitation type was rain, in 9 it was snow, and in 4 it was a mixed precipitation or freezing rain. Examples of the data from relatively steady-state portion of 5 events, three snow, one rain, and one rain and ice pellets are given in the following section. The systems were widespread stratiform in nature with cloud thicknesses ranging from 2 km to 6 km. As a result, no strong vertical velocities or turbulence, which would complicate the interpretation of the data obtained with the radar pointing vertically, were anticipated.

3. MICROPHYSICAL CHARACTERISTICS OF PRECIPITATING SYSTEMS

The first shown event, January 23, 1991, occurred in a precipitating system occurring in advance of a cold front bringing a fresh outbreak of continental arctic air to the region. Winds were strong (15 m s^{-1} to 20 m s^{-1}) from the southwest resulting in a flow with no off lake component. Cloud base at 500 m was around -7.0°C. Figure 1 gives the vertical profiles of Ze, V (positive velocities indicate motion towards the radar), and W from echo top to 0.5 km. The magnitudes of all three quantities was modest but there was a gradual increase in their values in going from cloud top to cloud base. These profiles are consistent with the footprint of ice crystal growth to snow by the *diffusion* process.

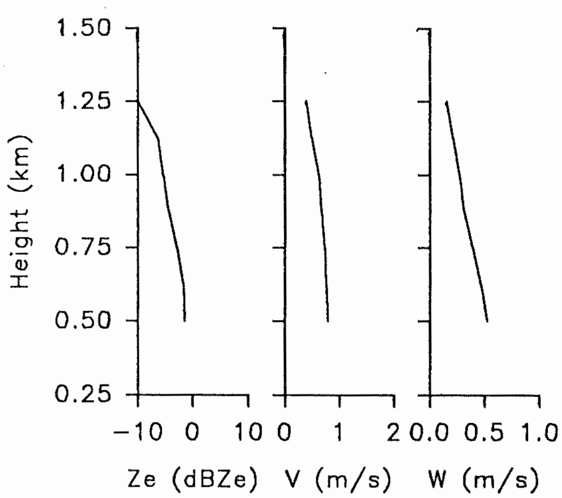

Figure 1: The vertical profile of equivalent reflectivity (Ze), fall velocity (V), and spectral width (W) for January 23, 1991.

The next snow example occurred on February 28, 1991 as a weak low was moving along a stationary front lying across Lake Ontario. There was a light easterly flow at the surface but the winds veered sharply with height to southerly by 0.5 km then to southwesterly by 1.5 km. Figure 2 gives the radar profiles for this case. Ze was low in the upper portions of the cloud but increased from -4 dBZe at 1.4 km to +4 dBZe by 1.2 km. There was a corresponding decrease in V from about 1.7 m s^{-1} to 1.0 m s^{-1} but little change in the spectrum width. This set of profiles with Ze increasing and V decreasing suggests that the diffusional growth occurring in the upper portions of the cloud was replaced by *aggregational growth* in the lower parts of the cloud. The height at which this change takes place corresponds to the level at which the wind flow went from off the land to off the lake.

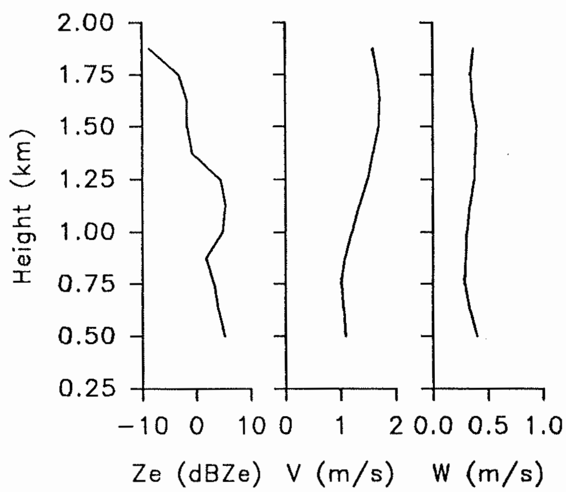

Figure 2: The same as Figure 1 for February 28, 1991.

The third example of solid precipitation (February 14, 1991) was taken as a warm front was approaching the area from the southwest. There was a well developed easterly flow in the lowest km. From 1.0 km to 2.0 km a sharp veering of the winds to southwest took place through the frontal surface. The temperature at cloud top was -10.0°C. Temperatures increased to -2.5°C at the top of the frontal inversion at 1.4 km. Through the front the temperature decreased to -5.0°C at 1.0 km. In the lowest km the temperature increased to a surface temperature of -0.7°C. Figure 3 gives the radar profiles in this case. Ze, higher in the upper portions of the cloud than in the previous two cases, increased to +8 dBZe at 1.7 km. Below that level it decreased to 0 dBZe at 1.0 km, the height of the base of the frontal inversion corresponding to the local minimum in temperature. V and W remained fairly constant above 1.0 km at 1.0 m s^{-1} and 0.2 m s^{-1} respectively. In the lowest km all three parameters increased their values steadily, Ze to +9 dBZe, V to 2.2 m s^{-1}, and W to 0.8 m s^{-1}. Based on these facts the hypothesis is that *diffusion* was the main growth mechanism above 2.2 km. This gave way to *aggregation* in the warmer temperatures (> -6°C) near the frontal surface. This is in keeping with the results of

Boatman and Reinking (1984) who found evidence of aggregation in upslope clouds at temperatures warmer than -7°C. In the stratus clouds below the front the increase in Ze, V, and W point to an active *riming* process.

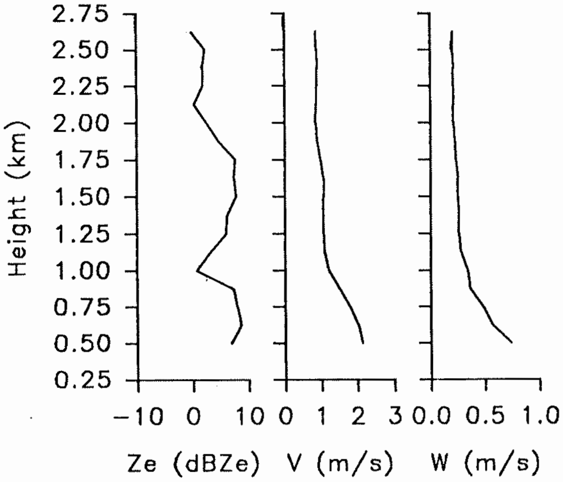

Figure 3: The same as Figure 1 for February 14, 1991

The next case on January 16, 1991 is an example of rain occurring at the surface in a warmer maritime arctic airmass in advance of a cold front. There was an easterly flow at the surface which gradually veered to southwesterly by 2.5 km. Figure 4 gives the temperature sounding taken at Toronto within 1 hour of the vertical scans by the radar. The temperature at cloud top was -10.0°C and at cloud base, reported at 800 m, it was 0.0°C. Also noteworthy is a 600 m thick isothermal layer at -1.4°C between 1.3 km and 1.9 km. The vertical profile of Ze shows a steady increase in values from +3 dBZe at 1.8 km to +23 dBZe at 1.0 km (Figure 5). There was a corresponding increase in V through this layer from 1.0 m s^{-1} to 4.0 m s^{-1} and in W from 0.2 m s^{-1} to 0.8 m s^{-1}. Below this level Ze and W remained relatively constant around 22 dBZe and 0.8 m s^{-1} respectively. V continued to increase although more slowly to 5.5 m s^{-1} by 0.5 km. The microphysical scenario in this case is that *diffusional growth* gives way to *aggregation*, then *melting* through the transition layer to above freezing temperatures. The pattern of radar parameters in the lowest km was somewhat unusual in that Ze and W did not show any noticeable decrease below their peaks at 1.0 km and V continued to decrease. Whether this is a reflection of the vertical bright band (Stewart, 1992) or an effect of the nearby lake is not yet clear and requires further investigation. Figure 6 gives an example of the full Doppler power spectral density data at selected levels taken during these scans. The figure gives the returned power as a function of the Doppler shifted radial velocities. The spectra displayed occur at the following places: at 2.3 km in the upper portions of the cloud; at 1.8 km at the top of the isothermal layer; at 1.3 km at the base of the isothermal layer; at 1.0 km at the bright band; and at 0.6 km just below cloud base. These spectra document details of the change from solid to liquid precipitation with broader spectra and higher fall velocities.

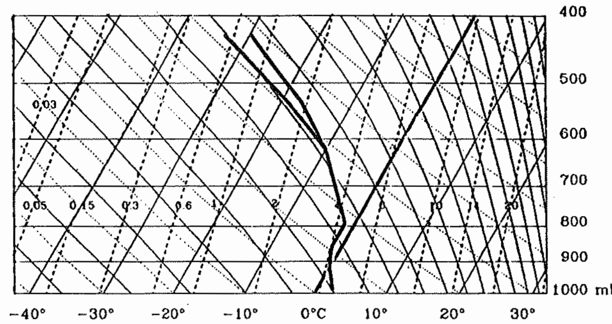

Figure 4: The temperature sounding taken at Toronto at 0700 LST on January 16, 1991.

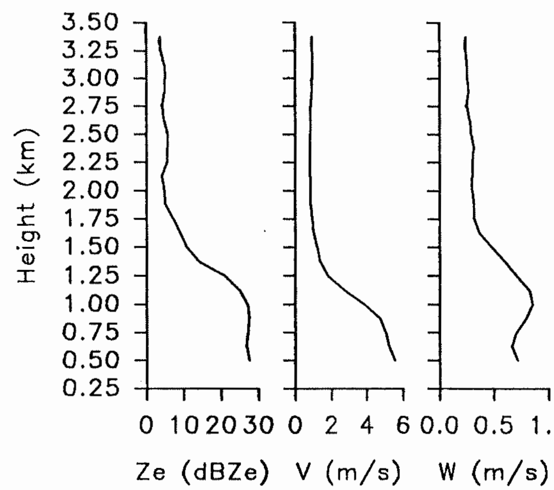

Figure 5: The same as Figure 1 for January 16, 1991.

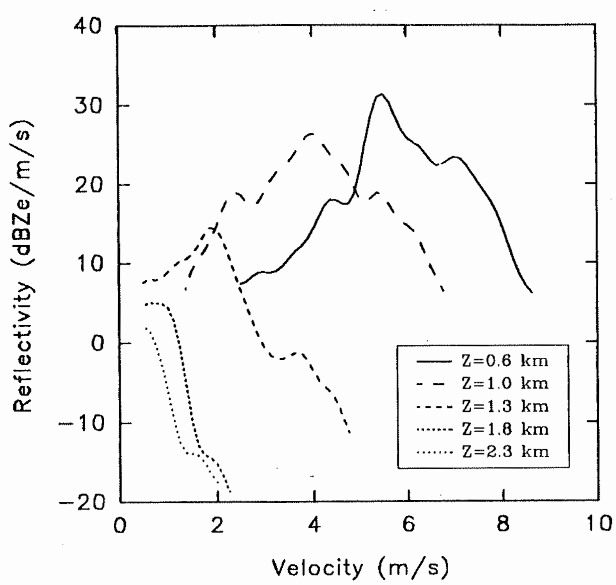

Figure 6: The Doppler spectrum at selected levels as a function of Doppler shifted radial velocities on January 16, 1991.

The final example (December 30, 1990) was taken while there was a mixture of ice pellets and rain occurring at the surface. The previous day had been unusually warm with surface temperatures of +8.1°C. Overnight a first cold front went through. The data shown in this case was taken as a second front went through marking the return of continental arctic air. Winds were northerly in the lowest 0.8 km. Then, they backed sharply to westerly by 1.3 km and increased in speed from 5 m s^{-1} to 20 m s^{-1} at 2.0 km. No local temperature sounding was available for this case. Figure 7 gives the radar derived profiles of Ze, V, and W and shows three distinct regimes. Ze steadily increased from 0 dBZe at 4.0 km to +6 dBZe at 2.3 km. In this layer V increased to 3.5 m s^{-1}, then decreased to 2.5 m s^{-1}, then remained steady. At the same time, W decreased, increased, then decreased again. One suggestion is that this reflects a partial *melting* process followed by *refreezing*. This could be occurring as a result of the warm air aloft in association with the first cold front that had gone through. From 2.0 km to 1.3 km there was the sharp increase then decrease in Ze and very sharp increase in V indicative of the *melting band*. In the lowest km Ze was relatively constant while V was steadily decreasing and W increasing. This reflects the *refreezing* as ice pellets were being formed. Figure 8, which shows examples of

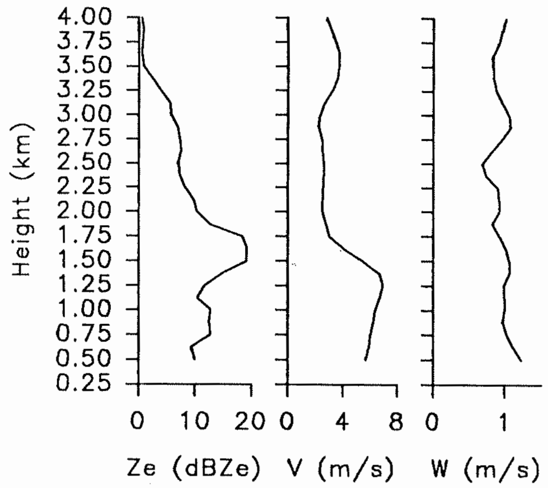

Figure 7: The same as Figure 1 for December 30, 1990.

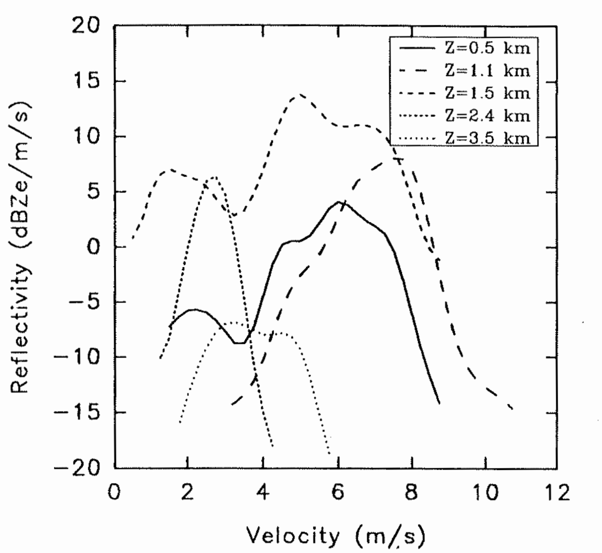

Figure 8: The same as Figure 6 for December 30, 1990.

the full Doppler power spectral density data at selected levels, supports this characterization. The spectrum at 3.5 km in the layer where partial melting was occurring is relatively broad; at 2.4 km where refreezing has taken place it is narrower with smaller velocities; at 1.5 km where the melting was occurring it is very broad and has the highest intensity; at 1.0 where the particles had all melted it has the highest fall velocities; and at 0.5 km where the transition to ice pellets was evolving there were lower velocities and higher spectral widths.

4. CONCLUDING REMARKS

The Toronto Winter Storms Program has gathered a great deal of information on the microphysical characteristics of winter storms in the Great Lakes area. Five examples have been presented which have shown that through a judicial use of an X-band Doppler radar, local radiosonde ascents, and surface weather observations the predominant microphysical footprints of the precipitating systems can be established. These microphysical scenarios have been presented as a function of the synoptic situation. The impact on the microphysics within these situations of the presence of the ice free lake to the south was clearly demonstrated. More comprehensive studies of this type will result in better conceptual models of the details of the precipitation processes on scales which current numerical models are unable to resolve.

Acknowledgements: The assistance of Norman Donaldson of the Atmospheric Environment Service (AES) in obtaining the upper air data and Arthur DiLeo of KelResearch Corporation in drafting the figures is gratefully acknowledged. The work was supported by DSS/AES contract No. KM175-0-8085/01-XSE.

REFERENCES

Boatman, J.F., and R.F. Reinking, 1984: Synoptic and mesoscale circulations and precipitation mechanisms in shallow upslope storms over the western high plains. *Mon. Wea. Rev.*, 112, 1725-1744.

Environment Canada, 1991: *Climatic Perspectives*. Vol. 13, AES, Downsview.

Hare, F.K., and M.K. Thomas, 1974: *Climate Canada*. Wiley Publishing, Toronto, 256 pp.

Hildebrand, P.H., and R.S. Sekhon, 1974: Objective determination of the noise level in Doppler spectra. *J. Appl. Meteor.*, 13, 808-811.

Keeler, R.J., and R.E. Passarelli, 1990: Signal processing for atmospheric radars. *Radar in Meteorology*, D. Atlas Ed., Amer. Meteor. Soc., 199-229.

Siggia, A.D., and J.M. Holmes, 1991: One pass velocity unfolding for VVP analysis. Preprints, *25th Intl. Conf. on Radar Meteorol.*, Paris, France, Amer. Meteor. Soc., 882-884.

Stewart, R.E., 1992: Precipitation types in the transition region of winter storms. *Bull. Amer. Meteor. Soc.*, 73, 287-296.

ON THE COUPLED ORGANIZATION OF PRECIPITATION TYPES AND RATES IN WINTER STORMS

Ronald E. Stewart, Norman R. Donaldson and Dia Yiu
Atmospheric Environment Service
Downsview, Ontario

1. INTRODUCTION

Understanding the type, location and amount of precipitation is one of the most basic questions to be addressed in the study of winter storms. The solution to this problem necessarily requires insight into the complete dynamic, thermodynamic and microphysical nature of the storms.

On the large scales, the general region where the various types of precipitation occur is determined by the overall temperature field. The sustained occurrence of freezing forms of precipitation furthermore normally depends upon strong wind shears (Brooks, 1914).

On the small scales, microphysical processes greatly affect the exact nature of the precipitation that strikes the surface. It is for example well-known that partial or complete phase changes determine whether particles initially in the form of snowflakes reach the surface in some other form such as freezing rain or ice pellets.

In this article, it is shown that small scale processes involving particle phase changes and associated terminal velocity and trajectory variations across the transition region affect precipitation rates as well as precipitation types. In this sense, precipitation rates and types are coupled features.

2. PARTICLE TRAJECTORIES

The transition region of winter storms is a very unique region from the point of view of particle trajectories. On the cold side of this region, precipitation remains in the form of low terminal velocity snowflakes, whereas on the warm side the particles begin in this form but evolve into high-terminal velocity raindrops at low levels. Within the transition region itself, a variety of precipitation types occur and these are characterized by a variety of terminal velocities. Even within a constant background wind field, particle trajectories from high levels to the surface consequently change a substantial amount across the transition region (Stewart and Donaldson, 1992)

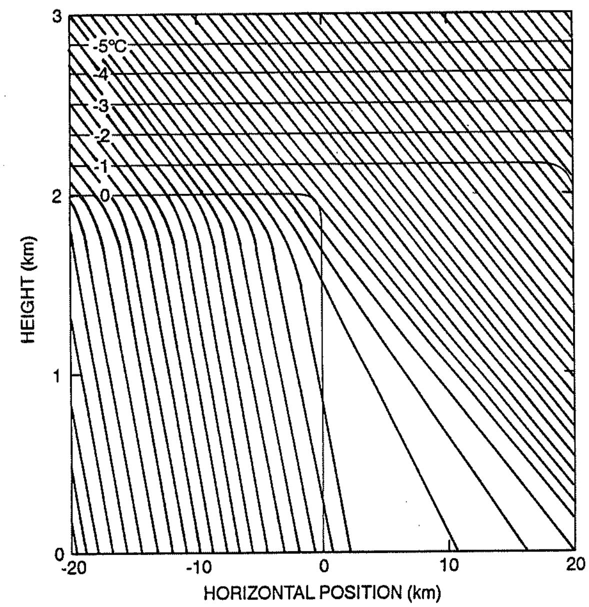

Figure 1: The background temperature field and the trajectories of particles with an initial 1 mm melted-equivalent diameter.

An illustration of the precipitation trajectory changes is shown in Figure 1. In this simple situation, it is assumed that a constant wind is directed from the left to the right and that the background temperature field is being maintained through weak ascent that is small enough to be ignored in comparison with the terminal velocities. All the initial particles are considered to be spherical snowflakes of density 10 kg/m^3 and to have a melted-equivalent diameter of 1 mm. The evolution of particles and their terminal velocity was determined through the use of the detailed numerical model discussed by Donaldson and Stewart (1992).

In this instance, the particle trajectories show an increase in the separation at temperatures close to but generally slightly below 0^oC. This arises because particles which fall through temperatures warm enough to undergo melting are able to achieve a high terminal velocity and they consequently fall to the surface rapidly. In contrast, particle which only fall through subfreezing regions always maintain their low terminal velocity and consequently fall further "downwind".

This separation between trajectories consequently affects observed precipitation rates at the surface. To determine this, assume that there is an initial 1 mm/h precipitation rate aloft of many-sized snowflakes which, upon melting, gives rise to a Marshall-Palmer size distribution of rain. By calculating the trajectories of all these different-sized particles and then by combining the results, a measure of precipitation rate can be determined (Figure 2). In this case, precipitation rates decrease to only 0.2 mm/h at temperatures just below $0^{o}C$. Note as well that if the initial precipitation rate is 10 mm/h, the relative decrease is not as pronounced. This variation in precipitation rate reduction occurs because of differences in the trajectories of different-sized particles. At the higher precipitation rate, there are more large particles than at the lower precipitation rate.

In addition, the types of particles that are produced at the surface evolve as well. Figure 3 shows the water fraction of precipitation across the transition region for the 1 mm equivalent diameter particles shown in Figure 1. Surface precipitation at the colder temperatures is initially all solid although some melting aloft and later refreezing has occurred. At warmer temperatures but still below $0^{o}C$, many of the particles reach the surface still partially melted.

By examining Figure 2 and 3 together, it is also evident that the lowest precipitation rates produced from the initial 1 and 10 mm/h values are associated with refrozen snowflakes and ice pellets in the former case and wet snow, refrozen snow and ice pellets in the latter case. These couplings are not accidental. The varying terminal velocities that give rise to the decrease in precipitation rate also dictates the types of precipitation.

Winds across the transition region can vary enormously and they produce corresponding variations in the associated precipitation rates and types (Stewart and Yiu, 1992). In some observed cases, winds are directed from right to left across the assumed temperature field of Figure 1 at all levels throughout the lower atmosphere. In such a situation, an increase in precipitation rate occurs and calculated enhancements have reached up to 19 mm/h over their initial background values. This arises due to the convergence in trajectories within this wind field. Such magnitudes of precipitation rate are normally only associated with convective activity! The enhancement furthermore occurs at temperatures just above $0^{o}C$ and associated forms of precipitation are typically rain mixed with wet snow.

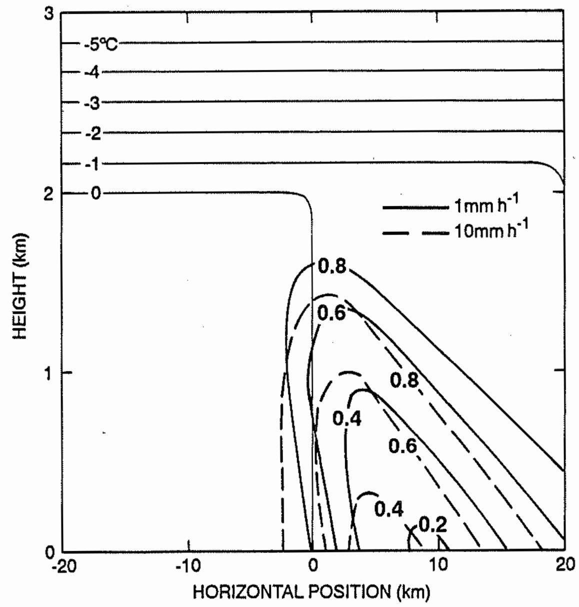

Figure 2: Fraction of initial precipitation rate assuming two initial values of 1 and 10 mm h-1.

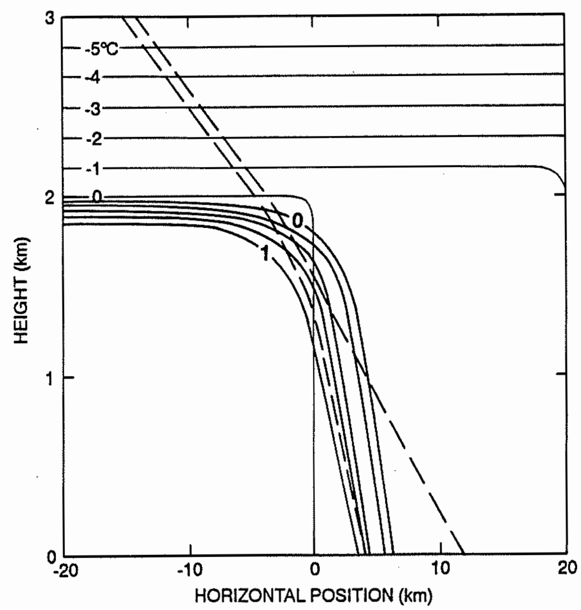

Figure 3: Melted fraction of particles with an initial melted equivalent diameter of 1 mm.

It is common across transition regions for winds to be directed to cold air at high levels and to warm air at low levels. Within such an environment, trajectories are forced to diverge initially and they converge shortly before reaching the surface. It is therefore expected that a peak in precipitation rate is produced at temperatures just above $0^{o}C$ and a decrease is produced at temperatures just below $0^{o}C$. The former situation is generally linked with rain and wet snow and the latter with ice pellets and snow.

3. CONCLUDING REMARKS

The types and rates of precipitation are two of the most important variables associated with the precipitation type transition regions of winter storms. The magnitudes of both these parameters also influence related factors such as visibility, accretion, and radar signatures.

Precipitation rates and types are both greatly influenced by particle trajectories. These two parameters, as well as their associated effects, are then strongly coupled and can only be understood together.

REFERENCES:

Brooks, C.F., 1914: The ice storms of New England. Harvard University Press, Cambridge, 8 pp.

Donaldson, N.R. and R.E. Stewart, 1991: Precipitation type characteristics in winter storms. Part I: basic simulations. J. Meteor. Soc. Japan (Submitted)

Stewart, R.E. and N.R. Donaldson, 1991: Precipitation type characteristics in winter storms. Part II: particle trajectories. J. Meteor. Soc. Japan (Submitted)

Stewart, R.E. and D. Yiu, 1991: Distributions of precipitation and associated parameters across precipitation type transitions over southern Ontario. Water. Res. Res. (Submitted)

On Snowfall over a Basin in Winter Monsoon

Tsuruhei Yagi and Masayuki Maki

National Research Institute for Earth Science and Disaster Prevention (NIED)

3-1,Tennodai,Tsukuba-shi,Ibaraki-ken,305,Japan

1. Introduction

On winter out-break of the polar air mass, the regionsfacing the Sea of Japan is directly swept by snow storms, which generally move eastward: cross over the hills and mountains and/or pass through the gorges, getting into the basins located down wind of them.

Smith(1979) has discussed the rainfall mechanisms over mountains with respect to ascending air flow and pointed out that there would exist three types of orographic effects. As being simillar in case of snowfall over a down-wind basin, up-wind mountains might play some significant roles on the distribution of precipitation.

In this view point, an observation ofsnowfall were carried out with 3.2 cm wavelength meteorological radar in the Shonai and Shinjo region of the Tohoku district, Japan from January 20 to 24 in 1986. Yagi et al. (1986) have reported the results of the previous year obser- vation. However the 1985 winter with respect to the report was relatively not so cold and had not so severe weather that the data obtained had been limited to somewhat qualitative ones. On the other hand, the 1986 winter was very severe enough to provide lots of data for the high quality analysis and interpretation of the mountain effects on snowfalls.

2. Topography and climate of snowfall in Tohoku district

First of all, topogrsphical features and climatological distributions of snowfall in Tohoku district are outlined.

Fig. 1 shows roughly explained terrains of Tohoku district. Regions under 200 m above mean sea level are dotted and hills and mountains are hatched. As general view, three ranges are recognized which run from north to south. And several basins (including the Shinjo basin) are seen between the western two ranges. Cross-section of west to east at Akita and Morioka induces a model which is illustrated at the bottom of figure; two basins appear in this case. In the cros-section at Yamagata and Sendai, a basin still appears. These basins have large cities and to link them a major railway and a highway go through from south to north. So it is stated that the basin terrain in Tohoku district is an important region in the view point of snowfall disaster on monsoon out-break.

On winter out-break of the polar air mass, a plain facing the Sea of Japan is directly swept by snow storms, which generally move eastwards; cross over the range (600 to 800 m above sea level) and/ or pass through a gorge, getting into a basin. However the snow storms could not go over the highest range which lays in thecenter of Tohoku district, according to climatological map (Wadachi, 1953).

3. Method of observation

Observation in 1986 was carried out in the Shinjo basin. A 3.2 cm wave length and transportable radar was set up at a small hill (140 m above sea level) for the observation. The point is the same as that of the 1985 observation and is marked white circle in Fig. 2. In this figure hills and mountains above 500 m and 1000 m are hatched and netted, respectively in connection with Yamagata Prefecture. Dewa hills link Mt. Chokai (2230 m) to Mt. Gassan (1980 m), dividing the Shonai plain and the Shinjo basin. These hills are 600 m to 800 m above sea level at the peaks. At the northern foot of Mt. Gassan, the Mogami river runs westwards through a gorge. The east Prefecture border is a part of the central high mountains of Tohoku district. The fan-shaped region between 240° and 30° is the covered area by radar. Its radius is 50 km. This area can observed the snow clouds which come from the Shonai plain to the Shinjo basin crossing over the Dewa hills and/or passing through the Mogami gorge. Solid points in the plain, the basin and the gorge are ground weather stations operatedby several official organizations.

Radar observation times were 08 hours to 18 hours and 20 hours to 24 hours in a day. In these times, measurements of reflectivity were made every 15 minutes. The elevation angle of the antenna was 2.5°. At this angle, the height of radar beam is 0.4 km at the range of 10 km and 12.3 km at the range of 30 km, respective- ly. The radar images were recorded by means of a pulse camera.

4. Method of analysis

On measuring precipitation intensity, $Z=2000R^{2.0}$ was assumed where Z is radar reflectivity factor (mm/m^6) and R is precipitation intensity (mm/hr) according to Gunn and Marshall (1958). ISO echo levels 1, 2, 3, ... corespond to precipitation intensities 1 mm/hr, 2 mm/hr, 4 mm/hr, ..., respectively.

For estimation of precipitation amount by radar within radar observation times, the fan-shaped observation area was divided by 2.5 mesh of Cartesian coordinates. And values of each mesh of every hours were estimated.

Ground precipitation amount were used from the data of the official weather observation stations.

Aerological data were used from those of Akita where located about 100 km north to the radar observation area as seen in Fig. 1.

5. Results

Synoptic atmospheric pressure patters during the observation period were of relatively strong monsoon type of high west-low east; westerly winds were generally predominant in Tohoku district. Fig. 3 shows wind structure up to 500 mb from 21st to 24th January 1986. It was seen that westerly winds had been continuous as a whole.

GMS cloud affairs over the present observation area were almost similar to those over Akita.

In Shonai and Shinjo, convective snowfall cloud echoes were prevailing. They moved eastwards from the plain to the basin via the hills and/or the gorge.

The major result for 1986 observation is that the horizontal distribution of precipitation, summed up from the radar reflectivities at the echo height, showed no significant differences between snowfalls which fell over hills and those which fell over gorges. These observational facts suggest that a snowfall echo, which might be called a snow cloud, does not tend to go through lower gorges more readily than high hills as seen in Figs. 4 and 5.

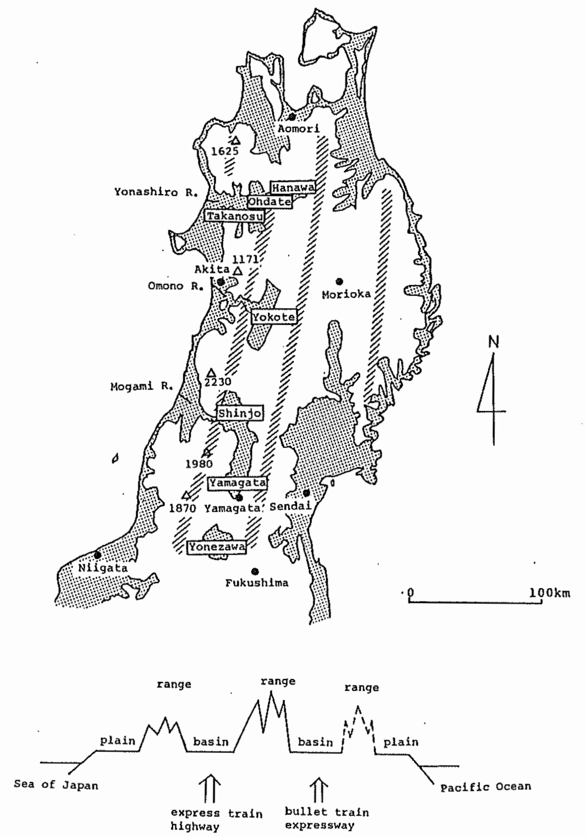

Fig. 1

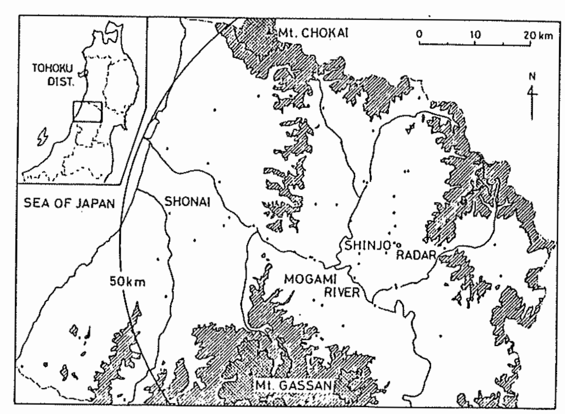

Fig. 2

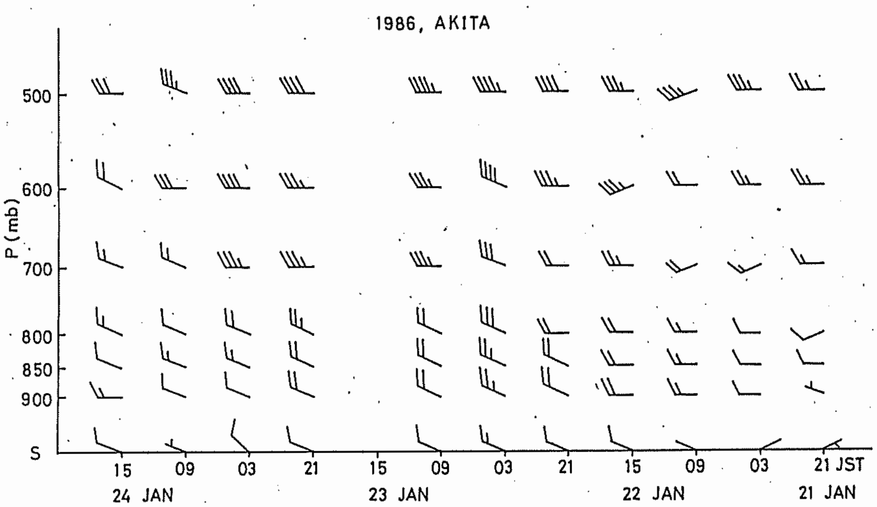
1986, AKITA
P (mb)
500
600
700
800
850
900
S
15
09
03
21
15
09
03
21
15
09
03
21 JST
24 JAN
23 JAN
22 JAN
21 JAN

Fig. 3

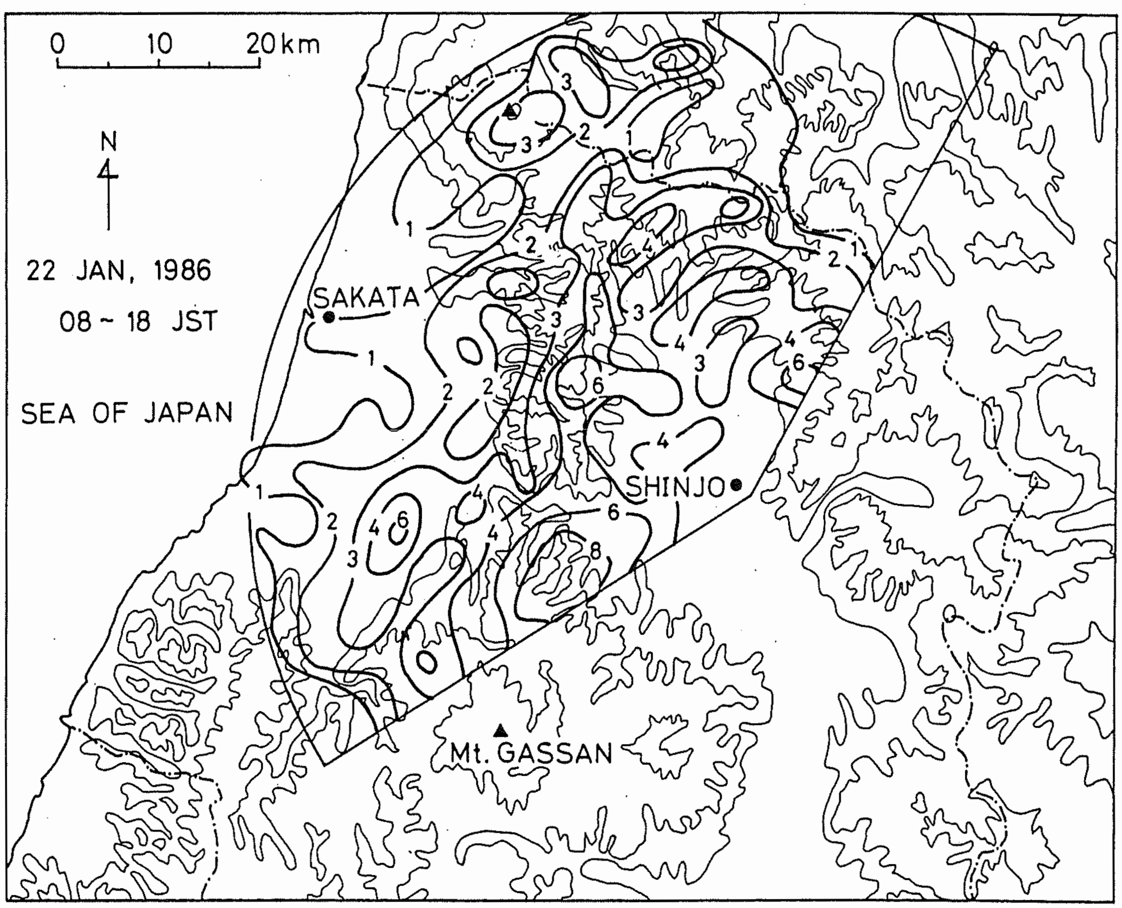
0
10
20km
N
22 JAN, 1986
08 ~ 18 JST
SAKATA
SEA OF JAPAN
SHINJO
Mt. GASSAN

Fig. 4

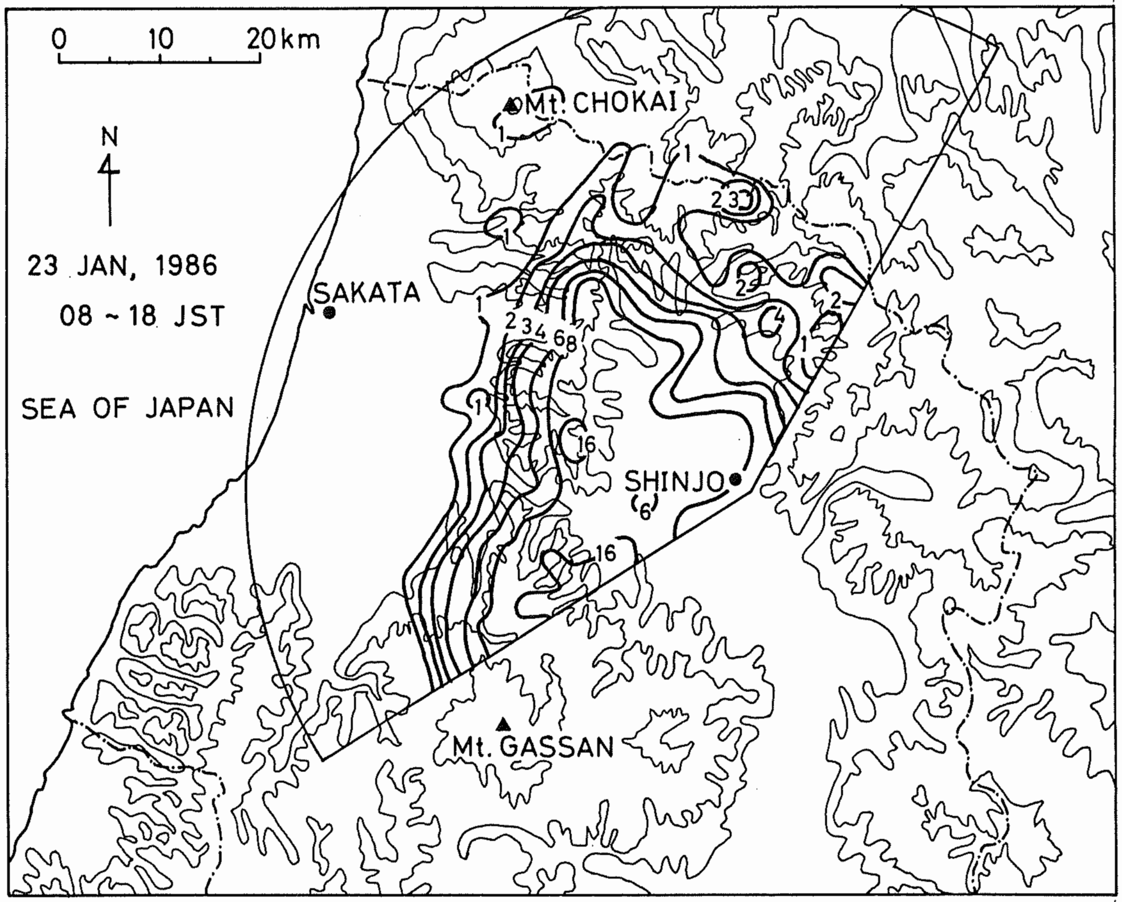
0
10
20km
N
23 JAN, 1986
08 ~ 18 JST
SAKATA
SEA OF JAPAN
Mt. CHOKAI
SHINJO
Mt. GASSAN

Fig. 5

Vertical structure of the Baiu fronts analyzed with the MU radar and an X-band Doppler radar

Shuji Shimizu, Hiroshi Uyeda, Ryuichi Shirooka*
Akira Watanabe[1], Akimasa Sumi[2] and Shoichiro Fukao[3]

Faculty of Science, Hokkaido University, Sapporo 060 Japan
[1]Faculty of Education, Fukushima University, Fukushima 960-12 Japan
[2]CCSR, The University of Tokyo, Tokyo, 113 Japan
[3]Radio Atmospheric Science Center, Kyoto University, Uji 611 Japan

1 Introduction

Heavy rainfalls are brought by the Baiu front from June to July in Japan every year. A large number of studies have been made on synoptic signature, mesoscale structure and precipitation mechanism of the Baiu front (Ninomiya and Akiyama, 1992; Kato and Kodama, 1992 and other). However little is known about the interactions between multi-scales (from mesoα to mesoγ and microα) and detailed structures of the Baiu front. Therefore it is necessary to make continuous observation of the Baiu fronts with remote sensors which can measure precipitation intensity and wind fields in a high resolution and over a wide range. In order to reveal the interactions between multi-scales and the detailed structures of the Baiu frontal rainband and around the front, observations with the MU radar and an X-band weather Doppler radar were carried out at Shigaraki, Japan.

The MU radar of Kyoto University, which is one of VHF radars (Fukao et al., 1988; Sato et al., 1991), is located at Shigaraki, Shiga Pref. The MU radar can continuously measure vertical profiles of horizontal and vertical wind in detailed above the height of 2km whether it has rain or not. While an X-band weather Doppler radar can measure reflectivities and Doppler velocities of rain clouds within a radius of 60km. Shirooka et al. (1991) revealed that horizontal winds obtained by the MU radar and VAD (Velocity Azimuth Display) method (Browning and Wexler, 1968) with an X-band Doppler radar coincides well. They also showed that comparative observation of the radars is useful for the study of detail structure of tropospheric meteorological phenomena.

In this study, comparative observations between the MU radar, the X-band Doppler radar of Hokkaido University and six hourly radiosonde observations were conducted on the Baiu front at Shigaraki, Japan. The observations were carried out from 30 June to 15 July 1990 and 20 June to 9 July in 1991. In particular, we are concerned with two cases of large rainfall intensity, 2-3 July and 12-13 July in 1990.

2 Method

Figure 1 shows the location of the MU radar and an X-band Doppler radar (transportable) of Hokkaido University, and an observational range (radius 60km) of the X-band radar. The range of Osaka District Meteorological Observatory radar (radius 200km) is also shown in the Figure 1. By the MU radar, vertical profile of horizontal winds is evaluated by using four azimuth beams (0°, 90°, 180°, 270°) that had a zenith angle of 10°, and vertical profiles of vertical wind is measured by using a vertical beam. The beam had a range resolution of 150m. Reflectivities from turbulence of the vertical beam were utilized for the analysis of layer structure of the troposphere. While the X-band radar observed reflectivities and Doppler velocities of PPI mode (at the elevation angles of 15°, 9°, 6° and 4°), and of that RHI mode with optional azimuths. And VAD wind calculation is conducted at an elevation angle of 15° and the height resolution of this elevation is about 65m. Radiosondes were released at Shigaraki every six hours (at 3, 9, 15, 21 JST). Precipitation amounts were measured at the radar site with a rain gauge.

*Present affiliation: Laboratory of Agro-meteorology, Hokkaido National Agricultural Experiment Station, Sapporo, Japan

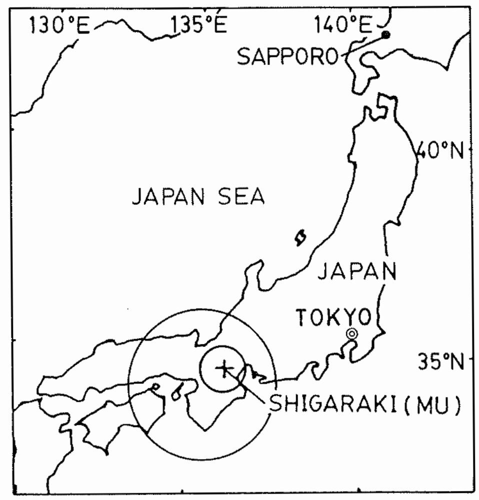

Fig. 1. The location of the MU radar and an X-band Doppler radar of Hokkaido University. A small circle (r=60km) is the observational range of the X-band and the large circle (r=200km) is the range of a weather radar of Osaka District Meteorological Observatory.

3 Results

3.1 Case 1 (2-3 July 1990)

From 2 to 3 July 1990, in wide area of the western Japan heavy rainfalls were brought by a cyclone that changed from Typhoon No.6. For 32 hours, from 1300 JST 2 July to 2100 JST 3 July, continuous rainfall was observed at the radar site by stratiform clouds, and the precipitation amounted to 78.0mm. In particular, between 0400 JST and 1400 JST 3 July the precipitation was concentrated. There was a cyclone on the east of Korea. The cyclone moved northeastward with cold, warm, and occluded fronts.

Figure 2 shows a time-height cross section of horizontal wind profiles, which were evaluated with the VAD method from velocity data of the X-band Doppler radar, and that of equivalent

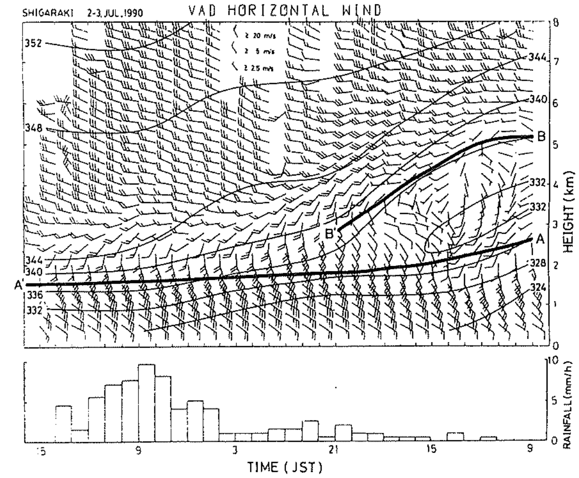

Fig. 2. Time-height cross sections of VAD wind profiles of the X-band Doppler radar, equivalent potential temperature (solid contours at intervals of 4°K) (top) and hourly rainfall amount at the radar site from 0900 JST 2 July to 1500 JST 3 July 1990 (bottom). Each flag, full barb and half barb corresponds to 20, 5 and 2.5 m/s, respectively. Thin solid lines A-A' and B-B' show large shear of horizontal wind.

potential temperature as solid contour from 0900 JST 2 July to 1500 JST 3 July. Hourly precipitations are shown in the bottom frame. Through this period, precipitation was recorded almost continuously. In particular, precipitation was concentrated to record 57.5mm from 0400 to 1400 JST 3 July. In the low level southeasterly wind was strong (~15m/s) through the period. While in the high level westerly wind dominated. From 0900

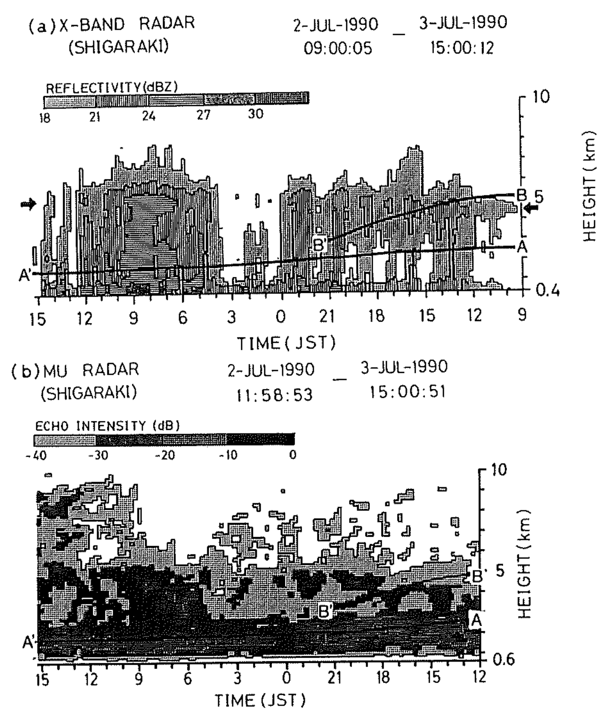

Fig. 3. Time-height cross section (a) of the X-band radar reflectivity from 0900 JST 2 July to 1500 JST 3 July 1990 and (b) of the MU radar echo intensity from 1200 JST 2 July to 1500 JST 3 July 1990 (no data before 1200 JST 2 July). A primary (A-A') and a upper secondary (B-B') warm front are also superposed.

to 2100 JST 2 July, weak southerly flow existed between the two levels. This flow corresponded to the area of a minimum equivalent potential temperature. Relative humidity obtained by radiosonde was less than 70% from 2 to 3km. It is analyzed from upper air charts that the southerly cold air entered this area around the edge of anticyclone in the middle level over the sea at the east of Japan. Curves A-A' and B-B' drawn by eye fitting show large shear of horizontal wind in the figure. They coincide with sharp gradients of equivalent potential temperature. This means that A-A' line corresponds to a primary warm front and B-B' line corresponds to an upper secondary warm front.

Figure 3 indicates the time-height cross sections of the X-band radar reflectivity and the MU radar echo intensity for the same period of Fig. 2 (except Fig. 3b that started from 1200 JST 3 July). Arrows in Fig. 3a indicate melting level height and corresponding height of the bright band, which ascended from 4.5km to 5.0km with the advection of warm air above 2km. The primary warm front (A-A') and the secondary warm front (B-B') are superposed in the figure. As B-B' descends from 5km to 3km, a large reflectivity of X-band radar spreads to the low level. From 0400 to 1400 JST, the large reflectivity appears at the heavy rainfall period. While strong echo intensity of the MU radar appears along A-A' and B-B' in Fig. 3b. This fact agreed that the strong echo intensity corresponded to the wind shear.

3.2 Case 2 (12-13 July 1990)

From 12 to 13 July 1990 strong rainfalls was observed for a short period at the radar site. On the Japan Sea, a cyclone which had changed from Typhoon No.7, moved northeast with a cold front and a warm front that overlapped a stationary front across Japan from north to south. However the rain observed at Shigaraki was associated with rainbands in the warm sector, and was not associated with the fronts.

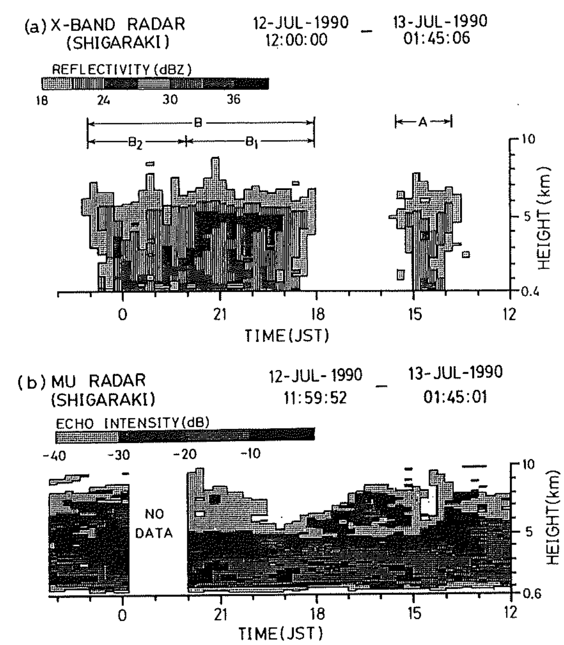

Fig. 4. As in Fig.3, except from 1200 JST 12 to 0200 JST 13 July 1990. From 2200 JST to 2330 JST data of the MU radar were not measured.

Figure 4 indicate time-height cross sections of the X-band radar reflectivity and the MU radar echo intensity from 1200 JST 12 July to 0200 JST 13 July. We roughly divided reflectivity of the X-band radar into two periods (A and B in Fig. 4a). And we subdivided the period B into two periods of B_1 and B_2. In the period B_1 a bright band is recognized at the height of about 5km and it ascends gradually to 5.5km. It indicates that the precipitation in this period was produced by stratiform clouds. While in the period B_2 the bright band is not recognized and echoes of the X-band radar and that of the Osaka District Meteorological Observatory radar, which have a large coverage, were isolated. Therefore the precipitation in this period was considered to be produced by convective clouds. Figure 4b shows that under a height of about 5km echo intensity is generally stationary, but after 'No Data' period strong echo intensity extends to the upper level. Because in this period convective echoes of RHI mode reached above the height of 10km, the ascent of the echo in Fig. 4b corresponds to the disturbance by the convective activities up to 10km. In the period between A and B a relatively strong echo (>-30dB) is seen at the altitude from 5 to 8km.

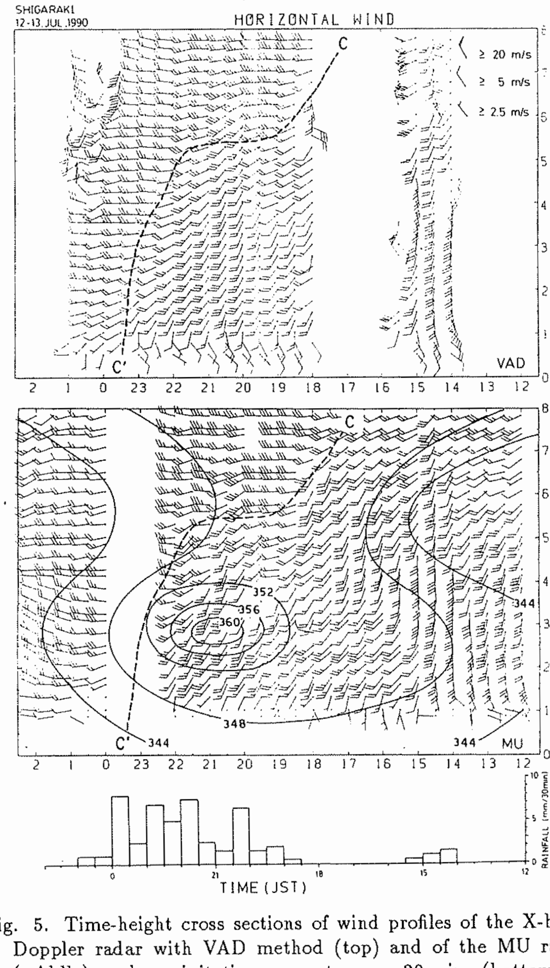

Fig. 5. Time-height cross sections of wind profiles of the X-band Doppler radar with VAD method (top) and of the MU radar (middle), and precipitation amounts every 30 min. (bottom) at Shigaraki from 1200 JST 12 July to 0200 JST 13 July 1990, except for no data of the MU radar from 2200 JST to 2300 JST 12. Dashed line C-C' indicates large shear of horizontal wind. Solid contours shows equivalent potential temperature (at the interval of 4°K).

Figure 5 shows a time-height cross section of horizontal wind profiles from 1200 JST 12 July to 0200 JST 13 July. Winds were evaluated with the VAD method from the velocity data of the X-band Doppler radar (top) and with the MU radar (middle). Solid contours of equivalent potential temperature are superposed on the middle frame. Precipitation amounts every 30 min. are shown in the bottom frame.

Southerly wind reached to the height of 8km from 1400 to 1500 JST 12 July corresponding to period A in Fig. 4a. After 1700 JST corresponding to period B in Fig. 4a, southwesterly flow existed in the middle level and westerly flow existed in the upper level. A dashed line (C-C'), which is drawn from vertical shear of winds with the VAD method and the MU radar, indicates that a boundary between the two levels existed. From 1700 to 1830 JST, the altitude of prominent vertical wind shear descended from 7.5 to 5km, namely down to the height of the bright band and to the melting layer. The descent of the shear layer corresponded to the descents of the snow echoes and of the shear layer identified in the snow echoes by the X-band Doppler radar (not shown).

From 1800 to 2200 JST (period B_1) the southwesterly flow became stronger than previous hours in the middle level and to the maximum at the height about 3km at 2100 JST. And equivalent potential temperature also had its maximum at the same time and height. This southeasterly warm air flowed into this area corresponded to the warm moist advection found in the upper air chart of 700mb at 2100 JST 12 July. This warm air flow also corresponded to the ascent of the bright band from 1800 to 2200 JST. On the other hand the dashed line suddenly descended to a low level after 2200 JST. In period B_2, a cold air flow into the upper height with westerly wind is prevailing.

Rainfalls were observed in the periods corresponding to the period A and B in Fig. 4a. Though after 1800 JST it continuously rained, before 2200 JST an inflow of moist warm air into the middle level caused stratiform rain (period B_1), while after 2200 JST an inflow of cold air into the middle and upper level caused convective rain (period B_2).

4 Discussion

In the first case, when there was an upper secondary warm front, precipitation rainfall intensity at the radar site was comparatively weak from 0900 to 2100 JST 2 July (Fig. 2). Because the middle level was dry (R.H.<70%) with sounding, this could be explained that precipitation particles generated over the upper secondary warm front evaporated with the fall of the particles. The cold layer was considered to be maintained by evaporation cooling. This coincided with the large reflectivity of the X-band radar spread to the lower level as the upper secondary warm front descended. And after 2100 JST when the front met the primary warm front, the large reflectivity reached to the ground and rainfall intensity increased from 1 to 2.5 mm/h. Namely, the upper secondary warm front was considered to suppress precipitation on the ground.

Heavy rainfall (10mm in one hour) and large reflectivity of the X-band radar lasted for 8 hours after 0400 JST 3 July. Simultaneously strong echo intensity of MU radar was also observed continuously. This echo intensity was considered to be associated with falls of precipitation particles. Though usually the MU radar observed echoes from atmospheric turbulences, in this case, echoes from precipitation particles prevailed (Shirooka et al.,1991). And the heavy rainfall was associated with a rise of equivalent potential temperature (about 4°K in 6hours) in the middle level as shown in Fig. 2.

In the second case, during period A from 1400 to 1530 JST 12 July, when rainfall intensity at the radar site was weak compared to the strong reflectivity of the X-band radar as shown in Fig. 4a. The reason was that southern edge of strong echo band passed over just several kilometers north of the radar site and a weaker echo passed over the site.

When there was no echo for the X-band radar, from 1500 to 1800 JST 12 July, a strong echo of the MU radar existed above 6km and it descended gradually to the melting layer. This corresponded to the descent of prominent vertical shear of winds shown as C-C' line in Fig. 5. This echo intensity was considered to be replacement of southwesterly winds with warm air extended to the upper level by westerly winds with cold air from a higher altitude. Also the formation of weak echoes of the X-band radar above the melting level was estimated to correspond to the cooling of warm moist air with southeasterly winds around the shear zone.

Winds near surface suddenly changed at 2330 JST 12 July. At this time the strongest rainfall intensity was observed (8.5mm in 30 minutes). After this strong rainfall, rainfall intensity decreased rapidly. And equivalent potential temperature descended to about 5°K in 6 hours near the surface. Judging from the above, a cold front was analyzed to have passed over Shigaraki area at about 2330 JST 12 July, though it was not analyzed on the surface map (not shown). While there was no echo on the radar of the Osaka District Meteorological Observatory which corresponded to the cold front on the surface map.

5 Concluding remarks

Based on the observations and analyses of the Baiu fronts, we have constructed conceptual models of weather systems that passed over Shigaraki area on 2-3 July and 12-13 July 1990 (Fig. 6). By the comparative observations of the MU radar and X-band Doppler radar, we caught the typical phenomena in the Baiu season, that is, (in the case 1, 2-3 July) precipitation associated with the warm front, and (in the case 2, 12-13 July) precipitation in the warm sector.

In the first case, as illustrated in Fig. 6a, southeasterly wind and westerly wind prevailed below and above the warm frontal surface respectively. Between the two layers, a southerly wind layer with cold air existed from 0900 to 2100 JST 2 July. Secondary warm frontal surface was analyzed between southerly wind layer and westerly wind layer above the primary warm front. Two fronts coincided with sharp gradients of equivalent potential temperature. In this period, rainfall intensity was limited to 1mm/h by a dry level. After 2100 JST 2 July, when the upper secondary warm front disappeared, rainfall intensity increased to 2.5mm/h. From 0400 to 1400 JST 3 July, according to the advection of the warm air to the middle and upper level, heavy rainfall and large reflectivity was observed.

In the second case, three different types of rainfalls were observed. A cloud corresponded to a narrow echo band which passed near Shigaraki and produced convective rainfall from 1400 to 1500 JST 12 July is shown on the right of the Fig. 6b. Southerly wind reached to the height of 8km. This rainfall was caused by instability due to warm moist advection to the low level. From 1800 to 2200 JST warm moist advection in the middle level intensified. Strong precipitation in this period was produced by stratiform clouds. After 2200 JST an instability formed by an inflow of cold air with westerly wind into the middle and upper level caused convective rain. And at 2330 JST a cold front, which was not showed on the surface map, was clarified to have passed over Shigaraki.

In this study, we clarified vertical structures and interactions between multi-scales of meteorological elements associated with the Baiu front: Detailed wind fields, precipitation amounts and thermodynamic features, which could not be seen by the synoptic analysis such as weather map analysis, were revealed by using the two radars with the detailed temporal and spatial resolution and by combining the radars with six hourly radiosondes.

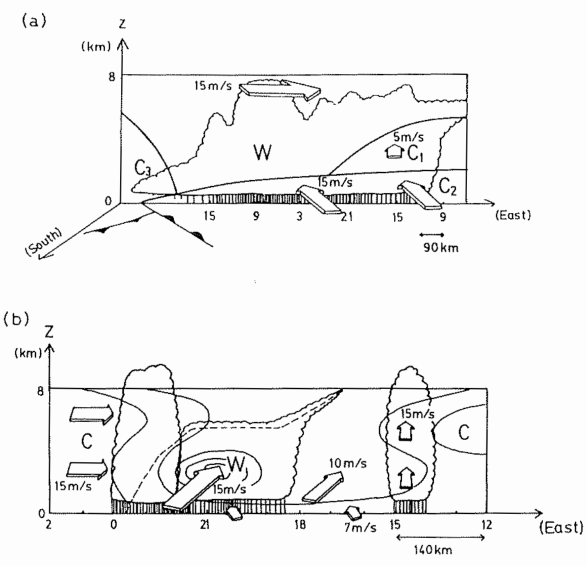

Fig. 6. Conceptual model of weather system that passed over Shigaraki on (a) 2-3 July 1990 and (b) 12-13 July 1990.

Acknowledgements. The authors express their thanks to Prof. Katsuhiro Kikuchi, Hokkaido University, for his encouragement throughout their study. The authors also offer thanks to the Osaka District Meteorological Observatory for providing its radar data. The MU radar belongs to and is operated by the Radio Atmospheric Science Center of Kyoto University. The expense of this research was partly supported by special grant for "Studies of Global Environmental Change with special reference to Asia and Pacific Regions" of the Ministry of Education, Science and Culture of Japan.

REFERENCES

Browning, K. A. and R. Wexler, 1968: The determination of kinematic properties of a wind field using Doppler radar. *J. Appl. Meteor.*, **7**, 105-113.

Fukao, S., M. D. Yamanaka, T. Sato, T. Tsuda and S. Kato, 1988: Three-dimensional air motions over the Baiu front observed by a VHF-band Doppler radar: A case study. *Mon. Wea. Rev.*, **116**, 281-292.

K. Kato and Y. Kodama, 1992: Formation of the quasi-stationary Baiu front to the south of the Japan Islands in early May of 1979. *J. Meteor. Soc. Japan*, **70**, 631-647.

Ninomiya, K . and T. Akiyama, 1992: Multi-scale features of Baiu, the summer monsoon over Japan and the East Asia. *J. Meteor. Soc. Japan*, **70**, 467-495.

Sato, T., N. Ao, M. Yamamoto, S. Fukao, T. Tsuda and S. Kato, 1991: A typhoon observed with the MU radar. *Mon. Wea. Rev.* **119**, 755-768.

Shirooka, R., H. Uyeda, S. Shimizu, S. Fukao, M. D. Yamanaka, G.Kotani, A. Watanabe and A. Sumi, 1991: Simultaneous observations of the Baiu front with the MU radar and an X-band Doppler radar. Fifth Intnl. Workshop on MST radar, Aberystwyth, August, 6pp.